COSMIC RAYS AT EARTH

Researcher's Reference Manual and Data Book

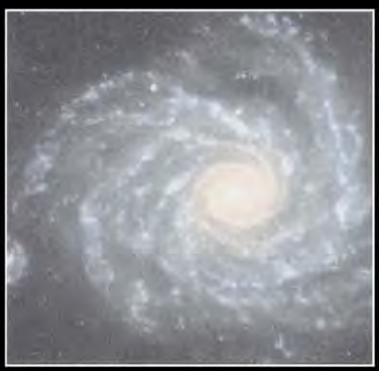

Peter K.F. Grieder

ELSEVIER

Cover

Left: Photograph of a hadronic interaction initiated by a high energy cosmic ray sulfur nucleus (red track) colliding with a target nucleus in photographic emulsion. The so-called leading fragment emerging from the vertex in a strong forward direction, deviating little from the direction of the incident momentum vector, is a fluorine nucleus (green track). It carries a large fraction of the initial primary energy. Relatively low energy alpha particles (long blue tracks) and larger nuclear fragments (dense short blue tracks), often referred to as evaporation products, mostly from the target nucleus, suggest that the collision partner of the primary was probably a bromine or silver nucleus. The thin irregularly dotted straight yellow tracks that are concentrated in a forward cone are relativistic (minimum ionizing) charged pions, forming a so-called pion jet. (Original photograph taken by C.Powell 1950; see "The Study of Elementary Particles by the Photographic Method", C. Powell, P. Fowler and D. Perkins, Pergamon Press, 1959. Coloring by David Parker.*(Science Photo Library, London, ref. No A134/005PFP).*

Right: Spectacular view of the large spiral galaxy NGC 1232; a possible source of cosmic rays? The picture was taken on September 21, 1998 with the Very Large Telescope (VLT) of the European Southern Observatory (ESO) (ESO PR Photo 37d/98; 23 September 1998). NGC 1232 is located 20°south of the celestial equator in the constellation Eridanus, at a distance of about 100 million light-years. *(Courtesy of ESO).*

This Page Intentionally Left Blank

This Page Intentionally Left Blank

COSMIC RAYS AT EARTH

Researcher's Reference Manual and Data Book

COSMIC RAYS AT EARTH

Researcher's Reference Manual and Data Book

Peter K.F. Grieder
Institute of Physics
University of Bern
Bern, Switzerland

2001

ELSEVIER

Amsterdam – London – New York - Oxford – Paris – Shannon -Tokyo

ELSEVIER SCIENCE B.V.
Sara Burgerhartstraat 25
P.O. Box 211, 1000 AE Amsterdam, The Netherlands

First edition 2001

Library of Congress Cataloging-in-Publication Data

Grieder, P. K. F.
Cosmic rays at earth : researcher's reference manual and data book / Peter K.F. Grieder.-- 1st ed.
p. cm.
Includes bibliographical references and index.
ISBN 0-444-50710-8 (hardcover)
1. Cosmic rays. I. Title.

QC485 .G715 2001
539.7'223--dc21

2001023791

British Library Cataloguing in Publication Data

Grieder, Peter K. F.
Cosmic rays at Earth : researcher's reference manual and data book
1.Cosmic rays
I.Title
539.7'223

ISBN 0444507108

ISBN: 0 444 50710 8

Transferred to digital printing 2005
Printed and bound by Antony Rowe Ltd, Eastbourne

To
Estelle, Marina and Ralph

Preface

In 1912 Victor Franz Hess made the revolutionary discovery that ionizing radiation is incident upon the Earth from outer space. He showed with ground based and balloon-borne detectors that the intensity of the radiation did not change significantly between day and night. Consequently the Sun could not be regarded as the source of this radiation and the question of its origin remained unanswered. Today, almost one hundred years later the question of the origin of the cosmic radiation still remains a mystery.

Hess' discovery has given an enormous impetus to large areas of science, in particular to physics, and has played a major role in the formation of our current understanding of universal evolution. For example, the development of new fields of research such as elementary particle physics, modern astrophysics and cosmology are direct consequences of this discovery, and other fields such as astronomy, geophysics and even biology are heavily affected.

Over the years the field of cosmic ray research has evolved in various directions:

Firstly, there is the field of particle physics that was initiated by the discovery of many so-called elementary particles in the cosmic radiation. In the fifties of the last century and the years that followed particle physics has almost completely been taken over by accelerator physics. The well defined particle beams of the big machines simplified enormously the analysis and interpretation of the results of countless accelerator experiments.

However, with a certain frustration that lingers on mostly among younger members of the accelerator physics community, that are faced with fewer and fewer but ever larger and costlier collaborations, where the individual gets lost in the bulk of participants, and because of the challenging recent discoveries made in cosmic ray physics and related fields, there is a strong trend from the accelerator physics community to reenter the field of cosmic ray physics, now reincarnated under the name of astroparticle physics.

Secondly, an important branch of cosmic ray physics that has rapidly evolved in conjunction with space exploration concerns the low energy portion of the cosmic ray spectrum. It includes heliospheric and magnetospheric physics as well as portions of geophysics. Here the interest is focused on the study of the combined influences of the Earth's and the Sun's magnetic fields on the cosmic radiation, on solar contributions to the very low energy radiation and on the so-called anomalous component. It is also this energy regime that is used to explore the time variation of the cosmic radiation and climatological aspects.

With the exception of solar neutrino experiments that must be carried out deep underground because of background problems, a large portion of the heliospheric research activities are carried out with satellite-borne equipment. However, balloon and ground based investigations, too, play an important role.

Thirdly, the branch of research that is concerned with the origin, acceleration and propagation of the cosmic radiation represents a great challenge for astrophysics, astronomy and cosmology. There several new and presently very popular fields of research that have rapidly evolved, such as high energy gamma ray and neutrino astronomy will continue to affect our current picture of the evolution of the Universe significantly.

In addition, high energy neutrino astronomy may soon initiate as a likely spin-off neutrino tomography of the Earth and thus open up a unique new branch of geophysical research of the interior of the Earth.

Finally, of considerable interest are the biological and medical aspects of the cosmic radiation because of its ionizing character and the inevitable irradiation to which we are exposed.

This book is a reference manual for researchers and students of cosmic ray physics and associated fields and phenomena. It is not intended to be a tutorial. However, in my opinion the book contains an adequate amount of background material that its content should be useful to a broad community of scientists and professionals.

About 20 years ago I wrote a similar book together with the late Claus Allkofer from the University of Kiel that was the first comprehensive data summary of cosmic rays in the atmosphere, at sea level and underground. The field of cosmic ray physics has enormously evolved in the past two decades. Particularly great efforts and achievements were made in the domains of muon and neutrino physics (underground physics) and in the exploration of the primary spectrum and composition.

It was the success of the first book and the numerous requests and encouragements that I have received in the course of the past years to create a new book with an extended scope that have motivated me to take up this big and difficult task. After numerous discussions with colleagues I decided to maintain basically the structure of the old book, but to extend the scope of topics significantly, and to add an extensive subject index.

Cosmic ray research is a vast field that is heavily interlaced with other branches of science such that it is difficult to draw clear-cut boundaries. Obviously this book cannot do justice to the entire field. Many important topics such as for example heliospheric phenomena or the primary radiation

are treated very superficially, others such as origin, propagation, arrival direction and anisotropy, extensive air showers and dark matter not at all. These topics together with many others are broad and highly specialized fields of their own and beyond the scope of this book.

The present book contains chiefly a data collection in compact form that covers the cosmic radiation in the vicinity of the Earth, in the Earth's atmosphere, at sea level and underground. Included are predominantly experimental but also theoretical data. In addition the book contains related data, definitions and important relations. The aim of this book is to offer the reader in a single volume a readily available comprehensive set of data that will save him the need of frequent time consuming literature searches.

Of course, a book like this can never be complete. Numerous papers had to be omitted to keep the volume within reasonable bounds. However, I believe it contains a large and representative sample of relevant cosmic ray and associated data. The extensive bibliography permits rapid access to the original publications from which the data have been extracted and to the more specific literature of related fields.

Bern, March 4, 2001 Peter K.F. Grieder

Comments for Reader

Organization of Data: The organization of the material presented in this book is evident from the titles of the chapters and sections. Chapters 2, 3 and 4 contain the bulk of the material on cosmic ray data on Earth that is presented here. The division of these data into the three chapters "Cosmic Rays in the Atmosphere" (Chapter 2), "Cosmic Rays at Sea Level" (Chapter 3) and "Cosmic Rays Underground, Underwater and Under Ice" (Chapter 4) has been chosen somewhat arbitrarily but appeared to be an acceptable grouping of the vast amount of information that is available. It was also a reasonable choice from the point of view of the different conditions under which experiments are being performed, the different techniques that are being used and interests that are being pursued as well as the standards of comparison that are employed, particularly among sea level experiments.

The boundary for placing an experiment, measurement or data set into Chapter 2 or 3 was chosen at approximately 300 m a.s.l.. Up to this level a large number of experimental sites are located and the comparison of data from different experiments in the narrow altitude window between sea level and 300 m does not pose a problem. However, the boundary for placing information either into Chapter 2 or 3 is slightly floating, depending on the particular experiment or data set under consideration. At altitudes above about 300 m the experimental sites are much more spread apart and the operating conditions vary significantly up to the highest ground based locations and, of course, for balloon-borne experiments. In-situ data taken with balloon-borne instruments within the atmosphere are summarized in Chapter 2, treated data that relate to the primary component, i.e., after subtraction of the atmospherically produced secondary component, are presented in Chapter 5. The content of Chapter 4 is evident.

Observation Levels: It will be noticed that sometimes different atmospheric depths are specified for the same site in different publications or data sets. Most authors do not offer an explanation. Moreover, occasionally altitude and atmospheric overburden may seem to be in minor disparity. In some cases this may be due to seasonal changes in barometric pressure. However, in some cases when data are being evaluated some authors take intentionally a somewhat larger overburden than corresponds to the vertical depth to account for the finite zenith-angular bin width and average zenith angle ($\theta > 0°$) within the "vertical" angular bin. Whenever given we have listed the published site data that had been used in the particular case.

References: The frequently used abbreviation PICRC stands for *Proceedings of the International Cosmic Ray Conference* and is used there where the proceedings are not part of a regular scientific journal or series.

Acknowledgements

The author is grateful to his colleagues from many universities and institutions around the world for having responded to his requests and having made available specific data and information that have helped to enrich the contents of this book.

Particular thanks are due to the following colleagues, in alphabetic order, for extensive and constructive discussions on topics closely related to their work and for their valuable comments and suggestions:

G. Bazilevskaya, J. Beer, P.L. Biermann, F. Bühler, A. Castellina, S. Cecchini, J. Clem, O. Eugster, E. Flückiger, T.K. Gaisser, J. Hörandel, L.W. Jones, B. Klecker, K. Marti, P. Minkowski, D. Müller, R. Protheroe, J. Ryan, O. Saavedra, M. Simon, A. Stephens, S. Tonwar, A.A. Watson, R.F. Wimmer-Schweingruber, and A.W. Wolfendale, N.E. Yanasak.

The general support of my colleagues at my own institution and of the library staff is greatly appreciated. The treasured help of our hardware and software wizard, Dr. U. Jenzer, merits special acknowledgement.

Bern, March 2001
Peter K.F. Grieder
Physikalisches Institut
University of Bern
Switzerland

This Page Intentionally Left Blank

Contents

Chapter 1

Cosmic Ray Properties, Relations and Definitions

1.1 Introduction

1.1.1 General Comments

This chapter contains a very rudimentary description of the relevant processes that govern the gross features of cosmic ray phenomena in the vicinity of the Earth, in the atmosphere and underground, and summarizes the mathematical relations that describe them. It also contains definitions of various concepts and frequently used quantities, and data of the atmosphere. It is not intended to be a tutorial for newcomers to the field.

Cosmic ray physics covers a wide range of disciplines ranging from particle physics to astrophysics and astronomy. Those who want to enter the field should consult appropriate text books that deal with the particular topics of interest (For an introduction see e.g. Sandström, 1965; Allkofer, 1975; for more specific topics such as extensive air showers see Galbraith, 1958; Khristiansen, 1980; Sokolsky, 1989; for high energy interactions, etc., see Gaisser, 1990).

The purpose of this chapter is twofold. For the researcher who is familiar with the field and is using the data in the subsequent chapters for his work, relations, definitions and cosmic ray related data that may not be readily available are placed at his finger tips. On the other hand, for those workers that are not particularly interested in cosmic ray research but need the data that are presented in the following chapters for their work, such as biologists, health physicists and others, it serves as an overview and brief introduction to cosmic ray physics.

1.1.2 Heliospheric Effects and Solar Modulation

The primary cosmic radiation which consists predominantly of protons, alpha particles and heavier nuclei is influenced by the galactic, the interplanetary, the magnetospheric and the geomagnetic magnetic fields while approaching the Earth. The interplanetary magnetic field (IMF) amounts to about 5 nanotesla [nT] (or 50 μG) at the Earth's orbit. The magnetospheric field is the sum of the current fields within the space bound by the magnetopause and is subject to significant variability, while the geomagnetic field is generated by sources inside the Earth and undergoes secular changes. The combined fields are typically 30 to 60 μT (0.3 - 0.6 G) at the Earth's surface, depending on the location. Time dependent variations are on the order of one percent. The electrically charged secondary cosmic ray component produced in the atmosphere is also subject to geomagnetic effects. Further details concerning these subjects are discussed in Section 1.8.

The cosmic ray flux is modulated by solar activity. It manifests an 11 year cycle and for certain effects also a 22 year cycle, and other solar influences. It should be remembered that the solar minimum and maximum cycle is 11 years and that the solar magnetic dipole flips polarity every solar maximum, thus imposing a 22 year cycle as well. Both cycles cause various effects on the galactic cosmic radiation in the heliosphere. The modulation effects decrease with increasing energy and become insignificant for particles with rigidities in excess of $\sim$10 GV. Solar modulation effects and terminology are summarized in Chapter 6.

1.2 Propagation of the Hadronic Component in the Atmosphere

1.2.1 Strong Interactions

Upon entering the atmosphere the primary cosmic radiation is subject to interactions with the electrons and nuclei of atoms and molecules that constitute the air. As a result the composition of the radiation changes as it propagates through the atmosphere. All particles suffer energy losses through hadronic and/or electromagnetic processes.

Incident hadrons are subject to *strong interactions* when colliding with atmospheric nuclei, such as nitrogen and oxygen. Above an energy of a few GeV, local penetrating particle showers are produced, resulting from the creation of mesons and other secondary particles in the collisions. Energetic

primaries and in case of heavy primaries their spallation fragments continue to propagate in the atmosphere and interact successively, producing more particles along their trajectories, and likewise for the newly created energetic secondaries. The most abundant particles emerging from energetic hadronic collisions are pions, but kaons, hyperons, charmed particles and nucleon-antinucleon pairs are also produced.

Energetic primary protons undergo on average 12 interactions along a vertical trajectory through the atmosphere down to sea level, corresponding to an *interaction mean free path* (i.m.f.p.), λ_i [g/cm^2], of about 80 g/cm^2. Thus, a hadron cascade is frequently created which is the parent process of an *extensive air shower* (EAS) (Auger et al., 1936, 1938; Auger, 1938; Kohlhörster et al., 1938; Jánossy and Lovell, 1938; Khristiansen, 1980). In energetic collisions atmospheric target nuclei get highly excited and evaporate light nuclei, mainly alpha particles and nucleons of energy $\leq$15 MeV in their rest frame.

The majority of the heavy nuclei of the primary radiation are fragmented in the first interaction that occurs at a higher altitude than for protons because of the much larger *interaction cross section*, σ_i [cm^2], and correspondingly shorter interaction mean free path, λ_i. The following expression describes the relation between cross section and interaction mean free path.

$$\lambda_i = \frac{N_A}{A}\sigma_i \quad [\mathrm{g/cm^2}] \,, \tag{1.1}$$

where N_A is *Avogadro's number* ($6.02{\cdot}10^{23}$), A the *mass number* of the target nucleus and σ_i the cross section for the particular interaction. For a projectile nucleus with mass number $A = 25$, the interaction mean free path is approximately 23 g/cm^2 in air, corresponding to about 50 interactions for a vertical trajectory through the atmosphere. Consequently there is practically no chance for a heavy nucleus to penetrate down to sea level.

The proton - nucleus (or more general the nucleon - nucleus) interaction cross section, $\sigma_{p,A}$, scales with respect to the proton - proton (or nucleon - nucleon) cross section, $\sigma_{p,p}$, approximately as

$$\sigma_{p,A}(E) = \sigma_{p,p}(E)\, A^{\alpha} \quad . \tag{1.2}$$

For nucleon projectiles $\alpha = 2/3$ and $\sigma_{p,p}(E)$ varies slowly over a range of many decades in energy from $\sim$ 40 mb at 10 GeV to $\sim$ 80 mb at 10^7 GeV. The energy dependence of the total and elastic proton-proton (pp), antiproton-proton ($\bar{p}p$) and pion-proton (π^+p, π^-p) cross sections as a function of energy is illustrated in Fig. 1.1 (Hernàndez et al., 1990; see also Caso et al., 1998.

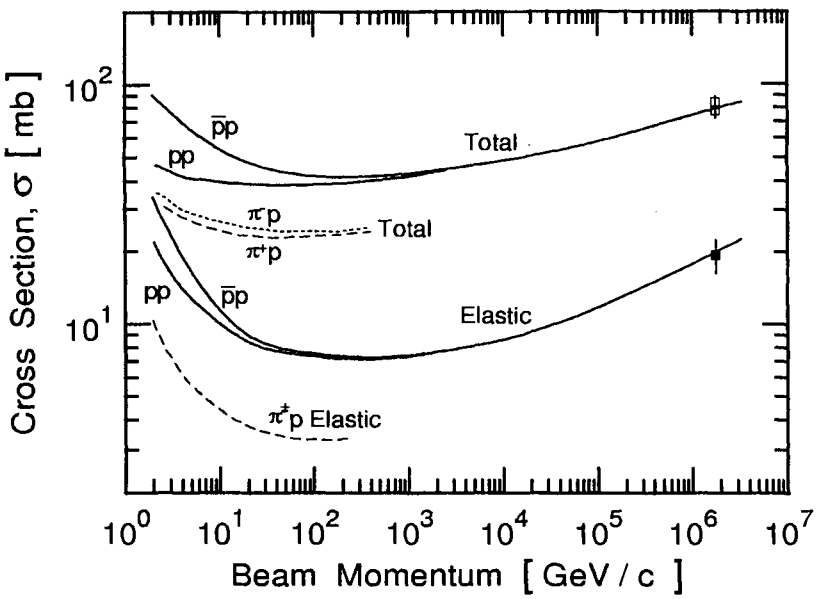

Figure 1.1: Total and elastic cross sections for proton-proton (pp), antiproton-proton ($\bar{p}p$), and pion-proton ($\pi^{\pm}p$) collisions as a function of beam momentum in the laboratory frame of reference (Hernàndez et al., 1990; see also Caso et al., 1998).

For details of $\bar{p}p$ cross sections see Abe et al., 1994). The high energy data were obtained with $\bar{p}p$ colliders.

For pion projectiles $\alpha = 0.75$ and $\sigma_{\pi,p}$ is approximately 26 mb. Figure 1.2 shows the projectile mass dependence of the interaction mean free path, $\lambda_i(A)$, in air.

A compilation of data from measurements of the energy dependence of the inelastic cross section for proton-air interactions is illustrated in Fig. 1.3 (Mielke et al., 1994). The data are from a wide variety of experiments, including very indirect cross section determinations from air shower studies at the higher energies. The solid curve, C, plotted in this figures represents a fit of the form

$$\sigma_{inel} = c + a\log(E) + \log^2(E) \ \text{[mb]}\,, \tag{1.3}$$

where the parameters have the values $a = -8.7 \pm 0.5$ [mb], $b = 1.14 \pm 0.05$ [mb], $c = 290 \pm 5$ [mb], and E is in [GeV].

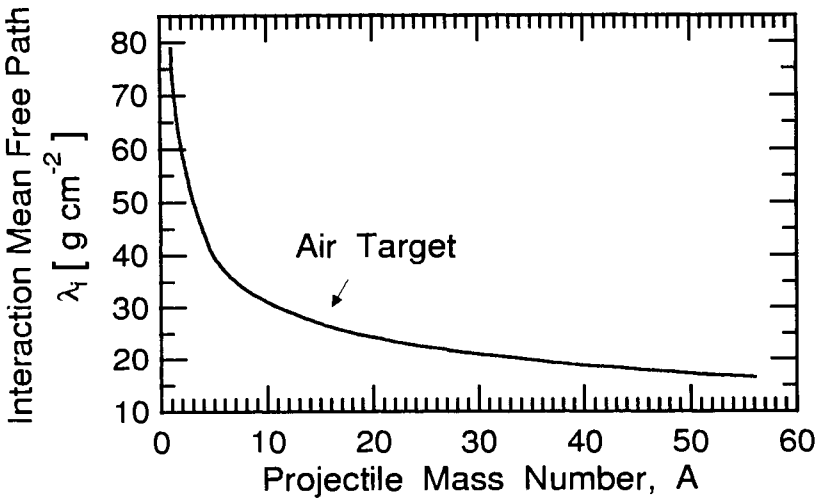

Figure 1.2: Interaction mean free path, λ_i, for high energy nuclear interactions in air versus projectile mass.

1.2.2 Energy Transport

Hadrons suffer energy losses due to strong interactions in collisions with nucleons and nuclei when propagating in a medium. These are characterized by the *total hadronic cross section*, $\sigma_{tot} = \sigma_{el} + \sigma_{inel}$, where σ_{el} and σ_{inel} are the *elastic* and *inelastic* parts of the total cross section, respectively, and the *inelasticity*, k.

A hadron having an initial energy E_0, undergoing n interactions with a mean inelasticity, $< k >$, will retain on average an energy, E, of

$$E = E_0 (1 - < k >)^n \, . \tag{1.4}$$

Nucleon (p, n) and antinucleon $(\overline{p}, \overline{n})$ initiated collisions are characterized by a high degree of *elasticity*, η, defined as $\eta = (1 - k)$, i.e., the incident nucleon or antinucleon retains on average a relatively large fraction ($\sim 50\%$) of its initial energy when emerging from a collision, usually much more than any of the secondary particles. This manifests itself in the so-called *leading particle effect*. At kinetic energies below $\sim$100 GeV *annihilation* of antinucleons must also be considered.

Under the assumption that $< k >= 0.5$ and $n = 12$, values that are typical for a vertically incident high energy proton traversing the full atmosphere

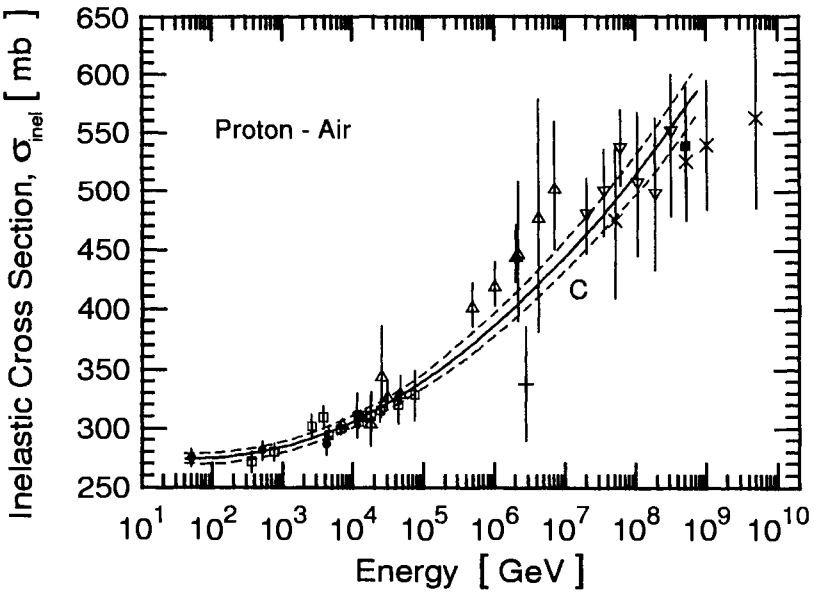

Figure 1.3: Compilation of inelastic cross sections for proton-air interactions as a function of energy (Mielke et al., 1994; Stanev, 2000). The symbols refer to the following references: •, C Mielke et al. (1994); □, Yodh et al. (1983); △, Gaisser et al. (1987); ▽, Honda et al. (1993); ■, Baltrusaitis et al. (1984); +, Aglietta et al. (1999); ×, Kalmykov et al. (1997).

down to sea level, the proton suffers an energy reduction by a factor of

$$\frac{E}{E_0} = (0.5)^{12} \simeq 2.5 \cdot 10^{-4} . \quad (1.5)$$

For pions and kaons the leading particle effect is also observed but it is less pronounced. Meson initiated interactions are in general more inelastic than nucleon or antinucleon initiated interactions.

1.3 Secondary Particles

1.3.1 Production of Secondary Particles

High energy strong interactions as well as electromagnetic processes, such as pair production, lead to the production of secondary particles. Charged pions as well as the less abundant kaons, other mesons, hyperons and nucleon-

Table 1.1: Parameters for Energy-Multiplicity Relation in Center of Mass Energy Range 3 GeV - 546 GeV. (Alner et al., 1987)

Equation	a	b	c
1.6	0.98 ± 0.05	0.38 ± 0.03	0.124 ± 0.003
1.7	-4.2 ± 0.21	4.69 ± 0.18	0.155 ± 0.003

antinucleon pairs emerging from strong interactions of energetic primaries with atmospheric target nuclei continue to propagate and contribute to the flux of hadrons in the atmosphere. Of all the secondaries pions (π^+, π^-, π^0) are the most abundant.

If sufficiently energetic secondary hadrons will themselves initiate new hadronic interactions, produce secondaries and build up a hadron cascade that forms the backbone of extensive air showers. However, unstable particles such as pions, kaons and other particles are also subject to decay.

The competition between interaction and decay is discussed in detail in Subsection 1.3.4. It depends on the mean life and energy of the particles and on the density of the medium in which they propagate. For a given particle propagating in the atmosphere the respective probabilities for the two processes become a function of energy, altitude and zenith angle.

Due to a very short mean life ($\tau \simeq 10^{-16}$ s) neutral pions decay almost instantly into two photons, contributing subsequently to electromagnetic channels.

The energy dependence of the average number of charged secondaries, i.e., the charged particle *multiplicity*, $< n^{\pm} >$, emerging from a high energy nucleon-nucleon collision, can be described with either of the following two relations (Alner et al., 1987).

$$< n^{\pm} > = a + b\ln(s) + c(\ln(s))^2 , \tag{1.6}$$

or

$$< n^{\pm} > = a + b s^c , \tag{1.7}$$

where s is the center of mass energy squared. For all inelastic processes Alner et al. (1987) specify for the constants a, b and c the values listed in Table 1.1.

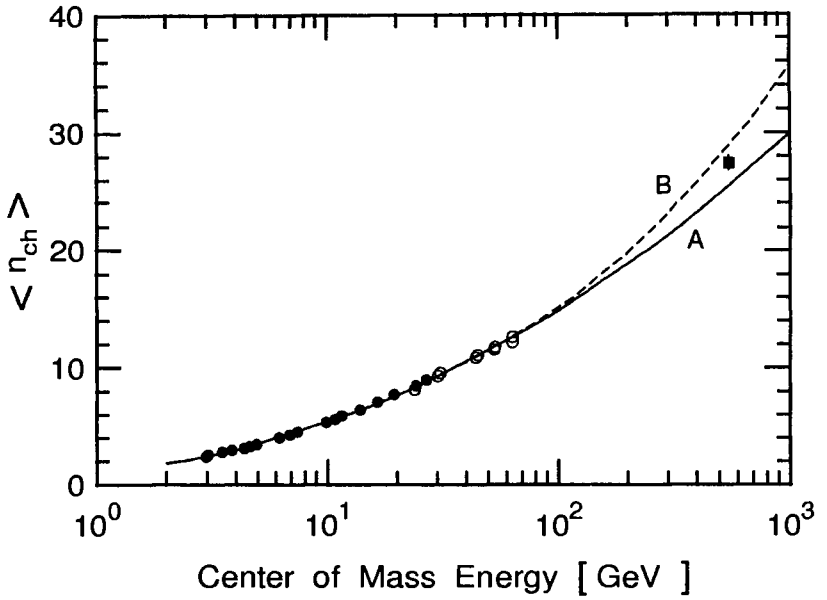

Figure 1.4: Mean charged multiplicity of inelastic pp or $\overline{p}p$ interactions as a function of center of mass energy, $\sqrt{s}$. The solid curve, A, is a fit to eq. 1.6, the dashed curve, B, to eq. 1.7 (after Alner et al., 1987).

The first term in eqs.1.6 and 1.7 represents the diffraction, fragmentation or isobar part, depending on the terminology used. The second and third terms, if applicable, account for the bulk of particles at high collision energies that result mostly from central processes. Figure 1.4 shows the center of mass energy dependence of the secondary particle multiplicity in proton-proton and proton-antiproton collisions obtained from experiments performed at CERN with the proton synchrotron (PS), the intersecting storage ring (ISR) and the proton-antiproton ($\overline{p}p$) collider (UA5 experiment, Alner et al., 1987). Relevant for particle production is the energy which is available in the center of mass. At high energies pp and $\overline{p}p$ interactions behave alike (see Fig. 1.1). The solid and dashed curves, A and B, are fits using eqs. 1.6 and 1.7, respectively, with the parameters listed in Table 1.1.

An earlier study of the energy-multiplicity relation that includes mostly data from cosmic ray emulsion stack and emulsion chamber experiments at energies up to 10^7 GeV in the laboratory frame was made by Grieder (1972 and 1977). This author found the same basic energy dependence as given in eq.1.7 but with a larger value for the exponent c. Part of the reason

for the higher value of c resulting from this work is probably due to the fact that the analysis included mostly nucleon-nucleus collisions which yield higher multiplicities than nucleon-nucleon collisions at comparative energies. Nucleus-nucleus collisions yield even higher multiplicities but they can easily be distinguished from nucleon-nucleus collisions when inspecting the track density of the incident particle in the emulsion.

1.3.2 Energy Spectra of Secondary Particles

The momentum or energy spectra of secondary particles produced in cosmic ray primary initiated interactions, or in subsequent interactions of secondaries of the first and higher generations of interactions with other target nuclei, can be calculated from our knowledge of high energy hadron - hadron collisions.

Several more or less sophisticated models are available to compute the spectra of the different kinds of secondaries, such as the CKP-model (Cocconi, 1958 and 1971; Cocconi et al., 1961), the scaling model (Feynman, 1969a and 1969b), the dual parton model (Capella et al., 1994; Battistoni et al., 1995; Ranft, 1995), the quark-gluon-string model (Kaidalov et al., 1986; Kalmykov and Ostapchenko, 1993), and others (see Gaisser, 1990). These models are frequently used in conjunction with Monte Carlo calculations to compute the total particle flux at a given depth in the atmosphere and to simulate extensive air shower phenomena.

At kinetic energies above a few GeV the differential energy spectrum of primary protons, $j_p(E)$, can be written as

$$j_p(E) \;=\; A_p\, E^{-\gamma_p}\;. \tag{1.8}$$

This expression which represents a *power law* is valid over a wide range of primary energies and applies essentially to all cosmic ray particles (for details see Chapter 5, Section 5.2). The secondary particle spectra have a form which is similar to that of the primary spectrum. For secondary pions it has the form

$$j_\pi(E) \;=\; A_\pi\, E^{-\gamma_\pi} \tag{1.9}$$

with an exponent, γ_π, very similar to that of the primary spectrum, i.e.,

$$\gamma_\pi \;\simeq\; \gamma_p\;. \tag{1.10}$$

For the less abundant kaons the same basic relation is valid, too.

1.3.3 Decay of Secondaries

Vertical Propagation in the Atmosphere

Charged pions have a mean life at rest of $2.6 \cdot 10^{-8}$ s and an interaction mean free path of $\sim$120 g/cm^2 in air. They decay via the processes

$$\pi^+ \rightarrow \mu^+ + \nu_\mu$$

and

$$\pi^- \rightarrow \mu^- + \overline{\nu}_\mu$$

into muons and neutrinos. At high energies their mean life, $\tau(E)$, is significantly extended by *time dilation.*

$$\tau(E) \;=\; \tau_{0,X} \left(\frac{E}{m_{0,X}\, c^2} \right) \;=\; \tau_{0,X}\, \gamma \quad [\mathrm{s}]\,, \tag{1.11}$$

where $\tau_{0,X}$ and $m_{0,X}$ are the mean life and mass of particle X under consideration at rest, E is the total energy, c the velocity of light, γ the *Lorentz factor*,

$$\gamma \;=\; \frac{1}{\sqrt{1-\beta^2}}\,, \tag{1.12}$$

and $\beta = v/c$, v [cm/s] being the velocity of the particle.

Pions that decay give rise to the muon and neutrino components which easily penetrate the atmosphere. Although the mean life of muons at rest is short, approximately $2.2 \cdot 10^{-6}$ s, the majority survives down to sea level because of time dilation. However, some muons decay, producing electrons and neutrinos.

$$\begin{aligned} \mu^+ &\rightarrow e^+ + \nu_e + \overline{\nu}_\mu \\ \mu^- &\rightarrow e^- + \overline{\nu}_e + \nu_\mu \end{aligned}$$

The situation is similar for kaons but their decay schemes are more complex, having many channels.

Neutral pions decay into gamma rays ($\pi^0 \rightarrow 2\gamma$) with a mean life of $8.4 \cdot 10^{-17}$ s at rest. The latter can produce electron-positron pairs which subsequently undergo bremsstrahlung, which again can produce electron-positron pairs, and so on, as long as the photon energy exceeds 1.02 MeV. Eventually, these repetitive processes build up an electromagnetic cascade or

shower in the atmosphere. Hence, a very energetic primary can create millions of secondaries that begin to spread out laterally more and more from the central axis of the cascade, along their path through the atmosphere because of transverse momenta acquired by the secondary particles at creation and due to scattering process. Such a cascade of particles is called an extensive air shower.

Because most of the secondary particles resulting from hadronic interactions are unstable and can decay on their way through the atmosphere, the decay probabilities must be known and properly accounted for, when calculating particle fluxes and energy spectra.

The mean life of an unstable particle of energy E is given by eq. 1.11. The distance l traveled during the time interval τ is

$$l = v\tau \simeq \gamma\beta c\tau_0 \quad [\text{cm}] , \tag{1.13}$$

where β, γ and τ_0 are as defined before. The *decay rate* per unit path length, l, can then be written as

$$\frac{1}{l} = \frac{1}{\gamma\beta c\tau_0} \quad [\text{cm}^{-1}] . \tag{1.14}$$

In a medium of *matter density* ρ [g/cm^3], the mean free path for spontaneous decay , λ_d [g/cm^2], is given by

$$\frac{1}{\lambda_d} = \frac{1}{\gamma\beta c\tau_0\rho} \quad [\text{g}^{-1}\,\text{cm}^2] \tag{1.15}$$

and the number of particles, dN, of a population, N_1, which decay within an element of thickness, dX [g/cm^2], is given by

$$dN = \frac{N_1}{\lambda_d} dX . \tag{1.16}$$

Hence, the number of particles remaining after having traversed the thickness X g/cm^2 is

$$N_2 = N_1 \exp\left(-\int \frac{dX}{\lambda_d}\right) \tag{1.17}$$

and the number of decays, N', is

$$N' = N_1 - N_2 = N_1\left\{1 - \exp\left(-\int \frac{dX}{\lambda_d}\right)\right\} . \tag{1.18}$$

The *decay probability* $W = N'/N_1$ is given by

$$W = 1 - \exp\left(-\int \frac{m_0}{\rho \tau_0 p} dX\right) \simeq \frac{m_0 X}{\rho \tau_0 p} . \quad (1.19)$$

Inclined Trajectories and Decay Enhancement

The above relation implies that if, in comparison to vertical incidence, an unstable particle is incident at a zenith angle $\theta > 0°$, the probability for decay along its prolonged path to a particular atmospheric depth X is *enhanced* by the factor $\sec(\theta)$. Hence,

$$W \simeq \frac{m_0 X \sec(\theta)}{\rho \tau_0 p} , \quad (1.20)$$

where

m_0 rest mass of unstable particle [GeV/c^2]	ρ density [g/cm^3]
X thickness traversed [g/cm^2]	θ zenith angle
τ_0 mean life of unstable particle at rest [s]	p momentum [GeV/c]

From this formula it is evident that for a given column of air traversed the decay probability of a particle depends on its mean life, its momentum (or energy), the density (or altitude) and zenith angle of propagation in the atmosphere. The decay probabilities for vertically downward propagating pions and kaons in the atmosphere at a depth of 100 g/cm^2 as a function of kinetic energy are illustrated in Fig. 1.5.

As mentioned before, on their way through the atmosphere, part of the charged pions and kaons decay into muons. The latter lose energy by ionization, bremsstrahlung and pair production, and decay eventually into electrons and neutrinos.

Decay of Muons

The decay probability for muons, W_μ, is derived in a manner similar to that for mesons. The corresponding *survival probability* is

$$S_\mu = (1 - W_\mu) . \quad (1.21)$$

It is shown in Fig. 1.6 for muons originating from an atmospheric depth of 100 g/cm^2 to reach sea level.

At a specific level in the atmosphere, the differential energy spectrum of muons is given by

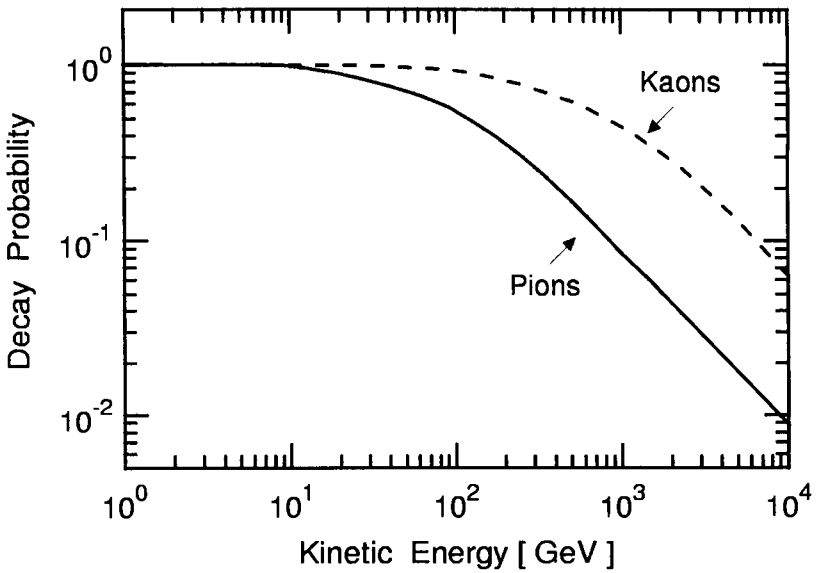

Figure 1.5: Decay probabilities of vertically downward propagating charged pions and kaons in the atmosphere versus kinetic energy at a depth of 100 g/cm^2.

$$j_\mu(E) \;=\; A_\pi\, W_\pi\, (E + \Delta E)^{-\gamma_\mu}\, (1 - W_\mu)\;, \tag{1.22}$$

where $\gamma_\mu \simeq \gamma_\pi$ and

A_π normalization constant for absolute intensity
ΔE energy loss by ionization
W_π pion decay probability
W_μ muon decay probability
γ_π exponent of pion differential spectrum
γ_μ exponent of muon differential spectrum

At very low energies, all mesons decay into muons, which subsequently decay while losing energy at a rate that increases as their energy decreases (see Fig. 1.10, Section 1.4). This leads to a maximum in the muon differential energy spectrum shown in Fig. 1.7.

1.3.4 Decay versus Interaction of Secondaries

At higher energies, mesons not only decay but also interact strongly with the nuclei that constitute the air. Thus, in the case of pions some decay

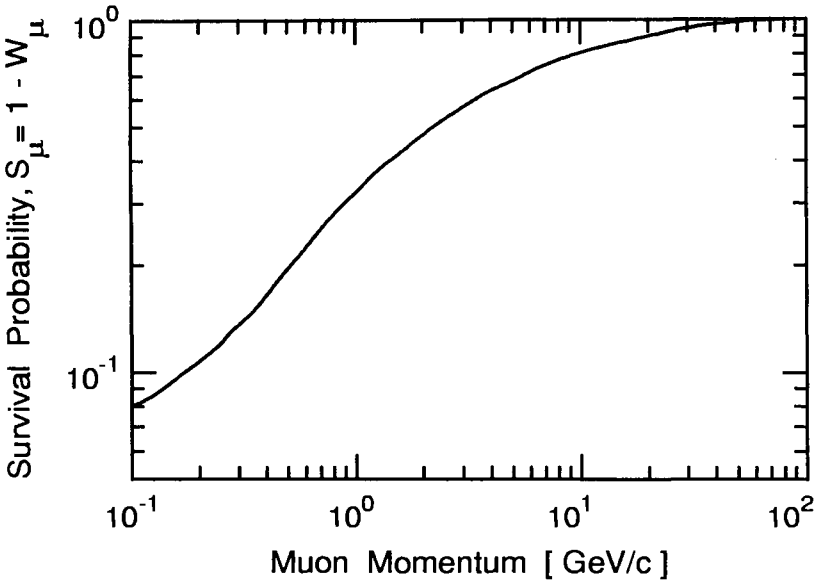

Figure 1.6: Survival probability of muons originating from an atmospheric depth of 100 g/cm^2 to reach sea level, versus muon momentum.

into muons while others interact and, hence, are losing energy. As pointed out before, the competition between the two processes depends essentially on the mean life and energy of the mesons, and on the density of the medium in which they propagate. At constant density the competition changes in favor of interaction with increasing energy since time dilation reduces the probability for decay. This trend is amplified with increasing density. These effects give rise to a steepening of the muon spectrum relative to the pion spectrum above a certain energy. The differential energy spectrum of the muons in this region can be expressed by the following formula which applies to pions and kaons, as indicated

$$j_\mu(E) = j_{\pi,K}(E) \left(\frac{B}{B+E} \right) . \tag{1.23}$$

B is a constant which accounts for the steepening of the spectrum,

$$B = \left(\frac{m_{\pi,K} c^2}{c\tau_{0,\pi,K}} \right) \left(\frac{RT}{<M>g} \right) \left(\frac{m_\mu}{m_{\pi,K}} \right) \quad [\text{GeV}] , \tag{1.24}$$

where

m_μ rest mass of muon
$m_{\pi,K}$ rest mass of pion or kaon

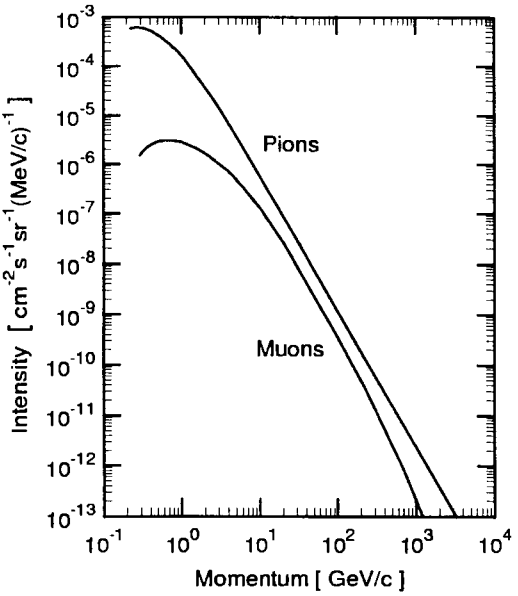

Figure 1.7: Muon differential momentum spectrum compared with the parent pion differential spectrum.

$\tau_{0,\pi,K}$ mean life of pion or kaon at rest
$RT/ < M > g = h_s$ atmospheric scale height
$< M >$ mean molecular mass of atmosphere.

For pions B has the value $B_\pi = 90$ GeV, for kaons $B_k = 517$ GeV. Since both, pions and kaons are present, the energy spectrum has the form

$$j_\mu(E) = j_\pi(E) \left(\frac{\alpha B_\pi}{E + B_\pi} + \frac{(1-\alpha) B_k}{E + B_k} \right) , \tag{1.25}$$

where α is the fraction of high energy pions and for the *spectral index* we can write $\gamma_\pi = \gamma_k = \gamma$.

For $B >> E$, i.e., in the energy range 10 to 100 GeV, the above formula leads to

$$j_\mu(E) \propto j_\pi(E) \tag{1.26}$$

For higher energies, $B << E$, the muon spectrum can be approximated by the expression

$$j_\mu(E) \propto j_\pi(E) \left(\frac{1}{E}\right) \tag{1.27}$$

which describes the previously mentioned steepening of the energy spectrum, as shown in Fig. 1.7.

The competition between decay and interaction of pions, kaons and charmed particles can be computed with the help of Figs. 1.8 and 1.9. Figure 1.8 shows the *mean decay lengths* of these particles in vacuum, $L_{X,vac}$, as a function of the Lorentz factor γ, and the *mean interaction lengths* in air, $L_{X,air}$, as a function of air density, ρ. In Fig. 1.9 we show the *critical altitude*, h_c, as a function of the kinetic energy for charged pions and kaons, and for K_L^0. The critical altitude is defined as the altitude at which the probabilities for decay and interaction of a particular particle at a given energy are equal.

1.4 Electromagnetic Processes and Energy Losses

All charged particles are subject to a variety of electromagnetic interactions with the medium in which they propagate that lead to energy losses. The significance of the different processes depends on the energy of the projectile and its mass, and on the nature of the target. In the following the different processes are outlined briefly.

1.4.1 Ionization and Excitation

According to the *Bethe-Bloch formula* (Bethe, 1933; Bethe and Heitler, 1934; Rossi, 1941 and 1952; Barnett et al., 1996; see also Chapter 4, Section 4.2), the energy loss, dE/dx, due to ionization and atomic excitation of a singly charged relativistic particle traversing the atmosphere in vertical direction ($\simeq$1030 g/cm^2) is 2.2 GeV. For such particles the rate of energy loss by ionization varies *logarithmically* with energy.

For a moderately relativistic particle with charge ze in matter with atomic number Z and atomic weight A the Bethe-Bloch formula can be written as (Fano, 1963)

$$-\left(\frac{dE}{dx}\right) = 4\pi N_A r_e^2 m_e c^2 z^2 \frac{Z}{A}\frac{1}{\beta^2}\left[\ln\left(\frac{2m_e c^2\gamma^2\beta^2}{I}\right) - \beta^2 - \frac{\delta}{2}\right] . \tag{1.28}$$

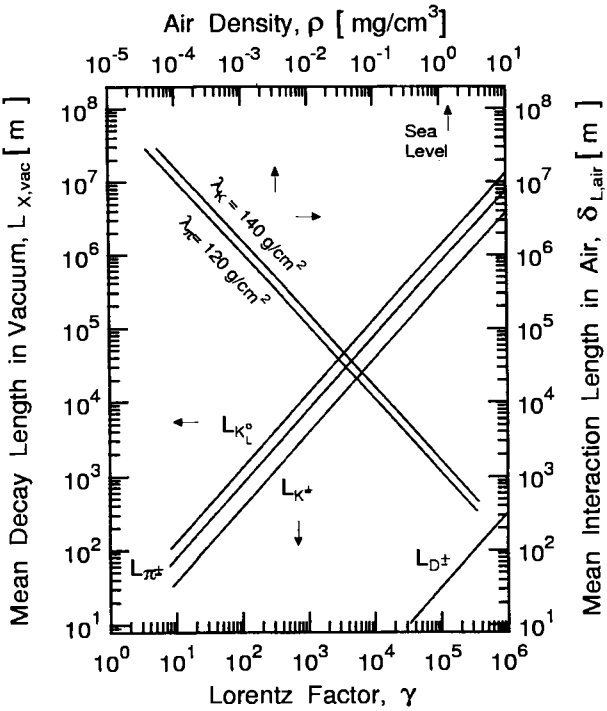

Figure 1.8: Mean decay length in vacuum, $L_{X,vac}$, as a function of Lorentz factor, γ, of charged pions, kaons and some charmed particles, and mean interaction length in air, $L_{X,air}$, as a function of air density, ρ, of pions and kaons for an i.m.f.p. of 120 g/cm^2 and 140 g/cm^2, respectively (Grieder, 1986).

Here m_e is the rest mass of the electron, r_e the classical radius of the electron, N_A Avogadro's number and $4\pi N_A r_e^2 m_e c^2 = 0.3071$ MeV cm^2 g^{-1}. γ is the Lorentz factor and $\beta = v/c$. I is the *ionization constant* and is approximately given by $16Z^{0.9}$ eV for $Z > 1$, and dx is the thickness or *column density* expressed in mass per unit area [g/cm^{-2}]. δ represents the *density effect* which approaches $2\ln\gamma$ plus a constant for very energetic particles (Crispin and Fowler, 1970; Sternheimer et al., 1984). (For details see the Appendix.)

1.4.2 Bremsstrahlung and Pair Production

At higher energies charged particles are subject to additional energy losses by *bremsstrahlung* (*bs*), *pair production* (*pp*), and *nuclear interactions* (*ni*) via

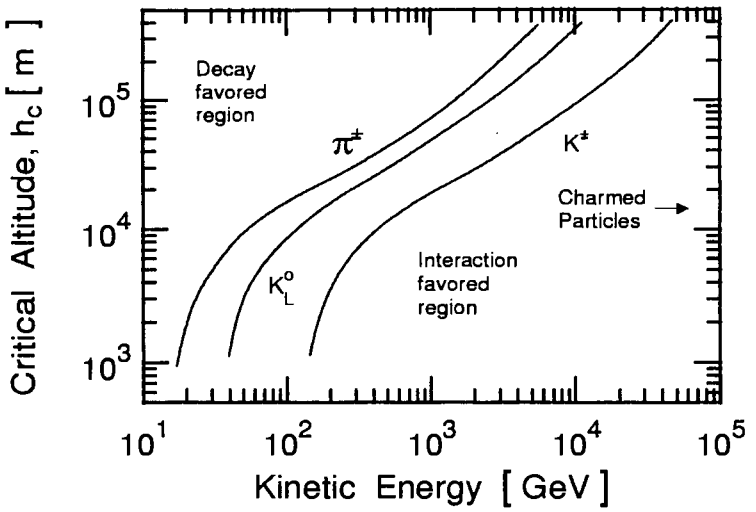

Figure 1.9: Critical altitude, h_c, of pions and kaons in the atmosphere as a function of kinetic energy. In the region above the curves decay is favored, below interaction is more likely. For details see text (Grieder, 1986).

photo-nuclear processes. The radiative energy losses rise nearly proportional with energy (Rossi, 1952). The corresponding expression for the energy loss, dE [eV], per unit thickness, dx [g/cm^2], including ionization is

$$\frac{dE}{dx} = a_{ion}(E) + b(E)\,E \quad [\mathrm{eV\,g^{-1}\,cm^2}]\,, \tag{1.29}$$

where $a_{ion}(E)$ represents the previously mentioned ionization losses and

$$b(E) = b_{bs}(E) + b_{pp}(E) + b_{ni}(E) \tag{1.30}$$

accounts for the other processes. Note that all terms are energy dependent.

The energy at which the energy loss by ionization and bremsstrahlung are equal is frequently called the *critical energy*, E_c (Rossi and Greisen, 1941; Rossi, 1952). Above the critical energy radiation processes begin to dominate. For *electrons* E_c can be approximated by (Berger and Seltzer, 1964)

$$E_c = \frac{800}{Z + 1.2} \quad [\mathrm{MeV}]\,, \tag{1.31}$$

where Z is the atomic charge of the medium in which the electrons propagate. E_c amounts to about 84.2 MeV in air at *standard temperature and pressure*

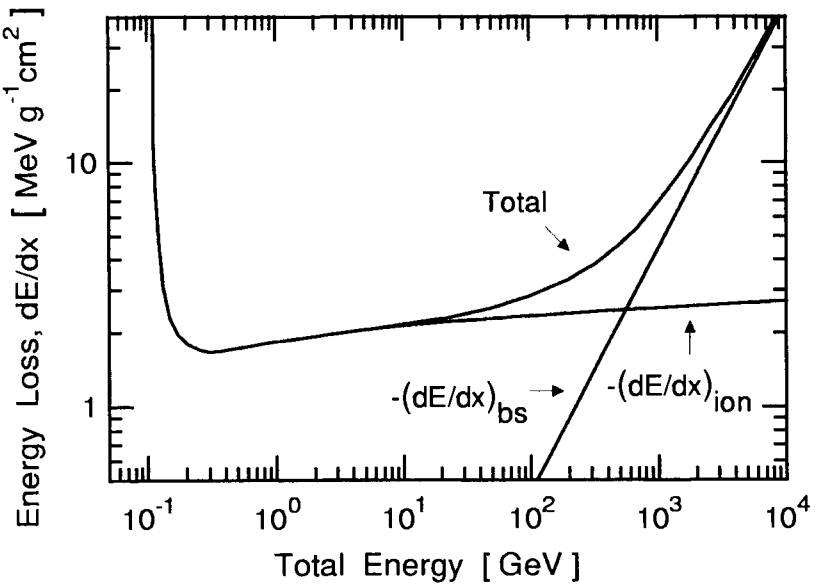

Figure 1.10: Example of the energy loss of charged particles by electromagnetic interactions. Shown is the energy loss of muons versus total energy in standard rock. (See text for explanation, Appendix for other materials.)

(STP). For *muons* $E_c \simeq 3.6$ TeV under the same conditions (Fig.1.10) (for details see Allkofer, 1975; Gaisser, 1990; Barnett et al., 1996).

Radiative processes are of great importance when treating high energy muon propagation in dense media such as is the case underground, underwater, or under ice. These topics are discussed in detail in Section 4.2. They can be neglected for heavy particles such as protons or nuclei in most cases.

Another quantity normally used when dealing with the passage of high energy electrons and photons through matter is the *radiation length*, X_0, expressed in [g/cm^2] or [cm] (Rossi and Greisen, 1941; Rossi, 1952). It is the characteristic unit to express thickness of matter in electromagnetic processes. A *radiation unit* is the mean distance over which a high-energy electron loses all but 1/e of its initial energy by bremsstrahlung. Moreover, it is also the characteristic scale length for describing high-energy electromagnetic cascades (Kamata and Nishimura, 1958; Nishimura, 1967).

Tsai (1974) has calculated and tabulated the radiation length (see also Barnett et al., 1996). An approximated form of his formula to calculate the radiation length X_0 is given below,

$$\chi_0 = \frac{716.4\,[\mathrm{g/cm^2}]A}{Z(Z+1)\ln(287/\sqrt{Z})} \quad [\mathrm{g/cm^2}] \ , \tag{1.32}$$

where Z is the atomic number and A the atomic weight of the medium. Radiation length and critical energy for different materials are listed in Table A.3 in the Appendix.

A simple approximation to compute the radiation length in air is given by Cocconi (1961).

$$\chi_{air} = 292\frac{1}{P}\frac{T}{273} \quad [\mathrm{m}] \quad \text{or} \quad 36.66\ \mathrm{g/cm^2} \ , \tag{1.33}$$

where P is the pressure in atmospheres [atm] and T the absolute temperature of the air in Kelvin [K].

1.5 Vertical Development in the Atmosphere

As a consequence of the different processes discussed above, the particle flux in the atmosphere increases with increasing atmospheric depth, X, reaching a maximum in the first 100 g/cm^2, then decreases continuously due to energy loss, absorption and decay processes. This maximum was first discovered by Pfotzer at a height of about 20 km and is called *Pfotzer maximum* (Pfotzer, 1936a and 1936b). Figure 1.11 shows the results of Pfotzer's experiment. Curve A is from his original publication showing counting rate versus atmospheric pressure and curve B shows the relative intensity versus altitude.

We distinguish between three major cosmic ray components in the atmosphere: The hadronic component which for energetic events constitutes the core of a cascade or shower, the photon-electron component which grows chiefly in the electromagnetic cascade process initiated predominantly by neutral pion decay, and the muon component arising mainly from the decay of charged pions, but also from kaons and charmed particles. The development of the three components is shown schematically in Fig. 1.12. Very energetic events of this kind are called *Extensive Air Showers* (EAS) (see Galbraith, 1958; Khristiansen, 1980; Gaisser, 1990). Because of their different nature, the three components have different altitude dependencies. This is shown in Fig. 1.13. In addition there is a neutrino component that escapes detection above ground because of the small neutrino cross section and background problems.

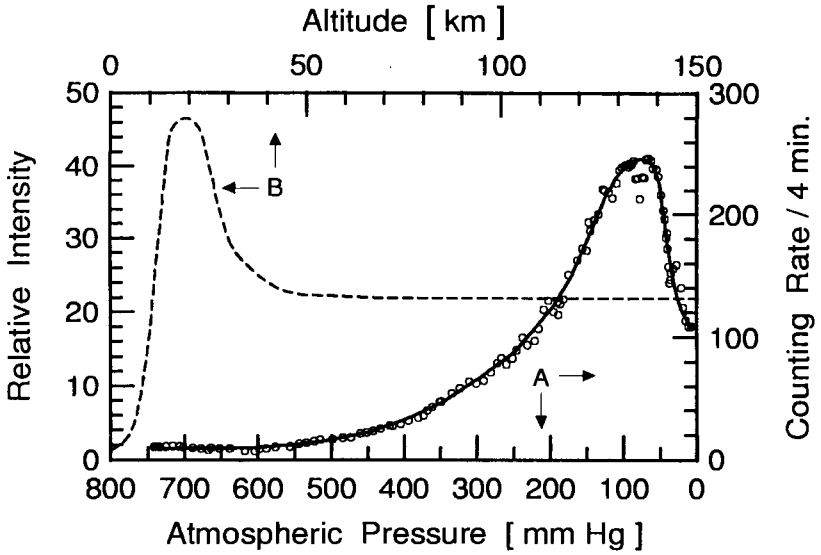

Figure 1.11: Average pressure dependence of the cosmic ray counting rate, after correction for accidental coincidences (curve A) and altitude dependence of the total cosmic ray flux (curve B) in arbitrary units, showing the Pfotzer maximum (Pfotzer , 1936a and 1936b).

1.6 Definition of Common Observables

In the following we have adopted the notation used by Rossi (1948), which has been widely accepted in the literature.

1.6.1 Directional Intensity

The *directional intensity*, $I_i(\theta, \phi)$, of particles of a given kind, i, is defined as the number of particles, dN_i, incident upon an element of area, dA, per unit time, dt, within an element of solid angle, $d\Omega$ (Fig. 1.14). Thus,

$$I_i(\theta, \phi) = \frac{dN_i}{dA\, dt\, d\Omega} \quad [\mathrm{cm}^{-2}\mathrm{s}^{-1}\mathrm{sr}^{-1}] \,. \tag{1.34}$$

Apart of its dependence on the zenith angle θ and azimuthal angle ϕ, this quantity also depends on the energy, E, and at low energy on the time, t. The time dependence is discussed in Section 1.8 and Chapter 6. Frequently, directional intensity is simply called *intensity*. Either the *total intensity* integrated over all energies, $I_i(\theta, \phi, \geq E, t)$, or the *differential intensity*,

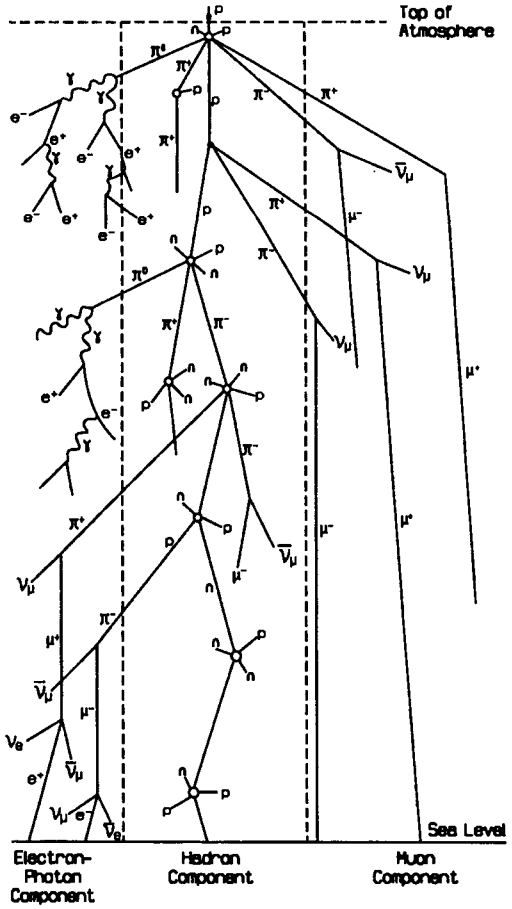

Figure 1.12: Cascade shower: Schematic representation of particle production in the atmosphere. Shown is a moderately energetic hadronic interaction of a primary cosmic ray proton with the nucleus of an atmospheric constituent at high altitude that leads to a small hadron cascade. In subsequent collisions of low energy secondaries with atmospheric target nuclei, nuclear excitation and evaporation of target nuclei may occur. Unstable particles are subject to decay or interaction, as indicated, and electrons and photons undergo bremsstrahlung and pair production, respectively. For completeness neutrinos resulting from the various decays are also shown. Note that the lateral spread is grossly exaggerated.

$I_i(\theta, \phi, E, t)$, can be determined. For $\theta = 0°$ the *vertical intensity* $I_{V,i} = I_i(0°)$ is obtained.

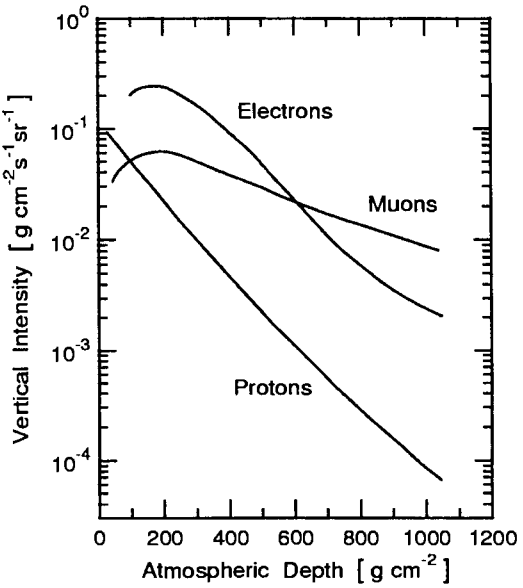

Figure 1.13: Altitude variation of the main cosmic ray components.

1.6.2 Flux

The *flux*, $J_{1,i}$, represents the number of particles of a given kind, i, traversing in a downward sense a horizontal element of area, dA, per unit time, dt. Dropping the subscript i, J_1 is related to I by the equation

$$J_1 = \int_{\cap} I(\theta, \phi) \cos(\theta) \, d\Omega \quad [\mathrm{cm}^{-2}\mathrm{s}^{-1}] \,, \tag{1.35}$$

where $\cap$ signifies integration over the upper hemisphere ($\theta \leq \pi/2$). If not specified otherwise the flux J_1 is usually meant to be the *integral flux* $J_1(\geq E)$.

1.6.3 Omnidirectional or Integrated Intensity

The *omnidirectional* or *integrated intensity*, J_2, is obtained by integrating the directional intensity I over all angles,

$$J_2 = \int I(\theta, \phi) \, d\Omega \,. \tag{1.36}$$

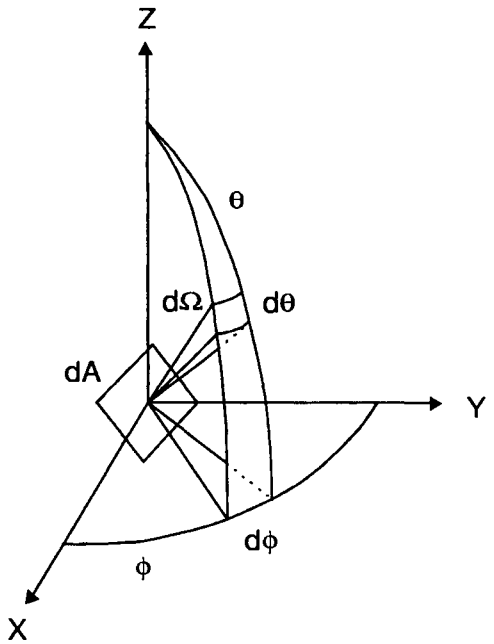

Figure 1.14: Concept of directional intensity and solid angle. The angles θ and ϕ are the zenith and azimuthal angles, respectively, and $d\Omega$ is a element of solid angle.

Since $d\Omega = \sin(\theta)\, d\theta\, d\phi$

$$J_2 = \int_{\theta=0}^{\pi} \int_{\phi=0}^{2\pi} I(\theta, \phi)\, \sin(\theta)\, d\theta\, d\phi$$

or,

$$J_2 = 2\pi \int_{\theta=0}^{\pi} I(\theta)\, \sin(\theta)\, d\theta \quad [\mathrm{cm}^{-2}\mathrm{s}^{-1}] \tag{1.37}$$

if no azimuthal dependence is present. By definition, the omnidirectional intensity J_2 is always greater than, or equal to the particle flux J_1.

$$J_2 \geq J_1 \,. \tag{1.38}$$

In order to compute the omnidirectional intensity, the angular dependence of the intensity $I(\theta, \phi)$ must be known. Measurements have shown that there is little azimuthal dependence for any of the components, except for small

changes due to the *east-west effect*, discussed in Section 1.8, which affects only the low energy component (see Chapter 2, Section 2.6, Chapter 3 ,Section 3.6 and Chapter 6, Section 6.1). However, the zenith angle dependence is significant.

1.6.4 Zenith Angle Dependence

If $I_i(\theta = 0°)$ is the vertical intensity of the i-th component, $I_i(0°)$, the *zenith angle dependence* can be expressed as

$$I_i(\theta) \;=\; I_i(0°)\,\cos^{n_i}(\theta)\;. \tag{1.39}$$

The exponent for the i-th component, n_i, depends on the atmospheric depth, X [g/cm^2], and the energy, E, i.e., $n_i = n_i(X, E)$ (see also Sections 2.6 and 3.6).

1.6.5 Attenuation Length

The *attenuation* of the hadronic component in the atmosphere is characterized by the *attenuation length* , Λ [g/cm^2]. Due to secondary particle production the attenuation length is larger than the interaction mean free path, λ_i, thus, $\Lambda > \lambda_i$. For the total cosmic ray flux in the atmosphere $\Lambda \simeq 120$ g/cm^2. The attenuation length is different for different kinds of particles. For the nucleon component in the lower atmosphere at mid latitude determined with neutron monitors one obtains about 140 g/cm^2, for neutrons only about 150 g/cm^2 (Carmichael and Bercowitch, 1969).

1.6.6 Altitude Dependence

The *altitude dependence* of the hadron flux can be written as follows:

$$I(0°, X_2) \;=\; I(0°, X_1)\,\exp\left(-\frac{X_2 - X_1}{\Lambda}\right)\;, \tag{1.40}$$

where $X_2 \geq X_1$. For a given *vertical depth* X [g/cm^2] in the atmosphere, the amount of matter traversed by a particle incident along an inclined trajectory subtending a zenith angle $\theta \leq 60°$, where the Earth's curvature can be neglected, is

$$X_s \;=\; X\,\sec(\theta) \quad [\mathrm{g\,cm^{-2}}]\;. \tag{1.41}$$

X_s is called the *slant depth* and X is frequently referred to as the *vertical column density* or *overburden*.

Assuming that the cosmic radiation impinges isotropically on top of the atmosphere, that the particle trajectories are not influenced by the Earth's magnetic field and that the intensity depends only on the amount of matter traversed, then

$$I(\theta, X) = I(0°, X) \exp\left(-X \frac{(1 - \sec(\theta))}{\Lambda}\right) . \tag{1.42}$$

Hence, $I(\theta, X)$ depends on $X \sec(\theta)$ only,

$$I(\theta, X) = I_V(X \sec(\theta)) , \tag{1.43}$$

and the omnidirectional intensity, J_2, is given by

$$J_2(X) = 2\pi \int_0^\pi I(\theta, X) \sin(\theta)\, d\theta$$

or explicitly

$$J_2(X) = 2\pi \int_0^\pi I_V(X \sec(\theta)) \sin(\theta)\, d\theta . \tag{1.44}$$

Differentiation of this expression leads to the *Gross transformation* (Gross, 1933; Jánossy, 1936; Kraybill, 1950 and 1954):

$$2\pi I_V(X) = J_2(X) - X \frac{dJ_2(X)}{dX} . \tag{1.45}$$

By means of this formula, the vertical intensity can be obtained from the omnidirectional intensity, or, vice versa. Note that for large zenith angles, i.e., for $\theta \geq 60°$ to $\geq 75°$, depending on the required accuracy, the Earth's curvature must be considered. For details concerning this topic see Subsection 1.7.2.

For both practical and historical reasons, cosmic radiation has originally been divided into two components, the *hard* or *penetrating* component and the *soft* component. This classification is based on the ability of particles to penetrate 15 cm of lead, which corresponds to a thickness of 167 g/cm^2. The soft component, which cannot penetrate this thickness, is composed mainly of electrons and low energy muons, whereas the hard penetrating component consists of energetic hadrons and muons. Which one is dominating depends on the altitude. At sea level the hard component consists mostly of muons.

1.6.7 Differential Energy Spectrum

The *differential energy spectrum*, $j(E)$, is defined as the number of particles, $dN(E)$, per unit area, dA, per unit time, dt, per unit solid angle, $d\Omega$, per energy interval, dE,

$$j(E) = \frac{dN(E)}{dA\, d\Omega\, dE\, dt} \quad [\mathrm{cm}^{-2}\,\mathrm{s}^{-1}\,\mathrm{sr}^{-1}\,\mathrm{GeV}^{-1}] \,. \tag{1.46}$$

It is usually expressed in units of $[\mathrm{cm}^{-2}\mathrm{s}^{-1}\mathrm{sr}^{-1}\mathrm{GeV}^{-1}]$ as indicated. However, the particle spectrum can as well be represented by a *momentum spectrum*, $j(p)$, per unit momentum, or, in *rigidity*, P, per unit rigidity, with P defined as

$$P = \frac{p\,c}{Z\,e} \quad [\mathrm{GV}] \,, \tag{1.47}$$

where $(p\,c)$ is the kinetic energy [GeV] of a relativistic particle, p being the momentum [GeV/c], and $(Z\,e)$ is the electric charge of the particle. The corresponding unit of rigidity is [GV]. The reason for using this unit is that different particles with the same rigidity follow identical paths in a given magnetic field.

1.6.8 Integral Energy Spectrum

The *integral energy spectrum*, $J(\geq E)$, is defined for all particles having an energy greater than E, per unit area, dA, per unit solid angle, $d\Omega$, and per unit time, dt, as follows:

$$J(\geq E) = \frac{dN(\geq E)}{dA\, d\Omega\, dt} \quad [\mathrm{cm}^{-2}\,\mathrm{s}^{-1}\,\mathrm{sr}^{-1}] \,. \tag{1.48}$$

It is usually expressed in units of $[\mathrm{cm}^{-2}\mathrm{s}^{-1}\mathrm{sr}^{-1}]$. The integral spectrum, $J(\geq E)$, is obtained by integration of the differential spectrum, $j(E)$:

$$J(\geq E) = \int_E^\infty j(E)\, dE \tag{1.49}$$

Alternatively $j(E)$ can be derived from $J(\geq E)$ by differentiation:

$$j(E) = -\frac{dJ(\geq E)}{dE} \,. \tag{1.50}$$

Most energy spectra can in part be represented by a power law with a constant exponent. For the integral spectrum we can write

$$J(\geq E) = C\, E^{-\gamma} \tag{1.51}$$

and for the differential spectrum

$$j(E) = C\,\gamma\,E^{-(\gamma+1)} = A\,E^{-(\gamma+1)}\,, \tag{1.52}$$

where C is a constant.

The exponent of the differential power law spectrum of the primary radiation, $(\gamma+1)$, is nearly constant from about 100 GeV to the beginning of the so-called *knee* (or bump) of the spectrum, which lies between 10^6 GeV and 10^7 GeV, and has a value of $\simeq 2.7$. Between the knee and the so-called *ankle* of the spectrum which lies between 10^9 GeV and 10^{10} GeV it has a value of $(\gamma+1) \simeq 3.0$ with slightly falling tendency, reaching about 3.15 at 10^{18} eV. Beyond the ankle the spectrum seems to flatten again with $(\gamma+1) \sim 2.7$. Details concerning the primary spectrum and composition are given in Chapter 5.

1.7 The Atmosphere

1.7.1 Characteristic Data and Relations

To provide a better understanding of the secondary processes which take place in the atmosphere, some of its basic features are outlined. The Earth's atmosphere is a large volume of gas with a density of almost 10^{19} particles per cm^3 at sea level. With increasing altitude the density of air decreases and with it the number of molecules and nuclei per unit volume, too. Since the real atmosphere is a complex system we frequently use an approximate representation, a simplified model, called the *standard isothermal exponential atmosphere* , where accuracy permits it.

The atmosphere consists mainly of nitrogen and oxygen, although small amounts of other constituents are present. In the *homosphere* which is the region where thermal diffusion prevails the atmospheric composition remains fairly constant. This region extends from sea level to altitudes between 85 km and 115 km, depending on thermal conditions. Beyond this boundary molecular diffusion is dominating. Table 1.2 gives the number of molecules, n_i, per cm^3 of each constituent, i, at standard temperature and pressure (STP), i.e., at 273.16 K and 760 mm Hg, and the relative percentage, q_i, of the constituents.

Specific regions within the atmosphere are defined according to their temperature variations. These include the *troposphere* where the processes which constitute the weather take place, the *stratosphere* which generally is without clouds, where ozone is concentrated, the *mesosphere* which lies between 50

Table 1.2: Composition of the Atmosphere (STP).

molecule	n_i [cm^{-3}]	$q_i = n_i/n_{air}$ [%]
air	$2.687 \cdot 10^{19}$	100
N_2	$2.098 \cdot 10^{19}$	78.1
O_2	$5.629 \cdot 10^{18}$	20.9
Ar	$2.510 \cdot 10^{17}$	0.9
CO_2	$8.87 \cdot 10^{15}$	0.03
He	$1.41 \cdot 10^{14}$	$5.0 \cdot 10^{-4}$
Ne	$4.89 \cdot 10^{14}$	$1.8 \cdot 10^{-3}$
Kr	$3.06 \cdot 10^{13}$	$1.0 \cdot 10^{-4}$
Xe	$2.34 \cdot 10^{12}$	$9.0 \cdot 10^{-6}$

and 80 km, where the temperature decreases with increasing altitude, and the *thermosphere* where the temperature increases with altitude up to about 130 km. The *temperature profile* of the atmosphere versus altitude is shown in Fig. 1.15. The layers between the different regions are called *pauses*, i.e., *tropopause, stratopause, mesopause and thermopause.*

The variation of density with altitude in the atmosphere is a function of the barometric parameters. The variation of each component can be represented by the *barometric law*,

$$n_i(X) = n_i(X_0) \left(\frac{T(h_0)}{T(h)} \right) \exp \left(- \int_{h_0}^{h} \frac{dh}{h_{s,i}} \right) , \qquad (1.53)$$

where

$n_i(X)$ number of molecules of i-th component at X [molecules/cm^3]
$n_i(X_0)$ number of molecules of i-th component at X_0 [molecules/cm^3]
$h_{s,i} = RT/M_i g(h)$ scale height of i-th component [cm]
R universal gas constant ($8.313 \cdot 10^7$ [erg mol^{-1} K^{-1}])
M_i atomic or molecular mass of the i-th component [g/mol]
h altitude (height) at X [cm]
X atmospheric depth at h [g/cm^2]
X_0 atmospheric depth at h_0 [g/cm^2] (usually sea level)
h_0 altitude (height) at X_0 [cm]
$T(h)$ temperature at h [K]
$T(h_0)$ temperature at h_0 [K]
$g(h)$ gravitational acceleration [cm s^{-2}]

In a *static isothermal atmosphere*, for which complete mixing equilibrium of all constituents is assumed, eq. 1.53 reduces to

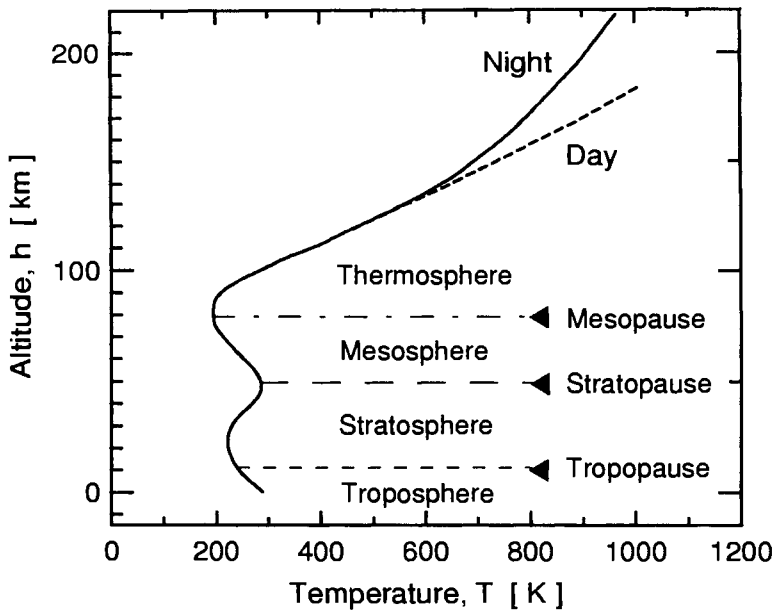

Figure 1.15: Schematic representation of the atmosphere showing its temperature profile.

Table 1.3: Scale Heights at Different Depths in the Atmosphere.

X [g/cm^2]	10	100	300	500	900
h_s [10^5cm]	6.94	6.37	6.70	7.37	8.21

$$n(h) = n(h_0) \exp\left(-\frac{h}{h_s}\right) , \tag{1.54}$$

where h_s [cm] is the mean *scale height* of the mixture (see Table 1.3).

For the *real atmosphere*, the same relation applies, but the scale height varies slightly with altitude. Table 1.3 gives some values of h_s for different atmospheric depths. A similar relation applies to the variation of pressure with altitude.

Fig. 1.16 shows the relation between density and altitude in an isothermal atmosphere, in the region which is important for cosmic ray propagation and transformation processes. In an inclined direction, i.e., for non-zero

zenith angles, the change of density per unit path length is less than in the vertical direction. Furthermore, for an incident particle the total thickness of atmosphere that must be traversed to reach a certain altitude increases with increasing zenith angle, as outlined above (cf eq. 1.41).

At large zenith angles the curvature of the Earth must be considered, requiring the Chapman function (Chapman, 1931) to compute the column density of a given path in the atmosphere. This topic is discussed in detail in Subsection 1.7.2. In horizontal direction, i.e., for $\theta = 90°$, the column density or atmospheric thickness is approximately 40 times larger than for $\theta = 0°$.

The relation between altitude and depth in the real atmosphere is illustrated in Fig. 1.17. The basic data of the COSPAR International Reference Atmosphere are given in Table A.1 in the Appendix (Barnett and Chandra, 1990).

1.7.2 Zenith Angle Dependence of the Atmospheric Thickness or Column Density

In a standard isothermal exponential atmosphere that is characterized by a constant scale height $h_s = (kT/Mg)$ [cm], where k is Boltzman's constant, T [K] the temperature in Kelvin, M [g/mol] the molecular weight and g [$\mathrm{cm^{-1}s^{-2}}$] the gravitational acceleration, the vertical column density X [$\mathrm{g/cm^2}$] of air overlaying a point P at altitude h [cm] is given by the common *barometer formula*

$$X(h) = X(h=0)e^{-(h/h_s)} \ [\mathrm{g/cm^2}] \ . \tag{1.55}$$

Flat Earth Approximation

For an inclined trajectory subtending a zenith angle $\theta \leq 60°$ the column density $X(h,\theta)$ measured from infinity to a given point P at altitude h in the atmosphere can be calculated neglecting the Earth's curvature, as shown in Fig. 1.18. In this case the column density increases with respect to the vertical column density proportional to the secant of the zenith angle, θ. Thus,

$$X(h, \theta \leq 60°) = X(h, \theta = 0°) \sec(\theta) \ [\mathrm{g/cm^2}] \ . \tag{1.56}$$

For less accurate calculations, this expression may even be used to zenith angles $\theta \leq 75°$.

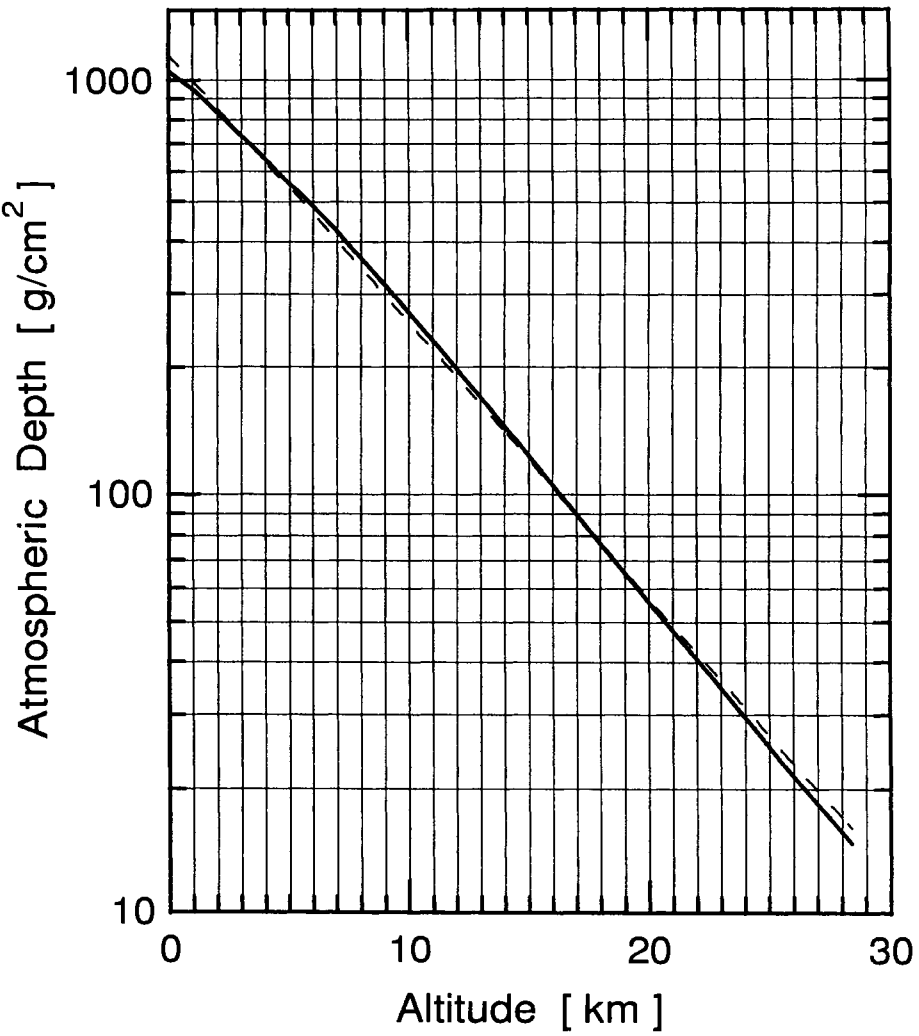

Figure 1.16: Relation between vertical depth and altitude in an isothermal atmosphere. The dashed line is an exponential fit to the overall data.

Curved Earth Atmosphere

For larger zenith angles the *curvature of the Earth* cannot be ignored as is evident from Fig. 1.19. The correct derivation of the formula to compute the true column density for inclined trajectories leads to the *Chapman function* (Chapman, 1931). The Chapman function gives the ratio of the total amount

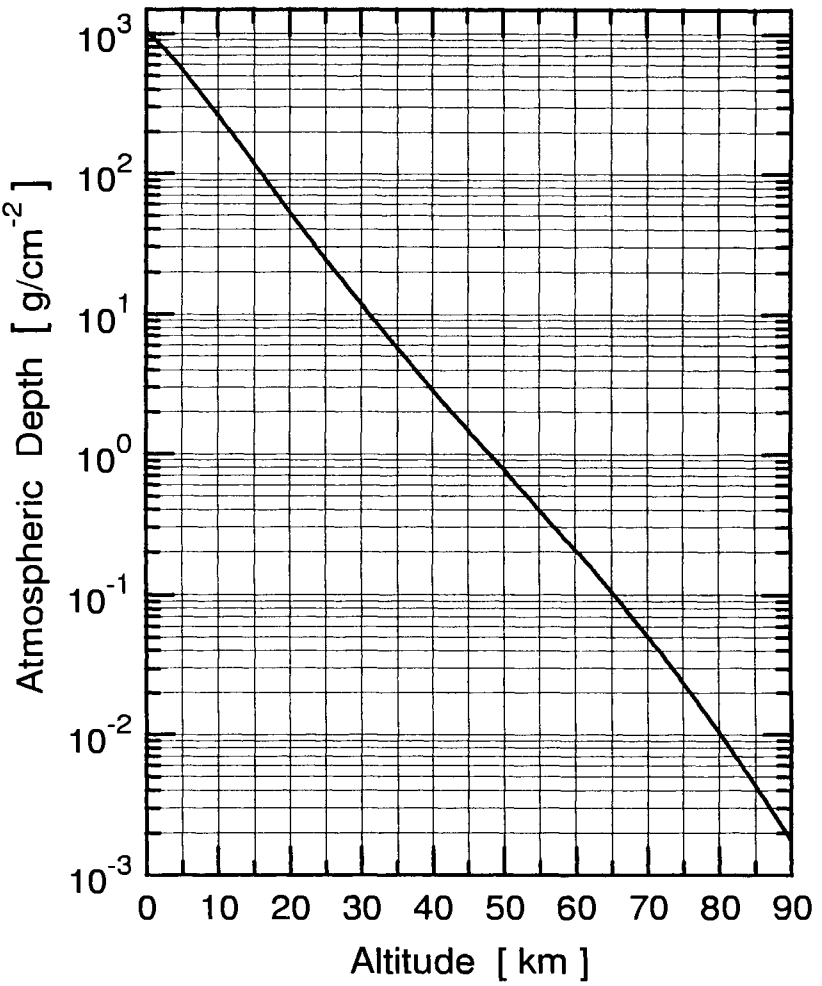

Figure 1.17: Relation between vertical depth or column density and altitude in the real atmosphere, after Cole and Kantor (1978).

of matter along an oblique trajectory subtending a zenith angle θ versus the amount of total matter in the vertical ($\theta = 0$) for a given point P in the atmosphere. This function has the following form:

$$Ch(x,\theta) \;=\; x\,\sin(\theta)\int_0^{\theta}\frac{\exp(x - x\,\sin(\theta)/\sin(\phi))}{\sin^2(\phi)}\,d\phi \;\;, \qquad (1.57)$$

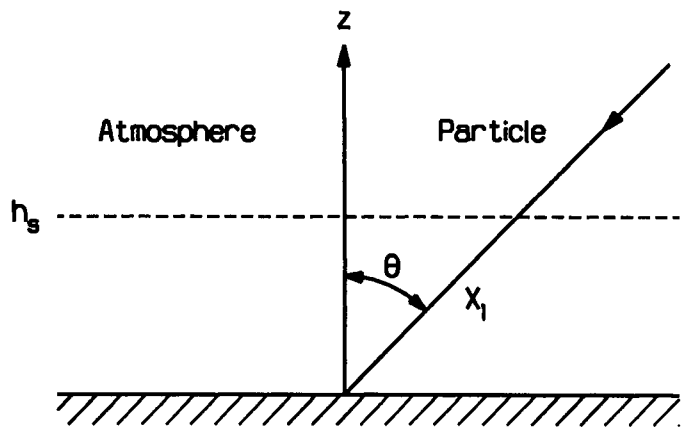

Figure 1.18: Atmospheric thickness or column density, X_1, encountered by a cosmic ray incident at a zenith angle θ to reach point P under the assumption that the Earth is flat. h_s represents the atmospheric scale height. (This approximation can be used for zenith angles $\theta \leq 60°$ to $\leq 75°$, depending on accuracy required.)

where

$$x = \frac{R_E + h}{h_s} \quad . \tag{1.58}$$

R_E is the radius of the Earth, h the altitude of point P in the atmosphere, and h_s is the appropriate scale height of the atmosphere.

Various authors have derived approximations to this expression (Fitzmaurice, 1964; Swider and Gardner, 1967). Swider and Gardner propose for zenith angles $\theta \leq (\pi/2)$ the equation

$$Ch\left(x, \theta \leq \frac{\pi}{2}\right) = \left(\frac{\pi x}{2}\right)^{1/2} \left(1 - erf\left[x^{1/2} \cos\frac{\theta}{2}\right]\right) \exp\left(x \cos^2\frac{\theta}{2}\right) \quad . \tag{1.59}$$

For $\theta = \pi/2$, i.e., for horizontal direction,

$$Ch(x, \frac{\pi}{2}) = (\pi x/2)^{1/2} \quad , \tag{1.60}$$

which is about equal to 40.

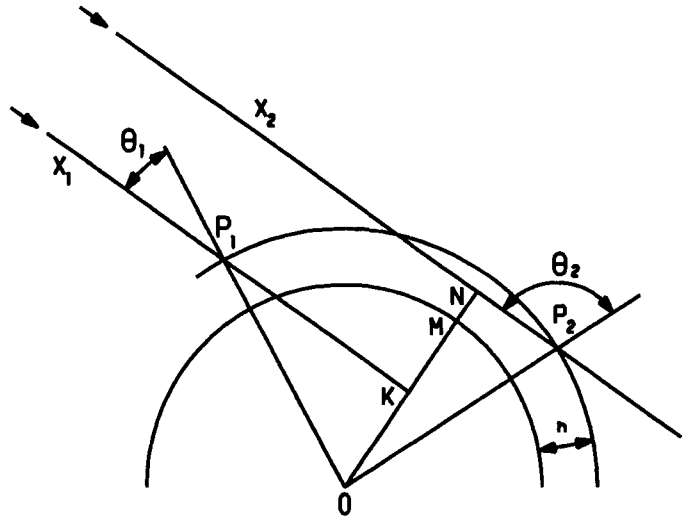

Figure 1.19: Atmospheric column density X_1 in curved atmosphere encountered by a cosmic ray incident under zenith angle $\theta_1 \leq \pi/2$ to reach point P_1 at altitude h. Also shown is the situation for point P_2 at $\theta > \pi/2$ and column density X_2, a situation that may arise when h is large.

For zenith angles in excess of $\pi/2$, a situation that may arise in satellite experiments (cf Fig. 1.19), the same authors propose the approximation

$$Ch\left(x, \theta \geq \frac{\pi}{2}\right) = \left(\frac{\pi x}{2}\sin(\theta)\right)^{1/2}\left(1 + erf\left[-\cot(\theta)\left(\frac{x\sin(\theta)}{2}\right)^{1/2}\right]\right) \times \left(1 + \frac{3}{8x\sin(\theta)}\right) \quad (1.61)$$

The zenith angle dependence of the atmospheric thickness or column density at sea level is illustrated in Fig. 1.20.

For further details concerning atmospheric column densities and attenuation for zenith angles $\theta \geq \pi/2$, such as may be relevant at great altitude in conjunction with satellites, the reader is referred to the articles by Swinder (1964) and Brasseur and Solomon (1986). The accuracy of certain approximations for the Chapman function is discussed by Swider and Gardner (1967).

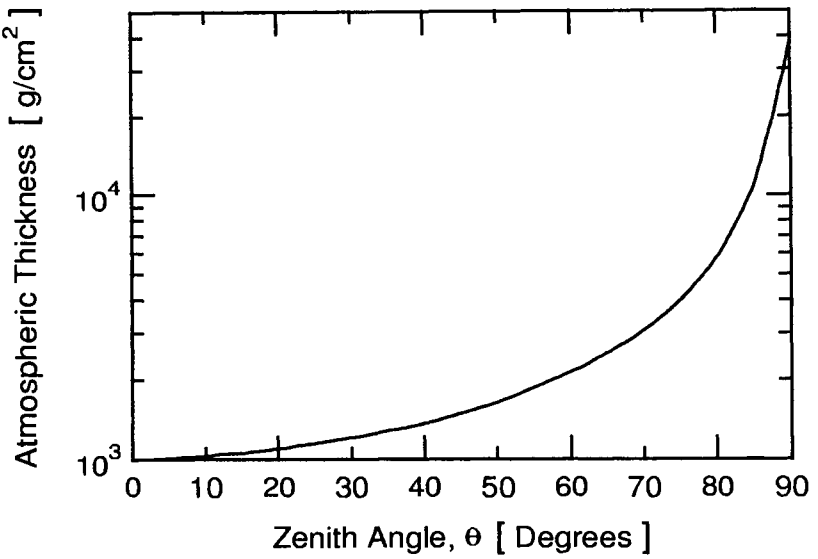

Figure 1.20: Relation between zenith angle and atmospheric thickness or column density at sea level for the "curved" Earth.

1.8 Geomagnetic and Heliospheric Effects

1.8.1 East-West, Latitude and Longitude Effects

Cosmic ray fluxes and spectra from eastern and western directions are different up to energies of about 100 GeV, because of the geomagnetic field and the *positive charge excess* of the primary radiation. This effect, which is called the *east-west effect* or *east-west asymmetry*, is strongest at the top of the atmosphere. It is illustrated in Fig. 1.21. Due to the zenith angle dependence of the cosmic ray intensity deep inside the atmosphere that goes roughly as $\cos^2(\theta)$ and is known as the $\cos^2(\theta)$-law, this asymmetry is less pronounced at sea level. Because of the dipole shape of the geomagnetic field there exists also an *azimuthal effect.*

Furthermore, due to the *geomagnetic cutoff* imposed by the geomagnetic field, the energy spectrum manifests a *latitude dependence* for energies up to about 15 GeV at vertical incidence. This is called the *latitude effect.* It is shown in Fig. 1.22.

There exists also a *longitude effect* which is due to the fact that the geomagnetic dipole axis is asymmetrically located with respect to the Earth's

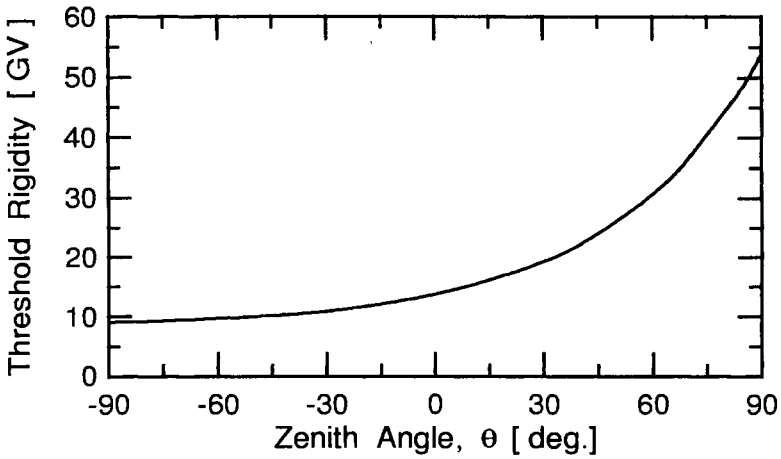

Figure 1.21: Threshold rigidity as a function of zenith angle in the east-west plane at an equatorial point at the top of the atmosphere, illustrating the east-west effect.

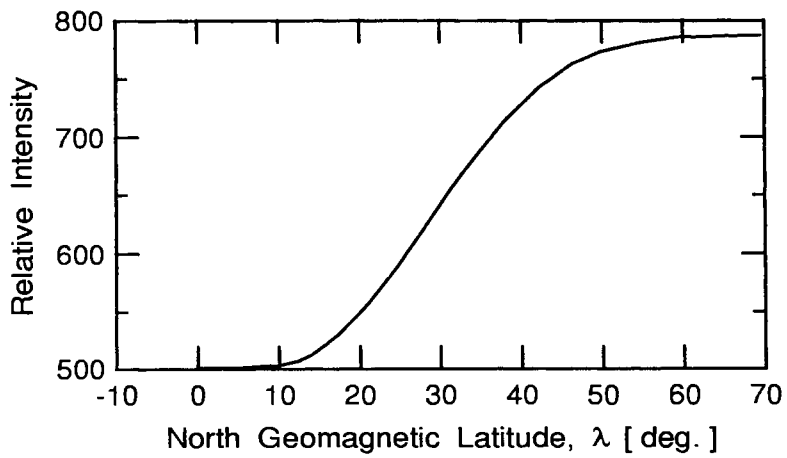

Figure 1.22: Relative variation of the cosmic ray intensity at an altitude of 9000 m as a function of geomagnetic latitude along the geographic meridian 80° (Neher, 1952). This is known as the latitude effect .

rotation axis. In addition there are local magnetic anomalies. The most dominant one is the *South Atlantic anomaly*, off the coast of Brazil. The longitude effect is illustrated in Fig. 1.23.

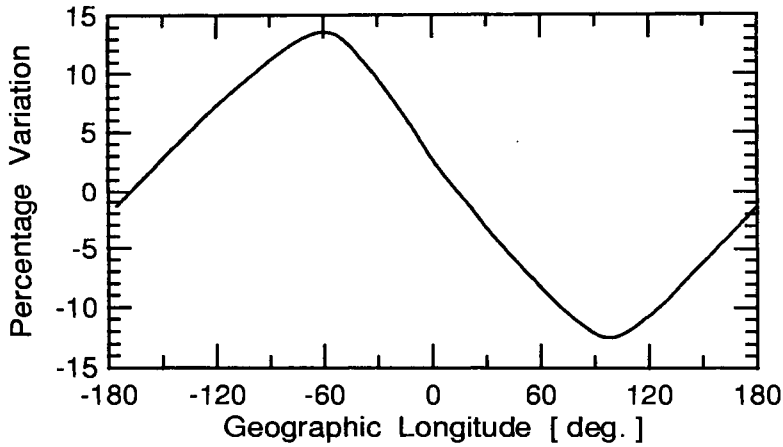

Figure 1.23: Variation of the cosmic ray intensity in percent as a function of geographic longitude recorded with a neutron monitor in an aircraft at constant pressure altitude ($\sim$ 18,000 feet or 5486 m) around the equator (Katz et al., 1958). This is known as the longitude effect.

1.8.2 Time Variation and Modulation

The solar activity influences the cosmic ray flux on Earth and the shape of the energy spectrum up to about 100 GeV/nucleon in various ways. The galactic or primary radiation and consequently the secondary radiation produced in the atmosphere, too, are subject to a periodic variation that follows the 11 year solar cycle.

Stochastic and relatively sudden changes, where the cosmic ray intensity may drop occasionally as much as 15 % to 30 % within tens of minutes to hours, followed by a gradual recovery to the previous average intensity within many hours or even days, are the so-called *Forbush decreases* (Forbush, 1937, 1938 and 1958). They are caused by magnetic shocks of solar origin. The above mentioned phenomena are referred to as *solar modulation effects.*

Occasional transient high energy phenomena on the Sun caused by *solar flares* ejecting relativistic particles are responsible for the so-called *ground level enhancement (GLE).* Such events provoke an increase of the intensity of the cosmic radiation anywhere between a few 10% to a few 100% with respect to the normal level due to the arrival of a superimposed low energy particle component.

Intensity variations are also due to changes of the geomagnetic cutoff,

discussed below. In addition, some of the intensity variations observed at sea level are seasonal and due to atmospheric effects caused by temperature and pressure changes.

Modulation effects are not discussed in detail in this volume. For these topics the reader is referred to the specialized literature. For an introduction see e.g. Parker (1963), Sandström (1965), Dorman (1974), Longair (1992). More specific information can be found in proceedings of topical conferences, see e.g. Kunow (1992), Moraal (1993). However, some selected heliospheric phenomena are summarized in Chapter 6.

1.8.3 Geomagnetic Cutoff

Charged particles approaching the Earth from outer space follow curved trajectories because of the geomagnetic field in which they propagate. As they enter the atmosphere they may also be subject to interactions with atmospheric constituents. Disregarding the existence of the atmosphere, the question whether a particle can reach the Earth's surface or not depends solely on the magnitude and direction of the local magnetic field, and on the rigidity and direction of propagation of the particle.

A practical measure to compare and interpret particle measurements made at different locations on Earth, in particular at different geomagnetic latitudes, is the *effective vertical cutoff rigidity*, P_c, frequently referred to as the *vertical cutoff rigidity*, or simply the *cutoff rigidity*. It must be emphasized that in general geomagnetic and geographic coordinates are not the same and P_c depends on location and time.

Moreover, the exact vertical cutoff rigidity of a particular geographic location varies somewhat with time because of the variability of the magnetospheric and geomagnetic fields. These variations may be as much as 20 percent at mid-latitude (Flückiger, 1982). Figure 1.24 shows the Störmer cutoff rigidity (Störmer, 1930) as a function of geomagnetic latitude for vertically incident positive particles and for positive particles incident under a zenith angle of 45° from the east and west, respectively (see Subsection 1.8.5 for the definition of the Störmer cutoff rigidity).

A frequently used method to compute the vertical cutoff rigidity of a particle is to consider an identical particle of opposite charge and opposite velocity being released in radial outward direction at the *reference altitude* of 20 km above sea level. The effective cutoff rigidity is defined as the rigidity required for the particle to overcome trapping in the geomagnetic field and being able to escape to infinity, taking into account the *penumbral bands*. All

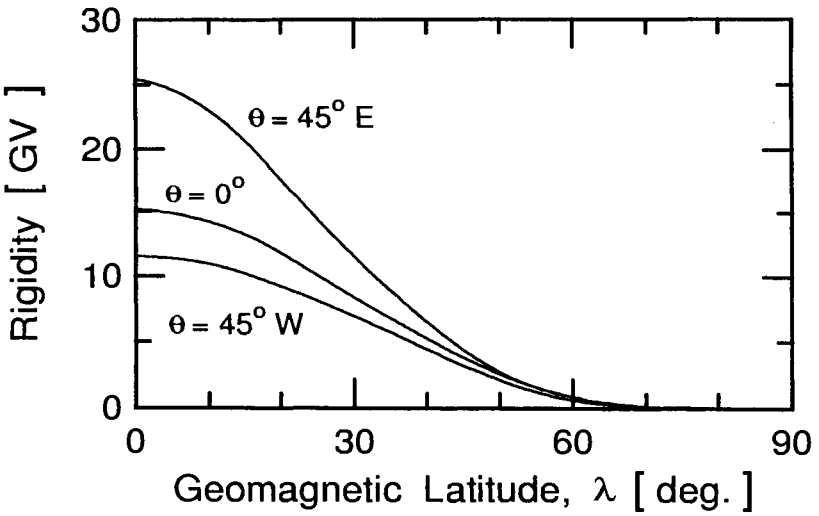

Figure 1.24: Störmer cutoff rigidity as a function of geomagnetic latitude, λ, for vertically incident positive particles ($\theta = 0°$), and for positive particles incident under a zenith angle of 45° from the east ($\theta = 45°$E) and west ($\theta = 45°$W), respectively (Rossi and Olbert, 1970).

kinds of interactions and energy loss mechanisms in the residual atmosphere as well as scattering are disregarded in this picture. The complexity of actual trajectories is shown in the specific example of Fig. 1.25.

1.8.4 Cosmic Ray Cutoff Terminology

Brief History

The study of cosmic ray access to locations within the geomagnetic field has greatly evolved over the past fifty years. Results obtained from theoretical investigations concerning this question have been instrumental in aiding the interpretation of a wide range of experimentally observed phenomena. These studies have ranged from examinations of the aurora, through attempts to account for the observed *directional asymmetries* detected in the primary and secondary cosmic ray fluxes, particularly at lower energies, to the determination of the relationship between primary and secondary cosmic rays and other topics.

The early work, initiated by Störmer (1930) and numerous other investigators in the years to follow, was mainly concerned with the distinction

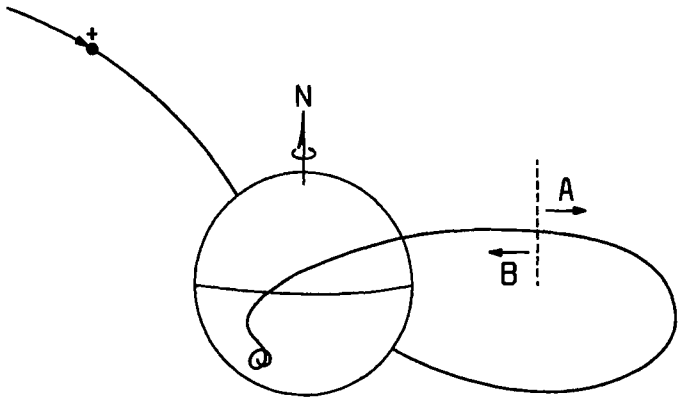

Figure 1.25: The trajectory within the geomagnetic field of a 5.65 GV cosmic ray particle en route to Williamtown, Australia (32.75° S, 151.80° E), where it will arrive with a zenith angle of 60° and azimuth of 150° east of geographic north (after Cooke et al., 1991).

between allowed directions of arrival of a particle from interplanetary space at a given location in the geomagnetic field, and directions that are inaccessible (for a review see Cooke et al., 1991). This work was based on analytic methods using a *dipole approximation* to describe the geomagnetic field, frequently ignoring the existence of a solid Earth, causing *shadow effects*. In such a picture bound *periodic orbits* play a significant role in delimiting the different access regions. With the beginning of the era of digital computers the field evolved rapidly. New aspects were developed and the terminology, too, was subject to changes.

Out of this work resulted the concept of *asymptotic cones of acceptance* for the worldwide network of cosmic ray stations and the construction of the *worldwide grid* of vertical cutoff rigidities of cosmic rays (McCracken et al., 1962, 1965 and 1968; Shea et al., 1968). As the work progressed the transition from the simple dipole representation of the geomagnetic field to the real-field, including the presence of the impenetrable Earth was made that led eventually to a new picture.

Whereas the early theoretical investigators viewed access conditions in what may be called the *direction picture*, describing the directions from which particles of a specific rigidity could or could not arrive, the modern computer calculations have usually a *rigidity picture* in which accessibility is considered as a function of particle rigidity in a single arrival direction. Thus, today we distinguish between the old geometrical terms, appropriate to the direction

picture, and the new rigidity picture.

As a result, confusion sometimes arises when comparing early and modern literature. Cooke et al. (1991) in their review have helped to clarify the situation, particularly for newcomers to the field. In the following we are summarizing the various definitions and the essential points of their article, using partly their own wording.

Summary of Trajectory Characteristics

In brief, it can be said that when trajectories calculated in a time-invariant but otherwise realistic model of the geomagnetic field are examined, many clearly defined cutoff structures can be found, including modified forms of the characteristic structures identified by the earlier workers as pertaining to the regions possessing the different types of access in a simple, axially symmetric, field. Although all the analytically identified structures can usefully be identified in computer-based studies, there has been good reason to introduce additional terminology in order to define useful quantities naturally associated with the standard sampling method of determining the real-field cutoff values in the presence of the Earth, in the rigidity domain.

These more recent definitions are presented in the following subsection, together with the definitions for the *classical terms*, suitably qualified to allow their application in real-field situations. The differences between the two groups are outlined.

1.8.5 Definitions of Geomagnetic Terms

The following definitions are subdivided by viewpoint, as indicated in Table 1.4. The subsequent list describes terms used in cutoff calculations. It is not exhaustive but seeks to portray the most useful quantities in each situation. Figure 1.26 helps to illuminate the various concepts and definitions.

Directional Definitions

The definitions listed under this subheading are appropriate for use with the directional picture. Each definition is for charged particles of a single specified rigidity value arriving at a particular point in the geomagnetic field (for details see Cooke et al., 1991). Figure 1.26 illustrates the various terms.

Allowed cone: The solid angle containing the directions of arrival of all trajectories which do not intersect the Earth and which cannot possess sections asymptotic to bound periodic orbits (because the rigidity is too high to permit such sections to exist in the directions of arrival concerned).

Table 1.4: Summary of terms used in cutoff calculations.
Terms describing phenomena which are equivalent in the two pictures are listed on the same line.
(Adopted from Cooke et al., 1991).

Direction Picture	Rigidity Picture
	Cutoff rigidity
Allowed cone	
Main cone	Main cutoff rigidity
	First discontinuity rigidity
Shadow cone	Shadow cutoff rigidity
Penumbra	Penumbra
Penumbral band	Penumbral band
	Primary band
Störmer cone	Störmer cutoff rigidity
Forbidden cone	
	Upper cutoff rigidity
	Lower cutoff rigidity
	Horizon-limited rigidity
	Effective cutoff rigidity
	Estimated cutoff rigidity

Main cone: The boundary of the allowed cone. The main cone is composed of trajectories which are asymptotic to the simplest bound periodic orbits and trajectories which graze the surface of the Earth. (For this purpose the surface of the Earth is generally taken to be at the top of the effective atmosphere.)

Forbidden cone: The solid angle region within which all directions of arrival correspond to trajectories which, in the absence of the solid Earth, would be permanently bound in the geomagnetic field. Access in these directions from outside the field is, therefore, impossible.

Störmer cone: The boundary of the forbidden cone. In an axially symmetric field the surface forms a right circular cone.

Shadow cone: The solid angle containing all directions of particle arrival which are excluded due to short-range Earth intersections of the approaching trajectories, while the particle loops around the local field lines.

Penumbra: The solid angle region contained between the main cone and the Störmer cone. In general the penumbra contains a complex structure of

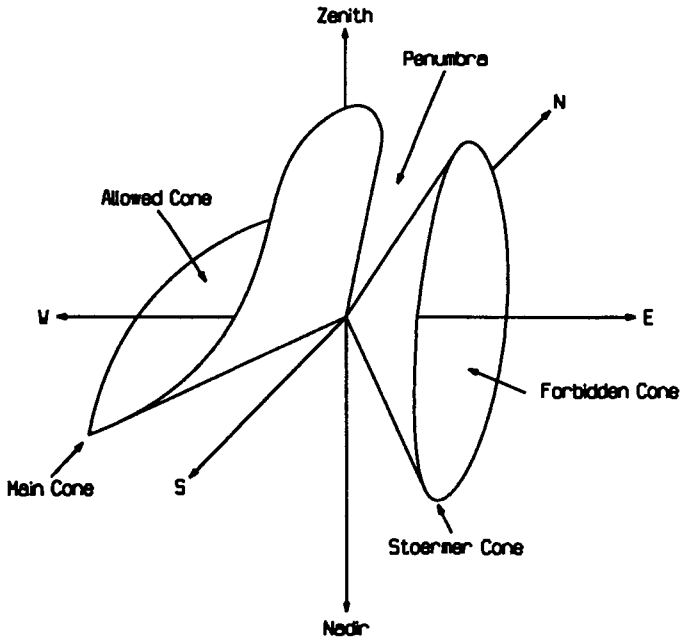

Figure 1.26: Spatial relationship between the allowed cone, main cone, penumbra, Störmer cone, and forbidden cone for positively charged cosmic ray nuclei with an arbitrary rigidity value at an arbitrary location in the magnetic dipole field (adapted from Cooke et al., 1991).

allowed and forbidden bands of arrival directions.

Penumbral band: A contiguous set of directions of arrival, within the penumbra, the members of which are either all allowed or all forbidden. Often, within any given forbidden band structure, it is possible to determine that a number of individual bands, each attributable to the Earth intersection of the associated trajectories in a different low point, are overlapping to produce the entire forbidden band structure observed.

Rigidity Picture Definitions

The following definitions are applicable to the rigidity picture. Each definition refers to particles arriving at a particular site within the geomagnetic field from a specified direction (for details see Cooke et al., 1991).

Cutoff rigidity: The location of a transition, in rigidity space, from allowed to forbidden trajectories as rigidity is decreased. Unless otherwise defined, the value normally quoted in representing the results of computer

calculations is, for practical reasons, the rigidity of the allowed member of the appropriate juxtaposed allowed/forbidden pair of trajectories computed as part of a spaced series of traces.

Main cutoff rigidity, P_m: The rigidity value at which the direction concerned is a generator of the main cone as defined in the direction picture. The associated trajectory is either one which is asymptotic to the simplest bound periodic orbit, or (owing to the presence of the solid Earth) is one which is tangential to the Earth's surface.

First-discontinuity rigidity, P_1: The rigidity associated with the first discontinuity in asymptotic longitude as the trajectory calculations are performed for successively lower rigidities, starting with some value within the allowed cone. The value of P_1 is approximately equal to the main cutoff as defined above.

Shadow cutoff rigidity, P_{sh}: The rigidity value at which the edge of the shadow cone lies in the direction concerned.

Penumbra: The rigidity range lying between the main and the Störmer cutoff rigidities.

Penumbral band: A continuous set of rigidity values, within the penumbra, all members of which have the same general access characteristics, either all allowed or all forbidden. Often, within any given forbidden band structure, it is possible to determine that a number of individual bands, each attributable to the Earth intersection of the associated trajectories in a different low point, are overlapping to produce the entire forbidden band structure observed.

Primary band: The stable forbidden penumbral band which is associated with the Earth intersection of a low point in the loop which lies at the last equatorial crossing before the trajectory (or its virtual extension in the assumed absence of the Earth) takes on the characteristic guiding center motion down the local magnetic field line.

Störmer cutoff rigidity, P_s: The rigidity value for which the Störmer cone lies in the given direction. In a dipole field (and perhaps also in the real geomagnetic field) direct access for particles of all rigidity values lower than the Störmer cutoff rigidity is forbidden from outside the field. In a dipole approximation to the geomagnetic field, one form of the Störmer equation gives the Störmer cutoff rigidity, in GV, as

$$P_s = \frac{\mathbf{M}\cos^4(\lambda)}{r^2[l + (1 - \cos^3(\lambda)\cos(\epsilon)\sin(\zeta))^{1/2}]^2} \tag{1.62}$$

where M is the dipole moment which has a normalized value of 59.6 when r is expressed in units of Earth radii, r being the distance from the dipole, λ is the geomagnetic latitude, ϵ the azimuthal angle measured clockwise from the geomagnetic east direction (for positive particles), and ζ is the angle from the local magnetic zenith direction.

Upper cutoff rigidity, P_u: The rigidity value of the highest detected allowed/forbidden transition among a set of computed trajectories. The upper cutoff rigidity can correspond to the main cutoff if and only if no trajectories asymptotic to bound periodic orbits lie at rigidities higher than this value. This can be identified from the nature of the trajectory associated with the main cutoff.

Lower cutoff rigidity, P_l: The lowest detected cutoff value (i.e. the rigidity value of the lowest allowed-forbidden transition observed in a set of computed trajectories). If no penumbra exists, P_l equals P_u.

Horizon-limited rigidity, P_h: The rigidity value of the most rigid particle for which an allowed trajectory is found in a set of computer calculations performed for a below horizon direction at a location above the surface of the Earth.

Effective cutoff rigidity, P_c: The total effect of the penumbral structure in a given direction may be represented usefully, for many purposes, by the *effective cutoff rigidity*, a single numeric value which specifies the equivalent total accessible cosmic radiation above and within the penumbra in a specific direction. *Effective cutoffs* may be either linear averages of the allowed rigidity intervals in the penumbra or functions weighted for the cosmic ray spectrum and/or detector response (Shea and Smart, 1970; Dorman et al., 1972). For a linear weighting this would have the form

$$P_c = P_u - \sum_{P_l}^{P_u} \Delta P_i(allowed) \tag{1.63}$$

where the trajectory calculations were performed at rigidity intervals ΔP_i.

Estimated cutoff rigidity, P_{est}: A value obtained by using an empirically normalized equation to approximate the cosmic ray cutoff variation in the location of a particular point within a magnetic field in order to estimate a cutoff value pertaining to the point. This value can be found by use of a variety of interpolation techniques, one of which is the application of the Störmer equation given above (eq. 1.63). Because the Störmer equation characterizes the spatial variation of the cutoff rigidity, with appropriate normalization it may be used to obtain useful estimates of the various cosmic ray cutoff

rigidities, over intervals of latitude, longitude, zenith and azimuth, for example. In practice, estimates of the value of any cutoff can be obtained from adjacent calculated values to a reasonable degree of accuracy by employing this method.

References

Abe, F., M. Albrow, D. Amidei, C. Anway-Wiese, G. Apollinari, M. Atac, P. Auchincloss, P. Azzi, N. Bacchetta, A.R. Baden, W. Badgett, M.W. Bailey, A. Bamberger, P. de Barbaro, A. Barbaro-Galtieri, V.E. Barnes, B.A. Barnett, G. Bauer, T. Baumann, F. Bedeschi, S. Behrends, S. Belforte, G. Bellettini, J. Bellinger, D. Benjamin, J. Benlloch, J. Bensinger, A. Beretvas, J.P. Berge, S. Bertolucci, K. Biery, S. Bhadra, M. Binkley, D. Bisello, R. Blair, C. Blocker, A. Bodek, V. Bolognesi, A.W. Booth, C. Boswell, G. Brandenburg, D. Brown, E. Buckley-Geer, H.S. Budd, G. Busetto, A. Byon-Wagner, K.L. Byrum, C. Campagnari, M. Campbell, A. Caner, R. Carey, W. Carithers, D. Carlsmith, J.T. Carroll,' R. Cashmore, A. Castro, Y. Cen, F. Cervelli, K. Chadwick, J. Chapman, T.J. Chapin, G. Chiarelli, W. Chinowsky, S. Cihangir, A.G. Clark, M. Cobal, D. Connor, M. Contreras, J. Cooper, M. Cordelli, D. Crane, J.D. Cunningham, C. Day, F. DeJongh, S. Dell'Agnello, M. Dell'Orso, L. Demortier, B. Denby, P.F. Derwent, T. Devlin, M. Dickson, R.B. Drucker, A. Dunn, K. Einsweiler, J. E. Elias, R. Ely, S. Eno, S. Errede, A. Etchegoyen, B. Farhat, M. Frautschi, G.J. Feldman, B. Flaugher, G.W. Foster, M. Franklin, J. Freeman, T. Fuess, Y. Fukui, A.F. Garfinkel, A. Gauthier, S. Geer, D.W. Gerdes, P. Giannetti, N. Giokaris, P. Giromini, L. Gladney, M. Gold, J. Gonzalez, K. Goulianos, H. Grassmann, G.M. Grieco, R. Grindley, C. Grosso-Pilcher, J. Grunhaus, C. Haber, S.R. Hahn, R. Handler, K. Hara, B. Harral, R.M. Harris, S.A. Hauger, J. Hauser,C. Hawk, T. Hessing, R. Hollebeek, L. Holloway, A. Hölscher, S. Hong, G. Houk, P. Hu, B. Hubbard, T. Huffman, R. Hughes, P. Hurst, J. Huth, J. Hylen, M. Incagli, T. Ino, H. Iso, C.P. Jessop, R.P. Johnson, U. Joshi, R.W. Kadel, T. Kamon, S. Kanda, D.A. Kardefis, I. Karliner, E. Kearns, L. Keeble, R. Kephart, P. Kesten, R.M. Keup, H. Keutelian, D. Kim, S.B. Kim, S.H. Kim, Y.K. Kim, L. Kirsch, K. Kondo, J. Konigsberg, K. Kordas, E. Kovacs, M. Krasberg, S.E. Kuhlmann, E. Kuns, A.T. Laasanen, S. Lammel, J.I. Lamoureux, S. Leone, J.D. Lewis, W. Li, P. Limon, M. Lindgren, T.M. Liss, N. Lockyer, M. Loreti, E.H. Low, D. Lucchesi, C.B. Luchini, P. Lukens, P. Maas, K. Maeshima, M. Mangano, J.P. Marriner, M. Mariotti, R. Markeloff, L.A. Markosky, J.A.J.

Matthews, R. Mattingly, P. McIntyre, A. Menzione, E.Meschi, T. Meyer, S. Mikamo, M. Miller, T. Mimashi, S. Miscetti, M. Mishina, S. Miyashita, Y. Morita, S. Moulding, J. Mueller, A. Mukherjee, T. Muller, L.F. Nakae, I. Nakano, C. Nelson, D. Neuberger, C. Newman-Holmes, J.S.T. Ng, M. Ninomiya, L. Nodulman, S. Ogawa, R. Paoletti, V. Papadimitriou, A. Para, E. Pare, S. Park, J. Patrick, G. Pauletta, L, Pescara, T.J. Phillips, A.G. Piacentino, R. Plunkett, L. Pondrom, J. Proudfoot, F. Ptohos, G. Punzi, D. Quarrie, K. Ragan, G. Redlinger, J. Rhoades, M. Roach, F. Rimondi, L. Ristori, W. J. Robertson, T. Rodrigo, T. Rohaly, A. Roodman, W.K. Sakumoto , A. Sansoni, R.D. Sard, A. Savoy-Navarro, V. Scarpine, P. Schlabach, E.E. Schmidt, O. Schneider, M.H. Schub, R. Schwitters, G. Sciacca, A. Scribano, S. Segler, S. Seidel, Y. Seiya, G. Sganos, N.M. Shaw, M. Sheaff, M. Shochet, J. Siegrist, A. Sill, P. Sinervo, J. Skarha, K. Sliwa, D.A. Smith, F.D. Snider, L. Song, T. Song, M. Spahn, P. Sphicas, A. Spies, R.St. Denis, L. Stanco, A. Stefanini, G. SuHivan, K. Sumorok, R.L. Swartz, Jr., M. Takano, K. Takikawa, S. Tarem, F. Tartarelli, S. Tether, D. Theriot, M. Timko, P. Tipton, S. Tkaczyk, A. Tollestrup, J. Tonnison, W. Trischuk, Y. Tsay, J. Tseng, N. Turini, F. Ukegawa, D. Underwood, S. Vejcik III, R. Vidal, R.G. Wagner, R.L. Wagner, N. Wainer, R.C. Walker, J. Walsh, A. Warburton, G. Watts, T. Watts, R. Webb, C. Wendt, H. Wenzel, W.C. Wester III, T. Westhusing, S.N. White, A.B. Wicklund, E. Wicklund, H.H. Wiiiiams, B.L. Winer, J. Wolinski, D.Y. Wu, X. Wu, J. Wyss, A. Yagil, K. Yasuoka, Y. Ye, G.P. Yeh, J. Yoh, M. Yokoyama, J.C. Yun, A. Zanetti, F. Zetti, S. Zhang, W. Zhang, and S. Zucchelli: (CDF Collaboration). Phys. Rev., D, 50, p. 5550 (1994).

Aglietta, M., B. Alessandro, P. Antonioli, F. Arneodo, L. Bergamasco, M. Bertaina, C. Castagnoli, A. Castellina, A. Chiavassa, G. Cini-Castagnoli, B. D'Ettore Piazzoli, G. Di Sciascio, W. Fulgione, P. Galeotti, P.L. Ghia, A. Lima de Godoi, M. Iacovacci, G. Mannocchi, C. Morello, G. Navarra, O. Saavedra, G.C. Trinchero, S. Valchierotti, P. Vallania, S. Vernetto, and C. Vigorito: PICRC, 1, p. 143 (1999).

Allkofer, O.C.: Introduction to Cosmic Radiation, Thiemig Verlag, München (1975).

Alner, G.J., K. Alpgard, P. Anderer, R.E. Ansorge, B. Asman, S. Berglund, K. Berkelman, D. Bertrand, C.N. Booth, C. Buffam, L. Burow, P. Carlson, J.-L. Chevalley, C. Declercq, R.S. DeWolf, B. Eckart, G. Ekspong, I. Evangelou, A. Eyring, J.-P. Fabre, M. Fischer, K.A. French, C. Fuglesang, J. Gaudaen, C. Geich-Gimbel, M. Gijsen, K. von Holt. R. Hospes, D. Johnson, K. Jon-And, Th. Kokott, M. Langer, F. Lotse, R. Mackenzie, M.N. Maggs, R. Meinke, Th. Müller, H. Mulkens, D.J. Munday, A. Odian, J.E.V. Ovens, M. Rosenberg, J.G. Rushbrooke, H. Saarikko, T. Saarikko, H. Schmickler, F.

Trian, L. Van hamme, Ch. Walck, C.P. Ward, D.R. Ward, G. Weber, T.O. White, G. Wilquet, and N. Yamdagni: UA5 Collaboration. Physics Reports, 154, p. 247-383 (1987).

Auger, P.: Comptes Rendus Acad. Sci., Paris, 207, p. 907 (1938) (in French).

Auger, Pierre, Louis Leprince-Ringuet, et Paul Ehrenfest, Jr.: J. Phys. et Radium, 7, No. 2, p. 58 (1936) (in French).

Auger, Pierre, Raymond Maze, et Mme. Thérèse Grivet-Meyer: Comptes Rendus Acad. Sci, Paris, 206, p. 1721 (1938) (in French).

Baltrusaitis, R.M., G.L. Cassiday, J.W. Elbert, P.R. Gerhardy, S. Ko, E.C. Loh, Y. Mizumoto, P. Sokolsky, and D. Steck: Phys. Rev. Lett., 52, p. 1380 (1984).

Barnett, J.J., and S. Chandra: Adv. Space Res., 10, No. 12, p. (12)7 (1990).

Barnett, R.M., C.D. Carone, D.E. Groom, T.G. Trippe, C.G. Wohl, B. Armstrong, P.S. Gee, G.S. Wagman, F. James, M. Mangano, K. Mönig, L. Montanet, J.L. Feng, H. Murayama, J.J. Hernàndez, A. Manohar, M. Aguilar-Benitez, C. Caso, M. Roos, N.A. Törnqvist, K.G. Hayes, K. Hagiwara, S. Kawabata, K. Nakamura, M. Tanabashi, K. Olive, K. Honscheid, P.R. Burchat, R.E. Shrock, S. Eidelman, R.H. Schindler, A. Gurtu, K. Hikasa, G. Conforto, R.L. Workman, C. Grab, and C. Amsler: Phys. Rev., D54, 1 (1996).

Battistoni, G., C. Forti, and J. Ranft: Astropart. Phys., 3, p. 157 (1995b).

Berger, M.J., and S.M. Seltzer: Tables of Energy Losses and Ranges of Electrons and Positrons, NASA Report, NASA-SP-3012 (Washington DC (1964).

Bethe, H.A.: Handbuch der Physik (Springer, Berlin), 24/1, p. 518 (1933).

Bethe, H.A., and W. Heitler: Proc. Roy. Soc., London, Ser. A 146, p. 83 (1934).

Brasseur, Guy, and Susan Solomon: Aeronomy of the Model Atmosphere, D. Reidel Publishing Company, Dordrecht / Boston / Lancaster (1986).

Capella, A., U. Sukhatme, C.-I. Tan, and J. Tran Thanh Van: Physics Reports, 236, p. 225 (1994).

Carmichael, H., and M. Bercovitch: Can. J. Phys., 47, No. 19, p. 2073 (1969).

Caso, C., G. Conforto, A. Gurtu, M. Aguilar-Benitze, C. Amsler, R.M. Barnett, P.R. Burchat, C.D. Carone, O. Dahl, M. Doser, S. Eidelman, J.L. Feng, M. Goodman, C. Grab, D.E. Groom, K. Hagiwara, K.G. Hayes, J.J. Hernàndez, K. Hikasa, K. Honscheid, F. James, M.L. Mangano, A.V. Mano-

har, K. Mönig, H. Murayama, K. Nakamura, K.A. Olive, A. Piepke, M. Roos, R.H. Schindler, R.E. Shrock, M. Tanabashi, N.A. Törnqvist, T.G. Trippe, P. Vogel, C.G. Wohl, R.L. Workman, W.-M. Yao: Europ. Phys. J., C3, p. 1 (1998).

Chapman, S.: Proc. Roy. Soc. (London), 43, p. 483 (1931).

Cocconi, Giuseppe: Phys. Rev., 111, p. 1699 (1958).

Cocconi, G.: In Handbuch der Physik, XLVI/1, p. 215. (S. Flügge, ed.). Springer Verlag Berlin (1961).

Cocconi, G., L.J. Koester, and D.H. Perkins: Lawrence Radiation Laboratory, UCID 1444, p. 1 (1961).

Cocconi, G.: Nucl. Phys., 28 B, p. 341 (1971).

Cole, A.E., and A.J. Kantor: Air Force Reference Atmosphere, AFGL-TR-78-0051 (1978).

Cooke, D.J., J.E. Humble, M.A. Shea, D.F. Smart, N. Lund, I.L. Rasmussen, B. Byrnak, P. Goret, N. Petrou: Nuovo Cimento,14 C, N. 3, p. 213 (1991).

Crispin, A., and G.N. Fowler: Rev. Mod. Phys., 42, p. 290 (1970).

Dorman, L.I., R.T. Gushchina, M.A. Shea, and D.F. Smart: Nauka, Moscow (1972).

Dorman, L.I.: Cosmic Rays. Variations and Space Explorations. North-Holland Publishing Company, Amsterdam, Oxford; American Elsevier Publishing Company, inc., New York (1974).

Fano, U.: Ann. Rev. Nucl. Sci., 13, p. 1 (1963).

Feynman, R.P.: Third International Conference on High-Energy Collisions (Stony Brook, N.Y.), p. 238 (1996a).

Feynman, R.P.: Phys. Rev. Lett., 23, p. 1415 (1969b).

Fitzmaurice, John A.: Applied Optics, 3, p. 640 (1964).

Flückiger, E.O.: Air Force Geophysical Laboratory, Hanscom AFB, Massachusetts 01731. Report AFGL-TR-82-0177, Environmental Research Paper No. 783 (1982).

Forbush, S.E.: Phys. Rev., 51, p. 1108 (1937).

Forbush, S.E.: Phys. Rev., 54, p. 975 (1938).

Forbush, S.E.: Jour. Geophys. Res., 63, p. 651 (1958).

Gaisser, Thomas K.: Cosmic Ray and Particle Physics. Cambridge University Press (1990).

Gaisser, T.K., U.P. Sukhatme, and G.B. Yodh: Phys. Rev., D 36, p. 1350 (1987).

Galbraith, W.: Extensive Air Showers, Butterworths Scientific Publisjers, London (1958).

Grieder, P.K.F.: Nuovo Cimento, 7 A, p. 867 (1972).

Grieder, P.K.F.: Rivista del Nuovo Cimento, 7, p. 1 (1977).

Grieder, P.K.F.: Proc. of the Japan-U.S. Seminar on Cosmic Ray Muon and Neutrino Phyysics/Astrophysics Using Deep Underground/ Underwater Detectors, June 1986, Tokyo, Japan, eds. Y. Ohashi and V.Z. Peterson. Institute for Cosmic Ray Research, University of Tokyo, p. 183 (1986).

Gross, B: Zeitschr. f. Physik, 83, p. 214 (1933).

Hernàndez, J.J., J. Stone, F.C. Porter, R.J. Morrison, L. Montanet, K. Gieselmann, M. Aguilar-Benitze, G. Conforto, C. Caso, M. Roos, N.A. Törnqvist, K.G. Hayes, K.R. Schubert, G. Höhler, K. Hagiwara, K. Hikasa, S. Kawabata, R.M. Barnett, J.J. Eastman, D.E. Groom, G.R. Lynch, A. Rittenberg, M. Suzuki, T.G. Trippe, C.G. Wohl, G.P. Yost, B. Armstrong, G.S. Wagman, K.A. Olive, R.E. Shrock, R.H. Schindler, R.A. Eichler: Phys. Lett., 239, p. 1 (1990).

Honda, M., M. Nagano, S. Tonwar, K. Kasahara, T. Hara, N. Hayashida, Y. Matsubara, M. Teshima, and S. Yoshida: Phys. Rev. Lett., 70, p. 525 (1993).

Jánossy, Ludwig: Zeitschr. f. Physik, 101, p. 129 (1936) Iin German).

Jánossy, L., and A.B.C. Lovell: Nature, 142, p. 716 (1938).

Kaidalov, A.B., K.A. Ter-Martirosyan, and Yu.M. Shabelsky: Yad. Fiz. 43, p. 1282 (1986).

Kalmykov, N.N., and S.S. Ostapchenko: Phys. At. Nucl., 56, p. 346 (1993).

Kalmykov, N.N., S.S. Ostapchenko, and A.I. Pavlov: Nucl. Phys. B (Proc. Suppl.) 52B, p. 17 (1997).

Kamata, K., and J. Nishimura: Progr. Theor. Phys., Suppl 6, p. 93 (1958).

Katz, L., P. Meyer, and J.A. Simpson: Nuovo Cimento 8, Suppl. II, p. 277 (1958).

Khristiansen, G.B.: Cosmic Rays of Superhigh Energies. Verlag Karl Thiemig, München (1980).

Kohlhörster, W., I. Matthes, and E. Weber: Naturwissenschaften, 26, p. 576 (1938) (in German).

Kraybill, H.L.: Phys. Rev., 77, p. 410 (1950).

Kraybill, H.L.: Phys. Rev., 93, p. 1362 (1954).

Kunow, H.: Proc. of the First Soltip Symposium, Liblice, Czechoslovakia 1991, p. 165. Fischer, S., and M. Vandas editors. Published by the Astronomical Institute of Czechoslovakia Academy of Sciences, Prague, Czechoslovakia (1992).

Longair, Malcolm, S.: High Energy Astrophysics. Cambridge University Press, Cambridge, 2nd. ed. (1992).

McCracken, K.G., U.R. Rao, and M.A. Shea: Massachusetts Institute of Technology, Technical Report No. 77, NYO-2670 (1962).

McCracken, K.G., U.R. Rao, B.C. Fowler, M.A. Shea, and D.F. Smart: Cosmic Ray Tables, IQSY Instruction Manual No. 10 (1965).

McCracken, K.G., U.R. Rao, B.C. Fowler, M.A. Shea, and D.F. Smart: Cosmic Rays, Annals of the IQSY, 1, edited by C.M. Minnis (MIT Press, Cambridge, MA., p. 198 (1968).

Mielke, H.H., M. Föller, J. Engler, and J. Knapp: J. Phys., G 20, p. 637 (1994).

Moraal, H.: Nucl. Phys. B, (Proc. Suppl.) 33A,B, p. 161 (ed. P.K.F. Grieder) (1993).

Neher, H.V.: Progr. in Elementary Particle and Cosmic Ray Physics, 1, p. 243 (ed. J.G. Wilson, North Holland Publ. Co., Amsterdam) (1952).

Nishimura, J.: Handbuch der Physik, 46/2, p. 1, Springer Verlag, Berlin (1967).

Parker, E.N.: Interplanetary Dynamical Processes. Interscience Monographs and Texts in Physics and Astronomy. J. Wiley and Sons N.Y. and London (1963).

Pfotzer, Georg: Zeitschr. f. Physik, 102, p. 23 (1936a).

Pfotzer, Georg: Zeitschr. f. Physik, 102, p. 41 (1936b).

Ranft, J.: Phys. Rev., D51, p. 64 (1995).

Rossi, B., and K. Greisen: Rev. Mod. Phys., 13, p. 240 (1941).

Rossi, B.: Rev. Mod. Phys., 20, p. 537 (1948).

Rossi, B.: High Energy Particles, Prentice-Hall, Inc., Englewood Cliffs, NJ, (1952).

Rossi, Bruno and Stanislaw Olbert: Introduction to the Physics of Space. McGraw Hill Book Co., New York (1970).

Sandström, A.E.: Cosmic Ray Physics. North Holland Publishing Co., Amsterdam (1965).

Shea, M.A., D.F. Smart, and J.R. McCall: Can. J. Phys., 46, p. S1098 (1968).

Shea, M.A., D.F. Smart: Acta Phys. Acad. Sci. Hung., 29, Suppl. 2, p. 533 (ed. A. Somogyi) (1970).

Sokolsky, Pierre: Introduction to Ultrahigh Energy Cosmic Ray Physics, Frontiers in Physics, Vol. 76, Addison-Weskey Publishing Co., New York (1989).

Stanev, Todor: PICRC, AIP Conf. Proc., 516, Brenda L. Dingus, David B. Kieda and Michael H. Salamon eds., American Institute of Physics (2000).

Sternheimer, R.M, S.M. Seltzer, and M.R. Berger: Atomic and Nuclear Data Tables, 30, p. 261 (1984).

Störmer, C.: Zeitschr. f. Astrophys., 1, p. 237 (1930).

Swider, Jr. William: Planet. Space Sci., 12, p. 761 (1964).

Swider, W., and M.E. Gardner: Environmental Research Papers No 272, Air Force Cambridge Research, Bedford, MA (1967).

Tsai, Y.S.: Rev. Mod. Phys., 46, p 815 (1974).

Yodh, G.B., S.C. Tonwar, T.K. Gaisser, and R.W. Ellsworth: Phys. Rev., D 27, p. 1183 (1983).

This Page Intentionally Left Blank

Chapter 2

Cosmic Rays in the Atmosphere

2.1 Introduction

This chapter includes data and results of cosmic ray experiments carried out at altitudes higher than sea level. Included are measurements performed on the ground at mountain levels covering altitudes between a few hundred meters and 6500 m above sea level (Qomolangma, foot of Mt. Everest, Tibet) as well as results of aircraft and balloon-borne experiments that cover essentially the entire atmosphere to its very fringes of just 2 or 3 g/cm^2 of residual atmosphere.

The high altitude data are also the backbone for the determination of the primary cosmic ray spectrum and mass composition over a wide range of energies that are complemented in the low energy domain by satellite measurements, and air shower data at high and ultra high energies. Spectra and composition of the primary radiation are presented in Chapter 5.

One should bear in mind that in view of the rapidly falling intensity of the cosmic radiation with increasing energy and because of the limited size and duration of aircraft and balloon-borne experiments the statistics of the data, particularly at higher energies and for the less abundant components of the radiation, are subject to poor statistics. Nevertheless, up to date a large number of experiments had been carried out and a remarkable stock of cosmic ray data from all levels in the atmosphere has become available over the years that is summarized in this chapter.

2.2 Charged Hadrons

2.2.1 Introduction

Hadron fluxes and energy spectra have been measured in the atmosphere at mountain altitudes up to 6500 m, with instruments on board of aircraft up to about 10 km and with balloon-borne equipment almost to the top of the atmosphere.

In principle energy spectra of hadrons can be measured with magnetic spectrometers, mass spectrometers, calorimeters or with range spectrometers. In order to separate protons from pions, two parameters must be known, e.g., momentum and energy or mass and velocity. This can be achieved in various ways by combining instruments such as a magnetic spectrometer with a calorimeter, or a mass spectrometer with a time-of-flight measurement. Early results have been obtained with the nuclear emulsion technique. The highest energies have been recorded with so-called emulsion chambers. These consist of layers of X-ray films, converter material, and nuclear emulsion. Integral flux measurements can easily be made with counter telescopes.

Singly charged hadrons identified by strong interactions can in principle be primary or secondary protons, charged pions, kaons or hyperons, deuterium, or tritium. Frequently only protons and pions are considered at greater atmospheric depth. A separation of protons and pions can be made by measuring the charged to neutral ratio. The ratio of secondary protons to neutrons must be equal to or greater than unity for reasons discussed below.

Low energy measurements are subject to solar modulation and depend on geomagnetic latitude. Some authors have not taken these effects into account for the interpretation of their data.

Various books and reviews have appeared in the past that describe the gross features of the cosmic radiation in the atmosphere and summarize the principal results (Rossi, 1964; Schopper et al., 1967; Allkofer, 1967 and 1975; Daniel and Stephens, 1974; Sokolsky, 1989).

2.2.2 Flux Measurements and Intensities

In principle the total flux of hadrons or of any single component can be obtained by integrating the energy or momentum spectrum. There are few recent data on general flux measurements in the atmosphere because the present interest is focused either on the exploration of the composition of the

Table 2.1: Vertical Intensity of Protons at Different Altitudes. (Schopper et al. 1967)

Energy [MeV]	Momentum [GeV/c]	Intensity $[cm^{-2}s^{-1}sr^{-1}]$	Altitude [m]	Reference
80 - 430	-	$(8.06 \pm 0.12) \cdot 10^{-4}$	3200	Kocharian (1955)
430 - 1220	-	$(6.06 \pm 0.13) \cdot 10^{-4}$		
> 80	-	$(1.69 \pm 0.02) \cdot 10^{-3}$		
> 1220	-	$2.81 \cdot 10^{-4}$		
50 - 370	-	$9.6 \cdot 10^{-4}$	3400	Whittemore (1952)
> 10000	-	$1.1 \cdot 10^{-5}$	2800	Hazen (1949)
-	0.37 - 1.04	$(1.215 \pm 0.03) \cdot 10^{-3}$	3250	Meshkowskii (1958)
-	0.59 - 0.77	$(9.6 \pm 1.2) \cdot 10^{-5}$	2700	Rosen (1954)
-	0.77 - 0.93	$(7.9 \pm 1.2) \cdot 10^{-5}$		

primary radiation, mostly with balloon or space bound instruments, or on the study of ultrahigh energy interactions of primary or secondary cosmic rays with well defined targets. Most of the early data were obtained with simple counter telescopes that were faced with the problem of particle identification.

Table 2.1 shows flux data of measurements compiled by Schopper et al. (1967). Additional data which give the percentage of protons to the total penetrating component, i.e., essentially protons, pions and neutrons combined, are shown in Table 2.2. The absolute intensity of single hadrons of energies $\geq$1 TeV at 3250 m is $(1.25 \pm 0.04) \cdot 10^{-5}$ $cm^{-2}s^{-1}sr^{-1}$ (Szaryan et al., 1973). The altitude dependence of the proton flux for $E \geq 1$ GeV was compiled by Schopper et al. (1967) and is shown in Fig. 2.1.

At an altitude of 2500 m (760 g/cm^2) the single hadron intensity in the high energy region has been measured by Berdzenishvili et al. (1981). Their results are given in Table 2.3.

At 3230 m the integral intensity of hadrons can be described by the expression

$$J(> E) = 3 \cdot 10^{-7} \cdot E^{-2.0} \quad [cm^{-2}s^{-1}sr^{-1}] , \tag{2.1}$$

with E in GeV (Jones et al., 1970).

Recent measurements of the hadron intensities at various altitudes had been carried out by Lu et al. (1997), using emulsion chambers. These authors made measurements at Qomolangma (the foot of Mt. Everest, 6500 m), at Mt. Kanbala (5450 m), Pamir (4370 m), Yangbajing (4300 m), Mt.

Table 2.2: Ratio of Protons to All Penetrating Hadrons (p, n, π). (Schopper et al., 1967).

Energy [MeV]	Momentum [GeV/c]	Proton content %	Altitude [m]	Reference
-	$0.5 \leq p \leq 50$	16 ± 3	2960	Allkofer (1964)
-	$0.5 \leq p \leq 20$	19.7 ± 3	2960	Allkofer (1964)
-	$0.2 \leq p \leq 20$	20.8 ± 3	2960	Allkofer (1964)
>400	-	7.9	3100	Gregory (1951)
-	$0.4 \leq p \leq 14$	12	3200	Kocharian (1956a,b)
-	$0.34 \leq p \leq 2.5$	14 ± 1	3250	Vaisenberg (1957)
-	$9.3 \leq p \leq 17$	4.8	3250	Alikhanian (1957)
-	≥ 0.3	19 ± 2	3400	Whittemore (1952)
-	$0.7 \leq p \leq 2.0$	20 ± 2	3400	Miller (1954)
> 300	-	12	3500	Lovati (1954)
-	> 0.31	11 ± 1	3650	Becker (1955)
-	$0.5 \leq p \leq 50$	24 ± 3	5200	Allkofer (1967)
-	$1 \leq p \leq 5$	50 ± 10	9000	Baradzei (1959)

Table 2.3: Hadron Intensities at 2500 m a.s.l.. (Berdzenishvili et al., 1981)

Energy Range	Intensity $[\mathrm{cm}^{-2}\mathrm{s}^{-1}\mathrm{sr}^{-1}]$
$I(E \geq 300$ GeV)	$(3.06 \pm 0.28) \cdot 10^{-8}$
$I(E \geq 1$ TeV)	$(3.33 \pm 0.83) \cdot 10^{-9}$
$I(E \geq 3$ TeV)	$(3.89 \pm 0.14) \cdot 10^{-10}$
$I(E \geq 5$ TeV)	$(8.3 \pm 5.5) \cdot 10^{-11}$

Fuji (3200 m) and Yunnan Station (3200 m). They found that the vertical intensity, I_h, at an atmospheric depth of 606 g/cm^2 and for energies $\geq$5 TeV is

$$I_h(E_h \geq 5\mathrm{TeV}) = (2.69 \pm 0.25) \cdot 10^{-10} \ [\mathrm{cm}^{-2}\,\mathrm{s}^{-1}\,\mathrm{sr}^{-1}] \qquad (2.2)$$

The altitude dependence of the hadron intensity is plotted in Fig. 2.2. We have also included some earlier data from the work of Shibuya (1987). In his paper a extensive list of earlier emulsion chamber measurements is given. From Fig. 2.2 one obtains for the attenuation of the hadronic component in the atmosphere the expression

$$I_h(E_h \geq 5\text{TeV}) \propto \exp(-X/\Lambda_{abs}) \tag{2.3}$$

where X is the atmospheric depth [g/cm^2] and $\Lambda_{abs} = 107.5 \pm 3.4$ g/cm^2.

It also follows from this work that the integral spectrum of hadrons of energy $\geq$5 TeV can be represented by a simple power law of the form $E^{-\gamma}$, with $\gamma = 1.85 \pm 0.2$.

Recently proton and helium intensities as a function of atmospheric depth had been measured with balloon-borne superconducting magnetic spectrometers. Circella et al. (1999) using the MASS instrument from Fort Sumner, NM (USA) at a vertical geomagnetic cutoff rigidity of 4.5 GV obtained the depth - intensity distribution for protons and helium nuclei in the kinetic energy bands $4.1 \leq E \leq 14.1$ GeV and $1.7 \leq E \leq 9.1$ GeV, respectively, in the upper atmosphere between about 5 and 380 g/cm^2 for protons and 5 and 120 g/cm^2 for helium. Their results are shown in Fig. 2.3.

More detailed data for protons are presented by Francke et al. (1999) from measurements with the CAPRICE94 instrument, flown from Lynn Lake (Canada) at a geomagnetic cutoff of about 0.5 GV. These authors recorded depth - intensity distributions of protons for eight energy windows that are illustrated in Fig. 2.4.

2.2.3 Energy Spectra

Early Measurements

Energy or momentum spectra have been measured at mountain altitudes from 2000 m up to nearly 5000 m. Many experiments were aimed at studying high energy hadronic interactions and energy spectra of the incident hadrons were by-products. Results of early measurements can be misleading because sometimes the total hadronic component had been interpreted as protons.

For momenta $\leq$ 2 GeV/c the proton spectrum has been measured by Kocharian (1955, 1956a, 1956b) at an altitude of 3200 m. The results are shown in Fig. 2.5. The apparatus consisted of a magnetic spectrometer, combined with a calorimeter. With an improved instrument measurements had been extended to 100 GeV. The results are shown in Fig. 2.6 (Kocharian, 1959). A compilation of proton energy spectra at a depth of 650 g/cm^2 has been made by Flückiger (1976a and 1976b). The experimental results have been compared with theoretical data from Monte Carlo calculations for different interaction mean free paths, ranging from 65 to 75 g/cm^2 for

nucleons, and from 75 to 120 g/cm^2 for pions. The data are presented in Fig. 2.7.

Other Monte Carlo calculations had been carried out to determine the energy spectra of protons at atmospheric depths ranging from $40 \leq X \leq 650$ g/cm^2 and for the energy range $0.05 \leq E \leq 100$ GeV (Flückiger, 1977 and 1978).

Higher energy regions of the spectrum of charged hadrons had been investigated by Nam et al. (1970). The apparatus consisted of an ionization calorimeter with lead absorbers, located at an altitude of 3340 m. It covered an energy range from 350 to 50000 GeV. The results are shown in Fig. 2.8. Also shown in the same figure are the measurements of Grigorov and Shestoperov (1967), Babayan et al. (1962) and Hayakawa et al. (1964).

In the range $1 \leq E \leq 100$ MeV energy spectra of protons have been measured at altitudes between 16 and 18 km at different geomagnetic cutoffs (Bogomolov et al., 1979). Fig. 2.9 shows the experimental spectra together with calculations of Aitbaev et al. (1981).

The energy spectrum of unaccompanied hadrons has been investigated by Siohan et al. (1978) in the energy range $100 \leq E \leq 10000$ GeV at an atmospheric depth of 730 g/cm^2 ($h = 2900$ m), using a calorimeter. Unaccompanied hadrons include primary protons that have traversed the atmosphere without undergoing strong interactions as well as secondary hadrons (protons, neutrons, pions, etc.) whose accompaniment has died out before reaching the observation level. It is unlikely that unaccompanied secondary hadrons are surviving fragments of primary nuclei because the energy of the latter is generally too large and cascade products are usually associated.

After several generations of collisions, one expects the intensity of secondary neutrons, I_n, to approach the intensity of secondary protons, I_p, because of charge exchange. However, the average number of interactions suffered by secondary hadrons that are unaccompanied at mountain altitudes is likely to be small and equilibrium will not be reached. One expects therefore that $I_n \leq I_p$ (see also section 1.3). A set of data points of the differential and integral energy spectra measured by Siohan et al. (1978) is given in Table 2.4. Plots of the differential and integral spectra are given in Figs. 2.10 and 2.11, respectively.

The zenith angle distribution of charged hadrons was studied by Siohan et al. (1978) for $0.9 \leq cos(\theta) \leq 0.1$ and $E \geq 22$ GeV. The results can be fitted with the expression

Table 2.4: Intensity of Single Charged Hadrons at an Altitude of 2900 m a.s.l. (730 g/cm^2). (Siohan et al., 1978)

Energy [GeV]	Events in Bin	Differential Intensity [cm^{-2}s^{-1}sr^{-1}GeV^{-1}]	Integral Intensity [cm^{-2}s^{-1}sr^{-1}]
107 - 128	219	$7.81 \pm 0.53 \cdot 10^{-9}$	$6.31 \pm 0.24 \cdot 10^{-7}$
128 - 149	160	$5.62 \pm 0.44 \cdot 10^{-9}$	
149 - 181	135	$3.12 \pm 0.27 \cdot 10^{-9}$	
181 - 225	121	$2.07 \pm 0.19 \cdot 10^{-9}$	
225 - 269	261	$1.07 \pm 0.07 \cdot 10^{-9}$	$1.58 \pm 0.06 \cdot 10^{-7}$
269 - 314	179	$7.26 \pm 0.54 \cdot 10^{-10}$	
314 - 381	140	$3.74 \pm 0.32 \cdot 10^{-10}$	
381 - 473	99	$1.96 \pm 0.20 \cdot 10^{-10}$	
473 - 542	105	$1.41 \pm 0.14 \cdot 10^{-10}$	$3.52 \pm 0.18 \cdot 10^{-8}$
542 - 659	99	$7.90 \pm 0.80 \cdot 10^{-11}$	
659 - 897	95	$3.70 \pm 0.40 \cdot 10^{-11}$	
871 - 1020	235	$1.80 \pm 0.12 \cdot 10^{-11}$	
1020 - 1170	147	$1.12 \pm 0.09 \cdot 10^{-12}$	
1170 - 1396	141	$7.15 \pm 0.60 \cdot 10^{-12}$	
1396 - 1623	87	$4.39 \pm 0.47 \cdot 10^{-12}$	
1623 - 1851	44	$2.21 \pm 0.32 \cdot 10^{-12}$	$1.90 \pm 0.15 \cdot 10^{-9}$
1851 - 2233	47	$1.41 \pm 0.20 \cdot 10^{-12}$	
2233 - 2616	28	$8.37 \pm 1.60 \cdot 10^{-13}$	$8.5 \pm 1.0 \cdot 10^{-10}$
2616 - 3000	17	$5.06 \pm 1.20 \cdot 10^{-13}$	
3001 - 3500	16	$2.64 \pm 0.66 \cdot 10^{-13}$	$4.0 \pm 0.6 \cdot 10^{-10}$
3500 - 4000	8	$1.32 \pm 0.46 \cdot 10^{-13}$	
4000 - 5000	9	$7.40 \pm 2.50 \cdot 10^{-14}$	$2.1 \pm 0.4 \cdot 10^{-10}$
5000 - 6000	7	$5.80 \pm 2.20 \cdot 10^{-14}$	
6000 - 8000	6	$2.50 \pm 1.00 \cdot 10^{-14}$	$7.4 \pm 2.5 \cdot 10^{-11}$
8000 - 10000	1	$4.10 \pm 4.10 \cdot 10^{-15}$	$2.5 \pm 1.4 \cdot 10^{-11}$
10000 - 15000	2	$3.30 \pm 2.30 \cdot 10^{-15}$	$1.6 \pm 1.2 \cdot 10^{-11}$
>15000	0	-	-

$$f(\theta) = A \cos^n(\theta) , \tag{2.4}$$

where $n = 7.3 \pm 0.5$ and A is a constant.

Low energy protons have been recorded with an instrument consisting of a magnetic spectrometer combined with a time of flight system by Barber

Table 2.5: Proton Intensities at an Atmospheric Depth of 747 g/cm^2 (2750 m a.s.l.). (Barber et al., 1980)

Velocity Interval	Momentum Interval [GeV/c]	p_{ave} [GeV/c]	N_p	Differential Intensity $[(\text{cm}^2\,\text{s}\,\text{sr}\,(\text{GeV/c}))^{-1}]$
$0.20 < \beta \leq 0.35$	0.20 - 0.35	0.31	113	$1.49 \pm 1.12 \cdot 10^{-3}$*
$0.35 < \beta \leq 0.50$	0.35 - 0.53	0.44	518	$9.37 \pm 2.25 \cdot 10^{-4}$*
$0.50 < \beta \leq 0.60$	0.54 - 0.70	0.60	646	$1.14 \pm 0.18 \cdot 10^{-3}$*
$0.60 < \beta \leq 0.65$	0.70 - 0.80	0.73	399	$1.14 \pm 0.09 \cdot 10^{-3}$
$0.65 < \beta \leq 0.70$	0.80 - 0.92	0.84	547	$1.21 \pm 0.09 \cdot 10^{-3}$
$0.70 < \beta \leq 0.75$	0.92 - 1.06	0.96	564	$9.45 \pm 0.66 \cdot 10^{-4}$
$0.75 < \beta \leq 0.80$	1.06 - 1.26	1.12	541	$6.58 \pm 0.47 \cdot 10^{-4}$
$0.80 < \beta \leq 0.85$	1.26 - 1.51	1.32	585	$4.87 \pm 0.36 \cdot 10^{-4}$
$0.85 < \beta \leq 0.90$	1.51 - 1.94	1.63	537	$2.68 \pm 0.23 \cdot 10^{-4}$
$0.90 < \beta \leq 0.95$	1.94 - 2.86	2.05	320	$1.22 \pm 0.21 \cdot 10^{-4}$

$\beta = v/c$, p_{ave} average momentum; N_p number of observed particles.
* corrected for magnetic-field decay effects.

(1980). Fig. 2.12 shows the differential proton spectrum at 747 g/cm^2 (2750 m) in the momentum range $0.3 \leq p \leq 2$ GeV/c. The differential intensities are listed in Table 2.5.

In the energy range $0.7 \leq E \leq 3$ TeV the integral spectrum has been determined at a level of 3250 m by Szaryan et al (1973). According to these authors it can be represented by

$$J(\geq E) = (1.25 \pm 0.09) \cdot 10^{-7} \cdot (100/E)^{3.0 \pm 0.06} \quad [\text{cm}^{-2}\text{s}^{-1}\text{sr}^{-1}]\,, \qquad (2.5)$$

with E in GeV.

The energy spectrum of vertical hadrons has been measured by the Pamir Collaboration (1979a) in the energy range $5 \leq E \leq 25$ TeV, at an altitude of 4370 m (596 g/cm^2), using an emulsion chamber. Fig. 2.13 shows their results. The integral intensity can be approximated by

$$J(\geq E) = (4.2 \pm 1.0) \cdot 10^{-9} \cdot E^{-2.0 \pm 0.2} \quad [\text{cm}^{-2}\text{s}^{-1}\text{sr}^{-1}]\,, \qquad (2.6)$$

with E in TeV.

The differential angular distribution of hadrons is shown in Fig. 2.14 for the regions $\theta < 25°$ and $\theta \geq 25°$, separately (Pamir Collaboration 1979a). The distribution can be represented by

$$I(\theta, E) = A\cos^{(n+1)}(\theta) , \tag{2.7}$$

where

$$n = 5.7 \pm 0.6 \text{ for } 6 \leq E \leq 10 \text{ TeV}$$
$$n = 6.3 \pm 0.8 \text{ for } E \geq 10 \text{ TeV}$$

The energy spectrum integrated over the solid angle for $\theta \leq 25°$ and energies up to about 100 TeV at an altitude of 4370 m is shown in Fig. 2.15 (Pamir Collaboration 1979b). The hadron energy, E_h, is determined from the energy deposited by the associated electromagnetic cascades, ΣE_γ, in the emulsion chamber. The relation between the two energy deposits is given by the empirical expression

$$E_h \simeq (4 - 5)\Sigma E_\gamma . \tag{2.8}$$

The differential momentum spectrum of charged hadrons in the momentum range $0.5 \leq p \leq 10$ GeV has been measured with a magnetic spectrometer at an altitude of 5200 m by Allkofer and Kraft (1965). It is shown in Fig. 2.16. Since there was no particle discrimination, the muonic component was separated on the assumption that the charge ratio is constant, i.e., $K_\mu = N_{\mu^+}/N_{\mu^-} = 1.25$. The positively charged hadrons ($p + \pi^+$) have been obtained from the relation

$$I_{\mu^+} = I_+ - K_\mu I_- , \tag{2.9}$$

where I_{μ^+} represents the intensity of positive muons and I_+ and I_- the intensity of positively and negatively charged particles, respectively.

In the momentum range $0.3 \leq p \leq 6$ GeV/c Baradzei et al. (1959) have measured the charged component (p, π, μ) at an altitude of 9000 m with a cloud chamber spectrometer in combination with a range telescope having a 9 cm thick lead absorber, using also the charge ratio relation. Since the cutoff momentum for the muons was $7.8 \cdot 10^8$ eV/c, corresponding to 9 cm of lead, particles below this momentum could only be protons and positive pions. Figs. 2.17 and 2.18 show the observed momentum spectra of all negatively (π^-, μ^-) and positively charged particles (p, π^+, μ^+), respectively. The dashed curve represents positively charged hadrons (p, π^+) only.

An emulsion chamber experiment has been carried out in an aircraft at a mean atmospheric depth of 260 g/cm^2 (Takahashi, 1978). The results give

the integral energy spectrum in the range $1 \leq E \leq 40$ TeV. The latter is shown in Fig. 2.19.

A compilation of experimental hadron energy spectra obtained by various groups has been made by Ellsworth et al. (1970). Individual measurements at a particular altitude differ from each other by as much as a factor of 10. Table 2.6 summarizes the data. Integral fluxes are given for atmospheric depths of 455 g/cm^2 (Ellsworth et al., 1970), 550 g/cm^2 (Kamata et al., 1967), 606 g/cm^2 (Jones et al., 1967), 686 g/cm^2 (Dobrotin, 1965), 698 g/cm^2 (Jones et al., 1972), and 730 g/cm^2 (Akashi et al., 1965a, 1965b, 1965c, and 1968).

Recent Measurements

A recent ground level measurement of the low energy proton spectrum at low altitude (600 m a.s.l., 945 g/cm^2) had been carried out by Golden et al. (1995) at Prince Albert, Saskatchewan, Canada ($P_c \approx 1$ GV) , with the Matter Antimatter Superconducting magnetic Spectrometer (MASS). The data are presented in Table 2.7 and Fig. 2.20 together with earlier sea level measurements of other authors that had been corrected for absorption to 945 g/cm^2 and a power law fit.

The EAS-TOP collaboration has constructed an unaccompanied hadron spectrum from the data of their hadron calorimeter on top of Gran Sasso, at an altitude of 2200 m a.s.l. (820 g/cm^2) (Castellina, 2000; Aglietta et al., 2001). This spectrum is shown in Fig. 2.21 and the most recent data from this experiment are listed in Table 2.8. The near sea level spectrum (110 m a.s.l.) of Mielke et al. (1994) is also shown in Fig. 2.21 for comparison.

2.2.4 Ratio of Neutral to Charged Hadrons

In some calorimeter experiments provisions were made to determine the ratio of neutral hadrons , N_n,(neutrons) to charged hadrons, N_c, (protons and pions). The ratios are given for different energy ranges and altitudes. Le Coultre (1971) gives for the ratio N_n/N_c a value of 0.73 ± 0.03 for $E \geq 12$ GeV and 0.64 ± 0.04 for $E \geq 15$ GeV, at an atmospheric depth of 967 g/cm^2. At a depth of 800 g/cm^2 and for an energy range $20 \leq E \leq 40$ GeV, Lal et al. (1971) obtained for $N_n/N_c = 0.66 \pm 0.07$. The data of Siohan et al. (1978) obtained at 2900 m are given in Table 2.9.

Fig. 2.22 shows the integral energy dependence of the ratio N_n/N_c for an energy range from 100 to about 3000 GeV from the work of Siohan et al. (1978) and McFall et al. (1979) at 730 g cm^{-2}. At an altitude of 3250 m and

Table 2.6: Summary of Hadron Intensity Measurements. (Ellsworth et al. 1970)

Energy [GeV]	Vert. Intensity $[cm^{-2}s^{-1}sr^{-1}]$	Atmospheric Depth	Reference
150	$8.3 \cdot 10^{-6}$		
300	$4.2 \cdot 10^{-6}$		
400	$2.5 \cdot 10^{-6}$		Ellsworth et al.
500	$(1.4 \pm 0.3) \cdot 10^{-6}$	455	(1970)
900	$(4.2 \pm 0.1) \cdot 10^{-7}$		
2000	$(5.5 \pm 0.8) \cdot 10^{-8}$		
6000± 5000	$(1.4 \pm 0.6) \cdot 10^{-9}$		
9000± 4000	$(8 + 4) \cdot 10^{-10}$		
2000	$(9 + 1) \cdot 10^{-10}$		Akashi et al.
3000	$(4.3 \pm 0.8) \cdot 10^{-10}$		(1965a, b, c, 1968)
4000	$(3 + 1) \cdot 10^{-10}$	550	Kamata et al.
5000	$(1.8 \pm 0.5) \cdot 10^{-10}$		(1968)
7000	$(8 \pm 3) \cdot 10^{-11}$		
10000	$(5 \pm 2) \cdot 10^{-11}$		
>100	$1.05 \cdot 10^{-6}$		
100 - 300	$0.9 \cdot 10^{-6}$		
300 - 1000	$1.2 \cdot 10^{-7}$	606	Jones (1967)
1000 - 3000	$1.3 \cdot 10^{-8}$		
300	$(1.2 \pm 0.2) \cdot 10^{-7}$		
400	$(6 \pm 1) \cdot 10^{-8}$		
600	$(3 \pm 1) \cdot 10^{-8}$	686	Dobrotin (1965)
800	$(2 \pm 1) \cdot 10^{-8}$		
1000	$(8 \pm 5) \cdot 10^{-9}$		
500	$(7.2 \pm 0.7) \cdot 10^{-9}$		
1000	$(1.3 \pm 0.1) \cdot 10^{-9}$		
2000	$(1.4 \pm 0.2) \cdot 10^{-10}$		
3000	$(2.5 \pm 0.1) \cdot 10^{-11}$		Grigorov et al.
5000	$(8.3 \pm 1.4) \cdot 10^{-10}$	698	(1965a, 1968)
8000	$(4.4 \pm 1.7) \cdot 10^{-10}$		
11000	$(1.4 \pm 0.5) \cdot 10^{-10}$		
10000	$(5.6 \pm 2.2) \cdot 10^{-11}$		
30000	$(1.9 \pm 0.8) \cdot 10^{-11}$		
2500	$(8 \pm 4) \cdot 10^{-11}$		
4000	$(5 \pm 4) \cdot 10^{-11}$		
6000	$(3 \pm 1) \cdot 10^{-11}$	730	Akashi (1968)
12000	$(6 \pm 1) \cdot 10^{-12}$		
25000	$(1.5 \pm 0.5) \cdot 10^{-12}$		

a mean energy of 100 GeV, Greisen and Walker (1953) have determined the inverse ratio, N_c/N_n, by means of a magnetic spectrometer and obtained a

Table 2.7: Differential Intensity of Protons at 945 g cm^{-2}.
(Prince Albert, Canada, $P_c \approx 1$ GV, Golden et al., 1995)

Deflection Interval [c/GV]	Median Momentum [GeV/c]	Median Energy [GeV]	Number of Events	Momentum Intensity $cm^{-2}s^{-1}sr^{-1}(GeV/c)^{-1}$	Energy Intensity $cm^{-2}s^{-1}sr^{-1}(GeV/c)^{-1}$	Error
0.05 - 0.14	11.64	10.74	17	$6.73 \cdot 10^{-7}$	$6.75 \cdot 10^{-7}$	24%
0.14 - 0.20	5.96	5.10	20	$4.76 \cdot 10^{-6}$	$4.82 \cdot 10^{-6}$	22%
0.20 - 0.24	4.56	3.72	16	$9.81 \cdot 10^{-6}$	$1.00 \cdot 10^{-5}$	25%
0.24 - 0.27	3.93	3.10	18	$1.95 \cdot 10^{-5}$	$2.01 \cdot 10^{-5}$	24%

Table 2.8: Single Hadron Differential Intensities at 820 g cm^{-2}
Measured by EAS-TOP (Aglietta et al., 2001; Castellina, 2000).

Energy Range [GeV]	$< E >$ [GeV]	Intensity [cm^2 s^{-1} sr^{-1} GeV^{-1}]	σ_{int} [cm^2 s^{-1} sr^{-1} GeV^{-1}]
32 - 56	41	$1.2 \cdot 10^{-7}$	$1.2 \cdot 10^{-9}$
56 - 100	73	$2.7 \cdot 10^{-8}$	$2.4 \cdot 10^{-10}$
100 - 178	129	$6.0 \cdot 10^{-9}$	$6.3 \cdot 10^{-11}$
178 - 316	229	$1.4 \cdot 10^{-9}$	$2.1 \cdot 10^{-11}$
316 - 562	408	$2.9 \cdot 10^{-10}$	$6.6 \cdot 10^{-12}$
562 - 1000	726	$4.7 \cdot 10^{-11}$	$1.8 \cdot 10^{-12}$
1000 - 1778	1290	$9.2 \cdot 10^{-12}$	$5.6 \cdot 10^{-13}$
1778 - 3162	2295	$1.7 \cdot 10^{-12}$	$1.6 \cdot 10^{-13}$
3162 - 5623	4081	$2.6 \cdot 10^{-13}$	$4.6 \cdot 10^{-14}$
5623 - 10000	7257	$8.4 \cdot 10^{-14}$	$1.8 \cdot 10^{-14}$
10000 - 17783	12904	$1.4 \cdot 10^{-14}$	$4.9 \cdot 10^{-15}$
17783 - 31623	22945	$9.0 \cdot 10^{-15}$	$5.2 \cdot 10^{-15}$

value of 1.68 ± 0.16. Jones et al. (1972) have summarized the data of experiments carried out at altitudes around 3000 m together with data from other altitudes, normalized to 3000 m. The data are illustrated in Fig. 2.23. A compilation of the altitude dependence of the ratio N_n/N_c has been made by Aguirre (1972). It is shown in Fig. 2.24 together with theoretical calculations of Garraffo et al. (1973) and Bhattacharyya et al. (1979).

Table 2.9: Ratio of Neutral to Charged Hadrons at an Altitude of 2900 m. (Siohan et al., 1978)

E [GeV]	110 – 220	220 – 450	≥ 450
N_n/N_c	0.40 ± 0.04	0.34 ± 0.03	0.35 ± 0.03

2.2.5 Pions and Pion to Proton Ratio

Differential intensities of negatively charged secondary pions in the atmosphere were recorded with the MASS instrument at 5 g/cm^2 above Prince Albert, Canada, and at 5.8 g/cm^2 above Fort Sumner, NM (Grimani et al., 1995; Brunetti et al., 1996 and Codino et al., 1997). The data are shown in Fig. 2.25 together with the theoretical spectrum of Stephens (1981).

The ratios of charged pions, $N_{\pi^\pm}$, to nucleons, $N_{p,n}$, and to protons, N_p, have also been determined at different altitudes and for different energy ranges. At an atmospheric depth of 976 g/cm^2 the ratio $N_{\pi^\pm}/N_{p,n}$ was found to be 0.18 ± 0.03 for energies ≥ 15 GeV (Le Coultre et al., 1971). At 2000 m Vardumyan et al. (1979) obtained a value of $1.5^{+0.20}_{-0.25}$ for the ratio $N_{\pi^\pm}/N_p$, in the momentum range $70 \leq p \leq 350$ GeV/c. In this work an exponent, γ, of 1.6 ± 0.2 was found for the slope of the integral energy spectrum of the hadron component in the same momentum range.

At a mean energy of 100 GeV and an altitude of 3250 m the following ratios were obtained: $N_{\pi^\pm}/N_{p,n} = 0.22 \pm 0.08$ and $N_{\pi^\pm}/N_p = 0.38 \pm 0.13$ (Avakian and Pleshko, 1968; Farrow, 1957). At a similar level (3220 m), in the momentum range $10 \leq p \leq 20$ GeV/c, Xu Chun-Xian et al. (1978) have used a magnetic spectrometer in conjunction with a multi-plate cloud chamber and determined the following ratios: $N_{\pi^\pm}/N_{p,\pi^+} = 0.53 \pm 0.05$ and $N_{\pi^-}/N_p = 0.9$.

At 2000 m Bostandzhyan et al. (1979) found for the ratio $N_{\pi^\pm}/N_p$ at energies up to 600 GeV the value $1.50^{+0.15}_{-0.20}$. In the energy range $450 \leq E \leq 2000$ GeV, at an altitude of 2900 m, Siohan et al. (1978) obtained the ratios $N_{\pi^\pm}/N_{p,n} = 0.85 \pm 0.05$ and $N_p/N_{p,\pi^\pm} = 0.54 \pm 0.03$ for the unaccompanied hadron flux.

Theoretical curves for $N_{\pi^\pm}/N_p$ as a function of energy are shown in Fig. 2.26 for atmospheric depths of 500, 700 and 1000 g/cm^2, and for assumed pion interaction mean free paths of 100 g/cm^2, (Garraffo et al., 1973). The experimental data of Brooke et al. (1964) are included in this figure for comparison. Another set of data showing the energy dependence of the ratio

$N_{\pi^\pm}/N_p$ over the range $1 \leq E \leq 500$ GeV is presented in Fig. 2.27 (Jones et al., 1972, extended by the author). With the exception of the data of Brooke et al. (1964), that were obtained near sea level, the data are from mountain level experiments recorded at altitudes around 3000 m.

2.2.6 Theoretical Aspects and Calculations

Starting with the primary energy spectrum at the top of the atmosphere, many authors have attempted to calculate the energy spectra of hadrons at different depths in the atmosphere. The different calculations do not all agree with each other mostly because different interaction models had been used. In addition, part of the disagreement appears to be due to deviating assumptions concerning the model of the atmosphere and the interaction mean free paths of nucleons and pions that affect the results significantly. Moreover large variations of the low energy secondary components are due to solar modulation because the latter affects the primary spectrum (see Chapter 6, Section 6.3). Thus, the particular phase of the 11 year solar cycle must be considered and the proper modulation parameter must be used (see Chapter 7, Section 7.2).

A very detailed calculation of the secondary proton spectra in the atmosphere at shallow depths for solar minimum and maximum has recently been carried out by Papini et al. (1996). Their results are given in Table 2.10.

Other calculations of older date have been carried out by the following authors:

Aitbaev et al. (1981), Bhattacharyya (1979), Bhattacharyya et al. (1975, 1979), Boyadzhyan and Pirogov (1978), Brooke et al. (1964), Dardo et al. (1979), De Oliveira-Castro (1979), Erlykin and Kuzina (1979), Flückiger (1976a, 1976b, 1977 and 1978), Ghosh et al. (1980), Ghosh and Bhattacharyya (1979), Jabs (1972), Liland and Pilkhun (1973), Liland (1975, 1978), Mandritskaya et al. (1979), Masarik and Beer (1999), Mitoyan (1979), Roychoudhury et al. (1979), Sarkar et al. (1977), Vardumyan et al. (1979), Xu Chun-Xian et al. (1978), and Yekutieli (1972).

Table 2.10: Predicted Secondary Proton Intensities at 3, 5 and 10 g/cm^2 of Residual Atmosphere for Solar Minimum and Maximum. (Papini et al., 1996)

Kinetic Energy	Secondary Proton Intensity [$cm^{-2}s^{-1}sr^{-1}GeV^{-1}$]					
	Solar Minimum			Solar Maximum		
[GeV]	3 g cm^{-2}	5 g cm^{-2}	10 g cm^{-2}	3 g cm^{-2}	5 g cm^{-2}	10 g cm^{-2}
0.02	$2.58 \cdot 10^{-1}$	$3.06 \cdot 10^{-1}$	$3.67 \cdot 10^{-1}$	$1.23 \cdot 10^{-1}$	$1.47 \cdot 10^{-1}$	$1.77 \cdot 10^{-1}$
0.03	$2.24 \cdot 10^{-1}$	$2.83 \cdot 10^{-1}$	$3.60 \cdot 10^{-1}$	$1.07 \cdot 10^{-1}$	$1.36 \cdot 10^{-1}$	$1.74 \cdot 10^{-1}$
0.04	$2.03 \cdot 10^{-1}$	$2.69 \cdot 10^{-1}$	$3.58 \cdot 10^{-1}$	$9.68 \cdot 10^{-2}$	$1.29 \cdot 10^{-1}$	$1.72 \cdot 10^{-1}$
0.05	$1.88 \cdot 10^{-1}$	$2.57 \cdot 10^{-1}$	$3.54 \cdot 10^{-1}$	$8.96 \cdot 10^{-2}$	$1.23 \cdot 10^{-1}$	$1.70 \cdot 10^{-1}$
0.07	$1.61 \cdot 10^{-1}$	$2.29 \cdot 10^{-1}$	$3.32 \cdot 10^{-1}$	$7.66 \cdot 10^{-2}$	$1.09 \cdot 10^{-1}$	$1.59 \cdot 10^{-1}$
0.10	$1.23 \cdot 10^{-1}$	$1.81 \cdot 10^{-1}$	$2.78 \cdot 10^{-1}$	$5.83 \cdot 10^{-2}$	$8.60 \cdot 10^{-2}$	$1.32 \cdot 10^{-1}$
0.15	$7.40 \cdot 10^{-2}$	$1.13 \cdot 10^{-1}$	$1.83 \cdot 10^{-1}$	$3.48 \cdot 10^{-2}$	$5.30 \cdot 10^{-2}$	$8.64 \cdot 10^{-2}$
0.20	$4.49 \cdot 10^{-2}$	$6.96 \cdot 10^{-2}$	$1.18 \cdot 10^{-1}$	$2.09 \cdot 10^{-2}$	$3.24 \cdot 10^{-2}$	$5.48 \cdot 10^{-2}$
0.30	$1.87 \cdot 10^{-2}$	$2.97 \cdot 10^{-2}$	$5.28 \cdot 10^{-2}$	$8.34 \cdot 10^{-3}$	$1.33 \cdot 10^{-2}$	$2.36 \cdot 10^{-2}$
0.40	$1.03 \cdot 10^{-2}$	$1.65 \cdot 10^{-2}$	$3.04 \cdot 10^{-2}$	$4.43 \cdot 10^{-3}$	$7.14 \cdot 10^{-3}$	$1.32 \cdot 10^{-2}$
0.50	$7.22 \cdot 10^{-3}$	$1.17 \cdot 10^{-2}$	$2.17 \cdot 10^{-2}$	$3.09 \cdot 10^{-3}$	$5.01 \cdot 10^{-3}$	$9.39 \cdot 10^{-3}$
0.70	$4.65 \cdot 10^{-3}$	$7.55 \cdot 10^{-3}$	$1.41 \cdot 10^{-2}$	$2.11 \cdot 10^{-3}$	$3.43 \cdot 10^{-3}$	$6.47 \cdot 10^{-3}$
1.0	$2.85 \cdot 10^{-3}$	$4.64 \cdot 10^{-3}$	$8.72 \cdot 10^{-3}$	$1.44 \cdot 10^{-3}$	$2.34 \cdot 10^{-3}$	$4.43 \cdot 10^{-3}$
1.5	$1.50 \cdot 10^{-3}$	$2.44 \cdot 10^{-3}$	$4.59 \cdot 10^{-3}$	$8.58 \cdot 10^{-4}$	$1.40 \cdot 10^{-3}$	$2.65 \cdot 10^{-3}$
2.0	$8.76 \cdot 10^{-4}$	$1.43 \cdot 10^{-3}$	$2.69 \cdot 10^{-3}$	$5.48 \cdot 10^{-4}$	$8.94 \cdot 10^{-4}$	$1.69 \cdot 10^{-3}$
3.0	$3.77 \cdot 10^{-4}$	$6.14 \cdot 10^{-4}$	$1.16 \cdot 10^{-3}$	$2.64 \cdot 10^{-4}$	$4.31 \cdot 10^{-4}$	$8.16 \cdot 10^{-4}$
4.0	$1.98 \cdot 10^{-4}$	$3.22 \cdot 10^{-4}$	$6.10 \cdot 10^{-4}$	$1.48 \cdot 10^{-4}$	$2.42 \cdot 10^{-4}$	$4.59 \cdot 10^{-4}$
5.0	$1.17 \cdot 10^{-4}$	$1.92 \cdot 10^{-4}$	$3.63 \cdot 10^{-4}$	$9.22 \cdot 10^{-5}$	$1.50 \cdot 10^{-4}$	$2.85 \cdot 10^{-4}$
7.0	$5.27 \cdot 10^{-5}$	$8.59 \cdot 10^{-5}$	$1.63 \cdot 10^{-4}$	$4.39 \cdot 10^{-5}$	$7.16 \cdot 10^{-5}$	$1.36 \cdot 10^{-4}$
10.0	$2.18 \cdot 10^{-5}$	$3.56 \cdot 10^{-5}$	$6.75 \cdot 10^{-5}$	$1.91 \cdot 10^{-5}$	$3.11 \cdot 10^{-5}$	$5.91 \cdot 10^{-5}$
15.0	$7.75 \cdot 10^{-6}$	$1.27 \cdot 10^{-5}$	$2.40 \cdot 10^{-5}$	$7.07 \cdot 10^{-6}$	$1.15 \cdot 10^{-5}$	$2.19 \cdot 10^{-5}$
20.0	$3.67 \cdot 10^{-6}$	$5.99 \cdot 10^{-6}$	$1.14 \cdot 10^{-5}$	$3.42 \cdot 10^{-6}$	$5.59 \cdot 10^{-6}$	$1.06 \cdot 10^{-5}$
30.0	$1.26 \cdot 10^{-6}$	$2.05 \cdot 10^{-6}$	$3.90 \cdot 10^{-6}$	$1.20 \cdot 10^{-6}$	$1.97 \cdot 10^{-6}$	$3.74 \cdot 10^{-6}$
40.0	$5.85 \cdot 10^{-7}$	$9.55 \cdot 10^{-7}$	$1.81 \cdot 10^{-6}$	$5.69 \cdot 10^{-7}$	$9.30 \cdot 10^{-7}$	$1.77 \cdot 10^{-6}$

References

Aglietta, M., B. Alessandro, P. Antonioli, F. Arneodo, L. Bergamasco, M. Bertaina, C. Castagnoli, A. Castellina, A. Chiavassa, G. Cini Castagnoli, B. D'Ettorre Piazzoli, G. Di Sciascio, W. Fulgione, P. Galeotti, P.L. Ghia, M. Iacovacci, G. Mannocchi, C. Morello, G. Navarra, O. Saavedra, G.C. Trinchero, P. Vallania, S. Vernetto, C. Vigorito, S. Valchierotti: Annual Report 2000, INFN-LNGS Laboratorio Nationale del Gran Sasso, R. Antolini ed., L'Aquila, Italy (2001) (in print).

Aguirre, C.: Resumen de labores del laboratorio de fisica cosmica, La Paz,

Bolivia, 46 (1972).

Aitbaev, F.B., E.V. Kolomeets, O.V. Krupennikov: PICRC, 5, p. 426 (1981).

Akashi, M., Z. Watanabe, J. Nishimura, K. Niu, T. Taira, N. Ogita, K. Ogata, T. Tsuneoka, A. Misaki, I. Mito, K. Nishikawa, Y. Oyama, A. Nishio, I. Ota, S. Dake, K. Yokoi, Y. Fujimoto, S. Hasegawa, A. Osawa, T. Shibata, T. Suzuki, C.M.G. Lattes, C.Q. Orsini, I.G. Pacca, M.T. Cruz, E. Okuno, T. Borello, M. Kawabata, A.M. Endler: PICRC, 2, p. 744 (1965a).

Akashi, M., Z. Watanabe, J. Nishimura, K. Niu, T. Taira, N. Ogita, K. Ogata, T. Tsuneoka, A. Misaki, I. Mito, K. Nishikawa, Y. Oyama, A. Nishio, I. Ota, S. Dake, K. Yokoi, Y. Fujimoto, S. Hasegawa, A. Osawa, T. Shibata, T. Suzuki, C.M.G. Lattes, C.Q. Orsini, I.G. Pacca, M.T. Cruz, E. Okuno, T. Borello, M. Kawabata, A.M. Endler: PICRC, 2, p. 835 (1965b).

Akashi, M., Z. Watanabe, J. Nishimura, K. Niu, T. Taira, N. Ogita, K. Ogata, T. Tsuneoka, A. Misaki, I. Mito, K. Nishikawa, Y. Oyama, A. Nishio, I. Ota, S. Dake, K. Yokoi, Y. Fujimoto, S. Hasegawa, A. Osawa, T. Shibata, T. Suzuki, C.M.G. Lattes, C.Q. Orsini, I.G. Pacca, M.T. Cruz, E. Okuno, T. Borello, M. Kawabata, A.M. Endler: PICRC, 2, p. 878 (1965c).

Akashi, M., Z. Watanabe, K. Nishikawa, Y. Oyama, S. Hazama, K. Ogata, T. Tsuneoka, T. Shirai, A. Nishio, I. Mito, K. Niu, I. Ohta, T. Taira, J. Nishimura, N. Ogita, Y. Fujimoto, S. Hasegawa, A. Osawa, T. Shibata, Y. Maeda, C.M.G. Lattes, N. Amato, D.V. Ferreora, C. Aguirre, M. Schönberg and M. Mantovani: Japanese - Brazilian Emulsion Chamber Group. Can. J. Phys., 46, p. S660 (1968).

Alikhanian, A.I. and A.O. Vaisenberg: J. Exp. Theoret. Phys., 32, p. 413 (1957).

Allkofer, O.C.: Fortschritte der Physik, 15, p. 113 (1967).

Allkofer, O.C.: Introduction to Cosmic Radiation, Thiemig Verlag, München (1975).

Allkofer, O.C. and E. Kraft: Nuovo Cimento, 39, p. 1051 (1965).

Allkofer, O.C. and J. Trümper: Zeitschr. f. Naturforschung, 19a, p. 1304 (1964).

Avakian, V.V. and M.P. Pleshko: Can. J. Phys., 46, p. S709 (1968).

Babayan, N.P., Ya.S. Babecky, Z.A. Buya, N.L. Grigorov, et al.: Izv. Akad. Nauk SSSR, Ser Fiz.,26, p. 558 (1962).

Baradzei, L.T., M.V. Solofev, Z.I. Tulinova and L.I. Filatova: Soviet Phys. JETP, 36(9), p. 1151 (1959).

Barber, H.B., T. Bowen, D.A. Delise, E.W. Jenkins, J.J. Jones, R.M. Kalbach, and A.E. Pifer: Phys. Rev., D 22, p. 2667 (1980).

Becker, J., D.P. Chanson, E.Nageotti, and P. Treille: J. Phys. Radium, 16, p. 191 (1955).

Berdzenishvili, O.L., Yu.A. Gromov, L.P. Garsevanishvili, D.M. Kotlyarevski, S.D. Kananov, I.Kh. Mandalyan, I.V. Morozov, I.M. Taglanov, and G.Z. Stemahetyan: PICRC, 5, p. 266 (1981).

Bhattacharyya, D.P. and D. Basu: Indian J. Phys., 49, p. 346 (1975).

Bhattacharyya, D.P., D. Basu, and R.K. Roychowdhury: J. Phys., G 1, p. L63 (1975).

Bhattacharyya, D.P., A.K. Ghosh, and D. Basu: Ann. Phys., 36, p. 170 (1979).

Bogomolov, E.A., et al.: Preprint LFTI, No.625, Leningrad (1979).

Bostandzhyan, N.Kh., D.T. Vardumyan, G.A. Marikyan, and K.A. K.A. Matevosyan: PICRC, 7, p. 127 (1979).

Boyadzhyan, N.G. and Yu.F. Pirogov: Sov. J. Nucl. Phys., 27, p. 400 (1978).

Brooke, G., M.A. Meyer, and A.W. Wolfendale: Proc. Phys. Soc., 83, p. 871 (1964).

Brunetti, M.T., A. Codino, C. Grimani, M. Menichelli, M. Miozza, I. Salvatori, R.L. Golden, B.L. Kimbell, S.A. Stephens, S.J. Stochaj, W.R. Webber, F. Massimo Brancaccio, P. Papini, S. Piccardi, P. Spillantini, G. Basini, F. Bongiorno, M. Ricci, J.F. Ormes, R.E. Streitmatter, M.P. De Pascal, A. Morselli, and P. Picozza: J. Phys., G 22, p. 145 (1996).

Castellina, A.: Paper presented at the "Congresso Nationale Gruppo Italiano di Fisica Cosmica", Italian Physical Society, Conference Proc., G. Sirone ed., Lecce, 24 - 26 May (2000).

Circella, M., G. Basini, R. Bellotti, M.T. Brunetti, A. Codino, E. Cafagna, C. De Marzo, M.P. De Pascale, R.L. Golden, C. Grimani, M. Hof, F. Massimo Brancaccio, M. Menichelli, W. Menn, J.W. Mitchell, A. Morselli, J.F. Ormes, P. Papini, C. Pfeifer, S. Piccardi, P. Picozza, M. Ricci, M. Simon, P. Spillantini, S.A. Stephens, S.J. Stochaj, and R.E. Streitmatter: PICRC, 7, p. 359 (1999).

Clark, M.A.: Phys. Rev., 87, p. 87 (1952).

Codino, A., M.T. Brunetti, C. Federico, C. Grimani, M. Lanfranchi, M. Menichelli, M. Miozza, R.L. Golden, S.J. Stochaj, S.A. Stephens, J.W. Mit-

chell, J.F. Ormes, R.E. Streitmatter, M. Hof, C. Pfeifer, W. Menn, M. Simon, G. Basini, M. Ricci, F.M. Brancaccio, P. Papini, S. Piccardi, P. Spillantini, M.P. De Pascal, A. Morselli, and P. Picozza: J. Phys., G 23, p. 1751 (1997).

Daniel, R.R. and S.A. Stephens: Rev. Geophys. Space Phys., 12, p. 233 (1974).

Dardo, M., S. Alessio, and K. Sitte: PICRC, 7, p. 81 (1979).

De Oliveira-Castro, F.M.: An. Acad. Bras. Cienc., 51, p. 65 (1979).

Dobrotin, N.: PRICRC, 9, p. 817 (1965).

Ellsworth, R. and G.B. Yodh: Acta Phys. Acad. Sci. Hung., 29, Suppl. 3, p. 321 (1970).

Erlykin, A.D. and N.P. Kuzina: PICRC, 7, p. 62 (1979).

Farrow, L.: Phys. Rev., 107, p. 1687 (1957).

Flückiger, E.: Helv. Phys. Acta, 49, p. 743 (1976a).

Flückiger, E.: Internal Report, University of Bern (1976b).

Flückiger, E.: Helv. Phys. Acta, 50, p. 633 (1977).

Flückiger, E.: Helv. Phys. Acta, 51, p. 496 (1978).

Francke, T., M. Boezio, G. Barbiellini, G. Basini, R. Bellotti, U. Bravar, F. Cafagna, P. Carlson, M. Casolino, M. Castellano, M. Circella, C. De Marzo, M.P. De Pascale, N. Finetti, R.L. Golden, C. Grimani, M. Hof, W. Menn, J.W. Mitchell, A. Morselli, J.F. Ormes, P. Papini, S. Piccardi, P. Picozza, M. Ricci, P. Schiavon, M. Simon, R. Sparvoli, P. Spillantini, S.A. Stephens, S.J. Stochaj, R.E. Streitmatter, M. Suffert, A. Vacchi, N. Weber, and N. Zampa: PICRC, 2, p. 80 (1999).

Garraffo, Z, A. Pignotti, and G. Zgrablich: Nucl. Phys., B 53, p. 419 (1973).

Ghosh, A.K. and D.P. Bhattacharyya: PICRC, 7, p. 136 (1979).

Ghosh, A.K. and D.P. Bhattacharyya: PICRC, 7, p. 142 (1979).

Ghosh, A.K. and D.P.Bhattacharyya: J. Phys., B, 30, p. 613, (1980).

Golden, R.L., S.A. Stephens, S.J. Stochaj, W.R. Webber, M.T. Brunetti, A. Codino, C. Grimani, M. Menichelli, I. Salvatori, M.P. De Pascale, A. Morselli, P. Picozza, G. Basini, F. Bongiorno, F. M. Brancaccio, M. Ricci, J.F. Ormes, R.E. Streitmatter, P. Papini: J. Geophys. Res., 100, p. 23515 (1995).

Gregory, B.P. and J.H. Tinlot: Phys. Rev., 81, p. 667 and 675 (1951).

Greisen, K. and W.D. Walker: Phys. Rev., 90, p. 915 (1953).

Grigorov, N.L., V.A. Sobinyakov, Ch.A. Tretyakov, V.Ya. Shestoperov, Kh.P. Babaian, and G.G. Dulyan: PICRC, 2, p. 860 (1965a).

Grigorov, N.L., I.N. Erofeeva, L.G. Mitshenko, V.S. Murzin, I.D. Rapoport, L.I. Saricheva, and G.L. Bashindjagian: PICRC, 2, p. 920 (1965b).

Grigorov, N.L., and V. Ya. Shestoperov: Vestnik MGU, Ser. Phys., 10, p. 41 (1967).

Grigorov, N.L., V.A. Sobinyakov, Ch.A. Tretyakov, and V.Ya. Shestoperov: Can. J. Phys., 46, p. S686 (1968).

Grimani, C., P. Papini, S.A. Stephens, G. Basini, F. Bongiorno, F. Massimo Brancaccio, M.T. Brunetti, A. Codino, N. Finetti, R.L. Golden, M. Hof, M. Menichelli, J.W. Mitchell, A. Morselli, J.F. Ormes, M.P. De Pascale, C. Pfeifer, S. Piccardi, P. Picozza, M. Ricci, I. Salvatori, M. Simon, P. Spillantini, S.J. Stochaj, and R.E. Streitmatter: PICRC, 4, p. 1029 (1995).

Hayakawa, Saito, Jun Nishimura, and Yoshiaki Yamamoto: Suppl. Progr. Theor. Phys., 32, p. 104 (1964).

Hazen, W.E., C.A. Randall, and O.L. Tiffany: Phys. Rev., 75, p 694 (1949).

Jabs, A.: Nuovo Cimento, 12A, p. 569 (1972).

Jones, L.W.: Univ. of Michigan, Techn. Report, 03106-30T (1967).

Jones, L.W., A.E. Bussian, G.D. DeMeester, B.W. Loo, D.E. Lyon, Jr., P.V. Ramana Murthy, R.F. Roth, K. N. Erickson, B. Cork: Phys. Rev. Lett., 25, p. 1679 (1970).

Jones, L.W., A.E. Bussian, G.D. DeMeester, B.W. Loo, D.E. Lyon, Jr., P.V. Ramana Murthy, R.F. Roth, P.R. Vishwanath, J.G. Learned, D.D. Reeder, R.J. Wilkes, K.N. Erickson, F.E. Mills, and B. Cork: Nucl. Phys., B 43, p. 477 (1972).

Kamata, K., M. LaPointe, J. Gaebler, I. Escobar, S. Shibata, O. Saavedra, A. Alarcon, K. Suga, K. Murakami, and Y. Toyoda: Can. J. Phys., 46, p. S63 (1968).

Kocharian, N.M.: J. Exp. Theoret. Phys., USSR, 28, p. 160 (1954).

Kocharian, N.M.: Sov. Phys.JETP, 1, p. 128 (1955).

Kocharian, N.M., M.T. Aivazian, Z.A. Kirakosian, and A.S. Aleksanian: J. Exp. Theoret. Phys., USSR, 30, p. 243 (1956a).

Kocharian, N.M., M.T. Aivazian, Z.A. Kirakosian, and A.S. Aleksanian: Sov. Phys. JETP, 3, p. 350 (1956b).

Kocharian, N.M., G.S. Saakian, and Z.A. Kirakosian: J. Exp. Theoret. Phys., USSR, 35, p. 1335 (1958).

Kocharian, N.M., G.S. Saakian, and Z.A. Kirakosian: Sov. Phys. JETP, 35, p. 933 (1959).

Lal, S., R. Raghavan, T.N. Rangaswamy, B.V. Sreekantan, and A. Subramanian: PICRC, 5, p. 260 (1963).

Lal, S., R. Raghavan, T.N. Rangaswamy, R.V. Sreekantan, and A. Subramanian: Proc.Indian Acad. Sci., A 73, p. 213 (1971).

LeCoultre, P.: Helv. Phys. Acta, 44, p. 115 (1971).

Liland, A.: Fortschr. Phys., 23, p. 571 (1975).

Liland, A.: Ark. Fys. Semin. Trondheim, 7, p. 1 (1978).

Liland, A. and H. Pilkhun: PICRC, 3, p. 1841 (1973).

Lovati, A., A. Mura, C. Succi,and G. Tagliaferri: Nuovo Cimento, 12, p. 526 (1954).

Lu, S.L., R. Ren, S.J. Zhou, C.R. Wang, M. He, N.J. Zhang, P.Y. Cao, and J.Y. Li: PICRC, 6, p. 89 (1997).

Mandritskaya, K.V., E.A. Osipova, I.V. Rakobolskaya, N.Vl. Sokolskaya, and A.Ya. Varkovitskaza, E.A. Zamachalova, and V.I. Zatsepin: PICRC, 7, p. 107 (1979).

Masarik, J., and J. Beer: J. Geophys. Res., 104, No. D10, p. 12099 (1999).

Meshkovskii, A.G., and L.I. Sokolov: Sov. Phys. JETP, 6, p. 424 (1958).

Mielke, H.H., M. Föller, J. Engler, and J. Knapp: J. Phys., G 20, p. 637 (1994).

Miller, C.E., J.E. Henderson, D.S. Potter, J. Todd, W.M. Sandstrom, G.R. Garrison, W.R. Davis, and F.M. Charbonnier: Phys. Rev., 93, p. 590 (1954).

Miller, C.E., J.E. Henderson, G.R. Garrison, D.S. Potter, W.M. Sandstrom, and J. Todd: Phys. Rev., 94, p. 167 (1954).

Mitoyan, S.V.: Izv. Akad. Nauk Arm. SSR Fiz., 14, p. 166 (1979).

Mylroi, M.G., and J.G. Wilson: Proc. Phys. Soc., Lond., A 64, p. 404 (1951).

Nam, R.A., S.I. Nikolsky, V.I. Sokolvsky, and V.I. Yakovlev: Acta Phys. Acad. Sci. Hung., 29, Suppl. 3, p. 263 (1970).

Pamir Collaboration: PICRC, 7, p. 75 (1979a).

Pamir Collaboration: PICRC, 7, p. 241 (1979b).

Papini, P., C. Grimani, and S.A. Stephens: Nuovo Cimento, 19 C, p. 367 (1996).

Rosen, A.Z.: Phys. Rev., 93, p. 211 (1954).

Rossi, B.: Cosmic Rays, McGraw Hill, New York (1964).

Roychoudhury, R.K. and D.P. Bhattacharyya: Ann. Phys., 36, p. 175 (1979).

Sarkar, K., D.P. Bhattacharyya, and D. Basu: Indian J. Phys., A, 51, p. 231 (1977).

Schopper, E., E. Lohrmann, and G. Mauck: Handbuch der Physik, Kosmische Strahlung XLVI/2, p. 372 (1967).

Shibuya, E.H.: PICRC, 8, p. 238 (1987).

Siohan, F., R.W. Ellsworth, A.S.Ito, J.R. Macfall, R.E. Streitmatter, S.C. Tonwar, and G.B. Yodh: J. Phys., G 4, p. 1169 (1978).

Sokolsky, Pierre: Introduction to Ultrahigh Energy Cosmic Ray Physics, Frontiers in Physics, Vol. 76, Addison-Weskey Publishing Co., New York (1989).

Subramanian, A.: Ph.D. Thesis, University of Madras (1962).

Szaryan, M.O., M.I. Keropyan, E.A. Mamidzhanyan, R.M. Martirosov, and M.M. Muradyan: Ivz. Akad. Nauk Arm. SSR Fiz., 37, p. 1356 (1973).

Stephens, S.A.: PICRC, 4, p. 282 (1981).

Takahashi, Y.: AIP Conf. Proc., 49, p. 166 (1978).

Takahashi, Y., J. Iwai, T. Ogata, and I. Ohta: PICRC, 7, p. 115 (1979).

Tinlot, J.: Phys. Rev., 74, p. 1197 (1948).

Vaisenberg, A.O.: Sov. Phys. JETP, 5, p. 352 (1957).

Vardumyan, D.T., G.A. Marikyan, and K.A. Matevosyan: Ivz. Akad. Nauk Arm. SSR Fiz., 14, p. 350 (1979).

Whittemore, W.L. and R.P. Shutt: Phys. Rev., 86, p. 940 (1952).

Xu Chun-Xian, Huo An-Xiang, Yuan Yn-Kui, Gu Yi-Dong, Li Ti-Pei, Shen Pei-Ro, Jia Guei-Bin, Xiao Qian-Yi, Yhang Cheng-Mo, and Chen Duan-Bao: Phys. Energ. Fortis and Phys. Nucl., 2, p. 423 (1978).

Yekutieli, G.: Nucl. Phys., B 47, p. 621 (1972).

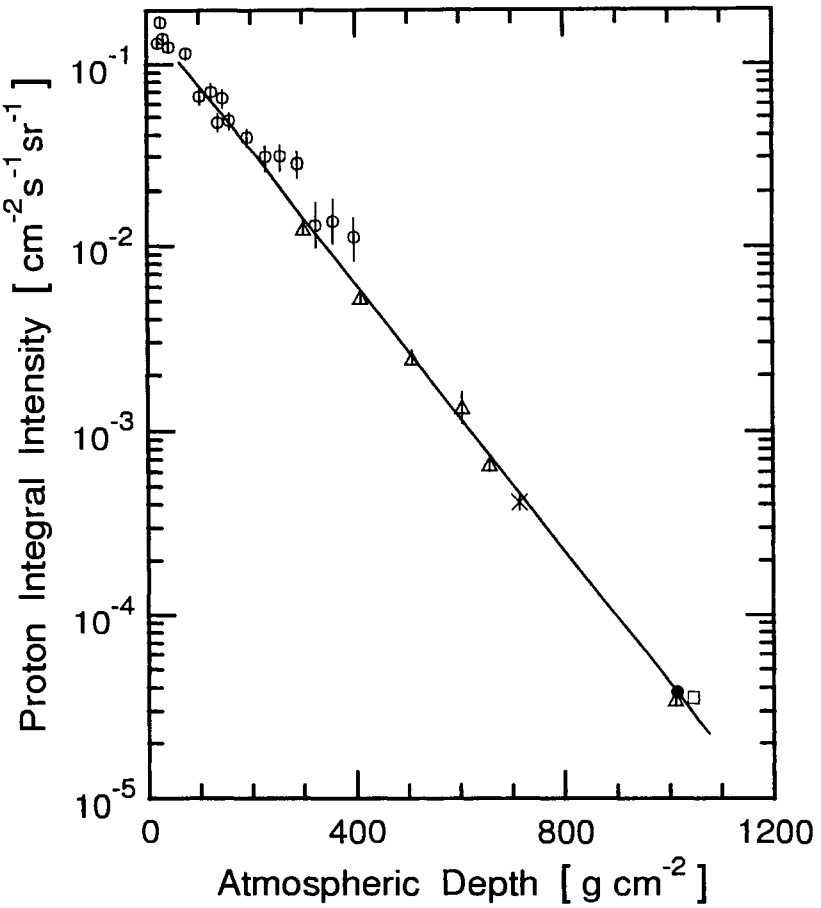

Figure 2.1: Altitude dependence of the vertical proton intensity for energies $E \geq 1$ GeV (Schopper et al.,1967).

○ Clark (1952)	△ Tinlot (1948)
□ Mylroi (1951)	• Normalizing Point
× Miller et al. (1954), Kocharyan (1955)	

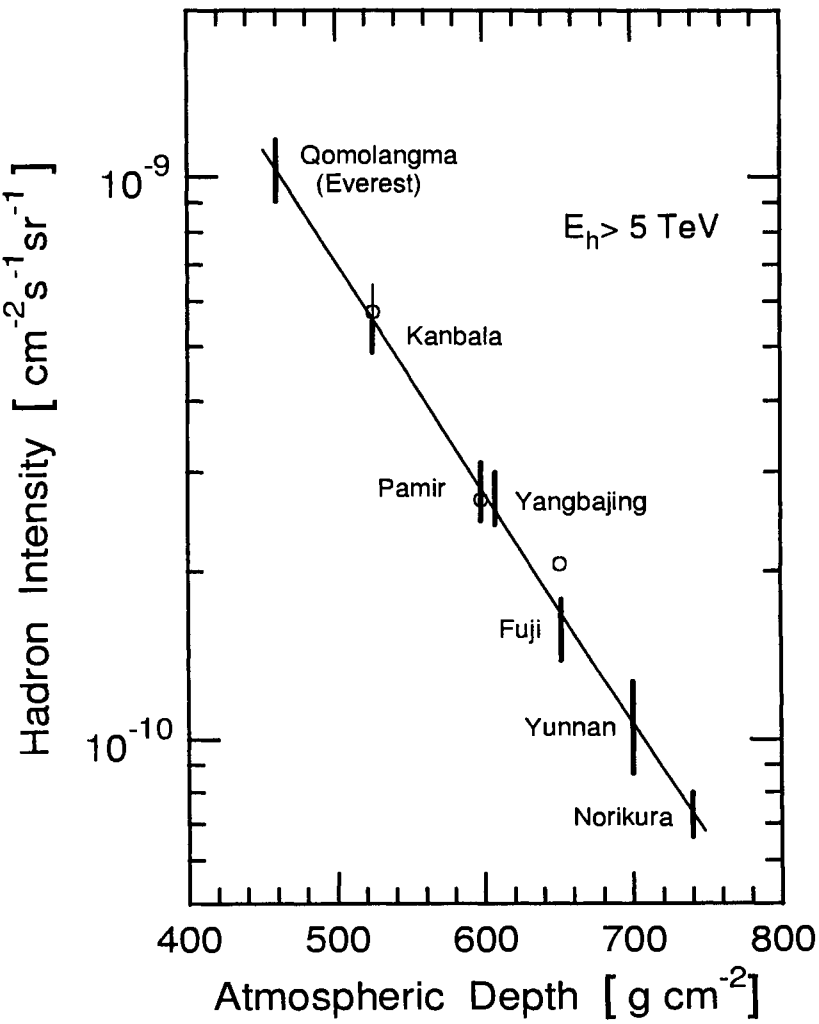

Figure 2.2: Variation of the hadron intensity with atmospheric depth measured at Qomolangma (6500 m, foot of Mt. Everest), Mt. Kanbala (5450 m), Pamir (4370 m), Yangbajing (4300 m), Mt. Fuji (3750 m) and the Yunnan Station (3200 m) by Lu et al. (1997) (vertical bars). Also shown are earlier data measured by Shibuya (1987) (o) and an old data point from Mt. Norikura. The straight line represents the fit with eq. 2.2 that gives the relation for the attenuation of the hadron component in the atmosphere.

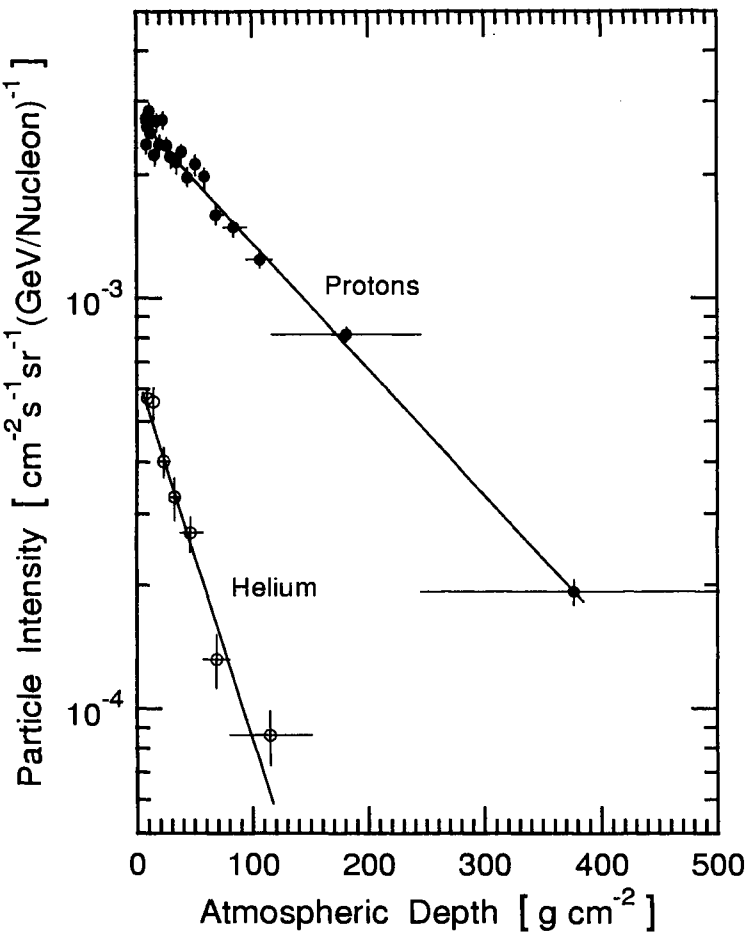

Figure 2.3: Proton and helium intensities as a function of atmospheric depth in the energy windows between $4.1 \leq E \leq 14.1$ GeV and $1.7 \leq E \leq 9.1$ GeV/nucleon, respectively (Circella et al., 1999). The measurement was made with the balloon-borne instrument MASS during ascent from Fort Sumner, NM (USA) in 1991 at a geomagnetic cutoff of 4.5 GV.

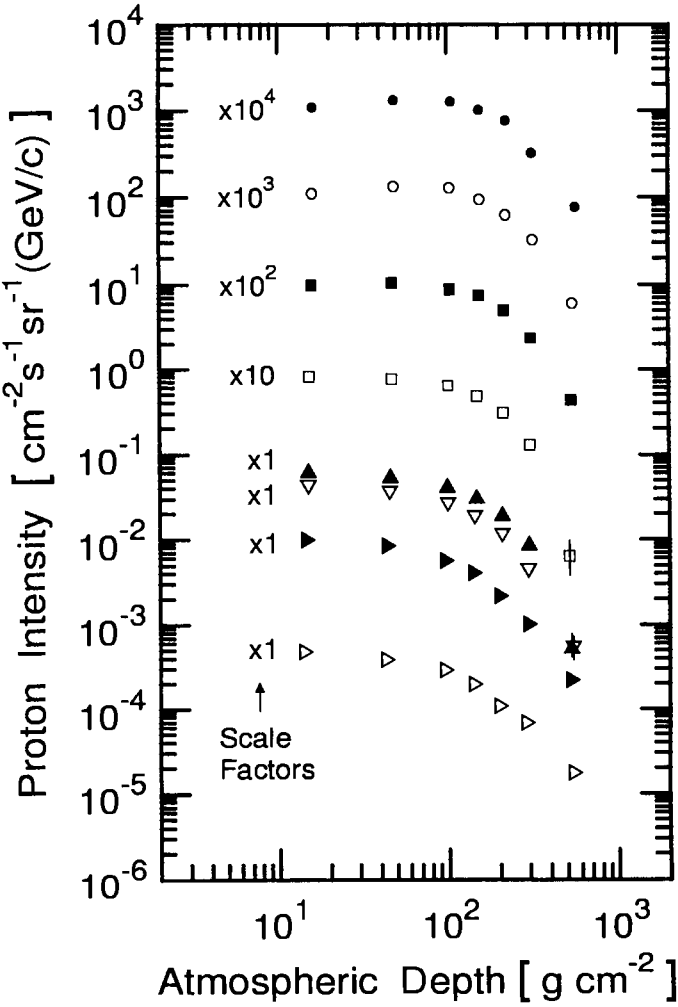

Figure 2.4: Atmospheric growth curves of protons for different momentum intervals as listed below, recorded with the CAPRICE94 instrument launched from Lynn Lake, Manitoba (Canada), August 8/9, 1994 (Francke et al., 1999). (Divide reading on ordinate by appropriate scale factor.)

• $0.53 \leq p \leq 0.75$ GeV/c	○ $0.75 \leq p \leq 0.97$ GeV/c
■ $0.97 \leq p \leq 1.23$ GeV/c	□ $1.23 \leq p \leq 1.55$ GeV/c
▲ $1.55 \leq p \leq 2.0$ GeV/c	▽ $2.0 \leq p \leq 3.2$ GeV/c
▶ $3.2 \leq p \leq 8.0$ GeV/c	▷ $8.0 \leq p \leq 40$ GeV/c

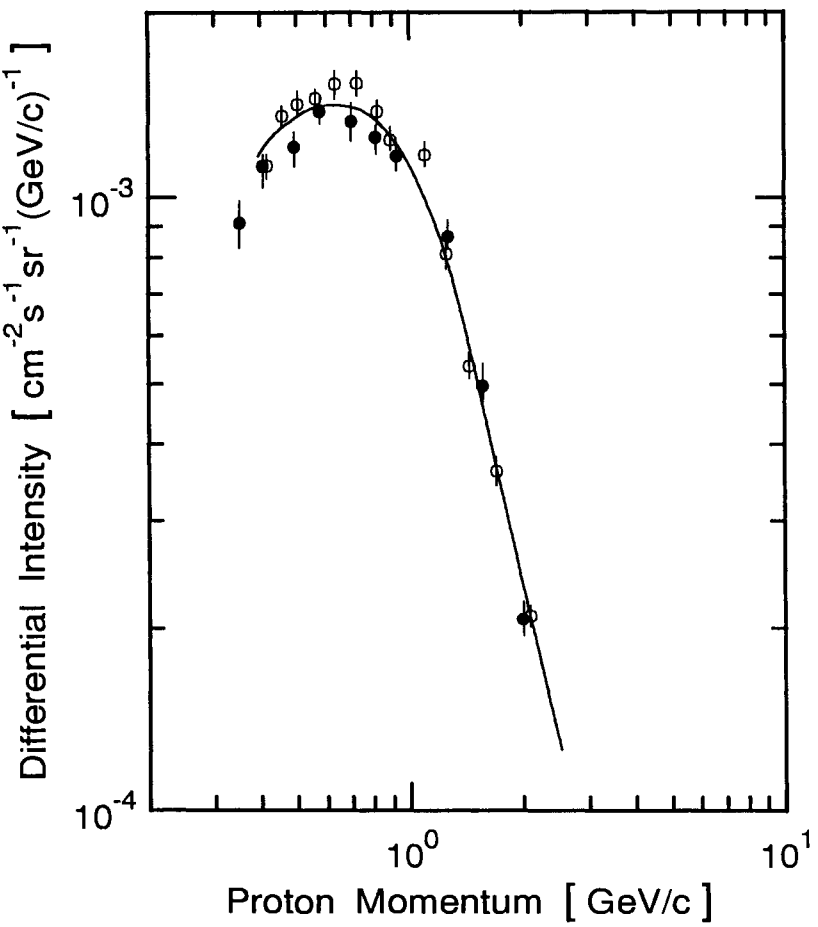

Figure 2.5: Differential momentum spectrum of low energy protons at an altitude of 3200 m. (Kocharian, 1954, 1955, 1956a and 1956b). The symbols o and • represent data from two versions of the experiment.

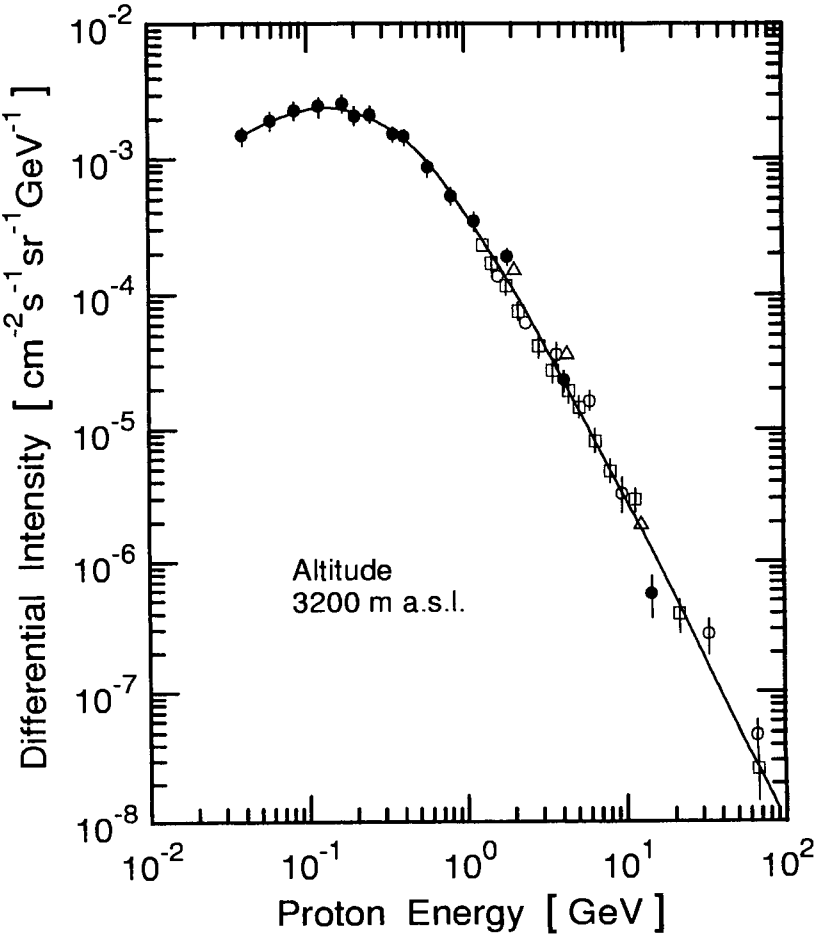

Figure 2.6: Differential energy spectrum of vertical protons at an altitude of 3200 m. (Kocharian et al., 1956a, 1956b, 1958 and 1959). The four sets of data (•, □, △, ○) show the results of four different experiments using different absorbers in the spectrometer.

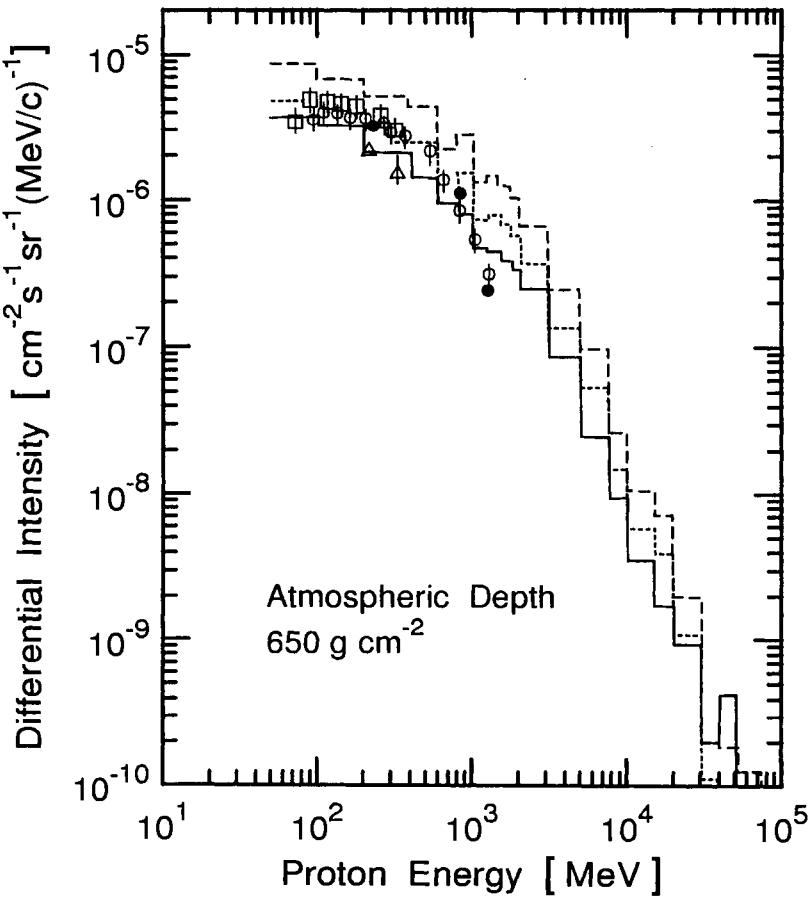

Figure 2.7: Differential momentum spectrum of protons at an atmospheric depth of 650 g/cm^2 (Flückiger, 1976a).

• Miller et al. (1954)	△ Rosen (1954)
□ Meshkowskii, Sokolov (1958)	○ Kocharian (1955)

—— Flückiger (1976), Monte Carlo, $\lambda_N = \lambda_N(E)$; $\lambda_\pi = 75$ g/cm^2

--- Flückiger (1976), Monte Carlo, $\lambda_N = 75$ g/cm^2; $\lambda_\pi = 120$ g/cm^2

···· Flückiger (1976), Monte Carlo, $\lambda_N = 65$ g/cm^2; $\lambda_\pi = 120$ g/cm^2

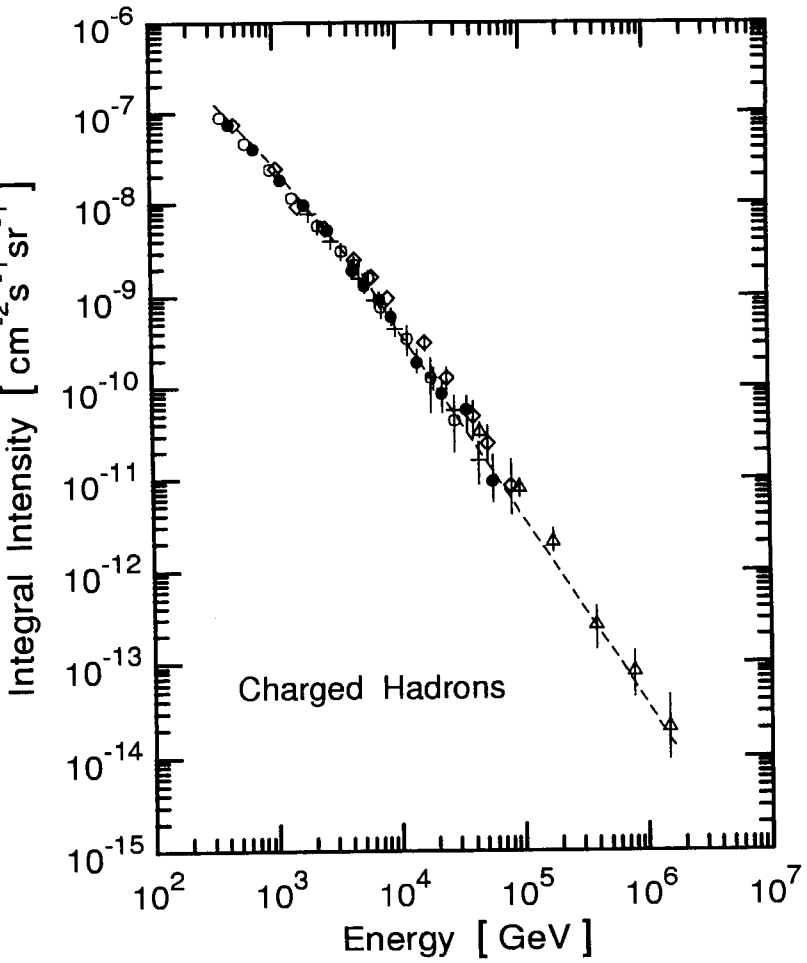

Figure 2.8: Integral energy spectrum of charged hadrons obtained by different experiments at an altitude of approximately 3000 m (Nam et al., 1970).

- o Nam et al. (1970), calorimeter data, 3340 m
- • Nam et al. (1970), burst data, 3340 m
- \+ Grigorov and Shestoperov (1967), burst data, 3250 m
- ◇ Babayan et al. (1962, 1965), bursts incl. structure 3250 m
- △ Hayakawa et al. (1964), photo-emulsion data, 2770 m

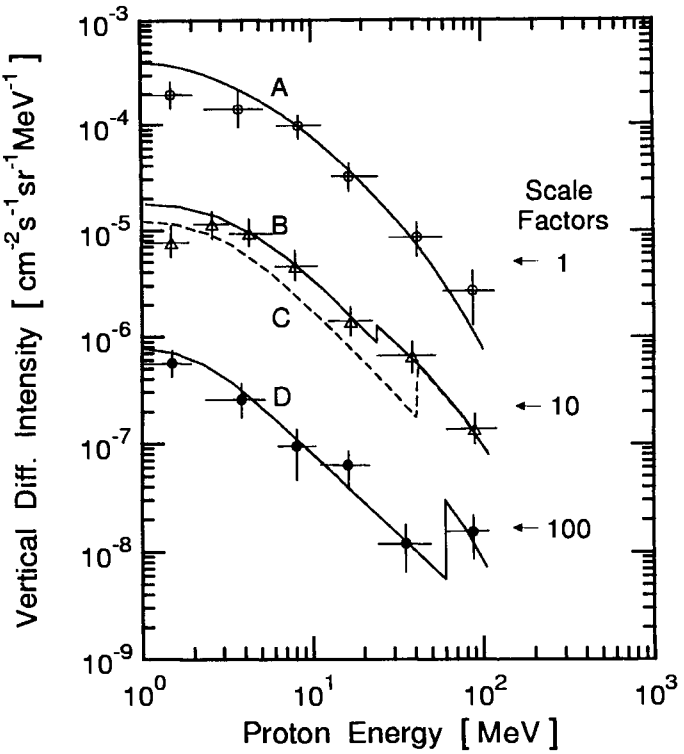

Figure 2.9: Differential energy spectra of protons at altitudes between 16 km and 18 km for different geomagnetic cutoff rigidities, P_c, and energies $\leq$ 100 MeV (Aitbaev et al., 1981; Bogomolov et al., 1979). (Multiply reading on ordinate with appropriate scale factor to get true intensity.)

o	$15.7 \leq h \leq 16.6$ km	P_c =	0.4 – 0.5 GV
△	$15.7 \leq h \leq 16.6$ km	P_c =	0.3 – 4.0 GV
•	$17.7 \leq h \leq 18.0$ km	P_c =	6.9 – 7.4 GV

Calculations by Aitbaev et al. (1981).

A	P_c = 0.5 GV	X = 100 g/cm^2
B	P_c = 3.0 GV	X = 100 g/cm^2
C	P_c = 5.0 GV	X = 100 g/cm^2
D	P_c = 7.0 GV	X = 80 g/cm^2

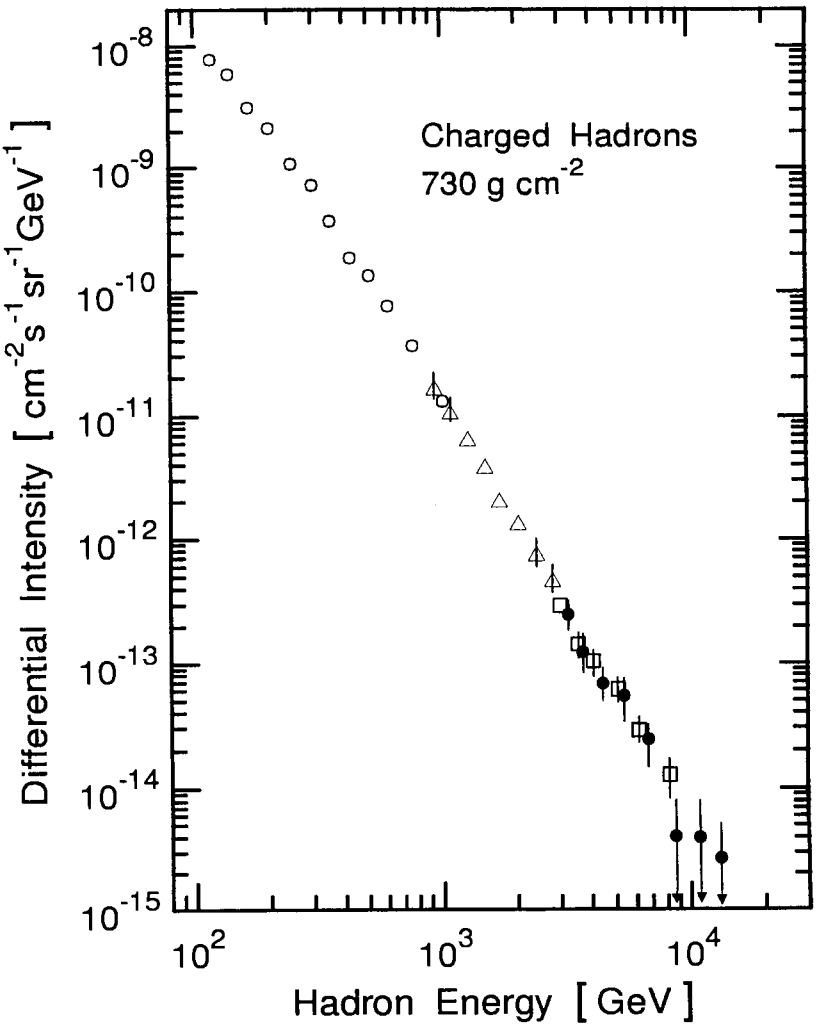

Figure 2.10: Differential energy spectrum of charged hadrons at an atmospheric depth of 730 g/cm^2 (Siohan et al., 1978). The symbols ○, △, and • represent data obtained for different geometric factors (area-solid-angle products). The symbols □ show the spectrum obtained using charged and neutral hadrons combined but is normalized to charged hadrons.

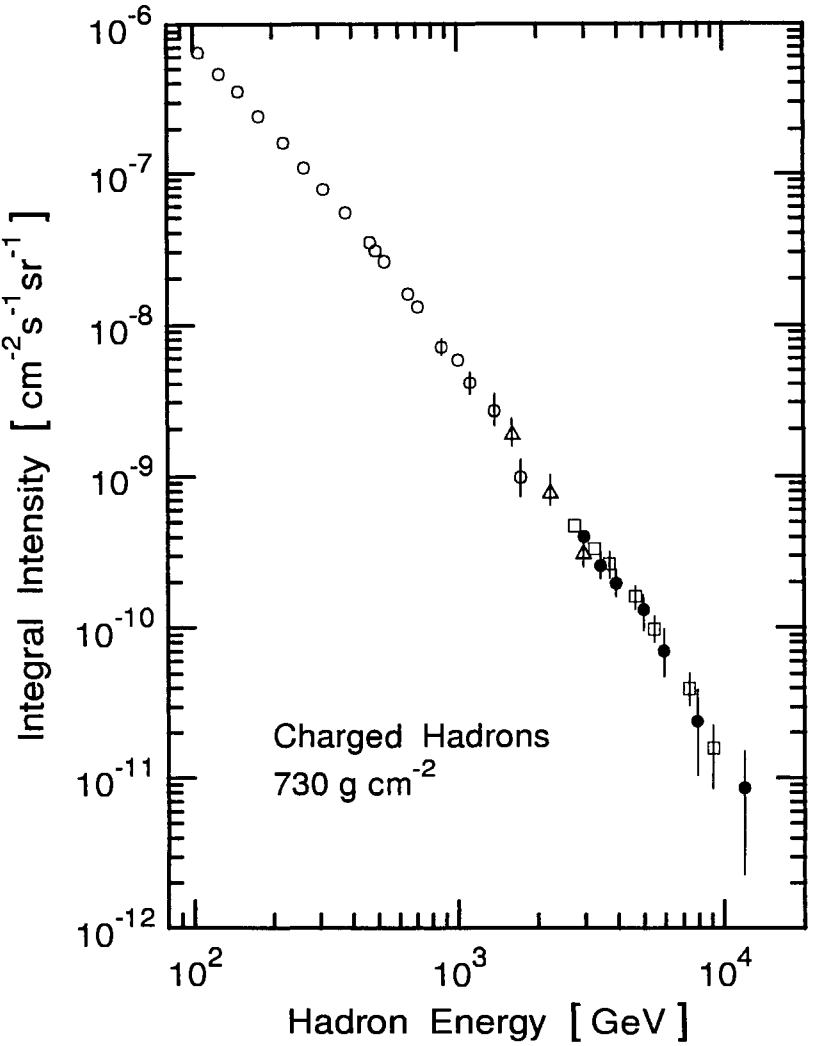

Figure 2.11: Integral energy spectrum of charged hadrons at an atmospheric depth of 730 g/cm^2 (Siohan et al.,1978). The symbols ○, ◇, △, and • represent data obtained for different geometric factors (area-solid-angle products). The symbol □ shows the spectrum obtained using charged and neutral hadrons combined but normalized to charged hadrons.

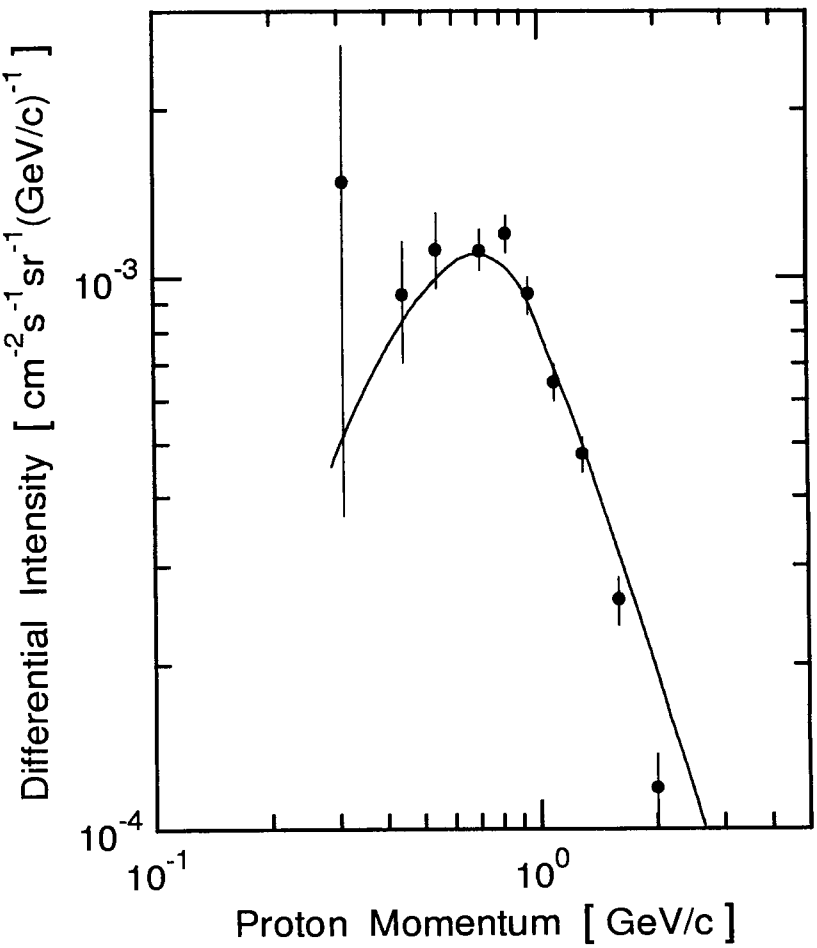

Figure 2.12: Differential momentum spectrum of vertical protons at an atmospheric depth of 747 g/cm^2 (2750 m) (Barber et al., 1980).

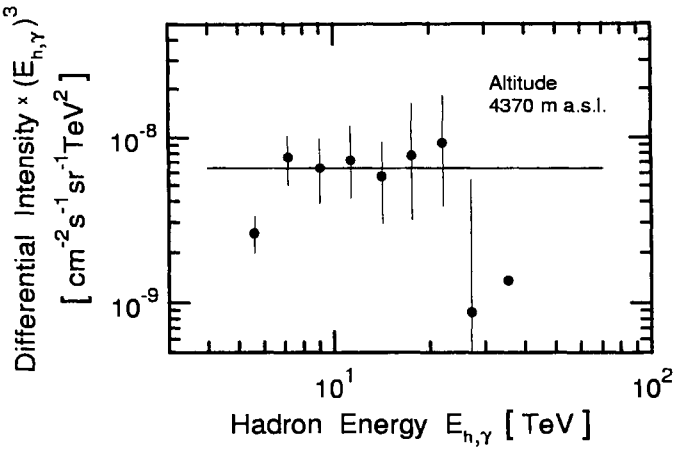

Figure 2.13: Differential energy spectrum of the vertical hadron flux at an altitude of 4370 m for the energy range $5 \leq E \leq 25$ TeV (Pamir Collaboration, 1979a). For details see text.

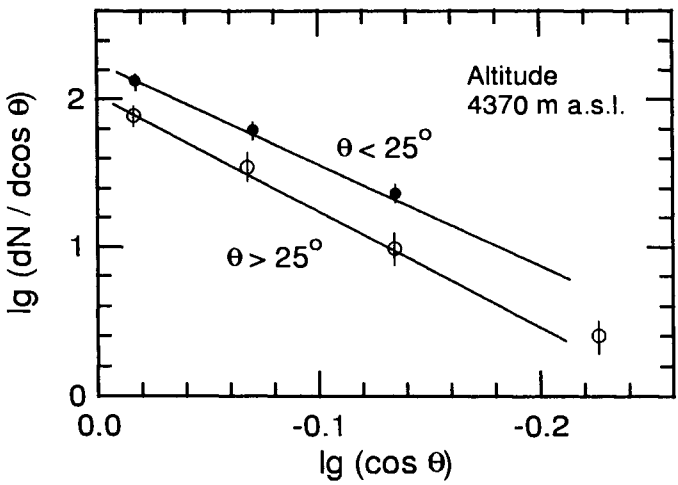

Figure 2.14: Angular distribution of hadrons at 4370 m (596 g/cm^2) in the energy range $5 \leq E \leq 25$ TeV for two different zenith angle regions (Pamir Collaboration, 1979a). For details see text.

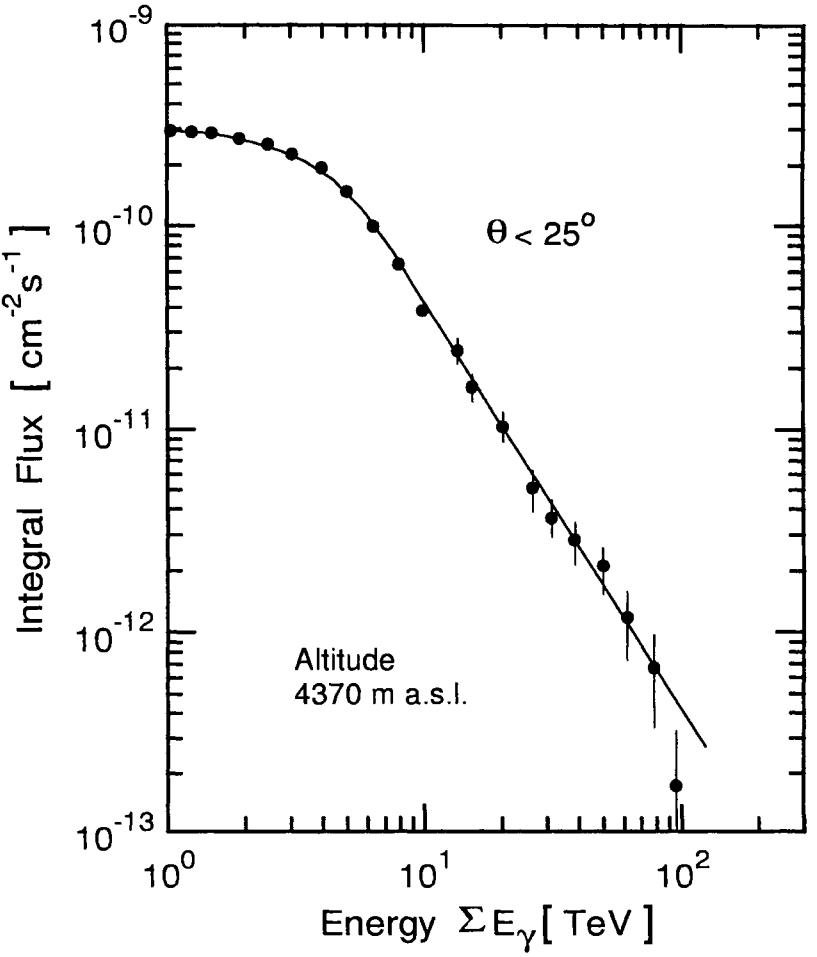

Figure 2.15: Integral spectrum of ΣE_{γ}, i.e., of the energy transferred by hadrons into the electromagnetic component inside the emulsion chamber. Included are particles with zenith angles $0° \leq \theta \leq 25°$ in the energy range $1 \leq E \leq 100$ TeV at an altitude of 4370 m (596 g/cm^2). The energy is estimated on the basis of the energy of the associated gamma ray families (Pamir Collaboration, 1979b).

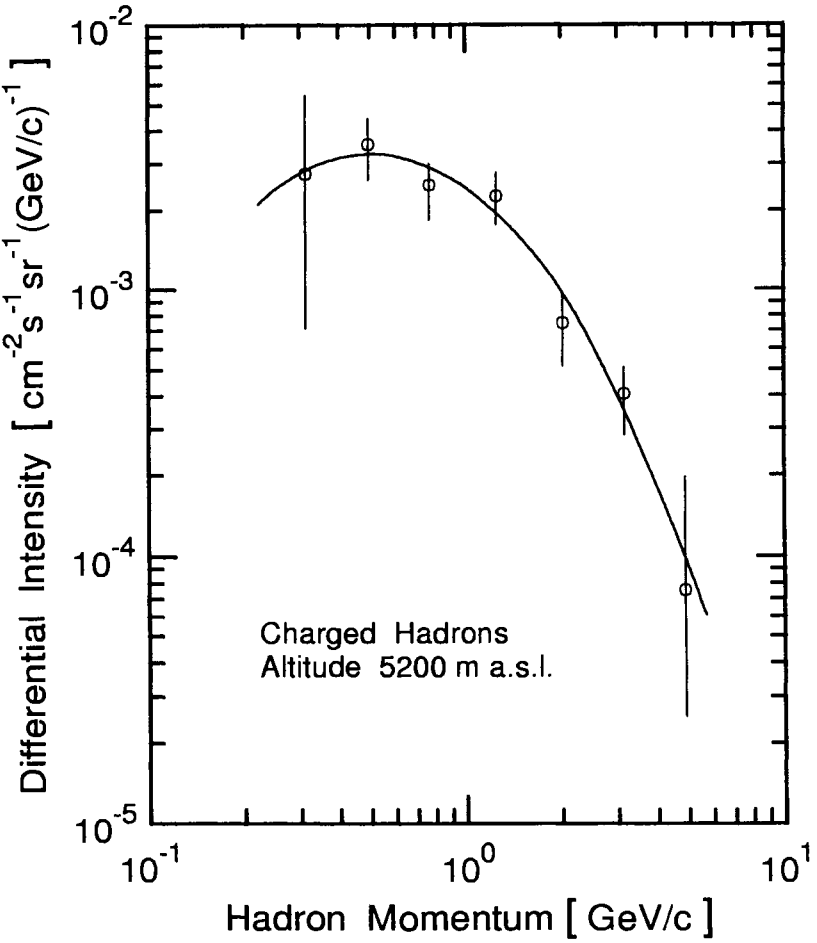

Figure 2.16: Differential momentum spectrum of charged hadrons at an altitude of 5200 m (Allkofer and Kraft, 1965).

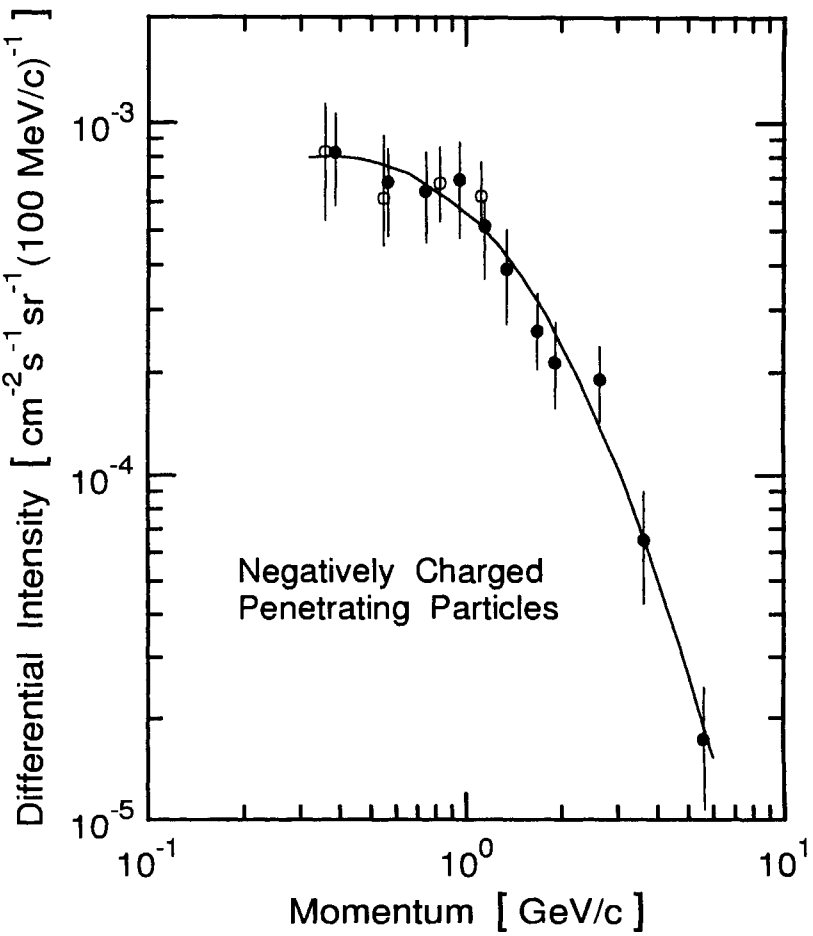

Figure 2.17: Differential momentum spectrum of negatively charged penetrating particles (π^-, μ^-) at an altitude of 9000 m (310 g/cm^2) (Baradzei et al., 1959). The two sets of data points represent two different sets of measurements.

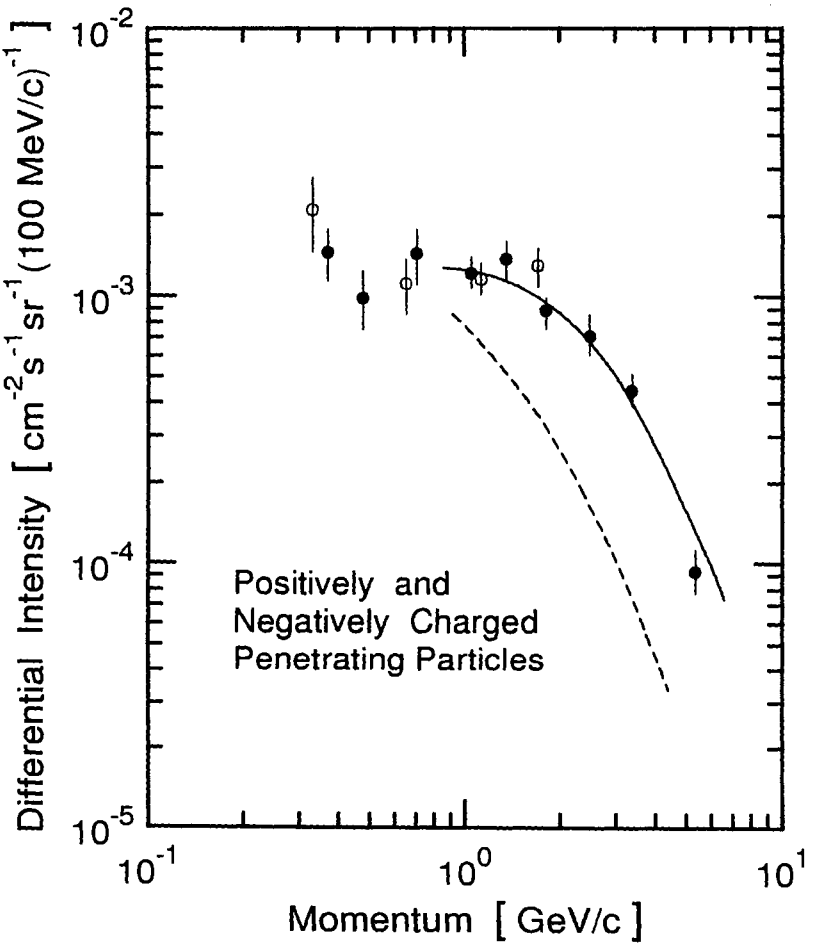

Figure 2.18: Differential momentum spectrum of positively charged penetrating particles (π^+, μ^+, p) at an altitude of 9000 m (310 g/cm^2) (Baradzei et al., 1959). The dashed line represents positively charged hadrons only. The two sets of data points represent two different sets of measurements.

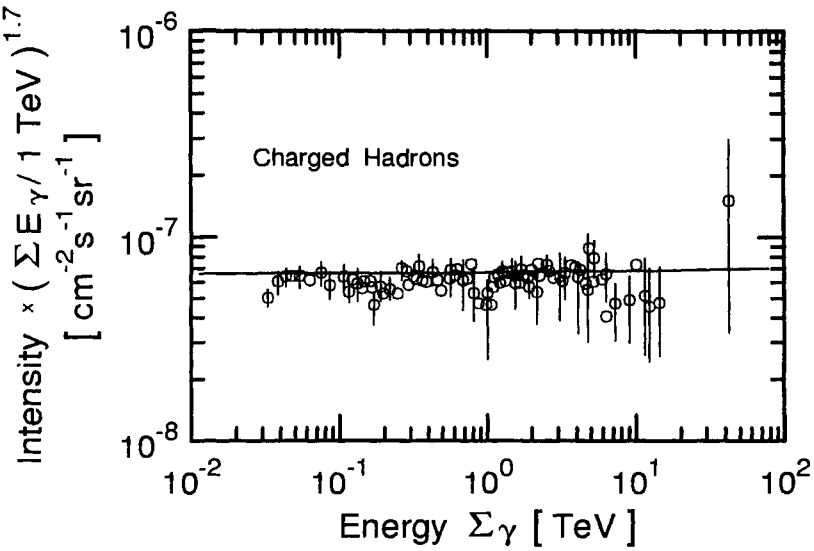

Figure 2.19: Integral energy spectrum of charged high energy hadrons at an atmospheric depth of 260 g/cm^2. The energies are given in terms of the energy of the associated gamma ray families (Takahashi, 1978 and 1979).

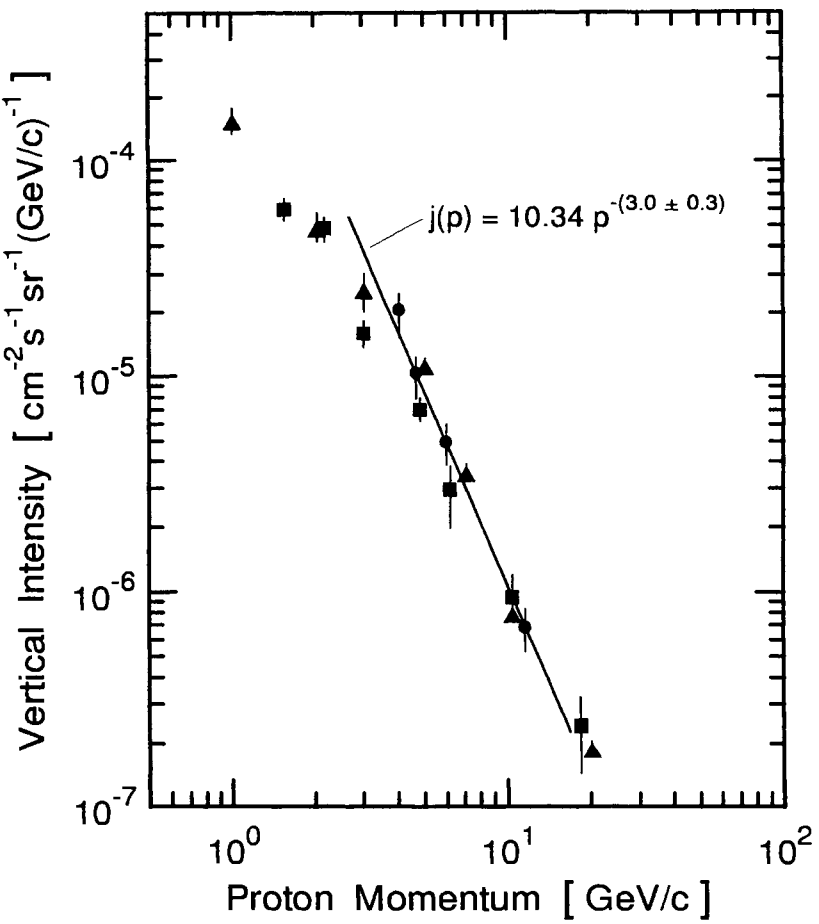

Figure 2.20: Differential proton momentum spectrum at 945 g/cm^2 and $P_c \approx 1$ GV (Golden et al., 1995). The data points from the work of Brooke and Wolfendale (1964) and Diggory et al. (1974) recorded at sea level are corrected to the level of 945 g/cm^2. The solid line is a power law fit to the data of Golden et al. (1995) and can be described by the expression given in the figure.

- ● Golden et al. (1995)
- ■ Brooke and Wolfendale (1964)
- ▲ Diggory et al. (1974)

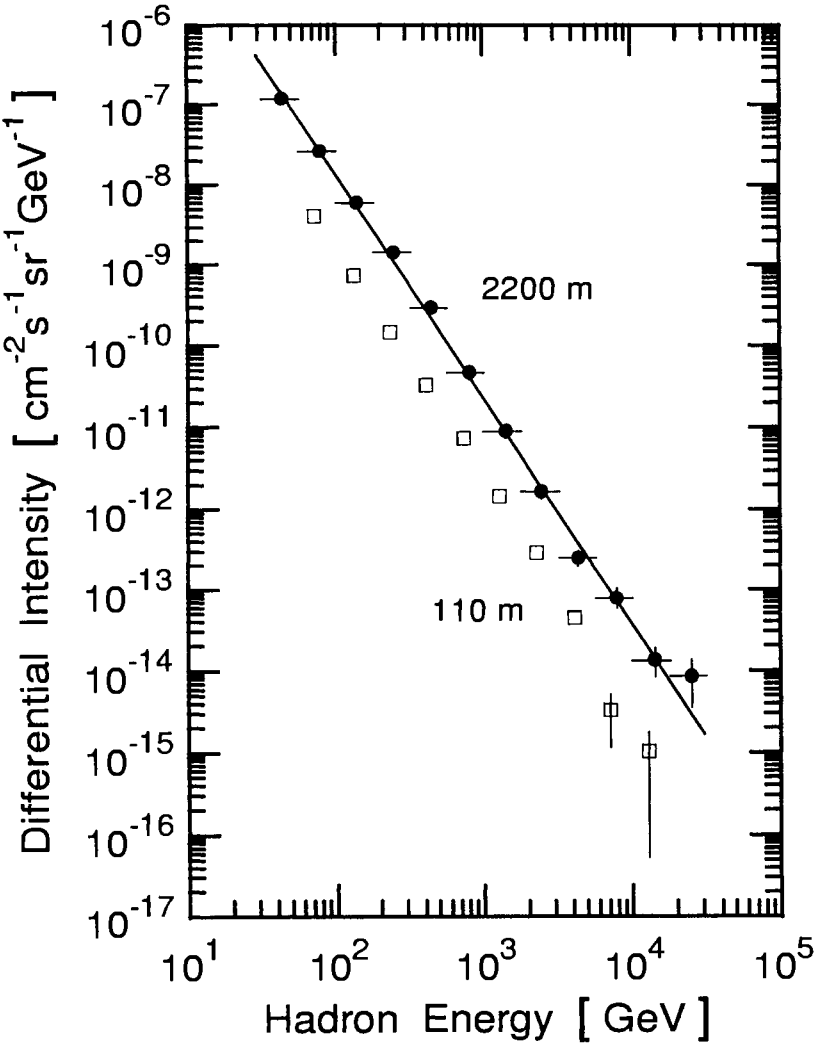

Figure 2.21: The all hadron differential energy spectrum recorded with the hadron calorimeter of the EAS-TOP experiment on top of Gran Sasso at 820 g/cm^2 (2200 m a.s.l.), • (Aglietta et al., 2001). The best power law fit to the data between 30 GeV and 30 TeV is given by the expression $I(E) = (2.25\pm0.20)\cdot10^{-11}\cdot(E/1000)^{-(2.79\pm0.06)}$ [cm^{-2}s^{-1}sr^{-1}GeV^{-1}] (solid line). Also shown for comparison is the hadron spectrum measured with the calorimeter at Karlsruhe at 110 m a.s.l., □ (Mielke et al., 1994).

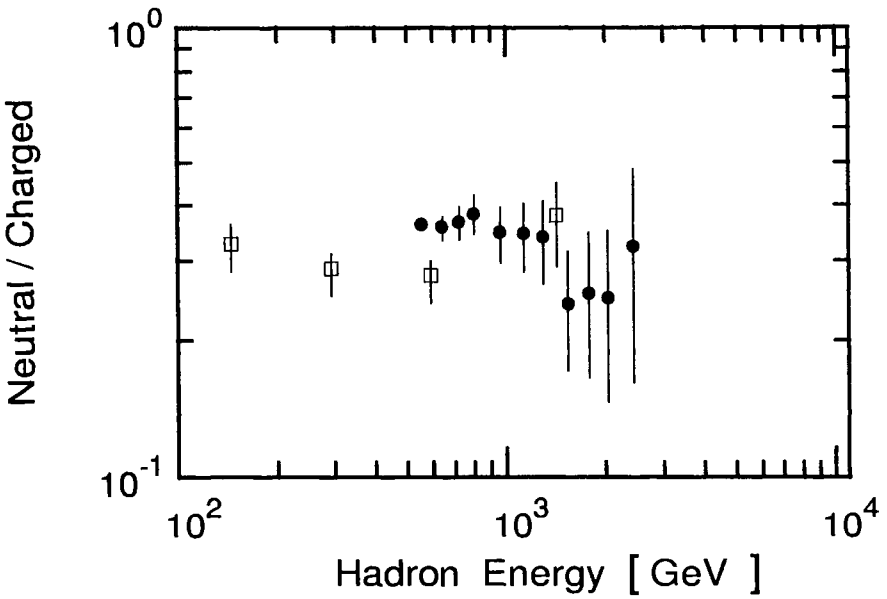

Figure 2.22: Energy dependence of the ratio of neutral to charged hadrons at an atmospheric depth of 730 g cm^{-2}.

- • Siohan et al. (1978)
- □ McFall et al. (1979)

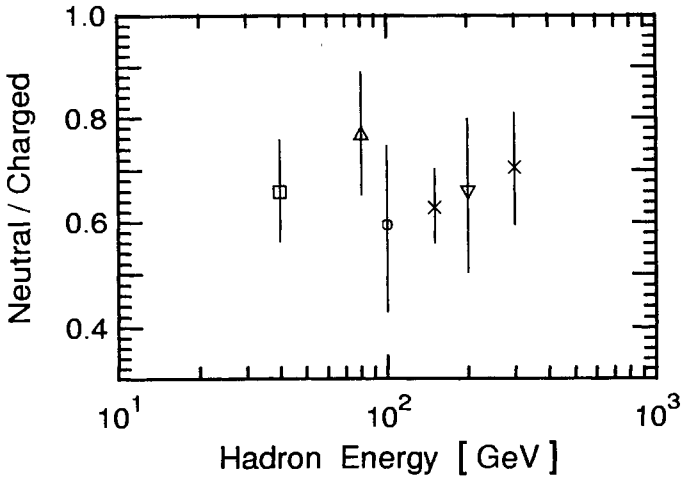

Figure 2.23: Energy dependence of the ratio of neutral to charged hadrons, normalized to an altitude of 3000 m (Echo Lake, Colorado) (Jones et al., 1972).

× Jones et al., (1972)	○ Avakian (1968)
▽ Farrow (1957)	△ Greisen and Walker (1953)
□ Lal et al. (1971)	

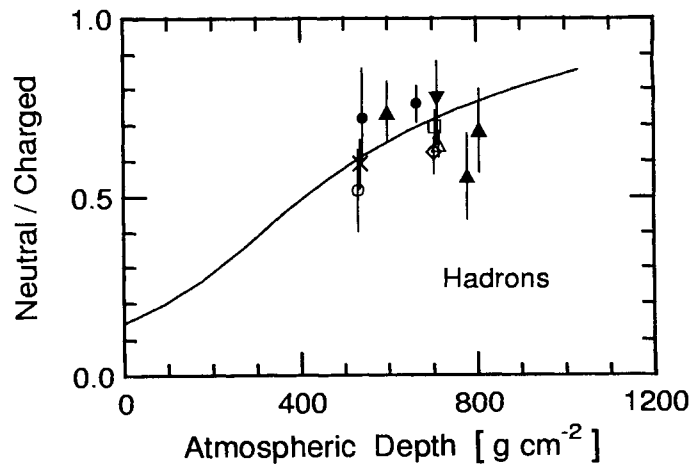

Figure 2.24: Compilation of data of the altitude dependence of the neutral to charged hadron ratios (Aguirre, 1972).

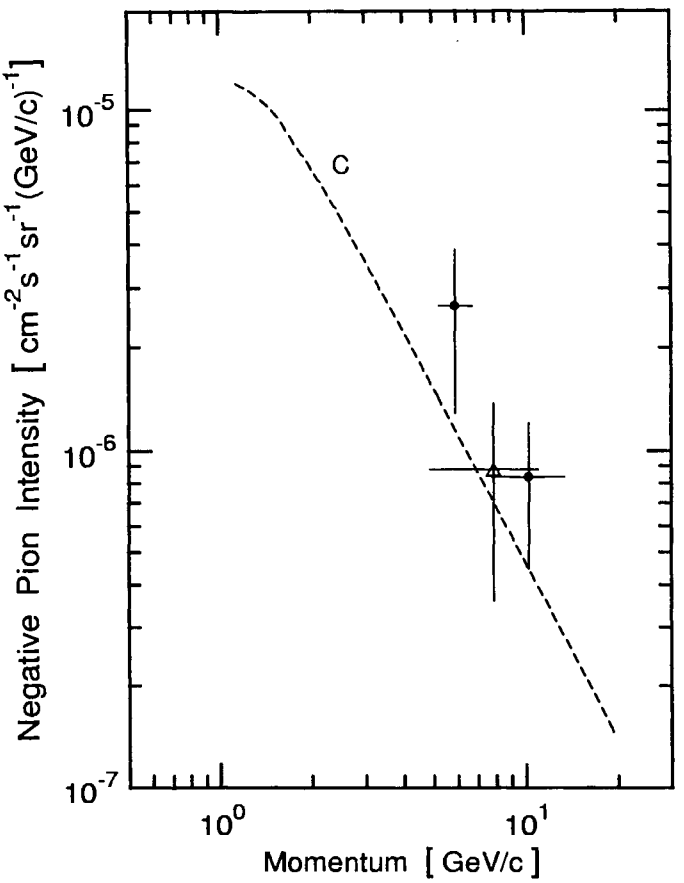

Figure 2.25: Measured and calculated negative differential pion intensities as a function of momentum near the top of the atmosphere (Codino et al., 1997).

△ Brunetti et al. (1996) at 5 g cm^{-2}
• Codino et al. (1997) at 5.8 g cm^{-2}

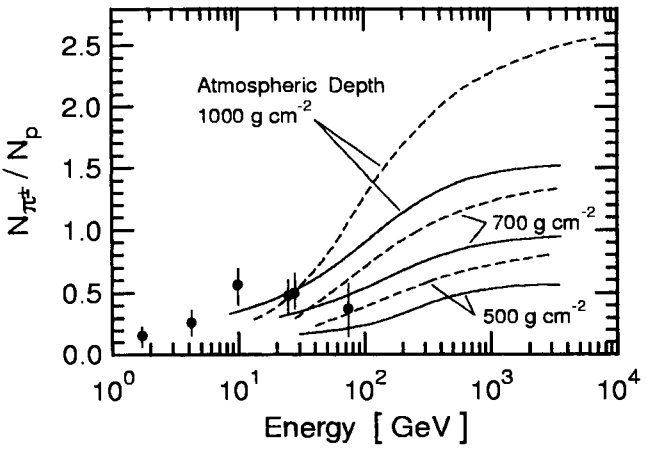

Figure 2.26: Theoretical charged pion to proton ratio as a function of energy at depths of 500, 700, and 1000 g/cm^2, for a pion interaction mean free path of $\pi_\lambda = 100$ g/cm^2 (solid) and 110 g/cm^2 (dashed curve) (Garraffo et al., 1973). The experimental points are from the work of Brooke et al. (1964).

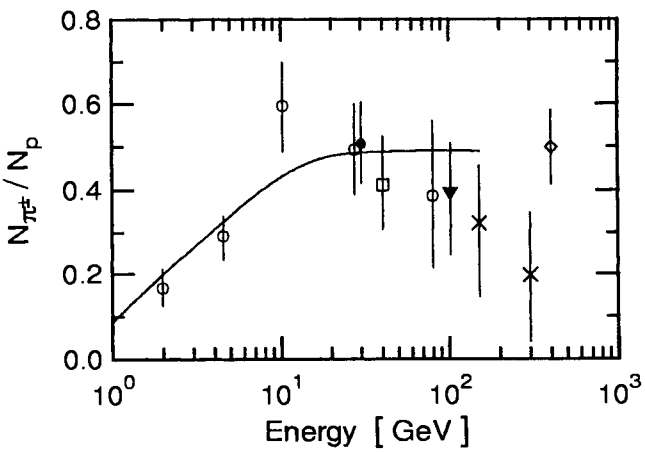

Figure 2.27: Energy dependence of the pion to proton ratio. The data apply to altitudes around 3000 m, except for those of Brooke et al. (1964) that were obtained at sea level. The curve is a fit to the data of Brooke et al..

• Subramanian (1962)	□ Lal et al. (1963)
o Brooke et al. (1964)	◇ Grigorov et al. (1965b)
▼ Avakian & Pleshko (1968)	× Jones et al. (1972)

2.3 Neutrons

2.3.1 Introduction

Atmospheric neutrons are secondary particles resulting from interactions of primaries with nuclei of air constituents. It is useful to distinguish low energy neutrons with energies less than about 10 MeV from high energy neutrons. Low energy neutrons are mostly evaporation products of excited nuclei and manifest an isotropic angular distribution. High energy neutrons can be produced as knock-on neutrons in peripheral collisions but also in charge exchange reactions of leading particles at very high energies. The angular distribution of high energy neutrons is anisotropic.

Neutrons produced in evaporation processes at high altitudes can be scattered out of the atmosphere (albedo neutrons). But also high energy neutrons can leak out from the atmosphere if the incident primaries subtend large zenith angles. Consequently, there are upward or outward as well as downward or inward directed neutrons in the atmosphere.

Because neutrons are produced by charged particles they inherit and also exhibit the latitude effect. Furthermore the flux of the low energy neutron component is modulated by the solar cycle. In addition, strong solar flares may cause significant neutron fluxes in the atmosphere.

A comprehensive summary on neutron flux data in the atmosphere is given by Korff et al. (1979).

2.3.2 Altitude Dependence of Flux and Intensities

In the energy range $8 \leq E \leq 200$ MeV flux measurements have been made at a latitude of 7.8° N near the equator at an altitude corresponding to a pressure of 4 - 6 mbar, using nuclear emulsion (Bhatt, 1976). Tables 2.11 and 2.12 show the results for different energy intervals.

The upward and downward directed fluxes have been measured with a scintillation counter system in the energy range $50 \leq E \leq 350$ MeV near the equator, at a vertical cutoff rigidity of 15 GV (Eyles, 1972). The downward flux is presented in Fig. 2.28. An albedo flux of $(2.4 \pm 1.0) \cdot 10^{-5}$ $cm^{-2}s^{-1}MeV^{-1}$ was found at an energy around 140 MeV and a depth corresponding to an atmospheric pressure of 3 mbar. In the lower energy range, $1 \leq E \leq 10$ MeV, the neutron flux has been determined at a latitude of 10° N, corresponding to a rigidity of 13.9 GV (Albernhe et al., 1971). The results are shown in Fig. 2.29. Zych and Frye (1970) obtained the ratio of the

Table 2.11: Differential Upward and Downward Neutron Intensities at Latitude $\lambda = 7.8°$ N and Atmospheric Pressure 5 mbar. (Bhatt, 1976)

Energy Interval [MeV]	Differential Neutron Intensity $[10^{-4}\,cm^{-2}s^{-1}sr^{-1}]$		
	Up	Down	Total
8 - 38	41	35	76 ± 10
38 - 70	23	29	52 ± 12
70 - 160	27	39	66 ± 24
8 - 160	91	103	194 ± 29

Table 2.12: Differential Upward / Downward Neutron Intensity Ratios and Total Neutron Intensities at Latitude $\lambda = 7.8°$ N and Atmospheric Pressure 5 mbar (Bhatt, 1976).

Neutron Energy Interval [MeV]	Up/Down Ratio*	Total Differential Neutron Intensity $[10^{-4}\,cm^{-2}s^{-1}sr^{-1}]$
8 - 24	1.12 ± 0.10	52 ± 7
24 - 48	1.27 ± 0.25	34 ± 10
48 - 160	0.70 ± 0.15	108 ± 26
8 - 160	1.07 ± 0.08	194 ± 29

* 4, 6 and 10 mbar data combined.

horizontal intensity to the albedo neutron flux on a balloon flight in Texas at latitude 42° N. The result is shown in Fig. 2.30.

The altitude dependence has been measured for different zenith angles with a liquid scintillator in the energy range $10 \leq E \leq 100$ MeV during balloon flights from Palestine, Texas (Preszler et al., 1974). Tables 2.13 and 2.14 show the upward and downward directed fluxes for zenith angles of 30°, 50° and 70°. Figs. 2.30, 2.31, 2.32, and 2.33 show the angular distribution for different energy intervals.

The zenith angle distribution has also been measured with a spark chamber system at a depth of 770 g/cm^2 in the energy range $80 \leq E \leq 300$ MeV

Table 2.13: Altitude Dependence of Upward-Moving Differential Neutron Intensity (Preszler et al., 1974).

Altitude		Intensity [$\times 10^{-4}$cm^{-2}s^{-1}sr^{-1}MeV^{-1}] at Zenith Angle θ											
		$10 < E_n < 30$ MeV			$30 < E_n < 50$ MeV			$50 < E_n < 100$ MeV					
[g/cm^2]	[km]	$\theta = 30°$	$\theta = 50°$	$\theta = 70°$	$\theta = 30°$	$\theta = 50°$	$\theta = 70°$	$\theta = 30°$	$\theta = 50°$	$\theta = 70°$			
246	10.8	12.1± 2.2	9.8± 1.4	5.7± 2.5	13.0± 3.1	2.4± 0.9	6.8± 2.4	4.9± 2.1	3.3± 1.3	3.7± 1.1			
109	15.9	9.7± 2.7	16.1± 2.3	23.2± 7.0	19.2± 4.8	5.0± 1.9	18.2± 5.3	7.9± 3.5	9.1± 2.7	3.7± 1.5			
78.8	18.0	5.6± 1.9	19.5± 2.6	5.2± 3.0	14.3± 3.8	5.9± 2.0	17.8± 5.1	6.9± 3.1	5.3± 2.0	3.8± 1.6			
58	20.0	10.4± 2.6	11.1± 1.9	9.0± 4.0	13.8± 4.0	4.6± 1.7	17.4± 5.2	13.1± 4.1	10.2± 2.8	6.0± 2.0			
38.8	22.4	10.1± 2.8	16.2± 2.5	14.9± 5.6	7.9± 3.2	5.8± 2.1	6.2± 2.8	13.9± 4.6	11.8± 3.3	9.4± 3.1			
26	25.0	10.0± 2.8	11.4± 2.0	6.6± 3.8	10.8± 3.4	6.8± 2.3	10.9± 3.9	10.3± 3.9	9.3± 2.8	6.9± 2.4			
16	28.0	10.6± 2.8	10.6± 1.8	4.1± 2.9	15.4± 4.3	4.5± 1.8	9.2± 3.5	9.0± 3.7	5.4± 2.2	3.7± 1.5			
11.5	30.5	8.5± 2.6	10.2± 1.9	1.6± 1.6	13.9± 4.2	2.3± 1.3	5.9± 2.4	4.7± 2.7	3.2± 1.6	3.5± 1.4			
7.3	33.5	14.0± 4.4	11.2± 2.6	11.2± 5.6	3.3± 2.3	2.9± 2.1	13.4± 6.0	9.7± 4.9	2.6± 1.8	4.1± 2.1			
5.3	35.7	5.9± 2.1	10.3± 1.9	14.5± 5.5	12.7± 4.2	2.9± 1.5	6.2± 2.8	5.7± 2.9	4.7± 1.9	5.5± 1.9			
5.2	35.9	8.0± 1.4	10.0± 1.0	5.7± 2.0	11.9± 2.2	4.9± 1.1	7.2± 1.8	3.0± 1.3	5.0± 1.1	6.0± 1.1			
4.9	36.2	11.8± 2.3	8.8± 1.4	6.7± 2.7	12.5± 3.0	5.1± 1.5	5.5± 2.3	7.5± 2.5	6.0± 1.7	5.1± 1.7			

(Heidbreder et al., 1971). The angular distribution can be described by the relation $I(\theta) = I(\theta = 0°) \cdot cos^n(\theta)$ with $n = 3.5 \pm 1.2$. The vertical

Table 2.14: Altitude Dependence of Downward-Moving Differential Neutron Intensity (Preszler et al., 1974).

Altitude		Intensity [$\times 10^{-4}$ cm^{-2}s^{-1}sr^{-1}MeV^{-1}] at Zenith Angle θ									
		$10 < E_n < 30$ MeV			$30 < E_n < 50$ MeV			$50 < E_n < 100$ MeV			
[g/cm^2]	[km]	$\theta = 30°$	$\theta = 50°$	$\theta = 70°$	$\theta = 30°$	$\theta = 50°$	$\theta = 70°$	$\theta = 30°$	$\theta = 50°$	$\theta = 70°$
246	10.8	8.2± 1.0	8.5± 0.7	3.5± 1.1	13.3± 1.6	5.9± 0.8	8.4± 1.3	9.5± 1.7	8.2± 1.1	4.3± 0.7
109	15.9	11.9± 1.7	9.2± 1.0	9.9± 2.5	17.2± 2.7	8.5± 1.4	9.6± 1.8	11.9± 2.4	12.0± 1.8	4.2± 1.0
78.8	18.0	11.9± 1.7	11.5± 1.1	6.3± 2.0	19.7± 2.7	6.4± 1.2	11.2± 2.3	12.5± 2.5	10.0± 1.7	4.2± 1.0
58	20.0	10.0± 1.7	11.1± 1.2	3.4± 1.0	15.0± 2.5	10.8± 2.5	8.4± 1.9	5.9± 1.7	8.9± 1.7	3.4± 0.9
38.8	22.4	10.1± 1.5	7.1± 0.9	6.3± 2.0	4.7± 1.3	5.3± 1.2	10.6± 2.4	5.9± 1.7	5.5± 1.2	6.5± 1.5
26	25.0	6.7± 1.3	6.2± 0.8	5.7± 1.9	6.8± 1.7	5.5± 1.2	5.8± 1.6	4.8± 1.4	5.5± 1.2	3.6± 1.3
16	28.0	6.3± 1.3	4.7± 0.7	2.5± 1.3	7.9± 1.7	3.4± 0.9	5.1± 1.5	2.6± 1.1	5.5± 1.3	2.8± 1.0
11.5	30.5	6.2± 1.3	4.6± 0.8	1.0± 0.7	6.3± 1.6	1.5± 0.6	4.7± 1.4	1.8± 0.9	2.8± 0.9	2.2± 0.6
7.3	33.5	2.0± 0.9	3.6± 0.9	0.0	5.2± 2.1	3.0± 1.0	4.0± 1.8	0.6± 0.6	1.3± 0.7	1.7± 0.7
5.3	35.7	3 4± 1.0	3.5± 0.6	1.9± 1.9	4.7± 1.3	1.4± 0.6	3.6± 1.3	2.9± 1.2	0.5± 0.3	4.3± 1.1
5.2	35.9	3.7± 0.6	3.5± 0.4	1.2± 0.5	3.6± 0.7	1.8± 0.4	2.1± 0.6	2.3± 0.6	1.5± 0.4	2.3± 0.4
4.9	36.2	3.6± 0.7	2.6± 0.4	0.7± 0.5	4.7± 1.0	0.4± 0.2	1.4± 0.6	0.4± 0.2	1.3± 0.5	1.8± 0.5

intensity is given as $I(0°) = 6.25 \cdot 10^{-3} \cdot E^{-1.5} \pm 41\%$ cm^{-2}s^{-1}sr^{-1}MeV^{-1}. At the depth of 4.6 g/cm^2 the zenith angle distribution has been determined

for different energy intervals in the range $10 \leq E \leq 100$ MeV (Preszler et al., 1976). Fig. 2.34 shows the results for 41° N. In Fig. 2.35 the results for the energy interval $80 \leq E \leq 100$ MeV are compared with earlier measurements.

Another experiment in the energy range $10 \leq E \leq 500$ MeV has been carried out near the geomagnetic equator, using a CsI(Tl) crystal (Daniel et al., 1970). Figs. 2.36 and 2.37 show the altitude dependence of the neutron flux at low and high altitudes, respectively. A flux of $(2.0 \pm 0.5) \cdot 10^{-2}$ $cm^{-2}s^{-1}$ was derived for the top of the atmosphere. Fig. 2.38 shows the altitude dependence for low energy neutrons in the interval $1 \leq E \leq 10$ MeV (Mendell and Korff, 1963) compared with calculations (Wilson, 1972). In this paper the asymmetry of the flux, i.e., the value $\alpha = (upward\ flux - downward\ flux)/(total\ flux)$ was calculated as a function of atmospheric depth for different energies (Fig. 2.39). The integral neutron flux at the Pfotzer maximum (100 g/cm^2) was found to be 0.36 ± 0.10 $cm^{-2}s^{-1}$ for the energy range $3.5 \leq E \leq 10.0$ MeV (St. Onge, 1977).

The angular distribution has been measured at a depth of 4 g/cm^2 at Palestine, Texas, in the energy range $10 \leq E \leq 60$ MeV (Lockwood et al., 1979). The results are compared with those of Preszler et al. (1976) in Fig. 2.40.

It can be concluded that both the downward and the upward directed fluxes reach their maxima at about 100 g/cm^2. In the deep atmosphere the angular distributions show that the more energetic neutrons of 50 to 100 MeV are peaked near 180° (vertically downward). Above 40 g/cm^2 the situation reverses. The fluxes are greater in the upward than in the downward direction, and the maximum intensity occurs near 90° (horizontal direction). Neutrons below 30 MeV have their characteristic peaks at all altitudes near 0° and 180°, with a minimum at 90°.

Armstrong et al. (1973) calculated the atmospheric depth dependence of neutrons in the energy window $1 \leq E \leq 10$ MeV at latitude 42° N, and compared the results with other calculations and experimental data. This is illustrated in Figs. 2.41 and 2.42. Their high altitude data shown in Fig. 2.41 include also calculations by Lingenfelter (1963) and Newkirk (1963), and measurements by Holt et al. (1966) and Haymes (1964). Fig. 2.42 shows their calculations for low altitudes together with measurements of Boella et al. (1963) and Holt et al. (1966).

2.3.3 Energy Spectra

Low energy measurements have been carried out in the range $2 \leq E \leq 10$ MeV (Lockwood et al.,1979). Fig. 2.43 shows the omnidirectional neutron intensity compared with other results.

The omnidirectional neutron intensity at different altitudes is shown in Fig. 2.44 (Preszler et al., 1974). The albedo flux was measured at an altitude corresponding to a pressure of 5 mbar at a latitude of 41° N (Preszler et al., 1976). Fig. 2.45 shows the neutron spectrum for the energy interval $10 \leq E \leq 200$ MeV.

The albedo spectrum has also been measured at a pressure of 5 mbar near the equator, at latitude 7.8° N (Bhatt, 1976). The results are compared with those of Kanbach et al. (1974), Reppin et al. (1973), Eyles et al. (1972), Claflin and White (1974), White et al. (1973), together with the theoretical curves of Lingenfelter (1963) and are shown in Fig. 2.46.

The neutron spectrum near the Pfotzer maximum has been obtained with an organic liquid scintillation detector in the energy range $5 \leq E \leq 20$ MeV (St. Onge, 1977). Fig. 2.47 shows the differential energy spectrum compared with other results up to energies of 100 MeV.

The neutron energy spectrum has been determined by Hewitt et al. (1978) during a series of flights at an altitude of 12.5 km and geomagnetic latitudes of 38° N, 45° N and 48° N. Fig. 2.48 shows the spectra together with results of Hess et al. (1959) and calculations by Armstrong et al. (1973) and Merker (1972).

Recently neutron energy spectra were measured by Manfredotti et al. (1997) at mountain altitude (3500 m or 650 g/cm^2, Matterhorn Laboratory, Italy, 45° 56′ N, 7° 42′ S) and in an aircraft on its flight from Milano to Los Angeles and back (average altitude ~10,000 m or ~270 g/cm^2). These authors have used four different kinds of passive detectors and unfolded their response using various codes. The results are shown in Fig. 2.49 and, in a different representation, in Fig. 2.50 together with the theoretical spectrum of Schraube et al. (1996) obtained for the level of the Zugspitze (Germany, altitude 2963 m) and results of Merker (1973) for an atmospheric depth of 700 g/cm^2.

2.3.4 Theoretical Contributions

Theoretical neutron energy spectra have been obtained with Monte Carlo calculations for the energy range $10^{-9} \leq E \leq 10^5$ MeV at various depths

in the atmosphere, for solar minimum and a latitude of 42° N (Armstrong et al., 1973). Figs. 2.51 and 2.52 show the neutron energy spectra from the top of the atmosphere down to sea level. Flückiger (1977) used a Monte Carlo calculation to compute the differential energy spectrum of neutrons at a depth of 650 g/cm^2. His spectrum has been compared with measurements and other calculations. A compilation of energy spectra of neutrons near the top of the atmosphere is shown in Fig. 2.53 (Armstrong et al., 1973). Additional calculations have been carried out by Hoffman et al. (1978), Ershkovich (1974) and Schraube et al. (1996).

References

Ahluwalia, H.S.: PICRC, 11, p. 3867 (1975).

Albernhe, F., I.M. Martin, R. Talon, and G. Vedrenne: Ann. Geophys.,27, p. 339 (1971).

Armstrong, T.W., K.C. Chandler, and J. Barish: J. Geophys. Res., 78, p. 2715 (1973).

Baird, G.A. and B.G. Wilson, Can. J. Phys., 44, p. 2131 (1966).

Bhatt, V.L., and V.R. Parikh: Acta Phys. Acad. Sci. Hung., 29, Suppl. 2, p. 721 (1970).

Bhatt, V.L.: J. Geophys. Res., 81, p. 4603 (1976).

Boella, G.G., G. Delgli Antoni, C. Dilworth, G. Gianelli, E. Rocca, L. Scarsi, and D. Shapiro, Nuovo Cimento, 29, p. 103, (1963).

Claflin, E.S. and R.S. White: J. Geophys. Res., 79, p. 959 (1974).

Daniel, R.R., G.S. Gokhale, G. Joseph, and P.J. Lavakare: Acta Phys. Acad. Sci. Hung., 29, Suppl. 2, p. 697 (1970).

Ershkovich, A.I.: J. Geophys. Res., 79, . 5295 (1974).

Eyles, C.J., A.D. Linney, and G.K. Rochester: Planet. Space Sci., 20, p. 1915 (1972).

Flückiger, E.: PICCR, 4, p. 144 (1977).

Freden, S.C. and R.S. White: J. Geophys. Res.,67, p. 25 (1962).

Haymes, R.C.: J. Geophys. Res., 69,p. 841 (1964).

Heidbreder, E., K. Pinkau, C. Reppin, and V. Schönfelder: J. Geophys. Res., 76, p. 2905 (1971).

Hess, W.N., H.W. Patterson, R. Wallace, and E.L. Chupp: Phys. Rev., 116, p. 445 (1959).

Hess W.N., E. H. Canfield and R. E. Lingenfelter: J. Geophys. Res., 66, p. 665 (1961).

Hewitt, J.E., L. Hughes, J.W. Baum, A.V. Kuehner, J.B. McCaslin, A. Rindi, A.R. Smith, L.D. Stephens, R.H. Thomas, R.V. Griffith, and C.G. Welles: Health Physics, 34, p. 375 (1978).

Hoffman, T.J., L.M. Petrie, S.N. Cramer, D.E. Bartine, and S.K. Fraley: Trans. Am. Nucl. Soc., 30, 595 (1978).

Holt, S.S., R.B. Mendell, and S.A. Korff: J. Geophys. Res., 71, p. 5109 (1966).

Jenkins, R.W., S.O. Ifedili, J.A. Lockwood, and H. Razdan: J. Geophys. Res., 76, p. 7470 (1971).

Kanbach, G., C. Reppin, and V. Schönfelder: J. Geophys. Res., 79, p. 5159 (1974).

Klumpar, D.M., J.A. Lockwood, R.N. St. Onge, and L.A. Friling: J. Geophys. Res., L 78, p. 7959 (1973).

Korff, S.A., R.B. Mendell, M. Merker, E.S. Light and H.J. Verschell: Atmospheric Neutrons. Final report. New York University, N.Y., Dept. of Physics (1979).

Lingenfelter, R.E.: J. Geophys. Res., 68, p. 5633 (1963).

Lockwood, J.A., C. Chen, L.A. Friling, and R.N. St. Onge: J. Geophys. Res., 81, p. 6211 (1976).

Lockwood, J.A., L. Hsieh, L.Friling, C. Chen, and D. Swartz: J. Geophys. Res., 84, p. 1402 (1979).

Luzov, A.A., Yu.G. Matyukhin, and V.E. Sdobnov: Izv. Akad. Nauk SSSR Ser. Fiz., 35, p. 2583 (1971).

Luzov, A.A., N.I. Pakhomov, and V.E. Sdobnov: Ivz. Akad. Nauk SSSR Ser. Fiz., 40, p. 666 (1976).

Manfredotti, C., C. Ongaro, A. Zanini, M. Cavaioli, and L. Tommasino: in SPIE Proceedings Series, ed. George Vourvopoulos, Vol. 2867, p. 619 (1997).

Mendell, R.B. and S.A. Korff: J. Geophys. Res., 68, p. 5487 (1963).

Merker, M.: Phys. Rev. Lett., 29, p. 1531 (1972).

Merker, M.: Health Physics, 25, p. 524 (1973).

Merker, M.: PICRC, 4, p. 1393 (1975).

Miyake, S. and K. Hinotani: J. Phys. Soc., 22, p. 845 (1957).

Newkirk, L.L.: J. Geophys. Res. 68, p. 1825 (1963).

O'Brien, K., H.A. Sandmeier, G.E. Hansen, and J.E. Campbell: J. Geophys. Res., 83, p. 114 (1978).

Preszler, A.M., G.M. Simnett, and R.S. White: J. Geophys. Phys. Rev. Lett.,28, p. 982 (1972).

Preszler, A.M., G.M. Simnett, and R.S. White: J. Geophys. Res., 79, p. 17 (1974).

Preszler, A.M., S. Moon, and R.S. White: J. Geophys. Res., 81, p. 4715 (1976).

Reppin, C., V. Schönfelder, G. Kanbach, and K. Pinkau: PICRC, 2, p. 834 (1971).

Reppin, C., G. Kanbach, and V. Schönfelder: PICRC, 2, p.903 (1973).

Schraube, J., J. Jakes, A. Sannikov, E. Weitzenegger, S. Roesler, and W. Heinricht: Proc. Internat. Conf. on Neutrons in Research and Industry, June 9 -15, Crete, Greece, pp 264 - 273 (1996).

St. Onge, R.N.: Phys. Rev., D, 16, p. 537 (1977).

White, R.S., S. Moon, A.M. Preszler, and G.M. Simnett: Space Res., 13, p. 683 (1973).

Wilson, J.W.: Trans. Amer. Nucl. Soc., 15, p. 969 (1972).

Zych, A.D., and G.M. Frye, Jr.: Acta Phys. Acad. Sci. Hung., 29, Suppl. 2, p. 709 (1970).

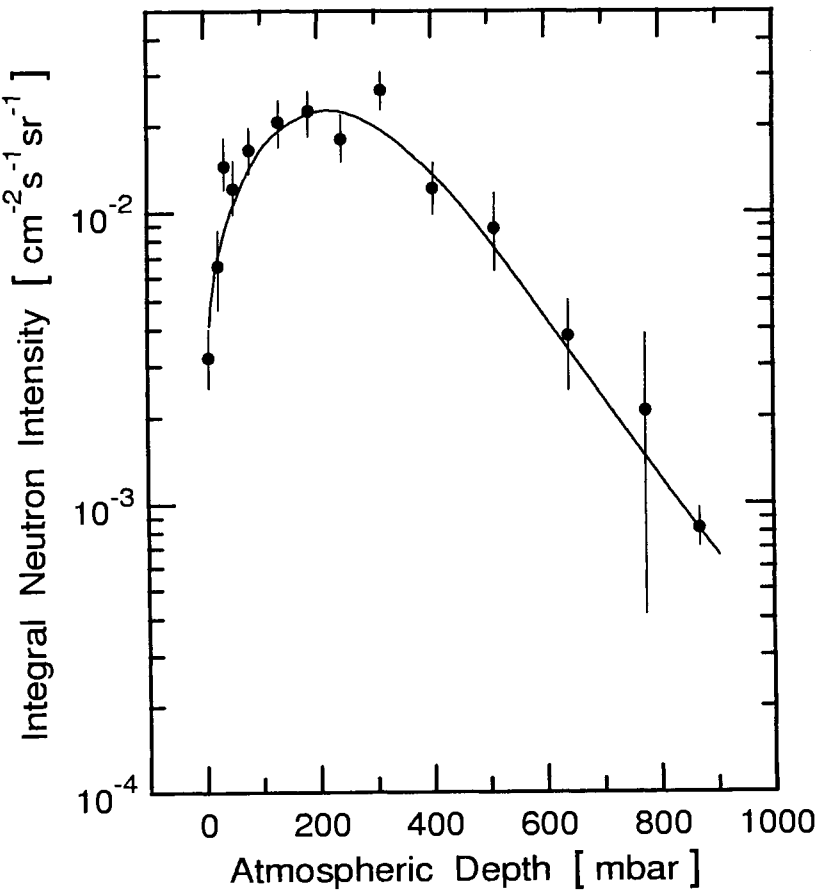

Figure 2.28: Neutron intensity versus atmospheric depth in mbar, in downward vertical direction, for energies $50 \leq E \leq 350$ MeV at a cutoff rigidity of 15 GV (Eyles, 1972). The balloon was launched from Makerere University, Kampala, Uganda.

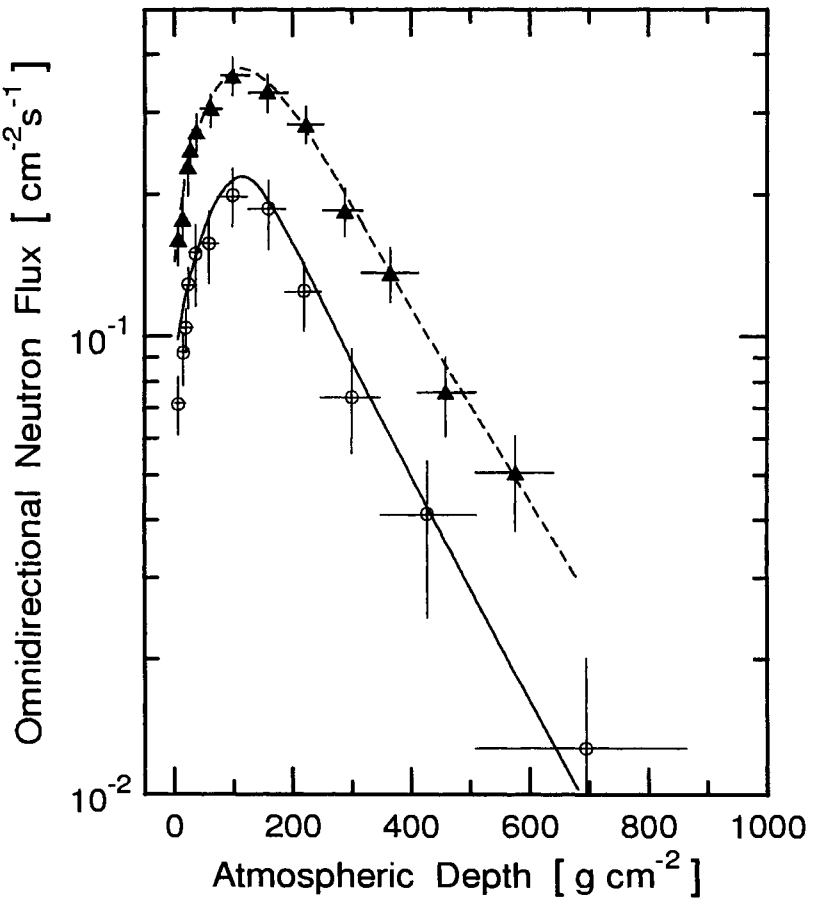

Figure 2.29: Altitude dependence of the neutron flux for two energy ranges measured at Guyana at a latitude of 10° N (Albernhe et al., 1971). The curves are fits to the data.

▲ 0.7 MeV - 4.5 MeV | ○ 1.0 MeV - 10 MeV

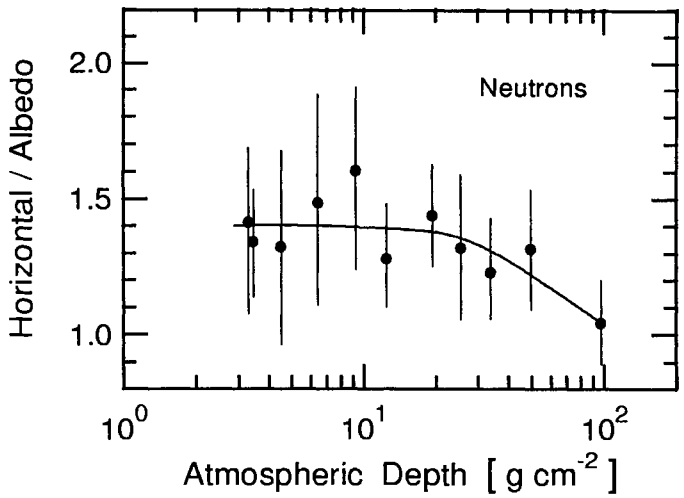

Figure 2.30: Ratio of horizontal to albedo flux versus atmospheric depth for neutrons of energy $12 \leq E \leq 100$ MeV, measured at Texas (Zych and Frye, 1970).

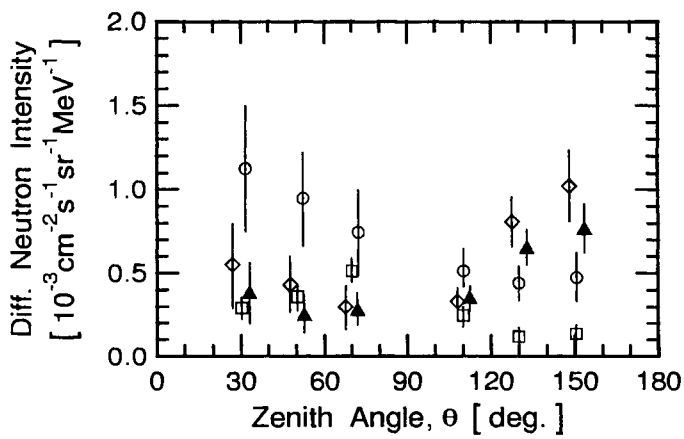

Figure 2.31: Differential neutron intensities corrected at various atmospheric depths as a function of zenith angle for the energy range $50 \leq E \leq 100$ MeV, measured over Palestine, TX, $\lambda = 41°$ N (Preszler et al., 1974).

▲ 246 g/cm^2 | ◇ 78.8 g/cm^2 | ○ 38.8 g/cm^2 | □ 4.9 g/cm^2

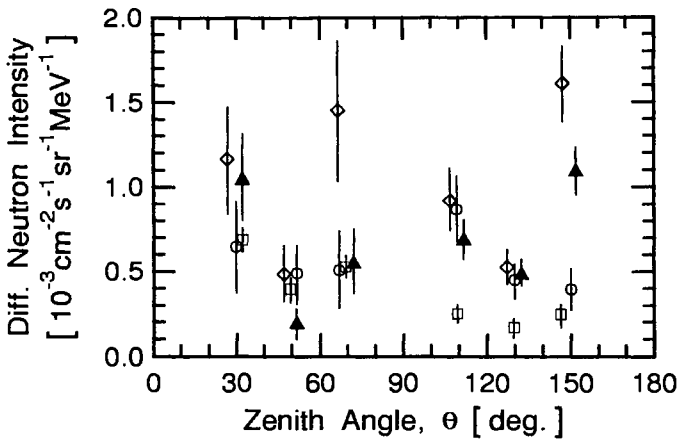

Figure 2.32: Differential neutron intensities corrected at various atmospheric depths as a function of zenith angle for the energy range $30 \leq E \leq 50$ MeV, measured over Palestine, TX, $\lambda = 41°$ N (Preszler et al., 1974).

▲ 246 g/cm^2 | ○ 38.8 g/cm^2 | ◇ 78.8 g/cm^2 | □ 4.9 g/cm^2

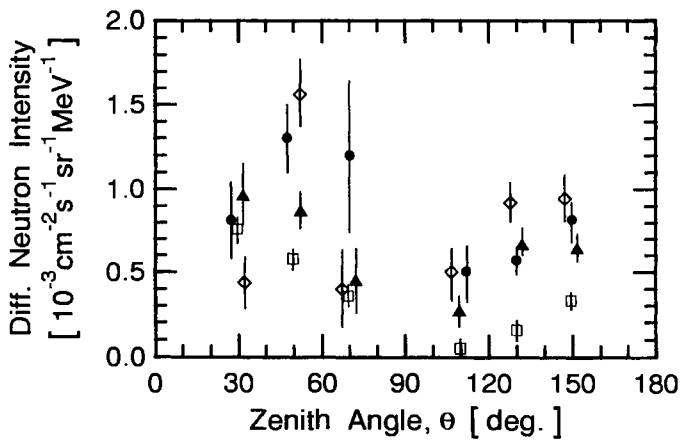

Figure 2.33: Differential neutron intensities corrected at various atmospheric depths as a function of zenith angle for the energy range $10 \leq E \leq 30$ MeV, measured over Palestine, TX, $\lambda = 41°$ N (Preszler et al., 1974).

▲ 246 g/cm^2 | ○ 38.8 g/cm^2 | ◇ 78.8 g/cm^2 | □ 4.9 g/cm^2

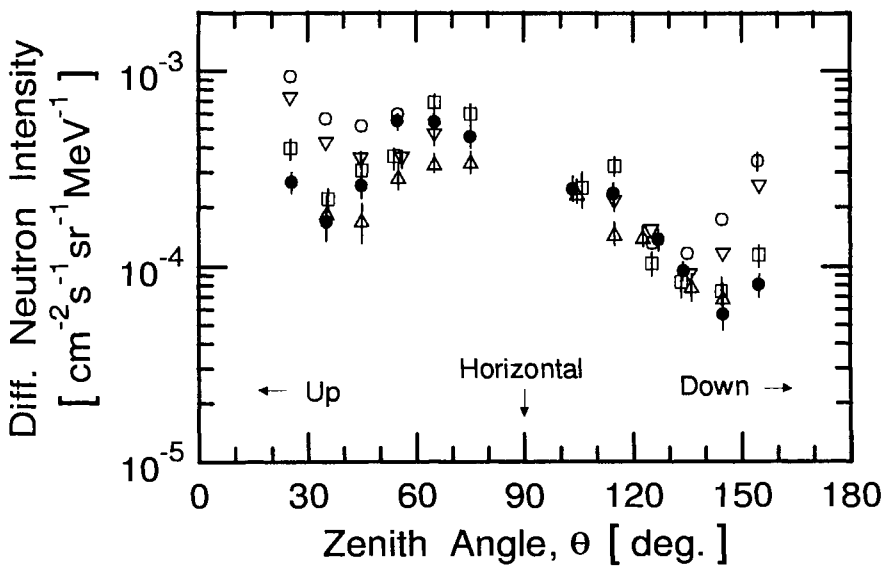

Figure 2.34: Zenith angle distribution of differential neutron intensity at 4.6 g/cm^2 and latitude 41° N for various energy intervals (Preszler et al., 1976).

○	$10 \leq E \leq 30$ MeV	●	$60 \leq E \leq 80$ MeV
▽	$30 \leq E \leq 50$ MeV	△	$80 \leq E \leq 100$ MeV
□	$50 \leq E \leq 60$ MeV		

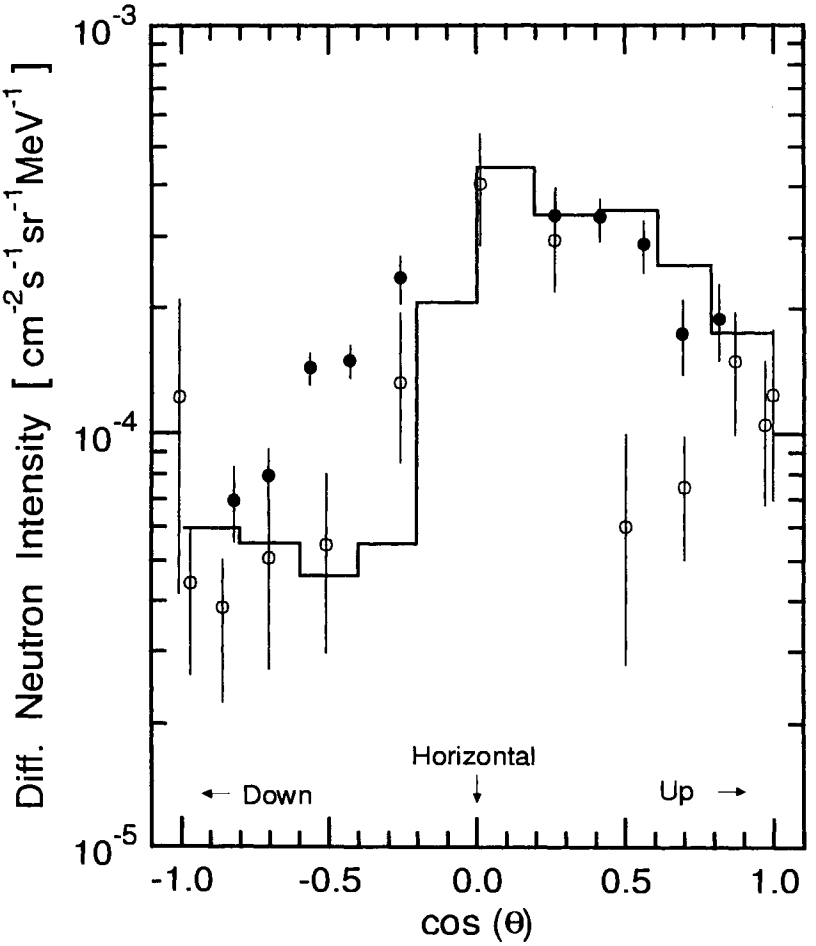

Figure 2.35: Experimental angular distribution of the neutron intensity at depth $X = 4.6$ g/cm^2 and latitude 41° N for the energy range $80 \leq E \leq 100$ MeV (Preszler et al., 1976). Also shown are the data obtained by Kanbach et al. (1974) and theoretical results of Merker (1975). (This figure is the mirror image of the originally published figure.)

- • Preszler et al. (1976) $80 \leq E \leq 100$ MeV, $X = 4.6$ g/cm^2
- ○ Kanbach et al. (1974) $90 \leq E \leq 110$ MeV, $X = 4.7$ - 8.6 g/cm^2
- ⌐⌙ Merker (1975) calc. $79 \leq E \leq 100$ MeV, $X = 0$ - 10 g/cm^2

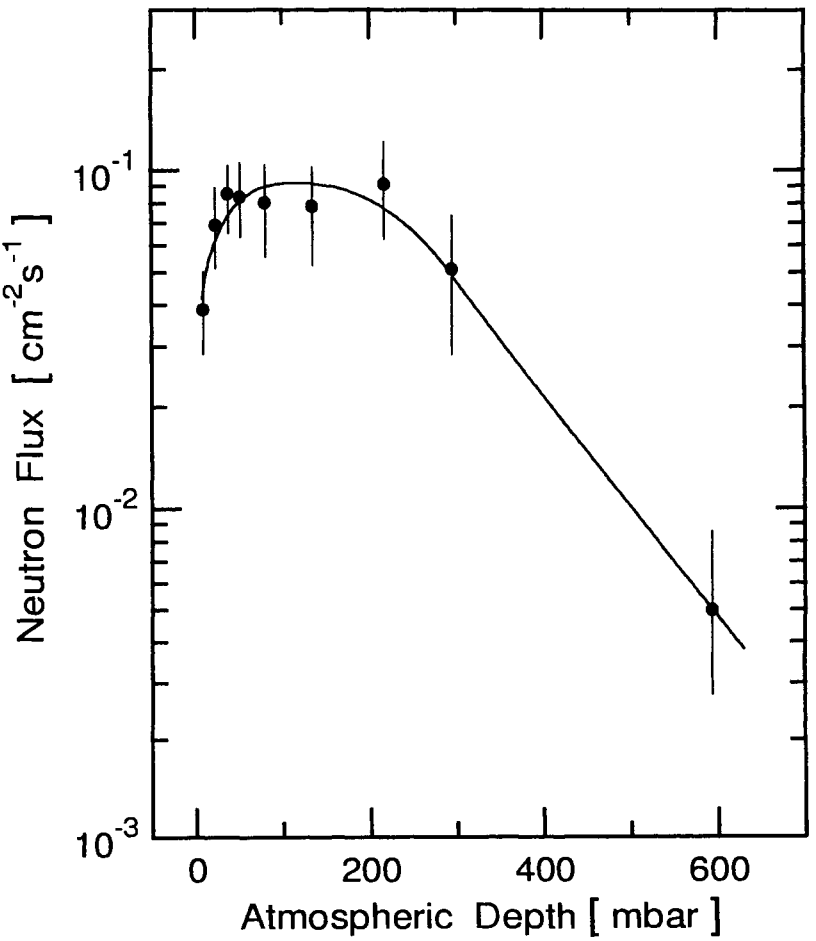

Figure 2.36: Altitude dependence of the neutron flux in the energy range $10 \leq E \leq 500$ MeV near the geomagnetic equator (Daniel et al., 1970).

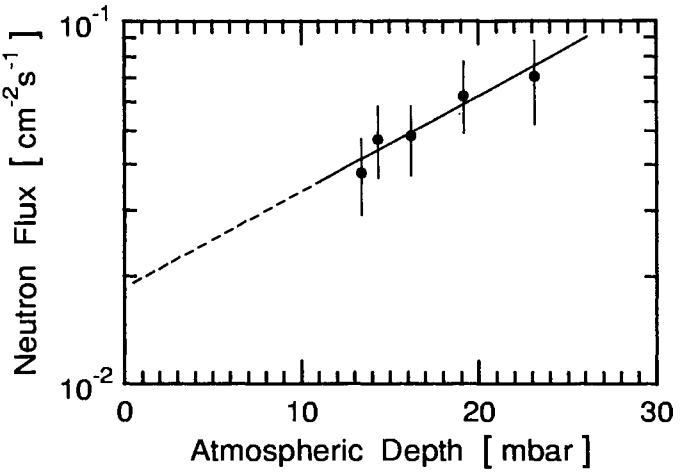

Figure 2.37: Altitude dependence of the neutron flux in the energy range $10 \leq E \leq 500$ MeV near the geomagnetic equator at low atmospheric depths (Daniel et al., 1970).

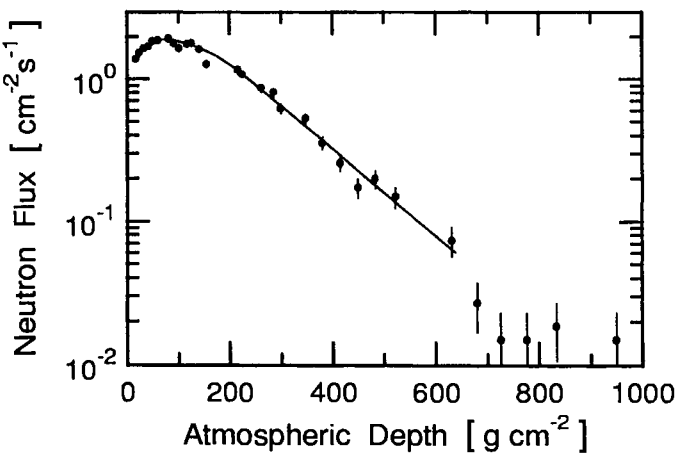

Figure 2.38: Altitude dependence of the neutron flux in the energy range $1 \leq E \leq 10$ MeV (Mendell and Korff, 1963).

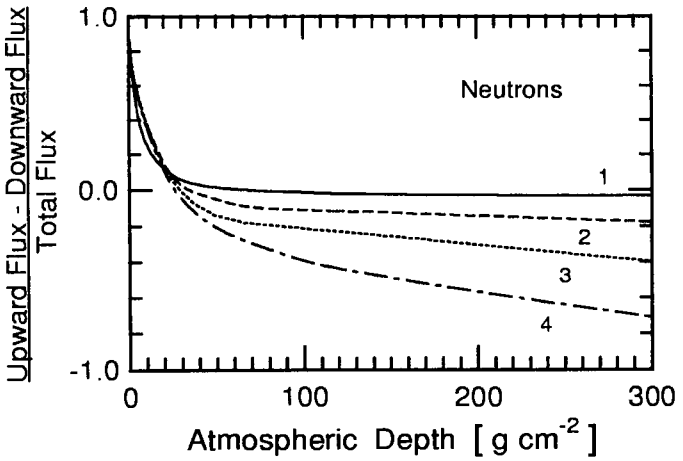

Figure 2.39: Asymmetry coefficient α of neutron flux versus atmospheric depth (Wilson, 1972).

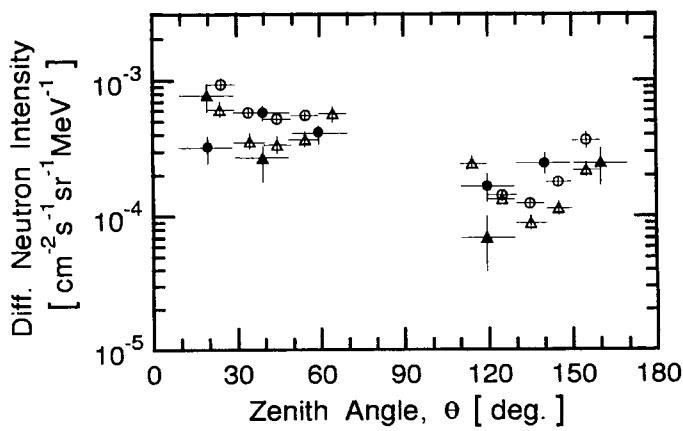

Figure 2.40: Experimental angular distribution of differential neutron intensities at 4 g/cm^2 for the energy range $10 \leq E \leq 60$ MeV at Palestine, TX, 41° N (Lockwood, 1979), compared with data by Preszler et al. (1976).

Lockwood et al. (1979)		Preszler et al. (1976)	
•	$10 \leq E \leq 30$ MeV	○	$10 \leq E \leq 30$ MeV
▲	$30 \leq E \leq 60$ MeV	△	$30 \leq E \leq 60$ MeV

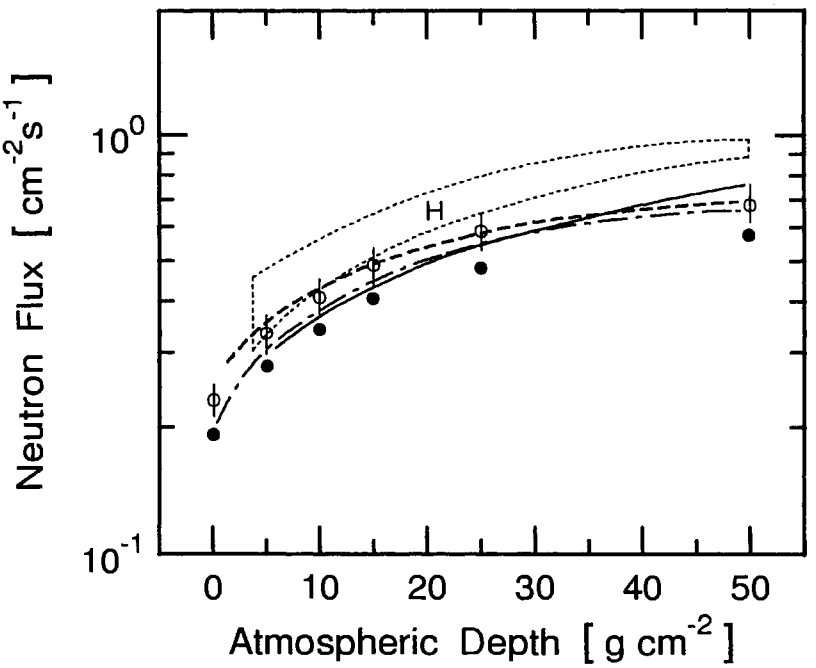

Figure 2.41: Calculated depth dependence of neutron flux in the energy range $1 \leq E \leq 10$ MeV near the top of the atmosphere compared with measurements (Armstrong et al., 1973).

——	Holt et al. (1966)	measurement
H	Haymes (1964) (1 - 14 MeV)	measurement
- - -	Lingenfelter (1963)	calculation
-·-	Newkirk (1963)	calculation
• , o	Armstrong et al. (1973)	calculation
•	incident protons only	calculation
o	incident protons + α	calculation

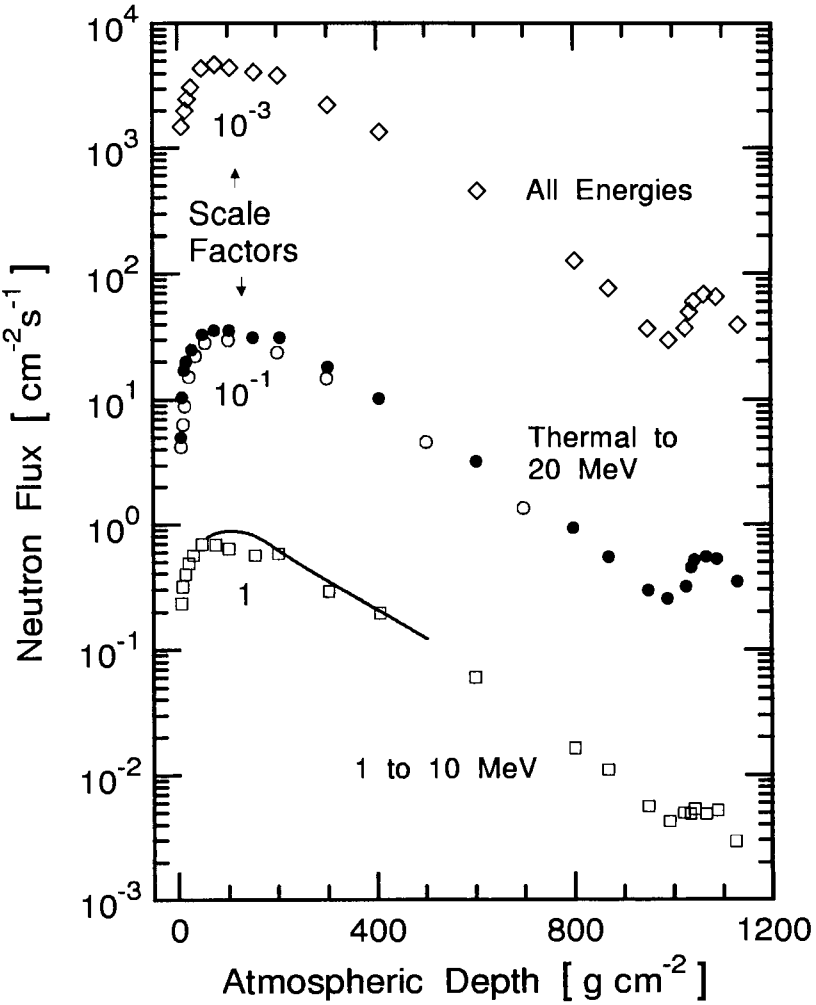

Figure 2.42: Calculated depth dependence of neutron intensity for different energy ranges compared with measurements during solar minimum at $\lambda = 42°$ (Armstrong et al., 1973). (Multiply readings on ordinate with appropriate scale factor to get true neutron flux.)

•	Armstrong et al. (1973)	calculation
o	Boella et al. (1963)	measurement
—	Holt et al. (1966)	measurement

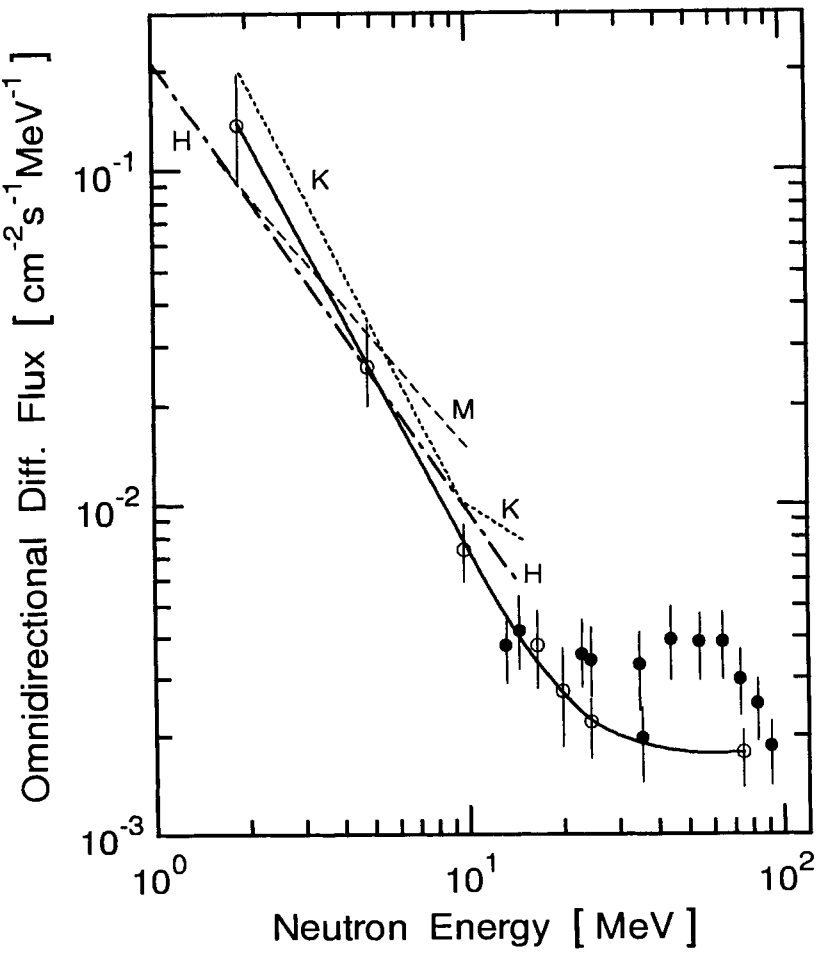

Figure 2.43: Omnidirectional differential neutron energy spectrum at latitude 42° N and atmospheric depth 5 g/cm^2 (Lockwood et al., 1979).

o , —	Lockwood et al. (1976)	K	Klumpar et al. (1973)
•	Preszler et al. (1976)	M	Merker et al. (1972)
H	Haymes (1964)		

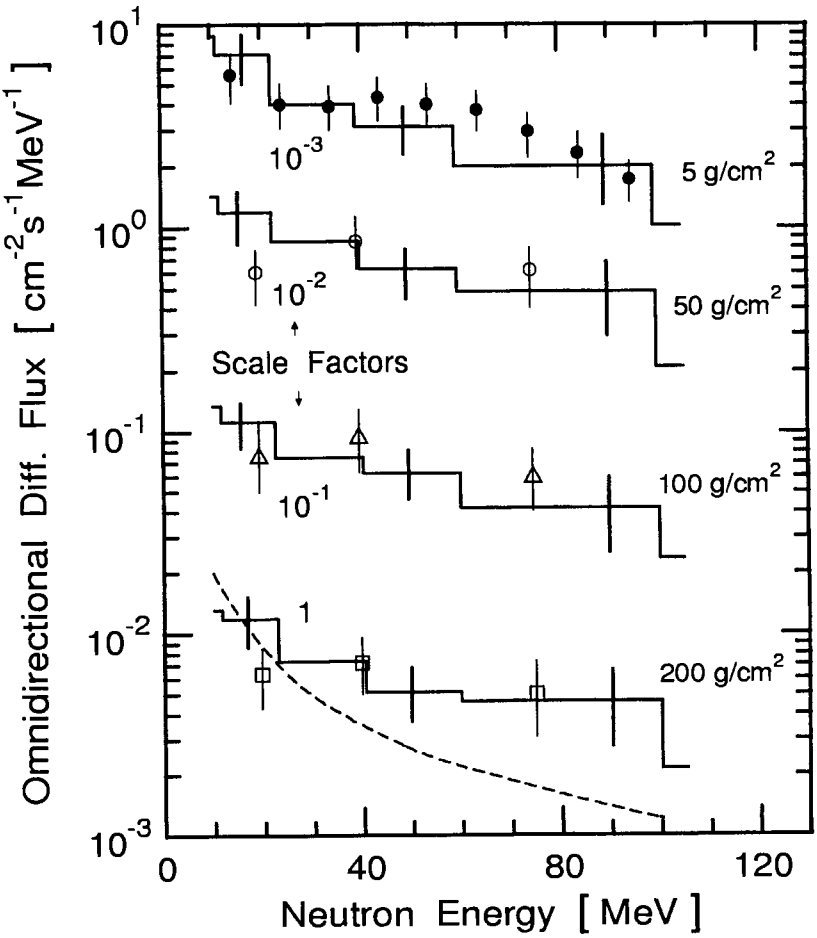

Figure 2.44: Energy dependence of the omnidirectional upward-moving neutron flux at various altitudes and latitude 41° N (Preszler et al., 1974). (Multiply readings on ordinate with appropriate scale factor to get true neutron flux.)

•, ○, △, □ Preszler et al. (1974)
--- Hess et al. (1959)
Armstrong et al. (1973)

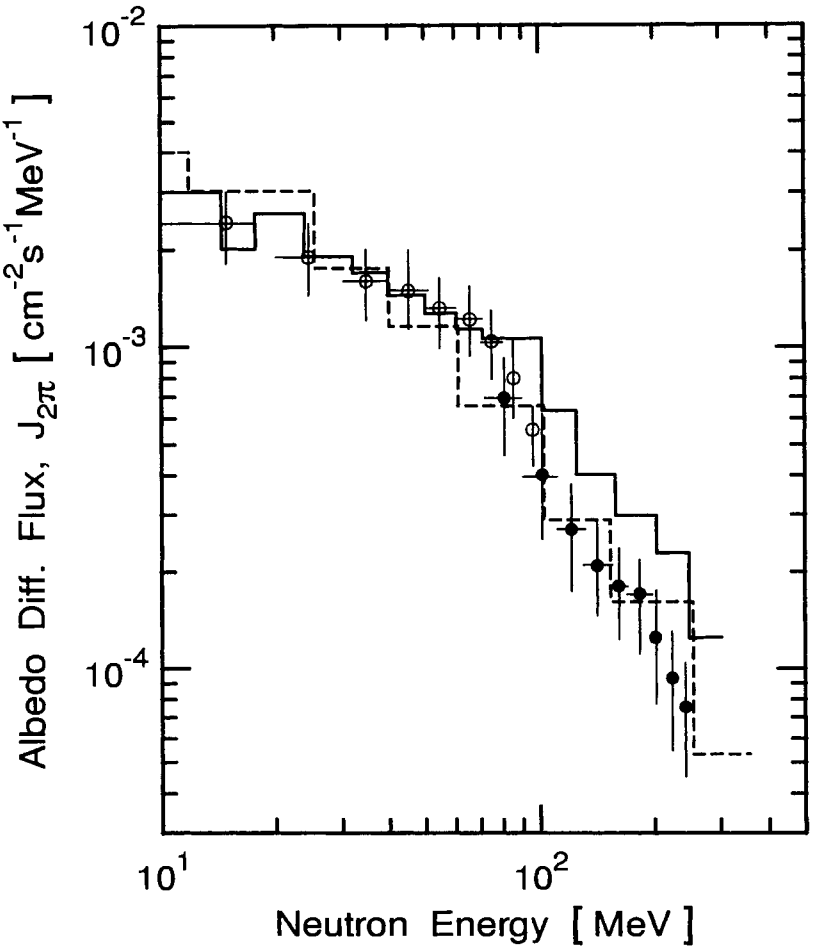

Figure 2.45: Differential albedo neutron spectrum at a pressure of 5 mbar and latitude 41° N (Preszler et al., 1976). Given is the leakage current, $J_{2\pi}$, integrated over a solid angle of 2π steradians.

o	Preszler et al. (1976)	measurements
•	Kanbach et al. (1974)	measurements
⊓	Armstrong et al. (1973)	calculation
⊓	Merker (1972)	calculation

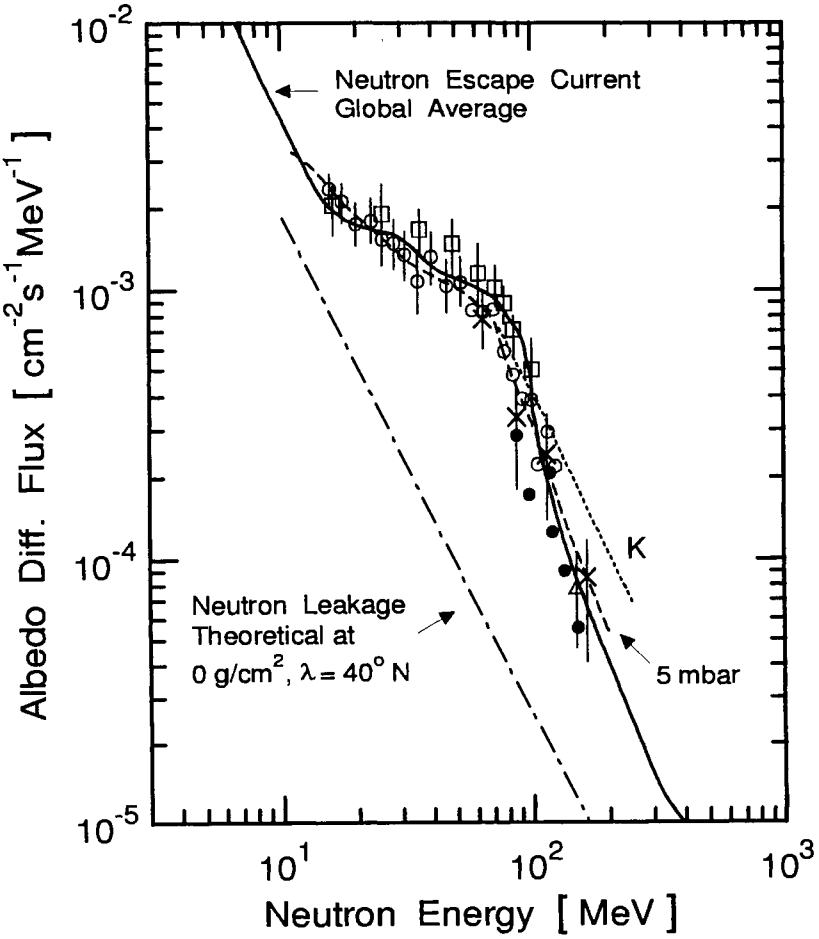

Figure 2.46: Differential albedo neutron spectrum at a pressure of 5 mbar and latitude 7.8° N (Bhatt, 1976).

- - - , o	Bhatt (1976)	5 mbar, 7.8° N
×	Bhatt (1976)	4 mbar, 7.8° N
□	White et al. (1973)	5.4 g/cm^2, 40° N
•	Reppin et al. (1973)	4.7 and 8.6 g/cm^2, 40° N
△	Eyles et al. (1972)	3 mbar, global average
——	Claflin and White (1974)	global average
- · -	Lingenfelter (1963)	calculation
K	Kanbach et al. (1974)	4.7 - 8.6 g/cm^2, 41° N

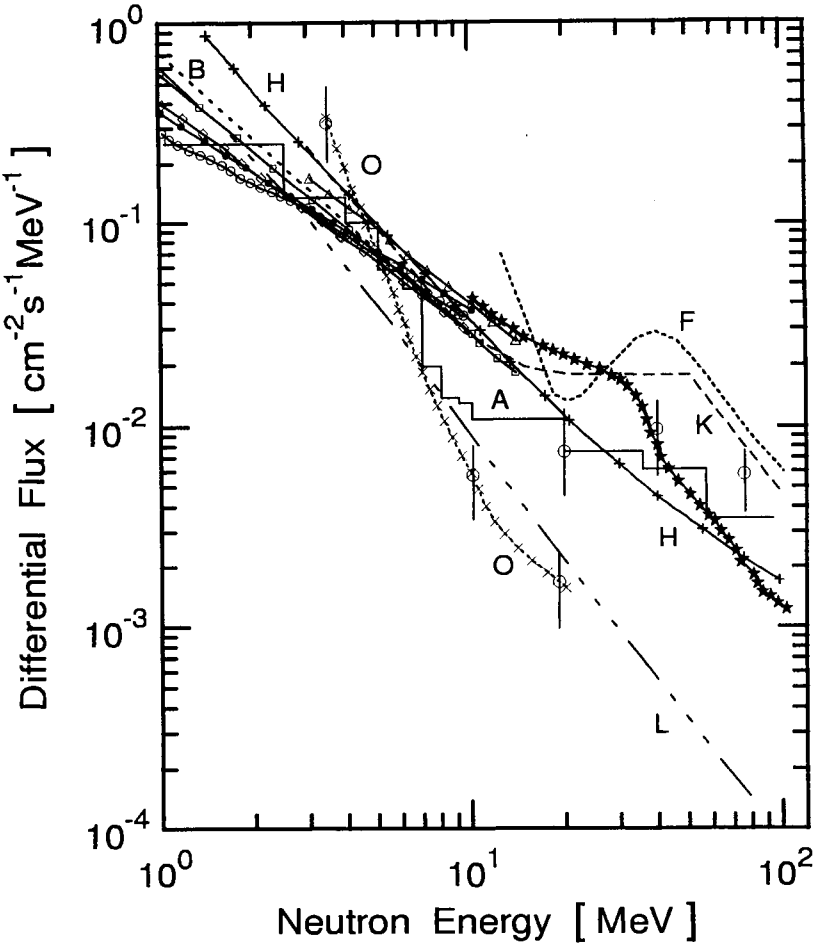

Figure 2.47: Differential neutron energy spectrum at Pfotzer maximum (~100 g/cm^2) and latitude 42° N (St. Onge, 1977).

O	St. Onge (1977)	B	Baird, Wilson (1966)
•	Holt et al. (1966)	L	Lingenfelter (1963)
△	Albernhe et al. (1971)	∞∞∞	Jenkins et al. (1971)
□	Haymes et al. (1964)	F	Freden et al. (1962)
◇	Mendell, Korff (1963)	★★★	Miyake et al. (1957)
o	Preszler et al. (1974)	H	Hess et al. (1961)
A	Armstrong (1973)	K	Klumpar et al. (1973)

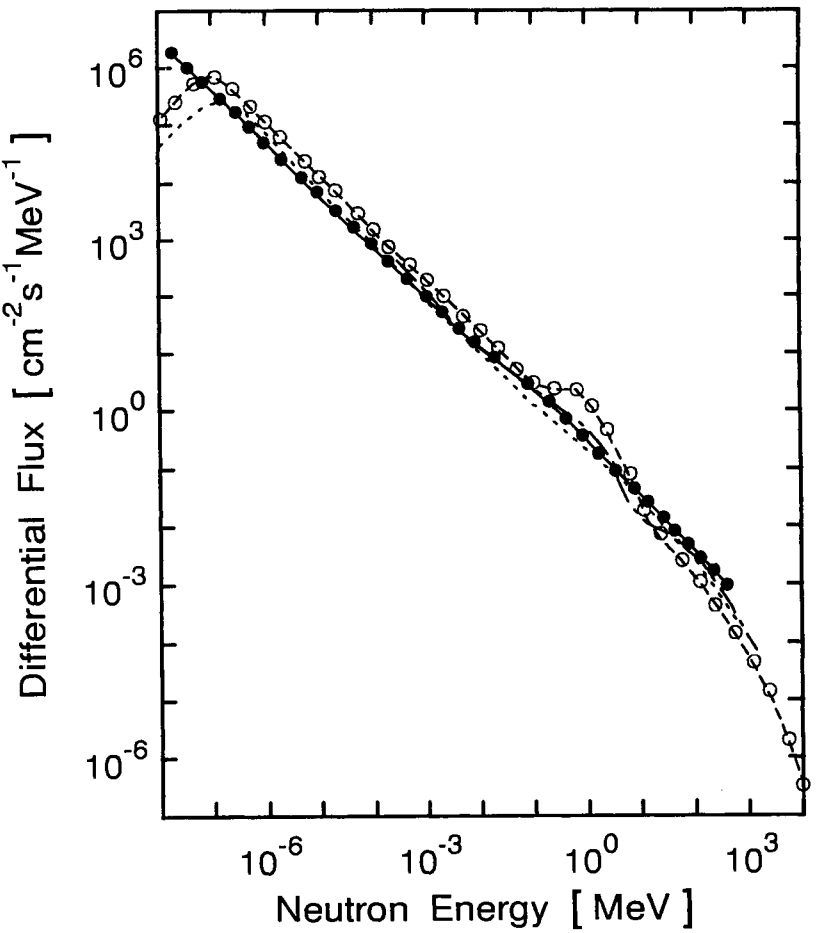

Figure 2.48: Differential neutron spectra at an altitude of 12.3 km and a latitude range from 38° to 48° N (Hewitt et al., 1978).

•	Hewitt et al. (1978)	measurement
o	Hess et al. (1961)	measurement at 200 g/cm^2, 44° N
....	Armstrong (1973)	calculation
- - -	Merker (1972)	calculation

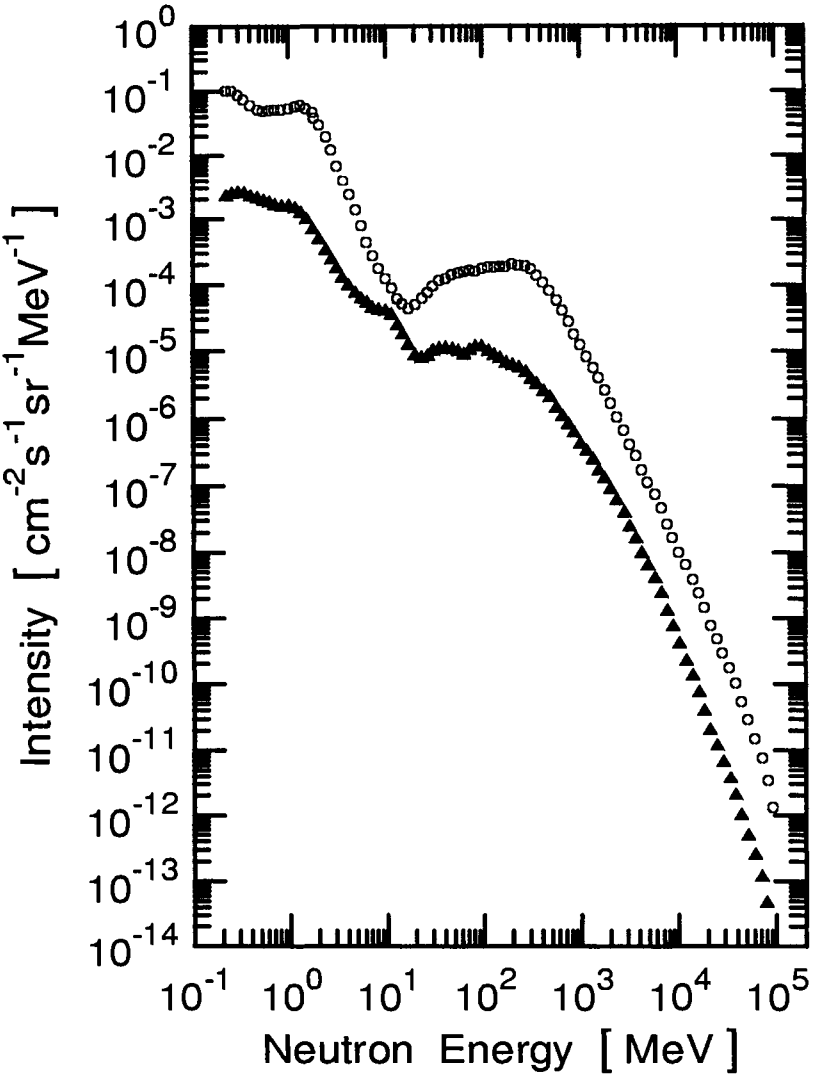

Figure 2.49: Neutron energy spectra obtained at altitudes of 3500 m and 11650 m using passive detectors and corresponding unfolding codes (Manfredotti et al., 1997).

- o Aircraft, altitude ~11650 m (~230 g/cm^2)
- ▲ Matterhorn Lab., Italy 3500 m (650 g/cm^2)

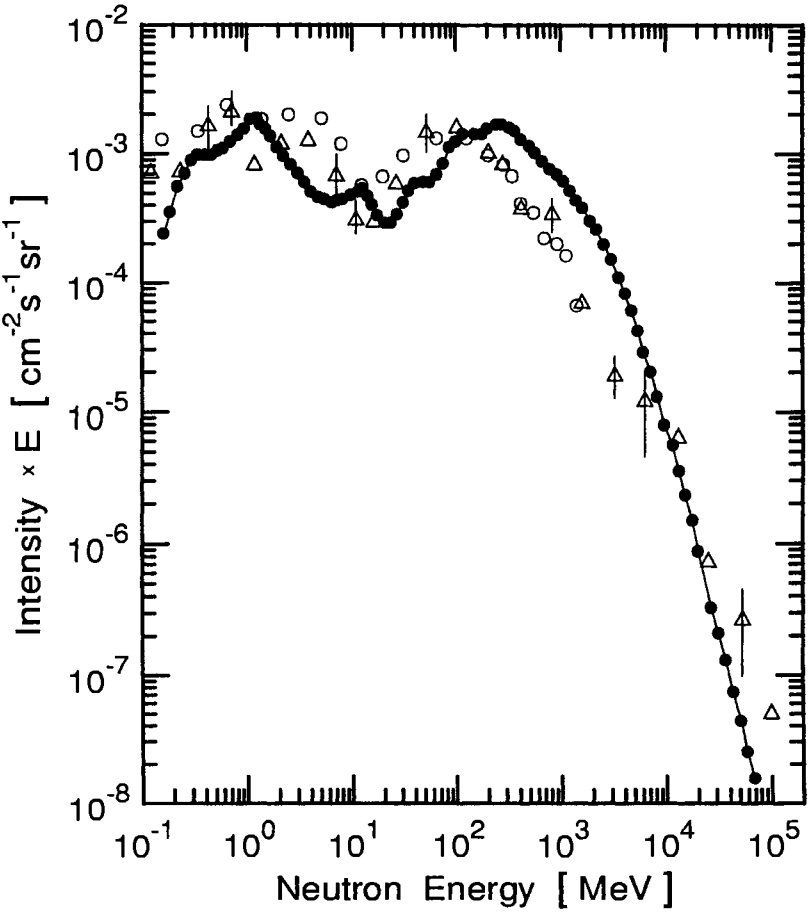

Figure 2.50: Neutron energy spectra obtained for different altitudes. Note that the intensity is multiplied with the energy. The solid line connects the full circles (after Manfredotti et al., 1997).

- • Manfredotti et al. (1997), 3500 m (650 g/cm^2)
- o Merker (1973) 700 g/cm^2 (~3200 m)
- △ Schraube et al. (1996), Zugspitze 2963 m

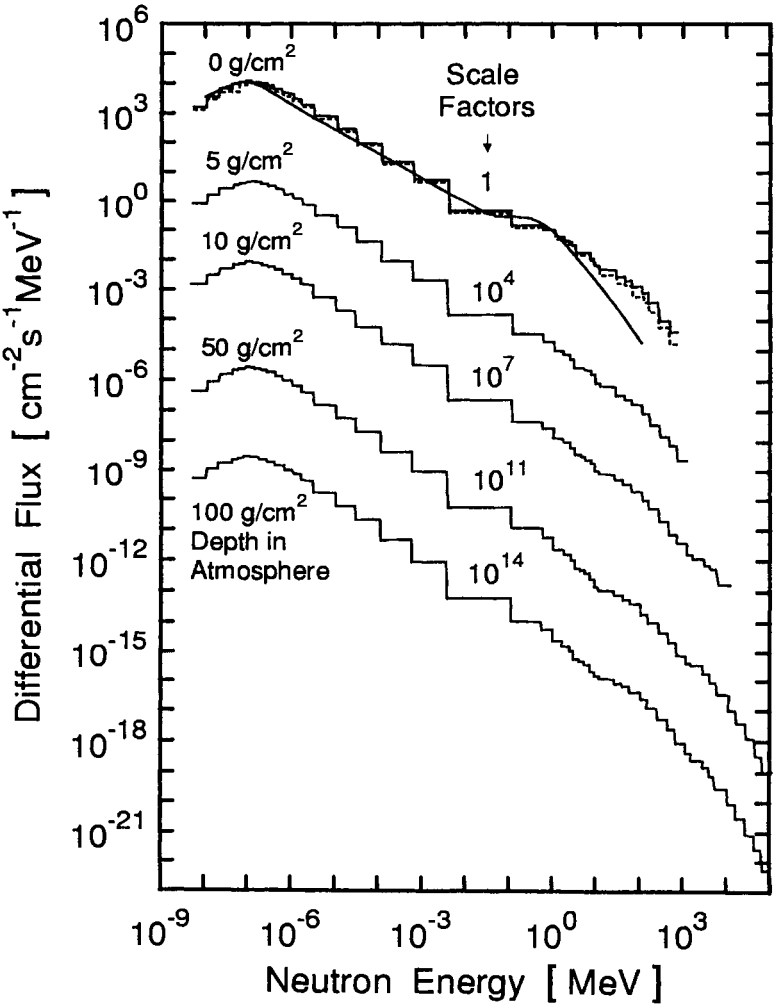

Figure 2.51: Omnidirectional differential energy spectra of neutrons at various depths in the atmosphere as indicated, for solar minimum and latitude 42° N (Armstrong et al., 1973). (Multiply reading with appropriate scale factor to get true flux.)

Armstrong et al. (1973)
incident protons + α
incident protons only
Lingenfelter (1963)

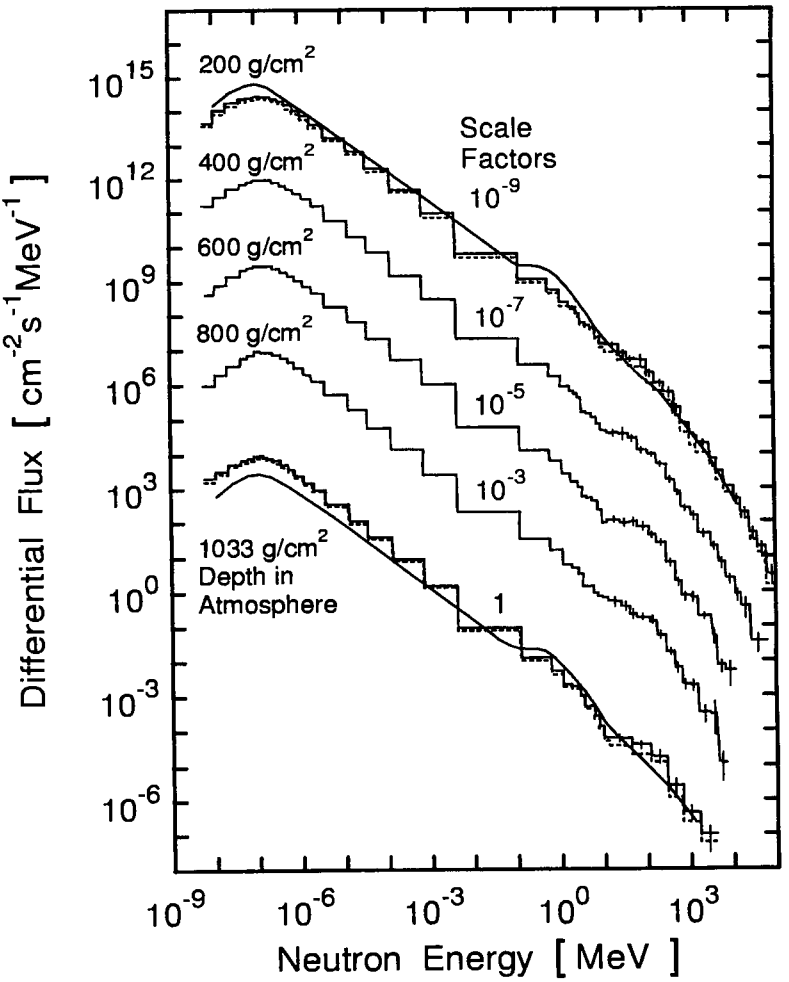

Figure 2.52: Omnidirectional differential energy spectra of neutrons at various depths in the atmosphere as indicated, for solar minimum and latitude 42° N (Armstrong et al., 1973). (Multiply reading with appropriate scale factor to get true flux.)

Armstrong et al. (1973)
incident protons + α
incident protons only
Hess et al. (1959) measurements

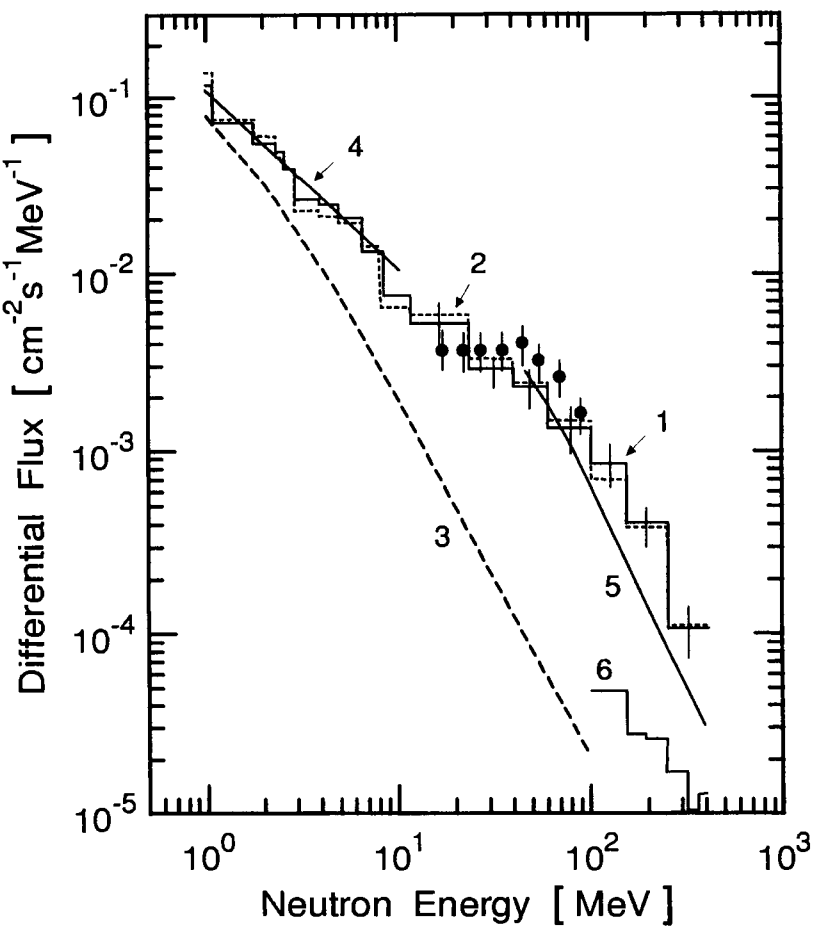

Figure 2.53: Differential energy spectrum of neutrons near the top of the atmosphere (Armstrong et al., 1973).

1	Armstrong et al. (1973)	0 g/cm^2	calculation
2	Armstrong et al. (1973)	5 g/cm^2	calculation
3	Lingenfelter (1963)	0 g/cm^2	calculation
4	Holt et al. (1966)	0 g/cm^2	measurement
5	Freden and White (1962)	0 g/cm^2	estimated
6	Heidbreder et al. (1970)	7 g/cm^2	measurement
•	Preszler et al. (1972)	5 g/cm^2	measurement

2.4 Gamma Rays

2.4.1 Introduction

Atmospheric gamma rays arise from a variety of processes and secondary particles that are produced by the primary radiation in interaction processes with atmospheric nuclei. The altitude dependence of the energy spectra of the gamma rays contains information on the secondary energy balance and the relative role of electromagnetic and neutron-induced processes, responsible for the production, absorption, and diffusion of these photons.

Several nuclear and electromagnetic processes are responsible for the gamma and X-ray fluxes in the atmosphere. The chief contributors are:

- neutral pion decay
- various decays of other unstable particles
- bremsstrahlung of electrons and positrons
- positron and electron annihilation
- inelastic scattering processes
- de-excitation of highly excited nuclei (after spallation or neutron capture)

Fig. 2.54 illustrates the processes schematically, together with the typical energies. Each π^0 contributes two quanta to the gamma ray spectrum, totaling at least 140 MeV. Electrons resulting from $\pi \rightarrow \mu \rightarrow e$ - decays and knock-on electrons have a probability of about 0.3 - 0.4 for producing photons via bremsstrahlung. The 0.51 MeV gamma lines are a measure for the electron - positron annihilation rate. Nuclear collisions produce neutrons with energies around 10 MeV that may be scattered or captured by ^{14}N and ^{16}O nuclei, leading to excited states which emit characteristic gamma lines. Gamma rays of energy less than about 2 MeV degrade slowly by multiple Compton scattering, losing only a small fraction of energy per collision, thus building up a continuum to lower energies until they are removed catastrophically by photoelectric absorption around 30 keV.

In the energy range up to approximately 10 MeV most of the experimental work has been carried out with scintillation telescopes. At higher energies combinations of scintillation and Cherenkov detectors have been

used frequently. But also spark chamber arrangements, emulsion stacks and combinations of both have been used. At even higher energies, beyond 1 TeV, data have been obtained with emulsion chambers. The latter consist of stacks of nuclear emulsion, interlaced with lead plates and sheets of X-ray film.

2.4.2 Energy Spectra Below 1 TeV

Daniel and Stephens (1974) reviewed the experimental data at a vertical geomagnetic threshold rigidity of 4 GV to 5 GV , corresponding to a latitude of 40° N, in the energy range $0.02 \leq E \leq 200$ GeV. These authors express the differential intensity per gram per square centimeter of air. Hence, data from a number of experiments made at 10 g/cm^2 could be pooled together. Fig. 2.55 shows the differential energy spectrum. It includes data from the work of Frye et al. (1966), Kniffen (1969), Hearn (1968), Valdez et al. (1970), Kinzer et al. (1970), Dahlbacka et al. (1972), Anand et al. (1973) together with calculations by Beuermann (1971),and Daniel and Stephens (1974). The data are averaged over geomagnetic latitudes less than about 40° N. They do not show any discernible variation over the solar cycle. In the energy range $100 \leq E \leq 2000$ MeV the integral spectrum can be represented by a simple power law:

$$J(\geq E) \;=\; A\,E^{-\gamma}\,. \tag{2.10}$$

Expressing energy E in [MeV] and area in [cm^2] the constant has the value $A = 1.3 \cdot 10^{-7}$ and $\gamma = 1.8$. Thus, over the range specified above the spectrum can be described by the following expression:

$$J(\geq E) \;=\; 1.3 \cdot 10^{-7} \cdot E^{-1.8} \quad [\mathrm{cm^{-2}s^{-1}sr^{-1}MeV^{-1}}]\,, \tag{2.11}$$

On February 27, 1973 Schönfelder and Lichti recorded the gamma ray spectrum in the energy range $1.5 \leq E \leq 10$ MeV at latitude 40° N over Palestine, Texas, at different altitudes (Schönfelder and Lichti, 1975). The results are shown in Fig. 2.56 for atmospheric depths of 2 and 10 g/cm^2, together with theoretical data by Beuermann (1971), Daniel and Stephens (1974), and Ling (1975). Figs. 2.57 and 2.58 show the spectra for depths of 50 and 100 g/cm^2, and 200 and 600 g/cm^2, respectively.

In the energy range $1 \leq E \leq 100$ MeV the vertical gamma ray flux has also been measured at a geomagnetic cutoff of 2.6 GV and an atmospheric depth of 2.4 g/cm^2, as shown in Fig. 2.59 (Scheel and Roehrs, 1972). The results are compared with those of Peterson et al. (1967), Frye et al. (1966),

Table 2.15: Differential Intensity of Downward Directed Gamma Rays at Cutoff Rigidity $P_c = 4.5$ GV and Depth $X = 4.2\ \mathrm{g\,cm^{-2}}$. (Ryan et al., 1977)

Energy [MeV]	Intensity $[\times 10^{-4}\mathrm{cm^{-2}s^{-1}sr^{-1}MeV^{-1}(g/cm^2)^{-1}}]$ at Zenith Angle, θ				
	$\theta = 5°$	$\theta = 15°$	$\theta = 25°$	$\theta = 35°$	$\theta = 45°$
2 - 3			6.9 ± 1.3	14 ± 1	
3 - 5		6.4 ± 0.9	6.3 ± 0.5	6.5 ± 0.5	9.5 ± 1.0
5 - 7.5	6.7 ± 5.3	3.8 ± 0.4	3.6 ± 0.4	4.8 ± 0.6	8.0 ± 1.0
7.5 - 10	1.8 ± 0.8	2.7 ± 0.4	1.9 ± 0.4	2.0 ± 0.4	3.5 ± 0.6
10 - 15		1.0 ± 0.2	1.2 ± 0.2	1.6 ± 0.3	2.9 ± 0.5
15 - 25		0.50 ± 0.08	0.68 ± 0.12	1.7 ± 0.2	

Table 2.16: Differential Intensity of Upward Directed Gamma Rays at Cutoff Rigidity $P_c = 4.5$ GV and Depth $X = 4.2\ \mathrm{g\,cm^{-2}}$. (Ryan et al., 1977)

Energy [MeV]	Intensity $[\times 10^{-3}\mathrm{cm^{-2}s^{-1}sr^{-1}MeV^{-1}(g/cm^2)^{-1}}]$ at Zenith Angle, θ				
	$\theta = 175°$	$\theta = 165°$	$\theta = 155°$	$\theta = 145°$	$\theta = 135°$
3 - 5		11 ± 4	18 ± 3	22 ± 3	
5 - 7.5		8.6 ± 1.5	10 ± 2	16 ± 3	31 ± 7
7.5 - 10	1.4 ± 0.9	6.1 ± 2.0	6.7 ± 2.0	8.6 ± 3.0	13 ± 5
10 - 15	6.4 ± 3.4	4.5 ± 2.0	4.0 ± 1.4	4.5 ± 1.9	5.4 ± 2.2
15 - 25	1.5 ± 0.4	0.78 ± 0.23	1.7 ± 0.4	2.1 ± 0.5	2.8 ± 0.8

Duthie et al. (1962), Fichtel et al. (1969) and with calculations of Beuermann (1971).

The energy spectra and fluxes of upward and downward propagating gamma rays have been measured on May 13, 1975 at an atmospheric depth around 3 g/cm^2 over Palestine, Texas, at a geomagnetic cutoff of 4.5 GV (Ryan et al., 1977). Tables 2.15 and 2.16 show the fluxes at 4.2 g/cm^2 for downward and upward propagating gamma rays, respectively. Analogous data are presented in Figs. 2.60 and 2.61, including theoretical results of Beuermann (1971), Ling (1975) and Daniel and Stephens (1974).

The flux of low energy gamma rays has been measured in the energy range $0.25 \leq E \leq 4.2$ MeV at 8° N geomagnetic latitude and an atmospheric depth of 6 g/cm^2 by Damle et al. (1971). The results are shown in Fig. 2.62 together with other experimental and theoretical data. Other low energy measurements have been carried out by Peterson et al. (1973) at depths of 3.6 , 95 and 350 g/cm^2. These results are given in Fig. 2.63. Fig. 2.64 shows a comparison of earlier data from the 3.5 g/cm^2 level with those of Peterson et al. (1973). Spectral measurements to energies as high as 10 MeV were made at 4 g/cm^2 and 12.5 GV geomagnetic cutoff on December 20, 1974 and October 7, 1979 by Buivan et al. (1979). Fig. 2.65 shows the results together with data from other groups (Kinzer et al., 1974; Staib et al., 1974).

The gamma ray spectrum of the atmosphere as observed from outer space was determined in the energy range $40 \leq E \leq 1000$ keV from a satellite (Imhof et al., 1976). Fig. 2.66 shows these spectra above the earth's polar caps and near the geomagnetic equator.

Above the equator, at 14.3 g/cm^2, the differential energy spectrum was determined with a small emulsion chamber (Anand et al., 1973). It is evident from Fig. 2.67 that over the energy range $90 \leq E \leq 1000$ GeV the differential spectrum can be described by the following expression:

$$j(E) = 1.1 \cdot 10^{-2} \cdot E^{-2.6} \quad [\mathrm{cm^{-2}s^{-1}sr^{-1}GeV^{-1}}] \,. \tag{2.12}$$

Nishimura et al. (1980) determined the energy spectrum of gamma rays over a somewhat larger energy range at a pressure of 4 mbar with an emulsion experiment. The results together with a predicted spectrum for that level are also plotted in Fig. 2.67.

Near the top of the atmosphere at 3.5 g/cm^2 and 6 g/cm^2, Klumpar et al. (1973) measured the gamma ray spectrum in the energy range $1 \leq E \leq 100$ MeV at cutoff rigidities of 0.3 GV (Fort Churchill, Canada) and 4.6 GV (Palestine, TX). The results are presented in Table 2.17.

Measurements at cutoffs of 4.5 GV and 11.5 GV have been carried out in the energy range $10 < E < 200$ MeV near the top of the atmosphere with a hybrid detector system consisting of nuclear emulsion and spark chambers (Kinzer et al., 1974). Figs. 2.68 and 2.69 show the vertical gamma ray spectra compared with other results for cutoff rigidities of 4.5 and 11.5 GV, respectively.

Energy spectra at different depths have been recorded at energies between 30 and 200 MeV at latitude 40° N in upward, downward and nearly horizontal directions (Thompson, 1974). Figs. 2.70, 2.71, and 2.72 show the spectra at

Table 2.17: Differential Gamma Ray Energy Spectrum Near Top of Atmosphere (Klumpar et al., 1973).

Energy [MeV]	Differential Flux [$cm^{-2}s^{-1}MeV^{-1}$]	
	Depth = 6.0 g/cm^{-2} Cutoff Rigidity = 0.3 GV (Ft. Churchill, CND)	Depth = 3.5 g/cm^{-2} Cutoff Rigidity = 4.6 GV (Palestine, TX)
1 - 4	$1.05 \cdot E^{-(2.2\pm0.3)}$	$0.82 \cdot E^{-(2.2\pm0.3)}$
4 - 10	$0.40 \cdot E^{-(1.5\pm03)}$	$0.36 \cdot E^{-(1.6\pm0.3)}$
	for E in [MeV]	for E in [MeV]

Table 2.18: Vertical Differential Atmospheric Gamma Ray Intensities at 3.5 g cm^{-2} (Schönfelder et al., 1980).

Energy [MeV]	Intensity [$cm^{-2}s^{-1}sr^{-1}MeV^{-1}$]
1.1 - 2.0	$(3.2 \pm 0.9) \cdot 10^{-3}$
2 - 3	$(1.5 \pm 0.5) \cdot 10^{-3}$
3 - 5	$(8.1 \pm 1.6) \cdot 10^{-4}$
5 - 10	$(2.75 \pm 0.7) \cdot 10^{-4}$
10 - 20	$(8.4 \pm 2.8) \cdot 10^{-5}$

different depths for mean zenith angles of 16°, 107°, and 168°, respectively.

A double Compton scattering telescope had been used by Ryan et al., (1979) to determine the vertical energy spectra of the gamma rays at atmospheric depths of 160, 330, 520, 820, and 1000 g/cm^2. With the exception of the sea level measurements that were made at Riverside (CA) (P_c = 5.4 GV), all other observations were made from a balloon, launched from Palestine (TX) (λ = 40°, P_c = 4.5 GV). The results are shown in Fig. 2.73 together with theoretical data.

Differential intensity measurements of the vertical gamma ray intensity at 3.5 g cm^{-2} were also obtained by Schönfelder et al. (1980). The results are given in Table 2.18.

Brunetti et al. (1999) carried out a recent series of measurements using a NaI(Tl) mono-crystal and determined the low energy gamma ray spectrum

at four widely different locations and altitudes, ranging from 5050 m (Kumbu Valley, Nepal) to 45 m a.s.l.. The data are plotted in Fig. 2.74.

2.4.3 Energy Spectra in the TeV-Range

While low energy gamma ray measurements are usually carried out with counters and individual track detectors, emulsion chambers and calorimeters are the principal tools for investigating high energy gamma rays. These detector systems consist of multi-layered sandwiches of converter plates, high-speed X-ray films and/or nuclear emulsion. Depending on the material and thickness of the converter plates and the chamber configuration, hadronic or electromagnetic processes can be studied.

In an emulsion chamber laid out for electromagnetic work, high energy electrons or gamma rays generate electromagnetic cascades in the converter material, usually lead, as they pass through the chamber, that are recorded in the photosensitive layers. In nuclear emulsion they produce visible tracks, in X-ray films easily detectable dark spots. The spot size is a measure for the size of the cascade, i.e., for the number of electrons at the particular location within the cascade. Because the gamma ray flux dominates over the electron flux at higher altitudes in the atmosphere, the electron component is frequently disregarded and the measured spectra are presented as gamma ray spectra.

Apanasenko et al. (1968) have measured the gamma ray spectrum at 200 g/cm^2 in the range $100 \leq E \leq 10^4$ GeV. It is illustrated in Fig. 2.75. The spectrum includes all photons within a zenith angle $\theta \leq 41°$. Its slope is essentially constant over the energy range investigated and it can again be represented by a simple power law, $J(\geq E) \propto E^{-\gamma}$, with $\gamma = 1.7$ to 1.9. In Fig. 2.76 we show the gamma ray spectrum over the range $1 \leq E \leq 40$ TeV at a level of 260 g/cm^2 (Takahashi, 1978; Takahashi et al., 1979).

Lu et al. (1981) determined the intensity of gamma rays of energy ≥ 2 TeV at an altitude of 6500 m (455 g/cm^2) and obtained a value of $(1.470 \pm 0.223) \cdot 10^{-9}$ cm^{-2}s^{-1}sr^{-1}. Wang et al. (1981) found for the vertical intensity at 5450 m a.s.l. (520 g/cm^2) and the same energy threshold a value of $(8.09 \pm 0.26) \cdot 10^{-10}$ cm^{-2}s^{-1}sr^{-1}. The entire gamma ray spectrum was investigated to energies as high as 50 TeV and a value of $\gamma = 1.96 \pm 0.07$ could be established for the integral spectrum.

The results of Yuda et al. (1973) for the vertical integral spectrum at 3776 m a.s.l. (630 g/cm^2), covering the energy range $1.5 \leq E \leq 8$ TeV are illustrated in Fig. 2.77. From this work a value of 2.2 ± 0.3 results for γ over

the corresponding portion of the spectrum.

Results from the work of Akashi et al. (1979 and 1981) carried out at the same altitude but over an energy range extended to nearly 100 TeV are presented in Fig. 2.78. The vertical integral spectrum resulting from this work can be described by the expression

$$J(\geq E) = (4.8 \pm 0.5) \cdot 10^{-11} \cdot \left(\frac{E}{5}\right)^{-1.95^{+0.2}_{-0.1}} \quad [\mathrm{cm}^{-2}\mathrm{s}^{-1}\mathrm{sr}^{-1}] \,, \qquad (2.13)$$

with energy E specified in TeV.

Bundles or so-called families of parallel high energy gamma rays (and/or hadrons) have also been observed in emulsion chambers. The energy flow of a gamma ray family, ΣE_γ, is determined by summing up the energy of all family members down to a minimum energy of 2 TeV. Fig. 2.79 shows the energy flow spectrum of gamma ray families (Akashi et al., 1981). Over the range $30 \leq E \leq 1200$ TeV the integral spectrum can again be represented by a simple power law with exponent, $\gamma = 1.40 \pm 0.05$.

High energy vertical gamma ray flux measurements including gamma ray families were made at 595 g/cm^2 by the Pamir Collaboration (1981), covering the range $6.3 \leq E \leq 125$ TeV. The results are shown in Fig. 2.80. This spectrum can be approximated by the expression

$$J(\geq E) = (7.61 \pm 0.76) \cdot 10^{-11} \cdot \left(\frac{E}{6.3}\right)^{-2.08 \pm 0.06} \quad [\mathrm{cm}^{-2}\mathrm{s}^{-1}\mathrm{sr}^{-1}] \,, \quad (2.14)$$

with energy, E, specified in TeV.

A survey of energy spectra of gamma rays at different altitudes has been given by Kanevskaya et al. (1977) and Erlykin et al. (1981). Fig. 2.81 summarizes the data and presents approximate spectra for atmospheric depths of 231, 257, 281, 314, 729, 798, 870, and 970 g/cm^2. It is evident from this figure that to some extent the data show a lack of systematic behavior.

From the more recent work of Capdevielle et al. (1987) we show in Fig. 2.82 the energy spectrum determined from an emulsion experiment having a total exposure of 400 hours at an atmospheric depth of approximately 100 g/cm^2 that was carried out on board of the supersonic jet liner Concorde. Also shown in the same figure is the spectrum obtained in a similar experiment by Ichimura (1987) who flew emulsion on a regular JAL jet liner at a depth of about 250 g/cm^2.

Table 2.19: Integral Gamma Ray Intensities at Mountain Altitudes for $E_\gamma \geq 1$ TeV. (Lu et al., 1981)

Location	Altitude [m]	Energy Range [TeV]	Spectral Index γ	Intensity [$cm^2 s^{-1} sr^{-1}$]
Mt. Everest (foot)	6500	2 - 10	2.2 ± 0.3	$1.47 \cdot 10^{-9}$
Mt. Kanbala	5450	2 - 50	2.0 ± 0.2	$7.32 \cdot 10^{-10}$
Mt. Chacaltaya	5200	0.2 - 50	2.07 ± 0.16	$6.3 \cdot 10^{-10}$
Mt. Fuji	3776	1 - 100	2.1 ± 0.1	$2.9 \cdot 10^{-10}$
Yunnan Station	3200	1 - 10	2.08 ± 0.2	$2.75 \cdot 10^{-10}$
Mt. Norikura	2700	0.6 - 2	1.92 ± 0.15	$1.0 \cdot 10^{-10}$

The spectral index, γ, is the exponent of the power law fit to the integral energy spectrum, $J(\geq E) \propto E^{-\gamma}$.

2.4.4 Altitude Dependence of Flux and Intensities

Data are also available on the altitude dependence of the gamma ray intensity in different energy regions and for different zenith angles. Fig. 2.83 to 2.85 show the altitude dependence of the intensity of gamma rays having energies ≥ 30 MeV at zenith angles of 16°, 107° and 168°, respectively, over the entire atmosphere (Thompson 1974).

Similarly, Fig. 2.86 shows the altitude dependence of the downward directed gamma ray intensity for the energy intervals 2 - 3 MeV, 5 - 7.5 MeV and 10 - 15 MeV, and Fig. 2.87 for the upward directed flux, in the upper regions of the atmosphere (Ryan et al., 1977). Another set of data of the downward directed intensity in the energy window $0.4 \leq E \leq 1.0$ MeV in the same atmospheric region obtained by Lockwood et al. (1981) is shown in Fig. 2.88. Analogous data that cover the entire atmosphere and a photon energy range up to 25 MeV are presented in Figs. 2.89 and 2.90 (Ryan et al., 1979).

For higher energy gamma rays a survey of intensity measurements at mountain altitudes is given in Table 2.19 (Lu et al., 1981). Intensity data for gamma rays having an energy ≥ 3.2 TeV are given in Fig. 2.91 (Pamir Collaboration, 1981).

In Fig. 2.92 we have made a compilation of the altitude dependence of the intensity of gamma rays with energy ≥ 5 TeV that includes data from all major ground based high altitude stations as well as two sets of data from measurements made on board of aircraft. One of these measurements

was made on board of the supersonic jet liner Concorde at an atmospheric depth of only 100 g/cm^2, the other on a normal JAL jet liner at about 250 g/cm^2 (Capdevielle et al., 1987). Included, too, is a series of recent measurements made by Lu et al. (1997) at altitudes as high as 6500 m a.s.l. (see also Shibuya, 1987). The companion figure for hadrons from the same experiments is shown in Fig. 2.2, Section 2.2.

The altitude dependence of the low energy gamma ray component can also be seen from the recent spectral studies at widely different altitudes of Brunetti et al. (1999), mentioned previously and shown in Fig. 2.74.

2.4.5 Zenith Angle Dependence

Four measurements had been carried out at zenith angles of 16°, 45°, 112° and 164° at the very shallow depth of only 3 g/cm^2 (Daniel and Stephens, 1974). The results, illustrated in Fig. 2.93, show clearly that the spectrum of the upward directed photons is significantly steeper at lower energies than corresponding spectral regions at small zenith angles. It also appears that the relative intensity towards the horizon increases and that the spectrum becomes harder.

The angular distribution of photons at 4.2 g/cm^2 belonging to different energy groups is shown in Fig. 2.94. The data include the zenith angle cuts from 0° to 50° for upward and from 130° to 180° for downward directed gamma rays (Ryan et al., 1977). Similar data obtained by the same authors at a depth of 2.5 g/cm^2 are presented in Fig. 2.95, together with predictions by Ling (1975) and Graser and Schönfelder (1977).

Another set of spectra covering the range $2 \leq E \leq 25$ MeV at different altitudes is presented in Figs. 2.96 and 2.97 for zenith angle intervals from 10° to 30° and from 140° to 170°, respectively (Ryan et al., 1979). Fig. 2.98 shows the same results in form of an angular distribution.

The zenith angle distribution at an altitude of 5450 m (520 g/cm^2) is shown in Fig. 2.99. It can be represented by the expression

$$I(\theta) \propto I(0°)\, cos^n(\theta) \tag{2.15}$$

with $n = 7.3 \pm 0.4$ (Wang et al., 1981).

The angular distribution of gamma rays of energies up to 100 TeV observed at 3776 m a.s.l. is shown in Fig. 2.100 (Akashi et al.,1979 and 1981).

Table 2.20: Compilation of 0.51 MeV Atmospheric Gamma Ray Data. (Daniel and Stephens, 1974)

Cutoff Rigidity [GV]	Measured [Year]	Float Altitude [g/cm^2]	Flux at Float in [photons/(cm^{2}s)]	References
1.3	1961	6.0	0.62 + 0.06*	Peterson (1963), (* revised)
4.4	1966	3.4	0.16 + 0.02	Chupp et al. (1970)
4.7	1967	3.6	0.20 + 0.02	Chupp et al. (1970)
4.8	1968	4.0	0.18 + 0.02	Chupp et al. (1970)
5.0	1966	3.6	0.10 + 0.005	Peterson et al. (1972)
10.0	1970	7.0	0.13 + 0.03	Nakagawa et al. (1971)
16.9	1968	22.0	0.14 + 0.01	Kasturirangan et al. (1972)
16.9	1968/1969	10.0	0.09 + 0.01	Prakashrao et al. (1971)
16.9	1969	6.0	0.08 + 0.01	Kasturirangan et al. (1972)
16.9	1971	4.7	0.031 + 0.005	Daniel et al. (1972)

2.4.6 Monochromatic Gamma Lines

The intensity of gamma rays resulting from electron - positron annihilation has been measured near the top of the atmosphere at different cutoff rigidities. Table 2.20 summarizes the data on the characteristic 0.511 MeV atmospheric gamma line (Daniel and Stephens, 1974). At 3.6 g/cm^2 and latitude 40° N a flux of 0.10 ± 0.005 photons/cm^{2}s was obtained (Peterson et al., 1973).

The altitude dependence of the 0.511 MeV gamma ray line has been determined with omnidirectional detectors and is shown in Figs. 2.101, 2.102 and 2.103 (Ling et al., 1977; Buivan et al., 1979 and Albernhe et al., 1979, respectively). Measurements with a high resolution detector were carried out by Ayre et al. (1981) at a latitude of 41° N. The dependence on geomagnetic latitude is shown in Fig. 2.104 (Albernhe et al., 1979). Similar measurements were carried out by Mahoney et al. (1981) on board the HEAO3 satellite.

Gamma lines resulting from neutron capture by atmospheric nuclei, inelastic scattering and induced radioactivity have been studied theoretically and experimentally. The most probable reactions occur with nuclei of ^{14}N and ^{16}O. The principal lines are due to de-excitation of ^{15}N and ^{16}O after neutron capture, inelastic scattering, or by de-excitation of ^{11}B and ^{13}C following (n, α) reactions. Table 2.21 summarizes the reactions and lists the predicted and measured fluxes (Peterson et al., 1973). Similar but satellite based measurements were made by Letaw et al. (1989) and Willett and Mahoney (1992).

Table 2.21: Atmospheric Gamma Ray Line Fluxes at 3.5 g/cm^2 Resulting from Nuclear Reactions (Peterson et al., 1973).

Nuclear Reactions			Predicted	Predicted		Predicted	Detector	Measured
Reaction	E_γ [MeV]	Transition Probability	Reaction Rate [photons/(g s)]	Flux [photons/(cm^{2}s)]	Efficiency	Counting Rates [counts/(cm^{2}s)]	Resolution %	Upper Limit Rate 1 σ [counts/(cm^{2}s)]
Capture Reactions (Thermal capture cross section 80 mb for (n,γ)								
$^{14}N(n,\gamma)^{15}N$	10.83	0.14	$0.211 \cdot 10^{-5}$	$1.35 \cdot 10^{-4}$	0.09	$1.22 \cdot 10^{-5}$	3.0	$5.6 \cdot 10^{-5}$
$^{14}N(n,\gamma)^{15}N$	5.54	0.32	$0.483 \cdot 10^{-5}$	$2.22 \cdot 10^{-4}$	0.11	$2.44 \cdot 10^{-5}$	4.3	$8.0 \cdot 10^{-5}$
$^{14}N(n,\gamma)^{15}N$	5.27	0.53	$0.80 \cdot 10^{-5}$	$3.59 \cdot 10^{-4}$	0.11	$3.98 \cdot 10^{-5}$	4.4	$8.2 \cdot 10^{-5}$
$^{14}N(n,\gamma)^{15}N$	7.31	0.09	$0.136 \cdot 10^{-5}$	$0.725 \cdot 10^{-4}$	0.10	$0.725 \cdot 10^{-5}$	3.7	$6.6 \cdot 10^{-5}$
$^{14}N(n,\gamma)^{15}N$	6.32	0.18	$0.272 \cdot 10^{-5}$	$1.34 \cdot 10^{-4}$	0.10	$1.34 \cdot 10^{-5}$	4.0	$7.3 \cdot 10^{-5}$
$^{14}N(n,\gamma)^{15}N$	4.49	0.16	$0.242 \cdot 10^{-5}$	$0.988 \cdot 10^{-4}$	0.11	$1.08 \cdot 10^{-5}$	4.8	$8.7 \cdot 10^{-5}$
$^{14}N(n,\gamma)^{15}N$	3.68	0.23	$0.347 \cdot 10^{-5}$	$1.24 \cdot 10^{-4}$	0.13	$1.61 \cdot 10^{-5}$	5.2	$9.6 \cdot 10^{-5}$
$^{14}N(n,\gamma)^{15}N$	3.53	0.09	$0.136 \cdot 10^{-5}$	$0.49 \cdot 10^{-4}$	0.13	$0.64 \cdot 10^{-5}$	5.2	$9.6 \cdot 10^{-5}$
Inelastic Scattering Reactions (For integrated neutron flux from threshold to 8 MeV)								
$^{14}N(n,n'\gamma)^{14}N$	2.31	-	$0.594 \cdot 10^{-4}$	$16.3 \cdot 10^{-4}$	0.18	$2.94 \cdot 10^{-5}$	6.6	$1.1 \cdot 10^{-4}$
$^{14}N(n,\alpha\gamma)^{11}B$	2.14	-	$0.517 \cdot 10^{-4}$	$13.6 \cdot 10^{-4}$	0.20	$2.72 \cdot 10^{-5}$	6.9	$1.1 \cdot 10^{-4}$
$^{14}N(n,\alpha\gamma)^{11}B$	4.46	-	$0.162 \cdot 10^{-4}$	$6.56 \cdot 10^{-4}$	0.11	$7.22 \cdot 10^{-5}$	4.8	$8.7 \cdot 10^{-5}$
$^{16}O(n,n'\gamma)^{16}O$	6.129	-	$2.98 \cdot 10^{-5}$	$14.7 \cdot 10^{-4}$	0.10	$1.47 \cdot 10^{-5}$	4.1	$7.6 \cdot 10^{-5}$
Inelastic Scattering Reactions (For integrated neutron flux from threshold to 16.5 MeV)								
$^{16}O(n,n'\gamma)^{16}O$	6.92	-	$0.71 \cdot 10^{-5}$	$3.67 \cdot 10^{-4}$	0.10	$3.67 \cdot 10^{-5}$	3.8	$6.6 \cdot 10^{-5}$
$^{16}O(n,n'\gamma)^{16}O$	7.117	-	$0.77 \cdot 10^{-5}$	$4.06 \cdot 10^{-4}$	0.10	$4.06 \cdot 10^{-5}$	3.8	$6.7 \cdot 10^{-5}$
$^{16}O(n,\alpha\gamma)^{13}C$	3.85	-	$0.53 \cdot 10^{-5}$	$1.98 \cdot 10^{-4}$	0.12	$2.38 \cdot 10^{-5}$	5.1	$9.4 \cdot 10^{-5}$
$^{16}O(n,\alpha\gamma)^{13}C$	3.68	-	$1.28 \cdot 10^{-5}$	$4.70 \cdot 10^{-4}$	0.13	$6.10 \cdot 10^{-5}$	5.2	$9.6 \cdot 10^{-5}$
$^{16}O(n,\alpha\gamma)^{13}C$	3.085	-	$0.59 \cdot 10^{-5}$	$1.92 \cdot 10^{-4}$	0.16	$3.07 \cdot 10^{-5}$	5.7	$9.9 \cdot 10^{-5}$

2.4.7 Theoretical Contributions

Numerous calculations have been carried out to explain the gamma ray spectrum, its angular distribution and altitude dependence. These topics are summarized in the following papers: Jabs and Wibberenz (1970), Beuermann (1971), Danjo (1972), Daniel and Stephens (1974), Galper and Prokhorova (1974), Matteson et al. (1974), Moyano and Schönfelder (1974), Thompson (1974), Graser and Schönfelder (1977), Bhattacharyya (1979), Ivanenko et al. (1979), Levina et al. (1979), Ryan et al. (1979), Erlykin et al. (1981), Fomin et al. (1981), and Shibata (1981).

References

Albernhe, F., G. Vedrenne, and I.M. Martin: J. Geophys. Res., 84, p. 6658 (1979).

Akashi, M., H. Nanjo, Z. Watanabe, I. Ohta, A. Misaki, K. Mizutani, K. Kasahara, E. Konishi, S. Torii, T. Yuda, I. Mito, T. Shirai, N. Tateyama, T. Taira, M. Shibata, H. Sugimoto, K. Taira and Y. Takahashi: PICRC, 7, p. 424 and 430 (1977).

Akashi, M., M. Amenomori, E. Konishi, H. Nanjo, Z. Watanabe, A. Misaki, K. Mizutani, K. Kasahara, T. Kobayashi, E. Mikumo, K. Sato, S. Torii, T. Yuda, I. Mito, T. Shirai, N. Tateyama, T. Taira, M. Shibata, H. Sugimoto, K. Taira and N. Hotta: PICRC, 7, p. 68 (1979).

Akashi, M., M. Amenomori, E. Konishi, H. Nanjo, Z. Watanabe, M. Ichiju, K. Mizutani, K. Kasahara, T. Kobayashi, E. Mikumo, K. Sato, S. Torii, T. Yuda, I.Mito, T. Shirai, N. Tateyama, T. Taira, M. Shibata, H. Sugimoto, K. Taira and N. Hotta: PICRC 5, p. 247 (1981).

Anand, K.C., R.R. Daniel, and S.A. Stephens: Pramana, 1, p.2 (1973).

Apanasenko, A.V., L.T. Baradzei, E.A. Kanevskaya, V.V. Rykov, Yu. A. Smorodin, and M.V. Solovyev: Can. J. Phys., 46, p. S700 (1968).

Ayre, C.A., P.N. Bhat, A. Owens, W.H. Summers, and M.G. Thompson: PICCR, 1, p. 103 (1981).

Baradzei, L.T., V.I. Rubtsow, and Yu.A. Smorodin and M.V. Soloiyev: Nukleonika, 9, p. 277 (1964).

Baradzei,L.T., E.A. Kanevskaya, Yu.A. Smorodin, and M.V. Soloviev: Acta Phys. Acad. Sci. Hung., 29, Suppl. 4, p. 33 (1970a).

Baradzei, L.T., E.A. Kanevskaya, Yu.A. Smorodin, and M.V. Soloviev: Acta Phys. Acad. Sci. Hung., 29, Suppl. 3, p. 81 (1970b).

Baradzei, L.T., E.A. Kanevskaya, Yu.A. Smorodin, and M.V. Soloviev: PICRC, 6, p. 2397 (1971).

Baradzei, L.T., V.K. Budilov, E.A. Kanevskaya, Yu.A. Smorodin, and E.V. Shalagina: PICRC, 3, p. 2269 (1973).

Baradzei, L.T., E.A. Kanevskaya, Yu.A. Smorodin: PICRC, 7, p. 453 (1977).

Beedle, R.E. and W.R. Webber: Can. J. Phys., 46, p. S1014 (1968).

Beuermann, K.P.: J. Geophys. Res., 76, p. 4291 (1971).

Bhattacharyya, D.P.: PICRC, 7, p. 130 (1979).

Bleeker, J.A.M. and A.J.M. Deerenberg: Astrophys. J., 159, p. 215 (1970).

Brasil - Japan Emulsion Chamber Collaboration. C.M.G. Lattes, W.A. Rodorigues, Jr., A. Turtelli, Jr., E.H. Shibuya, J.A. Chinellato, M. Luksys, C. Dobrigkeit, C.A.P. Ceneviva, N.M. Amato, N. Arata, T. Shibata, K. Yokoi, A. Ohsawa, Y. Fujimoto, S. Hasegawa, H. Kumano, T. Miyashita, K. Sawayanagi, H. Semba and M. Tamada: PICRC, 7, 2386 (1975).

Brini, D., F. Fuligni, and E. Horstman-Moretti: Proc. of Non-solar X- and Gamma Ray Astronomy Symposium, Rome, p. 321 (1969).

Brunetti, M., S. Cecchini, M. Galli, G. Giovannini, G. Longo, and A. Pagliarin: PICRC, 7, p. 355 (1999).

Buivan, N.A., K.R. Rao, and I.M. Martin: Astrophys. Space Sci., 64, p. 339 (1979).

Capdevielle, J.N., T. Ogata, M. Ichimura, T. Fujinaga, Y. Niihori, and T. Shibata: PICRC, 5, p. 182 (1987).

Carlson, A.G., J.E. Hooper and D.T. King: Phil. Mag., 41, p. 701 (1950).

Cherdyntseva, K.V. and S.I. Nikolski: Sov. Nucl. Phys., 23, p. 652 (1976).

Chupp, E.L., A.A. Sarkady, and H.P. Gilman: Planet. Space Sci., 15, p. 881 (1967).

Chupp, E.L., D.J. Forrest, A.A. Sarkady,and P.J. Lavakare: Planet. Space Sci., 18, p. 939 (1970).

Cline, T.L.: Phys. Rev. Lett., 7, p. 109 (1961).

Dahlbacka, G.H., P.S. Freier, and C.J. Waddington: Cosmic Phys. Rep., 161, p. 13 (1972).

Dahlbacka, G.H., P.S.Freier, and C.J. Waddington: Astrophys. J., 180, p. 371 (1973).

Damle, S.V., R.R. Daniel, G. Joseph, and P.J. Lavakare: PICRC, 1, p. 84 (1971).

Daniel, R.R., G. Joseph, and P.J. Lavakare: Astrophys. Space Sci., 18, p. 462 (1972).

Daniel R.R. and S.A. Stephens: Rev. Geophys. Space Phys.,12, p. 233 (1974).

Danjo, A.: J. Phys. Soc. Jap., 33, p. 890 (1972).

Duthie, J., P.H. Fowler, A. Kaddoura, D.H. Perkins and K. Pinkau: Nuovo Cimento, 24, p. 2 (1962).

Duthie (1968), after Scheel and Rohrs (1972).

Erlykin, A.D., N.P. Kuzina, and P.N. Lebedev: PICRC, 5, p. 243 (1981).

Fazio, G.G., H.F. Helmken, S.J. Cavrak, Jr., and D.R. Hearn: Can. J. Phys., 46, p. S427 (1968).

Fichtel, C.E., D.A. Kniffen, and H.B. Ogelman: Astrophys. J., 158, p. 193 (1969).

Fichtel, C.E., R.C. Hartman, D.A. Kniffen, and M. Sommer: Report GSFC X-662-71-209 (1971).

Fomin, Ju.A., T.G. Levina, G.B. Khristiansen, J. Kempa, A. Piotrowska, and J. Wdowczyk: PICRC, 5, p. 262 (1981).

Frye, G.M., F. Reines and A.H. Armstrong: J. Geophys. Res., 71, p. 3119 (1966).

Galper, A.M., and L.A. Prokhorova: Geomagn. Aeron., 14, p. 207 (1974).

Garmire, G.P.: Bull. Am. Phys. Soc., 15, p. 564 (1970).

Gorenstein, P., E.M. Kellogg, and H. Gursky: Astrophys. J., 156, p. 315 (1969).

Graser, U. and V. Schönfelder: J. Geophys. Res., 82, p. 1055 (1977).

Hearn, D.R.A.: Smithsonian Astrophysical Observatory, Spec. Rep., 277 (1968).

Hovestadt, D., and P. Meyer: Acta Phys. Acad. Sci. Hung., 29, Suppl. 2, p. 29 (1970).

Ichimura, M.: Report on Emulsion Technical Symposium, held at the Institute for Cosmic Ray Research, University of Tokyo, ICR (1987).

Imhof, W.L., G.H. Nakano, and J.B. Reagan: J. Geophys.Res., 81, p. 2835 (1976).

Israel, M.H.: J.Geophys. Res, 74, p. 4701 (1969).

Ivanenko, I.P., B.L. Kanevsky, and T.M. Roganova: PICRC, 7, p. 198 (1979a).

Ivanenko, I.P., B.L. Kanevsky, and T.M. Roganova: PICRC, 7, p. 101 (1979b).

Jabs, A. and G. Wibberenz: Z. Phys., 236, p. 101 (1970).

Japanese - Brasilian Collaboration: Suppl. Progr. Theor. Phys., 47, p. 1 (1971).

Kanevskaya, E.A., Yu.A. Smorodin, P.N. Lebedev, and L.T. Baradzei: PICRC, 7, p. 453 (1977).

Kasturirangan, K., U.R. Rao, and P.D. Bhavsar: Planet. Space Sci., 20, p. 1961 (1972).

Kinzer, R.L., G.H. Share, and N. Seeman: J. Geophys. Res., 79, p. 4567 (1974).

Klumpar, D.M., J.A. Lockwood, R.N. St. Onge, and L.A. Friling: J. Geophys. Res., 78, p. 7959 (1973).

Kniffen, D.A.: NASA Techn. Rep. R-308 (1969).

Letaw, John, R., G.H. Share, R.L. Kinzer, R. Silberberg, E.L.Chupp, D.J. Forrest, and E. Rieger: J. Geophys. Res., 94, p. 1211 (1989).

Levina, T.G., Yu.A. Fomin, G.B. Khristiansen, J. Wdowczyk, J. Kempa, and A. Piotrovska: PICRC, 7, p. 148 (1979).

Ling, J.C.: J. Geophys. Res., 80, p. 3241 (1975).

Ling, J.C., W.A. Mahoney, J.B. Willett, and A.S. Jacobson: J. Geophys. Res., 82, p. 1463 (1977).

Lockwood, J.A., W.R. Webber, L.A. Friling, J. Macri, and L. Hsieh: Astrophys. J., 248, p. 1194 (1981).

Lu, S.L., S. Su, J.L. Ren, and D.C. Wang: PICRC, 5, p. 254 (1981).

Lu, S.L., J.R. Ren, and S.J. Zhou: PICRC, 6, p. 89 (1997).

Mahoney, W.A., J.C. Ling, and A.S. Jacobson: J. Geophys. Res., 86, p. 11098 (1981).

Matteson, J.L., J.C. Ling, and L.E. Peterson: 9th ESLAB Symposium, Frascati, Italy, p. 137 (1974).

Moyano, C. and V. Schönfelder: Astrophys. Space Sci., 30, p. L17 (1974).

Mt. Fuji Collaboration: PICRC, 7, p. 68 (1979).

Mt. Fuji Collaboration: PICRC, 5, p. 247 (1981).

Nakagawa, S., M. Tsukuda, K. Okudaira, Y. Hirasima, M. Yoshimori, T. Yamagami, H. Murakami, and S. Iwama: PICRC, 1, p. 77 (1971).

Nishimura, J., M. Fujii, T. Taira, E. Aizu, H. Hiraiwa, T. Kobayashi, K. Niu, I. Ohta, R.L. Golden, T.A. Koss, J.J. Lord, and R.J. Wilkes: Astrophys. J., 238, p. 394 (1980).

Osborne, J.L. and A.W. Wolfendale: Proc. Phys. Soc., 84, p. 901 (1964).

Pamir Collaboration: PICRC, 5, p. 297 (1981).

Peterson, L.E.: J. Geophys. Res., 68, p. 979 (1963).

Peterson, L.E., A.S. Jacobsen and R.M. Pelling: J. Geophys. Res., 71, p. 5781 (1966).

Peterson, L.E., R.L. Jerde, and A.S. Jacobson: AIAA J., 5,p. 1921 (1967).

Peterson, L.E. and A.S. Jacobson: Publ. Astron. Soc. Pac., 82, p. 412 (1970).

Peterson, L.E., D.A. Schwartz, and J.C. Ling: (1972) unpublished.

Peterson, L.E., D.A. Schwartz, and J.C. Ling: J. Geophys. Res., 78, p. 7942 (1973).

Prakashrao, A.S., V.S. Iyengar, and U.R. Rao: Proc. Indian Acad. Sci., 73, p. 134 (1971).

Rockstroh, J. and W.R. Webber: J. Geophys. Res., 74, p. 504 (1969).

Ryan, J.M., B. Dayton, S.H. Moon, R.B. Wilson, A.D. Zych, and R.S. White: J. Geophys. Res., 82, p. 3593 (1977).

Ryan, James M., Mark C. Jennings, Martin D. Radwin, Allen D. Zych, and R. Stephen White: J. Geophys. Res., 84, p. 5279 (1979).

Scheel, J. and H. Roehrs: Z. Phys., 256, p. 226 (1972).

Schönfelder, V., and G. Lichti: J. Geophys. Res., 80, p. 3681 (1975).

Schönfelder, V., F. Graml, and F.-P. Penningsfeld: Astrophys. J., 240, p. 350 (1980).

Schwartz, D.A.: Ph.D. Thesis, Univ. of California, San Diego (1969).

Shibata, M.: PICRC, 5, p. 328 (1981).

Shibuya, E.H.: PICRC, 8, p. 238 (1987).

Soloviev, M.V.: Ph. D. Thesis, FIAN, Moscow (1969).

Staib, J.A., G. Frye, and A. Zych: PICRC, 2, p. 916 (1973).

Staib, J.A., G.M. Frye, and A.D. Zych: J. Geophys. Res., 79, p. 929 (1974).

Stephens, S.A.: Proc. Indian Acad. Sci., 72, p. 214 (1970).

Takahashi, Y., J. Iwai and I. Otha: PICRC, 7, p. 408 (1977).

Takahashi, Y.: AIP Conf. Proc., 49, p. 166 (1978).

Takahashi, Y., J. Iwai, T. Ogata, and I. Ohta: PICRC, 7, p. 115 (1979).

Thompson, D.J.: J. Geophys. Res., 79, p. 1309 (1974).

Valdez, J.V., P.S. Freier, and C.J. Waddington: Acta Phys. Acad. Sci. Hung., 29, Suppl. 2, p 79 (1970).

Verma, S.D.: J. Geophys. Res., 72, p. 915 (1967).

Vette, J.I., D. Gruber, J.L. Matteson, and L.E. Peterson: Astrophys. J., 160, p. L161 (1970).

Wang, C.R., M. He, N.J. Zhang, P.Y. Cao, J.Y. Li, J.R. Ren, S.L. Lu, Y.X. Wang, and D.C. Wang: PICRC, 5, p. 251 (1981).

White, R.S., R. Koga, and G. Simnett: PICRC, 1, p. 7 (1973).

Willett, J.B., and W.A. Mahoney: J. Geophys. Res., 97, p. 131 (1992).

Yuda, T., T. Taira, M. Shibata, and K. Taira: PICRC, 5, p. 3190 (1973).

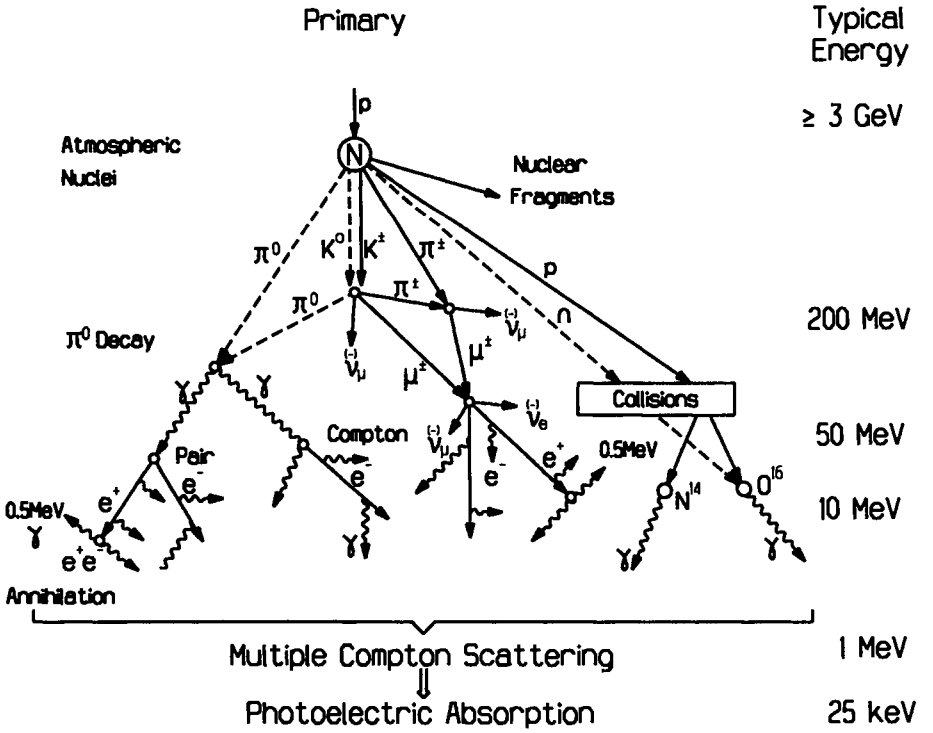

Figure 2.54: Schematic diagram of the main processes that are responsible for gamma ray production in the atmosphere. Shown is the typical electromagnetic cascade process as it takes place in the atmosphere. It is initiated predominantly by the decay products of secondary particles resulting from hadronic interactions caused by energetic primary hadrons in collisions with nuclei of the atmospheric constituents. The neutrinos that are being produced in various decays but which do not contribute to the growth of the cascade process are also indicated for completeness. Primary gamma rays and electrons make only minor contributions to the gamma ray flux in the atmosphere. The typical energy scale indicated on the right hand side of the figure shows the energy domain where the processes illustrated on the left are dominant in contributing to the gamma flux. The lateral spread of the cascade as shown in this figure is grossly exaggerated for reasons of illustration.

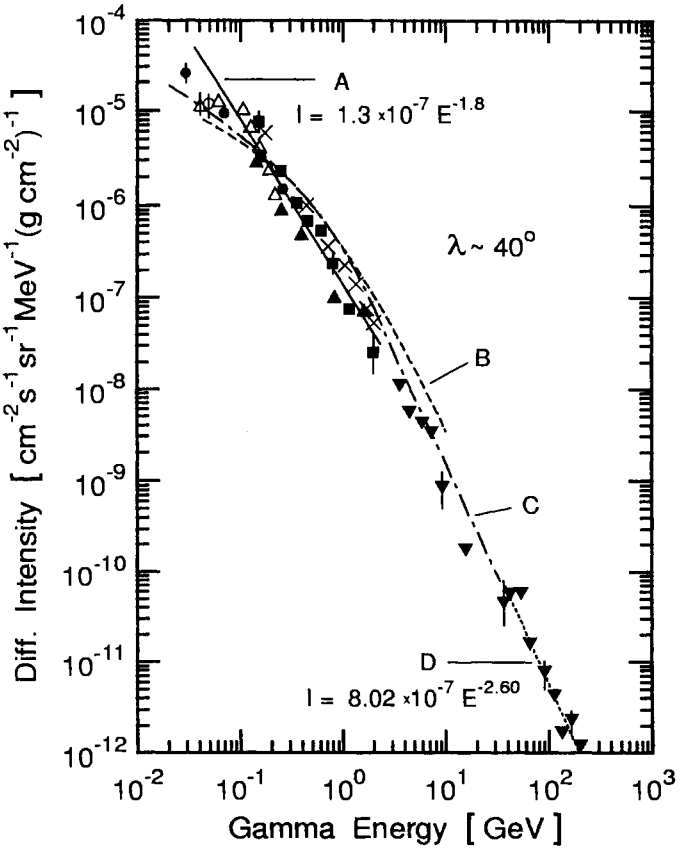

Figure 2.55: Differential energy spectra of gamma rays near the top of the atmosphere, at a depth of 10 g/cm^2 (Daniel and Stephens, 1974). Lines A and D are power law fits, as indicated, with E in GeV. Curves B and C are from calculations of Beuermann (1971) and Daniel and Stevens (1974), respectively.

- • Frye et al. (1966), $\lambda = 44°$ N, $P_c \sim 4 - 5$ GV, 11 g/cm^2
- × Dahlbacka et al. (1972, 1973), $P_c = 4.5$ GV
- ▲ Hearn (1968), $P_c \sim 4 - 5$ GV
- ■ Valdez et al. (1970), $P_c = 4.5$ GV, 3.4 mbar
- △ Kniffen et al. (1969, 1970), $P_c = 4.5$ GV, 2.9 g/cm^2
- o Kinzer et al. (1974), $P_c = 4.5$ GV, 4.5 g/cm^2, $P_c = 11.5$ GV, 2.5 g/cm^2
- ▼ Anand et al. (1973), Stephens (1970), $P_c = 16.9$ GV

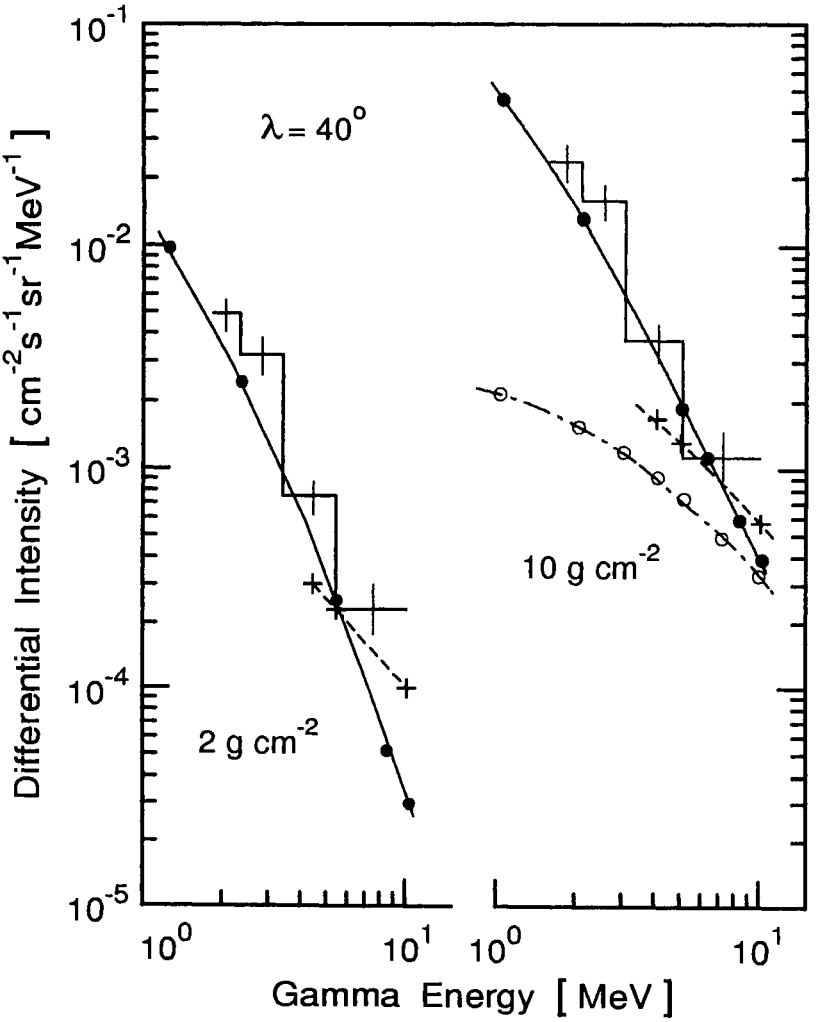

Figure 2.56: Experimental and theoretical differential energy spectra of vertical gamma rays at atmospheric depths of 2 and 10 g/cm^2, and a latitude of 40° N (Schönfelder and Lichti, 1975). The curves are drawn to guide the eye.

⌐└	Schönfelder and Lichti (1975)	experimental
+	Beuermann (1971)	calculation
o	Daniel and Stephens (1974)	calculation
•	Ling (1975)	calculation

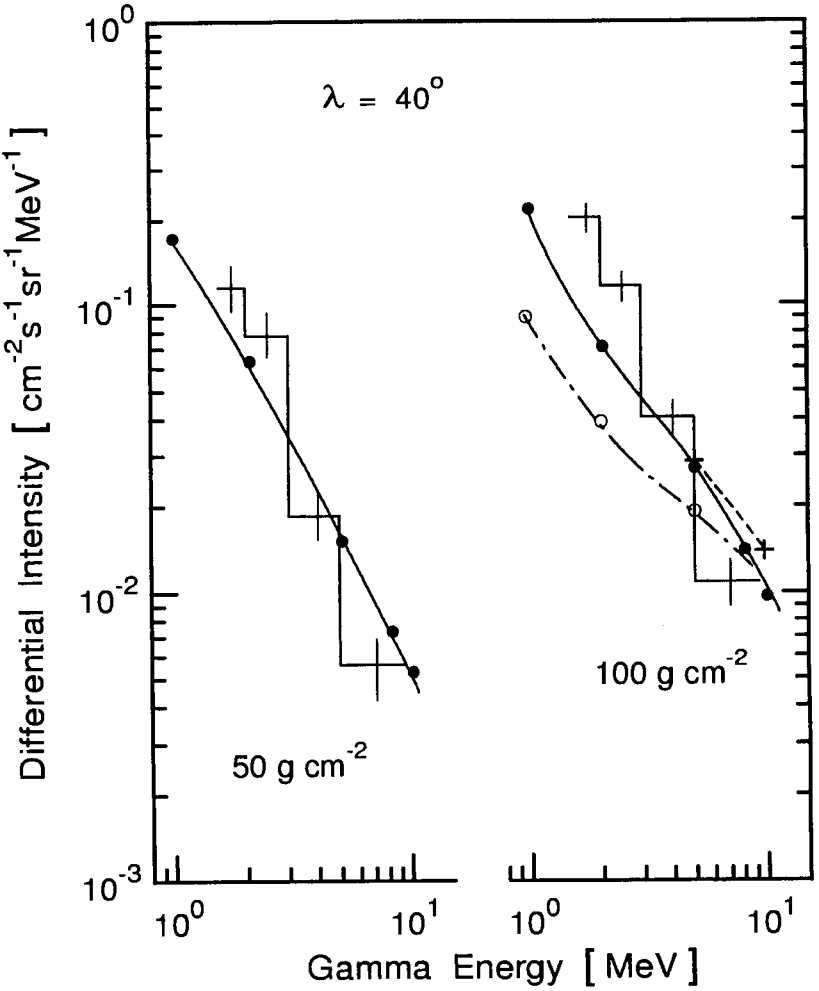

Figure 2.57: Experimental and theoretical differential energy spectra of vertical gamma rays at atmospheric depths of 50 and 100 g/cm^2, and a latitude of 40° N (Schönfelder and Lichti, 1975). The curves are drawn to guide the eye.

⌐⌙	Schönfelder and Lichti (1975)	experimental
+	Beuermann (1971)	calculation
o	Daniel and Stephens (1974)	calculation
•	Ling (1975)	calculation

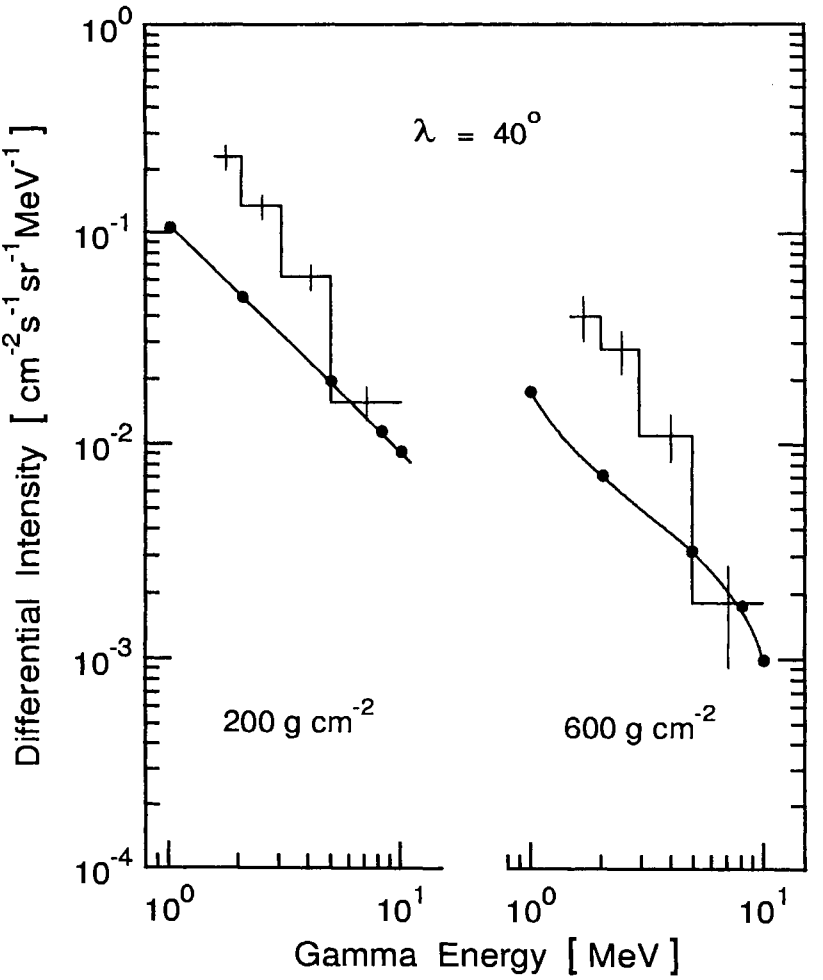

Figure 2.58: Experimental and theoretical differential energy spectra of vertical gamma rays at atmospheric depths of 200 and 600 g/cm^2, and a latitude of 40° N (Schönfelder and Lichti, 1975). The curves are drawn to guide the eye.

⌐⌙ Schönfelder and Lichti (1975) experimental
• Ling (1975) calculation

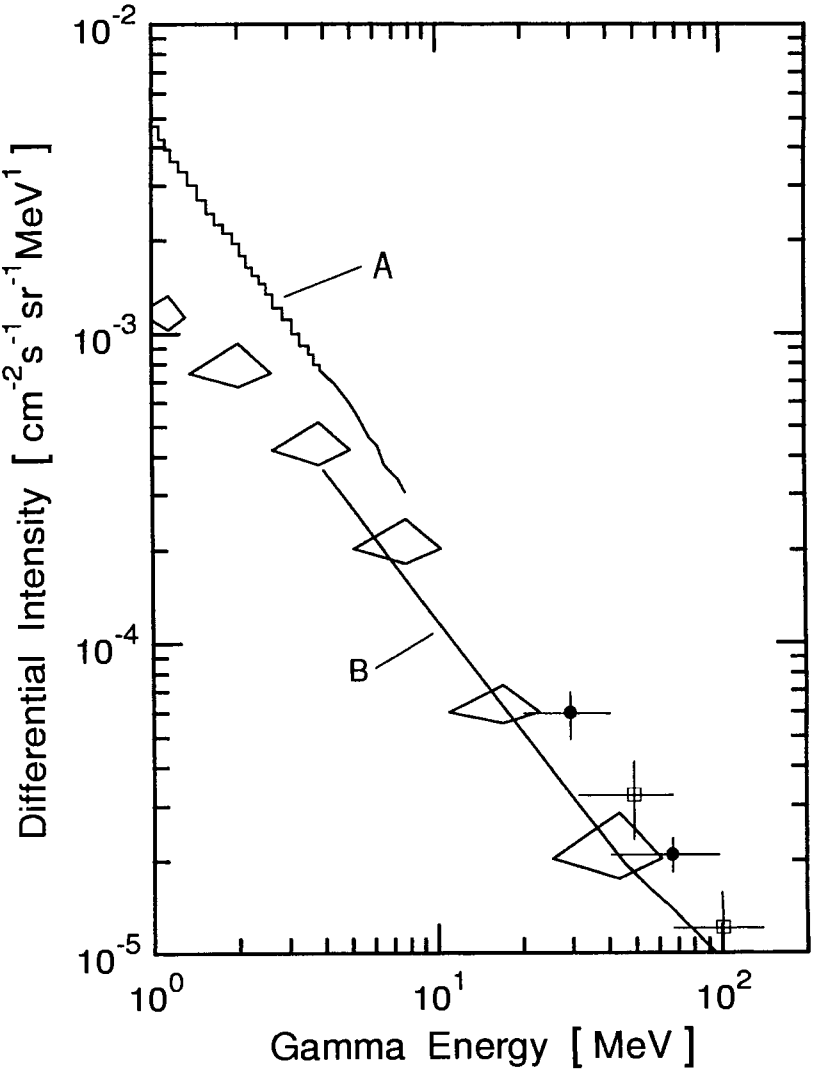

Figure 2.59: Compilation of data of the vertical differential energy spectrum of secondary photons at 2.4 g/cm^2 and cutoff rigidity of 2.6 GV (Scheel and Roehrs, 1972).

◇ Scheel and Rohrs (1972)	□ Fichtel (1971)
• Fry (1966), Duthie (1968)	A Peterson (1967)
B Beuermann (1971), calculations	

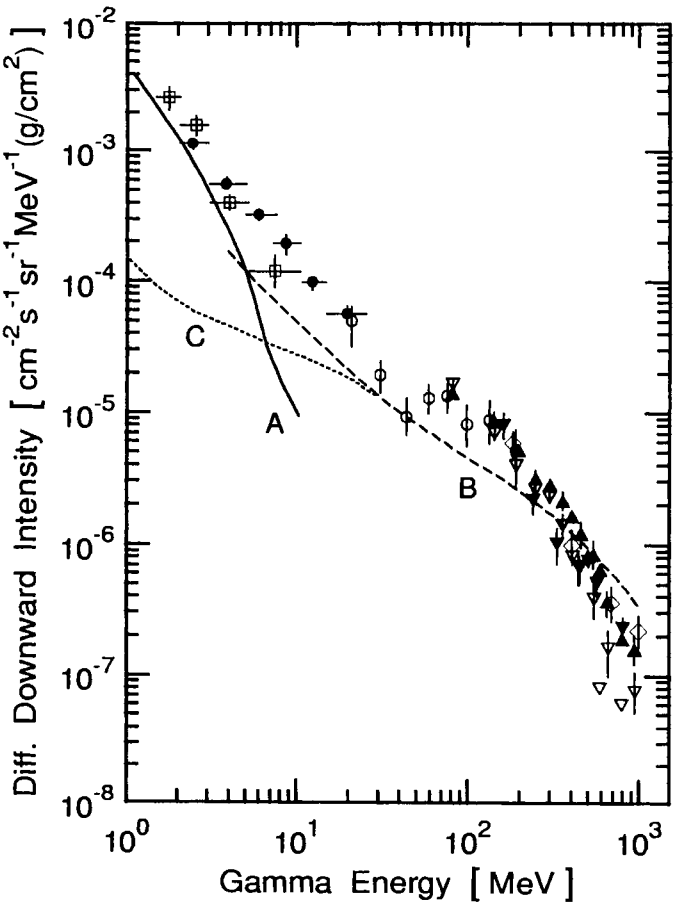

Figure 2.60: Gamma ray spectra of downward directed photons near the top of the atmosphere (4.2 g/cm^2) at a cutoff rigidity of 4.6 GV (Ryan et al., 1977). Curves A, B and C are the results of calculations.

A	Ling (1975)	B	Beuermann (1971)
C	Daniel and Stephens (1974)	o	Kinzer et al. (1974)
◇	Dahlbacka et al. (1973)	▲	Staib et al. (1974)
□	Schönfelder and Lichti (1975)	▽	Staib et al. (1974)
▼	Valdez et al. (1970)	•	Ryan et al. (1977)

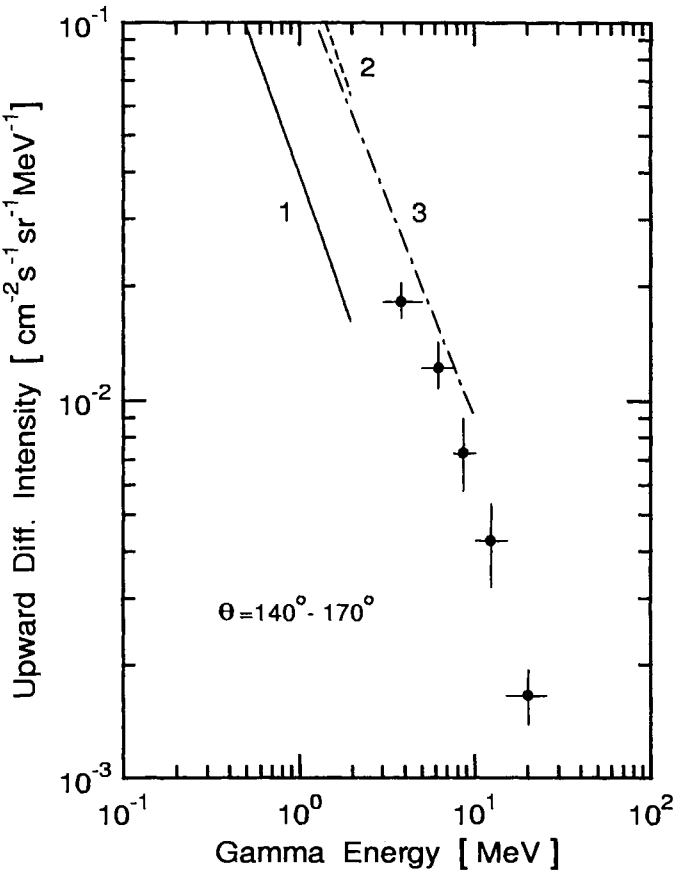

Figure 2.61: Gamma ray spectra of upward directed photons near the top of the atmosphere. The measurements of Imhof et al. (1976) were made from a satellite in a polar orbit at 750 km with a spectrometer collimated to ±45°. The zenith angle range of $\theta = 140° - 170°$ applies to the data of Ryan et al. (1977).

- Ryan et al. (1977), measurement at 4.2 g/cm^2 and $P_c = 4.5$ GV

1 Imhof et al. (1976), measurement at equator and altitude 750 km

2 Imhof et al. (1976), measurement in polar region at altitude 750 km

3 Ling (1975), calculation

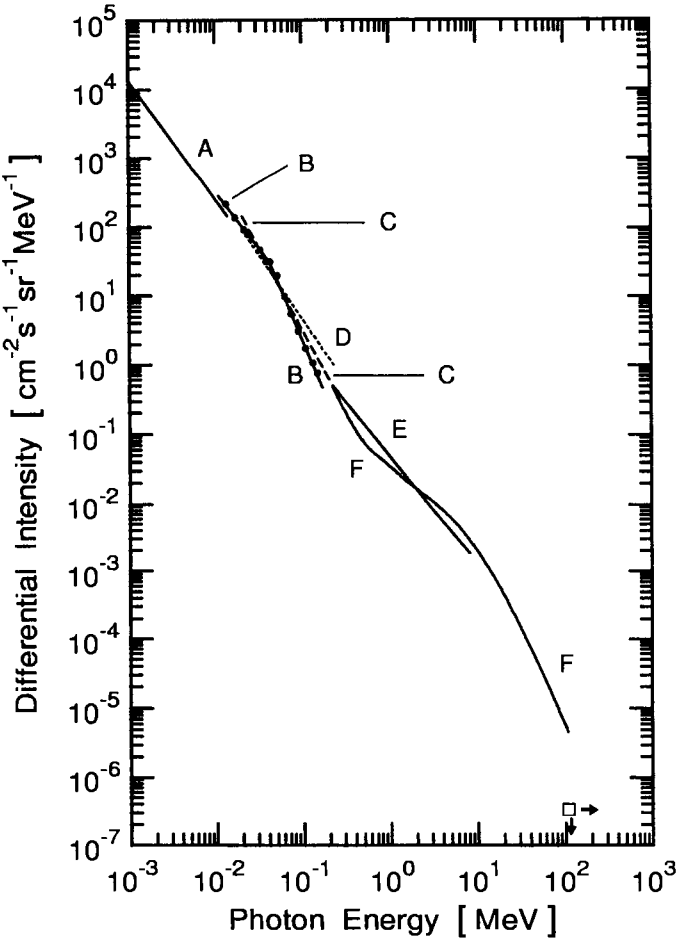

Figure 2.62: Compilation of diffuse photon spectra measured near the top of the atmosphere. The data of Damle et al. (1971) were taken at 6 g/cm^2 and latitude 8° N. Data from other authors were appropriately treated by Damle et al. to yield the above spectrum at 6 g/cm^2. The power law approximations of the energy dependence of the spectral regions covered by the different experiments are indicated below.

A	Gorenstein et al. (1969), $\propto E^{-1.7}$	D	Brini et al. (1969), $\propto E^{-1.8}$
•, B	Schwartz (1969), $\propto E^{-3.1}$ at $E \geq 40$ keV	E	Damle et al. (1971), $\propto E^{-1.5}$
C	Bleeker and Deerenberg (1970), $\propto E^{-2.45}$	□	Garmire (1970)
F	Vette et al. (1970), fit for $\propto E^{-2.3}$		

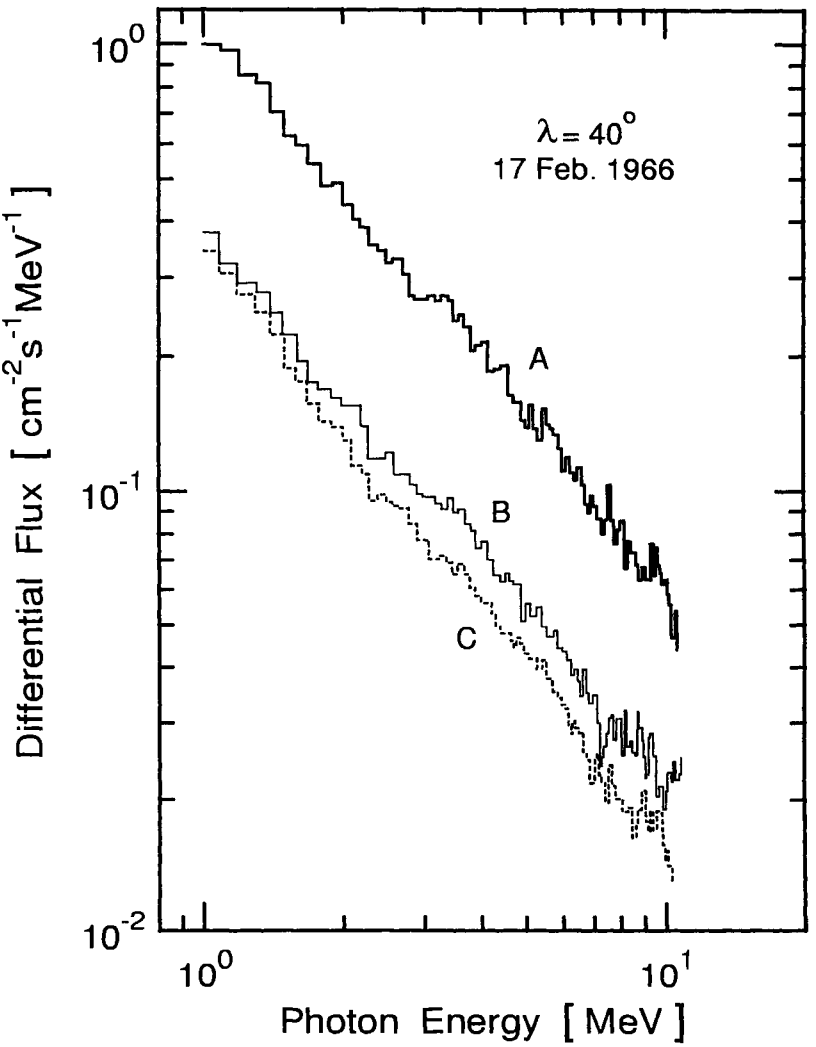

Figure 2.63: Low energy differential gamma ray spectra at latitude 40° N and different depths: A 95 g/cm^2, B 350 g/cm^2 and C 3.6 g/cm^2 (Peterson et al., 1973). Note the higher intensity at 95 g/cm^2 than at 350 g/cm^2.

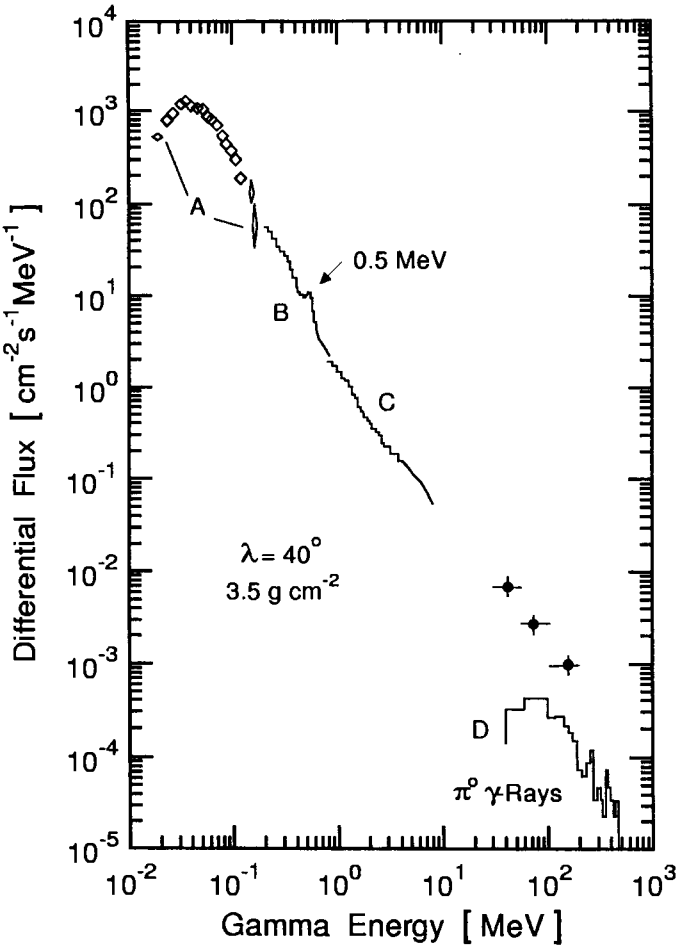

Figure 2.64: Gamma ray energy spectra measured at 3.5 g/cm^2 in the energy range $10^{-2} \leq E \leq 5 \cdot 10^2$ MeV (Peterson et al. 1973).

A , ◇	Peterson and Jacobson (1970)	B , C	Peterson et al. (1966)
D	Carlson et al. (1950)	•	Fichtel et al. (1969)

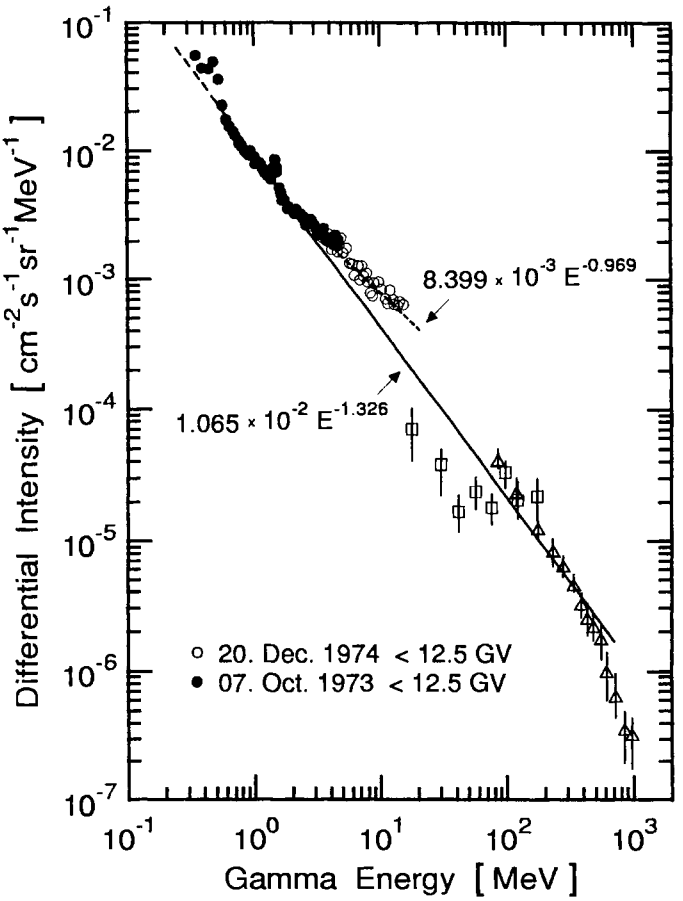

Figure 2.65: Energy spectrum of gamma rays at a depth of 4 g/cm^2 and a cutoff of 12.5 GV, recorded on October 7, 1973, and December 20, 1974, compared with other results (Buivan et al., 1979). The lines are power law fits as indicated with E in MeV.

• , o Buivan et al. (1979), 12.5 GV
□ Kinzer et al. (1974), 11.5 GV
△ Staib et al. (1974), 12 GV

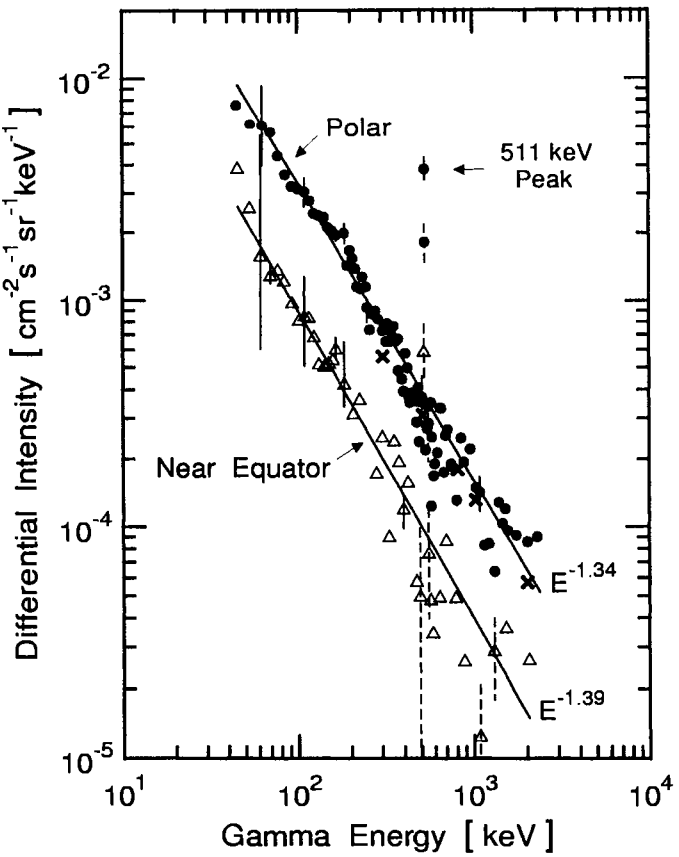

Figure 2.66: Atmospheric gamma ray spectra observed from a satellite in a polar orbit at 750 km over the earth's north polar cap (•) and near the geomagnetic equator (△). Dashed error bars are statistical uncertainties, solid error bars indicate the range of atmospheric fluxes corresponding to *reasonable* limits on the diffuse spectrum. According to the authors the intensity of the 0.511 MeV electron - positron annihilation line shown in the graph is expressed in flux per MeV (Imhof et al., 1976). The symbols × indicate the upward flux at 2.2 g/cm^2 and $\lambda = 40°$ according to a model of Ling (1975). The power law approximations for the two lines are also indicated in the figure.

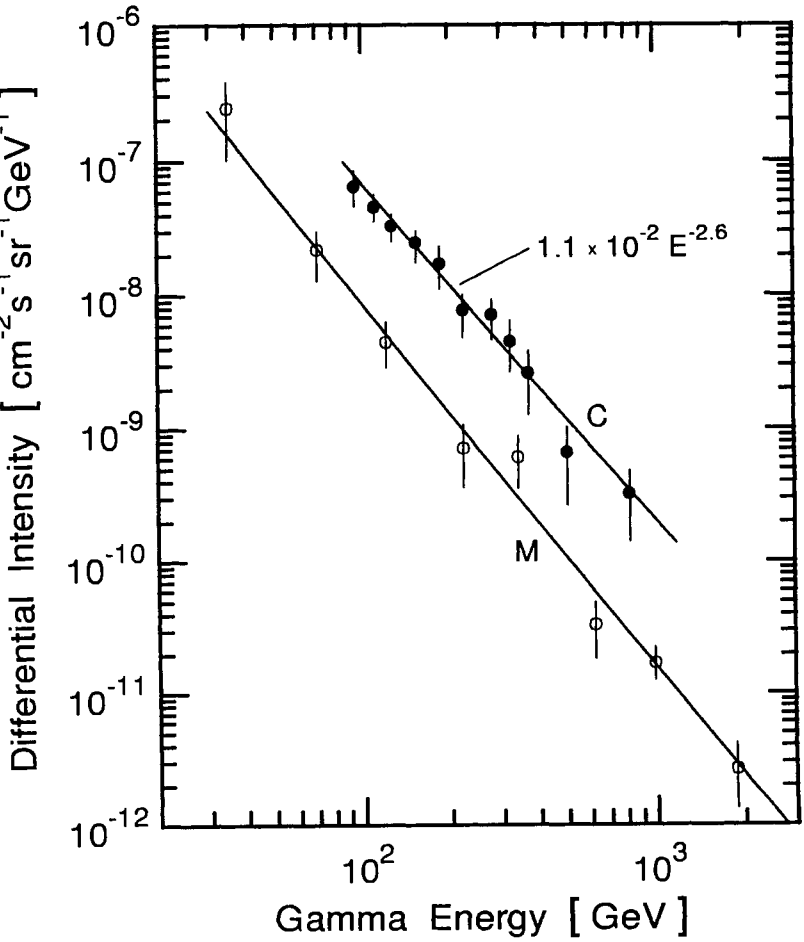

Figure 2.67: Differential energy spectrum of gamma rays at an atmospheric depth of 14.3 g/cm^2 over Hyderabad, near the geomagnetic equator with P_c = 16.9 GV (•). The line, C, represents a power law fit, as indicated, with E in GeV (Anand et al., 1973). Also shown is the spectrum obtained from an emulsion experiment at a residual atmosphere of 4 mbar (Nishimura et al., 1980) . Line M is a predicted spectrum for this level.

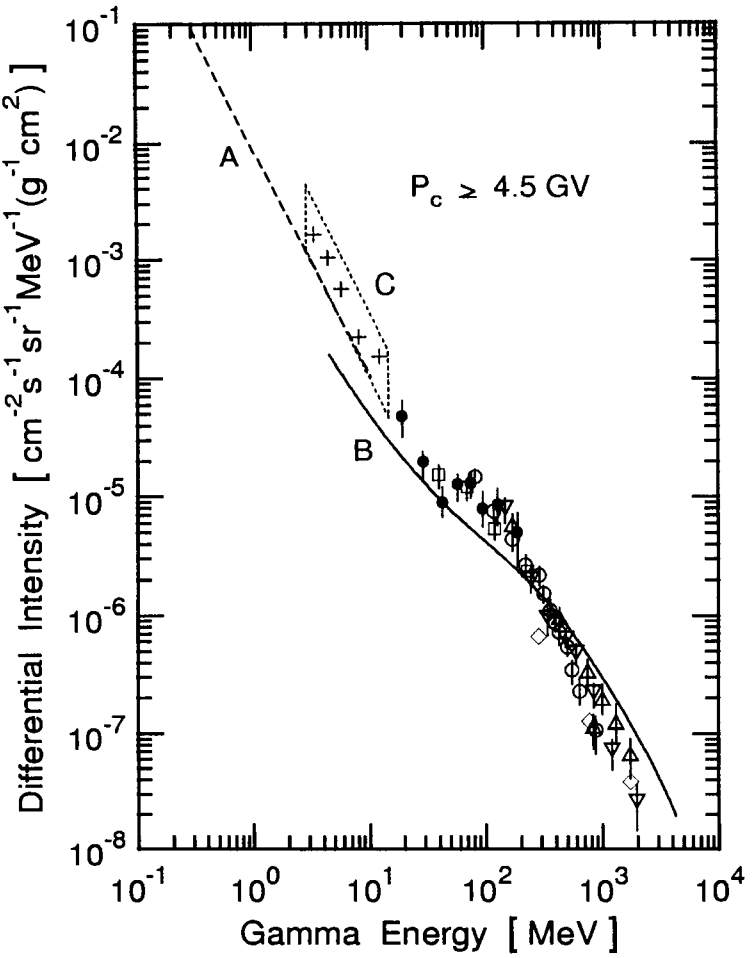

Figure 2.68: Compilation of gamma ray spectra near the top of the atmosphere at cutoff rigidity ≥4.5 GV (Kinzer et al., 1974).

A	Ling (1975), calculation	◇	Fazio et al. (1968)
B	Beuermann (1971), calculation	□	Fichtel et al. (1969)
C , +	White et al. (1973)	•	Kinzer et al. (1974)
o	Staib et al. (1973)	▽	Valdez et al. (1970)
△	Dahlbacka et al. (1973)		

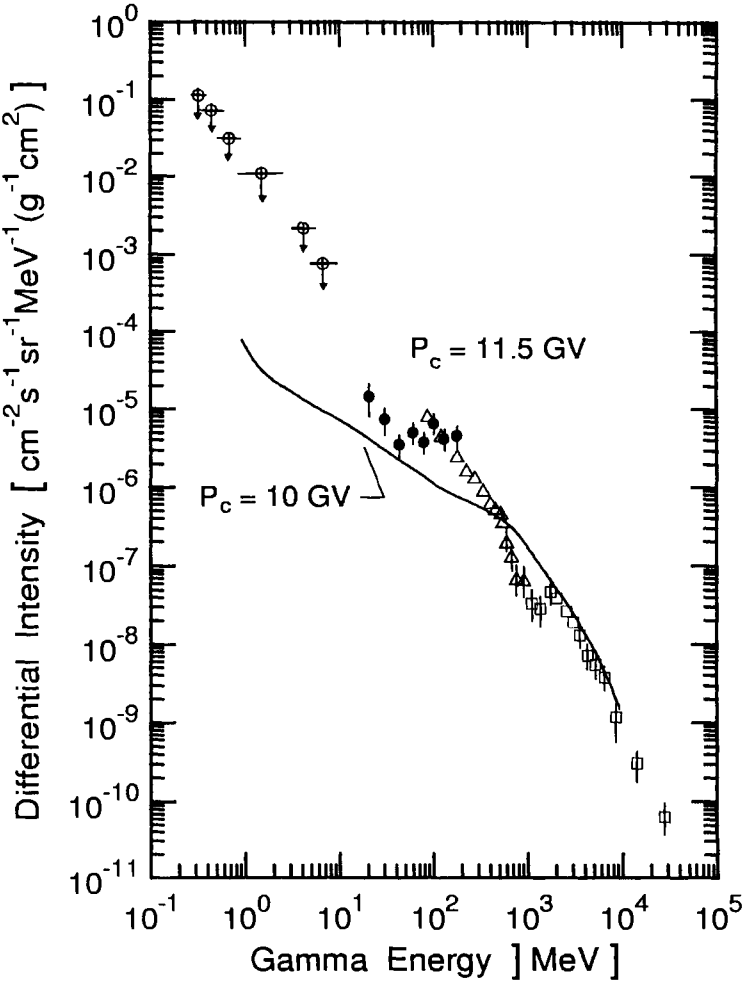

Figure 2.69: Compilation of differential gamma ray spectra near the top of the atmosphere at different cutoff rigidities, as indicated (Kinzer et al., 1974).

• Kinzer et al. (1974) 11.5 GV | ○ Daniel et al. (1972) 16.9 GV
△ Staib et al. (1973) 12 GV | □ Stephens (1970) 16.9 GV
—— Daniel and Stephens (1974) 10 GV (calculation)

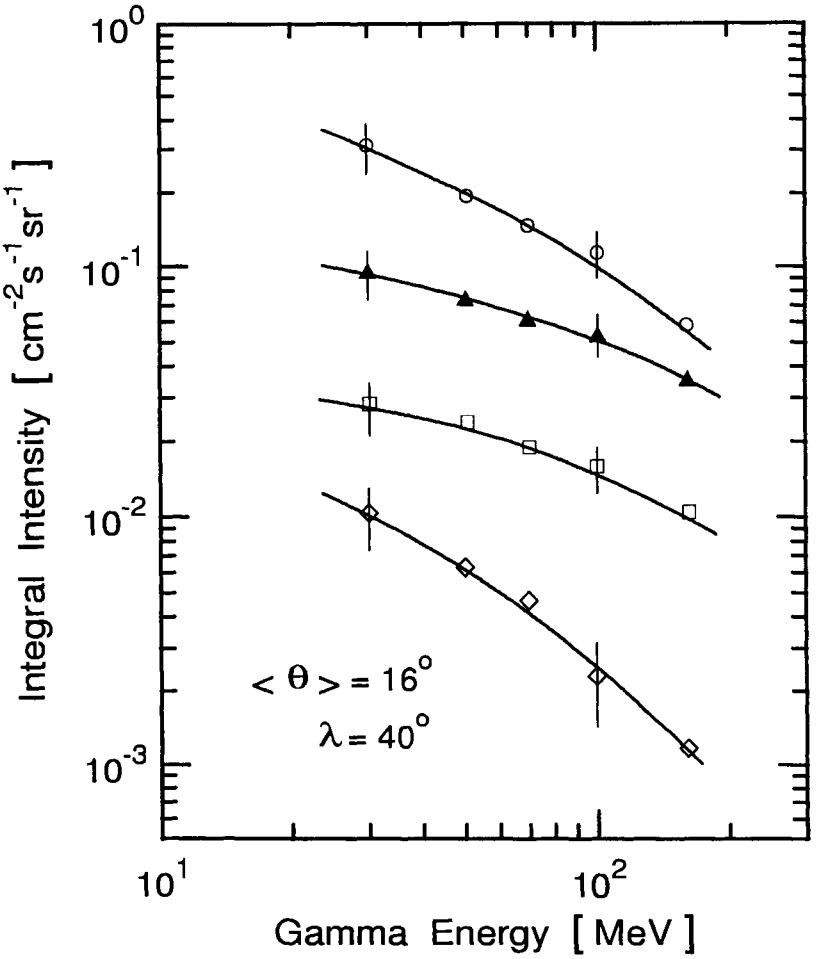

Figure 2.70: Integral energy spectra of gamma rays with an average zenith angle of 16° for four ranges of atmospheric depths recorded during ascent. The curves connecting the points are for visual reference only (Thompson , 1974).

◇ 1000 - 500 g/cm^2 | ○ 250 - 125 g/cm^2
▲ 50 - 20 g/cm^2 | □ 10 - 5 g/cm^2

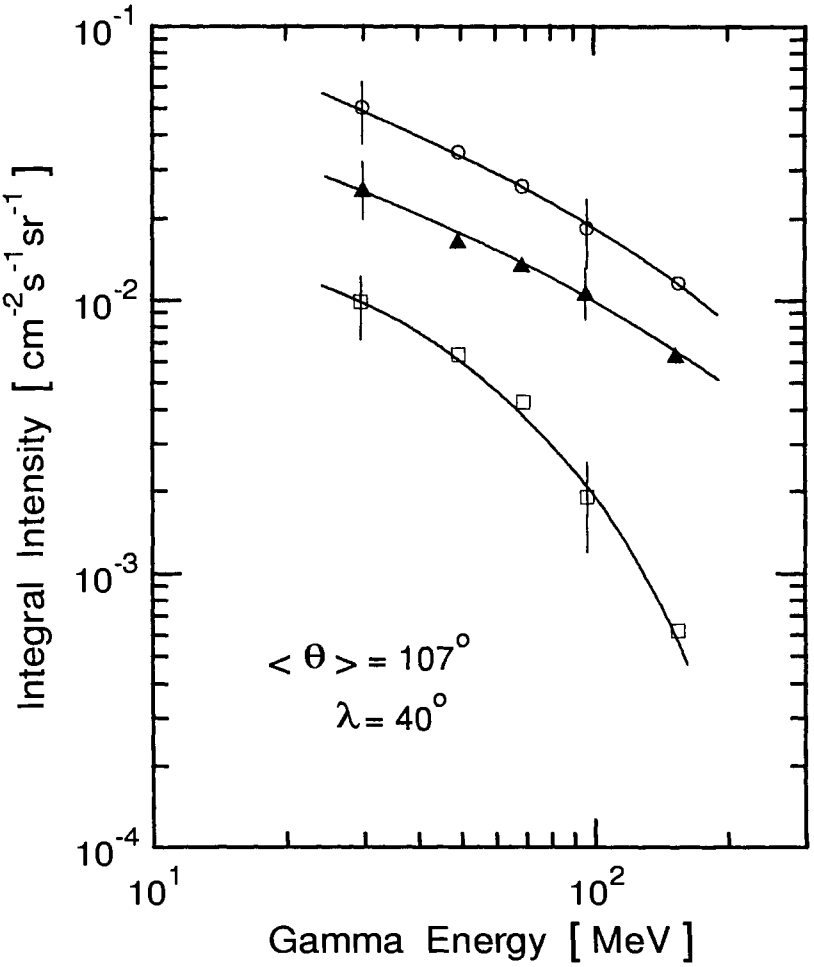

Figure 2.71: Integral energy spectra of gamma rays with an average zenith angle of 107° for three ranges of atmospheric depths recorded during ascent. The curves connecting the points are for visual reference only (Thompson , 1974).

□ 250 - 125 g/cm^2 | ▲ 125 - 50 g/cm^2
• 10 - 5 g/cm^2 |

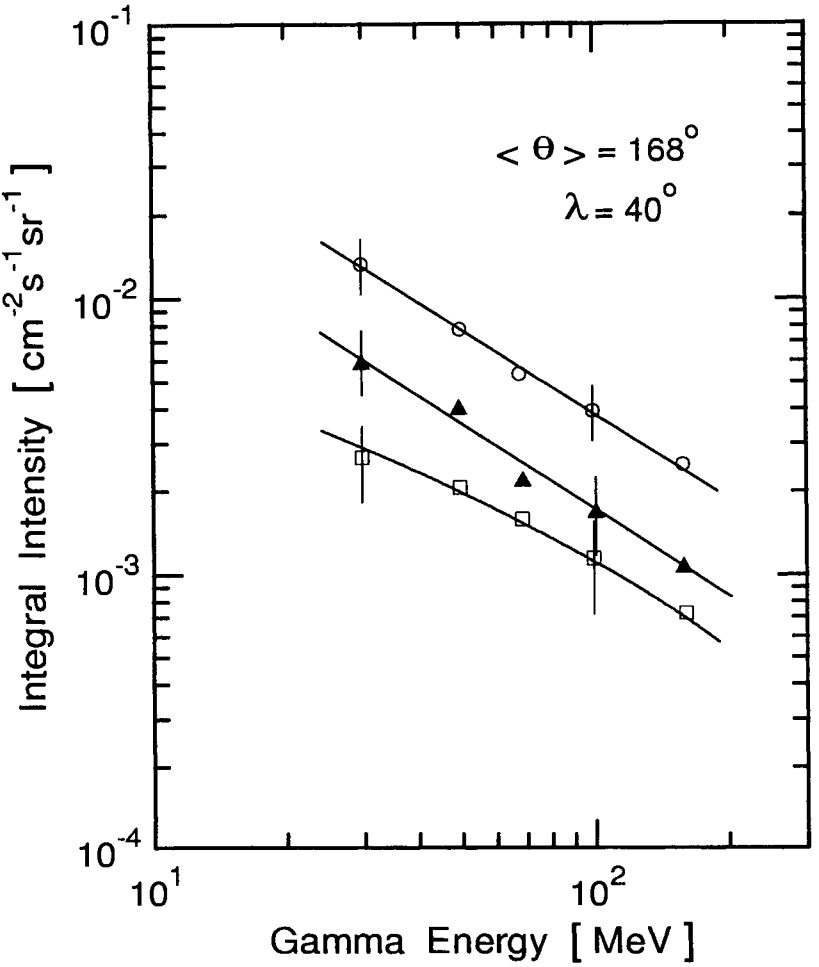

Figure 2.72: Integral energy spectra of gamma rays with an average zenith angle of 168° for three ranges of atmospheric depths recorded during ascent. The curves connecting the points are for visual reference only (Thompson , 1974).

□ 250 - 125 g/cm^2 | ▲ 125 - 50 g/cm^2
○ 5 - 4 g/cm^2 |

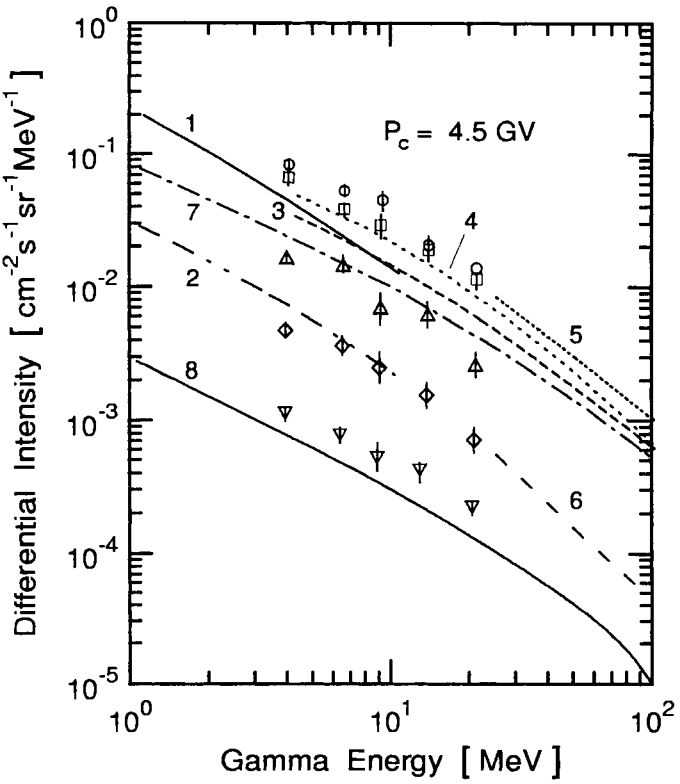

Figure 2.73: Compilation of vertical differential energy spectra of gamma rays at different atmospheric depths and cutoff rigidity of 4.5 GV (Ryan et al., 1979).

1	Ling (1975)	160 g/cm^2	○	Ryan et al. (1979)	160 g/cm^2
2	Ling (1975)	520 g/cm^2	□	Ryan et al. (1979)	330 g/cm^2
3	Beuermann (1971)	100 g/cm^2	△	Ryan et al. (1979)	520 g/cm^2
4	Beuermann (1971)	400 g/cm^2	◇	Ryan et al. (1979)	820 g/cm^2
5	Thompson (1974)	187 g/cm^2	▽	Ryan et al. (1979)	1000 g/cm^2
6	Thompson (1974)	750 g/cm^2			
7	Daniel and Stephens (1974)	100 g/cm^2			
8	Daniel and Stephens (1974)	1000 g/cm^2			

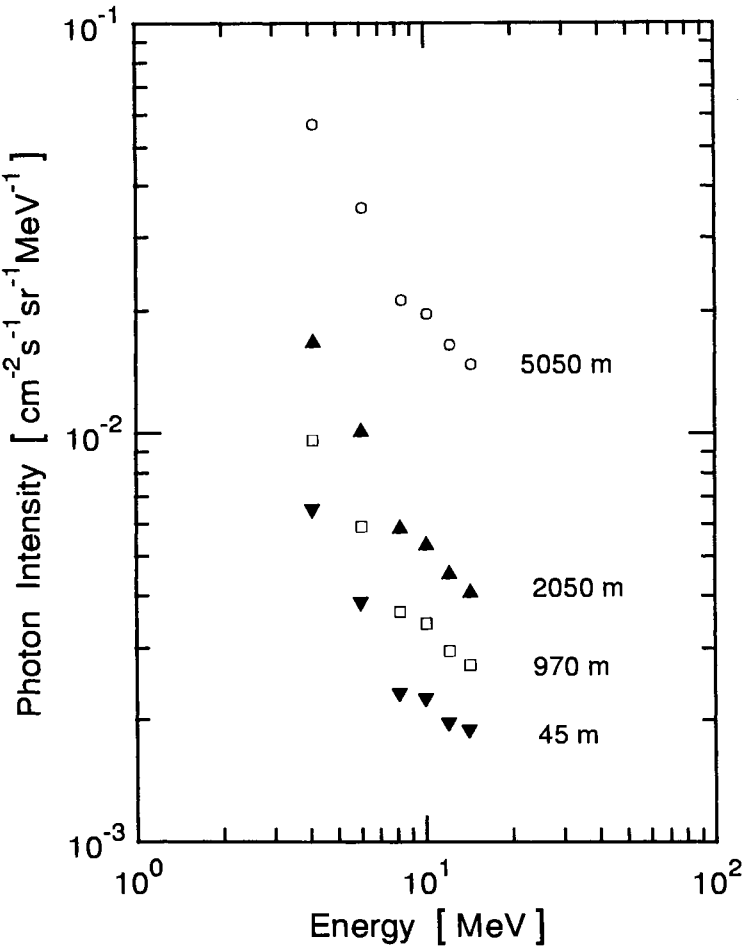

Figure 2.74: Comparison of differential photon energy spectra recorded with a NaI(Tl) mono-crystal in September 1997 at different locations and altitudes at ground level as listed below (Brunetti et al., 1999).

- o Kumbu Valley (Nepal), 5050 m a.s.l.
- ▲ EAS-TOP Lab., Gran Sasso (Italy), 2050 m a.s.l.
- □ LNGS Gran Sasso Lab. (Italy), 970 m a.s.l.
- ▼ University of Bologna (Italy), 45 m a.s.l.

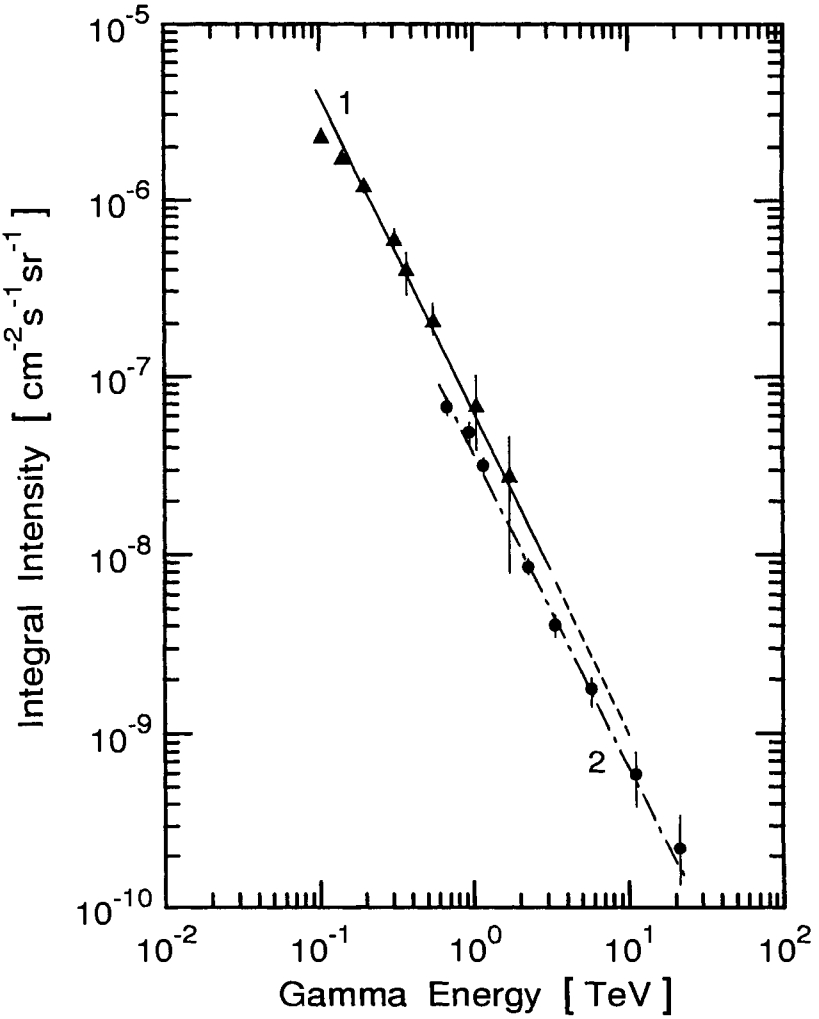

Figure 2.75: Vertical integral gamma ray spectra obtained during 425 hours of airplane flights at an atmospheric depth of 200 g/cm^2 (Apanasenko et al., 1968) . The dashed and dot-dashed lines approximate the data, the solid line indicates the ionization chamber data of Baradzei et al. (1964).

• X-ray film data | ▲ nuclear emulsion data

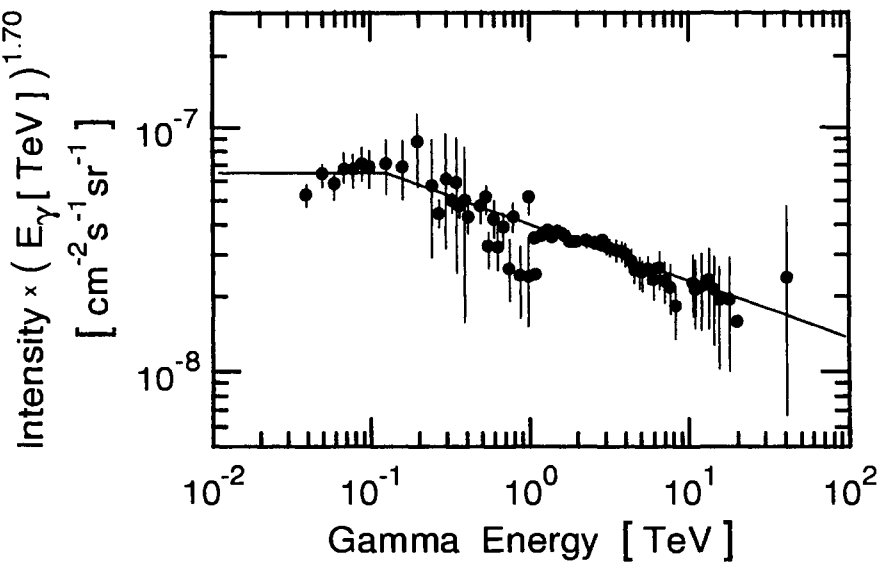

Figure 2.76: Energy spectrum of gamma rays in the energy range $1 \leq E \leq 40$ TeV at an atmospheric depth of 260 g/cm^2 (Takahashi et al., 1979). The line represents the result of a calculation using a scaling model.

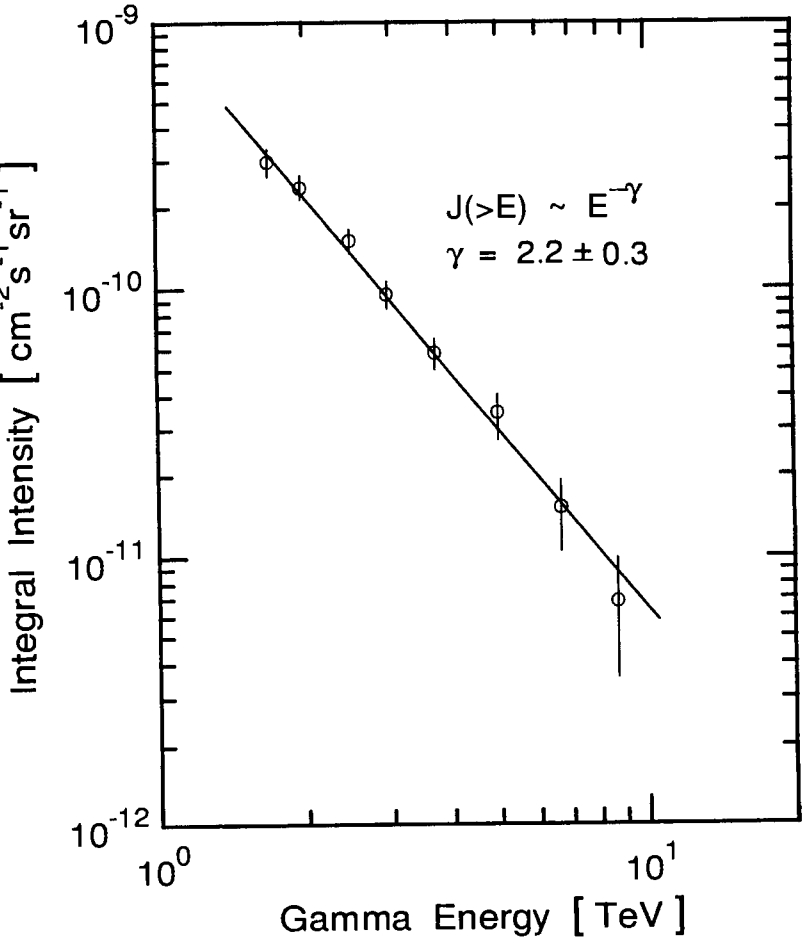

Figure 2.77: Vertical integral spectrum of gamma rays in the energy range $1.5 \leq E \leq 8$ TeV at the depth of 630 g/cm^2 (3776 m a.s.l.) (Yuda et al., 1973). The straight line shows a power law spectrum with a slope of -2.2, as indicated.

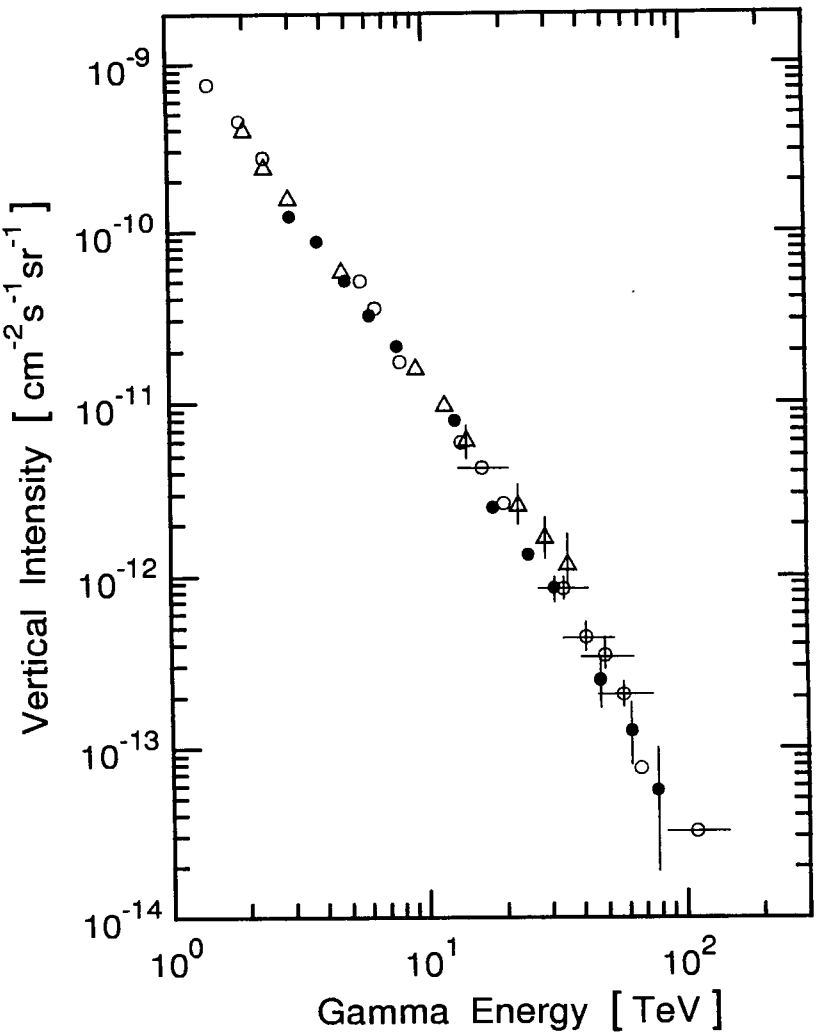

Figure 2.78: Vertical integral energy spectrum of gamma rays obtained at Mt. Fuji at an atmospheric depth of 630 g/cm^2 (3776 m a.s.l.) in the energy range $1 \leq E \leq 100$ TeV (Akashi et al., 1979). The different symbols show data from different emulsion chambers.

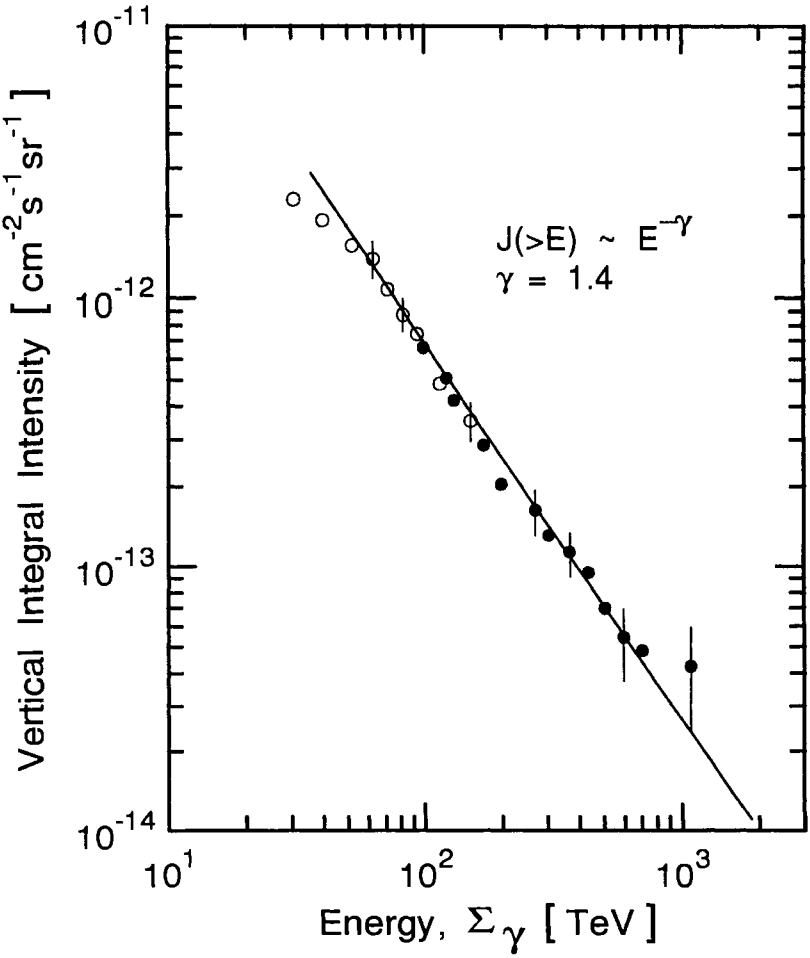

Figure 2.79: Energy flow spectrum of gamma ray families determined at Mt. Fuji at an atmospheric depth of 650 g/cm^2 (altitude 3776 m a.s.l.) in the energy range $30 \leq E \leq 1200$ TeV (Akashi et al., 1981). The two sets of data shown are for two different type chambers: o , thick type, and • thick and thin combined. The straight line shows a simple power law spectrum with spectral index of -1.4.

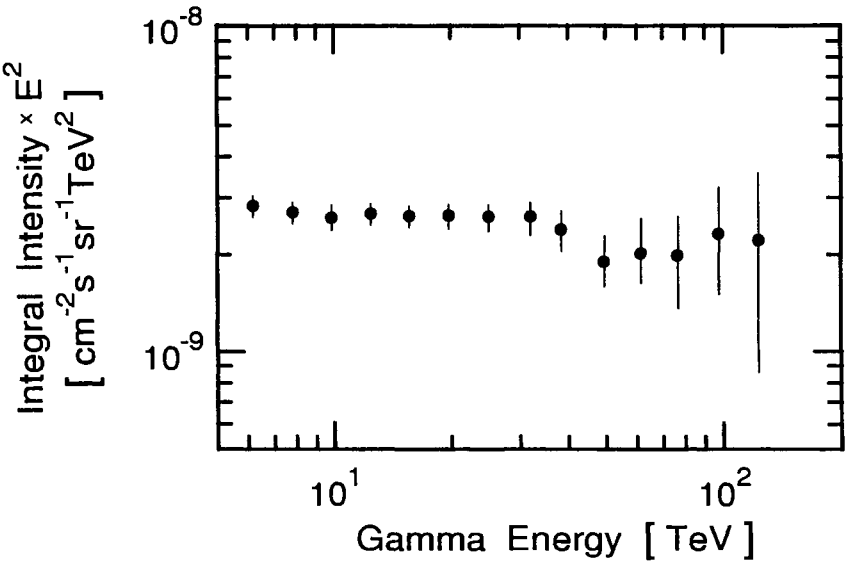

Figure 2.80: Vertical gamma ray spectrum observed at the Pamir station at an atmospheric depth of 595 g/cm^2 (4370 m a.s.l.), covering an energy range $6.3 \leq E \leq 125$ TeV (Pamir Collaboration, 1981).

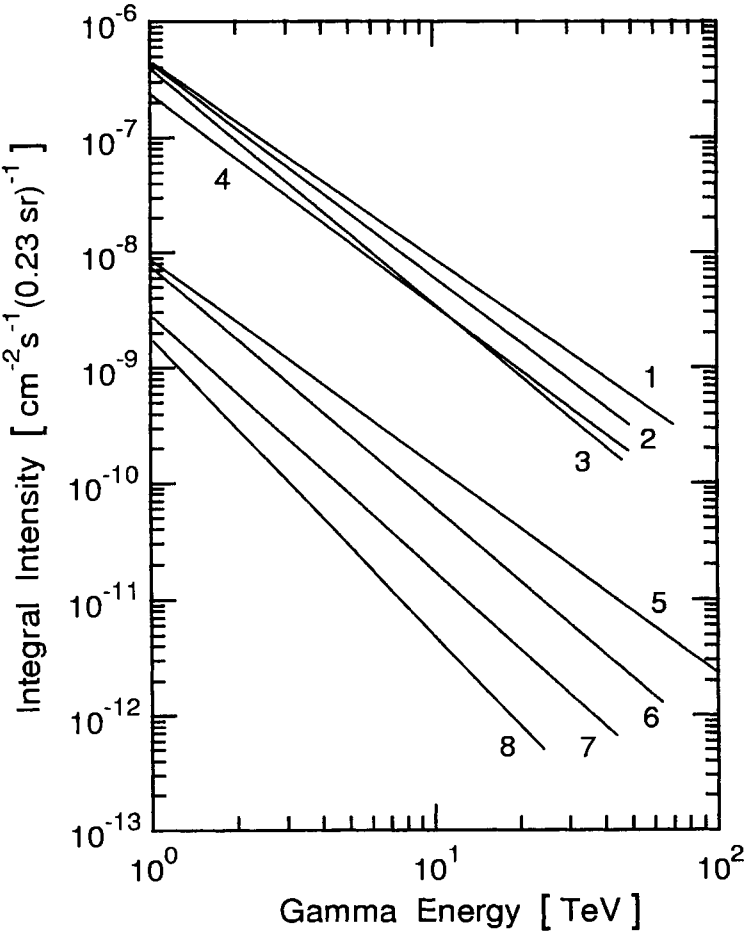

Figure 2.81: Compilation of energy spectra of the electromagnetic component at various atmospheric depths (Kanevskaya et al., 1977). No error bars are given by the authors. The lack of systematic behavior of the slope of the spectra at high altitude is evident.

1	235 g/cm^2	Duthie et al. (1962)	5	729 g/cm^2	Baradzei et al. (1969a)
2	257 g/cm^2	Osborne et al. (1964)	6	798 g/cm^2	Baradzei et al. (1969b)
3	281 g/cm^2	Baradzei et al. (1964)	7	870 g/cm^2	Baradzei et al. (1973)
4	314 g/cm^2	Soloviev (1969)	8	970 g/cm^2	Baradzei et al. (1971)

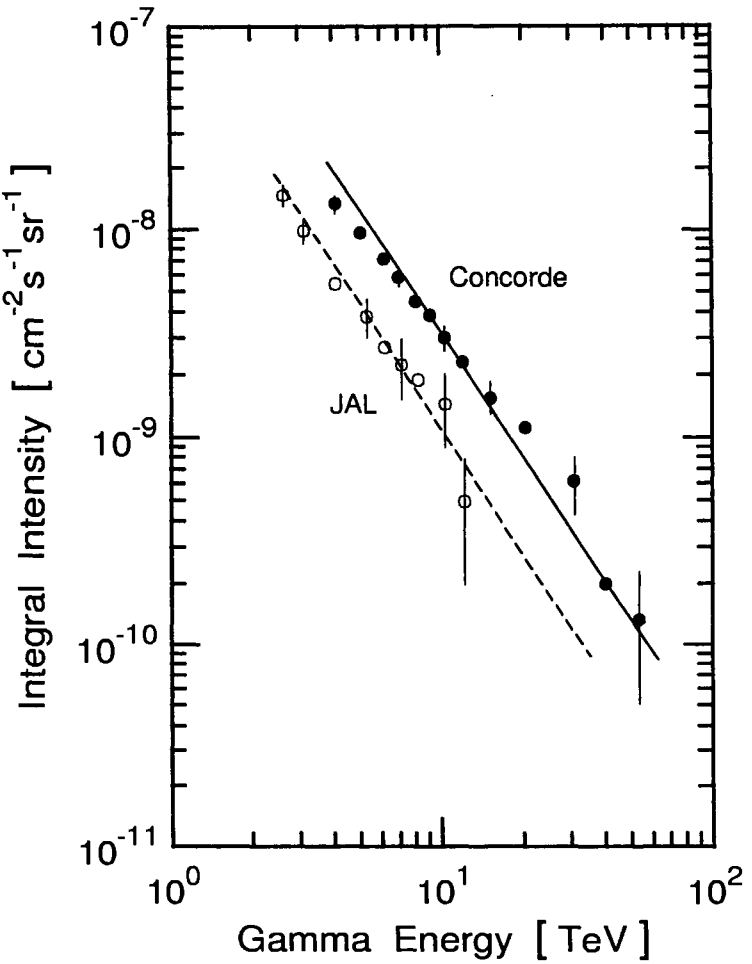

Figure 2.82: Integral vertical energy spectra of high energy gamma rays measured during 400 hours at a atmospheric depth of about 100 g/cm^2 on board of the supersonic jet liner Concorde and at about 250 g/cm^2 on board of a regular JAL jet liner. The solid and dashed lines are fits to the data.

- • Capdevielle et al. (1987), Concorde
- o Ichimura (1987), JAL

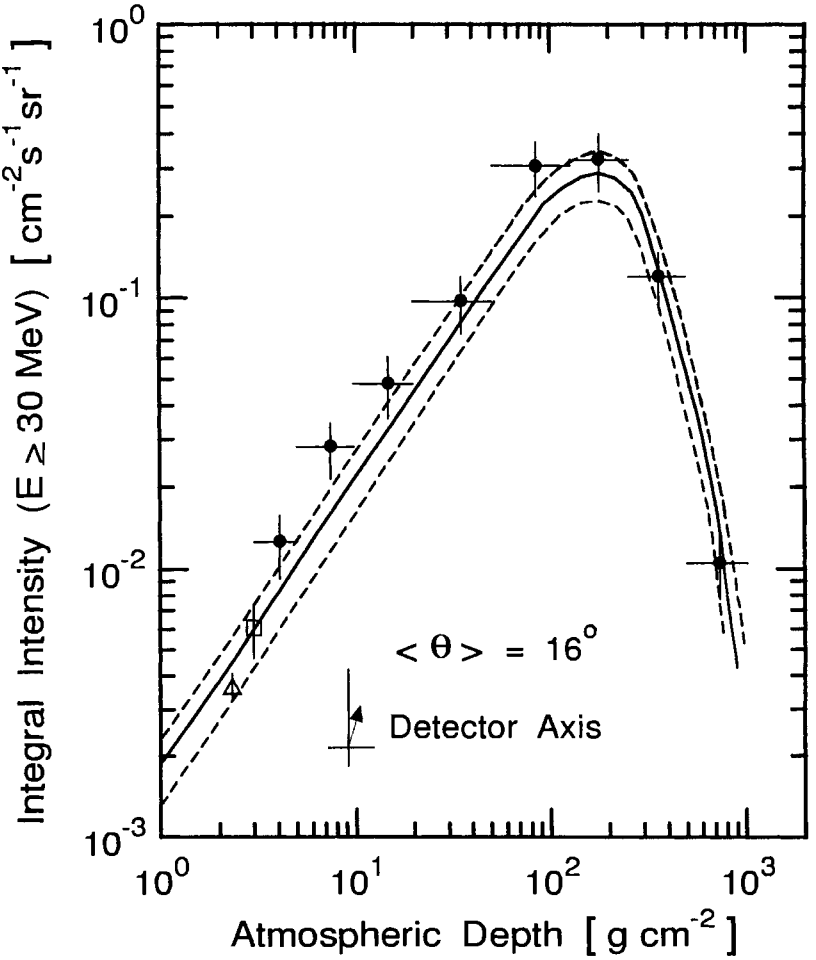

Figure 2.83: Total intensity of gamma rays with $E \geq 30$ MeV as a function of atmospheric depth for an average zenith angle of 16°. The solid line shows the calculated value, and the dashed lines the calculation uncertainty (Thompson, 1974).

△ Frye et al. (1966) | □ Fichtel et al. (1969)
• Thompson (1974) |

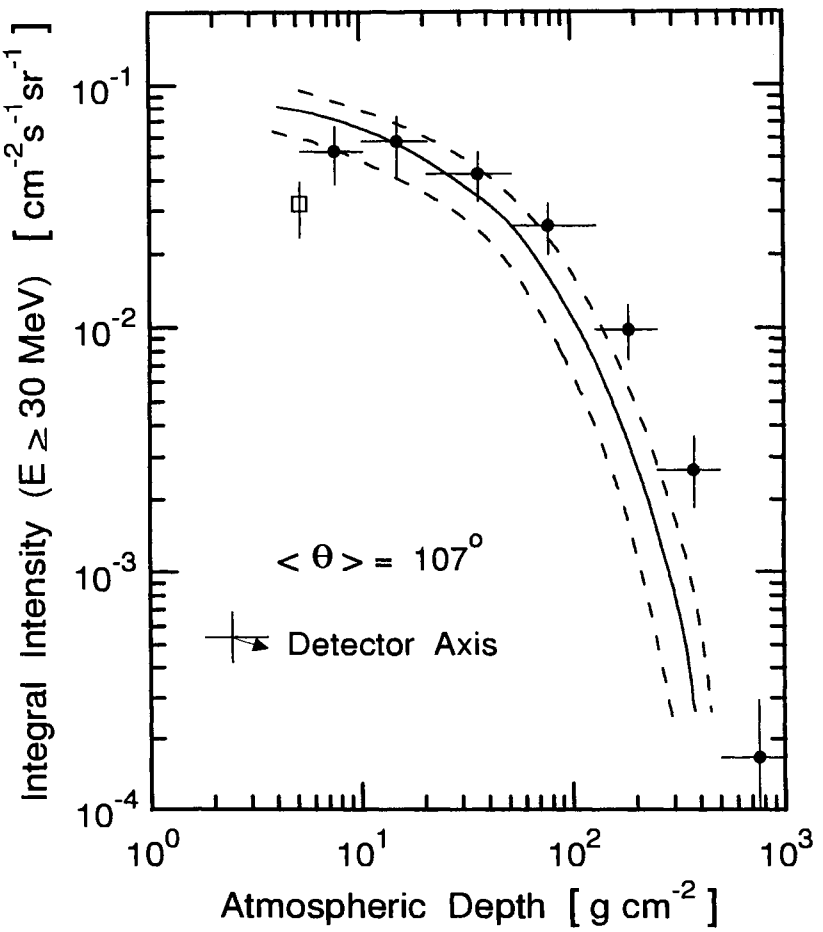

Figure 2.84: Total intensity of gamma rays with $E \geq 30$ MeV as a function of atmospheric depth for an average zenith angle of 107°. The solid line shows the calculated value, and the dashed lines the calculation uncertainty (Thompson, 1974).

□ Fichtel et al. (1969) | • Thompson (1974)

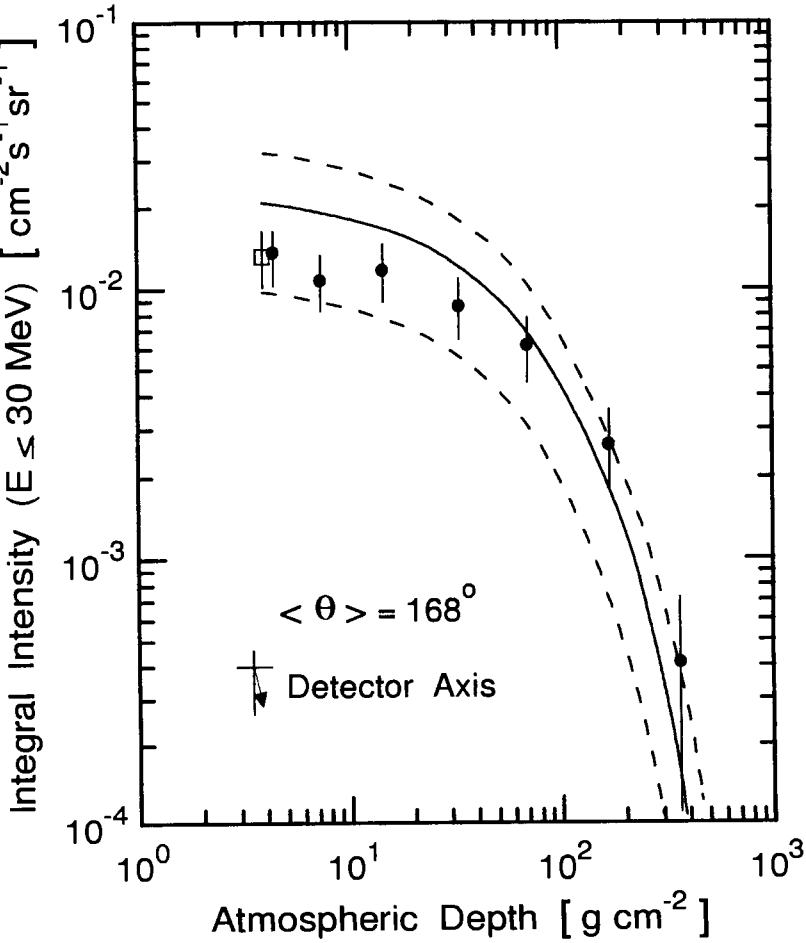

Figure 2.85: Total intensity of gamma rays with $E \geq 30$ MeV as a function of atmospheric depth for an average zenith angle of 168°. The solid line shows the calculated value, and the dashed lines the calculation uncertainty (Thompson, 1974).

□ Fichtel et al. (1969) | • Thompson (1974)

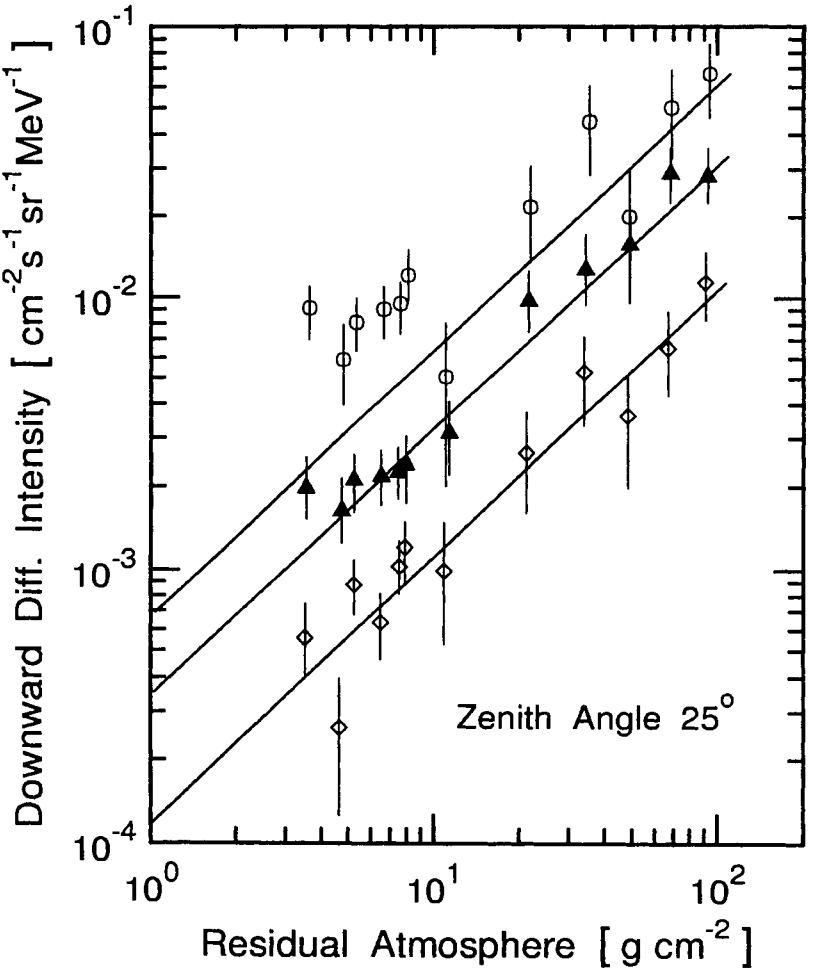

Figure 2.86: Altitude dependence of downward directed gamma ray intensity for the energy intervals 2 - 3 MeV, 5 - 7.5 MeV and 10 - 15 MeV (Ryan et al., 1977). The solid lines represent the respective least squares fit for the atmospheric component.

○ 2 - 3 MeV | ▲ 5 - 7.5 MeV
◇ 10 - 15 MeV |

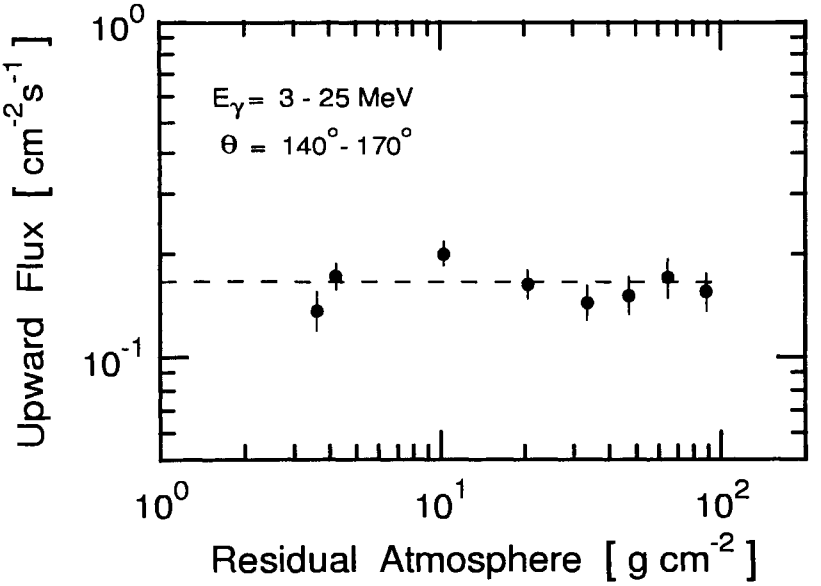

Figure 2.87: Altitude dependence of upward directed gamma ray flux for the energy range from 3 - 25 MeV (Ryan et al., 1977).

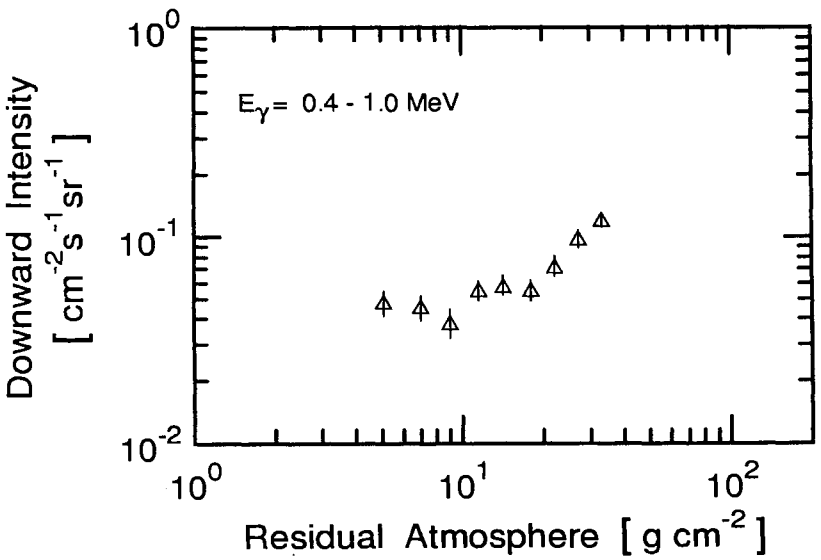

Figure 2.88: Altitude dependence of downward directed gamma ray intensity for the energy range from 0.4 - 1.0 MeV (Lockwood et al., 1981).

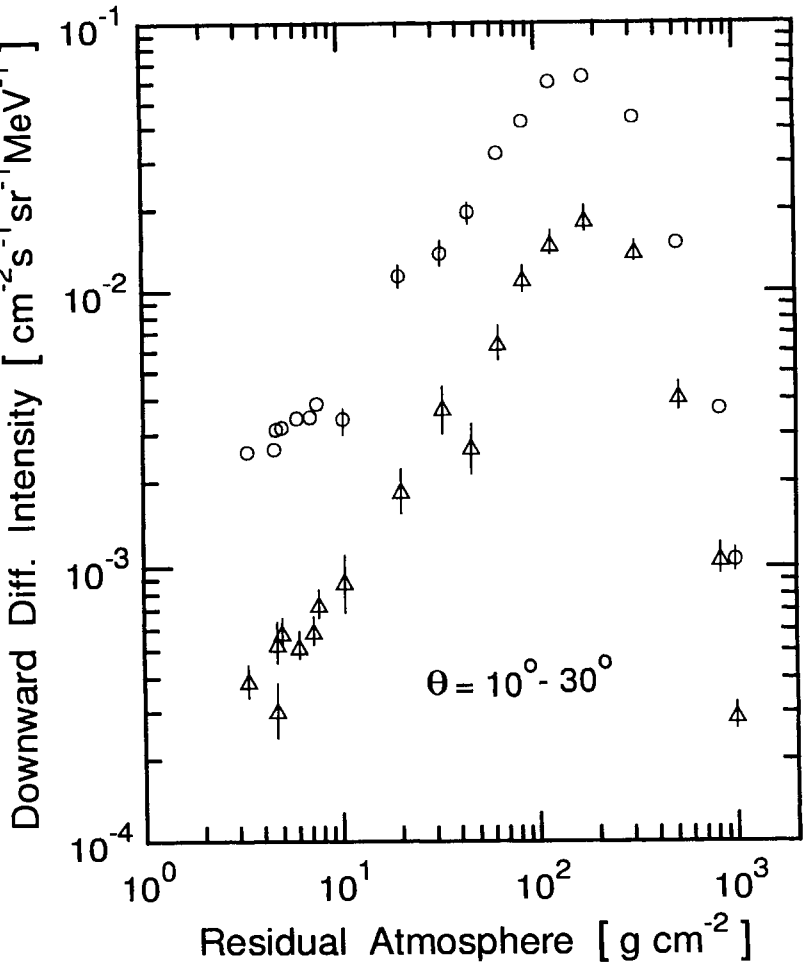

Figure 2.89: Altitude dependence of the downward directed gamma ray intensity for the energy ranges 3 - 10 MeV and 10 - 25 MeV, for the zenith angle interval from 10° to 30°. The data were recorded at Palestine, TX (P_c = 4.5 GV) during ascent (Ryan et al., 1979).

o 3 - 10 MeV | △ 10 - 25 MeV

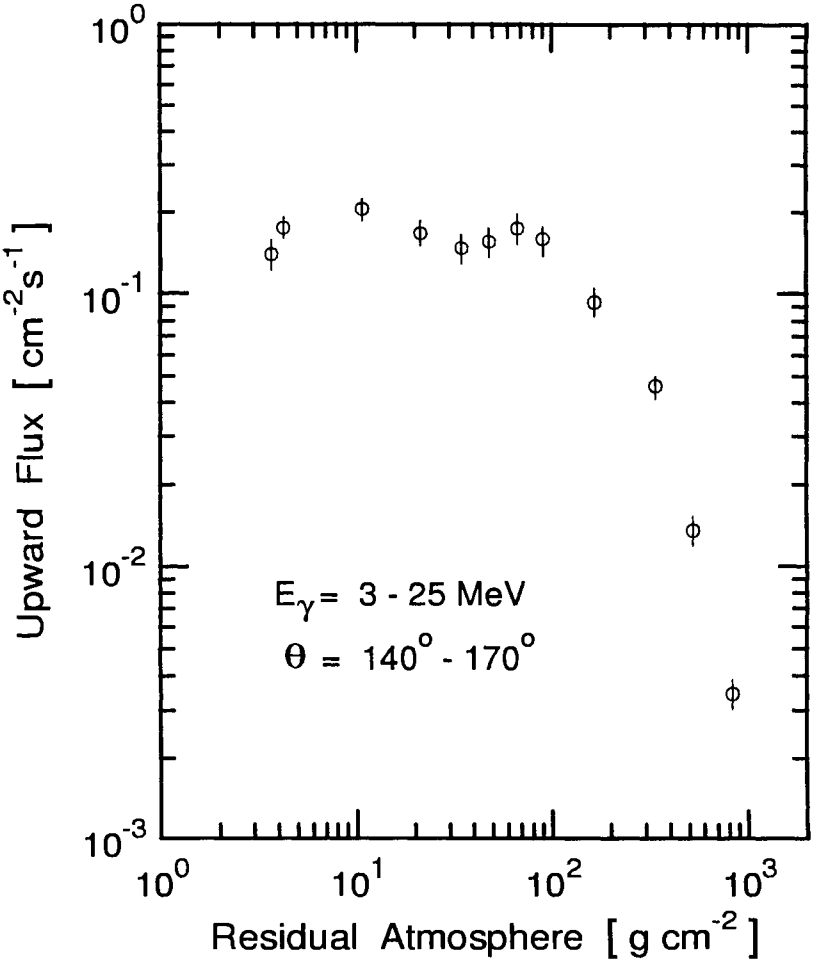

Figure 2.90: Altitude dependence of the upward directed gamma ray flux for the energy range 9 - 25 MeV within a zenith angle interval from 140° to 170°. The data were recorded at Palestine, TX (P_c = 4.5 GV) during ascent (Ryan et al., 1979).

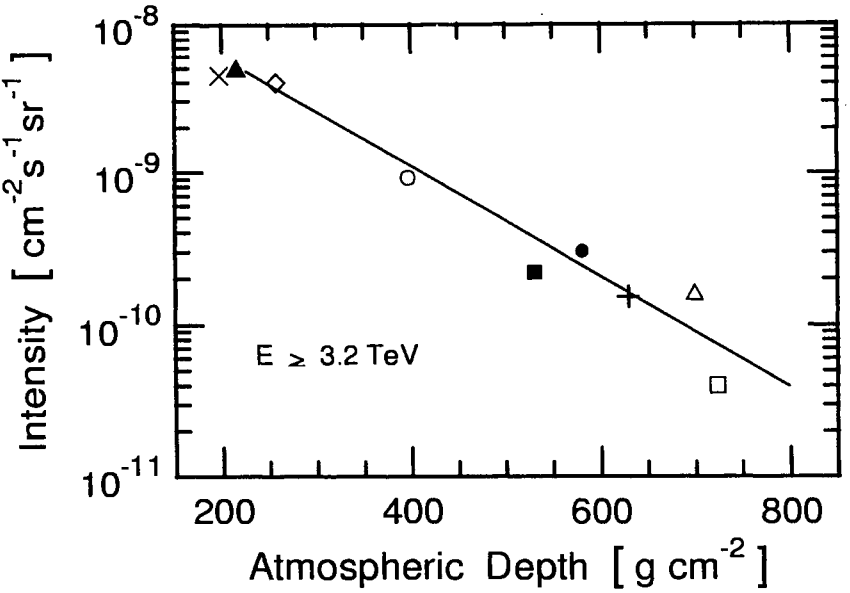

Figure 2.91: Compilation of altitude dependence of integral gamma ray intensities for energies $\geq$ 3.2 TeV (Pamir Collaboration, 1981).

- × Baradzei et al. (1970), Airplane, 197 g/cm^2
- ▲ Baradzei et al. (1977), Airplane, 225 g/cm^2
- ◇ Takahashi et al. (1977), Airplane, 260 g/cm^2
- ○ Cherdyntseva et al. (1976), Lenin Peak, 400 g/cm^2 (7050 m)
- ■ Japanese - Brasilian Collaboration (1971), Mt. Chacaltaya, 540 g/cm^2 (5200 m)
- • Pamir Collab. (1981), Pamir Mts., 595 g/cm^2
- \+ Akashi et al. (1979), Mt Fuji, 650 g/cm^2
- △ Baradzei et al. (1977), Mountain, 700 g/cm^2
- □ Akashi et al. (1981), Mt. Norikura, 725 g/cm^2

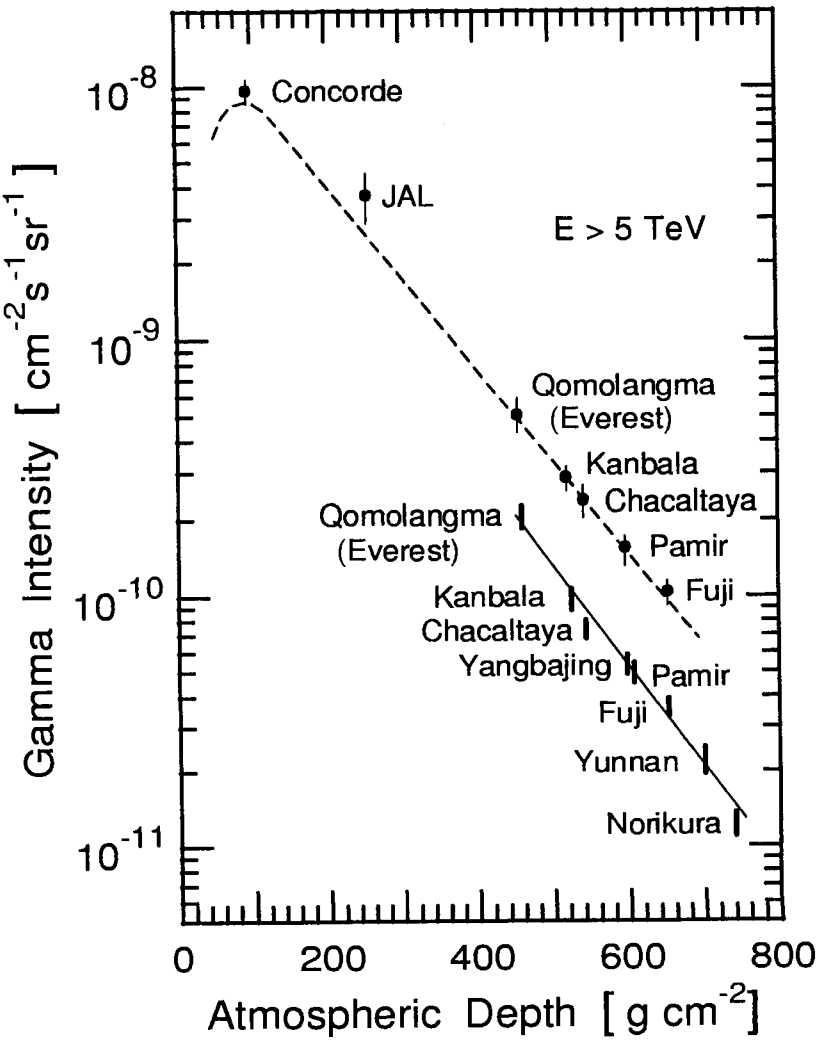

Figure 2.92: Altitude variation of the high energy gamma ray component ($E \geq 5$ TeV) in the atmosphere. The dashed line represents the prediction of a calculation of Shibuya (1987) using a scaling law. The solid line is an exponential fit to rescaled data according to Lu et al. (1997) (see also Lu et al. (1981).

• Capdevielle et al. (1987) | △ Shibuya (1987)
| Lu et al. (1997)

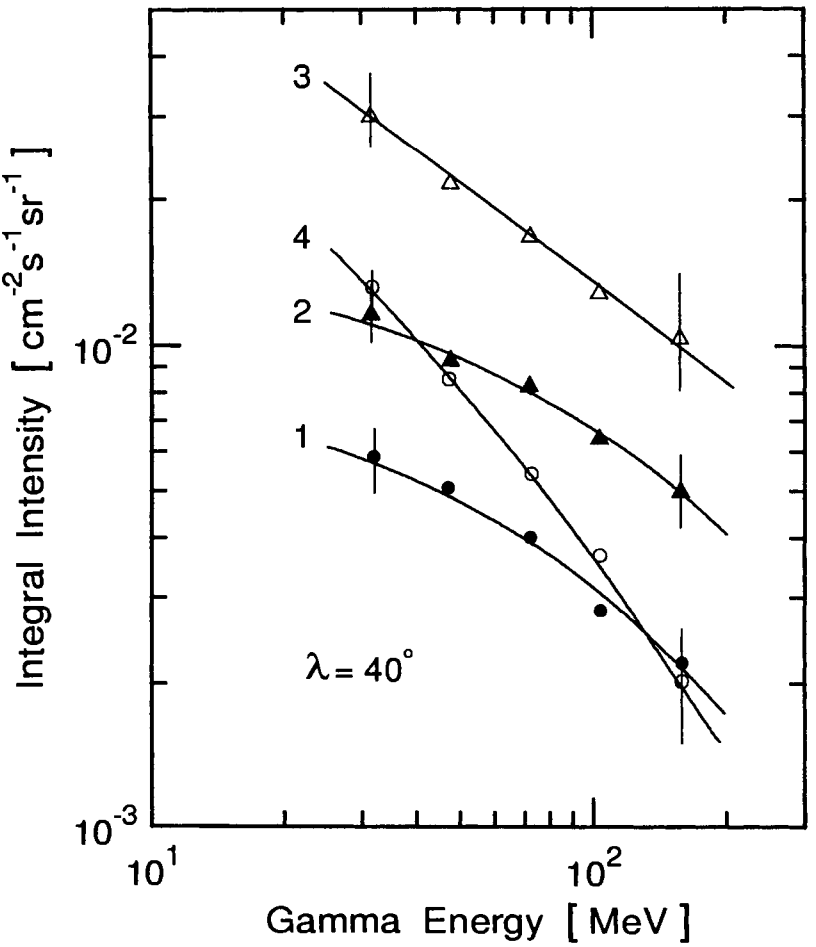

Figure 2.93: Integral energy spectra of gamma rays for various zenith angles at a depth of 3 g/cm^2 and latitude 40° N (Daniel and Stephens, 1974). The lines indicate the trend of the data. Note that the upward directed gamma rays (curve 4) show a much steeper spectrum at low energies than the downward directed radiation (curve 1).

1 , • θ = 16°	2 , ▲ θ = 45°
3 , △ θ = 112°	4 , ○ θ = 164°

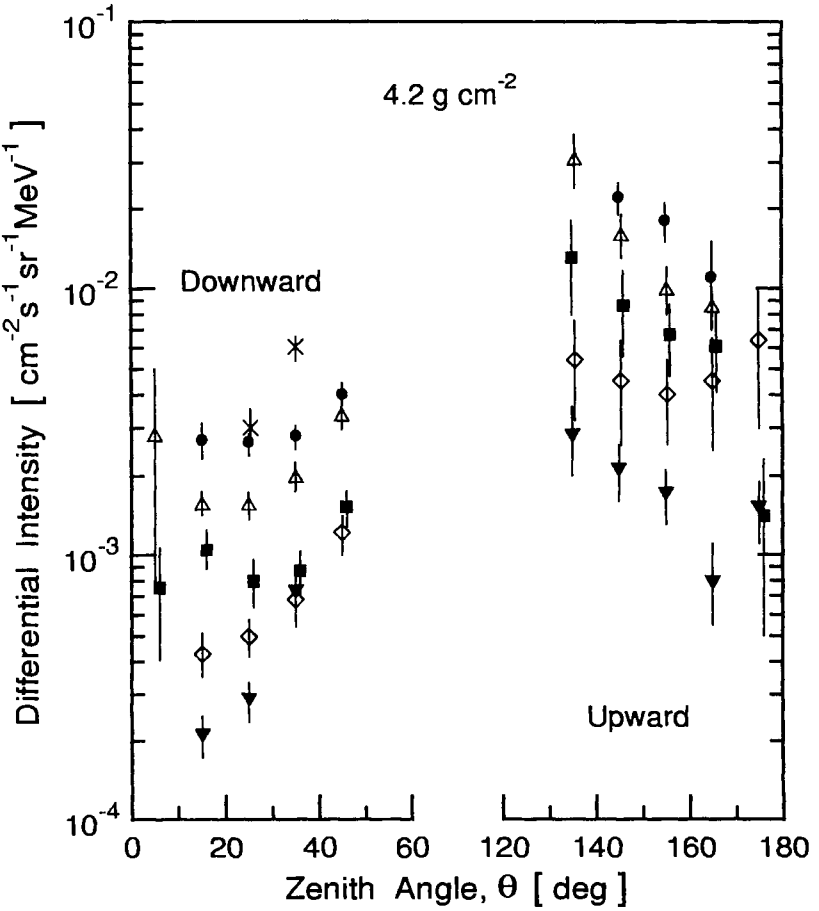

Figure 2.94: Angular distribution of atmospheric gamma rays at a depth of 4.2 g/cm^2 for upward and downward directed photons (Ryan et al., 1977).

×	2 - 3	MeV	•	3 - 5	MeV
△	5 - 7.5	MeV	■	7.5 - 10	MeV
◇	10 - 15	MeV	▼	15 - 25	MeV

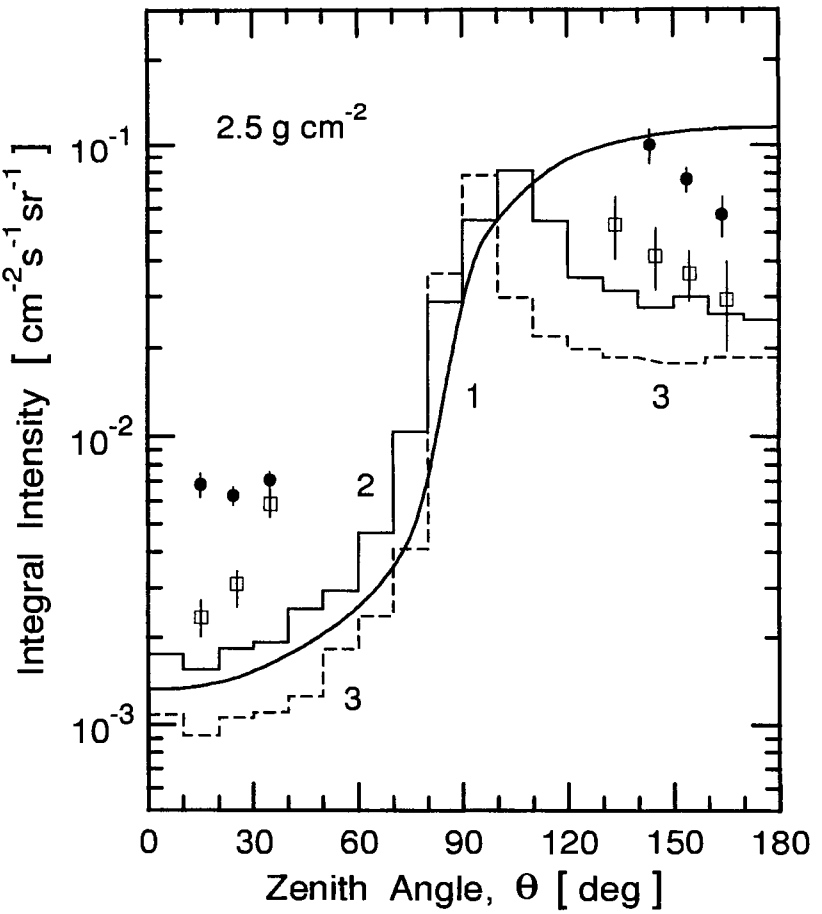

Figure 2.95: Angular distribution of gamma ray intensity at a depth of 2.5 g/cm^2 in the energy range $3 \leq E \leq 10$ MeV at a cutoff rigidity of 4.5 GV (Ryan et al., 1977).

1	Ling (1975), calculation	
2	Graser and Schönfelder (1977)	3 - 10 MeV
3	Graser and Schönfelder (1977)	10 - 30 MeV
•	Ryan et al. (1977)	3 - 10 MeV
□	Ryan et al. (1977)	10 - 25 MeV

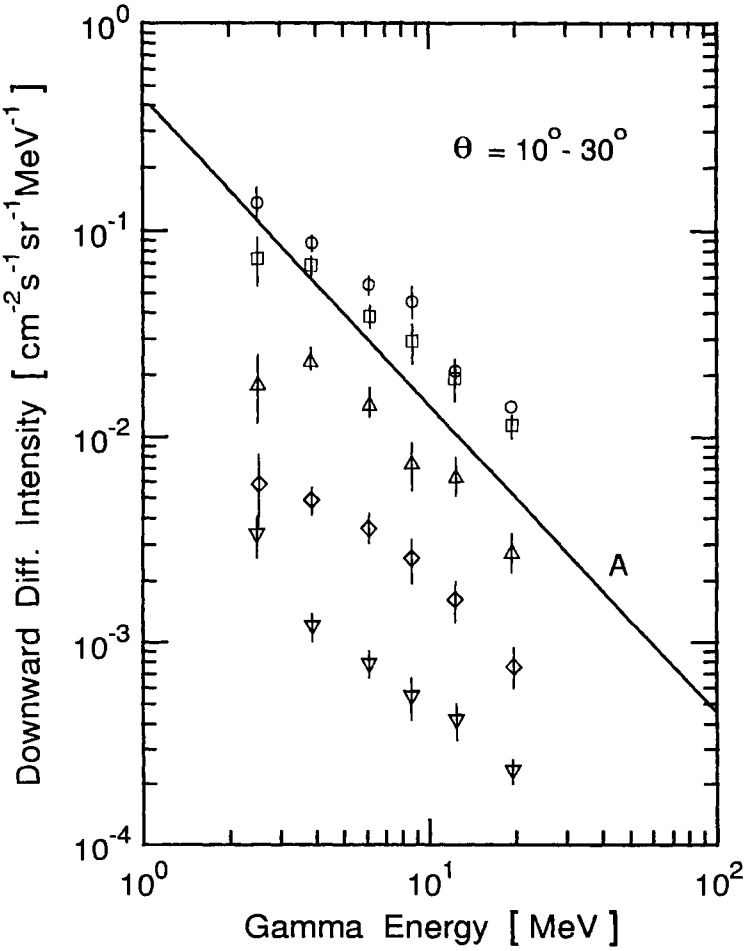

Figure 2.96: Differential energy spectra of downward directed gamma rays at various atmospheric depths within a zenith angle interval from 10° to 30° (Ryan et al., 1979). Line A is described by the expression $(4.3 \pm 0.5) \cdot 0.1\, E^{-\gamma}$, with $\gamma = 1.45 \pm 0.06$ (E in MeV), and is obtained from the high altitude growth curve, extrapolated to 100 g/cm^2. At and below 160 g/cm^2 the spectra are compatible with $\gamma = 1.09 \pm 0.05$.

○ 160 g/cm^2	□ 330 g/cm^2	△ 520 g/cm^2
◇ 820 g/cm^2	▽ 1000 g/cm^2	

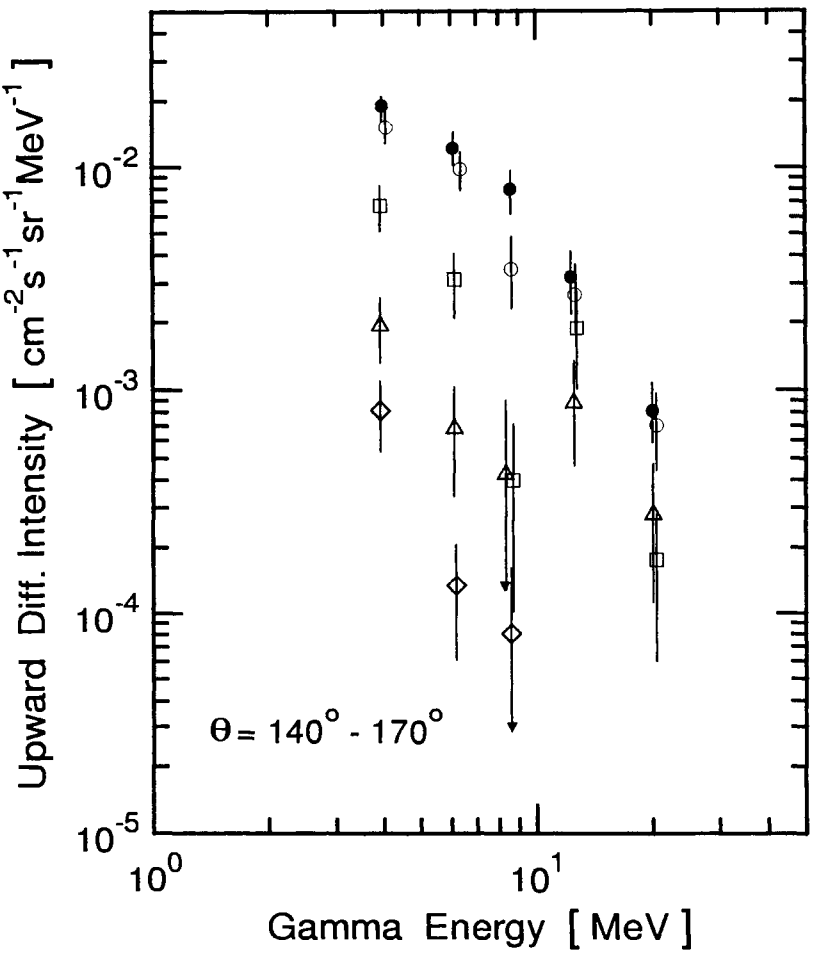

Figure 2.97: Differential energy spectra of upward directed gamma rays at various atmospheric depths within a zenith angle interval from 140° to 170° (Ryan et al., 1979).

• 10 g/cm^2	○ 160 g/cm^2	□ 330 g/cm^2
△ 520 g/cm^2	◇ 820 g/cm^2	

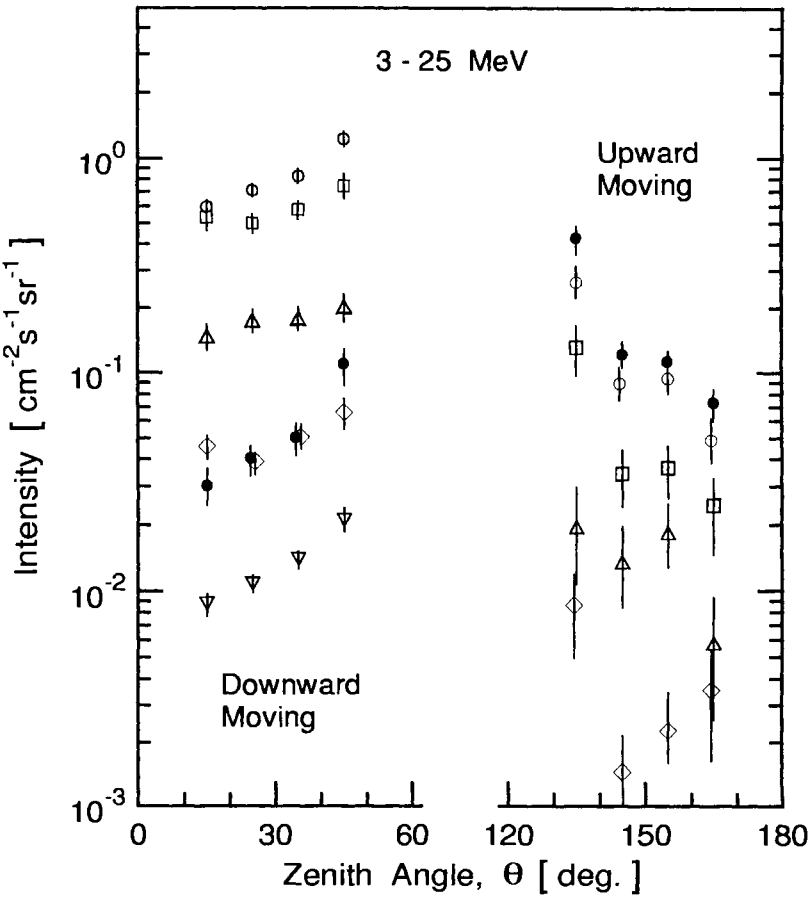

Figure 2.98: Zenith angle distribution of gamma rays of energy $3 \leq E \leq 25$ MeV at various atmospheric depths (Ryan et al., 1979) ($\lambda = 40°$).

•	10 g/cm^2	○	160 g/cm^2
□	350 g/cm^2	△	520 g/cm^2
◇	820 g/cm^2	▽	1000 g/cm^2

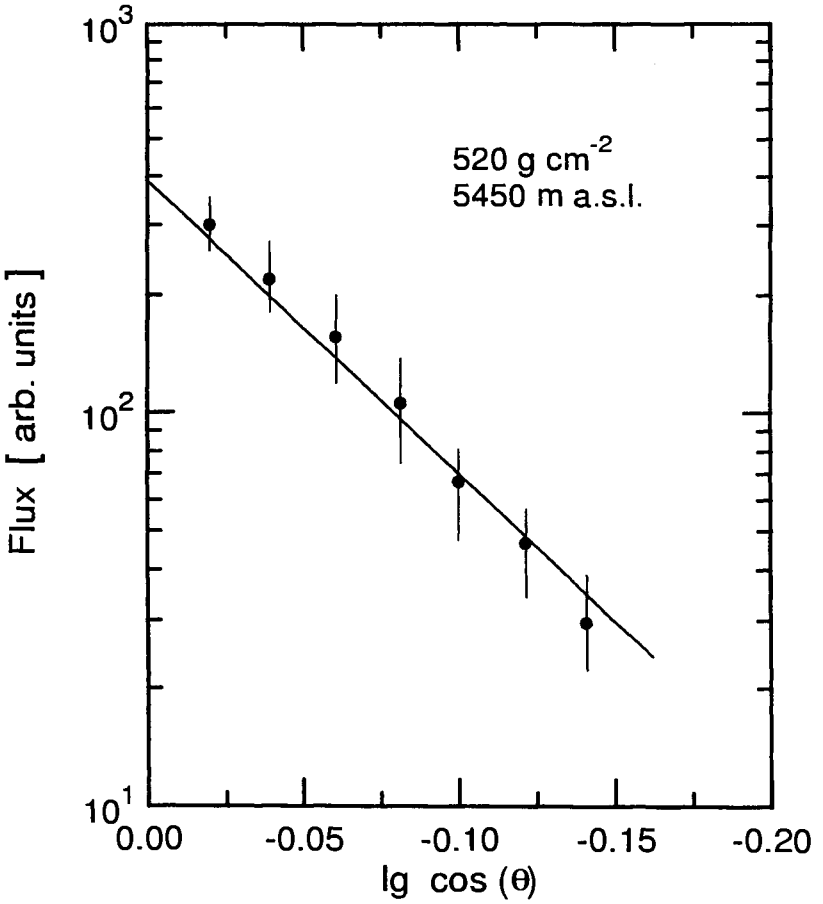

Figure 2.99: Zenith angle distribution of gamma rays of energy $\geq$ 2 TeV recorded at Mt. Kanbala (Tibet) at an altitude of 5450 m a.s.l. (520 g/cm^2) (Wang et al., 1981). The line which approximates the distribution is described by the function $I(\theta) \propto \cos^n(\theta)$ with $n = 7.3 \pm 0.4$.

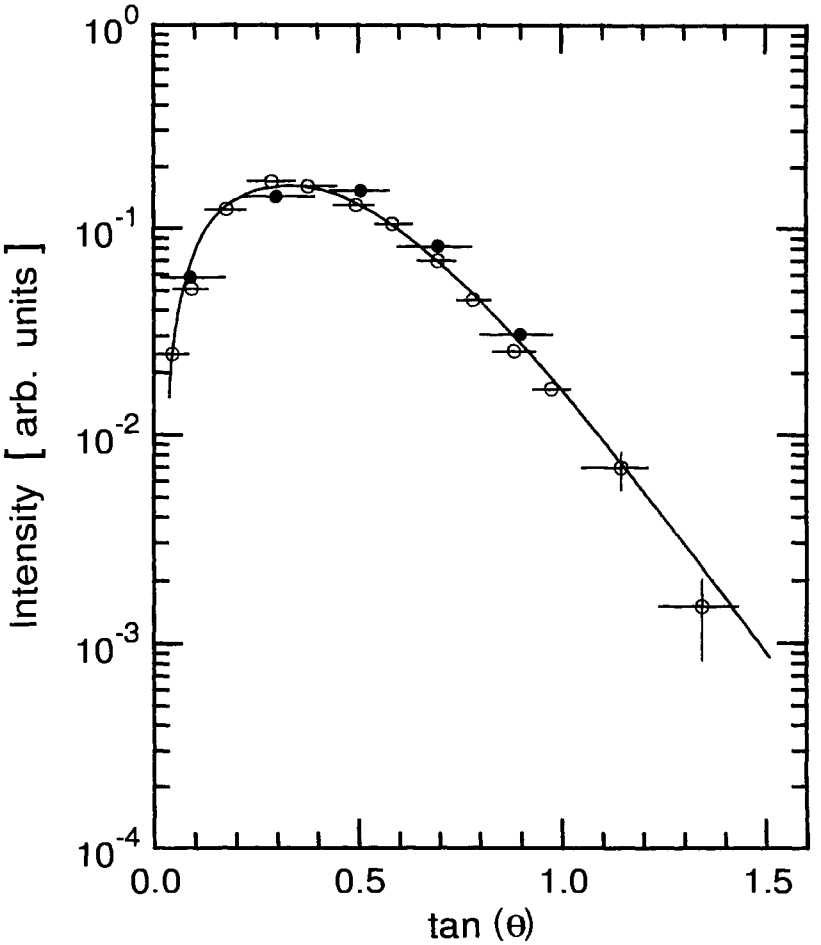

Figure 2.100: Zenith angle distribution of gamma rays in the energy range $1 \leq E \leq 100$ TeV recorded at Mt. Fuji at an altitude of 3776 m (650 g/cm^2) (Akashi et al., 1981). The two sets of data are for two types of emulsion chambers (see Fig. 2.79 for details). The curve is described by the function $I \propto \exp -(x/\cos\theta)$ with $x = 6$.

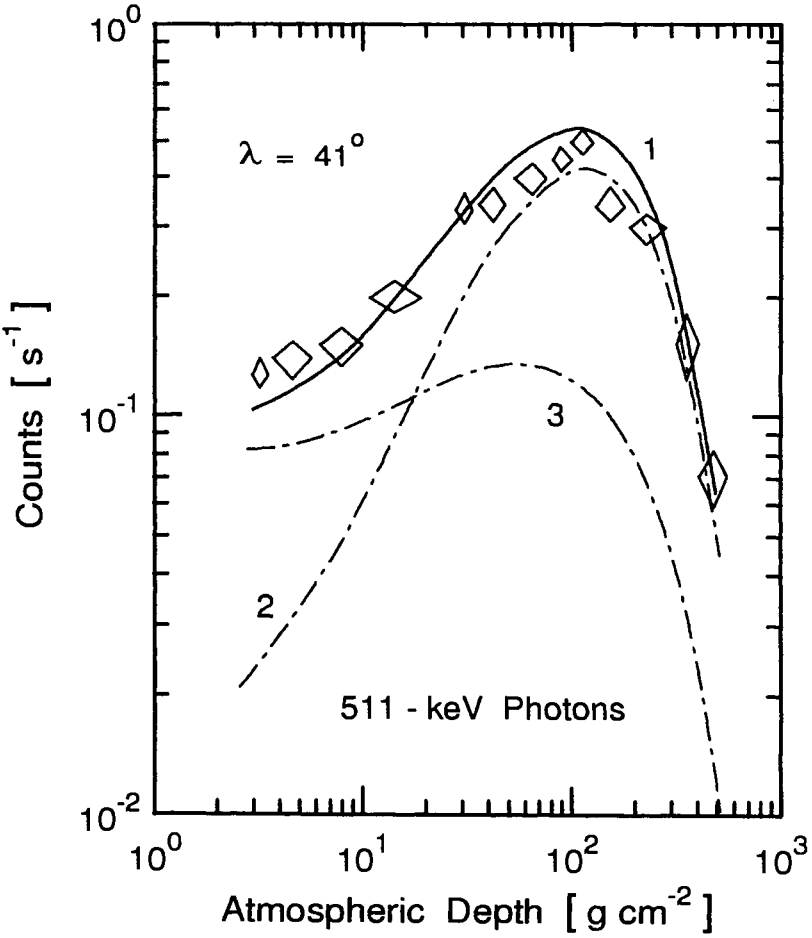

Figure 2.101: Altitude dependence of the 0.511 MeV e^+e^--annihilation line at latitude 41° N measured with a 40 cm^3 Ge-Li crystal detector system with an energy resolution of 0.5 % at 0.511 MeV and an angular resolution of 30° FWHM in a balloon. ◇ , net line counts, measured 10 June 1974. Errors are statistical. Curves 1, 2 and 3 are theoretical on the basis of a semi-empirical model (Ling et al., 1977). Curve 1, total atmospheric counts plus background due to positron annihilation resulting from β^+-decay of neutron and proton initiated reactions in material in and near the detector. Curve 2, atmospheric continuum background. Curve 3, component due to positron annihilation from β^+-decay only.

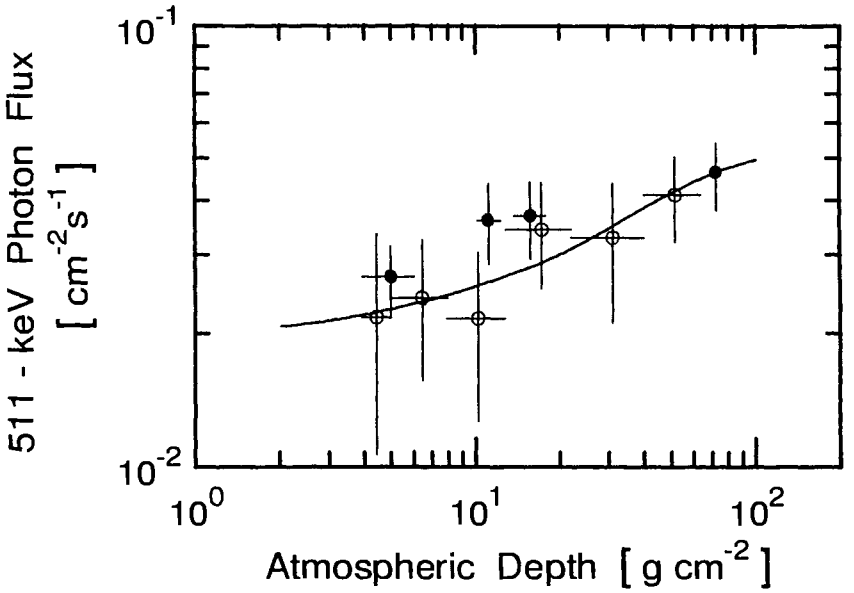

Figure 2.102: Two sets of data from different balloon flights (•, 20 Dec. 1974 and ○, 24 Feb. 1978) showing the atmospheric depth dependence of the 0.511 MeV annihilation line (Buivan et al., 1979). The line shows the prediction of a semi-empirical model.

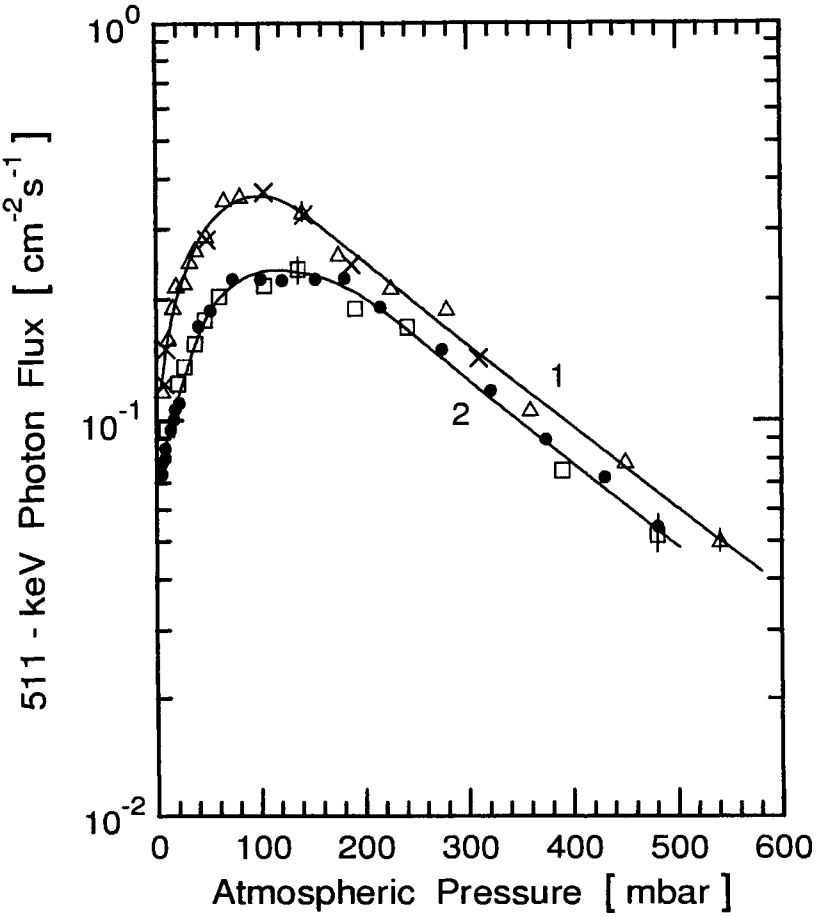

Figure 2.103: Altitude dependence of the 0.511 MeV electron - positron annihilation line at latitudes 45° N and 10° S (Albernhe et al., 1979). The data points × were obtained with a GeLi detector, the others with a NaI detector. The curves are fits to the data.

1 , △ , × 45° N | 2 , • , □ 10° S

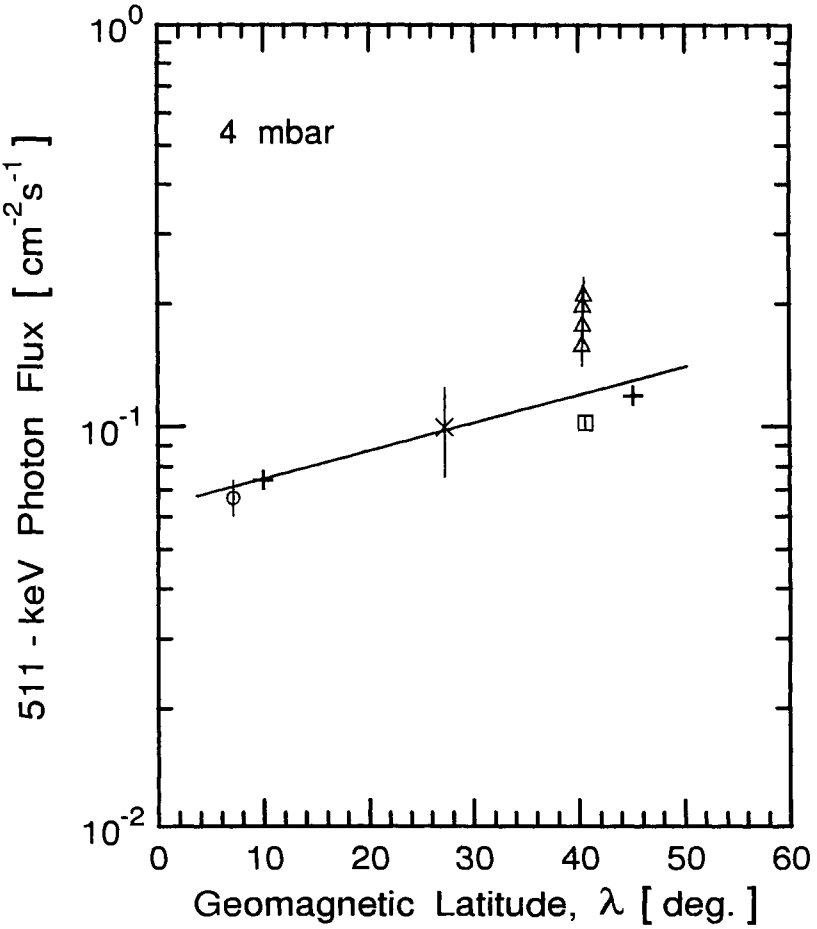

Figure 2.104: Geomagnetic latitude dependence of the 0.511 MeV gamma line at an atmospheric depth corresponding to a pressure of 4 mbar (Albernhe et al., 1979).

△ Chupp et al. (1967, 1970) | □ Peterson et al. (1973)
o Kasturirangan et al. (1972) |

2.5 Electrons (Negatrons and Positrons)

2.5.1 Introduction

The electron component in the atmosphere includes both primaries, incident from outer space, and secondaries that are created within the atmosphere. (Note that in general we use the term electrons to include both, negatrons and positrons combined.) The main sources of secondary electrons of either charge sign are short-lived particles, resulting from interactions of primary and secondary cosmic rays with nuclei that constitute the air. Gamma rays from neutral pion decay undergoing pair creation supply the bulk of electrons and positrons, followed by decaying muons and, in rare cases, charged pions. Another significant contribution comes from knock-on electrons (negatrons), ejected by primary and secondary cosmic rays from atomic shells and, finally, decay products of radioactive nuclei. The latter are by-products of the interactions in the atmosphere.

Experiments designed to investigate electron fluxes at energies below about 100 MeV are usually based on instruments that determine either the energy of the particles directly, or their energy loss, dE/dx. From 100 MeV to a few GeV gas Cherenkov counters and suitable combinations with dE/dx-counters are used for particle identification. At the highest energies ionization calorimeters and emulsion chambers have been used.

A comprehensive summary of electron data, including theoretical aspects, has been given by Daniel and Stephens (1974).

2.5.2 Altitude Dependence of Flux and Intensities

The development curves describing the electron intensity in the atmosphere as a function of atmospheric depth are different for different energy intervals. This is illustrated in Fig. 2.105 which shows the results of measurements by Rockstroh and Webber (1969), Beedle (1970), Beuermann et al. (1970) and Schmidt (1972), as presented by Daniel and Stephens (1974).

Fig. 2.106 shows the altitude dependence of the electron intensity in the energy range $35.6 \leq E \leq 54.0$ MeV (Fulks and Meyer, 1974). Analogous curves for the energy intervals $54 \leq E \leq 85$ MeV, $340 \leq E \leq 52$ MeV, $910 \leq E \leq 1570$ MeV and $2650 \leq E \leq 4300$ MeV, taken from the work of Fulks and Meyer (1974), are presented in Figs. 2.107 to 2.110, respectively. The different symbols identify different ascents of the instrument. In this set of figures theoretical curves of the primary (Fulks and Meyer, 1974) and secondary electron components (Daniel and Stephens, 1974) are also included.

The experimental work was carried out in 1972.

2.5.3 Energy Spectra

The majority of spectral measurements have been made at high geomagnetic latitudes. There, temporal intensity variations are observed at low energies. One of the causes for these variations is due to the 11 year solar cycle, another is the consequence of the large diurnal variations of the bulk of cosmic ray particles having energies less than 200 MeV. The latter is related to the stretching of the geomagnetic field lines on the night side of the earth, leading to drastic changes in the cutoff rigidity.

Over Fort Churchill, Canada, the cutoff rigidity varies from 210 MV at daytime to about 10 MV at night. Fig. 2.111 summarizes nighttime energy spectra of vertical electrons carried out at an atmospheric depth of 2.5 g/cm^2 over Fort Churchill during the period from 1965 to 1972. (Daniel and Stephens, 1974). These spectra are compared with several theoretical estimates. Since there exist no reentrant electrons above 100 MeV, the intensities must be due to electrons of primary origin and to secondaries produced in the overlaying atmosphere.The effect of solar modulation manifests itself in the energy range $20 \leq E \leq 1000$ MeV. A further complication arises from the albedo component, however, it affects the low energy region only. Fig. 2.112 shows data by Scheel and Roehrs (1972) which also include reentrant (downward directed) albedo electrons.

In 1972 Fulks and Meyer investigated the energy spectra of electrons at depths of 291 and 637 g/cm^2 over a wide range of energies during nighttime at high geomagnetic latitude, corresponding to a cutoff rigidity of 10 MV. Their results are shown in Fig. 2.113 (Fulks and Meyer, 1974). A compilation of data from different atmospheric depths is given in Fig. 2.114 (Daniel and Stephens, 1974).

Additional measurements have been made in 1973 at a geomagnetic latitude of 46° N (Galper et al., 1975). It could be shown that the exponent of the differential energy spectrum, γ, changes non-monotonically with atmospheric depth, as illustrated in Fig. 2.115.

Secondary fluxes of electrons and positrons resulting from the decay of mesons produced in nuclear interactions have been calculated by Orth and Buffington (1976) for an atmospheric depth of 5 g/cm^2. Fig. 2.116 shows the results obtained by Monte Carlo and analytic calculations.

A relatively recent ground level measurement at very low altitude (Prince Albert, Saskatchewan, Canada, 600 m a.s.l., 945 g/cm^2, $P_c \approx 1$ GV) had

Table 2.22: Differential Intensity of Electrons at 945 $g\,cm^{-2}$. (Golden et al., 1995).

Deflection Interval	Median Energy	Observed Number of Electrons		Intensity $[m^{-2}\ s^{-1}\ sr^{-1}\ (GV/c)^{-1}$		$e^+/(e^+ + e^-)$
[c/GV]	[GeV]	Negative	Positive	Negative	Positive	(Percent Error)
0.5 - 1.0	1.393	20	20	0.0494± 22%	0.0505± 22%	0.504± 16%
1.0 - 1.5	0.927	25	29	0.201± 20%	0.251± 19%	0.552± 15%
1.5 - 2.0	0.658	30	28	0.535± 18%	0.573± 19%	0.518± 13%
2.0 - 2.4	0.521	48	32	1.445± 14%	1.108± 18%	0.430± 9%
2.4 - 3.0	0.426	57	47	1.920± 13%	1.783± 15%	0.484± 9%
3.0 - 3.6	0.347	52	38	2.984± 14%	2.487± 17%	0.456± 9%
3.6 - 4.8	0.274	79	63	4.588± 12%	4.132± 13%	0.476± 8%
4.8 - 6.0	0.212	48	38	6.559± 15%	5.767± 17%	0.471± 12%
6.0 - 7.2	0.175	39	27	11.15± 17%	9.016± 20%	0.454± 14%
7.2 - 9.6	0.150	37	21	15.04± 20%	10.98± 27%	0.439± 18%

been carried out by Golden et al. (1995), using the Matter Antimatter Superconducting magnet Spectrometer (MASS) (see also Basini et al., 1993). The data which contain positron and negatron intensities separately are listed in Table 2.22. The energy spectrum of positrons and negatrons combined is illustrated in Fig. 2.117 together with old data of Beuermann and Wibberenz (1968). Also shown in the same figure is a theoretical spectrum of Daniel and Stephens (1974).

Other recent electron spectra were obtained by Codino et al. (1999) with the MASS91 instrument at 5.8 $g\,cm^{-2}$ and by Boezio et al. (2000) with the CAPRICE94 instrument at 3.9 $g\,cm^{-2}$. Their results are illustrated in Figs. 2.118 and 2.119, respectively. The data of Boezio et al. (2000) are also given in Table 2.23 where both the actually measured intensities and theoretical atmospheric secondary intensities of negatrons and positrons are listed separately.

2.5.4 Albedo Component

Secondary particles produced in interactions in the atmosphere that are propagating in the upward direction are referred to as *splash albedos* (SA). That fraction of these particles that leave the top of the atmosphere and get trapped in bound orbits in the geomagnetic field are guided to the conjugate location on the Earth, i.e., to the same geomagnetic latitude on the opposite hemisphere. They can enter the atmosphere with energies that are below the corresponding geomagnetic cutoff and appear to be of extraterrestrial ori-

Table 2.23: Negatron and Positron Intensities as a Function of Energy at 3.9 g/cm^2 (CAPRICE94) (Boezio et al., 2000).

Energy	Intensities [m^{-2} s^{-1} sr^{-1} GeV^{-1}]			
	Above Payload*)		Atmospheric Secondaries	
[GeV]	e^-	e^+	e^-	e^+
0.48	23 ± 2	17 ± 2	8.1	12.3
0.61	22 ± 2	10 ± 1	4.4	6.6
0.74	18 ± 1	6.7 ± 0.8	2.6	3.79
0.87	17 ± 1	5.9 ± 0.7	1.6	2.32
1.00	15 ± 1	4.2 ± 0.6	1.0	1.50
1.13	11 ± 1	3.4 ± 0.5	$7.0 \cdot 10^{-1}$	1.03
1.26	11 ± 1	1.9 ± 0.4	$5.0 \cdot 10^{-1}$	$7.4 \cdot 10^{-1}$
1.49	9.2 ± 0.6	2.0 ± 0.2	$3.1 \cdot 10^{-1}$	$4.4 \cdot 10^{-1}$
1.81	7.9 ± 0.5	$(9.9 \pm 1.6) \cdot 10^{-1}$	$1.7 \cdot 10^{-1}$	$2.38 \cdot 10^{-1}$
2.14	6.7 ± 0.5	$(9.8 \pm 1.6) \cdot 10^{-1}$	$1.1 \cdot 10^{-1}$	$1.41 \cdot 10^{-1}$
2.47	5.3 ± 0.4	$(5.3^{+1.5}_{-1.2}) \cdot 10^{-1}$	$7 \cdot 10^{-2}$	$9.0 \cdot 10^{-2}$
2.79	3.8 ± 0.3	$(3.0^{+1.1}_{-0.9}) \cdot 10^{-1}$	$5 \cdot 10^{-2}$	$6.1 \cdot 10^{-2}$
3.12	2.4 ± 0.3	$(2.7^{+1.1}_{-0.8}) \cdot 10^{-1}$	$3 \cdot 10^{-2}$	$4.3 \cdot 10^{-2}$
3.60	2.3 ± 0.2	$(2.7^{+0.7}_{-0.6}) \cdot 10^{-1}$	$2 \cdot 10^{-2}$	$2.7 \cdot 10^{-2}$
4.26	1.3 ± 0.1	$(1.5^{+0.6}_{-0.4}) \cdot 10^{-1}$	$1 \cdot 10^{-2}$	$1.6 \cdot 10^{-2}$
4.91	$(9.8 \pm 1.2) \cdot 10^{-1}$	$(6.4^{+4.3}_{-2.9}) \cdot 10^{-2}$	$8 \cdot 10^{-3}$	$1.04 \cdot 10^{-2}$
5.86	$(5.3 \pm 0.6) \cdot 10^{-1}$	$(3.6^{+2.5}_{-1.8}) \cdot 10^{-2}$	$5 \cdot 10^{-3}$	$5.9 \cdot 10^{-3}$
7.71	$(2.2 \pm 0.2) \cdot 10^{-1}$	$(3.5^{+1.4}_{-1.1}) \cdot 10^{-2}$	$2 \cdot 10^{-3}$	$2.5 \cdot 10^{-3}$
10.89	$(7.5 \pm 1.1) \cdot 10^{-2}$	$(5.4^{+6.2}_{-4.1}) \cdot 10^{-3}$	$8 \cdot 10^{-4}$	$8.7 \cdot 10^{-4}$
15.4	$(2.2^{+0.6}_{-0.5}) \cdot 10^{-2}$	-	$3 \cdot 10^{-4}$	-
21.2	$(1.1^{+0.4}_{-0.3}) \cdot 10^{-2}$	-	$1 \cdot 10^{-4}$	-
30.9	$(2.1^{+1.4}_{-0.9}) \cdot 10^{-3}$	-	$4 \cdot 10^{-5}$	-

*) The quoted errors are a combination of statistical and systematic errors.

gin. These particles are referred to as *reentrant albedos* (*RA*). On the other hand, particles having energies larger than the corresponding cutoff rigidity will not be trapped in the geomagnetic field. Since the source of reentrant albedo is the splash albedo below the geomagnetic threshold rigidity, fluxes due to splash and reentrant albedos over a given location are likely to be of comparable magnitude.

A compilation of albedo intensity data recorded at different locations near

Table 2.24: Albedo Intensities at Altitudes Between 14 and 35 km

Energy Range	Intensity
$35 \leq E \leq 420$ MeV	910 ± 120 m^{-2}s^{-1}sr^{-1}
$60 \leq E \leq 540$ MeV	340 ± 40 m^{-2}s^{-1}sr^{-1}

Table 2.25: Albedo Intensity at Top of Atmosphere

Energy Range	Intensity
$35 \leq E \leq 420$ MeV	1050 ± 150 m^{-2}s^{-1}sr^{-1}
$60 \leq E \leq 540$ MeV	390 ± 60 m^{-2}s^{-1}sr^{-1}

the top of the atmosphere is given in Fig. 2.120 (Daniel and Stephens, 1974). The albedo flux does not show any variation down to atmospheric depths of 50 g/cm^2. The observed discrepancies might be due to the fact that it is difficult to separate albedo electrons from the primary and secondary electron components. According to Verma (1967) the differential spectrum in the energy range $10 \leq E \leq 1100$ MeV over Fort Churchill can be described by the expression

$$j(E) = (5.4 \pm 0.5) \cdot 10^2 \cdot E^{-2.29} \quad [\mathrm{m^{-2}s^{-1}sr^{-1}(MeV)^{-1}}] \,. \tag{2.16}$$

The vertical intensity of double albedo electrons has been measured in the altitude range $14 \leq h \leq 35$ km (135 - 6 g/cm^2) for two energy ranges at the geomagnetic latitudes of 46° N and 49° N (Grachev et al., 1976). The data are presented in Table 2.24.

From these data the intensities at the top of the atmosphere had been derived. They are given in Table 2.25.

2.5.5 Positrons

Most of the instruments used in early experiments were not able to separate electrons from positrons. Thus electron flux and intensity data usually represent the sum of both, electrons and positrons. However, in some experiments the sign of the charge could be identified. A compilation of early electron as well as positron data for atmospheric depths of 2 to 4, 24 and 240 g/cm^2 is presented in Fig. 2.121 (Daniel and Stephens, 1974).

Hartman and Pellerin (1976) determined the altitude dependence of negatrons and positrons separately, using a magnetic spectrometer equipped with spark chambers. The respective data for the energy intervals $40 \leq E \leq 70$ MeV and $320 \leq E \leq 500$ MeV together with theoretical curves showing the primary and secondary components are presented in Figs. 2.122 to 2.125.

The two modern experiments mentioned previously, MASS91 and CAPRICE94, and many similar detectors are spectrometer type instruments that can determine the spectra of particles of either charge sign. The positron spectra determined by MASS91 at 5.8 $\mathrm{g\,cm^{-2}}$ and that of CAPRICE94 measured at 3.9 $\mathrm{g\,cm^{-2}}$ are shown in Figs. 2.118 and 2.119, respectively, and the latter is also given in Table 2.23.

2.5.6 Charge Ratio and Related Data

The ratio of negatrons to positrons, N_{e^-}/N_{e^+}, has been determined as a function of atmospheric depth during a magnetically quiet period (Voronov et al., 1975). The results are given in Fig. 2.126 together with theoretical curves by Beuermann (1971) and Daniel and Stephens (1974).

From the low altitude measurements of Golden et al. (1995) at 600 m a.s.l., mentioned earlier, the positron to electron ratio, $e^+/(e^+ + e^-)$, shown in Fig. 2.127 was obtained and is compared with a prediction of Daniel and Stephens (1974). The same measurements yielded also the ratios of $(e^+ + e^-)/\mu$ and p/μ, illustrated in Fig. 2.128.

The total electron spectrum, $(e^+ + e^-)$, and the positron spectrum only have been calculated by Orth and Buffington (1976) for an atmospheric depth of 5 $\mathrm{g/cm^2}$. The results are shown in Fig. 2.129 together with previous calculations by other authors.

References

Basini, G., F. Bongiorno, M.T. Brunetti, A. Codino, R.L. Golden, C. Grimani, B.L. Kimbell, F. Massimo Brancaccio, M. Menichelli, M. Miozza, A. Morselli, J.F. Ormes, P. Papini, M.P. de Pascale, P. Picozza, M. Ricci, I. Salvatori, E.S. Seo, P. Spillantini, S.A. Stephens, S. Stochaj, R.E. Streitmatter, and W.R. Webber: PICRC, 3, p. 773 (1993).

Beedle, R.E.: Ph.D.thesis, Univ. of New Hampshire, Durham (1970).

Beuermann, K.P.: J. Geophys. Res., 76, p. 4291 (1971).

Beuermann, K.P. and G. Wibberenz: Can. J. Phys., 46, p. S1034 (1968).

Beuermann, K.P., C.J. Rice, E.C. Stone, and R.E. Vogt: Acta Phys. Acad. Sci. Hung., 29, Suppl. 1, p. 173 (1970).

Boezio, M., P. Carlson, T. Francke, N. Weber, M. Suffert, M. Hof, W. Menn, M. Simon, S.A. Stephens, R. Bellotti, F. Cafagna, M. Castellano, M. Circella, C. De Marzo, N. Finetti, P. Papini, S. Piccardi, P. Spillantini, M. Ricci, M. Casolino, M.P. De Pascale, A. Morselli, P. Picozza, R. Sparvoli, G. Barbiellini, U. Bravar, P. Schiavon, A. Vacchi, N. Zampa, C. Grimani, J.W. Mitchell, J.F. Ormes, R.E. Streitmatter, R.L. Golden, and S.J. Stochaj: Astrophys. J., 532, p. 653 (2000).

Codino, A., M.T. Brunetti, C. Federico, C. Grimani, M. Lanfranchi, M. Menichelli, M. Miozza, R.L. Golden, S.J. Stochaj, S.A. Stephens, J.W. Mitchell, J.F. Ormes, R.E. Streitmatter, M. Hof, C. Pfeifer, W. Menn, M. Simon, G. Basini, M. Ricci, F.M. Brancaccio, P. Papini, S. Piccardi, P. Spillantini, M.P. De Pascal, A. Morselli, and P. Picozza: J. Phys., G 23, p. 1751 (1997).

Daniel, R.R., and S.A. Stephens: Rev. Geophys. and Space Phys., 12, p. 233 (1974).

Fulks, G. and P. Meyer: J. Geophys., 40 p. 751 (1974).

Galper, A.M., B.I. Luchkov, and L.A. Prokhorova: Izv. Akad. Nauk SSSR, Ser. Fiz., 38, p. 1990 (1974).

Galper, A.M., V.M. Grachev, V.V. Dmitrenko, V.G. Kirillov - Ugryumov, L.I. Potapov, S.E. Ulin, and A.M. Shermanzon: PICRC, 4, p.1412 (1975).

Golden, R.L., S.A. Stephens, S.J. Stochaj, W.R. Webber, M.T. Brunetti, A. Codino, C. Grimani, M. Menichelli, I. Salvatori, M.P. De Pascale, A. Morselli, P. Picozza, G. Basini, F. Bongiorno, F. M. Brancaccio, M. Ricci, J.F. Ormes, R.E. Streitmatter, P. Papini: J. Geophys. Res., 100, p. 23515 (1995).

Grachev, V.M., V.V. Dmitrienko, L.I. Potapov, S.E. Ulin, and Eh.M. Shermanzon: Izv. Akad. Nauk SSSR, Ser. Fiz., 40, p. 561 (1976).

Hartman, R.C. and C.J. Pellerin: Astrophys. J., 204, p. 927 (1976).

Hovestadt, D. and P. Meyer: Acta Phys. Acad. Sci. Hung., 29, Suppl. 2, p. 525 (1970).

Hovestadt, D., P. Meyer, and P.J.Schmidt: Astrophys. Lett., 9, p. 165 (1971).

Israel, M.H.: J. Geophys. Res., 74, p. 4701 (1969).

Krieger, R.: Diplomarbeit, Kiel (1965).

Orth, C.D. and A. Buffington: Astrophys. J., 206, p. 312 (1976).

Perola, G.C. and L. Scarsi: Nuovo Cimento, 46, p. 718 (1966).
Rockstroh, J. and W.R. Webber: J. Geophys. Res., 74, p. 5041 (1969).
Scheel, J., H. Roehrs: Z. Phys., 256, p. 226 (1972).
Schmidt, P.J.: J. Geophys. Res., 77, p. 3295 (1972).
Stephens, S.A.: Acta Phys. Acad. Sci. Hung., 29, Suppl. 2, p. 727 (1970).
Verma, S.D.: J. Geophys. Res., 72, p. 915 (1967a).
Verma, S.D.: Proc. Indian Acad. Sci., 66A, p. 125 (1967b).
Voronov, S.A., B.I. Luchkov, and V.A. Fedorov: PICRC, 4, p. 1405 (1975).

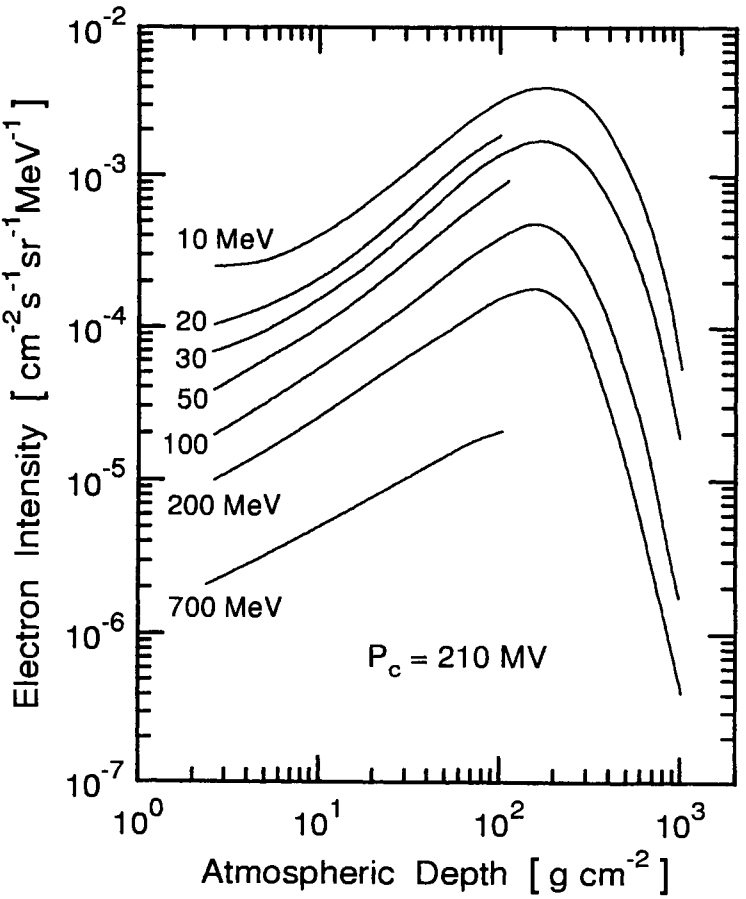

Figure 2.105: Depth - intensity relation of electrons (negatrons and positrons combined) of different energies in the atmosphere over Fort Churchill, Canada, during the period of minimum solar activity (Daniel and Stephens, 1974).

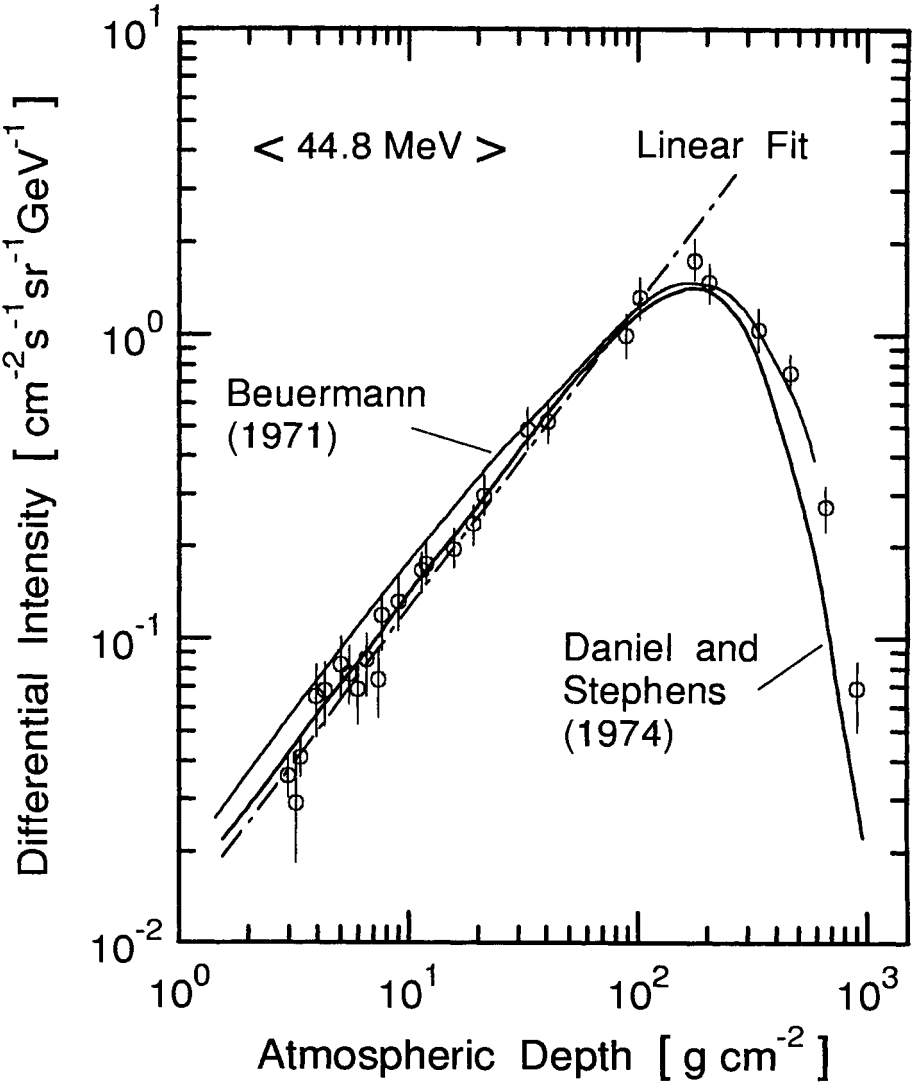

Figure 2.106: Depth- intensity relation of electrons in the atmosphere for the energy interval $35.6 \leq E \leq 54$ MeV at a cutoff rigidity of 210 MV (Fulks and Meyer, 1974). Shown, too, are predictions by Beuermann (1971) and Daniel and Stephens (1974), as well as a linear fit.

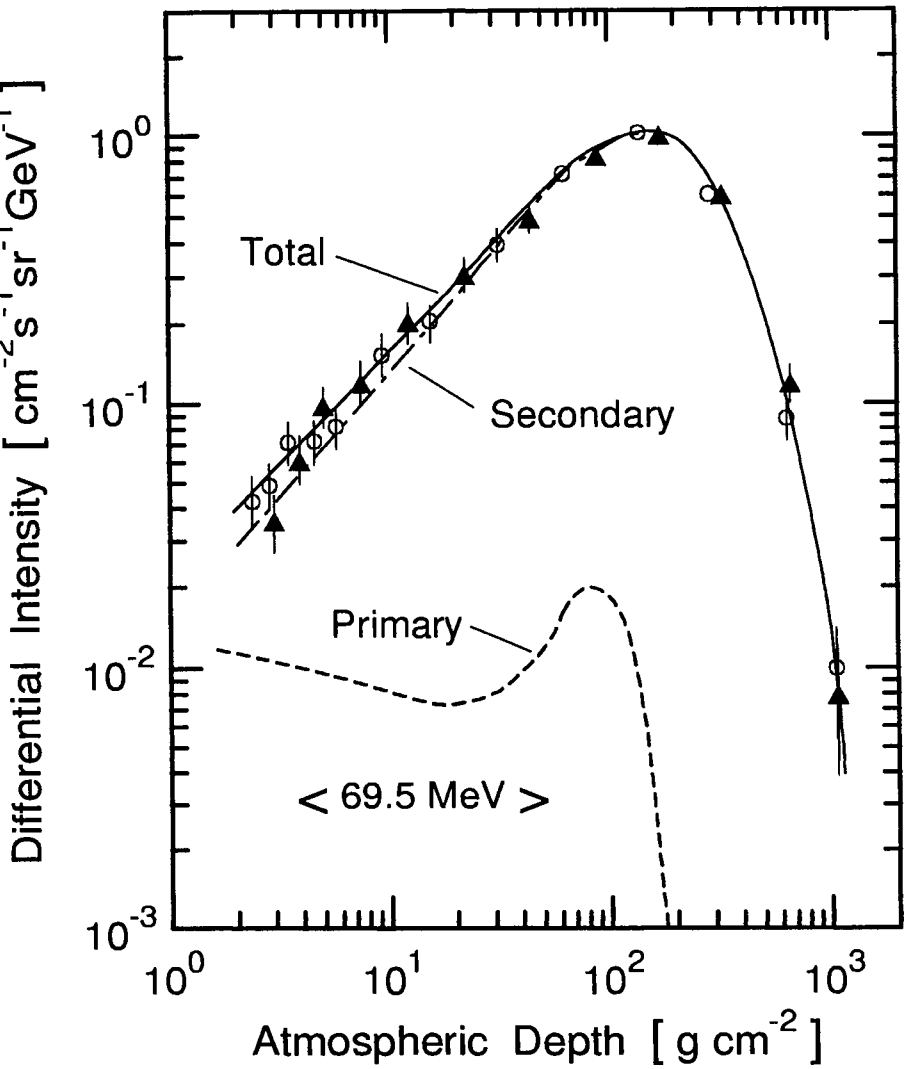

Figure 2.107: Depth - intensity relation of electrons in the atmosphere for the energy interval $54 \leq E \leq 85$ MeV at a cutoff rigidity of 210 MV, measured in 1972. Different symbols stand for different balloon ascents (Fulks and Meyer, 1974).

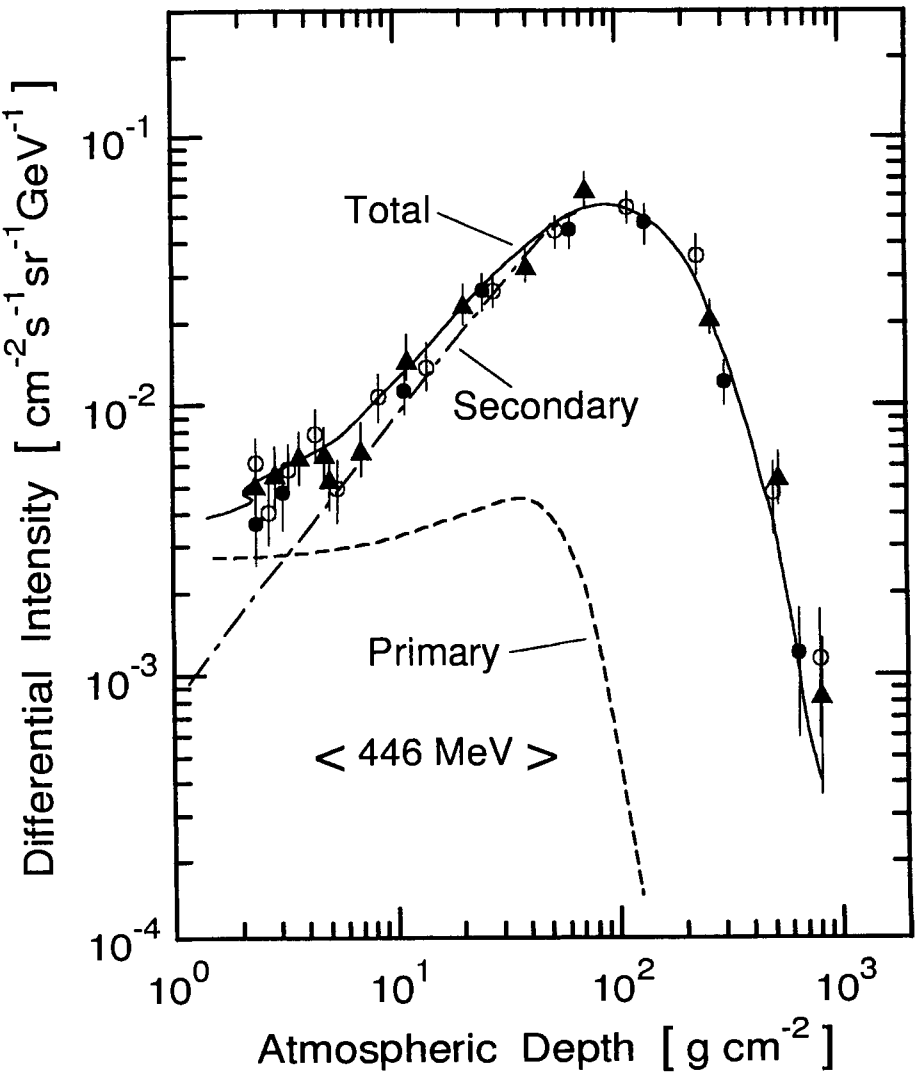

Figure 2.108: Depth - intensity relation of electrons in the atmosphere for the energy interval $340 \leq E \leq 552$ MeV at a cutoff rigidity of 210 MV, measured in 1972. Different symbols stand for different balloon ascents (Fulks and Meyer, 1974).

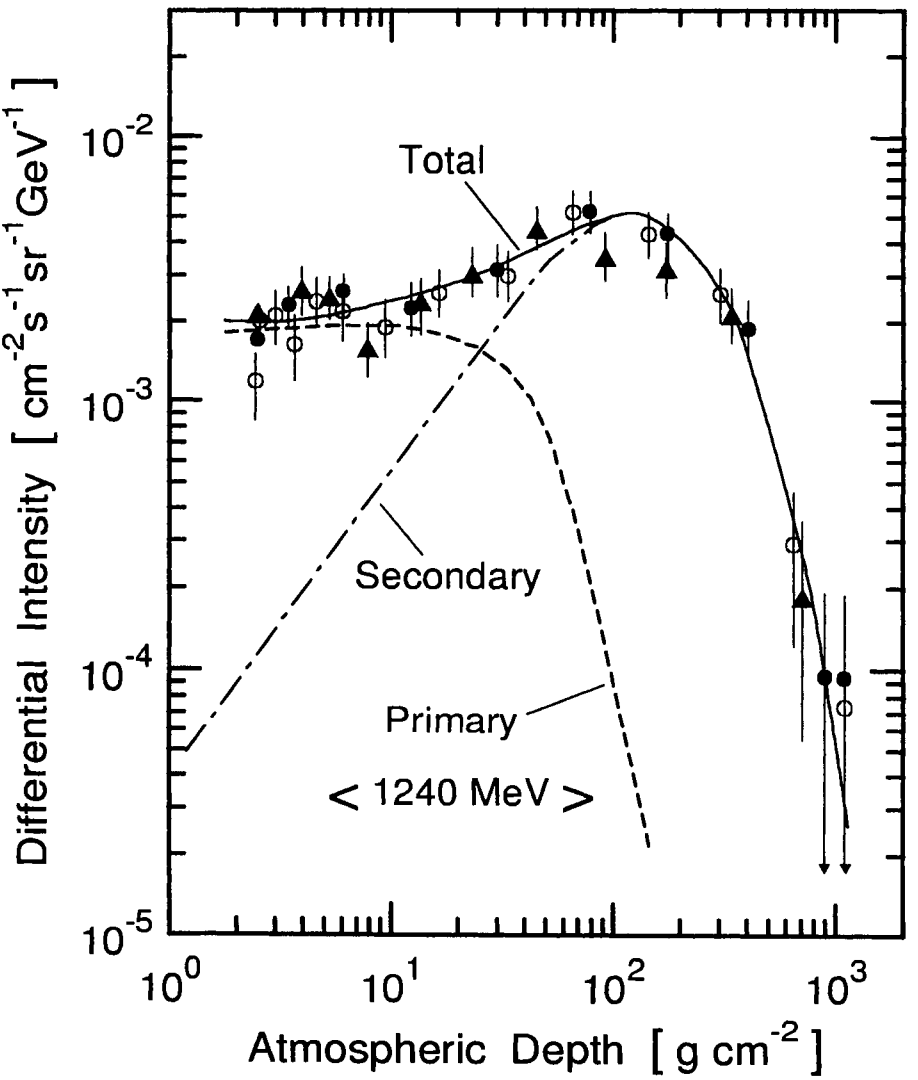

Figure 2.109: Depth - intensity relation of electrons in the atmosphere for the energy interval $910 \leq E \leq 1570$ MeV at a cutoff rigidity of 210 MV, measured in 1972. Different symbols stand for different balloon ascents (Fulks and Meyer, 1974).

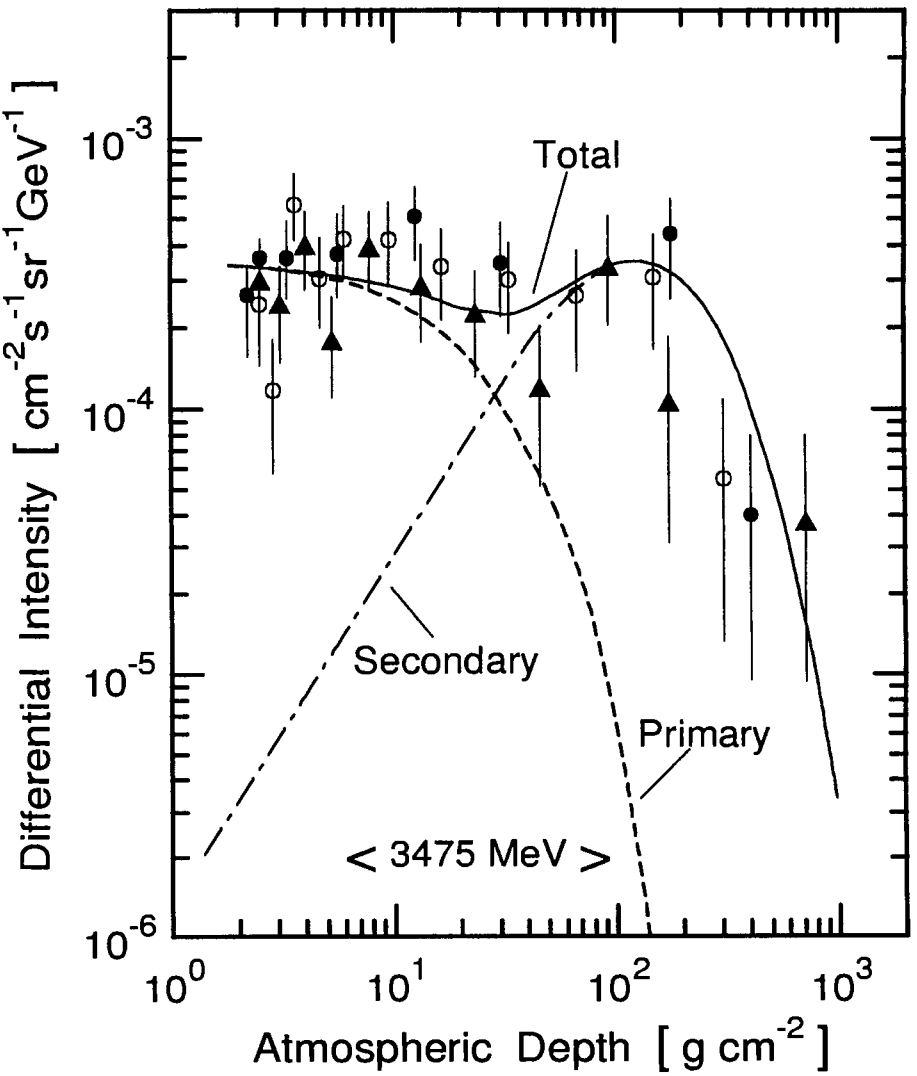

Figure 2.110: Depth - intensity relation of electrons in the atmosphere for the energy interval $2650 \leq E \leq 4370$ MeV at a cutoff rigidity of 210 MV, measured in 1972. Different symbols stand for different balloon ascents (Fulks and Meyer, 1974).

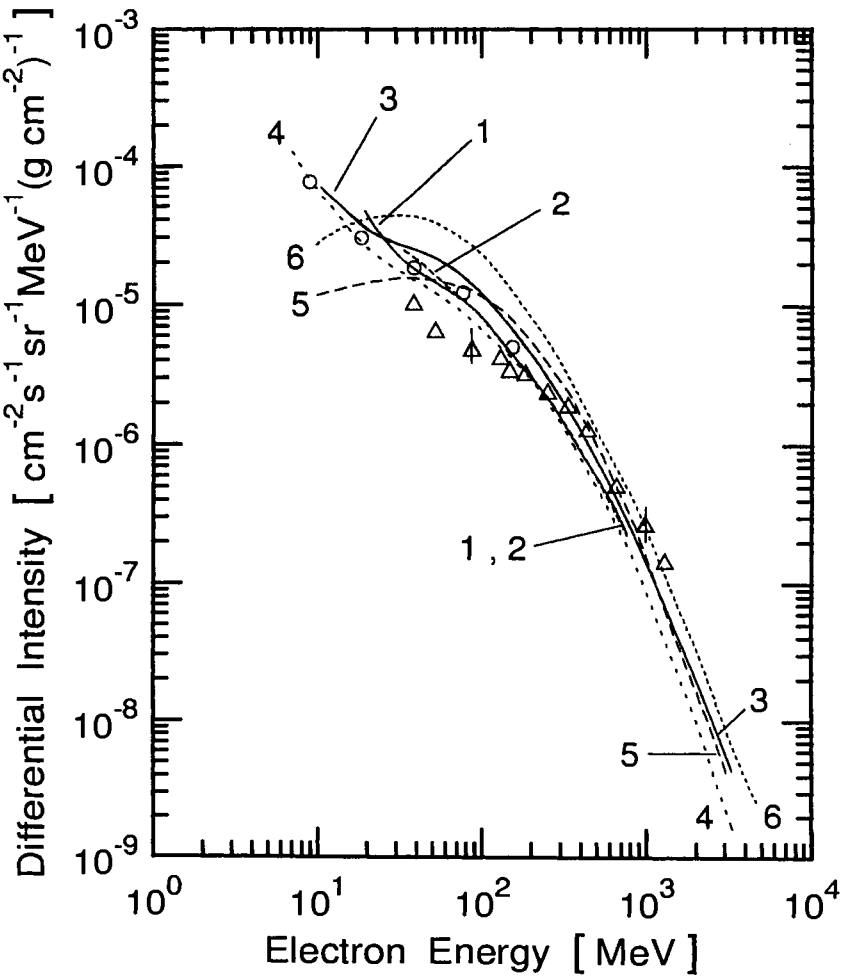

Figure 2.111: Observed and calculated differential energy spectra of vertical electrons, expressed per g/cm^2 at a depth around 2.5 g/cm^2 over Fort Churchill during the period of minimum solar activity (Daniel and Stephens 1974).

	Experimental:		Theoretical:
o	Beuermann et al. (1970)	3	Beuermann (1971)
△	Rockstroh and Webber (1969)	4	Daniel and Stephens (1974)
1	Schmidt (1972)	5	Verma (1967b)
2	Hovestadt et al. (1971)	6	Perola and Scarsi (1966)

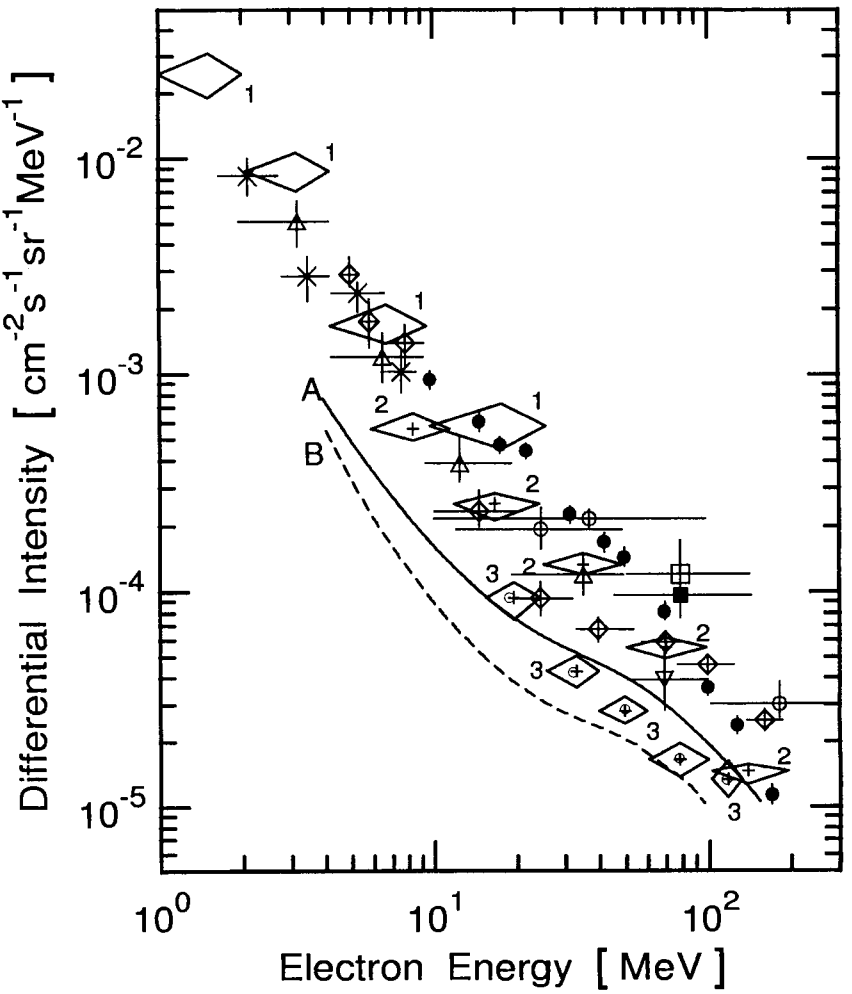

Figure 2.112: Differential spectra of low energy secondary electrons and reentrant albedos below geomagnetic cutoff at the fringes of the atmosphere. The directional distribution is within the accuracy of the measurement isotropic (Scheel and Röhrs, 1972).

1	Krieger (1968)	4.7 g/cm^2	3	Rockstroh and Webber (1969)	2.5 g/cm^2
2	Beuermann (1968)	2.3 g/cm^2	△	Scheel and Röhrs (1972)	2.4 g/cm^2
▽	Israel (1967)	5 g/cm^2	□	Schmocker and Earl (1962)	4.5 g/cm^2
◇	Beedle (1966)		■	Schmocker and Earl (1962)	6 g/cm^2
×	Brunstein (1962)	5.5 g/cm^2	•	Hovestadt and Meyer (1968)	2.3 g/cm^2
○	Verma (1965)	4 g/cm^2	A	Beuermann calculations (1971)	4 g/cm^2
			B	Beuermann calculations (1971)	2 g/cm^2

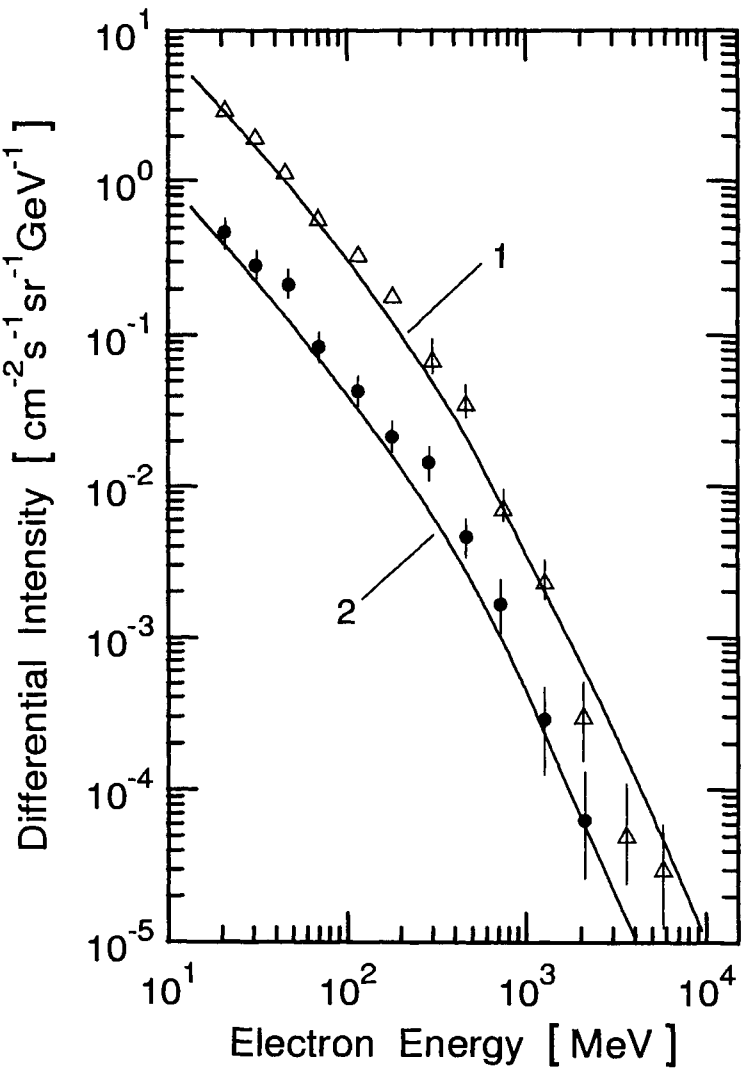

Figure 2.113: Differential energy spectra of energetic electrons at depths of 291 and 637 g/cm^2 over Fort Churchill, Canada (Fulks and Meyer, 1974).

△ Fulks and Meyer (1974), measurement at 291 g cm^{-2}
• Fulks and Meyer (1974), measurement at 637 g cm^{-2}
1 , 2 Daniel and Stephens (1974), theoretical

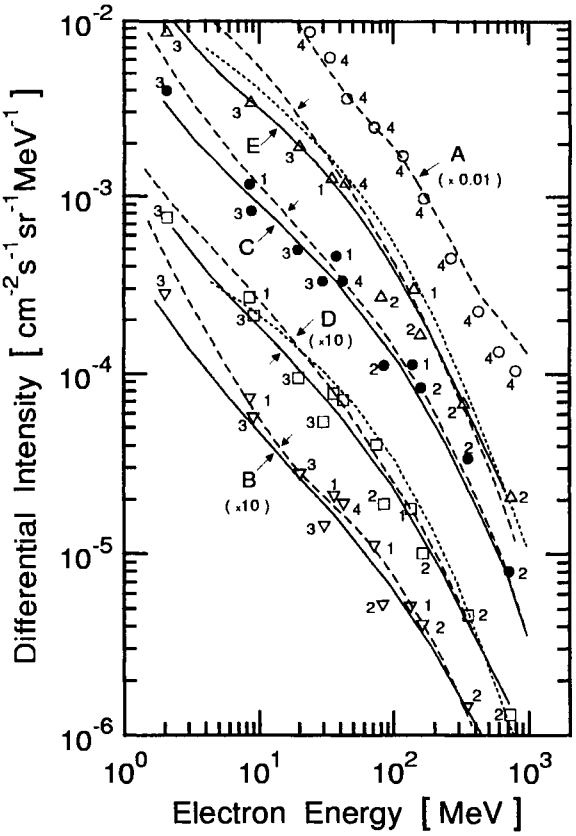

Figure 2.114: Observed and theoretical differential energy spectra of electrons at various atmospheric depths over Fort Churchill for the period of minimum solar modulation (Daniel and Stephens 1974). The symbols and letters identify the altitudes, the numbers the experiment. Note the scale factors attached to A, B and C. The ordinate readings for curve A (o) must be multiplied by 0.01 to get the true intensities, those of the curve groups B (∇) and C (•) must both be multiplied by 10.

1	Beuermann et al. (1970)	A	2.6 g/cm^2
2	Rockstroh and Webber (1969)	B	12 g/cm^2
3	Beedle (1970)	C	25 g/cm^2
4	Schmidt (1972)	D	50 g/cm^2
....	Beuermann (1971) calc.	E	100 g/cm^2
– –	Daniel and Stephens (1974), calculation		
——	best eye fit to experimental data		

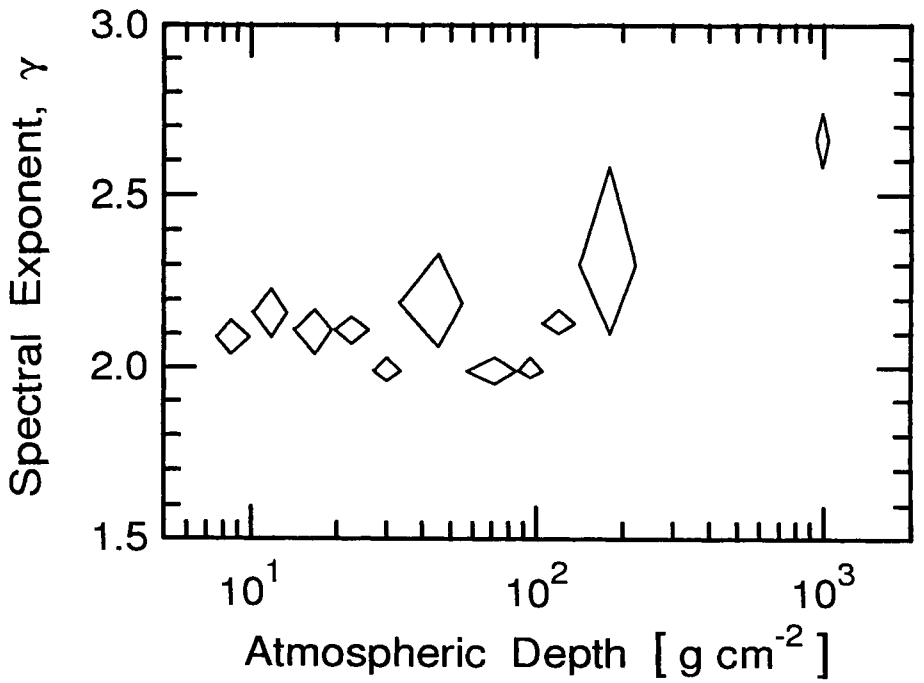

Figure 2.115: Atmospheric depth dependence of the exponent of the differential energy spectrum, $j(E) \propto E^{-\gamma}$, of electrons of energy ≥ 30 MeV (Galper et al., 1975). The contours indicate the size of the errors.

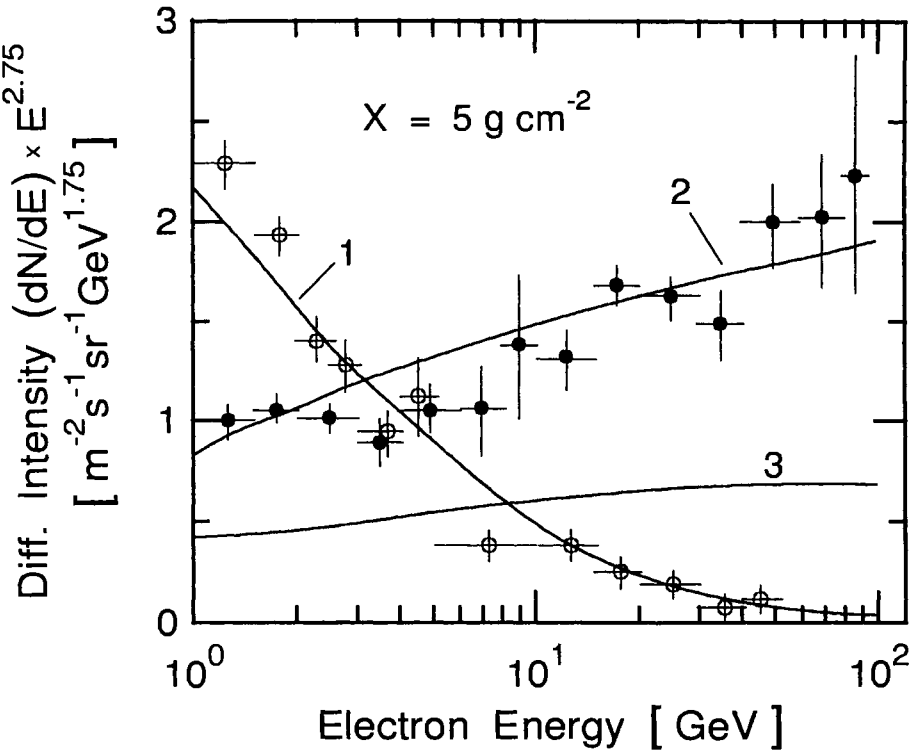

Figure 2.116: Theoretical differential energy spectra of electrons in the range $1 \leq E \leq 100$ GeV, originating from different parents and resulting from Monte Carlo and analytic calculations, as listed below (Orth and Buffington, 1976).

- ○ Monte Carlo ($e^+ + e^-$) from $\pi^\pm$
- • Monte Carlo ($e^+ + e^-$) from π°
- 1 Analytic calculations ($e^+ + e^-$) from $\pi^\pm$
- 2 Analytic calculations ($e^+ + e^-$) from π°
- 3 Analytic calculations ($e^+ + e^-$) from *Kaons*

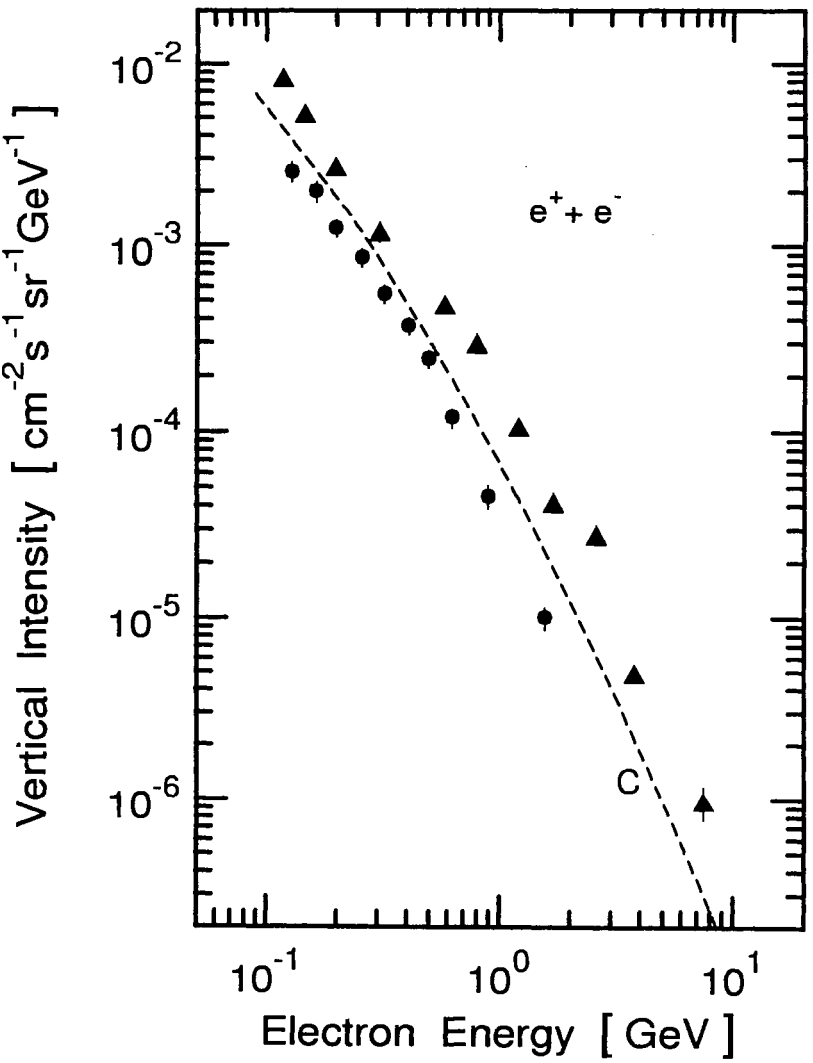

Figure 2.117: Differential energy spectrum of electrons (positrons and negatrons combined), recorded at Prince Albert, Saskatchewan, Canada (600 m a.s.l., 945 g/cm^2) (Golden et al., 1995). Also shown are old data of Beuermann and Wibberenz (1968) and a theoretical spectrum, C, of Daniel and Stephens (1974).

- • Golden et al. (1995)
- ▲ Beuermann and Wibberenz (1968)

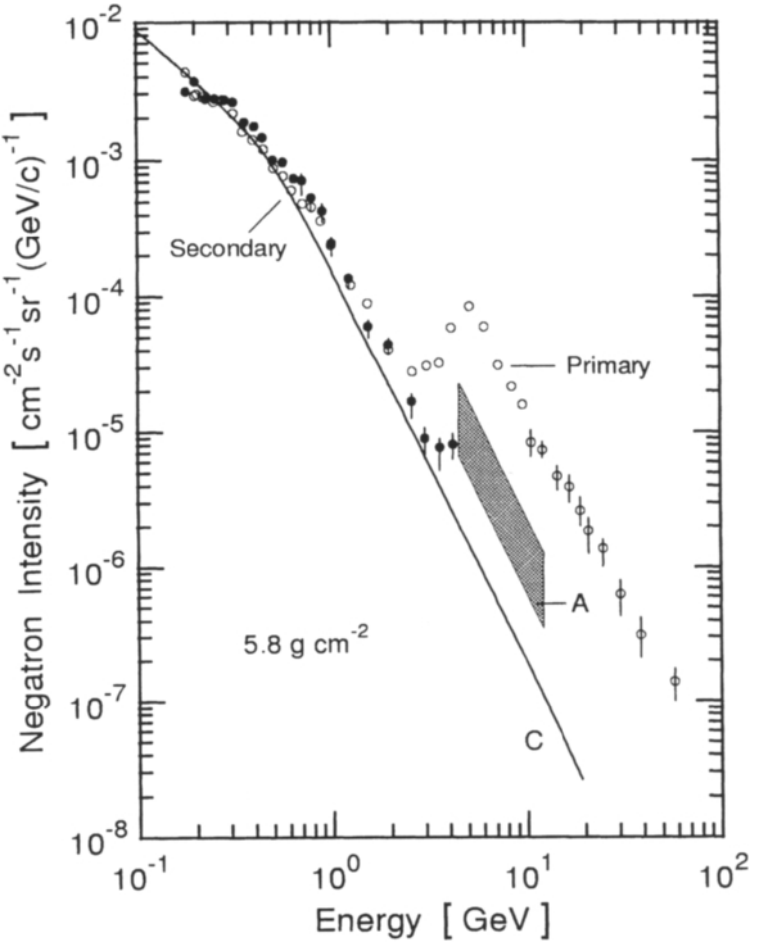

Figure 2.118: Energy spectra of negatrons and positrons in the atmosphere at a depth of 5.8 gcm^{-2} measured with the MASS91 instrument (Codino et al., 1997). The solid line, C, is a prediction of the secondary electron intensity according to Stephens (1981) and the shaded area, A, represents the domain where primary positrons can be expected (Golden et al., 1994). The predominantly primary and secondary components are indicated.

o Measured e^- at 5.8 g cm^{-2}	• Measured e^+ at 5.8 g cm^{-2}
C Calculated secondaries	A Expected primary e^+

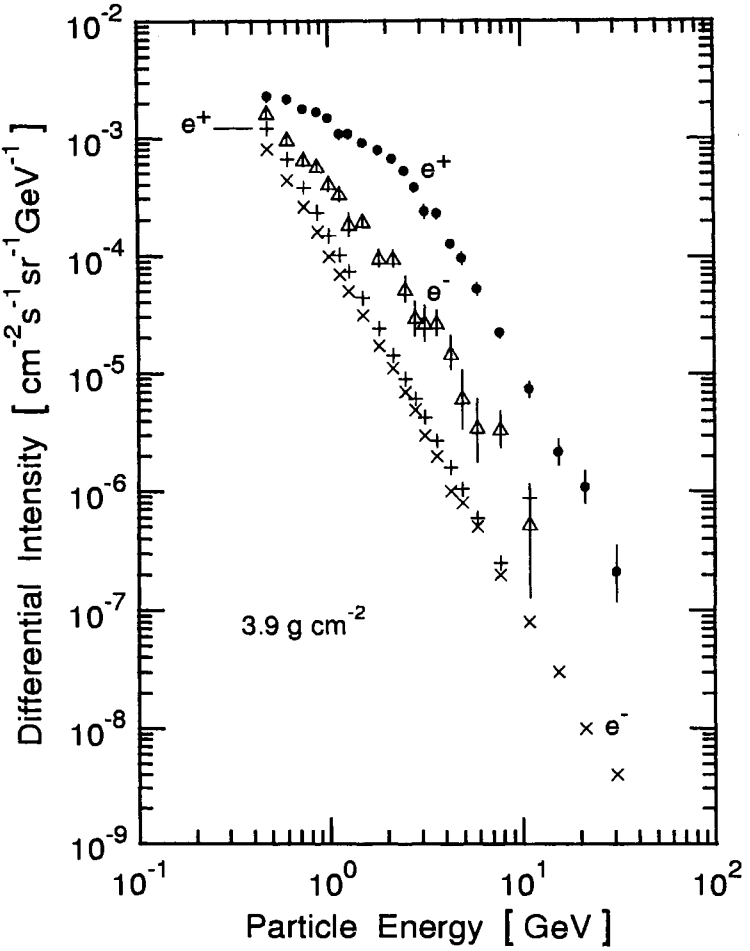

Figure 2.119: Energy spectra of negatrons and positrons in the atmosphere at a depth of 3.9 gcm^{-2} measured with the CAPRICE94 instrument (Boezio et al., 2000). Shown are the intensities measured above the payload and the calculated intensities of secondary atmospheric negatrons and positrons. The figure is a plot of the data listed in Table 2.23.

- • Measured e^+ at 3.9 gcm^{-2}
- △ Measured e^- at 3.9 gcm^{-2}
- \+ Calculated atmospheric secondary e^+
- × Calculated atmospheric secondary e^-

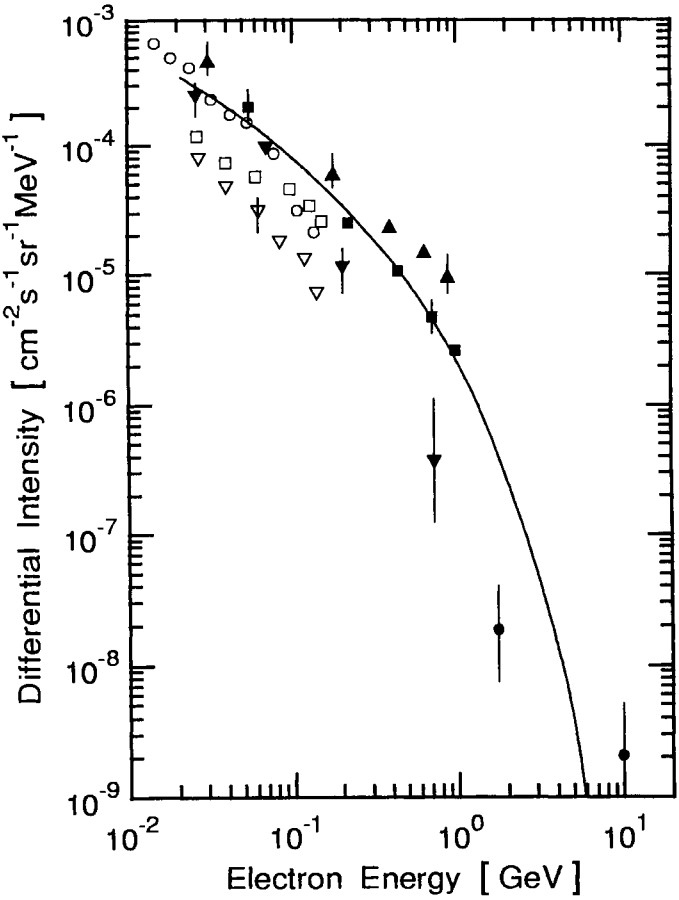

Figure 2.120: Differential energy spectra of splash albedo, SA, and reentrant albedo electrons, RA, at different latitudes near the top of the atmosphere. The solid curve is an envelope for all data (Daniel and Stephens, 1974).

	Fort Churchill:	
▼	Israel (1969)	SA in 1967
□	Rockstroh and Webber (1969)	RA in 1966
▽	Rockstroh and Webber (1969)	RA in 1968
o	Hovestadt and Meyer (1970)	RA in 1968
	Palestine, Texas:	
■	Verma (1967a)	RA in 1965
▲	Verma (1967a)	SA in 1965
	Hyderabad:	
•	Stephens (1970b)	RA in 1970

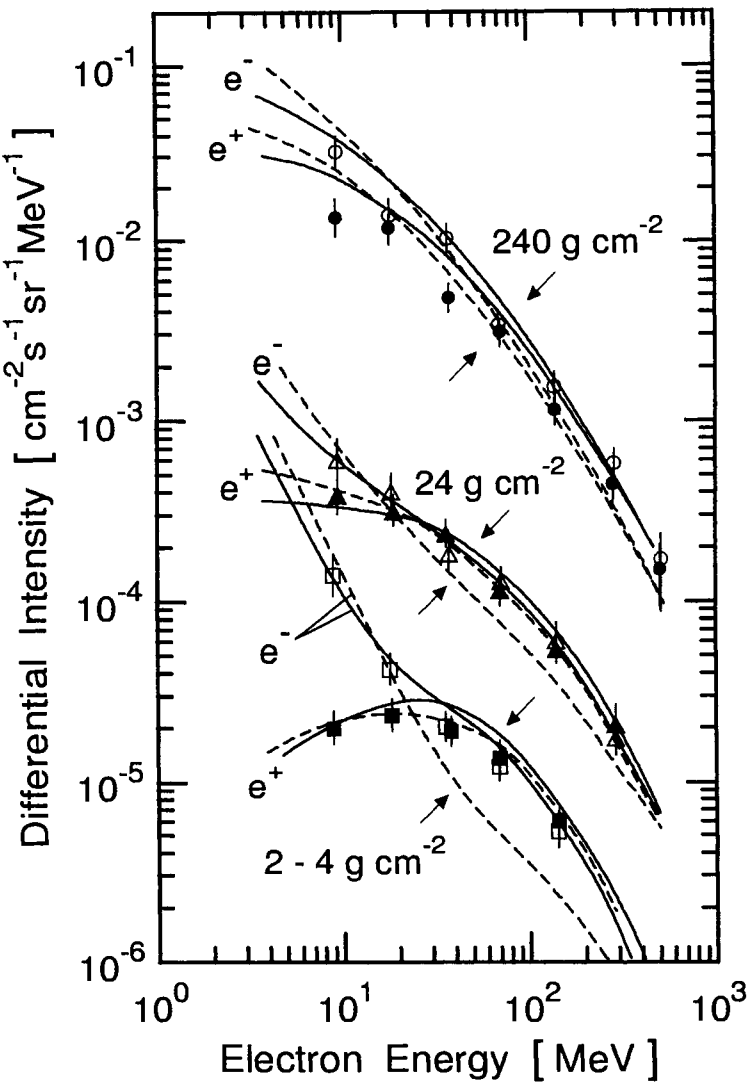

Figure 2.121: Observed (all symbols, Beuermann, 1971) and calculated (curves) differential energy spectra of secondary positrons and negatrons at various atmospheric depths over Fort Churchill, Canada (Daniel and Stephens, 1974).

□, △, ○ electrons | —— Beuermann (1971)
■, ▲, ● positrons | – – Daniel and Stephens (1974)

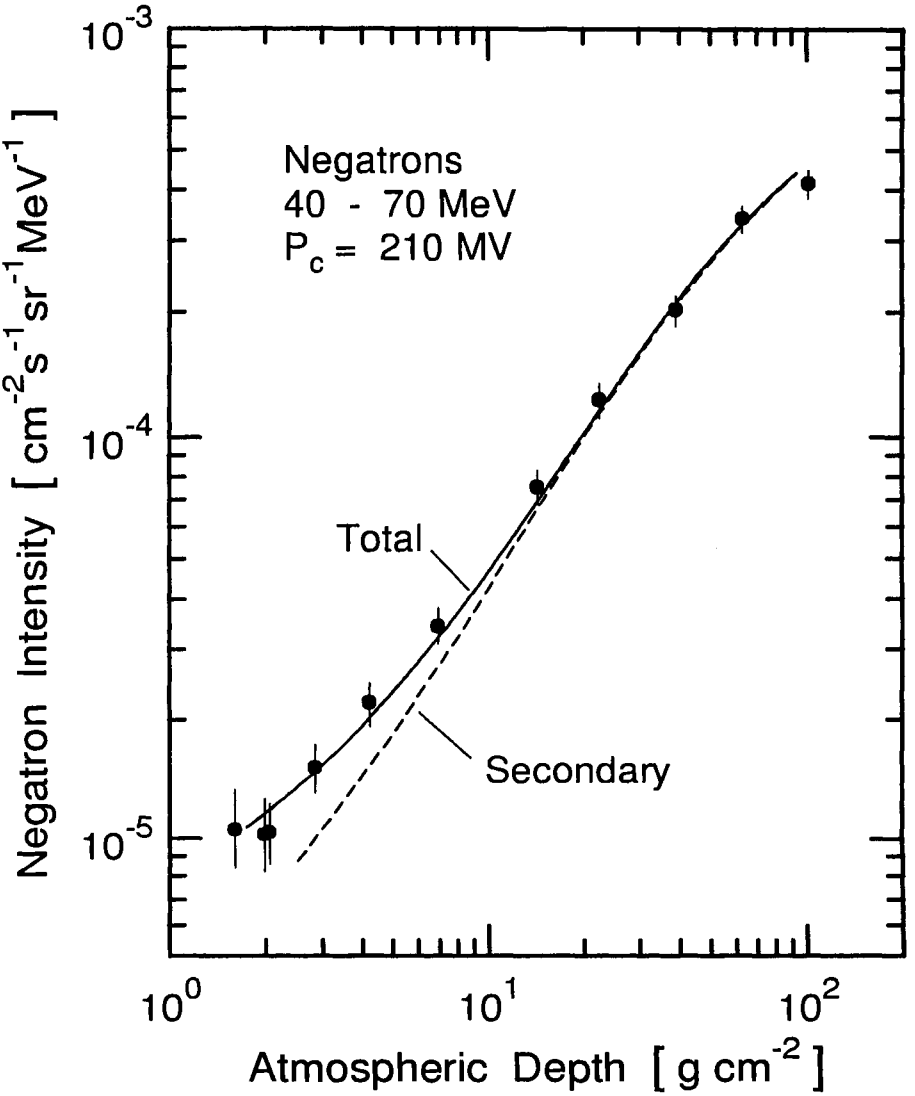

Figure 2.122: Altitude dependence of negatrons for the energy interval $40 \leq E \leq 70$ MeV at a cutoff rigidity of 210 MV, recorded in 1974. The curves are fits to the total (primary and secondary) and the computed secondary intensities (Hartman and Pellerin, 1976).

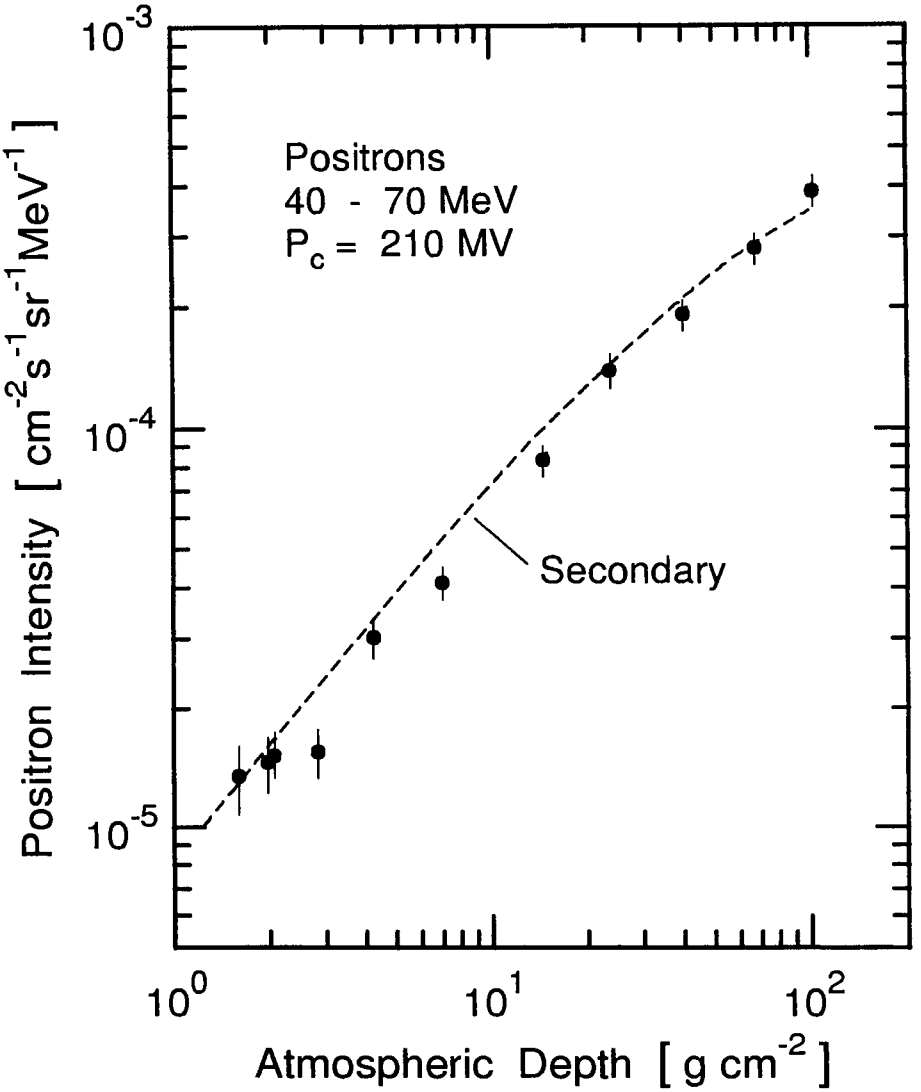

Figure 2.123: Altitude dependence of positrons for the energy interval $40 \leq E \leq 70$ MeV at a cutoff rigidity of 210 MV, recorded in 1974. The curve is a fit (Hartman and Pellerin, 1976).

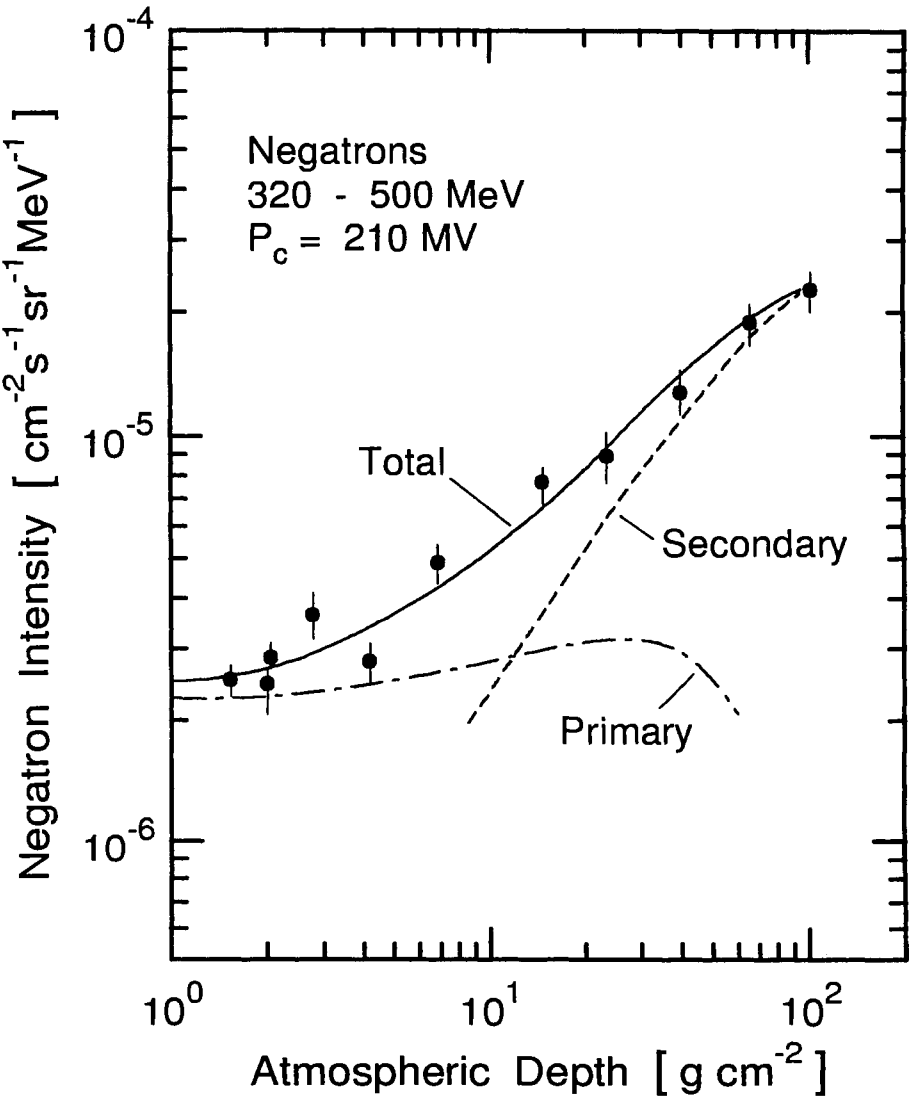

Figure 2.124: Altitude dependence of negatrons for the energy interval $320 \leq E \leq 500$ MeV at a cutoff rigidity of 210 MV, recorded in 1974. The solid curve is a fit to the total measured intensity, the dashed curves to the estimated primary and secondary intensities (Hartman and Pellerin, 1976).

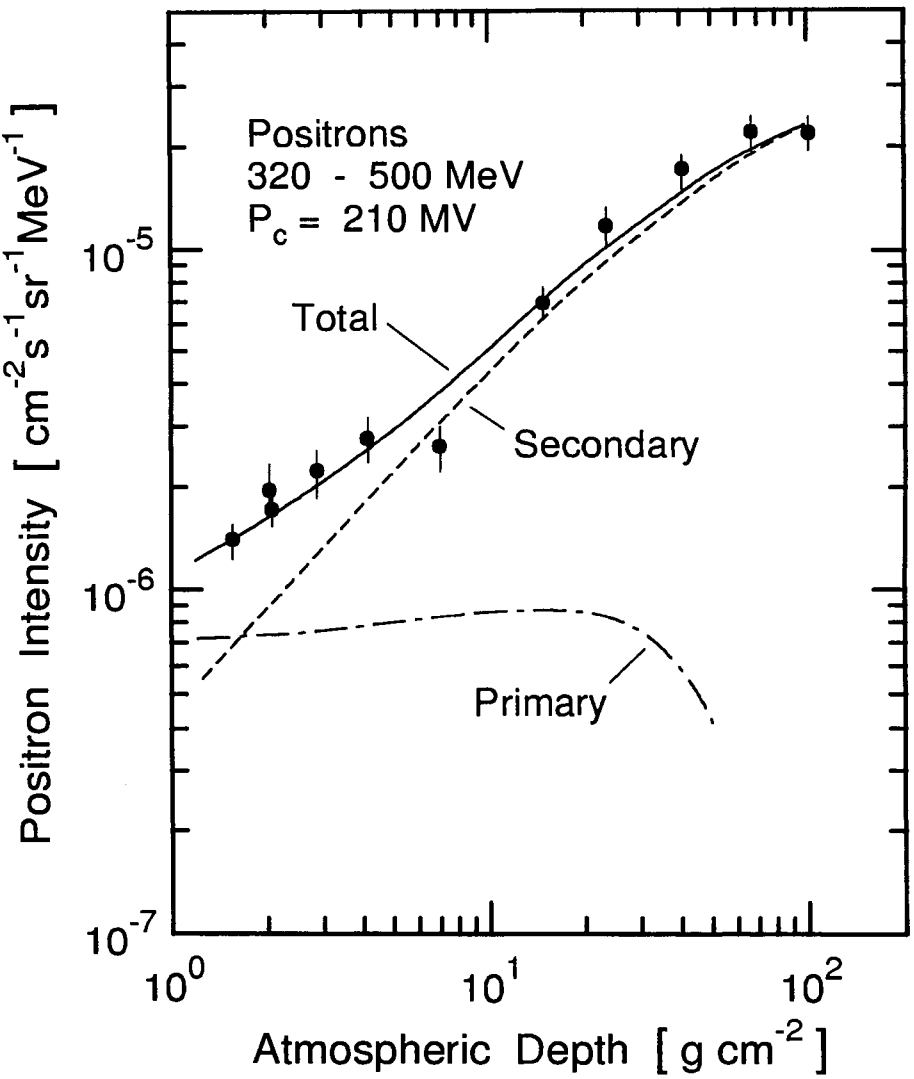

Figure 2.125: Altitude dependence of positrons for the energy interval $320 \leq E \leq 500$ MeV at a cutoff rigidity of 210 MV, recorded in 1974. The solid curve is a fit to the total measured intensity, the dashed curves to the estimated primary and secondary intensities (Hartman and Pellerin, 1976).

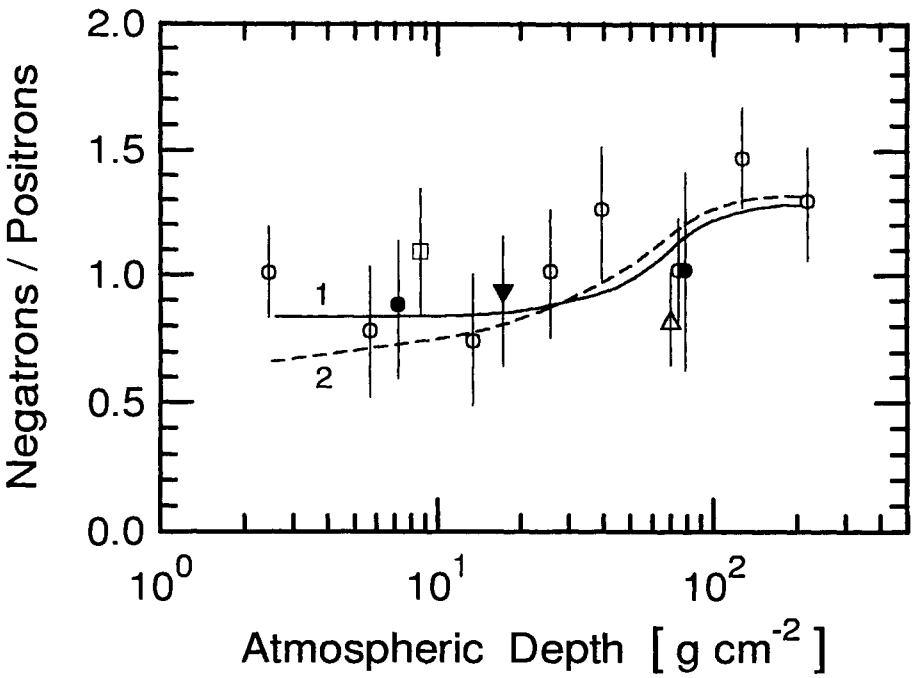

Figure 2.126: Ratio of negatrons to positrons for energies $100 \leq E \leq 1500$ MeV during magnetically quiet periods as a function of atmospheric depths (Voronov et al., 1975).

□	Voronov et al., (1975)	Oct. 12. 1972
△	Voronov et al., (1975)	Aug. 2. 1973
•	Voronov et al., (1975)	Sept. 12. 1973
▼	Voronov et al., (1975)	Sept. 21. 1973
o	Beuermann (1971)	experiment
1	Beuermann (1971)	theory
2	Daniel and Stephens (1974)	theory

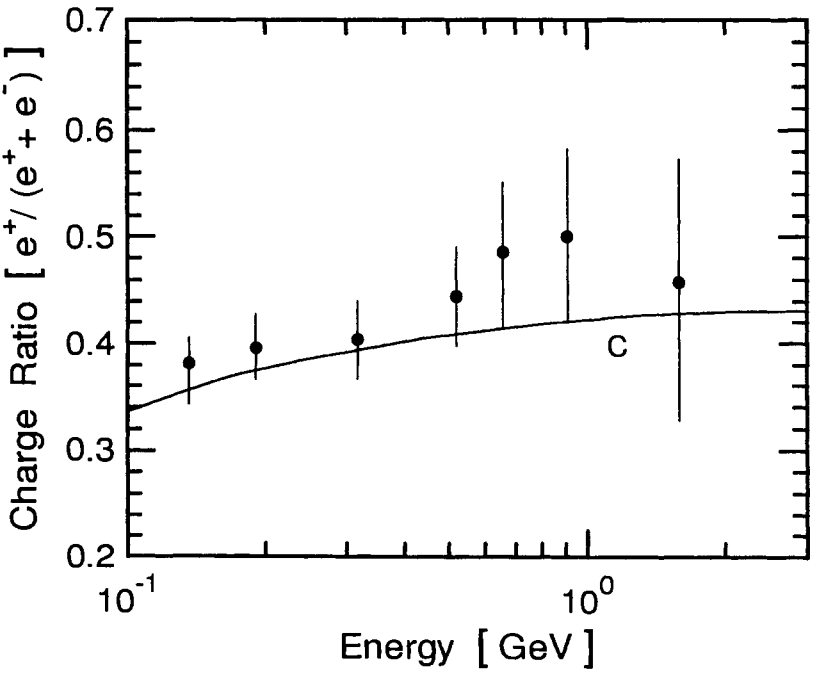

Figure 2.127: Energy dependence of the fraction of positrons measured at 600 m a.s.l. (945 g/cm^2) (Golden et al., 1995). The data are compared with a prediction of Daniel and Stephens (1974), curve C.

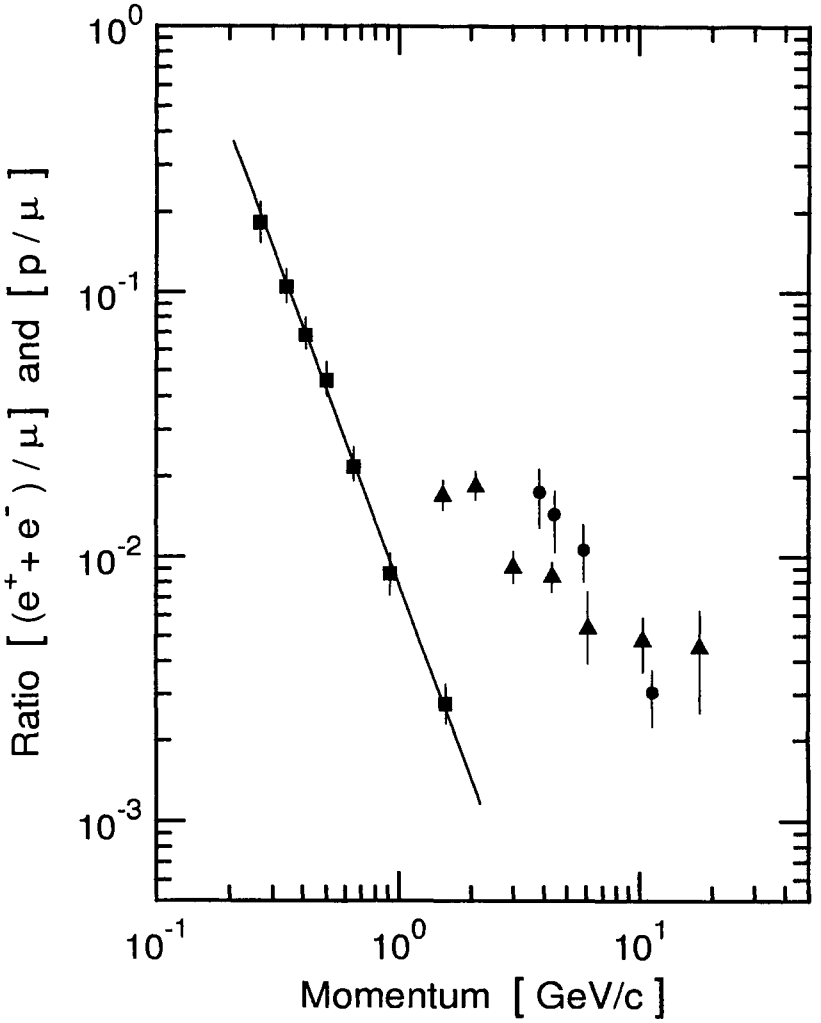

Figure 2.128: The ratio of electrons ($e^+ + e^-$) to muons ($\mu^+ + \mu^-$) and protons (p) to muons ($\mu^+ + \mu^-$) plotted as a function of momentum, measured at 600 m a.s.l. (945 g/cm^2) (Golden et al., 1995). The ratios from another experiment, also shown, are corrected for the attenuation from sea level to 945 g/cm^2.

- ■ Golden et al. (1995) $(e^+ + e^-)/(\mu^+ + \mu^-)$
- ▲ Brooke and Wolfendale (1964) $p/(\mu^+ + \mu^-)$
- • Golden et al. (1995) $p/(\mu^+ + \mu^-)$

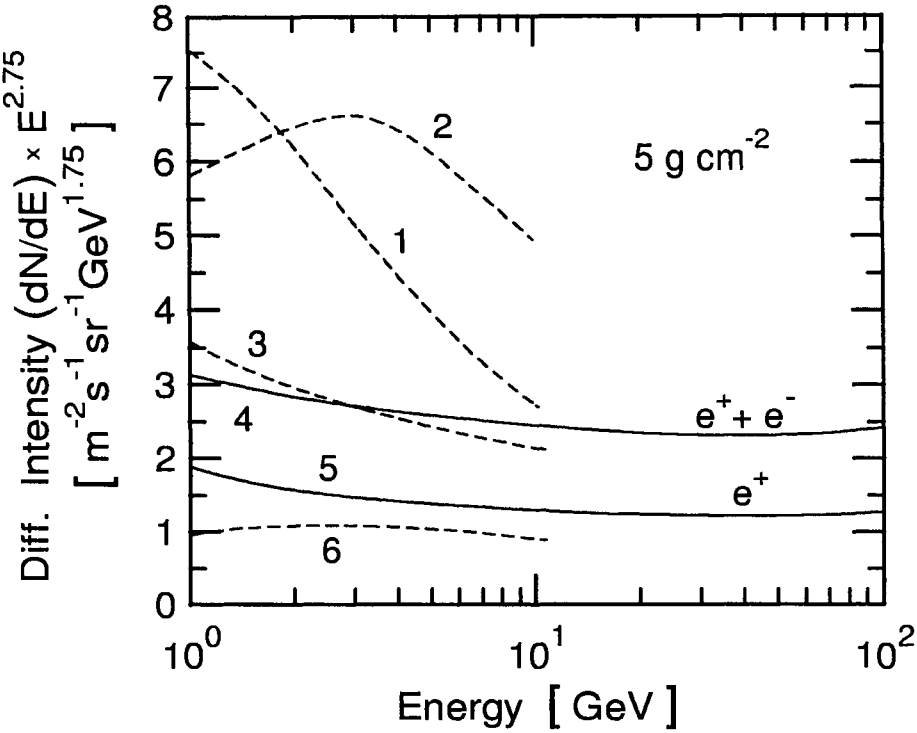

Figure 2.129: Compilation of calculated total secondary intensities of electrons and positrons combined (curves 1, 2, 3, 4 and 6) and positrons only (curve 5) in the energy range $1 \leq E \leq 100$ GeV at an atmospheric depth of 5 g/cm^2 (Orth and Buffington, 1967). Note that curve 6 had been scaled down by a factor of ten, thus the readings of intensity for curve 6 must be multiplied by 10 to get the true values.

1 Verma (1967b)
2 Beuermann (1971)
3 Daniel and Stephens (1974)
4 Orth and Buffington (1976)
5 Orth and Buffington (1976), e^+ only
6 Perola and Scarsi (1966), intensity $\times 0.1$

2.6 Muons

2.6.1 Introduction

Muons are chiefly the decay products of charged pions and to a much lesser extent of charged kaons. At very high energies, in the TeV range, a small contribution arises from the decay of charmed particles, such as D-mesons and other, massive particles. Over a long period only few measurements have been made with a first generation of instruments to determine the flux and the momentum or energy spectra of muons in the atmosphere. Most of the early experiments had been carried out with counter telescopes using absorbers and with magnetic spectrometers located at various altitudes on the ground and in aircraft. Because of the crudity of some of the instruments there is uncertainty in some cases whether interfering components, such as protons and electrons, have contaminated the measurements or could be eliminated completely.

More recently muon measurements were carried out in horizontal direction with the more refined large ground based magnetic spectrometer at Mt. Aragats, Armenia (3250 m a.s.l.) (Asatiani et al. 1983). In addition, the vertical muon intensity was explored over a wide range of atmospheric depths with a series of new complex balloon-borne instruments employing superconducting magnets. (Bellotti et al., 1996 and 1999; Carlson et al., 1999; Coutu et al., 1999; Franke et al., 1999; Golden et al., 1995; Krizmanic et al. 1999; and Schneider et al. 1995). These rather small instruments have a minimum of matter in the spectrometer and permit to make very precise measurements even at very low energies but their maximum detectable momentum is at present limited to about 100 GeV/c. The low energy capabilities are particularly important for the accurate determination of the low energy muon spectrum and charge ratio which are relevant in connection with the atmospheric neutrino anomaly. Some of these experiments were stimulated partly because of questions related to neutrino oscillations (see e.g. Perkins 1993 and 1994).

2.6.2 Altitude Dependence of Integral Intensity

Ground Based Measurements

The altitude dependence of the integral vertical muon intensity in the lower regions of the atmosphere between 650 and 950 $\mathrm{g\,cm^{-2}}$ has been investigated by Blokh et al. (1977) with a scintillation telescope, shielded by 10 cm of lead. The result of this work is plotted in Fig. 2.130. In Fig. 2.131 we show

the well known Rossi depth-intensity curve of the integral muon component in the atmosphere for energies $\geq$ 0.3 GeV (Rossi, 1948). Also indicated in this figure is a similar curve from the work of Murakami et al. (1979) for muons of energy $\geq$ 0.316 GeV.

Shen and Chiang (1979) used a magnetic spectrometer in conjunction with a counter hodoscope to determine the intensity at 3220 m. These authors found the following value for the vertical muon intensity, I_v, for energies $\geq$ 2 GeV:

$$I_v(\geq 2\ GeV) \ = \ (4.9 \pm 0.2) \cdot 10^{-3} \quad [\mathrm{cm}^{-2}\mathrm{s}^{-1}\mathrm{sr}^{-1}] \ . \tag{2.17}$$

For the angular interval from 78.4° to 90°, corresponding to a mean zenith angle of 86.2°, i.e., in almost horizontal direction, the intensity at 3220 m was found to be

$$I_h(\geq 2\ GeV) \ = \ (9.68 \pm 0.32) \cdot 10^{-5} \quad [\mathrm{cm}^{-2}\mathrm{s}^{-1}\mathrm{sr}^{-1}] \ . \tag{2.18}$$

At the same altitude, according to Jing-Gui-Ru et al. (1978), the vertical integral momentum spectrum for muons with momenta $p \geq 4$ GeV/c can be represented by the expression

$$I_v(\geq p) \ = \ C\,(p+4)^{-1.86 \pm 0.06} \quad [\mathrm{cm}^{-2}\mathrm{s}^{-1}\mathrm{sr}^{-1}] \ , \tag{2.19}$$

where C is a constant.

Balloon-Borne Measurements

Circella et al. (1993) flew an instrument called the *Matter - Antimatter Space Spectrometer (MASS)* on September 5, 1989 from Prince Albert, Saskatchewan (Canada) ($P_c \approx 1$ GV) and recorded the altitude dependence of the negative muon intensity during ascent, covering the momentum range from 0.3 - 100 GeV/c (MASS89). The data are presented in Fig. 2.132. Krizmanic et al. (1995) flew an instrument called the *Isotope Matter Antimatter eXperiment (IMAX)* July 16-17, 1992 from Lynn Lake, Manitoba (Canada) at latitude 56° N and geomagnetic cutoff $\approx$100 MeV over an altitude range from 360 m to 36 km, covering the momentum interval from 0.42 GeV/c to 0.47 GeV/c. Muon intensities recorded in this experiment are also shown in Fig. 2.132.

In another series of experiments Bellotti et al. (1999) using MASS91 from Fort Sumner, NM (U.S.A.), Krizmanic et al. (1999) using the IMAX92 instrument from Lynn Lake, and Francke et al. (1999) using an instrument called the *Cosmic AntiParticle Ring Imaging Cherenkov Experiment*

(CAPRICE) (CAPRICE94) also from Lynn Lake, recorded so-called growth curves of the muon component in the atmosphere during balloon ascents. The measurements were carried out at each level for a number of momentum intervals. Their results are shown in Figs. 2.133 to 2.136 for positive and negative muons separately. Because of background problems mostly due to protons the positive muon momentum window is rather narrow.

2.6.3 Momentum and Energy Spectra

In this subsection we discuss first early data from measurements in the atmosphere that were carried out with ground based instruments at well defined altitudes, arranged sequentially in ascending order with respect to altitude. Subsequently we present results of modern ground based measurements carried out with superconducting magnetic spectrometers. These are followed by data from air-borne spectrometer experiments (aircraft and balloon-borne) of recent date.

Ground Based Measurements

At an altitude of 2960 m (Zugspitze, Germany), Allkofer and Trümper (1964) determined the differential momentum spectrum of muons in the range $0.2 \leq p \leq 50$ GeV/c with a magnetic spectrometer. Their data are shown in Fig. 2.137 for both positive and negative muons combined in vertical direction. Similarly, Kocharian et al. (1956) determined the vertical differential momentum spectrum at the Alagez Laboratory, on Mt. Aragats (Armenia) at 3250 m up to 10 GeV/c. The results are included in Fig. 2.137 together with the integral spectrum obtained by the same authors, with the same spectrometer, that was operated to higher momenta (Kocharian at al., 1959).

Allkofer and Trümper (1964) did also determine the muon momentum spectra at a zenith angle of 37.5° in eastern and western directions at 2960 m. The spectra have not been corrected for electron and proton contaminations. The results are shown in Fig. 2.138.

Later spectral measurements in the near horizontal direction at a somewhat higher altitude (3250 m), covering the zenith angle range $80° \leq \theta \leq 90°$ with mean angle $\theta \simeq 84°$ were obtained with the large ground-based magnetic spectrometer on Mt Aragats in Armenia (Asatiani et al., 1975). The differential spectrum which covers the range $10 \leq p \leq 2000$ GeV/c at a mean zenith angle of 84° is shown in Fig. 2.139. These date are normalized at 50 GeV/c using the calculation of Ashton et al (1966).

Table 2.26: Differential Energy Spectrum of Positive and Negative Muons Combined at Mt. Aragats (3250 m), at Zenith Angle $< \theta > = 84°$ (Asatiani et al. 1983).

Kinetic Energy [GeV]	Differential Intensity $[cm^{-2} s^{-1} sr^{-1} GeV^{-1}]$
32.3	$1.30 \pm 0.03 \cdot 10^{-6}$
40.1	$1.56 \pm 0.03 \cdot 10^{-6}$
49.8	$1.13 \pm 0.03 \cdot 10^{-6}$
63.8	$6.89 \pm 0.13 \cdot 10^{-7}$
88.7	$3.53 \pm 0.08 \cdot 10^{-7}$
126.3	$1.51 \pm 0.04 \cdot 10^{-7}$
218.7	$4.03 \pm 0.11 \cdot 10^{-8}$
417.1	$7.79 \pm 0.46 \cdot 10^{-9}$
679.9	$2.08 \pm 0.19 \cdot 10^{-9}$
1016.1	$6.42 \pm 0.94 \cdot 10^{-10}$

After significantly improving the spectrometer a new series of measurements was carried out. The resulting differential intensities for positive and negative muons combined are given in Table 2.26 and the spectrum is plotted in Fig. 2.139 (Asatiani et al., 1983). The instrument's axis was oriented N 70° W and its azimuthal aperture was $\varphi = \pm 10°$. In addition, this work yielded differential muon spectra at narrow zenith angle intervals near the horizontal direction that are plotted in Fig. 2.140.

The highest ground based muon spectra were recorded by Allkofer and Kraft (1965) at Mt. Chacaltaya (Bolivia) at 5260 m a.s.l.. The measurements were made in vertical direction and covered the momentum range $0.2 \leq p \leq 50$ GeV/c. The results are shown in Fig. 2.141.

Basini et al. (1991) recorded the spectrum of positive and negative muons with the MASS instrument mentioned in Subsection 2.6.2 (Circelle et al., 1993) on August 30, 1989 at ground level (600 m a.s.l.) at Prince Albert, Saskatchewan (Canada), between 0.25 GeV/c and 100 GeV/c. The preliminary differential spectrum is displayed in Fig. 2.142 together with the final differential and integral spectra by De Pascale et al (1993). The differential and integral spectra of De Pascale et al. (1993) are also given in tabulated form in Tables 2.27 and 2.28. For comparison the differential and integral spectra of Allkofer et al. (1971a and 1971b) at sea level and the integral spec-

Table 2.27: Differential Muon Intensity at 600 m a.s.l. (920 $g\,cm^{-2}$) (De Pascale et al., 1993).

Rigidity Interval [GV]			Diff. Int. $[cm^{-2}s^{-1}sr^{-1}(GV)^{-1}]$	
Minimum	Maximum	Median	Positive Muons	Negative Muons
0.247	0.321	0.283	$1.595 \cdot 10^{-3} \pm 11.0\%$	$2.390 \cdot 10^{-3} \pm 10.0\%$
0.321	0.393	0.356	$2.064 \cdot 10^{-3} \pm 7.9\%$	$2.013 \cdot 10^{-3} \pm 8.8\%$
0.393	0.463	0.428	$1.759 \cdot 10^{-3} \pm 7.4\%$	$2.279 \cdot 10^{-3} \pm 7.1\%$
0.463	0.564	0.513	$1.788 \cdot 10^{-3} \pm 5.9\%$	$2.128 \cdot 10^{-3} \pm 5.8\%$
0.564	0.633	0.598	$1.660 \cdot 10^{-3} \pm 6.5\%$	$2.023 \cdot 10^{-3} \pm 6.3\%$
0.633	0.722	0.677	$1.673 \cdot 10^{-3} \pm 5.8\%$	$1.961 \cdot 10^{-3} \pm 5.6\%$
0.722	0.841	0.780	$1.649 \cdot 10^{-3} \pm 5.1\%$	$1.939 \cdot 10^{-3} \pm 4.8\%$
0.841	1.008	0.922	$1.365 \cdot 10^{-3} \pm 4.7\%$	$1.814 \cdot 10^{-3} \pm 4.1\%$
1.008	1.198	1.101	$1.316 \cdot 10^{-3} \pm 4.5\%$	$1.609 \cdot 10^{-3} \pm 4.0\%$
1.198	1.478	1.334	$1.094 \cdot 10^{-3} \pm 4.1\%$	$1.328 \cdot 10^{-3} \pm 3.6\%$
1.478	1.931	1.694	$8.756 \cdot 10^{-4} \pm 3.7\%$	$1.093 \cdot 10^{-3} \pm 3.2\%$
1.931	2.508	2.205	$6.789 \cdot 10^{-4} \pm 3.6\%$	$7.705 \cdot 10^{-4} \pm 3.3\%$
2.508	3.579	3.004	$4.244 \cdot 10^{-4} \pm 3.3\%$	$5.404 \cdot 10^{-4} \pm 2.9\%$
3.579	5.008	4.238	$2.634 \cdot 10^{-4} \pm 3.5\%$	$3.145 \cdot 10^{-4} \pm 3.1\%$
5.008	8.341	6.456	$1.274 \cdot 10^{-4} \pm 3.3\%$	$1.506 \cdot 10^{-4} \pm 3.1\%$
8.341	12.51	10.19	$5.025 \cdot 10^{-5} \pm 4.3\%$	$5.983 \cdot 10^{-5} \pm 3.9\%$
12.51	16.68	14.42	$2.124 \cdot 10^{-5} \pm 6.2\%$	$2.523 \cdot 10^{-5} \pm 5.7\%$
16.68	25.01	20.36	$8.653 \cdot 10^{-6} \pm 6.7\%$	$1.246 \cdot 10^{-5} \pm 5.7\%$
25.01	33.34	28.80	$3.788 \cdot 10^{-6} \pm 9.9\%$	$4.709 \cdot 10^{-6} \pm 8.8\%$
33.34	50.01	40.64	$1.389 \cdot 10^{-6} \pm 11.5\%$	$1.430 \cdot 10^{-6} \pm 11.3\%$
50.01	100.01	70.16	$2.423 \cdot 10^{-7} \pm 15.8\%$	$5.176 \cdot 10^{-7} \pm 10.7\%$

trum of Karmakar et al. (1973) at 122 m a.s.l. had been added to Fig. 2.142 as well as the theoretical differential spectrum of Stephens (1979a).

Very recently Nozaki (2000) carried out precision measurements of the muon component with the BESS97-99 instrument (*Balloon-borne Experiment with a Superconducting solenoid Spectrometer*) at ground level at Lynn Lake (Canada), located at 360 m a.s.l. ($\simeq$ 960 $g\,cm^{-2}$, $P_c \simeq 0.5$ GV) and at Tsukuba, Japan (sea level, $P_c \simeq 11.5$ GV) to study the local differences and geomagnetic effects. The Lynn Lake spectrum is illustrated in Fig. 2.143 and both spectra together in Fig. 3.71 of Chapter 3, Section 3.6.

Table 2.28: Integral Muon Intensity at 600 m a.s.l. (920 $g\,cm^{-2}$) (De Pascale et al., 1993).

Rigidity	Integral Intensity $[cm^{-2}s^{-1}sr^{-1}]$		
[GV]	Negative Muons	Positive Muons	All Muons
> 0.247	$4.307 \cdot 10^{-3} \pm 2.5\%$	$5.253 \cdot 10^{-3} \pm 2.5\%$	$9.560 \cdot 10^{-3} \pm 2.5\%$
> 0.321	$4.189 \cdot 10^{-3} \pm 2.5\%$	$5.075 \cdot 10^{-3} \pm 2.5\%$	$9.264 \cdot 10^{-3} \pm 2.5\%$
> 0.393	$4.040 \cdot 10^{-3} \pm 2.5\%$	$4.930 \cdot 10^{-3} \pm 2.5\%$	$8.970 \cdot 10^{-3} \pm 2.4\%$
> 0.463	$3.917 \cdot 10^{-3} \pm 2.4\%$	$4.771 \cdot 10^{-3} \pm 2.4\%$	$8.689 \cdot 10^{-3} \pm 2.4\%$
> 0.564	$3.737 \cdot 10^{-3} \pm 2.4\%$	$4.556 \cdot 10^{-3} \pm 2.4\%$	$8.293 \cdot 10^{-3} \pm 2.4\%$
> 0.633	$3.622 \cdot 10^{-3} \pm 2.4\%$	$4.416 \cdot 10^{-3} \pm 2.4\%$	$8.037 \cdot 10^{-3} \pm 2.3\%$
> 0.722	$3.472 \cdot 10^{-3} \pm 2.4\%$	$4.241 \cdot 10^{-3} \pm 2.3\%$	$7.713 \cdot 10^{-3} \pm 2.3\%$
> 0.841	$3.276 \cdot 10^{-3} \pm 2.4\%$	$4.010 \cdot 10^{-3} \pm 2.3\%$	$7.286 \cdot 10^{-3} \pm 2.3\%$
> 1.008	$3.048 \cdot 10^{-3} \pm 2.3\%$	$3.707 \cdot 10^{-3} \pm 2.3\%$	$6.756 \cdot 10^{-3} \pm 2.3\%$
> 1.198	$2.798 \cdot 10^{-3} \pm 2.3\%$	$3.401 \cdot 10^{-3} \pm 2.3\%$	$6.199 \cdot 10^{-3} \pm 2.2\%$
> 1.478	$2.491 \cdot 10^{-3} \pm 2.3\%$	$3.029 \cdot 10^{-3} \pm 2.3\%$	$5.520 \cdot 10^{-3} \pm 2.2\%$
> 1.931	$2.095 \cdot 10^{-3} \pm 2.3\%$	$2.534 \cdot 10^{-3} \pm 2.3\%$	$4.630 \cdot 10^{-3} \pm 2.2\%$
> 2.508	$1.703 \cdot 10^{-3} \pm 2.4\%$	$2.090 \cdot 10^{-3} \pm 2.3\%$	$3.793 \cdot 10^{-3} \pm 2.2\%$
> 3.579	$1.249 \cdot 10^{-3} \pm 2.5\%$	$1.511 \cdot 10^{-3} \pm 2,4\%$	$2.760 \cdot 10^{-3} \pm 2.3\%$
> 5.008	$8.724 \cdot 10^{-4} \pm 2.7\%$	$1.062 \cdot 10^{-3} \pm 2.6\%$	$1.934 \cdot 10^{-3} \pm 2.4\%$
> 8.341	$4.478 \cdot 10^{-4} \pm 3.3\%$	$5.596 \cdot 10^{-4} \pm 3.1\%$	$1.008 \cdot 10^{-4} \pm 2.6\%$
> 12.51	$2.384 \cdot 10^{-4} \pm 4.1\%$	$3.103 \cdot 10^{-4} \pm 3.7\%$	$5.487 \cdot 10^{-4} \pm 3.1\%$
> 16.68	$1.499 \cdot 10^{-4} \pm 4.9\%$	$2.052 \cdot 10^{-4} \pm 4.3\%$	$3.551 \cdot 10^{-4} \pm 3.5\%$
> 25.01	$7.779 \cdot 10^{-5} \pm 6.5\%$	$1.014 \cdot 10^{-4} \pm 5.7\%$	$1.792 \cdot 10^{-4} \pm 4.5\%$
> 33.34	$4.623 \cdot 10^{-5} \pm 8.3\%$	$6.214 \cdot 10^{-5} \pm 7.2\%$	$1.084 \cdot 10^{-4} \pm 5.6\%$
> 50.01	$2.308 \cdot 10^{-5} \pm 12.0\%$	$3.831 \cdot 10^{-5} \pm 9.0\%$	$6.139 \cdot 10^{-5} \pm 8.0\%$
> 100.01	$1.096 \cdot 10^{-5} \pm 17.0\%$	$1.243 \cdot 10^{-5} \pm 16.0\%$	$2.339 \cdot 10^{-5} \pm 15.0\%$

Aircraft and Balloon-Borne Measurements

At the level of 9000 m Baradzei et al. (1959) determined the vertical component of the spectrum of negatively charged particles under a lead absorber of thickness 9 cm in the range $0.3 \leq p \leq 6$ GeV/c. Fig. 2.144 shows this spectrum. The particles are mostly negative muons.

Bogomolov et al. (1979) made differential muon intensity measurements at very low energies between 0.1 GeV and 2 GeV in the altitude intervals 15.5 to 16 km (cutoff rigidity 0.4 - 0.5 GV) and 16 - 18 km (cutoff rigidity 6.9 - 7.4 GV). The data have very poor statistics and are not shown here (see Narasimham 1987).

On September 5, 1989 the MASS89 instrument was flown from Prince

Albert (Canada) to an altitude of 36 km to determine the negative muon momentum spectrum at different atmospheric depths during ascent. Results from a preliminary analysis by Circella et al. (1993) are given in Fig. 2.145 and final results for a somewhat different level selection in Fig. 2.146 (Bellotti et al., 1996).

On September 23, 1991 Basini et al. (1995) launched an improved version of the balloon borne instrument MASS (MASS91) from Ft. Sumner, NM (U.S.A.) (geomagnetic cutoff $\approx$ 4.5 GV). They explored the negative muon momentum spectrum between 0.33 GeV/c and 40 GeV/c at different atmospheric depths. The results are illustrated in Fig. 2.147 (Bellotti et al., 1999).

More recent measurements were carried out with the HEAT instrument launched August 23, 1995 from Lynn Lake at a vertical geomagnetic cutoff rigidity well below 1 GV (HEAT95) (Coutu et al., 1999). The results of this experiment are plotted in Fig. 2.148.

Accurate measurements of muon spectra at the ceiling altitudes of balloon-borne experiments at levels between 5.8 and 3.9 $\mathrm{g\,cm^{-2}}$ were made with MASS89 (Grimani et al., 1993; Brunetti et al., 1996), MASS91 (Codino et al., 1997; Bellotti et al., 1999), and CAPRICE94 (Francke et al., 1999). The two latter experiments offer spectra of positive and negative muons. The spectra are shown in Fig. 2.149. In addition, the spectrum obtained with MASS89 at 5 $\mathrm{g\,cm^{-2}}$ is also given in Table 2.29.

2.6.4 Charge Ratio

Momentum Dependence of Charge Ratio

Due to the fact that the primary cosmic radiation is essentially positively charged, the secondary component in the atmosphere has a positive charge excess, too. The secondary muon charge ratio, $K_\mu = N_{\mu^+}/N_{\mu^-}$, can be determined with relatively simple apparatuses. In many cases older data deviate significantly from each other. This is mostly because the instruments could not always clearly distinguish protons or electrons from muons in each case.

At an altitude of 2960 m (Zugspitze, Germany), Allkofer and Trümper (1964) have measured the charge ratio of muons in the momentum range $0.1 \leq p \leq 20$ GeV/c. At a somewhat higher altitude, at 3250 m (Alagez Laboratory, Mt. Aragats, Armenia), Alikhanian and Vaisenberg (1957) and Vaisenberg (1957) determined the charge ratio with their spectrometer in the momentum range $0.1 \leq p \leq 2.5$ GeV/c. These measurements were extended

Table 2.29: Differential Energy Spectrum of Negative Muons at 5 $g\,cm^{-2}$. (MASS89) (Brunetti et al., 1996)

Kinetic Energy [GeV]	Differential Intensity $[cm^{-2}\,s^{-1}\,sr^{-1}\,GeV^{-1}]$
0.316 - 0.631	$(1.492 \pm 0.130) \cdot 10^{-3}$
0.631 - 1.00	$(9.21 \pm 0.82) \cdot 10^{-4}$
1.00 - 1.26	$(5.72 \pm 0.72) \cdot 10^{-4}$
1.26 - 1.58	$(4.16 \pm 0.54) \cdot 10^{-4}$
1.58 - 2.00	$(2.46 \pm 0.36) \cdot 10^{-4}$
2.00 - 3.00	$(1.47 \pm 0.14) \cdot 10^{-4}$
3.00 - 4.00	$(5.8 \pm 0.9) \cdot 10^{-5}$
4.00 - 6.00	$(2.9 \pm 0.4) \cdot 10^{-5}$
6.00 - 9.00	$(1.3 \pm 0.2) \cdot 10^{-5}$
9.00 - 15.0	$(3.1 \pm 1.0) \cdot 10^{-6}$

by Kocharian et al. (1959) to about 15 GeV/c. The three sets of data are presented in Fig. 2.150. A similar experiment was carried out by Allkofer and Kraft (1965) at 5260 m a.s.l. (Mt. Chacaltaya in Bolivia). The proton component was not completely eliminated in this experiment, thus the hump in the charge ratio could be due to proton contamination. This set of data is also included in Fig. 2.150.

In later efforts muon charge ratio measurements were carried out by Asatiani et al. (1975 and 1983) with the magnetic spectrometer on Mt Aragats (3250 m) between about 10 GeV/c and 4 TeV/c over the zenith angle range $80° \leq \theta \leq 90°$. The data are shown in Fig. 2.151. We have also added the data of Ashley et al. (1975a, 1975b) from the Utah underground detector, located at an altitude of approximately 1500 m a.s.l., $\simeq$1400 $hg\,cm^{-2}$ underground, that cover the momentum range from about 1 TeV/c to 8 TeV/c and zenith angles between 40° and 90° to this figure. The mean zenith angle of the latter data increases with muon energy as indicated in the figure caption.

Basini et al. (1991) made similar measurements in the vertical direction with the superconducting magnetic spectrometer MASS89, mentioned above, on August 30, 1989 on the ground at 600 m a.s.l. (920 $g\,cm^{-2}$) at Prince Albert (Canada) over the momentum interval from 0.25 GeV/c to 100 GeV/c. The preliminary data of these authors together with the final results of this experiment (De Pascale et al., 1993) are also given in Fig. 2.151. Also

included in this figure is the theoretical charge ratio obtained by Stephens (1979b) for the muon momentum range from 1 GeV/c to 100 GeV/c. In addition the data of De Pascale et al. (1993) are listed in Table 2.30.

Table 2.30: Muon Charge Ratio at 600 m a.s.l. (920 $g\,cm^{-2}$) (De Pascale et al., 1993).

Rigidity Interval, [GV]			Charge Ratio
Minimum	Maximum	Median	
0.247	0.393	0.320	1.207 ± 0.130
0.393	0.564	0.479	1.233 ± 0.088
0.564	0.722	0.643	1.192 ± 0.081
0.722	1.008	0.865	1.258 ± 0.068
1.008	1.478	1.228	1.218 ± 0.057
1.478	2.508	1.948	1.192 ± 0.049
2.508	5.008	3.568	1.237 ± 0.046
5.008	12.51	8.008	1.185 ± 0.047
12.51	33.34	19.89	1.292 ± 0.075
33.34	100.01	55.87	1.409 ± 0.173

Another set of data from modern ground based measurements of the momentum dependence of the muon charge ratio acquired at altitudes between 360 m and 1270 m a.s.l. is illustrated in Fig. 2.152. We have added the data points from an older near sea level experiment for comparison.

Results from similar measurements near the top of the atmosphere between 5.8 and 3.9 $g\,cm^{-2}$ are summarized in Fig. 2.153.

Altitude Dependence of Charge Ratio

In Table 2.31 we have summarized muon charge ratios obtained from early experiments carried out at different altitudes on the ground and on board of aircraft.

Basini et al. (1995) have also determined the muon charge ratio for three momentum windows between 0.33 GeV/c and 1.5 GeV/c at different atmospheric depths with the MASS2 (MASS91) instrument during the previously mentioned launch from Ft. Sumner (Figs. 2.154 to 2.157).

Similarly, Schneider et al. (1995) used an instrument called the *High*

Table 2.31: Altitude Dependence of Charge Ratio (Allkofer, 1967).

Height [m a.s.l.]	Momentum [GeV/c]	Charge Ratio μ^+/μ^-	Reference
88	0.48	1.08 ± 0.007	Quercia (1950)
200	0.34	1.24 ± 0.15	Conversi (1950)
700	0.34	0.99 ± 0.14	Conversi (1950)
2000	0.50	1.20	Bassi (1949)
2000	1.40	1.48	Bassi (1949)
3500	0.18	0.89 ± 0.10	Correll (1947)
3500	0.48	1.13 ± 0.002	Quercia (1950)
5100	0.48	1.14 ± 0.002	Quercia (1950)
7100	0.48	1.13 ± 0.02	Quercia (1950)
9000	0.50	1.70 ± 0.4	Baradzei (1959)
10000	0.34	1.54 ± 0.24	Conversi (1950)

Energy Antimatter Telescope (HEAT) (HEAT94). It was flown on May 3, 1994 from Ft. Sumner, NM (U.S.A.), and reached 5 $g\,cm^{-2}$ in 2.5 hours. The muon charge ratio was measured in the momentum interval 0.3 to 0.9 GeV/c over an atmospheric depth range from 7 to 850 g/cm^2. The data are given in Fig. 2.158. Early data of Conversi (1950) and Quercia (1950) are also indicated in the same figure. From a subsequent experiment (HEAT95) Tarlé et al. (1997) reported the values listed in Table 2.32 for the altitude dependence of the muon charge ratio for the same momentum window.

Krizmanic et al. (1995) recorded the charge ratio during the flight of their IMAX92 instrument from Lynn Lake (Canada) over an altitude range from 360 m to 36 km. Preliminary data for a momentum interval between 0.42 GeV/c and 0.47 GeV/c are included in Fig. 2.158 and the final results are summarized in Fig. 2.159.

Other recent data on the altitude dependence of the charge ratio of muons are summarized in Fig. 2.160 where the results from measurements with HEAT95 (Coutu et al., 1997 and 1998), MASS91 (Codino et al., 1997; Bellotti et al., 1999) and CAPRICE94 (Francke et al., 1999) are given.

Table 2.32: Muon Charge Ratio as a Function of Atmospheric Depth for Rigidity Interval $0.3 \leq |R| \leq 0.9$ GV Measured with HEAT95 at Lynn Lake, Canada (360 m, 960 g/cm^2, $P_c \simeq 0.5$ GV), Aug. 23, 1995. (Tarlé et al., 1997).

Depth Range g cm^{-2}]	Mean Depth [g cm^{-2}]	Total [s]	N_{μ^+}	N_{μ^-}	Charge Ratio
3-4	3.45	4203	144	98	1.47 ± 0.19
4-7	5.24	1509	42	37	1.14 ± 0.26
7-13	9.62	1199	63	45	1.40 ± 0.27
13-32	23.2	1453	245	174	1.41 ± 0.14
32-67	48.9	1307	363	274	1.32 ± 0.11
67-140	105	1571	939	748	1.255 ± 0.062
140-250	189	1285	1310	1145	1.144 ± 0.046
250-350	299	1163	471	422	1.116 ± 0.075
350-840	500	1163	620	579	1.071 ± 0.062
840-960	957	5335	838	775	1.081 ± 0.054

2.6.5 Theoretical Contributions

Calculations of the muon component in the atmosphere have been carried out by the following authors:

Agrawal et al., (1996), Bhattacharyya (1972), Bugaev et al. (1998), Gaisser (1990), Garraffo et al. (1973), Jabs (1969), Liland (1975), Lipari (1993), Maeda (1973), Stephens (1979a and 1979b), Torsti and Terho (1973), Yekutieli (1972) (see also Chapter 3, Subsection 3.6.8 and Chapter 4).

References

Agrawal, Vivek, T.K. Gaisser, P. Lipari, and T. Stanev: Phys. Rev., D 53, p. 1314 (1996).

Alikhanian, A.I., and A.O. Vaisenberg: Soviet Phys. JETP, 5, p. 349 (1957).

Allkofer, O.C.: Z. Fortschritte der Physik, 15, p. 113 (1967).

Allkofer, O.C., and E. Kraft: Nuovo Cimento, 39, p. 1051 (1965).

Allkofer, O.C., and J. Trümper: Z. Naturforsch., 19 A, p. 1304 (1964).

Allkofer, O.C., K. Carstensen, and W.D. Dau: Phys. Lett., 36 B, p. 425 (1971a).

Allkofer, O.C., K. Carstensen, and W.D. Dau: Phys. Lett., 36B, Erratum, p. 428 (1971b).

Ambriola, M.L., G. Barbiellini, S. Bartalucci, R. Bellotti, D. Bergström, V. Bidoli, M. Boezio, U. Bravar, F. Cafagna. P. Carlson, M. Casolino, F. Ciacio, M. Circella, C.N. De Marzo, M.P. De Pascale, N. Finetti, T. Francke, S. Grinstein, M. Hof, F. Khalchukov, J. Kremer, W. Menn, J.W. Mitchell, A. Morselli, J.F. Ormes, P. Papini, S. Piccardi, P. Picozza, M. Ricci, P. Schiavon, M. Simon, R. Sparvoli, P. Spillantini, S.A. Stephens, S.J. Stochaj, R.E. Streitmatter, M. Suffert, A. Vacchi, and N. Zampa: Nucl. Phys., B (Proc. Suppl.) 85, p. 355 (2000).

Asatiani, T.L., S.V. Alchudzhyan, K.A. Gayaryan, L.I. Kozliner, V.M. Kreshcyan, G.S. Martirosyan, and S.V. Ter-Antonuan: PICRC, 6, p. 2024 (1975).

Asatiani, T.L., A.V. Abrahamian, S.V. Alchudzhyan, V.A. Ivanov, L.I. Kozliner, G.S. Martirosyan, V.A. Melkumiants, A.K. Pogossian, and S.V. Ter-Antonuan: PICRC, 7, p. 47 (1983).

Ashley, G.K., J.W. Keuffel, and M.O. Larson: PICRC, 12, p. 4282 (1975a).

Ashley, G.K., et al.: Phys. Rev. D 12, p. 20 (1975b).

Ashton, F., Y. Kamiya, P.K. MacKeown, J.L. Osborne, J.B. Pattison, P.V. Ramana Murthy, and A.W. Wolfendale: Proc. Phys. Soc. 88, p. 79 (1966).

Baradzei, L.T., M.V. Solov'ev, Z.I. Tulinova, and L.I. Filatova: Soviet Phys. JETP, 36, p. 1151 (1959).

Barrett, P.H., L.M. Bollinger, G. Cocconi, Y. Eisenberg, and K. Greisen: Rev. Mod. Phys., 24, p. 133 (1952).

Basini, G., B. Bongiorno, A. Codino, R.L. Golden, C. Grimani, B.L. Kimbell, M. Menichelli, A. Morselli, J.F. Ormes, M.P. de Pascale, P. Picozza, M. Ricci, I. Salvatori, E. Seo, P. Spillantini, S.A. Stephens, R.E. Streitmatter, S.J. Stochaj, and W.R. Webber: PICRC, 4, p. 544 (1991).

Basini, G., R. Bellotti, F. Bongiorno, M.T. Brunetti, F. Cafagna, M. Circella, A. Codino, G. De Cataldo, C.N. De Marzo, M.P. De Pascale, N. Finetti, N. Giglietto, R.L. Golden, C. Grimani, M. Hof, F. Massimo Brancaccio, M. Menichelli, J.W. Mitchell, A. Morselli, J.F. Ormes, P. Papini, S. Piccardi, P. Picozza, M. Ricci, I. Salvatori, M. Simon, P. Spillantini, P. Spinelli, S.A. Stephens, S.J. Stochaj, and R.E. Streitmatter: PICRC, 1, p. 585 (1995).

Bassi, P., E. Clementel, I. Filosofo, and G. Puppi: Nuovo Cimento, 6, p. 484 (1949).

Bellotti, R., F. Cafagna, M. Circella, G. De Cataldo, C.N. De Marzo, N. Giglietto, P. Spinelli, R.L. Golden, S.A. Stephens, S.J. Stochaj, W.R. Webber, M.P. De Pascale, A. Morselli, P. Picozza, J.F. Ormes, R.E. Streitmatter, F. Massimo Brancaccio, P. Papini, S. Piccardi, P. Spillantini, G. Basini, and F. Bongiorno, M. Ricci, M.T. Brunetti, A. Codino, C. Grimani, M. Menichelli and I. Salvatori: Phys. Rev., D 53, p. 35 (1996).

Bellotti, R., F. Cafagna, M. Circella, C.N. De Marzo, R.L. Golden, S.J. Stochaj, M.P. De Pascale, A. Morselli, P. Picozza, S.A. Stephens, M. Hof, W. Menn, M. Simon, J.W. Mitchell, J.F. Ormes, R.E. Streitmatter, N. Finetti, C. Grimani, P. Papini, S. Piccardi, P. Spillantini, G. Basini, and M. Ricci: Phys. Rev., D 60, p. 052002-1 (1999).

Bhattacharyya, D.P.: Z. Phys, 257, p. 292 (1972).

Blokh, Y.L., L.I. Dorman, and I.Y. Libin: Nuovo Cimento, 37 B, p. 198 (1977).

Bogomolov, E.A., et al.: Preprint LFTI, N. 629 (1979).

Brunetti, M.T., A. Codino, C. Grimani, M. Menichelli, M. Miozza, I. Salvatori, R.L. Golden, B.L. Kimbell, S.A. Stephens, S.J. Stochaj, W.R. Webber, F. Massimo Brancaccio, P. Papini, S. Piccardi, P. Spillantini, G. Basini, F. Bongiorno, M. Ricci, J.F. Ormes, R.E. Streitmatter, M.P. De Pascal, A. Morselli, and P. Picozza: J. Phys., G 22, p. 145 (1996).

Bugaev, E.V., A. Misaki, V.A. Naumov, T.S. Sinegovskaya, S.I. Sinegovsky, and N. Takahashi: Phys. Rev., D 58, p. 54001 (1998).

Bull, R.M., W.F. Nash, and B.C. Rastin: Nuovo Cimento, 40, p. 365 (1965).

Carlson, P., M.L. Ambriola, G. Barbiellini, S. Bartalucci, R. Bellotti, D. Bergström, V. Bidoli, M. Boezio, U. Bravar, F. Cafagna, M. Casolin, M. Castellano, E. Ciacio, M. Circella, C. DeMarzo, M.P. De Pascale, N. Finetti, T. Francke, S. Grinstein, M. Hof, F. Khalchukov, J. Kremer, W. Menn, J.W. Mitchell, A. Morselli, J.F. Ormes, P. Papini, S. Piccardi, P. Picozza, M. S.J. Stochaj, Muon Ricci, P. Schiavon, M. Simon, R. Sparvoli, P. Spillantini, S.A. Stephens, R.E. Streitmatter, M. Suffert, A. Vacchi, and N. Zampa: PICRC, 2, p. 84 (1999).

Circella, M., F. Cafagna, G. Basini, R. Bellotti, F. Bongiorno, M.T. Brunetti, A. Codino, C. De Marzo, M.P. De Pascale, R.L. Golden, C. Grimani, F. Massimo Brancaccio, M. Menichelli, J.W. Mitchell, A. Morselli, J.F. Ormes, P. Papini, P. Picozza, M. Ricci, I. Salvatori, E.S. Seo, P. Spillantini, S.J. Stochaj, R.E. Streitmatter, and W.R. Weber: PICRC, 4, p. 503 (1993).

Codino, A., M.T. Brunetti, C. Federico, C. Grimani, M. Lanfranchi, M. Menichelli, M. Miozza, R.L. Golden, S.J. Stochaj, S.A. Stephens, J.W. Mit-

chell, J.F. Ormes, R.E. Streitmatter, M. Hof, C. Pfeifer, W. Menn, M. Simon, G. Basini, M. Ricci, F.M. Brancaccio, P. Papini, S. Piccardi, P. Spillantini, M.P. De Pascal, A. Morselli, and P. Picozza: J. Phys., G 23, p. 1751 (1997).

Conversi, M.: Phys. Rev., 79, p. 749 (1950).

Correll, M.: Phys. Rev., 72, p. 1054 (1947).

Coutu, S., et al.: Proc. 29th Internat. Conf. on High Energy Physics, Vancouver (1998).

Coutu, S., S.W. Barwick, J.J. Beatty, A. Bhattacharyya, C.R. Bower, C. Chaput, G.A. deNolfo, M.A. DuVernois, A. Labrador, S. McKee, D. Müller, J.A. Musser, S.L. Nutter, E. Schneider, S.P. Swordy, G. Tarlé, A.D. Tomasch, and E. Torbet: PICRC, 2, p. 68 (1999).

De Pascale, M.P., A. Morselli, P. Picozza, R.L. Golden, C. Grimani, B.L. Kimbell, S.A. Stephens, S.J. Stochaj, W.R. Weber, G. Basini, F. Bongiorno, F.M. Brancaccio, M. Ricci, J.F. Ormes, E.S. Seo, R.E. Streitmatter, P. Papini, P. Spillantini, M.T. Brunetti, A. Codino, M. Menichelli, and I. Salvatori: J. Geophys. Res., 98 (A3), p. 3501 (1993).

Francke, T., M. Boezio, G. Barbiellini, G. Basini, R. Bellotti, U. Bravar, F. Cafagna, P. Carlson, M. Casolino, M. Castellano, M. Circella, C. De Marzo, M.P. De Pascale, N. Finetti, R.L. Golden, C. Grimani, M. Hof, W. Menn, J.W. Mitchell, A. Morselli, J.F. Ormes, P. Papini, S. Piccardi, P. Picozza, M. Ricci, P. Schiavon, M. Simon, R. Sparvoli, P. Spillantini, S.A. Stephens, S.J. Stochaj, R.E. Streitmatter, M. Suffert, A. Vacchi, N. Weber, and N. Zampa: PICRC, 2, p. 80 (1999).

Gaisser, T.K., et al.: (1995), after Francke et al. (1999).

Garraffo, Z., A. Pignotti, and G. Zgrablich: Nucl. Phys., 53, p. 419 (1973).

Golden, R.L., S.A. Stephens, S.J. Stochaj, W.R. Webber, M.T. Brunetti, A. Codino, C. Grimani, M. Menichelli, I. Salvatori, M.P. De Pascale, A. Morselli, P. Picozza, G. Basini, F. Bongiorno, F. M. Brancaccio, M. Ricci, J.F. Ormes, R.E. Streitmatter, P. Papini: J. Geophys. Res., 100, p. 23515 (1995).

Grimani, C., S.A. Stephens, G. Basini, F. Bongiorno, F. Massimo Brancaccio, M.T. Brunetti, A. Codino, R.L. Golden, B.L. Kimbell, M. Menichelli, M. Miozza, A. Morselli, J.F. Ormes, P. Papini, M.P. De Pascale, P. Picozza, M. Ricci, I. Salvatori, P. Spillantini, S.J. Stochaj, R.E. Streitmatter, and W.R. Weber: PICRC, 4, p. 507 (1993).

Jabs, A.: Z. Phys. 222, p. 1 (1969).

Jing-Gui-Ru, Huo An-Xiang, Yan Yu-Kui, Wang Li-An, Li Yan-Guo, Su

Deng-Ji, Meng Xiang-Cheng, Yao Wei-Zhong, Zhou Yin-Zao, Feng Shao-Hua, and Wnag Li-Hui: Phys. Energ. Fortis and Phys. Nucl., 2, p. 417 (1978).

Karmakar, N.L., A. Paul and N. Chaudhuri: Nuovo Cimento 17 B, p. 173 (1973).

Kocharian, N.M., M.T. Aivazian, Z.A. Kirakosian, and A.S. Aleksanian: Soviet Phys. JETP, 3, p. 350 (1956).

Kocharian, N.M., G.S. Saakian, and Z.A. Kirakosian: Soviet Phys. JETP, 8, p. 933 (1959).

Kremer, J., M. Boezio, M.L. Ambriola, G. Barbiellini, S. Bartalucci, G. Basini, R. Bellotti, D. Bergström, V. Bidoli, U. Bravar, F. Cafagna, P. Carlson, M. Casolino, M. Castellano, F. Ciacio, M. Circella, C. De Marzo, M.P. De Paseale, T. Francke, N. Finetti, R.L. Golden, C. Grimani, M. Hof, W. Menn, J.W. Mitchell, A. Morselli, J.F. Ormes, P. Papini, S. Piccardi, P. Picozza, M. Ricci, P. Schiavon, M. Simon, R. Sparvoli , P. Spillantini, S.A. Stephens, S.J. Stochaj, R.E. Streitmatter, M. Suffert, A. Vacchi, N. Weber, and N. Zampa: PICRC, 2, p. 76 (1999).

Krizmanic, J.F., A.J. Davis, L.M. Barbier, E.R. Christian, R.L. Golden, M. Hof, K.E. Krombel, A.W. Labrador, R.A. Mewaldt, J.W. Mitchell, J.F. Ormes, I.L. Rasmussen, O. Reimer, S.M. Schindler, M. Simon, S.J. Stochaj, R.E. Streitmatter, and W.R. Weber: PICRC, 1, p. 593 (1995).

Krizmanic, John F., A.J. Davis, L.M. Barbiei, E.R. Christian, R.L. Golden, M. Hof, K.E. Krombel, A.W. Labrador, R.A. Mewald, J.W. Mitchell, J.F. Onnes, I.L. Rasmussen, 0. Reimer, S.M. Schindler, M. Simon, S.J. Stochaj, R.E. Streitmatter, and W.R. Webber: PICRC, 2, p. 56 (1999).

Liland, A.: Fortschr. Phys., 23, p. 571 (1975).

Lipari, Paolo: Astropart. Phys., 1, p. 195 (1993).

Maeda, K.: Fortschr. Phys., 21, p. 113 (1973).

Murakami, K., K. Nagashima, S. Sagisaka, Y. Mishima, and A. Inoue: Nuovo Cimento, 2C, p. 635 (1979).

Narasimham, P.V.: PICRC, 8, p. 288 (1987).

Nozaki, M., et al.: PICRC, Invited and Rapporteur Papers, AIP Conf. Proc., 516, p. 330 (2000).

Perkins, D.H.: Nucl. Phys., B 399, p. 3 (1993).

Perkins, D.H.: Astropart. Phys. 2, p. 249 (1994).

Quercia, I.F., B. Rispoli, and S. Sciuti: Nuovo Cimento, 7, p. 277 (1950).

Rastin, B.C.: J. Phys., G 10, p. 1609 (1984).

Rossi, B.: Rev. Mod. Phys., 20, p. 537 (1948).

Schneider, E., S.W. Barwick, J.J. Beatty, C.R. Bower, C. Chaput, S. Coutu, G. de Nolfo, D. Ficenec, J. Knapp, D.M. Lowder, S. McKee, D. Müller, J.A. Musser, S.L. Nutter, S.P. Swordy, K.K. Tang, G. Tarlé, A.D. Tomasch, and E. Torbet: PICRC, 1, p. 690 (1995).

Shen Chang-quan and Chiang In-lin: PICRC, 10, p. 8 (1979).

Smith, J.A., and N.M. Duller: Journ. Geophys. Res., 64, p. 2297 (1959).

Stephens, S.A.: PICRC, 10, p. 90 (1979a).

Stephens, S.A.: PICRC, 10, p. 96 (1979b).

Stephens, S.A.: PICRC, 4, p. 282 (1981).

Stephens, S.A., and R.L. Golden: PICRC, 6, p. 173 (1987).

Tarlé, G., S.W. Barwick, J.J. Beatty, A. Bhattacharyya, C.R. Bower, C. Chaput, S. Coutu, G.A. de Nolfo, J. Knapp, D.M. Lowder, S. McKee, D. Müller, J.A. Musser, S.L. Nutter, E. Schneider, S.P. Swordy, A.D. Tomasch, and E. Torbet: PICRC, 6, p. 321 (1997).

Torsti, J.J. and R.W. Terho: Nuovo Cimento, 16, p. 376 (1973).

Vaisenberg, A.O.: Soviet Phys. JETP, 5, p. 352 (1957).

Vulpescu, B., J. Wentz, I.M. Brancus, H. Rebel, A.F. Badea. H. Bozdog, M. Duma, A. Haungs, H.-J. Mathes, M. Petcu, and M. Roth: Nucl. Instr. Meth., A 414, p. 205 (1998).

Yekutieli, G.: Nucl. Phys., 47, p. 621 (1972).

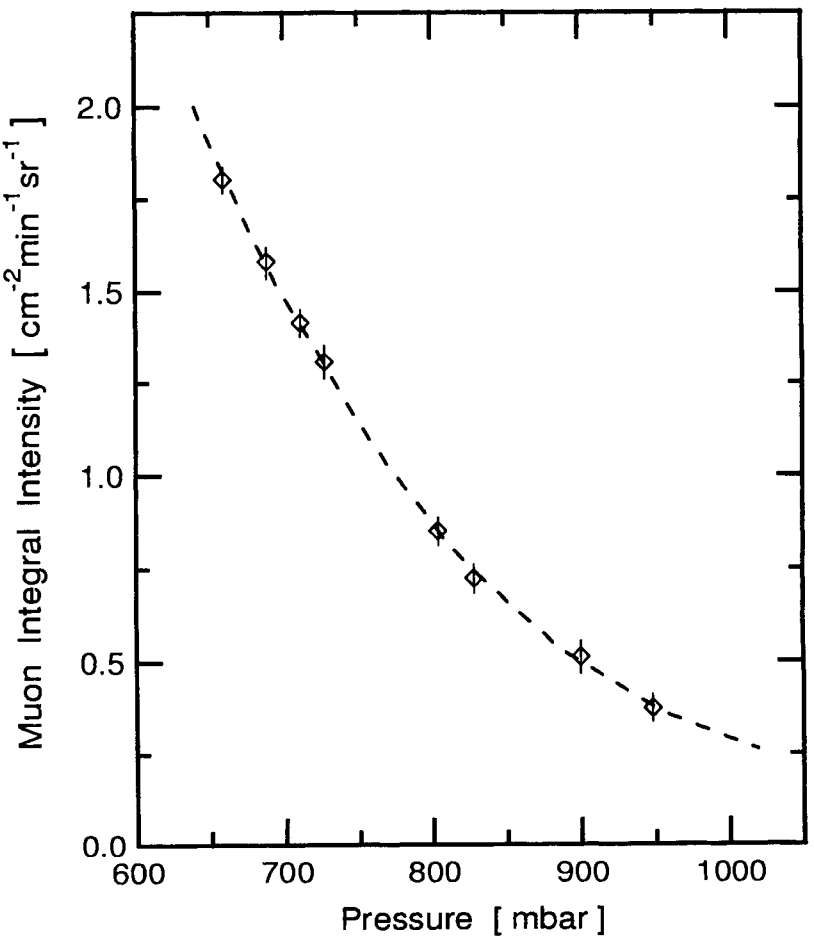

Figure 2.130: Vertical muon intensity versus atmospheric pressure. (Blokh et al., 1977). For the conversion from pressure to altitude in meters, see Chapter 1, Section 1.7 and the Appendix.

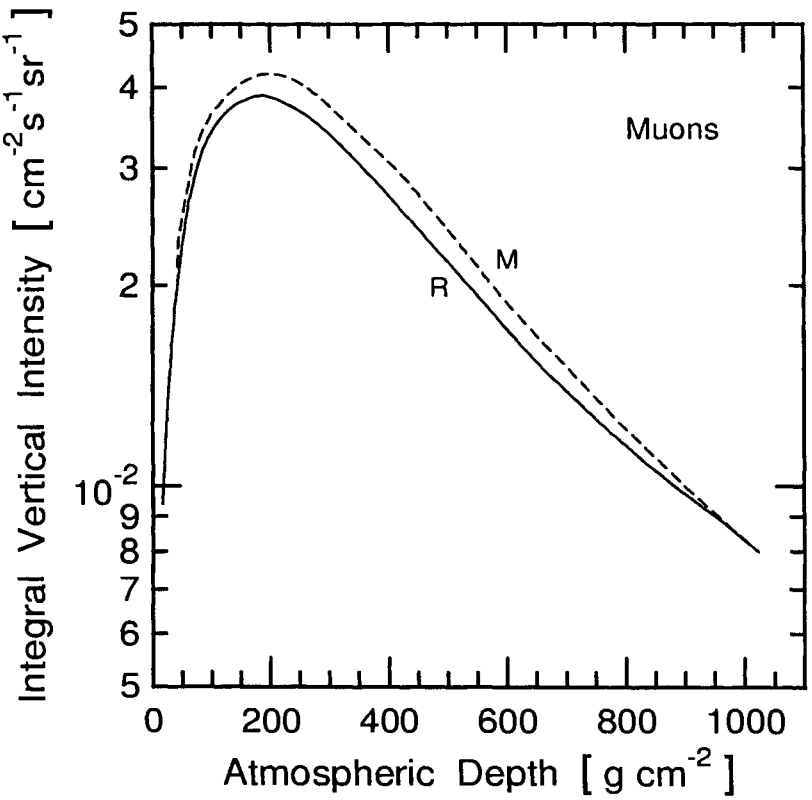

Figure 2.131: Muon integral intensity as a function of atmospheric depth for muons of energy $\geq$0.3 GeV. The solid curve R is the old Rossi curve (Rossi, 1948), the dashed curve is from a calculation of Murakami et al. (1979).

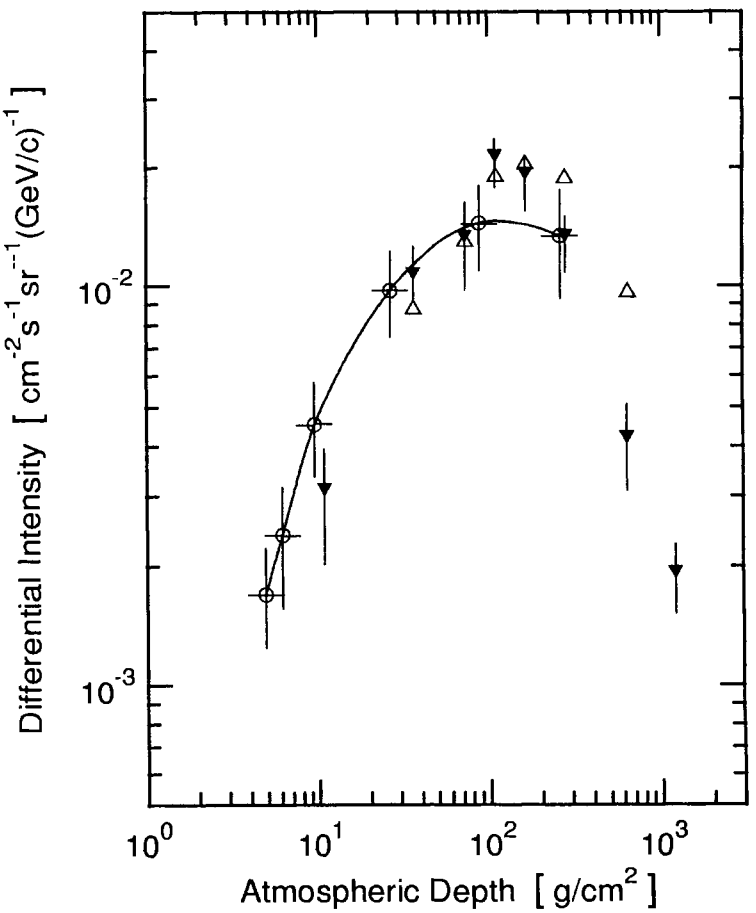

Figure 2.132: Differential intensity of negative muons in different momentum windows as a function of atmospheric depth determined with the IMAX and MASS spectrometers. The curve is a splined link connecting the data points of Krizmanic et al. (1995), drawn by the author.

- o Krizmanic et al. (1995) 0.42 - 0.47 GeV/c
- ▼ Circella et al. (1993) 0.3 - 0.4 GeV/c
- △ Circella et al. (1993) 0.3 - 100 GeV/c

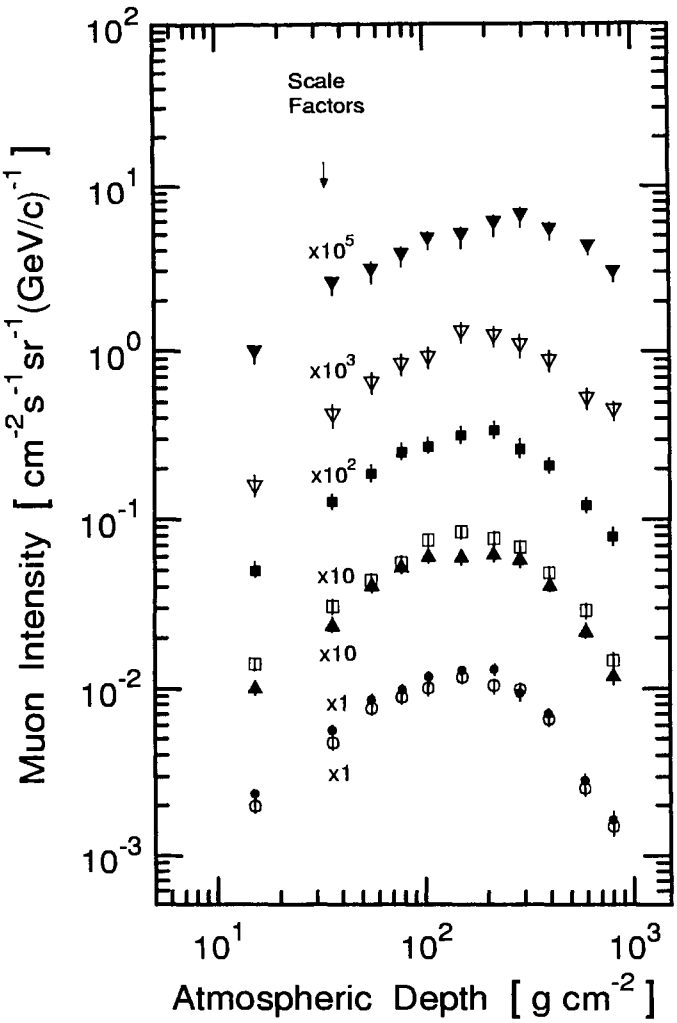

Figure 2.133: Atmospheric growth curves of positive and negative muons for different momentum intervals as listed below, recorded with the MASS91 instrument launched from Fort Sumner, NM (U.S.A.) (Bellotti et al., 1999). (Divide reading on ordinate by appropriate scale factor to get true intensity.)

▼	μ^-	$4.0 \leq p \leq 40$ GeV/c	▽	μ^-	$2.5 \leq p \leq 4.0$ GeV/c
■	μ^-	$1.5 \leq p \leq 2.5$ GeV/c	□	μ^+	$0.9 \leq p \leq 1.5$ GeV/c
▲	μ^-	$0.9 \leq p \leq 1.5$ GeV/c	•	μ^+	$0.3 \leq p \leq 0.9$ GeV/c
o	μ^-	$0.3 \leq p \leq 0.9$ GeV/c			

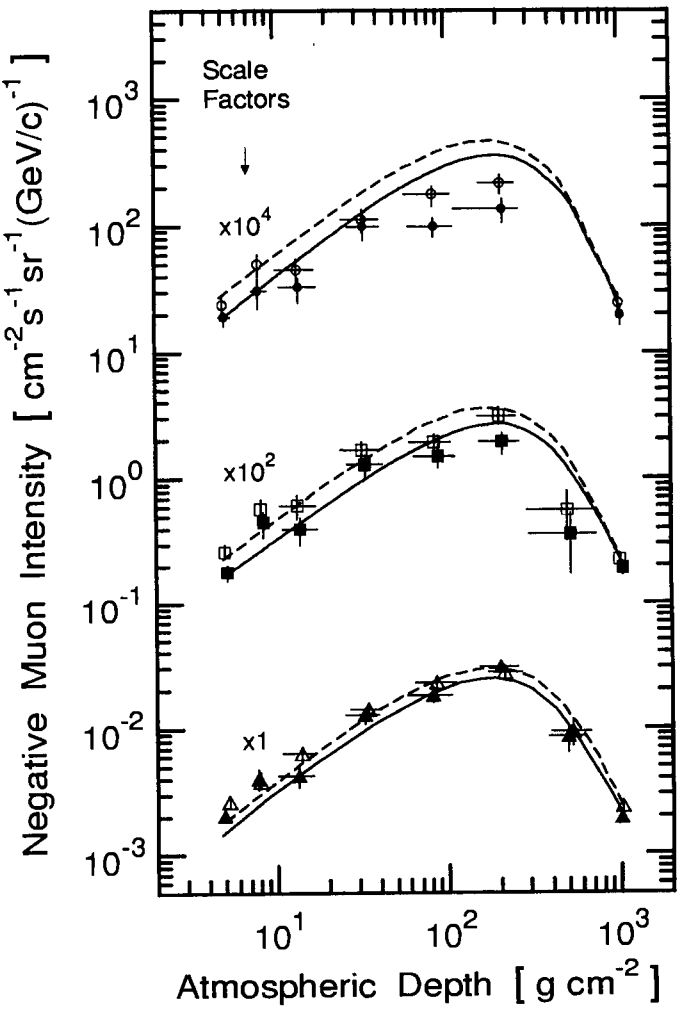

Figure 2.134: Atmospheric growth curves of positive and negative muons for different momentum intervals as listed below, recorded with the IMAX92 instrument launched from Lynn Lake, Manitoba (Canada), July 16-17, 1992 (Krizmanic et al., 1999). (Divide reading on ordinate by appropriate scale factor.)

•	μ^-	$0.22 \leq p \leq 0.32$ GeV/c	○	μ^+	$0.22 \leq p \leq 0.32$ GeV/c
■	μ^-	$0.37 \leq p \leq 0.42$ GeV/c	□	μ^+	$0.37 \leq p \leq 0.42$ GeV/c
▲	μ^-	$0.42 \leq p \leq 0.47$ GeV/c	△	μ^+	$0.42 \leq p \leq 0.47$ GeV/c

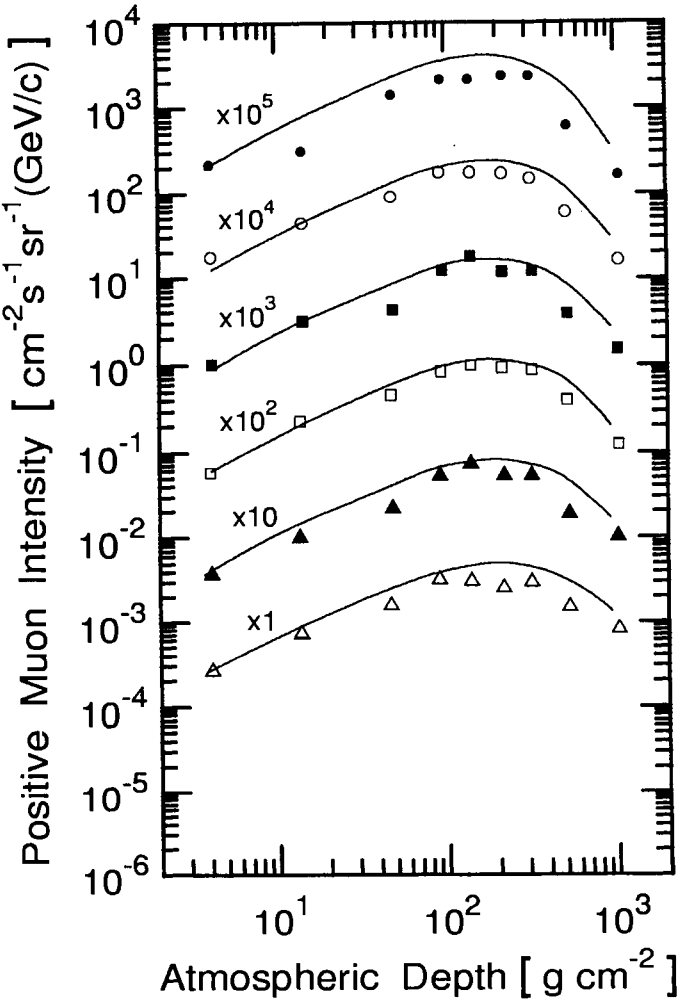

Figure 2.135: Atmospheric growth curves of positive muons for different momentum intervals as listed below, recorded with the CAPRICE94 instrument launched from Lynn Lake, Manitoba (Canada), August 8/9, 1994 (Francke et al., 1999). (Divide reading on ordinate by appropriate scale factor to get true intensity.)

• $0.30 \leq p \leq 0.53$ GeV/c	○ $0.53 \leq p \leq 0.75$ GeV/c
■ $0.75 \leq p \leq 0.97$ GeV/c	□ $0.97 \leq p \leq 1.23$ GeV/c
▲ $1.23 \leq p \leq 1.55$ GeV/c	△ $1.55 \leq p \leq 2.0$ GeV/c

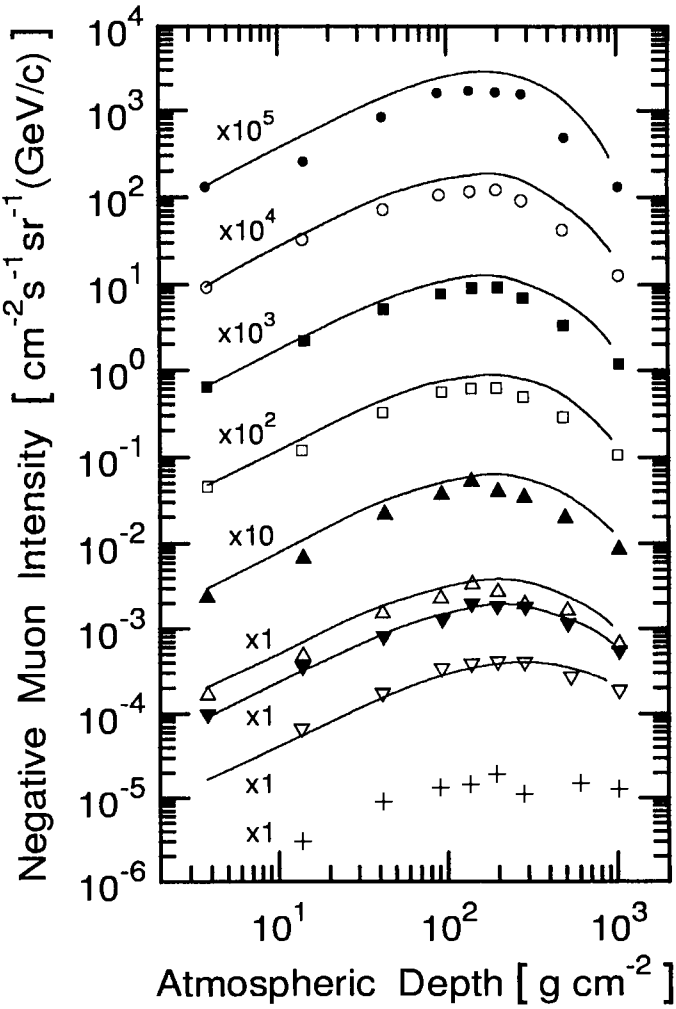

Figure 2.136: Atmospheric growth curves of negative muons for different momentum intervals as listed below, recorded with the CAPRICE94 instrument launched from Lynn Lake, Manitoba (Canada), August 8/9, 1994 (Francke et al., 1999). (Divide reading on ordinate by appropriate scale factor.)

• $0.30 \leq p \leq 0.53$ GeV/c	○ $0.53 \leq p \leq 0.75$ GeV/c
■ $0.75 \leq p \leq 0.97$ GeV/c	□ $0.97 \leq p \leq 1.23$ GeV/c
▲ $1.23 \leq p \leq 1.55$ GeV/c	△ $1.55 \leq p \leq 2.0$ GeV/c
▼ $2.0 \leq p \leq 3.2$ GeV/c	▽ $3.2 \leq p \leq 8.0$ GeV/c
+ $8.0 \leq p \leq 40$ GeV/c	

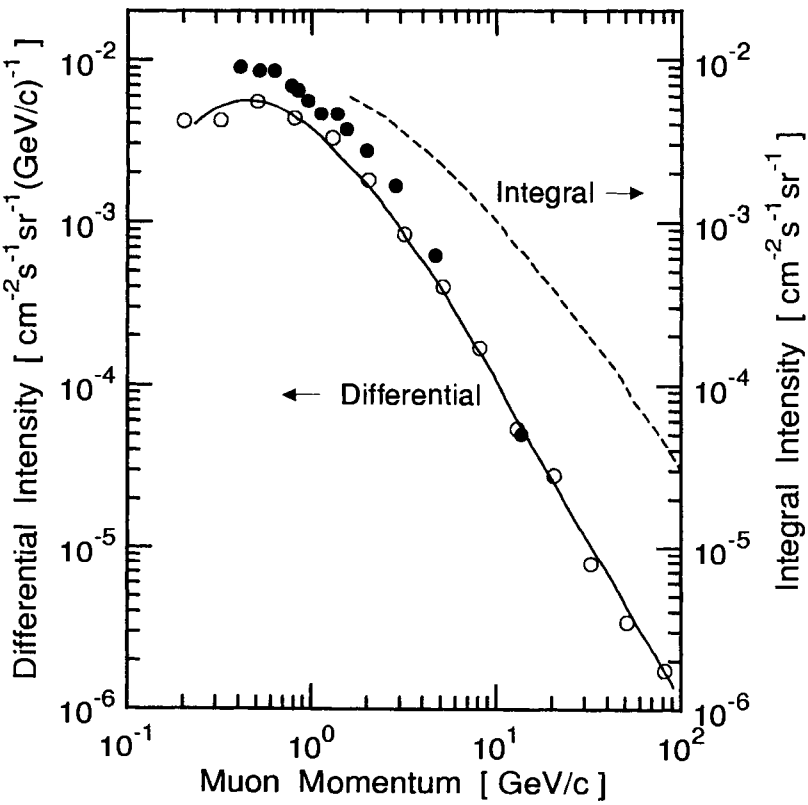

Figure 2.137: Vertical differential momentum spectrum of positive and negative muons combined at an altitude of 2960 m (Zugspitze, Germany) (Allkofer and Trümper, 1964), and of low energy muons at 3250 m (Mt. Aragats, Armenia) (Kocharian et al., 1956). Also shown is the integral momentum spectrum of muons at 3250 m (Mt. Aragats, Armenia) (Kocharian, 1959).

o, — Allkofer and Trümper (1964), 2960 m, differential
• Kocharian et al. (1956), 3250 m, differential
- - - Kocharian et al. (1959), 3250 m, integral

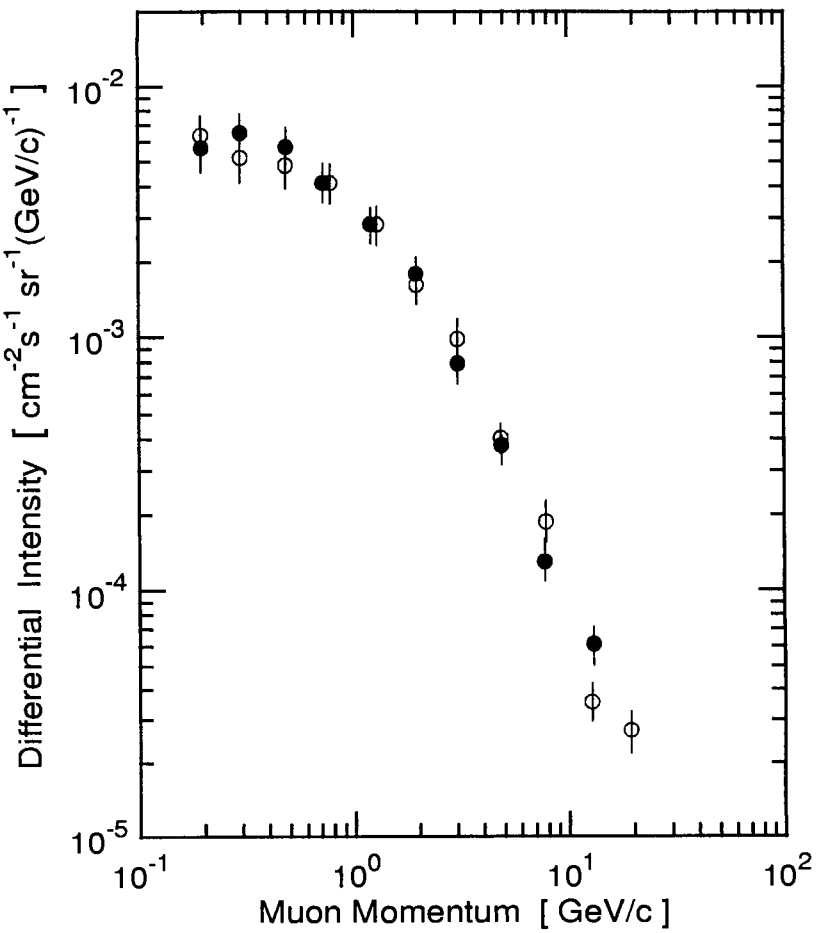

Figure 2.138: Differential momentum spectra of positive and negative muons combined at a zenith angle of 37.5° in eastern and western directions, at an altitude of 2960 m (Zugspitze, Germany) (Allkofer and Trümper, 1964). The data are not corrected for proton and electron contamination.

• 37.5° east | ○ 37.5° west

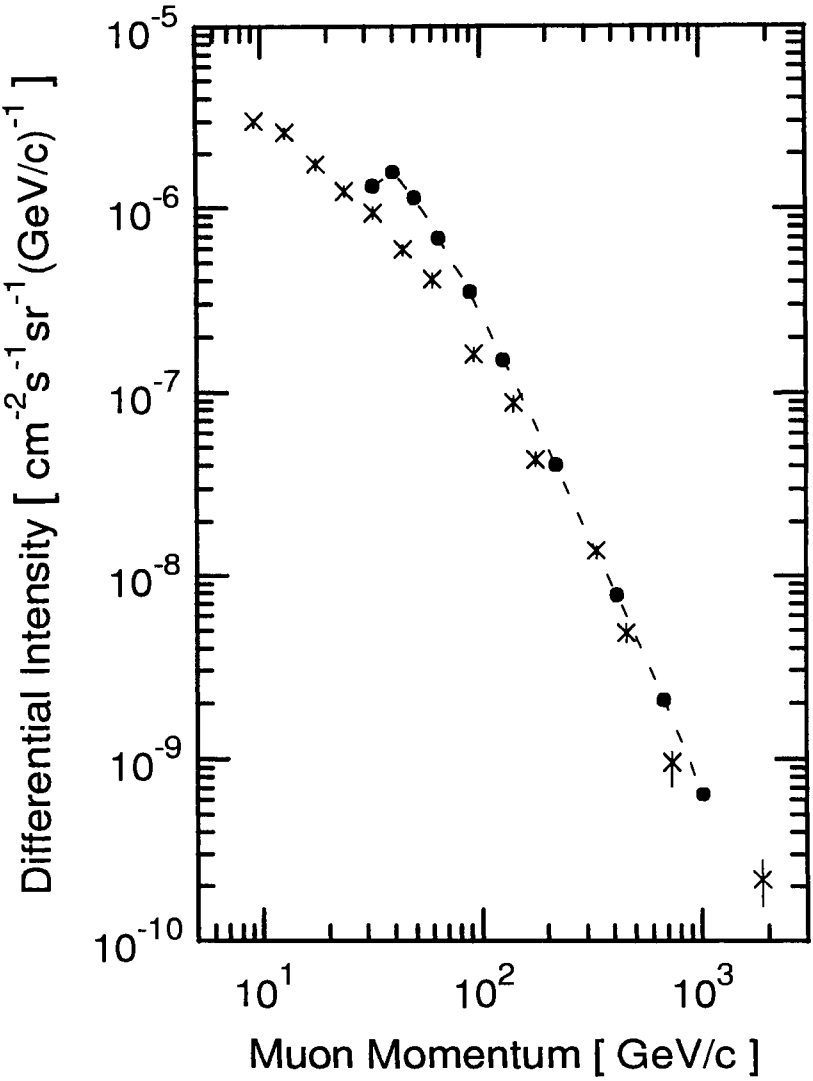

Figure 2.139: Differential energy spectrum of positive and negative muons combined, obtained with the magnetic spectrometer at Mt. Aragats, Armenia (3250 m, 670 g cm^{-2}), covering the zenith angle range $80° \leq \theta \leq 90°$ with a mean zenith angle of 84°. The errors are within the symbols. The curve connects the points.

× Asatiani et al. (1975) | • Asatiani et al. (1983) |

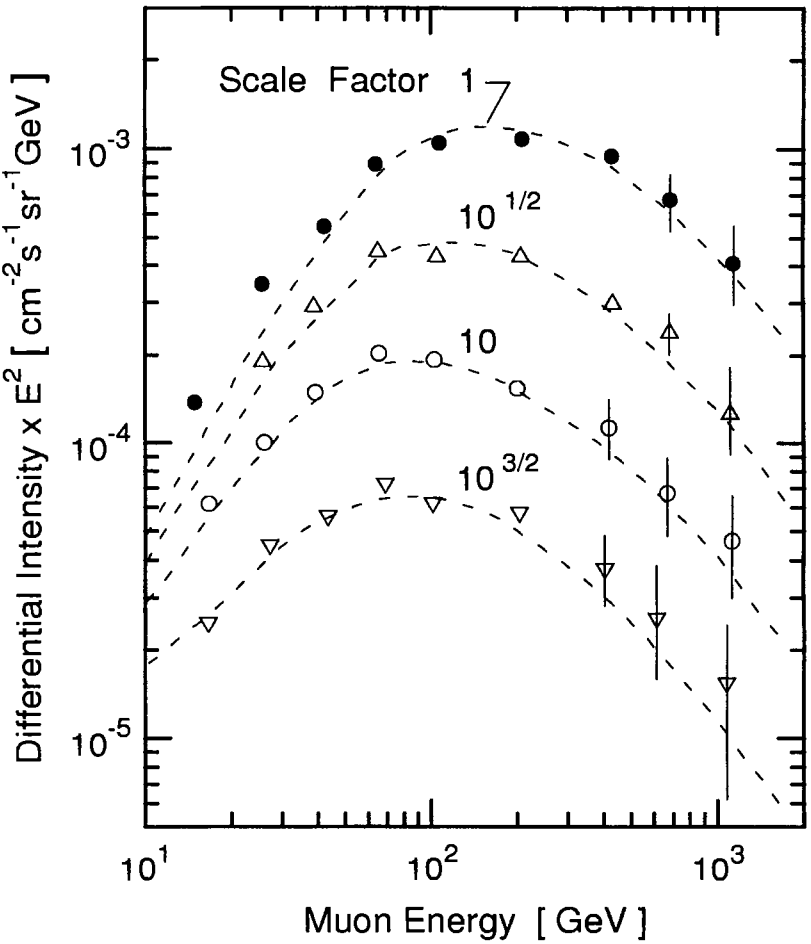

Figure 2.140: Differential energy spectra of positive and negative muons combined, obtained with the magnetic spectrometer at Mt. Aragats, Armenia (3250 m, 670 $g\,cm^{-2}$) for different zenith angle intervals (Asatiani et al. 1983). The curves are from model calculations based on the work of Bull et al. (1965) using the method developed by Barrett et al. (1952) with corrections by Smith and Duller (1959). (Multiply intensity reading by proper scale factor and divide by the energy squared to get true intensity.)

∇ 80° – 82° | o 82° – 84° | $\triangle$ 84° – 86° | • 86° – 88°

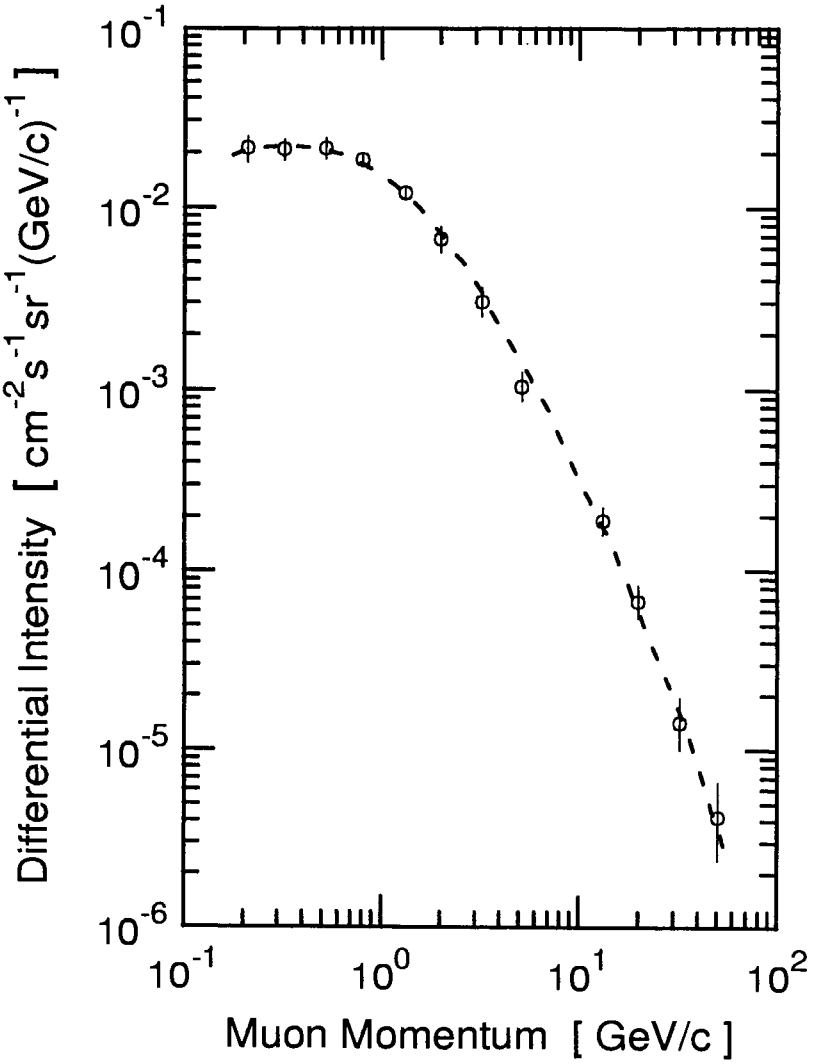

Figure 2.141: Vertical differential momentum spectrum of muons at an altitude of 5260 m (Mt. Chacaltaya, Bolivia) (Allkofer and Kraft, 1965).

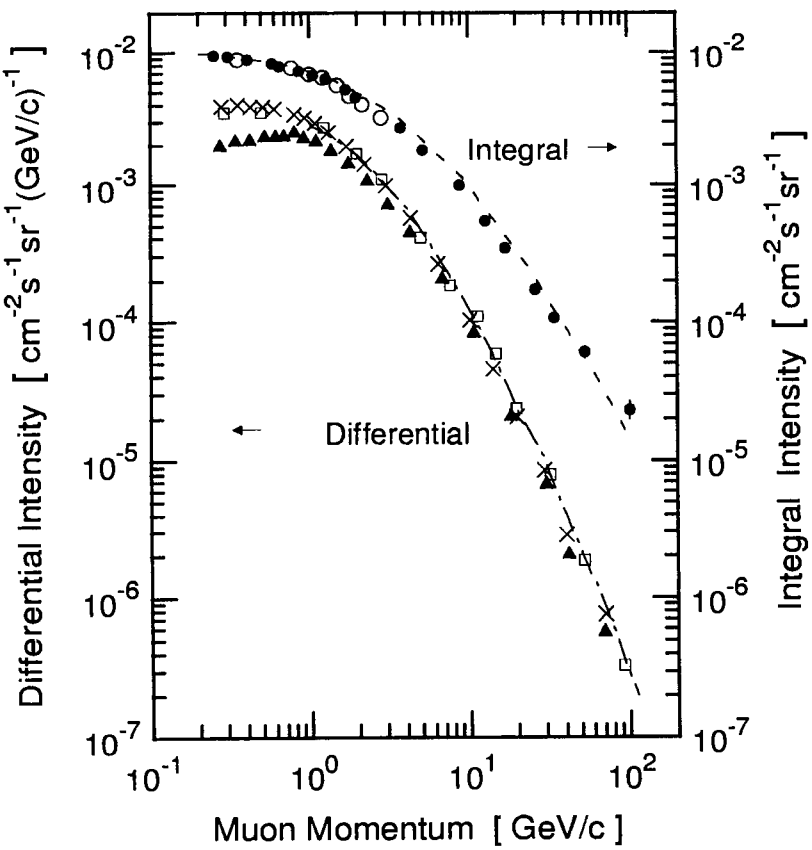

Figure 2.142: Differential and integral momentum spectra of positive and negative muons at 920 g cm^{-2} (600 m a.s.l.) measured at Prince Albert (Canada) ($P_c \approx 1$ GV). For details see text. Also shown is the differential sea level spectrum of Allkofer et al. (1971a, b), the integral spectrum at 122 m a.s.l. of Karnakar et al. (1973), and a theoretical spectrum by Stephens (1979a).

× De Pascale et al. (1993), 600 m, differential
▲ Basini et al. (1991), 600 m, differential
□ Allkofer et al. (1971b, d), s.l., differential
- · - Stephens (1979a), differential, theory
• De Pascale et al. (1993), 600 m, integral
o Karmakar et al. (1973), 122 m, integral
- - - Allkofer et al. (1971a, b), s.l., integral

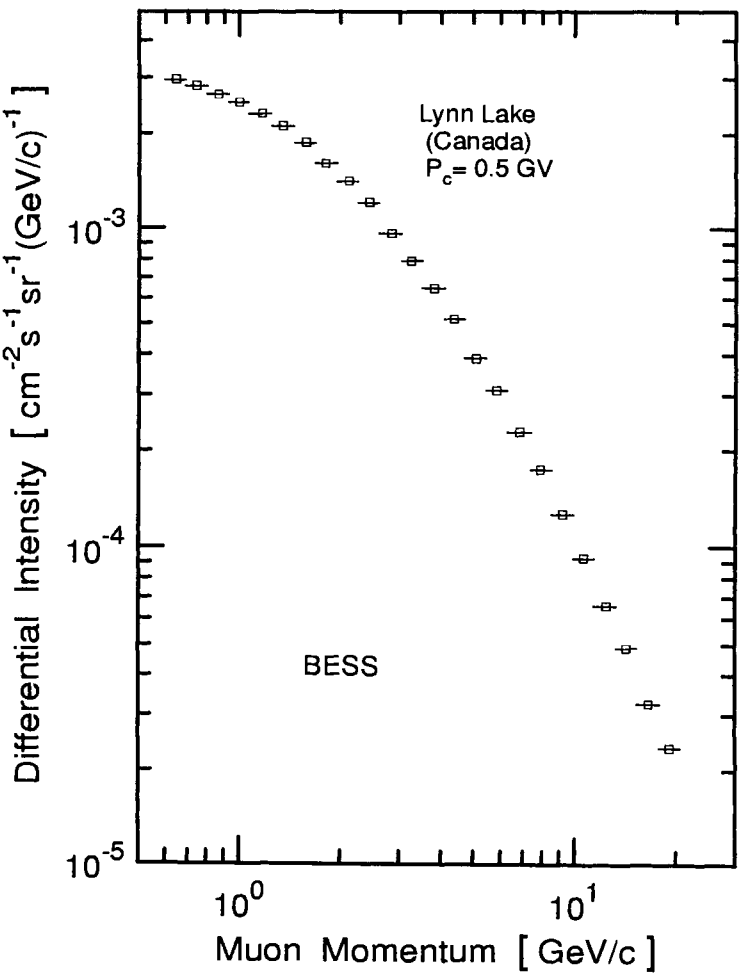

Figure 2.143: Precision measurement of the muon momentum spectrum carried out with the BESS instrument at Lynn Lake (Canada), □, altitude 360 m a.s.l., $\simeq$ 960 g cm^{-2}, $P_c \simeq 0.5$ GV (BESS 97 - 99) (Nozaki, 2000).

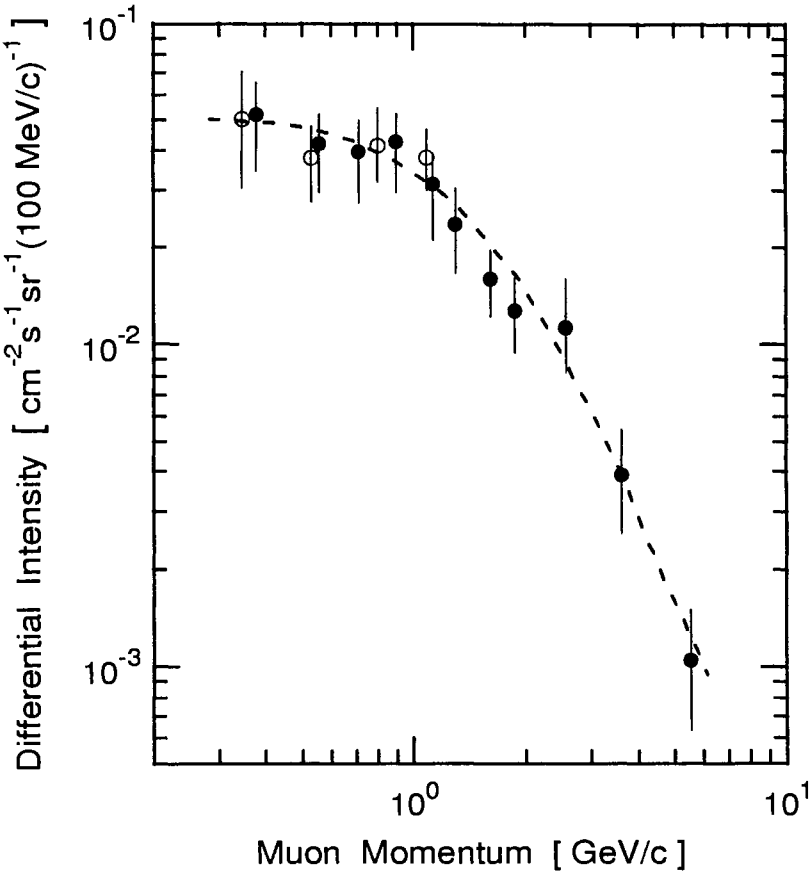

Figure 2.144: Vertical differential momentum spectrum of negative muons at an altitude of 9000 m (Baradzei et al., 1959). Full and Open circles represent two different sets of measurements. The dashed curve is a fit.

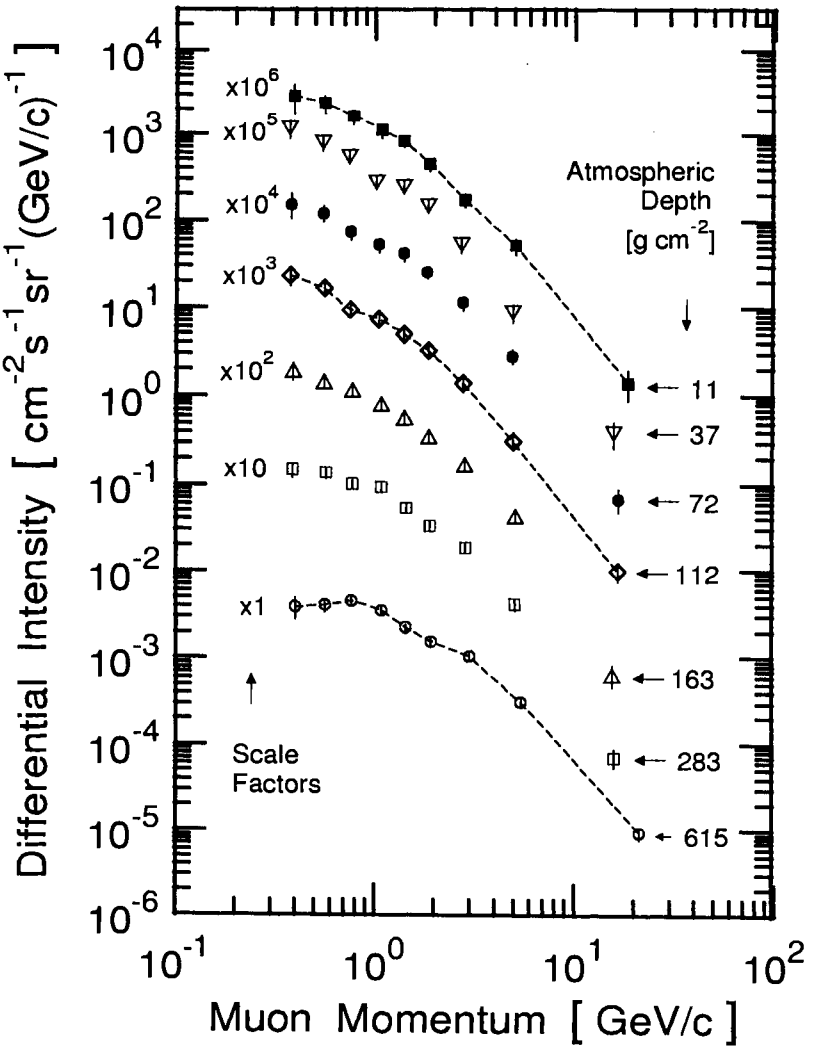

Figure 2.145: Differential momentum spectra of negative muons measured at different atmospheric depths above Prince Albert (Canada) ($P_c \approx 1$ GV) (Circella et al. 1993). (Divide reading on ordinate by appropriate scale factor to get true intensity.)

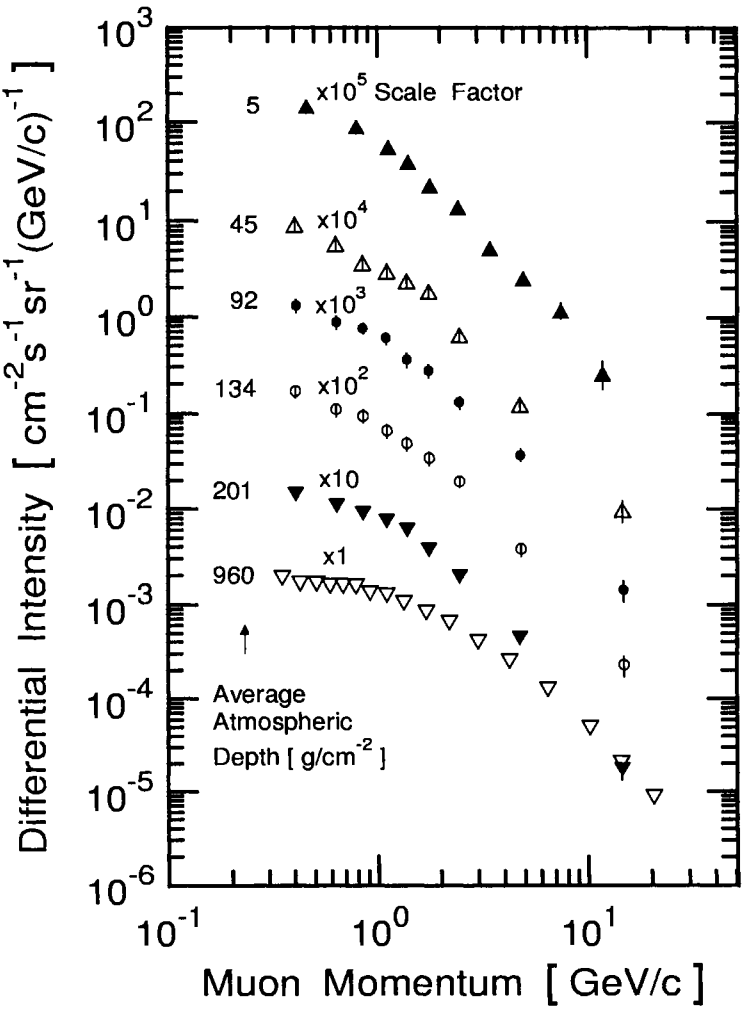

Figure 2.146: Negative muon momentum spectra at various depths in the atmosphere measured with the MASS89 instrument, launched from Prince Albert, Saskatchewan (Canada). The depth intervals are listed below (Bellotti et al., 1996). (Divide reading on ordinate by appropriate scale factor to get true intensity.)

▲ 5 g cm^{-2} | △ 25 - 70 g cm^{-2} | • 70 - 115 g cm^{-2}
o 115 - 160 g cm^{-2} | ▼ 160 - 250 g cm^{-2} | ▽ 960 g cm^{-2}

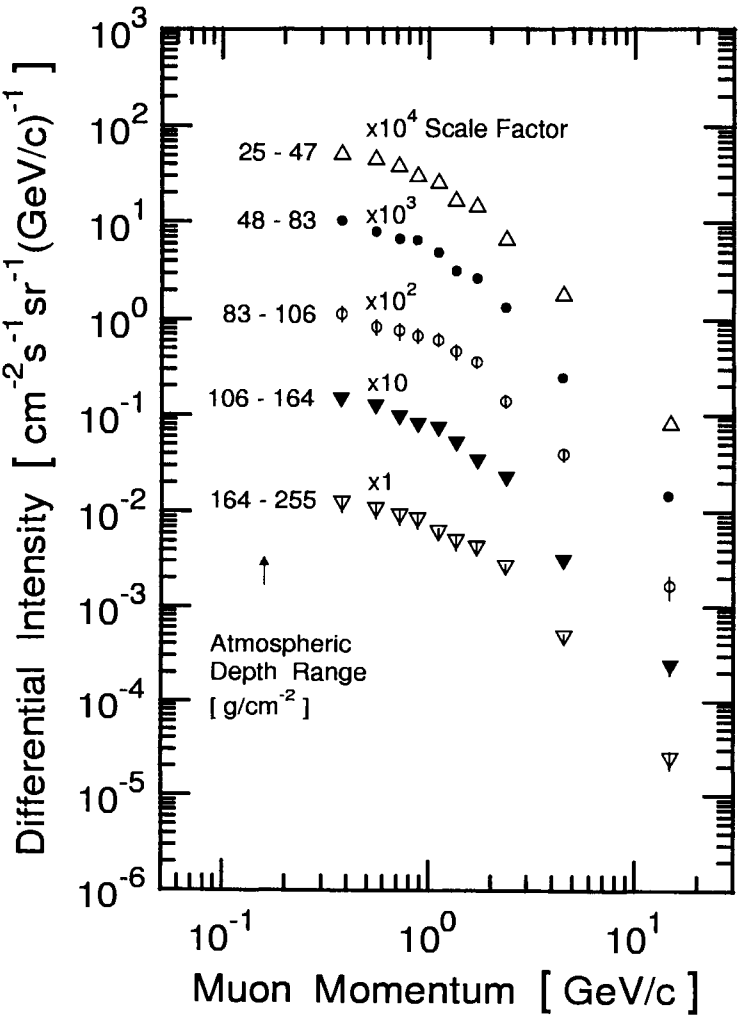

Figure 2.147: Negative muon momentum spectra at various depths in the atmosphere measured with the MASS91 instrument launched from Fort Sumner, NM (U.S.A.) (Bellotti et al., 1999). (Divide reading on ordinate by appropriate scale factor to get true intensity.)

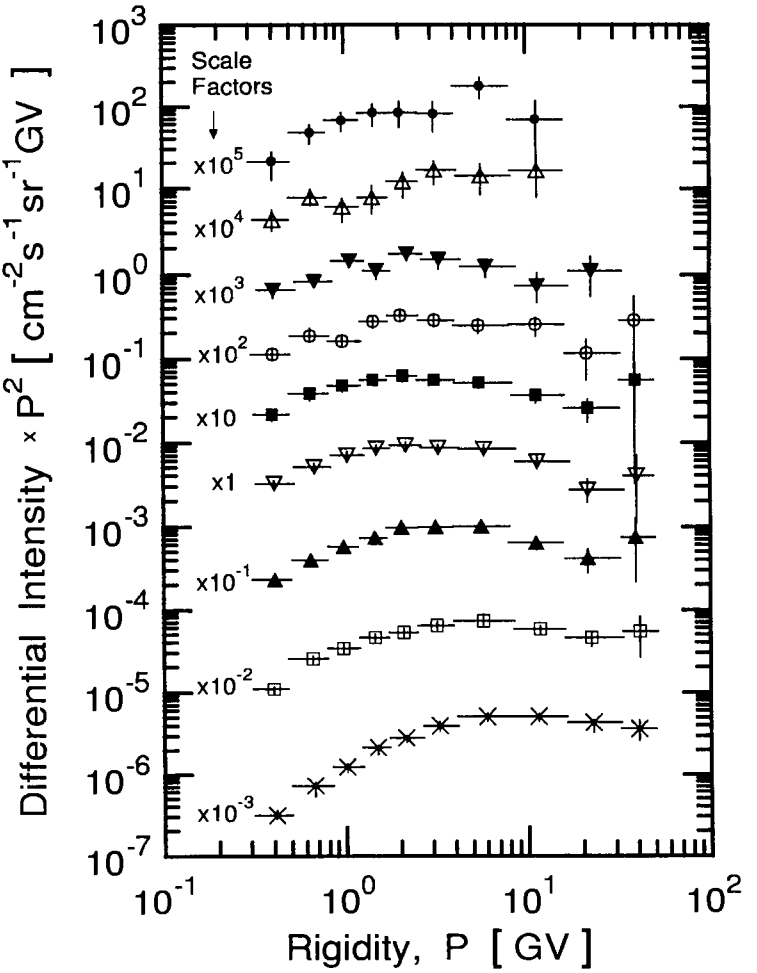

Figure 2.148: Differential rigidity spectra of negative muons at various depths in the atmosphere measured with the HEAT95 instrument, launched from Lynn Lake, Manitoba (Canada) ($P_c \simeq 1$ GV). The depth intervals are listed below (Coutu et al., 1999). (Divide reading on ordinate by appropriate scale factor to get true intensity.)

• 4 - 7 g cm^{-2}	△ 7 - 13 g cm^{-2}	▼ 13 - 32 g cm^{-2}
○ 32 - 67 g cm^{-2}	■ 67 - 140 g cm^{-2}	▽ 140 - 250 g cm^{-2}
▲ 250 - 350 g cm^{-2}	□ 350 - 840 g cm^{-2}	× 840 - 960 g cm^{-2}

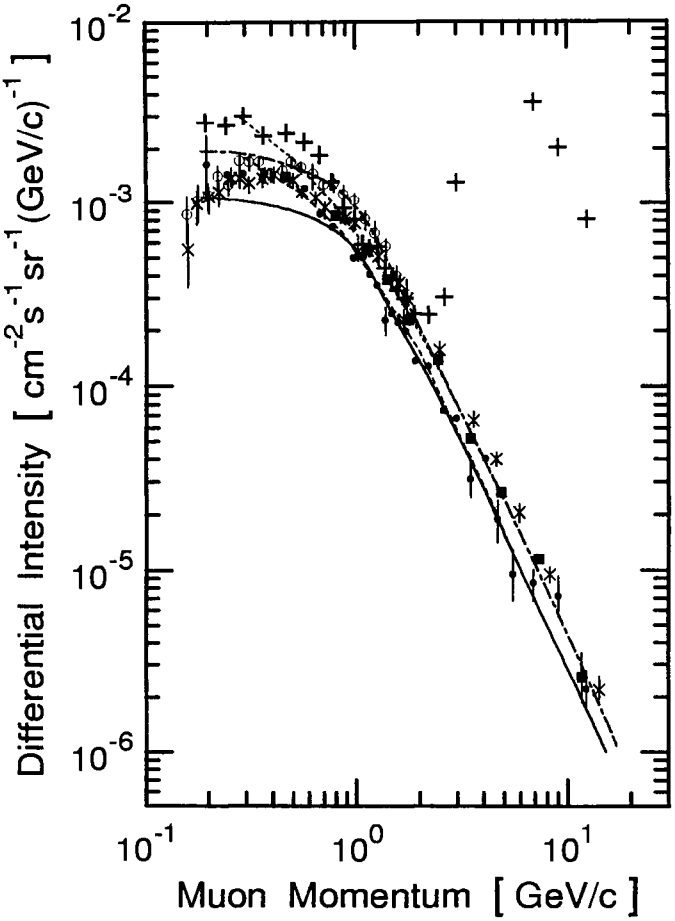

Figure 2.149: Momentum spectra of positive and negative muons determined by different experiments in the upper atmosphere as listed below. The solid and dot-dashed curves are predictions for negative and positive muons, respectively, after Stephens (1981), the dashed and the dotted curves are analogous curves from a calculation of Gaisser et al. (1995).

- • μ^- 3.9 g cm^{-2}, CAPRICE94 (Francke et al., 1999)
- ■ μ^- 5.0 g cm^{-2}, MASS89 (Brunetti et al., 1996)
- × μ^- 5.8 g cm^{-2}, MASS91 (Codino et al., 1997)
- o μ^+ 5.8 g cm^{-2}, MASS91 (Codino et al., 1997)
- \+ μ^+ 3.9 g cm^{-2}, CAPRICE94 (Francke et al., 1999)

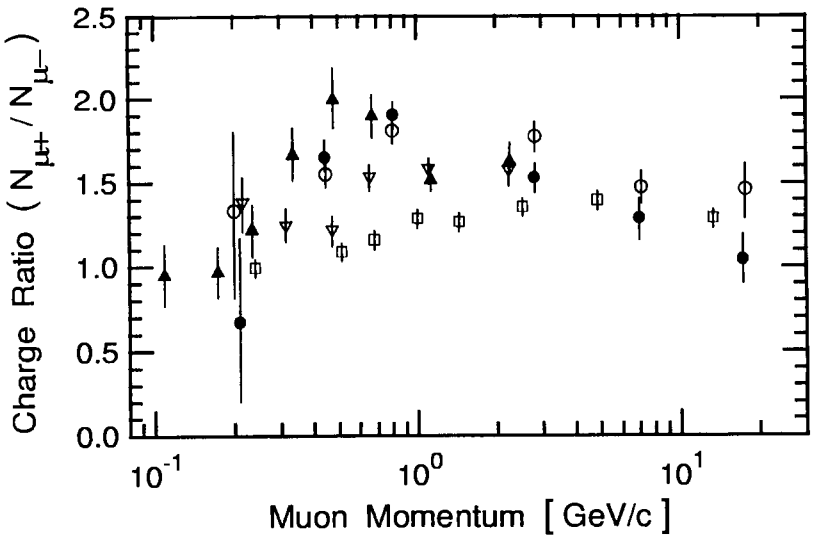

Figure 2.150: Muon charge ratio measured at an altitude of 2960 m (Zugspitze, Germany) in the momentum range $0.2 \leq p \leq 20$ GeV/c (•) (Allkofer and Trümper, 1964), at altitude 3250 m (Mt. Aragats, Armenia) in the momentum range $0.1 \leq p \leq 2.5$ GeV/c (▲) (Vaisenberg, 1957), at the same altitude and same place in the momentum range $0.2 \leq p \leq 20$ GeV/c (□) (Kocharian et al., 1959), and at altitude 5260 m (Mt. Chacaltaya, Bolivia) in the momentum range $0.2 \leq p \leq 20$ GeV/c (o) (Allkofer and Kraft, 1965). The data of Vaisenberg (1957) apply to two different measurement conditions: ▲, charge ratio obtained without the use of any absorbers, showing a strong positive excess, presumably due to protons, and, ▽, charge ratio under 9 cm of lead.

- • Allkofer and Trümper (1964), 2960 m
- ▲ Vaisenberg (1957), unshielded, 3250 m
- ▽ Vaisenberg (1957), under 8.6 g cm^{-2} Pb, 3250 m
- □ Kocharian et al. (1959), 3250 m
- o Allkofer and Kraft (1965), 5260 m

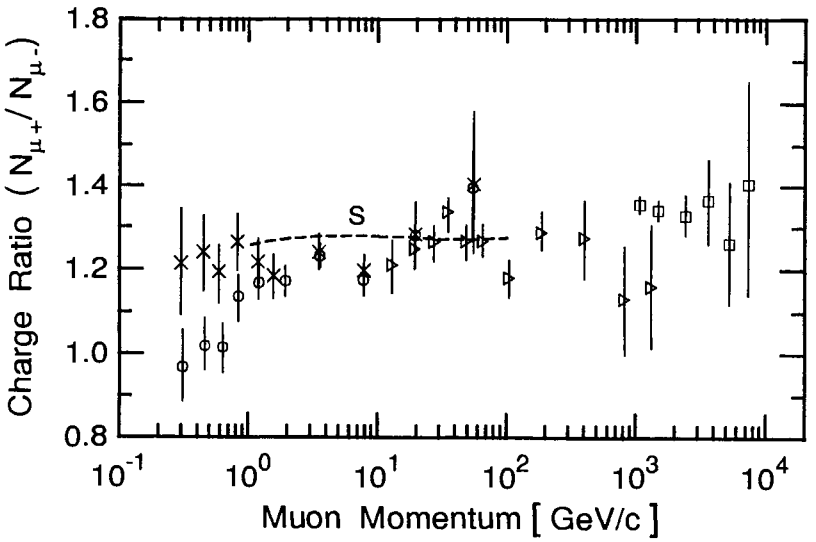

Figure 2.151: Charge ratio of muons as a function of energy in the lower atmosphere. The data by Asatiani et al. (1983) (altitude 3250 m a.s.l.) are for near horizontal muons. Included are also the data of Ashley et al. (1975a, 1975b) for high energy inclined muons recorded at the Utah underground laboratory (altitude ~1500 m a.s.l., depth ≃1400 hg cm^{-2}). The mean zenith angle of these data increases with energy and is 51°, 60°, 69°, 74°, 77° and 78°, respectively, for the six values indicated. (For details see text.)

- o Basini et al. (1991) vertical, 600 m a.s.l.
- × De Pascale et al. (1993) vertical, 600 m
- □ Ashley et al. (1975a, b), inclined, 1500 m
- ▷ Asatiani et al. (1983) horizontal, 3250 m
- - - Stephens (1979b), theoretical, sea level

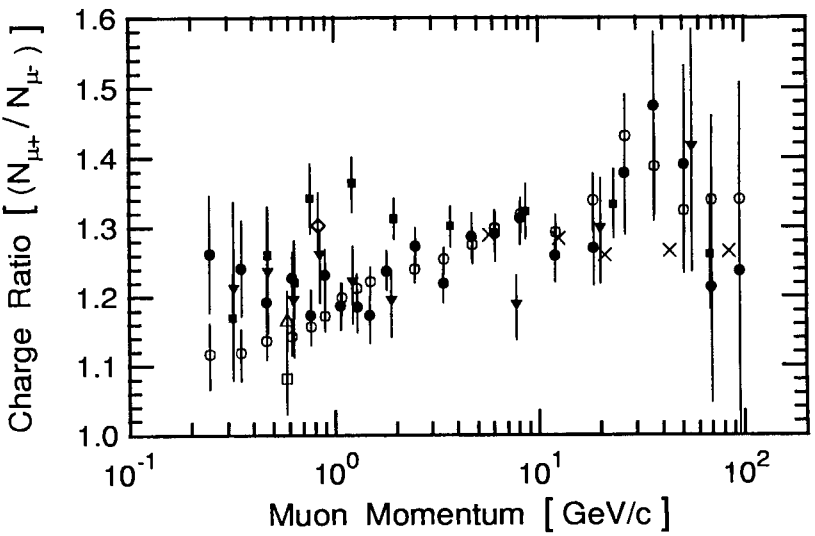

Figure 2.152: Muon charge ratios as a function of momentum measured at the ground at different locations and altitudes, as listed below. For comparison we have added the data of two near sea level experiments.

- • Kremer et al. (1999), Lynn Lake, 360 m (CAPRICE94)
- o Kremer et al. (1999), Ft. Sumner, 1270 m (CAPRICE97)
- □ Tarlé et al. (1997), Lynn Lake, 360 m (HEAT95)
- △ Schneider et al. (1995), Ft. Sumner, 1270 m (HEAT94)
- ■ Golden et al. (1995), Prince Albert, 600 m (MASS89)
- ▼ De Pascale et al. (1993), Prince Albert, 600 m (MASS89)
- × Rastin (1984a), Nottingham, 50 m (magn. spectrometer)
- ◇ Vulpescu et al. (1998), Karlsruhe, 110 m (WILLI97)

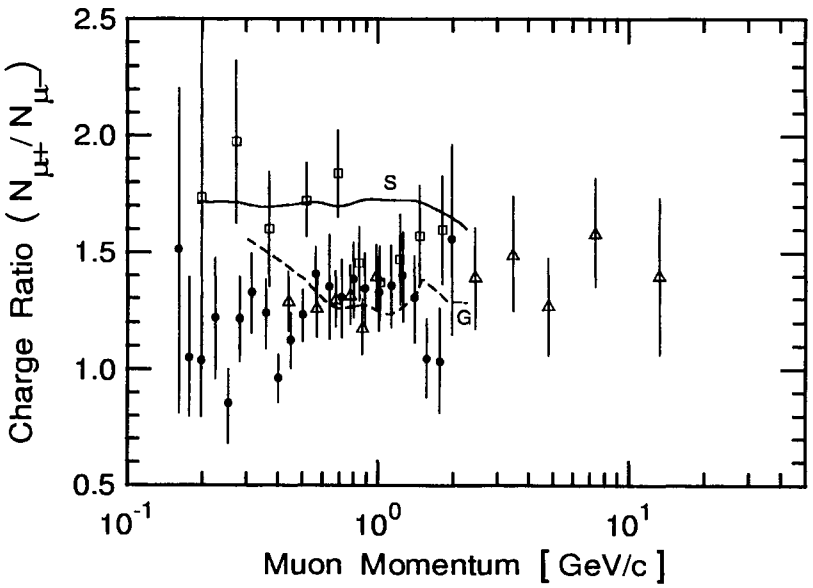

Figure 2.153: Muon charge ratios as a function of momentum measured at high altitudes in the atmosphere at different locations, as listed below. Curves G and S are predicted charge ratios according to Gaisser et al. (1995) and Stephens (1981), respectively.

•	Codino et al. (1997)	Ft. Sumner, 5.8 $g\,cm^{-2}$	(MASS91)
□	Francke et al. (1999)	Lynn Lake, 3.9 $g\,cm^{-2}$	(CAPRICE94)
△	Carlson et al. (1999)	Ft. Sumner, 5.5 $g\,cm^{-2}$	(CAPRICE98)

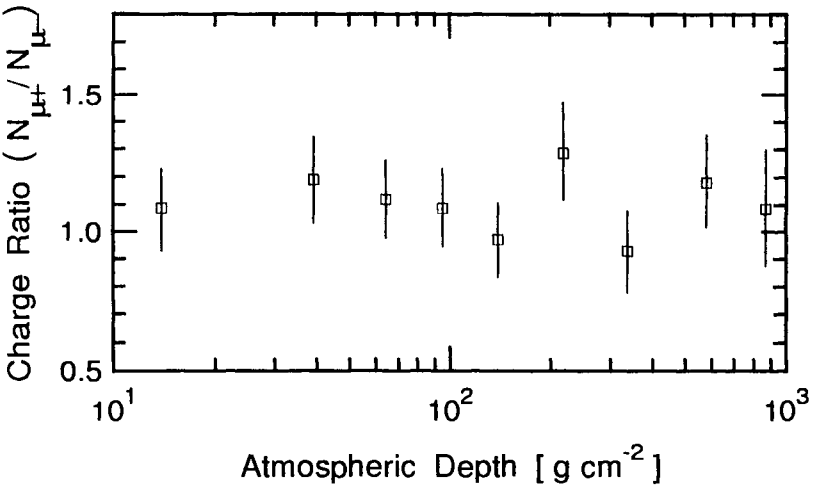

Figure 2.154: Muon charge ratio as a function of atmospheric depth for $0.33 \leq p \leq 0.65$ GeV/c (Basini et al. 1995).

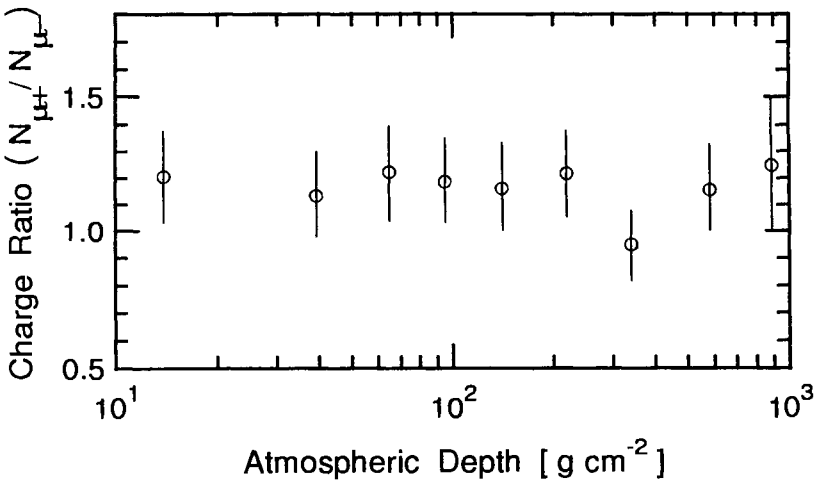

Figure 2.155: Muon charge ratio as a function of atmospheric depth for $0.65 \leq p \leq 1.0$ GeV/c (Basini et al. 1995).

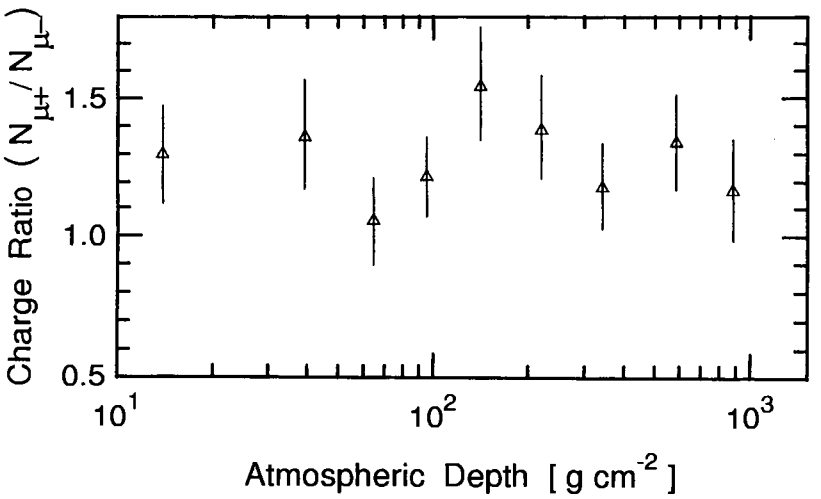

Figure 2.156: Muon charge ratio as a function of atmospheric depth for $1.0 \leq p \leq 1.5$ GeV/c (Basini et al. 1995).

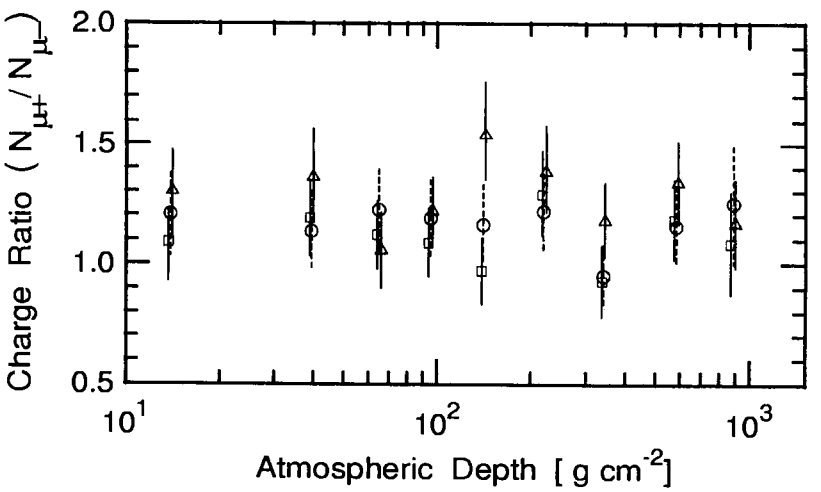

Figure 2.157: Muon charge ratio as a function of atmospheric depth. Shown are the data of the previous three figures combined (Figs. 2.154 - 2.156 (Basini et al. 1995).

□ 0.33 - 0.65 GeV/c | ○ 0.65 - 1.0 GeV/c | △ 1.0 - 1.5 GeV/c

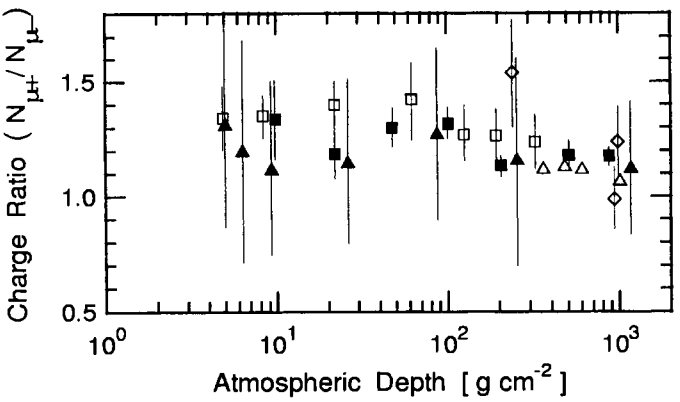

Figure 2.158: Muon charge ratio as a function of atmospheric depth for different momentum windows or cutoff energies.

■ 0.3 GeV/c $\leq p_\mu \leq$ 0.9 GeV/c, Schneider et al. (1995), HEAT94
▲ 0.42 GeV/c $\leq p_\mu \leq$ 0.47 GeV/c, Krizmanic et al. (1995), IMAX92
◇ > 0.4 GeV, Conversi (1950) △ 0.46 GeV, Quercia et al. (1950)
□ MC-Simulation, Schneider et al. (1995)

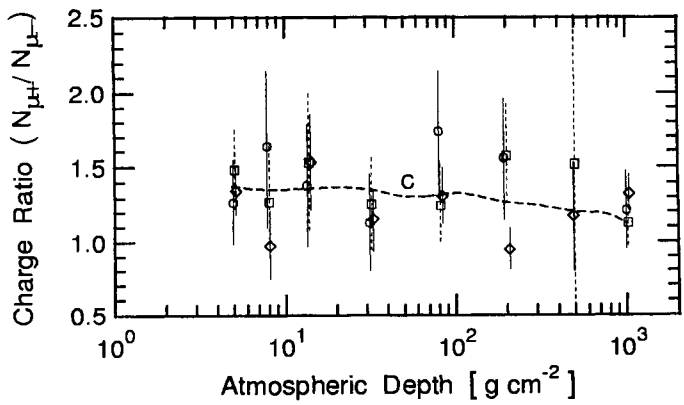

Figure 2.159: Muon charge ratio as a function of atmospheric depth for different momentum intervals as listed below, determined with IMAX92 launched from Lynn Lake (Canada) (Krizmanic et al., 1999). Two of the data point sets (○ and ◇) are drawn slightly displaced with respect to (□, dashed error bars) to prevent overlapping. C is a prediction after Barr et al. (1989).

○ 0.22- 0.32 GeV/c | □ 0.37 - 0.42 GeV/c | ◇ 0.42 - 0.47 GeV/c

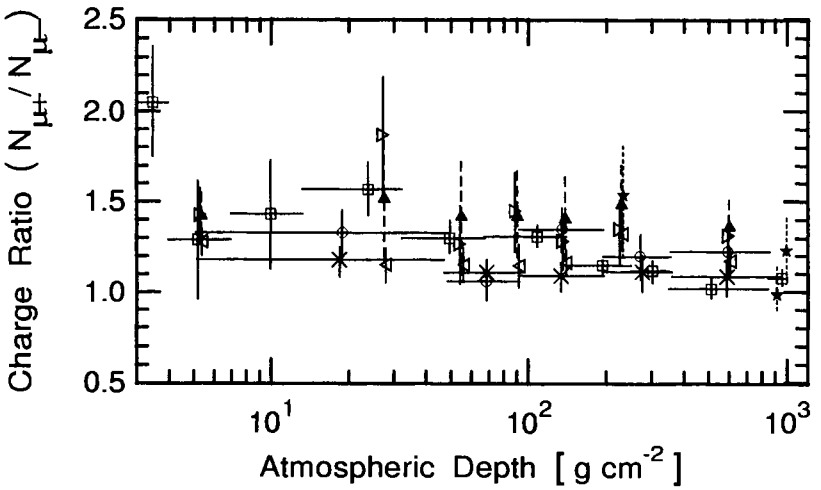

Figure 2.160: Muon charge ratio as a function of atmospheric depth. Shown are the data from different experiments and for different momentum intervals, as listed below. Two of the CAPRICE98 data point sets ($\triangleright$ and $\triangleleft$) are drawn slightly displaced with respect to those with the dashed error bars to prevent overlapping.

$\triangleleft$	$0.31 \leq p \leq 1.0$ GeV/c	CAPRICE98 (Ambriola et al., 2000)
$\triangleright$	$2.0 \leq p \leq 4.5$ GeV/c	CAPRICE98 (Ambriola et al., 2000)
$\blacktriangle$	$4.5 \leq p \leq 15$ GeV/c	CAPRICE98 (Ambriola et al., 2000)
$\times$	$0.3 \leq p \leq 0.9$ GeV/c	MASS91 (Bellotti et al., 1999)
o	$0.9 \leq p \leq 1.5$ GeV/c	MASS91 (Bellotti et al., 1999)
$\square$	$0.3 \leq p \leq 0.9$ GeV/c	HEAT95 (Coutu et al., 1997, 1998)
$\star$	$0.315 \leq p \leq 0.348$ GeV/c	(Conversi, 1950)

2.7 Nuclei

2.7.1 Introduction

Apart from protons and alpha particles, the mass spectrum of primary cosmic ray nuclei is usually divided into five mass groups. These comprise the *light* or L-group (Li, Be, B), the *medium* or M-group (C, N, O, F), the *heavy* or H-group (Ne to K), the *very heavy* or VH-group (Ca to Ac), frequently referred to as the *iron* group, and the *super heavy* or SH-group ($90 \leq Z \leq 112$).

The flux of heavy primary nuclei is rapidly attenuated with increasing atmospheric depth because of fragmentation. Thus new nuclei of smaller mass and charge are produced. But even these have little chance to penetrate deep into the atmosphere. The rapid fragmentation is due to the fact that the interaction mean free path of nuclei in air decreases from 75 g/cm^2 for protons to 14 g/cm^2 for iron nuclei. It is even shorter for the very rare nuclei beyond the iron group. Thus, the flux of primary or secondary nuclei that survive on their way through the atmosphere down to sea level is vanishing small.

2.7.2 Altitude Dependence of Flux and Intensities

Only very few experiments have been carried out to determine the flux of nuclei in the atmosphere. Nuclear emulsion and plastic sheets such as Lexan have been used as detector material to determine the flux of so-called *enders*, i.e., of nuclei that come to a stop in the detector. During the period from 1965 to 1966 measurements have been carried out to determine the flux of nuclei with charge $Z \geq 6$ at atmospheric depths up to about 80 g/cm^2 (Fukui et al., 1969). It was found that the flux of enders, incident under a particular zenith angle, θ, is a function of the path length measured from the top of the atmosphere. Fig. 2.161 shows the flux of enders versus the product of the vertical atmospheric depth, X, and the secant of the zenith angle, i.e., $X \cdot sec\theta$, for nuclei of charge $6 \leq Z \leq 9$. Fig. 2.162 shows the same graph for nuclei with charge $Z \geq 10$.

The vertical fluxes of nuclei belonging to different charge groups have been determined over the atmospheric depth range $40 \leq X \leq 120$ g/cm^2 with plastic stacks containing cellulose-nitrate as detector material (Allkofer et al., 1973; Allkofer and Heinrich, 1974a and 1974b). The charge spectra for three intervals of the investigated atmospheric depth range measured at a geomagnetic cutoff of 2.5 GV ($\simeq$625 MeV/nucleon) are presented in Figs. 2.163a to 2.163c, respectively.

Table 2.33: Time Integrated Flux of Cosmic Ray Nuclei at High Altitude. The measurements were carried out on board of the supersonic aircraft Concorde between London and New York (average cruising altitude 15 km, accumulated flight time 834 h above 9 km) (Zhou et al., 1999).

Nucleus	Energy Interval [MeV/Nucleon]	Time Integrated Differential Flux $[\mathrm{cm}^{-2}\,(\mathrm{MeV/Nucleon})^{-1}]$
He	$7 \leq E \leq 22$	$(3.43 \pm 0.49) \cdot 10^{-3}$
Li	$8 \leq E \leq 60$	$(1.24 \pm 0.50) \cdot 10^{-4}$
Be	$10 \leq E \leq 150$	$(3.06 \pm 1.53) \cdot 10^{-5}$
B	$11 \leq E \leq 155$	$(2.98 \pm 1.49) \cdot 10^{-5}$
C	$13 \leq E \leq 250$	$(4.07 \pm 1.36) \cdot 10^{-5}$
N	$14 \leq E \leq 400$	$(1.39 \pm 0.62) \cdot 10^{-5}$
O	$15 \leq E \leq 800$	$(5.46 \pm 2.73) \cdot 10^{-6}$

The altitude dependence of the vertical differential intensity was investigated experimentally and theoretically using fragmentation parameters for nuclear emulsion and air targets (Allkofer and Heinrich, 1974). Fig. 2.164 shows the experimental data for different charge groups as a function of atmospheric depth. Fig. 2.165 compares the results of the M-group and H-group with those of Fukui et al. (1969). Figs. 2.166 and 2.167 show the altitude dependence of nuclei of energies $\geq$ 360 MeV/nucleus and $\geq$ 1200 MeV/nucleus, respectively.

With a plastic detector of 15 m^2 area, exposed at a depth of 603 $\mathrm{g/cm}^2$, tracks of particles with $Z/\beta > 10$ ($\beta = v/c$) could be recorded (Price and Kinoshita, 1981). For particles with $Z \geq 4$ and $\beta \geq 0.3$ a flux of about 100 $\mathrm{m}^{-2}\mathrm{yr}^{-1}$ could be observed.

In a recent measurement Zhou et al. (1999) have determined the time integrated flux of nuclei from helium to oxygen on board the supersonic jetliner Concorde, accumulated during 150 flights, totaling 835 hours above an altitude of 9 km. The actual cruising altitude varied from about 13.5 km to 17 km ($\simeq 130 - 100\,\mathrm{g\,cm}^{-2}$. The results are presented in Table 2.33.

Table 2.34: Fragmentation Probabilities of Cosmic Ray Nuclei in Collisions with Light Nuclei of Nuclear Emulsion and in Air. (Allkofer and Heinrich, 1974)

Fragmentation Type	Emulsion (1)	(2)	(3)	(4)	Sum (1-4)[a]	Mean (1-4)	Air (5)
H1 → H1		0.20 0.09	0.18 0.04	0.12 0.04	0.23 0.10	0.17 0.03	0.17
→ H2		0.36 0.12			0.20 0.09	0.27 0.08	0.27
→ H3	0.37 0.12	0.08 0.06			0.20 0.09	0.23 0.06	0.23
→ M	0.11 0.08	0.16 0.08	0.14 0.04	0.13 0.04	0.23 0.10	0.15 0.03	0.15
→ L	0.26 0.10	0.36 0.12	0.22 0.05		0.13 0.07	0.24 0.04	0.24
H2 → H2		0.09 0.09			0.10 0.06	0.10 0.05	0.10
→ H3	0.37 0.22	0.27 0.16			0.40 0.14	0.36 0.10	0.36
→ M	0.18 0.13	0.18 0.13			0.20 0.09	0.19 0.06	0.19
→ L	0.22 0.13	0.18 0.13			0.40 0.14	0.31 0.10	0.31
H3 → H3	0.07 0.03	0.19 0.05			0.09 0.03	0.10 0.02	0.20
→ M	0.25 0.05	0.28 0.07			0.39 0.07	0.30 0.04	0.30
→ L	0.28 0.05	0.22 0.06			0.26 0.05	0.26 0.03	0.26
M → M	0.12 0.03	0.20 0.03	0.16 0.02	0.19 0.04	0.11 0.02	0.16 0.01[b]	0.16
→ L	0.17 0.03	0.19 0.03	0.21 0.02	0.13 0.04	0.23 0.03	0.20 0.02[b]	0.04
L → L		0.15 0.04	0.13 0.03	0.13 0.06	0.11 0.03	0.13 0.03[b]	0.02

(1) Saito (1971), (2) Judek & Heerden (1966), (3) Waddington (1960), (4) Püschel (1958), (5) Allkofer and Heinrich (1974).

[a] Fragmentation probabilities determined from lists of fragmentations. [b] In the weighted mean values for the M- and L-group the results of Lohrmann and Teucher (1959), Cester et al. (1958), Koshiba et al. (1958) and Aizu et al. (1960) are included.

Table 2.35: Deuteron Intensities at 747 g/cm^2 (Barber et al. 1980).

Momentum Interval [GeV/c]	Average Momentum [GeV/c]	Number Observed	Intensity [cm^{-2}s^{-1}sr^{-1}(GeV/c)$^{-1}$]
0.70 - 1.08	0.89	10	$1.93 \pm 0.73 \cdot 10^{-5}$
1.08 - 1.41	1.24	8	$1.57 \pm 0.64 \cdot 10^{-5}$
1.41 - 1.60	1.50	3	$0.98 \pm 0.60 \cdot 10^{-5}$
1.60 - 1.84	1.72	7	$1.79 \pm 0.75 \cdot 10^{-5}$
1.84 - 2.50	2.17	1	$\leq 3.52 \cdot 10^{-6}$ *

* 90% confidence upper limit assuming Poisson statistics.

2.7.3 Fragmentation Probabilities of Nuclei

The fragmentation of nuclei of the cosmic radiation while undergoing collisions with target nuclei of photographic emulsion or air in the atmosphere had been studied by many authors (Aizu et al., 1960; Allkofer and Heinrich, 1974; Cester et al., 1958; Freier and Waddington, 1975; Judek and van Heerden, 1966; Koshiba et al., 1958; Lohrmann and Teucher, 1959; Powell et al., 1959; Püschel, 1958; Saito, 1971; Waddington, 1960). Table 2.34 is a survey of results from different experiments showing the fragmentation probabilities for collisions between cosmic ray nuclei and light nuclei of nuclear emulsion. Also given are the derived fragmentation probabilities for air (Allkofer and Heinrich, 1974).

More recently extensive studies of nuclear fragmentation have been carried out with accelerator experiments using heavy ion beams (Ogilvie et al., 1991; Wolter et al., 1999; and others). Reviews of this subject can be found in Hüfner (1985) and Moretto and Wozniak (1991).

2.7.4 Momentum Spectra

The vertical momentum spectrum of low energy deuterons has been measured in a counter experiment at an atmospheric depth of 747 g/cm^2 (2750 m) (Barber et al., 1980). The results are shown in Fig. 2.168, together with a calculated spectrum. The data are also given in tabulated form in Table 2.35.

Table 2.36: Predicted and Measured Intensities of Light Nuclei at Depth 747 g/cm^2 and Velocity Interval $0.35 < \beta \leq 0.70$, $\beta = v/c$ (Barber et al. 1980).

Nucleus	Momentum Interval [GeV/c]	Number Observed	Intensity $[cm^{-2}s^{-1}sr^{-1}(GeV/c)^{-1}]$ Observed	Predicted
^{3}H	1.05 - 2.76	$\leq$ 2	$\leq 1.9 \cdot 10^{-6}$	$4.98 \cdot 10^{-8}$
^{3}He	1.05 - 2.76	$\leq$ 2	$\leq 1.9 \cdot 10^{-6}$	$1.42 \cdot 10^{-8}$
^{4}He	1.39 - 3.65	$\leq$ 13	$(2.2 \pm 1.1) \cdot 10^{-6}$	$1.94 \cdot 10^{-8}$

The limits for the abundances of ^{3}H (tritium) and the two helium isotopes, ^{3}He and ^{4}He, all at 747 g/cm^2, are given in Table 2.36.

2.7.5 Theoretical Aspects

Starting with the primary isotopic composition Price et al. (1980) have calculated the integral flux of heavy cosmic ray nuclei for various depths in the atmosphere.

If $N_i(X)$ represents the number of particles of type i that traverse X g/cm^2 of atmosphere, then the differential equation governing the behavior of $N_i(X)$ is given by

$$\frac{dN_i}{dX} = -\sigma_{i,i}\left(\frac{N_o}{A_T}\right)N_i + \sum_j \sigma_{i,j}\left(\frac{N_o}{A_T}\right)N_j \,, \qquad (2.20)$$

where $\sigma_{i,i}$ is the cross section for type i projectiles, $\sigma_{i,j}$ the total production cross section for type j secondaries, N_0 is Avogadro's number, and A_T is the average mass number of the target nucleus, usually 14.4 for air. The validity of this one-dimensional equation depends on the assumptions that the interactions are velocity-preserving and that there is no net scattering.

The intensity was numerically integrated over all zenith angles and finite energies, from infinity (0 g/cm^2) to depth X. The contributions of various isotopes of the same element have been added. Fig. 2.169 shows the fluxes of nuclei with charges ranging from 5 to 28 at depths 0, 300, 540, 600, 650, and 1034 g/cm^2.

Additional calculations have been carried out to obtain the differential

energy spectra of the four charge groups at various depths and angles in the atmosphere (Kolomeets et al., 1979). Figs. 2.170a to 2.170c show vertical differential energy spectra for α-particles, the L-group (Li, Be, B), M-group (C, N, O, F) and the H-group (Ne to K) at 40, 80 and 160 g/cm^2, respectively. Figs. 2.171a to 2.171d show three differential energy spectra each, corresponding to the zenith angles of 0°, 60° and 80°, for the four charge groups at 30 g/cm^2, respectively. Analogous spectra are given in Figs. 2.172a to 2.172d for a depth of 60 g/cm^2.

Extensive calculations on fragmentation and cascading of cosmic ray nuclei have been carried out by Freier and Waddington (1975). The depth-intensity relation of the different components resulting from various primary nuclei have been obtained. Charge ratio for different groups of nuclei in the upper atmosphere have been calculated by Alessio and Dardo (1979).

References

Aizu, H., Y. Fujimoto, S. Hasegawa, M. Koshiba, I. Mito, J. Nishimura, and K. Kokoi: Prog. Theor. Phys. Suppl., 16, p. 56 (1960).

Akimov Yu.K., O.V. Savchenko, and L.M. Soroko: Zh. Eksp. Teor. Fiz., 41, p. 708 (1961).

Alessio, S., and M. Dardo: Nuovo Cimento, 2C, p. 465 (1979).

Allkofer, O.C., H. Dispert, and W. Heinrich: PICRC, 2, p. 897 (1973).

Allkofer, O.C. and W. Heinrich: Nucl. Phys. B, 71, p. 429 (1974a).

Allkofer, O.C. and W. Heinrich: Health Phys., 27, p. 543 (1974b).

Bakich, A.M., L.S. Peak, P.A. Riley, and M.M. Winn: PICRC, 6, p. 53 (1979).

Barber, H.B., T. Bowen, D.A. Delise, E.W. Jenkins, J.J. Jones, R.M. Kalbach, and A.E. Pifer: Phys. Rev. D, 22, p. 2667 (1980).

Beauchamp, W.T., T. Bowen, A.J. Cox, and R. M. Kalbach: Phys. Rev. D, 6, p. 1211 (1972).

Bhasin V.S. and I.M. Duck: Phys. Lett., B, 46, p. 309 (1973).

Cester, R., A. Debenedetti, C.M. Carelli, B. Quassiati, L. Tallone, and M. Vigone: Nuovo Cimento, 7, p. 371 (1958).

Daniel, R.R. and N. Durgaprasad: Nuovo Cimento, Suppl., 23, p 82 (1962).

Fleischer, R.L., H.R. Hart, G.E. Nichols, and P.B. Price: Phys. Rev. D, 4, p. 24 (1971).

Freier, Phyllis S., and C.J. Waddington: Astrophys. and Space Sci., 38, p. 419 (1975).

Fukui, K., Y.K. Lim, and P.S. Young: Nuovo Cimento, 61B, p. 210 (1969).

Hüfner, J.: Phys. Rep., 125, p. 129 (1985).

Judek, B., and I.J. van Heerden: Can. J. Phys., 44, 1121 (1966).

Kolomeets, E.V.,O.V. Krupennikov, O.A. Barsukov, and V.L. Shmonin: PICRC, 7, p. 121 (1979).

Koshiba, M., G. Schultz, and M. Schein: Nuovo Cimento, 2, p. 1 (1959).

Lohrmann, E., and M.W. Teucher: Phys. Rev., 115, p. 636 (1959).

Moretto, L.G., and G.J. Wozniak: Ann. Rev. Nucl. Part. Phys., 43, p. 374 (1993).

Ogilvie, C.A., J.C. Adloff, M. Begemann-Blaich, P. Bouissou, J. Hubele, G. Imme, I. Iori, P. Kreutz, G.J. Kunde, S. Leray, V. Lindenstruth,Z. Liu, U. Lynen, R.J. Meijer, U. Milkau, W.F.J. Müller, C. Ngô, J. Pochodzalla, G. Raciti, G. Rudolf, H. Sann, S. Schüttauf, W. Seidel, L. Stuttge, W. Trautmann, and A. Tucholski: Phys. Rev. Lett., 67, p. 1214 (1991).

Powell, C.F., P.H. Fowler, and D.H. Perkins: Study of Elementary Particles by the Photographic Method, Pergamon Press, London (1959).

Price, P.B., F. Askary and G. Tarle: Proc. Natl. Acad. Sci. , 77, p. 44 (1980).

Price, P.B. and K. Kinoshita: PICRC, 5, p. 51 (1981).

Püschel, W.: Zeitschr. f. Naturforsch., 13a, p. 801 (1958).

Waddington, C.J.: Phil. Mag., 5, p. 311 (1960).

Webber, W.R. and J.F. Ormes: J. Geophys. Res., 72, p. 5957 (1967).

Wolter, W., M.L. Cherry, A. Dabrowska, P. Deines-Jones, R. Holynski, B.S. Nilsen, A. Olszewski, M. Szarska, A. Trzupek, C.J. Waddington, J.P. Wefel, B. Wilczyńska, H. Wilczyński, B. Wosiek, and K. Woźniak: PICRC, 1, p. 5 (1999).

Yock, P.C.M.: Nucl. Phys. B, 86, p. 216 (1975).

Zhou, D., W. Heinrich, D. O'Sullivan, J. Donnelly, J. Byrne, and E. Flood: PICRC, 3, p. 101 (1999).

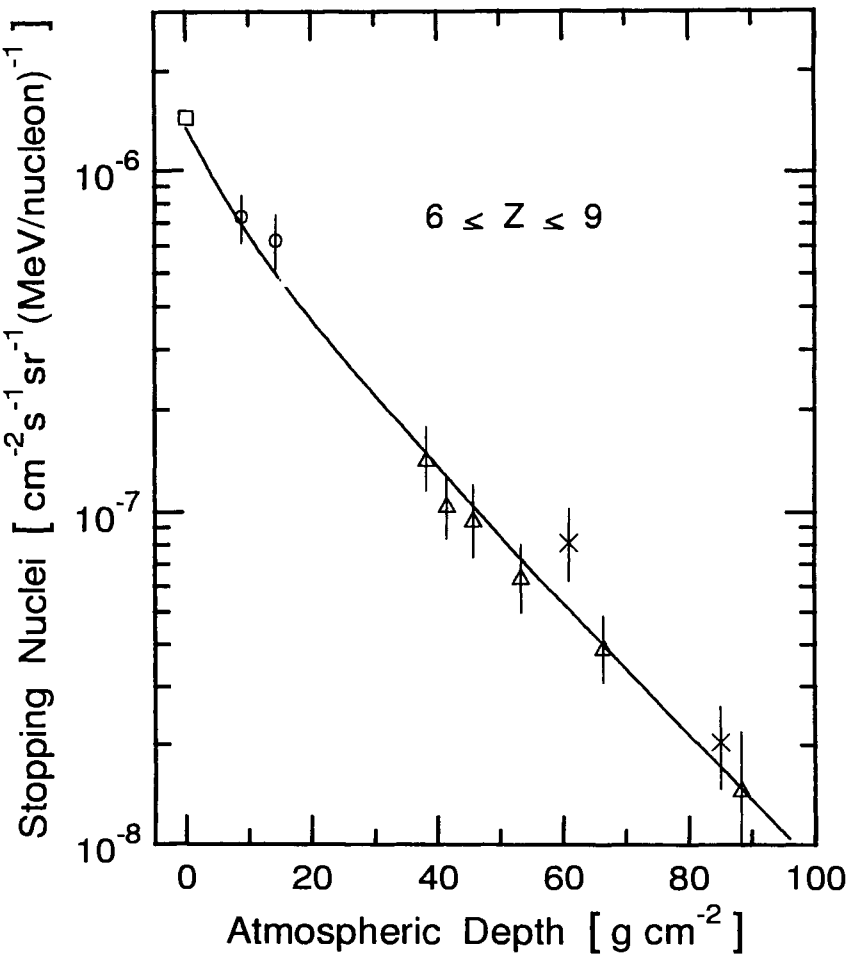

Figure 2.161: Differential intensity of stopping nuclei detected in nuclear emulsion for charges $6 \leq Z \leq 9$ (Fukui et al., 1969).

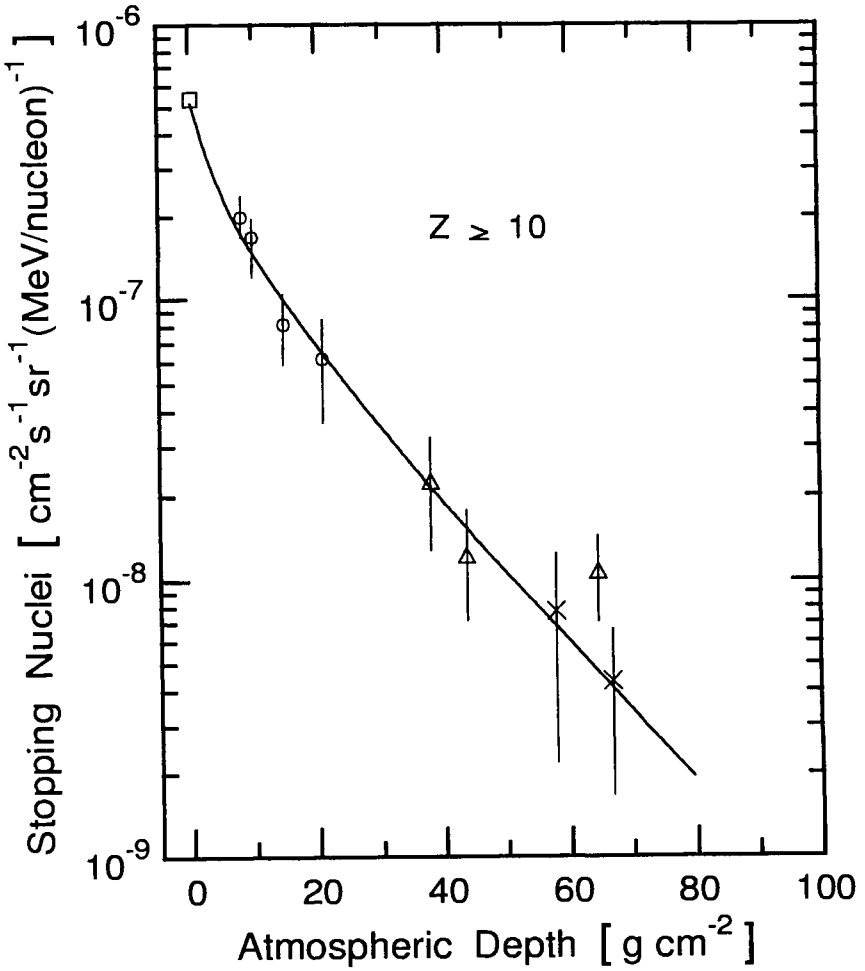

Figure 2.162: Differential intensity of stopping nuclei detected in nuclear emulsion for charges $Z \geq 10$ (Fukui et al., 1969).

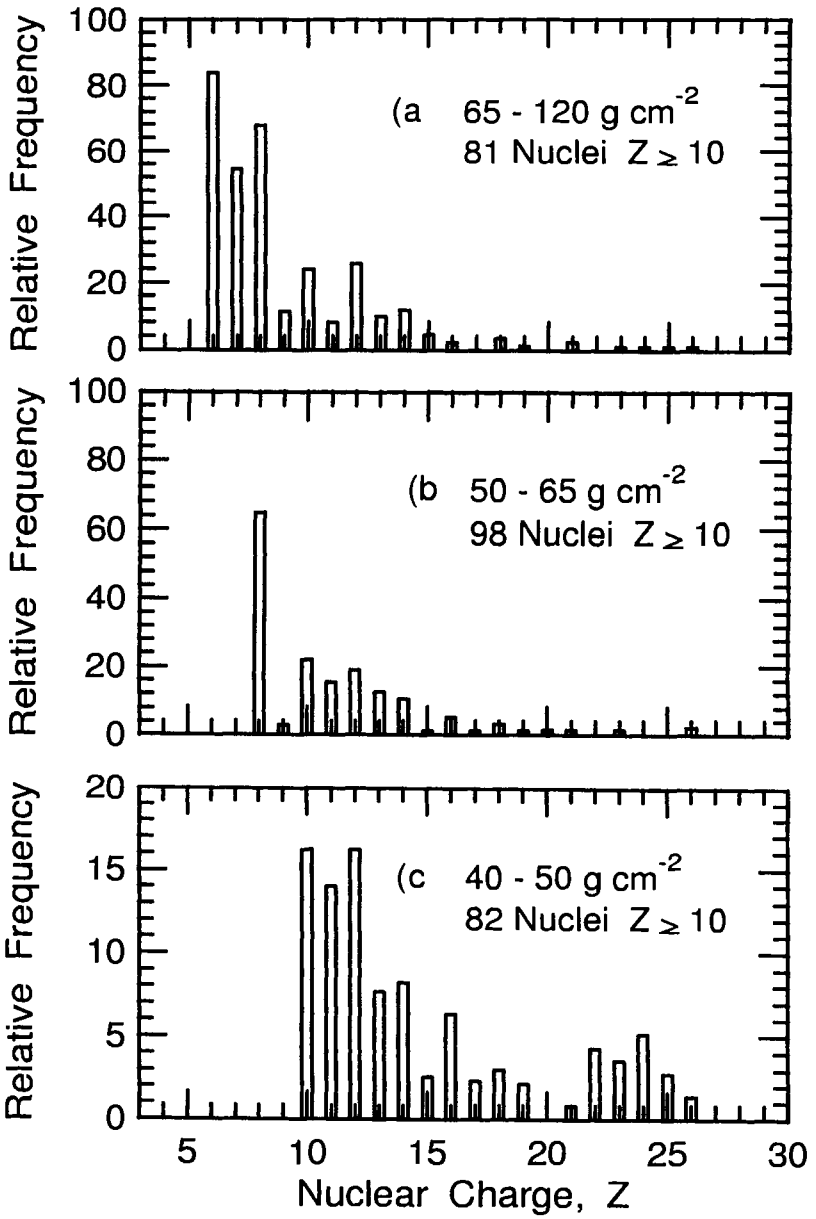

Figure 2.163: Charge spectra of heavy nuclei measured at three different atmospheric depths, as indicated: a) 65 – 120 g/cm^2, b) 50 – 65 g/cm^2, and c) 40 – 50 g/cm^2. The geomagnetic cutoff was 2.5 GV ($\simeq$625 MeV/nucleon) (Allkofer and Heinrich, 1974a).

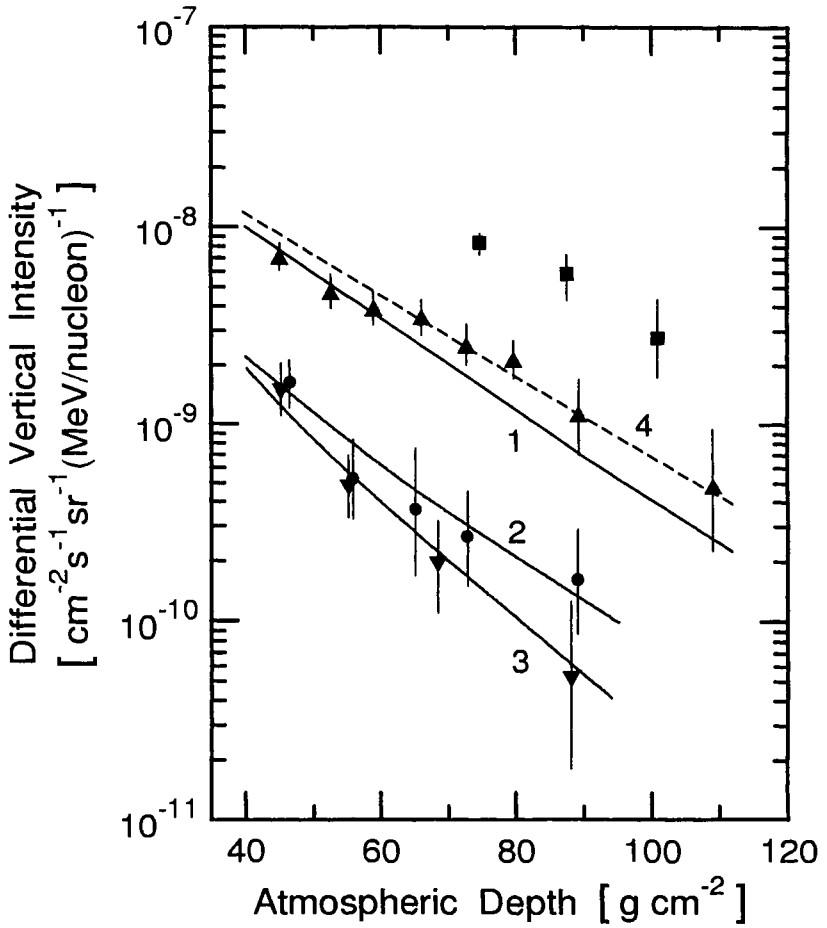

Figure 2.164: Measured and calculated differential vertical intensities of heavy nuclei as a function of atmospheric depth for $E \leq 500$ MeV/nucleus (Allkofer and Heinrich, 1974a). The solid and dashed lines are calculated intensities using different weighted mean values for the fragmentation probabilities.

■ M-group $(6 \leq Z \leq 9)$ | ▲ $H3$-group $(10 \leq Z \leq 14)$
• $H2$-group $(15 \leq Z \leq 19)$ | ▼ $H1$-group $(20 \leq Z \leq 28)$

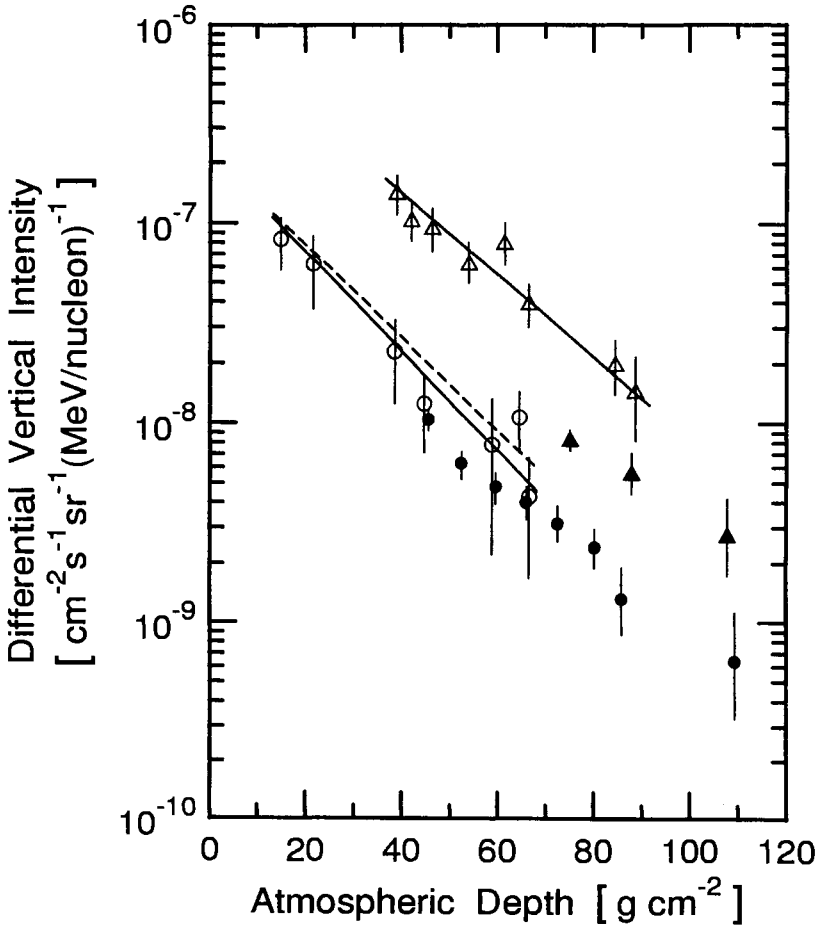

Figure 2.165: Comparison of the differential vertical flux of nuclei of the M- and H-groups as a function of atmospheric depth for $E \leq 500$ MeV/nucleus (Allkofer and Heinrich, 1974a). The solid and dashed lines are calculated intensities using different weighted mean values for the fragmentation probabilities.

M-group ($6 \leq Z \leq 9$)	H-group ($Z \geq 10$)
△ Fukui et al. (1969)	○ Fukui et al. (1969)
▲ Allkofer and Heinrich (1974a)	● Allkofer and Heinrich (1974a)

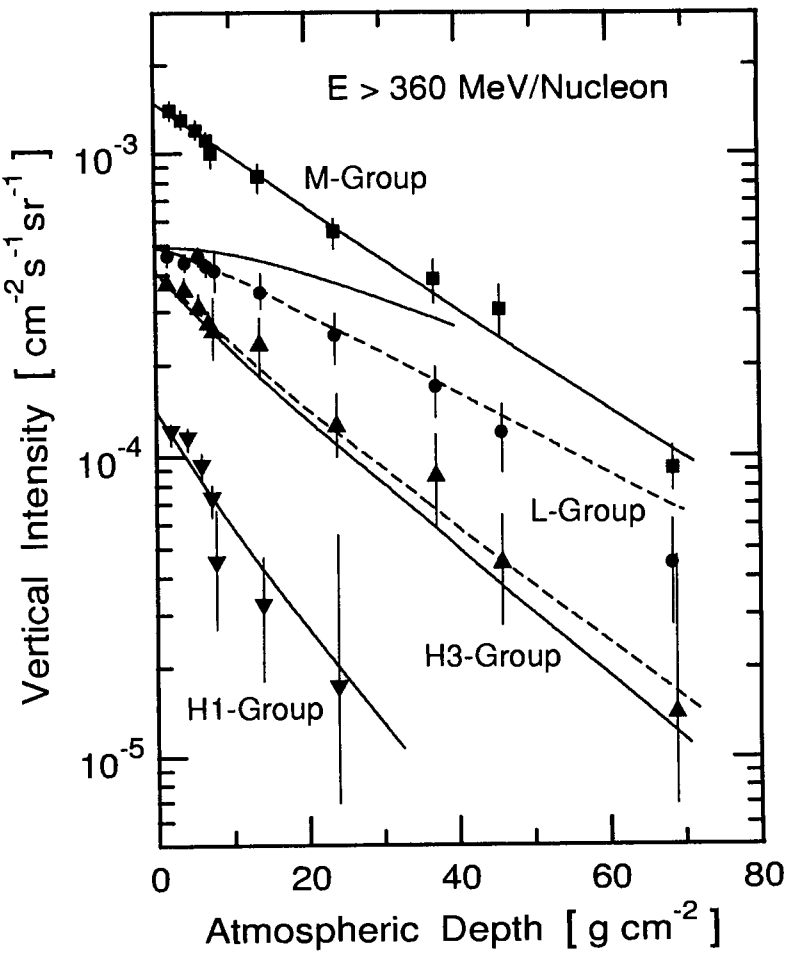

Figure 2.166: Integral vertical intensity of nuclei of different charge groups and $E \geq 360$ MeV/nucleus, as a function of atmospheric depth (Allkofer and Heinrich, 1974a). The charge groups included are: L-group $3 \leq Z \leq 5$, M-group $6 \leq Z \leq 9$, H3-group $10 \leq Z \leq 14$, and H1-group $20 \leq Z \leq 28$. The solid and dashed lines are calculated intensities using different weighted mean values for the fragmentation probabilities.

▼ , ▲ , ● , ■ Webber et al. (1967)
—— Allkofer and Heinrich (1974a), calculation
– – Allkofer and Heinrich (1974a), calculation

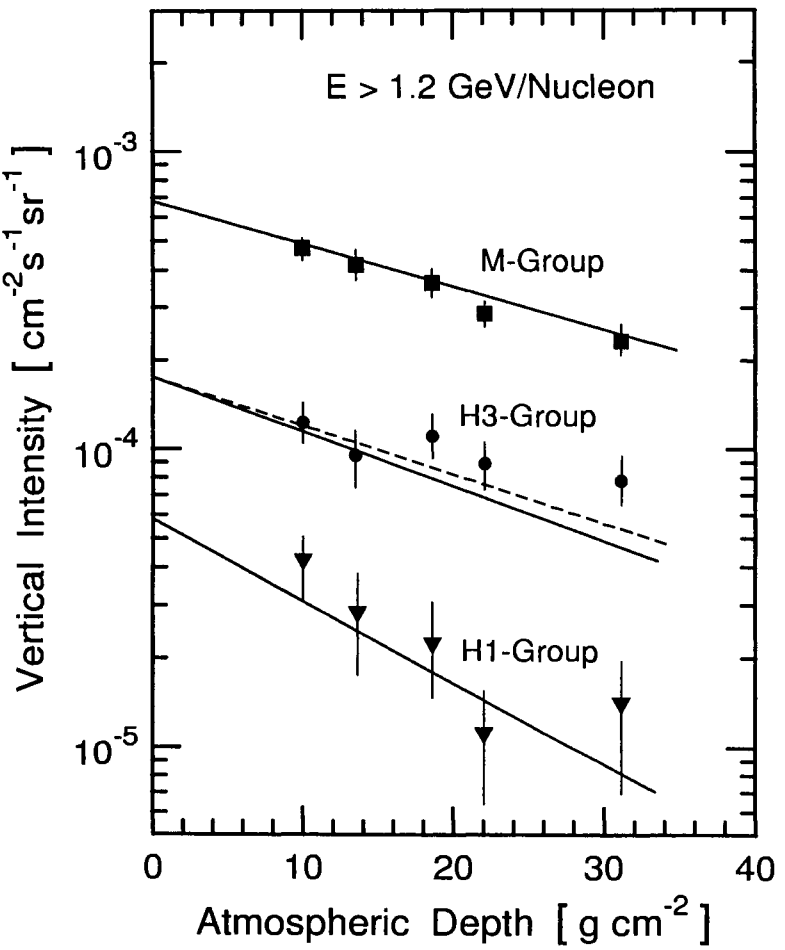

Figure 2.167: Integral vertical intensity of nuclei of different charge groups and $E \geq 1200$ MeV/nucleus, as a function of atmospheric depth (Allkofer and Heinrich, 1974a). The charge groups included are: M-group $6 \leq Z \leq 9$, H3-group $10 \leq Z \leq 14$, H1-group $20 \leq Z \leq 28$. The solid and dashed lines are calculated intensities using different weighted mean values for the fragmentation probabilities.

▼ , ● , ■ Daniel et al. (1962)
—— Allkofer and Heinrich (1974a), calculations
– – Allkofer and Heinrich (1974a), calculation

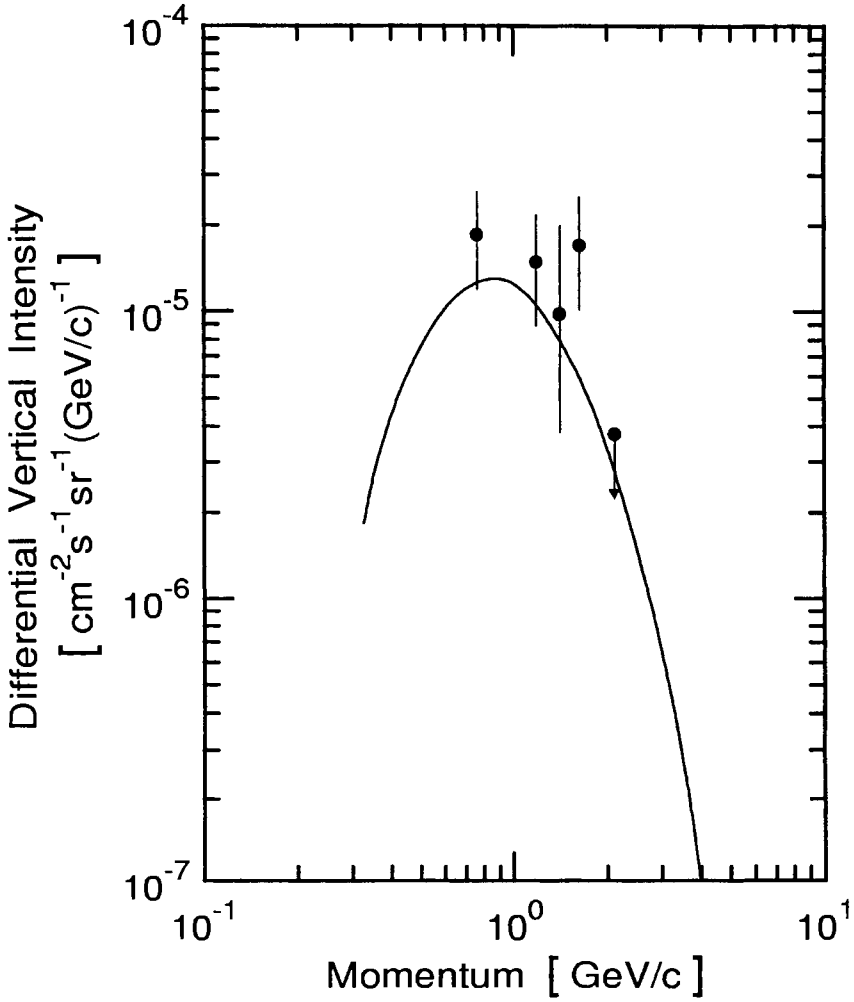

Figure 2.168: Deuteron vertical differential momentum spectrum at an atmospheric depth of 747 g/cm^2 (2750 m). The solid line is a theoretical spectrum (Barber et al., 1980).

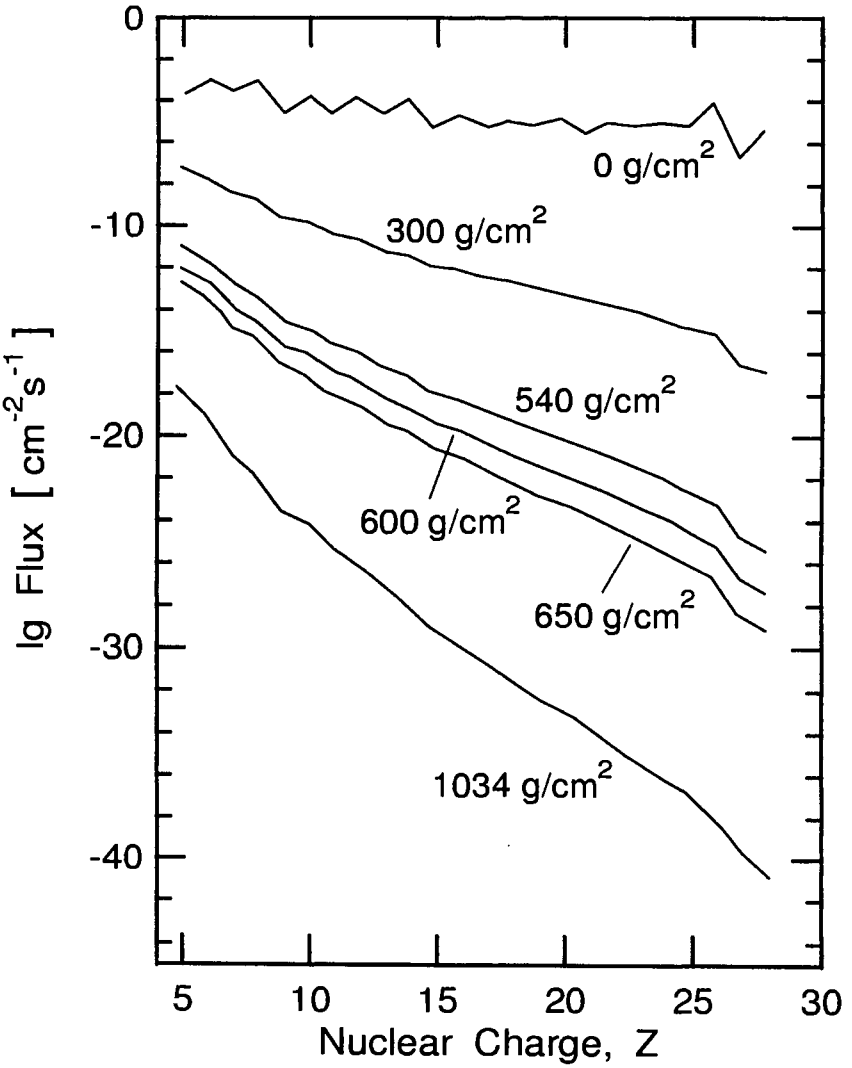

Figure 2.169: Calculated flux of energetic nuclei versus charge at top of atmosphere, and at depths of 300, 540, 600, 650 and 1034 g/cm^2 (Price et al., 1980).

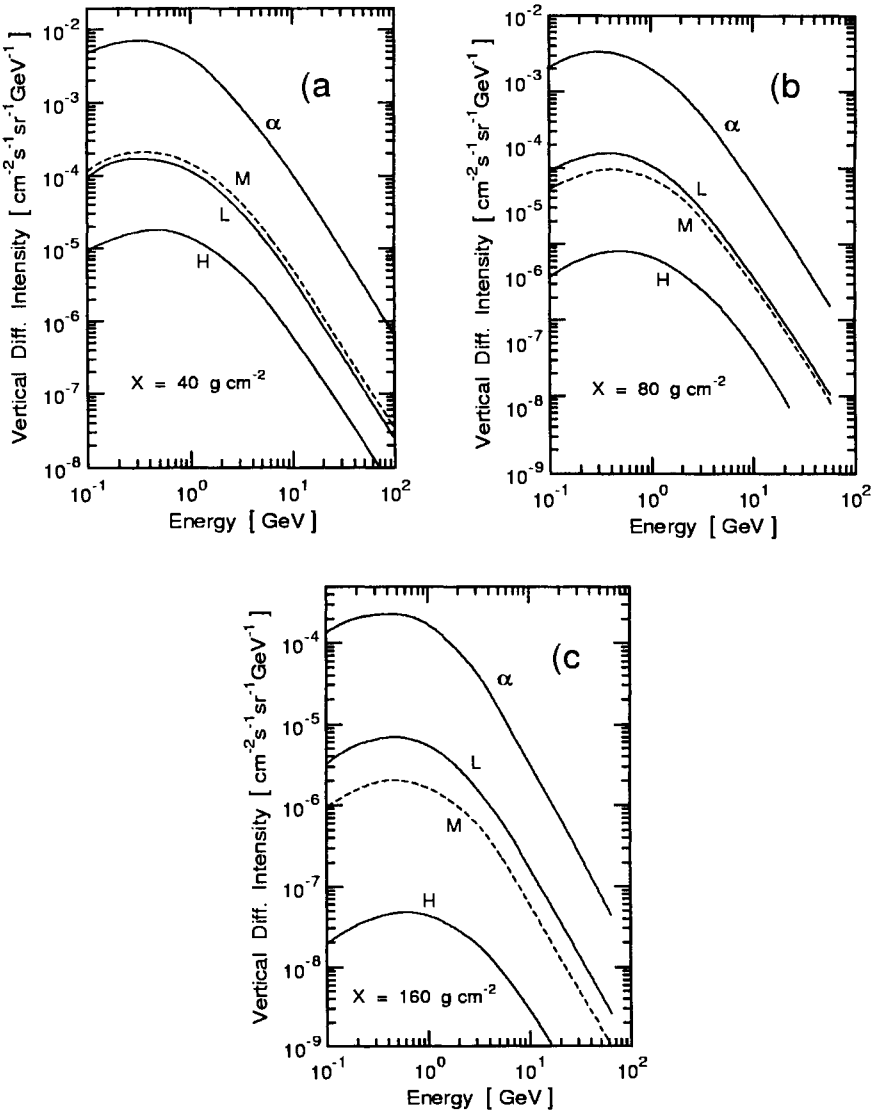

Figure 2.170: Calculated vertical differential energy spectra for different charge groups at atmospheric depths of 40, 80 and 160 g/cm^2, illustrated in graphs (a, (b and (c, respectively (Kolomeets et al., 1979).

α : α-particles	L-group: Li, Be, B
M-group: C, N, O, F	H-group: Ne to K

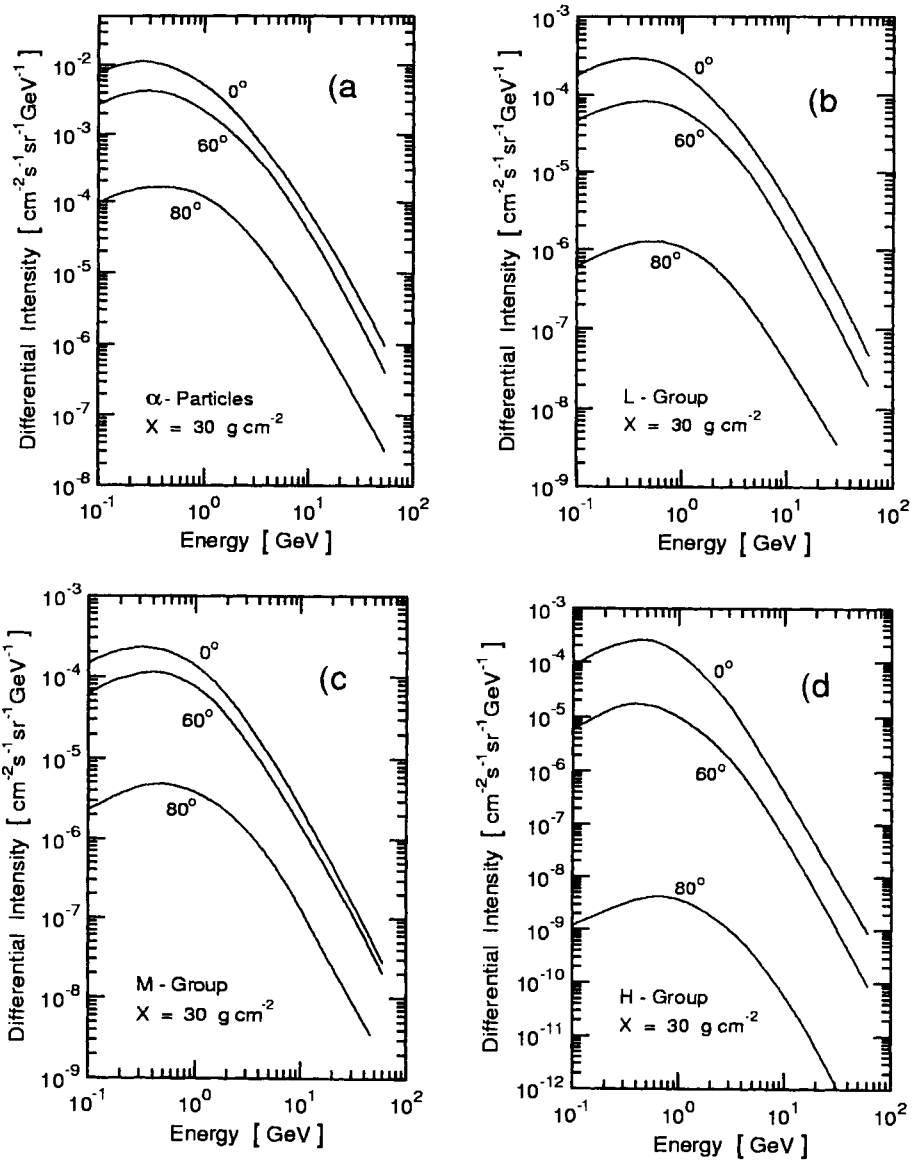

Figure 2.171: Calculated energy spectra of alpha particles and L-, M- and H-group particles at a depth of 30 g/cm^2 in the atmosphere, for different zenith angles, presented in graphs (a to (d, respectively (Kolomeets et al., 1979).

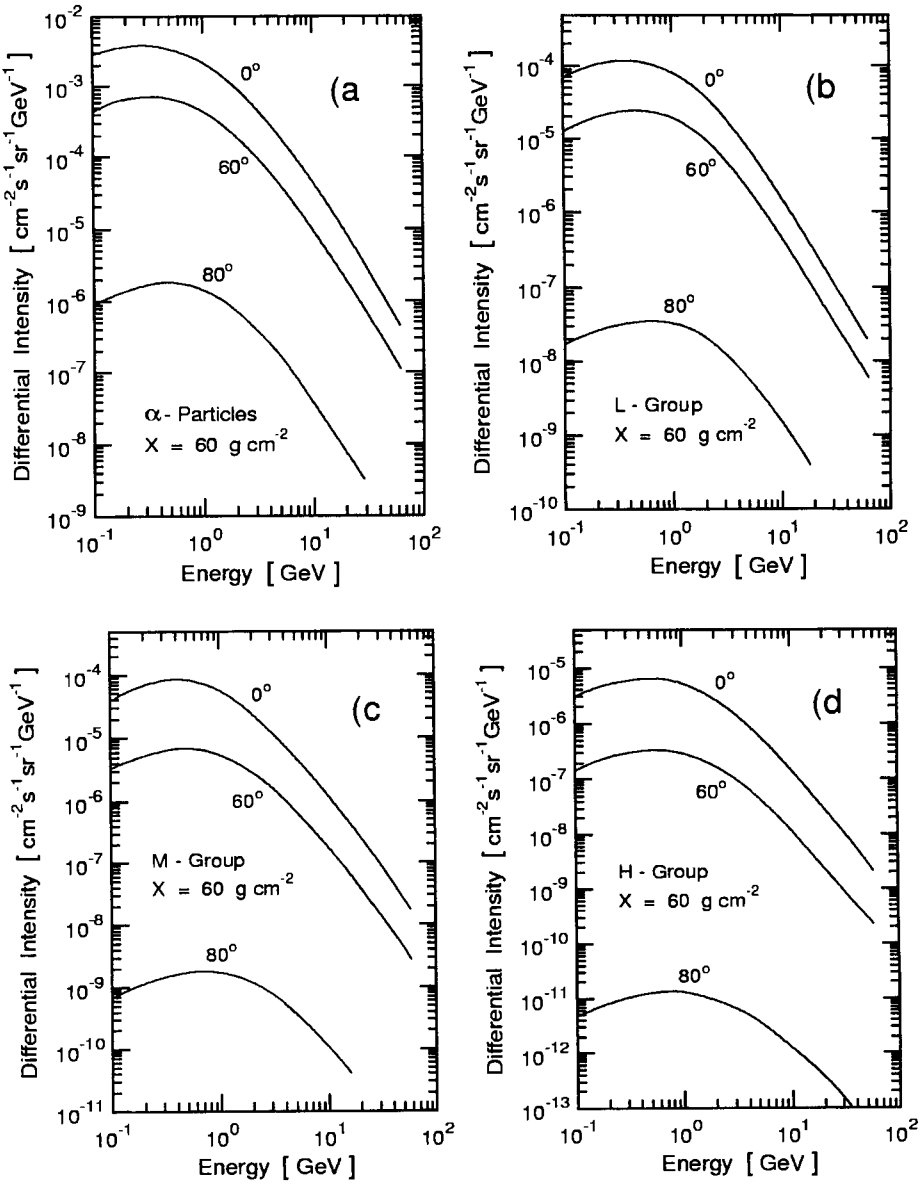

Figure 2.172: Calculated energy spectra of alpha particles and L-, M- and H-group particles at a depth of 60 g/cm^2 in the atmosphere, for different zenith angles, presented in graphs (a to (d, respectively (Kolomeets et al., 1979).

2.8 Antinucleons, Antinuclei

2.8.1 Introduction

Since the discovery of the antiproton ($\overline{p}$) at the Bevatron accelerator by Chamberlain et al. (1955), the existence of antinucleons in the cosmic radiation had been expected on theoretical grounds. Evidence for the existence of antiprotons in the primary cosmic radiation was delivered by Golden and collaborators in a balloon-borne experiment June 21-22, 1979, launched from Palestine, Texas (Golden et al., 1978, 1979a and 1979b). The instrument consisted of a superconducting magnet spectrometer combined with a gas Cherenkov detector, scintillators and high resolution multiwire proportional counters. The measurements were made under an average residual atmosphere of 5.4 g/cm^2. The geomagnetic cutoff during the flight varied from 4.55 GV/c to 5.55 GV/c and the data acquisition period lasted $2.84 \cdot 10^4$ s ($\simeq$7.89 hrs).

Figure 2.173 shows a plot of the number of observed particles as a function of magnetic deflection. This plot is typical for magnetic spectrometer measurements. Events to the right of zero deflection are positively charged and those on the left negative. Note that the scales of the ordinates on the left and right hand sides of the plot are different. On the extreme left of the plot one would expect negatively charged pions and muons of atmospheric origin which have a Lorentz factor below the imposed threshold of 23.6 (Golden et al., 1979b). The enhanced signal in the deflection region between -0.18 and -0.08 GV/c is attributed to antiprotons. To extract the primary flux of antiprotons above the geomagnetic threshold from the total of recorded $\overline{p}$ events, the number of atmospherically produced $\overline{p}$ must be subtracted.

Subsequent to the pioneering work of Golden and collaborators many more experiments were carried out to confirm the results of Golden, to improve the statistics and, above all, to determine the spectrum of the primary antiprotons. These topics are discussed in Chapter 5, Section 5.6 and modulation related effects in Chapter 6, Section 6.3.

2.8.2 Experimental Data

With the exception of balloon-borne experiments at the fringes of the atmosphere mentioned above that search for antiparticles in the primary cosmic radiation, almost no data exist on antiparticles of cosmic origin within the atmosphere. The reason for this lack of information is due to the fact that the detection of antinucleons ($\overline{N}$) in the atmosphere is extremely difficult,

particularly detection of antineutrons ($\overline{n}$).

But also the detection of antiprotons is impeded by a high level of background of negatively charged particles such as e^-, π^-, k^- and others, and a number of severe criteria must be applied to filter out the small fraction of antiprotons (e.g. Golden et al., 1978).

The overwhelming majority of all the antiprotons in the atmosphere are produced locally in high energy interactions of primary and secondary cosmic ray hadrons, mostly nucleons, with nucleons of nuclei of air constituents, chiefly nitrogen and oxygen. Extracting the small fraction of primary antiprotons from a sample of antiproton data in the atmosphere is an extremely difficult task and can only be done reliably for a data sample acquired near the fringes of the atmosphere where secondary production is small.

For reasons of baryon number conservation antinucleons are always produced in pairs. i.e.,

$$\begin{aligned} p+p &\rightarrow p+p+p+\overline{p}+\text{anything} \\ p+p &\rightarrow p+p+n+\overline{n}+\text{anything} \\ p+n &\rightarrow p+n+p+\overline{p}+\text{anything} \\ \pi^{\pm}+p &\rightarrow \pi^{\pm}+p+p+\overline{p}+\text{anything} \\ &\text{etc..} \end{aligned}$$

So far, only one direct measurement has been made at greater depth in the atmosphere, at an altitude of 2750 m (747 g/cm^2), using a spectrometer with a superconducting magnet in conjunction with a time-of-flight array (Barber et al. 1980). Two possible antiproton candidates were found. With a 90% confidence level the upper limit of the vertical differential intensity of antiprotons, $I_{\overline{p}}(p)$, at a depth of 747 g/cm^2 in the momentum range $0.19 \leq p \leq 0.92$ GeV/c is

$$I_{\overline{p}}(0.19 \leq p_{\overline{p}} \leq 0.92\text{GeV/c}) \;=\; 1.1 \cdot 10^{-5} \quad [\text{cm}^{-2}\text{s}^{-1}\text{sr}^{-1}(\text{GeV/c})^{-1}]\,. \quad (2.21)$$

2.8.3 Theoretical Studies and Expected Intensities

Starting with the primary cosmic ray spectrum and the production cross section for antinucleons in air, Barber et al. (1980) computed the differential momentum spectrum of antiprotons for momenta $\leq$ 10 GeV/c that is produced by the primary cosmic radiation at a depth of 747 g/cm^2 in the atmosphere. The result is shown in Fig. 2.174.

Similarly, with the aid of a more sophisticated Monte Carlo simulation Ding et al. (1979) calculated the flux of antiprotons and the ratios of antiprotons to negative pions, $\overline{p}/\pi^-$, and of antiprotons to protons, $\overline{p}/p$, for an altitude of 3200 m. The calculations have been made under three different assumptions for the average secondary particle multiplicity, $< n >$, and two different multiplicity distributions. These included: *a)* $< n > \propto E^{0.25}$ and a poissonian distribution, E being the energy in the laboratory frame of reference; *b)* $< n > \propto ln(s)$ and the KNO-distribution (Koba et al., 1972), s being the center of mass energy squared; and *c)* $< n > \propto E^{0.25}$ and the KNO-distribution, respectively. The results do not differ appreciably. For the third case the following results have been obtained:

$$I_{\overline{p}}(\leq 10\ GeV) = 2.87 \cdot 10^{-7} \quad [\mathrm{cm^{-2}s^{-1}sr^{-1}}] \tag{2.22}$$

$$N_{\overline{p}}/N_{\pi^-} = 0.050 \text{ for } E \geq 10 \text{ GeV} \tag{2.23}$$

$$N_{\overline{p}}/N_p = 0.081 \text{ for } E \geq 10 \text{ GeV} . \tag{2.24}$$

Other attempts to estimate the secondary antiproton spectrum in the atmosphere were made by Stephens (1981a and 1981b), Bowen and Moats (1986) and Pfeifer et al. (1993 and 1996), using the proton - proton collision characteristics. The results thus obtained were then scaled to account for the primary cosmic ray mass composition and the different atmospheric nuclear target masses. Further simplifying assumptions were made for the propagation of antinucleons in the atmosphere and it was also assumed that the target nucleon is at rest.

Recently, Stephens (1997) has carried out a far more detailed calculation of the intensity of the secondary antiproton component in the atmosphere. This was urgently needed in view of the fact that background uncertainties due to locally produced antiprotons are essentially the limiting factor determining the accuracy of any primary antiproton flux measurement with balloon-borne instruments at the fringes of the atmosphere.

In his calculation Stephens included among other refinements the Fermi motion of the target nucleons in nuclei of air constituents in the kinematics of the interactions for the production of antinucleons. This addition plays an important role in reducing the production threshold for $\overline{p}$ because of the increased center of mass energy that is available and enhances the production of low energy antiprotons.

The results of Stephens (1997) for the differential intensities of secondary antiprotons at shallow depths near the top of the atmosphere, at 3, 5 and 10 g/cm^2, for solar minimum and maximum are given in Tables 2.37 and 2.38. The same data are illustrated in Fig. 2.175 together with values at a residual atmosphere of 20 g/cm^2 and earlier results of Stephens (1981b) and Bowen and Moats (1986).

Secondary antiproton intensities for different depths across the atmosphere from 100 g/cm^2 down to sea level were also calculated by Stephens and are shown in Fig. 2.176. Stephens' spectrum at 700 g/cm^2 differs very significantly from the comparative spectrum of Barber et al. (1980) at low energies for reasons discussed above.

References

Barber, H.B., T. Bowen, D.A. Delise, E.W. Jenkins, J.J. Jones, R.M. Kalbach, and A.E. Pifer: Phys. Rev., D 22, p. 2667 (1980).

Bowen, T., and A. Moats: Phys. Rev., D 33, p. 651 (1986).

Chamberlain, Owen, Emilio Segrè, Clyde Wiegand, and Thomas Ypsilantis: Phys. Rev., 100, p. 947 (1955).

Ding, Ling-Kai, Qing-qi, Zhu: PICRC, 7, p. 95 (1979).

Golden, R.L., G.D. Badhwar, J.L. Lacy, and J.E. Zipse: Nucl. Instr. Meth., 148, p. 179 (1978).

Golden, R.L., S. Horan. B.G. Mauger, G.D. Badhwar, J.L. Lacy, S.A. Stephens, R.R. Daniel, and J.E. Zipse: PICRC, 12, p. 76 (1979a).

Golden, R.L., S. Horan. B.G. Mauger, G.D. Badhwar, J.L. Lacy, S.A. Stephens, R.R. Daniel, and J.E. Zipse: Phys. Rev. Lett., 43, p. 1196 (1979b).

Koba, Z., H.B. Nielsen and P. Olesen: Nucl. Phys. B, 40, p. 317 (1972).

Pfeifer, Ch., U. Heinbach, and M. Simon: PICRC, 2, p. 148 (1993).

Pfeifer, Ch., S. Roesler, and M. Simon: Phys. Rev., C, 54, p. 882 (1996).

Stephens, S.A.: PICRC, 2, p. 214 (1981a).

Stephens, S.A.: Astrophys. Space Sci., 76, p. 87 (1981b).

Stephens, S.A., and R.L. Golden: Space Sci. Rev., 46, p. 31 (1987).

Stephens, S.A.: Astropart. Phys., 6, p. 229 (1997).

Table 2.37: Secondary Antiproton Intensities in the Atmosphere at Solar Minimum. (Stephens 1997)

Kinetic Energy [GeV]	Intensity $[cm^{-2} s^{-1} sr^{-1} GeV^{-1}]$ Residual Atmosphere		
	3 g/cm^2	5 g/cm^2	10 g/cm^2
0.05	$1.231 \cdot 10^{-8}$	$2.993 \cdot 10^{-8}$	$9.461 \cdot 10^{-8}$
0.07	$1.363 \cdot 10^{-8}$	$3.347 \cdot 10^{-8}$	$1.086 \cdot 10^{-7}$
0.10	$1.579 \cdot 10^{-8}$	$3.382 \cdot 10^{-8}$	$1.248 \cdot 10^{-7}$
0.15	$2.110 \cdot 10^{-8}$	$4.778 \cdot 10^{-8}$	$1.494 \cdot 10^{-7}$
0.20	$2.907 \cdot 10^{-8}$	$6.108 \cdot 10^{-8}$	$1.777 \cdot 10^{-7}$
0.25	$3.982 \cdot 10^{-8}$	$7.872 \cdot 10^{-8}$	$2.118 \cdot 10^{-7}$
0.30	$5.300 \cdot 10^{-8}$	$1.002 \cdot 10^{-7}$	$2.530 \cdot 10^{-7}$
0.40	$8.546 \cdot 10^{-8}$	$1.528 \cdot 10^{-7}$	$3.518 \cdot 10^{-7}$
0.50	$1.228 \cdot 10^{-7}$	$2.131 \cdot 10^{-7}$	$4.628 \cdot 10^{-7}$
0.70	$2.023 \cdot 10^{-7}$	$3.407 \cdot 10^{-7}$	$6.948 \cdot 10^{-7}$
1.0	$3.091 \cdot 10^{-7}$	$5.112 \cdot 10^{-7}$	$1.001 \cdot 10^{-6}$
1.5	$4.191 \cdot 10^{-7}$	$6.876 \cdot 10^{-7}$	$1.322 \cdot 10^{-6}$
2.0	$4.502 \cdot 10^{-7}$	$7.365 \cdot 10^{-7}$	$1.406 \cdot 10^{-6}$
2.5	$4.342 \cdot 10^{-7}$	$7.095 \cdot 10^{-7}$	$1.351 \cdot 10^{-6}$
3.0	$3.962 \cdot 10^{-7}$	$6.471 \cdot 10^{-7}$	$1.230 \cdot 10^{-6}$
4.0	$3.079 \cdot 10^{-7}$	$5.028 \cdot 10^{-7}$	$9.553 \cdot 10^{-7}$
5.0	$2.328 \cdot 10^{-7}$	$3.801 \cdot 10^{-7}$	$7.222 \cdot 10^{-7}$
7.0	$1.367 \cdot 10^{-7}$	$2.233 \cdot 10^{-7}$	$4.247 \cdot 10^{-7}$
10	$7.022 \cdot 10^{-8}$	$1.148 \cdot 10^{-7}$	$2.185 \cdot 10^{-7}$
15	$3.014 \cdot 10^{-8}$	$4.928 \cdot 10^{-8}$	$9.396 \cdot 10^{-8}$
20	$1.585 \cdot 10^{-8}$	$2.585 \cdot 10^{-8}$	$4.932 \cdot 10^{-8}$
25	$9.372 \cdot 10^{-9}$	$1.533 \cdot 10^{-8}$	$2.927 \cdot 10^{-8}$
30	$6.045 \cdot 10^{-9}$	$9.891 \cdot 10^{-9}$	$1.889 \cdot 10^{-8}$
40	$2.972 \cdot 10^{-9}$	$4.864 \cdot 10^{-9}$	$9.294 \cdot 10^{-9}$
50	$1.691 \cdot 10^{-9}$	$2.768 \cdot 10^{-9}$	$5.291 \cdot 10^{-9}$
70	$7.110 \cdot 10^{-10}$	$1.164 \cdot 10^{-9}$	$2.226 \cdot 10^{-9}$
100	$2.789 \cdot 10^{-10}$	$4.566 \cdot 10^{-10}$	$8.737 \cdot 10^{-10}$
200	$4.377 \cdot 10^{-11}$	$7.168 \cdot 10^{-11}$	$1.372 \cdot 10^{-10}$

Table 2.38: Secondary Antiproton Intensities in the Atmosphere at Solar Maximum. (Stephens 1997)

Kinetic Energy [GeV]	Intensity $[cm^{-2} s^{-1} sr^{-1} GeV^{-1}]$ Residual Atmosphere		
	3 g/cm^2	5 g/cm^2	10 g/cm^2
0.05	$1.140 \cdot 10^{-8}$	$2.771 \cdot 10^{-8}$	$8.765 \cdot 10^{-8}$
0.07	$1.261 \cdot 10^{-8}$	$3.099 \cdot 10^{-8}$	$1.006 \cdot 10^{-7}$
0.10	$1.460 \cdot 10^{-8}$	$3.536 \cdot 10^{-8}$	$1.155 \cdot 10^{-7}$
0.15	$1.946 \cdot 10^{-8}$	$4.413 \cdot 10^{-8}$	$1.381 \cdot 10^{-7}$
0.20	$2.676 \cdot 10^{-8}$	$5.629 \cdot 10^{-8}$	$1.636 \cdot 10^{-7}$
0.25	$3.657 \cdot 10^{-8}$	$7.240 \cdot 10^{-8}$	$1.953 \cdot 10^{-7}$
0.30	$4.859 \cdot 10^{-8}$	$9.199 \cdot 10^{-8}$	$2.329 \cdot 10^{-7}$
0.40	$7.817 \cdot 10^{-8}$	$1.400 \cdot 10^{-7}$	$3.229 \cdot 10^{-7}$
0.50	$1.122 \cdot 10^{-7}$	$1.949 \cdot 10^{-7}$	$4.241 \cdot 10^{-7}$
0.70	$1.846 \cdot 10^{-7}$	$3.110 \cdot 10^{-7}$	$6.354 \cdot 10^{-7}$
1.0	$2.820 \cdot 10^{-7}$	$4.666 \cdot 10^{-7}$	$9.153 \cdot 10^{-7}$
1.5	$3.832 \cdot 10^{-7}$	$6.290 \cdot 10^{-7}$	$1.210 \cdot 10^{-6}$
2.0	$4.132 \cdot 10^{-7}$	$6.762 \cdot 10^{-7}$	$1.292 \cdot 10^{-6}$
2.5	$4.003 \cdot 10^{-7}$	$6.543 \cdot 10^{-7}$	$1.246 \cdot 10^{-6}$
3.0	$3.669 \cdot 10^{-7}$	$5.994 \cdot 10^{-7}$	$1.140 \cdot 10^{-6}$
4.0	$2.881 \cdot 10^{-7}$	$4.704 \cdot 10^{-7}$	$8.942 \cdot 10^{-7}$
5.0	$2.194 \cdot 10^{-7}$	$3.583 \cdot 10^{-7}$	$6.812 \cdot 10^{-7}$
7.0	$1.306 \cdot 10^{-7}$	$2.133 \cdot 10^{-7}$	$4.058 \cdot 10^{-7}$
10	$6.785 \cdot 10^{-8}$	$1.109 \cdot 10^{-7}$	$2.112 \cdot 10^{-7}$
15	$2.942 \cdot 10^{-8}$	$4.810 \cdot 10^{-8}$	$9.172 \cdot 10^{-8}$
20	$1.551 \cdot 10^{-8}$	$2.537 \cdot 10^{-8}$	$4.841 \cdot 10^{-8}$
25	$9.226 \cdot 10^{-9}$	$1.509 \cdot 10^{-8}$	$2.882 \cdot 10^{-8}$
30	$5.964 \cdot 10^{-9}$	$9.758 \cdot 10^{-9}$	$1.864 \cdot 10^{-8}$
40	$2.939 \cdot 10^{-9}$	$4.811 \cdot 10^{-9}$	$9.193 \cdot 10^{-9}$
50	$1.675 \cdot 10^{-9}$	$2.742 \cdot 10^{-9}$	$5.241 \cdot 10^{-9}$
70	$7.056 \cdot 10^{-10}$	$1.155 \cdot 10^{-9}$	$2.209 \cdot 10^{-9}$
100	$2.771 \cdot 10^{-10}$	$4.537 \cdot 10^{-10}$	$8.681 \cdot 10^{-10}$
200	$4.356 \cdot 10^{-11}$	$7.134 \cdot 10^{-11}$	$1.366 \cdot 10^{-10}$

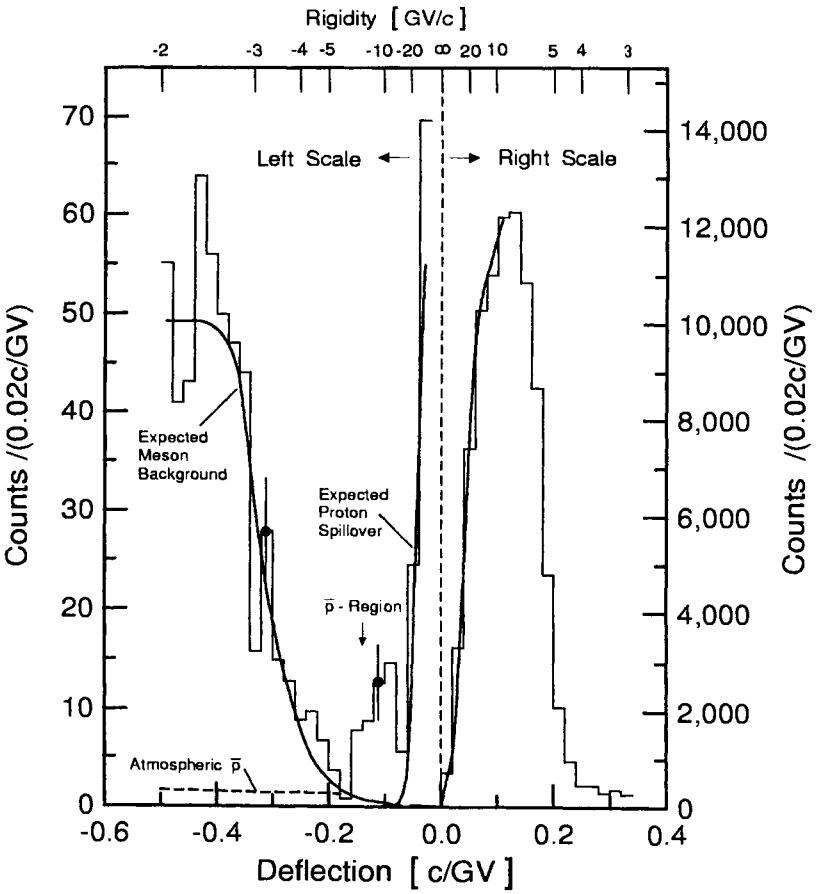

Figure 2.173: Number of observed particles as a function of magnetic deflection. The proton spill-over marked on the negative deflection side is the extension of the scaled up version of the proton deflection spectrum shown on the positive side (Stephens and Golden, 1987).

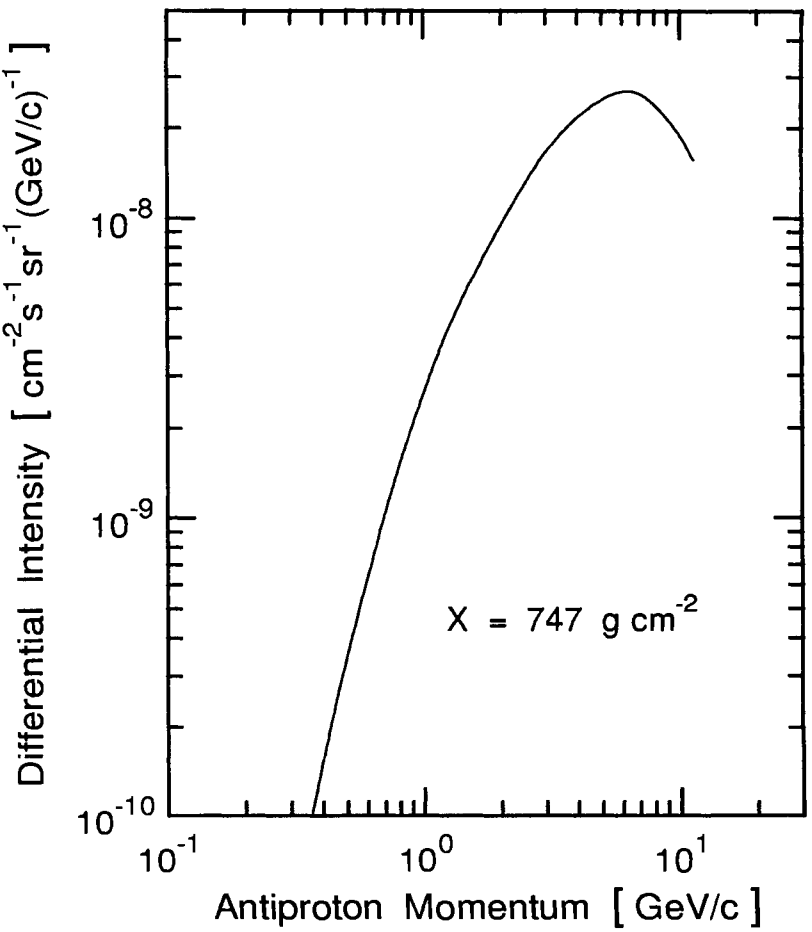

Figure 2.174: Predicted differential momentum spectrum for antiprotons at an atmospheric depth of 747 g/cm^2 (Barber et al., 1980).

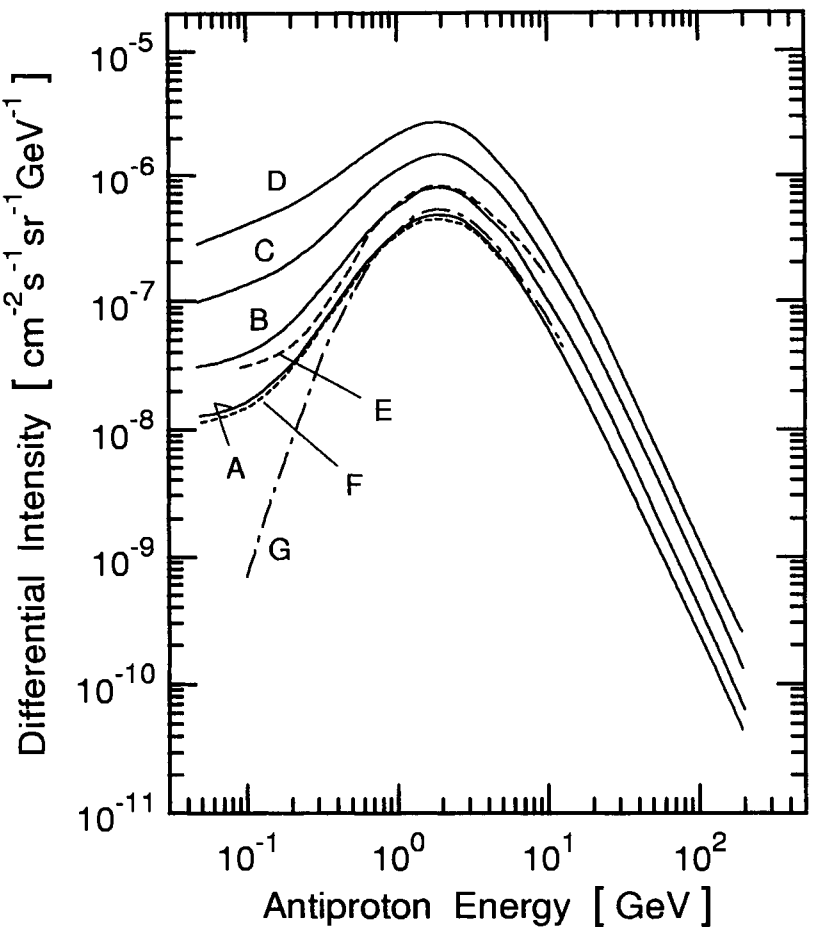

Figure 2.175: Theoretical differential energy spectra of secondary antiprotons at very shallow depths in the atmosphere produced by cosmic rays for the solar minimum period (curves A to D) and for solar maximum (curve F) (Stephens, 1997). Also shown are the results of calculations by Bowen and Moats (1986), curve E, and Stephens (1981), curve G.

A	3 g/cm^2	B	5 g/cm^2
C	10 g/cm^2	D	20 g/cm^2
E	5 g/cm^2	F	3 g/cm^2
G	3 g/cm^2		

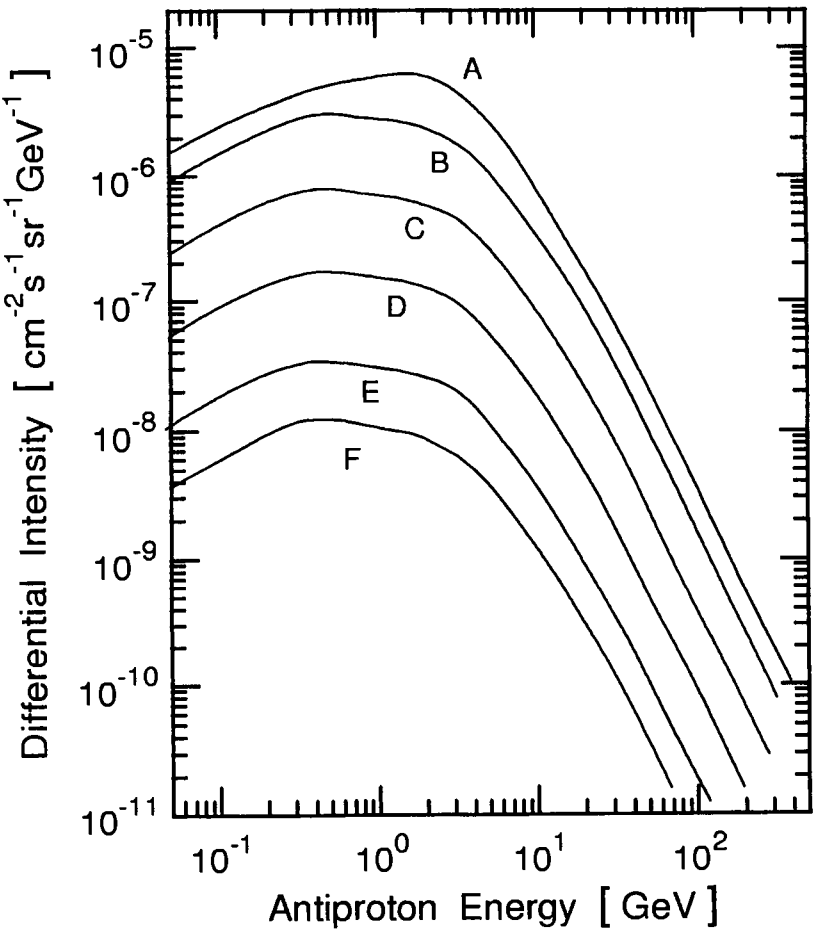

Figure 2.176: Theoretical differential energy spectra of secondary antiprotons at different depths in the atmosphere produced by cosmic rays (Stephens, 1997).

A	100 g/cm^2	B	300 g/cm^2
C	500 g/cm^2	D	700 g/cm^2
E	900 g/cm^2	F	1030 g/cm^2

This Page Intentionally Left Blank

Chapter 3

Cosmic Rays at Sea Level

3.1 Introduction

The interaction processes of the primary cosmic radiation in the atmosphere lead to different secondary particle components which have been described in Chapter1. Due to the specific interaction mechanisms to which the various particle types are subjected, the attenuation of their fluxes along their way through the atmosphere is different. Another important aspect is the mean life of unstable particles. Although they are mostly relativistic and experience a prolonged lifetime due to time dilation, the probability of surviving from the point of production to sea level depends on the particle type, its charge state, energy, zenith angle of propagation and mean life at rest.

Energetic protons and neutrons lose energy mostly by strong interactions, heavy nuclei are fragmented in collisions with nuclei of air molecules, and electrons and photons undergo electromagnetic energy loss processes. In addition all charged particles are subject to ionization losses. Particles with mean lives shorter than 10^{-12} s have almost no chance at all to survive down to sea level unless they are locally produced. Muons with a mean life of $2.2 \cdot 10^{-6}$ s at rest survive to great atmospheric depths, provided they are adequately energetic. There they represent the bulk of charged particles.

Another important component are neutrinos of all kinds. However, because of their small cross section and weak interaction behavior, and because of major background problems, no cosmic ray neutrino experiments have been carried out in the atmosphere or at sea level. Since the neutrino flux is not significantly different underground as compared to sea level, the neutrino component is studied exclusively deep underground, underwater or under ice to insure sufficient shielding and adequate background reduction. Because of the different nature of the problems involved we discuss atmospheric neu-

trinos in Chapter 4, Section 4.5, astrophysical neutrinos, i.e., neutrinos from supernovae or of cosmic origin, in Chapter 5, Section 5.5, and solar neutrinos in Chapter 6, Section 6.6.

In the following we are presenting the data of cosmic ray particles at sea level. These include charged hadrons, neutrons, gamma rays, electrons, muons, nuclei and antinucleons. The material is presented in this sequence. Even though the flux of nuclei at sea level is almost nonexistent compared to higher altitudes, as discussed in Chapter 2, a separate section is devoted to this subject to summarize the scant information, mostly of theoretical nature, that is available. Some comments and references on antinucleons are also given. The topic of *cosmogenic nuclei*, i.e., of isotopes that are produced by the cosmic radiation in the atmosphere and in the Earth's crust, is discussed in connection with questions that are related to the constancy of the cosmic radiation in Chapter 6, Section 6.3 and mostly in Chapter 7, Section 7.2 . A comprehensive review of the different particle components at ground level has been given in the book, Cosmic Rays at Ground Level, edited by A. W. Wolfendale (1973) (see also Allkofer, 1975).

References

Allkofer, O.C.: Introduction to Cosmic Radiation, Thiemig Verlag, München (1975).

Wolfendale, A.W., ed.: Cosmic Rays at Ground Level, The Institute of Physics, London (1973).

3.2 Charged Hadrons

3.2.1 Flux Measurements and Intensities

Since the rate of ionization losses of a singly charged particle in any given medium is a function of the velocity of the particle only, the low energy spectrum of protons can be obtained by observing the rates of particles that are stopped in absorbers of suitable thickness. This method has been used in many experiments. In general proton momenta have been measured either with magnetic spectrometers or by comparing their rates of ionization losses and their ranges. Table 3.1 and Fig. 3.1 summarize the early proton intensity measurements at low momenta (Brooke, 1973).

3.2.2 Momentum and Energy Spectra

At low energies the proton spectrum has been investigated with magnetic spectrometers in conjunction with neutron monitors. Positively charged nuclear active particles have been identified as protons and positive pions, negatively charged as negative pions. There is also a small calculable contribution of positive and negative kaons and some few misidentified muons in both charge channels. A survey has been given by Brooke (1973).

In the momentum range $0.3 \leq p \leq 80$ GeV/c data have been obtained by Meshkovskii and Sokolov (1958), Brooke and Wolfendale (1964) and by Diggory et al. (1974). Fig. 3.2 shows the results together with Monte Carlo data by Barber et al. (1980). The differential intensities of single protons obtained in early measurements by Brooke and Wolfendale (1964) are given in Table 3.2 and the more recent results of Diggory et al. (1974) in Table 3.3.

It should be noted that the data of Brooke and Wolfendale (1964) shown in Table 3.1 have been normalized to the absolute muon intensity given by Ashton et al. (1972) whereas the data in Table 3.2 are normalized to the integral intensity of 1 GeV/c muons obtained by Rossi (1948). On the other hand, the data of Diggory et al. (1974) are normalized to the intensity given by Allkofer et al. (1970a, 1971a and 1971b). The latter is about 26% larger than the Rossi intensity. Thus, to compare the data of Diggory et al. with those of Brooke and Wolfendale shown in Table 3.2 the latter should be raised by 26%.

The proton momentum spectrum in the range $1 \leq p \leq 100$ GeV/c is shown in Fig. 3.3 (Brooke, 1973). Above 5 GeV/c the differential spectrum can be represented by a power law , i.e., $j(E) \propto E^{-\gamma}$. The exponent, γ, of

Table 3.1: Low Momentum Vertical Proton Intensities.
(Brooke 1973)

Observer	Momentum Interval [MeV/c]	Intensity $\times 10^8$ $\left[\left(\text{cm}^2\,\text{s}\,\text{sr}\,\frac{\text{MeV}}{\text{c}}\right)^{-1}\right]$
Rochester and Bound(1940)*	340 – 400	15 ± 6
Merkle et al. (1950)	480 – 880	23 ± 3
Goldwasser and Merkle (1951)	780 – 1100	20 ± 5
Mylroi and Wilson (1951)*	530 – 710	21.8 ± 5.7
	710 – 930	11.6 ± 2.1
	930 – 1350	7.1 ± 1.2
	1500	5.6 ± 1.0
	2000	2.7 ± 0.6
York (1952b)	550 – 750	28 ± 3
	750 – 880	$10.7 \pm 0\ 8$
Ballam and Lichtenstein (1954)	757 – 842	13.5 ± 4.3
	842 – 983	12.4 ± 2.6
	983 – 1105	13.3 ± 3.2
	1105 – 1217	10.0 ± 3.4
Rosen (1954)	590 – 770	9.1 ± 1.9
	770 – 930	$12.1 \pm 2\ 3$
Filthuth (1955)	180 – 210	2.2 ± 0.3
	210 – 236	$3.7\ ^{+0.4}_{-1.1}$
	236 – 260	$3.3\ ^{+0.4}_{-0.8}$
	275 – 312	6.5 ± 0.5
	332 – 358	8.0 ± 1
	432 – 446	8.3 ± 1
	456 – 469	11 ± 1
	615	10 ± 1
	730	8.4 ± 1
	887	4.8 ± 1

* Re-normalized using the absolute muon intensity given by Ashton et al. (1972).

this spectrum is 2.9.

In the high energy region spectra have been obtained by Ashton and Saleh (1975a and 1975b), Babecki et al. (1961) and Siohan et al. (1977).

Table 3.1: Low Momentum Vertical Proton Intensities (continued). (Brooke 1973)

Observer	Momentum Interval [MeV/c]	Intensity $\times 10^8$ $\left[\left(\text{cm}^2\,\text{s}\,\text{sr}\,\frac{\text{MeV}}{\text{c}}\right)^{-1}\right]$
Ogilvie (1955)	590 – 700	14 ± 4
	700 – 1100	7.8 ± 1
	850 – 1240	6.5 ± 0.5
	950 – 1300	6.0 ± 0.7
	1050 – 1400	5.5 ± 0 7
McDiarmid (1959)	716 – 739	24 ± 3
	739 – 828	13 ± 1
Brooke and Wolfendale (1964)*	740	20.3 ± 3.7
	1030	10.5 ± 0.94
	1530	3.65 ± 0.38
	2120	2.37 ± 0.21
Hook and Turver (1972) (unpublished)	1000	6.0 ± 0.24
	2000	2.4 ± 0.22

* Re-normalized using the absolute muon intensity given by Ashton et al. (1972).

The latter used an ionization calorimeter located at an atmospheric depth of 960 g/cm^2. With this apparatus three categories of energy spectra have been obtained:

a) Single unaccompanied hadrons.

b) Associated single hadrons, i.e., single hadrons which are accompanied by one or more parallel tracks in the calorimeter which do not produce a cascade. These can be shower electrons or very low energy hadrons.

c) Associated multiple hadrons, i.e., events with two or more interacting hadrons.

Fig. 3.4 shows the integral energy spectrum in the range $500 \leq E \leq 10^4$ GeV for singly charged hadrons, all charged hadrons and gives an upper limit for all hadrons (including neutrons). A least squares fit to a power law spectrum yields the following expression for the differential spectrum in the energy range $250 \leq E \leq 1200$ GeV.

Table 3.2: Differential Intensities of Protons at Sea Level and Proton to Muon Ratio from four Experiments Combined. (Brooke and Wolfendale, 1964)

Momentum [GeV/c]	Intensity* $[\mathrm{cm}^{-2}\mathrm{s}^{-1}\mathrm{sr}^{-1}(\mathrm{MeV/c})^{-1}]$	$p/\mu^{\pm}$ [%]
0.75	$(1.50 \pm 0.28) \cdot 10^{-7}$	5.44 ± 1.01
1.03	$(8.40 \pm 0.75) \cdot 10^{-8}$	3.45 ± 0.31
1.53	$(2.85 \pm 0.30) \cdot 10^{-8}$	1.51 ± 0.16
2.12	$(2.26 \pm 0.20) \cdot 10^{-8}$	1.64 ± 0.15
2.94	$(7.64 \pm 0.88) \cdot 10^{-9}$	0.848 ± 0.098
4.60	$(3.40 \pm 0.36) \cdot 10^{-9}$	0.772 ± 0.082
6.16	$(1.40 \pm 0.46) \cdot 10^{-9}$	0.53 ± 0.17
10.3	$(4.6 \pm 1.2) \cdot 10^{-10}$	0.48 ± 0.12
18.0	$(1.17 \pm 0.47) \cdot 10^{-10}$	0.44 ± 0.18
27.5	$(2.95 \pm 0.94) \cdot 10^{-11}$	0.32 ± 0.10
79.0	$(2.3 \pm 1.4) \cdot 10^{-12}$	0.50 ± 0.31

* Normalized using the absolute muon intensity given by Rossi (1948).

Table 3.3: Differential Intensities of Low Energy Protons at Sea Level. (Diggory et al. 1974)

Proton Momentum [GeV/c]	Intensity $[\mathrm{cm}^{-2}\mathrm{s}^{-1}\mathrm{sr}^{-1}(\mathrm{GeV/c})^{-1}]$
1	$(7.45^{+0.10}_{-0.18}) \cdot 10^{-5}$
2	$(2.37^{+0.5}_{-0.3}) \cdot 10^{-5}$
3	$(1.22^{+0.2}_{-0.3}) \cdot 10^{-5}$
5	$(5.31 \pm 0.18) \cdot 10^{-6}$
7	$(1.66 \pm 0.09) \cdot 10^{-6}$
10	$(3.76 \pm 0.30) \cdot 10^{-7}$
20	$(9.27^{+0.78}_{-1.31}) \cdot 10^{-8}$

$$j(E) = (3.0 \pm 0.5) \cdot 10^{-11} \left(\frac{E[\mathrm{GeV}]}{300} \right)^{-3.05 \pm 0.4} \quad [\mathrm{cm}^{-2}\mathrm{s}^{-1}\mathrm{sr}^{-1}\mathrm{GeV}^{-1}] \,. \quad (3.1)$$

The corresponding integral energy spectrum can be fitted by

$$J(>E) = (4.4 \pm 0.7) \cdot 10^{-9} \left(\frac{E[\mathrm{GeV}]}{300} \right)^{-2.05 \pm 0.4} \quad [\mathrm{cm}^{-2}\mathrm{s}^{-1}\mathrm{sr}^{-1}] \,. \quad (3.2)$$

A least squares fit to the differential spectrum of all hadrons in the energy range $300 \leq E \leq 1700$ GeV leads to

$$j(E) = (1.0 \pm 0.15) \cdot 10^{-10} \left(\frac{E[\mathrm{GeV}]}{300} \right)^{-2.6 \pm 0.3} \quad [\mathrm{cm}^{-2}\mathrm{s}^{-1}\mathrm{sr}^{-1}\mathrm{GeV}^{-1}] \,. \quad (3.3)$$

An integral spectrum point was obtained for energies ≥ 2000 GeV:

$$I(>2000\ \mathrm{GeV}) = (1.4 \pm 0.7) \cdot 10^{-10} \quad [\mathrm{cm}^{-2}\mathrm{s}^{-1}\mathrm{sr}^{-1}] \,. \quad (3.4)$$

Fig. 3.5 shows a comparison of the results obtained by Siohan et al. (1977), Babecki et al. (1961) and Ashton and Saleh (1975a and 1975b).

Recent Spectral Measurements

A relatively new measurement of the unaccompanied hadron spectrum was made by the Kascade team with their unique calorimeter essentially at sea level (110 m) (Mielke et al., 1994; Klages et al., 1997 and Schatz et al., 1998). The results of this work are given in Table 3.4 and plotted in Fig. 3.6. This figure includes a compilation of hadron spectral measurements from other experiments made by the same authors.

3.2.3 Zenith Angle Dependence

There exist no experimental proton energy spectra for different zenith angles. Theoretical data for mean solar activity and rigidities of 4.4 GV and 15 GV are presented in Tables 3.5 and 3.6, respectively (Flückiger, 1977). Fig. 3.7 shows the calculated angular dependence together with curves given by Bel'skii and Romanov(1966) and by Lohrmann (1955) as shown by Flückiger (1977).

3.2.4 Charged Pions

Energy spectra of charged pions have been obtained by Brooke and Wolfendale (1964), Diggory et al. (1974), Ashton and Saleh (1975a, 1975b), Cowan and Mathews (1971), Baruch et al. (1973), and by Dmitriev (1960). Table 3.7

Table 3.4: Single Hadron Intensities Measured at 110 m a.s.l. The errors are statistical only. A systematic uncertainty of 20% below 1 TeV and of 30% in the TeV region has to be added (Mielke et al., 1994).

Mean Energy [GeV]	Energy Range [GeV]	Hadron Number	Hadron Flux $[m^2 s^{-1} sr^{-1} GeV^{-1}]$
4.1	3.2 - 5.6	902	$(6.1 \pm 0.20) \cdot 10^{-2}$
7.2	5.6 - 10	5170	$(1.7 \pm 0.03) \cdot 10^{-2}$
1.3	1.0 - 18	7335	$(4.8 \pm 0.06) \cdot 10^{-3}$
23	1.8 - 32	8365	$(9.8 \pm 0.10) \cdot 10^{-4}$
41	32 - 56	9420	$(2.0 \pm 0.02) \cdot 10^{-4}$
72	56 - 100	7840	$(3.9 \pm 0.05) \cdot 10^{-5}$
129	100 - 178	4595	$(7.7 \pm 0.11) \cdot 10^{-6}$
229	178 - 316	1980	$(1.4 \pm 0.03) \cdot 10^{-6}$
407	316 - 562	853	$(3.2 \pm 0.11) \cdot 10^{-7}$
724	561 - 1000	361	$(7.4 \pm 0.40) \cdot 10^{-8}$
1290	1000 - 1780	122	$(1.4 \pm 0.13) \cdot 10^{-8}$
2290	1780 - 3160	48	$(2.9 \pm 0.42) \cdot 10^{-9}$
4070	3160 - 5620	13	$(4.2 \pm 1.20) \cdot 10^{-10}$
7240	5620 - 10000	2	$(3.3 \pm 2.30) \cdot 10^{-11}$
12900	10000 - 17800	1	$(9 \pm 9) \cdot 10^{-11}$

gives the differential intensities of single negative pions in the momentum range $1 \leq E \leq 20$ GeV/c (Diggory et al., 1974). Fig. 3.8 shows the spectra of unaccompanied negative pions obtained by Diggory et al. (1974) and Brooke and Wolfendale (1964). The difference between the data could be due to the fact that older results have been normalized to the muon flux given by Rossi (1948), whereas the newer results have been normalized to the value given by Allkofer et al. (1970a, 1971a and 1971b). A summary of pion data is given in Fig. 3.9 (Brooke, 1973).

Fig. 3.10 shows the differential energy spectrum of charged pions ($\pi^+ + \pi^-$) in the energy range $40 \leq E \leq 7000$ GeV, obtained by Ashton and Saleh (1975a). At low energies (≤ 100 GeV) the data of these authors are consistent with the results of Brooke and Wolfendale (1964), but differ from those of Diggory et al. (1974) by about a factor of two. The shape of the spectrum can be represented by the expression

Table 3.5: Calculated Differential Proton Spectrum at Sea Level and Cutoff Rigidity 4.4 GV for Different Zenith Angles at Mean Solar Activity (Flückiger 1977).

Kinetic Energy	Proton Intensity [$cm^{-2}\,s^{-1}\,sr^{-1}\,MeV^{-1}$] in Zenith Angle Interval				
[MeV]	0° – 15°	15° – 30°	30° – 45°	45° – 60°	60° – 90°
50 – 100	$5.1 \cdot 10^{-7}$	$3.9 \cdot 10^{-7}$	$1.6 \cdot 10^{-7}$	$4.4 \cdot 10^{-7}$	$6.6 \cdot 10^{-8}$
100 – 200	$1.9 \cdot 10^{-7}$	$3.3 \cdot 10^{-7}$	$1.9 \cdot 10^{-7}$	$1.8 \cdot 10^{-7}$	$3.1 \cdot 10^{-7}$
200 – 400	$4.3 \cdot 10^{-7}$	$1.3 \cdot 10^{-7}$	$8.3 \cdot 10^{-8}$	$5.4 \cdot 10^{-8}$	$5.8 \cdot 10^{-9}$
400 – 600	$2.1 \cdot 10^{-7}$	$5.9 \cdot 10^{-8}$	$3.1 \cdot 10^{-8}$	0.0	$7.6 \cdot 10^{-9}$
600 – 800	$1.2 \cdot 10^{-7}$	$4.1 \cdot 10^{-8}$	$3.6 \cdot 10^{-8}$	$1.9 \cdot 10^{-8}$	0.0
800 – 1000	$9.0 \cdot 10^{-8}$	$3.2 \cdot 10^{-8}$	$2.2 \cdot 10^{-8}$	$5.3 \cdot 10^{-9}$	
1000 – 1250	$6.6 \cdot 10^{-8}$	$5.9 \cdot 10^{-8}$	$6.9 \cdot 10^{-9}$	0.0	
1250 – 1500	$4.7 \cdot 10^{-8}$	$1.7 \cdot 10^{-8}$	$1.4 \cdot 10^{-8}$	0.0	
1500 – 1750	$4.5 \cdot 10^{-8}$	$4.1 \cdot 10^{-8}$	$1.1 \cdot 10^{-8}$	0.0	
1750 – 2000	$6.0 \cdot 10^{-8}$	$2.6 \cdot 10^{-8}$	$5.1 \cdot 10^{-9}$	$3.3 \cdot 10^{-9}$	
2000 – 3000	$2.9 \cdot 10^{-8}$	$1.3 \cdot 10^{-8}$	$2.3 \cdot 10^{-9}$	$1.7 \cdot 10^{-9}$	
3000 – 5000	$1.0 \cdot 10^{-8}$	$1.9 \cdot 10^{-9}$	$8.1 \cdot 10^{-10}$	0.0	
5000 – 7500	$2.1 \cdot 10^{-9}$	0.0	0.0		
7500 – 10000	$2.3 \cdot 10^{-10}$	$1.1 \cdot 10^{-9}$			
10000 – 15000	$1.5 \cdot 10^{-10}$	0.0			
15000 – 20000	$1.6 \cdot 10^{-10}$				
20000 – 30000	0.0				
30000 – 40000	$2.9 \cdot 10^{-11}$				
40000 – 50000	0.0				
50000 – 75000	0.0				
75000 – 100000	0.0				

$$j(E) \propto E^{-2.55\pm0.10} \tag{3.5}$$

3.2.5 Charge and Particle Ratios

Fig. 3.11 shows the energy dependence of the ratio of positive and negative pions to protons at sea level, as given by Diggory et al. (1974), with additional data from Brooke et al. (1964) and Subrahmanian (1962). The latter have been obtained at an atmospheric depth of 800 g/cm^2. The results of a recent measurement of the pion to nucleon ratio was made by Kronmayer et al. (1995) and is shown in Fig. 3.12 together with various theoretical

Table 3.6: Calculated Differential Proton Spectrum at Sea Level and Cutoff Rigidity 15 GV for Different Zenith Angles at Mean Solar Activity (Flückiger 1977).

Kinetic Energy	Proton Intensity $[cm^{-2} s^{-1} sr^{-1} MeV^{-1}]$ in Zenith Angle Interval				
[MeV]	$0° - 15°$	$15° - 30°$	$30° - 45°$	$45° - 60°$	$60° - 90°$
50 – 100	$2.7 \cdot 10^{-7}$	$2.4 \cdot 10^{-7}$	$1.0 \cdot 10^{-7}$	$1.3 \cdot 10^{-7}$	$4.5 \cdot 10^{-8}$
100 – 200	$1.3 \cdot 10^{-7}$	$1.1 \cdot 10^{-7}$	$8.1 \cdot 10^{-8}$	$6.7 \cdot 10^{-8}$	$7.9 \cdot 10^{-8}$
200 – 400	$1.4 \cdot 10^{-7}$	$5.9 \cdot 10^{-8}$	$5.3 \cdot 10^{-8}$	$2.4 \cdot 10^{-8}$	$5.8 \cdot 10^{-9}$
400 – 600	$1.3 \cdot 10^{-7}$	$4.0 \cdot 10^{-8}$	$2.6 \cdot 10^{-8}$	0.0	$7.0 \cdot 10^{-9}$
600 – 800	$7.3 \cdot 10^{-8}$	$3.0 \cdot 10^{-8}$	$1.5 \cdot 10^{-8}$	$4.5 \cdot 10^{-9}$	
800 – 1000	$7.6 \cdot 10^{-8}$	$3.1 \cdot 10^{-8}$	$1.6 \cdot 10^{-8}$	$5.3 \cdot 10^{-9}$	
1000 – 1250	$5.6 \cdot 10^{-8}$	$4.9 \cdot 10^{-8}$	$6.9 \cdot 10^{-9}$	0.0	
1250 – 1500	$4.6 \cdot 10^{-8}$	$1.5 \cdot 10^{-8}$	$1.1 \cdot 10^{-8}$	0.0	
1500 – 1750	$4.5 \cdot 10^{-8}$	$9.6 \cdot 10^{-9}$	$1.0 \cdot 10^{-8}$	0.0	
1750 – 2000	$3.3 \cdot 10^{-8}$	$2.4 \cdot 10^{-8}$	$4.7 \cdot 10^{-9}$	$3.3 \cdot 10^{-9}$	
2000 – 3000	$2.5 \cdot 10^{-8}$	$9.2 \cdot 10^{-9}$	$2.2 \cdot 10^{-9}$	$1.7 \cdot 10^{-9}$	
3000 – 5000	$8.2 \cdot 10^{-9}$	$1.9 \cdot 10^{-9}$	$8.1 \cdot 10^{-10}$		
5000 – 7500	$2.1 \cdot 10^{-9}$	0.0			
7500 – 10000	$2.3 \cdot 10^{-10}$	$1.1 \cdot 10^{-9}$			
10000 – 15000	$1.5 \cdot 10^{-10}$				
15000 – 20000	$1.6 \cdot 10^{-10}$				
20000 – 30000	0.0				
30000 – 40000	$2.9 \cdot 10^{-11}$				
40000 – 50000	0.0				
50000 – 75000	0.0				
75000 – 100000	0.0				

predictions. The data of Kronmayer et al. (1995) are also given in tabulated form in Table 3.8

A compilation of data of the energy dependence of the ratio of protons to muons from many experiments is presented in Fig. 3.13.

Similarly, data of the ratio of charged pions to positive and negative muons obtained by Brooke et al. (1964) are given in Fig. 3.14.

The energy dependence of the so-called neutral-to-charged ratio which is essentially the ratio of neutrons to charged hadrons has been measured by Kronmayer et al. (1995) near sea level (Karlsruhe, 110 m a.s.l.) and is

Table 3.7: Low Energy Differential Single Negative Pion Intensities at Sea Level (Diggory et al. 1974).

Pion Momentum [GeV/c]	Intensity $[cm^{-2} s^{-1} sr^{-1} (GeV/c)^{-1}]$
1	$(5.68 \pm 0.25) \cdot 10^{-6}$
2	$(2.08 \pm 0.08) \cdot 10^{-6}$
3	$(8.60 \pm 0.39) \cdot 10^{-7}$
5	$(6.48 \pm 0.46) \cdot 10^{-7}$
7	$(4.02 \pm 0.37) \cdot 10^{-7}$
10	$(1.67 \pm 0.21) \cdot 10^{-7}$
20	$(8.53 \pm 1.30) \cdot 10^{-8}$

Table 3.8: Ratio of Charged Pions to Nucleons at Sea Level. (Kronmayer et al., 1995)

Energy Range [GeV]	$< E >$ [GeV]	Ratio Pions / Nucleons
10 - 18	13	0.38 ± 0.12
18 - 32	23	0.44 ± 0.11
32 - 56	41	0.49 ± 0.13
56 - 100	72	0.67 ± 0.15
100 - 180	130	0.56 ± 0.10
180 - 320	230	0.63 ± 0.11
320 - 560	405	0.88 ± 0.23
560 - 1000	725	1.58 ± 0.88
1000 - 1800	1300	0.43 ± 0.51

given in Fig. 3.15. Results from other experiments, including the work of McFall et al. (1979) from mountain altitude (730 $g cm^{-2}$) are also presented for comparison. The numeric data of the work of Kronmayer et al. are given in Table 3.9.

3.2.6 Theoretical Contributions

Theoretical energy spectra and fluxes of charged hadrons in the atmosphere have been computed by Torsti (1975), O'Brien (1971 and 1975), Hook and

Table 3.9: Neutral to Charged Ratio of Unaccompanied Hadrons at Sea Level (Kronmayer et al., 1995).

Energy Range [GeV]	$< E >$ [GeV]	Ratio Neutral/Charged
10 - 18	13	(0.56 ± 0.07)
18 - 32	23	(0.53 ± 0.06)
32 - 56	41	(0.50 ± 0.06)
56 - 100	72	(0.42 ± 0.05)
100 - 180	130	(0.47 ± 0.04)
180 - 320	230	(0.44 ± 0.04)
320 - 560	405	(0.36 ± 0.06)
560 - 1000	725	(0.24 ± 0.10)
1000 - 1800	1300	(0.53 ± 0.29)

Turver (1974), and Flückiger (1977).

References

Allkofer, O.C. and K. Clausen: Acta Phys. Acad. Sci. Hung., 29, Suppl. 2, p. 689 (1970).

Allkofer, O.C., W.D. Dau, and H. Jokisch: Phys. Lett. B, 31, p. 606 (1970a).

Allkofer, O.C., K. Clausen, and P. Knoblich: Proc. VI. Inter-American Seminar on Cosmic Rays, La Paz, IV, p. 930 (1970b).

Allkofer, O.C., K. Carstensen, W.D. Dau: Phys. Lett., 36B, Erratum, p. 428 (1971a).

Allkofer, O.C., K. Carstensen, and W.D. Dau: PICRC, 4, p. 1314 (1971b).

Ashton, F., K. Tsuji, and A.W. Wolfendale: Nuovo Cimento, 9 B, p. 344 (1972).

Ashton, F. and A.J. Saleh: PICRC, 7, p. 2507 (1975a).

Ashton, F. and A.J. Saleh: Nature 256, p. 387 (1975b).

Babecki, J., Z. Buja, N.L. Grigorov, J. Laskiewicz, J. Massalski, A. Oles and V. Ya. Shestoperov: Sov. Phys. JETP 40 (13), p. 1089 (1961).

Ballam, J. and P.G. Lichtenstein: Phys. Rev., 93, p. 851 (1954).

Barber, H.B., T. Bowen, D.A. Delise,E.W. Jenkins, J.J. Jones, R.M. Kalbach, and A.E. Pifer: Phys. Rev., D 22, p. 2667 (1980).

Baruch, J.E.F., G. Brooke, and E.W. Kellermann: PICRC 3, p. 2301 (1973).

Bel'skii, S.A. and A.M. Romanov: Bull. Acad. Sci. USSR, Phys. Ser. (USA), 29, p. 1503 (1966).

Brooke, G. and A.W. Wolfendale: Proc. Phys. Soc., 83, p. 843 (1964).

Brooke, G., M.A. Meyer, and A.W. Wolfendale: Proc. Phys. Soc., 83, p. 871 (1964).

Brooke, G.: Cosmic Rays at Ground Level. (A.W. Wolfendale, ed.). The Institute of Physics, London, Chapter 3, p. 57 (1973).

Cowan, E.W. and K. Matthews: Phys. Rev., D 4, p. 37 (1971).

Dardo, M., S. Alession, and K. Sitte: PICRC, 7, p. 81 (1979).

Diggory, I.S., J.R. Hook, I.A. Jenkins, and K.E. Turver: J. Phys. A, 7, p. 741 (1974).

Dmitriev, V.A., G.V. Kulikov, and G.B. Khristiansen: Sov. Phys. JETP, 37 (10), p. 637 (1960).

Erlykin, A.D., and N.P. Kuzina: PICRC, 7, p. 62 (1979).

Filthuth, H.: Zeitschrift für Naturforschung, 10a, p. 219 (1955).

Flückiger, E.: Helv. Phys. Acta, 50, p. 633 (1977).

Garaffo, Z., A. Pignotti, and G. Zgrablich: Nucl. Phys., B 53, p. 419 (1973).

Goldwasser, E.L. and T.C. Merkle: Phys. Rev., 83, p. 43 (1951).

Hook, J.R. and K.E. Turver: Private communication (1972), after Brooke (1973).

Hook, J.R. and K.E. Turver: J. Phys. A, 7, p. 765 (1974).

Klages, H.O., W.D. Apel, K. Bekk, E. Bollmann, H. Bozdog, I.M. Brancus, M. Brendle, A. Chilingarian, K. Daumiller, P. Doll, J. Engler, M. Föller, P. Gabriel, H.J. Gils, R. Glasstetter, A. Haungs, D. Heck, J. Hörandel, K.-H. Kampert, H. Keim, J. Kempa, J. Knapp, H.J. Mathes, H.J. Mayer, H.H. Mielke, D. Mühlenberg, J. Oehlschläger, M. Petcu, U. Raidt, H. Rebel, M. Roth, G. Schatz, H. Schieler, G. Schmalz, H.J. Simonis, T. Thouw, J. Unger, G. Völker, B. Vulpescu, G.J. Wagner, J. Wdowczyk, J. Weber, J. Wentz, Y. Wetzel, T. Wibig, T. Wiegert , D. Wochele, J. Wochele, J. Zabierowski, S. Zagromski , B. Zeitnitz: Proc. 9th Internat. Symposium on Very High Energy Cosmic Ray Interactions, Karlsruhe (1996). Nucl. Phys., 52B, p. 92 (1997).

Kronmayer, H., H.-H. Mielke, J. Engler, and J. Knapp: J. Phys., G 21, p. 439 (1995).

Lohrmann, E.: Nuovo Cimento, 1, p. 1126 (1955).

Lumme, M., M. Nieminen, J. Peltonen, J.J. Torsti, E. Vainikka, and E. Valtonen: J. Phys., G 10, p. 683 (1984).

McDiarmid, I.B.: Can. J. Phys., 37, p. 79 (1959).

McFall, J.R., R.W. Ellsworth, A.S. Ito, F. Siohan, R.E. Streitmatter, S.C. Tonwar, P.R. Vishwanath, and G.B. Yodh: J. Phys, G 5, p. 861 (1979).

Merkle, T.C., E.L. Goldwasser, and R.B. Brode: Phys. Rev., 79, p. 926 (1950).

Meshkovskii, A.G. and L.I. Sokolov: Sov. Phys. JETP (U.S.S.R.), 33, p. 542 (1957), and Sov. Phys. JETP, 6, p. 424 (1958).

Mielke, H.H., M. Föller, J. Engler, and J. Knapp: J. Phys., G 20, p. 637 (1994).

Milroy, M.G. and J.G. Wilson: Proc. Phys. Soc., Lond., A 64, p. 404 (1951).

Nieminen, M., J.J. Torsti, E. Valtonen, H. Arvela, M. Lumme, J. Peltonen, and E. Vainikka: J. Phys., G 11, p. 421 (1985).

O'Brien, K.: Nuovo Cimento, 3 A, p. 521 (1971).

O'Brien, K.: J. Phys., A 8, p. 1530 (1975).

Ogilvie, K.W.: Can. J. Phys., 33, p. 746 (1955).

Rochester, G.D. and M. Bound: Nature, 146, p. 745 (1940).

Rosen, A.Z.: Phys. Rev., 93, p. 211 (1954).

Rossi, B.: Rev. Mod. Phys., 20, p. 537 (1948).

Schatz, G., W.D. Apel, K. Bekk, E. Bollmann, H. Bozdog, I.M. Brancus, M. Brendle, J.N. Capdevielle, A. Chilingarian, K. Daumiller, P. Doll, J. Engler, M. Föller, P. Gabriel, H.J. Gils, R. Glasstetter, A. Haungs, D. Heck, J. Hörandel, K.-H. Kampert, H. Keim, J. Kempa, H.O. Klages, J. Knapp, H.J. Mathes, H.J. Mayer, H.H. Mielke, D. Mühlenberg, J. Oehlschläger, M. Petcu, Chr. Rämer, U. Raidt, H. Rebel, M. Roth, H. Schieler, G. Schmalz, H.J. Simonis, T. Thouw, J. Unger, G. Völker, B. Vulpescu, G.J. Wagner, J. Wdowczyk, J. Weber, J. Wentz, Y. Wetzel, T. Wibig, T. Wiegert , D. Wochele, J. Wochele, J. Zabierowski, S. Zagromski , B. Zeitnitz: Nucl. Phys., 60 B, p. 151 (1998).

Siohan, F., R.W. Ellsworth, M. Lapointe, J.R. Macfall, A. Stottlemyer, and G.B. Yodh: J. Phys., G 3, p. 1157 (1977).

Subramanian, A.: Thesis University of Madras (1962).
Torsti, J.J.: Nuovo Cimento, 25 B, p. 829 (1975).
York, C.M.: Phys. Rev., 85, p. 998 (1952).

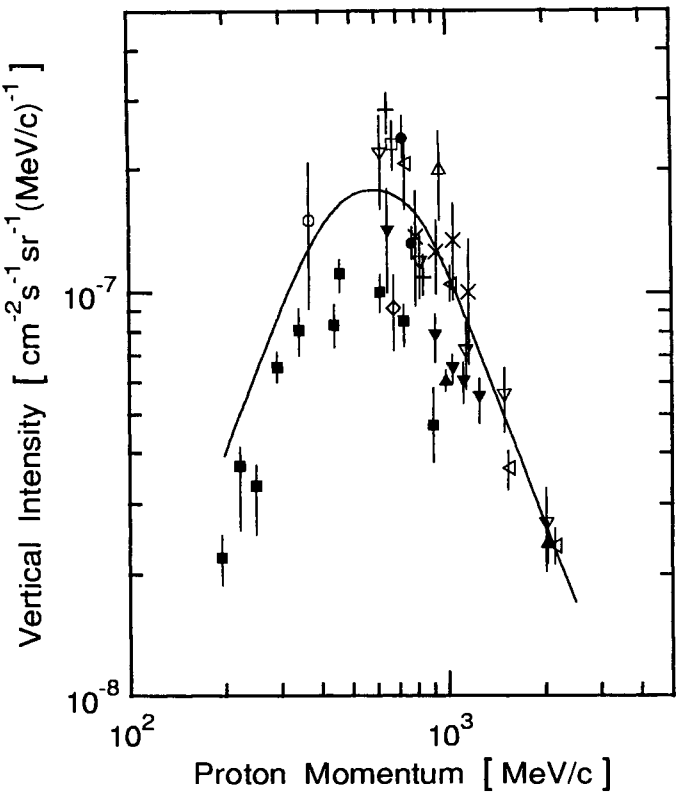

Figure 3.1: Measurements of the vertical proton intensity for momenta less than 2.5 GeV/c. The curve is based on the original data shown in the graph and listed below, except for the data of Filthuth (1955), the values of which had been increased by 70%, the percentage they are lower than other comparative data (Brooke, 1973).

○	Rochester and Bound (1940)	◇	Rosen (1954)
□	Merkle et al. (1950)	■	Filthuth (1955)
△	Goldwasser and Merkle (1951)	▼	Ogilvie (1955)
▽	Milroy and Wilson (1951)	•	McDiarmid (1959)
+	York (1952)	◁	Brooke and Wolfendale (1964)
×	Ballam and Lichtenstein (1954)	▲	Hook and Turver (1972)

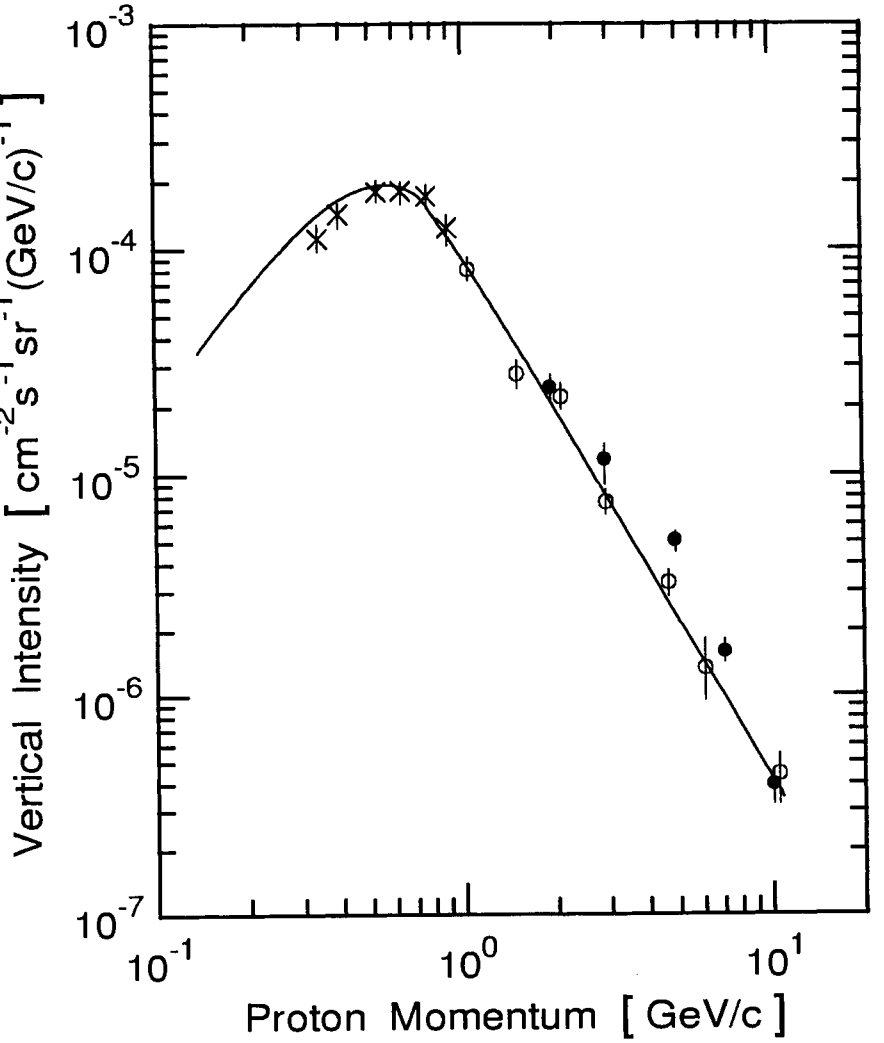

Figure 3.2: Differential momentum spectrum of protons at sea level (Barber et al., 1980).

× Meshkovskii and Sokolov (1958)
o Brooke and Wolfendale (1964)
• Diggory et al. (1974)

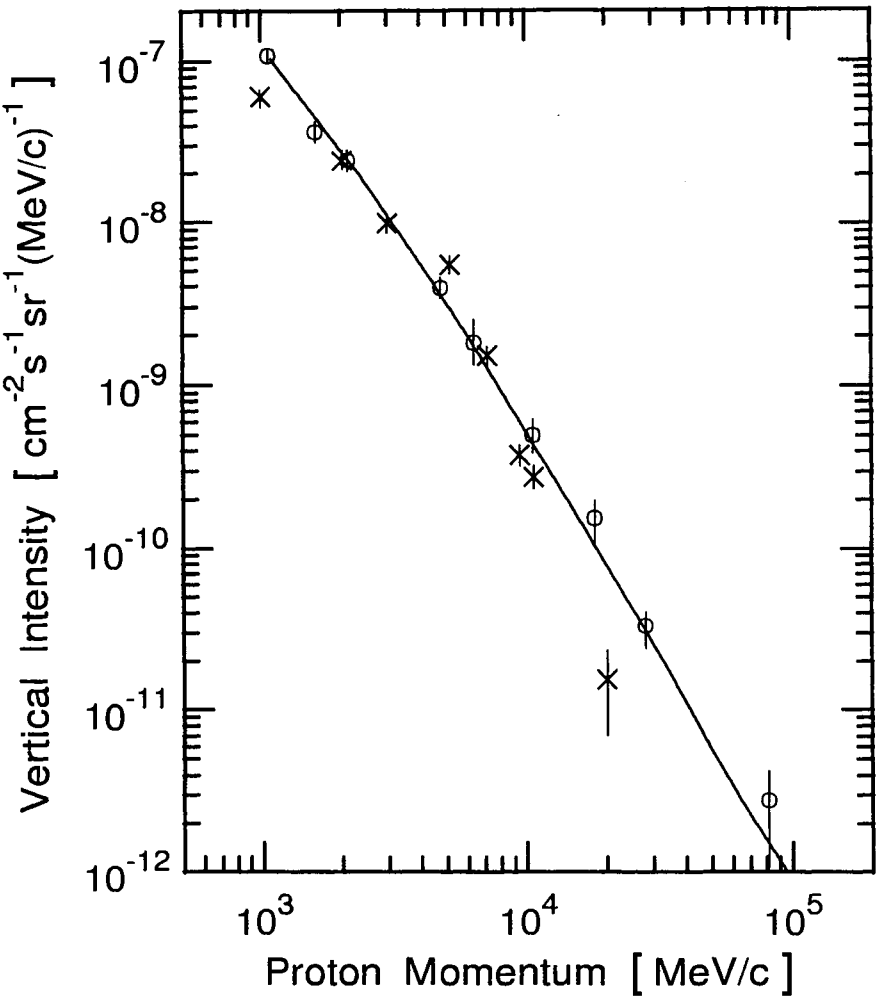

Figure 3.3: Vertical differential momentum spectrum of protons at sea level. The solid curve is the suggested best estimate of the spectrum and includes all the data given in Table 3.1. If the spectrum is approximated by a power law its best fit exponent is -2.9 (Brooke, 1973).

o Brooke and Wolfendale (1964)
× Hook and Turver (1972)

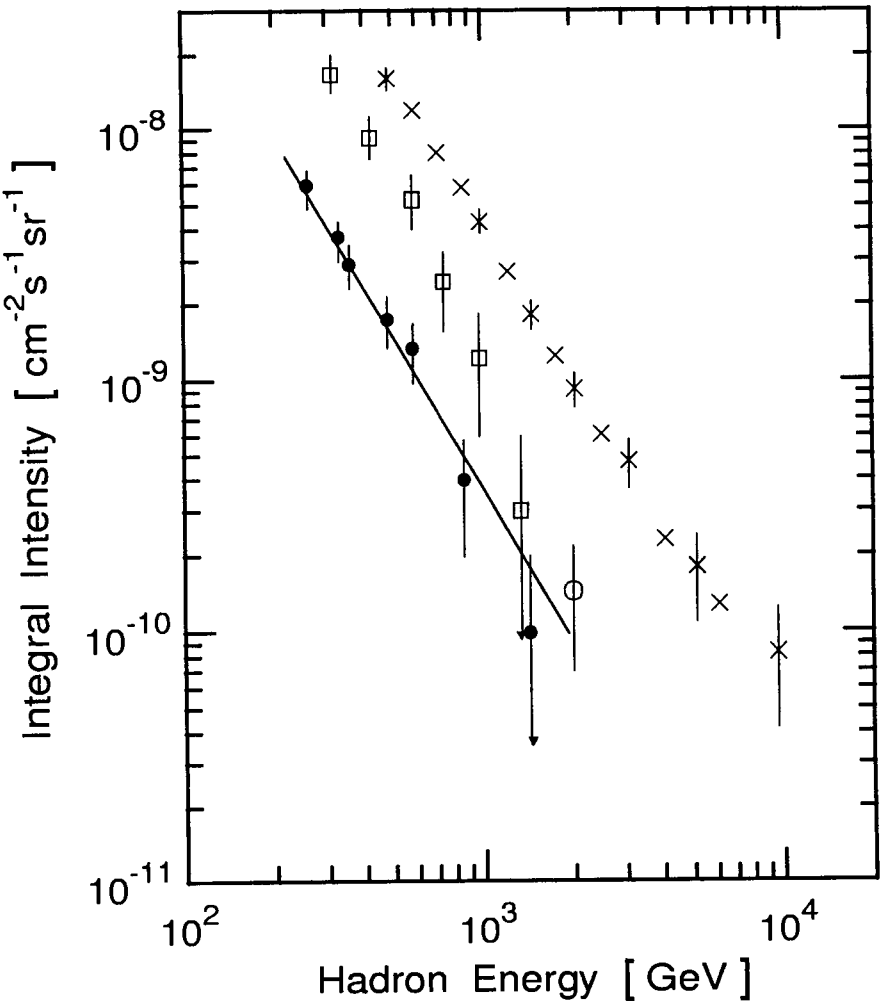

Figure 3.4: Integral spectrum of vertical high energy charged hadrons at sea level. Also shown is an upper limit for all hadrons (Siohan et al., 1977).

● , —— single, unaccompanied charged hadrons
□ , o all charged hadrons
× upper limit to all hadrons

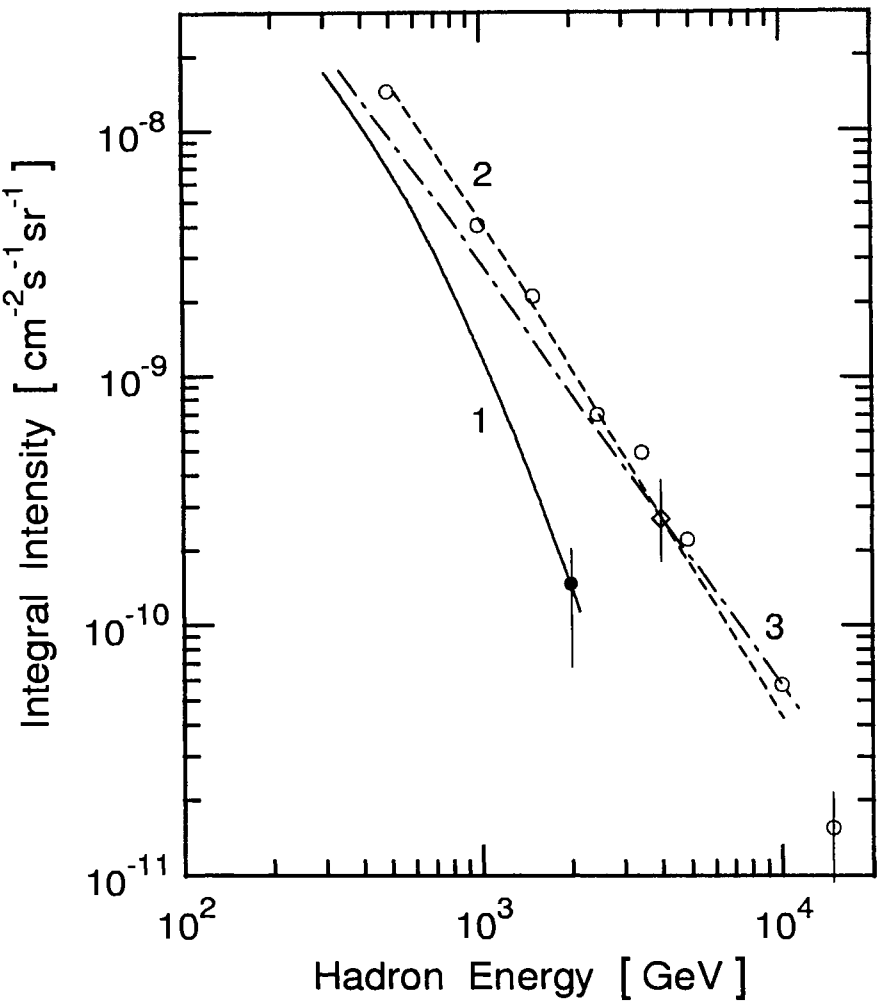

Figure 3.5: Comparison of high energy integral spectra of hadrons obtained in various experiments at sea level (Siohan et al., 1977). Curve 2 includes about 10 % of neutral contamination resulting from heavily accompanied hadrons with $\geq$6 charged tracks.

1 , • Siohan et al. (1977), charged hadrons only
2 , ◇ Siohan et al. (1977), upper limit
3 Ashton and Saleh (1975b), charged and neutral
o Babecki et al. (1961), charged and neutral

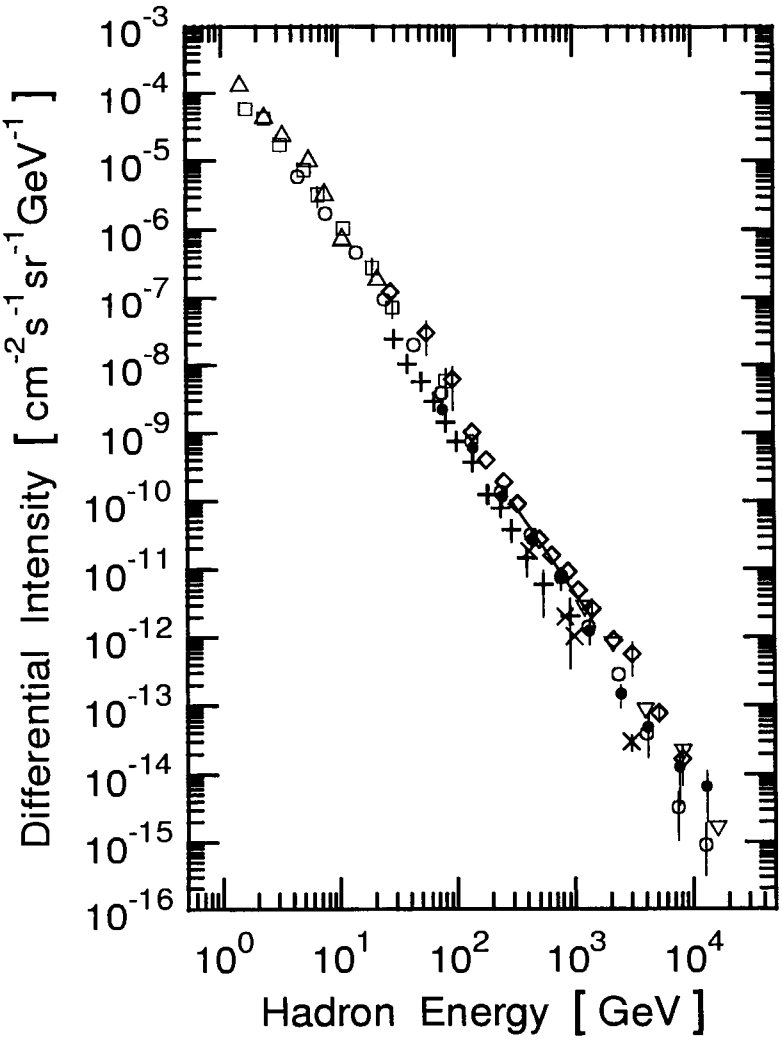

Figure 3.6: Compilation of single hadron differential energy spectra at sea level (Mielke et al, 1994; Klages et al., 1997).

○	Klages et al. (1997)	◇	Ashton and Saleh (1975b)
□	Brooke & Wolfendale (1964)	△	Diggory et al. (1974)
▽	Baruch et al. (1979)	+	Fickle and Lamb (1979)
×	Cowan & Matthews (1971)	– – –	Siohan et al. (1977)
•	Schatz et al. (1998); Klages et al. (1997); Mielke et al. (1994)		

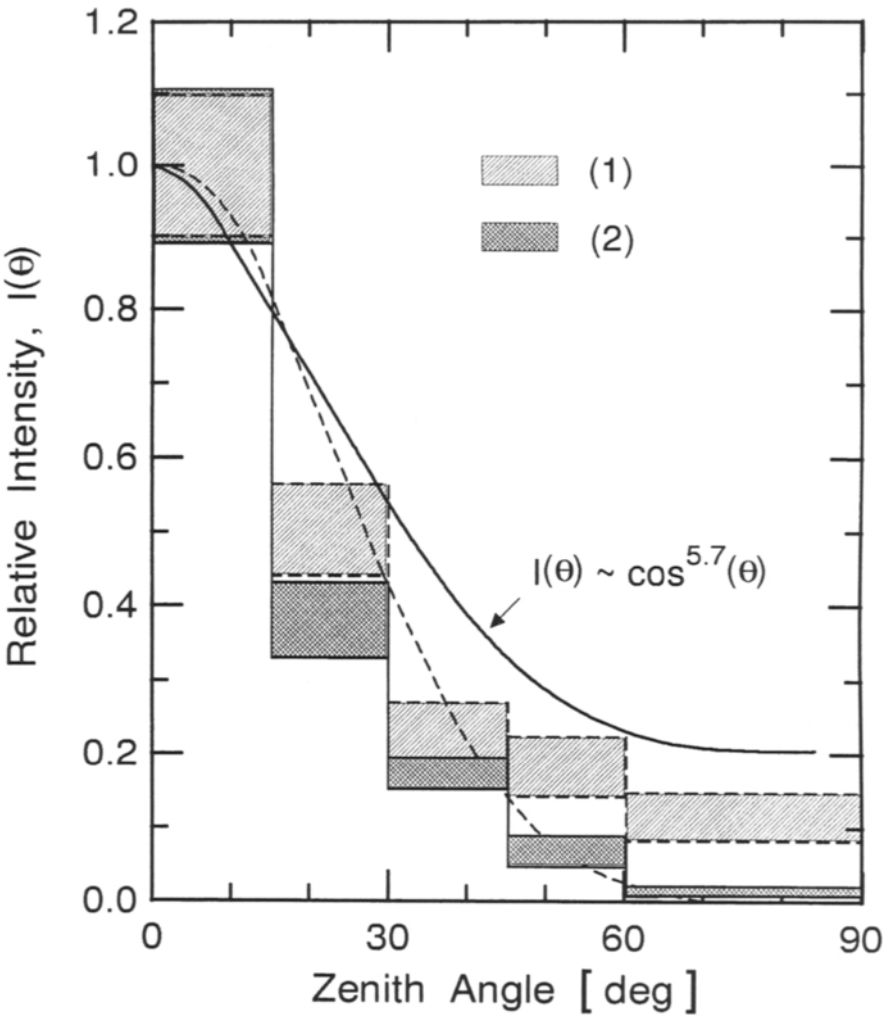

Figure 3.7: Zenith angular distribution of protons at sea level (1033 g/cm^2) (Flückiger, 1977).

– – Lohrmann (1955)
—— Bel'skii and Romanov (1966)
1 Flückiger (1977), Monte Carlo for $E \geq 50$ MeV
2 Flückiger (1977), Monte Carlo for $E \geq 200$ MeV

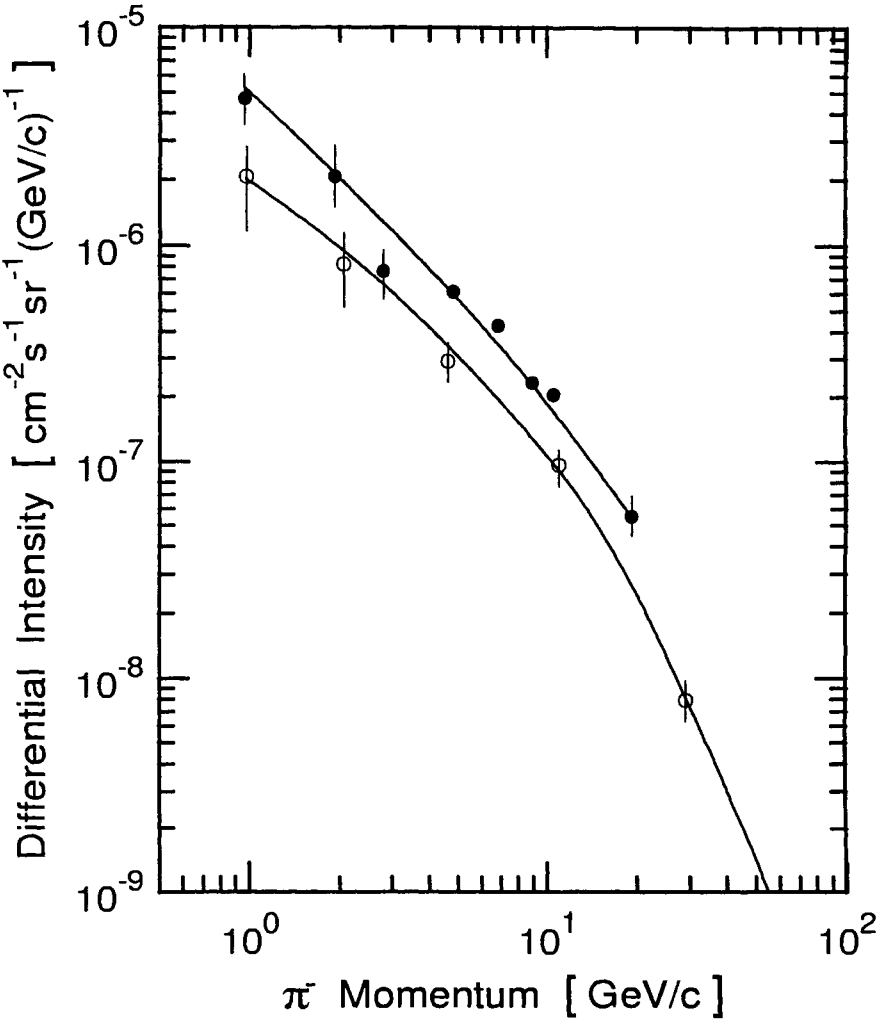

Figure 3.8: Vertical differential momentum spectrum of single unaccompanied negative pions at sea level (Diggory et al., 1974).

- o Brooke et al. (1964)
- • Diggory et al. (1974)

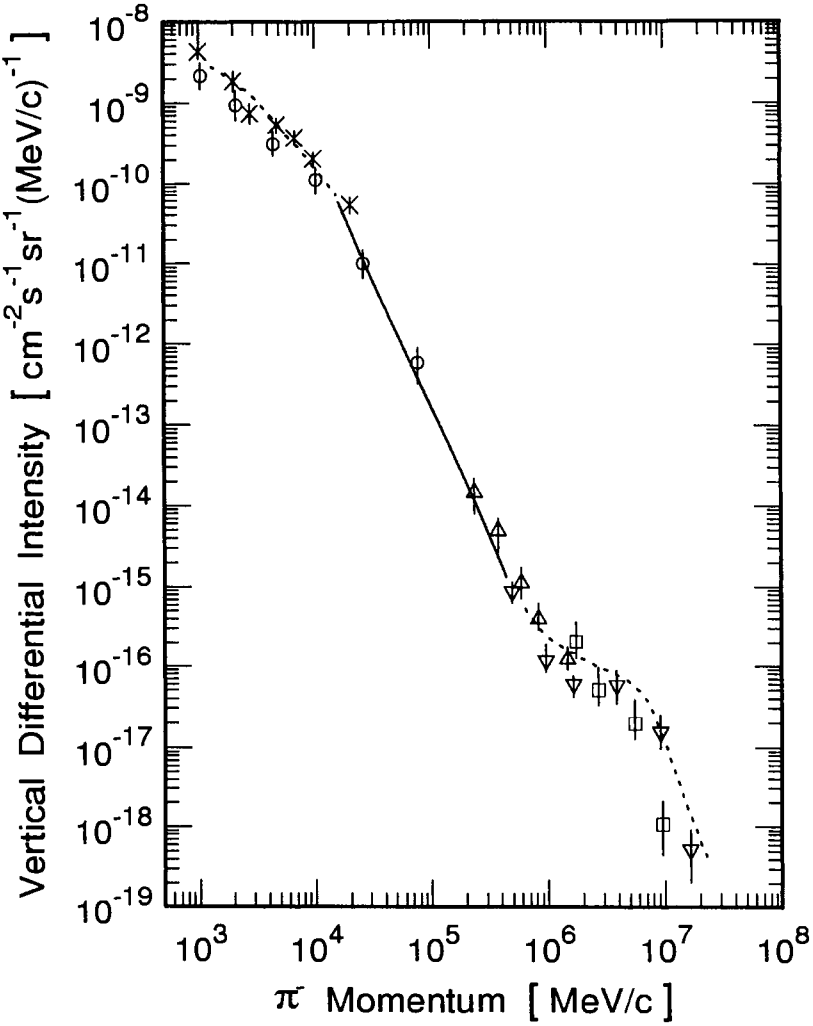

Figure 3.9: Vertical differential momentum spectrum of negative pions near sea level (Brooke, 1973). The intensities were obtained assuming a charged pion to proton ratio of 0.5. The dotted lines show the effect when this ratio is assumed to be 2.05, as found by Cowan and Matthews (1971).

□ Dmitriev et al. (1960)	o Brooke et al. (1964)
△ Cowan and Matthews (1971)	× Hook and Turver (1972)
▽ Baruch et al. (1973)	

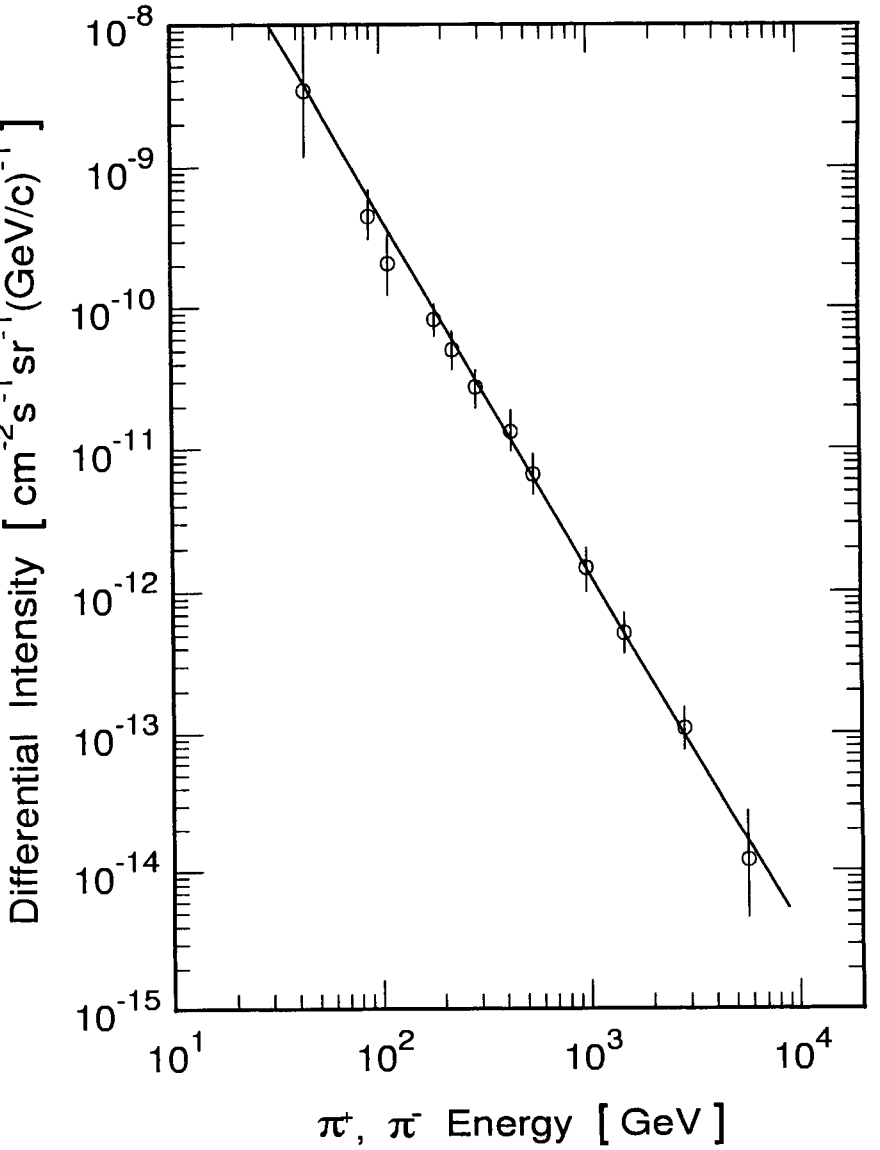

Figure 3.10: Differential energy spectrum of charged pions ($\pi^+ + \pi^-$) at sea level (Ashton and Saleh, 1975a, see also Ashton and Saleh, 1975b).

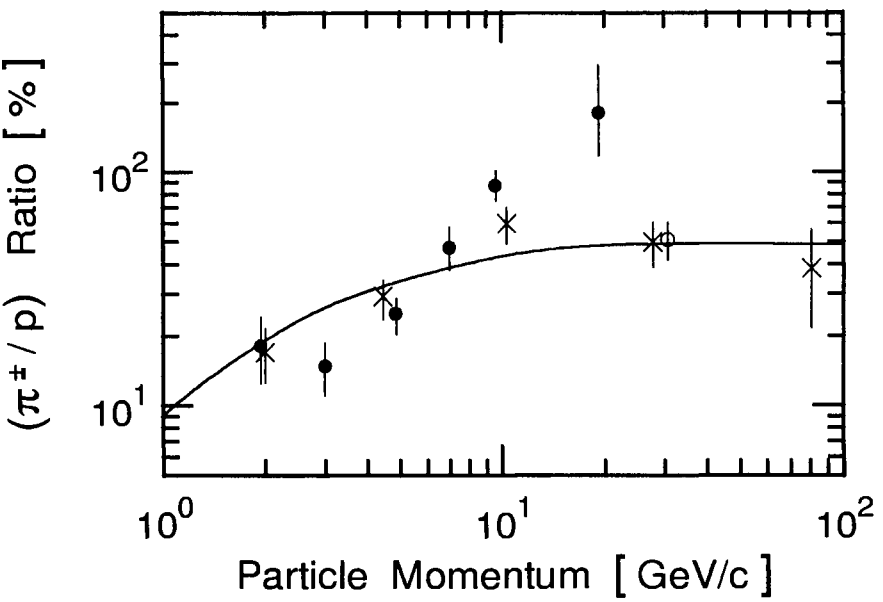

Figure 3.11: Early data of the ratio of single pions ($\pi^+ + \pi^-$) to protons as a function of momentum at sea level. Also shown for comparison is one date set at mountain level.

- × Brooke et al. (1964), sea level
- • Diggory et al. (1974), sea level
- o Subrahmanian (1962), 800 g/cm^2

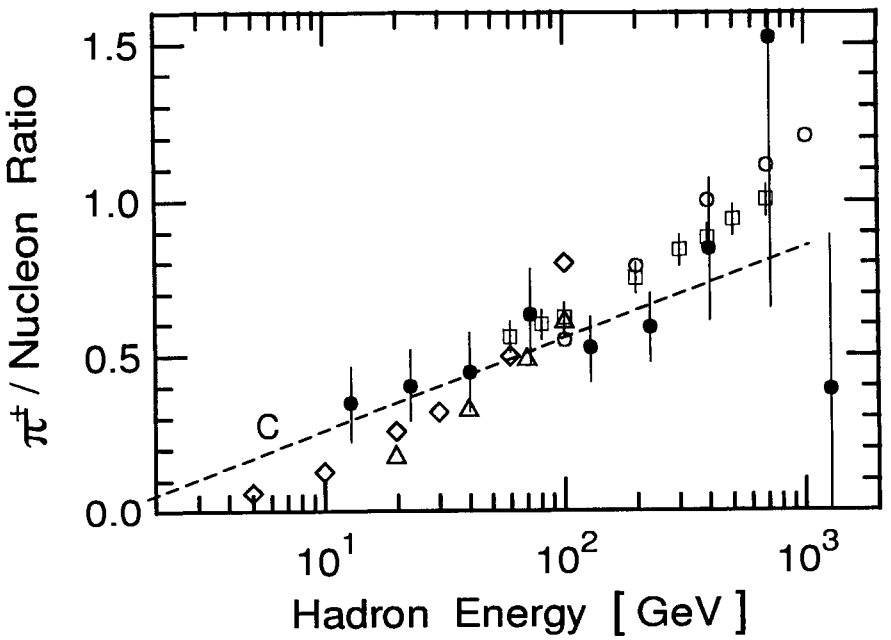

Figure 3.12: Experimental (full symbols) and predicted (open symbols) ratios of charged pions to nucleons as a function of energy at sea level (Kronmayer et al., 1995). C is a linear fit to the experimental data.

- • Kronmayer et al. (1995)
- □ Kronmayer et al. (1995), CORSIKA
- ◇ Lumme et al. (1984)
- ○ Erlykin and Kuzina (1979)
- △ Garaffo et al. (1973)

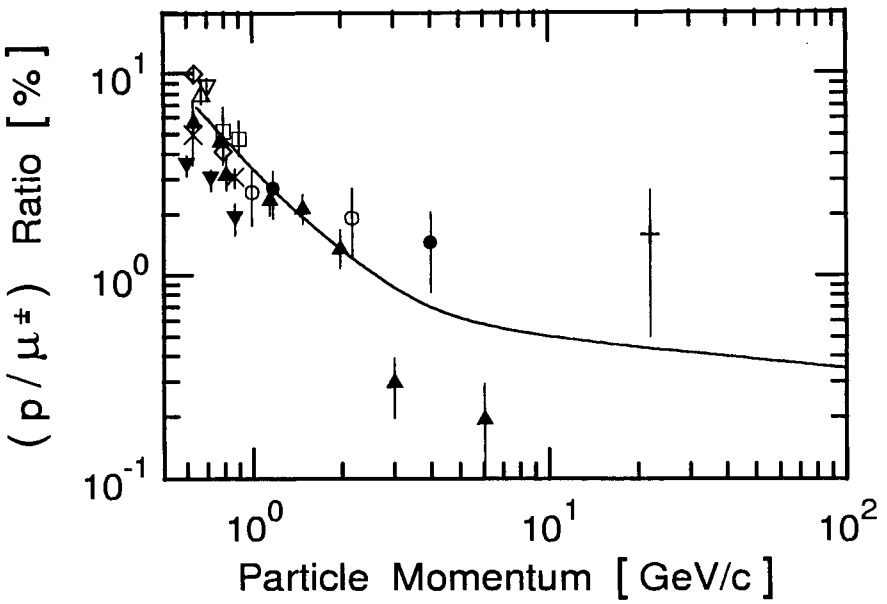

Figure 3.13: Ratio of protons to muons as a function of momentum at sea level. The curve is the best fit result of four sets of measurements by Brooke and Wolfendale (1964).

——	Brooke and Wolfendale (1964)
o	Allkofer and Clausen (1970)
•	Allkofer et al. (1970b)
□	Ballam and Lichtenstein (1954)
▼	Filthuth (1955)
+	Pak and Greisen (1962)
∇	McDiarmid (1959)
△	Merkle et al. (1950)
▲	Mylroi and Wilson (1951)
×	Ogilvie (1955)
◇	York (1952)

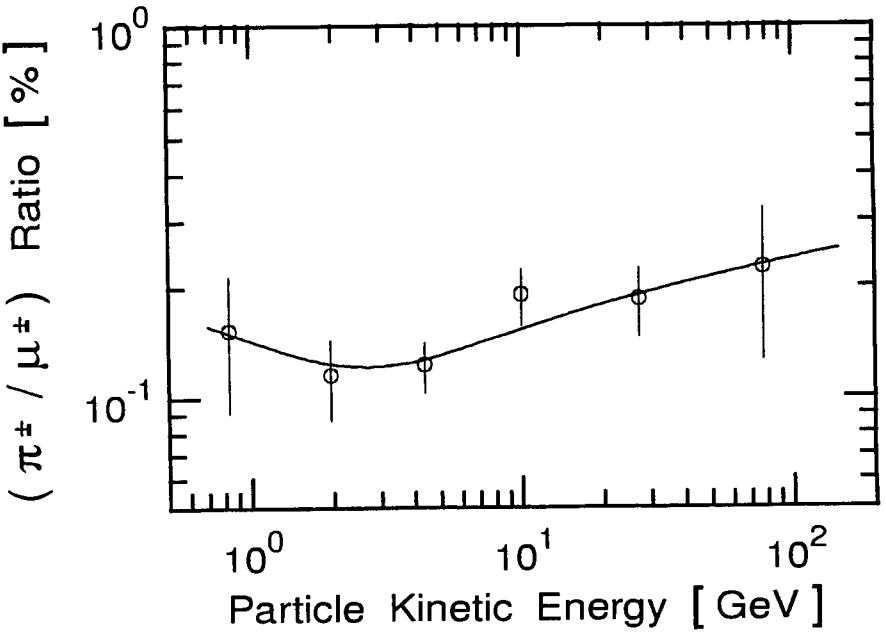

Figure 3.14: Ratio of positive and negative pions to muons as a function of kinetic energy at sea level (Brooke et al., 1964).

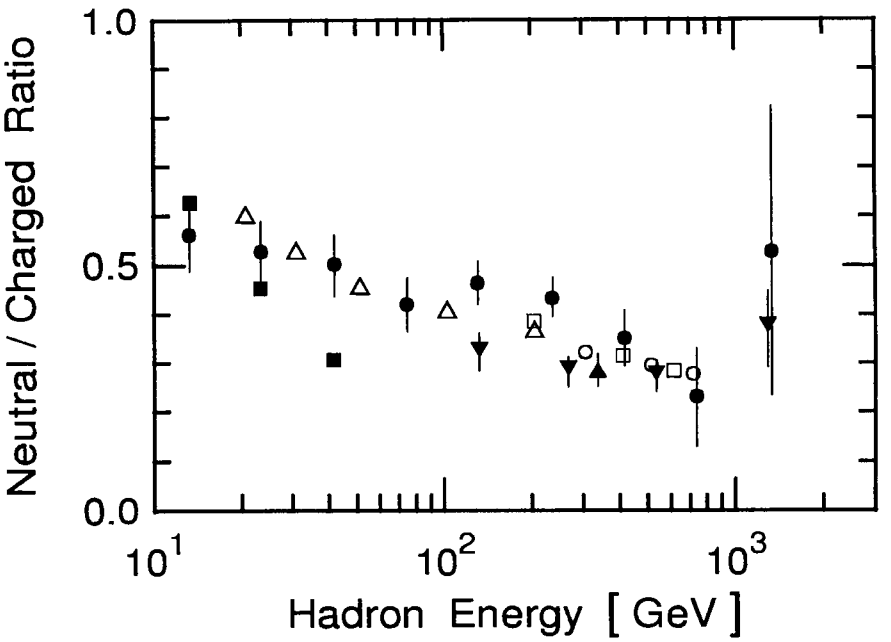

Figure 3.15: Experimental (full symbols) and predicted (open symbols) ratios of neutral to charged hadrons as a function of energy at sea level Kronmayer et al. (1995). Also shown for comparison is the ratio obtained by McFall et al. (1979) at 730 $g\,cm^{-2}$.

- ● Kronmayer et al. (1995)
- △ Garaffo et al. (1973)
- ▲ Cowan and Matthews (1971)
- ○ Erlykin and Kuzina (1979)
- ■ Nieminen et al. (1985)
- □ Dardo et al. (1979)
- ▼ McFall et al. (1979)

3.3 Neutrons

3.3.1 Flux Measurements and Intensities

Only a few experiments have been carried out to determine the intensity and the energy spectra of neutrons at sea level. They have been reviewed by Ashton (1973).

The vertical differential neutron intensity in the energy range $80 \leq E \leq 300$ MeV was found to be $1.54 \cdot 10^{-3} \cdot E^{-1.5} \pm 33\%$ $\mathrm{cm^{-2}s^{-1}sr^{-1}MeV^{-1}}$ (Heidbreder et al., 1971). The omnidirectional intensity has been measured by Hajnal et al. (1971) and was found to be $8.2 \cdot 10^{-3}$ $\mathrm{cm^{-2}s^{-1}}$.

3.3.2 Energy Spectra

In the low energy region energy spectra have been measured by Ashton et al. (1971), Heidbreder et al. (1971), and Hess et al. (1959). The results obtained by Ashton et al. (1971) together with proton data from the work of Brooke and Wolfendale (1964), and a calculated spectrum by Hughes and Marsden (1966) are shown in Fig. 3.16 (Ashton, 1973).

High energy data have been obtained by Milroy and Wilson (1951), and Ashton et al. (1970), and recently by Kronmayer et al. (1995). Fig. 3.17 shows the differential energy spectrum of neutrons in the energy range $10 \leq E \leq 1000$ GeV together with the proton spectrum of Brooke and Wolfendale (1964), for comparison (Ashton, 1973). From this figure it can be seen that the high energy intensities of protons and neutrons are essentially the same. The intensities measured by Kronmayer et al. (1995) are also given in tabulated form in Table 3.10 (the term neutral used in this table means essentially neutrons).

A compilation of differential neutron intensity data in the energy range $1 \leq E \leq 10^6$ MeV has been made by Heidbreder et al. (1971). Fig. 3.18 shows the results for the geomagnetic latitude of 50° N. Another compilation over the same energy range was made by Flückiger (1976) together with a Monte Carlo calculation. A calculated spectrum is presented in Fig. 3.19 and compared with measurements in the energy range $10^2 \leq E \leq 10^5$ MeV (Armstrong et al., 1973). Another calculation has been made by Bhattacharyya et al. (1979).

Table 3.10: Neutral Hadron Intensity at Sea Level (Kronmayer et al., 1995)

Energy Range [GeV]	$< E >$ [GeV]	Neutral Intensity $[cm^{-2}s^{-1}sr^{-1}GeV^{-1}]$
10 - 18	13	$(1.4 \pm 0.3) \cdot 10^{-7}$
18 - 32	23	$(2.4 \pm 0.5) \cdot 10^{-8}$
32 - 56	41	$(5.1 \pm 1.1) \cdot 10^{-9}$
56 - 100	72	$(1.0 \pm 0.2) \cdot 10^{-9}$
100 - 180	130	$(2.4 \pm 0.5) \cdot 10^{-10}$
180 - 320	230	$(5.0 \pm 1.1) \cdot 10^{-11}$
320 - 560	405	$(8.1 \pm 1.9) \cdot 10^{-12}$
560 - 1000	725	$(1.1 \pm 0.4) \cdot 10^{-12}$
1000 - 1800	1300	$(3.4 \pm 1.4) \cdot 10^{-13}$

3.3.3 Zenith Angle Dependence

Measurements of the zenith angle distribution show that it can be approximated by the expression

$$I(\theta) = I(0°) \cos^n(\theta) \tag{3.6}$$

with $n = 3.5 \pm 1.2$, up to zenith angles of 60° (Heidbreder et al., 1971).

References

Armstrong, T.W., K.C. Chandler, and J. Barish: J. Geophys. Res., 78, p. 2715 (1973).

Ashton, F., and R.B. Coats: Proc. Phys. Soc., 1, p. 169 (1968).

Ashton, F., N.I. Smith, J. King, and E.A. Mamidzhanian: Acta Phys. Acad. Sci. Hung, 29,Suppl. 3, p. 25 (1970).

Ashton, F., H.J. Edwards, and G.N. Kelly: J. Phys. A4, p. 352 (1971).

Ashton, F.: in Cosmic rays at ground level. (A.W. Wolfendale, ed.). The Institute of Physics, London, Chapter 4, p. 75 (1973).

Bhattacharyya, D.P., A.K. Ghosh, and D. Basu: Ann. Phys., 36, p.170 (1979).

Brooke, G., and A.W. Wolfendale: Proc. Phys. Soc., 83, p. 843 (1964).

Clementel, E., and F. Ferrari: Nuovo Cimento, 9, p. 572 (1952).

Flückiger, E.: Internal Report, University of Bern (1976).

Hajnal, F., E. McLaughlin, M.S. Weinstein, K. O'Brien: NTIS, Springfield, VA. 22151, p. 22 (1971).

Heidbreder, E., K. Pinkau, C. Reppin, and V. Schönfelder: J. Geophys. Res., 76, p. 2905 (1971).

Hess, W.N., H.W. Patterson, R. Wallace, and E.L. Chupp: Phys. Rev., 116, p.445 (1959).

Hess, W.N., E.H. Canfield, and R.E. Lingenfelter: J. Geophys. Res., 66, p. 665 (1961).

Hughes, E.B., and P.L. Marsden: J. Geophys. Res. 71, p. 1435 (1966).

Hughes, E.B., P.L. Marsden, G. Brooke, M.A. Meyer, and A.W. Wolfendale: Proc. Phys. Soc., 83, p. 239 (1964).

Kastner, J., B.G. Oltmann, and L.D. Marinelli: Progress report, The Natural Radiation Environment, University of Chicago Press, Chicago, Il (1964).

Kronmayer, H., H.-H. Mielke, J. Engler, and J. Knapp: J. Phys., G 21, p. 439 (1995).

Mendell, R.B., and S.A. Korff: J. Geophys. Res., 68, p. 5487 (1963).

Milroy, M.G., and J.G. Wilson: Proc. Phys. Soc. A., 64, p. 404 (1951).

Nieminen, M., J.J. Torsti, E. Valtonen, H. Arvela, M. Lumme, J. Peltonen, and E. Vainikka: J. Phys., G 11, p. 421 (1985).

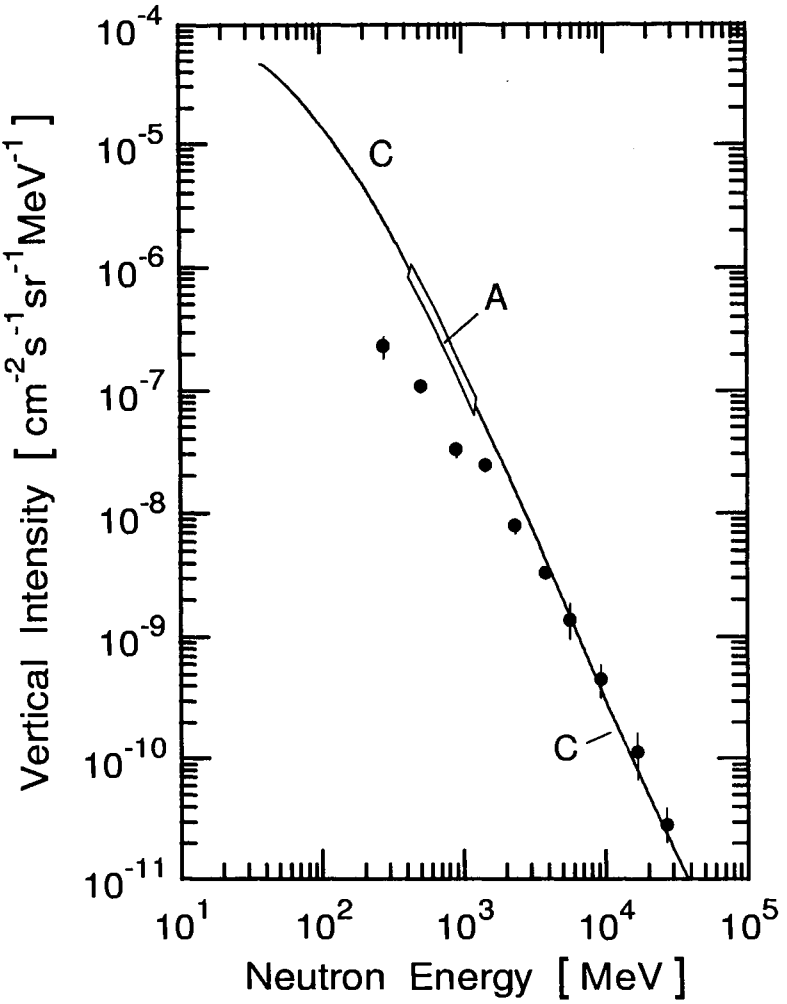

Figure 3.16: Low energy vertical differential neutron spectrum. A proton spectrum has been added for comparison (Ashton, 1973).

A Ashton et al. (1971), experimental
• Brooke and Wolfendale (1964), protons
C Hughes and Marsden (1966), theoretical

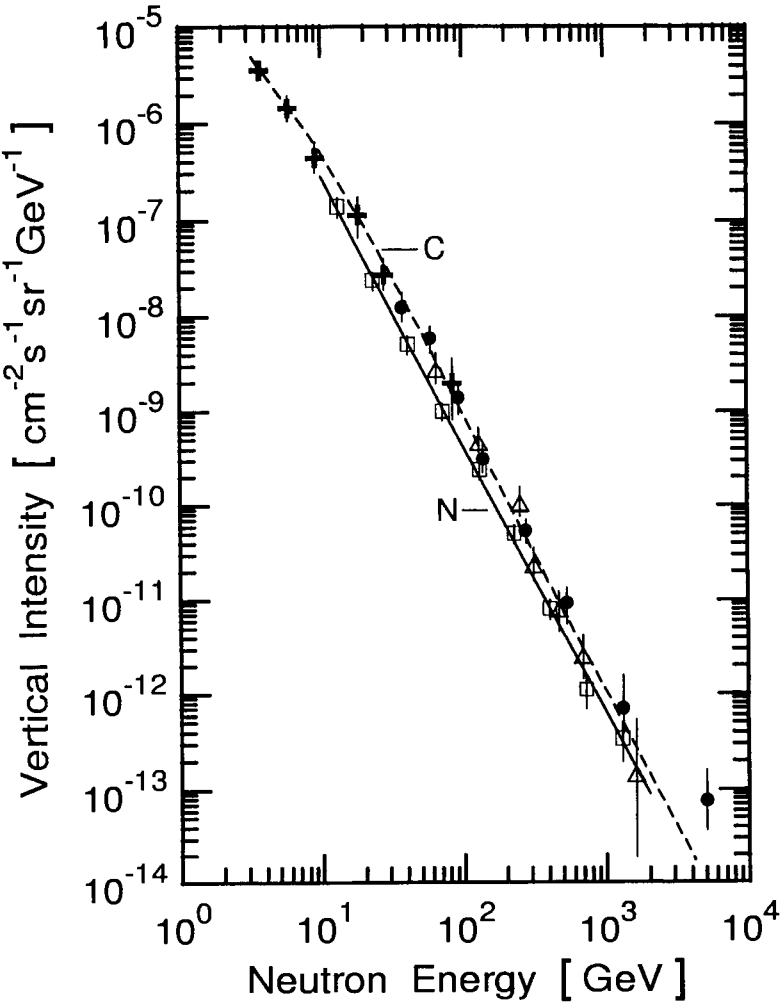

Figure 3.17: High energy vertical differential neutron spectrum. A proton spectrum has been added for comparison. Curve C is described by the function $j(E)dE = KE^{-\gamma}dE$, where $\gamma = 2.95 \pm 0.10$ (Ashton et al. 1973).

△ , •	Ashton et al. (1970, 1973), neutrons
□	Kronmayer et al. (1995), neutrons
N	Nieminen et al. (1984), neutrons
+	Brooke and Wolfendale(1964), protons

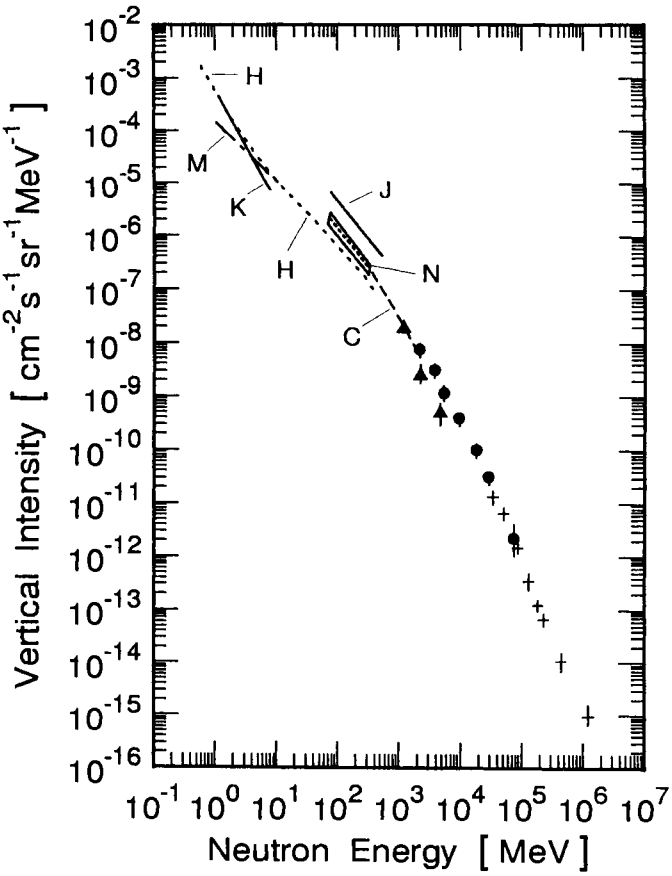

Figure 3.18: Vertical differential energy spectrum of neutrons in the energy range 1 MeV to 10^6 MeV at sea level (1030 g/cm^2), normalized to a geomagnetic latitude of 50° N. Proton data have been added for comparison (Heidbreder et al., 1971).

C Clementel and Ferrari (1952), neutrons, theoretical
H Hess et al.(1959, 1961), neutrons, $I(\theta) = \text{const.}$
J Hess et al. (1959, 1961), neutrons, $I(\theta) \propto \cos^{3.5}(\theta)$
M Mendell and Korff, neutrons (1963)
K Kastner et al. (1964), neutrons
+ Ashton and Coats (1968), neutrons
N Heidbreder et al. (1971) neutrons
▲ Milroy and Wilson (1951), protons
• Brooke and Wolfendale (1964), protons

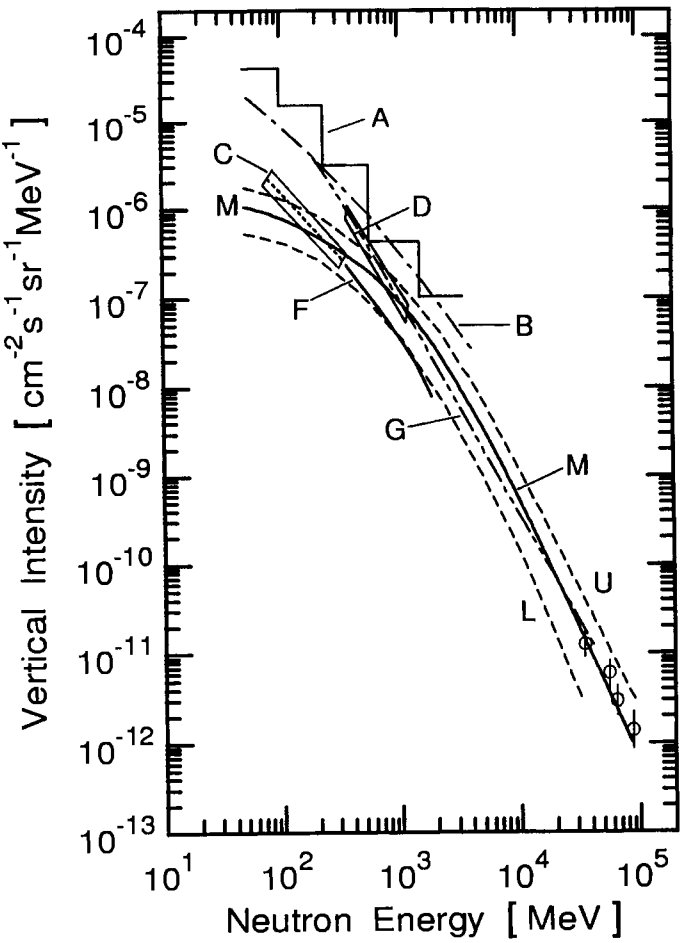

Figure 3.19: Vertical differential energy spectra of neutrons at sea level (Flückiger, 1976).

A	Armstrong et al. (1973), Monte Carlo
B	Hess et al. (1959), measurement
C	Heidbreder et al. (1971), measurement
D	Ashton et al. (1971), measurement
F	Clementel and Ferrari (1952), theoretical
G	Hughes and Marsden (1966), estimate
M	Flückiger (1976), Monte Carlo, $\lambda_N = \lambda_N(E)$, $\lambda_\pi = 75$ g/cm^2
U , L	upper and lower limits of spectrum M
o	Ashton et al. (1970), measurement

3.4 Gamma Rays

3.4.1 Experimental Aspects and Data

No flux data and energy spectra exist for gamma rays only at sea level. All measurements include both, electrons and gamma rays combined. Thus, most of the data for gamma rays given in this chapter include electrons as well.

The ratio of photons to electrons of energies $\geq$ 100 MeV was found to be unity. According to Palmatier (1952) the corresponding photon intensity I is

$$I(E \geq 100\ MeV) = 10^{-3} \quad [\mathrm{cm}^{-2}\mathrm{s}^{-1}\mathrm{sr}^{-1}] \,. \tag{3.7}$$

In one experiment electrons and gamma rays have been separated at an atmospheric depth of 760 g/cm^2 (Beuermann and Wibberenz, 1968). The differential energy spectrum obtained by this measurement is shown in Fig. 3.20 together with a calculation of the photon spectrum at the same depth (Daniel and Stephens, 1974). The exponent, γ, of the differential energy spectrum, which can be represented by the expression $j(E) \propto E^{-\gamma}$, is 2.0. The calculated differential energy spectrum at sea level is shown in Fig. 3.21 (Daniel and Stephens, 1974). For comparison, the spectra of electrons and positrons are also indicated.

References

Beuermann, K.P. and G. Wibberenz: Can. J. Phys., 46, p. S1034 (1968).

Daniel, R.R. and S.A. Stephens: Rev. Geophys. and Space Phys., 12, p. 233 (1974).

Palmatier, E.D.: Phys. Rev., 88, p. 761 (1952).

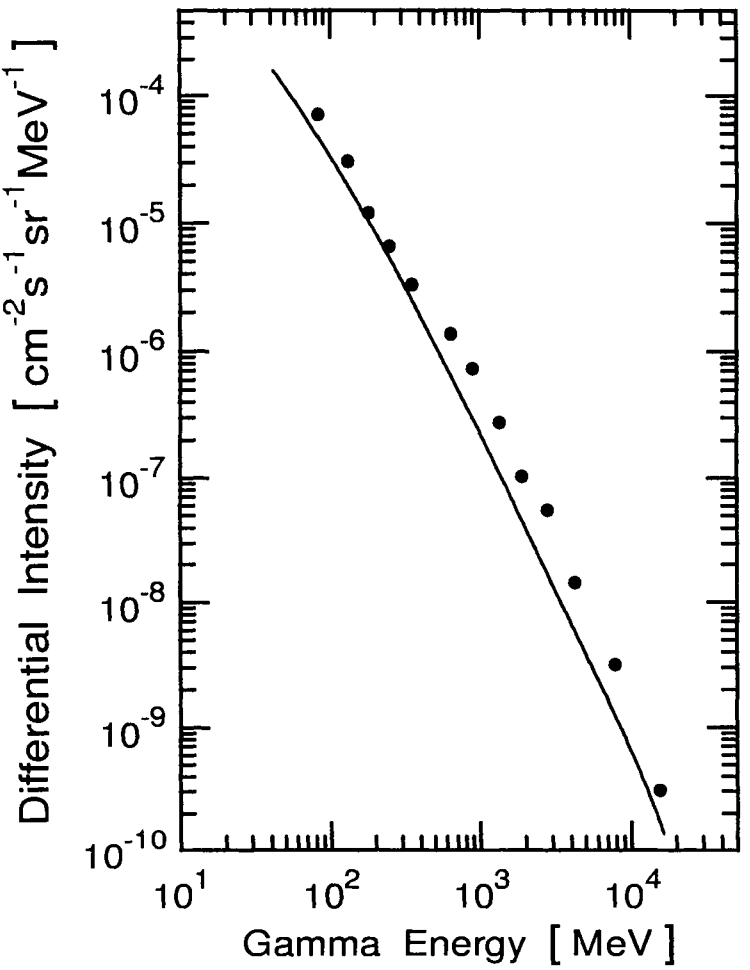

Figure 3.20: Differential energy spectrum of photons at an atmospheric depth of 760 g/cm^2.

o Beuermann and Wibberenz (1968), experimental
— Daniel and Stephens (1974), theoretical

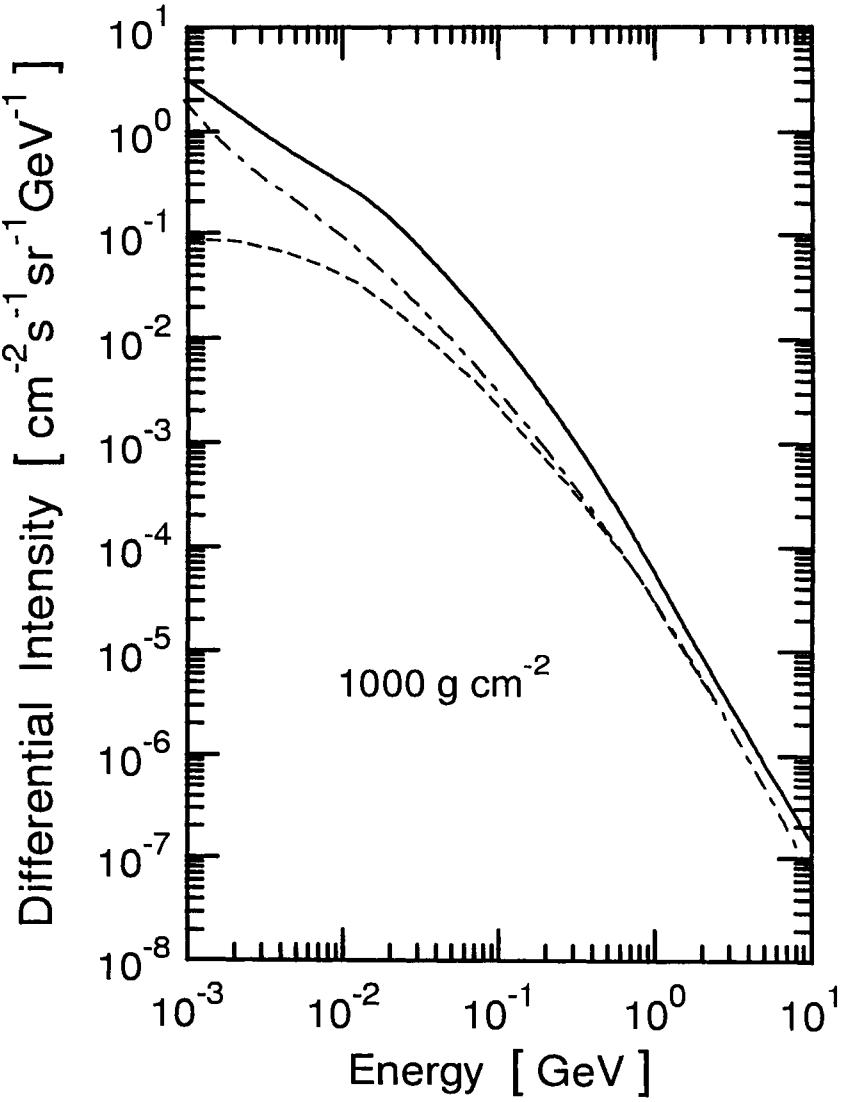

Figure 3.21: Calculated differential energy spectrum of photons, electrons and positrons at sea level (Daniel and Stephens, 1974).

—— photons
— · — electrons
— — positrons

3.5 Electrons (Negatrons and Positrons)

3.5.1 Flux Measurements and Intensities

As pointed out before, the secondary cosmic radiation is divided into a hard and a soft component. By definition the hard component is able to penetrate 15 cm of lead, which corresponds to 167 g/cm^2. The soft component which consists mostly of electrons (negatrons and positrons) and photons is almost completely absorbed in such a massive shield. Its flux at sea level amounts to about 35% - 40% of that of the muons.

The vertical intensity I_v and the flux J_1 are generally known. Assuming for the angular dependence

$$I(\theta) = I_v \cos^n(\theta) \tag{3.8}$$

the following relation between the flux and the vertical intensity can be derived.

$$J_1 = 2\pi \left(\frac{I_v}{n+2} \right) \tag{3.9}$$

Measurements of the soft component have been carried out by Greisen (1942). The following data are given for the vertical intensity I_v and the flux J_1 at sea level:

$$I_v = 3.1 \cdot 10^{-3} \quad [\mathrm{cm^{-2}s^{-1}sr^{-1}}] \tag{3.10}$$

$$J_1 = 5.2 \cdot 10^{-3} \quad [\mathrm{cm^{-2}s^{-1}}] \, . \tag{3.11}$$

A somewhat higher vertical intensity was measured by Chou (1953), namely

$$I_v = 3.3 \cdot 10^{-3} \quad [\mathrm{cm^{-2}s^{-1}sr^{-1}}] \, . \tag{3.12}$$

The intensity for energies ≥ 80 MeV amounts to $(30 \pm 6)\%$ of the total flux of the soft component. Pugacheva and Yamburenko (1973) have given the following value for the vertical intensity:

$$I_v(\geq 80\mathrm{MeV}) = 1.0 \cdot 10^{-3} \quad [\mathrm{cm^{-2}s^{-1}sr^{-1}}] \, . \tag{3.13}$$

An integral value for the vertical intensity for $E \geq 500$ MeV has been given by Wibberenz (1962).

Based on vertical intensity measurements at an altitude of 3000 m, Beuermann and Wibberenz (1968) derived the vertical intensity and the flux of electrons and positrons for $E \geq 100$ MeV at sea level. They obtained

$$I_v(\geq 100\text{MeV}) = (8.8 \pm 0.8) \cdot 10^{-4} \quad [\text{cm}^{-2}\text{s}^{-1}\text{sr}^{-1}] \tag{3.14}$$

$$J_1(\geq 100\text{MeV}) = (1.0 \pm 0.1) \cdot 10^{-3} \quad [\text{cm}^{-2}\text{s}^{-1}] \,. \tag{3.15}$$

Adding the flux of photons, a value of

$$J_1(\geq 100\text{MeV}) = (2.7 \pm 0.3) \cdot 10^{-3} \quad [\text{cm}^{-2}\text{s}^{-1}] \tag{3.16}$$

can be given for the total soft component (Beuermann and Wibberenz, 1968).

3.5.2 Energy Spectra

Sea level energy spectra have been measured by Allkofer and Knoblich (1970), Beedle (1970), Beuermann and Wibberenz (1968), and Wibberenz (1962).

The differential momentum spectrum for the range $0.1 \leq p \leq 0.8$ GeV/c is shown in Fig. 3.22 (Allkofer and Knoblich, 1970). Fig. 3.23 shows the energy spectrum for the range $80 \leq E \leq 3700$ MeV (Pugacheva et al., 1973) together with low energy values from Palmatier (1952). The integral spectrum for $E \geq 80$ MeV can be represented by

$$J(\geq E) = 2.2 \cdot 10^{-5} E^{-1.45} \quad [\text{cm}^{-2}\text{s}^{-1}\text{sr}^{-1}] \,. \tag{3.17}$$

with E in [GeV].

A combined differential energy spectrum consisting of measured and calculated data is shown in Fig. 3.24 (Daniel and Stephens, 1974). Since the spectrum at sea level is independent of the geomagnetic latitude, values of different latitudes could be summarized in this figure. Between 100 and 1000 MeV a power law spectrum can be fitted with an exponent of -2.0. Beyond about 1 GeV a value of -2.8 is required.

3.5.3 Charge Ratio

The charge ratio of positrons to negatrons has been determined up to 6 GeV with a magnetic spectrograph, combined with a calorimeter (Allkofer and Knoblich, 1970). The results are shown in Table 3.11. The charge ratio shows values less than one, as expected, because of processes like the Compton

Table 3.11: Intensities and Charge Ratio of Electrons at Sea Level. (Allkofer and Knoblich 1974)

Momentum Interval [GeV/c]	Mean Momentum [GeV/c]	Intensity $[cm^{-2}\,s^{-1}\,sr^{-1}\,(GeV/c)^{-1}]$	Charge Ratio (e^+/e^-)
0.05 - 0.5	0.20	$(2.20 \pm 0.26) \cdot 10^{-3}$	0.52 ± 0.13
0.5 - 1.0	0.64	$(2.75 \pm 0.69) \cdot 10^{-4}$	0.60 ± 0.31

effect and knock-on production, that generate negatrons only. Theoretical energy spectra for negatrons and positrons are shown in Fig. 3.25 (Daniel and Stephens, 1974).

3.5.4 Zenith Angle Dependence

The zenith angle dependence of the observed intensities can be fitted with a $\cos^2(\theta)$ distribution for $\theta \leq 60°$, in the energy range $1.3 \leq E \leq 35$ MeV (Beedle, 1970). For electrons of energy $2 \leq E \leq 20$ GeV a value of $n = 2.0 \pm 0.5$ was obtained for the exponent (Kameda, 1960). The angular dependence observed by Beuermann and Wibberenz (1968) is shown in Fig. 3.26. The exponent which results from this work is $n > 3.6$ for $E \geq 100$ MeV.

References

Allkofer, O.C., K. Clausen, and P. Knoblich: Proc. of the VI. Inter-American Seminar on Cosmic Rays, La Paz, Bolivia, 4, p. 930 (1970).

Allkofer, O.C. and P. Knoblich: Nuovo Cimento, 3, p. 6 (1970).

Beedle, R.E. and W.R. Webber: Can. J. Phys., 46, p. S1014 (1968).

Beedle, R.E.: Ph. D. Thesis, University of New Hampshire, Durham ¿ (1970).

Beuermann, K.P. and G. Wibberenz: Can. J. Phys., 46, p. S1034 (1968).

Chou, C.N.: Phys. Rev., 90, p. 473 (1953).

Daniel, R.R. and S.A. Stephens: Rev. Geophys. and Space Phys., 12, p. 233 (1974).

Greisen, K.: Phys. Rev., 61, p. 212 (1942).

Kameda, T. and T. Maeda: J. Phys. Soc. Japan 15, p. 1367 (1960).

Palmatier, E.D.: Phys. Rev., 88,p. 761 (1952).

Pugacheva, G.I. and N.S. Yamburenko: Geomagn. and Aeron. (USSR), 13, p. 778 (1973).

Wibberenz, G.: Z. Phys., 167, p. 284 (1962).

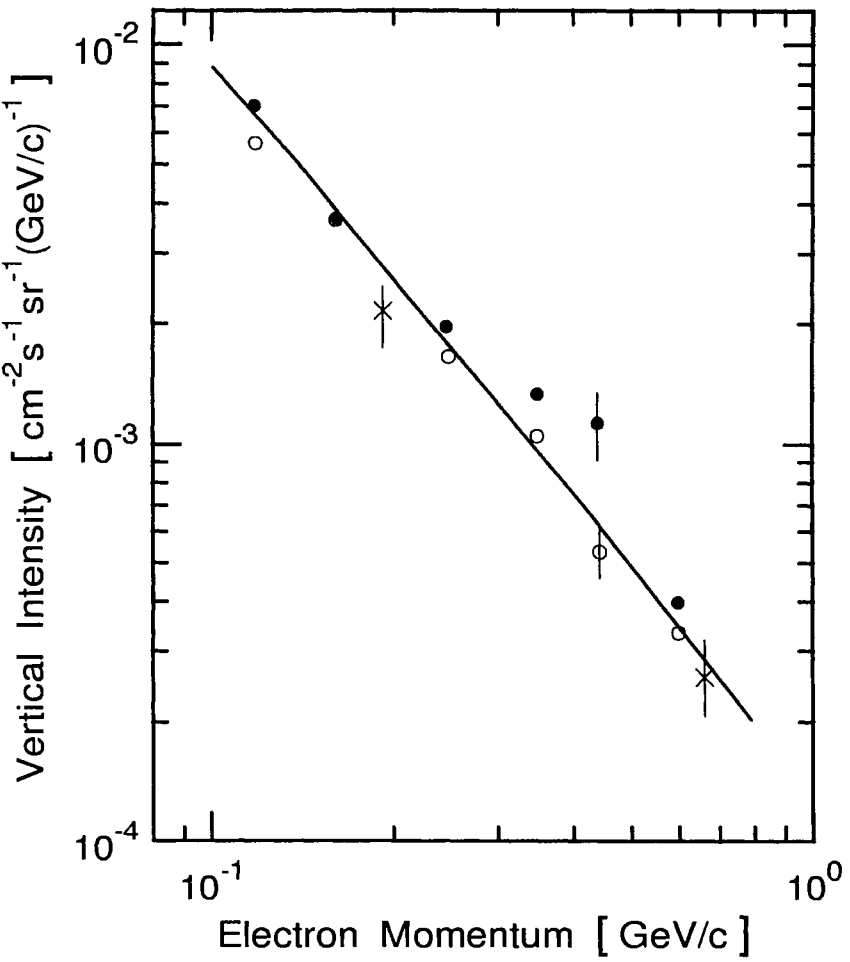

Figure 3.22: Differential electron spectrum ($e^+ + e^-$) at sea level in the momentum range $0.1 \leq p \leq 1$ GeV/c (Allkofer and Knoblich, 1970).

• , ○ Wibberenz (1962)
× Allkofer and Knoblich (1970)

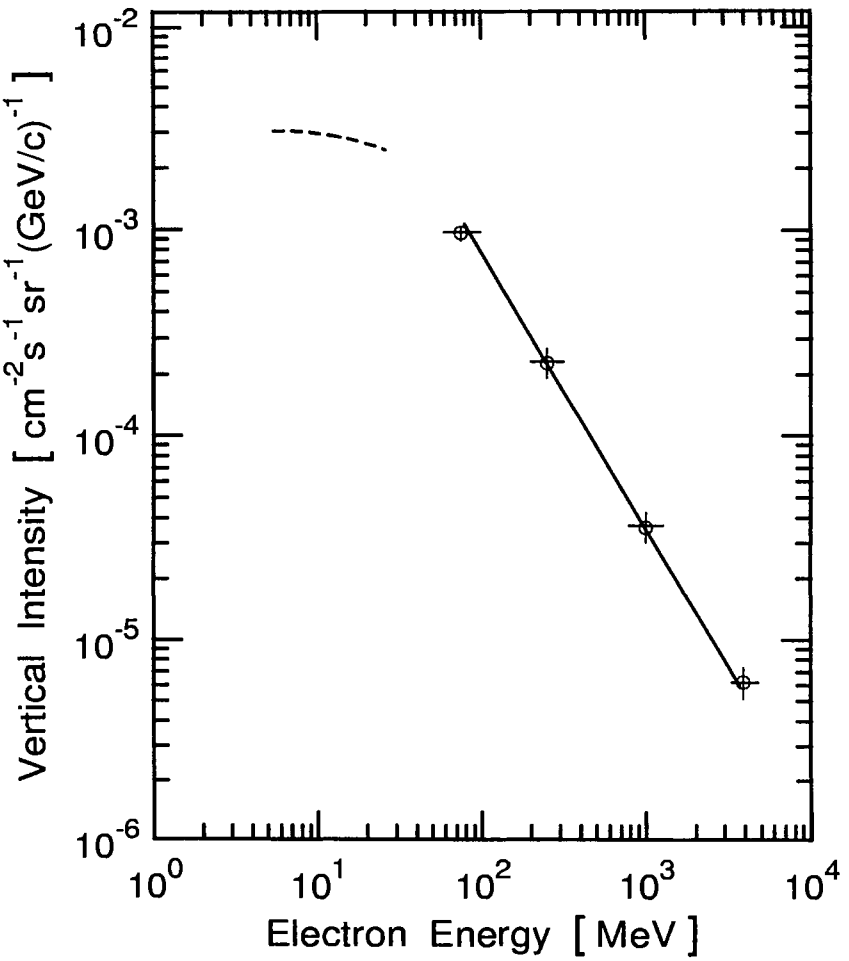

Figure 3.23: Integral energy spectrum of electrons ($e^+ + e^-$) at sea level in the range $10 \leq E \leq 5000$ MeV (Pugacheva and Yamburenko, 1973).

– – Palmatier (1952)
o Pugacheva and Yamburenko (1973)

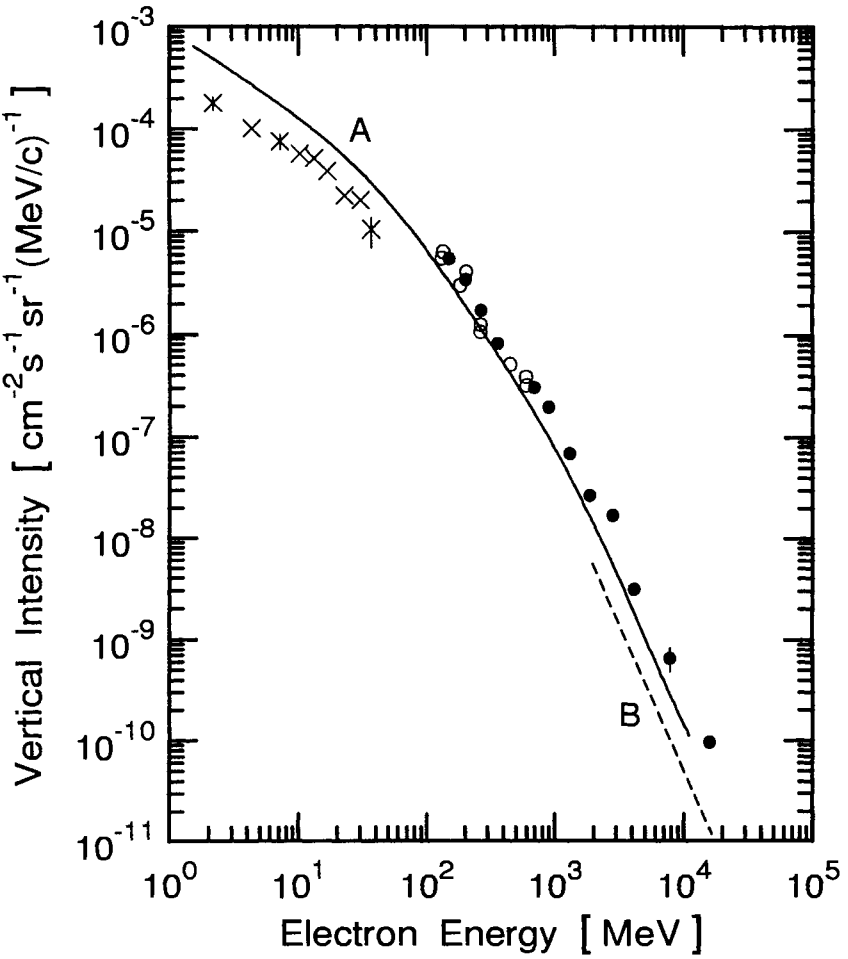

Figure 3.24: Experimental and theoretical differential energy spectra of electrons ($e^+ + e^-$) at sea level (Daniel and Stephens, 1974).

- o Allkofer and Knoblich (1970), measurements
  Wibberenz (1962), measurements
- • Beuermann and Wibberenz (1968), measurements
- × Beedle (1970), measurements
- A Daniel and Stephens (1974), calculation for electrons at 1000 g/cm^2
- B Kameda (1960), measurements

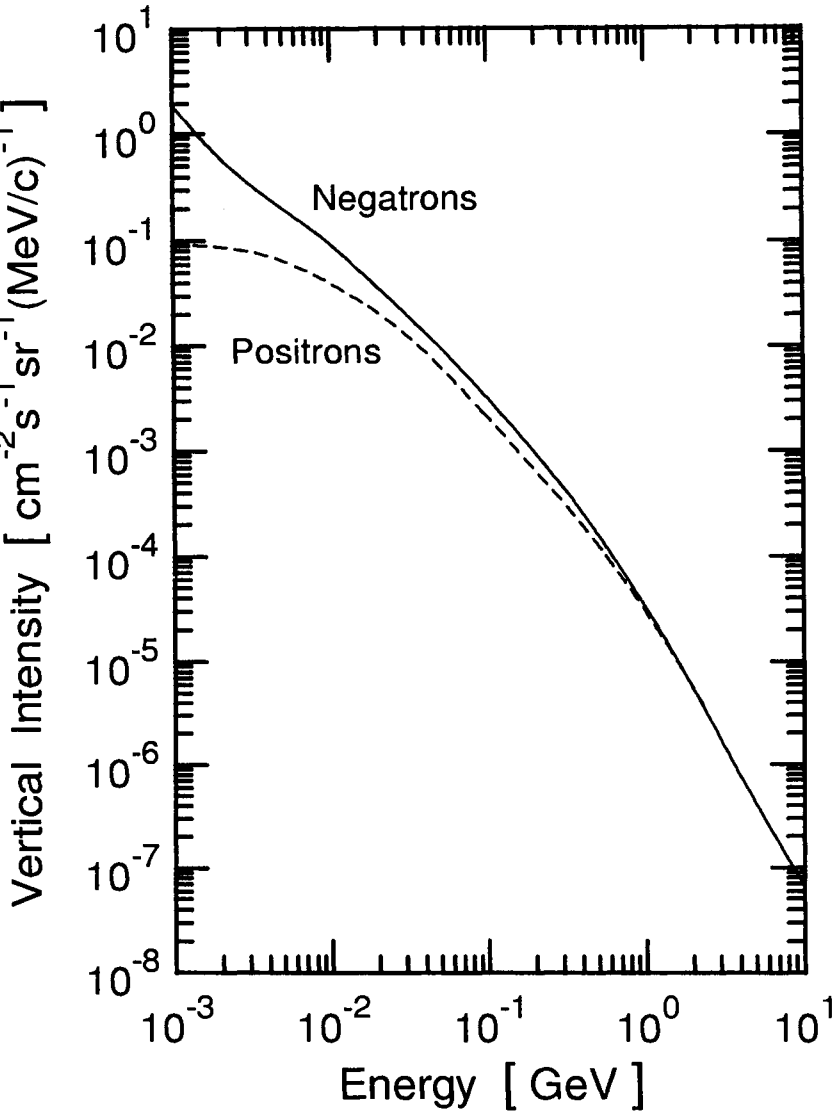

Figure 3.25: Calculated differential energy spectra of negatrons (solid curve) and positrons (dashed curve) at sea level (Daniel and Stephens, 1974).

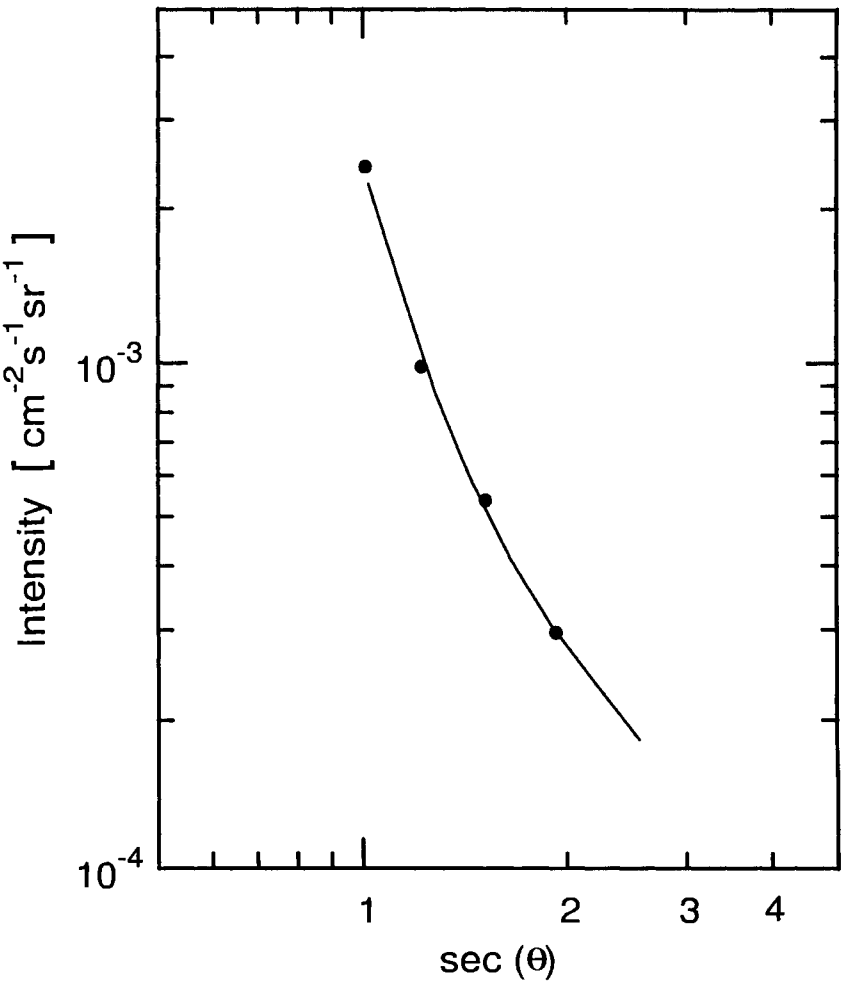

Figure 3.26: Angular dependence of the electron ($e^+ + e^-$) intensity at sea level for energies $\geq$ 100 MeV (Beuermann and Wibberenz, 1968).

3.6 Muons

3.6.1 Introduction

With the exception of photons and neutrinos, muons are the most abundant component of the secondary cosmic radiation at sea level. Consequently much more information is available on muons than on any other component. In addition muon data reveal information on high energy processes in the atmosphere and on the primary radiation, in particular on its spectrum and composition. Comprehensive reviews on this subject have been presented in rapporteur papers at international cosmic ray conferences and in review articles (Allkofer, 1967 and 1979a; Thompson, 1973; Kitamura, 1981; Narasimham, 1987; and Ryazhskaya, 1995). A recent summary of theoretical aspects of atmospheric muons, including contributions from charm decay and comparisons with experimental data is given by Bugaev et al. (1998).

3.6.2 Absolute Flux Measurements and Intensities

The vertical muon intensity at sea level is an important physical quantity. At low momenta ($p_\mu \leq 5$ GeV/c) it depends on the geomagnetic latitude, λ, of the location where the measurement is made and on the solar activity. Geomagnetic effects are discussed in Chapter 1, Section 1.8 and Chapter 6, Section 6.2, and details of the latitude effect in Subsection 3.6.6 below. Muon measurements up to 1973 had been summarized by Allkofer and Jokisch (1973).

The so-called hard component which penetrates 15 cm of lead (167 g/cm^2) consists mostly of muons ($p_\mu \geq 0.3$ GeV/c), less than 1% are protons or other particles. The following values have been given for the *vertical integral intensity*, $I_v(\geq p)$, the *flux*, $J_1(\geq p)$, and the *omnidirectional intensity*, $J_2(\geq p)$, of the hard component at a latitude of 50° and an altitude of 259 m a.s.l. (1007 g cm^{-2}) (Ithaca, N.Y.) (Greisen 1942). The data apply to muons of momentum $\geq$0.35 GeV/c, accounting for slightly inclined trajectories in the absorber because of the finite opening angle of the muon telescope.

$$I_v(\geq 0.35 GeV/c) = 0.82 \cdot 10^{-2} \quad [\mathrm{cm^{-2}s^{-1}sr^{-1}}] \tag{3.18}$$

$$J_1(\geq 0.35 GeV/c) = 1.27 \cdot 10^{-2} \quad [\mathrm{cm^{-2}s^{-1}}] \tag{3.19}$$

$$J_2(\geq 0.35 GeV/c) = 1.68 \cdot 10^{-2} \quad [\mathrm{cm^{-2}s^{-1}}] \, . \tag{3.20}$$

Based on measurements by Greisen, Rossi (1948) derived the *vertical differential intensity*, $I_v(p)$, for a muon momentum of 1 GeV/c, obtaining a value of

$$I_v(1\,GeV/c) = 2.45 \cdot 10^{-6} \quad [\mathrm{cm^{-2}s^{-1}sr^{-1}(MeV/c)^{-1}}] \,. \tag{3.21}$$

Newer measurements using more modern detectors and precise correction factors have led to higher values (Allkofer et al. 1970a, 1970b, 1970c, 1970d, and 1971d erratum to 1970a). According to these measurements the absolute vertical differential muon intensity at 1 GeV/c is

$$I_v(1\,GeV/c) = 3.09 \cdot 10^{-6} \pm 5\% \quad [\mathrm{cm^{-2}s^{-1}sr^{-1}(MeV/c)^{-1}}] \,, \tag{3.22}$$

or

$$I_v(1\,GeV/c) = 3.09 \cdot 10^{-3} \quad [\mathrm{cm^{-2}s^{-1}sr^{-1}(GeV/c)^{-1}}] \,, \tag{3.23}$$

which is 26% higher than the Rossi intensity. The vertical integral intensity, the flux and the omnidirectional intensity have been derived from this intensity and have been found to be 16% higher than the Greisen data (Greisen 1942; Allkofer et al. 1975a). They have the following values for a lower momentum cutoff at 0.35 GeV/c:

$$I_v(> 0.35\,GeV/c) = (0.94 \pm 0.05) \cdot 10^{-2} \quad [\mathrm{cm^{-2}s^{-1}sr^{-1}}] \tag{3.24}$$

$$J_1(> 0.35\,GeV/c) = (1.44 \pm 0.09) \cdot 10^{-2} \quad [\mathrm{cm^{-2}s^{-1}}] \,, \tag{3.25}$$

$$J_2(> 0.35\,GeV/c) = (1.90 \pm 0.12) \cdot 10^{-2} \quad [cm^{-2}s^{-1}] \,. \tag{3.26}$$

In 1970 worldwide re-measurement of the muon intensities had been initiated to clarify the situation. New differential and integral measurements were carried out, predominantly at sea level and at low momenta. The new values are between 10% and 30% higher. Table 3.12 gives a summary of the results obtained by various authors (see also Allkofer and Jokisch, 1973). A compilation of differential data is shown in Fig. 3.27 and of integral data

Table 3.12: Vertical Absolute Integral Intensities of Muons at or near Sea Level (ordered by latitude).

Authors	Geomagn. Lat. [°N]	Geomagn. P_c [1] [GV]	Altitude [m]	Momentum [GeV/c]	Intensity $\times 10^3$ [$cm^{-2}s^{-1}sr^{-1}$]
Allkofer et al. (1968)	9	14.1	s.l.	$\geq$0.32	7.25±0.1
Chandrasekharan et al. (1950)	9	-	555	$\geq$0.27	7.6
Sinha and Basu (1959)	12	16.5	30	$\geq$0.27	7.3±0.2
De et al. (1972)	12	16.5	30	$\geq$0.954	6.86±0.03
Karmakar et al. (1973)	16	15.0	122	$\geq$0.353	8.99±0.05
				$\geq$1.0	6.85±0.04
Gokhale (1953)	19	-	-	$\geq$0.32	7.3±0.1
Gokhale and Balasubrahmanyam	19	-	124	$\geq$0.27	7.55±0.1
Fukui et al. (1957)	24	12.6	s. l.	$\geq$0.34	7.35±0.20
				$\geq$0.54	6.87±0.25
Kitamura and Minorikawa (1953)	25	12.6	-	$\geq$0.34	7.2±0.1
Baschiera et al. (1979)	42	4.5	238	$\geq$ 0.457	8.75 ± 0.33
				$\geq$ 0.918	7.27 ± 0.26
Wentz et al. (1995)	44.5	3.4	116	$\geq$0.6	8.54 ± 0.34
Rossi (1948)	$\geq$50	~1.8	s.l.	$\geq$0.32	8.3
Pomerantz (1949)	52	2.0	89	$\geq$0.31	8.2±0.1
Allkofer et al. (1970a, e, and 1971d erratum	53	2.4	s. l.	$\geq$0.985	7.49±0.30
				$\geq$1.239	6.76±0.27
Allkofer et al. (1971b, c),				$\geq$ 0.4 [2]	9.18
Allkofer & Clausen (1970)				$\geq$1.0	7.22
Kraushaar (1949)	53	1.6	259	$\geq$0.28	8.87±0.05
Greisen (1942)	54	1.5	259	$\geq$0.33	8.2±0.1
			s. l.	$\geq$0.33	8.3±0.1 [2]

[1] Cutoff rigidities, P_c, are listed as given in references. They may vary with time and model employed.

[2] Results after corrections made by Rossi (1948).

Table 3.12: Vertical Absolute Integral Intensities of Muons at or near Sea Level (ordered by latitude) (continued).

Authors	Geomagn. Lat. [°N]	Geomagn. P_c [1] [GV]	Altitude [m]	Momentum [GeV/c]	Intensity $\times 10^3$ [$cm^{-2} s^{-1} sr^{-1}$]
Allkofer (1965)	55	2.2	s. l.	$\geq$0.320	8.5±0.2
Allkofer (1965)				$\geq$0.320	8.4±0.1
Crookes & Rastin (1972)	53	2.5	40	$\geq$0.35	9.13±0.12
Crookes and Rastin (1971b, 1973)				> 7.3	1.40 ± 0.02
				> 8.5	1.19 ± 0.06
Barbouti and Rastin (1983)	53	2.5	40	$\geq$ 0.438	8.868 ± 1.3%
				$\geq$ 0.815	7.661 ± 1.1%
				$\geq$ 1.728	5.563 ± 1.1%
				$\geq$ 2.681	4.152 ± 1.2%
				$\geq$ 3.639	3.20 ± 1.1%
Hayman et al. (1962)	57.5	1.8	s.l.	$\geq$0.320	$\geq$7.6±0.06
Ashton et al. (1972)	57.5	2.1	s. l.	$\geq$0.88	8.22±0.4
				$\geq$1.0	7.58±0.4 [2]
Ayre et al. (1971a, b, and 1973a)	57.5	2.1	s. l.	> 3.48	2.86 ± 0.04
				> 7.12	1.31 ± 0.02

[1] Cutoff rigidities, P_c, are listed as given in references. They may vary with time and model employed.

[2] Obtained by combining with the measurements of Allkofer et al. (1970a) and Allkofer and Clausen (1970) around 1 Gev/c.

in Figs. 3.28 and 3.29. The discrepancies between the very early and the more recent measurements are evident. Newer measurements of the vertical intensity at low momenta carried out by different authors are in agreement with each other, as shown in Fig. 3.30 (Flint et al. 1973).

High resolution low energy vertical measurements by Karmakar et al. (1973), Ng et al. (1974b), and others have led to the results listed in Table 3.13. A more recent summary of muon measurements has been given by Shen et al. (1981) and Kitamura (1981).

A very recent integral measurement made by Wentz et al. (1995) in Karlsruhe, Germany, at 110 m a.s.l. yielded a value of $(8.54 \pm 0.34) \cdot 10^{-3}$

Table 3.13: Low Momentum Vertical Differential Muon Intensities at Sea Level.

Authors	Cutoff P_c [GV]	Momentum [GeV/c]	Intensity $\times 10^3$ [$cm^{-2}s^{-1}sr^{-1}$ $(GeV/c)^{-1}$]
Rossi (1948)	~1.8	1.0	2.45
Ng et al. (1974b)	2.1	0.85 ± 0.03	4.09 ± 0.21
		1.16 ± 0.04	3.29 ± 0.19
Allkofer et al. (1970d)	2.4	1.32	2.57 ± 0.21
Allkofer et al. (1970a, e,		1.0	$3.21 \pm 5\%$
and 1971d erratum)		1.112	2.90 ± 0.2
Allkofer and Clausen (1970)		1.24	2.73 ± 0.23
Allkofer and Jockisch (1973)		1.0	$3.09 \pm 8\%$ *
Baschiera et al. (1979)	4.5	0.314	3.25 ± 0.17
		0.805	3.60 ± 0.18
Bateman et al. (1971)	4.9	3.0	$1.0 \pm 3\%$
Basu and Sinha (1956/57)	16.5	0.30	2.89 ± 0.1
De et al. (1972b)	16.5	1.131	2.32 ± 0.2

* new standard

$cm^{-2}s^{-1}sr^{-1}$ at a threshold energy of 0.5 GeV ($p \simeq 0.6$ GeV/c).

The zenith angle dependence of the muon intensity is discussed in Subsection 3.6.4 where absolute intensities for a wide range of zenith angles are summarized.

3.6.3 Momentum and Energy Spectra

The momentum spectrum of muons has been measured many times. Most experiments were carried out with magnetic spectrometers. The upper limit of the momentum range of early measurements was just a few GeV/c, today it is in excess of 20 TeV/c for large spectrometers. In the highest energy region spectral data had been obtained with emulsion chambers, muon pair meters and burst detectors (Mitsui et al. 1979, 1983a and 1983b). Because of the low event rate at high energies large installations are required. Many spectra were measured at large zenith angles, close to the horizontal direction.

Vertical Spectra

Momentum spectra of vertical muons have been measured in Kiel with a variety of spark chamber spectrometers in different energy regions (Allkofer et al. 1970a, 1970c, and 1971d erratum to 1970a; Knoblich 1968). The results were merged to form a single momentum spectrum, covering the range $0.2 \leq p \leq 1000$ GeV/c (Allkofer et al. 1971b and 1971c). The differential and integral spectra from this work are shown in Fig. 3.31. The values are also given in Table 3.14 (Allkofer et al. 1971b). The corresponding exponents of the power law representations, $j_\mu(p) \propto E^{-\delta}$ and $J_\mu(\geq p) \propto E^{-\gamma}$, respectively, can be taken from Table 3.15. A comparison with previous results is shown in Figs. 3.32 and 3.33.

In somewhat later work Karmakar et al. (1973) made high precision absolute measurements of low momentum muons in North Bengal at geographic coordinates $\sim 27°\,3'$ N and $\sim 88°\,30'$ E, just slightly above sea level, at altitude 122 m and mean atmospheric pressure of 995.5 mb. The local geomagnetic cutoff energy was 15 GeV. The results are given in Table 3.16.

De et al. (1974) obtained the following expression that gives a good fit to the experimental differential spectrum over the momentum range $0.2 \leq p \leq 20$ GeV/c at low latitude (12°N) and sea level.

$$j_\mu(p) = 2.47 \cdot 10^{-3} p^{-0.4854 - 0.3406 \ln(p)} \quad [\mathrm{cm^{-2} s^{-1} sr^{-1} (GeV/c)^{-1}}] \,, \quad (3.27)$$

where p is in GeV/c and the constant refers to the differential muon intensity at 1 GeV/c obtained by these authors in their experiment.

For high latitudes most of the absolute spectra can be well represented (within 8%) by the relation

$$j_\mu(p) = 3.09 \cdot 10^{-3} p^{-0.5483 - 0.3977 \ln(p)} \quad [\mathrm{cm^{-2} s^{-1} sr^{-1} (GeV/c)^{-1}}] \,. \quad (3.28)$$

The spectrum is normalized at the standard momentum of 1 GeV/c to the value stated in eq. 3.23.

Menon and Ramana Murthy (1967) assembled a so-called composite vertical integral energy spectrum of muons from a variety of early measurements made with different experimental installations and types of apparatuses, covering the energy range $20 \leq E \leq 7000$ GeV. The spectrum is presented in tabulated form in Table 3.17 and as a plot in Fig. 3.34.

Detailed spectral measurements were carried out by Rastin and co-workers at Nottingham, England (Rastin 1984a). These data are summarized

Table 3.14: Vertical Absolute Differential Muon Intensities at Sea Level at Kiel in the Momentum Range $0.2 \leq p \leq 1000$ GeV/c. (Allkofer et al. 1971b)

Momentum Range [GeV/c]	Mean Momentum [GeV/c]	Differential Intensity $[cm^{-2}s^{-1}sr^{-1}(GeV/c)^{-1}]$
0.2 - 0.5	0.34	$(3.92 \pm 0.62) \cdot 10^{-3}$
0.5 - 0.8	0.64	$(3.59 \pm 0.49) \cdot 10^{-3}$
0.8 - 2.0	1.32	$(2.57 \pm 0.29) \cdot 10^{-3}$
2.0 - 4.0	2.86	$(1.11 \pm 0.13) \cdot 10^{-3}$
4,0 - 6.0	4.91	$(4.13 \pm 0.59) \cdot 10^{-4}$
0.98 - 1.24	1.11	$(2.90 \pm 0.20) \cdot 10^{-3}$
0.2 - 0.4	0.29	$(3{,}57 \pm 0.35) \cdot 10^{-3}$
0.4 - 0.6	0,50	$(3.70 \pm 0.35) \cdot 10^{-3}$
0.6 - 1.0	0.79	$(3.41 \pm 0.28) \cdot 10^{-3}$
1.0 - 1.5	1.24	$(2.73 \pm 0.23) \cdot 10^{-3}$
1.5 - 2.5	1.95	$(1.73 \pm 0.15) \cdot 10^{-3}$
2.5 - 4.0	3.17	$(7{,}92 \pm 0.65) \cdot 10^{-4}$
4,0 - 6.0	4.91	$(4.24 \pm 0.37) \cdot 10^{-4}$
6.0 - 10	7.76	$(1.84 \pm 0.17) \cdot 10^{-4}$
10 - 13	11.4	$(1.13 \pm 0.01) \cdot 10^{-4}$
13 - 17	14.8	$(6.04 \pm 0.08) \cdot 10^{-5}$
17 - 25	20.5	$(2.51 \pm 0.03) \cdot 10^{-5}$
25 - 40	31.4	$(8.01 \pm 0.13) \cdot 10^{-6}$
40 - 70	52.3	$(1.89 \pm 0,05) \cdot 10^{-6}$
70 - 128	93.0	$(3.38 \pm 0.14) \cdot 10^{-7}$
128 - 250	175.0	$(5.19 \pm 0.37) \cdot 10^{-8}$
250 - 450	329.0	$(7.84 \pm 1.12) \cdot 10^{-9}$
450 - 1000	642.0	$(6.40 \pm 1.92) \cdot 10^{-10}$

in differential and integral form in Table 3.18 and presented in Fig. 3.35. In addition some high energy data points obtained with MARS, the Magnetic Automated Research Spectrograph at Durham, England (Thompson et al. 1977), and one set of horizontal data ($\theta = 89°$) from the work of Komori et al. (1977) using the MUTRON detector in Tokyo are also included.

Table 3.15: Differential and Integral Momentum Spectra of Vertical Muons at Kiel. δ and γ are the respective spectral exponents of power law fits (Allkofer et al. 1971b).

Momentum [GeV/c]	Differential Intensity $[\frac{cm^{-2}s^{-1}sr^{-1}}{(GeV/c)}]$	δ	Integral Intensity $[cm^{-2}s^{-1}sr^{-1}]$	γ
0.2	$3.73 \cdot 10^{-3}$	0.06	$9.94 \cdot 10^{-3}$	0.05
0.4	$3.72 \cdot 10^{-3}$	0.16	$9.18 \cdot 10^{-3}$	0.13
0.8	$3.10 \cdot 10^{-3}$	0.38	$7.81 \cdot 10^{-3}$	0.28
1.0	$2.79 \cdot 10^{-3}$	0.49	$7.22 \cdot 10^{-3}$	0.35
1.5	$2.14 \cdot 10^{-3}$	0.73	$6.00 \cdot 10^{-3}$	0.50
2.0	$1,67 \cdot 10^{-3}$	0.93	$5.05 \cdot 10^{-3}$	0.63
3.0	$1.06 \cdot 10^{-3}$	1,24	$3.72 \cdot 10^{-3}$	0.82
5.0	$4.97 \cdot 10^{-4}$	1.63	$2.26 \cdot 10^{-3}$	1.08
7.0	$2.73 \cdot 10^{-4}$	1.87	$1.52 \cdot 10^{-3}$	1.24
10	$1.33 \cdot 10^{-4}$	2.10	$9.42 \cdot 10^{-4}$	1.40
15	$540 \cdot 10^{-5}$	2.32	$5.13 \cdot 10^{-4}$	1.57
20	$2.70 \cdot 10^{-5}$	2.46	$3.21 \cdot 10^{-4}$	1.68
30	$9.59 \cdot 10^{-6}$	2.63	$1.57 \cdot 10^{-4}$	1.82
50	$2.36 \cdot 10^{-6}$	2.83	$593 \cdot 10^{-5}$	1.99
70	$8.92 \cdot 10^{-7}$	2.95	$2.98 \cdot 10^{-5}$	2.09
100	$3.04 \cdot 10^{-7}$	3.07	$1.38 \cdot 10^{-5}$	2.20
150	$8.51 \cdot 10^{-8}$	3.20	$5.55 \cdot 10^{-6}$	2.30
200	$3,35 \cdot 10^{-8}$	3.28	$2.84 \cdot 10^{-6}$	2.36
300	$8.70 \cdot 10^{-9}$	3.37	$1.07 \cdot 10^{-6}$	2.43
500	$1.52 \cdot 10^{-9}$	3.46	$3.03 \cdot 10^{-7}$	2.50
700	$4.71 \cdot 10^{-10}$	3.50	$1.30 \cdot 10^{-7}$	2.54
1000	$1.34 \cdot 10^{-10}$	3.54	$5.23 \cdot 10^{-8}$	2.56

At very high energies the spectrum was obtained from underground range measurements, from muon burst measurements, and from X-ray film emulsion chambers. Fig. 3.36 shows the muon momentum spectrum thus obtained from 10 to 10^5 GeV/c (Carstensen 1978, Allkofer et al. 1978b, 1978c, Allkofer 1979b). Note that the intensities are multiplied by the energy squared.

Another compilation of vertical differential sea level muon spectral data made by the author which includes very recent work as well is presented in

Table 3.16: Vertical Absolute Integral Muon Intensities at 122 m a.s.l. and Geomagnetic Latitude 16°N (Cutoff Energy $E_c = 15$ GeV) (Karmakar et al., 1973).

Cutoff Momentum [GeV/c]	Absolute Intensity $\times 10^3$ $[cm^{-2} s^{-1} sr^{-1}]$	
	before msc(*	after msc(*
0.353±0.025	8.45±0.05	8.99±0.05
0.725±0.036	7.41±0.05	7.81±0.05
0.977±0.043	6.64±0.04	6.95±0.04
1.158±0.048	6.03±0.04	6.32±0.04
1.440±0.053	5.42±0.04	5.65±0.04
1.730±0.057	4.70±0.03	4.90±0.03
2.050±0.061	4.04±0.03	4.20±0.03
2.431±0.065	3.49±0.02	3.65±0.02
2.681±0.069	3.04±0.02	3.20±0.02

(* msc: multiple scattering correction.

Table 3.17: Composite Vertical Sea Level Muon Integral Energy Spectrum(* (Menon and Ramana Murthy, 1967)

Muon Energy ≥[GeV]	Intensity $[cm^{-2} s^{-1} sr^{-1}]$	Error [standard deviation]
20	$2.5 \cdot 10^{-4}$	5%
40	$7.8 \cdot 10^{-5}$	6%
70	$2.7 \cdot 10^{-5}$	8%
100	$1.3 \cdot 10^{-5}$	10%
200	$2.9 \cdot 10^{-6}$	12%
400	$5.5 \cdot 10^{-7}$	16%
700	$1.25 \cdot 10^{-7}$	20%
1000	$5.1 \cdot 10^{-8}$	22%
2000	$8.0 \cdot 10^{-9}$	25%
4000	$1.1 \cdot 10^{-9}$	35%
7000	$2.0 \cdot 10^{-10}$	60%

(* Assembled from magnetic spectrometer, depth-intensity, burst and γ-ray measurements.

Table 3.18: Best-fit Vertical Muon Differential and Integral Spectra at Sea Level (Rastin 1984a).

Muon Momentum [GeV/c]	Differential Intensity $[cm^{-2}\ s^{-1}sr^{-1}(GeV/c)^{-1}]$	Integral Intensity $[cm^{-2}\ s^{-1}\ sr^{-1}]$
0.35	$2.85 \cdot 10^{-3}$	$9.13 \cdot 10^{-3}$
0.40	$2.90 \cdot 10^{-3}$	$8.98 \cdot 10^{-3}$
0.50	$2.94 \cdot 10^{-3}$	$8.69 \cdot 10^{-3}$
0.60	$2.92 \cdot 10^{-3}$	$8.40 \cdot 10^{-3}$
0.70	$2.87 \cdot 10^{-3}$	$8.11 \cdot 10^{-3}$
0.80	$2.80 \cdot 10^{-3}$	$7.83 \cdot 10^{-3}$
0.90	$2.71 \cdot 10^{-3}$	$7.55 \cdot 10^{-3}$
1.0	$2.62 \cdot 10^{-3}$	$7.29 \cdot 10^{-3}$
1.5	$2.12 \cdot 10^{-3}$	$6.10 \cdot 10^{-3}$
2.0	$1.69 \cdot 10^{-3}$	$5.16 \cdot 10^{-3}$
3.0	$1.10 \cdot 10^{-3}$	$3.80 \cdot 10^{-3}$
4.0	$7.40 \cdot 10^{-4}$	$2.90 \cdot 10^{-3}$
5.0	$5.17 \cdot 10^{-4}$	$2.27 \cdot 10^{-3}$
6.0	$3.75 \cdot 10^{-4}$	$1.83 \cdot 10^{-3}$
7.0	$2.80 \cdot 10^{-4}$	$1.51 \cdot 10^{-3}$
8.0	$2.16 \cdot 10^{-4}$	$1.25 \cdot 10^{-3}$
9.0	$1.69 \cdot 10^{-4}$	$1.06 \cdot 10^{-3}$
10	$1.35 \cdot 10^{-4}$	$9.05 \cdot 10^{-4}$
15	$5.28 \cdot 10^{-5}$	$4.79 \cdot 10^{-4}$
20	$2.58 \cdot 10^{-5}$	$2.93 \cdot 10^{-4}$
25	$1.45 \cdot 10^{-5}$	$1.96 \cdot 10^{-4}$
30	$8.69 \cdot 10^{-6}$	$1.40 \cdot 10^{-4}$
40	$3.90 \cdot 10^{-6}$	$8.23 \cdot 10^{-5}$
50	$2.11 \cdot 10^{-6}$	$5.35 \cdot 10^{-5}$
60	$1.26 \cdot 10^{-6}$	$3.72 \cdot 10^{-5}$
70	$8.03 \cdot 10^{-7}$	$2.72 \cdot 10^{-5}$
80	$5.42 \cdot 10^{-7}$	$2.06 \cdot 10^{-5}$
90	$3.81 \cdot 10^{-7}$	$1.60 \cdot 10^{-5}$
100	$2.77 \cdot 10^{-7}$	$1.28 \cdot 10^{-5}$
150	$7.85 \cdot 10^{-8}$	$5.18 \cdot 10^{-6}$
200	$3.12 \cdot 10^{-8}$	$2.67 \cdot 10^{-6}$
250	$1.50 \cdot 10^{-8}$	$1.58 \cdot 10^{-6}$
300	$8.20 \cdot 10^{-9}$	$1.02 \cdot 10^{-6}$

Table 3.18: Best-fit Vertical Muon Differential and Integral Spectra at Sea Level (Rastin 1984a, continued).

Muon Momentum [GeV/c]	Differential Intensity $[cm^{-2}\ s^{-1}sr^{-1}(GeV/c)^{-1}]$	Integral Intensity $[cm^{-2}\ s^{-1}\ sr^{-1}]$
400	$3.11 \cdot 10^{-9}$	$5.08 \cdot 10^{-7}$
500	$1.45 \cdot 10^{-9}$	$2.93 \cdot 10^{-7}$
600	$7.75 \cdot 10^{-10}$	$1.87 \cdot 10^{-7}$
700	$4.55 \cdot 10^{-10}$	$1.27 \cdot 10^{-7}$
800	$2.86 \cdot 10^{-10}$	$9.07 \cdot 10^{-8}$
900	$1.89 \cdot 10^{-10}$	$6.74 \cdot 10^{-8}$
1000	$1.31 \cdot 10^{-10}$	$5.16 \cdot 10^{-8}$
1500	$3.14 \cdot 10^{-11}$	$1.84 \cdot 10^{-8}$
2000	$1.13 \cdot 10^{-11}$	$8.81 \cdot 10^{-9}$
2500	$5.11 \cdot 10^{-12}$	$4.97 \cdot 10^{-9}$
3000	$2.67 \cdot 10^{-12}$	$3.11 \cdot 10^{-9}$

Fig. 3.37. The intensities are multiplied by the third power of the momentum to obtain a compressed representation. Very new measurements in the low energy range were carried out by Wada et al. (1995) with the magnetic spectrometer at Okayama (Japan) in both, vertical and horizontal directions (Saito et al. 1991; Tsuji et al. 1995). Their vertical data are also included in Fig. 3.37.

The uncompressed vertical integral muon spectrum at sea level is displayed in Fig. 3.38. Shown are the directly measured and fully corrected vertical integral intensities obtained with the Kiel-DESY spectrometer in Hamburg, Germany (Allkofer et al. 1971b; Jokisch et al. 1979), the vertical spectrum which had been computed from the horizontal MUTRON (Tokyo) spectrum (Matsuno et al. 1984) and, to extend the energy range, the vertical sea level spectrum derived from the Fréjus underground experiment located at the French-Italian border (Rhode 1993). The theoretical spectrum computed by Gaisser (1990) (see eq. 3.34) is also shown for comparison.

Very recently a precision momentum spectrum was measured by the BESS *Balloon-borne Experiment with a Superconducting solenoid Spectrometer* Collaboration (Nozaki, 2000) at Tsukuba, Japan ($P_c \simeq 11.5$ GV, sea level, BESS 95) which is presented in Fig. 3.39. A similar measurement was made by

the same collaboration at Lynn Lake, Canada ($P_c \simeq 0.5$ GV, 360 m a.s.l., BESS 97-99), to study the geomagnetic effects. Both spectra are shown in Fig. 3.71, Subsection 3.6.6 where these effects are discussed.

Inclined and Horizontal Spectra

The highest energy muons that have been recorded with magnetic spectrometers have been detected in near horizontal direction, which is more favorable. The reason is simply that very high energy pions emerging from the first generation of interactions of primaries that enter the earth's atmosphere tangentially travel longer in a low density medium than when propagating vertically. Consequently, for a given pion energy the likelihood for decay, which is in competition with interaction, is larger in horizontal direction, thus enhancing the muon flux. These arguments do not apply to directly produced muons from charmed particles.

The momentum spectrum in the range $10 \leq p \leq 1000$ GeV/c has been determined very precisely in the angular range from $75° \leq \theta \leq 87.5°$ with large acceptance instruments (Allkofer et al. 1977a and 1977b). Fig. 3.40 shows the spectra for zenith angles of 75°, 79°, 81°, 84°, and 87.5°. The figure also includes a set of data from the MUTRON detector in Tokyo (Kitamura et al., 1975). In addition some data of Asatiani et al. (1975) recorded at an altitude of 3250 m a.s.l. have been added for comparison. The curves were calculated with a Maeda-type model (Maeda 1973). Different sets of data are compiled in Fig. 3.41 for the angular range $0° \leq \theta \leq 79°$ (Carstensen 1978, Allkofer 1979b).

Beyond 3 TeV there exist also emulsion chamber data from sea level measurements obtained at very shallow depth underground (40 m.w.e. at Moscow) for zenith angles of 72° and 45° that are given in Fig. 3.42 (Ivanova et al. 1979; Ivanenko et al. 1985). Some other data points have been added to extend the spectra to lower momenta.

The highest resolutions have been achieved with the magnetic spectrometers MUTRON, located in Tokyo, Japan (Higashi et al. 1978; Kawashima et al. 1981; Mitsui et al. 1980 and 1983c; Muraki et al. 1979 and 1983), and DEIS, located in Tel Aviv, Israel (Allkofer et al. 1977a, 1977b 1979b 1981; Jokisch et al. 1979). These instruments explored the momentum spectrum to 25 TeV/c. Fig. 3.43 shows spectra obtained with these instruments for different zenith angles over the range from 78° to 90° (Allkofer et al. 1981). A compilation of different differential and integral spectra for this energy region is given in Figs. 3.44 and 3.45, respectively, together with the calculated spectra of Murakami et al. (1979) and Allkofer (1979a).

The final absolute spectrum obtained with MUTRON at a zenith angle of 89° is presented in Fig. 3.46 together with the spectrum from DEIS (Matsuno et al. 1984). The spectra are multiplied by the momentum to the third power. The MUTRON data for 89° are also given in differential and integral form in Tables 3.19 and 3.20, respectively. Essentially the same data are shown in regular representation in Fig. 3.47 with the exception that the MUTRON spectrum covers the zenith angle range from 87° – 90° (Kitamura 1981).

Recently, Gettert et al. (1993) carried out an experiment at Karlsruhe and determined the horizontal muon energy spectrum between 250 GeV/c and 15 TeV/c, and Tsuji et al. (1995) measured the low energy portion of the muon spectrum at zenith angles between 70° and 78°. The data of Gettert et al. (1993) are incorporated in Fig. 3.47.

3.6.4 Zenith and Azimuthal Angular Dependence

Low Energy Effects

The earth's magnetic field gives rise to an *azimuthal dependence* and an *east-west asymmetry* of the muon intensity, because the primary cosmic ray particles are predominantly positively charged. It is mostly the low energy component that is affected to the extent that the path lengths are different for charged particles coming from the east or west. As a result the absorption and decay probabilities of unstable particles are influenced and the low energy charge ratio is modified, as mentioned before.

Zenith Angular Muon Enhancement

At higher energies the muon spectrum is modified by another effect. The parent particles of muons, chiefly pions and kaons, can either decay or interact strongly. Which one of the processes will dominate depends on the particle's energy and the density of the atmosphere along its trajectory. The latter is a function of altitude and zenith angle.

In particular, pions and kaons resulting from collisions of primaries that are incident upon the atmosphere at a zenith angle $\theta > 0°$ propagate along the same general direction as the primaries. However, they require longer trajectories and more time to traverse a given column of $X = X_s$ [g cm^{-2}] of air than vertically propagating particles. This is because the rate of change of density along an inclined trajectory is smaller per unit path length than along a vertical trajectory. Consequently, the competition between interaction and decay of pions and kaons of a given energy changes in favor of decay

Table 3.19: Differential Momentum Spectrum of Muons at Zenith Angle $\theta = 89°$. (MUTRON, fully corrected, Matsuno et al. 1984)

Momentum		Muon	Differential Intensity	Statistical
Range [GeV/c]	Mean [GeV/c]	Number	$\left[\frac{1}{cm^2\ s\ sr\ (GeV/c)}\right]$	Error
100 - 126	112	70142	$5.69 \cdot 10^{-8}$	$\pm 2.15 \cdot 10^{-10}$
126 - 158	141	60560	$3.99 \cdot 10^{-8}$	$\pm 1.62 \cdot 10^{-10}$
158 - 200	177	50136	$2.41 \cdot 10^{-8}$	$\pm 1.08 \cdot 10^{-10}$
200 - 251	223	40643	$1.60 \cdot 10^{-8}$	$\pm 7.94 \cdot 10^{-11}$
251 - 316	281	31519	$9.88 \cdot 10^{-9}$	$\pm 5.57 \cdot 10^{-11}$
316 - 398	354	23608	$5.90 \cdot 10^{-9}$	$\pm 3.84 \cdot 10^{-11}$
398 - 501	444	16946	$3.37 \cdot 10^{-9}$	$\pm 2.59 \cdot 10^{-11}$
501 - 631	559	11765	$1.88 \cdot 10^{-9}$	$\pm 1.73 \cdot 10^{-11}$
631 - 794	704	7893	$1.02 \cdot 10^{-9}$	$\pm 1.15 \cdot 10^{-11}$
794 - 1000	886	5628	$5.29 \cdot 10^{-10}$	$\pm 7.05 \cdot 10^{-12}$
1000 - 1259	1115	3114	$2.71 \cdot 10^{-10}$	$\pm 4.86 \cdot 10^{-12}$
1259 - 1585	1403	1858	$1.31 \cdot 10^{-10}$	$\pm 3.04 \cdot 10^{-12}$
1585 - 1995	1766	1104	$6.23 \cdot 10^{-11}$	$\pm 1.88 \cdot 10^{-12}$
1995 - 2512	2222	646	$2.97 \cdot 10^{-11}$	$\pm 1.17 \cdot 10^{-12}$
2512 - 3162	2797	350	$1.29 \cdot 10^{-11}$	$\pm 6.90 \cdot 10^{-13}$
3162 - 3981	3520	221	$6.62 \cdot 10^{-12}$	$\pm 4.45 \cdot 10^{-13}$
3981 - 5012	4431	135	$3.25 \cdot 10^{-12}$	$\pm 2.80 \cdot 10^{-13}$
5012 - 6310	5576	81	$1.59 \cdot 10^{-12}$	$\pm 1.77 \cdot 10^{-13}$
6310 - 7943	7018	47	$7.33 \cdot 10^{-13}$	$\pm 1.07 \cdot 10^{-13}$
7943 - 10000	8832	31	$3.76 \cdot 10^{-13}$	$\pm 6.75 \cdot 10^{-14}$
10000 - 12589	11116	13	$1.18 \cdot 10^{-13}$	$\pm 3.27 \cdot 10^{-14}$
12589 - 15849	13990	8	$5.18 \cdot 10^{-14}$	$\pm 1.83 \cdot 10^{-14}$
15849 - 19953	17606	7	$3.50 \cdot 10^{-14}$	$\pm 1.32 \cdot 10^{-14}$
19953 - 25119	22162	4	$1.10 \cdot 10^{-14}$	$\pm 5.50 \cdot 10^{-15}$

with increasing zenith angle, thus causing muon enhancement with increasing zenith angle and energy. The quantities X and X_s stand for vertical and inclined columns of air (or matter), respectively, often referred to as the *column density*, measured in $[\mathrm{g\,cm^{-2}}]$. X_s is also called the *slant depth*.

Table 3.20: Integral Momentum Spectrum of Muons at Zenith Angle $\theta = 89°$. (MUTRON, fully corrected, Matsuno et al. 1984)

Momentum [TeV/c]	Muon Number	Integral Intensity [$cm^{-2} s^{-1} sr^{-1}$]	Statistical Error
0.10	326499	$6.90 \cdot 10^{-6}$	$\pm 1.21 \cdot 10^{-8}$
0.13	256357	$5.42 \cdot 10^{-6}$	$\pm 1.07 \cdot 10^{-8}$
0.16	195797	$4.15 \cdot 10^{-6}$	$\pm 9.55 \cdot 10^{-8}$
0.20	145661	$3.08 \cdot 10^{-6}$	$\pm 8.07 \cdot 10^{-9}$
0.25	105018	$2.22 \cdot 10^{-6}$	$\pm 6.85 \cdot 10^{-9}$
0.32	73499	$1.55 \cdot 10^{-6}$	$\pm 5.72 \cdot 10^{-9}$
0.40	49891	$1.05 \cdot 10^{-6}$	$\pm 4.70 \cdot 10^{-9}$
0.50	32945	$6.95 \cdot 10^{-7}$	$\pm 3.83 \cdot 10^{-9}$
0.63	21180	$4.46 \cdot 10^{-7}$	$\pm 3.06 \cdot 10^{-9}$
0.79	13287	$2.79 \cdot 10^{-7}$	$\pm 2.42 \cdot 10^{-9}$
1.00	7659	$1.70 \cdot 10^{-7}$	$\pm 1.94 \cdot 10^{-9}$
1.26	4545	$1.00 \cdot 10^{-7}$	$\pm 1.48 \cdot 10^{-9}$
1.59	2687	$5.87 \cdot 10^{-8}$	$\pm 1.14 \cdot 10^{-9}$
2.00	1583	$3.40 \cdot 10^{-8}$	$\pm 8.62 \cdot 10^{-10}$
2.51	937	$1.96 \cdot 10^{-8}$	$\pm 6.51 \cdot 10^{-10}$
3.16	587	$1.18 \cdot 10^{-8}$	$\pm 4.97 \cdot 10^{-10}$
3.98	366	$7.00 \cdot 10^{-9}$	$\pm 3.80 \cdot 10^{-10}$
5.01	231	$4.04 \cdot 10^{-9}$	$\pm 2.82 \cdot 10^{-10}$
6.31	150	$2.31 \cdot 10^{-9}$	$\pm 2.08 \cdot 10^{-10}$
7.94	103	$1.32 \cdot 10^{-9}$	$\pm 1.51 \cdot 10^{-10}$
10.00	72	$6.97 \cdot 10^{-10}$	$\pm 8.43 \cdot 10^{-11}$
12.59	59	$3.88 \cdot 10^{-10}$	$\pm 6.97 \cdot 10^{-11}$
15.85	51	$2.14 \cdot 10^{-10}$	$\pm 4.99 \cdot 10^{-11}$
19.95	44	$1.17 \cdot 10^{-10}$	$\pm 3.31 \cdot 10^{-11}$
25.12	40	$6.44 \cdot 10^{-11}$	$\pm 2.26 \cdot 10^{-11}$

Many authors have investigated the muon enhancement phenomenon theoretically and experimentally. Its energy dependence is well illustrated in Fig. 3.48 which shows the muon intensity resulting from pion and kaon de-

cays separately as a function of zenith angle for different muon threshold energies from a calculation of Maeda (1970 and 1973) using a diffusion equation (see also Subsection 3.6.8, Fig. 3.80). The difference between the two contributing channels, pions and kaons, is chiefly due to the respective mass and mean lifetime differences. Identical production spectra of the form shown below were used for pions and kaons,

$$F(E_{\pi,K}) \;=\; A_{\pi,K}\, E_{\pi,K}^{-2.7}\;, \tag{3.29}$$

where $A_{\pi,K}$ is normalized for vertical intensity at sea level.

The interaction and propagation model that was used by Maeda (1973) was rather rudimentary. Identical nuclear absorption mean free paths of 120 $\mathrm{g\,cm^{-2}}$ were used for nucleons, pions and kaons propagating in the atmosphere. In some cases energy dependent absorption paths were used, too. However, in spite of these simplifications and other model shortcomings the well known characteristic features of the zenith angle dependence of the muon intensity and spectrum in the atmosphere and at ground level are well demonstrated by the results of this calculation.

The enhancement effect manifests itself even better when plotting the ratio of vertical to inclined differential intensities versus zenith angle, θ, or versus $\cos(\theta)$, for different energies, as shown in Fig. 3.49 (Maeda, 1973). In another representation illustrated in Fig. 3.50 due to Bergamasco et al. (1983) the said ratio plotted as a function of $\sec(\theta)$ shows a linear relation down to zenith angles of about 70°. At larger angles the curvature of the earth leads to the breakdown of this linear relationship.

Prompt, Isotropic Muon Component

There exists a small, zenith angle independent, so-called prompt or direct muon component that originates from the decay of charmed particles. Because of the very short mean lifetime of charmed particles they decay almost instantly near their point of production and cause no muon enhancement effect. Prompt muons reflect the isotropic character of the primary radiation. Their contribution is small in comparison to the bulk of all muons but they begin to manifest themselves at high energies ($E \geq 1$ TeV) and large zenith angles where there are few muons. The topic of prompt or direct muons is discussed in greater detail in Section 4.3 since underground installations are most suitable for their detection.

Table 3.21: Low Momentum Absolute Muon Intensities at Large Zenith Angles near Sea Level (North - South Azimuth). (Karmakar et al., 1973, extended by the author)

Reference	Geomagn. Latitude [°N]	Momentum [GeV/c]	Zenith Angle $\theta°$	Absolute Intensity $\times 10^5$ [$cm^{-2} s^{-1} sr^{-1}$]
Jakeman (1956) (101 m a.s.l.)	56.8	$>\sim 0.4$	88.4	4.20±0.30
			88.8	3.00±0.38
			89.2	2.55±0.26
			89.6	2.94±0.25
			90	2.40±0.27
Wilson (1959) (101 m a.s.l.)	56.8	$>\sim 1.0$	87	6.75±0.46
			87.5	4.75±0.31
			88	4.11±0.95
			88.5	2.89±0.19
			89	3.34±0.19
Crookes and Rastin (1972) (40 m a.s.l.)	53	≥ 0.35	45	436±6
			60	210±3
			80	27.9±0.4
Karmakar et al. (1973) (122 m a.s.l.)	16	≥ 0.30	75	54.34±0.85
			80	22.84±0.49
			85	7.05±0.30
			89	1.28±0.10

Experimental Zenith Angle Distributions

Extensive measurements of the zenith angle dependence of the absolute intensity of muons of momentum ≥ 0.35 GeV/c at sea level over a wide range of zenith angles have been made by Crookes and Rastin (1972). The data were taken with the axial direction of the spectrometer in the magnetic N-S azimuth. Their results are shown in Fig. 3.51 together with those of Jakeman (1956), Wilson (1959), Hicks et al. (1971) and Karmakar et al. (1973). Also shown in the same figure are the integral intensities of muons between 1 GeV/c and 100 GeV/c over a zenith angle interval from 65° to 85° obtained by Allen and Apostolakis (1961). Additional details are given in Table 3.21.

Some of these data are also shown in Fig. 3.52, plotted as a function of

Table 3.22: Zenith Angle Dependence of Integral Muon Intensity at Sea Level for Momenta $\geq$1 GeV/c (Gettert et al. 1993).

Angular Interval θ	$< \theta >$	Intensity $[cm^{-2}s^{-1}sr^{-1}]$
71° – 83.5°	75.4°	$3.60 \cdot 10^{-4}$
76° – 85.5°	79.3°	$2.25 \cdot 10^{-4}$
79° – 90°	83.6°	$1.20 \cdot 10^{-4}$
85° – 90°	86.8°	$0.45 \cdot 10^{-4}$

$\sec(\theta)$, together with similar but recent measurements carried out by Gettert et al. (1993) in Karlsruhe (Germany) (~110 m a.s.l.), covering a zenith angle range from 71° to 90°. The latter data, obtained with the spectrometer oriented in the east-west direction, are given in Table 3.22.

Tsuji et al. (1995) used the Okayama spectrometer, located at a geographic latitude of 34.7°, to measure the zenith angle dependence of the integral intensity while scanning over a zenith angle range from -31° pointing east to 78° pointing west during daily rotations of the telescope in azimuthal direction from east to west, as indicated in Fig. 3.53.

The momentum spectra in the range $0.2 \leq p \leq 50$ GeV/c have been determined at zenith angles of 30° and 60° in eastern and western directions at Melbourne, Australia (Moroney and Parry 1954). The spectra are shown in Figs. 3.54 to 3.57 for $30°E$, $30°W$, $60°E$ and $60°W$, respectively. Since the normalization has been made with respect to the Rossi value, the intensities have to be increased by 26% to agree with modern data. Similar measurements were made by Judge and Nash (1965). Figs. 3.58 and 3.59 show the momentum spectra recorded at Kiel (Gernamy) at a zenith angle of 45°, pointing east and west, respectively (Allkofer and Andresen 1967). Measurements of the angular dependence at low geomagnetic latitude have been made by Bhattacharyya (1974a and 1974b).

Integral intensity measurements in the zenith angle range from 75° to 90° were made by Flint et al. (1972) for momenta $\geq 0.28 \pm 0.01$ GeV/c. The results are given in Table 3.23.

The enhancement of the differential muon intensity at high energies has been measured at College Station, Texas, near sea level, and is shown in

Table 3.23: Zenith Angle Dependence of Integral Muon Intensity at Sea Level for Momenta $\geq 0.28 \pm 0.01$ GeV/c (Flint et al. 1972).

Zenith Angle	Intensity $[cm^{-2}s^{-1}sr^{-1}]$
75°	$(5.26 \pm 0.16) \cdot 10^{-4}$
77°	$(4.11 \pm 014) \cdot 10^{-4}$
79°	$(2.92 \pm 0.10) \cdot 10^{-4}$
81°	$(2.02 \pm 0.06) \cdot 10^{-4}$
82°	$(1.61 \pm 0.05) \cdot 10^{-4}$
83°	$(1.33 \pm 005) \cdot 10^{-4}$
85°	$(8.37 \pm 0.28) \cdot 10^{-5}$
88.7° [a]	$(2.80 \pm 0.12) \cdot 10^{-5}$
86.5° [b,c]	$(5.86 \pm 0.21) \cdot 10^{-5}$
87.4° [a,c]	$(4.28 \pm 0.17) \cdot 10^{-5}$
88° [b,c]	$(3.58 \pm 0.21) \cdot 10^{-5}$

[a] Telescope axis horizontal; [b] Telescope axis at 88°; [c] Wide angle telescope.

Table 3.24 (Abdel-Monem 1977).

The experimental zenith angle dependence of the muon intensity at $\theta \leq 75°$ can be described by the expression (see Budini and Molière 1953, and Greisen 1942)

$$I(\theta) = I(0°) \cos^n(\theta) , \tag{3.30}$$

where n is a function of momentum, $n = n(p)$. Its average value at 1 GeV is $n = 1.85 \pm 0.10$. The momentum dependence of n resulting from several experiments is shown in Fig. 3.60. A compilation of values of n from different measurements at low threshold momenta is given in Table 3.25.

Extensive calculations of the zenith angle dependence of the muon momentum spectrum had been made by Maeda (1973). A comprehensive theoretical study of the enhancement of the muon intensity at large zenith angles and high energies as well as the opposite effect for low energy muons has been carried out by Stephens (1979a). His results are summarized in Fig. 3.61 and compared to experimental data of Allkofer et al. (1979c).

Table 3.24: Measured Muon Enhancement at Zenith Angles of 65° and 80° as a Function of Momentum at College Station (TX) near Sea Level. (Abdel-Monem et al. 1977)

Muon Momentum [GeV/c]	Enhancement $I(65°)/I(0°)$	Enhancement $I(80°)/I(0°)$
1.6	0.240± 0.004	0.054± 0.002
4	0.325± 0.006	0.082± 0.003
7	0.424± 0.015	0.122± 0.007
10	0.502± 0.012	0.172± 0.008
15	0.632± 0.025	0.252± 0.016
25	0.971± 0.094	0.450± 0.057
40	1.330± 0.116	0.638± 0.083
70	1.661± 0.422	0.812± 0.258
110	1.996± 0.334	1.054± 0.256

Table 3.25: Exponent n of Zenith Angle Distribution $\cos^n(\theta)$ of Low Energy Muons at Sea Level.

Momentum [GeV/c]	Geomagn. Latitude	n	Reference
0.3	47°S	3.3	Moroney and Parry
$> \sim 0.33$		2.1	(1954)
>0.4		1.91±0.10	
>1.0		1.85±0.11	
>1.5	12°N	1.81±0.12	Bhattacharyya
>2.0		1.75±0.11	(1974b)
>2.4		1.81±0.08	
>3.0		1.83±0.09	
>0.33	50°N	2.1	Greisen (1940)
$> \sim 10$	-	1.6±0.1	Sheldon and Duller (1962)
>0.7	53°N	1.96±0.22	Judge and Nash (1965)
>0.35	53°N	2.16±0.01	Crookes and Rastin (1972)

3.6.5 Charge Ratio

General Remarks

The primary cosmic radiation consists almost entirely of positively charged particles. This charge excess is modified by interactions in the atmosphere that produce new generations of particles that tend to reduce the *positive charge excess*, s, defined as

$$s = \frac{N_{\mu+} - N_{\mu-}}{N_{\mu+} + N_{\mu-}}, \tag{3.31}$$

because of charge symmetry in the particle production mechanisms. $N_{\mu+}$ and $N_{\mu-}$ are the number of positive and negative muons, respectively, traversing a detector in a specified momentum and time interval.

The muon *charge ratio*, K_μ, is defined as

$$K_\mu = \frac{N_{\mu+}}{N_{\mu-}}, \tag{3.32}$$

At low momenta ($\leq$5 GeV/c) the charge ratio depends weakly on the *geomagnetic latitude* and on *azimuthal direction*. These topics are discussed in Subsection 3.6.6 of this chapter.

Magnetic spectrometers are mostly used to determine the charge ratio. However, some researchers have used the delayed coincidence method that exploits the different behavior of negative and positive muons when they come to rest in an absorber (Vulpescu et al., 1998). Vulpescu et al. (1998) have summarized the bulk of low energy data that exist on the muon charge ratio. We present their table at the back of this section (Table 3.30). The method of charge determination is also indicated and the geomagnetic cutoff rigidities, P_c, of the locations where the measurements were made, too. The data are from measurements made at or near sea level except for those of De Pascale et al. (1993) and Schneider et al. (1995) that were made at 600 m and 1270 m a.s.l., respectively, as indicated in the table.

Because of systematic errors in the momentum determination, the charge ratios obtained by different groups deviate from each other. Since statistics are very poor at high energies, the energy dependence is sometimes difficult to recognize. In the vertical the charge ratio changes slightly with energy.

Energy Dependence of Charge Ratio

Figs. 3.62 and 3.63 show a compilation of charge ratio data for vertical and horizontal directions, respectively, of measurements carried out before 1973

(Thompson 1973), covering the momentum range from 1 GeV/c to 1 TeV/c. The large uncertainties are evident from the wide scatter of the data, particularly for the horizontal measurements and in general at high energies where statistics are poor.

Further compilations of charge ratio data made by the author, covering different energy windows at sea level are presented in Figs. 3.64, 3.65 and 3.66. In Fig. 3.65 we have added the high energy data from the Utah underground experiment located at about 1500 m a.s.l. ($\simeq$1400 hg cm^{-2}; Davis et al., 1971; Lowe et al., 1975) to enlarge the momentum range. Theoretical predictions by Stephens 1979a and 1979b together with the experimental results of Stephens and Golden (1987) are included in Figs. 3.64 and 3.66.

Charge ratio data obtained at the highest energies with horizontal instruments (MUTRON, DEIS) are summarized in Fig. 3.67 and discussed in various articles (see e.g. Kitamura 1981). Included in this figure are the final data from the large spectrometers MUTRON, DEIS and Kiel - DESY. The MUTRON data are also tabulated in Table 3.26. Also included are the underground data of the Utah experiment, mentioned before (Ashley et al. 1973, 1975a and 1975b), and some data points from the so-called world survey (Allkofer et al. 1978a and 1978b). In the momentum range $100 \leq p \leq 10^4$ GeV/c it is uncertain whether the charge ratio tends to increase slightly or remains constant. The integral charge ratio is 1.23 ± 0.01 at $E \geq 100$ GeV and 1.30 ± 0.05 at $E \geq 1.2$ TeV (Allkofer et al. 1981).

Zenith and Azimuthal Angle Dependence of Charge Ratio

The charge ratio exhibits a zenith angle dependence partly because the atmospheric depth increases with increasing zenith angle, and likewise the primary energy which is responsible for the processes that generate muons of a definite momentum at sea level (Thompson 1973; Ng and Wolfendale 1974). At large zenith angles, near the horizontal, and particularly at low energies, where geomagnetic effects manifest themselves strongly, the charge ratio is significantly affected, even the integrated values.

A detailed experimental and theoretical analysis of the zenith angle dependence of the muon charge ratio at large zenith angles had been carried out by Allkofer et al. (1979c) using the DEIS spectrometer at Tel-Aviv. The results are presented in Fig. 3.68.

The azimuthal dependence of the charge ratio in the low momentum region due to different path lengths of the particles under the influence of the geomagnetic field when approaching from the east or west can be seen in

Table 3.26: Muon Charge Ratio Versus Momentum at Zenith Angle $\theta = 89°$. (MUTRON, fully corrected, Matsuno et al. 1984)

Momentum [GeV/c]	Charge Ratio
71 - 100	1.243 ± 0.011
100 - 141	1.258 ± 0.010
141 - 200	1.239 ± 0.010
200 - 282	1.252 ± 0.012
282 - 398	1.264 ± 0.014
398 - 631	1.260 ± 0.016
631 - 1000	1.306 ± 0.024
1000 - 1995	1.276 ± 0.034
1995 - 3981	1.394 ± 0.083
3981 - 10000	1.17 ± 0.14
10000 - 25119	1.32 ± 0.49

Fig. 3.69 for a zenith angle of 45° (Allkofer and Andresen 1967).

3.6.6 Geomagnetic Latitude Dependence

Because of the geomagnetic field, there is a *cutoff rigidity*, P_c, for each point and direction on earth (see Chapter 1). Consequently variations of the muon flux and muon momentum spectrum with geomagnetic latitude are expected in the low energy region for momenta up to about 5 GeV/c. Note that geomagnetic and geographic latitudes are not identical. In addition there is an *atmospheric latitude effect* caused by the latitude dependence of the column density of the atmosphere.

The *geomagnetic latitude effect* is defined as the ratio, L, of the muon intensity at latitude λ_1, $I(\lambda_1, p)$, divided by the muon intensity at latitude λ_2, $I(\lambda_2, p)$, thus,

$$L = (\lambda_1, p)/I(\lambda_2, p) \tag{3.33}$$

One of the first theoretical treatments of the latitude effect was made by Olbert (1954). This analysis was based on the work of Kraushaar (1949) and the air-borne measurements of Conversi (1950) (see Chapter 2, Section 2.6). The latitude effect is also evident from Tables 3.12 and 3.13 where

the geomagnetic latitude and the cutoff rigidities are given for the different low energy intensity measurements, and Fig. 3.70 illustrates the differential intensities and spectra for different latitudes (Allkofer et al. 1968).

Recent precision measurements of the muon momentum spectra at Lynn Lake, Canada ($P_c \simeq 0.5$ GV, 360 m a.s.l., BESS 97-99) and at Tsukuba, Japan ($P_c \simeq 11.5$ GV, sea level, BESS 95) have been carried out by Nozaki (2000) with the BESS instrument. The spectra are illustrated in Fig. 3.71. The Tsukuba spectrum is the same as the one which is shown separately in Fig. 3.39, Subsection 3.6.3. The gradually diminishing systematic differences with increasing momentum that are mostly due to the different geomagnetic cutoffs are evident.

The relative contributions of the geomagnetic and atmospheric latitude effects to the total latitude effect are resolved in Fig. 3.72 for different muon energies (Allkofer et al. 1972). The relative influence of the geomagnetic cutoff on the muon intensities recorded at different locations on the globe is shown in Fig. 3.73.

The differential and integral momentum spectra at the equator and at Kiel, Germany, corresponding to cutoff rigidities of 14 GV and 2.3 GV, respectively, are shown in Figs. 3.74 and 3.75, respectively (Allkofer et al., 1975b).

A compilation of differential and integral muon spectral data at the latitude of 12° N is given in Fig. 3.76. The data are from the work of De et al. (1974) and other workers. In addition, spectra for different muon directions at latitude 12° N are shown in Fig. 3.77 (Bhattacharyya, 1976).

The latitude effect on the charge ratio for vertically incident muons had also been studied. Allkofer and Dau (1972) carried out charge ratio measurements at Kiel, Germany ($P_c = 2.3$ GV), and in equatorial regions ($P_c = 14$ GV) with the same spectrometer to avoid systematic errors. The results of these measurements can be compared in Fig. 3.78. From these data we conclude that there is almost no dependence of the charge ratio on geomagnetic latitude for vertically incident muons. However, for near horizontal muons the effect is very strong at low momenta and trails off to become insignificant above about 100 GeV/c (cf. Figs. 3.68 and 3.69, Subsection 3.6.4).

3.6.7 Backscattered Muons at Ground Level

The flux of upward directed muons at ground level resulting from backscattering in the ground represents an important background for underground neutrino experiments, particularly if located at shallow depths. Such muons

can be misinterpreted as the result of underground reactions initiated by neutrinos traversing the earth. Abbrescia et al. (1993) have investigated this problem and measured the upward directed flux of muons of energy $\geq$4 GeV at ground level. The results are shown in Fig. 3.79 and compared with a theoretical prediction by Elbert et al. (1991).

3.6.8 Theoretical Contributions

Some theoretical contributions to specific topics presented in this sections are discussed above in connection with the experimental data and are included in the appropriate figures. General aspects of muon physics are discussed in Chapter 4, Section 4.2. In the following we give the results of some fairly recent calculations of muon spectra, zenith angle dependencies and muon charge ratios that are of some relevance for the atmospheric neutrino data summarized in Chapter 4, Section 4.5.

Theoretical Muon Energy Spectra

Theoretical papers dealing with different aspects of the unaccompanied muon component of the cosmic radiation in the atmosphere are listed at the end of this subsection. However, to give an example of the characteristic features of the muon energy spectrum and its dependence on zenith angle, including the zenith angular enhancement we show in Fig. 3.80 theoretical energy spectra for vertical, strongly inclined and horizontally incident muons at sea level obtained by Maeda (1970 and 1973) in calculations using a diffusion equation. The enhancement effect is discussed in Subsection 3.6.4, where additional details concerning Maeda's calculations are mentioned.

As mentioned before, it must be kept in mind that at low momenta ($\leq$5 GeV/c) the energy spectrum depends weakly on the *geomagnetic latitude* and also on *azimuthal direction.* These topics are discussed in Subsections 3.6.6 and 3.6.4, respectively. They are relevant when computing atmospheric neutrino fluxes for neutrino oscillation studies.

An analytic expression giving a good fit to the muon energy spectrum observed in the atmosphere was obtained by Gaisser (1990) (eq. p. 71) and is given below.

$$\frac{dj_\mu(E_\mu,\cos(\theta))}{dE_\mu} \approx 0.14\,A\,E_\mu^{-\gamma}\left(\frac{1}{1+\frac{1.1E_\mu\cos(\theta)}{115GeV}}+\frac{0.054}{1+\frac{1.1E_\mu\cos(\theta)}{850GeV}}\right) \quad [\mathrm{cm^{-2}s^{-1}sr^{-1}GeV^{-1}}] \quad (3.34)$$

Here E_μ and j_μ are the muon energy and intensity, θ is the zenith angle and γ the spectral index.

Of the many theoretical muon spectra we show in Fig. 3.81 the one we have constructed from tabulated data of an analytic calculation of Lipari (1993) (Table 3.27). The energy dependence of the ratio of positive to negative muons resulting from the same calculation is listed in Table 3.28.

Furthermore, we have added the tabulated spectrum from a calculation of Agrawal et al. (1996) (Table 3.29). We have included the data of Lipari and Agrawal et al. because they are the result of the first step of the calculations which had been used by the respective authors to compute the atmospheric electron and muon neutrino and antineutrino spectra and ratios, presented in Chapter 4, Section 4.5. It is important to note that in either case the muon spectra are based on a variety of assumptions and approximations and disregard geomagnetic effects.

Additional calculations and theoretical studies that deal with muon fluxes and intensities, energy and momentum spectra, charge ratios, and their dependence on azimuth, latitude and zenith angle can be found in the following papers (see also Chapter 2, Section 2.6):

Abdel-Monem et al. (1976), Badhwar et al. (1977), Bedewi and Goned (1971), Bhattacharyya (1979), Bugaev et al. (1993, 1994 and 1998), Butkevich et al. (1989), Chakrabarti et al. (1979), Das and De (1979 and 1980), Gaisser (1974), Honda et al. (1995), Komori (1977), Liland (1975 and 1980), Maeda (1970 and 1973), Minorikawa (1977), Mitsui et al. (1986), Naumov et al. (1992), O'Brien (1971a), Ramana Murthy (1972), Stephens (1981), Thompson et al. (1977a), Torsti (1976), and Volkova et al. (1980) (see also Chapter 2, Subsection 2.6.5 and Chapter 4).

Table 3.27: Muon Intensity, $\mu^+ + \mu^-$, at sea level.
(Lipari, 1993)

Muon Energy GeV	Intensity [$cm^{-2}s^{-1}sr^{-1}GeV^{-1}$] cos$\theta$							
	1	0.6	0.4	0.3	0.2	0.1	0.05	0.0
1.0	$2.24 \cdot 10^{-3}$	$4.04 \cdot 10^{-4}$	$1.19 \cdot 10^{-4}$	$3.62 \cdot 10^{-5}$	$9.00 \cdot 10^{-6}$	$1.08 \cdot 10^{-6}$	$2.37 \cdot 10^{-7}$	$5.15 \cdot 10^{-8}$
3.16	$8.16 \cdot 10^{-4}$	$2.80 \cdot 10^{-4}$	$1.06 \cdot 10^{-4}$	$4.42 \cdot 10^{-5}$	$1.33 \cdot 10^{-5}$	$1.88 \cdot 10^{-6}$	$4.23 \cdot 10^{-7}$	$6.45 \cdot 10^{-8}$
10.0	$1.10 \cdot 10^{-4}$	$6.78 \cdot 10^{-5}$	$3.95 \cdot 10^{-5}$	$2.37 \cdot 10^{-5}$	$1.05 \cdot 10^{-5}$	$2.28 \cdot 10^{-6}$	$6.16 \cdot 10^{-7}$	$8.88 \cdot 10^{-8}$
31.6	$6.80 \cdot 10^{-6}$	$6.09 \cdot 10^{-6}$	$5.07 \cdot 10^{-6}$	$4.11 \cdot 10^{-6}$	$2.80 \cdot 10^{-6}$	$1.17 \cdot 10^{-6}$	$4.75 \cdot 10^{-7}$	$9.54 \cdot 10^{-8}$
100	$2.48 \cdot 10^{-7}$	$2.81 \cdot 10^{-7}$	$2.91 \cdot 10^{-7}$	$2.84 \cdot 10^{-7}$	$2.59 \cdot 10^{-7}$	$1.87 \cdot 10^{-7}$	$1.21 \cdot 10^{-7}$	$4.55 \cdot 10^{-8}$
316	$6.06 \cdot 10^{-9}$	$8.12 \cdot 10^{-9}$	$9.78 \cdot 10^{-9}$	$1.08 \cdot 10^{-8}$	$1.18 \cdot 10^{-8}$	$1.18 \cdot 10^{-8}$	$1.04 \cdot 10^{-8}$	$6.78 \cdot 10^{-9}$
1000	$1.14 \cdot 10^{-10}$	$1.69 \cdot 10^{-10}$	$2.24 \cdot 10^{-10}$	$2.67 \cdot 10^{-10}$	$3.28 \cdot 10^{-10}$	$4.02 \cdot 10^{-10}$	$4.19 \cdot 10^{-10}$	$3.69 \cdot 10^{-10}$
3160	$1.87 \cdot 10^{-12}$	$2.91 \cdot 10^{-12}$	$4.06 \cdot 10^{-12}$	$5.06 \cdot 10^{-12}$	$6.65 \cdot 10^{-12}$	$9.14 \cdot 10^{-12}$	$1.04 \cdot 10^{-11}$	$1.05 \cdot 10^{-11}$
$1.00 \cdot 10^4$	$2.81 \cdot 10^{-14}$	$4.50 \cdot 10^{-14}$	$6.47 \cdot 10^{-14}$	$8.26 \cdot 10^{-14}$	$1.13 \cdot 10^{-13}$	$1.64 \cdot 10^{-13}$	$1.95 \cdot 10^{-13}$	$2.07 \cdot 10^{-13}$
$3.16 \cdot 10^4$	$4.06 \cdot 10^{-16}$	$6.58 \cdot 10^{-16}$	$9.60 \cdot 10^{-16}$	$1.24 \cdot 10^{-15}$	$1.72 \cdot 10^{-15}$	$2.60 \cdot 10^{-15}$	$3.16 \cdot 10^{-15}$	$3.42 \cdot 10^{-15}$
$1.00 \cdot 10^5$	$5.78 \cdot 10^{-18}$	$9.41 \cdot 10^{-18}$	$1.38 \cdot 10^{-17}$	$1.79 \cdot 10^{-17}$	$2.51 \cdot 10^{-17}$	$3.85 \cdot 10^{-17}$	$4.72 \cdot 10^{-17}$	$5.16 \cdot 10^{-17}$
$3.16 \cdot 10^5$	$8.18 \cdot 10^{-20}$	$1.33 \cdot 10^{-19}$	$1.96 \cdot 10^{-19}$	$2.55 \cdot 10^{-19}$	$3.59 \cdot 10^{-19}$	$5.53 \cdot 10^{-19}$	$6.81 \cdot 10^{-19}$	$7.47 \cdot 10^{-19}$
$1.00 \cdot 10^6$	$1.16 \cdot 10^{-21}$	$1.89 \cdot 10^{-21}$	$2.78 \cdot 10^{-21}$	$3.61 \cdot 10^{-21}$	$5.08 \cdot 10^{-21}$	$7.86 \cdot 10^{-21}$	$9.68 \cdot 10^{-21}$	$1.06 \cdot 10^{-20}$

Table 3.28: Muon Charge Ratio, μ^+ / μ^-, at Sea Level.
(Lipari, 1993)

Muon Energy GeV	Ratio $[\mu^+ / \mu^-]$ cosθ 1	0.6	0.4	0.3	0.2	0.1	0.05	0.00
1.0	1.28	1.28	1.29	1.29	1.29	1.29	1.29	1.30
3.16	1.29	1.29	1.29	1.29	1.29	1.29	1.30	1.30
10.0	1.30	1.30	1.30	1.30	1.30	1.29	1.30	1.30
31.6	1.31	1.31	1.30	1.30	1.30	1.30	1.30	1.30
100	1.34	1.32	1.32	1.31	1.31	1.31	1.30	1.31
316	1.39	1.36	1.35	1.34	1.33	1.32	1.32	1.32
1000	1.45	1.42	1.40	1.39	1.37	1.35	1.34	1.34
3160	1.50	1.49	1.47	1.45	1.43	1.41	1.39	1.39
$1.00 \cdot 10^4$	1.53	1.52	1.51	1.51	1.49	1.47	1.46	1.46
$3.16 \cdot 10^4$	1.53	1.53	1.53	1.53	1.52	1.51	1.51	1.51
$1.00 \cdot 10^5$	1.54	1.54	1.54	1.54	1.53	1.53	1.53	1.53

Table 3.29: Atmospheric Muon Intensities as a Function of Zenith Angle. The Values are $dN_\mu/d(\ln E_\mu)$, in Units of $[\mathrm{cm}^{-2}\,\mathrm{s}^{-1}\,\mathrm{sr}^{-1}]$.
(Agrawal et al., 1996)

Muon Energy [GeV]	Muon Intensity $[\mathrm{cm}^{-2}\mathrm{s}^{-1}\,\mathrm{sr}^{-1}]$ cos(θ) 1.0	0.75	0.50	0.25	0.15	0.05
1	$4.03 \cdot 10^{-3}$	$1.63 \cdot 10^{-3}$	$3.78 \cdot 10^{-4}$	$3.15 \cdot 10^{-5}$	$2.49 \cdot 10^{-6}$	$7.16 \cdot 10^{-7}$
2	$4.11 \cdot 10^{-3}$	$1.98 \cdot 10^{-3}$	$6.59 \cdot 10^{-4}$	$6.41 \cdot 10^{-5}$	$1.27 \cdot 10^{-5}$	$1.20 \cdot 10^{-6}$
3	$3.59 \cdot 10^{-3}$	$2.03 \cdot 10^{-3}$	$7.47 \cdot 10^{-4}$	$9.46 \cdot 10^{-5}$	$2.38 \cdot 10^{-5}$	$1.68 \cdot 10^{-6}$
5	$2.61 \cdot 10^{-3}$	$1.68 \cdot 10^{-3}$	$7.87 \cdot 10^{-4}$	$1.43 \cdot 10^{-4}$	$3.44 \cdot 10^{-5}$	$2.92 \cdot 10^{-6}$
10	$1.33 \cdot 10^{-3}$	$1.02 \cdot 10^{-3}$	$6.19 \cdot 10^{-4}$	$1.76 \cdot 10^{-4}$	$6.27 \cdot 10^{-5}$	$5.47 \cdot 10^{-6}$
20	$5.29 \cdot 10^{-4}$	$4.63 \cdot 10^{-4}$	$3.51 \cdot 10^{-4}$	$1.55 \cdot 10^{-4}$	$7.02 \cdot 10^{-5}$	$9.97 \cdot 10^{-6}$
30	$2.80 \cdot 10^{-4}$	$2.60 \cdot 10^{-4}$	$2.18 \cdot 10^{-4}$	$1.20 \cdot 10^{-4}$	$6.37 \cdot 10^{-5}$	$1.24 \cdot 10^{-5}$
50	$1.15 \cdot 10^{-4}$	$1.15 \cdot 10^{-4}$	$1.07 \cdot 10^{-4}$	$7.46 \cdot 10^{-5}$	$4.97 \cdot 10^{-5}$	$1.38 \cdot 10^{-5}$
100	$2.94 \cdot 10^{-5}$	$3.22 \cdot 10^{-5}$	$3.39 \cdot 10^{-5}$	$3.09 \cdot 10^{-5}$	$2.50 \cdot 10^{-5}$	$1.11 \cdot 10^{-5}$
200	$6.45 \cdot 10^{-6}$	$7.51 \cdot 10^{-6}$	$8.90 \cdot 10^{-6}$	$9.97 \cdot 10^{-6}$	$9.48 \cdot 10^{-6}$	$6.27 \cdot 10^{-6}$
300	$2.54 \cdot 10^{-6}$	$3.04 \cdot 10^{-6}$	$3.73 \cdot 10^{-6}$	$4.73 \cdot 10^{-6}$	$4.75 \cdot 10^{-6}$	$3.76 \cdot 10^{-6}$
500	$7.33 \cdot 10^{-7}$	$9.17 \cdot 10^{-7}$	$1.19 \cdot 10^{-6}$	$1.70 \cdot 10^{-6}$	$1.77 \cdot 10^{-6}$	$1.69 \cdot 10^{-6}$
1000	$1.30 \cdot 10^{-7}$	$1.66 \cdot 10^{-7}$	$2.29 \cdot 10^{-7}$	$3.69 \cdot 10^{-7}$	$3.99 \cdot 10^{-7}$	$4.58 \cdot 10^{-7}$
2000	$2.24 \cdot 10^{-8}$	$2.92 \cdot 10^{-8}$	$4.09 \cdot 10^{-8}$	$7.02 \cdot 10^{-8}$	$7.85 \cdot 10^{-8}$	$1.01 \cdot 10^{-7}$
3000	$7.66 \cdot 10^{-9}$	$9.82 \cdot 10^{-9}$	$1.40 \cdot 10^{-8}$	$2.63 \cdot 10^{-8}$	$2.91 \cdot 10^{-8}$	$3.87 \cdot 10^{-8}$
5000	$1.96 \cdot 10^{-9}$	$2.89 \cdot 10^{-9}$	$3.84 \cdot 10^{-9}$	$7.32 \cdot 10^{-9}$	$7.87 \cdot 10^{-9}$	$1.10 \cdot 10^{-8}$

Table 3.30: Compilation of Low Energy Muon Charge Ratios. Methods: A - delayed coincidence, B - magnetic spectrometer (Vulpescu et al., 1998)

Mean Momentum [GeV/c]	Charge Ratio μ^+/μ^-	Method	Geomagn. Cutoff [GV]	Reference
0.35	1.24 ± 0.15	A	1.9	Conversi (1950)
0.4	1.24 ± 0.05	A	6.4	
1.15	1.172 ± 0.019			
1.90	1.241 ± 0.018			
2.75	1.251 ± 0.018	B	2.9	Owen & Wilson (1951)
4.90	1.263 ± 0.019			
6.76	1.240 ± 0.023			
11.48	1.229 ± 0.036			
0.6	1.14 ± 0.07			
1.6	1.20 ± 0.07			
1.7	1.16 ± 0.10			
2.6	1.39 ± 0.12	B	3.0	Moroney & Parry (1954)
3.4	1.28 ± 0.08			
4.3	1.36 ± 0.12			
9.0	1.38 ± 0.12			
0.85	0.88 ± 0.13			
1.71	1.03 ± 0.11	B	12.2	Fukui (1955)
3.72	1.27 ± 0.14			
10	1.27 ± 0.15			
6.7	1.39 ± 0.08			
11	1.35 ± 0.08	B	2.9	Holmes et al. (1961)
18	1.29 ± 0.08			
6.7	1.229 ± 0.049			Hayman &
10.4	1.223 ± 0.038	B	2.1	Wolfendale (1962)
17.5	1.233 ± 0.037			
4.32	1.33 ± 0.10	B	2.6	Coates & Nash (1962)
4.3	1.217 ± 0.033	B	2.6	Rastin et al. (1965)
7.4	1.284 ± 0.094			
10.6	1.249 ± 0.076	B	12.0	Kawaguchi et al. (1965)
15.3	1.312 ± 0.068			
0.325	0.98 ± 0.13			
0.515	1.25 ± 0.13			
0.71	1.46 ± 0.20	B	14.1	Allkofer et al. (1968)
0.995	1.50 ± 0.13			
1.4	1.20 ± 0.12			

Table 3.30: Compilation of Low Energy Muon Charge Ratios (continued). Methods: A - delayed coincidence, B - magnetic spectrometer (Vulpescu et al., 1998)

Mean Momentum [GeV/c]	Charge Ratio μ^+/μ^-	Method	Geomagn. Cutoff [GV]	Reference
2.42	1.64 ± 0.12			
5.4	1.32 ± 0.12	B	14.1	Allkofer et al. (1968)
1	30.95 ± 0.14			(continued)
19	1.07 ± 0.18			
4.0	1.22 ± 0.04			
6.1	1.27 ± 0.04			
9.2	1.26 ± 0.06	B	2.6	Baber et al. (1968)
12.4	1.25 ± 0.08			
17.1	1.27 ± 0.09			
0.5	1.337 ± 0.098			
1.34	1.469 ± 0.087			
2.67	1.606 ± 0.130	B	2.3	Allkofer & Clausen (1970)
4.57	1.364 ± 0.131			
8.31	1.275 ± 0.140			
3.8	1.249 ± 0.024			
6	1.229 ± 0.020			
9.2	1.256 ± 0.027	B	2.6	Appleton et al. (1971)
12.7	1.312 ± 0.039			
17.2	1.263 ± 0.038			
0.46	1.17 ± 0.11			
0.90	1.43 ± 0.10			
1.60	1.51 ± 0.10	B	14.1	
2.40	1.71 ± 0.14			
3.80	1.36 ± 0.10			
11.40	1.06 ± 0.07			Allkofer & Dau (1972)
0.46	1.37 ± 0.14			
0.90	1.41 ± 0.10			
1.60	1.51 ± 0.12	B	2.3	
2.40	1.66 ± 0.16			
3.80	1.53 ± 0.14			
11.40	1.22 ± 0.10			
3	1.20 ± 0.06			
5.3	1.24 ± 0.07			
8.4	1.26 ± 0.11	B	4.8	Abdel-Monem et al. (1973)
12.1	1.24 ± 0.12			
18.8	1.24 ± 0.15			

Table 3.30: Compilation of Low Energy Muon Charge Ratios (continued). Methods: A - delayed coincidence, B - magnetic spectrometer (Vulpescu et al., 1998)

Mean Momentum [GeV/c]	Charge Ratio μ^+/μ^-	Method	Geomagn. Cutoff [GV]	Reference
9.7	1.277 ± 0.008			
11.9	1.252 ± 0.017			
12.4	1.295 ± 0.007			
13.6	1.284 ± 0.014	B	2.1	Thompson et al. (1973)
13.9	1.286 ± 0.003			
16.1	1.281 ± 0.016			
19.6	1.288 ± 0.015			
14.4	1.32 ± 0.05	B	5.8	Burnett et al. (1973b)
17.4	1.25 ± 0.05			
0.23	1.02 ± 0.17			
0.31	1.24 ± 0.23	A	15.6	Singhal (1983)
0.52	0.99 ± 0.17			
0.74	1.46 ± 0.24			
4.48	1.361 ± 0.034			
4.96	1.336 ± 0.026			
5.37	1.322 ± 0.025			
5.67	1.336 ± 0.031			
5.91	1.320 ± 0.028			
6.18	1.308 ± 0.026			
6.49	1.302 ± 0.024			
6.84	1.310 ± 0.023			
7.24	1.231 ± 0.020	A	2.6	Rastin (1984b)
7.70	1.271 ± 0.020			
8.25	1.257 ± 0.019			
8.91	1.257 ± 0.018			
9.70	1.249 ± 0.017			
10.69	1.239 ± 0.016			
11.94	1.247 ± 0.016			
13.58	1.251 ± 0.016			
15.81	1.285 ± 0.016			
19.05	1.263 ± 0.016			
0.8	0.97 ± 0.06			
0.9	0.95 ± 0.05	B	4.9	Stephens & Golden (1987)
1.0	1.04 ± 0.04			
2.0	1.12 ± 0.03			

Table 3.30: Compilation of Low Energy Muon Charge Ratios (continued). Methods: A - delayed coincidence, B - magnetic spectrometer (Vulpescu et al., 1998)

Mean Momentum [GeV/c]	Charge Ratio μ^+/μ^-	Method	Geomagn. Cutoff [GV]	Reference
3.0	1.18 + 0.03			
8.0	1.27 + 0.03			
10	1.44 + 0.07			
11.2	1.26 + 0.07	B	4.9	Stephens & Golden (1987)
13.0	1.17 + 0.06			(continued)
15.3	1.23 + 0.05			
18.1	1.14 + 0.04			
0.320	1.207 + 0.130			
0.479	1.233 + 0.088			
0.643	1.192 + 0.081			
0.865	1.258 + 0.068			
1.228	1.218 + 0.057	B	0.7	De Pascale et al. (1993)
1.948	1.192 + 0.049			(600 m a.s.l.)
3.568	1.237 + 0.046			
8.008	1.185 + 0.047			
19.89	1.292 + 0.075			
5.1	1.32 + 0.04	A	2.9	Grandegger (1993)
5.1	1.28 + 0.02	A	2.9	Jannakos (1995)
0.49	1.08 + 0.24			
0.82	1.22 + 0.26	B	4.3	Basini (1995)
1.24	1.13 + 0.18			
0.44	1.12 + 0.27	B	0.4	Krizmanic et al. (1995)
0.59	1.17 + 0.04	B	4.3	Schneider et al. (1995)
				(1270 m a.s.l.)
0.59	1.081 + 0.054	B	0.4	Tarlé et al. (1997)
0.86	1.30 + 0.05	A	5.6	Vulpescu et al. (1998)

References

Abbrescia, M., M. Ambrosio, G.C. Barbarino, G. Bressi, D. Campana, R. Cardarelli, F. Guarino, M. Iacovacci, G. Iaselli, A. Lanza, S. Natali, S. Nuzzo, G. Osteria, P. Pistilli, A. Ranieri, F. Romano, R. Santonico, and V. Silvestrini: PICRC, 4, p. 430 (1993).

Abdel-Monem, M.S., J.R. Benbrook, A.R. Osborne, W.R. Sheldon, N.M. Duller, and P.J. Green: PICRC, 3, p. 1811 (1973).

Abdel-Monem, M.S., J.R. Benbrook, A.R. Osborne, W.R. Sheldon, L.M. Choate, C.E. Magnuson, N.M. Duller, and J.P. Green: PICRC, 6, p. 2043 (1975).

Abdel-Monem, M.S., J.R. Benbrook, A.R. Osborne, and W.R. Sheldon: Nuovo Cimento, 34 A, p. 210 (1976).

Abdel-Monem, M.S.: PICRC, 6, p. 46 (1977).

Achar, C.V., V.S. Narasimham, P.V. Ramana Murthy, D.R. Creed, J.B.M. Pattison, and A.W. Wolfendale: Proc. Phys. Soc., 86, p. 1305 (1965).

Agrawal, Vivek, T.K. Gaisser, P. Lipari, and T. Stanev: Phys. Rev., D 53, p. 1314 (1996).

Alexander, D.: Ph.D. Thesis Durham (1970).

Allen, K.E. and A.J. Apostolakis: Proc. R. Soc. A, 265, p. 117 (1961).

Allkofer, O.C.: University of Kiel, Internal Report (1965).

Allkofer, O.C.: Fortschr. Phys., 15, p. 113 (1967).

Allkofer, O.C.: PICRC, 14, p. 385 (1979a).

Allkofer, O.C.: Proc. 1978 DUMAND Summer Workshop, Scripps Institution of Oceanography, La Jolla, CA 92093. Code A-010, A. Roberts (ed.), 1, p. 13 (1979b).

Allkofer, O.C., and R.D. Andresen: Nuovo Cimento, 51 B, p. 329 (1967).

Allkofer, O.C., and K. Clausen: Acta Phys. Acad. Sci. Hung., 29, Suppl. 2, p. 689 (1970).

Allkofer, O.C., and W.D. Dau: Acta Phys. Acad. Sci. Hung., 29, Suppl. 2, p. 611 (1970).

Allkofer, O.C., and W.D. Dau: Phys. Lett., 38 B, p. 439 (1972).

Allkofer, O.C., and H. Jokisch: Nuovo Cimento, 15 A, p. 371 (1973).

Allokfer, O.C., and K. Clausen: Acta Phys. Acad. Sci. Hung., 29, Suppl. 2, p. 689 (1970).

Allkofer, O.C., R.D. Andresen, and W.D. Dau: Can. J. Phys., 46, p. S301 (1968).

Allkofer, O.C., W.D. Dau, and H. Jokisch: Phys. Lett., 31 B, p. 606 (1970a).

Allkofer, O.C., K. Carstensen, W.D. Dau, W. Heinrich, E. Kraft, and M. Weinert: Nucl. Instrum. and Methods, 83, p. 317 (1970b).

Allkofer, O.C., K. Carstensen, W.D. Dau, W. Heinrich, E. Kraft, and M. Weinert: Acta Phys. Acad. Sci. Hung., 29, Suppl. 4, p. 13 (1970c).

Allkofer, O.C., K. Clausen, and P. Knoblich: Proc. VI. Inter-American Seminar on Cosmic Rays, La Paz, IV, p. 930 (1970d).

Allkofer, O.C., W.D. Dau, and H. Jokisch: Proc. VI. Inter-American Seminar on Cosmic Rays, La Paz, IV, p. 937 (1970e).

Allkofer, O.C., K. Carstensen, W.D. Dau, E. Fähnders, W. Heinrich, and H. Jokisch: PICRC, 4, p. 1319 (1971a).

Allkofer, O.C., K. Carstensen, and W.D. Dau: Phys. Lett., 36 B, p. 425 (1971b).

Allkofer, O.C., K. Carstensen, and W.D. Dau: PICRC, 4, p. 1314 (1971c).

Allkofer, O.C., K. Carstensen, and W.D. Dau: Phys. Lett., 36 B, Erratum, p. 428 (1971d).

Allkofer, O.C., R.D. Andresen, K. Clausen, and W.D. Dau: J. Geophys. Res., 77, p. 4251 (1972).

Allkofer, O.C., K. Carstensen, W.D. Dau, and H. Jokisch: J. Phys., G 1, p. L51 (1975a).

Allkofer, O.C., K. Clausen, and W.D. Dau: Lett. Nuovo Cimento, 12, p. 107 (1975b).

Allkofer, O.C., G. Bella, E. Bohm, K. Carstensen, W.D. Dau, A. Entis, W. Greve, G. Hartmann, H. Jokisch, G. Klemke, B. Leugers, Y. Oren, A. Seidman, R.C. Uhr, and Y. Yeivin: PICRC, 9, p. 62 (1977a).

Allkofer, O.C., K. Carstensen, W.D. Dau, H. Jokisch, and H.J. Meyer: PICRC, 6, p. 38 (1977b).

Allkofer, O.C., K. Carstensen, W.D. Dau, and H. Jokisch: Phys. Rev. Lett., 41, p. 832 (1978a).

Allkofer, O.C., G. Bella, O. Binder, B. Bleichert, E. Bohm, K. Carstensen, W.D. Dau, H. Jokisch, G. Klemke, Y. Oren, and R.C. Uhr: Proc. VI. European Cosmic Ray Symposium KIEL, p. 72, and University if Kiel Report IFKKI 78/3 (1978b).

Allkofer, O.C., G. Bella, B. Bleichert, E. Bohm, K. Carstensen, W. D. Dau, H. Jokisch, G. Klemke, Y. Oren, and R.C. Uhr: Proc. VI. European Cosmic Ray Symposium KIEL, p. 71 (1978c).

Allkofer, O.C., T. Kitamura, A. Okada and W. Vernon: PICRC, 10, p. 411 (1979a).

Allkofer, O.C., G. Bella, B.M. Bleichert, E. Böhm, K. Carstensen, W.D. Dau, H. Jokisch, G. Klemke, Y. Oren, and R.C. Uhr: PICRC, 10, p. 50 (1979b).

Allkofer, O.C., G. Bella, O.H. Binder, K. Carstensen, W.D. Dau, H. Jokisch, G. Klemke, Y. Oren, and R.C. Uhr: PICRC, 10, p. 56 (1979c).

Allkofer, O.C., T. Kitamura, A. Okada, and W. Vernon: Proc. 1978 DUMAND Summer Workshop, Scripps Institution of Oceanography, La Jolla, CA 92093. Code A-010, A. Roberts (ed.), 1, p. 37 (1979d).

Allkofer, O.C., K. Carstensen, G. Bella, W.D. Dau, H. Jokisch, G. Klemke, Y. Oren, and R.C. Uhr: PICRC, 10, p. 321 (1981).

Amineva, T.P., K.V. Cherdyntseva, G.B. Khristiansen, S.A. Dubrovina, I.P. Ivanenko, M.A. Ivanova, N.N. Kalmykov, K.V. Mandritskaya, E.A. Sokolskaya, A.Y. Varkovitskaya, and G.T. Zatsepin: PICRC, 6, p. 2387 (1971).

Appleton, I.C., M.T. Hogue, and B.C. Rastin: Nucl. Phys., B 26, p. 365 (1971).

Asatiani, T.L., S.V. Alchudzhyan, K.A. Gayaryan, L.I. Kozliner, V.M. Kreshcyan, G.S. Martirosyan, and S.V. Ter-Antonuan: PICRC, 6, p. 2024 (1975).

Asbury, J.G., W.A. Cooper, L. Voyvodic, R.J. Walker, and T.P. Wangler: Nuovo Cimento, 66 B, p. 169 (1970).

Ashley, G.K., J.W. Keuffel, and M.O. Larson: PICRC, 4, p. 1359 (1971).

Ashley, G.K.: Private communication (1972) (after Thompson 1973).

Ashley, G.K., J.W. Keuffel, and M.O. Larson: PICRC, 3, p. 1828 (1973).

Ashley, G.K., J.W. Keuffel, and M.O. Larson: PICRC, 12, p. 4282 (1975a).

Ashley, G.K., J.W. Keuffel, and M.O. Larson: Phys. Rev. D 12, p. 20 (1975b).

Ashton, F. and A.W. Wolfendale: Proc. Phys. Soc., 81, p. 593 (1963).

Ashton, F., Y. Kamiya, P.K. MacKeown, J.L. Osborne, J.B. Pattison, P.V. Ramana Murthy, and A.W. Wolfendale: Proc. Phys. Soc. 88, p. 79 (1966).

Ashton, F., K. Tsuji, and A.W. Wolfendale: Nuovo Cimento, 9 B, p. 344 (1972).

Aurela, A.M., P.K. MacKeown, and A.W. Wolfendale: Proc. Phys. Soc., 89,

p. 401 (1966).

Aurela, A.M., and A.W. Wolfendale: Ann. Acad. Sci. Fenn. A 6, p. 226 (1967).

Ayre, C.A., M.A. Hamdan, F.W. Holroyd, C.J. Hume, B.C. Nandi, M.G. Thompson, S.C. Wells, M.R. Whalley, and A.W. Wolfendale: PICRC, 4, p. 1309 (1971a).

Ayre, C.A., M.A. Hamdan, F.W. Holroyd, C.J. Hume, B.C. Nandi, M.G. Thompson, S.C. Wells, M.R. Whalley, and A.W. Wolfendale: J. Phys., A 4, p. L89 (1971b).

Ayre, C.A., M.A. Hamdan, C.J. Hume, M.G. Thompson, S.C. Wells, M.R. Whalley, and A.W. Wolfendale: PICRC, 4, p. 1364 (1971c).

Ayre, C.A., J.M. Baxendale, B.J. Daniel, C.J. Hume, M.G. Thompson, M.R. Whalley, and A.W. Wolfendale: PICRC, 3, p. 1754 (1973a).

Ayre, C.A., J.M. Baxendale, B.J. Daniel, C.J. Hume, B.C. Nandi, M.G. Thompson, M. Whalley, and A.W. Wolfendale: PICRC, 3, p. 1822 (1973b).

Ayre, C.A., J.M. Baxendale, C.J. Hume, B.C. Nandi, M.G. Thompson, and M.R. Whalley: J. Phys. G, 1, p. 584 (1975).

Baber, S.R., W.F. Nash, and B.C. Rastin: Nucl. Phys., B 4, p. 549 (1968).

Badhwar, G.D., S.A. Stephens, and R.L. Golden: Phys. Rev. D, 15, p. 820 (1977).

Baradzei, L.T., E.A. Kanevskaya, Yu.A. Smorodin, and M.V. Soloviyev: PICRC, 6, p. 2397 (1971).

Barbouti, A.I., and B.C. Rastin: J. Phys., G 9, p. 1577 (1983).

Baschiera, B., G. Basini, H. Bilokon, B. D'Ettorre Piazzoli, G. Mannocchi, C. Castagnoli, and P. Picchi: Nuovo Cimento, 2 C, p. 473 (1979).

Basini, G., R. Bellotti, F. Bongiorno, M.T. Brunetti, F. Cafagna, M. Circella, A. Codino, G. De Cataldo, C.N. De Marzo, M.P. De Pascale, N. Finetti, N. Giglietto, R.L. Golden, C. Grimani, M. Hof, F. Massimo Brancaccio, M. Menichelli, J.W. Mitchell, A. Morselli, J.F. Ormes, P. Papini, S. Piccardi, P. Picozza, M. Ricci, I. Salvatori, M. Simon, P. Spillantini, P. Spinelli, S.A. Stephens, S.J. Stochaj, and R.E. Streitmatter: PICRC, 1, p. 585 (1995a).

Basu, N. and M.S. Sinha: Trans. Bose Res. Inst., 21, p. 67 (1956-57).

Bateman, B.J., W.G. Cautrell, D.R. Durda, N.M. Duller, P.J. Green, A.V. Jelinek, T.A. Nagy and W.R. Sheldon: Phys. Lett., 36 B, p. 144 (1971).

Baxendale, J.M., C.J. Hume, and M.G. Thompson: J. Phys., G 1, p. 781 (1975a).

Baxendale, J.M., B.J. Daniel, R. Hawkes, J.L. Piggott, M.G. Thompson, and R. Thornley: PICRC, 6, p. 2011 (1975b).

Bedewi, F.El., and A. Goned: J. Phys. A, 4, p. 660 (1971).

Berger, Ch., et al.: (Fréjus Collaboration) Phys. Lett., 227 B, p. 489 (1989).

Bhattacharyya, D.P.: Z. Phys., 234, p. 17 (1970).

Bhattacharyya, D.P.: Ph.D. Thesis Calcutta University (1971).

Bhattacharyya, D.P.: J. Phys. A: Math. Nucl. Gen., 6, p. 582 (1973).

Bhattacharyya, D.P.: J. Phys. A, 7, p. 158 (1974a).

Bhattacharyya, D.P.: Nuovo Cimento, 24, p. 78 (1974b).

Bhattacharyya, D.P.: Phys. Rev. D, 13, p. 566 (1976).

Bhattacharyya, D.P.: Aus. J. Phys., 32(4), p. 369 (1979).

Brancus, I.M., B. Vulpescu, J. Wentz, H. Rebel, A.F. Badea, H. Bozdog, M. Duma, A. Haungs, H.J. Mathes, M. Petcu, and M. Roth: PICRC, 2, p. 48 (1999).

Bruscoli, M., and M. Pieri: DFF 182/2/93, Firenze (unpublished) (1993).

Bugaev, Edgar V., Vadim A. Naumov, Sergey I. Sinegovsky, Akeo Misaki, Nobusuke Takahashi, and Elena S. Zaslavskaya: Proceedings of Nestor Workshop, p. 268 (1993).

Bugaev, Edgar V., Vadim A. Naumov, Sergey I. Sinegovsky, Akeo Misaki, Nobusuke Takahashi, and Elena S. Zaslavskaya: Università degli Studi di Firenze, Dipartimento di Fisica and Instituto Nationale di Fisica Nucleare Sezione di Firenza, Preprint DFF 204/4/1994 (1994).

Bugaev, E.V., A. Misaki, V.A. Naumov, T.S. Sinegovskaya, S.I. Sinegovsky, and N. Takahashi: Phys. Rev., D 58, p. 54001 (1998).

Burnett, T.H., G.E. Masek, T. Maung, E.S. Miller, H. Ruderman, and W. Vernon: PICRC, 3, p. 1764 (1973a).

Burnett, T.H., L.J. LaMay, G.E. Masek, T. Maung, E.S. Miller, H. Ruderman, and W. Vernon: Phys. Rev. Lett., 30, p. 937 (1973b).

Butkevich, A.V., L.G. Dedenko, and I.M. Zheleznykh: Yad. Fiz., 50, p. 142 (1989). Sov. J. Nucl. Phys., 50, p. 90 (1989).

Carstensen, K.: Thesis, Kiel (1978).

Chakrabarti, A.K., A.K. Das, and A.K. De: Can J. Phys., 57, p. 921 (1979).

Chandrasekharan, K.S., G.S. Gokhale, and A.S. Rao: Proc. Ind. Acad. Sci., 32, p. 95 (1950).

Chin, S., Y. Hanayama, T. Hara, S. Higasi, T. Kitamura, S. Miono, M. Nakagawa, S. Ozaki, T. Takahashi, K. Tsuji, Y. Watase, K. Kobayakawa, and H. Shibata: Acta Phys. Acad. Sci. Hung., 29, Suppl. 4, p. 65 (1970).

Coates, D.W., and W.F. Nash: Austr. J. Phys., 15, p. 420 (1962).

Conversi, M.: Phys. Rev., 79, p. 749 (1950).

Cottrell, D.M., R.J. Piserchio, J.R. Thompson and J.J. Lord: Proc. VI. Inter-American Seminar on Cosmic Rays, 4, p. 1019 (1970).

Crookes, J.N. and B.C. Rastin: PICRC, 4, p. 1325 (1971a).

Crookes, J.N. and B.C.Rastin: PICRC, 4, p. 1369 (1971b).

Crookes, J.N. and B.C. Rastin: Nucl. Phys., B 39, p. 493 (1972).

Crookes, J.N. and B.C. Rastin: Nucl. Phys., B 58, p. 93 (1973).

Das, A.K. and A.K. De: PICRC, 10, p. 110 (1979).

Das, A.K. and A.K. De: J. Phys., G 6, p. 637 (1980).

Davis, K.H., S.M. Fall, R.B. Ingebretsen, and R.O. Stenerson: Phys. Rev., D 4, p. 607 (1971).

De, A.K., P. Ghosh, S. Mitra, P.C. Bhattacharyya, and A.K. Das: Phys. Rev. D, 5, p. 1068 (1972a).

De, A.K., P. Ghosh, S. Mitra, P.C. Bhattacharyya, and A.K. Das: J. Phys., A 5, p. 1236 (1972b).

De, A.K.,P. Ghosh, and A.K. Das: J. Phys., A 7, p. 150 (1974).

De Pascale, M.P., A. Morselli, P. Picozza, R.L. Golden, C. Grimani, B.L. Kimbell, S.A. Stephens, S.J. Stochaj, W.R. Webber, G. Basini, F. Bongiorno, F.M. Brancaccio, M. Ricci, J.F. Ormes, E.S. Seo, R.J. Streitmatter, P. Papini, P. Spillantini, M.T. Brunetti, A. Codino, M. Menichelli, and I. Salvatori: J. Geophys. Res. 98 (A3), p. 3501 (1993).

Del Rosario, L. and J. Davila-Aponte: Phys. Rev., 88, p. 998 (1952).

Elbert, J., M. Iacovacci, and V. Silvestrini: Europhys. Lett, 14 (2), p, 181 (1991).

Filosofo, I., E. Pohl, and J. Pohl-Ruling: Nuovo Cimento, 12, p. 809 (1954).

Flint, R.W. and W.F. Nash: PICRC, 4, p. 1346 (1971a).

Flint, R.W. and W.F. Nash: Nucl. Phys. B 33, p. 632 (1971b).

Flint, R.W., R.B. Hicks, and S. Standil: Can. J. Phys., 50, p. 843 (1972).

Flint, R.W., R.B. Hicks, and S. Standil: Phys. Rev., D 8, p. 1300 (1973).

Fujii, A., S. Iida, Y. Kamiya, S. Kawaguchi, and A. Takenaka: Lett. Nuovo. Cimento, 1, p. 845 (1969).

Fukui, S., T. Kitamura, and Y. Murata: J. Phys. Soc. Japan, 10, p. 735 (1955).

Fukui, S., T. Kitamure and Y. Murata: J. Phys. Soc. Japan 12, p. 854 (1957).

Gaisser, T.K.: J. Geophys. Res., 79, p. 2281 (1974).

Gaisser, T.K.: Cosmic Rays and Particle Physics, Cambridge (1990).

Gandegger, W.: KfK Report 5122, Kernforschungszentrum Karlsruhe (1993).

Gettert, M., J. Unger, R. Trezeciak, J. Engler, and J. Knapp: PICRC, 4, p. 394 (1993).

Ghosh, S. and S. Sengupta: Indian J. Phys., 41, p. 788 (1967).

Gokhale, G.S.: Private communication (1953) (after Allkofer et al. 1968).

Gokhale, G.S. and Balasubrahmanyan: as quoted by Fukui et al. (1957).

Greisen, K.I.: Phys. Rev., 61, p. 212 (1942).

Greisen, K.I., and N. Nereson: Phys. Rev., 62, p. 316 (1942).

Hayman, P.J. and A.W. Wolfendale: Proc. Phys. Soc., 80, p. 710 (1962).

Hicks, R.B., R.W. Flint, and S. Standil: Can. Journ. Phys., 49, p. 2079 (1971).

Higashi, S., K. Honda, S. Ozaki, T. Takahashi, Y. Teramoto, T. Kitamura, K. Mitsui, S. Miyake, Y. Muraki, I. Nakamura, Y. Ohashi, A. Okada, S. Ida, Y. Kamiya, Y. Kawashima, H. Shibata, K. Kobayakawa, S. Mikamo, and Y. Minorikawa: N.I.M., 150, p. 387 (1978).

Holmes, J.E.R., B.G. Owen, and A.L. Rodgers: Proc. Phys. Soc., 78, p. 505 (1961).

Honda, K., S. Higashi, S. Iida, Y. Kamiya, Y. Kawashima, T. Kitamura, K. Kobayakawa, S. Matsuno, S. Mikamo, Y. Minorikawa, K. Mitsui, S. Miyake, Y. Muraki, I. Nakamura, Y. Ohashi, A. Okada, S. Ozaki, H. Shibata, T. Suda, T. Takahashi and Y. Teramoto: PICRC 10, p. 59 (1979).

Honda, M., T. Kajita, K. Kasahara, and S. Midorikawa: Phys. Rev., D 52, p. 4985 (1995).

Ivanenko, I.P., M.A. Ivanova, L.A. Kuzmichev, N.P. Ilyina, K.V. Mandritskaya, E.A. Osipova, I.V. Rakobolskaya, amd G.T. Zatsepin: PICRC, 8, p. 210 (1985).

Ivanova, M.A., L.A. Kuzmichev, K.V. Mandritskaya, E.A. Osipova, I.V.

Rakobolskaya, N.V. Sokolskaya, A.Y. Varkovitskaya, G.T. Zatsepin, and V.I. Zatsepin: PICRC, 10, p. 35 (1979).

Jain, S.K.: Proc. Indian National Sci. Acad., 46A, p. 146 (1980).

Jakeman, D.: Can. J. Phys., 34, p. 432 (1956).

Jannakos, T.E.: KfK Report 5520, Forschungszentrum Karlsruhe (1995).

Jokisch, H., K. Carstensen, W.D. Dau, H.J. Meyer, and O.C. Allkofer: Phys. Rev. D 19, p. 1368 (1979).

Judge, R.J.R. and W.F. Nash: Nuovo Cimento, 35, p. 999 (1965).

Kamiya, Y., S. Kawaguchi, and S. Iida: PICRC, 4, p. 1354 (1971).

Kaneko, S., T. Kubozoe, and M. Takahata: J. Phys. Soc. Japan, 10, p. 915 (1955).

Karmakar, N.L., A. Paul and N. Chaudhuri: Nuovo Cimento 17 B, p. 173 (1973).

Kasha, H., C.B.J. Hawkins, and R.J. Stefanski: Can. J. Phys., 46, p. S306 (1968).

Kawaguchi, S., T. Sakai, H. Oda, H. Ueno and Y. Kamiya: PICRC, 2, p. 941 (1965).

Kawashima, Y., T. Kitamura, S. Matsuno, K. Mitsui, Y. Muraki, Y. Ohashi, A. Okada, T. Suda, Y. Minorikawa, K. Kobayakawa, Y. Kamiya, I. Nakamura and T. Takahashi: PICRC 7, p. 16 (1981).

Khalchukov, F.F., E.V. Korolka, V.A. Kudryavtsev, A.S. Malgin, O. Ryazhskaya, and G.T. Zatsepin: PICRC 8, p. 12 (1985).

Kitamura, Y., and O. Minakawa: Progr. Theor Phys., 10, p. 239 (1953).

Kitamura, T., K. Mitsui, Y. Muraki, I. Nakamura, Y. Ohashi, A. Okada, Y. Minorikawa, V.S. Narasimham: PICRC, 6, p. 2031 (1975).

Kitamura, T.: PICRC, 13, p. 361 (1981).

Knoblich, P.: Ph.D. Thesis, University of Kiel (1968).

Komori, H.: PICRC, 6, p. 26 (1977).

Kong, D.F.L, S.Y. Lau, and L.K. Ng: PICRC, 6, p. 1859 (1977).

Krasilnikov, D.D., G.V. Skripin, N.P. Chirkov, and G.V. Shafer: PICRC, 6, p. 2421 (1971).

Kraushaar, W.L.: Phys. Rev. 76, p. 1045 (1949).

Krishnaswamy, M.R., M.G.K. Menon, V.S. Narasimham, K. Hinotani, N. Ito, S. Miyake, J.L. Osborne, A.J. Parsons, and A.W. Wolfendale: Proc. R.

Soc. A, 323, p. 511 (1971).

Krizmanic, J.F., A.J. Davis, L.M. Barbier, E.R. Christian, R.L. Golden, M. Hof, K.E. Krombel, A.W. Labrador, R.A. Mewaldt, J.W. Mitchell, J.F. Ormes, I.L. Rasmussen, O. Reimer, S.M. Schindler, M. Simon, S.J. Stochaj, R.E. Streitmatter, and W.R. Weber: PICRC, 1, p. 593 (1995).

Lamanna, E. et al. (MACRO Collaboration): PICRC, 4, p. 391 (1993).

Leipuner, L., R. Larsen, L. Smith, R. Adair, B. Higgs, H. Kasha, and R. Kellogg: PICRC, 3, p. 1771 (1973).

Liland, A.: Fortschr. Phys., 23, p. 571 (1975).

Liland, A.: Ark. Fys. Semin. Trondheim (Norway) Co.: AFYTAA , 10, p. 1 (1980).

Lipari, Paolo: Astropart. Phys., 1, p. 195 (1993).

Lowe, G.H., M.O. Larson, H.E. Bergeson, J.W. Cardon, J.W. Keuffel, and J. West: Phys. Rev., D 12, p. 651 (1975).

MacKeown, P.K., S.S. Said, J. Wdowczyk, and A.W. Wolfendale: PICRC, 2, p. 937 (1965).

Maeda, K.: VI.Inter-American Seminar on Cosmic Rays, La Paz, IV, p. 847 (1970).

Maeda, K.: Fortschr. Phys., 21, p. 113 (1973).

Matsuno, S., F. Kajino, Y. Kawashima, T. Kitamura, K. Mitsui, Y. Muraki, Y. Ohashi, A. Okada, T. Suda, Y. Minorikawa, K. Kobayakawa, Y. Kamiya, N. Nakamura, and T. Takahashi: Phys. Rev. D, 29, p. 1 (1984).

Menon, M.G.K. and P.V. Ramana-Murthy: Progr. Elementary Particles and Cosmic Rays, 9, p. 161 (1967).

Meyer, B.S., J.P.F. Sellschop, M.F. Crouch, W.R. Kropp, H.W. Sobel, H.S. Gurr, J. Lathrop, and F. Reines: Phys. Rev., D 1, p. 2229 (1970).

Minorikawa, Y., and T. Saito: PICRC, 6, p. 12 (1977).

Mitsui, K., A. Okada, Y. Kawashima, T. Kitamura, S. Matsuno, Y. Muraki, Y. Ohashi, T. Suda, T. Takahashi, S. Higashi,S. Ozaki, I. Nakamura, Y. Kamiya, K. Kobayakawa, H. Shibata, Y. Minorikawa, and S. Mikamo: PICRC 10, p. 29 (1979).

Mitsui, K., A. Okada, T. Kitamura, S. Miyake, Y. Muraki, Y. Ohashi, T. Suda, S. Ozaki, and S. Mikamo: N.I.M., 169, p. 96 (1980).

Mitsui, K., A. Okada, Y. Kawashima, T. Kitamura, S. Matsuno, Y. Muraki, Y. Ohashi, T. Suda, T. Takahashi, S. Higashi,S. Ozaki, I. Nakamura, Y.

Kamiya, K. Kobayakawa, H. Shibata, Y. Minorikawa, and S. Mikamo: Nuovo Cimento 73 A, p. 209 (1983a).

Mitsui, K., A. Okada, Y. Kawashima, T. Kitamura, S. Matsuno, Y. Muraki, Y. Ohashi, T. Suda, T. Takahashi, S. Higashi,S. Ozaki, I. Nakamura, Y. Kamiya, K. Kobayakawa, H. Shibata, Y. Minorikawa, and S. Mikamo: Nuovo Cimento 73 A, p. 235 (1983b).

Mitsui, K., A. Okada, Y. Kawashima, T. Kitamura, S. Matsuno, Y. Muraki, Y. Ohashi, T. Suda, I Nakamura, K. Kobayakawa, H. Inazawa, Y. Minorikawa, and S. Mikamo: J. Phys. G 9, p. 573 (1983c).

Mitsui, K., Y. Minorikawa, and H. Komori: Nuovo Cimento, 9 C, N. 5, p. 995 (1986).

Miyake, S., V.S. Narasimham, and P.V. Ramana Murthy: Nuovo Cimento, 32, p. 1505 (1964).

Mizutani, K., T. Shirai, M. Akashi, and Z. Watanshe: PICRC, 4, p. 1392 (1971).

Moroney, J.R. and J.K. Parry: Aust. J. Phys., 7, p. 423 (1954).

Murakami, K., S. Sagisaka, A. Inoue, Y. Mishima, and K. Nagashima: PICRC, 10, p. 70 (1979).

Muraki, Y., Y. Ohashi, T. Kitamura, K. Mitsui, S. Miyake, A. Okada, P.V. Ramana-Murthy, K. Honda, Y. Kawashima, T. Takahashi, Y. Teramoto, S. Higashi, S. Ozaki, I. Nakamura, Y. Kamiya, S. Iida, K. Kabayakawa, S. Shibata, Y. Minorikawa and S. Mikamo: Phys. Rev. Lett. 43, p. 974 (1979).

Muraki, Y., Y. Kawashima, T. Kitamura, S. Matsuno, K. Mitsui, S. Miyake, Y. Ohashi, T. Suda, P.V. Ramana-Murthy, S. Higashi, K. Honda, S. Ozaki, T. Takahashi, Y. Teramoto, Y. Kamiya, I. Nakamura, K. Kabayakawa, H. Shibata, Y. Minorikawa and S. Mikamo: Phys. Rev. D 28, p. 40 (1983).

Nakamura, I., T. Kitamura, K. Mitsui, Y. Muraki, Y. Ohashi, A. Okada and T. Takahashi: PICRC 10, p. 19 (1979).

Nandi, B.C., and M.S. Sinha: Acta Phys. Acad. Sci. Hung., 29, Suppl. 4, p. 87 (1970).

Nandi, B.C., and M.S. Sinha: Nucl. Phys., B 40, p. 289 (1972a).

Nandi, B.C. and M.S. Sinha: J. Phys., A 5, p. 1384 (1972b).

Narasimham, V.S.: Ph.D. Thesis, University of Bombay (1967).

Naumov, Vadim A., Sergey I. Sinegovsky, and Edgar V. Bugaev: Proc. 2nd. Internat. Nestor Workshop, Pylos, Greece, ed. L.K. Resvanis, University of Athens, p. 119 (1992).

Ng, L.K. and A.W. Wolfendale: Nuovo Cimento, 22 A, p. 251 (1974a).

Ng, L.K., M.G. Thompson, and M.R. Whalley: Nuovo Cimento, 22 B, p. 328 (1974b).

Nozaki, M.: PICRC, Invited and Rapporteur Papers, AIP Conf. Proc., 516, p. 330 (2000).

O'Brien, K.: Phys. Rev., D 4, p. 635 (1971a).

Olbert, S.: Phys. Rev., 96, p. 1400 (1954).

Osborne, J.L., A.W. Wolfendale, and N.S. Palmer: Proc. Phys. Soc., 84, p. 901 (1964).

Owen, B.G. and J.G. Wilson: Proc. Phys. Soc., 68 A, p. 409 (1955).

Palmer, N.S., and W.F. Nash: Can. J. Phys., 46, p. S313 (1968).

Pine, J., R.J. Davisson, and K. Greisen: Nuovo Cimento, 14, p. 1181 (1959).

Pomerantz, M.A.: Phys. Rev., 75, p. 1721 (1949).

Ramana-Murthy, P.V. and A. Subramanian: Phys. Lett., 39 B, p. 646 (1972).

Rastin, B.C.: J. Phys., G 10, p. 1609 (1984a).

Rastin, B.C.: J. Phys., G 10, p. 1629 (1984b).

Rastin, B.B., S.R. Barber, R.M. Bull, and W.F. Nash: PICRC, 2, p. 981 (1965).

Rhode, Wolfgang: Dissertation University of Wuppertal, Germany, (1993).

Rossi, B.: Rev. Mod. Phys., 20, p. 537 (1948).

Saito, K., I. Yamamoto, T. Tomiyama, and M. Nakamura: PICRC, 4, p. 575 (1991).

Schneider, E., S.W. Barwick, J.J. Beatty, C.R. Bower, C. Chaput, S. Coutu, G. de Nolfo, D. Ficenec, J. Knapp, D.M. Lowder, S. McKee, D. Müller, J.A. Musser, S.L. Nutter, S.P. Swordy, K.K. Tang, G. Tarlé, A.D. Tomasch, and E. Torbet: PICRC, 1, p. 690 (1995).

Sheldon, W.R.: Private communication (1971), after Allkofer et al. (1971b).

Shen, Pei-ruo, T. Aoki, Y. Kawashima, K. Mitsui, T. Kitamura, and I. Nakamura: PICRC, 10, p. 305 (1981).

Singhal, K.P.: PICRC, 7, p. 27 (1983).

Sreekantan, B.V., S. Naranan, and P.V. Ramana Murthy: Proc. Ind. Acad. Sci., A 43, p. 113 (1956).

Stephens, S.A.: PICRC, 10, p. 90 (1979a).

Stephens, S.A.: PICRC, 10, p. 96 (1979b).

Stephens, S.A.: PICRC, 4, p. 282 (1981).

Stephens, S.A., and R.L. Golden: PICRC, 6, p. 173 (1987).

Stockel, C.T.: J. Phys., A 2, p. 639 (1969).

Subramanian, A., S. Naranan, P.V. Ramana Murthy, A.B. Sahiar, and S. Lal: Nuovo Cimento, 7, p. 110 (1958).

Tarlé, G., S.W. Barwick, J.J. Beatty, A. Bhattacharyya, C.R. Bower, C. Chaput, S. Coutu, G.A. de Nolfo, J. Knapp, D.M. Lowder, S. McKee, D. Müller, J.A. Musser, S.L. Nutter, E. Schneider, S.P. Swordy, A.D. Tomasch, and E. Torbet: PICRC, 6, p. 321 (1997).

Tebb, R.G.P., W.F. Nash, and C.A. Deacon: PICRC, 4, p. 1340 (1971).

Thompson, M.G.: Cosmic Rays at Ground Level. A.W. Wolfendale (ed.), The Institute of Physics, London, p. 17 (1973).

Thompson, M.G., R. Thornley, and M.R. Whalley: J. Phys., G 3(2), p. L39 (1977a).

Thompson, M.G., R. Thornley, M.R. Whalley, and A.W. Wolfendale: PICRC, 6, p. 21 (1977b).

Torsti, J.J. and E. Valtonen: Phys. Scr., 14, p. 187 (1976).

Tsuji, S., T. Wada, Y. Yamashita, I. Yamamoto, H. Asada, T. Katayama, K. Kohno, S. Tagasira, H. Takei, Y. Tsutsui, and K. Saitoh: PICRC, 1, p. 614 (1995).

Volkova, L.V., L.A. Kuzmichev and G.T. Zatsepin: PICRC, 6, p. 6 (1977).

Volkova, L.V.: Yad. Fiz., 31, p. 1510 (1980); Sov. J. Nucl. Phys., 31, p. 784 (1980).

Volkova, L.V., W. Fulgione, P. Galeotti, and O. Saavedra: Nuovo Cimento, C 10, p. 465 (1987).

Vulpescu, B., J. Wentz, I.M. Brancus, H. Rebel, A.F. Badea. H. Bozdog, M. Duma, A. Haungs, H.-J. Mathes, M. Petcu, and M. Roth: Nucl. Instr. Meth., A 414, p. 205 (1998).

Wada, T., H. Asada, T. Katayama, K. Kono, N. Nishiyama, S. Tsujii, Y. Tsutsui, K. Saito, T. Tagashira, T. Takei, K. Noda, T. Tomiyama, I. Yamamoto, and Y. Yamashita: PICRC, 1, p. 1068 (1995).

Wentz, J., A. Haungs, H.J. Mathes, H. Rebel, F. Herm, and M. Kretschmer: PICRC, 1, p. 520 (1995).

Whalley, M.R.: Ph.D. Thesis, Durham (1974).

Wilson, B.G.: Can. J. Phys., 37, p. 19 (1959).

Wolfendale, A.W.: Private communication (1971) (after Allkofer et al. 1971b).

Wright, A.G.: J. Phys., A 7, p. 2085 (1974).

Zatsepin, G.T., et al.: Izv. Akad. Nauk SSSR, Ser Fiz., 55, p. 740 (1991).

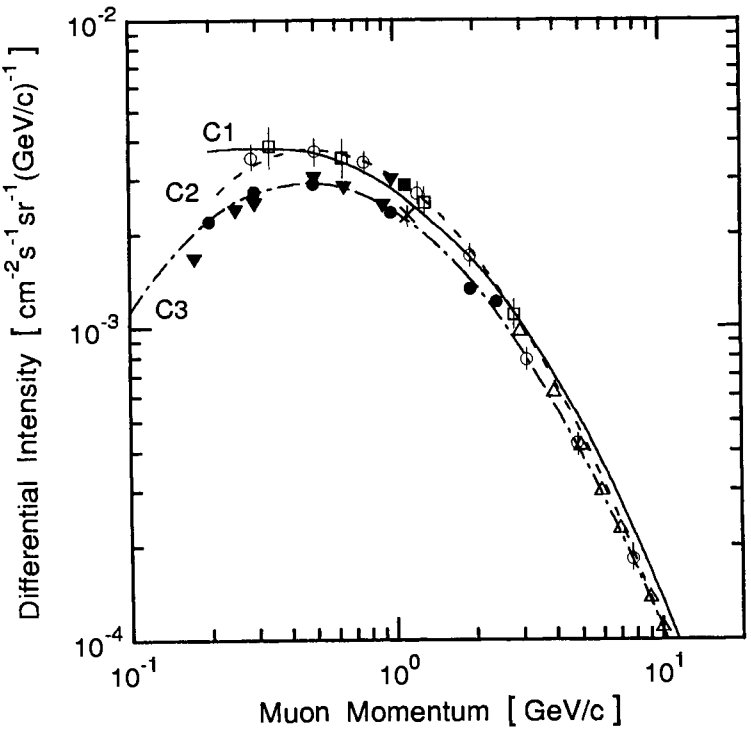

Figure 3.27: Absolute differential intensities and momentum spectra of vertical muons at sea level constructed from individual measurements. The numbers in brackets after the references are the respective vertical cutoff rigidities in GV. The solid and dashed curves are fits obtained by Allkofer et al. (1971b) and Thompson (1973), the dash - dot curve is the Rossi curve (1948). (Allkofer and Jokisch 1973, extended by the author).

□	Allkofer et al. (1970d) and Knoblich (1968) [2.4 GV]	○	Allkofer and Clausen (1970) [2.4 GV]
■	Allkofer et al. (1970a, e, 1971d) [2.4 GV]	△	Bateman et al. (1971) [4.9 GV]
•	Rossi (1948)	×	De et al. (1972b) and Allkofer and Dau (1970) [16.5 GV]
C1	Allkofer et al. (1971b), fit	▼	Fukui et al. (1957) [12.6 GV]
C3	Rossi (1948), fit	C2	Thompson (1973), fit

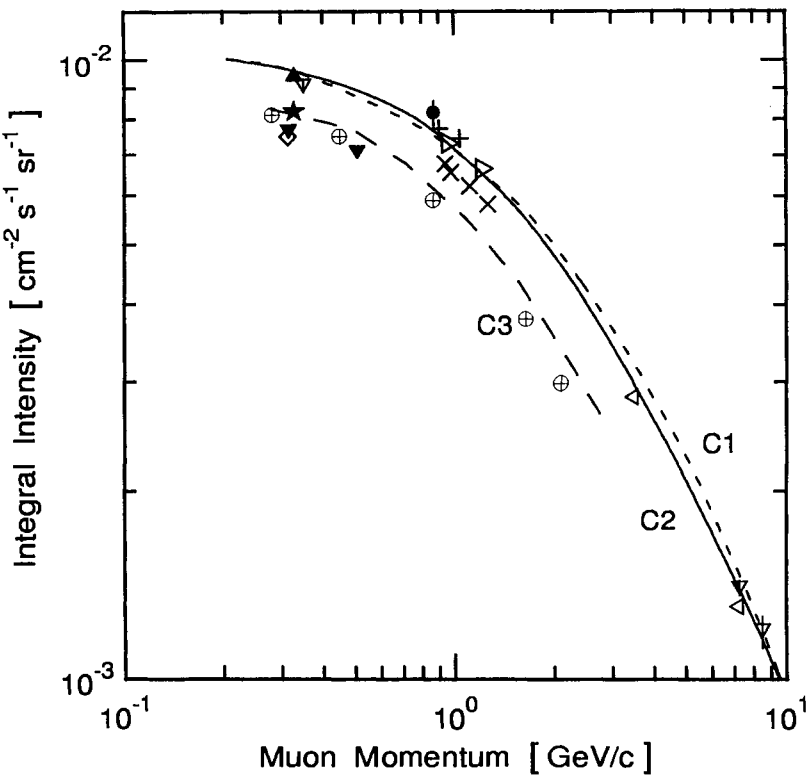

Figure 3.28: Absolute integral intensities and momentum spectra of vertical muons at sea level constructed from various measurements. The numbers in brackets after the references are the respective vertical cutoff rigidities in GV.

- ▷ Allkofer et al. (1970a, e, 1971d) [2.4 GV]
- ▽ Crookes and Rastin (1971a, b, 1972) [2.5 GV]
- ▼ Fukui et al. (1957) [12.6 GV]
- ★ Greisen (1942) [1.5 GV]
- ⊕ Rossi (1948)
- C1 Allkofer et al, (1971b)
- C3 Rossi (1948)
- • Ashton et al. (1972) [2.1 GV]
- ◁ Ayre et al. (1971a, b) [2.1 GV]
- ◇ Bhattacharyya (1970) [16.5 GV]
- × De et al. (1972b) and Allkofer and Dau (1970) [16.5 GV]
- ▲ Greisen and Nereson (1942) [1.5 GV], corrected
- \+ Karmakar et al (1973) [15 GV]
- C2 Allkofer and Jokisch (1973)

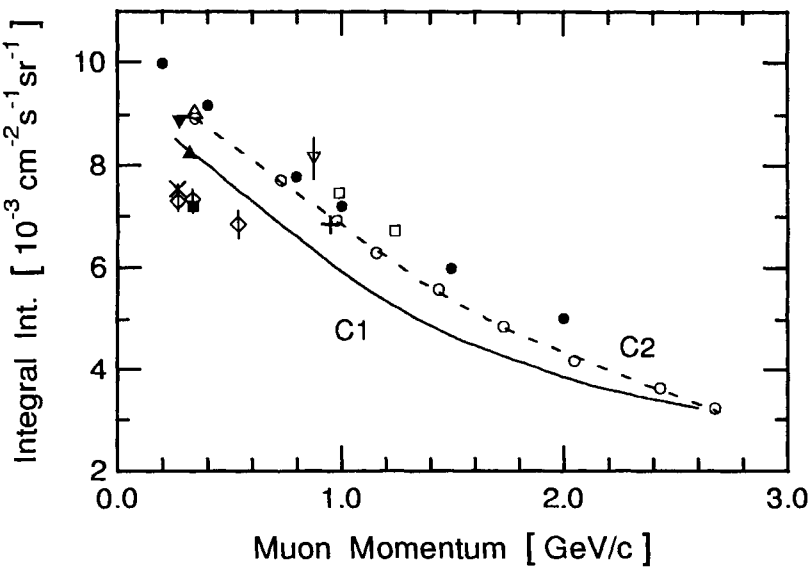

Figure 3.29: Compilation of vertical absolute integral muon intensity data and momentum spectrum measurements near sea level, presented on a linear plot (Karmakar et al., 1973). The solid line, C1, is the old integral spectrum of Rossi (1948), the dashed line, C2, the best fit to the data of Karmakar et al.(1973).

□	Allkofer et al. (1970a)	▽	Ashton et al. (1972)
•	Allkofer et al. (1971b, c)	+	De et al. (1972a)
△	Crookes and Rastin (1972)	◇	Fukui et al. (1957)
×	Gokhal and Balasubrahmanyan (1957)	▲	Greisen (1942)
		▼	Kraushaar (1949)
■	Kitamura and Minorikawa (1953)	—	Rossi (1948)
o , - - -	Karmakar et al. (1973)		

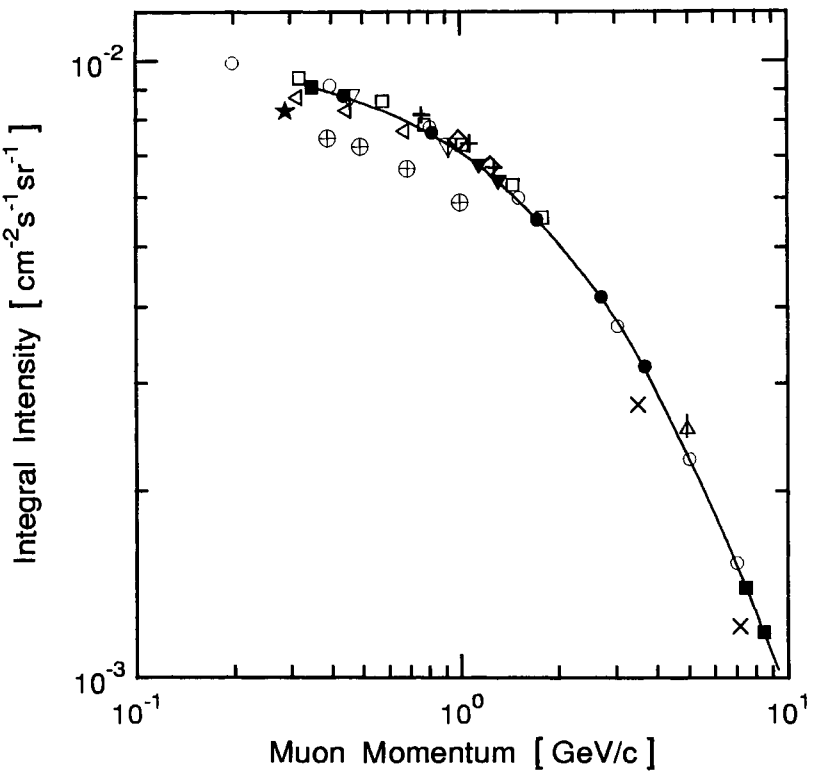

Figure 3.30: Absolute integral intensities obtained by various authors and best-fit absolute integral momentum spectrum of low energy muons at sea level. The solid curve is a fit by Crookes and Rastin.

o	Allkofer et al. (1971b)	◇	Allkofer et al. (1970a)
×	Ayre et al. (1975)	•	Barbouti and Rastin (1983)
▽	Baschiera et al. (1979)	■	Crookes and Rastin (1973a, b)
▼	De et al. (1972a)	◁	Flint et al. (1973)
△	Kong et al. (1977)	⊕	Hayman and Wolfendale (1962)
+	Ng et al. (1974b)	★	Rossi (1948)
□	Shen et al. (1981)	—	Crookes and Rastin (1973a), fit

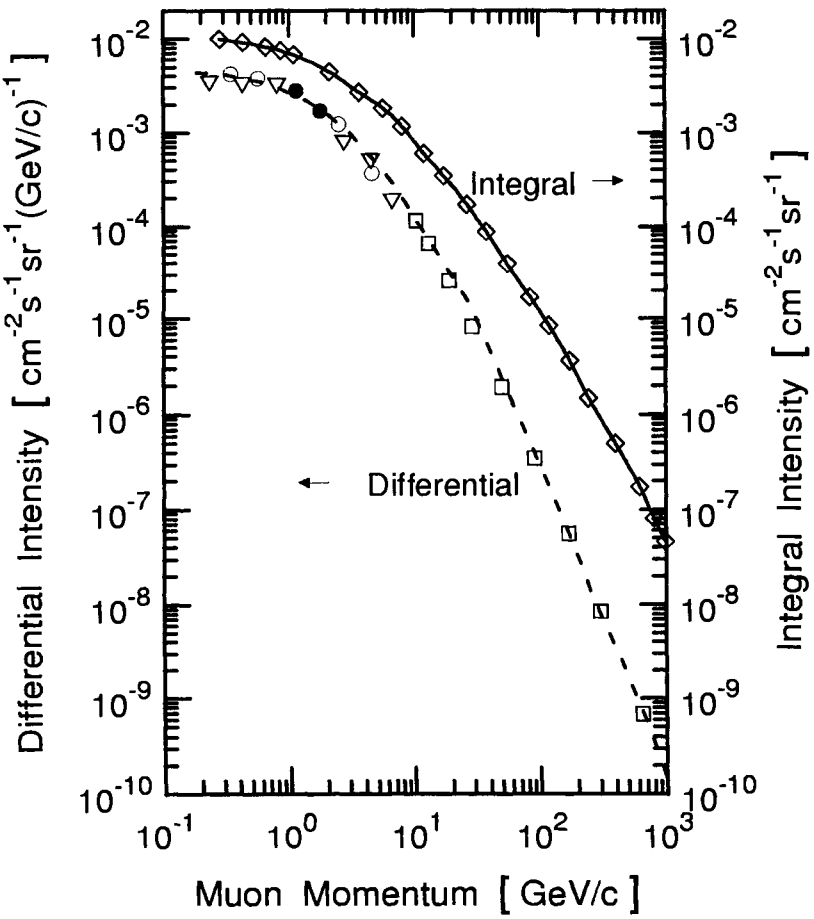

Figure 3.31: Absolute vertical differential and integral momentum spectra of muons in the range $0.2 \leq p \leq 1000$ GeV/c at sea level (Allkofer et al. 1971b and 1971c) obtained with four experiments. The absolute intensity was calibrated at 1 GeV/c and at 1.11 GeV/c (Allkofer et al. 1970a and 1971d).

○ Exp. 1: 0.2 - 6.0 GeV/c	▽ Exp. 3: 0.2 - 10.0 GeV/c
● Exp. 2: 0.98 - 1.24 GeV/c	□ Exp. 4: 10 - 1000 GeV/c
◇ Combined integral spectrum	

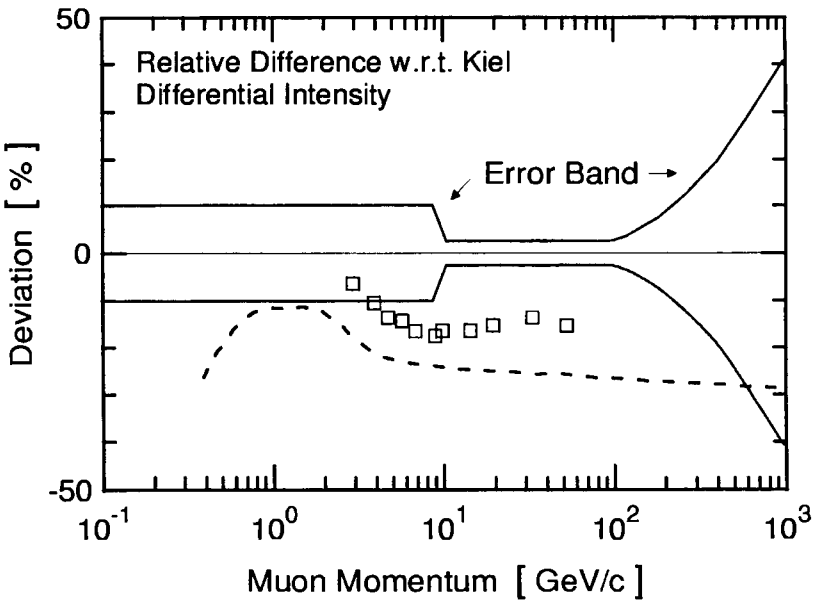

Figure 3.32: Relative deviations of experimental vertical differential muon spectra with respect to the Kiel standard (Allkofer et al. 1971b).

- - - Hayman and Wolfendale (1962) | □ Sheldon (1971)

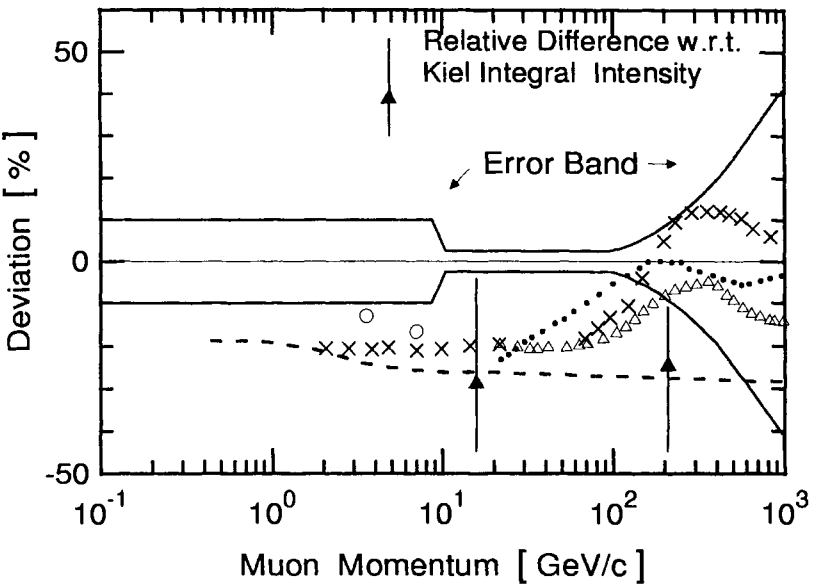

Figure 3.33: Relative deviations of experimental vertical integral muon spectra with respect to the Kiel standard (Allkofer et al. 1971b).

×	Aurela and Wolfendale (1966), and Aurela et al. (1967)		
- - -	Hayman and Wolfendale (1962)	▲	Cottrell et al. (1970)
△	Osborne and Wolfendale (1964)	o	Wolfendale (1971)
· · ·	Menon and Ramana Murthy (1967)		

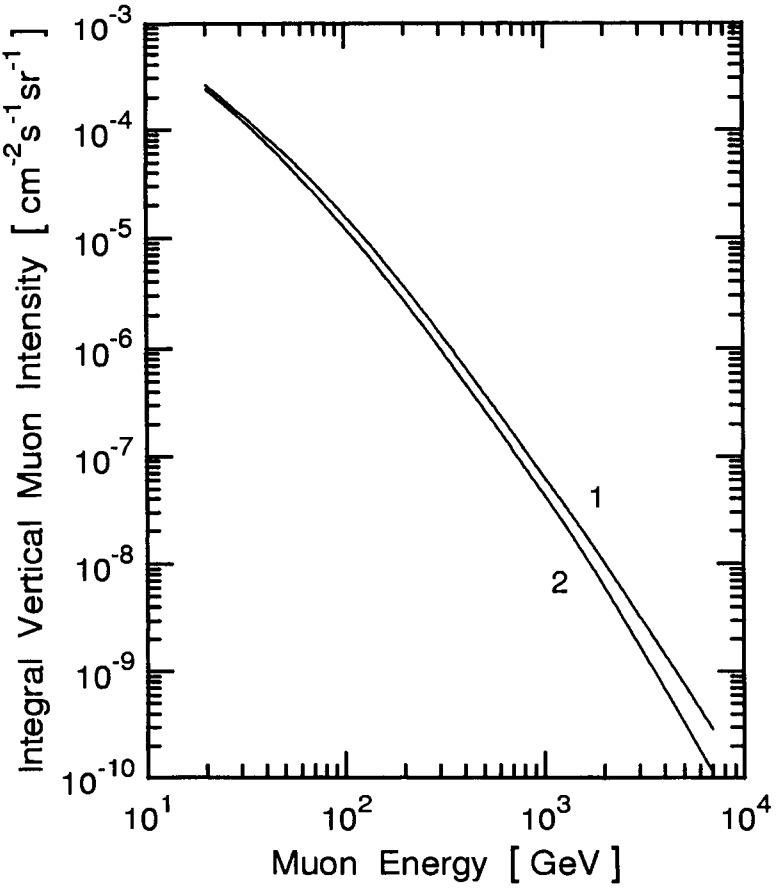

Figure 3.34: Composite vertical integral energy spectrum of muons at sea level assembled from magnetic spectrometer, depth-intensity, burst spectra and high altitude high energy γ-spectra measurements (Menon and Ramana Murthy, 1967). The two curves represent the spread of experimental data.

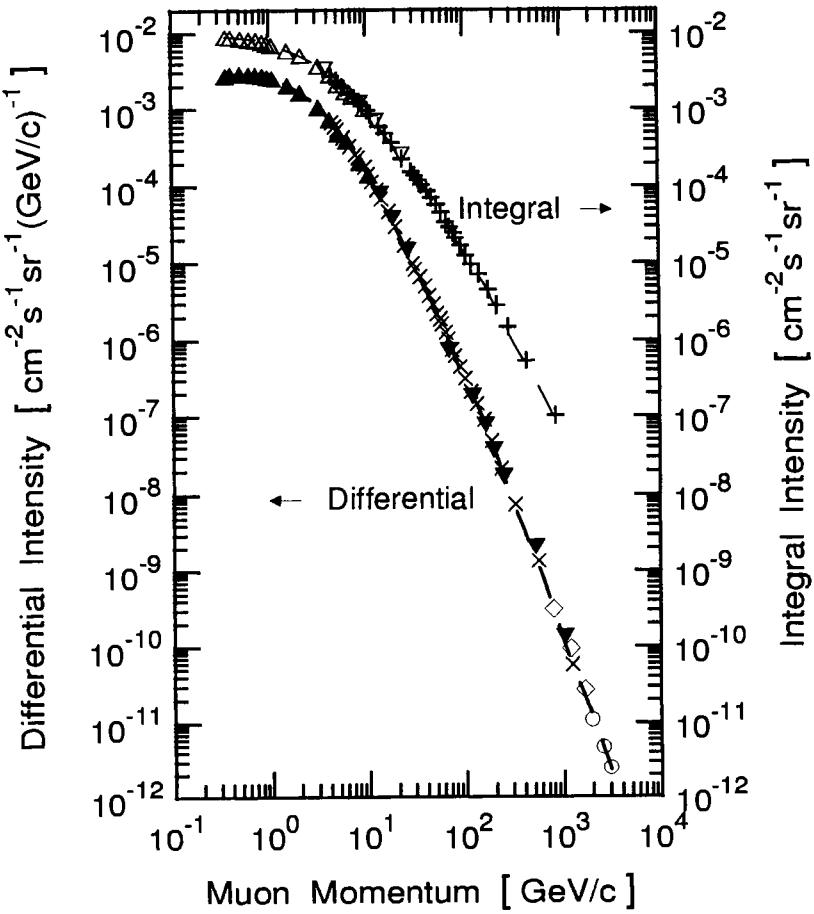

Figure 3.35: Differential and integral vertical muon momentum spectra determined from measurements at Nottingham (sea level) (Rastin, 1984). Also shown are a few high energy data points from the work of Komori (1977), Komori and Mitsui (1979) and Thompson et al. (1977b).

▼, ▽	Appleton et al. (1971)	▲, △	Barbouti and Rastin (1983)
×, +	Rastin (1984a)	o	Komori (1977) and Komori and Mitsui (1979)
◇	Thompson et al. (1977b)		
– –	best fit, Rastin (1984a)		

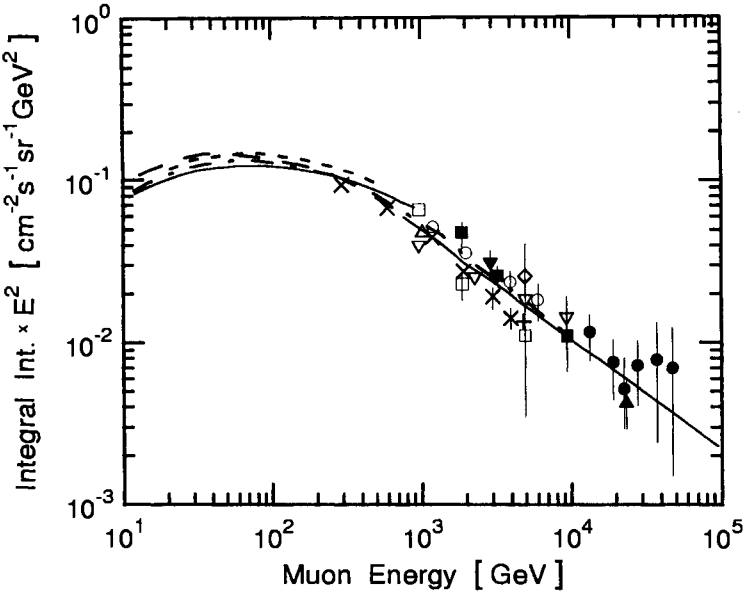

Figure 3.36: Vertical muon energy spectrum at sea level in the range $10 \leq p \leq 10^5$ GeV determined by direct measurements and through indirect methods (Carstensen, 1978, Allkofer et al 1978b, c, Allkofer 1979b).

γ-cascade data:	×	Osborne and Wolfendale (1964)
γ-burst data	o	Amineva et al. (1971)
	△	Krasilnikov et al. (1971)
	□	Mizutani et al. (1971)
	◇	Chin et al. (1970)
	+	Baradzei et al. (1971)
	▽	Krasilnikov et al. (1971)
underground data	•	Krishnaswamy et al. (1971)
	■	Miyake et al. (1964)
	▼	Achar et al. (1965)
	▲	Meyer et al. (1970)
calculations	– –	Allkofer et al. (1971a)
	——	Ng et al. (1974b)
	– · –	Wright (1974)
	- - -	Ayre et al. (1975)
	——	Carstensen (1978)

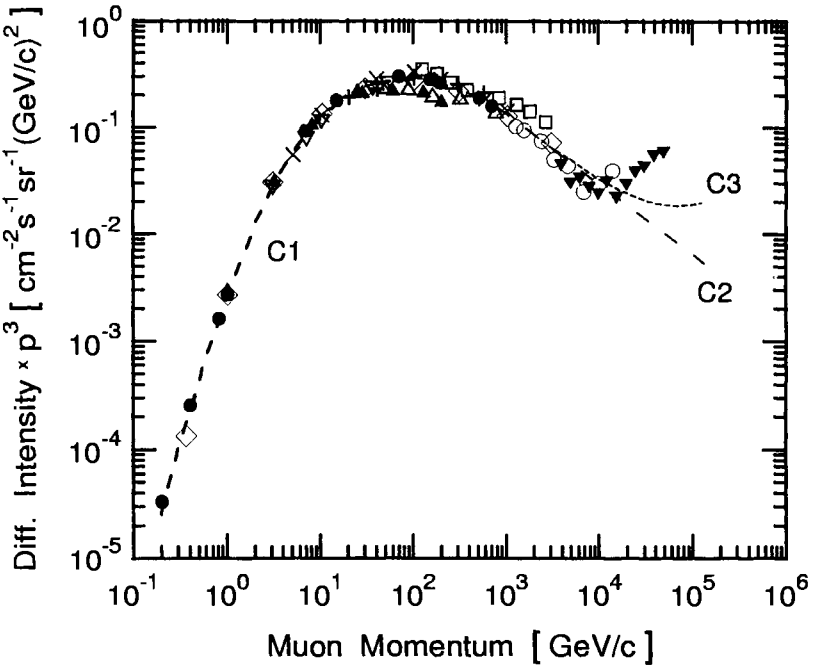

Figure 3.37: Compilation of vertical differential muon spectra at sea level in the momentum range $0.1 \leq p \leq 10^5$ GeV/c. The ordinate is multiplied by the momentum to the third power to compress the plot and emphasize the differences.

absolute measurements	▽	Bateman et al. (1971)
	•	Allkofer et al. (1971b)
	+	Ayre et al. (1975)
	◇	Rastin (1984a)
non-absolute measurements	×	Nandi and Sinha (1972b)
	□	Thompson (1977b)
	△	Bruscoli and Pieri (1993)
	▲	Wada et al. (1995)
indirect determinations	o	Khalchukov et al. (1985)
	▼	Zatsepin et al. (1991)
fit	C1	fit to experimental data by author
model calculations	C2	π-, K-decay only
	C3	π-, K-, charm decay, Volkova et al. (1987)

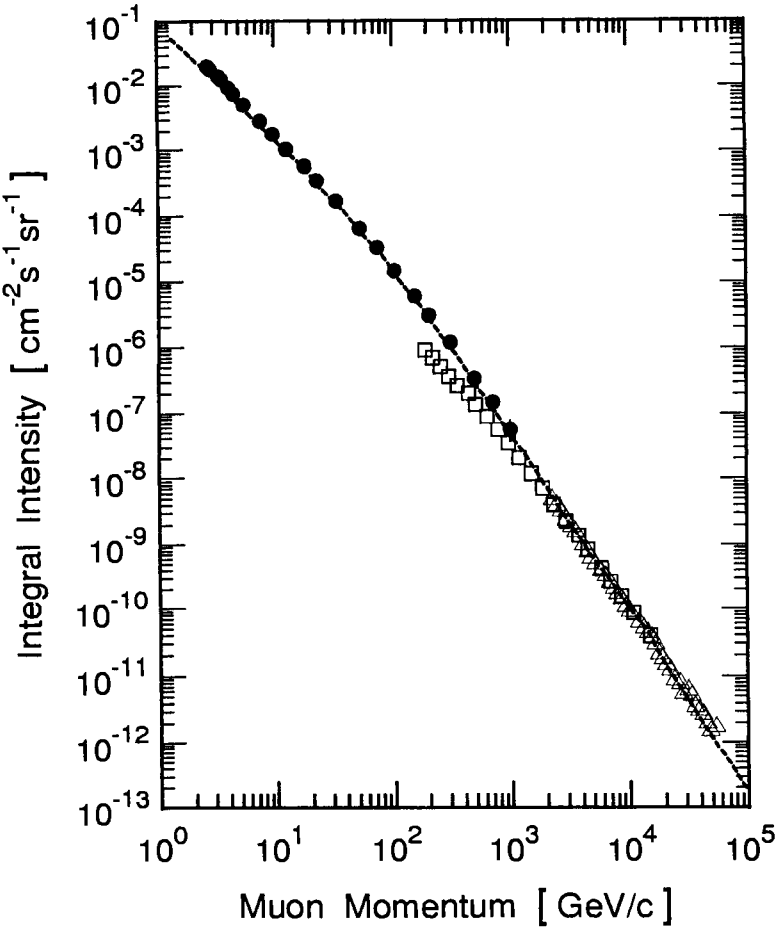

Figure 3.38: Combined vertical integral muon momentum spectrum at sea level in the range $1 \leq p \leq 10^5$ GeV/c. The data by Berger et al. are derived from the Fréjus underground experiment (for details see Rhode, 1993), those from Matsuno et al. (1984) from the MUTRON horizontal data. The spectrum of Gaisser (1990) is the result of a calculation.

• Allkofer et al. (1971b)	□ Matsuno et al. (1984)
△ Berger et al. (1989)	- - - Gaisser (1990), Theory

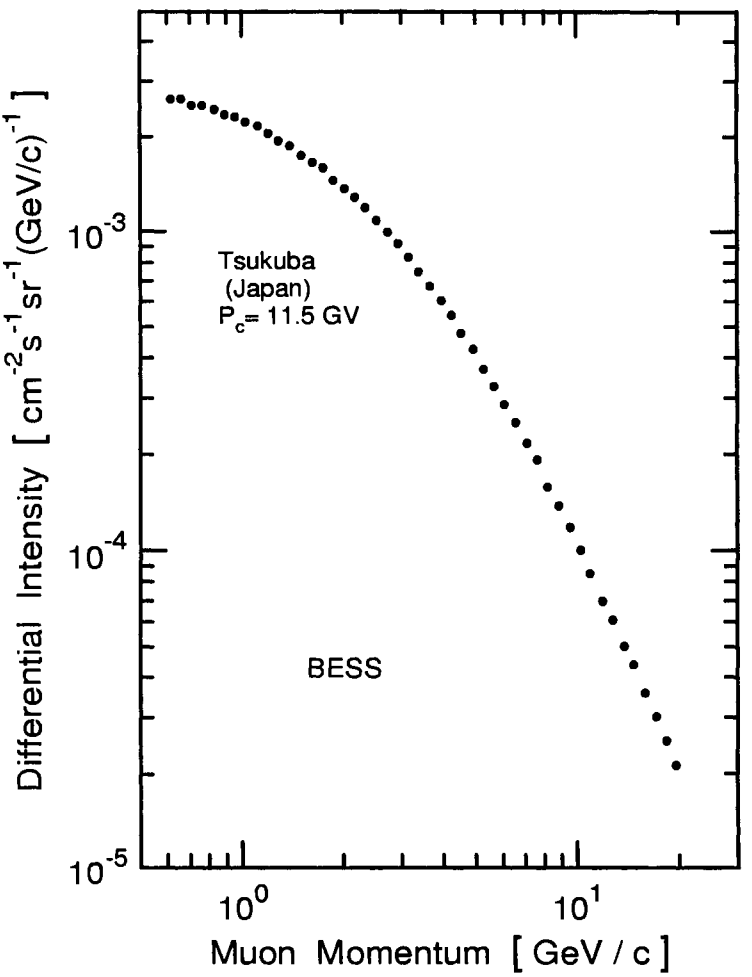

Figure 3.39: Precision measurement of the muon momentum spectrum carried out with the BESS instrument at Tsukuba (Japan), sea level, $P_c \simeq 11.5$ GV (BESS 95) (Nozaki, 2000). The same spectrum is shown in Fig. 3.71 together with the spectrum taken at Lynn Lake (Canada), 360 m a.s.l., $P_c \simeq 0.5$ GV, with the same instrument, to study differences due to geomagnetic effects.

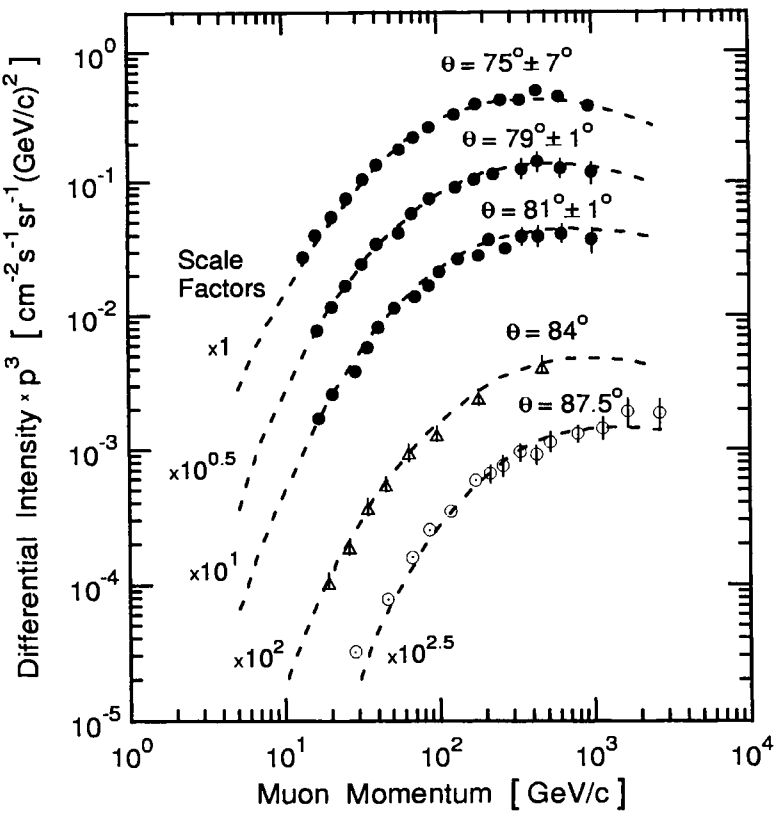

Figure 3.40: Differential momentum spectra of muons at sea level for different zenith angles near horizontal direction (Allkofer et al. 1977b). The ordinate is multiplied by the momentum to the third power to compress the spectra. In addition, the spectra had been divided by the scale factors, as indicated, to shift successive curves downward for better presentation. Thus, the reading at the ordinate for a given point on a curve must be multiplied by the appropriate scale factor to get the true intensity. Note that the data by Asatiani et al. (1975) were obtained at altitude 3250 m; they were added for completeness.

• Allkofer et al. (1977b)	△ Asatiani et al. (1975)
o Kitamura et al. (1975)	- - - Maeda (1973), calculation

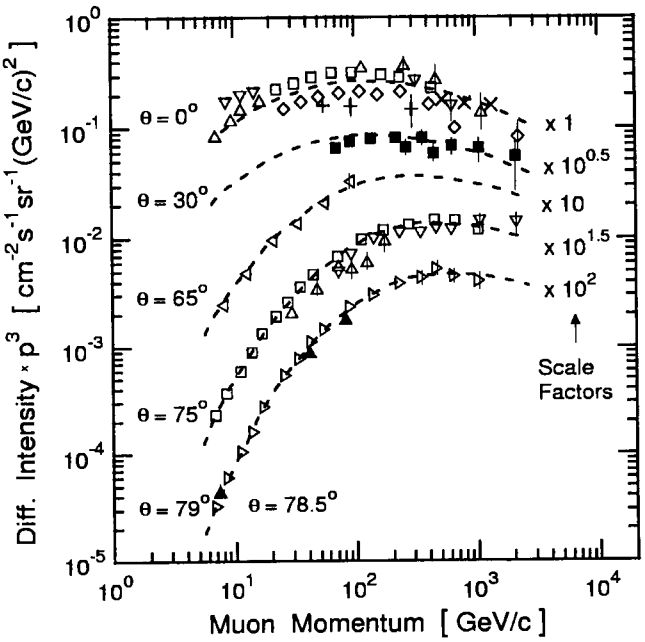

Figure 3.41: Differential momentum spectra of muons at sea level for different zenith angles, θ. The ordinate is multiplied by the momentum to the third power to compress the spectra. In addition, the spectra had been divided by the scale factors, as indicated, to shift the successive curves downward for better presentation. Thus, the reading at the ordinate for a given point on a curve must be multiplied by the appropriate scale factor to get the true intensity. (Carstensen 1978, Allkofer et al. 1978b, c, Allkofer 1979b).

Zenith Angle		
θ = 0°	▽	Allkofer et al. (1971a, b)
	△	Nandi and Sinha (1970, 1972b)
	+	Abdel-Monem et al. (1973)
	◇	Burnett et al. (1973a, b)
	□	Whalley (1974)
	×	Baxendale et al. (1975a, b)
θ = 30°	■	Leipuner et al. (1973)
θ = 65°	◁	Abdel-Monem et al. (1975)
θ = 75°	□	Carstensen (1978), Allkofer (1978b, c)
	△	Asbury et al. (1970)
	▽	Leipuner et al. (1973)
θ = 78.75°	▲	Ashton and Wolfendale (1963)
θ = 79°	▷	Carstensen (1978), Allkofer (1978b, c)
	- - -	Maeda, calculation (1973)

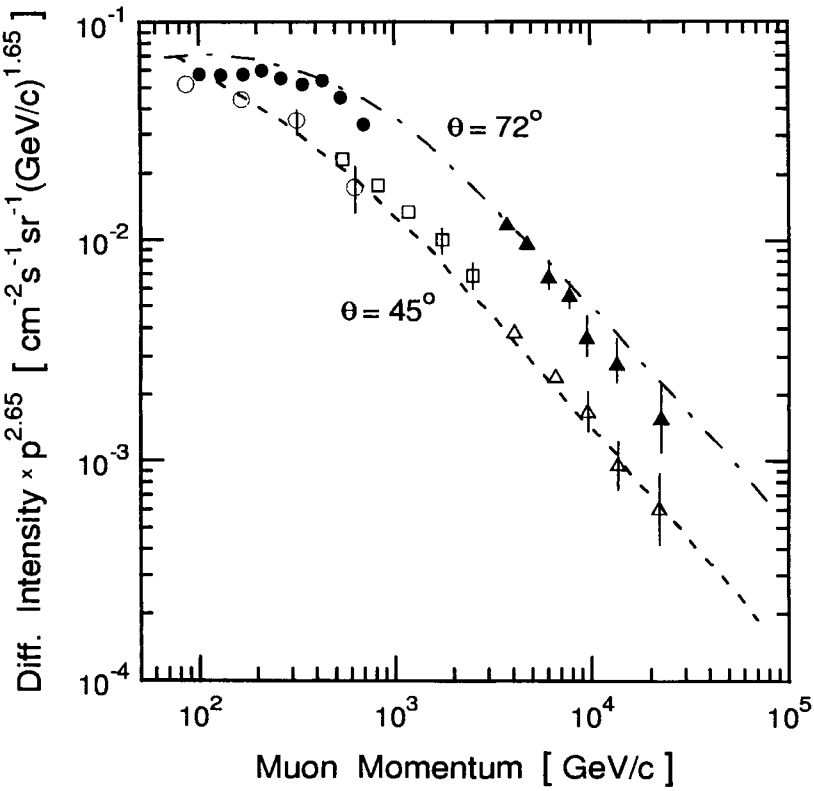

Figure 3.42: Differential muon momentum spectra at sea level for different zenith angles. The data by Ivanova et al. (1979) are from emulsion experiments. (Note that the intensities are multiplied by $p^{2.65}$.)

○	Allkofer et al. (1971a),	$\theta = 0°$
●	Allkofer et al. (1978b, c),	$\theta = 75°$
□	Thompson et al. (1977b),	$\theta = 0°$
▲	Ivanova et al. (1979),	$\theta = 72°$
△	Ivanova et al. (1979),	$\theta = 45°$
- - -	Volkova et al. (1977),	calculation

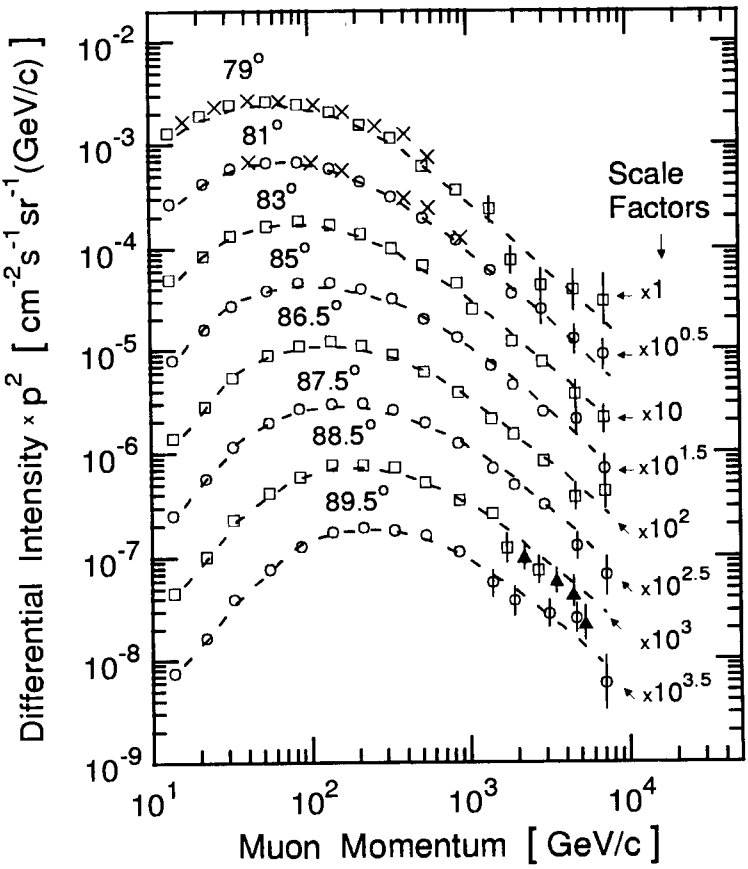

Figure 3.43: Differential muon spectra in the zenith angle range $78° - 90°$ at sea level (Allkofer et al. 1981). The ordinate is multiplied by the momentum squared. In addition, the spectra had been divided by the scale factors, as indicated, to shift successive curves downward for better presentation. Thus, the reading at the ordinate for a given point on a curve must be multiplied by the appropriate scale factor to get the true intensity. The statistical errors are less than 2% below 500 GeV/c and about 4% at 1000 GeV/c.

□, o DEIS 78° - 90°, Allkofer et al. (1979b, 1981)
× Kiel-DESY, Allkofer et al. (1977b)
▲ MUTRON, Muraki et al. (1979)
- - - model calculation, Maeda (1970, 1973)

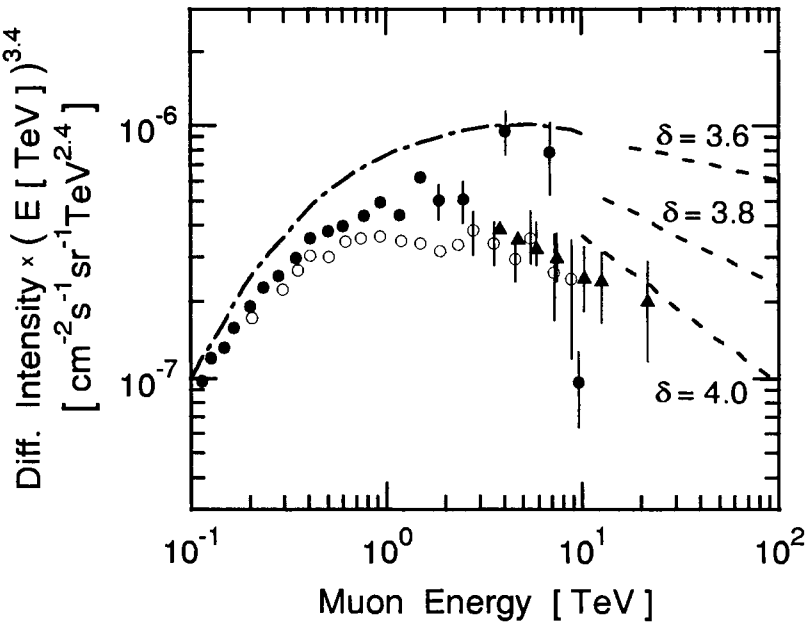

Figure 3.44: Comparison of near horizontal differential muon spectra at sea level (Allkofer 1979a). δ is the asymptotic exponent of the power law approximation, $j(E) \propto E^{-\delta}$, of the muon energy at production. (Note that the intensities are multiplied by $E^{3.4}$.)

- — · — model calc. 89°, Murakami et al. (1979)
- - - - fit, Allkofer et al. (1979a)
- • DEIS 88° - 89°, magnetic spectrometer, Allkofer et al. (1979b)
- o MUTRON 87° - 90°, magnetic spectrometer, Honda et al. (1979)
- ▲ Moscow 72°, X-ray film, Ivanova et al. (1979)

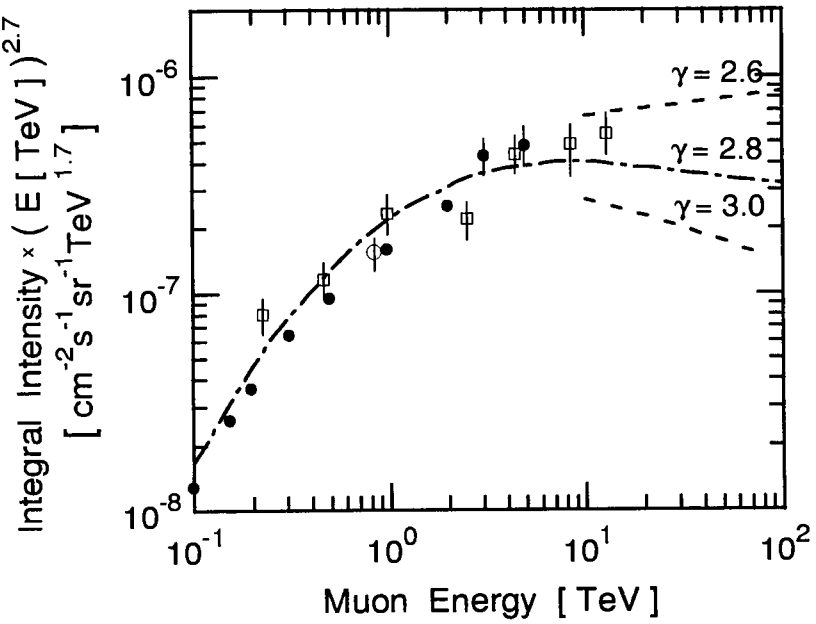

Figure 3.45: Comparison of near horizontal integral muon spectra at sea level (Allkofer 1979a). γ is the asymptotic exponent of the power law approximation, $J(> E) \propto E^{-\gamma}$, of the muon energy at sea level. (Note that the intensities are multiplied by $E^{2.7}$.)

– · – model calc. 89°, Murakami et al. (1979)
– – – fit, Allkofer et al. (1979a)
• DEIS 88° - 89°, magnetic spectrometer, Allkofer et al. (1979b)
o MUTRON 87° - 90°, magnetic spectrometer, Honda et al. (1979)
□ MUTRON 77°, pair meter, Nakamura et al. (1979)

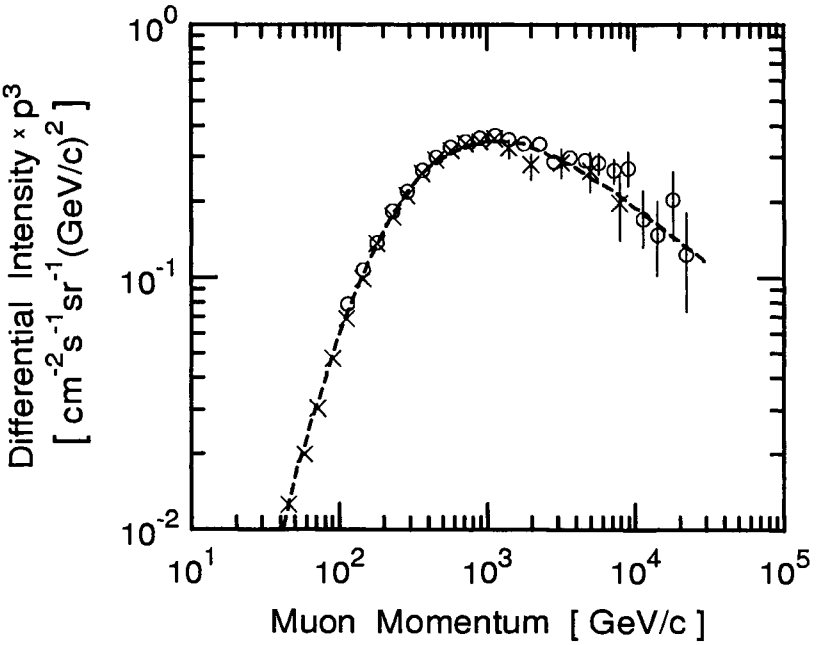

Figure 3.46: Comparison of the absolute differential muon momentum spectra obtained by the experiments DEIS and MUTRON at a zenith angle of 89°. The ordinate is multiplied by the momentum to the third power. All corrections are included (Matsuno et al., 1984).

×	DEIS	Allkofer et al. (1981)	- - - fit by author
o	MUTRON	Matsuno et al. (1984)	

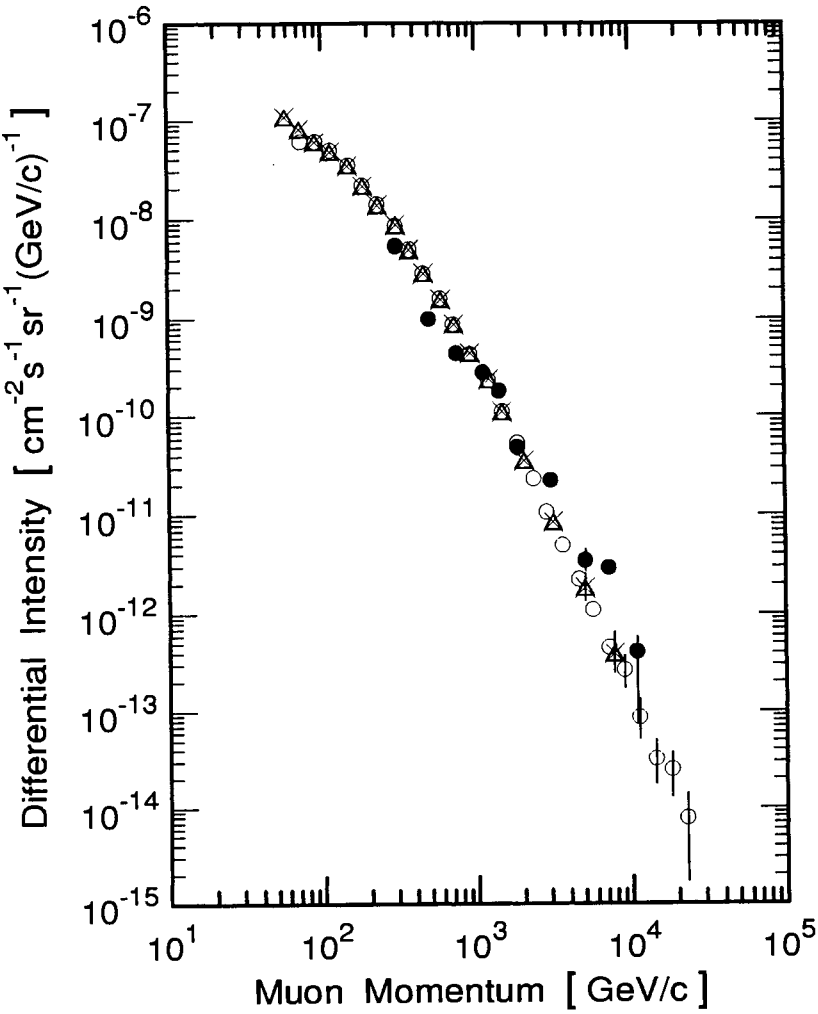

Figure 3.47: Comparison of the MUTRON and DEIS differential muon momentum spectra for the zenith angle range $87° \leq \theta \leq 90°$ at sea level (Kitamura 1981 and Allkofer et al. 1977b, respectively). Also shown is the more recent Karlsruhe spectrum for $85° \leq \theta \leq 90°$ (Gettert et al. 1993).

× DEIS, | ○ MUTRON | • Karlsruhe

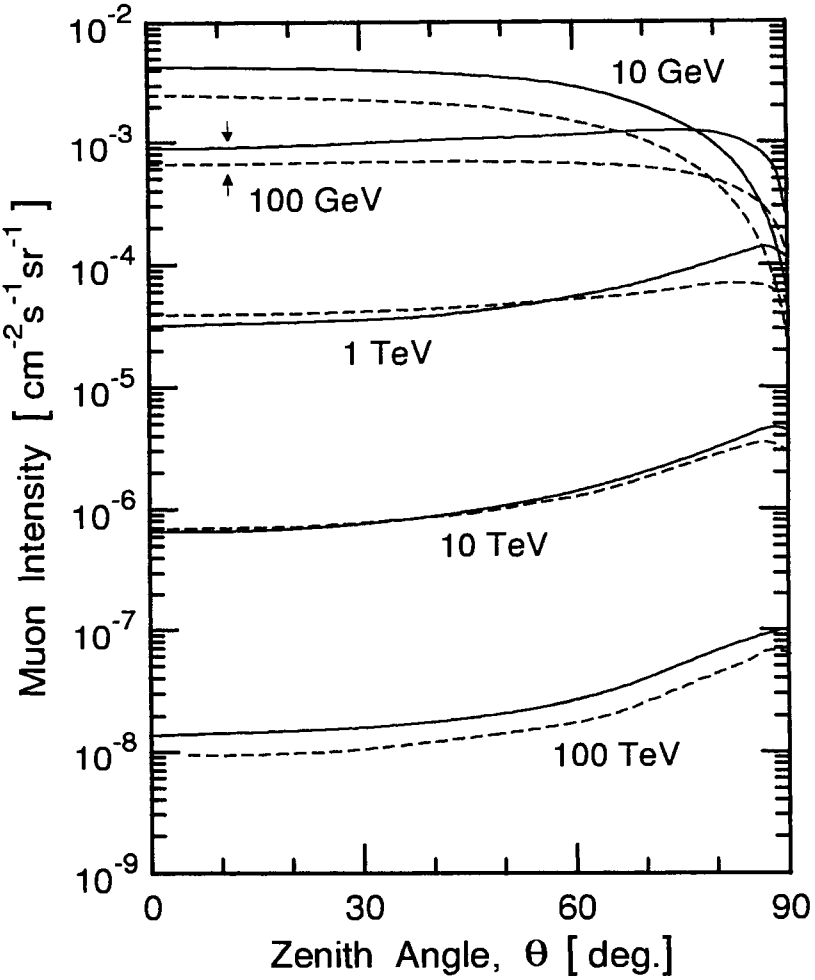

Figure 3.48: Zenith angle dependence of the integral intensity of muons originating from pion (solid curves) and kaon (dashed curves) decays for different threshold energies at sea level obtained from a calculation using a diffusion equation (Maeda, 1970 and 1973). The same production spectra are used in either case. The zenith angular muon enhancement with increasing energy is evident. The same general trend is also observed at Mt. Chacaltaya altitude (5260 m a.s.l.). For details see text.

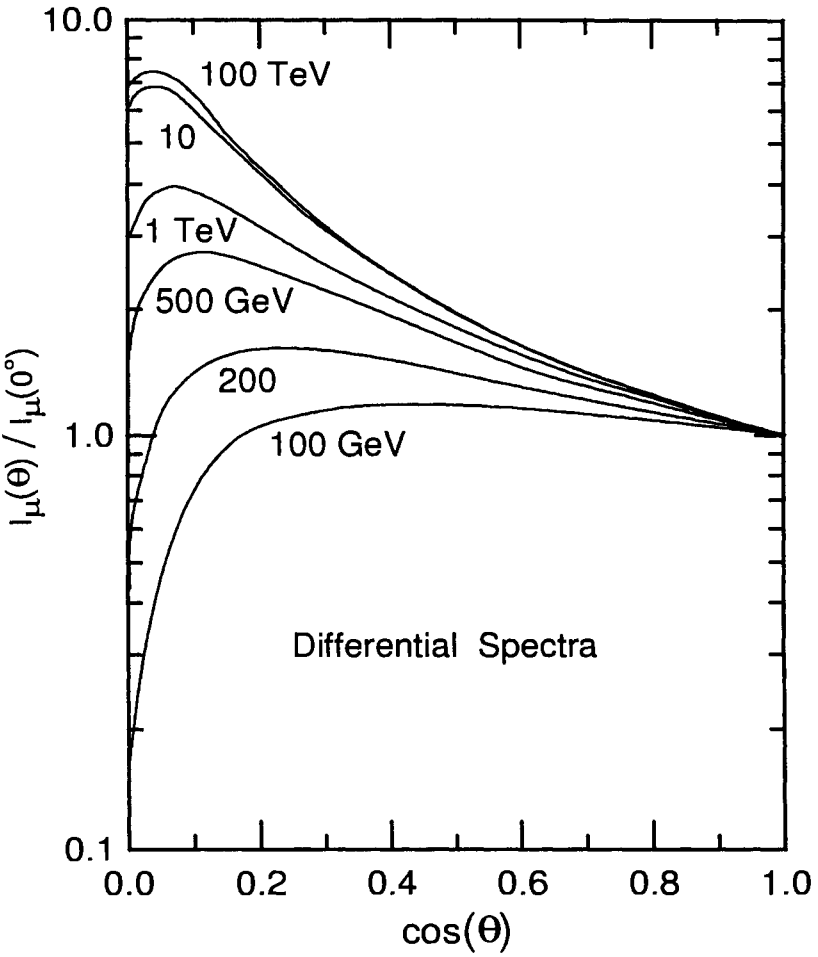

Figure 3.49: Relative differential intensities of atmospheric muons at sea level resulting from pion decay only as a function of $\cos(\theta)$, θ being the zenith angle. The calculation is based on a relatively simple diffusion equation using identical attenuation mean free paths for nucleons and pions in the atmosphere of 120 $g\,cm^{-2}$ (Maeda, 1970, 1973). More realistic assumptions do not change the basic features of the plot.

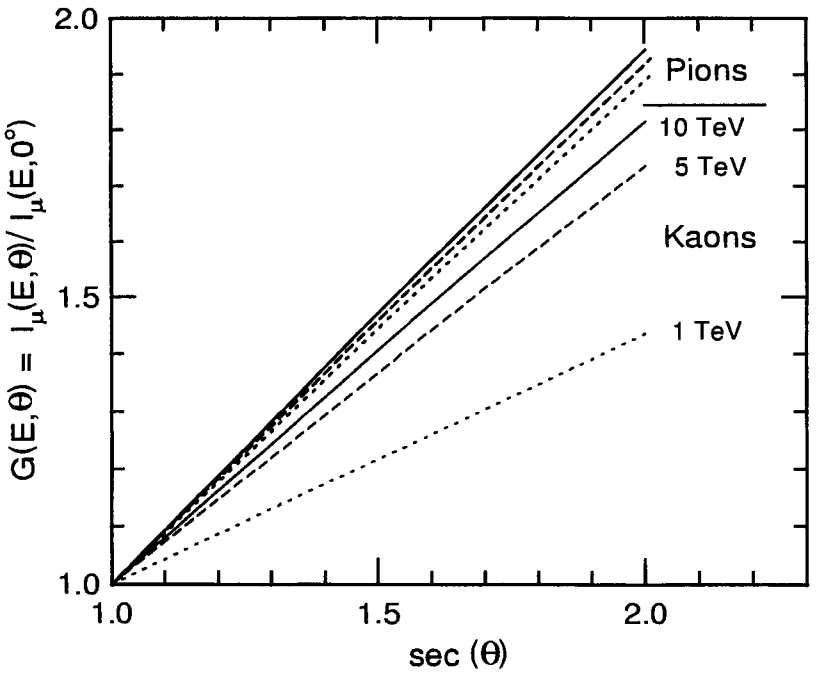

Figure 3.50: Enhancement factor, $G(E,\theta)$, as a function of $\sec(\theta)$ in the zenith angular range $0° \leq \theta \leq 60°$ at an atmospheric depth of $X = 700$ g cm^{-2} for muons of energies 1 TeV (dotted lines), 5 TeV (dashed lines), and 10 TeV (solid lines) from pion and kaon decays, respectively, as indicated (Bergamasco et al., 1983).

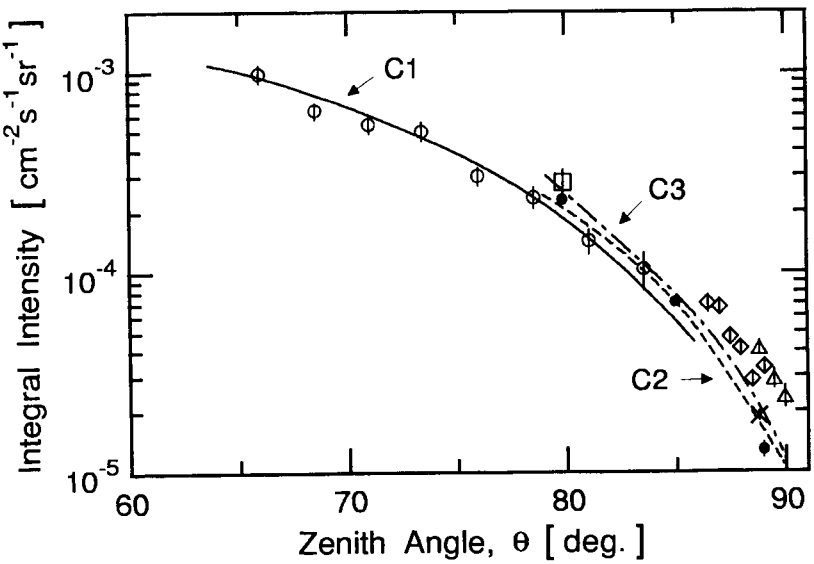

Figure 3.51: Variation of absolute integral intensity of muons with zenith angle, θ, at sea level illustrated in a semi-log plot. Curve C1 is a fit to the data of Allen and Apostolakis (1961) for momenta $1 \leq p \leq 100$ GeV/c. Curves C2 and C3 are from an early calculation of Ashton et al. (1966) for muons from pion and kaon decays using production ratios of $K/\pi = 0.0$ and $K/\pi = 0.4$, respectively.

△ Jakeman (1956)	◇ Wilson (1959)
○ Allen and Apostolakis (1961)	× Hicks et al. (1971)
□ Crookes and Rastin (1972)	• Karmakar et al. (1973)

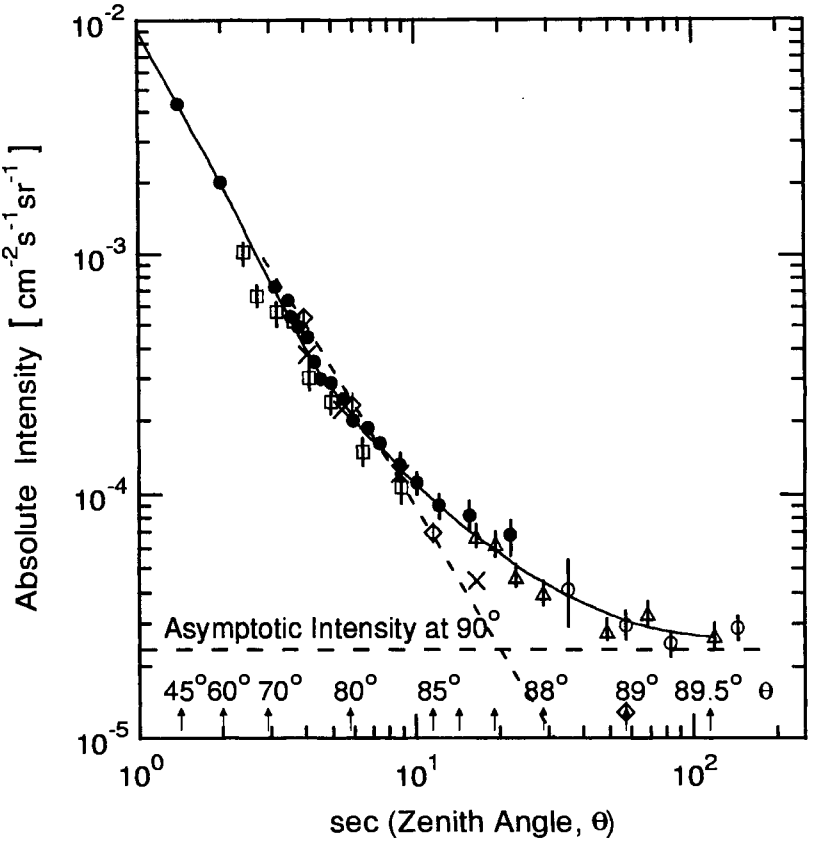

Figure 3.52: Variation of the absolute integral muon intensity versus secant zenith angle, θ, for different conditions near sea level. For additional data see Table 3.21. • Crookes and Rastin (1972) for muons penetrating 10.3 cm of Pb (total absorber thickness including roof was 184.7 g cm^{-2}), corresponding to a muon momentum > 0.35 GeV/c. □ Allen and Apostolakis (1961), × Gettert et al. (1993), both sets of data apply to muons with momenta $\geq$1 GeV/c. ○ Jakeman (1956) used 19 cm of Pb requiring muon momenta $>\sim$ 0.4 GeV/c, and △ Wilson (1959) 42 cm of Pb corresponding to muon momenta ($>\sim$ 1 GeV/c). ◇ Karmakar et al. (1973) had minimum muon energies between 0.35 and 2.7 GeV/c, recorded at low geomagnetic latitude. The solid curve is a best fit by Crookes and Rastin (1972), the dashed straight line a least-square fit to the data of Karmakar.

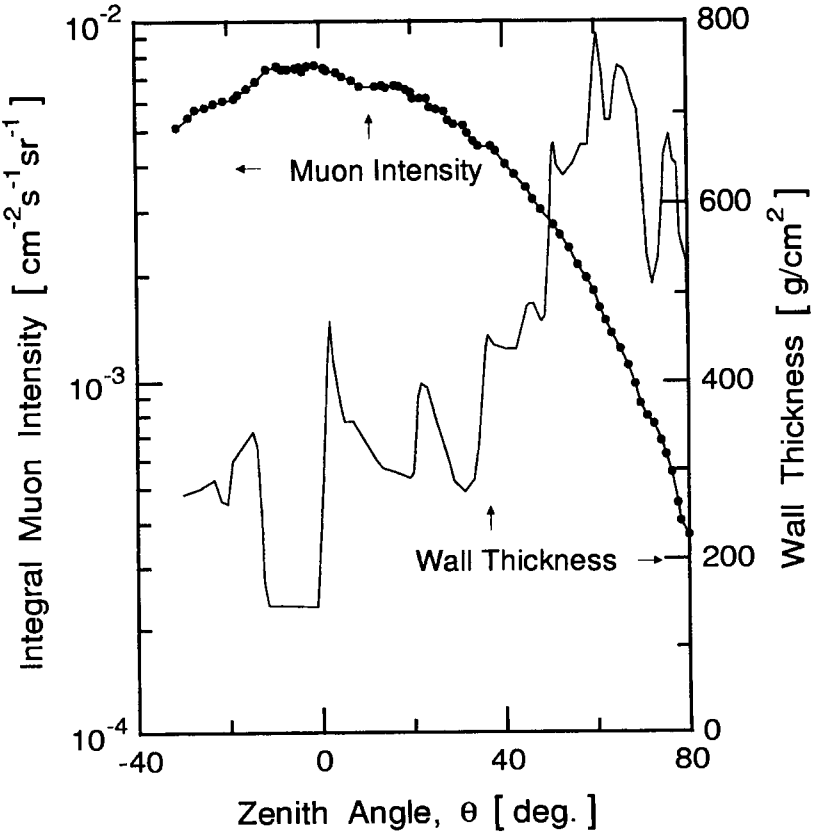

Figure 3.53: Zenith angle dependence of the integral muon intensity above 1 GeV/c at sea level, recorded at Okayama, Japan ($\approx$ 134° E, $\approx$ 34.7° N, 3.3 m a.s.l.) (Tsuji et al. 1995). The irregularities are mostly due to the roof and wall profile, also indicated.

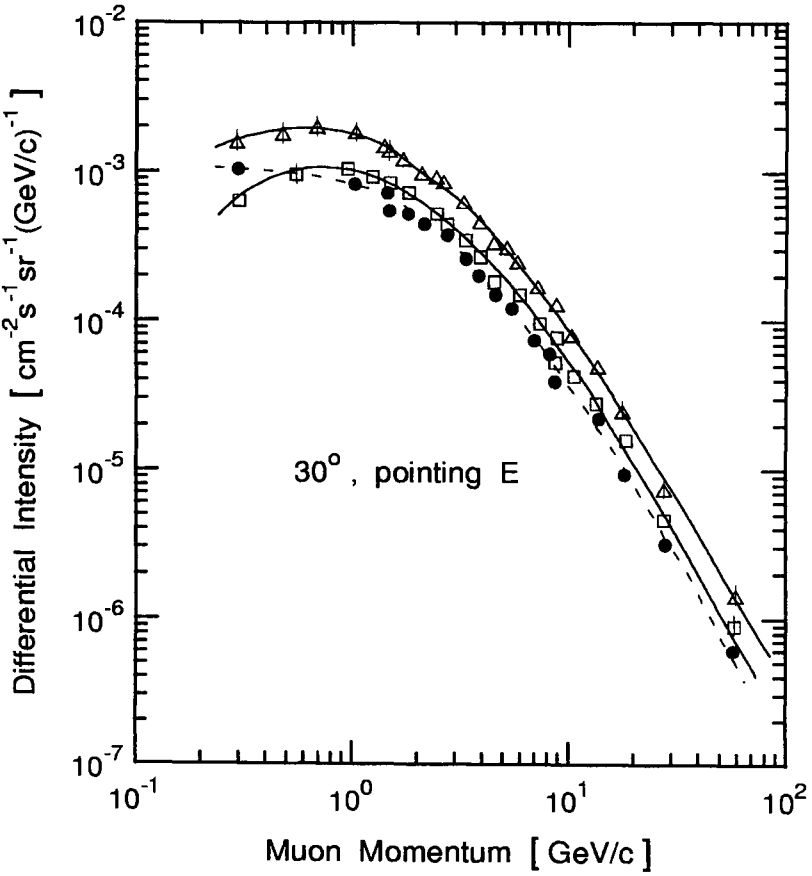

Figure 3.54: Differential momentum spectra of positive, negative and all muons at sea level (Melbourne, Australia), for a zenith angle of 30°, pointing east (Moroney and Parry 1954).

△ all muons, □ positive muons, • negative muons

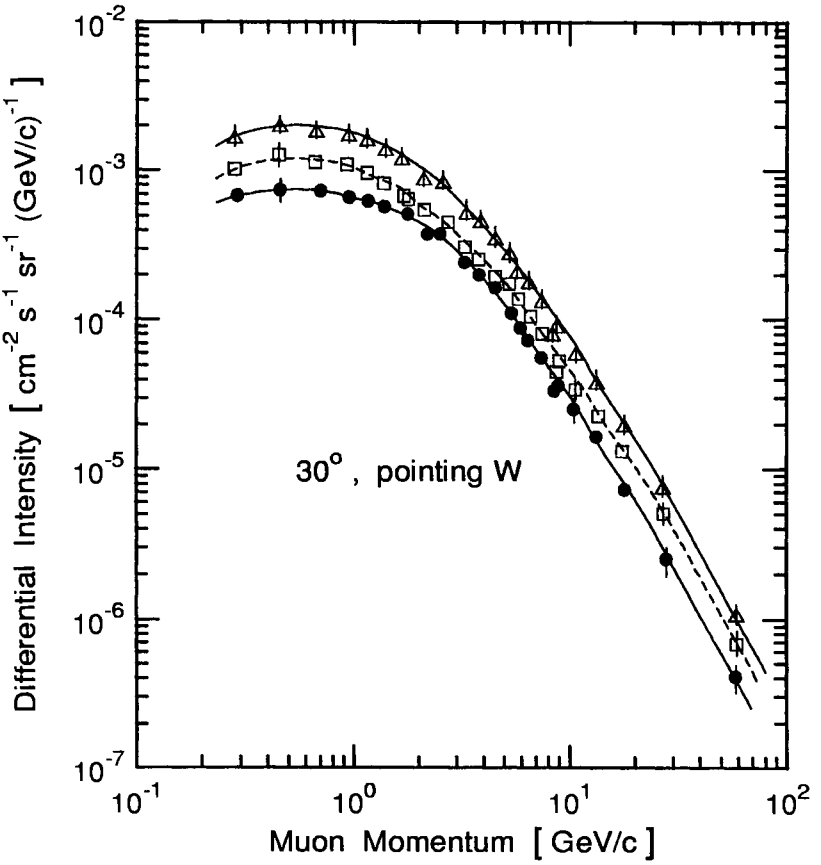

Figure 3.55: Differential momentum spectra of positive, negative and all muons at sea level (Melbourne, Australia), for a zenith angle of 30°, pointing west (Moroney and Parry 1954).

△ all muons, □ positive muons, • negative muons

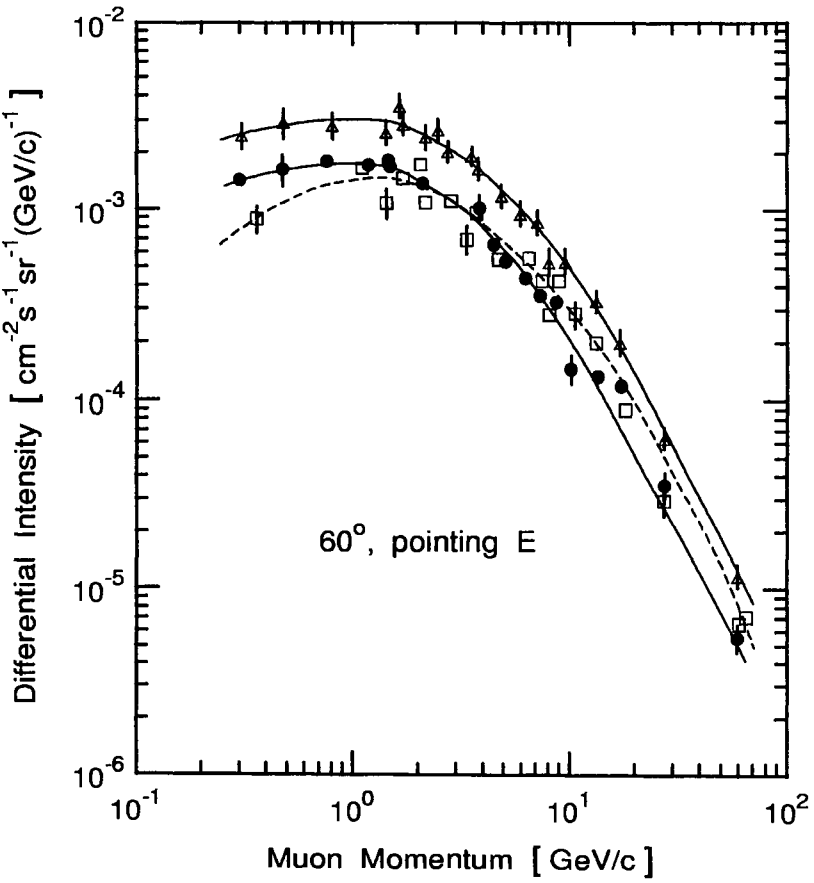

Figure 3.56: Differential momentum spectra of positive, negative and all muons at sea level (Melbourne, Australia), for a zenith angle of 60°, pointing east (Moroney and Parry 1954).

△ all muons, □ positive muons, • negative muons

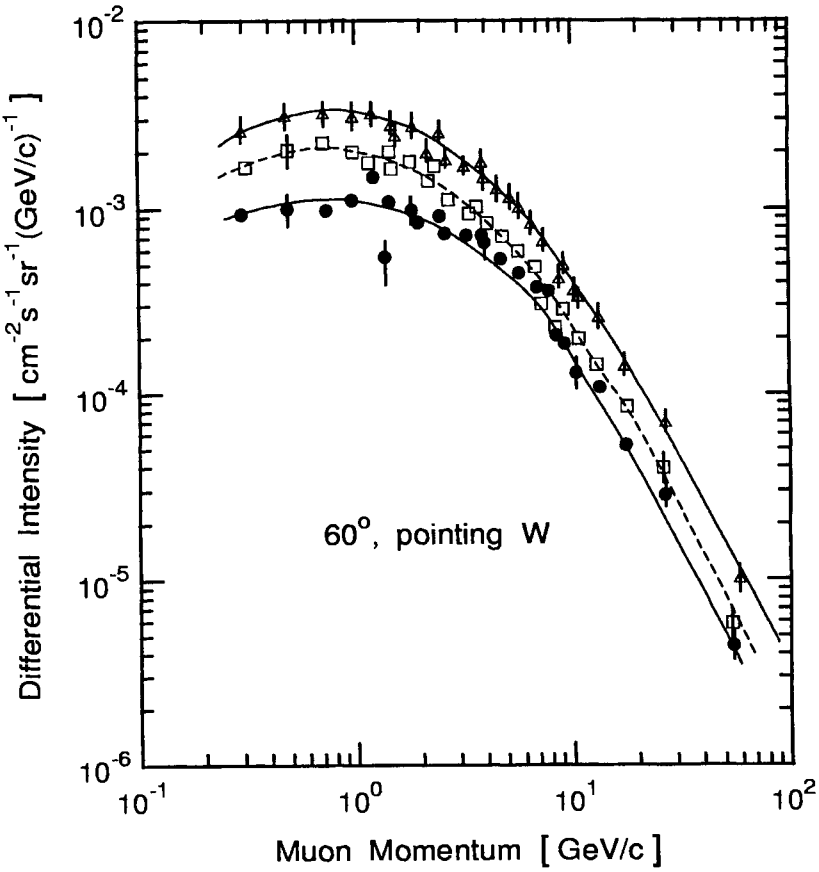

Figure 3.57: Differential momentum spectra of positive, negative and all muons at sea level (Melbourne, Australia), for a zenith angle of 60°, pointing west (Moroney and Parry 1954).

△ all muons, □ positive muons, • negative muons

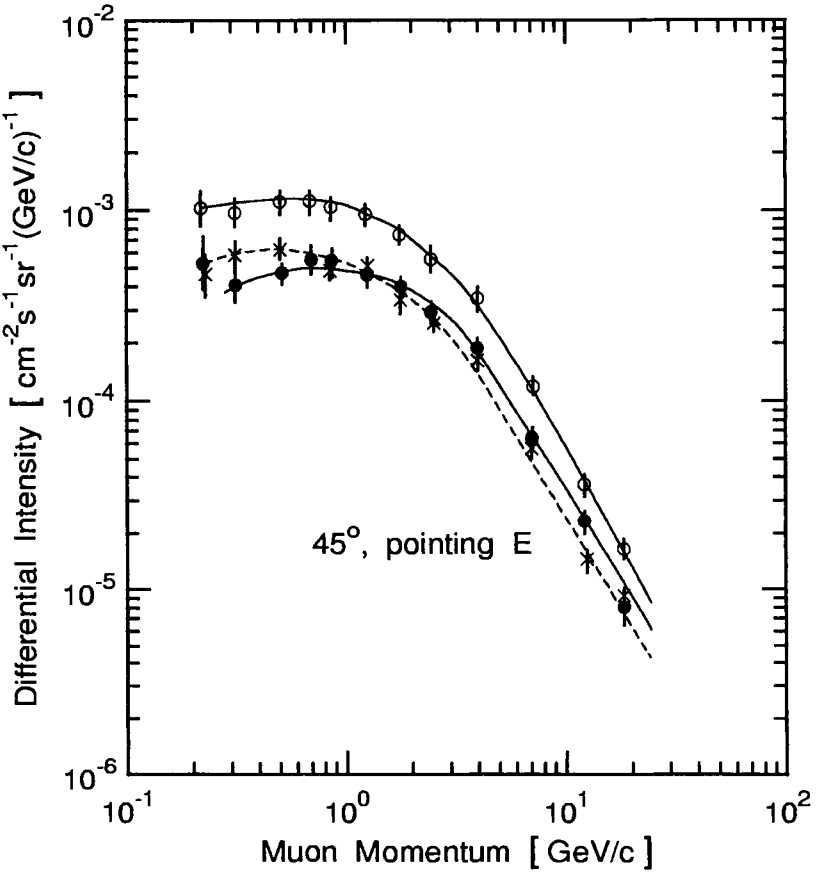

Figure 3.58: Differential momentum spectra of positive, negative and all muons at sea level, for a zenith angle of 45°, pointing east, recorded at Kiel (geographic latitude 54° N) (Allkofer and Andresen 1967).

○ all muons, ● positive muons, × negative muons

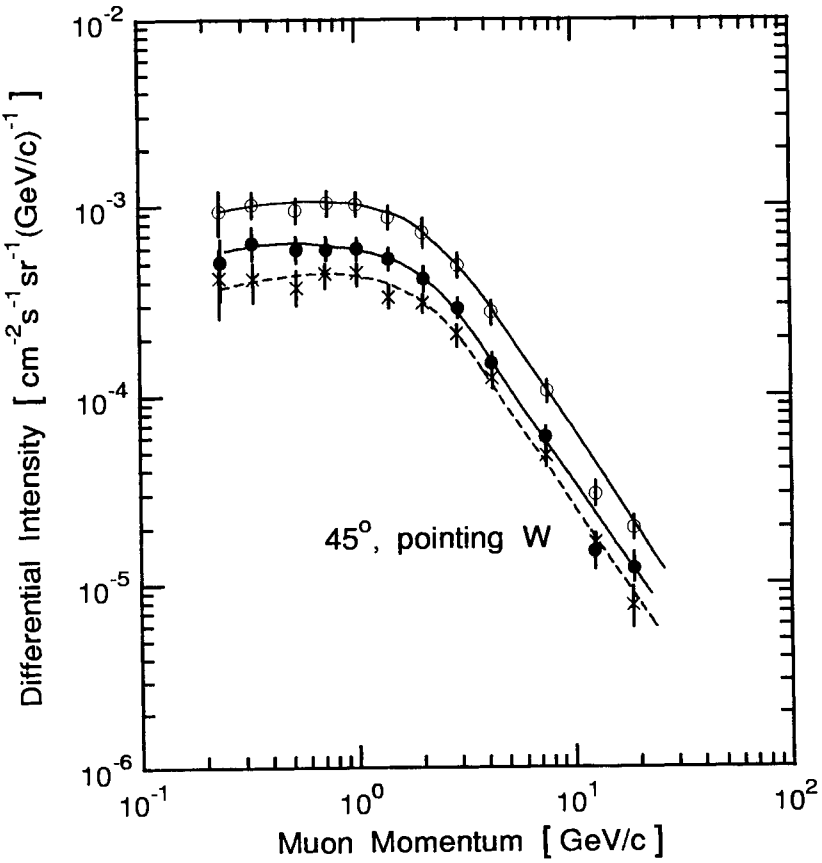

Figure 3.59: Differential momentum spectra of positive, negative and all muons at sea level, for a zenith angle of 45°, pointing west, recorded at Kiel (geographic latitude 54° N) (Allkofer and Andresen 1967).

o all muons, • positive muons, × negative muons

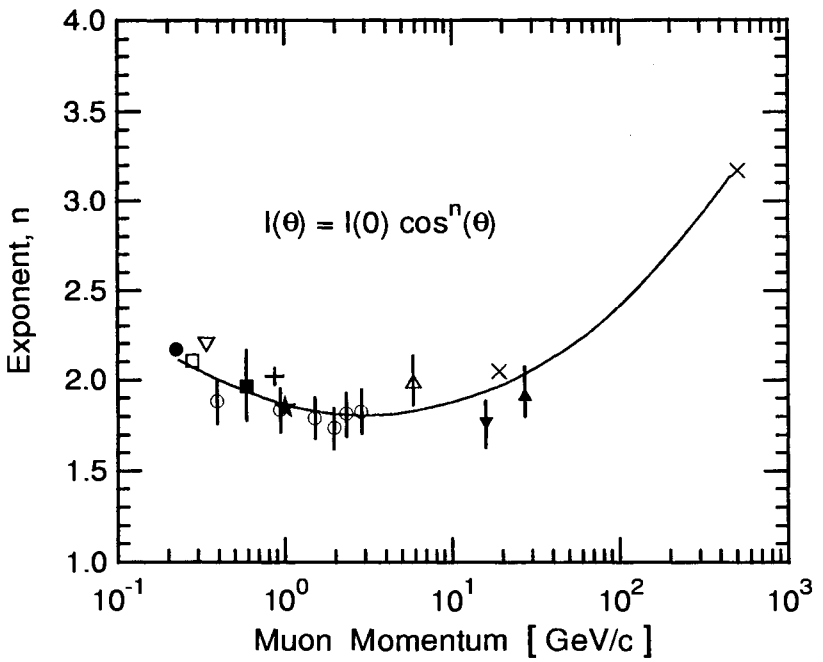

Figure 3.60: Momentum dependence of the exponent, n, of the zenith angular distribution of muons, $I(\theta, > p) = I(0°, \geq p)\cos^n(\theta)$ at sea level (Bhattacharyya, 1974b).

▽ Crookes and Rastin (1972)	□ Greisen (1942)
△ Crookes and Rastin (1973)	• Judge and Nash (1965)
■ Ghosh and Sengupta (1967)	× Narasimham (1967)
▲ Sreekantan et al. (1956)	▼ Stockel (1969)
o Bhattacharyya (1974b)	+ Wentz et al. (1995)

★ World mean, Bhattacharyya (1974b)

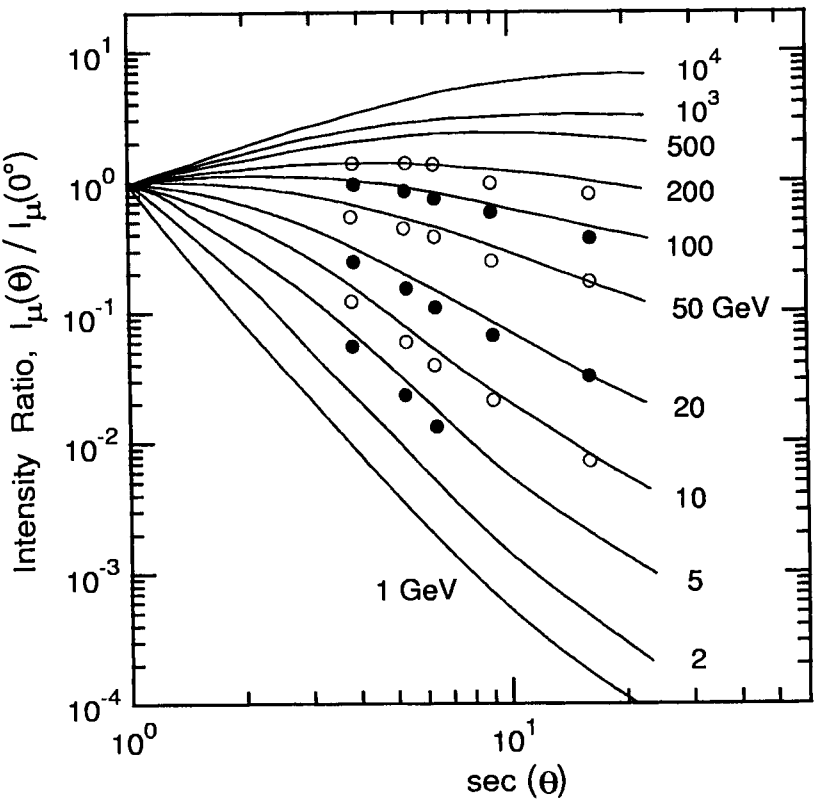

Figure 3.61: Ratio of the intensity of muons at zenith angle $\theta > 0°$ to the vertical intensity at $\theta = 0°$ as a function of sec(θ) for different energies. The solid lines are predictions from calculations by Stepens (1979a), the full and open circles are data from experiments carried out at Kiel, Germany (Allkofer et al., 1971c).

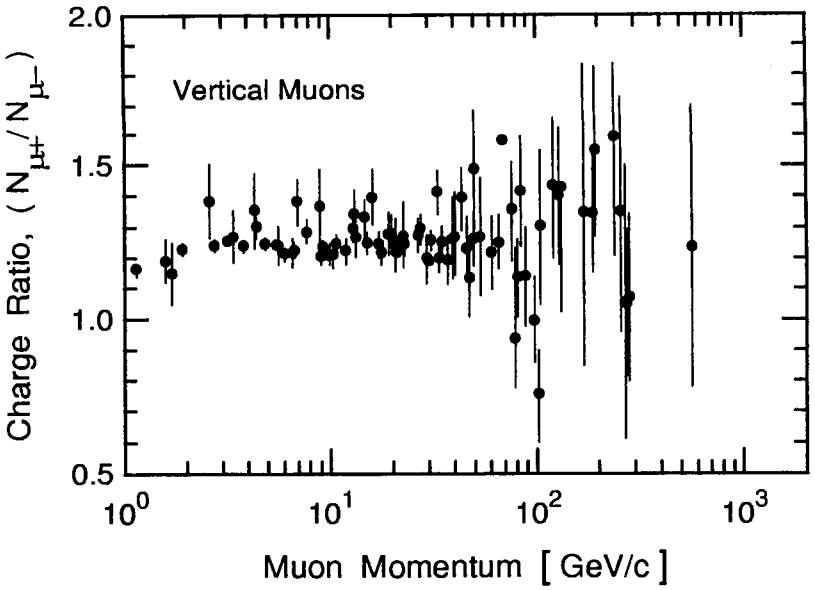

Figure 3.62: Compilation of early muon charge ratios as a function of momentum for vertical direction at sea level. The different contributors are listed below but not separately identified in the figure (Thompson 1973, extended by the author). (Note that some of the data were not actually recorded at sea level but apply to sea level as well.)

Alexander (1970)
Allkofer et al. (1971a)
Ashley (1972)
Aurela et al. (1966)
Filosofo et al. (1954)
Fujii et al. (1969)
Holmes et al. (1961)
Kasha et al. (1968)
MacKeown et al. (1965)
Nandi and Sinha (1972a)
Palmer and Nash (1967)
Allkofer et al. (1970c)
Appleton et al. (1971)
Ashton and Wolfendale (1963)
Ayre et al. (1971c)
Flint and Nash (1971a, b)
Hayman and Wolfendale (1962)
Kamiya et al. (1971)
Kawaguchi et al. (1965)
Moroney and Parry (1954)
Owen and Wilson (1955)
Pine et al. (1959)

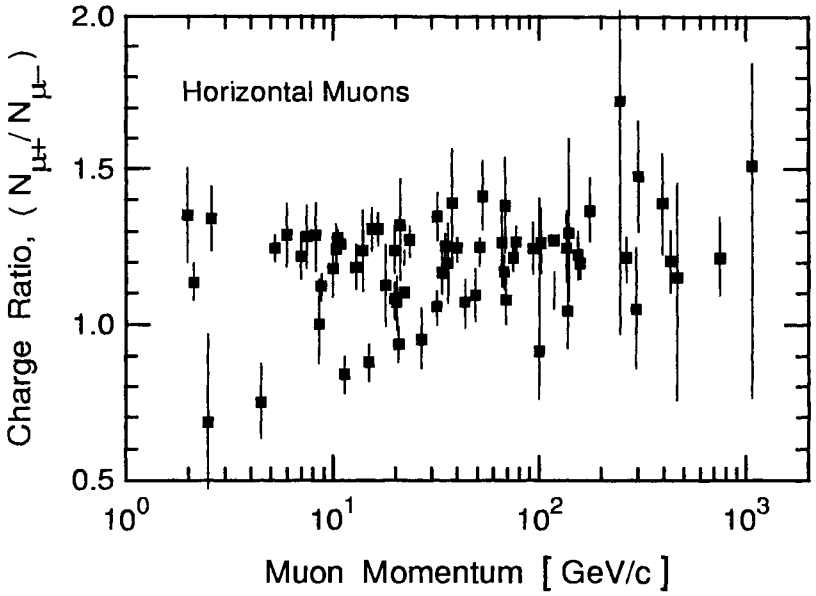

Figure 3.63: Compilation of early muon charge ratios as a function of momentum for horizontal direction at sea level. The different contributors are listed in the caption of Fig. 3.62 but not separately identified (Thompson 1973, extended by the author). (Note that some of the data were not actually recorded at sea level but apply to sea level as well.)

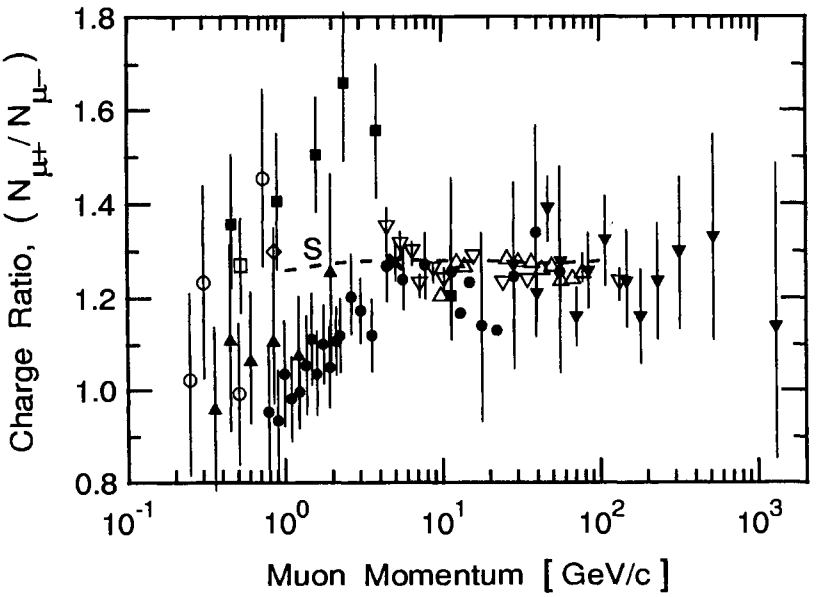

Figure 3.64: Compilation of muon charge ratio data versus momentum for vertical direction at sea level. The dashed curve S is a prediction.

■ Allkofer and Dau (1972)	△ Ayre et al. (1973b)
▲ Jain (1980)	▽ Rastin (1984b)
▼ Rastin (1984b)	o Singhal (1983)
□ Brancus et al. (1999)	◇ Vulpescu et al. (1998)
• Stephens and Golden (1987)	× Grandegger (1993)
S Stephens (1979b)	

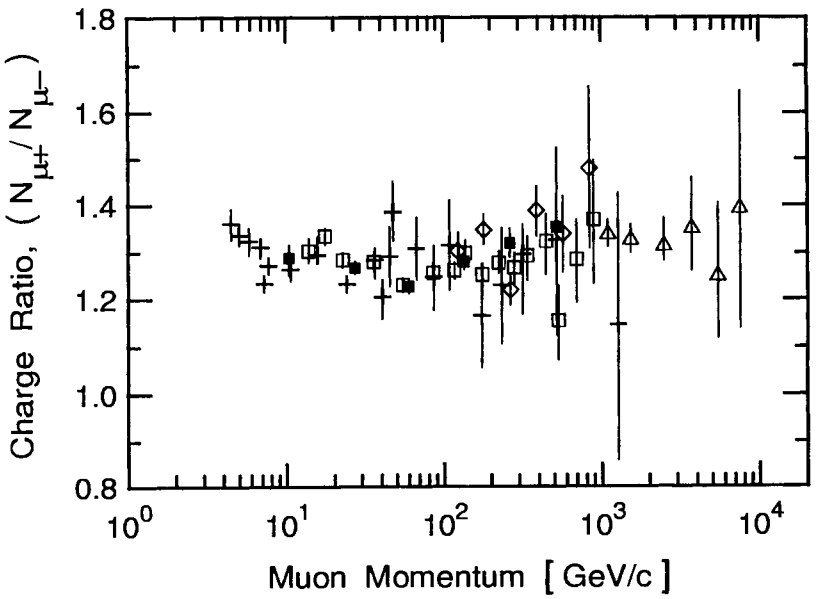

Figure 3.65: Compilation of muon charge ratio data versus momentum for vertical direction. With the exception of the data by Ashley et al. (1975), that are from the Utah underground experiment located at an altitude of about 1500 m, the data apply to sea level. The latter represent essentially the situation at sea level and were added to extend the scope to higher momenta.

■ Allkofer et al. (1978a)	△ Ashley et al. (1975)
□ Burnett et al. (1973a, b)	+ Rastin (1984b)
◇ Thompson et al. (1977b)	

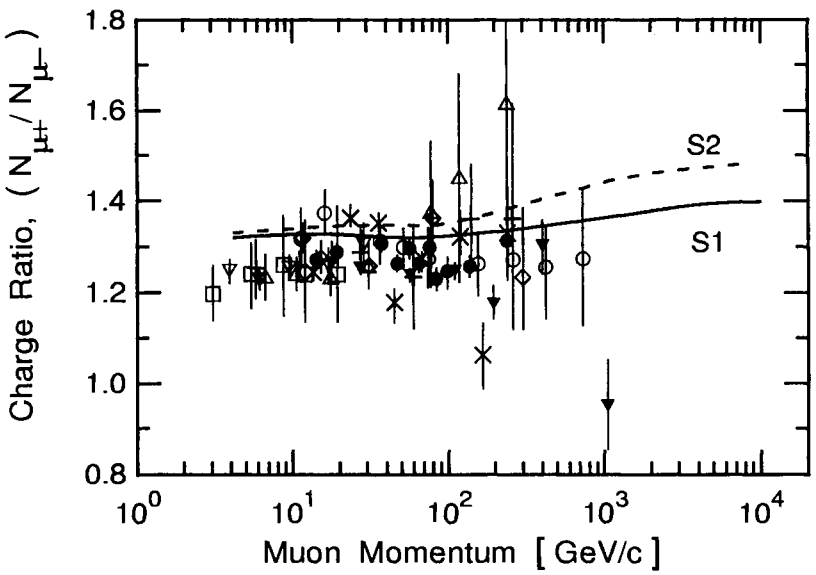

Figure 3.66: Compilation of muon charge ratio data versus momentum for vertical incidence. With the exception of the data by Ashley et al. (1975), that are from the Utah underground experiment, the data apply to sea level. Curves S1 and S1 are predictions for different pion and kaon production models.

□	Abdel-Monem et al. (1973)	◇	Allkofer et al. (1971b)
•	Baxendale et al. (1975a, b)	▽	Appleton et al. (1971)
▼	Flint and Nash (1971a, b)	○	Kamiya et al. (1971)
+	Nandi and Sinha (1972a)	×	Tebb et al. (1971)
△	Hayman and Wolfendale (1962)	S1, S2	Stephens (1979b), Theory

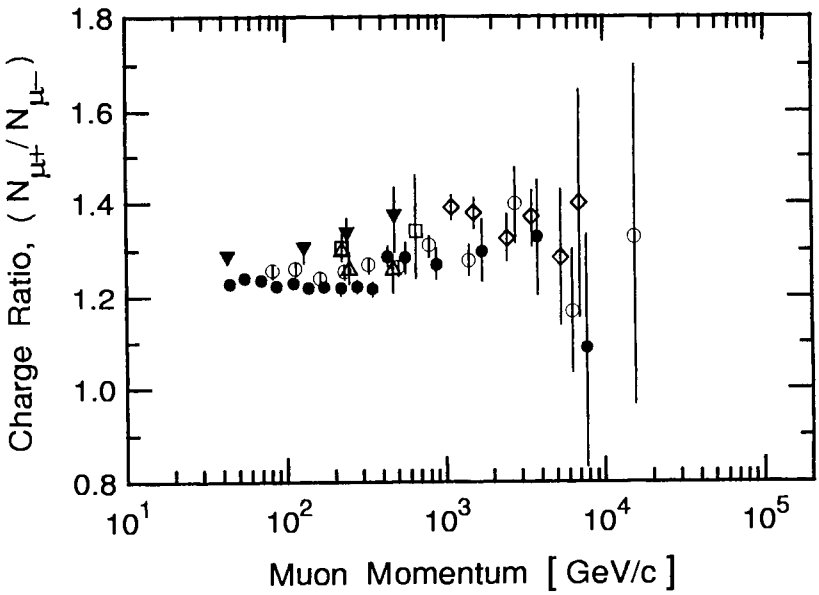

Figure 3.67: Compilation of charge ratio data of high momentum muons at sea level. The Utah underground data from higher altitude are also included.

- ▼ Kiel-DESY 75° ± 7°, Allkofer et al. (1977b)
- □ World survey 0°, Allkofer et al. (1978a, b, c, 1979c)
- △ World survey 70° - 90°, Allkofer et al. (1978a, 1979c, d)
- • DEIS 78° - 90°, Allkofer et al. (1981)
- ○ MUTRON 89°, Matsuno et al. (1984), see also MUTRON 89°, Kawashima et al. (1981), Kitamura (1981)
- ◇ Utah 40° - 80°, Ashley et al. (1971, 1975a, b)

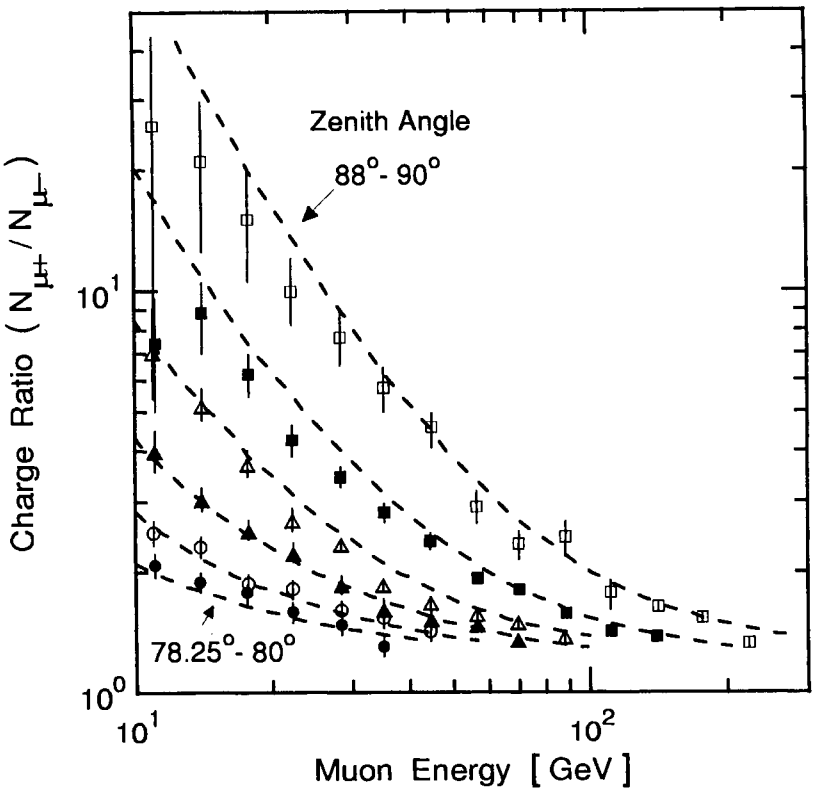

Figure 3.68: The effect of the geomagnetic field on the muon charge ratio at large zenith angles, θ, in the east - west direction in the energy window between 10 and 200 GeV. The experimental data are from the DEIS magnetic spectrometer at Tel-Aviv (latitude 32.1°, longitude 34.2°). The curves are predictions from model calculations for a geomagnetic field of 0.42 Gauss. The asymptotic value for the charge ratio was assumed to be 1.25 (Allkofer et al., 1979c).

●	$78.25° \leq \theta \leq 80°$	○	$80° \leq \theta \leq 82°$
▲	$82° \leq \theta \leq 84°$	△	$84° \leq \theta \leq 86°$
■	$86° \leq \theta \leq 88°$	□	$88° \leq \theta \leq 90°$

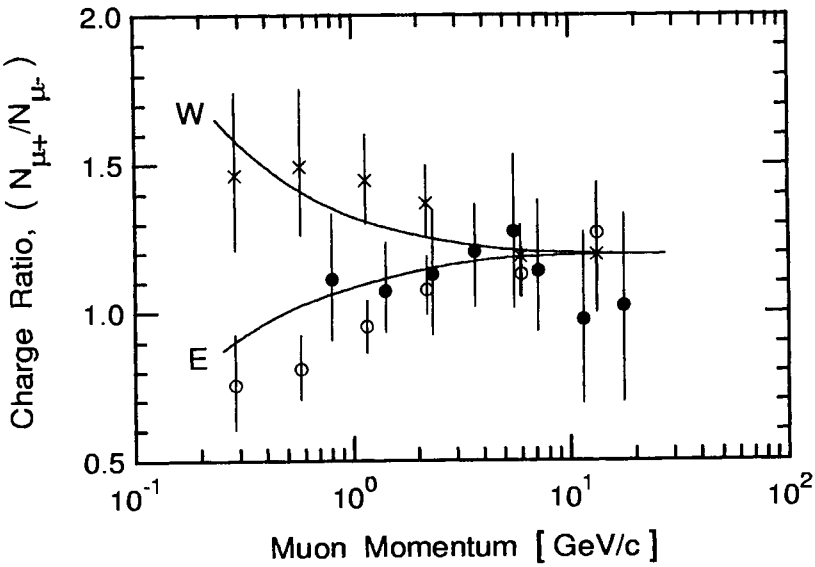

Figure 3.69: Charge ratio of low energy muons in the east - west geomagnetic plane at a zenith angle of 45° pointing east and west, respectively, at sea level (Allkofer and Andresen 1967).

o	east, Allkofer and Andresen (1967)	$P_c = 2.4$ GV
×	west, Allkofer and Andresen (1967)	$P_c = 2.4$ GV
•	east, Judge and Nash (1965)	$P_c = 2.5$ GV

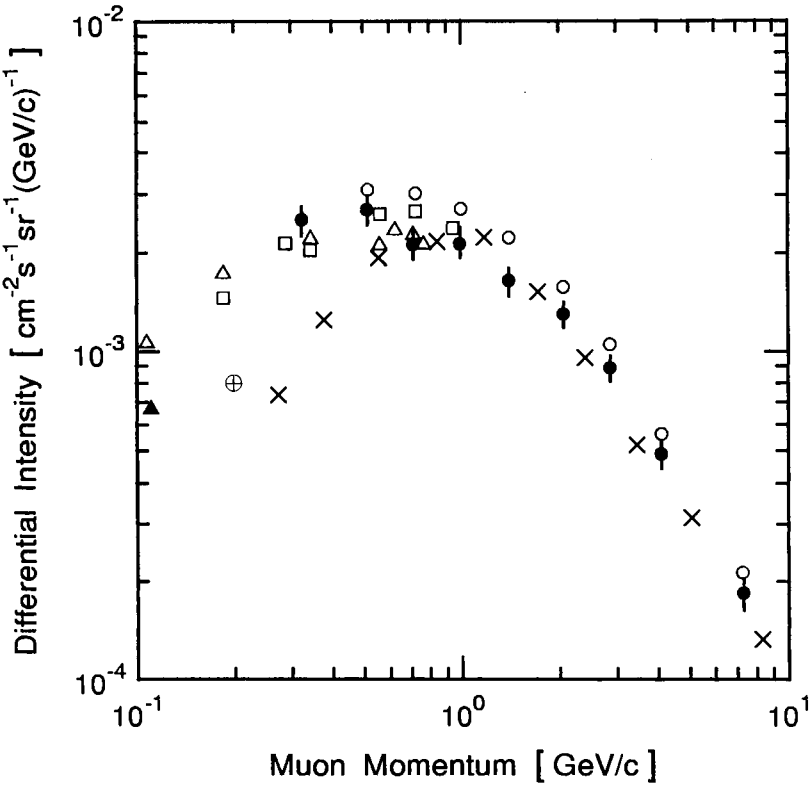

Figure 3.70: Differential momentum spectra of muons at sea level for various latitudes and cutoff energies, E_c (Allkofer et al. 1968, 1972).

△	del Rosario and Davila-Aponte (1952)	$\lambda = 29°$ N	$E_c = 8.8$ GeV
×	Fukui et al. (1955)	$\lambda = 24°$ N	$E_c = 11.6$ GeV
▲	Kaneko et al. (1955)	$\lambda = 24°$ N	$E_c = 11.6$ GeV
□	Fukui et al. (1957)	$\lambda = 24°$ N	$E_c = 11.6$ GeV
⊕	Subramanian et al. (1958)	$\lambda = 11°$ N	$E_c = 17.4$ GeV
○	Hayman and Wolfendale (1962)	$\lambda = 57.5°$ N	$E_c = 1.8$ GeV
●	Allkofer et al. (1968)	$\lambda = 9°$ N	$E_c = 14.1$ GeV

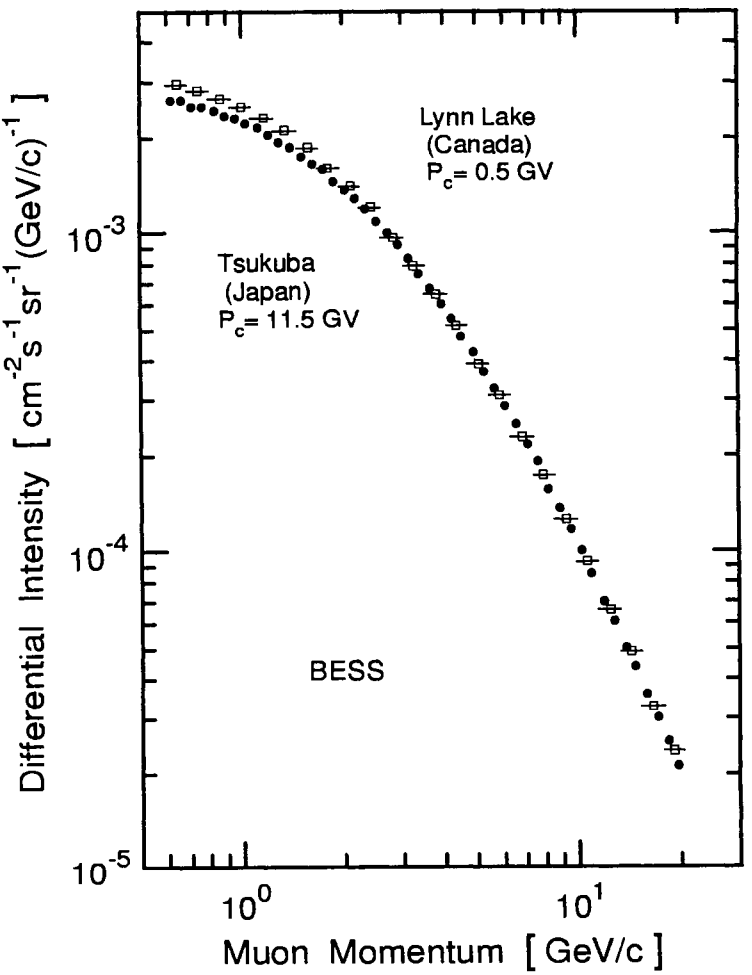

Figure 3.71: Precision measurements of the muon momentum spectra carried out with the BESS instrument at Lynn Lake (Canada), □, altitude 360 m a.s.l., $P_c \simeq 0.5$ GV (BESS 97 - 99) and at Tsukuba (Japan), •, sea level, $P_c \simeq 11.5$ GV (BESS 95) (Nozaki, 2000).

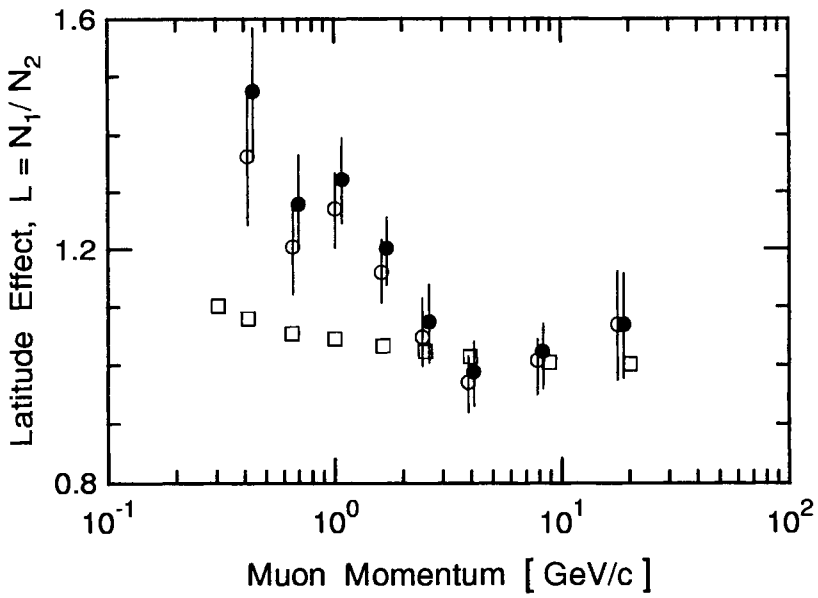

Figure 3.72: Experimentally determined latitude effect of the vertical differential muon flux. The contributions from the geomagnetic and atmospheric latitude effects that add up to the total latitude effect are individually resolved. N_1 denotes the muon flux at Kiel with vertical cutoff rigidity P_c = 2.3 GV, N_2 is the flux at the equator with P_c = 14 GV (Allkofer et al. 1972).

• total effect | o geomagnetic effect | □ atmospheric effect

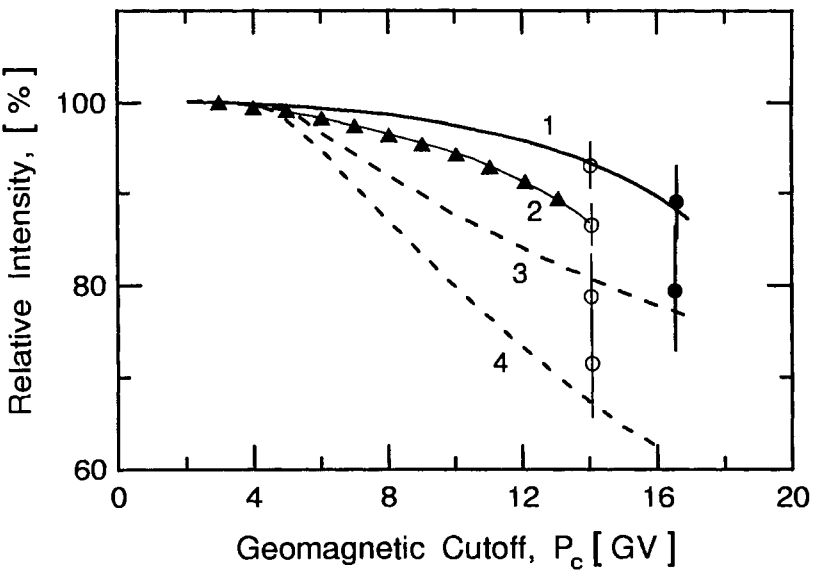

Figure 3.73: Latitude effect of the muon flux. Shown are relative integral and differential muon intensities at sea level as a function of the geomagnetic cutoff rigidity P_c for two different muon threshold momenta and at two muon momenta.

1	$p > 1.2$ GeV/c	2	$p > 0.3$ GeV/c
3	$p = 1.2$ GeV/c	4	$p = 0.5$ GeV/c
- - -	Diff. intensities	___	Integral intensities

o Magnet spectrograph, Atlantic, diff., integral (Allkofer et al., 1972)

• Range spectrograph, Calcutta, integral (Allkofer et al., 1970e, De et al., 1972a)

▲ Muon monitor, Leningrad to equator, integral (Dorman et al., 1970)

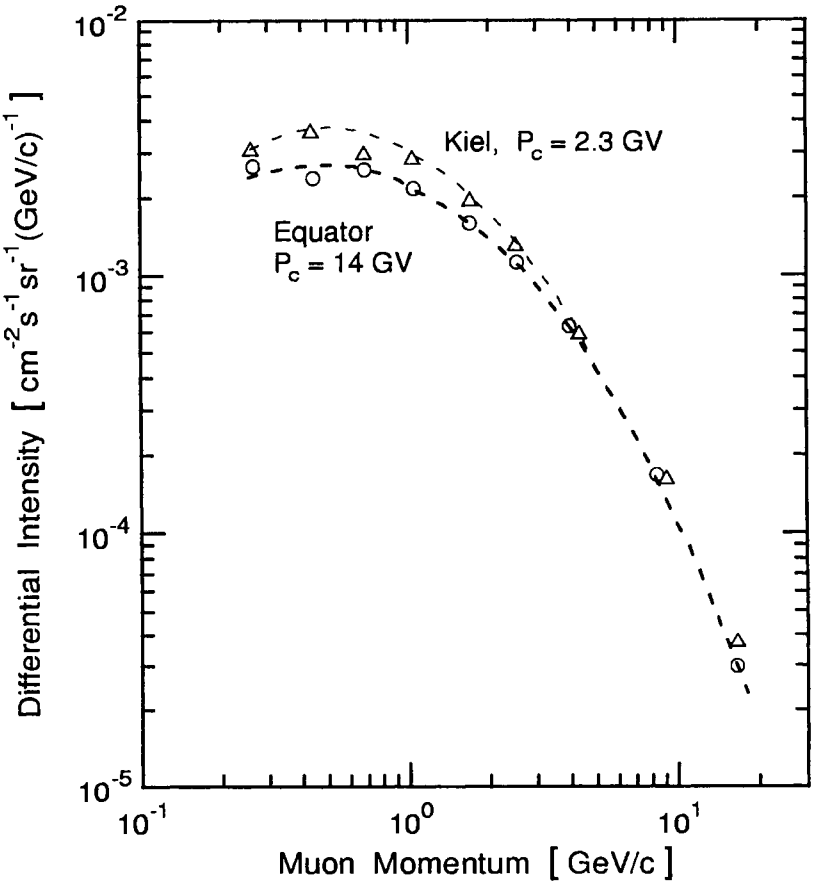

Figure 3.74: Differential momentum spectra of muons at sea level, recorded at the equator (P_c = 14 GV) and at Kiel (P_c = 2.3 GV) (Allkofer et al. 1975b).

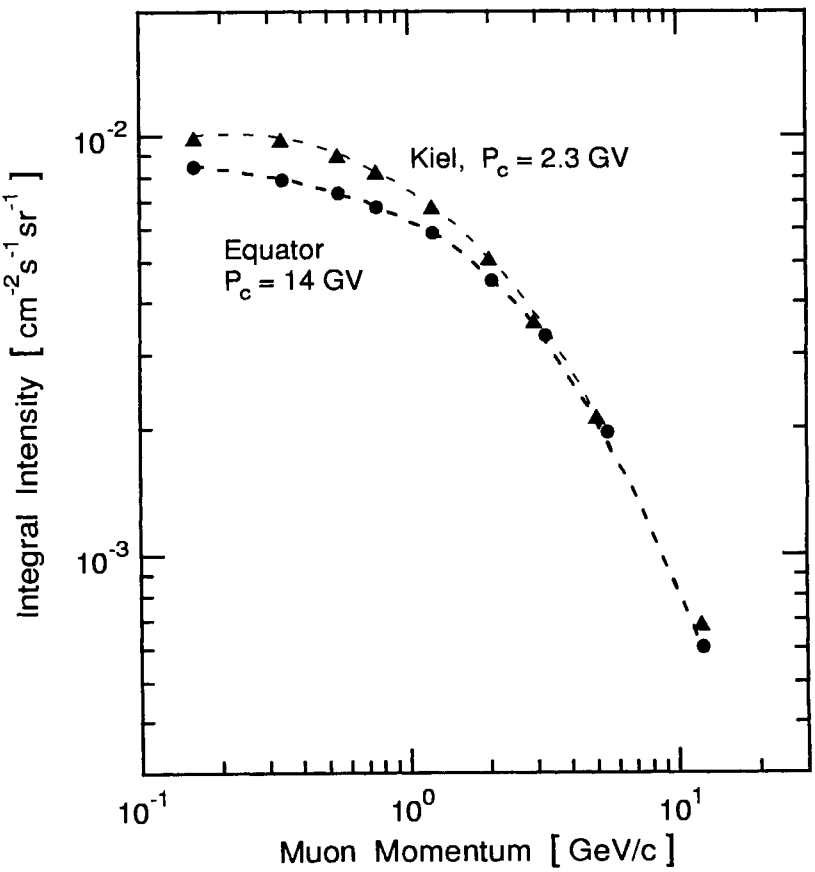

Figure 3.75: Integral momentum spectra of muons at sea level, recorded at the equator (P_c = 14 GV) and at Kiel (P_c = 2.3 GV) (Allkofer et al. 1975b).

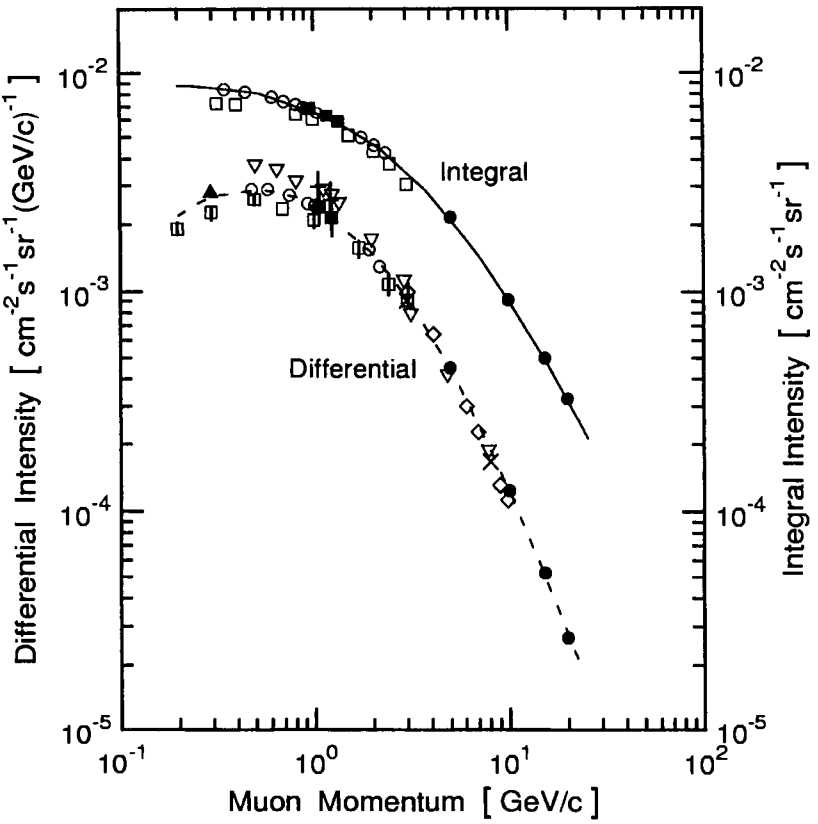

Figure 3.76: Vertical differential and integral momentum spectra of muons recorded in Calcutta at sea level and latitude $\lambda = 12°$ N (De et al., 1972b and 1974).

○	De et al. (1974)	□	Bhattacharyya (1970, 1971, 1973)
■	De et al. (1972a, 1972b)	•	Nandi and Sinha (1970, 1972b)
▲	Basu and Sinha (1956)	—	int. form-fit spectrum at $12°N$
▽	Allkofer et al. (1971b)	- - -	diff. form-fit spectrum at $12°N$

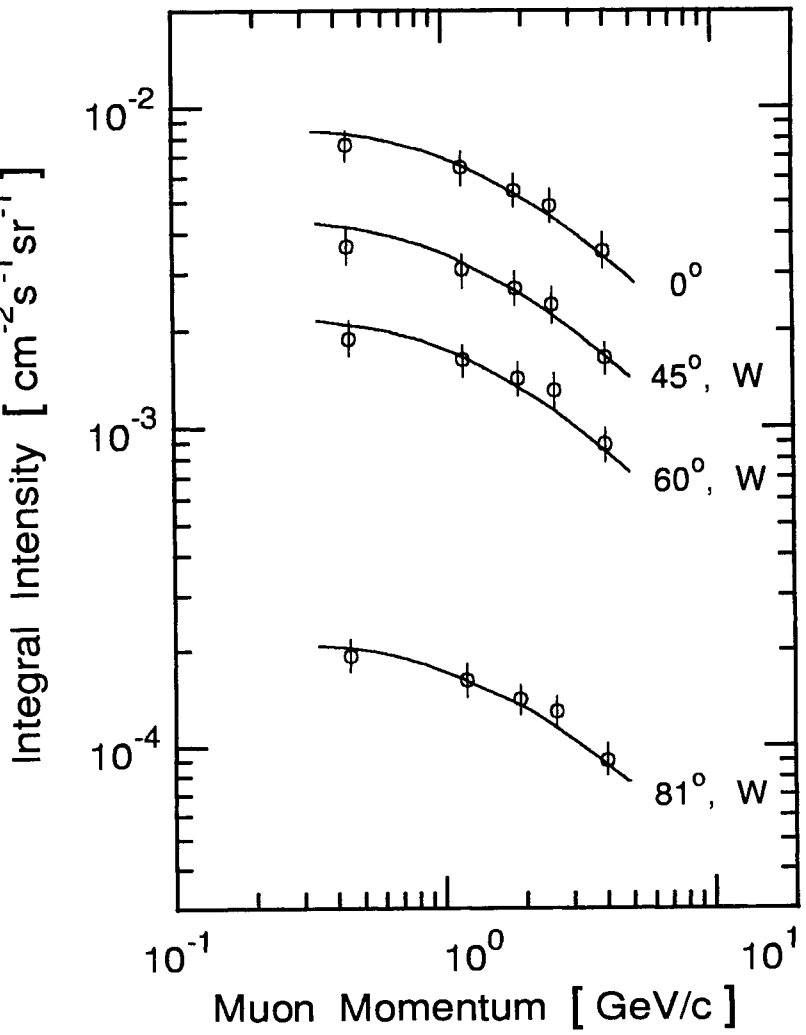

Figure 3.77: Integral momentum spectra of muons at sea level and latitude 12° N, for different zenith angles, pointing west (Bhattacharyya, 1976).

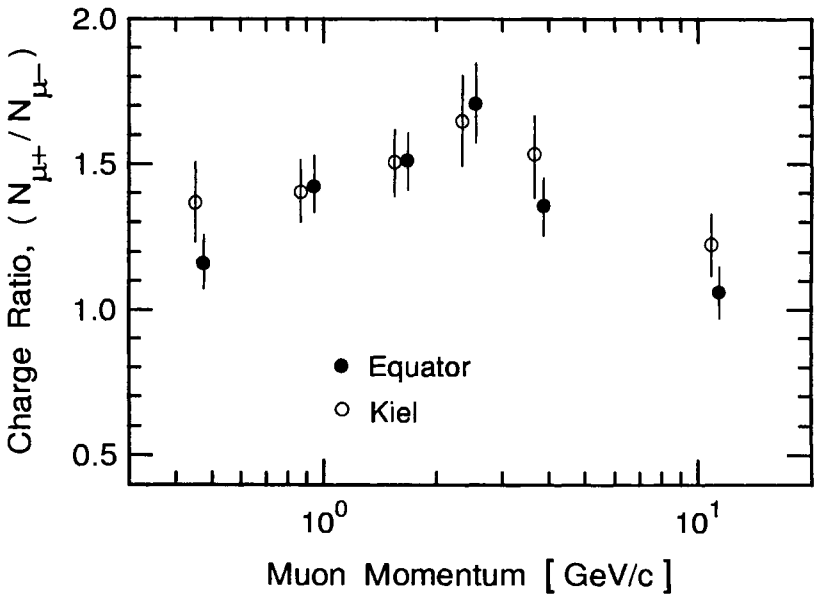

Figure 3.78: Muon charge ratio in equatorial regions, • (P_c = 14 GV) and at Kiel, ○ (P_c = 2.3 GV) for vertically incident muons. The latitude dependence is negligible except possibly at the lowest energies. However, it gets very significant for near horizontal muons of low energy moving perpendicularly to the field. (Allkofer and Dau 1972).

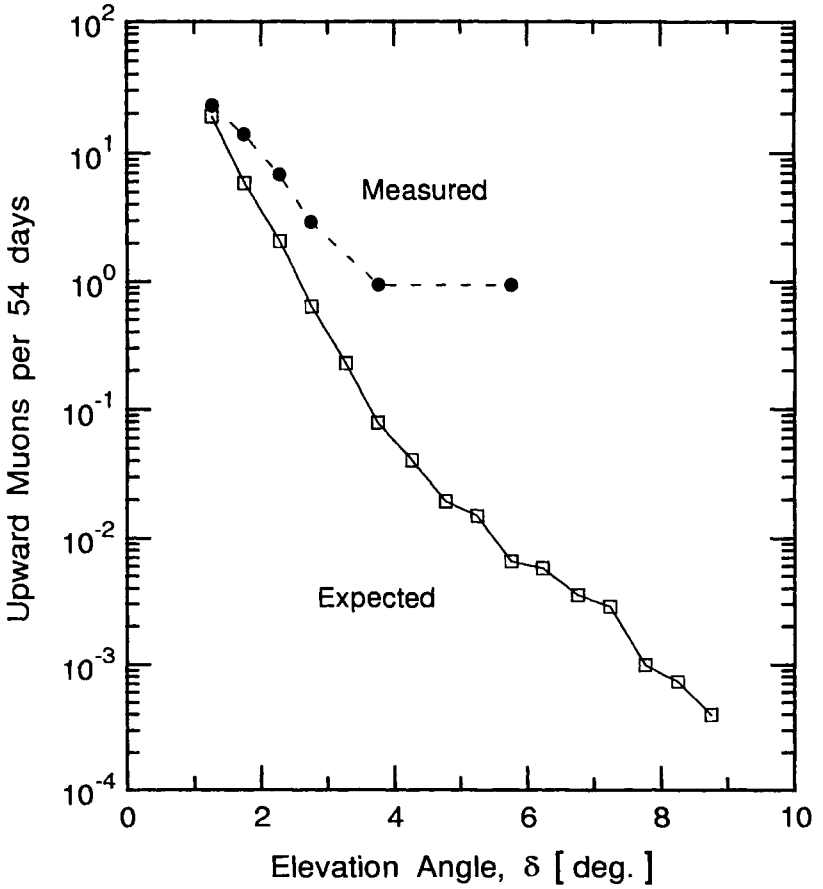

Figure 3.79: Ground level measurement of upward directed atmospheric muons of energy $\geq$4 GeV resulting from backscattering in the ground compared with a prediction. The horizontal telescope had an area of 2 m^2 and a horizontal depth of 11.07 m. (Abbrescia et al. (1993).

- Abbrescia et al. (1993), exp. | □ Elbert et al. (1991), theory

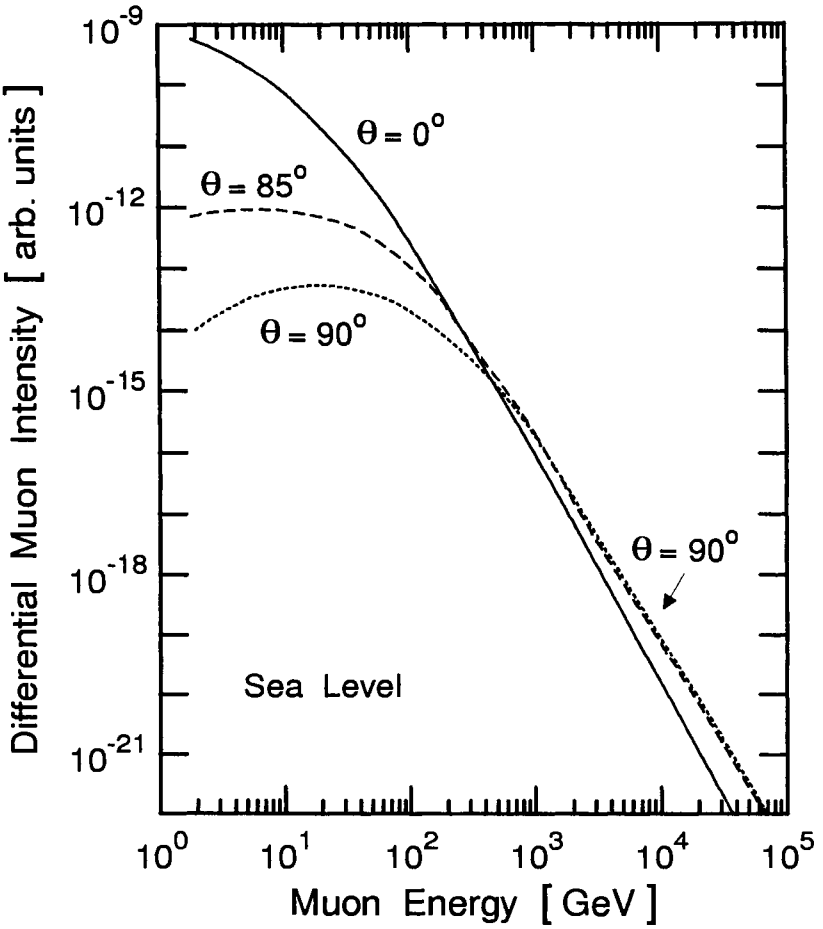

Figure 3.80: Theoretical differential energy spectra of atmospheric muons in an isothermal atmosphere at sea level at three different zenith angles, θ, as indicated (adopted from Maeda, 1970). The spectra were obtained with a diffusion equation. The muon enhancement at high energy and large zenith angles is evident.

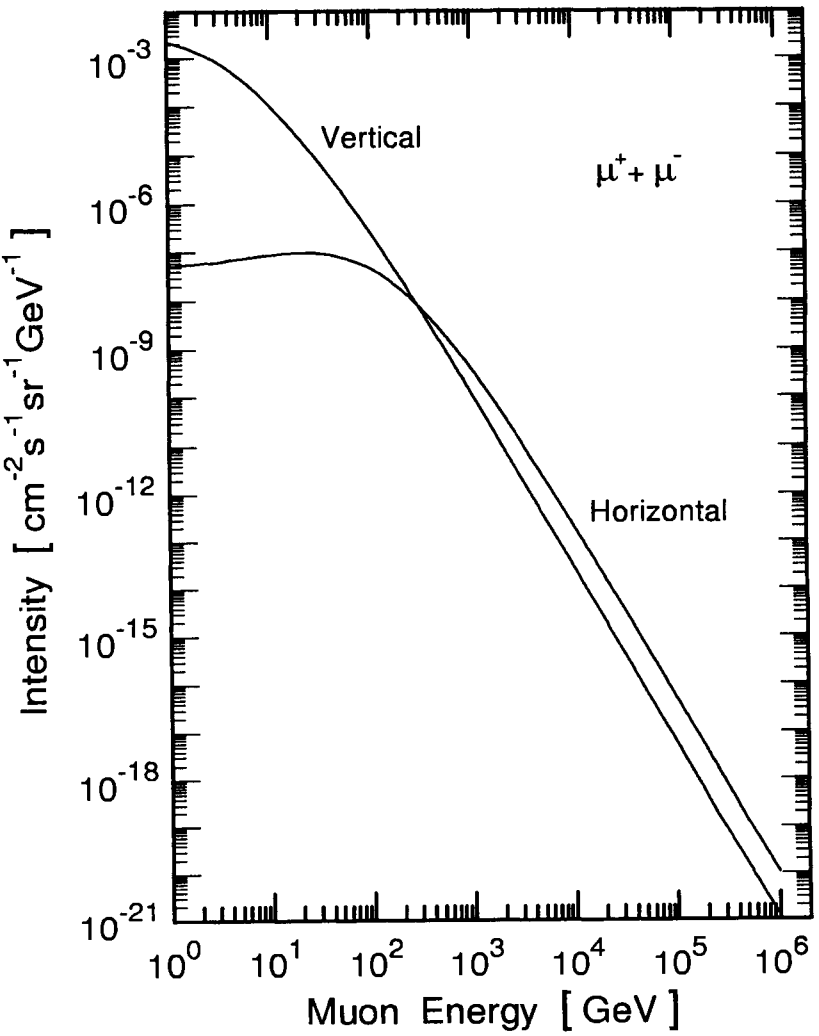

Figure 3.81: Theoretical differential energy spectra of atmospheric muons in horizontal and vertical directions at sea level plotted by the author from tabulated data of Lipari (1993). The spectra are the result of an analytic calculation using various assumptions and approximations and served as basis for computing neutrino spectra presented in Chapter 4, Section 4.5.

3.7 Nuclei

3.7.1 General Comments

Because of the rapid exponential absorption of energetic nuclei in the earth's atmosphere, the flux of primary nuclei that survive down to sea level without being subjected to a single collision is vanishingly small, even for light nuclei, such as helium. But also secondary nuclei, produced by fragmentation of heavy primaries in collisions with atmospheric nuclei, have little chance for survival down to sea level. Consequently very large detectors would be needed to carry out flux measurements of nuclei at great atmospheric depth. So far no experiment aimed at this task has been carried out at low altitude. However, starting out with the known primary composition on top of the atmosphere, Price et al. (1980) have calculated the flux of nuclei with charges $5 \leq Z \leq 28$ at sea level. Fig. 3.82 shows the results, integrated over all zenith angles, for the entire primary energy range.

There exist some data on the deuteron intensity at sea level (Ashton et al., 1970). The results are shown in Fig. 3.83 together with a calculated spectrum (Barber et al., 1980).

References

Ashton, F., H.J. Edwards, and G.N. Kelly: Acta Phys. Acad. Sci. Hung., 29, Suppl. 3, p. 327 (1970).

Barber, H.B., T. Bowen, D.A. Delise, E.W. Jenkins, J.J. Jones, R.M. Kalbach, and A.E. Pifer: Phys. Rev. D, 22, p. 2667 (1980).

Price, P.B., F. Askary, and G. Tarle: Proc. Nat. Acad. Sci. USA, 77, No. 1, p. 44 (1980).

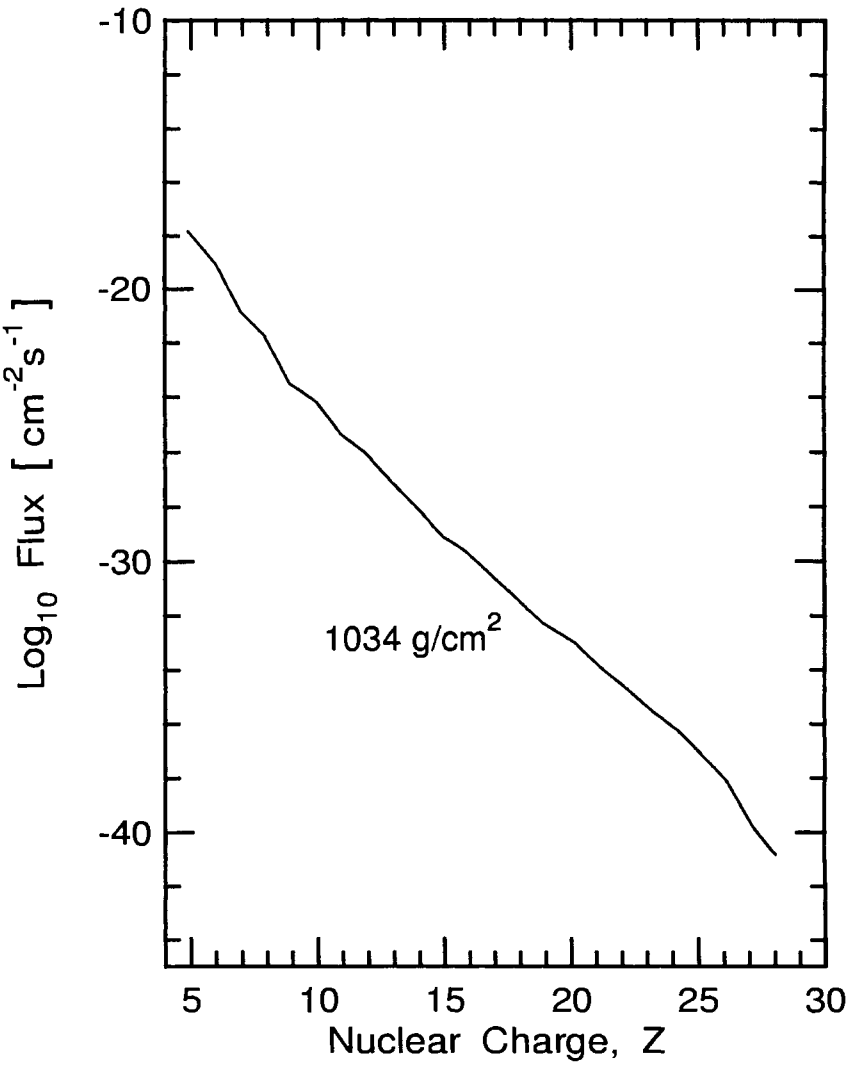

Figure 3.82: Calculated flux of nuclei with charges $5 \leq Z \leq 28$ at sea level, integrated over all zenith angles, for the entire energy range (Price et al., 1980).

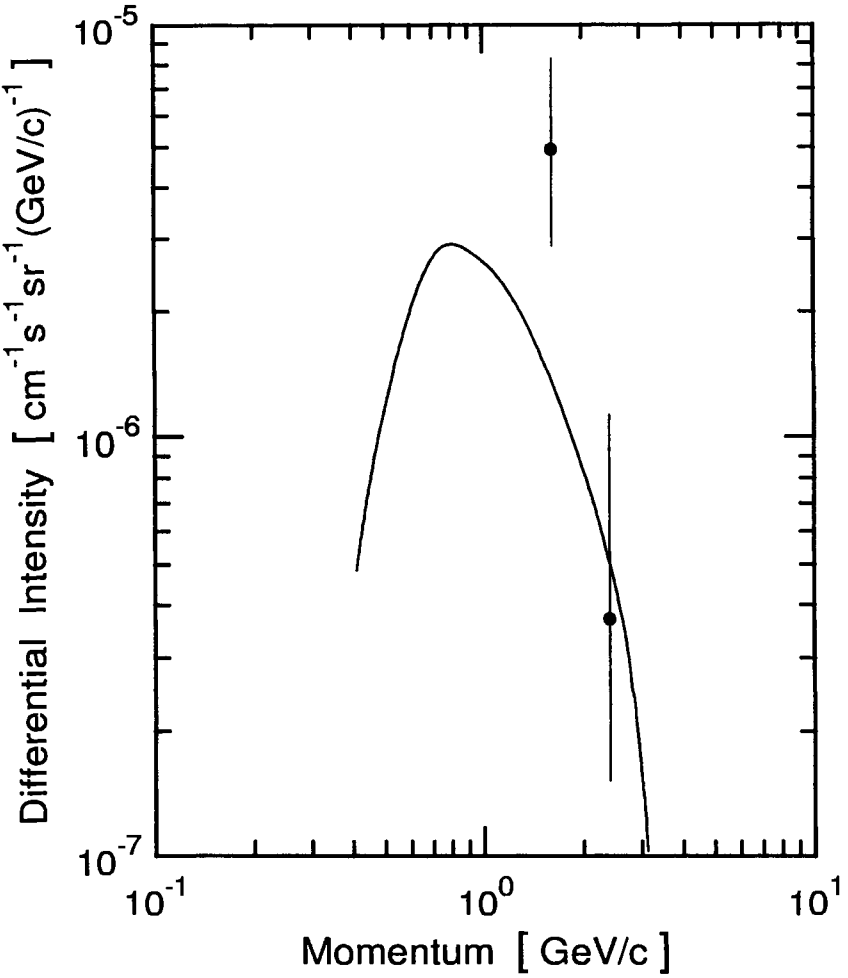

Figure 3.83: Vertical differential momentum spectrum of deuterons at sea level.

• Ashton et al. (1970)
— Barber et al. (1980) calculation

3.8 Antinucleons, Antinuclei

3.8.1 General Comments

Apart from delayed hadron measurements in extensive air showers from which the existence of energetic antinucleons can be inferred in conjunction with air shower simulations (Chatterjee et al., 1965; Murthy et al., 1968; Grieder, 1970a, 1970b, 1970c and 1977), there are no data on directly identified unaccompanied antinucleons at sea level.

References

Chatterjee, B.K., G.T. Murthy, S. Naranan, B.V. Sreekantan, M.V. Srinivasa Rao, and S.C. Tonwar: PICRC, 2, p. 802 (1965).

Grieder, P.K.F.: Acta Phys. Acad. Sci. Hung., 29, S3, p. 563 (1970a).

Grieder, P.K.F.: Acta Phys. Acad. Sci. Hung., 29, S3, p. 569 (1970b).

Grieder, P.K.F.: Institute for Nuclear Study, University of Tokyo Report INS J-125, November (1970c).

Grieder, P.K.F.: Rivista del Nuovo Cimento, 7, p. 1 (1977).

Murthy, G.T., K. Sivaprasad, M.V. Srinivasa Rao, S.C. Tonwar, R.H. Vatcha, and P.R. Vishwanath: Can. J. Phys., 46, p. S147 (1968).

This Page Intentionally Left Blank

Chapter 4

Cosmic Rays Underground, Underwater and Under Ice

4.1 Introduction

Cosmic ray particles which penetrate the atmosphere and enter the Earth's crust or its oceans lose energy by the same processes while propagating in these media as in the air. However, the situation changes dramatically for unstable particles due to the much higher density of these media as compared to air. At a given kinetic energy the likelihood for an unstable particle such as a pion or kaon to interact rather than decay is much higher when propagating in a dense medium such as earth, rock, ice or water than in the atmosphere. On the other hand, electrons are quickly absorbed as a result of cascade processes and stable hadrons are removed by nuclear interactions and, if charged, by ionization. Therefore, muons and neutrinos are the sole survivors of the cosmic radiation at great depth underground or underwater.

However, apart from the decay products of radioactive isotopes in the materials of the detector or its vicinity there is a minute flux of secondary particles such as pions, muons, electrons, gamma rays and neutrons, resulting mostly from muon but also neutrino induced interactions in the detector itself, or its surroundings. As expected, the angular distribution of this component does not manifest the sharp downward peak of the surviving atmospherically produced muon component.

Muon intensities have been measured at different levels under rock and in the sea down to depths of about 10^6 g/cm^2, and in ice to shallower depths. Underwater measurements have the great advantage that the overburden is exactly known, leaving no ambiguities about density and composition variations along a particle trajectory as in the case of an underground site. The

study of underground/underwater muons is important for several reasons.

By measuring the intensity of muons at different depths, information is obtained on the electromagnetic processes, including photo-nuclear processes, that reduce their flux. Based on intensity measurements at lower energies and electromagnetic cross sections extrapolated to high energies, muon spectral measurements can be extended to the TeV energy region with the help of deep underground flux data. Moreover, high energy muon data can be used to investigate the primary spectrum and multi-muon data permit to explore the primary mass composition.

Another aspect of muon measurements deep underground is to establish data for background estimations in heavily shielded underground areas that house neutrino experiments. There the muon flux as well as the flux of muon induced secondaries, particularly muons and electrons, must be known very accurately because the products of muon (electron) neutrino interactions themselves are muons (electrons). Similar arguments apply to site choice and planning of low-level counting laboratories deep underground.

Last but not least, the relation between depth and muon intensity is of considerable geophysical interest.

Underground and to a somewhat lesser extend underwater neutrino physics, too, have become fields of major activity that have strongly evolved during the last two decades. After the first attempts to detect solar as well as cosmic ray neutrinos deep underground in the early sixties in South Africa and India, several new generations of ever larger and more sophisticated neutrino experiments have come into operation or are currently under construction or in the planning phase.

Great efforts are under way to solve the solar neutrino puzzle with highly dedicated experiments using mostly specific neutrino reactions that have different predominantly low threshold energies. But also astrophysical aspects have received much attention and attempts are now in progress to look for neutrino point sources. Finally, the question of neutrino oscillations is also being tackled by cosmic ray physicists using solar as well as atmospheric neutrinos and, in united efforts with the accelerator community, neutrinos from accelerator beam dumps.

4.2 Theoretical Aspects of Muon Physics

4.2.1 Introductory Comments

In this subsection we discuss very briefly some of the theoretical aspects that are relevant for the evaluation and interpretation of the experimental results summarized in Sections 4.3 and 4.4. Emphasis is given to the energy loss mechanisms that are the basis for computing the range-energy relation, for linking the sea level muon spectrum with the muon intensities and spectra at different depths underground, underwater or under ice, and vice versa, and for computing the high energy portion of the sea level muon energy spectrum from the depth-intensity relation. The latter is a method to explore that spectrum to the highest energies and to link it with the primary spectrum and composition.

4.2.2 Energy Loss and Survival Probability of Muons in Dense Matter

Muons propagating in matter are subject to the following energy loss mechanisms: *ionization* and *atomic excitation* (Rossi, 1952; Sternheimer, 1956; Sternheimer and Peierls, 1971), *direct electron pair production* (Kelner and Kotov, 1968; Kokulin and Petrukhin, 1971; Wright, 1973), *bremsstrahlung* (Bethe and Heitler, 1934; Petrukhin and Shestakov, 1968; Kelner and Kotov, 1968), and *photo-nuclear interactions* (Kobayakawa, 1967 and 1985; Bezrukov and Bugaev, 1981). The references listed are those of the basic papers where the models and computational approaches to treat the particular process are discussed. Reviews concerning these topics are found in Kotov and Logunov (1970), Bergamasco and Picchi (1971), Vavilov et al. (1974), Wright (1974), Grupen (1976), Lohmann et al. (1985), and Bugaev et al. (1993 and 1994). Direct muon pair production and other higher order processes are usually disregarded unless specific aims are pursued.

The total energy loss relation for muons can be written as

$$-\frac{dE}{dx} = a(E) + b(E)\,E\ . \tag{4.1}$$

The term $a(E)$ in eq. 4.1 stands for energy losses due to ionization and atomic excitation. It has a weak logarithmic energy dependence and is therefore frequently regarded as constant for deep underground applications.

For a moderately relativistic particle with charge ze in matter with atomic number Z and atomic weight A the term $a(E)$ is given by the *Bethe-Bloch*

formula (Fano, 1963; see also Chapter 1, Subsection 1.4.1), which can be written as

$$-\left(\frac{dE}{dx}\right) = 4\pi N_A r_e^2 m_e c^2 z^2 \frac{Z}{A}\frac{1}{\beta^2}\left[\ln\left(\frac{2m_e c^2\gamma^2\beta^2}{I}\right) - \beta^2 - \frac{\delta}{2}\right] . \quad (4.2)$$

Here m_e is the electron rest mass, r_e the classical radius of the electron and $4\pi N_A r_e^2 m_e c^2 = 0.3071$ MeV cm^2 g^{-1}. $\gamma = 1/(1-\beta^2)^{0.5}$ is the Lorentz factor and $\beta = v/c$, v being the velocity of the particle and c the velocity of light. I is the *ionization constant* and is approximately given by $16Z^{0.9}$ eV for $Z > 1$, and dx is the mass per unit area or the *column density*, usually expressed in g/cm^{-2}. δ represents the *density effect* which approaches $2\ln\gamma$ plus a constant for very energetic particles (Crispin and Fowler, 1970; Sternheimer et al., 1984; for further details see the Appendix).

The term $b(E)$ is a composite term, $b(E) = b_{br}(E) + b_{pp}(E) + b_{ni}(E)$, and represents the sum of the losses resulting from bremsstrahlung, pair production and photo-nuclear interactions, respectively. Each of these mechanisms is energy dependent and the mathematical expressions are relatively complex.

Figure 4.1 shows the energy dependence of the three processes that contribute to b, and of the sum in Mont Blanc rock (Bergamasco et al., 1983). Results of a similar calculation by Inazawa and Kobayakawa (1985) for standard rock, sea water and fresh water are presented in Fig. 4.2. A very new calculation of the energy loss of muons in standard rock, was carried out by Rhode (1993). The results are given in Fig. 4.3 where the contributions of the different mechanisms, including ionization, as well as the sum are shown as a function of muon energy.

Since the energy loss of muons in matter is not continuous muons do not have a unique range. *Fluctuations* in range arise from catastrophic processes, in particular from bremsstrahlung. They must be taken into account when calculating the muon intensity underground from the energy spectrum of the muons at the surface of the Earth.

For range calculations of high energy muons in thick absorbers the *survival probability* is a relevant quantity. It is usually determined by means of Monte Carlo calculations that include all four processes mentioned above and account for fluctuations. Catastrophic interactions become very important at high energies. They dominate the energy loss at energies greater than about 600 GeV.

Some time ago Tannenbaum (1991) pointed out that discrepancies exist between the bremsstrahlung *screening function* used by Petrukhin and

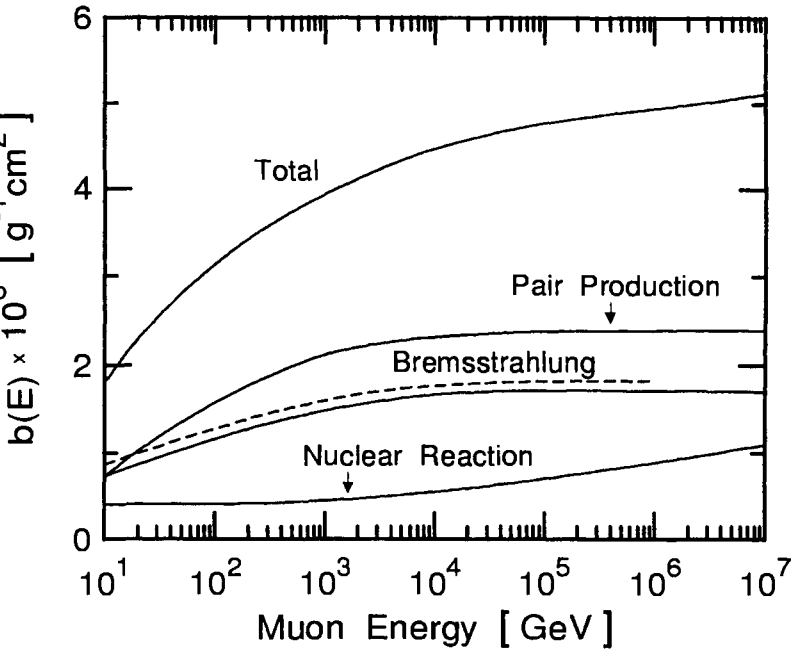

Figure 4.1: Energy dependence of the coefficient b of the energy loss equation 4.1 and of the separate contributions from direct pair production (b_{pp}), bremsstrahlung (b_{br}) and photo-nuclear interactions (b_{ni}) in standard rock, after Bergamasco et al. (1983). Shown, too, is the result of Lipari and Stanev (1993) (dashed curve) for bremsstrahlung using Rozental screening which lies about 10% above the result of Bergamasco et al. who used the Petrukhin and Shetakov screening functions.

Shestakov (1968), and those of Rozenthal (1968) and Tsai (1974) (see also Sternheimer et al., 1984). Moreover, deviations between theory and experiment are confirmed (Sakumoto et al., 1992).

Lipari and Stanev (1993) modified the screening function and carried out Monte Carlo simulations of muon propagation to great depth underground and underwater. They noticed that their modification to the screening function causes noticeable changes in the energy loss due to bremsstrahlung and affects the muon survival probability. The results of some of their work are illustrated in Figs. 4.1 and 4.4. In Fig. 4.1 we have added their curve showing the energy dependence of the parameter b_{br} for bremsstrahlung using a Rozental-like screening function, for comparison. The latter lies roughly 10% above the corresponding curve of Bergamasco et al. (1983), calculated with

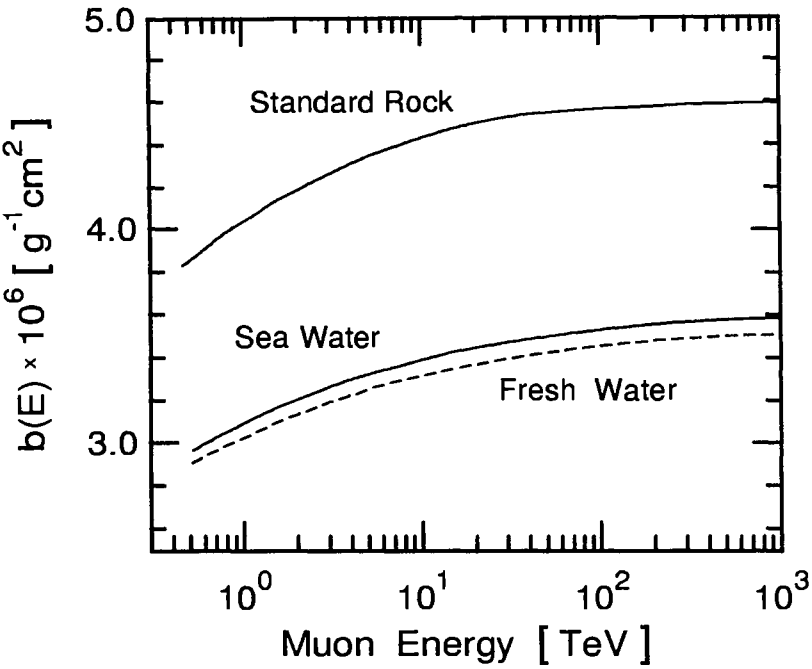

Figure 4.2: Energy dependence of the b-term (all contributions) in fresh water, sea water and standard rock according to Inazawa and Kobayakawa (1985).

the Petrukhin and Shestakov screening function.

The differences resulting for the survival probability using either Petrukhin and Shestakov or Rozental screening is evident from Fig. 4.4. Lipari and Stanev (1993) state that at 10 TeV the relative energy losses due to bremsstrahlung (Rozenthal function), pair production and nuclear interactions are 0.36, 0.51 and 0.12, respectively.

More recently several authors have revisited the problem of muon energy losses and propose more accurate relations, different computational approaches, and present new data on the energy loss and survival probability of muons in various media (Bugaev et al., 1985a, 1985b, 1994, 1998 and references listed therein; Naumov et al., 1992).

A summary of formulas for the cross sections of processes contributing to the energy loss of muons in matter and a comprehensive collection of computed energy loss data of muons in a variety of pure and compound materials, covering the energy range from 1 GeV to 10 TeV, is given in

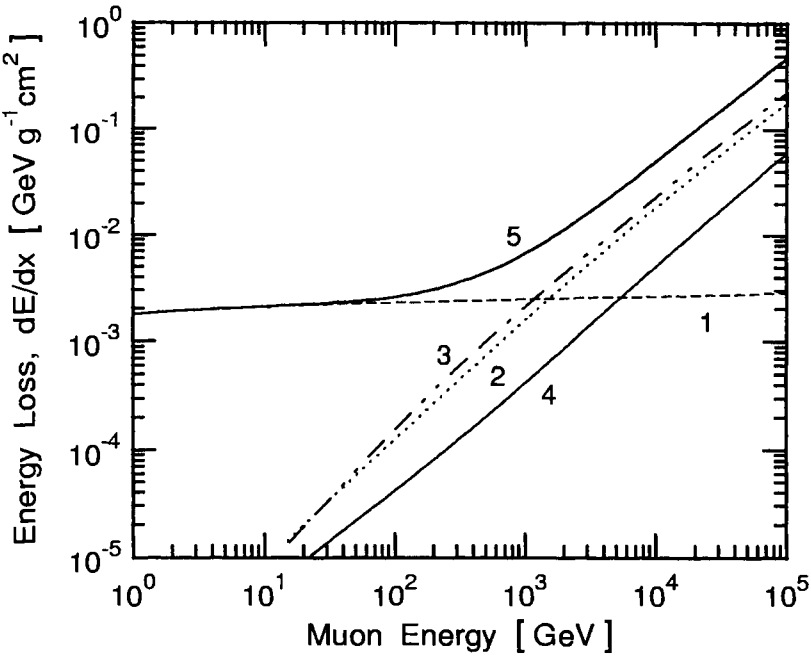

Figure 4.3: Energy loss, dE/dx, of muons in standard rock. Shown is the near constant loss which is due to ionization (curve 1), the energy dependent contributions from bremsstrahlung (curve 2), pair production (curve 3) and nuclear interactions (curve 4), as well as the sum of all four mechanisms (curve 5), after Rhode (1993).

tabulated form in a paper by Lohmann et al. (1985). Portions of the tables concerning materials relevant to cosmic ray research are reproduced in Tables A.5 and A.6, in the Appendix.

Practical Energy Loss Expressions

The mathematical expressions for the energy losses resulting from the different processes listed above are relatively complex and can be found in the references given above. However, for muons propagating in specific media they can be written in convenient form, lumping constants together, such that they can be used readily for computations. In the following we list the complete set of equations for *standard rock* with $\rho = 2.650$, $Z/A = 0.50$ and $Z^2/A = 5.50$ (Menon and Ramana Murthy, 1967; Kotov and Logunov, 1970; Grupen, 1976).

i) Energy loss by *ionization and excitation.* For energies $>> 10^{11}$ eV the

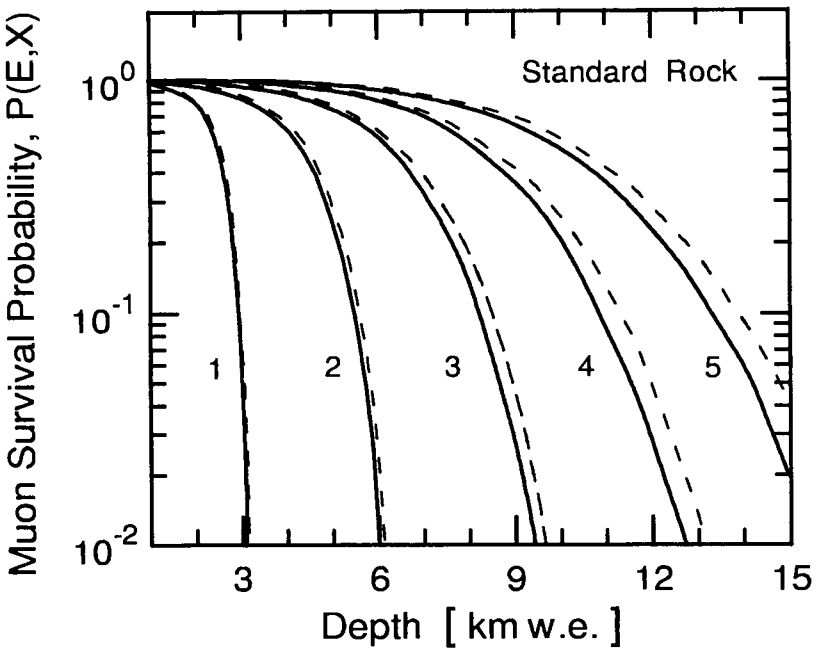

Figure 4.4: Survival probabilities of muons in standard rock calculated with the Rozental (1968) (solid curves) and Petrukhin and Shestakov (1968) (dashed curves) screening functions for muons of different energy. Curves 1, 2, 3, 4 and 5 are for muons of energy 1, 3.16, 10, 31.6 and 100 TeV, respectively (after Lipari and Stanev, 1993).

differential energy loss due to ionization is equal to

$$-\left(\frac{dE}{dx}\right)_{ion} = a + d \ln \frac{E'_{max}}{m_\mu c^2} \tag{4.3}$$

and

$$E'_{max} = \frac{E^2}{E + \left(\frac{m_\mu^2 c^2}{2m_e}\right)}, \tag{4.4}$$

where E and m_μ are the energy and rest mass of the muon, m_e the mass of the electron, and E'_{max} is the maximum transferable energy.

For standard rock (Z/A = 0.5; Z^2/A = 5.5; Z = 11; A = 22; ρ = 2.65 gcm^{-3}) the ionization loss is given by

$$-\left(\frac{dE}{dx}\right)_{ion} = 1.84 + 0.076 \ln \frac{E'_{max}}{m_\mu c^2} \ [\text{MeV g}^{-1} \text{ cm}^2] \ . \tag{4.5}$$

For water the expression changes to

$$-\left(\frac{dE}{dx}\right)_{ion} = 2.15 + 0.0853 \ln \frac{E'_{max}}{m_\mu c^2} \ [\text{MeV g}^{-1} \text{ cm}^2] \ . \quad (4.6)$$

ii) Energy loss by *bremsstrahlung.*

$$-\left(\frac{dE}{dx}\right)_{br} = 1.77 \cdot 10^{-6} E \ [\text{MeV g}^{-1} \text{ cm}^2] \ . \quad (4.7)$$

iii) Energy loss by *direct electron pair production.*

$$-\left(\frac{dE}{dx}\right)_{br} = 2.40 \cdot 10^{-6} E \ [\text{MeV g}^{-1} \text{ cm}^2] \ . \quad (4.8)$$

iv) Energy loss by *photo-nuclear processes.*

$$-\left(\frac{dE}{dx}\right)_{br} = 0.48 \cdot 10^{-6} E \ [\text{MeV g}^{-1} \text{ cm}^2] \ . \quad (4.9)$$

The accuracy of eq. 4.9 is rather uncertain and the values quoted by different authors are not identical. The more generalized equations for any Z and A can be found in the reviews listed at the beginning of this section.

Summing the terms for the different energy loss modes given above, eqs. 4.3 and 4.7 to 4.9, one obtains for the total energy loss of muons in standard rock and energy given in units of MeV

$$-\left(\frac{dE}{dx}\right)_{total} = 1.84 + 4.65 \cdot 10^{-6} E + 0.076 \ln \frac{E'_{max}}{m_\mu c^2} \ [\text{MeV g}^{-1} \text{ cm}^2] \ . \quad (4.10)$$

For different rock the energy proportional term must be modified to account for the different value of Z^2/A. Depending on rock composition and theoretical approach chosen, parameter b can have values that lie in the range between $3.6 \cdot 10^{-6}$ and $5.5 \cdot 10^{-6}$ g^{-1} cm^2.

Theoretical data of the energy loss of muons underwater from a calculation of Davitaev et al. (1970) are presented in tabulated form in Section 4.4, Table 4.26.

4.2.3 Average Range-Energy Relation of Muons

From the theoretical foundations of the energy loss of muons summarized above, the survival probability for an atmospheric muon of given energy at

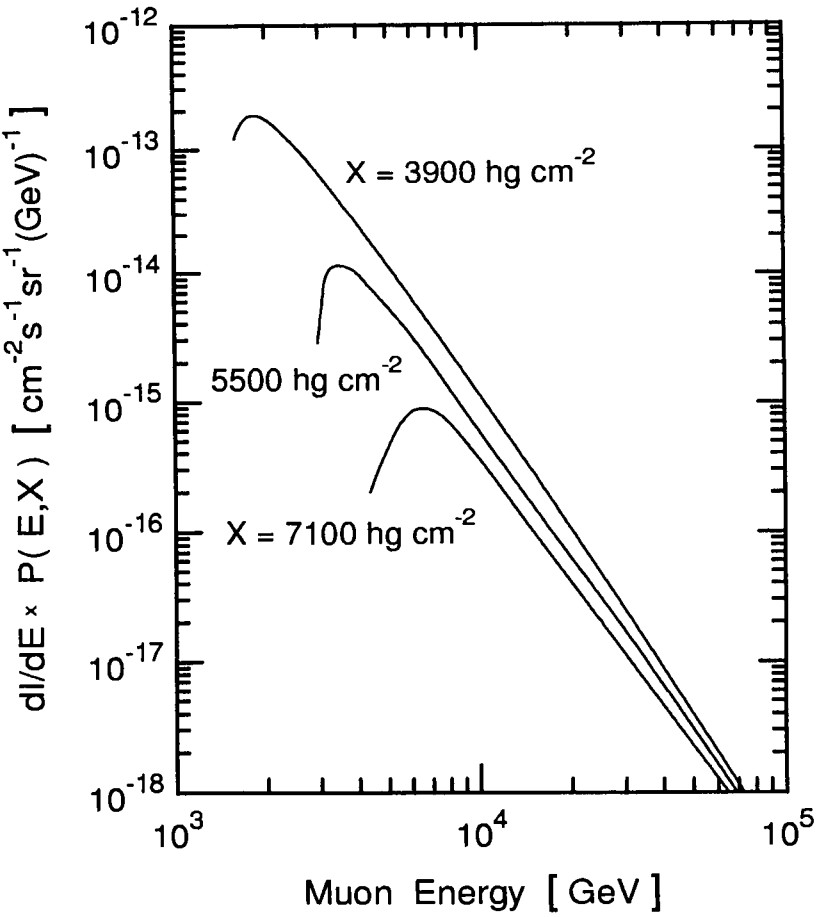

Figure 4.5: Intensity probability distribution of atmospheric muons that contribute to the muon flux at a particular level underground, as indicated, versus muon energy (Bergamasco et al., 1983).

the Earth's surface to reach a particular level underground can be calculated. Folding the atmospheric muon spectrum with the survival probability for a given depth underground, one obtains the intensity probability distribution of the muons that contribute to the muon intensity underground as a function of energy. The result of such a calculation by Bergamasco et al. (1983) is illustrated in Fig. 4.5 for three depths.

The mean range, $R_\mu(E)$, expressed in g/cm^2, can be obtained by integra-

tion of eq. 4.1 (Kotov and Logunov, 1970; Miyake, 1973). Letting $a(E) = a$ being constant we can write

$$R_\mu(E) = -\int_0^E \left(\frac{dx}{dE}\right) dE = \int_0^E \frac{dE}{a + b(E)E} = \frac{1}{b} \ln\left(\frac{a + bE}{a}\right) . \quad (4.11)$$

Solving for E we get the *range-energy relation*

$$E = \left(\frac{a}{b}\right)\left(e^{b R_\mu} - 1\right) \quad (4.12)$$

where we now insert for a the weakly energy dependent expression

$$a = 1.84 + 0.076 \ln\left(\frac{E^2}{e m_\mu c^2 (E + eA)}\right) \ [\text{MeV g}^{-1} \text{ cm}^2] . \quad (4.13)$$

The constants are $A = 11.3$ GeV, $e = 2.718$, and a frequently used value for b is $3.6 \cdot 10^{-6}$ g^{-1} cm^2. Average range-energy relations for three different values of b are illustrated in Fig. 4.6 (Menon and Ramana Murthy, 1967).

For relatively low energy muons ($E << 100$ GeV), where $bE << a$, this relation simplifies to

$$R_\mu = \frac{E}{a} . \quad (4.14)$$

Theoretical data of the range of muons underwater obtained from a calculation by Rogers and Tristam (1984) covering a momentum range from 1 to 100 GeV/c are given in Table 4.27 of Section 4.4.

4.2.4 Range Fluctuations of Muons Underground and in Water

Whenever the range of a muon is comparable to the radiation length of muons in the medium (5680 hg cm^{-2} in standard rock), the concept of continuous energy loss is no longer valid. Fluctuations begin to play an important role and must be accounted for when interpreting data from range-energy or depth-intensity measurements. Modern Monte Carlo calculations take care of the problem of fluctuations when simulating the propagation of muons to great depth underground. However, before that time some authors have developed theoretical methods to handle fluctuations (Mando and Sona, 1953; Hayman et al., 1962 and 1963; Zatsepin and Mikhalchi, 1962 and 1965; Nishimura,

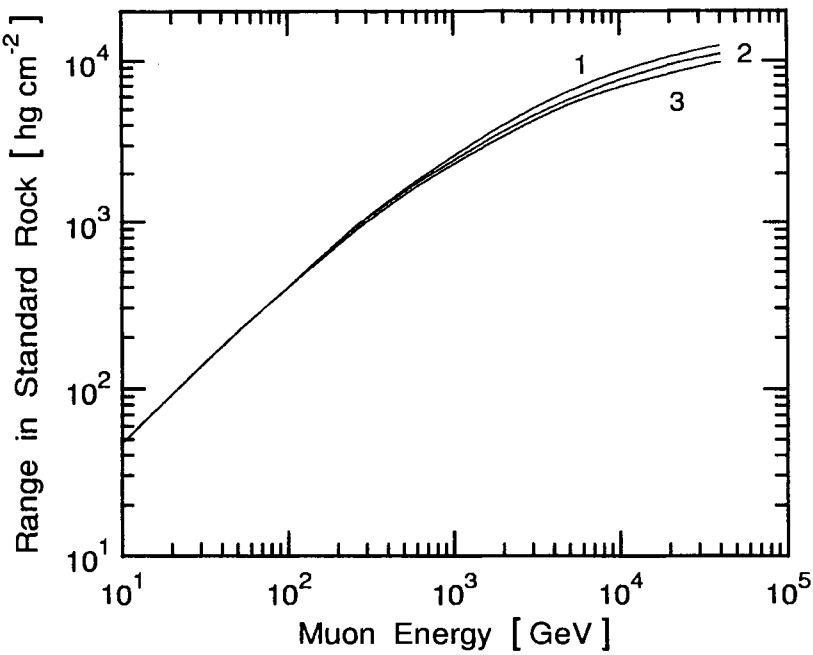

Figure 4.6: Average range-energy relation of muons based on the assumption of continuous energy loss. Curves 1, 2 and 3 are for values of $b = 3.0 \cdot 10^{-6}$, $b = 3.6 \cdot 10^{-6}$ and $b = 4.2 \cdot 10^{-6}$, respectively (after Menon and Ramana Murthy, 1967).

1964; and Kiraly et al., 1972). These methods are based on the introduction of a *correction factor*, R_C, which is defined as

$$R_C = I(X)/I_f(X) \, . \tag{4.15}$$

$I(X)$ is the calculated intensity at a specified level X underground for an assumed muon energy spectrum of given spectral index γ at the Earth's surface, neglecting fluctuations, and $I_f(X)$ is the intensity including fluctuations. The intensities are obtained by solving the diffusion equations (see Bergamasco et al., 1983; Maeda, 1970 and 1973).

More recently Minorikawa and Mitsui (1985) have used the same approach developed by Zatsepin and Mikhalchi (1965) (see also Gurentsov et al., 1976) to compute the correction factor R_C and applied it to various experiments. R_C depends on the spectral index γ of the muons at the surface and on the range. Table 4.1 lists a compilation of correction factors from different authors for three different spectral indices, valid for the depth ranges indicated

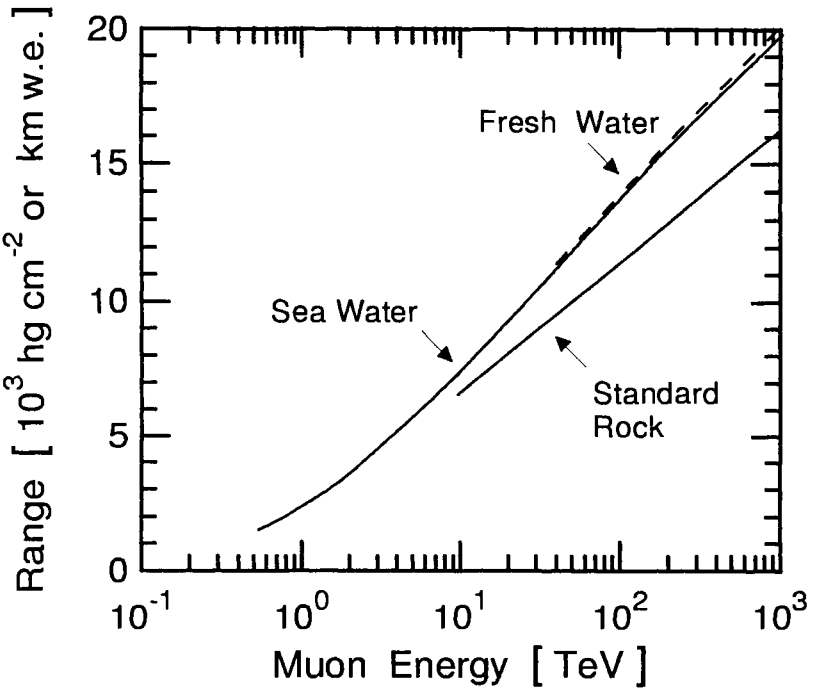

Figure 4.7: Range-energy relation of muons in fresh water, sea water and standard rock (Inazawa and Kobayakawa, 1985).

(Menon and Ramana Murthy, 1967). These correction factors are used to calculate the high energy portion of the muon energy spectrum at the surface of the Earth from intensity data underground. The intensities observed at different depths have to be multiplied by the R_C values of Table 4.1 to correct for fluctuations in the energy loss of muons. For a more detailed account of the different approaches the reader is referred to the article by Menon and Ramana Murthy (1967).

In Fig. 4.7 we show corrected range-energy spectra in standard rock, fresh water and sea water from a calculation by Inazawa and Kobayakawa (1985), and in Fig. 4.8 the correction factor R_C as a function of muon range for three different spectral indices of the muon spectrum at the surface.

Table 4.1: Intensity Correction Factors, R_C, Accounting for Fluctuations for Different Spectral Slopes, γ and Depths. (Menon and Ramana Murthy, 1967)

Depth (Rock) [hg cm^{-2}]	Reference*)	Correction factor, R_C for $\gamma = 2.5$	$\gamma = 3.0$	$\gamma = 3.5$
2000	1)	0.97	-	-
	2)	0.93	0.88	0.81
	3)	0.93	0.88	0.82
	4)	1.19	1.19	1.17
	5) case 1	0.93	0.88	0.83
	5) case 2	0.83	0.73	0.63
4000	2)	0.81	0.69	0.60
	3)	0.80	0.69	0.60
	4)	0.92	0.83	0.76
	5) case 1	0.87	0.78	0.69
	5) case 2	0.62	0.46	0.33
	6)	0.95	0.84	0.73
6000	2)	0.66	0.51	0.41
	3)	0.67	0.51	0.41
	4)	0.66	0.53	0.44
	5) case 1	0.79	0.66	0.55
	5) case 2	0.43	0.27	0.16
	6)	0.86	0.68	0.55
8000	2)	0.54	0.36	0.24
	3)	0.55	0.37	0.27
	6)	0.69	0.51	0.38
10000	2)	0.40	0.27	0.14

*) 1) Mando and Sona (1953); 2) Zatsepin and Mikhalichi (1965); 3) Nishimura (1964); 4) Bollinger (1951); 5) Hayman et al. (1962, 1963); 6) Miyake et al. (1964). For full references see end of section.

4.2.5 Average Depth-Intensity Relation of Muons

By expressing the high energy portion of the integral energy spectrum of muons at sea level as

$$J(\geq E) = A E^{-\gamma} , \tag{4.16}$$

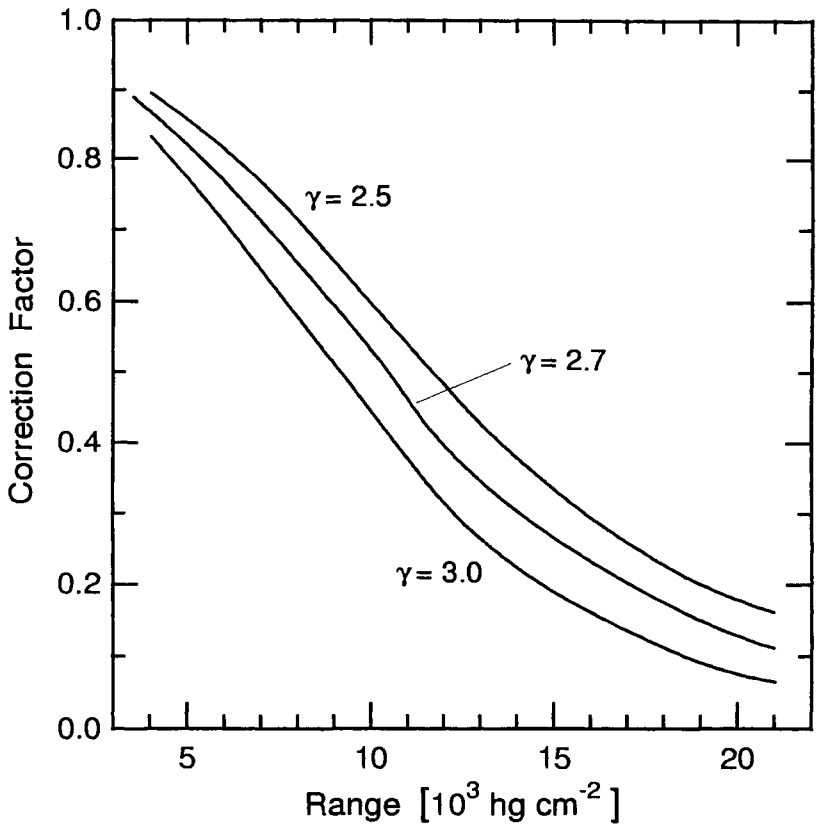

Figure 4.8: Fluctuation correction factor in sea water for different exponents γ of the integral energy spectrum of muons at sea level (Inazawa and Kobayakawa, 1985).

where A is a constant and γ the spectral exponent, and using the range-energy relation, eq. 4.12, the vertical intensity $I(X)$ at depth X can be written as

$$I(X) = A\left(\frac{a}{b}\left(e^{bX}-1\right)\right)^{-\gamma} . \tag{4.17}$$

Here a and b are the energy loss parameters defined earlier.

For $e^{bX} >> 1$, and using

$$B = \frac{1}{b}(Aa)^{-\gamma} , \tag{4.18}$$

the following depth-intensity relation is obtained:

$$I(X) = Be^{-bX\gamma} . \tag{4.19}$$

If the intensity is measured in an inclined direction under a zenith angle $\theta > 0°$ and a flat surface topography at a vertical depth X, the depth-intensity relation must be modified by the factor $\sec(\theta)$ because of the muon enhancement in the atmosphere, outlined in Section 3.6. Moreover, another factor of $\sec(\theta)$ must be introduced in the exponent because of the slant depth, X_s, which is larger than X for an inclined trajectory underground. Thus

$$I(X,\theta) \;=\; B\,\sec(\theta)\,e^{-b\,X\,\gamma\,\sec(\theta)}\;. \tag{4.20}$$

For *small depths* in the vertical direction, a series expansion of the previous equation (eq. 4.19) yields

$$I(X) \;=\; A'\,(a\,X)^{-\gamma}\;, \tag{4.21}$$

where A' is a constant. This equation shows that the shape of the muon spectrum is reproduced. For *large depths* one gets

$$I(X) \;\simeq\; e^{-b\,X\,\gamma}\;. \tag{4.22}$$

Thus the intensity decreases exponentially with depth. The principal energy loss process at small depths (and low energies) is ionization, represented by the factor a, whereas at large depths (and high energies) the electromagnetic processes, accounted for by b, are more important. Energy losses due to ionization exhibit only small fluctuations because the loss is due to many single processes. In contrast, as pointed out above, the bremsstrahlung mechanism which is dominating at high energies, is a single process in which a large fraction of the energy can get lost. Consequently large fluctuations are produced in the depth-intensity relation at larger depths.

The consequence resulting from the difference between the screening functions of Petrukhin and Shestakov (1968) and Rozental (1968) for the theoretical depth-intensity relation, as pointed out before, are shown in Fig. 4.9 (Lipari and Stanev, 1993).

Experimental data of muons underground and underwater are presented in Sections 4.3 and 4.4.

4.2.6 Indirect Determination of the Energy Spectrum Underground and Average Energy

The vertical muon intensity at depth X, $I(X,0°)$, is related to the muon differential energy spectrum at the surface,

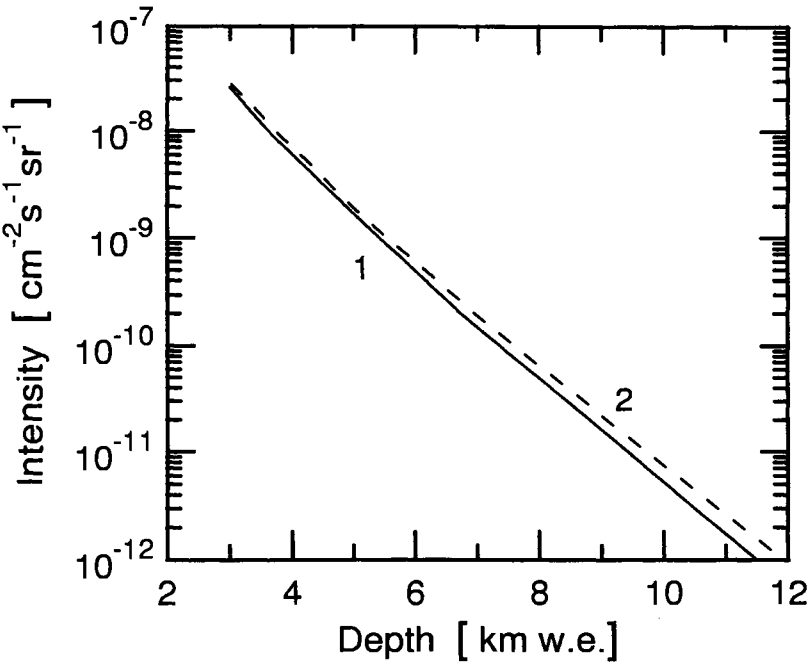

Figure 4.9: Depth-intensity relation calculated with the Petrukhin and Shestakov (1968) (curve 1, solid) and the Rozental (1968) (curve 2, dashed) screening functions in standard rock using an atmospheric differential muon energy spectrum of the form $E_\mu^{-3.7}$ (after Lipari and Stanev, 1993).

$$j(E,0°) = BE^{-(\gamma+1)} , \tag{4.23}$$

by the relation

$$I(X,0°) = \int_{E_{th}}^{\infty} P(E,X)\, j(E,0°)\, dE , \tag{4.24}$$

where γ is the spectral index of the integral muon energy spectrum at the surface, $P(E,X)$ the survival probability that a muon of energy E reaches depth X, and E_{th} is the energy threshold corresponding to $P(E_{th},X) = 0$. The energy spectrum is then calculated with the help of a minimizing procedure.

If we are neglecting fluctuations that are embedded in the survival probability, $P(E,X)$, we can easily derive the vertical energy spectrum at depth X using eqs. 4.1 and 4.19, which yields

$$j(E,X) = Be^{-bX\gamma} \cdot \left(E + \frac{a}{b}(1 - e^{-bX})\right)^{-(\gamma+1)} . \qquad (4.25)$$

In this equation the first exponent describes the attenuation of the high energy muon flux, whereas the expression in parenthesis determines the shape of the local energy spectrum underground.

The *average energy* of the muons at depth X is given by the relation

$$E_{ave} = \left(\frac{a}{b\,(\gamma - 1)}\right)(1 - e^{-bX}) . \qquad (4.26)$$

Some important facts that result from the mathematical treatment above should be remembered (Castagnoli et al., 1995):

1. The energy spectrum underground is flat at energies $E << E_{ave}$.
2. The slope of the spectrum at the surface is reproduced for $E >> E_{ave}$.
3. At shallow depths where $bX << 1$ the average muon energy is nearly proportional to X.
4. At great depths where $bX > 1$ ($X > 2 \cdot 10^3$ hg cm^{-2}) the spectral slope varies slowly with depth.
5. The average energy approaches the asymptotic limit $a/[b(\gamma - 1)]$.

Rhode (1993) computed the muon energy spectra for different levels underground using the energy loss dependencies shown earlier in Fig. 4.3. The results of his calculations are illustrated in Fig. 4.10.

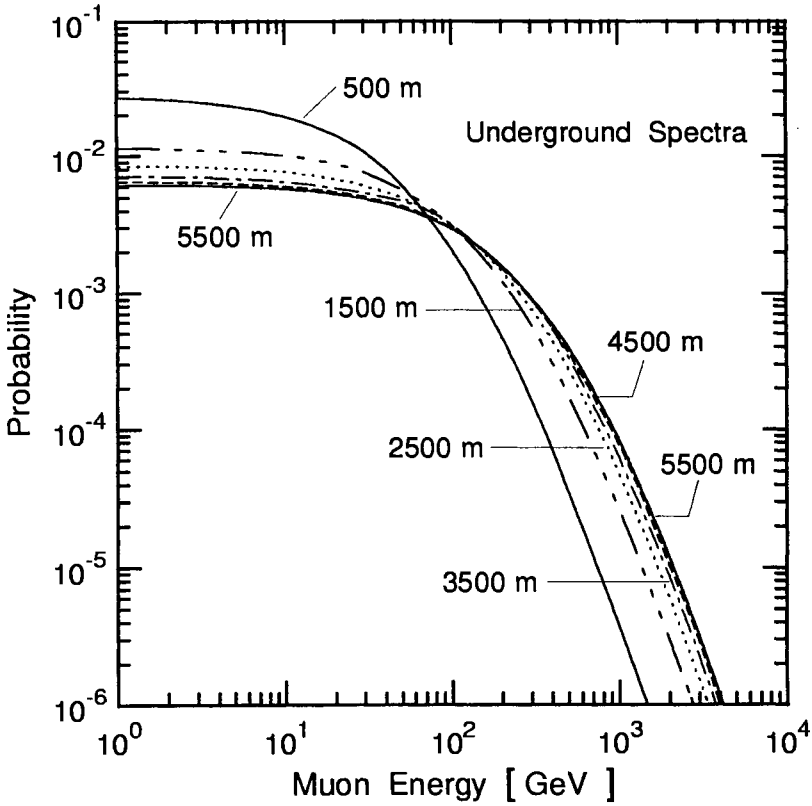

Figure 4.10: Energy spectra of muons underground in standard rock for energy loss coefficients according to Rozental (1968) of $a = 0.217$ GeV (m w.e.)$^{-1}$ and $b = 4.5 \cdot 10^{-4}$ (m w.e.)$^{-1}$, and different depth as indicated (after Rhode, 1993) (for details see text).

References

Bergamasco, L. and P. Picchi: Nuovo Cimento, 3 B, p. 134 (1971).

Bergamasco, L., A. Castellina, B. D'Ettorre Piazzoli, G. Mannocchi, P. Picchi, and S. Vernetto: Nuovo Cimento, 6C, p. 569 (1983).

Bethe, H.A., and W. Heitler: Proc. Roy. Soc., London, Ser. A 146, p. 83 (1934).

Bezrukov, L.B., and E.V. Bugaev: Yad. Phys., 33, p. 1195 (1981), or, Sov. J. Nucl. Phys., 33, p. 635 (1981).

Bollinger, I.M.: Ph. D. thesis, Cornell University (1951).

Bugaev, E.V., V.A. Naumov, and S.I. Sinegovsky: Sov. J. Nucl. Phys., 41, p. 245 (1985a).

Bugaev, E.V., V.A. Naumov, and S.I. Sinegovsky: Proc. of the Acad. of Sci. of the USSR. Phys, Ser. 49, p. 1389 (1985b).

Bugaev, Edgar V., Vadim A. Naumov, Sergey I. Sinegovsky, Akeo Misaki, Nobusuke Takahashi, and Elena S. Zaslavskaya: Proceedings of Nestor Workshop, p. 268 (1993).

Bugaev, Edgar V., Vadim A. Naumov, Sergey I. Sinegovsky, Akeo Misaki, Nobusuke Takahashi, and Elena S. Zaslavskaya: Università degli Studi di Firenze, Dipartimento di Fisica and Instituto Nationale di Fisica Nucleare Sezione di Firenza, Preprint DFF 204/4/1994 (1994).

Bugaev, E.V., A. Misaki, V.A. Naumov, T.S. Sinegovskaya, S.I. Sinegovsky, and N. Takahashi: Phys. Rev., D 58, p. 54001 (1998).

Castagnoli, C., A. Castellina, O. Saavedra, T.M. Kirina, R.P. Kokoulin, and A.A. Petrukhin: Phys. Rev., D 52, p. 2673 (1995).

Crispin, A., and G.N. Fowler: Rev. Mod. Phys., 42, p. 290 (1970).

Fano, U.: Ann. Rev. Nucl. Sci., 13, p. 1 (1963).

Grupen, C.: Fort. d. Phys., 23, p. 127 (1976).

Gurentsov, V.I., G.T. Zatsepin, and E.D. Mikhalchi: Sov. J. Nucl. Phys., 23, No 5 (1976).

Hayman, P.J., N.S. Palmer, and A.W. Wolfendale: Proc. Phys. Soc., 80, p. 800 (1962).

Hayman, P.J., N.S. Palmer, and A.W. Wolfendale: Proc. Roy. Soc., 275, p. 391 (1963).

Inazawa, H., and K. Kobayakawa: PICRC, 8, p. 83 (1985).

Kelner, S.R., and Yu.D. Kotov: Sov. J. Nucl. Phys., 7, p. 237 (1968).

Kobayakawa, K.: Nuovo Cimento 47B, p. 156 (1967).

Kokoulin, R.P., and A.A. Petrukhin: PICRC, 6, p. 2436 (1971).

Kotov, Yu.,D., and V.M. Logunov: Acta Phys. Acad. Sci. Hung., 29, Suppl. 4, p. 73 (1970).

Lipari, Paolo, and Todor Stanev: PICRC, 4, p. 411 (1993).

Lohmann, W., R. Kopp, and R. Voss: CERN Yellow Report 85-03 (1985).

Maeda, K.: VI.Inter-American Seminar on Cosmic Rays, La Paz, IV, p. 847 (1970).

Maeda, K.: Fortschr. Phys., 21, p. 113 (1973).

Makarov, V.V, A.A. Lgutin, A.G. Prokopets, and A.I. Goncharov: PICRC, 1, p. 630 (1995).

Mando, M., and P.G. Sona: Nuovo Cimento, 10, p. 1275 (1953).

Menon, M.G.K. and P.V. Ramana-Murthy: Progr. Elementary Particles and Cosmic Rays, North Holland, Amsterdam, 9, p. 161 (1967).

Minorikawa, Y., and K. Mitsui: PICRC, 8, p. 94 (1985).

Miyake, S., V.S. Narasimham, and P.V. Ramana Murthy: Nuovo Cimento, 32, p. 1505 (1964).

Miyake, S.: PICRC, 5, p. 3638 (1973).

Naumov, V.A., S.I. Sinegovsky, and E.V. Buhaev: Proc. 2nd. Internat. Nestor Workshop, Pylos, Greece, ed. L.K. Resvanis, University of Athens, p. 119 (1992).

Nishimura, J.: PICRC, 6, p. 224 (1964).

Petrukhin, A.A., and V.V. Shestakov: Can. J. Phys., 46, p. S377 (1968).

Rhode, Wolfgang: Ph. D. Thesis (Dissertation), Fachbereich Physik, Bergische Universität, Gesamthochschule Wuppertal, Germany. WUB-DIS 93-11 (1993).

Rossi, B: High Energy Particles, Prentice Hall, Englewood Cliffs, NJ (1952).

Rozenthal, I.L.: Usp. Phys. Nauk, 94, p. 91 (1968); Soviet Phys. Uspekhi 11, p. 49 (1968).

Sakumoto, W.K., P. de Barbaro, A. Bodek, H.S. Budd, B.J. Kim, F.S. Merritt, M.J. Oreglia, H. Schellman, B.A. Schumm, K.T. Bachmann, R.E. Blair, C. Foudas, B.J. King, W.C. Lefmann, W.C. Leung, S.R. Mishra, E. Oltman, P.Z. Quintas, S.A. Rabinowitz, F. Sciulli, W.G. Seligman, M.H. Shaevitz, R.H. Bernstein, F.O. Borcherding, H.E. Fisk, M.J. Lamm, W. Marsh, K.W. Merritt, P.H. Sandler, and W.H. Smith: Phys. Rev. D 45, p. 3042 (1992).

Sternheimer, R.M.: Phys. Rev., 103, p. 511 (1956).

Sternheimer, R.M., and R.F. Peierls: Phys. Rev., B 3, p. 3681 (1971).

Sternheimer, R.M, S.M. Seltzer, and M.R. Berger: Atomic and Nuclear Data Tables, 30, p. 261 (1984).

Tannenbaum, M.J.: CERN Preprint, CERN-PPE/91-134 (1991).

Tsai, Y.S.: Rev. Mod. Phys., 46, p 815 (1974).

Vavilov, Yu.N., Yu.A. Trubkin, and V.M. Fedorov: Sov. J. Nucl. Phys., 18, p. 434 (1974).

Wright, A.G.: J. Phys., A 6, p. 79 (1973).

Wright, A.G.: J. Phys. A, 7, p. 2085 (1974).

Zatsepin, G.T., and E.D. Mikhalchi: PICRC, 3, p. 356 (1962).

Zatsepin, G.T., and E.D. Mikhalchi (1965), quoted by Menon and Ramana Murthy (1967).

4.3 Muons Underground

4.3.1 General Comments

Underground measurements of cosmic ray muon intensities have been carried out under a variety of different conditions, such as different locations, depths, environmental conditions, using different detector types and geometries, and, most important, under different rock compositions. The statistics of the early experiments is generally rather poor because of very low counting rates due to small detector dimensions. Early data are therefore mutually not very consistent, also because of instrumental deficiencies (Stockel, 1967).

Since the late seventies and early eighties a number of ever larger detectors, such as NUSEX (NUcleon Stability EXperiment), LSD (Large Scintillation Detector), Baksan, Fréjus, IMB (Irvine - Michigan - Brookhaven), Kamiokande, LVD (Large Volume Detector), MACRO (Monopole Astrophysics Cosmic Ray Observatory), Soudan I and II, and others, came into operation and improved the muon data statistics significantly. Some of these detectors were originally designed for proton decay or neutrino experiments, and the search for monopoles and certain forms of dark matter. However, they all have excellent muon capabilities.

Apart from Superkamiokande that was commissioned in 1996, a new generation of freely expandable giant detectors are currently in the planning phase or under construction. They are chiefly designed as neutrino telescopes and employ the water masses of deep lakes, the deep ocean or the ice masses of the Earth's polar regions as Cherenkov medium for the detection of neutrino reaction products. As a bi-product of their principal goal, which is neutrino astronomy, they will improve the high energy muon data by orders of magnitude in the future.

Nevertheless, valuable data could be obtained from the early experiments. From these Miyake and others developed a number of empirical formulas that describe the depth - intensity relation, the zenith angle dependence and the energy spectrum of muons underground and underwater rather well on average (Miyake, 1963 and 1973). Theoretical aspects concerning these problems are summarized in Section 4.2. Results from underwater experiments are discussed and presented in Section 4.4. An excellent modern review covering theoretical as well as experimental topics of muon physics underground and underwater had been given by Bugaev et al. (1993 and 1994).

4.3.2 Rock Composition, Standard Rock and Conversion Formula

The energy spectrum of muons incident upon the Earth at sea level at energies on the order of a few tens of GeV is more or less a global constant. Depending on the nature of the medium which acts as an absorber the incident spectrum will lead to different range spectra. At low energies the energy losses of muons are dominated by atomic collision processes and ionization which depend mainly on the average value of Z/A of the target, Z being the electric charge and A the atomic mass. Since the average Z/A for most of the rocks is within a few percent of 0.50, the effective thickness or depth, X, of different rocks can all be considered equivalent up to thicknesses of $\sim 1.5 \cdot 10^5$ g cm^{-2}. Depth under water, however, requires a correction of the order of 10% since Z/A of water is 0.555.

At great depth ($X \geq 1.5 \cdot 10^5$ g cm^{-2}), the situation is different. At the high energies that are relevant at these depths, the energy losses of muons are dominated by pair production and bremsstrahlung. These depend on the average Z^2/A of the medium in which the muons propagate. Since the values for the average Z^2/A of rocks from different sites deviate considerably, it is necessary to consider this ratio when comparing data from different experiments.

To simplify matters, intensities are usually converted to intensities under *standard rock* (Mandò and Ronchi, 1952; Menon and Ramana Murthy, 1967). Depth is expressed in [g cm^{-2}] of overburden. Frequently depth is also expressed in *meters water equivalent*, [m w.e.]. To simplify matters even more, it is customary to express depth as well as slant depth underground in *hectograms per square centimeter*, [hg cm^{-2}] (1 hg cm^{-2} = 100 g cm^{-2}, and 1 hg cm^{-2} of water corresponds to a column of 1 m of water).

Standard Rock, Definition

Standard rock (SR) is defined as rock consisting of atoms of an average atomic charge Z = 11 and an average atomic mass A = 22, with Z/A = 0.5, Z^2/A = 5.5 and density ρ = 2.650 g cm^{-3} (Bollinger, 1951; Barrett et al., 1952; Hayman and Wolfendale 1963; Menon and Ramana Murty 1967). Note that some early workers have used values of Z = 10, A = 20, ρ = 2.9 g cm^{-3} (George, 1952), and Z = 12, A = 24, ρ = 2.6 g cm^{-3} (Mandò and Ronchi, 1952), to normalize underground data from different sites.

The average values of Z/A and Z^2/A of a medium are defined as

$$Z/A = \sum_i f_i Z_i/A_i \quad (4.27) \quad \text{and} \quad Z^2/A = \sum_i f_i Z_i^2/A_i \quad (4.28)$$

respectively, where Z_i, A_i, and f_i are the atomic number, atomic weight and fractional weight, respectively, of the i-th element present in the medium,

$$f_i = A_i / \sum_i A_i \,. \quad (4.29)$$

Rock Conversion Formula and Underground / Underwater Intensity Relation

Most muon measurements underground are carried out under different environmental conditions. In particular, the rock composition of the overburden varies from experiment to experiment and must be carefully accounted for when comparing data from different sites. Table 4.2 lists the relevant rock parameters of some experimental sites.

Many authors have studied the problem of muon propagation in different media and for different energy regions and have derived formulas to convert data from one kind of rock to another. The widely accepted and extensively used conversion formula given below converts depth in rock characterized by Z and A, $X_{Z,A}$, to depth in standard rock, X_{SR}, with $Z = 11$ and $A = 22$ (Menon and Ramana Murthy, 1967).

$$X_{SR} = \frac{1}{b_{SR}} \ln\left(1 + \frac{b_{SR}}{b_{Z,A}}\left(e^{(b_{Z,A}X_{Z,A})} - 1\right)\right) \quad (4.30)$$

Here b_{SR} and $b_{Z,A}$ are the energy proportional terms in the energy loss equation for muons appropriate for standard rock with $Z = 11$, $A = 22$, and arbitrary rock with Z and A. The a-term which accounts for the ionization losses is disregarded since it is practically the same for all rocks.

Equation 4.30 is a reasonable approximation because the b-terms are only weakly energy dependent. Computing muon ranges by numerical integration of the energy loss formula using the energy dependent functions $a(E)$ and $b(E)$ yields more accurate values (for details see Section 4.2 where some theoretical background and references are given). Results obtained from calculations by Kotov and Logunov (1970), and Wright (1973) are given in Fig. 4.11, which shows the conversion factor, $F(X, Z, A)$, given as

$$F(X, Z, A) = \frac{X_{SR}}{X_{Z,A}} = \frac{X(E, 11, 22)}{X(E, Z, A)} \,, \quad (4.31)$$

Table 4.2: Rock Parameters of Underground Sites / Water Parameters. (for Depths of Sites see Appendix, Table C.5)

Site	$< \rho >$	<Z>	<A>	Z/A	Z^2/A	Ref.
Baksan	2.74±0.01	11.9	24.04	0.495	5.89	1)
CWI*	2.71	11.08	22.21	0.499	5.53	2)
Fréjus	2.74	10.12	20.34	0.498	5.035	3)
Gotthard	2.645±0.015	-	-	-	-	4)
Gran Sasso	2.71	11.41	22.88	0.499	5.69	5)
Homestake	2.84	10.0	-	-	-	6)
IMB*	2.39	11.8	23.6	0.5	5.90	7)
Ithaca	2.65	12.6	25.2	0.50	6.3	8)
KGF*	3.02	12.62	25.24	0.495	6.31	9)
KGF*	3.02	13.13	26.53	0.495	6.50	10)
LSGM*	2.73	11.4	22.8	0.50	5.7	11)
Mont Blanc	2.60	10.34	20.94	0.494	5.12	12)
Mont Blanc	2.68	10.36	20.94	0.494	5.11	13)
Nagoya	2.67	11.475	23.18	0.495	5.68	14)
Shimizu	2.8	-	-	-	-	15)
Soudan II	2.74	12.56	25.15	0.499	6.273	16)
Utah	2.55±0.04	11	22	0.50	5.50	17)
Standard Rock	2.650	11.0	22.0	0.50	5.50	18)
H_2O	1.00	6.66	12.01	0.555	3.7	19)
Sea Water (Pacific Hawaii) salinity 3.45 %	1.027	7.433	14.787	0.553	3.26	20) 21)

* CWI Case-Witwatersrand-Irvine, South Africa; IMB Irvine-Michigan-Brookhaven, USA; KGF Kolar Gold Fields, India; LSGM Lake Shore Gold Mine Ontario, CND.
1) Alexeyev, et al. (1979a and 1979b), Andreyev, et al. (1987); 2) Reines et al. (1965), Reines (1967), Meyer et al. (1970); 3) Rhode (1993); 4) Czapek et al. (1990); 5) Ambrosio, et al. (1993, 1995), Kudryavtsev et al. (1995); 6) Cherry (2000); 7) Svoboda (1985); 8) Bollinger (1951); 9) Menon (1967), Miyake et al. (1964); 10) Menon et al. (1968); 11) Barton (1961); 12) Castagnoli et al. (1965); 13) Baschiera et al. (1979); 14) Mizutani and Ohta (1975), Mizutani et al. (1979) (Okutadami Tunnel); 15) Miyazaki (1949); 16) DeMuth (1999), Goodman (2000); 17) Cassiday et al. (1971), Bergeson et al. (1973); 18) Menon and Ramana Murthy (1967); 19) Rogers and Tristam (1984); 20) Hasted et al. (1948); 21) Turekian, K.K., (1969).
For full references see end of section.

where E stands for the energy that enters via the b-terms of eq. 4.30.

Thus depth in a medium consisting of matter with Z and A must be

multiplied by this factor to convert it to depth in standard rock. The deviation between curves a and b of Fig. 4.11 at shallow depths is believed to arise because of the use of the approximate Sternheimer formula by Kotov and Logunov (1970) in place of the complete formula quoted by Barton and Stockel (1969). The significantly lower values of curve c are probably due to poor parameter choice.

4.3.3 Depth-Intensity Relations and Data

The intensity of muons as a function of depth underground can be calculated from our knowledge of the sea level muon spectrum and the physics of muon propagation and interactions in rock or other media, provided that we know the relevant physical parameters of these media. The basic equations to carry out such calculations are summarized in Section 4.2. Additional details for further study of the subject can be found in the references listed there.

Empirical Depth-Intensity Relations

At a vertical depth, X, underground the vertical intensity of muons can be calculated with the widely used empirical formula of Miyake (1963).

$$I(X,0^\circ) \;=\; (X+a)^\alpha \left(\frac{K}{X+H}\right) e^{-(\beta X)} \quad . \tag{4.32}$$

This is the original formula. It has the three important features built in, namely: (i) the low energy muon spectrum from a few GeV to a few tens of GeV, reflecting the pion and kaon production spectrum which is relevant at shallow depths, where the first term dominates; (ii) the changing slope of the muon spectrum around 100 GeV, reflecting the rising importance of nuclear interactions for the muon parents in the competition between decay and interaction, where the first two terms dominate; (iii) the domain where the energy losses are proportional to the muon energy and the exponential term dominates.

Frequently a slightly simplified version of this equation, also known as Miyake's formula, but without parameter a and with appropriately adjusted constants, is used by many authors (Menon and Ramana Murthy, 1967). Thus,

$$I(X,0^\circ) \;=\; B\,\frac{X^\alpha}{(X+H)}\,e^{-(\beta X)} \quad . \tag{4.33}$$

At small depths this relation reduces essentially to a power law, and at very great depths ($X > 4000$ m w.e.) to an exponential law.

Referring to eq. 4.32 the parameters a, H, K, α and β are constants to be adjusted to fit the experimental data. At the Kolar Gold Fields installations the following values were frequently used in early days: $a = 11$, $H = 400$, $K = 174$, $\alpha = 1.53$, and $\beta = 8.0 \cdot 10^{-4}$. X is measured from the top of the atmosphere in units of [hg cm^{-2}] or in meters of water equivalent [m w.e.], and the intensity is given in units of [cm^{-2}s^{-1}sr^{-1}]. With the above values inserted eq. 4.32 takes the form

$$I(X, 0°) = \frac{174}{X + 400}(X + 10)^{-1.53}\, e^{-8.0 \cdot 10^{-4} X} \quad [\mathrm{cm^{-2}s^{-1}sr^{-1}}] \,. \qquad (4.34)$$

This formula is valid for depth $X \geq 100$ hg cm^{-2} of standard rock. A more refined expression that covers the depth range from 10 to 10^4 hg cm^{-2} was obtained by Barbouti and Rastin (1983) which reads

$$I(X, 0°) = \left(\frac{K}{(X^{\alpha} + a)(X + H)}\right) e^{-(\beta X)} \quad [\mathrm{cm^{-2}s^{-1}sr^{-1}}] \,. \qquad (4.35)$$

The values of the different parameters are as follows: $a = 75$, $H = 200$ hg cm^{-2}, $K = 270.7$ hg cm^{-2}, $\alpha = 1.68$, and $\beta = 5.5 \cdot 10^{-4}$ hg^{-1} cm^2, with X in hg cm^{-2} of standard rock and the intensity $I(0°, X)$ in [cm^{-2}s^{-1}sr^{-1}].

At very large depths ($X \geq 4 \cdot 10^3$ hg cm^{-2}), the vertical depth-intensity relation can be approximated with the expression (Menon et al., 1967; Meyer et al., 1970; Miyake, 1973)

$$I(X, 0°) = A\, e^{-X/\Lambda} \quad [\mathrm{cm^{-2}s^{-1}sr^{-1}}] \,, \qquad (4.36)$$

where A is a constant. However, different experiments yield different values for A and Λ, and Λ may depend on X in some cases, as shown in Table 4.3. More recent fits to experimental data are given by eqs. 4.37 and 4.38 below and the relations for inclined muon trajectories with zenith angles $0° < \theta \leq 90°$ in Subsection 4.3.4.

Exploratory and Early Experimental Data

A compilation of *absolute vertical intensities* obtained with different experiments underground during the period from 1951 to 1970 was made by Crookes and Rastin (1973) and is given in Table 4.4. Also indicated in the table is the technique that was used. With the exception of the data by Sreekantan and Naranan (1952) the data are from *direct vertical measurements* and do not include converted data from inclined measurements. Note that depth is

Table 4.3: Values of A and Λ of eq. 4.36 for Different Depths X.

X [hg cm^{-2}]	A [cm^{-2}s^{-1}sr^{-1}]	Λ [hg cm^{-2}]	References
4000	$0.98 \cdot 10^{-6}$	810±50	Menon et al. (1967)
4000 to 9000	$1.04^{+0.21}_{-0.13} \cdot 10^{-6}$	804^{+35}_{-39}	Meyer et al. (1970)
3900 to 10000	$(7.63 \pm 0.48) \cdot 10^{-7}$	810.44 ± 0.84	Battistoni et al. (1985)
3000	-	625*	Miyake (1973)
4000	-	700*	
6000	-	825*	
10000	-	900*	

* These values are also used in the expression for the zenith angle distribution given by Miyake (1973) (see eq. 4.43, Subsection 4.3.4).

measured from the top of the atmosphere. For the depth range from 10 to 10^3 hg cm^{-2} the flux values are also illustrated in Fig. 4.12.

On the other hand, Table 4.5 contains a list of vertical muon intensities obtained with different experiments from *inclined measurements*. The resulting data were converted to vertical intensities by considering the slant depth in the rock, as discussed in Subsection 4.3.4 below, and the sec(θ) enhancement of energetic muons in the atmosphere, described in Sections 2.6 and 3.6 (Menon and Ramana Murthy, 1967). For completeness the directly measured vertical intensities obtained at the respective levels are also listed in the table.

An early world survey by Menon and Ramana Murthy (1967) including data from experiments carried out between 1938 and 1964 is given in Fig. 4.13 and a quick reference of vertical intensities at a few standard depths in Table 4.6.

At shallow to moderate depths under rock measurements had been made by Krishnaswamy et al. (1968), Stockel (1969), Bergamasco and Picchi (1971), Crookes and Rastin (1972), and Wright (1973, 1974). The results are shown in Fig. 4.14 together with some data from great depths by Miyake

Table 4.4: Absolute Vertical Muon Intensities (Crookes and Rastin, 1973).

Authors Apparatus	Depth Below Top of Atmosphere [hg cm^{-2}]	Absolute Vertical Intensity [cm^{-2}s^{-1}sr^{-1}]
Randall and Hazen (1951) Geiger counters in two-fold coincidence.	860	$(2.17 \pm 0.02) \cdot 10^{-6}$
Bollinger (1951) Hodoscoped Geiger counters operated in conjunction with a two-fold Geiger coincidence.	1510 1850	$(3.90 \pm 0.08) \cdot 10^{-7}$ $(1.91 \pm 0.04) \cdot 10^{-7}$
Sreekantan and Naranan (1952) Hodoscoped Geiger counters plus two-fold Geiger coincidence.*	110 391 485 694 895	$(2.87 \pm 0.23) \cdot 10^{-4}$ $(1.76 \pm 0.24) \cdot 10^{-5}$ $(1.24 \pm 0.13) \cdot 10^{-5}$ $(5.55 \pm 0.70) \cdot 10^{-5}$ $(2.37 \pm 0.27) \cdot 10^{-6}$
Barrett et al. (1952) Hodoscoped Geiger counters plus four-fold Geiger coincidence.	1584	$(3.25 \pm 0.05) \cdot 10^{-7}$
Avan and Avan (1955) Photographic emulsion.	310 590 1290	$(3.80 \pm 0.17) \cdot 10^{-5}$ $(7.3 \pm 0.4) \cdot 10^{-6}$ $(8.0 \pm 0.6) \cdot 10^{-7}$

* Calculated from $I(0) = I(\theta)/\cos^n(\theta)$ with $n = 3$ at 110 hg cm^{-2} and $n = 4$ at all other depths.

et al. (1964), Menon et al. (1968) and Meyer et al. (1970). The depth is measured from the top of the atmosphere. For comparison, underwater measurements carried out by Higashi et al. (1966) and Davitaev et al. (1970) that are discussed in greater detail in Section 4.4 are presented in Fig. 4.15 with the depth converted to and expressed in hg cm^{-2} of standard rock. The depth is again given from the top of the atmosphere.

Bergamasco et al. (1971) have been carrying out measurements at a particular site in the Mont Blanc tunnel that allowed to cover a depths range from 50 m w.e to 4330 m w.e.. At this site the rock parameters are fairly well known. (see Table 4.2). The results of this work are shown in Table 4.7.

Table 4.4: Absolute Vertical Muon Intensities (Crookes and Rastin, 1973). (continued)

Authors Apparatus	Depth Below Top of Atmosphere [hg cm^{-2}]	Absolute Vertical Intensity [cm^{-2}s^{-1}sr^{-1}]
Miyake et al. (1964) Coincidence from two layers of plastic scintillators.	833 1888	$(2.51 \pm 0.15) \cdot 10^{-6}$ $(1.77 \pm 0.07) \cdot 10^{-7}$
Castagnoli et al. (1965) Two narrow-angle telescopes each involving a coincidence between plastic scintillators.	149 299 1319	$(1.70 \pm 0.04) \cdot 10^{-4}$ $(4.60 \pm 0.01) \cdot 10^{-5}$ $(5.60 \pm 0.07) \cdot 10^{-7}$
Achar et al. (1965a, b) Plastic scintillation detector plus neon flash tubes.	826 1881	$(2.39 \pm 0.15) \cdot 10^{-6}$ $(2.00 \pm 0.12) \cdot 10^{-7}$
Krishnaswamy et al. (1968) Plastic scintillation detector plus crossed neon flash tubes.	764 1510	$(2.7 \pm 0.1) \cdot 10^{-6}$ $(3.4 \pm 0.1) \cdot 10^{-7}$
Stockel (1969) Telescope employing two trays of Geiger counters and a plastic scintillation counter.	71.6 734 1068	$(5.00 \pm 0.17) \cdot 10^{-4}$ $(3.12 \pm 0.15) \cdot 10^{-6}$ $(1.03 \pm 0.04) \cdot 10^{-6}$
Sheldon et al. (1970) A hodoscoped arrangement of three trays of crossed Geiger counters operating in six-fold coincidence.	890	$(1.65 \pm 0.09) \cdot 10^{-6}$

A vertical depth-intensity distribution for moderate to large depths measured at the Utah laboratory is shown in Fig. 4.16 (Cassiday et al. 1971; Cannon and Stenerson, 1971).

In the CWI (Case-Witwatersrand-Irvine) laboratory, located under 8890 hg cm^{-2} of standard rock, the vertical muon intensity had been determined over a very large depth range from measurements carried out at different inclinations with respect to the vertical, i.e., at different slant depths (Crouch

Table 4.5: Summary of Early Muon Intensity Measurements Underground. (Menon and Ramana Murthy, 1967)

Authors Location	Depth from Top of Atmosphere [hg cm^{-2}] actual rock	Vertical Intensity [cm^{-2} s^{-1} sr^{-1}]	Depth from Top of Atmosphere [hg cm^{-2}] standard rock
Miyazaki (1949) [a]	1410	$5.0 \cdot 10^{-7}$	-
Shimizu Tunnel	3010	$(1.7 \pm 0.25) \cdot 10^{-8}$	-
Bollinger (1951) [b]	1510	$3.90 \cdot 10^{-7}$	1510
Ithaca Salt Mine	1850	$1.91 \cdot 10^{-7}$	1850
Intensities	1577	$3.30 \cdot 10^{-7}$	1577
computed from	1965	$(1.2 \pm 0.1) \cdot 10^{-7}$	1965
inclined	2155	$(7.7 \pm 0.8) \cdot 10^{-8}$	2155
measurements	2445	$(4.8 \pm 0.6) \cdot 10^{-8}$	2445
at 1510 m	2170	$(2.8 \pm 0.4) \cdot 10^{-8}$	2170
	3150	$(1.5 \pm 0.3) \cdot 10^{-8}$	3150
	3785	$(7.2 \pm 1.8) \cdot 10^{-9}$	3785
	4650	$(2.9 \pm 1.1) \cdot 10^{-9}$	4650
	6800	$(2.8 \pm 1.9) \cdot 10^{-10}$	6800
Intensities	1915	$1.59 \cdot 10^{-7}$	1915
computed from	2030	$1.19 \cdot 10^{-7}$	2030
inclined	2160	$9.8 \cdot 10^{-8}$	2160
measurements	2470	$6.3 \cdot 10^{-8}$	2470
at 1850 m	2805	$4.1 \cdot 10^{-8}$	2805
	2905	$2.7 \cdot 10^{-8}$	2905
	3330	$(1.1 \pm 0.2) \cdot 10^{-8}$	3330
	4000	$(6.5 \pm 1.1) \cdot 10^{-9}$	4000
	5130	$(1.2 \pm 0.3) \cdot 10^{-9}$	5130
	8560	$(1.6^{+1.4}_{-0.7}) \cdot 10^{-10}$	8560

[a] The counting rates given by Miyazaki have been normalized at 1400 hg cm^{-2} of rock with the smooth curve in Fig. 4.13. The rock composition is unknown.

[b] The vertical cosmic ray intensities have been obtained after applying the necessary corrections, as discussed in the text, from the angular distribution experiments carried out at depths of 1510 hg cm^{-2} and 1850 hg cm^{-2} of rock from the top of the atmosphere.

Table 4.5: Summary of Early Muon Intensity Measurements Underground. (Menon and Ramana Murthy, 1967) (continued)

Authors Location	Depth from Top of Atmosphere [hg cm^{-2}] actual rock	Vertical Intensity [cm^{-2} s^{-1} sr^{-1}]	Depth from Top of Atmosphere [hg cm^{-2}] standard rock
Barton (1961)	1670	$(2.27 \pm 0.24) \cdot 10^{-7}$	1690
Lake Shore	3290	$(8.1 \pm 2.4) \cdot 10^{-9}$	3350
Gold Mine (CND)	5060	$< 2.0 \cdot 10^{-9}$	5160
Miyake et al.	816	$(2.51 \pm 0.15) \cdot 10^{-6}$	833
(1964)	1812	$(1.77 \pm 0.07) \cdot 10^{-7}$	1888
Kolar Gold	3410	$(1.42 \pm 0.14) \cdot 10^{-8}$	3690
Fields	4280	$(3.24 \pm 0.35) \cdot 10^{-9}$	4570
	6380	$(1.92 \pm 0.47) \cdot 10^{-10}$	6930
	8400	$\leq 10^{-11}$	9210
Castagnoli et	149	$(1.70 \pm 0.04) \cdot 10^{-4}$	149
al. (1965)	299	$(4.60 \pm 0.01) \cdot 10^{-5}$	299
Mont Blanc	1334	$(5.60 \pm 0.07) \cdot 10^{-7}$	1319
Tunnel	4109 ± 110	$(1.00 \pm 0.23) \cdot 10^{-8}$	4009

et al., 1978). (We note that slightly different vertical depths are specified for the CWI experiment in different publications.) At very large depths the muon flux is due to neutrino induced reactions. This is illustrated in Fig. 4.17.

More recent vertical muon intensity measurements at shallow rock depths in the range from 20 to 223 hg cm^{-2} have been carried out by Liu-Zhong-he et al. (1979). These data are shown in Fig. 4.18. Similarly, Barbouti and Rastin (1983) made absolute intensity measurement at Nottingham (40 m a.s.l.), also at shallow depth, under homogeneous absorbers such as lead and iron of different but well defined thicknesses and converted the data to equivalent standard rock overburdens. The results are given in Table 4.8. They are also included in the compilation of underground muon intensities of Fig. 4.19 that covers the period from 1952 to 1983. This figure is complementary to Fig. 4.13.

Starting with the primary energy spectrum the vertical muon depth-

Table 4.6: Composite Vertical Muon Intensity Versus Depth Based on Early Experimental Data. (Menon and Ramana Murthy, 1967)

Depth below Top of Atmosphere [hg cm $^{-2}$] (Standard Rock)	Vertical Intensity [$cm^{-2} s^{-1} sr^{-1}$]
100	$2.70 \cdot 10^{-4}$
200	$7.40 \cdot 10^{-5}$
400	$1.56 \cdot 10^{-5}$
700	$4.00 \cdot 10^{-6}$
1000	$1.46 \cdot 10^{-6}$
2000	$1.53 \cdot 10^{-7}$
4000	$8.60 \cdot 10^{-9}$
7000	$1.80 \cdot 10^{-10}$
9000	$\leq 10^{-11}$

Table 4.7: Vertical Muon Intensities in the Mont Blanc Tunnel. Depth is Measured in m w.e. from Top of Atmosphere. (Bergamasco et al., 1971)

Depth [m w.e]	Vertical Intensity [$cm^{-2} s^{-1} sr^{-1}$]
50	$(2.36 \pm 0.02) \cdot 10^{-4}$
106	$(2.36 \pm 0.02) \cdot 10^{-4}$
158	$(1.20 \pm 0.01) \cdot 10^{-4}$
238	$(5.00 \pm 0.05) \cdot 10^{-5}$
4270	$(4.79 \pm 0.23) \cdot 10^{-9}$

intensity curve had been calculated and compared with measurements by O'Brien (1972). The result is shown in Fig. 4.20.

A world survey of vertical underground muon intensities made by Crouch (1985 and 1987) is presented in Figs. 4.21 and 4.22, and in Table 4.9. All data are converted to standard rock and measurements made at large angles are corrected for the Earth's curvature. Fig. 4.21 covers a very large depth

Table 4.8: Absolute Vertical Muon Intensities under Different Absorbers Measured at 40 m a.s.l. (Barbouti and Rastin, 1983).

Depth Below Top of Atmosphere in Standard Rock [hg cm^{-2}]	Absorber Thickness Pb-equivalent [hg cm^{-2}]	Absolute Vertical Intensity [cm^{-2}s^{-1}sr^{-1}]
11.62*	1.85 ± 0.01	$(9.13 \pm 0.12) \cdot 10^{-3}$
12.12	2.59 ± 0.01	$(8.87 \pm 0.12) \cdot 10^{-3}$
14.32	5.54 ± 0.01	$(7.66 \pm 0.09) \cdot 10^{-3}$
19.28	12.23 ± 0.01	$(5.56 \pm 0.06) \cdot 10^{-3}$
24.24	18.73 ± 0.01	$(4.15 \pm 0.05) \cdot 10^{-3}$
29.06	25.04 ± 0.01	$(3.20 \pm 0.04) \cdot 10^{-3}$
47.72**	33.0 ± 0.1	$(1.40 \pm 0.02) \cdot 10^{-3}$
52.42**	37.7 ± 0.1	$(1.19 \pm 0.06) \cdot 10^{-3}$

* Crookes and Rastin (1972); ** Crookes and Rastin (1973).

range to almost $2 \cdot 10^5$ hg cm^{-2} in double-logarithmic representation and includes a large depth region where neutrino induced muons only are present. The figure also includes some data points from underwater measurements by Fyodorov et al. (1985). The smooth curve which gives a good fit to the data is described by the following expression.

$$I(X, 0°) = e^{(A_1 + A_2 X)} + e^{(A_3 + A_4 X)} + A_5 \ \ [\mathrm{cm}^{-2}\mathrm{s}^{-1}\mathrm{sr}^{-1}] \ , \qquad (4.37)$$

where $A_1 = -11.24 \pm 0.18$, $A_2 = -0.00264 \pm 0.00014$, $A_3 = -13.98 \pm 0.14$, $A_4 = -0.001227 \pm 0.000021$, $A_5 = (2.18 \pm 0.21) \cdot 10^{-13}$, and X is in hg cm^{-2}.

Fig. 4.22 shows partly the same data in semi-logarithmic representation over a smaller depth range down to the beginning of the region where neutrino induced muons are dominating. Also shown in the same figure are results from calculations by Bugaev et al. (1993 and 1994) that are based on different muon production processes, mentioned in the caption.

Figure 4.23 is a compilation of data from many experiments at the Kolar Gold Fields, including some more recent work. The data are again compared with results from some of the model calculations of Bugaev et al. (1993 and 1994).

Table 4.9: World Survey of Vertical Muon Depth-Intensity Data in Standard Rock (Crouch, 1987).

Depth [hg cm^{-2}]	Intensity [cm^{-2}s^{-1}sr^{-1}])	Error	Reference
1068	$1.03 \cdot 10^{-6}$	$5.07 \cdot 10^{-8}$	Stockel (1969)
1500	$3.90 \cdot 10^{-7}$	$1.46 \cdot 10^{-8}$	Bollinger (1951)
1535	$3.40 \cdot 10^{-7}$	$1.51 \cdot 10^{-8}$	Krishnaswamy et al. (1970a)
1574	$3.31 \cdot 10^{-7}$	$1.17 \cdot 10^{-8}$	Barrett et al. (1952)
1840	$1.91 \cdot 10^{-7}$	$7.71 \cdot 10^{-9}$	Bollinger (1951)
1853	$2.00 \cdot 10^{-7}$	$1.36 \cdot 10^{-8}$	Achar et al. (1965a, b)
1853	$1.77 \cdot 10^{-7}$	$9.52 \cdot 10^{-9}$	Miyake et al. (1964)
2235	$9.70 \cdot 10^{-8}$	$6.11 \cdot 10^{-9}$	Stockel (1969)
2622	$3.10 \cdot 10^{-8}$	$5.70 \cdot 10^{-9}$	Fyodorov et al. (1985)
3493	$5.90 \cdot 10^{-9}$	$2.30 \cdot 10^{-9}$	Fyodorov et al. (1985)
3534	$1.15 \cdot 10^{-8}$	$8.01 \cdot 10^{-10}$	Krishnaswamy et al. (1970a)
3562	$1.42 \cdot 10^{-8}$	$1.53 \cdot 10^{-9}$	Miyake et al. (1964)
4255	$4.10 \cdot 10^{-9}$	$2.00 \cdot 10^{-9}$	Fyodorov et al. (1985)
4312	$4.63 \cdot 10^{-9}$	$6.23 \cdot 10^{-10}$	Achar et al. (1965a, b)
4508	$3.24 \cdot 10^{-9}$	$4.04 \cdot 10^{-10}$	Miyake et al. (1964)
6808	$1.92 \cdot 10^{-10}$	$4.97 \cdot 10^{-11}$	Miyake et al. (1964)
7486	$1.10 \cdot 10^{-10}$	$2.15 \cdot 10^{-11}$	Krishnaswamy et al. (1971a)
8742	$1.87 \cdot 10^{-11}$	$3.05 \cdot 10^{-12}$	Meyer et al. (1970)
9141	$1.13 \cdot 10^{-11}$	$6.30 \cdot 10^{-12}$	
9358	$1.36 \cdot 10^{-11}$	$3.60 \cdot 10^{-12}$	
9660	$4.59 \cdot 10^{-12}$	$1.30 \cdot 10^{-12}$	
10060	$3.77 \cdot 10^{-12}$	$8.90 \cdot 10^{-13}$	
10580	$2.56 \cdot 10^{-12}$	$5.90 \cdot 10^{-13}$	
11250	$9.07 \cdot 10^{-13}$	$2.90 \cdot 10^{-13}$	
12100	$6.84 \cdot 10^{-13}$	$2.00 \cdot 10^{-13}$	
13210	$3.48 \cdot 10^{-13}$	$1.20 \cdot 10^{-13}$	Crouch et al. (1978)
14660	$2.57 \cdot 10^{-13}$	$8.90 \cdot 10^{-14}$	
16610	$2.34 \cdot 10^{-13}$	$7.70 \cdot 10^{-14}$	
19320	$1.67 \cdot 10^{-13}$	$6.00 \cdot 10^{-14}$	
23300	$2.81 \cdot 10^{-13}$	$7.20 \cdot 10^{-14}$	
29620	$2.15 \cdot 10^{-13}$	$5.90 \cdot 10^{-14}$	
41050	$1.87 \cdot 10^{-13}$	$5.20 \cdot 10^{-14}$	
67440	$1.88 \cdot 10^{-13}$	$4.90 \cdot 10^{-14}$	
182700	$2.61 \cdot 10^{-13}$	$5.40 \cdot 10^{-14}$	

Data from Modern Mostly Large Experiments

In the late seventies and early eighties a number of new, mostly large deep underground experiments came into operation. Some of these were initially designed and optimized for a particular task, such as proton decay studies, supernova watch, monopole and dark matter searches, cosmic ray muon physics, and neutrino investigations of various kinds. Others were intended to be more multipurpose instruments that could tackle a variety of problems simultaneously. Consequently different techniques were employed for different detectors but all have muon detection capability.

Since some of these detectors have very large dimensions they can explore the spectral and other features of the cosmic ray muon component to much higher energies and with far better statistics than their predecessors. In the following we summarize the data from the different experiments.

In Fig. 4.24 we show vertical muon depth-intensity data that were computed from measurements made with the Baksan underground installation in Russia at different zenith angles, as indicated, and different azimuthal angles (Andreyev et al., 1987 and 1990). Similarly, the results from the NUSEX (NUcleon Stability EXperiment) (Aglietta et al., 1990a), Gotthard (Czapek et al., 1990) and Fréjus (Berger et al., 1989a, 1989b and 1990) experiments are shown in Fig. 4.25. We have added to both figures the results from the prediction by Bugaev et al. (1994), mentioned previously, for comparison. A more detailed display of the Fréjus results can be found in Fig. 4.36 of Subsection 4.3.5, where measurements on through-going and stopping muons in the Fréjus detector are discussed, and likewise in Fig. 4.87 of Section 4.5 where similar data on neutrino induced muons are presented.

Recent data from measurements made with the LVD at Gran Sasso are illustrated in Fig. 4.26 (Aglietta et al., 1995a; Giusti et al., 1995; Sartorelli et al., 1995 and Aglietta et al., 1997). Shown are the slant depth intensities as well as the vertical intensities. The difference of the respective intensities is a measure of the fraction of directly produced muons.

Precision measurements of the muon intensities underground were made with the MACRO detector, covering the slant depth range from 3200 hg cm^{-2} to 6950 hg cm^{-2}. The results were converted in the usual manner to vertical intensities and are listed in Table 4.10. A very recent compilation of depth-intensity data of many of the large new experiments, including Baksan, Fréjus, LVD, MACRO, NUSEX, Soudan I and II, and the old Cornell data, is shown in Figs. 4.27 and 4.28 (Ambrosio et al., 1995 and 1996).

The vertical depth intensity data of these experiments can be described

Table 4.10: Vertical Muon Intensities Measured with the MACRO Detector. (Ambrosio et al., 1995)

Depth [hg cm^{-2}] SR	$I(h) \pm \Delta I(h)$ [cm^{-2} s^{-1} sr^{-1}]	Depth [hg cm^{-2}] SR	$I(h) \pm \Delta I(h)$ [cm^{-2} s^{-1} sr^{-1}]
3200	$(2.00 \pm 0.01) \cdot 10^{-8}$	4550	$(3.29 \pm 0.07) \cdot 10^{-9}$
3250	$(1.85 \pm 0.01) \cdot 10^{-8}$	4600	$(3.05 \pm 0.07) \cdot 10^{-9}$
3300	$(1.73 \pm 0.01) \cdot 10^{-8}$	4650	$(2.92 \pm 0.04) \cdot 10^{-9}$
3350	$(1.59 \pm 0.01) \cdot 10^{-8}$	4700	$(2.72 \pm 0.06) \cdot 10^{-9}$
3400	$(1.48 \pm 0.01) \cdot 10^{-8}$	4762	$(2.61 \pm 0.04) \cdot 10^{-9}$
3450	$(1.39 \pm 0.01) \cdot 10^{-8}$	4850	$(2.32 \pm 0.06) \cdot 10^{-9}$
3500	$(1.30 \pm 0.01) \cdot 10^{-8}$	4950	$(2.02 \pm 0.06) \cdot 10^{-9}$
3550	$(1.215 \pm 0.008) \cdot 10^{-8}$	5050	$(1.86 \pm 0.03) \cdot 10^{-9}$
3600	$(1.144 \pm 0.008) \cdot 10^{-8}$	5150	$(1.60 \pm 0.04) \cdot 10^{-9}$
3650	$(1.058 \pm 0.007) \cdot 10^{-8}$	5250	$(1.40 \pm 0.02) \cdot 10^{-9}$
3700	$(1.000 \pm 0.007) \cdot 10^{-8}$	5350	$(1.28 \pm 0.04) \cdot 10^{-9}$
3750	$(9.44 \pm 0.07) \cdot 10^{-9}$	5450	$(1.05 \pm 0.03) \cdot 10^{-9}$
3800	$(8.85 \pm 0.06) \cdot 10^{-9}$	5550	$(9.6 \pm 0.2) \cdot 10^{-10}$
3850	$(8.23 \pm 0.06) \cdot 10^{-9}$	5650	$(8.7 \pm 0.2) \cdot 10^{-10}$
3900	$(7.73 \pm 0.07) \cdot 10^{-9}$	5750	$(7.5 \pm 0.1) \cdot 10^{-10}$
3950	$(7.20 \pm 0.07) \cdot 10^{-9}$	5850	$(6.8 \pm 0.2) \cdot 10^{-10}$
4000	$(6.75 \pm 0.06) \cdot 10^{-9}$	5950	$(5.8 \pm 0.5) \cdot 10^{-10}$
4050	$(6.37 \pm 0.06) \cdot 10^{-9}$	6050	$(5.2 \pm 0.3) \cdot 10^{-10}$
4100	$(5.88 \pm 0.06) \cdot 10^{-9}$	6150	$(4.6 \pm 0.2) \cdot 10^{-10}$
4150	$(5.49 \pm 0.06) \cdot 10^{-9}$	6250	$(4.3 \pm 0.1) \cdot 10^{-10}$
4200	$(5.15 \pm 0.05) \cdot 10^{-9}$	6350	$(3.6 \pm 0.7) \cdot 10^{-10}$
4250	$(4.82 \pm 0.06) \cdot 10^{-9}$	6450	$(3.2 \pm 0.4) \cdot 10^{-10}$
4300	$(4.51 \pm 0.05) \cdot 10^{-9}$	6550	$(2.7 \pm 0.3) \cdot 10^{-10}$
4350	$(4.21 \pm 0.07) \cdot 10^{-9}$	6650	$(2.7 \pm 0.5) \cdot 10^{-10}$
4400	$(3.94 \pm 0.07) \cdot 10^{-9}$	6750	$(2.2 \pm 0.3) \cdot 10^{-10}$
4450	$(3.69 \pm 0.09) \cdot 10^{-9}$	6850	$(2.2 \pm 0.3) \cdot 10^{-10}$
4500	$(3.46 \pm 0.03) \cdot 10^{-9}$	6950	$(2.0 \pm 0.3) \cdot 10^{-10}$

with an expression of the form

$$I(X, 0^\circ) \;=\; A \left(\frac{X_0}{X} \right)^{\alpha} e^{-(X/X_0)} + K \;, \tag{4.38}$$

where the parameters A, X_0 and α have different values for different exper-

Table 4.11: Parameters for Vertical Depth-Intensity Relation of eq. 4.38 in Standard Rock.

Experiment Reference	$A \cdot 10^6$ [$\mathrm{cm^{-2}\,s^{-1}\,sr^{-1}}$]	α	X_0 [$\mathrm{hg\,cm^{-2}}$]	$K \cdot 10^{13}$ [$\mathrm{cm^{-2}\,s^{-1}\,sr^{-1}}$]
Fréjus Rhode + (1996)	(2.18 ± 0.05)	2.0	1127 ± 4	0
LVD Aglietta + (1995a)	(1.77 ± 0.02)	2.0	1211 ± 3	(2.98 ± 1.15)
MACRO Ahlen + (1994)	(1.97 ± 0.02)	1.15 ± 0.01	983 ± 2	0

iments and depth ranges. For depths less than ~5 km w.e. the constant K which accounts for the neutrino induced muon component can be neglected. At great depths, values of K ranging from $K = (2.17 \pm 0.21) \cdot 10^{-13}$ $\mathrm{cm^{-2}\,s^{-1}\,sr^{-1}}$ (Crouch, 1987) to $K = (2.98 \pm 1.15) \cdot 10^{-13}$ $\mathrm{cm^{-2}\,s^{-1}\,sr^{-1}}$ (Giusti et al., 1995) were found. Table 4.11 lists the parameters of eq. 4.38 for some experiments.

4.3.4 Zenith Angle Dependence and Relations

In this subsection we discuss mostly muons from normal processes, such as the decay of pions and kaons in the atmosphere. These muons constitute the bulk of all the muons in the atmosphere as well as underground to depths of about 8 km w.e.. Beyond this depth neutrino induced muons become significant and below about 13 km w.e. they are the dominating component. Effects due to *prompt muons* resulting from the decay of *charmed particles* will be mostly ignored here, they are discussed separately in Subsection 4.3.6. Note that atmospheric muons underground show *no azimuthal dependence*, like energetic muons at the surface. Only low energy muons in the atmosphere down to sea level manifest an azimuthal dependence because of the geomagnetic field.

In an underground laboratory at a vertical depth of X $\mathrm{g\,cm^{-2}}$ with a flat surface topography, and assuming a flat Earth and atmosphere, the path length X_s of an inclined trajectory with zenith angle θ is given by the relation

$$X_s = X \sec(\theta) \quad [\mathrm{g\,cm^{-2}}] \,. \tag{4.39}$$

X_s is referred to as the *slant depth.*

The angular distribution of energetic atmospheric muons of normal origin is proportional to $\sec(\theta)$ at the Earth's surface. This linear relationship is an approximation which is valid only for energetic muons subtending zenith angles $\leq 60°$ (for details see Subsection 3.6.4). From eq. 4.36 it is evident that the muons will be attenuated by a factor $\exp(-X \sec(\theta)/\Lambda)$ upon penetrating to depth X under zenith angle θ. Because of the assumption of a flat Earth this expression as well as eq. 4.39 are subject to the same zenith angular restriction as mentioned above. For larger zenith angles the Earth's curvature must be considered in analogy to the curved atmosphere, discussed in Chapter 1, Subsection 1.7.2.

If the vertical muon flux at depth X is compared with the flux at an angle θ for the same path length inside the rock, $(X_s = X)$, i.e., at a more shallow vertical depth, then an *enhanced intensity* is expected at $\theta > 0°$. This is because the atmospheric muon intensity itself manifests an enhancement at $\theta > 0°$ with respect to $\theta = 0°$. This topic is discussed in Chapter 3, Subsection 3.6.4.

According to Miyake (1973) (see also Bollinger, 1951; Budini and Molière, 1953) the following expression is valid to describe the zenith angle distribution of muons at *shallow depths* underground.

$$I(X,\theta) \;=\; I(X,0°)\,\cos^n(\theta)\;, \tag{4.40}$$

where

$$n \;=\; 1.53 + 8.0\cdot 10^{-4}\,X + \epsilon\;. \tag{4.41}$$

X is in $\mathrm{hg\,cm^{-2}}$, and ϵ is a small correction that arises from muon decay and ionization losses at shallow depths only. Note that the exponent n is a function of depth X and depends on the low energy cutoff of the detector. With increasing depth the zenith angle distribution of the muon intensity gets steeper and consequently n increases, too. At great depth the distribution is sharply peaked to the vertical. According to Stockel (1969) eq.4.40 is valid to a zenith angle of $\theta \simeq 60°$ down to depths of $\simeq 2000$ $\mathrm{hg\,cm^{-2}}$ and according to Menon et al. (1967) it is inadequate below 4000 $\mathrm{hg\,cm^{-2}}$ for $\theta \geq 40°$.

At *intermediate depths* or at large angles at shallow depths the angular distribution can be expressed as

$$I(X,\theta) \;=\; I(X,0°)\,\cos^{1.53}(\theta)\,e^{-8.0\cdot 10^{-4}X(\sec(\theta)-1)}\;. \tag{4.42}$$

At *very large depths* the angular distribution can be approximated by the expression

$$I(X,\theta) \;=\; I(X,0°)\,\sec(\theta)\,e^{-X\left(\frac{\sec(\theta)-1}{\Lambda}\right)} \tag{4.43}$$

where Λ has different values for different depths as given by Miyake (1973) (see Table 4.3).

For the whole depth range the angular distribution can be described by the following empirical formula (Miyake, 1973).

$$I(X,\theta) \;=\; \frac{174}{X\cos(\theta)+400}\,(X+10\,\sec(\theta))^{-1.53}\left(\frac{X+75}{X+50+25\,\sec(\theta)}\right)$$
$$\cdot e^{-8.0\cdot 10^{-4}(X+10\,\sec(\theta))} \qquad [\mathrm{cm^{-2}s^{-1}sr^{-1}}]\,, \tag{4.44}$$

where X is the slant depth in $\mathrm{hg\,cm^{-2}}$. This expression is valid for KGF-rock but it covers all data within an error of 10 percent. The different terms of this relation represent the pion decay into muons, the production energy spectrum, muon decay, and the depth-energy relation.

If the angular variation is expressed as $I(X,\theta) = I(X,0°)\cos^n(\theta)$ (see eq. 4.40), where $I(X,0°)$ is the vertical intensity at depth X, the variation of n as a function of depth X can be obtained.

At shallow depth (31.6 $\mathrm{hg\,cm^{-2}}$ below sea level, or 43.0±1 $\mathrm{hg\,cm^{-2}}$ below the top of the atmosphere, including 134±1 $\mathrm{g\,cm^{-2}}$ of absorber in the telescope) the variation of the *absolute* muon intensity as a function of zenith angle was measured by Crookes and Rastin (1973). The results are given in Table 4.12.

Early studies of the depth dependence of the zenith angle distribution of the muon intensity underground, in particular of the exponent n of eq. 4.40 as a function of depth X, were made by Miyake et al. (1964). The data are summarized in Table 4.13. Table 4.14 contains a similar set of data acquired by Castagnoli et al. (1965) in the Mont Blanc tunnel. Results from measurements made by Stockel (1969) at four different depths (sites at Holborn and at Tilmanstone Colliery, Kent), are illustrated in Fig. 4.29. The intensities are in arbitrary units but the steepening of the slope of the distribution with increasing depth is well demonstrated.

Bergeson et al. (1967, 1968 and 1971) and Keuffel et al. (1970) made similar measurements with the Utah detector to larger depths and compared the data with a previous world survey (Fig. 4.30). In this figure the intensities

Table 4.12: Angular Distribution of Muons at Shallow Depths.
(Crookes and Rastin 1973)

Axial Zenith Angle [deg.]	Depth Below Sea Level [hg cm^{-2}]	Absolute Muon Intensity [cm^{-2}s^{-1}sr^{-1}]	Muon Energy at Sea Level [GeV]
0	31.6±1.0	$1.40 \pm 0.02 \cdot 10^{-3}$	7.5
30	42.4±0.2	$8.7 \pm 0.3 \cdot 10^{-4}$	9.7
45	52.7±0.3	$6.2 \pm 0.25 \cdot 10^{-4}$	11.7
60	72.7±0.4	$3.0 \pm 0.1 \cdot 10^{-4}$	15.5

Table 4.13: Depth Dependence of Exponent n of Zenith Angle Distribution of the Muon Intensity, eq. 4.40.
Kolar Gold Fields Experiment, India (Miyake et al., 1964).

Depth from Surface [a] [m]	Depth from Top of Atmosphere (actual rock) [b] [hg cm^{-2}]	n	Absolute Vertical Intensity [cm^2 s^{-1} sr^{-1}]
270 ± 0.3	816	2.3	$(2.51 \pm 0.15) \cdot 10^{-6}$
600 ± 0.3	1812	3.1	$(1.77 \pm 0.07) \cdot 10^{-7}$
1130 ± 0.3	3410	4.5	$(1.42 \pm 0.14) \cdot 10^{-8}$
1415 ± 0.3	4280	5.2	$(3.24 \pm 0.35) \cdot 10^{-9}$
2110 ± 0.3	6380	6.6	$(1.92 \pm 0.47) \cdot 10^{-10}$
2760 ± 0.3	8400	-	$\leq 10^{-11}$ (from atmos. muons) $\leq 1.5 \cdot 10^{-12}$ (from neutrinos)

[a] Known to the nearest 30 cm.

[b] The errors in the depth estimates owing to modulations in the surface topography are about ±1.7%. In addition there may be an error of zero to 2% depending on the percentage (0 to 10% by volume) of rocks other than horn-blende schist.

are plotted as a function of sec(θ) for fixed slant depths, X_s. The data were obtained by varying the zenith angle and selecting the appropriate azimuth to keep X_s constant. These authors found that the zenith angle distribution is flatter than expected on the basis of muon production via pion and kaon decays and concluded that a significant *isotropic component*, resulting from

Table 4.14: Depth Dependence of Exponent n of Zenith Angle Distribution of the Muon Intensity, eq. 4.40.
Mont Blanc Tunnel Experiment, Italy - France (Castagnoli et al., 1965).

Depth from Top of Atmosphere (actual rock) [hg cm^{-2}]	n	Absolute Vertical Intensity [cm^2 s^{-1} sr^{-1}]
140	2.0	$(1.70 \pm 0.04) \cdot 10^{-4}$
290	2.2	$(4.60 \pm 0.01) \cdot 10^{-5}$
1325	3.0	$(5.60 \pm 0.07) \cdot 10^{-7}$
4100	5 - 6	$(1.00 \pm 0.23) \cdot 10^{-8}$

direct processes (charmed particle decays), is needed to explain the results (Keuffel effect). Re-analysis of the data and new measurements at Utah as well as elsewhere, discussed in Subsection 4.3.6, made it clear that the isotropic component is very small at low and moderate energies.

Krishnaswamy et al., (1970a, 1970b, 1971b, 1971c and 1971d) carried out similar investigations at different depths down to 3375 hg cm^{-2} with their detectors at the Kolar Gold Fields. The apparatus had an angular resolution of $\Delta\theta = \pm 1.5°$ and the data were evaluated in 5° angular bins. The results are shown in Fig. 4.31 as plain zenith angle distributions together with theoretical distributions, assuming a constant kaon to pion production ratio of $K/\pi = 0.2$. The same authors have also studied the angular distribution of muon pairs underground which show the same characteristic features (Krishnaswamy et al., 1970b).

The rock density given by Krishnaswamy et al. (1970a) is slightly different at different depths (3.03, 3.05, and 3.02 g cm^{-3} at 754, 1500 and 3375 hg cm^{-2}, respectively), resulting in somewhat different values of Z/A (0.495) and Z^2/A (6.4) than given in Table 4.2.

A more recent study using the proton decay detector at the Kolar Gold Fields, located at a depth of 6045 hg cm^{-2}, was conducted by Adarkar et al. (1990a and 1990b). The apparatus had an angular resolution of $\Delta\theta = \pm 0.8°$ and the data were evaluated in 5° angular bins. The results are shown in Fig. 4.32 together with theoretical curves for atmospheric and neutrino induced muons. The former curve was obtained assuming a pion production spectrum

in the atmosphere of the form

$$F(E_\pi)\,dE_\pi \;=\; AE_\pi^{\gamma}\,dE_\pi \quad , \tag{4.45}$$

with a production ratio of kaons to pions of $K/\pi = 0.15$, and a ratio of prompt muons from charmed particle decays to pions of $f_p^{'} = \mu_p/\pi = 0.1\%$. Using the survival probabilities, the range-energy relation and the detector acceptance (area-solid-angle product), the sea level muon spectrum was converted to the angular distribution underground, including the $\sec(\theta)$ effect for the muons from pion and kaon decays. The flux was then normalized to the experimental data underground and the exponent γ fitted to the data. The best fit was obtained with a spectral index of $\gamma_\pi = 2.7$.

The simulation calculations show that the variation of the K/π ratio has little effect on the zenith angle distribution at these large energies because of the comparatively small mass difference between pions and kaons. To investigate the contribution of prompt muons, the ratio of pions and kaons to prompt muons, f_p, was varied, and the expected and observed intensity distributions compared for shape. The effect of the fraction of prompt muons manifests itself in the ratio of muons stopping in a given target to the muons traversing it, and in deviations from the theoretical depth-intensity and angular distributions. Further details concerning these topics are discussed in Subsections 4.3.5 and 4.3.6.

A very new series of high statistics measurements of the zenith angle distribution was made by the MACRO team at four different slant depth intervals (Ambrosio et al., 1995). From these data the authors determined the vertical muon intensities, as shown in Fig. 4.33.

A compilation of data on the depth dependence of the exponent n of the zenith angle distribution $\cos^n(\theta)$ of muons underground is illustrated in Fig. 4.34. As mentioned before the exponent n depends also on the lower momentum cutoff imposed by the measuring instrument (Stockel, 1969; Crookes and Rastin, 1973).

4.3.5 Stopping Muons

The motivation to study stopping muons underground arises from a variety of problems. Comparison of the depth and therefore the energy dependence of the spectrum of through-going and stopping muons underground yields information on the origin of the low energy component, i.e., whether they are of atmospheric or neutrino induced origin. From the portion of stopping muons that result from decaying mesons in the atmosphere one can obtain the muon

Table 4.15: Intensity of Stopping Muons Underground.

Depth, X $[\mathrm{hg\,cm^{-2}}]$	Intensity $[\mathrm{cm^{-2}s^{-1}sr^{-1}}100\,\mathrm{g^{-1}cm^2}]$	References
24	$(6.6 \pm 1.1) \cdot 10^{-5}$	Higashi et al. (1973)
Surface	$(2.62 \pm 0.15) \cdot 10^{-4}$	Bhat and Ramana Murthy (1973a, b)
96	$(7.67 \pm 0.4) \cdot 10^{-6}$	
417	$(7.90 \pm 0.5) \cdot 10^{-8}$	
985	$(6.90 \pm 0.7) \cdot 10^{-9}$	

energy spectrum at the detector location underground. This spectrum is dependent only on the spectral index γ and the energy loss mechanisms in the rock. Direct measurement of the low energy portion of the muon spectrum in a detector offers therefore the possibility to determine the spectral index γ together with the energy loss parameters a and b independently of the depth dependence of the through-going muon flux.

In addition, the spectral index of the neutrino flux can be determined from the ratio of the absolute fluxes of stopping to through-going neutrino induced muons. From the above mentioned wealth of information the portion of stopping negative muons can be estimated. This data is relevant for background estimates for critical low level spallation experiments that are sensitive to muon capture induced reactions.

Last but not least prompt muon production via charmed particles and other direct processes can be investigated with stopping muons, and likewise speculations that possible deviations from the expected behavior of muons underground might reveal hitherto unknown high energy leptonic processes or components. These topics are discussed in Subsection 4.3.6.

Measurements on stopping muons have been made by many authors. The intensity of stopping muons as measured at the Kolar Gold Fields at different depths, X, is given in Table 4.15 (Bhat and Ramana Murthy, 1973a and 1973b).

Ratio of Stopping to Through-going Muons

When dealing with stopping muons one usually specifies the ratio, r, defined as the number of muons stopping in an absorber of thickness 100 $\mathrm{g\,cm^{-2}}$ to the number of through-going muons. This ratio is a function of depth.

Table 4.16: Ratio of Stopping to Through-going Muons Underground.

Depth, X [hg cm^{-2}]	Ratio, r [per 100 g cm^{-2}]	References
24	$(3.0 \pm 0.5) \cdot 10^{-2}$	Higashi et al. (1973)
24	$(2.8 \pm 0.5) \cdot 10^{-5}$*	Higashi et al. (1973)
60	$(3.5 \pm 0.3) \cdot 10^{-2}$	
850	$(4.5 \pm 0.9) \cdot 10^{-3}$	Alexeyev et al. (1973a, b)
1150	$(4.2 \pm 0.7) \cdot 10^{-3}$	
985	$(4.6 \pm 0.5) \cdot 10^{-3}$	Bhat and Ramana Murthy (1973a, b)

* Ratio of stopping accompanied muon flux to through-going muon flux.

Fig. 4.35 shows a compilation of results of many measurements made before 1976, together with theoretical predictions (Grupen et al., 1972 and 1976). In Table 4.16 we summarize the results of some early measurements which also include one value for the ratio of stopping accompanied muons to all through-going muons from the work of Higashi et al. (1973).

Recent investigations of stopping muons were carried out with the Fréjus detector (Rhode, 1993 and 1994). The results are displayed in Fig. 4.36, showing the depth dependence of stopping as well as through-going muons. Also shown are fits to the data and theoretical distributions of neutrino induced through-going and stopping muons. An extension of this plot to depths of 50 km w.e. is presented in Section 4.5 (Fig. 4.87) that deals with neutrino data.

The zenith angle distribution of stopping muons, μ_{st}, has been determined at a vertical depth of 417 hg cm^{-2} in the Kolar Gold Fields by Bhat and Ramana Murthy (1978). They found that the experimentally obtained distribution could be represented by the relation

$$I_{\mu_{st}}(\theta) \;=\; I_{\mu_{st}}(0^\circ)\,\cos^n(\theta)\;. \qquad (4.46)$$

where $n = 2.23 \pm 0.33$, evaluated for all events within the investigated zenith angle range of $0^\circ \leq \theta \leq 70^\circ$.

In earlier work Bhat and Ramana Murthy (1973) and others have recognized that stopping muons underground consist of two populations of different origin. One results from slowed-down atmospheric muons, the other from the decay of low energy pions that are locally produced by high energy

muons in inelastic scattering processes on nuclei of rock constituents. The two populations have different angular distributions.

Bhat and Ramana Murthy (1978) conclude from their work that $12.9 \pm 0.6\%$ of all stopping muons at this depth are locally produced and have an intensity distribution that has a zenith angle dependence of the form

$$I_{\mu_{loc}}(\theta) \propto \cos(\theta) \,. \tag{4.47}$$

The approximate ratio, r, of stopping to through-going muons per $\mathrm{g\,cm^{-2}}$ at depth X can be calculated on the basis of the energy loss equation for muons and spectral considerations. According to Alexeyev et al. (1973a and 1973b) it is

$$r = \left(\frac{a}{E'_\mu} + b_n \, n_0 (< E_\mu >)^z \right) \quad [\mathrm{g^{-1}cm^2}] \,. \tag{4.48}$$

Here $< E_\mu >$ is the mean muon energy in GeV at depth X and a is the mean ionization energy loss in rock, $a = 2 \cdot 10^6$ $\mathrm{eV\,g^{-1}cm^2}$. Because of the flat shape of the muon energy spectrum underground, which can be written as

$$\frac{dj_\mu}{dE} \sim \frac{1}{(A + E_\mu)^\gamma} \,, \tag{4.49}$$

the value of

$$E'_\mu = \frac{j_\mu}{(dJ_\mu/dE)_{max}} \tag{4.50}$$

is close to $< E_\mu >$, where $(dj_\mu/dE)_{max}$ is the maximum of the differential muon energy spectrum. In practice $E'_\mu = 0.7 < E_\mu >$. The exponent $z \simeq 0.7$ and the quantity n_0 are related to the hadronic cascades initiated by photo-nuclear interactions of muons. It is estimated to be about 0.4 (Bugaev, 1968), and $b_n = 5.7 \cdot 10^{-7}$ $\mathrm{g^{-1}cm^2}$ is the muon energy loss coefficient for this process (Bezrukov et al., 1972).

Inserting some of the numeric factors, eq. 4.48 can be rewritten for practical applications as

$$r \simeq \left(\frac{0.3}{< E_\mu >} \right) + 5.7 \cdot 10^{-5} \, n_0 (< E_\mu >)^{0.7} \quad [100\,\mathrm{g^{-1}cm^2}] \,. \tag{4.51}$$

4.3.6 Prompt or Direct Muons

Experimental Aspects

Muons resulting from charmed particle decays and other so-called prompt or direct processes, often referred to as X-processes, do not manifest the zenith angle dependence which is characteristic for muons from so-called normal processes, i.e., from pion and kaon decays (see Subsection 3.6.4). This is because the mean lifetime of charmed particles is too short so that they have a vanishing chance to interact in the low density environment of the upper atmosphere. They decay directly, producing prompt muons. The angular distribution of these muons in the atmosphere is therefore isotropic like that of the primaries and the zenith angle dependence at depth X underground is expected to have the form

$$I_{\mu_p}(X,\theta) \;=\; A_{\mu_p}\, e^{-\left(\frac{X\,\sec(\theta)}{\Lambda}\right)} \,. \tag{4.52}$$

The spectral index of prompt muons is identical to that of the primary spectrum and their fraction is expected to increases with increasing energy. The relatively slow fall-off with energy of the flux increases their importance at high energies and large depths.

Neglecting neutrino induced muons, the total muon intensity underground can be written as

$$I(X,\theta) \;=\; I(X,0^\circ)\,G(X,\theta) \;+\; I_p(X) \,, \tag{4.53}$$

where θ is the zenith angle, $G(X,\theta) \approx \sec(\theta)$ usually referred to as the enhancement, X is the depth or column of rock traversed, and $I_p(X)$ is the intensity of the prompt (isotropic) muon component at X.

Measurements made by Bergeson et al. (1973) at two slant depths for a range of zenith angles, shown in Fig. 4.37, illustrate the relation stated above (see also Subsection 4.3.4). The plotted muon intensity $I(X,\theta)$ versus $\sec(\theta)$ reveals that the data points fall on a straight line, as expected, that intersects the intensity axis close to zero at $\sec(\theta) = 0$. The value at $\sec(\theta) = 0$ is essentially the intensity of prompt muons, $I_p(X)$. The experiment shows that the ratio $I_p(X)/I(X,0^\circ)$ is very small and, if present, manifests itself only at large depth which implies high energy.

Similar work carried out by Krishnaswamy et al. (1971c and 1971d) reveals no evidence in support of the existence of a prompt muon component, and in many other experiments it remains undetectable. Likewise, Cassiday et al. (1973) at a depth of 1500 hg cm^{-2} and Bakatanov et al. (1979) at 850

hg cm^{-2} show that their experimental data can be explained by conventional processes.

On the other hand, Bergamasco et al. (1983) find from their work at the Mont Blanc laboratory, using a spark chamber arrangement, an isotropic component on the level of 5% (Fig. 4.38). Similarly, Afanasieva et al. (1987), using an emulsion chamber located 5 to 6 meters underground, indicate that the fraction of prompt muons increases with energy from about 0.08% at a muon energy of 1 TeV to 0.18% at 100 TeV. Moreover, in a very recent analysis of data from the LVD detector, Aglietta et al. (1997) conclude from zenith angle distributions at different depths shown in Fig. 4.39 that the upper limit on the ratio of the flux of prompt to normal muons is $f_p \leq 2 \cdot 10^{-3}$ (90% C.L.).

As mentioned in Subsections 4.3.4 and 4.3.5, the portion of muons originating from prompt processes to that resulting from pion and kaon decays manifests itself in the ratio, r, of stopping to through-going muons in a given absorber. This ratio reflects the spectral difference between the two muon groups. The investigation is based on comparison of the experimental data with results from simulation calculations, whereby the ratio f_p of prompt muons, μ_p, to normal muons, $\mu_{\pi,K}$, i.e., $f_p = \mu_p/\mu_{\pi,K} = N_\psi/N_{\pi,K}$, is varied. Here N_ψ stands for the number of charmed particles and possibly other direct processes, and $N_{\pi,K}$ for the number of pions and kaons.

The result of such an analysis is shown in Fig. 4.40 (Krishnaswami et al., 1983; Adarkar et al., 1990a and 1990b). Variation of the K/π ratio has little effect at these large energies because of the comparatively small mass difference between pions and kaons (see also Fig, 3.50, Section 3.6).

Differences between theoretical and experimental depth-intensity distributions had been discussed by Andreyev et al. (1990). These authors conclude from their work with the large liquid scintillator at Baksan that muons from prompt processes constitute about 0.15±0.5% of the muon flux in the zenith angle interval 50° to 70°, corresponding to a depth range from 1000 hg cm^{-2} to 11000 hg cm^{-2}.

Theoretical Aspects of Prompt Muons

Theoretical studies concerning prompt muon production were carried out by many authors since the mid sixties. Most calculations are based on semi-empirical models of charm production and the results vary strongly from author to author. Contributions to this field were made by Aglietta et al. (1995b), Battistoni et al. (1996), Bugaev et al. (1988, 1989a, 1989b, 1994

and 1998), Castagnoli et al. (1984), Castellina et al. (1985), Elbert et al. (1983), Inazawa and Kobayakawa (1983 and 1985), Inazawa et al. (1986a and 1986b), Kobayakawa (1967), Komori and Mitsui (1982), Thunman et al. (1996), Volkova et al. (1987), Zas et al. (1993), and others.

In Fig. 4.41 we show the results of a calculation by Volkova et al. (1987) of the spectra of prompt muons originating from different processes. The main contributions come from semi-leptonic decays of D-mesons (D^+, D^-, D^0, $\overline{D^0}$) and charmed baryons, Λ_c. Also shown is the theoretical spectrum of muons from pion and kaon decays, and the results of the Mont Blanc experiment (Bergamasco et al., 1983). The theoretical spectra are subject to relatively large uncertainties, as indicated. The intensities shown in Fig. 4.41 seem to be rather high.

Inazawa and Kobayakawa (1985) carried out some calculations to estimate the effect of prompt muon production on the depth-intensity curve, assuming a maximum likely prompt muon spectrum of the form

$$J_p(> E) = 2.11 \cdot 10^{-9} \cdot E^{-1.44} \; [\mathrm{cm^{-2} s^{-1} sr^{-1}}] \qquad (4.54)$$

with E in TeV. The results of this calculation are shown in Fig. 4.42. Also indicated in the same figure are the depth-intensity distributions of conventional vertical muons and of inclined muons observed at a vertical depth of 4800 hg cm^{-2} and different slant depths.

Theoretical estimates of the energy where the flux of prompt muons at sea level may reach 50% of the total muon flux range anywhere from 30 TeV to 1000 TeV and more (Bugaev et al., 1994 and 1998).

4.3.7 Energy Loss Data of Muons

The theoretical foundations for carrying out energy loss calculations of muons propagating in dense media to great depths underground are discussed in Section 4.2. Lohmann et al. (1985) produced tables of energy losses of muons from 1 GeV to 10 TeV in various elements and compounds commonly used in high energy physics. Some of their data comprising materials that are frequently used in cosmic ray research, including standard rock and water, are reproduced in Tables A.5 and A.6 in the Appendix.

Mitsui (1992) studied the energy loss of muons in iron and water experimentally and theoretically, using data from measurements on horizontal muons analyzed with the MUTRON detector at sea level. The results are summarized in Fig. 4.43. Shown are the energy losses as a function of muon energy from 100 GeV to 1000 TeV resulting from two different calculations.

Table 4.17: Energy Loss Parameters a and b.
(Rhode, 1993)

Rock Type	$\sigma_{br}^{*)}$	b [(m w.e.)$^{-1}$]	a [GeV (m w.e.)$^{-1}$]		a/b [GeV]	
			calc.	exp.	calc.	exp.
Fréjus	P&S	$4.24 \cdot 10^{-4}$	0.217	0.215±0.004	513	507±8
Fréjus	R	$4.38 \cdot 10^{-4}$	0.217	0.215±0.004	495	490±8
Standard	P&S	$4.50 \cdot 10^{-4}$	0.217	0.215±0.004	482	477±8
Standard	R	$4.66 \cdot 10^{-4}$	0.217	0.215±0.004	466	460±8

*) P&S: Petrukhin and Shestakov (1968); R: Rozental (1968).

One is based on quantum electrodynamics, the other uses an empirical formula. Also indicated are the experimental data obtained with the MUTRON detector.

The energy loss parameters a and b of eq. 4.1, Section 4.2, have been determined by many authors. In Table 4.17 we list the results obtained by Rhode (1993) in an evaluation for Fréjus and standard rocks, using the Petrukhin and Shestakov (1968) as well as the Rozental (1968) formulas for the bremsstrahlung cross section, σ_{br} (for details see Section 4.2). For a, which is essentially independent of rock type, calculated and experimentally determined values are listed.

4.3.8 Range-Energy Data of Muons Underground

Theoretical Range-Energy Data

Results from an early calculation by Menon and Ramana Murthy (1967) of the average range-energy relation of muons are included in Section 4.2, Fig. 4.6, where the theoretical foundations for range-energy calculations are given. Similarly, range fluctuations that are important at great depth where high energy muons are relevant are also discussed there. Correction factors accounting for fluctuation-induced muon enhancement underground are given by Kiraly et al. (1972). Included in this paper is a survey of previous work dealing with this topic.

A very new calculation of the average range of muons as a function of energy in dense media, considering the problem of range fluctuations, was performed by Makarov et al. (1995). Their results for standard rock, Baksan

Table 4.18: Muon Range, $R(E, E_{th})$, in Various Rocks and in Water. (Threshold Energy $E_{th} = 1$ GeV, Makarov et al., 1995)

E	$\overline{R}(E)$ [g cm^{-2}]			
[GeV]	SR	Baksan	KGF	Water
10^2	$4.08 \cdot 10^4$	$4.11 \cdot 10^4$	$4.12 \cdot 10^4$	$3.63 \cdot 10^4$
$2 \cdot 10^2$	$7.48 \cdot 10^4$	$7.51 \cdot 10^4$	$7.49 \cdot 10^4$	$6.80 \cdot 10^4$
$4 \cdot 10^2$	$1.30 \cdot 10^5$	$1.30 \cdot 10^5$	$1.29 \cdot 10^5$	$1.22 \cdot 10^5$
$6 \cdot 10^2$	$1.74 \cdot 10^5$	$1.73 \cdot 10^5$	$1.71 \cdot 10^5$	$1.68 \cdot 10^5$
$8 \cdot 10^2$	$2.09 \cdot 10^5$	$2.08 \cdot 10^5$	$2.05 \cdot 10^5$	$2.07 \cdot 10^5$
10^3	$2.40 \cdot 10^5$	$2.37 \cdot 10^5$	$2.33 \cdot 10^5$	$2.41 \cdot 10^5$
$2 \cdot 10^3$	$3.45 \cdot 10^5$	$3.39 \cdot 10^5$	$3.31 \cdot 10^5$	$3.65 \cdot 10^5$
$4 \cdot 10^3$	$4.61 \cdot 10^5$	$4.50 \cdot 10^5$	$4.37 \cdot 10^5$	$5.10 \cdot 10^5$
$6 \cdot 10^3$	$5.31 \cdot 10^5$	$5.17 \cdot 10^5$	$5.01 \cdot 10^5$	$5.99 \cdot 10^5$
$8 \cdot 10^3$	$5.82 \cdot 10^5$	$5.65 \cdot 10^5$	$5.47 \cdot 10^5$	$6.64 \cdot 10^5$
10^4	$6.21 \cdot 10^5$	$6.02 \cdot 10^5$	$5.82 \cdot 10^5$	$7.15 \cdot 10^5$
$2 \cdot 10^4$	$7.41 \cdot 10^5$	$7.17 \cdot 10^5$	$6.91 \cdot 10^5$	$8.73 \cdot 10^5$
$4 \cdot 10^4$	$8.61 \cdot 10^5$	$8.32 \cdot 10^5$	$8.00 \cdot 10^5$	$1.03 \cdot 10^6$
$6 \cdot 10^4$	$9.31 \cdot 10^5$	$8.99 \cdot 10^5$	$8.63 \cdot 10^5$	$1.12 \cdot 10^6$
$8 \cdot 10^4$	$9.80 \cdot 10^5$	$9.46 \cdot 10^5$	$9.08 \cdot 10^5$	$1.19 \cdot 10^6$
10^5	$1.02 \cdot 10^6$	$9.82 \cdot 10^5$	$9.43 \cdot 10^5$	$1.24 \cdot 10^6$
$2 \cdot 10^5$	$1.14 \cdot 10^6$	$1.09 \cdot 10^6$	$1.05 \cdot 10^6$	$1.39 \cdot 10^6$
$4 \cdot 10^5$	$1.25 \cdot 10^6$	$1.21 \cdot 10^6$	$1.16 \cdot 10^6$	$1.54 \cdot 10^6$
$6 \cdot 10^5$	$1.32 \cdot 10^6$	$1.27 \cdot 10^6$	$1.22 \cdot 10^6$	$1.63 \cdot 10^6$
$8 \cdot 10^5$	$1.37 \cdot 10^6$	$1.32 \cdot 10^6$	$1.26 \cdot 10^6$	$1.69 \cdot 10^6$
10^6	$1.41 \cdot 10^6$	$1.35 \cdot 10^6$	$1.30 \cdot 10^6$	$1.74 \cdot 10^6$
$2 \cdot 10^6$	$1.52 \cdot 10^6$	$1.46 \cdot 10^6$	$1.40 \cdot 10^6$	$1.89 \cdot 10^6$
$4 \cdot 10^6$	$1.63 \cdot 10^6$	$1.57 \cdot 10^6$	$1.50 \cdot 10^6$	$2.04 \cdot 10^6$
$6 \cdot 10^6$	$1.70 \cdot 10^6$	$1.63 \cdot 10^6$	$1.56 \cdot 10^6$	$2.12 \cdot 10^6$
$8 \cdot 10^6$	$1.75 \cdot 10^6$	$1.68 \cdot 10^6$	$1.60 \cdot 10^6$	$2.18 \cdot 10^6$
10^7	$1.78 \cdot 10^6$	$1.71 \cdot 10^6$	$1.64 \cdot 10^6$	$2.23 \cdot 10^6$

and KGF rocks, and water are given in Table 4.18

Experimental Range-Energy Data

Direct information on the range-energy relationship for muons can be obtained from the muon integral energy spectrum, measured at sea level, and

the depth-intensity curve, since a given muon intensity underground will correspond to a certain threshold energy at sea level and also a certain absorber thickness in terms of standard rock. Crookes and Rastin (1973) have used their best-fit sea level integral muon energy spectrum with the depth-intensity curve to produce the range-energy curve of Fig. 4.44.

Over the range of muon energies covered by these results (0.4 - 100 GeV) the dominant mode of energy loss is ionization. Shown, too, is a theoretical curve using the energy loss expression given by Sternheimer (1956) plus the terms to allow for bremsstrahlung, pair production and nuclear interactions. The probable cause for the deviation of the theoretical curve from the experimental points at low energies could be that the empirical relationship does not accurately represent the shape of the depth-intensity variation for depths less than 14 hg cm^{-2} of standard rock.

4.3.9 Momentum and Energy Spectra of Muons Underground and Derived Sea Level Spectrum

Theoretical Spectra

The computational approach to determine the energy spectrum of muons underground is discussed in Section 4.2. There theoretical results are summarized in Fig. 4.10 for different depths in rock.

Directly Measured Spectra Underground

Early attempts to determine the energy spectrum of underground muons were made by George and Shrikantia (1956) using emulsion at a depth of 57 m w.e.. Likewise, Nash and Pointon (1956) made measurements at 40 m w.e., using the scattering technique in a multi-plate cloud chamber, covering a momentum range of approximately 0.2 - 0.8 GeV/c.

First measurements of the underground muon momentum spectrum using magnetic spectrographs were made in Moscow at a depth of 40 m w.e. by Daion and Potapov (1959a and 1959b), in England at a depth of 38 m w.e. by Ashton et al. (1960), and in a tunnel in Australia under 70 hg cm^{-2} of rock by Murdoch et al. (1960). The results of the work of Daion and Potapos and of Murdoch et al. are shown in Fig. 4.45. Also shown are theoretical curves based on calculations by these authors, using muon spectra above ground, at sea level, with differential spectral exponents of $\gamma = 2.5$, 2.85 and 3.0, as indicated in the figure.

In later work at Moscow, Vernov et al. (1965) used burst measurements

to determine the energy of muons at 40 m w.e.. More recently, Mizutani and Ohta (1975, 1977 and 1979) determined the muon energy spectrum at a depth of 850 hg cm^{-2} to energies of several TeV, using an emulsion chamber. Their results are shown in Fig. 4.46.

Average Energy of Muons Underground

In view of the problems that arise in the direct determination of the energy spectrum of muons deep underground, where the experimental conditions are extremely difficult and statistics poor, the concept of average energy, defined in Section 4.2, is very useful. This method is based on multiple electromagnetic interactions of muons in an adequately thick detector in which electron-positron pairs are produced and analyzed in a so-called pair meter. This technique has also been used at sea level to explore the spectrum of ultrahigh energy horizontal muons. It can also be used to study high energy muon interactions.

This method had been employed in connection with the NUSEX detector in the Mont Blanc Laboratory by Castagnoli et al. (1997) (see also Castagnoli et al., 1995). They determined the average energy of muons as a function of depth underground experimentally and theoretically. The data are shown in Fig. 4.47 together with theoretical expectations by other authors and a very recent experimental determination by the MACRO group (Ambrosio et al., 1999a). We have also added older experimental data of Alexeyev et al. (1973a). A previous attempt to determine the muon spectrum underground using a transition radiation detector was made by Calicchio et al. (1987).

Sea Level Spectra Derived from Underground Measurements

As a by-product of underground measurements that is of equal or even greater interest than the local energy spectrum at a given depth in rock or water is the sea level energy spectrum of the muons at the Earth's surface derived from depth-intensity measurements. The latter offer at present the only practical method to extend spectral studies of muons to ultrahigh energies that represent one of several approaches to explore spectrum and composition of the primary radiation. For this reason several authors present the results of their underground measurements directly in the form of surface spectra at sea level. Some of these data are discussed in Section 3.6.

Khalchukov et al. (1985) (see also Enikeev et al., 1981) have used the 100 ton scintillator tank located in Artyomovsk at 570 m w.e.. They determined the muon spectrum using the energy deposit of muon initiated electromag-

netic cascades only. Hadronic cascades were eliminated in the analysis on the grounds of different neutron numbers. From their measurements underground the authors constructed the muon spectrum at sea level above ground (Fig. 4.48). Likewise, Zatsepin et al. (1994) (see also Il'ina et al., 1995) have used an X-ray emulsion chamber to determine the near horizontal muon spectrum using basically the same method as Khalchukov et al. (1985) (Fig. 4.49).

The vertical muon differential energy spectrum at the surface (sea level) derived from measurements made with the MACRO detector underground, having excellent statistics, is shown in Fig. 4.50 together with earlier data from small experiments at sea level. Essentially the same data are shown in Fig. 4.51 in differential form with the intensities multiplied by E_μ^3 to emphasize the energy dependence of the intensity (Ambrosio et al., 1995; Bussino et al., 1995). The fitted and theoretical curves were obtained with a slightly refined version of the analytic expression of Gaisser (1990) (eq. p. 71) for the muon spectrum at sea level.

$$\frac{dJ_\mu(E_\mu,\cos(\theta))}{dE_\mu} = 0.14\,A\,E_\mu^{-\gamma}\left(\frac{1}{1+\frac{1.1E_\mu\cos(\theta^*)}{115GeV}}+\frac{0.054}{1+\frac{1.1E_\mu\cos(\theta^*)}{850GeV}}+f_p\right)$$

$$[\mathrm{cm}^{-2}\mathrm{s}^{-1}\mathrm{sr}^{-1}\mathrm{GeV}^{-1}] \quad (4.55)$$

Here $\cos(\theta)$ had been substituted by $\cos(\theta^*)$, θ^* being the local zenith angle at the point of production of the muon in the atmosphere, and the spectral index γ was set to 2.7. The additional term, f_p, not present in the original Gaisser formula and ignored by Ambrosio et al. (1995) had been introduced by Aglietta et al. (1997) to account for the prompt muon component.

In another analysis Aglietta et al. (1997) have used the depth-vertical intensity data obtained with the LVD detector to get a fit for the sea level muon spectrum using eq. 4.55 and obtained for the parameters A, γ and f_p the following values: $A = 1.8 \pm 1.0$, $\gamma = 2.77 \pm 0.05$ and $f_p < 2 \cdot 10^{-3}$ (95% C.L.).

In the past several authors have derived expressions similar to eq. 4.55 to describe the muon spectrum in the atmosphere at sea level (see eg. Miyake, 1973).

4.3.10 Multi-Muon Events and Decoherence

Sources of Multi-Muon Events

Multi-muon events can originate from three different processes:

Photoproduction. High energy muons can interact with matter surrounding the detector system or in the detector itself. In this case the produced particles have tracks that are diverging from the vertex in the rock or apparatus and are frequently of much lower energy.

Extensive Air Showers. In energetic hadron-hadron collisions, several hadrons with decay channels into muons can be produced. In spite of the fact that the decay probability of the unstable, newly created fast particles is small,the large number that participate in the nuclear cascade in the shower core can still produce many muons in the TeV range. These muons are strongly collimated near the shower axis and produce almost parallel tracks.

Massive Particles. Multi-muon events can also arise from the decay of massive particles with decay channels that lead to two or more muons. These events have the vertex somewhere in the atmosphere, the muon number is less abundant and the separation of muons can be appreciably larger than in the previously mentioned cases.

Measurement of Multi-Muon Events

High energy multi-muon events have been observed at different levels underground and with very different detector systems and geometries. They are characterized by their frequency distribution or *multiplicity* and track separation, referred to as *decoherence*. The latter is expressed in units of $[\mathrm{m}^{-4}\,\mathrm{s}^{-1}\,\mathrm{sr}^{-1}]$.

Multiplicity as well as decoherence distributions measured with a finite size detector are biased by detector dimensions and geometry. Clusters of n simultaneous muons that extend over an area larger than that of the detector are misinterpreted as having a smaller multiplicity. Likewise, muon pairs with separations that exceed the detector dimension cannot be recognized as such, nor can muon pairs or clusters having separations less than the detector resolution be recognized as such. Thus different detectors obtain quite different results unless the data are properly corrected for detector geometry and efficiency.

Multiplicity Distributions

Multi-muon events have been recorded with the Utah detector at different depths and zenith angles, under rock ($\rho = 2.55\ \mathrm{g\,cm}^{-3}$, $Z^2/A = 5.65$). The

data are summarized in Table 4.19 (Lowe et al., 1975). Additional Utah data are given in Table 4.20 and Figs. 4.52 and 4.53 show the results for zenith angles of 47.5° and 62.5°, respectively (Elbert et al., 1975). At a depth of 3375 hg cm^{-2}, multi-muon events have been recorded at zenith angles $\geq 20°$ and energies ≥ 2 TeV in the Kolar Gold Fields (Krishnaswamy et al., 1979). The results are presented in Fig. 4.54, in arbitrary units.

A summary for different depth is given in Fig. 4.55 (Totsuka and Koshiba, 1974). Fig. 4.56 shows the muon multiplicity distribution at a mean slant depth of 1380 hg cm^{-2} (Suda et al., 1974).

In the Baksan detector, which has an effective area of 250 m^2, the ratio, κ, of muon pairs and multiple muon events combined, $J(\geq 2\mu)$, to single muons, $J(1\mu)$, has been measured in the depth range $850 \leq X \leq 10^4$ hg cm^{-2} for $0° \leq \theta \leq 90°$ and was found to be (Chudakov et al., 1979)

$$\kappa = \frac{J(\geq 2\mu)}{J(1\mu)} = 3 \cdot 10^{-2} . \tag{4.56}$$

In later work at Baksan, Budko et al. (1987) found that the multiplicity distributions for different muon threshold energies ($E_{\mu,th}$ = 0.25, 0.83, 1.2, and 1.7 TeV) have the same slope.

A compilation of more recent data from Baksan (Chudakov et al., 1991), Fréjus (Berger et al., 1989b) and NUSEX (Aglietta et al., 1990b) are shown in Fig. 4.57. Separate sets of data from the Fréjus and MACRO detectors are given in Fig. 4.58 (Berger et al., 1989a and 1989b) and Fig. 4.59 (Ahlen et al., 1994; Ambrosio et al., 1996; Bernardini et al., 1994; Palamara et al., 1996), respectively. For muon multiplicities $m \geq 2$ the Fréjus data are well fitted by the empirical expression

$$\Phi_m = \frac{K}{m^\nu} \; (m \geq 2) \qquad \text{with} \qquad \nu = \frac{\nu_1}{1 + a\, m} \tag{4.57}$$

with $K = (5.6 \pm 0.5) \cdot 10^{-9}$ cm^{-2}s^{-1}, $\nu_1 = 4.63 \pm 0.11$, and $a = (0.66 \pm 0.16) \cdot 10^{-2}$, with a correlation coefficient for ν_1 and a of 0.918.

The multi-muon fluxes recorded with the Fréjus detector are presented in Table 4.21. Fluxes specified in a later paper (Berger et al., 1989b) are insignificantly different from those given here. The characteristic distance, r_m, of the lateral distribution given in the table is based on the assumption that the distribution can be represented by the expression

$$\left(\frac{1}{N}\right) \frac{dN}{dr} = \frac{r}{r_m^2} e^{-\left(\frac{r}{r_m}\right)} \tag{4.58}$$

Table 4.19: Multi-Muon Events Recorded with the Utah Detector. (Lowe et al., 1975)

Depth	Zenith Angle	Rates of n-Fold Muon Multiplicity in 80 m^2 Detector $[s^{-1}sr^{-1}]$				
		$n = 1$	$n = 2$	$n = 3$	$n = 4$	$n = 5$
$[hg\,cm^{-2}]$	[deg.]					
$3.2 \cdot 10^3$	47.5	$(7.86 \pm 0.40) \cdot 10^{-2}$	$(1.58 \pm 0.10) \cdot 10^{-3}$	$(1.82 \pm 0.14) \cdot 10^{-4}$	$(5.9 \pm 0.9) \cdot 10^{-5}$	$(2.5 \pm 0.7) \cdot 10^{-5}$
	52.5	$(8.44 \pm 0.53) \cdot 10^{-2}$	$(1.55 \pm 0.11) \cdot 10^{-3}$	$(1.84 \pm 0.17) \cdot 10^{-4}$	$(5.2 \pm 1.3) \cdot 10^{-5}$	$(2.6 \pm 0.7) \cdot 10^{-5}$
	47.5	$(2.14 \pm 0.15) \cdot 10^{-2}$	$(3.98 \pm 0.34) \cdot 10^{-4}$	$(4.4 \pm 0.8) \cdot 10^{-5}$	$(1.6 \pm 0.4) \cdot 10^{-5}$	$(4.0 \pm 2.0) \cdot 10^{-6}$
	52.5	$(2.39 \pm 0.18) \cdot 10^{-2}$	$(4.29 \pm 0.38) \cdot 10^{-4}$	$(5.3 \pm 0.6) \cdot 10^{-5}$	$(1.9 \pm 0.3) \cdot 10^{-5}$	$(5.9 \pm 1.1) \cdot 10^{-6}$
	57.5	$(2.76 \pm 0.20) \cdot 10^{-2}$	$(4.49 \pm 0.37) \cdot 10^{-4}$	$(5.2 \pm 0.5) \cdot 10^{-5}$	$(1.31 \pm 0.16) \cdot 10^{-5}$	$(4.3 \pm 0.9) \cdot 10^{-6}$
	62.5	$(3.13 \pm 0.22) \cdot 10^{-2}$	$(4.25 \pm 0.33) \cdot 10^{-4}$	$(4.24 \pm 0.48) \cdot 10^{-5}$	$(1.6 \pm 0.5) \cdot 10^{-5}$	$(2.8 \pm 1.1) \cdot 10^{-6}$
$4.0 \cdot 10^3$	62.5	$(9.12 \pm 0.80) \cdot 10^{-3}$	$(1.38 \pm 0.12) \cdot 10^{-4}$	$(1.7 \pm 0.2) \cdot 10^{-5}$	$(3.5 \pm 0.9) \cdot 10^{-6}$	$(1.3 \pm 0.6) \cdot 10^{-6}$
	67.5	$(1.11 \pm 0.09) \cdot 10^{-2}$	$(1.34 \pm 0.14) \cdot 10^{-4}$	$(1.38 \pm 0.30) \cdot 10^{-5}$	$(3.2 \pm 2.1) \cdot 10^{-6}$	$(0.93 \pm 0.44) \cdot 10^{-6}$
	72.5	$(1.46 \pm 0.11) \cdot 10^{-2}$	$(1.34 \pm 0.24) \cdot 10^{-4}$	$(1.28 \pm 0.40) \cdot 10^{-5}$	$(0.78 \pm 0.97) \cdot 10^{-6}$	0.0
$4.8 \cdot 10^3$	62.5	$(3.31 \pm 0.70) \cdot 10^{-3}$	$(5.52 \pm 0.80) \cdot 10^{-5}$	$(5.3 \pm 1.9) \cdot 10^{-6}$	0.0	
	67.5	$(4.41 \pm 0.42) \cdot 10^{-3}$	$(5.58 \pm 0.62) \cdot 10^{-5}$	$(5.2 \pm 1.9) \cdot 10^{-6}$	$(0.43 \pm 0.35) \cdot 10^{-6}$	$(0.49 \pm 0.35) \cdot 10^{-6}$
	72.5	$(4.65 \pm 0.44) \cdot 10^{-3}$	$(5.2 \pm 0.6) \cdot 10^{-5}$	$(3.4 \pm 0.9) \cdot 10^{-6}$	$(1.4 \pm 0.6) \cdot 10^{-6}$	0.0
$5.6 \cdot 10^3$	67.5	$(1.39 \pm 0.16) \cdot 10^{-3}$	$(1.5 \pm 0.4) \cdot 10^{-5}$	$(2.0 \pm 0.9) \cdot 10^{-6}$	0.0	
	72.5	$(1.90 \pm 0.22) \cdot 10^{-3}$	$(2.0 \pm 0.4) \cdot 10^{-5}$	$(1.5 \pm 0.6) \cdot 10^{-6}$	$(0.17 \pm 0.24) \cdot 10^{-6}$	
	77.5	$(2.42 \pm 0.26) \cdot 10^{-3}$	$(0.99 \pm 0.19) \cdot 10^{-5}$	$(0.75 \pm 0.46) \cdot 10^{-6}$	0.0	
$6.4 \cdot 10^3$	72.5	$(7.7 \pm 1.2) \cdot 10^{-4}$	$(1.2 \pm 0.3) \cdot 10^{-5}$	$(1.8 \pm 1.0) \cdot 10^{-6}$	$(0.5 \pm 0.6) \cdot 10^{-6}$	
	77.5	$(8.8 \pm 1.1) \cdot 10^{-4}$	$(0.37 \pm 0.12) \cdot 10^{-5}$	$(0.23 \pm 0.28) \cdot 10^{-6}$	0.0	
$7.2 \cdot 10^3$	72.5	$(3.3 \pm 0.5) \cdot 10^{-4}$	$(0.35 \pm 0.13) \cdot 10^{-5}$	$(0.42 \pm 0.50) \cdot 10^{-6}$		
	77.5	$(3.5 \pm 0.5) \cdot 10^{-4}$	$(0.25 \pm 0.11) \cdot 10^{-5}$	0.0		
$8.0 \cdot 10^3$	77.5	$(1.34 \pm 0.25) \cdot 10^{-4}$	$(0.15 \pm 0.07) \cdot 10^{-5}$			
	82.5	$(2.0 \pm 0.3) \cdot 10^{-4}$	0.0			

Table 4.20: Multiple Muons in the Utah Detector.
(Detector size: for $n < 10$, 80 m^2; for $n \geq 10$, 100 m^2).
(Elbert et al., 1975)

Zenith Angle [deg.]	Depth [hg cm^{-2}]	Muon Multiplicity n	Measured Rate [$s^{-1}sr^{-1}$]
47.5	$2.4 \cdot 10^3$	1	$(0.786 \pm 0.040) \cdot 10^{-1}$
		2	$(0.158 \pm 0.010) \cdot 10^{-2}$
		3	$(0.182 \pm 0.014) \cdot 10^{-3}$
		4	$(0.592 \pm 0.094) \cdot 10^{-4}$
		5	$(0.251 \pm 0.070) \cdot 10^{-4}$
	$3.2 \cdot 10^3$	1	$(0.214 \pm 0.015) \cdot 10^{-1}$
		2	$(0.398 \pm 0.034) \cdot 10^{-3}$
		3	$(0.439 \pm 0.077) \cdot 10^{-4}$
		4	$(0.159 \pm 0.041) \cdot 10^{-4}$
62.5	$3.2 \cdot 10^3$	1	$(0.313 \pm 0.022) \cdot 10^{-4}$
		2	$(0.425 \pm 0.033) \cdot 10^{-3}$
		3	$(0.424 \pm 0.048) \cdot 10^{-4}$
		4	$(0.162 \pm 0.048) \cdot 10^{-4}$
	$4.0 \cdot 10^3$	1	$(0.912 \pm 0.080) \cdot 10^{-2}$
		2	$(0.138 \pm 0.012) \cdot 10^{-3}$
		3	$(0.170 \pm 0.018) \cdot 10^{-4}$
	$4.8 \cdot 10^3$	1	$(0.331 \pm 0.070) \cdot 10^{-2}$
		2	$(0.552 \pm 0.080) \cdot 10^{-4}$
72.5	$4.0 \cdot 10^3$	1	$(0.146 \pm 0.011) \cdot 10^{-1}$
		2	$(1.34 \pm 0.24) \cdot 10^{-4}$
	$4.8 \cdot 10^3$	1	$(0.465 \pm 0.044) \cdot 10^{-2}$
		2	$(0.518 \pm 0.059) \cdot 10^{-4}$
	$5.6 \cdot 10^3$	1	$(0.190 \pm 0.022) \cdot 10^{-2}$
		2	$(0.202 \pm 0.038) \cdot 10^{-4}$
	$6.4 \cdot 10^3$	1	$(0.773 \pm 0.118) \cdot 10^{-3}$
	$7.2 \cdot 10^3$	1	$(0.328 \pm 0.046) \cdot 10^{-3}$
	$8.0 \cdot 10^3$	1	$(0.113 \pm 0.018) \cdot 10^{-3}$
30.0	$1.6 \cdot 10^3$	10 - 14	$(0.456 \pm 0.036) \cdot 10^{-4}$
		15 - 19	$(0.147 \pm 0.019) \cdot 10^{-4}$
		20 - 29	$(0.600 \pm 0.130) \cdot 10^{-5}$
	$2.0 \cdot 10^3$	10 - 14	$(0.177 \pm 0.020) \cdot 10^{-4}$
		15 - 19	$(0.500 \pm 0.110) \cdot 10^{-5}$

Table 4.21: Multi-Muon Flux Recorded with the Fréjus Detector. (Fréjus Collaboration, 1987)

Muon Multiplicity m	Event Flux $[cm^2s^{-1}]$	Characteristic Distance r_m [m]
2	$(2.16 \pm 0.05) \cdot 10^{-10}$	1.75 ± 0.04
3	$(4.67 \pm 0.30) \cdot 10^{-11}$	1.70 ± 0.09
4	$(9.51 \pm 1.09) \cdot 10^{-12}$	1.39 ± 0.04
5	$(3.28 \pm 1.24) \cdot 10^{-12}$	1.39 ± 0.04 for n > 4

where r is the distance between the muon and the unknown event axis, and the characteristic distance, r_m, is assumed to depend on multiplicity and incident direction.

The large detectors mentioned above, including LVD (Aglietta et al., 1994) give a far more realistic picture of the true flux of multi-muons than the previous generation of much smaller instruments. The latter missed a significant fraction of high multiplicity events and large corrections had to be implemented to estimate the true flux.

Decoherence Distributions and Angular Spread

The lateral separation of muons in di-muon events and of pairs in multi-muon events has been measured in several experiments. One method is to determine the decoherence curve. This curve shows the rate of pairs of coincident muons in two small detectors as a function of detector separation, divided by the product of the areas of the detectors. In large detectors where two or more muon tracks are recorded simultaneously, the decoherence distribution can be determined directly, whereby the limitations imposed by the detector mentioned above must be observed.

Early results of decoherence studies from different groups are summarized in Fig. 4.60 (Totsuka and Koshiba, 1974) and phenomenological considerations are discussed by Davis et al. (1971). In Figs. 4.61 and 4.62 muon pair decoherence curves are shown for different zenith angles and depths (Bergeson et al., 1975; Lowe et al., 1976). Fig. 4.63 shows the di-muon separation distributions at a depth of 1840 hg cm^{-2} for the angular range $0° \leq \theta \leq 60°$, observed at the Kolar Gold Fields (Krishnaswamy et al., 1979). Similar data recorded at different depths (754, 1500, 3375 and 6045 hg cm^{-2}) at the same

site are discussed by Krishnaswamy et al. (1977).

The decoherence curve obtained with the Homestake detector, a 300 ton water Cherenkov counter system located at a depth of 4200 m w.e., is shown in Fig. 4.64 (Cherry et al., 1981 and 1982). Also shown in this figure are earlier data from the Utah detector and two theoretical distributions (Elbert and Stanev, 1983). Likewise, Chudakov et al. (1990) made extensive measurements at Baksan. One set of data shows the decoherence curves for different zenith angle intervals and more or less constant slant depth (Fig. 4.65). The other set is restricted to the zenith angle window between 50° and 60° and different slant depths corresponding to muon threshold energies between 0.28 TeV and 3.16 TeV (Fig. 4.66).

Very recent decoherence measurements on muons underground were carried out with the large MACRO detector, measuring 77 m × 12 m × 9 m (Ahlen et al., 1994; Battistoni et al., 1995; Ambrosio et al., 1996, 1997 and 1999b; Sioli, 2000). The distribution depends rather strongly on the event selection criteria and the corrections applied to the raw data. The most recent data (Sioli, 2000) are shown in Fig. 4.67. The results of the work of Ahlen et al. (1994), obtained with the lower part of the detector having an acceptance of 3100 m^2 sr are shown in Fig. 4.68 together with a data sample obtained by Battistoni et al. (1995) which shows the muon pair separation for events with a multiplicity $m \geq 8$.

Furthermore, Battistoni et al. (1995) have also measured the *decorrelation distribution* with the MACRO detector. This distribution shows the relative angle subtended by a muon pair as a function of pair separation (Fig. 4.69).

Theoretical Contributions to Multi-Muon Events

Theoretical studies of multi-muon events had been carried out by many authors, frequently in connection with air shower studies, using Monte Carlo simulations (Ambrosio et al., 1997; Battistoni et al., 1995; Bilokon et al., 1990; Boziev et al., 1990; Budko et al., 1987; Chudakov, 1979; Cline, 1982; Davis et al., 1971; Elbert, 1979 and 1982; Elbert et al., 1981; Forti et al., 1990; Gaisser and Stanev, 1982 and 1985; Goned et al., 1975; Grieder, 1977, 1985 and 1986).

References

Achar, C.V., V.S. Narasimham, P.V. Ramana Murthy, D.R. Creed, J.B.M. Pattison, and A.W. Wolfendale: PRICRC, 2, p. 989 (1965a).

Achar, C.V., V.S. Narasimham, P.V. Ramana Murthy, D.R. Creed, J.B.M. Pattison, and A.W. Wolfendale: Proc. Phys. Soc., 86, p. 1305 (1965b).

Adarkar, H., et al.: Proc. Internat. Symposium on Underground Physics Experiments, ed. K. Nakamura (1990a).

Adarkar, H., S.R. Dugad, M.R. Krishnaswamy, M.G.K. Menon, N.K. Mondal, V.S. Narasimham, B.V. Sreekantan, Y. Hayashi, N. Ito, S. Kawakami, T. Nakamura, K. Tanaka, and S. Miyake: PICRC, 9, p. 310 (1990b).

Afanasieva, T.N., M.A. Ivanova, I.P. Ivanenko, N.P. Il'ina, L.A. Kuzmichev, K.V. Mandritskaya, E.A. Osipova, I.V. Rakobolskaya, L.V. Volkova, and G.T. Zatsepin: PICRC, 6, p. 161 (1987).

Aglietta, M., G. Badino, G. Bologna, C. Castagnoli, A. Castellina, B. D'Ettorre Piazzoli, W. Fulgione, P. Galeotti, G. Mannochi, P. Picchi, O. Saavedra, G. Trinchero,, and S. Vernetto: Nucl. Phys. B, (Proc. Suppl.) 14, p. 193 (1990a).

Aglietta, M., G. Badino, G. Bologna, C. Castagnoli, A. Castellina, B. D'Ettorre Piazzoli, W. Fulgione, P. Galeotti, G. Mannochi, P. Picchi, O. Saavedra, G. Trinchero,, and S. Vernetto: PICRC, 9, p. 352 (1990b).

Aglietta, M., et al., LVD Collaboration: Nucl. Phys. B, (Proc. Suppl.) 35, p. 243 (1994).

Aglietta, M., et al., LVD Collaboration: Astropart. Phys., 3, p. 311 (1995a).

Aglietta, M., et al., LVD Collaboration: PICRC, 1, p. 544 (1995b).

Aglietta, M., et al., LVD Collaboration: Report No INFN/AE-97/35 (1997).

Ahlen, S., et al.: MACRO Collaboration, INFN Laboratori Nazionali del Gran Sasso, Report No LNGS-94/114 December (1994).

Alexeyev, E.N., A.E. Chudakov, V.A. Gurentsov, S.P. Mikheev, and V.A. Tizengausen: PICRC, 3, p. 1936 (1973a).

Alexeyev, E.N., V.A. Gurentsov, S.P. Mikheev, V.A. Tizengausen, and A.E. Chudakov: Izv. Akad. Nauk, SSSR, 37, p. 1488 (1973b).

Alexeyev, E.N., Yu.M. Andreyev, A.E. Chudakov, A.A. Gitelson, V.I. Gurentsov, Ya.S. Elensky, Yu.V. Malovichko, V.Ya. Markov, V.I. Stepanov: PICRC, 10, p. 12 (1979a).

Alexeyev, E.N., V.V. Alexeyenko, Yu.M. Andreyev, V.N. Bakatanov, A.N.

Budkevich, A.E. Chudakov, M.D. Gal'perin, A.A. Gitelson, V.I. Gurentsov, A.E. Danshin, V.A. Dogujaev, V.L. Dadykin, Ya.S. Elensky, V.A. Kozyarivsky, I.M. Kogai, N.F. Klimenko, A.A. Kiryishin, Yu.N. Konovalov, B.A. Makoev, V.Ya. Markov, Yu.Ya. Markov, Yu.V. Malovichko, N.A. Metlinsky, A.R. Mikhelev, S.P. Mikheyev, Yu.S. Novosel'tsev, V.G. Sporshikov, V.V. Sklyarov, Yu.V. Sten'kin, V.I. Stepanov, Yu.R. Sula-Petrovsky, T.I. Tulupova, A.V. Voevodsky, V.I. Volchenko, V.N. Zakidyshev: PICRC, 10, p. 276 (1979b).

Alexeyev, E.N., L.N. Alexeyeva, A.E. Chudakov, and I.V. Krivosheina: PICRC, 6, p. 277 (1987).

Allkofer, O.C., W.D. Dau, and H. Jokisch: Phys. Lett., B 31, p. 606 (1970).

Allkofer, O.C., K. Carstensen, and W.D. Dau: Phys. Lett., B 36, p. 425 (1971).

Ambrosio, M. et al., MACRO Collaboration: INFN - Laboratori Nazionali del Gran Sasso, Italy. Report No LNGS-93/71 (1993).

Ambrosio,M., et al., MACRO Collaboration: INFN - Laboratori Nazionali del Gran Sasso, Italy. Report No. LNGS - 95/03 (1995).

Ambrosio,M., et al., MACRO Collaboration: INFN - Laboratori Nazionali del Gran Sasso, Italy. Report No. INFN/AE - 96/28 (1996).

Ambrosio,M., et al., MACRO Collaboration: INFN - Laboratori Nazionali del Gran Sasso, Italy. Report No. INFN/AE - 97/28 (1997).

Ambrosioe, M., R. Antolini, C. Aramo, G. Auriemma, A. Baldini, G.C. Barbarino, B.C. Barish, G. Battistoni, R. Bellotti, C. Bemporad, P. Bernardini, H. Bilokon, V. Bisi, C. Bloise, C. Bower, S. Bussino, F. Cafagna, M. Calicchio, D. Campana, M. Carboni, M. Castellano, S. Cecchini, F. Cei, V. Chiarella, B.C. Choudhary, S. Coutu, L. De Benedictis, G. De Cataldo, H. Dekhissi, C. De Marzo, I. De Mitri, J. Derkaoui, M. De Vincenzi, A. Di Credico, 0. Erriquez, C. Favuzzi, C. Forti, P. Fusco, G. Giacomelli, G. Giannini, N. Giglietto, M. Giorgini, M. Grassi, L. Gray, A. Grillo, F. Guarino, P. Guarnaccia, C. Gustavino, A. Habig, K. Hanson, R. Heinz, Y. Huang, E. Iarocci, E. Katsavounidis, E. Kearns, H. Kim, S. Kyriazopoulou, E. Lamanna, C. Lane, D.S. Levin, P. Lipari , N.P. Longley, M.I. Longo, F. Maaroufi, G. Mancarella, G. Mandrioli, S. Manzoor, A. Margiotta Neri, A. Marini, D. Martello, A. Marzari-Chiesa, M.N. Mazziotta, C. Mazzotta, D.G. Michael, S. Mikheyev, L. Miller, P. Monacelli, T. Montaruli, M. Monteno, S. Mufson, J. Musser, D. Nicoló, C. Orth, G. Osteria, M. Ouchrif, 0. Palamara, V. Patera, L. Patrizii, R. Pazzi, C.W. Peck, S. Petrera, P. Pistilli, V. Popa, V. Pugliese, A. Rainò, J. Reynoldson, F. Ronga, U. Rubizzo, C. Satriano,

L. Satta, E. Scapparone, K. Scholberg, A. Sciubba, P. Serra-Lugaresi, M. Severi, M. Sioli, M. Sitta, P. Spinelli, M. Spinetti, M. Spurio, R. Steinberg, J.L. Stone, L.R. Sulak, A. Surdo, G. Tarlè, V. Togo, D. Ugolotti, M. Vakili, C.W. Walter, and R. Webb, MACRO Collaboration: Astropart. Phys., 10, p. 11 (1999a).

Ambrosio, M. et al., MACRO Collaboration: Phys. Rev., D 60, p. 032001 (1999b).

Andreyev, Yu.M., V.I. Gurentsov, and I.M. Kogai: PICRC, 6, p. 200 (1987).

Andreyev, Yu.M., A.E. Chudakov, V.I. Gurentsov, and I.M. Kogai: PICRC, 9, p. 301 (1990).

Appleton, I.C., M.T. Hogue, and B.C. Rastin: Nucl. Phys., B 26, p. 365 (1971).

Ashton, F., A.W. Wolfendale, and W.F. Nash: PICRC, 1, p. 302 (1959), N.M. Gerasimova, ed. (printed 1960).

Avan, L. and M. Avan: Compt. Rend., 241, p. 1122 (1955).

Ayre, C.A., J.M. Baxendale, C.J. Hume, B.C. Nandi, M.G. Thompson, and M.R. Whalley: J. Phys. G, 1, p. 584 (1975).

Bakatanov, V.N., A.E. Chudakov, A.E. Danshin, N.F. Klimenko, Yu.F. Novosel'tsev, and Yu.V. Sten'kin: PICRC, 10, p. 179 (1979).

Barbouti, A.I., and B.C. Rastin: J. Phys., G 9, p. 1577 (1983).

Barrett, P.H., L.M. Bollinger, G. Cocconi, Y. Eisenberg, and K. Greisen: Rev. Mod. Phys., 24, p 133 (1952).

Barton, J.C.: Phil. Mag., 6, p. 1271 (1961).

Barton, J.C., and M. Slade: PICRC, p. 1006 (1965).

Barton, J.C., and C.T. Stockel: J. Phys. A, 2, p. 650 (1969).

Baschiera, B., L. Bergamasco, C. Castagnoli and P. Picchi: Lett. Nuovo Cimento, 4, p. 121 (1970).

Baschiera, B., L. Bergamasco, C. Castagnoli and P. Picchi: Lett. Nuovo Cimento, 1, p. 901 (1971).

Baschiera, B., G. Basini, H. Bilokon, B. D'Ettorre Piazzoli, G. Mannocchi, C. Castagnoli, and P. Picchi: Nuovo Cimento, 2 C, p. 473 (1979).

Battistoni, G., E. Bellotti, C. Bloise, G. Bologna, P. Campana, C. Castagnoli, A. Castellina, V. Chiarella, A. Ciocio, D. Cundy, B. D'Ettorre Piazzoli, E. Fiorini, P. Galeotti, E. Iarocci, C. Liguori, G. Mannocchi, G. Murtas, P. Negri, G. Nicoletti, P. Picchi, M. Price, A. Pullia, S. Ragazzi, M. Rollier, O.

Saavedra, L. Satta, S. Vernetto, and L. Zanotti: PICRC, 2, p. 158 (1985).

Battistoni, G., et al., MACRO Collaboration: PICRC, 1, p. 528 (1995).

Battistoni, G., C. Bloice, C. Forti, M. Greco, J. Ranft, and A. Tanzini: Astropart. Phys., 4, p. 351 (1996).

Bergamasco, L. and P. Picchi: Nuovo Cimento, 3B, p. 134 (1971).

Bergamasco, L., B. D'Ettorre Piazzoli, and P. Picchi: Nuovo Cimento, 4B, p. 59 (1971).

Bergamasco, L., A. Castellina, B. D'Ettorre Piazzoli, G. Mannocchi, P. Picchi, and S. Vernetto: Nuovo Cimento, 6C, p. 569 (1983).

Berger, Ch., M. Fröhlich, H. Mönch, R. Nisius, F. Raupach, P. Schleper, Y. Benadjal, D. Blum, C. Bourdarios, B. Dudelzak, P. Eschstruth, S. Jullian, D. Lalanne, F. Laplanche, C. Longuemare, C. Paulot, O. Perdereau, Ph. Roy, G. Szklarz, L. Behr, B. Degrange, U. Nguyen-Khac, S. Tisserant, C. Arpesella, P. Bareyre, R. Barloutaud, A. Borg, G. Chardin, J. Ernwein, J.F. Glicenstein, L. Mosca, L. Moscoso, J. Becker, K.H. Becker, H.J. Daum, S. Demski, B. Jacobi, B. Kuznik, R. Mayer, H. Meyer, R. Möller, M. Schubnell, B. Seyffert, Y. Wei, and P. Wintgen: Phys. Lett., B 227, p. 489 (1989a).

Berger, Ch., M. Fröhlich, H. Mönch, R. Nisius, F. Raupach, P. Schleper, Y. Benadjal, D. Blum, C. Bourdarios, B. Dudelzak, P. Eschstruth, S. Jullian, D. Lalanne, F. Laplanche, C. Longuemare, C. Paulot, O. Perdereau, Ph. Roy, G. Szklarz, L. Behr, B. Degrange, Y. Minet, U. Nguyen-Khac, P. Serri, S. Tisserant, R.D. Tripp, C. Arpesella, P. Bareyre, R. Barloutaud, A. Borg, G. Chardin, J. Ernwein, J.F. Glicenstein, L. Mosca, L. Moscoso, J. Becker, K.H. Becker, H.J. Daum, S. Demski, B. Jacobi, B. Kuznik, R. Mayer, H. Meyer, R. Möller, M. Schubnell, B. Seyffert, Y. Wei, and P. Wintgen: Phys. Rev. D 40, p. 2163 (1989b).

Berger, Ch., M. Fröhlich, H. Mönch, R. Nisius, F. Raupach, Y. Benadjal, D. Blum, C. Bourdarios, B. Dudelzak, P. Eschstruth, S. Jullian, D. Lalanne, F. Laplanche, C. Longuemare, C. Paulot, O. Perdereau, Ph. Roy, G. Szklarz, L. Behr, B. Degrange, Y. Minet, U. Nguyen-Khac, S. Tisserant, C. Arpesella, P. Bareyre, R. Barloutaud, A. Borg, G. Chardin, J. Ernwein, J.F. Glicenstein, L. Mosca, L. Moscoso, J. Becker, K.H. Becker, H.J. Daum, B. Jacobi, B. Kuznik, H. Meyer, R. Möller, M. Schubnell, and Y. Wei: Z. Phys., C 48, p. 221 (1990).

Bergeson, H.E., J.W. Keuffel, M.O. Larson, E.R. Martin, and G.W. Mason: Phys. Rev. Lett., 19, p. 1487 (1967).

Bergeson, H.E., J.W. Keuffel, M.O. Larson, G.W. Mason, and J.L. Osborne: Phys. Rev. Lett., 21, p. 1089 (1968).

Bergeson, H.E., G.L. Bolingbroke, G. Carlson, D.E. Groom, J.W. Keuffel, J.L. Morrison, and J.L. Osborne: Phys. Rev. Lett., 27, p. 160 (1971).

Bergeson, H.E., G.W. Carlson, J.W. Keuffel, and J.L. Morrison: PICRC, 3, p. 1722 (1973).

Bergeson, H.E., J.W. Elbert,J.W. Keuffel, M.O. Larson, G.H. Lowe, J.L. Morrison, W.J. West, and G.W. Mason: Phys. Rev. Lett., 35, p. 1681 (1975).

Bernardini, P., et al., MACRO Collaboration: Nucl. Phys. B, (Proc. Suppl.) 35 B, p. 229 (1994).

Bezrukov, L.B., et al.: Yadernaya Fisica 15, p. 313 (1972).

Bhat, P.N. and P.V. Ramana Murthy: Lett. Nuovo Cimento, 4, p. 543 (1972).

Bhat, P.N. and P.V. Ramana Murthy: J. Phys. A, 6, p. 1960 (1973a).

Bhat, P.N. and P.V. Ramana Murthy: PICRC, 3, p. 1923 (1973b).

Bhat, P.N. and P.V.Ramana Murthy: J. Phys. G, 4, p. 453 (1978).

Bilokon, H., B. D'Ettorre Piazzoli, C. Forti, T.K. Gaisser, L. Satta, and T. Stanev: PICRC, 9, p. 366 (1990).

Bollinger, I.M.: Phys. Rev., 79, p. 207A (1950).

Bollinger, I.M.: Ph. D. thesis, Cornell University (1951).

Boziev, S.N., A.E. Chudakov, and A.V. Voevodsky: PICRC, 9, p. 38 (1990).

Budini, P., and G. Molière: in Kosmische Strahlung, ed. W. Heisenberg (Springer, Berlin) (1953).

Budko, E.V., A.E. Chudakov, V.A. Dogujaev, O.V. Suvorova, A.L. Tsyabuk, and A.V. Voevodsky: PICRC, 6, p. 221 (1987).

Bugaev, E.V.: Proceedings of Union Conference on Cosmic Ray Physics, Tashkent, I, 2, p. 74 (1968).

Bugaev, E.V., et al.: Preprint No. P-0347, Institute for Nuclear Research, Moscow (1984).

Bugaev, E.V., V.A. Naumov, S.I. Sinegovsky, and E.S. Zaslavskaya: PICRC, 6, p. 165 (1987).

Bugaev, E.V., V.A. Naumov, S.I. Sinegovsky, and E.S. Zaslavskaya: Nuovo Cimento, C 12, p. 41 (1989a).

Bugaev, E.V., V.A. Naumov, S.I. Sinegovsky, and E.S. Zaslavskaya: Izv. Akad. Nauk SSSR, Ser. Fiz. 53, p. 342 (1989b). Proc. of the Acad. of Sci. of the USSR. Phys. Ser. 53, p. 135 (1989b).

Bugaev, Edgar V., Vadim A. Naumov, Sergey I. Sinegovsky, Akeo Misaki, Nobusuke Takahashi, and Elena S. Zaslavskaya: Proceedings of Nestor Workshop, p. 268 (1993).

Bugaev, Edgar V., Vadim A. Naumov, Sergey I. Sinegovsky, Akeo Misaki, Nobusuke Takahashi, and Elena S. Zaslavskaya: Università degli Studi di Firenze, Dipartimento di Fisica and Instituto Nationale di Fisica Nucleare Sezione di Firenza, Preprint DFF 204/4/1994 (1994).

Bugaev, E.V., A. Misaki, V.A. Naumov, T.S. Sinegovskaya, S.I. Sinegovsky, and N. Takahashi: Phys. Rev., D 58, p. 54001 (1998).

Bussino, S., et al., the MACRO Collaboration: PICRC, 1, p. 540 (1995).

Calicchio, M., C. De Marzo, O. Erriquez, C. Favuzzi, N. Giglietto, E. Nappi, F. Posa, and P. Spinelli: Phys. Lett., B 193, p. 131 (1987).

Cannon, T.M. and R.O. Stenerson: J. Phys. A, 4, p. 266 (1971).

Cassiday, G.L., P.C. Gilbert, and D.M. White: Phys. Rev. Lett., 27, p. 164 (1971).

Cassiday, G.L., J.W. Keuffel, and J.A. Thompson: Phys. Rev. D, 7, p. 2022 (1973).

Castagnoli, C., A. De Marco, A. Longhetto, and P. Penengo: Nuovo Cimento, 35, p. 969 (1965).

Castagnoli, C., P. Picchi, A. Castellina, B. D'Ettorre Piazzoli, G. Mannocchi, and S. Vernetto: Nuovo Cimento, A82, p. 78 (1984).

Castagnoli, C., A. Castellina, O. Saavedra, T.M. Kirina, R.P. Kokoulin, and A.A. Petrukhin: Phys. Rev., D 52, p. 2673 (1995).

Castagnoli, C., A. Castellina, O. Saavedra, T.M. Kirina, R.P. Kokoulin, and A.A. Petrukhin: Astropart. Phys., 6, p. 187 (1997).

Castellina, A., B. D'Ettorre Piazzoli, G. Mannocchi, P. Picchi, and S. Vernetto: Nuovo Cimento, 8C, p. 93 (1985).

Cherry, M.L., M. Deakyne, K. Lande, C.K. Lee, R.J. Steinberg and E.J. Fenyves: PICRC 10, p. 342 (1981).

Cherry, M.L., M. Deakyne, K. Lande, C.K. Lee, R.J. Steinberg, B. Cleveland, R. Davis, Jr., and E.J. Fenyves: Proceedings of the Workshop on Very High Energy Cosmic Ray Interactions, University of Pennsylvania, Philadelphia (ed. L.M. Cherry, K. Lande, and R.I. Steinberg), p. 278 (1982).

Cherry, M.L.: Private communication (2000).

Chudakov, A.E.: PICRC, 10, p. 192 (1979).

Chudakov, A.E., V.A. Dogujaev, A.A. Kiryushin, V.Ya. Markov, A.R. Mikhelev, V.I. Stepanov, and A.V. Voevodsky: PICRC, 10, p. 188 (1979).

Chudakov, A.E., A.L. Tsyabuk, and V. Voevodsky: PICRC, 9, p. 348 (1990).

Chudakov, A.E., A.L. Tsyabuk, and V. Voevodsky: PICRC, 2, p. 5 (1991).

Clay, J., and A. van Gemert: Physica, 6, p. 497 (1939).

Cline, D.B.: Proceedings of the Workshop on Very High Energy Cosmic Ray Interactions, University of Pennsylvania, Philadelphia (ed. L.M. Cherry, K. Lande, and R.I. Steinberg), p. 411 (1982).

Coats, R.B., S. Ozaki, R.O. Stenerson, H.E. Bergeson, J.W. Keuffel, M.O. Larson, G.H. Lowe, J.L. Osborne, and J.H. Parker: J. Phys. A, 3, p 689 (1970).

Crookes, J.N. and B.C. Rastin: Nucl. Phys. B, 39, p. 493 (1972).

Crookes, J.N. and B.C. Rastin: Nucl. Phys. B, 58, p.93 (1973).

Crouch, M.F., P.B. Landecker, J.F. Lathrop, F. Reines, W.G. Sandie, H.W. Sabel, H. Coxell and J.P.F. Sellschop: Phys. Rev. D 18, p. 2239 (1978).

Crouch, Marshall: PICRC, 8, p. 20 (1985).

Crouch, Marshall: PICRC, 6, p. 165 (1987).

Czapek, G., B. Hahn, W. Krebs, and L. Müller: J. Phys. G., 16, p. 1101 (1990).

Daion, M.I., and L.I. Potapov: Sov. Physics, JETP, 36 (9), p. 697 (488) (1959a).

Daion, M.I., and L.I. Potapov: Sov. Physics, JETP, 36 (9), p. 921 (650) (1959b).

Davis, K.H., S.M. Fall, R.B. Ingebretsen, and R.O. Stenerson: Phys. Rev. D, 4, p. 607 (1971).

Davitaev, L.N., V.M. Fyodorov, Yu.A. Trubkin, Yu.N. Vavilov: Acta Phys. Acad. Sci. Hung., 29, Suppl. 4, p. 53 (1970).

De, A.K., P. Ghosh, S. Mitra, P.C. Bhattacharyya, and A.K. Das: J. Phys., A 5, p. 1236 (1972).

DeMuth, David, M.: Thesis University of Minnesota (1999).

Elbert, J.W., J.W. Keuffel, G.H. Lowe, J.L. Morrison, and G.W. Mason: Phys. Rev., D 12, p. 660 (1975).

Elbert, J.W.: PICRC, 10, p.405 (1979).

Elbert, J.W.: Proceedings of the Workshop on Very High Energy Cosmic Ray Interactions, University of Pennsylvania, Philadelphia (ed. L.M. Cherry, K.

Lande, and R.I. Steinberg), p. 312 (1982).

Elbert, J.W., and Todor Stanev: PICRC, 5, p. 229 (1983).

Elbert, J.W., J.W. Keuffel, and J.A. Thompson: Phys. Rev. Lett., 29, p. 1270 (1972).

Elbert, J.W., J.W. Keuffel, G.H. Lowe, J.L. Morrison, and G.W. Mason: Phys. Rev. D, 12, p. 660 (1975).

Elbert, J.W., T.K. Gaisser, and Todor Stanev: PICRC, 7, p. 42 (1981).

Elbert, J.W., T.K. Gaisser, and T. Stanev: Phys. Rev., D27, p. 1448 (1983).

Enikeev, R.I., V.A. Kudryavtsev, A.S. Mal'grin, O.G. Ryazhskaya, and G.T. Zatsepin: PICRC, 10, p. 329 (1981).

Follett, D.H. and J.D. Crawshaw: Proc. R. Soc. A, 155, p. 546 (1936).

Forti, C., H. Bilokon, B. D'Ettorre Piazzoli, T.K. Gaisser, L. Satta, and Todor Stanev: Phys. Rev., D 42, p. 3668 (1990).

Fréjus Collaboration (Aachen - Orsay - Ecole Polytechnique - Saclay - Wuppertal): PICRC 6, p. 216 (1987).

Fyodorov, V.M., V.P. Pustovetov, Yu.A. Trubkin, and A.V. Kirilenkov: PICRC, 8, p. 39 (1985).

Gaisser, Thomas K.: Cosmic Ray and Particle Physics. Cambridge University Press (1990).

Gaisser, T.K., and T. Stanev: Proceedings of the Workshop on Very High Energy Cosmic Ray Interactions, University of Pennsylvania, Philadelphia (ed. L.M. Cherry, K. Lande, and R.I. Steinberg), p. 295 (1982).

Gaisser, T.K., and T. Stanev: Nucl. Instr. Meth., A235 (1985).

George, E.P.: in Progress in Cosmic Ray Physics, ed. J.G. Wilson, North-Holland Publ. Co., Amsterdam, 1, p. 393 (1952).

George, E.P., and G.S. Shrikantia: Nucl. Phys., 1, p. 54 (1956).

Giusti, P., et al., LVD Collaboration: PICRC, 1, p. 548 (1995).

Goned, A., T.R. Stewart, A.W. Wolfendale, and J. Wdowczyk: Nuovo Cimento, 29A, p. 317 (1975).

Goodman, M.: Private communication (2000).

Green, P.J., N.M. Duller, C.E. Magnuson, L.M. Choate, W.R. Sheldon, A.R. Osborne, J.R. Benbrook, and Abdel-Monem: Phys. Rev., D 20, p. 1598 (1979).

Greisen, K.: Phys. Rev., 61, p. 212 (1942).

Grieder, P.K.F.: Rivista del Nuovo Cimento, 7, p. 1 (1977).

Grieder, P.K.F.: PICRC, 8, p. 179 (1985).

Grieder, P.K.F.: in Cosmic Ray Muon and Neutrino Physics / Astrophysics Using Deep Underground / Underwater Detectors, ed. Y. Ohashi and V.Z. Peterson, Institute for Cosmic Ray Research, University of Tokyo, p. 183 (1986).

Grupen, C., A.W. Wolfendale, and E.C.M. Young: Nuovo Cimento, 10B, p. 144 (1972).

Grupen, C.: Fort. d. Phys., 23, p. 127 (1976).

Gurentsov, V.I.: Preprint No. P-0380, Inst. for Nucl. Res., Moscow (1984).

Hasted et al. (1948), after Higashi et al. (1966).

Hayman, P.J., and A.W. Wolfendale: Proc. Phys. Soc., 80, p. 710 (1962).

Hayman, P.J., N.S. Palmer, and A.W. Wolfendale: Proc. Roy. Soc., 275, p. 391 (1963).

Higashi, S., T. Kitamura, S. Miyamoto, Y. Mishima, T. Takahashi, and Y. Watase: Nuovo Cimento, 43A, p. 334 (1966).

Higashi, S., S. Ozaki, S. Miono, T. Takahashi, and K. Tsuji: PICRC, 3, p. 1930 (1973).

Il'ina, N.P., N.N. Kalmykov, I.V. Rakobolskaya, and G.T. Zatsepin: PICRC, 1, p. 524 (1995).

Inazawa, Hiroshi, and Keizo Kobayakawa: Progr. Theor. Phys., 69, p. 1195 (1983).

Inazawa, H., and K. Kobayakawa: PICRC, 8, p. 83 (1985).

Inazawa, H., K. Kobayakawa, and T. Kitamura: J. Phys. G, 12, p. 59 (1986a).

Inazawa, H., K. Kobayakawa, and T. Kitamura: Nuovo Cimento, C 9, p. 382 (1986b).

Judge, R.J.R. and W.F. Nash: Nuovo Cimento, 35, p. 999 (1965).

Kasahara, Susan, M.: Ph. D. Thesis, University of Minnesota, unpublished (1994).

Keuffel, J.W., J.L. Osborne, G.L. Bolingbroke, G.W. Mason, M.O. Larson, G.H. Lowe, J.H. Parker, R.O. Stenerson, and H.E. Bergeson: Acta Phys. Acad. Sci. Hung., 29, Suppl. 4, p. 183 (1970).

Khalchukov, F.F., E.V. Korolka, V.A. Kudryavtsev, A.S. Malgin, O.G. Ryazhskaya, and G.T. Zatsepin: PICRC 8, p. 12 (1985).

Kiraly, E., P. Kiraly, and J.L. Osborne: J. Phys. A, 5, p. 444 (1972).

Komori, H., and K. Mitsui: J. Phys. G, 8, p. L197 (1982).

Kong, Doreen F.L, S.Y. Lau, and L.K. Ng: PICRC, 6, p. 1859 (1975).

Kotov, Yu.D., and V.M. Logunov: Acta Phys. Acad. Sci. Hung., 29, Suppl. 4, p. 73 (1970).

Krishnaswamy, M.R., M.G.K. Menon, V.S. Narasimham, S. Kawakami, S. Kino, and S. Miyake: Phys. Lett., 27B, p. 535 (1968).

Krishnaswamy, M.R., M.G.K. Menon, V.S. Narasimham, S. Kawakami, S. Miyake, and A. Mizohata: Acta Phys. Acad. Sci. Hung., 29, Suppl. 4, p. 221 (1970a).

Krishnaswamy, M.R., M.G.K. Menon, V.S. Narasimham, S. Kawakami, S. Miyake, and A. Mizohata: Acta Phys. Acad. Sci. Hung., 29, Suppl. 4, p. 227 (1970b).

Krishnaswamy, M.R., M.G.K. Menon, V.S. Narasimham, H. Hinotani, N. Ito, S. Miyake, J.L. Osborne, A.J. Parson, and A.W. Wolfendale: Proc. Roy. Soc. London, A 323, p. 511 (1971a).

Krishnaswamy, M.R., M.G.K. Menon, V.S. Narasimham, H. Hinotani, S. Kawakami, S. Miyake: PICRC, 7, p. 2875 (1971b).

Krishnaswamy, M.R., M.G.K. Menon, V.S. Narasimham, H. Hinotani, S. Kawakami, S. Miyake: PICRC, 7, p. 2881 (1971b).

Krishnaswamy, M.R., M.G.K. Menon, V.S. Narasimham, H. Hinotani, S. Kawakami, S. Miyake: PICRC, 7, p. 2886 (1971b).

Krishnaswamy, M.R., M.G.K. Menon, V.S. Narasimham, N. Ito, S. Kawakami, and S. Miyake: PICRC, 6, p. 161 (1977).

Krishnaswamy, M.R., M.G.K. Menon, N.K. Mondal, V.S. Narasimham, Y. Hayashi, N. Ito, S. Kawakami, and S. Miyake: PICRC, 13, p. 383 (1979).

Krishnaswamy, M.R., M.G.K. Menon, N.K. Mondal, V.S. Narasimham, Y. Hayashi, N. Ito, S. Kawakami, and S. Miyake: PICRC, 11, p. 450 (1983).

Kropp, W.R., F. Reines and R.M. Woods: Phys. Rev. Lett. 20, p. 1451 (1968).

Kudryavtsev, V.A., et al., (LVD Collaboration): PICRC 1, p. 557 (1995).

Lagutin, A.A, et al.: Izv. RAN, Ser. fiz. 58 (12), p. 159 (1994).

Lamanna, E., et al., the MACRO Collaboration: PICRC, 4, p. 391 (1993).

Larson, M.O.: Ph. D. Thesis, University of Utah (1968).

Lipari, P., and T. Stanev: Phys. Rev., D 44, p. 3543 (1991).

Liu-Zhong-be, Wang Dien-rong, and Liu Jian-guo: PICRC, 10, p. 9 (1979).

Lohmann, W., R. Kopp, and R. Voss: CERN Yellow Report 85-03 (1985).

Lowe, G.H., M.O. Larson, H.E. Bergeson, J.W. Cardon, J.W. Keuffel, and J. West: Phys. Rev. D, 12, p. 651 (1975).

Lowe, G.H., H.E. Bergeson, J.W. Keuffel, M.O. Larson, J.L. Morrison, and W.J. West: Phys. Rev. D, 13, p. 2925 (1976).

Makarov, V.V, A.A. Lgutin, A.G. Prokopets, and A.I. Goncharov: PICRC, 1, p. 630 (1995).

Mandò, M., and L. Ronchi: Nuovo Cimento, 9, p. 517 (1952).

Menon, M.G.K.: Proc. Roy. Soc., 301, p. 137 (1967).

Menon, M.G.K. and P.V. Ramana Murthy: Progr. Elementary Particles and Cosmic Rays, North Holland, Amsterdam, 9, p. 161 (1967).

Menon, M.G.K., S. Naranan, V.S. Narasimham, K. Hinotani, N. Ito, S. Miyake, D.R. Creed, J.L. Osborne, J.B.M. Pattison, and A.W. Wolfendale: Proc. Phys. Soc., 90, p. 649 (1967).

Menon, M.G.K., S. Naranan, V.S. Narashinham, K. Hinotani, N. Ito,S. Miyake, D.R. Creed, J.L. Osborne and A.W. Wolfendale: Can. J. Phys. 46, p. S344 (1968).

Meyer, B.S., J.P.F. Sellschop, M.F. Crouch, W.R. Kropp, H.W. Sobel, H.S. Gurr, J. Lathrop, and F. Reines: Phys. Rev., D 1, p. 2229 (1970).

Meyer, H., M.W. Teucher and E. Lohrmann: Nuovo Cimento 28, p. 1399 (1963).

Mitsui, K: Phys. Rev., D 45, p. 3051 (1992).

Miyake, S.: J. Phys. Soc. Japan, 18, p. 1093 (1963).

Miyake, S.: PICRC, 5, p. 3638 (1973).

Miyake, S., V.S. Narashinham, and P.V. Ramana Murthy: Nuovo Cimento, 32, p. 1505 (1964).

Miyazaki, Y.: Phys. Rev., 76, p. 1733 (1949).

Mizutani, K. and I. Ohta: PICRC, 6, p. 1900 (1975).

Mizutani, K. and I. Ohta: PICRC, 6, p. 93 (1977).

Mizutani, K., I. Ohta, and K. Taira: PICRC, 10, p. 40 (1979).

Moroney, J.R. and J.K. Parry: Aust. J. Phys., 7, p. 423 (1954).

Murdoch, H.S., K.W. Ogilvie, and H.D. Rathgeber: PICRC, 1, p. 304 (1959), N.M. Gerasimova, ed. (printed 1960).

Nandi, B.C. and M.S. Sinha: J. Phys., A 5, p. 1384 (1972).

Nash, W.F., and A.J. Pointon: Proc. Phys. Soc., A69, p. 725 (1956).

Naumov, Vadim A., Sergey I. Sinegovsky, and Edgar V. Bugaev: Proc. 2nd. Internat. Nestor Workshop, Pylos, Greece, ed. L.K. Resvanis, University of Athens, p. 119 (1992).

O'Brien, K.: Phys. Rev. D, 5, p.597 (1972).

Palamara, O., et al., MACRO Collaboration: Nucl. Phys. B, (Proc. Suppl.) 48, p. 444 (1996).

Paul, C.R. and N. Chaudhuri: Nuovo Cimento B, 36(2), p. 165 (1976).

Paul, C.R. and N. Chaudhuri: Nuovo Cimento B, 37(1), p. 35 (1977).

Percy, J.C., and I.W. Rogers: PICRC 6, p. 99 (1977).

Petrukhin, A.A., and V.V. Shestakov: Can. J. Phys., 46, p. S377 (1968).

Randall, C.A. and W.E. Hazen: Phys. Rev., 81, p. 144 (1951).

Randall, C.A. and W.E. Hazen: Nuovo Cimento, 8, p. 878 (1958).

Rastin, B.C.: J. Phys., G 10, p. 1609 (1984).

Reilly, T.D.: Ph. D. Thesis, Case Western Reserve University (1969).

Reines, F., M.F. Crouch, T.L. Jenkins, W.R. Kropp, H.S. Gurr, G.R. Smith, H.W. Sobel, J.P.F. Sellschop, and B. Meyer: PICRC, 2, p. 1051 (1965).

Reines, F.: Proc. Roy. Soc., 301, p. 125 (1967).

Reines, F., W.R. Kropp, H.W. Sobel, H.S. Gurr, J. Lathrop, M.F. Crouch, J.P.F. Sellschop, and B.S. Meyer: Phys. Rev., D4, p. 80 (1971).

Rhode, Wolfgang: Ph. D. Thesis (Dissertation), Fachbereich Physik, Bergische Universität, Gesamthochschule Wuppertal, Germany. WUB-DIS 93-11 (1993).

Rhode, Wolfgang: Nucl. Phys. B (Proc. Suppl.) 35, p. 250 (1994).

Rhode, W., K. Daum, P. Bareyre, R. Barloutaud, G. Chardin, B. Degrange, J. Ernwein, B. Kuznik, H. Meyer, L. Mosca, L. Moscoso, O. Perdereau, M. Schubnell, S. Tisserant, and Y. Wei: Astropart. Phys., 4, p. 217 (1996).

Rogers, I.W., and M. Tristam: J. Phys. G., 10, p. 983 (1984).

Rozenthal, I.L.: Usp. Phys. Nauk, 94, p. 91 (1968); Soviet Phys. Uspekhi 11, p. 49 (1968).

Ruddick, K.: Soudan Collaboration, Internal Report PDK-435, unpublished (1990).

Sartorelli, G., et al., LVD Collaboration: PICRC, 1, p. 734 (1995).

Sheldon, W.R., W.G. Cantrell, N.M. Duller, F.Cambou, G. Vedrenne, R. Bazer-Bachi, A.St. Marc, and E. Barough: Acta Phys. Acad. Sci. Hung., 29, Suppl. 4, p. 209 (1970).

Sheldon, W.R., J.R. Benbrook, N.M. Duller, W.G. Cantrell, A.R. Bazer-Bachi, Gilbert Vedrenne, and Claude Dunet: Phys. Rev., D, 17, p. 114 (1978).

Short, A.M.: Proc. Phys. Soc. 81, p. 841 (1963).

Sioli, M., MACRO Collaboration: Nucl. Phys., B (Proc. Suppl.) 85, p. 349 (2000).

Sreekantan, B.V. and S. Naranan: Proc. Ind. Acad. Sci., 36, p. 97 (1952).

Sreekantan, B.V., S. Naranan, and P.V. Ramana Murthy: Proc. Ind. Acad. Sci., 43, p. 113 (1956).

Sternheimer, R.M.: Phys. Rev., 103, p. 511 (1956).

Stockel, C.T.: J. Phys. A, 2, p. 639 (1969).

Stockel, C.T.: Thesis, University of London (1967). (quoted by Wright (1973).

Suda, T.,Y. Totsuka, and M. Koshiba: J. Phys. Soc. Japan, 36, p 351 (1974).

Svoboda, R.: Ph.D. Thesis University of Hawaii at Manoa (1985).

Thunman, M., G. Ingelman, and P. Gondolo: Astropart. Phys., 5, p. 309 (1996).

Totsuka, Y. and M. Koshiba: J. Phys. Soc. Japan, 36, p 341 (1974).

Turekian, K.K.: in Handbook of Geochemistry, p. 309. Springer Verlag, K.H. Wedepohl ed., (1969).

Vernov, S.N., G.B. Khristiansen, Yu.A. Netchin, O.V. Vedeneev, and B.A. Khrenov: PICRC, 2, p. 952 (1965).

Volkova, L.V., G.T. Zatsepin, and L.D. Kuzmichev: Sov. J. Nucl. Phys., 29, p. 645 (1979).

Volkova, L.V., W. Fulgione, P. Galeotti, and O. Saavedra: Nuovo Cimento, 10C, p. 465 (1987).

Wilson, V.C.: Phys. Rev., 53, p. 337 (1938).

Wright, A.G.: PICRC, 3, p. 1709 (1973).

Wright, A.G.: J. Phys. A, 7, p. 2085 (1974).

Zas, E., et al.: Astropart. Phys., 1, p. 297 (1993).

Zatsepin, G.T., et al.: Izv. Akad. Nauk Ser. Fiz., 58, N12, p. 119 (1994).

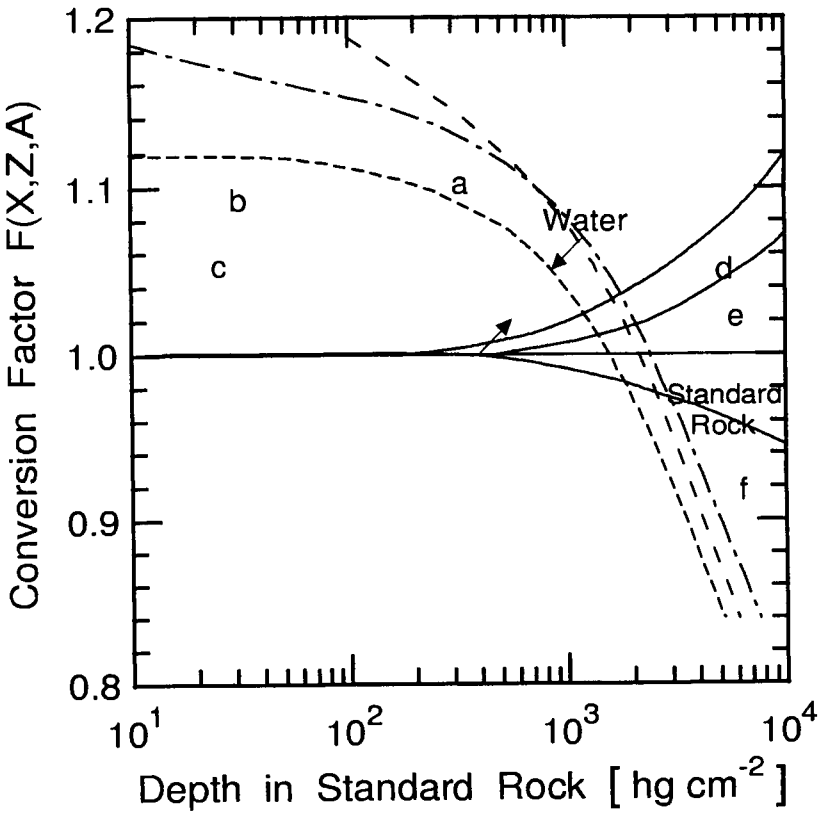

Figure 4.11: Conversion factor $F(X, Z, A)$ for water and rock to standard rock as a function of depth (after Wright, 1973). Curves *a*, *d*, *e* and *f* are the result of calculations by Kotov and Logunov (1970), *b* is from a computation of Wright (1973), and *c* represents formula 4.30 including the ionization loss term. Curves *a*, *b* and *c* are for water, curves *d*, *e* and *f* are in rock with Z = 13, 12 and 11, respectively. For details see text.

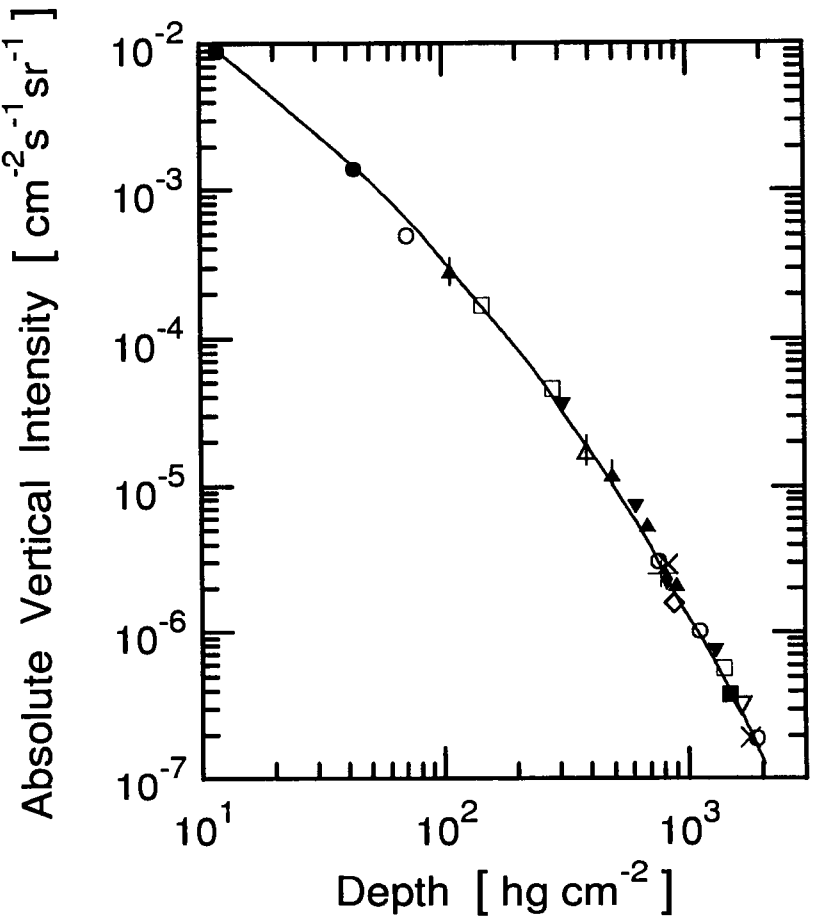

Figure 4.12: Depth-intensity data for vertical muons at shallow to moderate depths under rock (Crookes and Rastin, 1973). (Depth is measured from the top of the atmosphere).

- • Crookes and Rastin (1973)
- ▲ Sreekantan and Naranan (1952)
- \+ Krishnaswamy et al. (1968)
- △ Randall and Hazen (1951)
- □ Castagnoli et al. (1965)
- ▼ Avan and Avan (1955)
- ○ Stockel (1969)
- ■ Bollinger (1951)
- ♦ Achar et al. (1965a, b)
- × Miyake et al. (1964)
- ▽ Barrett et al. (1952)
- ◇ Sheldon et al. (1970)

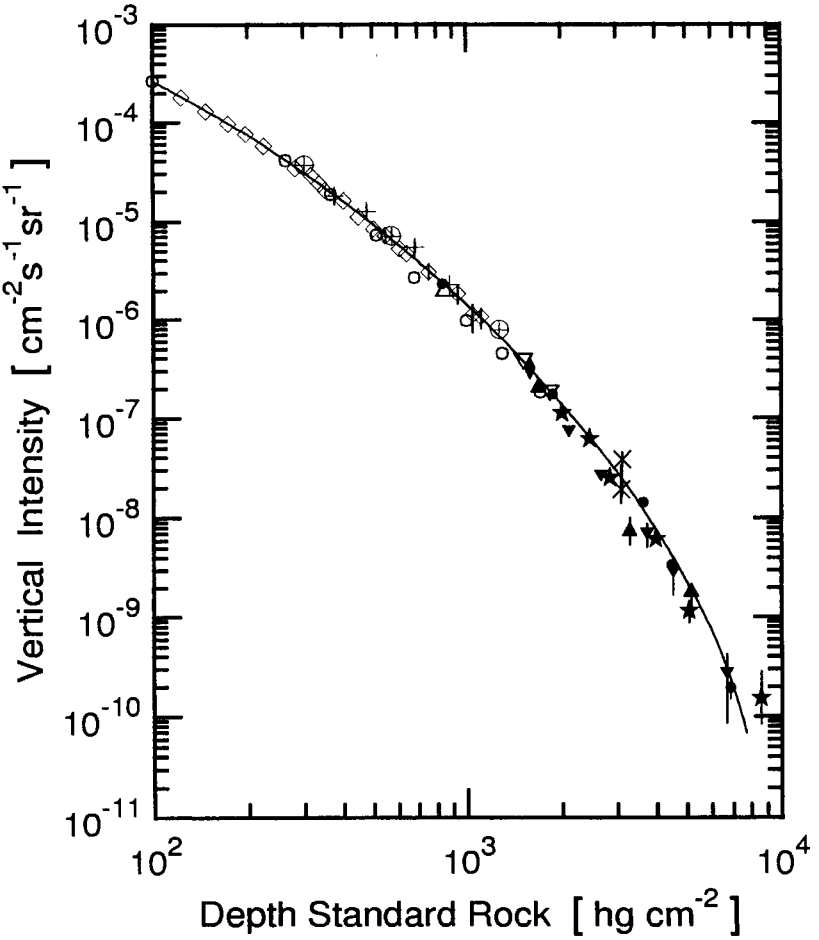

Figure 4.13: Summary of early vertical muon depth-intensity data at moderate to large depths in standard rock underground (Barrett et al., 1952; Miyake et al., 1964; Menon and Ramana Murthy, 1967). (Depth is measured from the top of the atmosphere).

- ⊕ Avan and Avan (1955)
- ▲ Barton (1961)
- ★ Bollinger (1951)
- o Clay and van Gemert (1939)
- × Miyazaki (1949)
- \+ Sreekantan and Naranan (1952) and Sreekantan et al. (1956)
- ♦ Barrett et al. (1952)
- ▼ Bollinger (1951)
- ▽ Bollinger (1951)
- • Miyake et al. (1964)
- △ Randall and Hazen (1951)
- ◇ Wilson (1938)

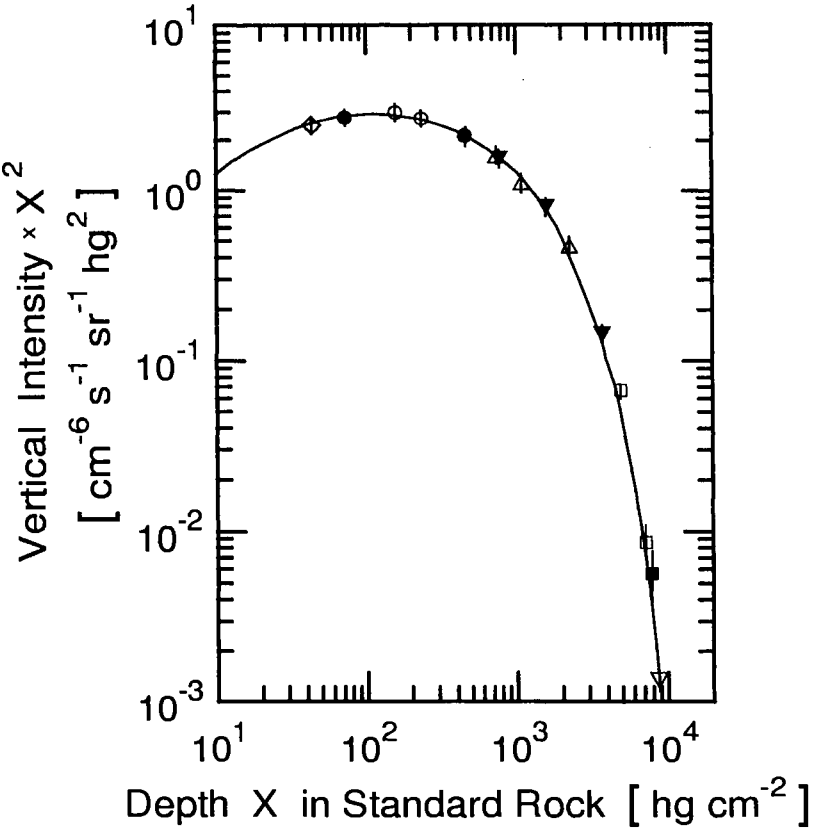

Figure 4.14: Depth-intensity relation for vertical muons at predominantly shallow depths under rock. Included are also a few data points from great depths. Note that depth, X, is measured from the top of the atmosphere in standard rock. The ordinate is multiplied by X^2 (after Wright, 1973, 1974).

- ▼ Krishnaswamy et al. (1968)
- o Bergamasco and Picchi(1971)
- ◇ Crookes and Rastin (1973)
- □ Miyake et al. (1964)
- ▽ Meyer et al. (1970)
- △ Stockel (1969)
- • Wright (1973)
- × Barrett et al. (1952)
- ■ Menon et al. (1968)

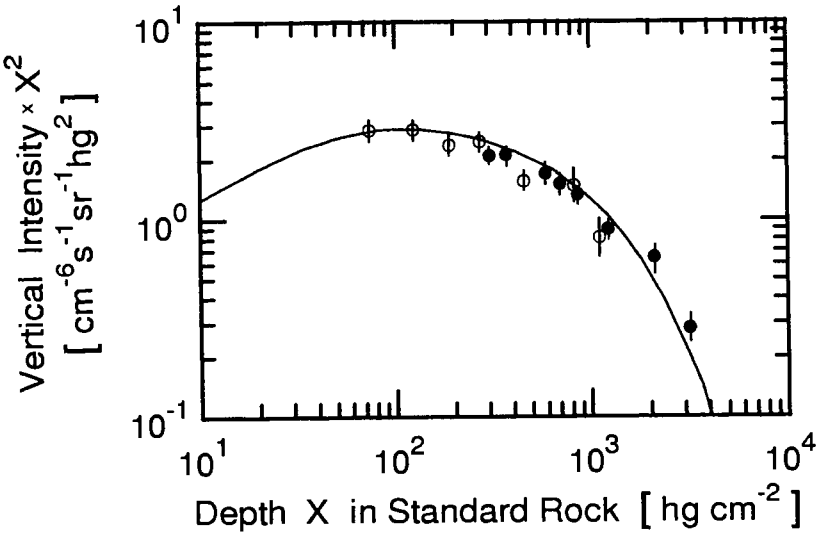

Figure 4.15: Depth-intensity relation for vertical muons recorded at shallow depths under water but converted to and plotted in depth expressed in $\mathrm{hg\,cm^{-2}}$ of standard rock. Note that depth, X, is measured from the top of the atmosphere. The ordinate is multiplied by X^2 (after Wright, 1974).

o Higashi et al. (1966) | • Davitaev et al. (1970)

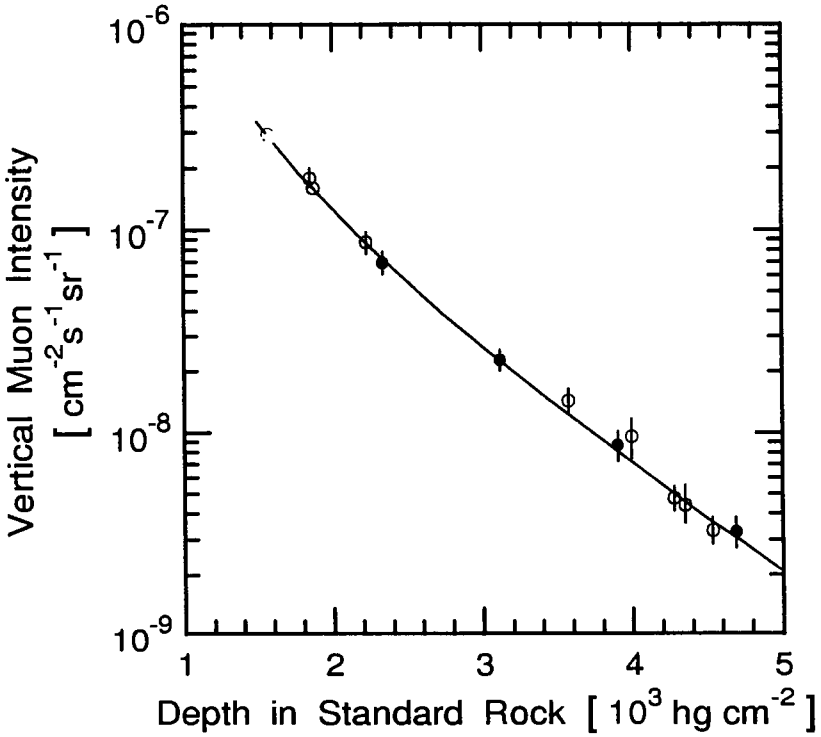

Figure 4.16: Depth-intensity relation for moderate to great depths underground showing an early world survey and the Utah data. The curve is a fit to the world survey data only (Cassiday et al., 1971).

• Utah data | ○ World survey

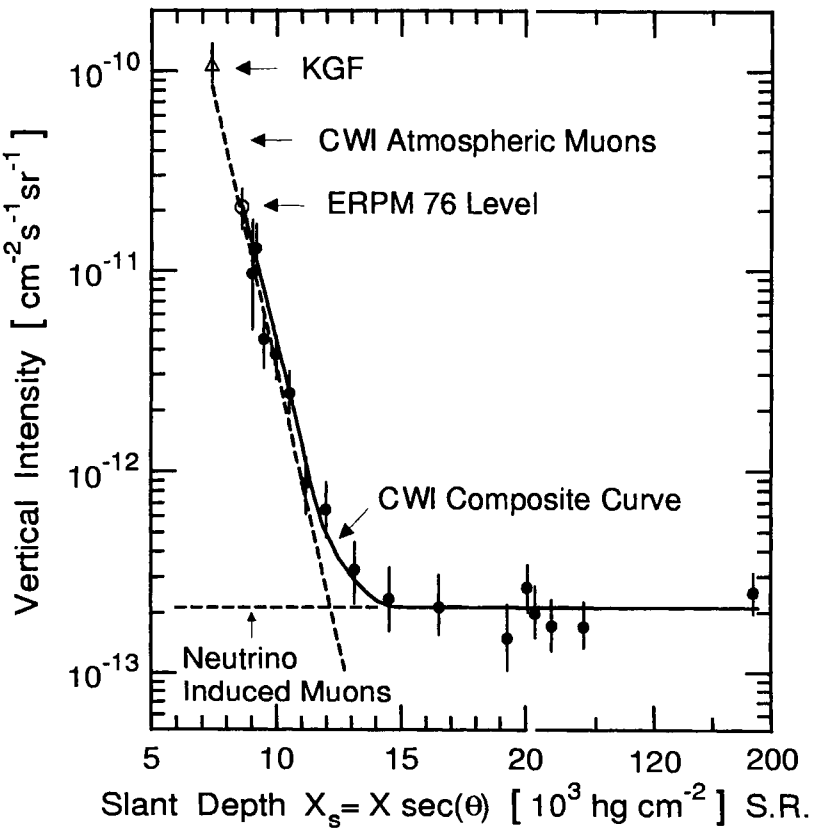

Figure 4.17: Muon intensity versus slant depth, X_s, in standard rock, deduced from the muon angular distribution at 8890 hg cm^{-2} vertical depth. o ERPM - East Rand Proprietary Mine; △ KGF - Kolar Gold Fields; • CWI - Case Witwatersrand Irvine. (Crouch et al., 1978).

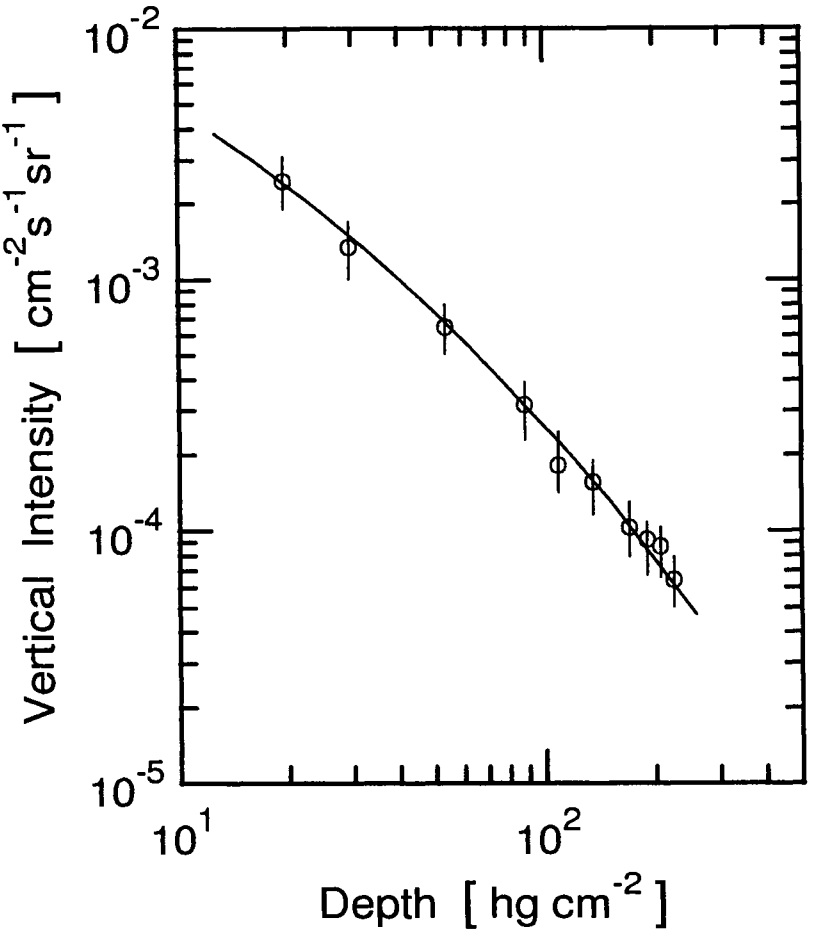

Figure 4.18: Depth-intensity relation for vertical muons at shallow depths under rock (20 - 223 hg cm^{-2}) from measurements of more recent date. The experiment was carried out in the Geleshan tunnel at Chongqing, China (Liu Zhong-he et al., 1979).

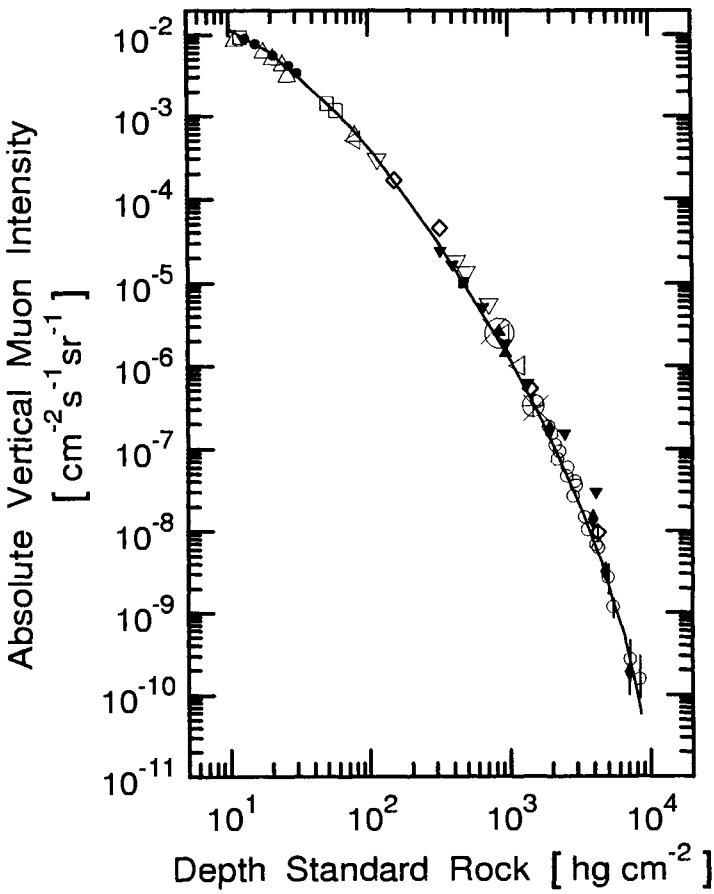

Figure 4.19: Absolute vertical depth-intensity spectrum compiled by Barbouti and Rastin (1983). Depth is measured from the top of the atmosphere. The size of the symbols is not related to the errors, some are shown enlarged to improve their legibility.

○ Achar et al. (1965a, b)	• Barbouti and Rastin (1983)
o Barrett et al. (1952)	◇ Castagnoli et al. (1965)
□ Crookes and Rastin (1973)	▼ Davitaev et al. (1970)*
× Krishnaswamy et al. (1970a)	♦ Miyake (1963, 1964)
△ Percy and Rogers (1977)	▲ Sheldon et al. (1978)
▽ Sreekantan and Naranan (1952) and Sreekantan et al. (1956)	◁ Stockel (1969)
	■ Wright (1974)
— Nottingham best fit 1973	* underwater data
⊕ Avan and Avan (1955)	

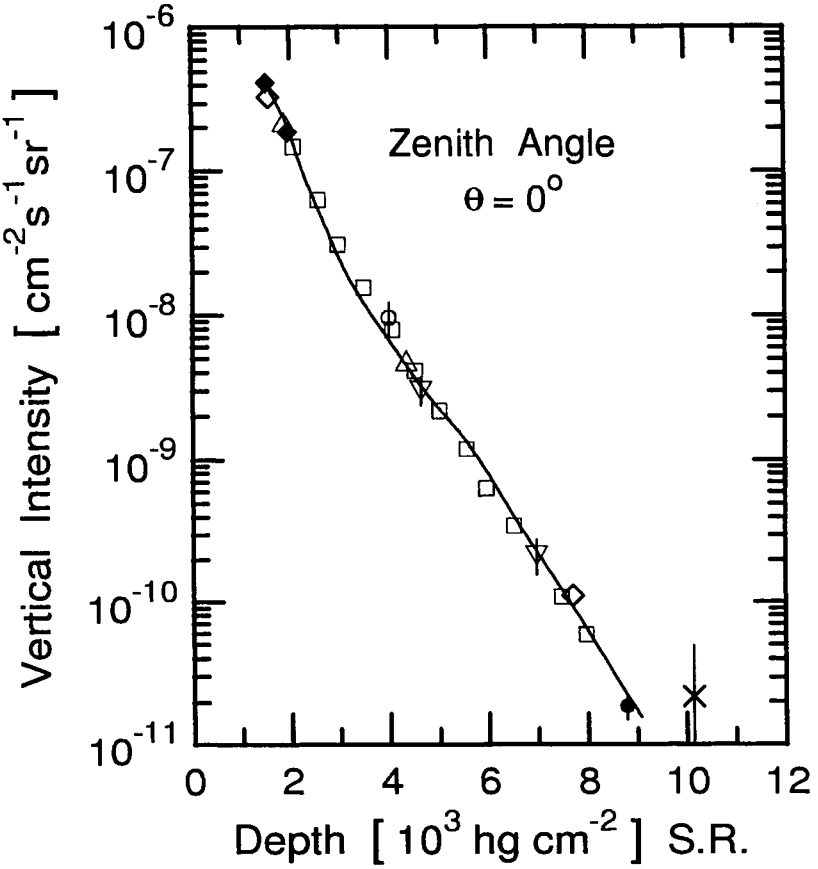

Figure 4.20: Theoretical vertical muon attenuation curve compared with measurements at different depths in standard rock (O'Brien, 1972).

- ○ Castagnoli et al. (1965)
- □ Larson (1968), World Survey
- ◇ Barrett et al. (1952)
- • Meyer et al. (1963)
- △ Achar et al. (1965a, b)
- — O'Brien (1972)
- ♦ Bollinger (1951)
- × Menon et al. (1968)
- ▽ Miyake et al. (1964)

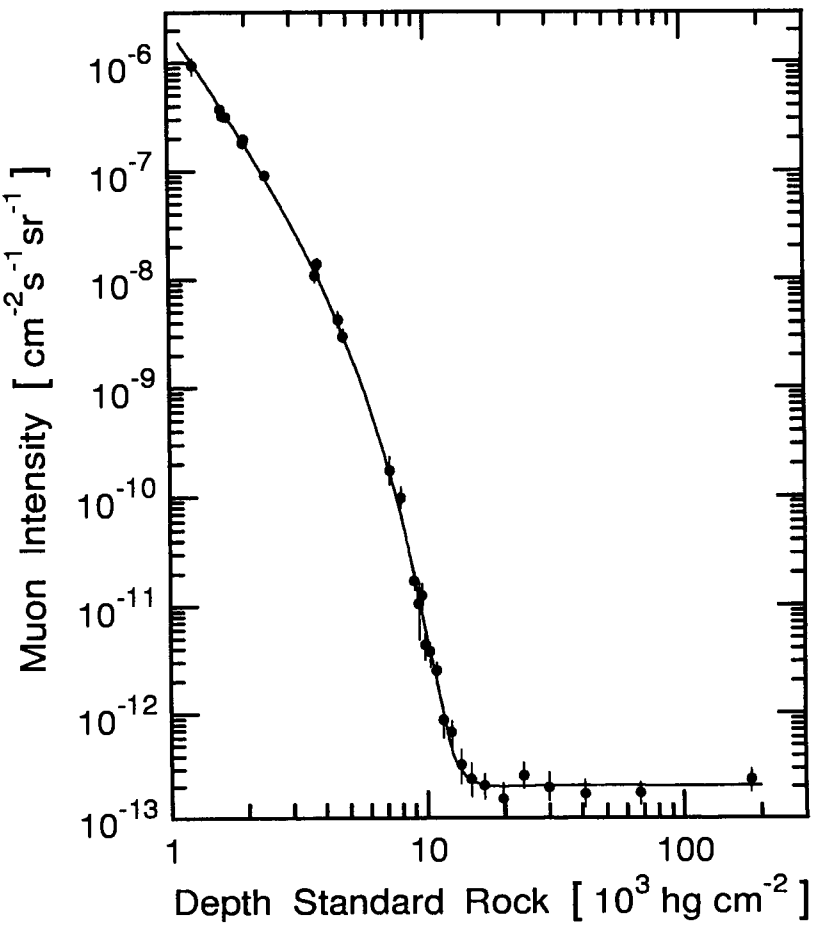

Figure 4.21: Vertical muon intensity as a function of slant depth in standard rock. Shown is a compilation of Crouch (1987) covering a very wide range of depths. Included are data from the following experiments: Stockel (1969), Bollinger (1950), Krishnaswamy et al. (1970a), Barrett et al. (1952), Achar et al. (1965a, b), Miyake et al. (1964), Krishnaswamy et al. (1971a), Meyer et al., (1970), Fyodorov et al. (1985). The curve is a fit with two exponentials.

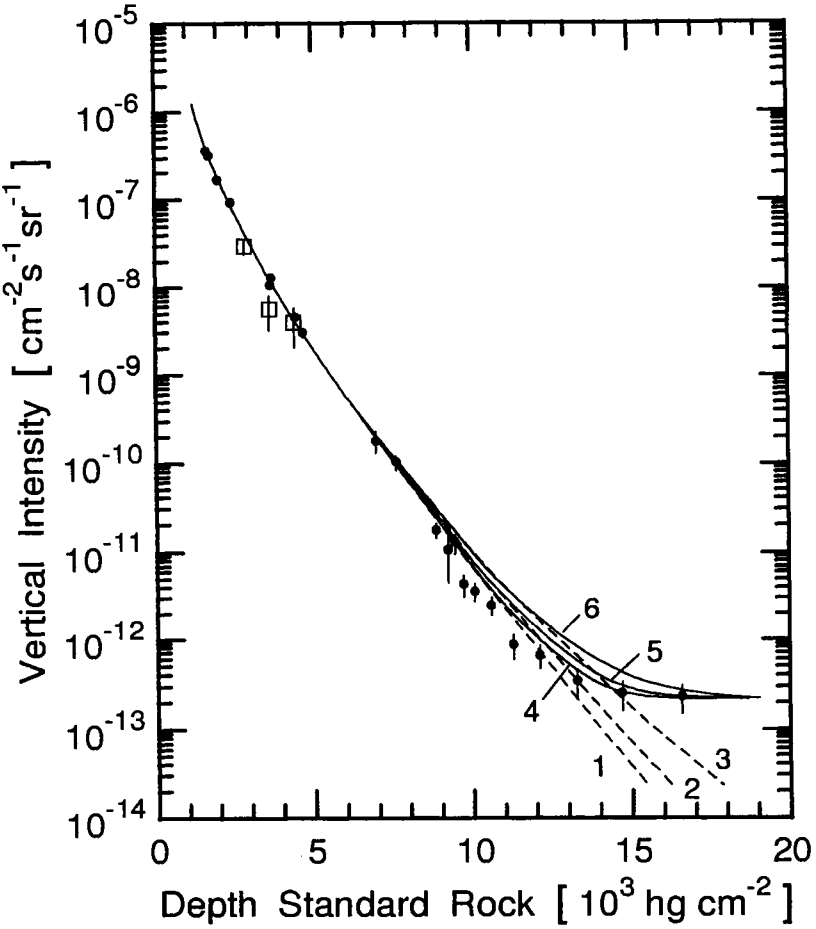

Figure 4.22: Comparison of calculated vertical muon depth-intensity spectra in standard rock for different assumptions, after Bugaev et al. (1993), and experimental world survey data compiled by Crouch (1985). The dashed curves represent muon intensities from the following sources: Curve 1 pions and kaons only; curve 2 pions, kaons and prompt production according to the RQPM model (Recombination Quark-Parton Model); curve 3 pions, kaons and prompt production according to Volkova et al. (1987). The solid curves 4, 5 and 6 correspond to curves 1, 2 and 3, and are for the same intensities, but include a constant contribution form the neutrino background (after Bugaev et al., 1993 and 1994).

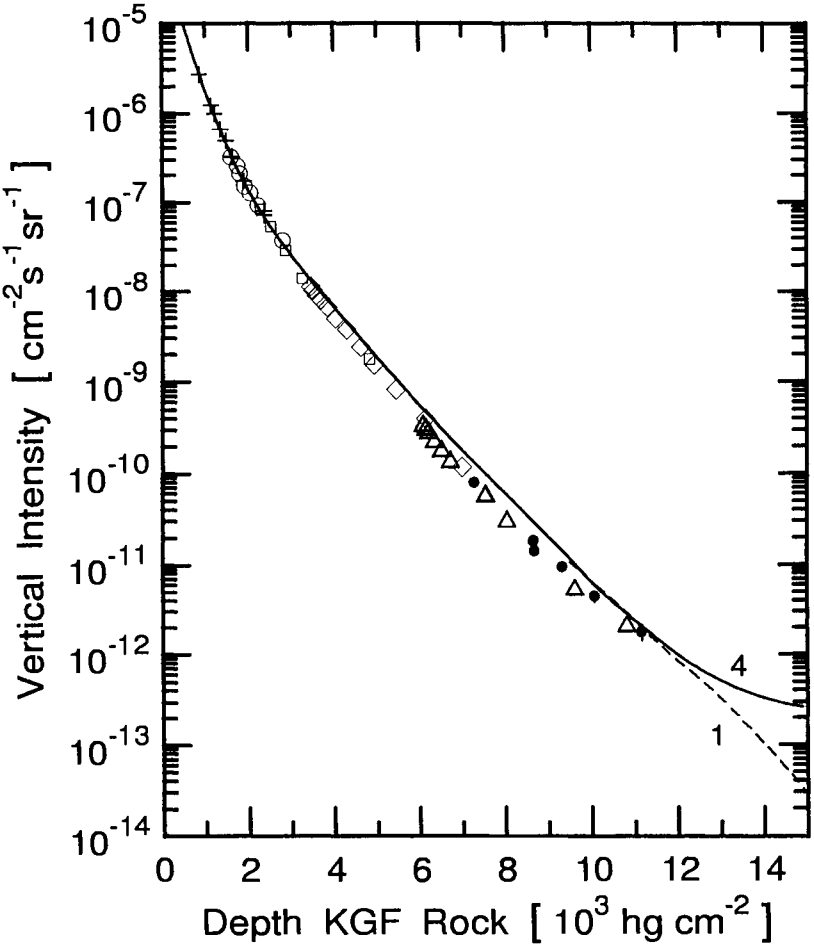

Figure 4.23: Compilation of muon vertical depth-intensity distributions obtained from different experiments over an extended period at the Kolar Gold Fields (KGF) (Adarkar et al., 1990a). + vertical depth 754 hg cm^{-2}; ○ vertical depth 1500 hg cm^{-2}; ◇ vertical depth 3375 hg cm^{-2}; □ horizontal telescope at 3375 hg cm^{-2}; △ proton decay detector at 6045 hg cm^{-2}; • proton decay detector at 7000 hg cm^{-2}. The dashed and solid curves are calculated vertical intensities in standard rock and the same as those in Fig. 4.22 with the same numbers.

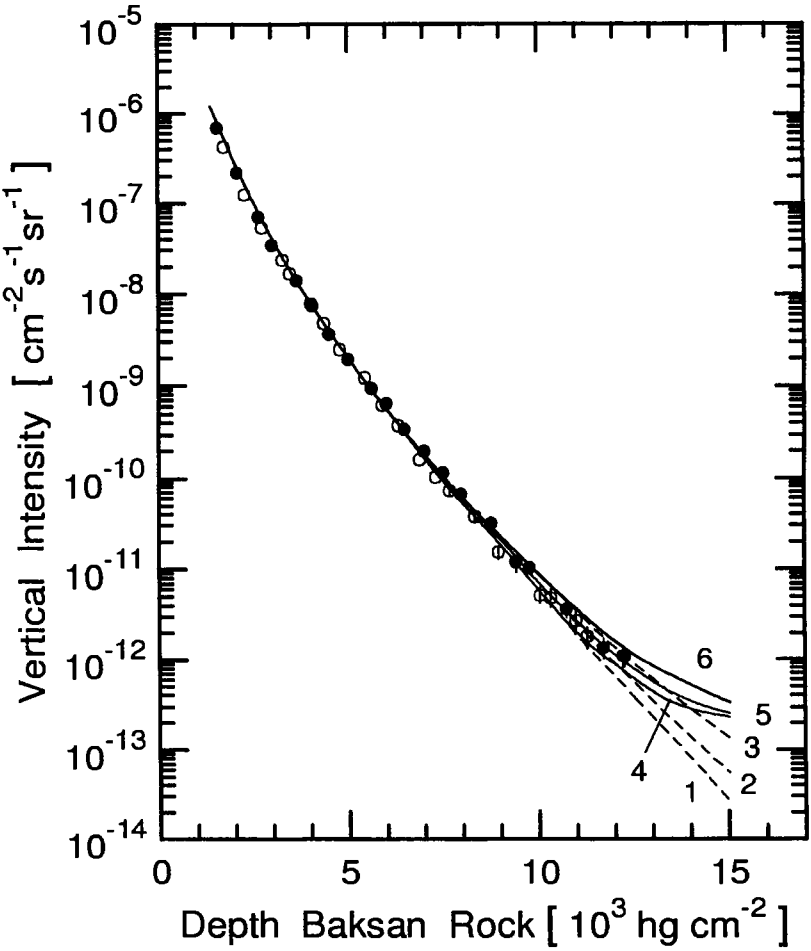

Figure 4.24: Muon vertical depth-intensity data obtained from inclined measurements at Baksan at two different zenith angles, θ, and different azimuthal angles. (o) $50° \leq \theta \leq 70°$; (•) $70° \leq \theta \leq 85°$ (Andreyev et al., 1987 and 1990). The dashed and solid curves are calculated vertical intensities in standard rock and the same as those in Fig. 4.22 with the same numbers.

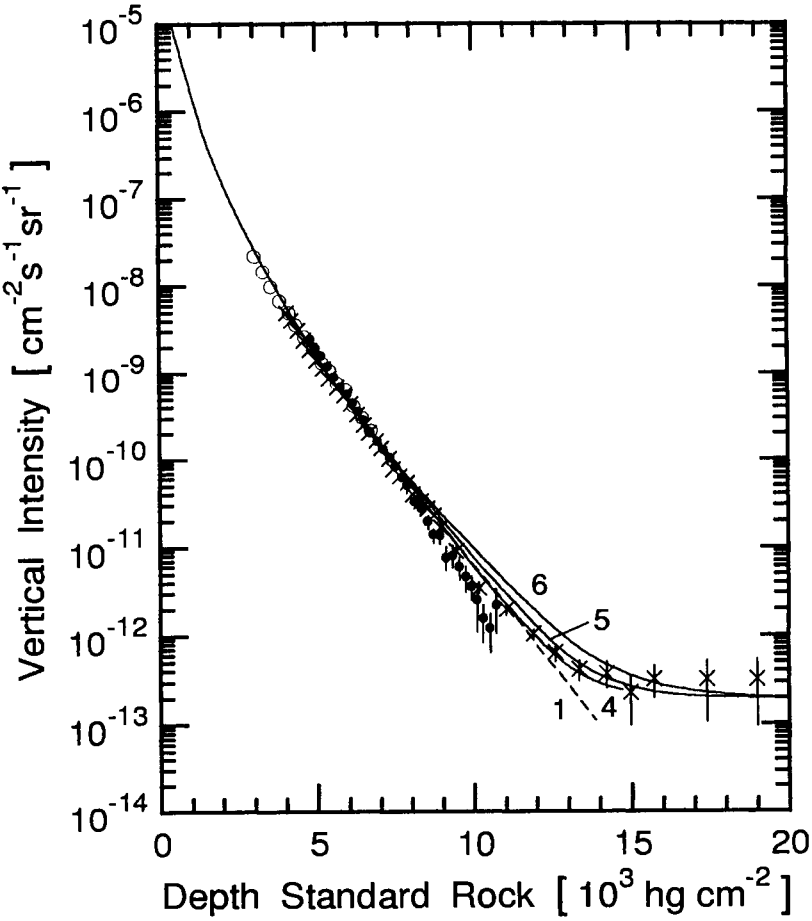

Figure 4.25: Muon vertical depth-intensity distributions obtained with the Fréjus (×) (Berger et al., 1989a, 1989b and 1990), NUSEX (•) (Aglietta et al., 1990a) and Gotthard (o) (Czapek et al., 1990) detectors. The dashed and solid curves are calculated vertical intensities in standard rock and the same as those in Fig. 4.22 with the same numbers.

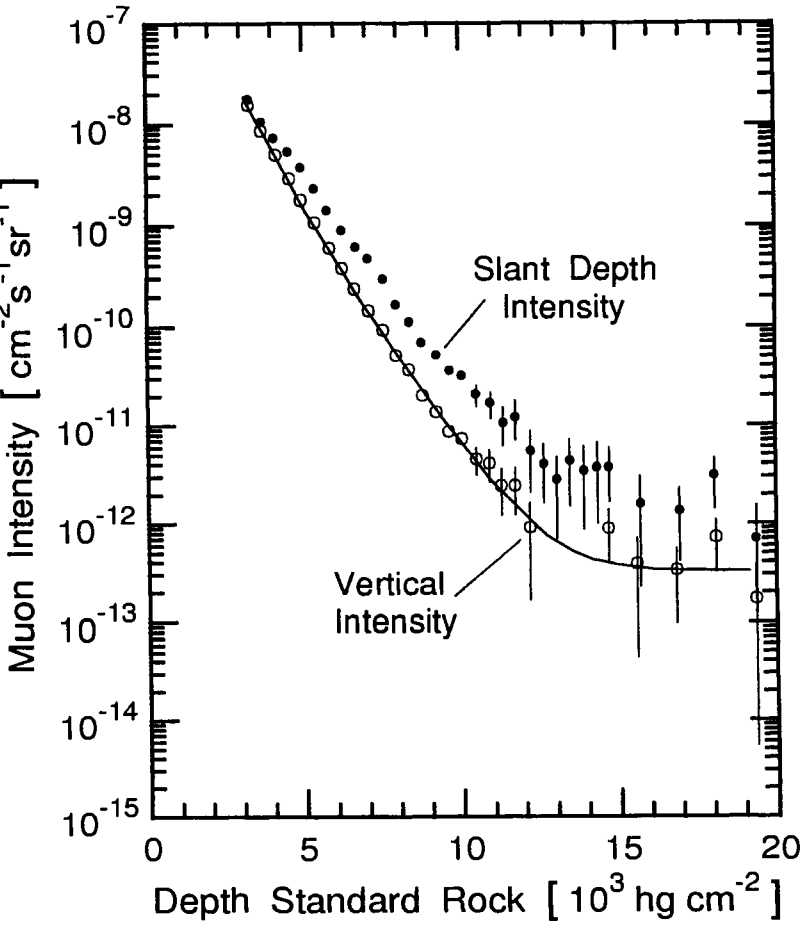

Figure 4.26: Muon intensity as a function of slant depth (•) obtained with the LVD detector, and vertical muon intensity as a function of depth (○) computed from the slant depth data (Giusti et al., 1995; Sartorelli et al., 1995). The curve is a fit using eq. 4.38.

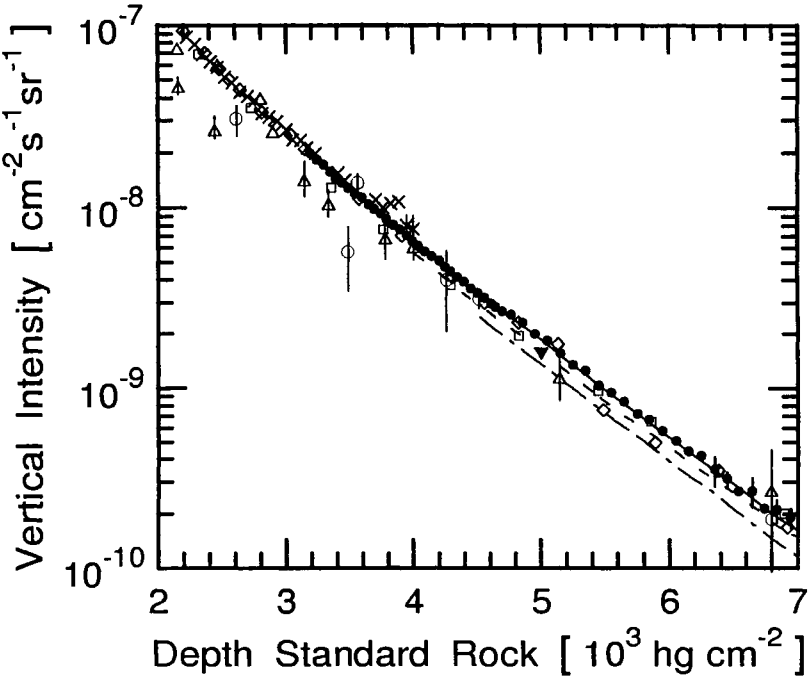

Figure 4.27: Compilation of vertical muon intensities versus depth in standard rock for different experiments (Ambrosio et al., 1995, 1996; Bussino et al., 1995). The thin solid curve is a fit of the MACRO data to eq. 4.38. The dashed curve is a fit to the Fréjus data (Berger et al., 1989a and 1989b) and the dot-dash curve is a fit to the NUSEX data (Aglietta et al., 1990a). The Crouch compilation, Fig. 4.22 (Crouch, 1987), for depths $\geq$4500 hg cm^{-2} (not shown in this figure) follows a line that lies between the MACRO and Fréjus fits, and the corresponding LVD distribution of Fig. 4.26 lies between the Fréjus and Crouch data.

- • Ambrosio et al. (1995, 1996)
- △ Bollinger (1950) Cornell
- ▼ Berger et al. (1989a, b) Fréjus
- × Kasahara (1994) Soudan 2
- □ Andreyev et al. (1987) Baksan
- ○ Crouch (1987) compilation
- ◇ Ruddick (1990) Soudan 1

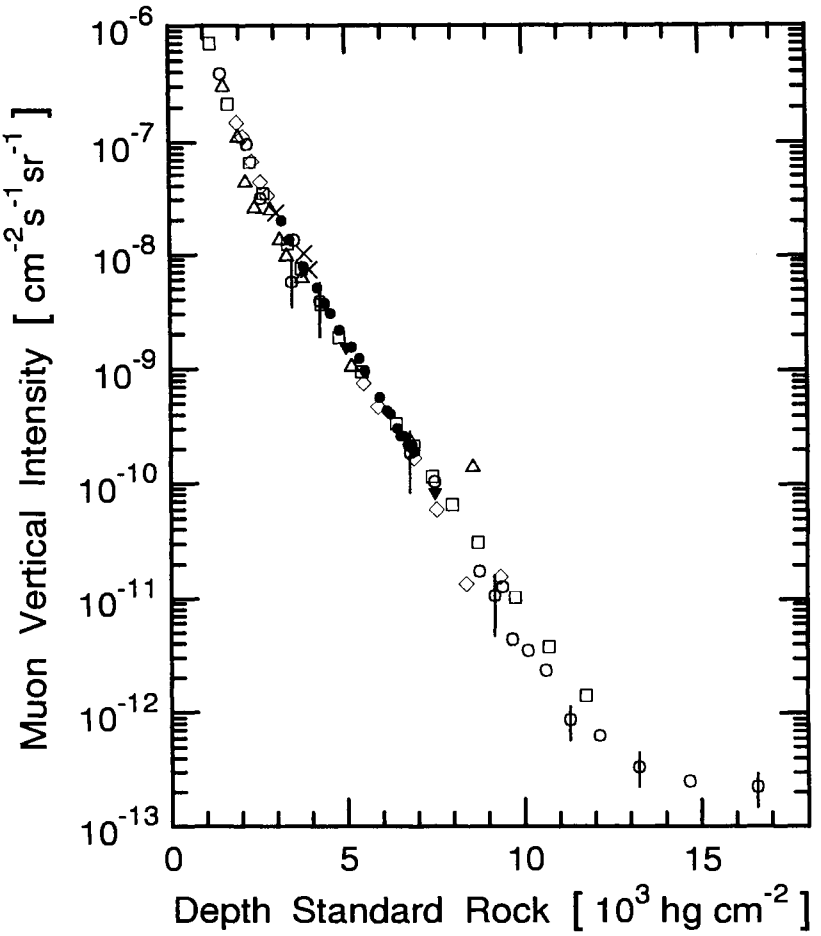

Figure 4.28: Compilation of vertical muon intensities versus depth in standard rock for different experiments (Ambrosio et al., 1995 and 1996). The data are from the same experiments as those in Fig. 4.27 but cover a wider range.

- • Ambrosio et al. (1995, 1996)
- △ Bollinger (1950) Cornell
- ▼ Berger et al. (1989a, b) Fréjus
- × Kasahara (1994) Soudan 2
- □ Andreyev et al. (1987) Baksan
- ○ Crouch (1987) compilation
- ◇ Ruddick (1990) Soudan 1

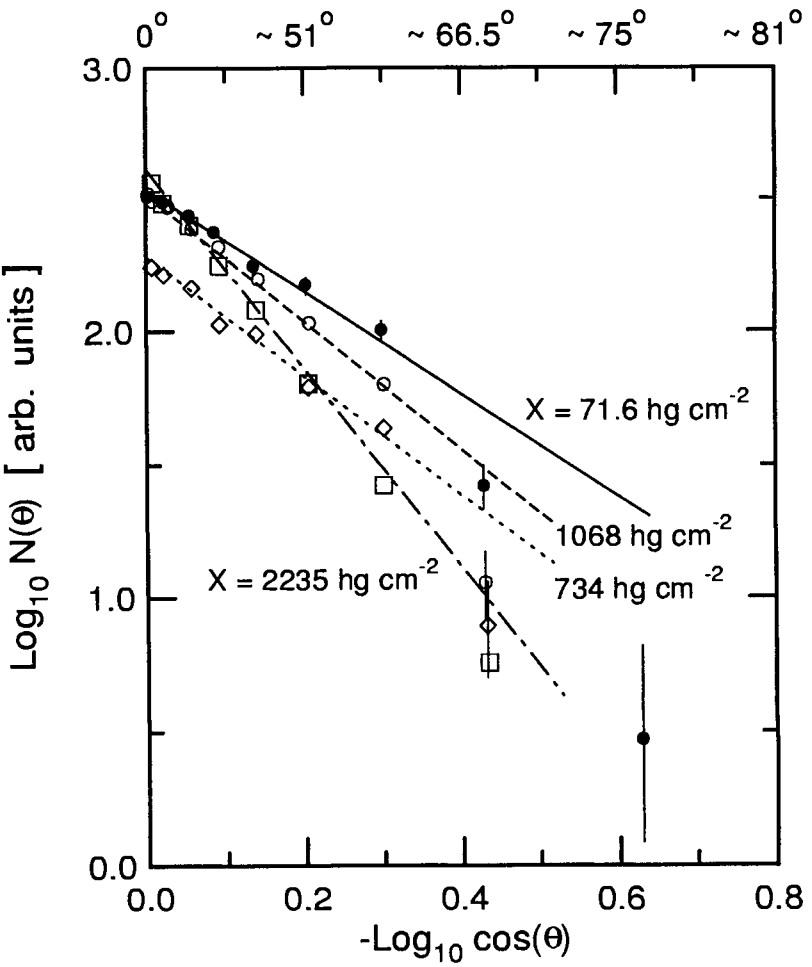

Figure 4.29: Angular distributions of muons at various vertical depths underground, as indicated (Stockel, 1969). The vertical intensities and the slopes, n, of the angular distributions determined at the different depths are as follows:

Symbol	Depth [hg cm^{-2}]	Intensity [cm^{-2}s^{-1}sr^{-1}]	Slope n
•	71.6	$5.00 \pm 0.17 \cdot 10^{-4}$	1.85 ± 0.10
◇	734	$3.12 \pm 0.15 \cdot 10^{-6}$	2.1 ± 0.1
○	1068	$1.03 \pm 0.04 \cdot 10^{-6}$	2.4 ± 0.1
□	2235	$9.7 \pm 0.5 \cdot 10^{-8}$	3.6 ± 0.2

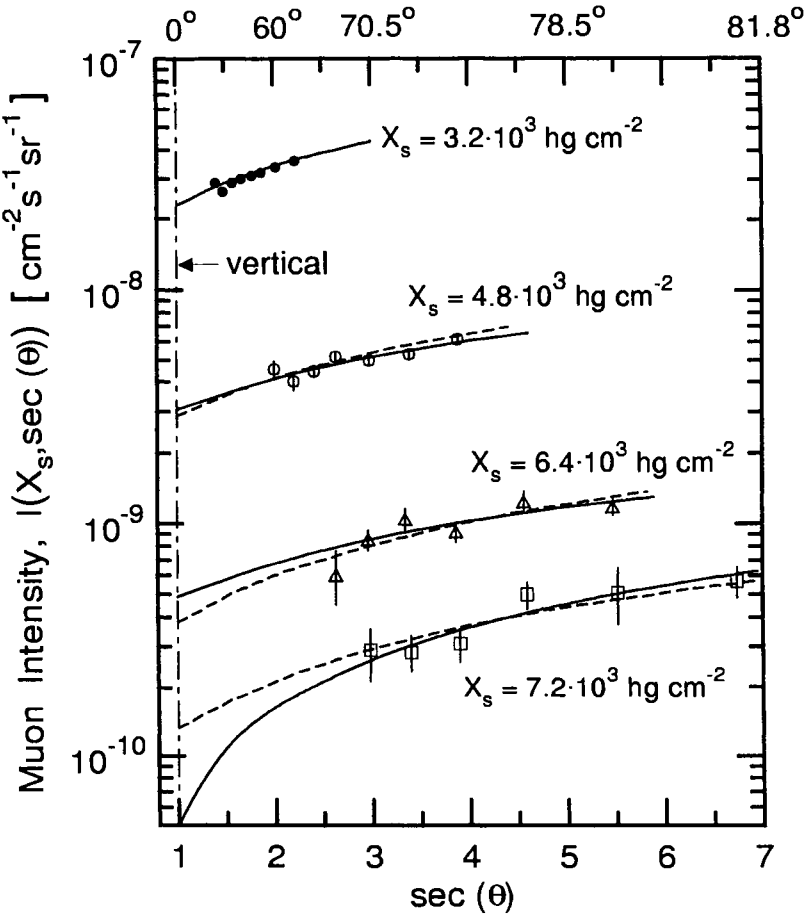

Figure 4.30: Zenith angle distributions at several constant slant depths cuts. Shown is the muon intensity versus $\sec(\theta)$, θ being the zenith angle, for constant slant depths of $X_s = 3.200$ hg cm^{-2} (•), 4800 hg cm^{-2} (○), 6400 hg cm^{-2} (△), and 7200 hg cm^{-2} (□) (Bergeson et al., 1971). The solid curves are fits to the Utah data, the dashed curves represent the world survey. (The data in the original publication are shown in linear representation in separate figures).

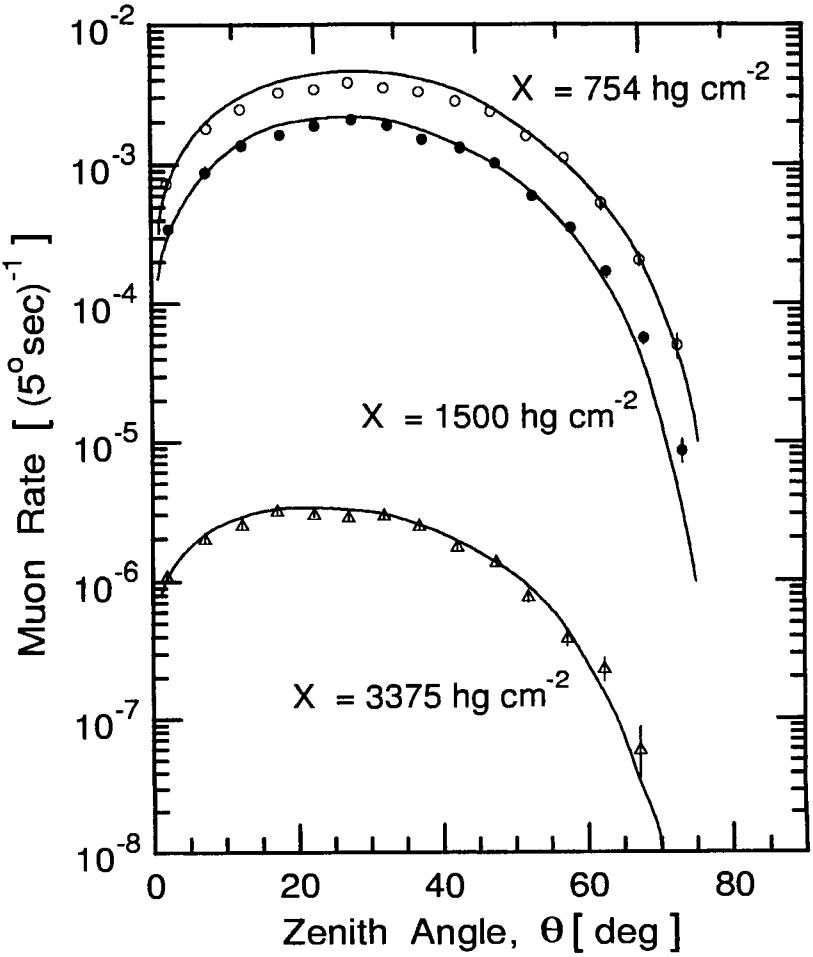

Figure 4.31: Zenith angle distribution of atmospheric muons at vertical depths $X = 754\,\mathrm{hg\,cm^{-2}}$ (o), $1500\,\mathrm{hg\,cm^{-2}}$ (•) and $3375\,\mathrm{hg\,cm^{-2}}$ ($\triangle$) underground in the Kolar Gold Fields (Krishnaswamy et al., 1970a). The curves are theoretically expected distributions computed from known vertical muon intensities.

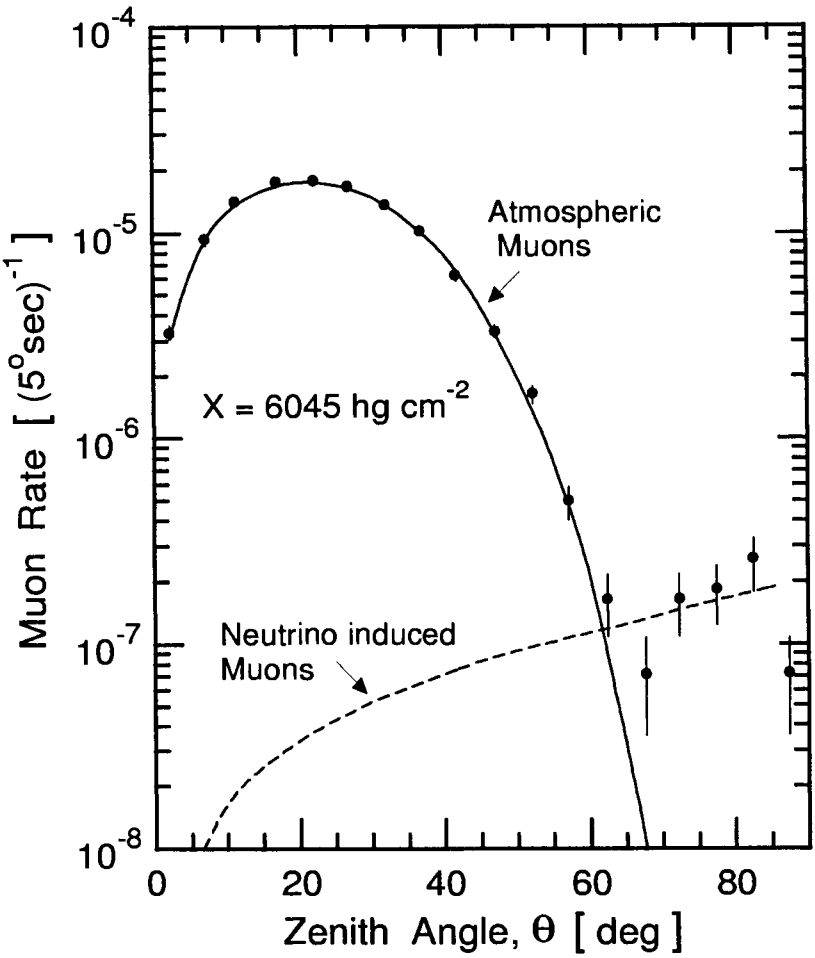

Figure 4.32: Zenith angle distribution of muons at a vertical depth of 6045 hg cm^{-2} underground in the Kolar Gold Fields (Adarkar et al., 1990a, b). The solid and dashed curves show the theoretically expected distribution of atmospheric and neutrino induced muons, respectively. The experimental data were collected in 5° bin intervals and the angular resolution was 0.8°. The detector measured 6 m × 4 m × 3.9 m in phase I and 6 m × 6 m × 6.5 m in phase II.

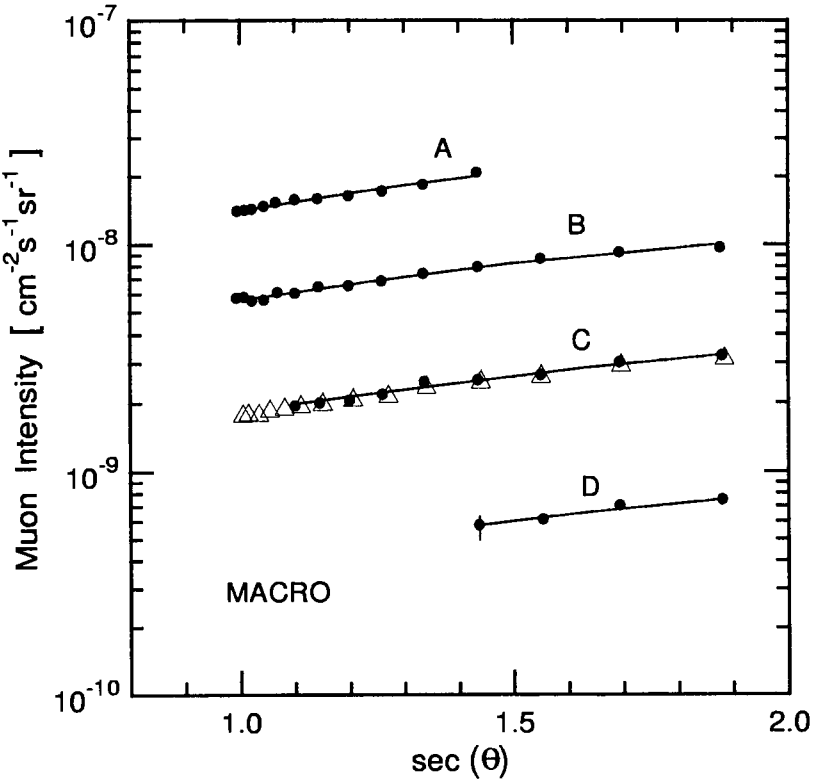

Figure 4.33: Vertical muon intensity versus sec(θ) for four ranges of slant depths determined with the MACRO detector: A) 3150 $\leq X_s \leq$ 3750, B) 3850 $\leq X_s \leq$ 4550, C) 4650 $\leq X_s \leq$ 5550, and D) 5650 $\leq X_s \leq$ 6950 hg cm^{-2}. The symbols Δ show the data A) to D) scaled to a slant depth X_s = 5400 hg cm^{-2} (Ambrosio et al., 1995). The energy of the muons involved ranges from about 1 TeV to 20 TeV, corresponding to a primary energy range between 10 TeV and 200 TeV.

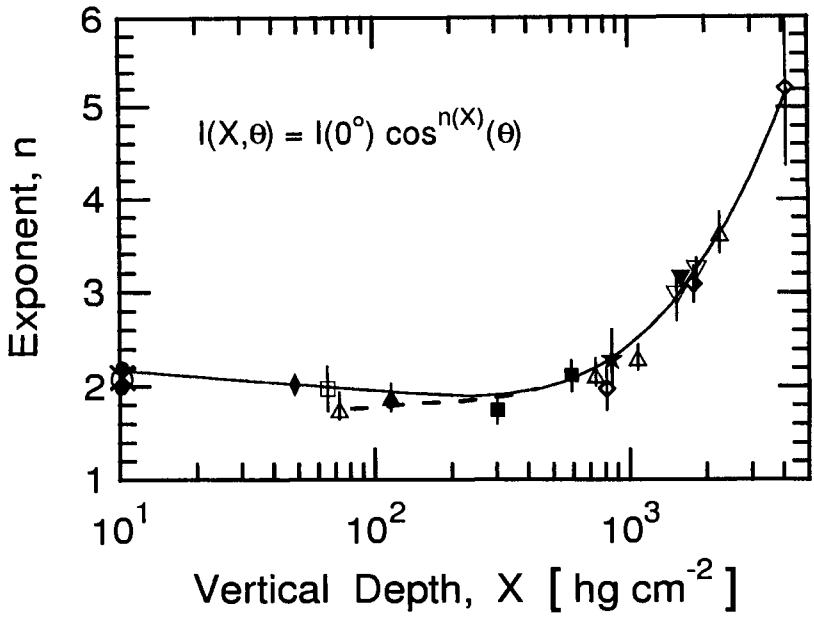

Figure 4.34: Variation of the exponent, n, of the muon zenith angle distribution, $I(\theta) = I(0°)\cos^n(\theta)$, with depth underground. The solid curve represents the best fit to all the data, the broken line is a fit to the earlier data using a somewhat different relation and normalization. Depth is given below the top of the atmosphere (after Stockel, 1969; Crookes and Rastin, 1973).

- ♦ Crookes and Rastin (1973)
- ▲ Sreekantan and Naranan (1952)
- □ Follett and Crawshaw (1936)
- o Moroney and Parry (1954)
- ★ Randall and Hazen (1958)
- • Judge and Nash (1965)
- × Greisen (1942)
- ▽ Bollinger (1951)
- ▼ Barrett et al. (1952)
- ◇ Achar et al. (1965a, b)
- ■ Avan and Avan (1955)
- △ Stockel (1969)

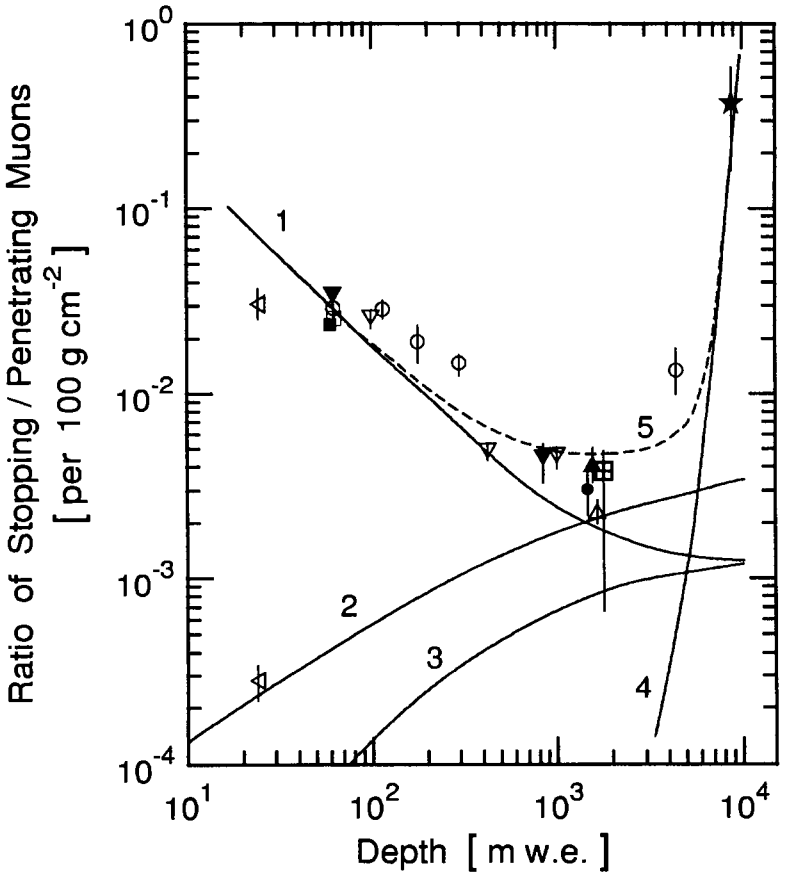

Figure 4.35: Summary of theoretical and experimental data of the ratio of stopping to through-going muons underground in an absorber of thickness 100 g cm^{-2}. Depth is given in units of meters water equivalent (m w.e.).

■ Short (1963)	□ Barton and Slade (1965)
• Kropp et al. (1968)	△ Reilly (1969)
o Baschiera et al. (1970, 1971)	★ Reines et al. (1971)
⊞ Krishnaswamy et al. (1971b)	▽ Bhat and Ramana Murthy (1972, 1973b)
▲ Elbert et al. (1972)	▼ Alexeyev et al. (1973a, b)
◁ Higashi et al. (1973)	
1 residual atmospheric muons	2 $\mu^{+,-}$ from nucl. interactions
3 $\mu^{+,-}$ from photoprod. $\pi^{+,-}$	4 $\mu^{+,-}$ from ν-interactions
5 sum of (1) to (4)	

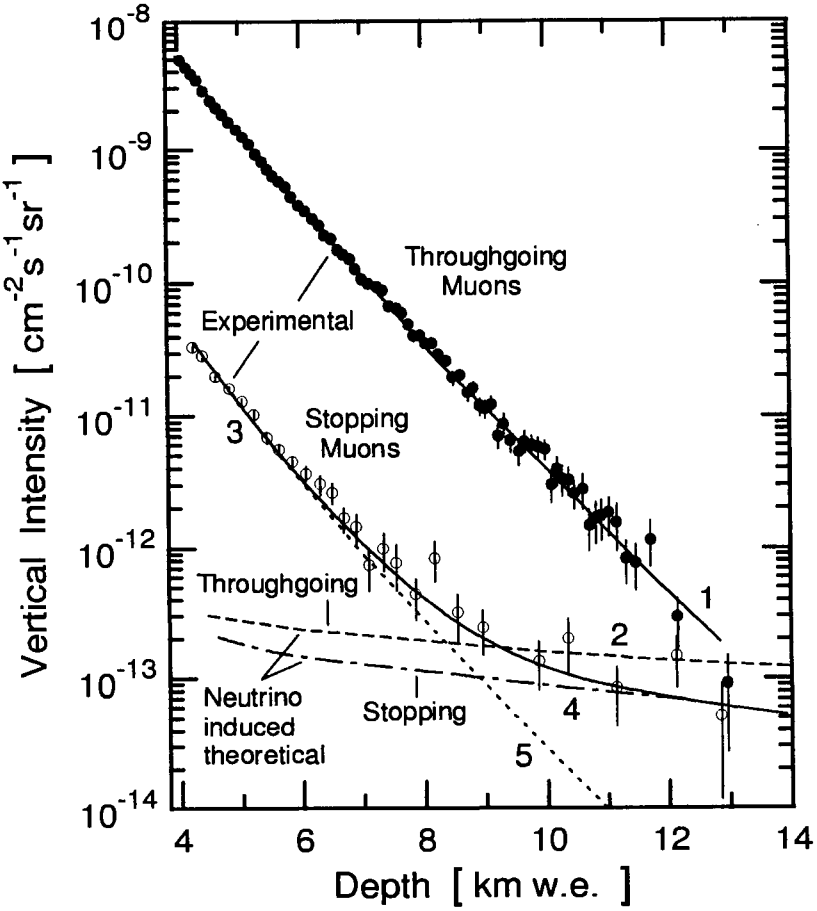

Figure 4.36: Vertical depth-intensity relation of through-going and stopping muons, respectively, recorded with the Fréjus detector (Rhode 1993, 1996). Curves 1 and 3 are fits to the experimental data, curves 2, 4 and 5 are theoretical distributions. Curves 2 and 4 are for neutrino induced through-going and stopping muons, respectively, and curve 5 is for stopping atmospheric muons. Intensities recorded at zenith angles $\theta > 0°$ were multiplied by $\cos(\theta^*)$ for conversion to vertical intensity (θ^* is the local zenith angle measured at the point of creation of the particle in the atmosphere and not as seen at the detector).

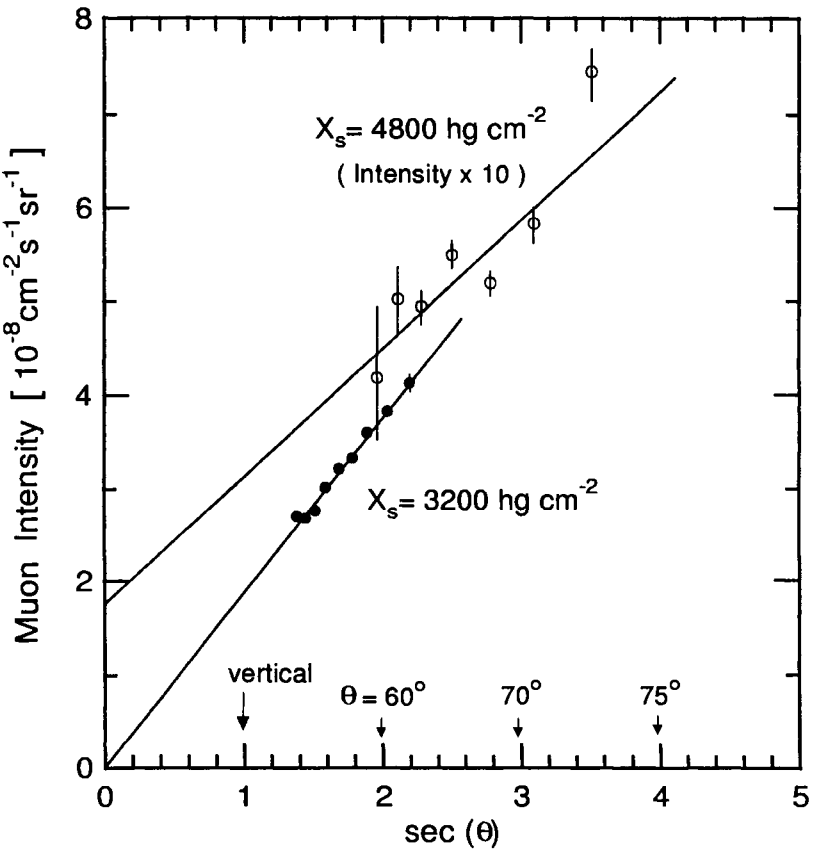

Figure 4.37: Zenith angular enhancement, $G(X, \theta)$, of the muon intensity at the two fixed slant depths of 3200 hg cm^{-2} and 4800 hg cm^{-2}, respectively, measured with the Utah detector (Bergeson et al., 1973). The intercepts of the lines with the ordinate at $\sec(\theta) = 0$ are a measure of the isotropic component originating from prompt muons ($G(X, \theta) \approx \sec(\theta)$). (Note that the intensities plotted for 4800 hg cm^{-2} are multiplied by 10.)

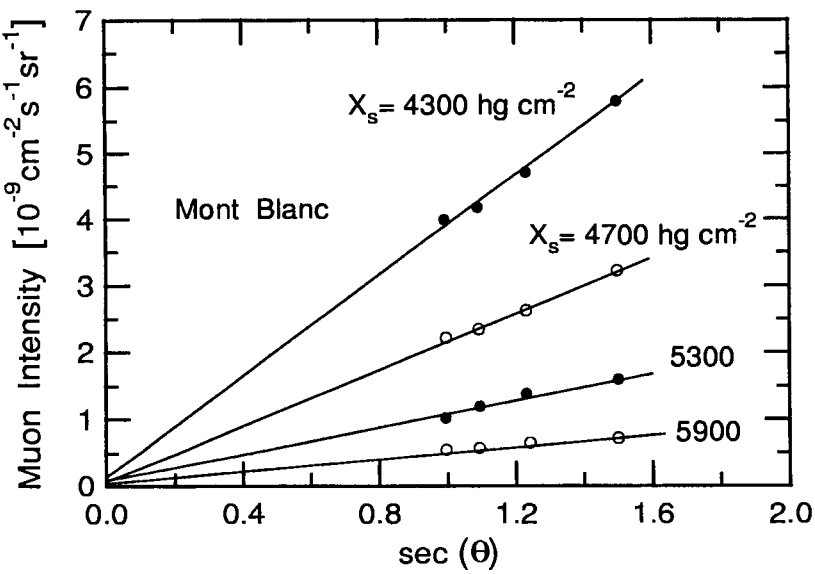

Figure 4.38: Experimental intensities of muons as a function of sec(θ) at four slant depths underground, as indicated. The solid lines represent the expected angular dependencies (Bergamasco et al., 1983).

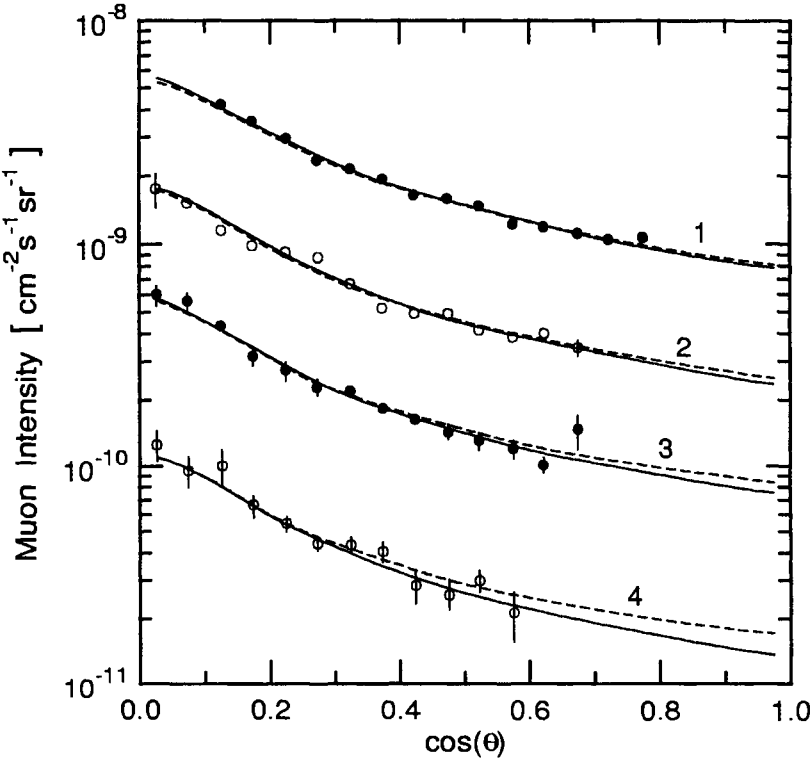

Figure 4.39: Zenith angle dependence of the muon intensity as determined with the LVD detector at Gran Sasso for four different depth ranges: 1) 5 - 6 km w.e., 2) 6 - 7 km w.e., 3) 7 - 8 km w.e., 4) 8 - 10 km w.e.. The solid curves are calculated distributions using eq. 4.55 which neglects the production of prompt muons, the dashed curves represent the same equation with the prompt contribution, $f_p = 2 \cdot 10^{-3}$, added (Aglietta et al., 1997).

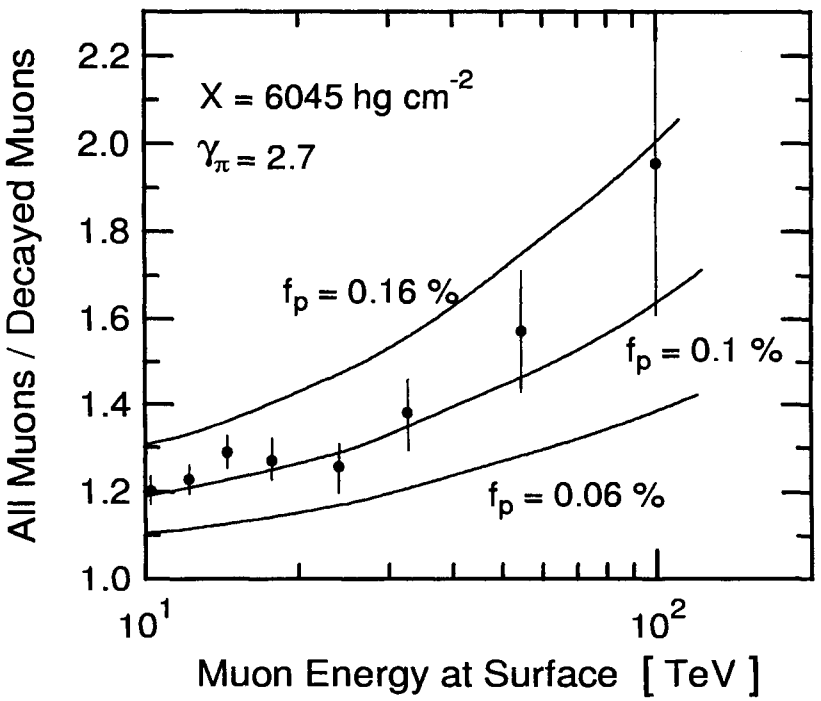

Figure 4.40: Ratio of all muons to decayed muons at a vertical depth of 6045 hg cm^{-2} at the Kolar Gold Fields (Krishnaswami et al., 1983; Adarkar et al., 1990a, b). The curves are theoretical distributions obtained for a differential pion production spectrum with exponent $\gamma_\pi = 2.7$, and for a ratio of prompt muons to pions only of $f_p' = 0.06\%$, 0.1% and 0.16%, as indicated.

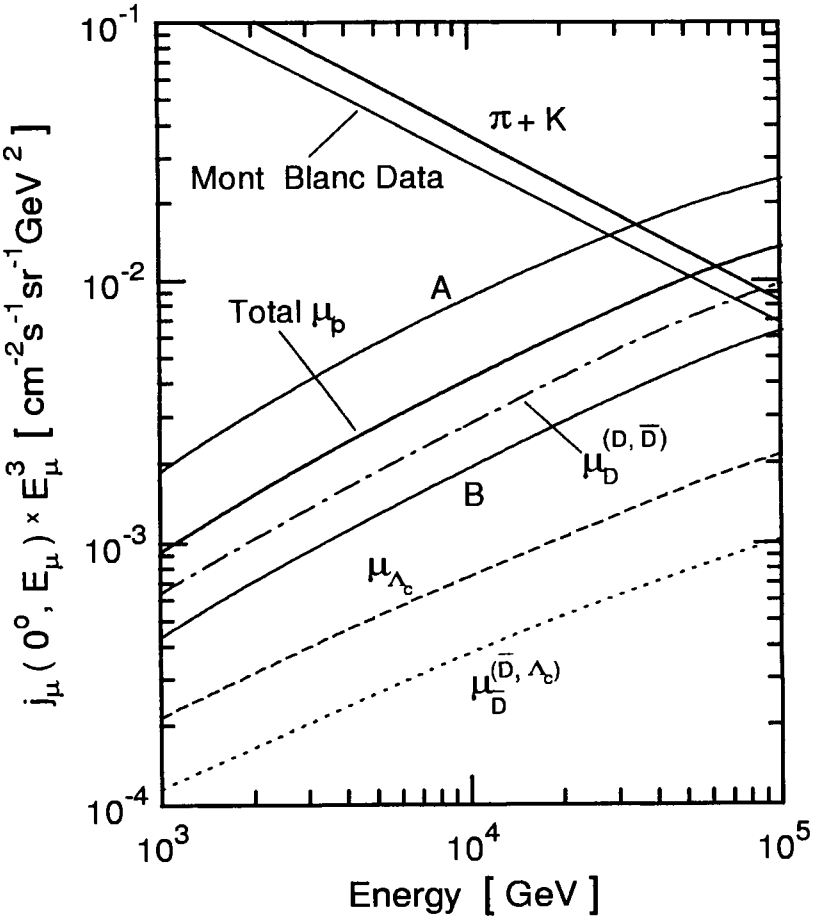

Figure 4.41: Differential spectra of vertical muons at sea level multiplied by E_μ^3, E_μ being the muon energy. Shown is a theoretical spectrum of muons from pion and kaon decays only (Volkova et al., 1979) and the spectrum from the Mont Blanc experiment (Castagnoli et al., 1984) together with predictions for the contribution of prompt muons from the decay of charmed particles, as indicated. Curves A and B indicate the likely upper and lower boundaries of the total intensity of prompt muons, μ_p, and reflect the degree of uncertainty of the predictions (after Volkova et al., 1987). $\mu_D^{D,\overline{D}}$ stands for muons from D-mesons generated in $D\overline{D}$ pairs, $\mu_{\overline{D}}^{\overline{D},\Lambda_c}$ for muons from $\overline{D}$-mesons generated in $\overline{D}, \Lambda_c$ pairs, and μ_{Λ_c} for muons from Λ_c-hyperons.

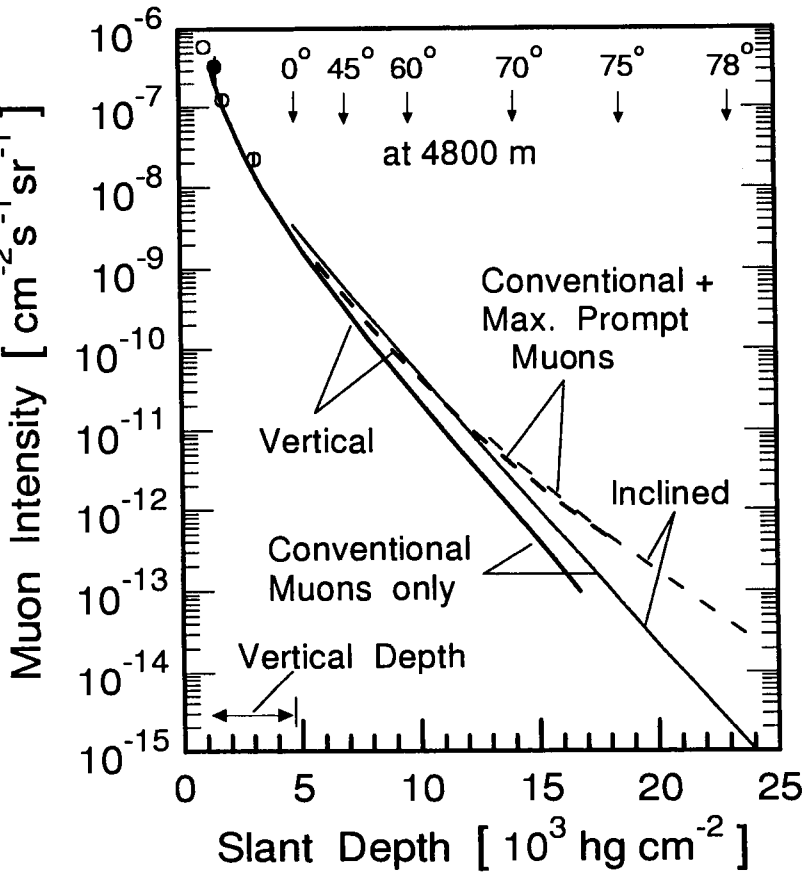

Figure 4.42: Theoretical intensities versus vertical depth to 4800 m and slant depth beyond 4800 m underwater of muons originating from different processes (Inazawa and Kobayakawa, 1985). Shown is the vertical depth-intensity relation of muons of conventional origin only and of the sum of conventional plus an estimated maximum of prompt muons. Also shown are the inclined intensities versus slant depth at 4800 hg cm^2 and beyond of the same muon groups. (For details see text.)

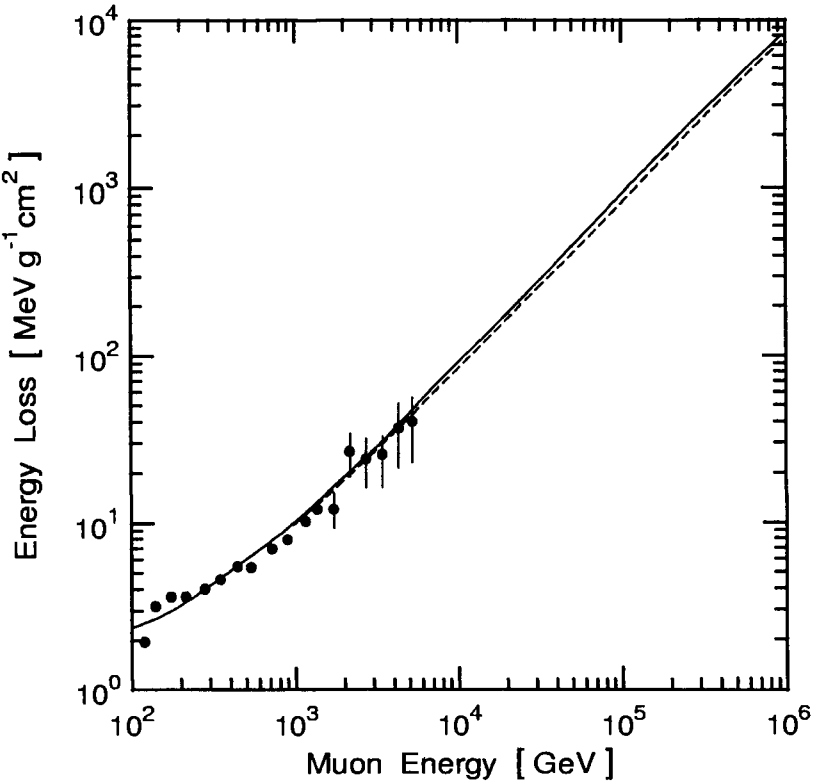

Figure 4.43: Mean energy loss of muons as a function of muon energy. The dashed line shows the expectation by quantum electrodynamics, the solid line that calculated with an empirical formula. The experimental points are from measurements with the MUTRON detector (Mitsui, 1992).

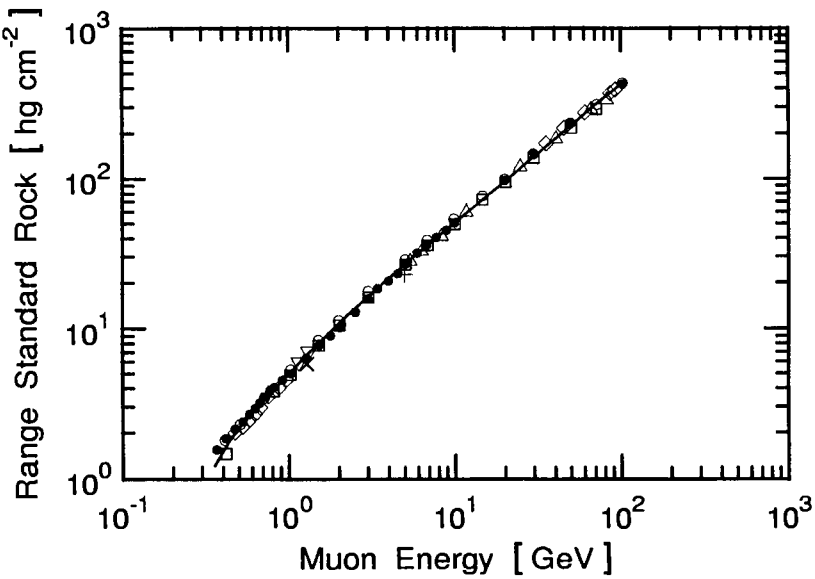

Figure 4.44: Muon range-energy spectrum for shallow depth in standard rock. The curve was computed using the energy loss expression by Sternheimer (1956) plus the term to allow for bremsstrahlung, pair production and nuclear interactions (after Barbouti and Rastin, 1983).

□	Allkofer et al. (1971)	▽	De et al. (1972)
•	Barbouti and Rastin (1983)	△	Appleton et al. (1971)
○	Hayman and Wolfendale (1962)	×	Allkofer et al. (1970)
◇, —	Diffusion Theory, $\gamma = 2.68$	+	Kong et al. (1975)

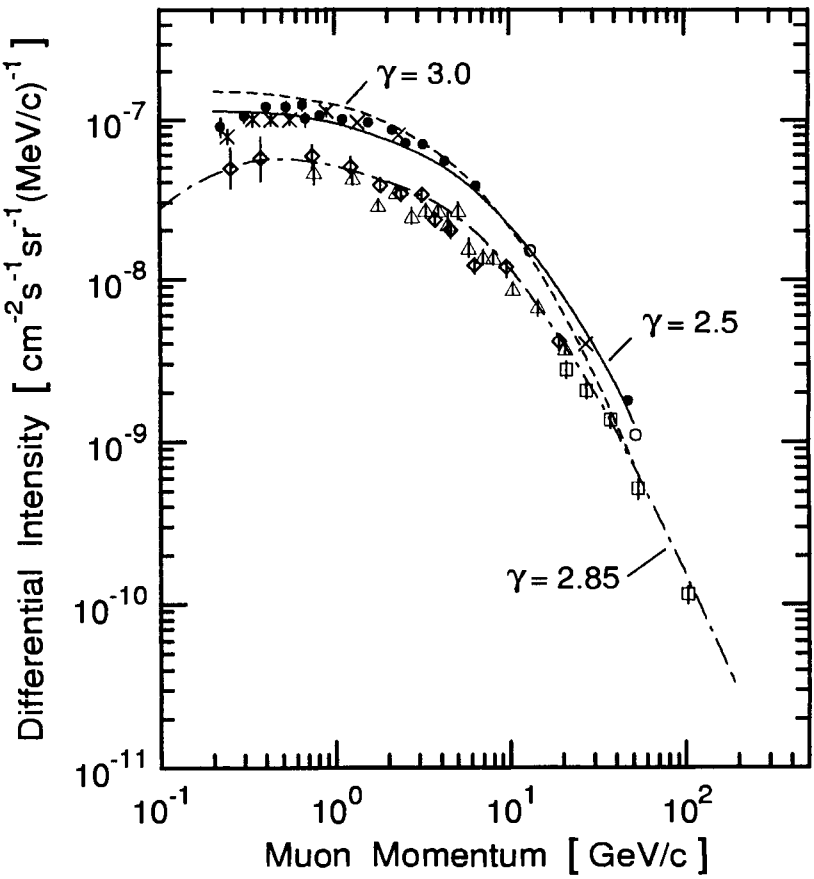

Figure 4.45: First muon momentum spectra measured with magnetic spectrographs underground. Shown are three sets of data from measurements at Moscow at a depth of 40 m w.e. by Daion and Potapov (1959a and 1959b), •, × and ○, and two theoretical curves by the same authors based on calculations using sea level muon spectra with differential spectral indices of $\gamma = 2.5$ and 3.0, respectively. The second set of data is from work of Murdoch et al. (1960) of the Sydney group who made measurements in a tunnel under 70 hg cm^{-2} of rock, ◇, △ and □. The curve that connects their points is from a calculation using a surface spectrum at sea level with a differential exponent of $\gamma = 2.85$.

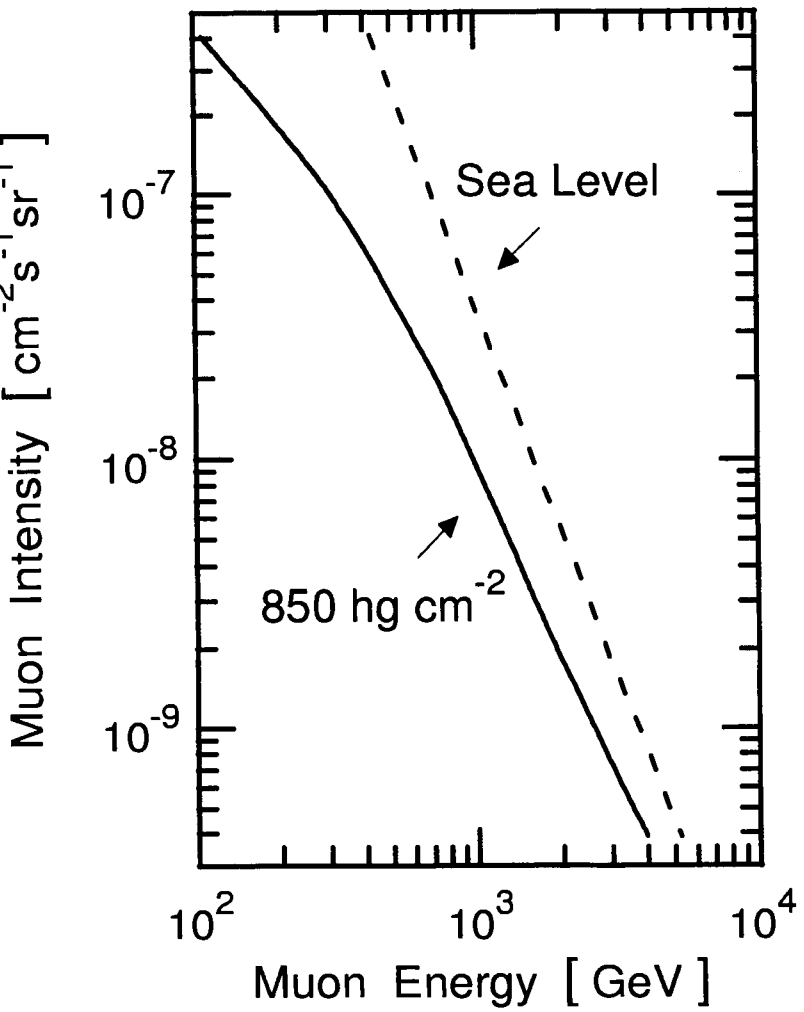

Figure 4.46: The Integral energy spectrum of muons at 850 hg cm^{-2} underground and an approximate one-exponent sea level spectrum for comparison (Mizutani and Ohta, 1977 and 1979).

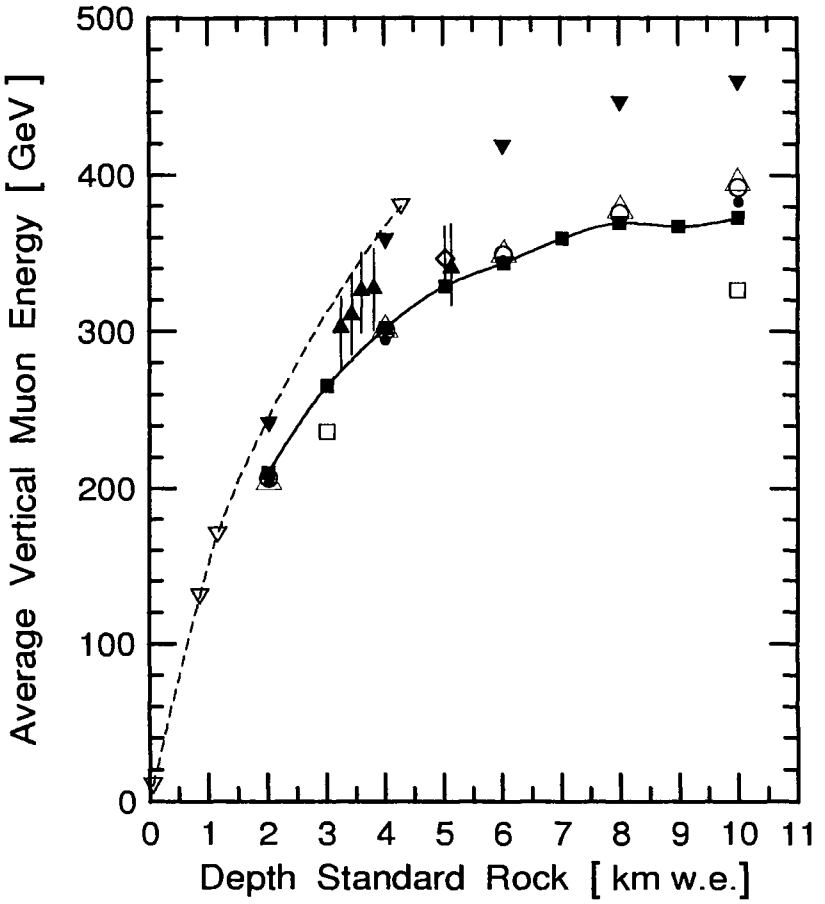

Figure 4.47: Comparison of the measured (exp.) average energy of vertical muons versus depth with theoretical data from different authors. The solid curve connects the data points of Castagnoli et al. (1997), the dashed those of Alexeyev et al. (1973a).

- ▼ Gurentsov (1984)
- • Lagutin et al. (1994)
- □ Lipari and Stanev (1991)
- ◇ Castagnoli et al. (1997), exp.
- ▲ Ambrosio et al. (1999a), exp.
- ○ Lagutin et al. (1994)
- △ Bugaev et al. (1984)
- ■ Castagnoli et al. (1997), exp.
- ▽ Alexeyev et al. (1973a), exp.

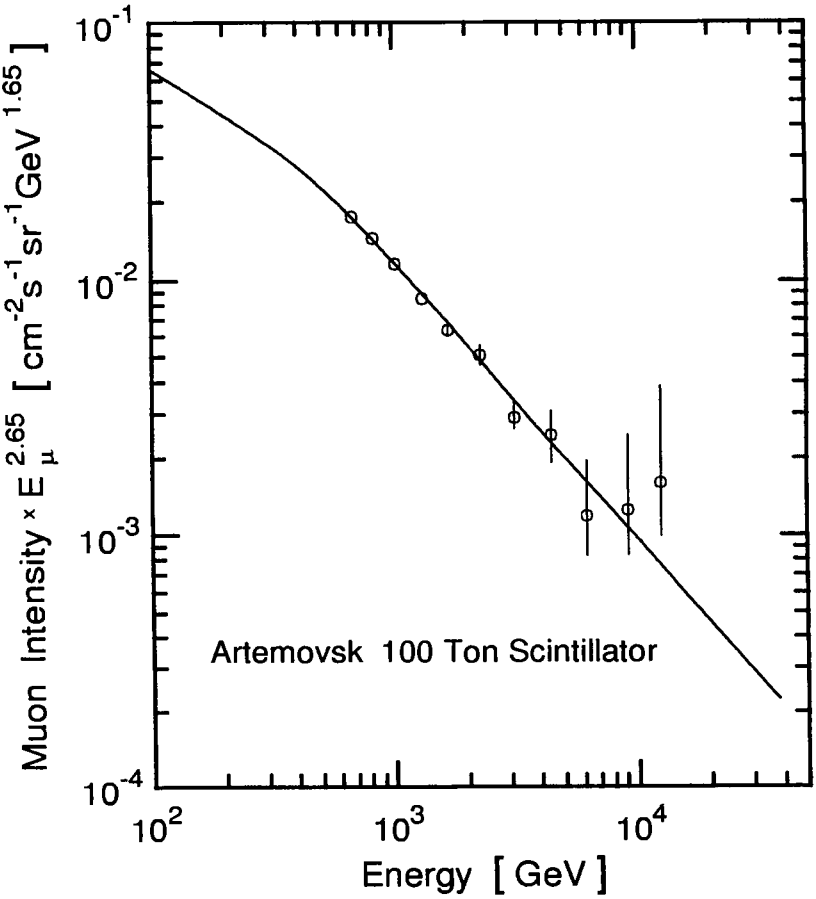

Figure 4.48: Vertical muon spectrum at sea level derived from data measured at 570 m w.e. underground with the 100 ton scintillator tank at Artyomovsk (Khalchukov et al., 1985).

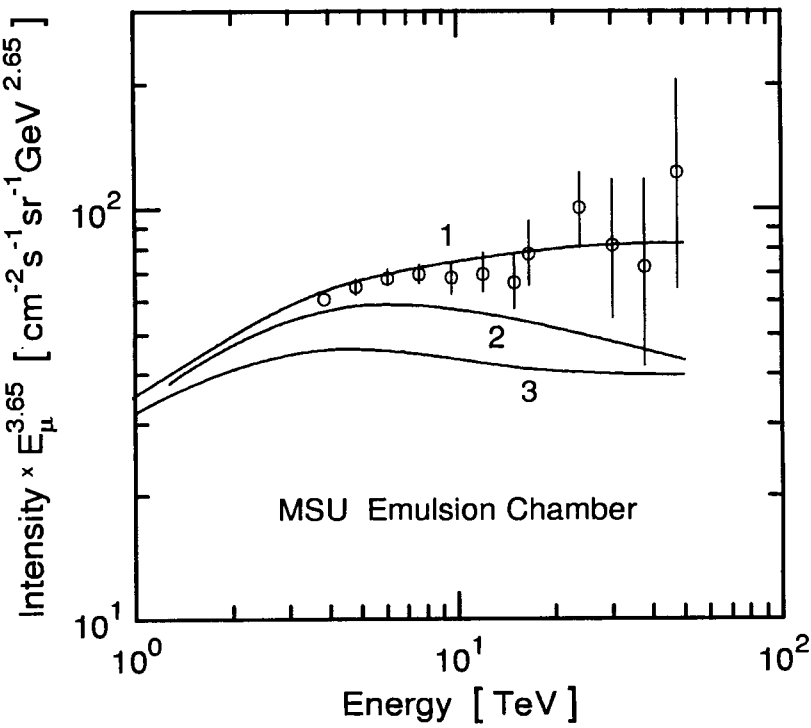

Figure 4.49: Differential energy spectrum of near horizontal muons (66° - 89°) detected with emulsion 40 m w.e. underground (Zatsepin et al., 1994). The intensities are multiplied by $E^{3.65}$ to emphasize deviations from this widely accepted slope of the spectrum underground. Curves 1, 2 and 3 are the result of model calculations for primary power law nucleon spectra with exponents $\gamma_N = 1.65$ constant, $\gamma_N = 1.65$ to 10 TeV and 3.14 above, and $\gamma_N = 1.65$ to 40 TeV and 3.22 above, respectively (Il'ina et al., 1995).

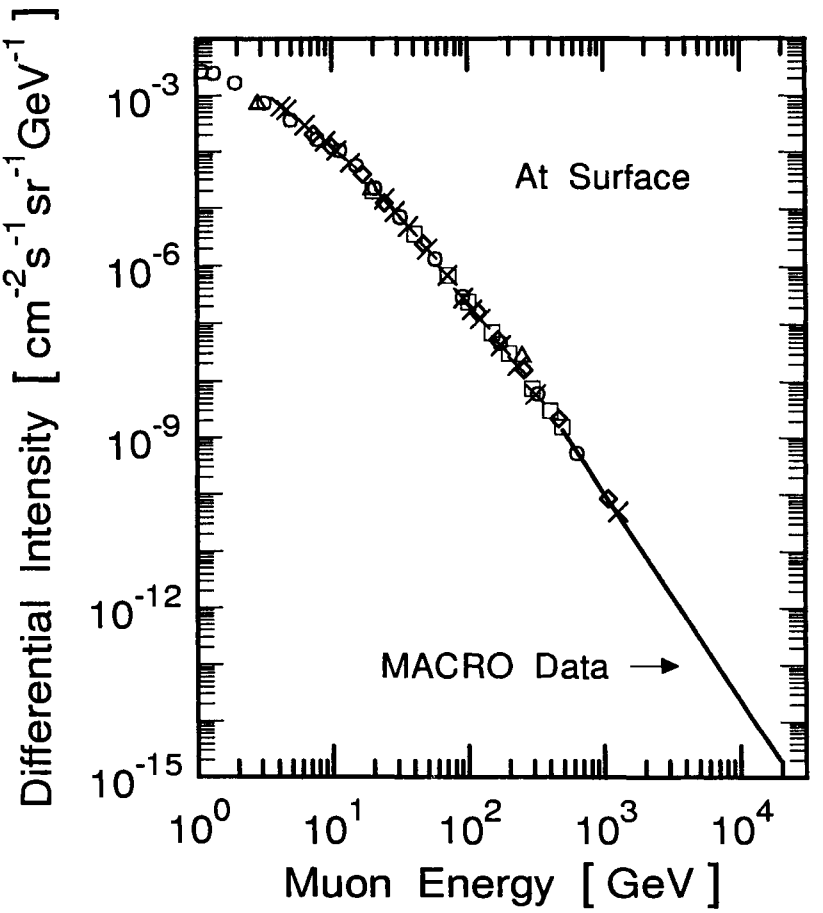

Figure 4.50: Differential muon energy spectrum at surface and sea level constructed from data of different experiments above and under ground. The solid line extending to the right of the many separate data points that are from measurements above ground is the fit to the MACRO data as shown in Figs. 4.27 and 4.28 (Ambrosio et al., 1995, 1996).

o	Allkofer et al. (1971)	□	Ayre et al. (1975)
△	Green et al. (1979)	◇	Nandi and Sinha (1972)
×	Rastin (1984)	——	Ambrosio et al. (1995, 1996)

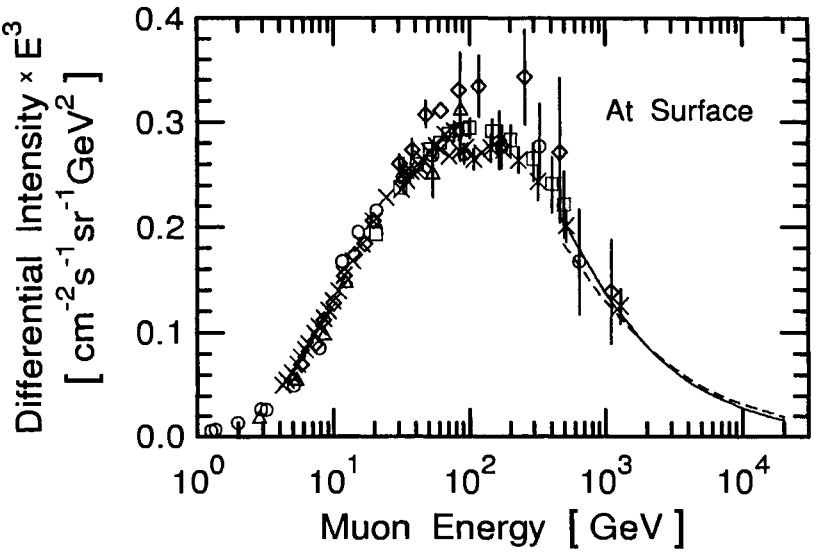

Figure 4.51: Differential muon energy spectrum at surface and sea level constructed from data of different experiments above and under ground. The figure shows the same data as Fig. 4.50 but in a different representation to eliminate the energy dependence of the flux behavior. (Ambrosio et al., 1995, 1996; Bussino et al., 1995). The thin solid curve is a fit of the data to eq. 4.55, the dashed line the expression itself. (For additional sea level data see Chapter 3, Section 3.6, for ground level data above sea level see Chapter 2, Section 2.6.)

o	Allkofer et al. (1971)	□	Ayre et al. (1975)
△	Green et al. (1979)	◇	Nandi and Sinha (1972)
×	Rastin (1984)	——	Gaisser (1990)

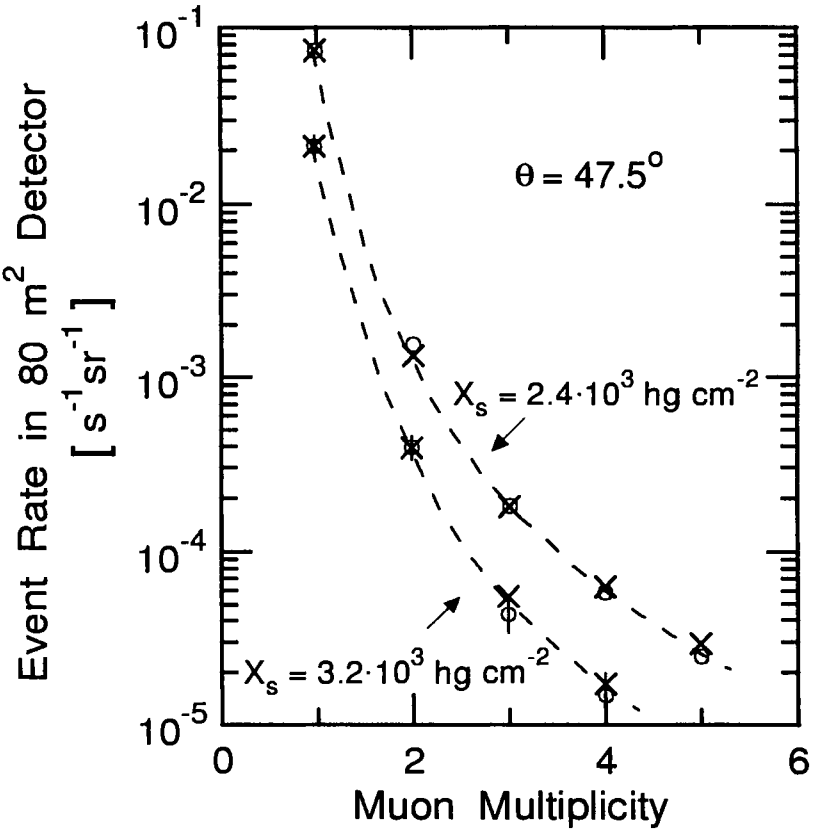

Figure 4.52: Muon multiplicity in the Utah detector at a zenith angle of $\theta = 47.5°$ and two different slant depths (Elbert et al., 1975).

o Experimental data | – – , × Prediction

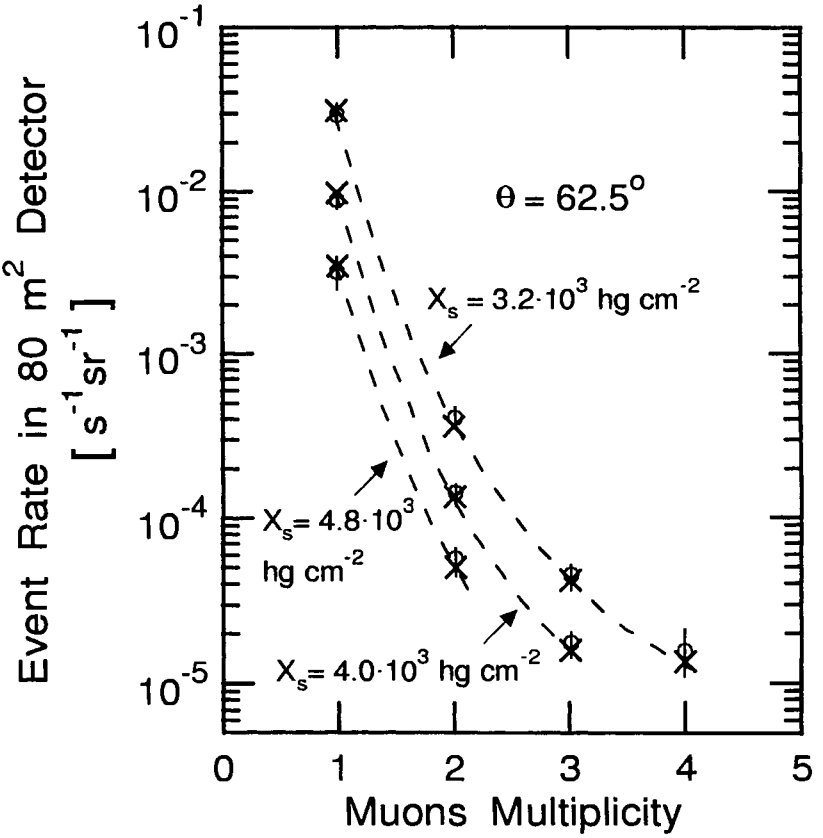

Figure 4.53: Muon multiplicity in the Utah detector at a zenith angle of $\theta = 62.5°$ and three different slant depths (Elbert et al., 1975).

o Experimental data | – – , × Prediction

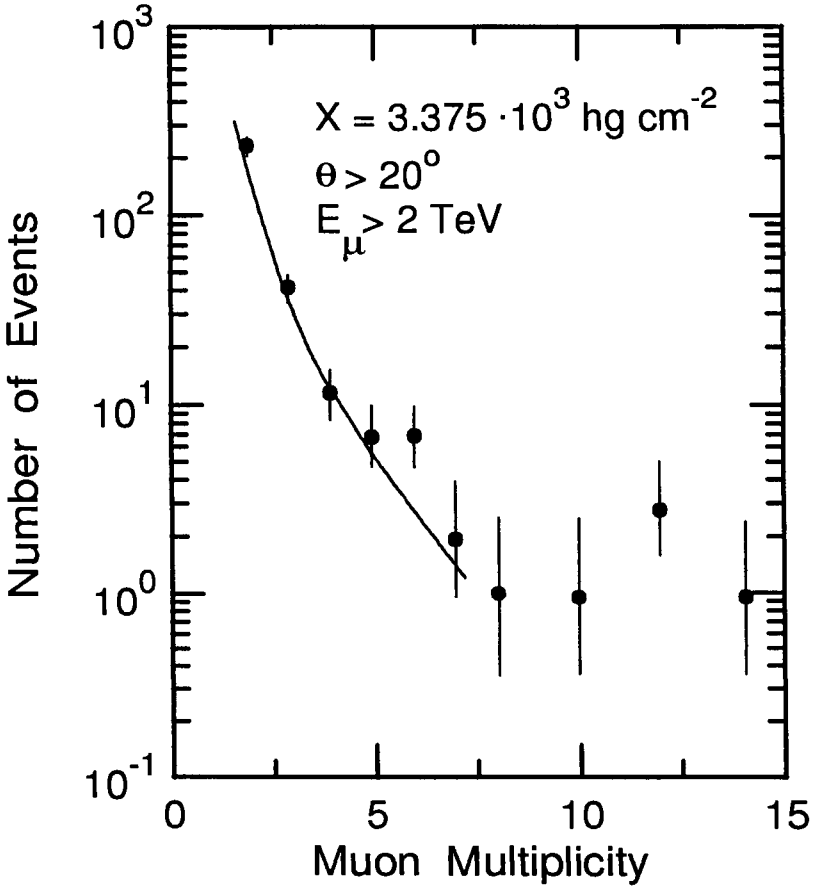

Figure 4.54: Muon multiplicity at a vertical depth of 3375 hg cm^{-2} in the Kolar Gold Fields (Krishnaswamy et al., 1979).

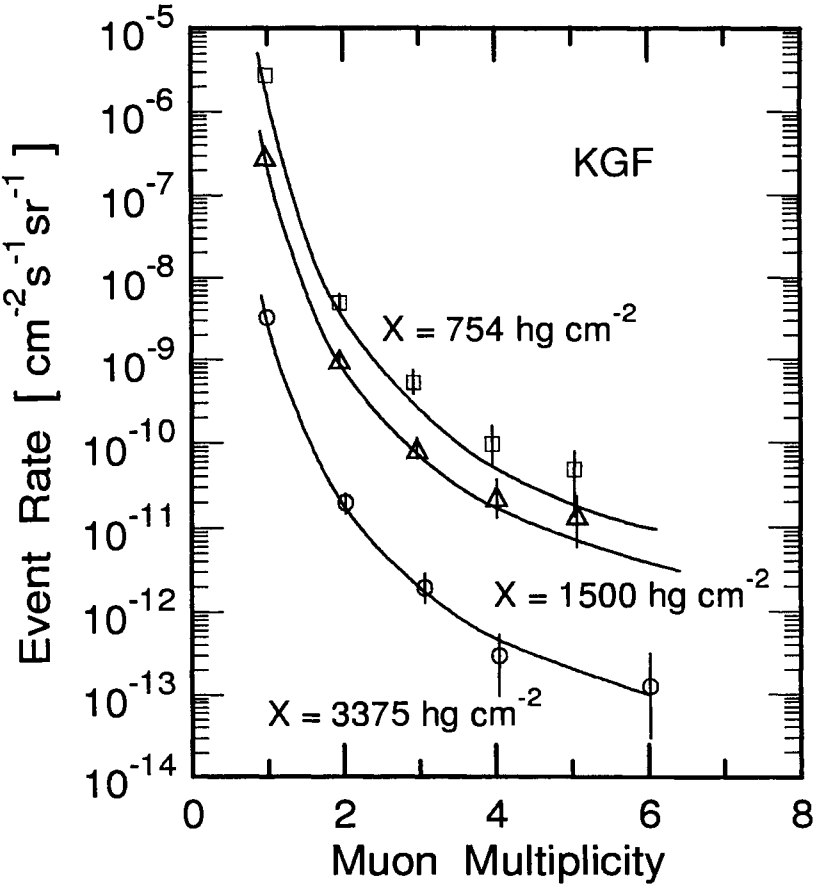

Figure 4.55: Multiplicity distributions of muons at three different vertical depths in the Kolar Gold Fields (KGF) laboratory (Totsuka and Koshiba, 1974). The curves are fits to the data.

□ 754 hg cm^{-2} | △ 1500 hg cm^{-2} | ○ 3375 hg cm^{-2}

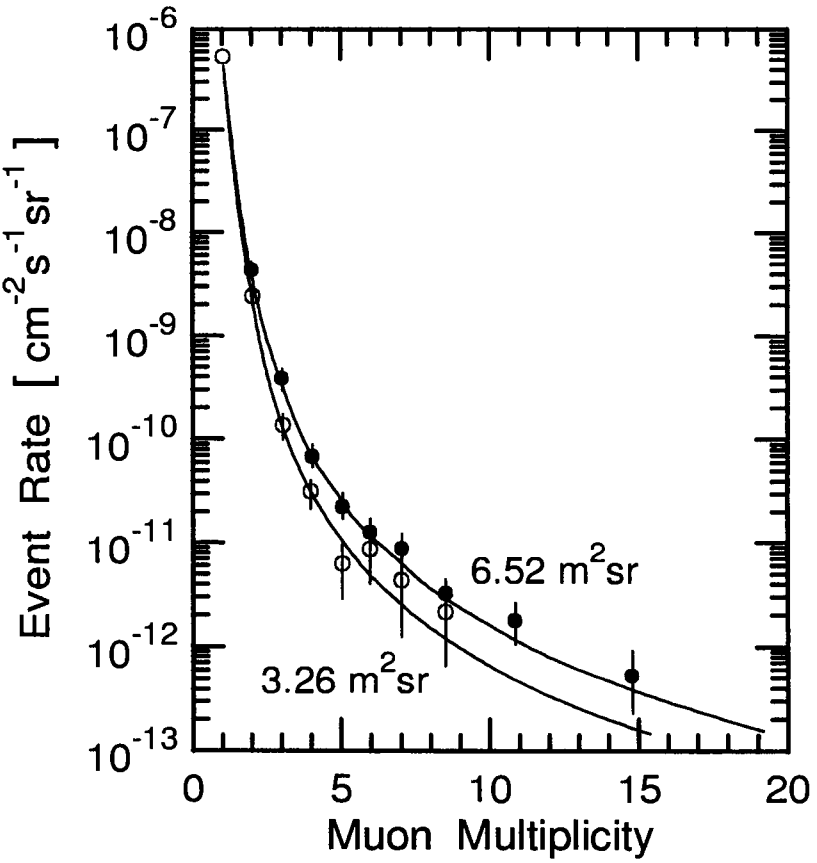

Figure 4.56: Multiplicity distributions of muons at a mean slant depth of X_s = 1380 hg cm^{-2} ($E_\mu \geq 450$ GeV) for full and half detector areas, respectively. The mean zenith angle is 20°. The curves are fits to the data points (Suda et al., 1974).

- • area - solid angle product $S_1 = 6.52$ m^2 sr
- ○ area - solid angle product $S_2 = 3.26$ m^2 sr

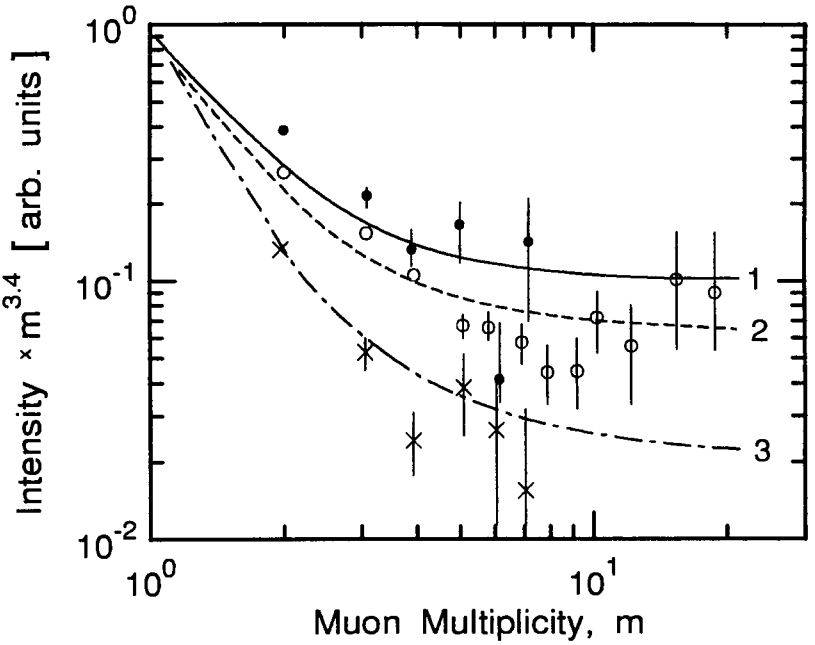

Figure 4.57: Comparison of muon multiplicities, m, from three underground detectors for only slightly different threshold energies: • Baksan (170 m^2, $E_\mu \geq 3.2$ TeV), o Fréjus (80 m^2, $E_\mu \geq 3.1$ TeV), and × NUSEX (12 m^2, $E_\mu \geq 3.5$ TeV). The intensities are multiplied by the multiplicity m to the power of 3.4. Curves 1, 2, and 3 are from simulation calculations with a differential muon spectral index at ground level of $\gamma = 2.7$ and apply to the respective experiments in the sequence listed above. (Chudakov et al., 1991).

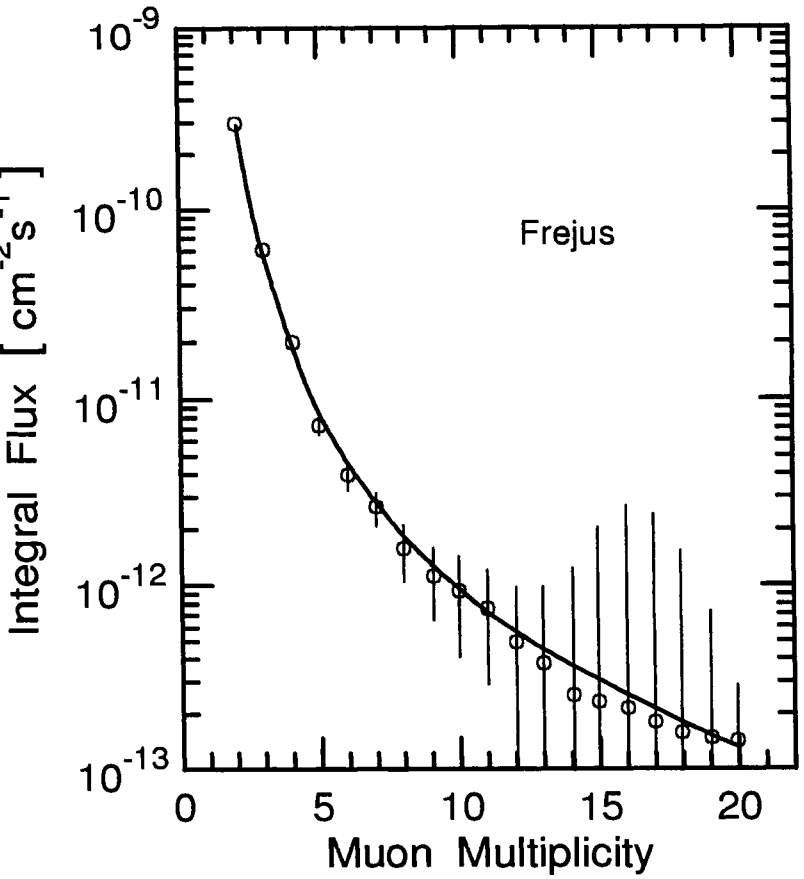

Figure 4.58: Integral flux of multi-muons as a function of true muon multiplicity, after corrections, obtained with the Fréjus detector at a depth of 4850 hg cm^{-2}. The curve is a fit to the empirical expression, eq. 4.57 (after Berger et al., 1989a and 1989b).

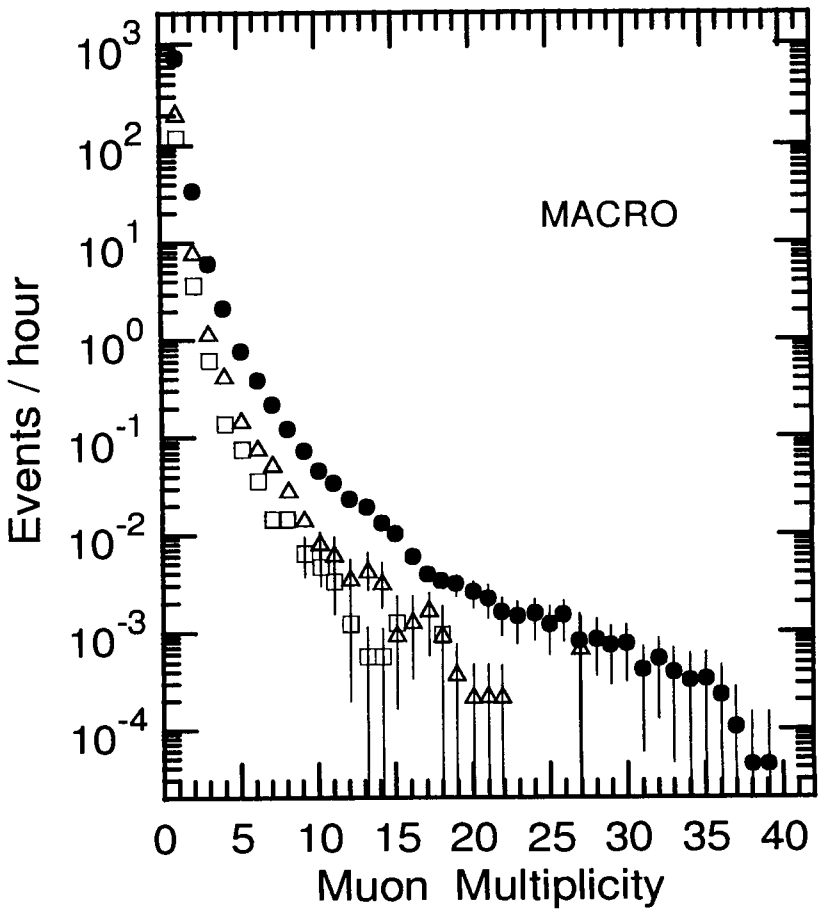

Figure 4.59: Muon multiplicity distributions as seen with one (□), two (△) and six (•) MACRO super module detectors at Gran Sasso (depth approx. 4000 m w.e.). A super module measures 12 m × 12 m × 4.8 m (Ahlen et al., 1994; Ambrosio et al., 1996).

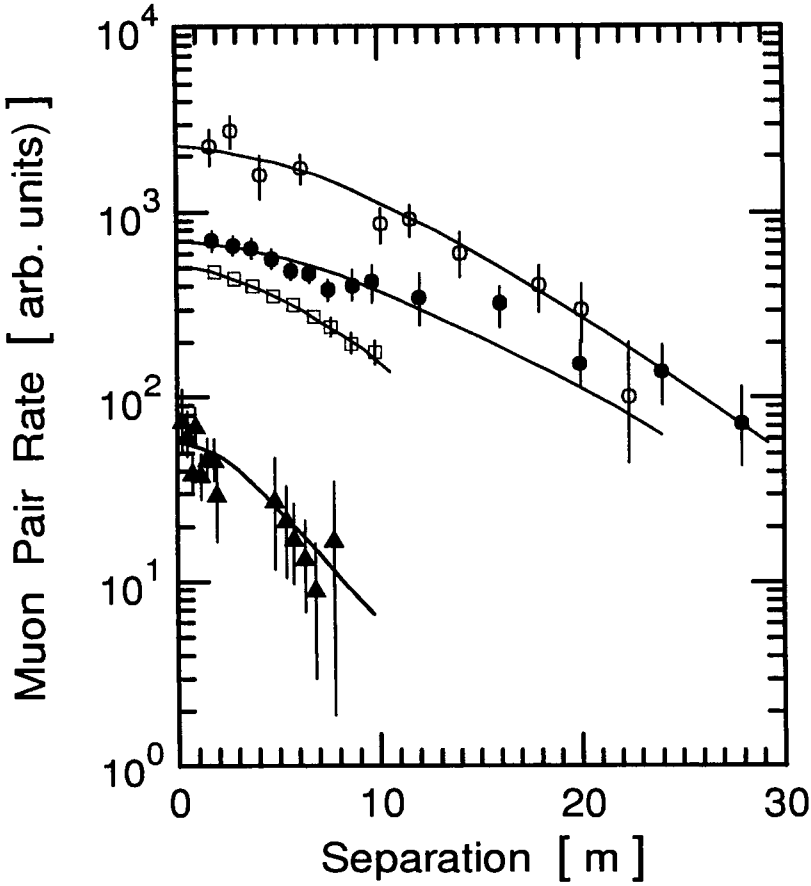

Figure 4.60: Decoherence distributions obtained by different experiments at different vertical depths (Totsuka and Koshiba, 1974).

- ○ 1600 hg cm^{-2} vertical depth; $\theta = 0°$ (Barrett et al., 1952) Cornell
- ● 2500 hg cm^{-2} , $40° \leq \theta \leq 60°$, 6.52 m^{2}sr detector (Coats et al., 1970)
- □ 2500 hg cm^{-2} , $40° \leq \theta \leq 60°$, 3.26 m^{2}sr detector (Coats et al., 1970)
- ▲ 3375 hg cm^{-2} vertical depth; $\theta = 0°$ (Krishnaswamy et al., 1968) KGF

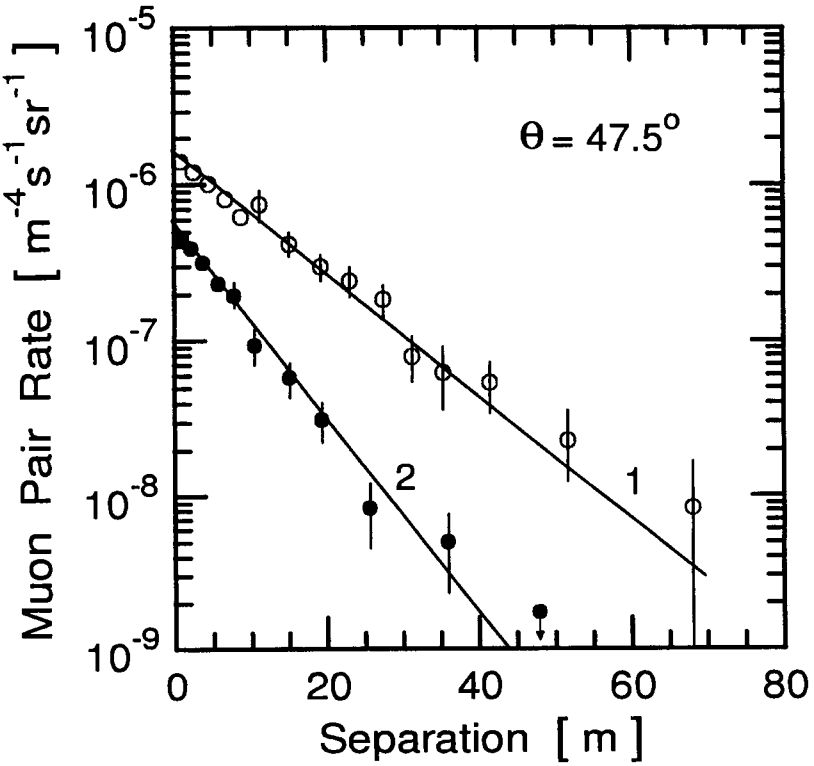

Figure 4.61: Decoherence distribution for muon pairs at zenith angle $\theta = 47.5°$ and slant depths of $X_s = 2400$ hg cm^{-2} (o, curve 1), and $X_s = 3200$ hg cm^{-2} (•, curve 2) recorded with the Utah detector. The symbol with the downward pointing arrow attached shows the location of the upper bound of a hypothetical single count in the last bin of curve 2 where no actual counts were recorded. (Bergeson et al., 1975; Lowe et al., 1976).

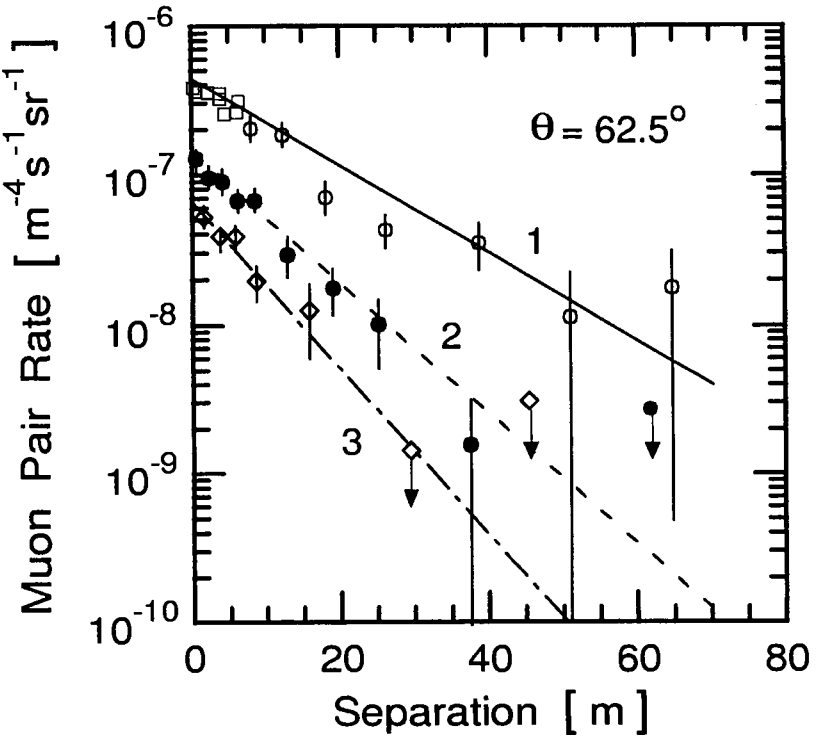

Figure 4.62: Decoherence distribution for muon pairs at zenith angle $\theta = 62.5°$ and slant depths of $X_s = 3200$ hg cm^{-2} (□, ○, curve 1), $X_s = 4000$ hg cm^{-2} (•, curve 2), and $X_s = 4800$ hg cm^{-2} (◇, curve 3) obtained with the Utah detector. The symbols with the downward pointing arrows attached show the location of the upper bound of a hypothetical single count in the last bin where no actual counts were recorded. (Bergeson et al., 1975; Lowe et al., 1976).

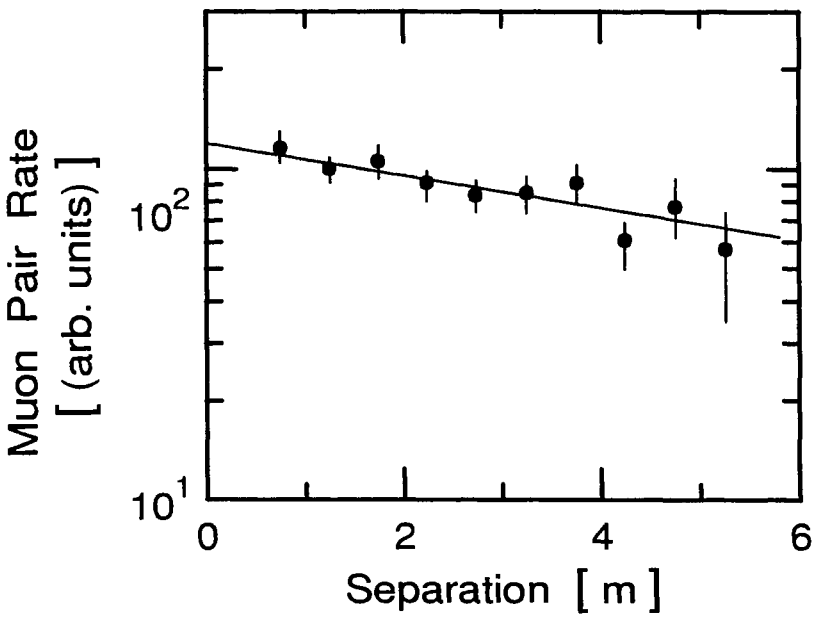

Figure 4.63: Decoherence distribution for muon pairs at a vertical depth of 1840 hg cm^{-2} and an angular range $0° \leq \theta \leq 60°$ (Krishnaswamy et al., 1979). The data from different angular regions have been corrected for the same uniform area at each separation.

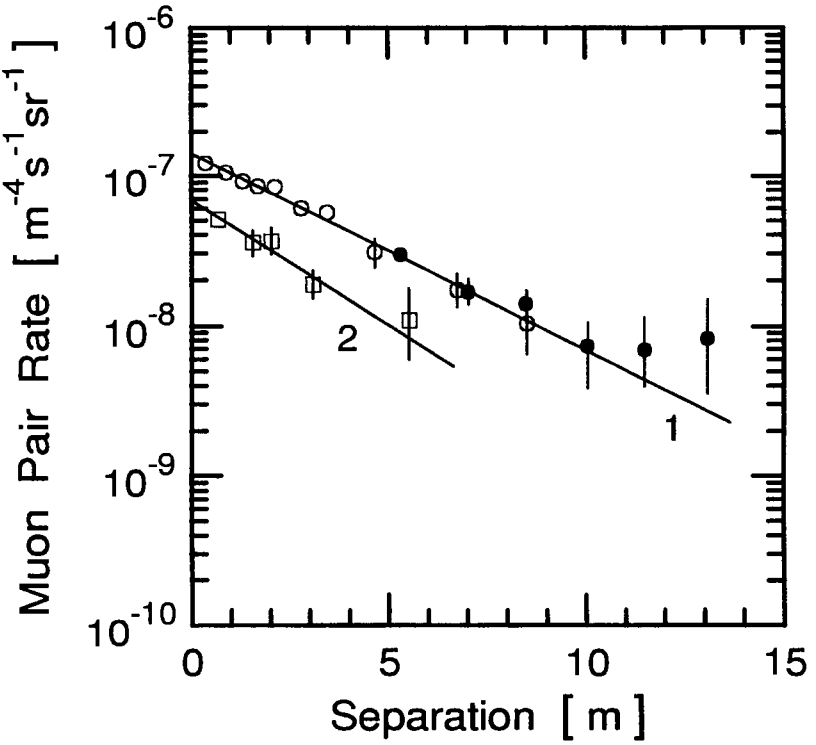

Figure 4.64: Comparison of decoherence rates from the Homestake detector for zenith angles $0° \leq \theta \leq 20°$, located at a depth of 4200 m w.e. with earlier data from the Utah detector (Cherry et al., 1981 and 1982) and calculations by Elbert and Stanev (1983).

- o Utah, $\theta = 62.5°$, 4000 m w.e. | □ Utah, $\theta = 62.5°$, 4800 m w.e.
- • Homestake, $0° \leq \theta \leq 20°$, 4200 m w.e.

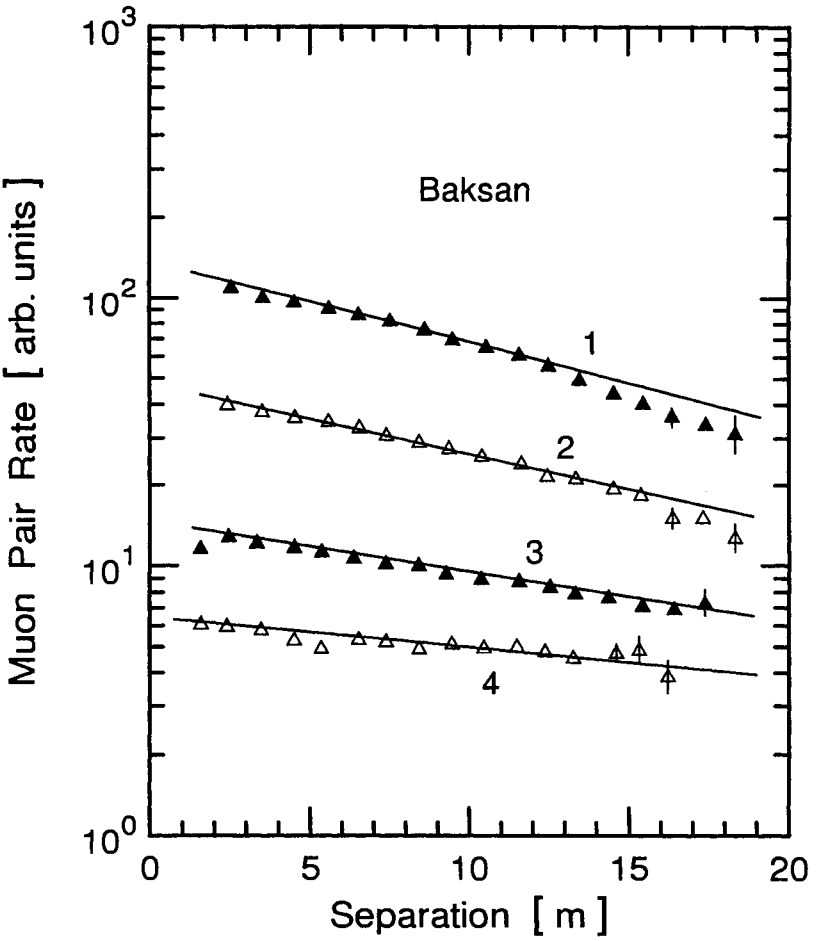

Figure 4.65: Decoherence curves measured at Baksan for a range of zenith angles at nearly the same slant depth, X_s, and threshold energies, E_{th}. The parameter r_0 is defined in the text (Chudakov et al., 1990).

Curve	E_{th} [TeV]	r_0 [m]	θ	X_s [hg/,cm^{-2}]
1	0.235	8.2	0° - 20°	940
2	0.244	8.1	20° - 40°	970
3	0.270	7.8	40° - 60°	1040
4	0.309	9.0	60° - 70°	1160

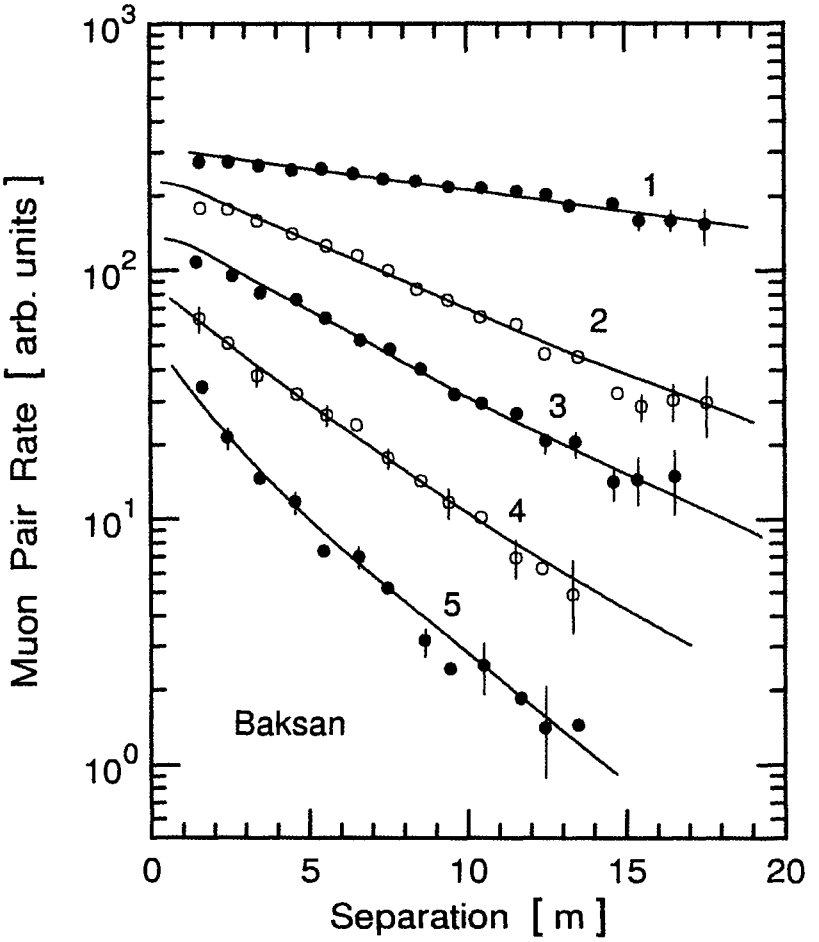

Figure 4.66: Decoherence curves measured at Baksan for a zenith angle interval between 50° and 60° and different muon threshold energies, E_{th}. The parameter r_0 is defined in the text (Chudakov et al., 1990).

Curve	E_{th} [TeV]	r_0 [m]	X_s [hg cm^{-2}]	Curve	E_{th} [TeV]	r_0 [m]	X_s [hg cm^{-2}]
1	0.28	7.0	1070	2	0.85	2.3	2510
3	1.34	1.7	3190	4	1.96	1.3	3970
5	3.16	0.9	4970				

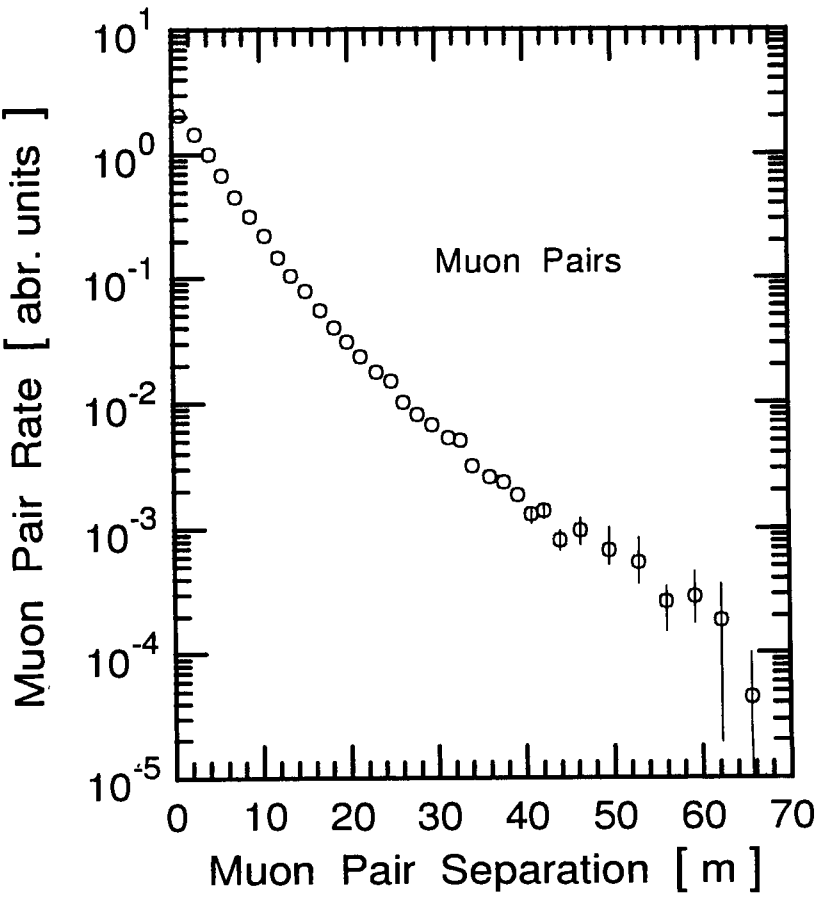

Figure 4.67: Muon pair separation distribution in arbitrary units, measured with the MACRO detector at Gran Sasso. The data include all pairs (•) (Sioli et al., 2000).

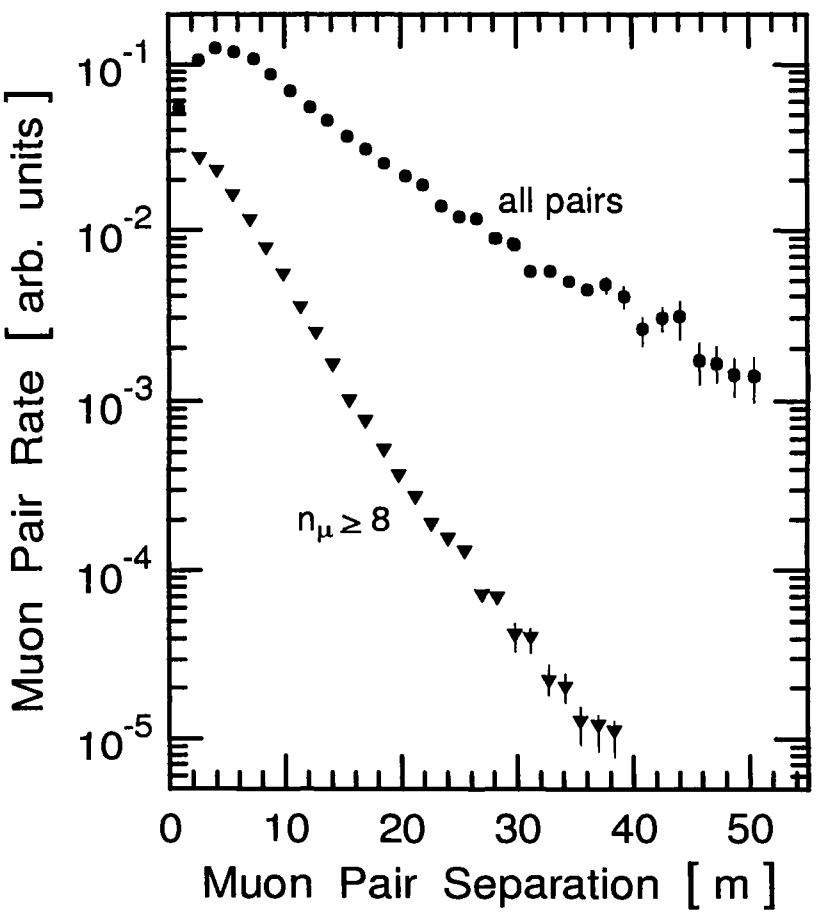

Figure 4.68: Muon pair separation distribution in arbitrary units, measured with the MACRO detector at Gran Sasso. The data include all pairs (•) (Ahlen et al., 1994; Ambrosio et al., 1996 and 1997), and muons in groups with $n_\mu \geq 8$ (▼) (Battistoni et al., 1995). The two data sets are from different runs and should not be brought into relation.

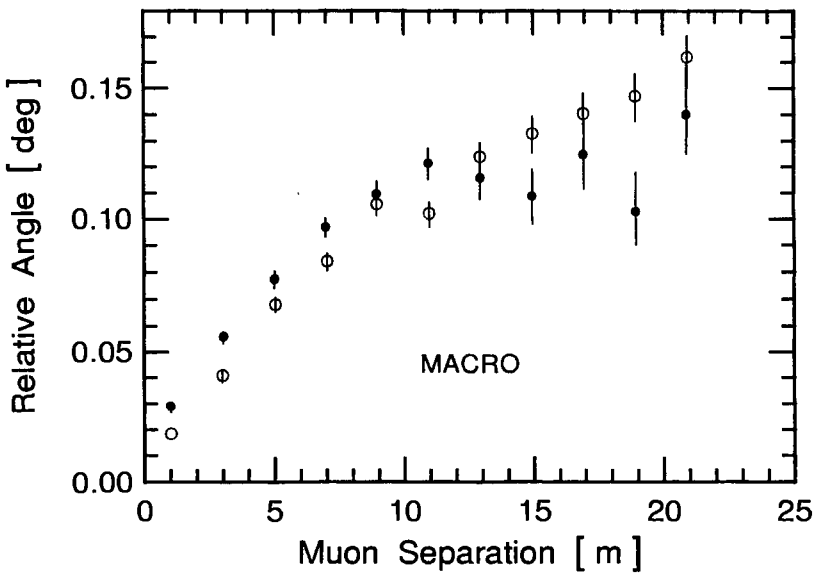

Figure 4.69: Decorrelation curve, or the dependence of the relative angle [degrees] between double muon tracks as a function of track separation [m] in multi-muon events as seen by the MACRO detector at Gran Sasso. • experimental data, ○ results from a Monte Carlo calculation including muon bremsstrahlung (Battistoni et al., 1995).

4.4 Muons Under Water and Ice

4.4.1 General Comments

Measurements of muon intensities in a large and highly homogeneous dense medium, such as a large and deep body of water like the ocean, are of fundamental importance to study muon propagation and energy loss, and to verify the validity of the theory. Theoretical predictions of the depth-intensity relation of muons have attained a degree of accuracy and reliability that experimental data obtained in deep mines or tunnels underground can no longer be used for fine tuning of theoretical formulas because of the uncertainties in rock composition and density along the muon trajectories.

In addition, with the rising interest in high energy neutrino astronomy and the planning of highly shielded, giant neutrino telescopes in the form of very large optical detector matrices aimed at detecting the Cherenkov signatures of high energy muons and also electrons created in neutrino reactions at great depth in lakes, oceans and the polar ice caps, extensive efforts were initiated in the early eighties to explore mostly the muon component in these media (see f.i., Markov, 1960; Markov and Zheleznykh, 1961; Roberts, 1979a, 1979b and 1992; Wilkins, 1979; Learned, 1980; Stenger, 1981; Halzen and Learned, 1988; Barwick, 1991; Belolaptikov et al., 1991; Resvanis, 1992a, 1993 and 1996).

This work was accompanied by exhaustive studies of the optical and related properties and parameters of these media at prospective future array sites, including optical background studies. These topics are discussed separately in Chapter 7, Section 7.5. An excellent review of muon physics underground and underwater of more general nature had been given by Bugaev et al. (1993 and 1994).

4.4.2 Intensity versus Depth in Water

Pioneering work in this field was carried out by Higashi et al. (1966) in Sugura Bay, Shizuokaken (Japan), who made measurements down to depths of 1380 m. Their results are shown in Table 4.22 and Fig. 4.70. Davitaev et al. (1970) made measurements of the muon intensities in the Black Sea, the Mediterranean and the Atlantic to depths of 420 m, 2000 m and 3190 m, respectively. Their combined data are listed in Table 4.23 and plotted in Fig. 4.71.

Percy and Rogers (1977), Rogers et al. (1981) and Rogers and Tristam (1983 and 1984) made measurements at very shallow depths in fresh wa-

Table 4.22: Absolute Vertical Intensity of Muons Versus Depth in Sea Water (Higashi et al., 1966.)

Depth [m]	Intensity $[cm^{-2}s^{-1}sr^{-1}]$
50	$5.58 \cdot 10^{-4}$
90	$2.05 \cdot 10^{-4}$
150	$(6.80 \pm 0.17) \cdot 10^{-5}$
220	$(3.47 \pm 0.15) \cdot 10^{-5}$
380	$(7.94 \pm 0.27) \cdot 10^{-6}$
715	$(2.30 \pm 0.20) \cdot 10^{-6}$
960	$(7.50 \pm 0.66) \cdot 10^{-7}$
1380	$(3.50 \pm 1.40) \cdot 10^{-7}$

Table 4.23: Vertical Muon Intensity as a Function of Depth in Sea Water (Davitaev et al., 1970)

Depth [m]	Intensity $[cm^{-2}s^{-1}sr^{-1}]$
250	$2.32 \cdot 10^{-5}$
300	$1.67 \cdot 10^{-5}$
500	$5.20 \cdot 10^{-6}$
600	$3.30 \cdot 10^{-6}$
750	$1.92 \cdot 10^{-6}$
1090	$6.42 \cdot 10^{-7}$
1970	$1.58 \cdot 10^{-7}$
3190	$3.04 \cdot 10^{-8}$

ter. Their exploratory work was carried out in the Hanningfield Reservoir in Essex (GB) to depths of 12.5 m, followed by experiments in Lake Geneva, Switzerland, to depths of 175 m using a scintillation counter telescope. The results are given in Table 4.24 and also presented in Fig. 4.71. For a comparison with similar measurements under rock the reader is referred to Fig. 4.15, Subsection 4.3.3.

More recently measurements were made by Fyodorov et al. (1985, 1986) in the Caribbean and the Pacific to depths in excess of 5000 m, by the

Table 4.24: Absolute Vertical Intensity of Muons versus Depth in Fresh Water (Rogers and Tristam, 1984)

Depth [hg cm^{-2}]	Intensity [cm^{-2}s^{-1}sr^{-1}]
10.3	$(3.70 \pm 0.32) \cdot 10^{-3}$
18.0	$(2.24 \pm 0.15) \cdot 10^{-3}$
20.9	$(1.83 \pm 0.18) \cdot 10^{-3}$
38.4	$(9.61 \pm 0.85) \cdot 10^{-4}$
45.6	$(7.59 \pm 0.72) \cdot 10^{-4}$
59.0	$(4.99 \pm 0.41) \cdot 10^{-4}$
71.7	$(3.90 \pm 0.33) \cdot 10^{-4}$
100	$(2.02 \pm 0.18) \cdot 10^{-4}$
111	$(1.80 \pm 0.16) \cdot 10^{-4}$
143	$(1.10 \pm 0.10 \cdot 10^{-4}$
175±4	$(7.39 \pm 0.88) \cdot 10^{-5}$

DUMAND Collaboration (Babson et al., 1990) in the Pacific near Kailua Kona, Hawaii, and by the NESTOR Collaboration (Anassontzis et al., 1993) near Pylos, Greece, in the Mediterranean, the two latter to depths of 4200 m. The data of Babson et al. (1990) are illustrated in Fig 4.72. For comparison we have added to this figure data points from the earlier work by Vavilov et al. (1970) and Fyodorov et al. (1985) together with data from Higashi et al. (1966). Intensities predicted by the Miyake formula (Miyake, 1963) and results from inclined measurements, converted to vertical intensities, are also shown. Vertical intensities obtained by the NESTOR group in three different experiments that were carried out more than one year apart each are shown in Fig. 4.73 together with the Miyake prediction and data from other experiments. Some of these data are tabulated in Table 4.25.

The only moderately deep (~1170 m) and fairly large fresh water array currently in operation is the Lake Baikal installation (Belolaptikov et al., 1991 and 1997). The results of this work are illustrated in Fig. 4.73 and in the world survey on underwater muon intensities of Bugaev et al. (1993 and 1994), presented in Fig. 4.74. Also shown is a theoretical prediction by Bugaev et al. (1993).

Table 4.25: Muon Vertical Intensities in the Deep Sea

Reference	Location	Depth [m]	Intensity $[cm^{-2}s^{-1}sr^{-1}]$
Vavilov et al. (1970)	Black Sea	1090	$(6.0 \pm 0.31) \cdot 10^{-7}$
	Mediterr.	1970	$(1.45 \pm 0.13) \cdot 10^{-7}$
	Atlantic	3190	$(2.55 \pm 0.23) \cdot 10^{-8}$
Fyodorov et al. (1985)	Carrib.	2925	$(3.1 \pm 0.5) \cdot 10^{-8}$
	Atlantic	4025	$(5.9^{+2.0}_{-2.5}) \cdot 10^{-9}$
		5020	$(4.1^{+1.6}_{-2.0}) \cdot 10^{-9}$
Babson et al. (1990)	Pacific	2090	$(9.84 \pm 6.5) \cdot 10^{-8}$
		2633	$(8.04 \pm 3.3) \cdot 10^{-8}$
		3160	$(2.04 \pm 0.83) \cdot 10^{-8}$
		3707	$(1.31 \pm 0.40) \cdot 10^{-8}$
		4157	$(4.57 \pm 1.32) \cdot 10^{-9}$

4.4.3 Zenith Angle Dependence at Great Depth in Water

The zenith angle distribution of muons under water was measured in Lake Baikal, at the DUMAND site in the Pacific and at the NESTOR site in the Mediterranean (Anassontzis et al., 1995) . Figure 4.75 shows event rates versus $\cos(\theta)$ on a linear scale obtained from the Baikal and DUMAND experiments. The Lake Baikal data are from a vertical depth of 1170 m, located at a surface distance to shore of about 3.6 km (Belolaptikov et al., 1993a and 1994). Lake bottom depth at the site is about 1370 m. The DUMAND data which are of poorer statistics, were obtained at a vertical depth of 4000 m, approximately 30 km off-shore, west of Keahole Point, Hawaii (Babson et al., 1990). The depth of the sea floor at this site is 4800 m.

In Fig. 4.76 we show the zenith angle distribution of the muon intensity at three depths (3338 m, 3697 m, 4108 m) recorded at the NESTOR site at slightly different locations and different dates. Indicated, too, are curves that are fits of the form as given in the caption.

Newer measurements made with the Baikal underwater array NT-36 at the same depth (1170 m), giving absolute intensities versus $\cos(\theta)$ on a logarithmic scale with good statistics, are presented in Fig. 4.77 (Belolaptikov

et al., 1995a and 1995b). We have also constructed the linear representation of these data and show it in the same figure.

4.4.4 Intensity versus Depth in Ice

First attempts to detect muons in polar ice were made by the AMANDA collaboration at shallow depth (217 m) in Greenland ice (Lowder et al., 1991). Encouraged by the results the work was continued at much greater depth in the Antarctic ice cap at the South Pole. However, initial studies there indicated that light scattering on tiny air bubbles at depths around 800 m to 1000 m made it impossible to reconstruct muon trajectories (Askebjer et al., 1995). New measurements at greater depth (1.5 to 2.0 km), now in progress, are more promising for reasons discussed in Chapter 7, Section 7.5, and have yielded first results that are displayed in Fig. 4.73 (Andres et al., 2000).

4.4.5 Theoretical Contributions

Davitaev et al. (1970) calculated on the basis of the usual processes considered for the depth-energy relation, i.e., ionization and excitation, pair production, bremsstrahlung and nuclear interactions, the average energy loss versus depth in water (for details see Sections 4.2 and 4.3). The results are shown in Table 4.26. The values at shallow depth have big errors because of large steps in the integration. Subsequently, theoretical studies of the propagation and intensities of muons in fresh water, sea water and ice were made by Vavilov et al., 1974.

Rogers and Tristam (1984) calculated the range of relatively low momentum muons (1 to 100 GeV/c) in water, considering the usual energy loss processes and taking for the mean ionization potential of water 80 eV, $Z/A = 0.555$, $Z^2/A = 3.7$, and for the photonuclear cross section $\sigma_{ph} = 125\,\mu$b. The results of this work are shown in Table 4.27. Convoluting these data with the results of their measurements underwater these authors obtained the integral sea level intensities at standard momenta which are also included in the table.

Table 4.26: Theoretical Energy Loss of Muons versus Depth in Water (Davitaev et al., 1970)

Depth [hg cm^{-2}]	Energy Loss [GeV]	Depth [hg cm^{-2}]	Energy Loss [GeV]
100	26.32	3500	1710
200	53.96	4000	2149
500	143.2	5000	3270
1000	312.8	6000	4818
1500	511.5	7000	6961
2000	744.1	8000	9931
2500	1016	9000	14059
3000	1336	10000	19806

Table 4.27: Muon Ranges in Water and Integral Sea Level Intensities (Rogers and Tristam, 1984)

Momentum [GeV/c]	Range [m of water]	Intensity [cm^{-2}s^{-1}sr^{-1}]
1	3.94	$(6.29 \pm 0.40) \cdot 10^{-3}$
1.5	6.29	$(5.04 \pm 0.33) \cdot 10^{-3}$
2	8.56	$(4.17 \pm 0.28) \cdot 10^{-3}$
3	13.0	$(3.04 \pm 0.21) \cdot 10^{-3}$
5	21.6	$(1.87 \pm 0.13) \cdot 10^{-3}$
7	29.9	$(1.29 \pm 0.09) \cdot 10^{-3}$
10	42.2	$(8.28 \pm 0.61) \cdot 10^{-4}$
15	62.1	$(4.71 \pm 0.36) \cdot 10^{-4}$
20	81.7	$(3.03 \pm 0.23) \cdot 10^{-4}$
30	120.0	$(1.53 \pm 0.12) \cdot 10^{-4}$
50	194.0	$(5.80 \pm 0.48) \cdot 10^{-5}$
70	266.0	$(2.84 \pm 0.24) \cdot 10^{-5}$
100	370.0	$(1.25 \pm 0.11) \cdot 10^{-5}$

References

Anassontzis, E.G., I.F. Barinov, M. Barone, A.O. Deyneko, V.A. Gaidash, P. Ioannou, G. Kalkanis, S. Katsanevas, Ch. Kourkoumelis, V.V. Ledenev, A.A. Permyakov, M.N. Platonov, P. Pramantiotis, L.K. Resvanis, V.Kh. Rukol, N.A. Sheremet, N.M. Surin, D.U. Vasilenko, G. Voulgaris, L.M. Zakharov, I.M. Zheleznykh, and V.A. Zhukov: PICRC 4, p. 554 (1993).

Anassontzis, E., P. Assimakopoulus, M. Barone, G. Fanourakis, C. Goudis, G. Grammatikakis, P. Hantzion, P. Ioannou, S. Katsanevas, C. Markou, J. McNutt, L. Moraitis, A. Nicolaidis, P. Pramantiotis, L.K. Resvanis, I. Siotis, S.A. Sotiriou, G. Voulgaris, P.K.F. Grieder, P. Minkowski, E. Torrente, L. Sulak, A.E. Ball, B. Langeset, H. Bradner, S. Bottai, A. Cartacci, L. Dell'Angelo, M.P. DePascale, F. Grianti, B. Monteleoni, V.A. Naumov, V. Valente, J.G. Learned, V.J. Stenger, U. Keusen, P. Koske, J. Rathlev, G. Voigt, G. DeMarchis, L. Piccari, M. Bonori, A. Capone, F. Massa, E. Valente, I.F. Barinov, A.V. Butkevich, L.G. Dedenko, A.O. Deineko, V.A. Gaidash, S.K. Karaevsky, A.A. Mironovich, A.A. Permyakov, N.M. Surin, A.V. Trenikhin, L.A. Zakharov, I.M. Zheleznykh, V.A. Zhukov, T.A. Demidova, A.P. Eremeev, M.N. Platonov, V.K. Rucol, N.A. Sheremet, V.I. Albul, V.V. Ledenev, A.A. Paramonov, N. de Botton, P.H. Carton, M. Cribier, F. Feinstein, Ph. Gorest, J.-C. Languillat, S. Loucatos, L. Moscoso, J.-P. Passérieux, Ph. Rebourgeard, F. Rondeaux, J. Poinsignon, Y. Sacquin, J.-P. Schuller, A. Tabary, D. Vignaud, D. Vilanova, U. Camerini, R. March: NESTOR Proposal 1995, Dept. of Physics, University of Athens (1995).

Andres, E., P. Askebjer, S.W. Barwick, R. Bay, L. Bergström, A. Biron, J. Booth, A. Bouchta, S. Carius, M. Carlson, D. Cowen, E. Dalberg, T. DeYoung, P. Ekström, B. Erlandson , A. Goobar, L. Gray, A. Hallgren, F. Halzen, R. Hardtke, S. Hart, Y. He, H. Heukenkamp, G. Hill, P.0. Hulth, S. Hundertmark, J. Jacobsen, A. Jones, V. Kandhadai, A. Karle, B. Koci, P. Lindahl, I. Liubarsky, M. Leuthold, D.M. Lowder, P. Marciniewski, T. Mikolajski, T. Miller, P. Miocinovic, P. Mock, R. Morse, P. Niessen, C. Pérez de los Heros, R. Porrata, D. Potter, P.B. Price, G. Przybylski, A. Richards, S. Richter, P. Romenesko, H. Rubinstein, E. Schneider, T. Schmidt, R. Schwarz, M. Solarz, G.M. Spiczak, C. Spiering, 0. Streicher, Q Sun, L. Thollander, T. Thon, S. Tilav, C. Walck, C. Wiebusch, R. Wischnewski, K. Woschnagg, and G. Yodh: Astropart. Phys., 13, p. 1 (2000).

Askebjer, P., S.W. Barwick, L. Bergström, A. Bouchat, S. Carius, A. Coulthard, K. Engel, B. Erlandsson, A. Goobar, L. Gray, A. Hallgren, F. Halzen, P.O. Hulth, J. Jacobson, S. Johansson, V. Kandhadai, I. Liubarsky, D. Lowder, T. Miller, P.C. Mock, R. Morse, R. Porrata, P.B. Price, A. Richards, H.

Rubinstein, E. Schneider, Q. Sun, S. Tilav, C. Walck, and G. Yodh: Science, 267, p. 1147 (1995).

Babson, J., B. Barish, R. Becker-Szendy, H. Bradner, R. Cady, J. Clem, S.T. Dye, J. Gaidos, P. Gorham, P.K.F. Grieder, M. Jaworski, T. Kitamura, W. Kropp, J.G. Learned, S. Matsuno, R. March, K. Mitsui, D. O'Connor, Y. Ohashi, A. Okada, V. Peterson, L. Price, F. Reines, A. Roberts, C. Roos, H. Sobel, V.J. Stenger, M. Webster, and C. Wilson: Phys. Rev., D 42, p. 3613 (1990).

Barwick, S.W., F. Halzen, D.M. Lowder, J. Lynch, T. Miller, R. Morse, P.B. Price, A. Westphal, and G.B. Yodh: PICRC, 4, p. 658 (1991).

Belolaptikov, I.A., L.B. Bezrukov, B.A. Borisovets, E.V. Bugaev, G.V. Domogatsky, L.A. Donskich, A.A. Doroshenko, M.D. Galperin, Zh.A.M. Djilkibaev, A.M. Klabukov, S.I. Klimushin, O.J. Lanin, B.K. Lubsandorzhiev, A.I. Panfilov, I.A. Sokalsky, I.I. Trofimenko, N.M. Budnev, A.G. Chensky, V.I. Dobrynin, O.A. Gress, A.P. Koshechkin, J.B. Lanin, G.A. Litunenko, A.V. Lopin, V.A. Naumov, M.I. Nemchenko, Yu.V. Parfenov, A.A. Pavlov, O.P. Pokalev, V.A. Primin, A.A. Shestakov, A.A. Sumanov, V.A. Tarashansky, V.L. Zurbanov, A.V. Golikov, E.S. Zaslavskaya, V.B. Kabikov, L.A. Kuzmichov, E.A. Osipova, G.N. Dudkin, V.Yu. Egorov, M.N. Gushtan, A.A. Lukanin, A.M. Ovcharov,V.M. Padalko, A.H. Padusenko, J. Krabi, T. Mikolajski, Ch. Spiering, R. Wischnewski, L. Jenek, D. Kiss, L. Tanko, Yu.S. Kusner, V.A. Poleschuk, and P.P. Sherstyankin: Nucl. Phys., B (Proc. Suppl.) 19, p. 388 (1991).

Belolaptikov, I.A., L.B. Bezrukov, B.A. Borisovets, N.M. Budnev, A. G. Chensky, Zh.A.M. Djilkibaev, V.I. Dobrynin, G.V. Domogatsky, L.A. Donskych, A.A. Doroshenko, S.V. Fialkovsky, O.A. Gress, A.V. Golikov, R. Heller, H. Heukenkamp, V.B. Kabikov, A.M. Klabukov, A.I. Klimov, S.I. Klimushin, T.A. Konopleva, A.P. Koshechkin, J. Krabi, V.F. Kulepov, L.A. Kuzmichov, O.J. Lanin, B.K. Lubsandorzhiev, M.B. Milenin, T. Mikolajski, R.R. Mirgazov, S.A. Nikiforov, N.V. Ogievietzky, E.A. Osipova, A.H. Padusenko, A.I. Panfilov, Yu.V. Parfenov, A.A. Pavlov, D.P. Petuchov, K.A. Pocheikin, P.G. Pochil, O.P. Pokalev, M.I. Rosanov, A.V. Rzhetshizki, V.Yu. Rubzov, S.I. Sinegovsky, I.A. Sokalsky, Ch. Spiering, O. Streicher, V.A. Tarashansky, T. Thon, I.I. Trofimenko, R. Wischnewski, and V.L. Zurbanov: Proc. 3nd. NESTOR Workshop, October 19 - 21, 1993, Pylos, Greece, (L.K. Resvanis, ed.), University of Athens, Greece, p. 213 (1993a).

Belolaptikov, I.A., L.B. Bezrukov, B.A. Borisovets, N.M. Budnev, E.V. Bugaev, A. G. Chensky, Zh.A.M. Djilkibaev, V.I. Dobrynin, G.V. Domogatsky, L.A. Donskych, A.A. Doroshenko, G.N. Dudkin, V.Yu. Egorov, S.V. Fi-

alkovsky, A.V. Golikov, O.A. Gress, M.N. Gushtan, R. Heller, H. Heukenkamp, V.B. Kabikov, A.M. Klabukov, A.I. Klimov, S.I. Klimushin, T.A. Konopleva, A.P. Koshechkin, J. Krabi, V.F. Kulepov, L.A. Kuzmichov, O.J. Lanin, A.L. Lopin, B.K. Lubsandorzhiev, M.B. Milenin, T. Mikolajski, R.R. Mirgazov, M.I. Nemchenko, S.A. Nikiforov, N.V. Ogievietzky, E.A. Osipova, A.H. Padusenko, A.I. Panfilov, Yu.V. Parfenov, A.A. Pavlov, K.A. Pocheikin, P.G. Pochil, O.P. Pokalev, M.I. Rosanov, A.V. Rzhetshizki, V.Yu. Rubzov, S.I. Sinegovsky, I.A. Sokalsky, Ch. Spiering, A.A. Sumanov, V.A. Tarashansky, T. Thon, I.I. Trofimenko, R. Wischnewski, and V.L. Zurbanov: PICRC, 4, p. 573 (1993b).

Belolaptikov, I.A., L.B. Bezrukov, B.A. Borisovets, N.M. Budnev, A.G. Chensky, Zh.A.M. Djilkibaev, V.I. Dobrynin, G.V. Domogatsky, L.A. Donskych, A.A. Doroshenko, S.V. Fialkovsky, A.V. Golikov, O.A. Gress, R. Heller, H. Heukenkamp, V.B. Kabikov, A.M. Klabukov, A.I. Klimov, S.I. Klimushin, T.A. Konopleva, A.P. Koshechkin, J. Krabi, V.F. Kulepov, L.A. Kuzmichov, O.J. Lanin, B.K. Lubsandorzhiev, M.B. Milenin, T. Mikolajski, R.R. Mirgazov, N.I. Moseiko, S.A. Nikiforov, N.V. Ogievietzky, E.A. Osipova, A.H. Padusenko, A.I. Panfilov, Yu.V. Parfenov, A.A. Pavlov, D.P. Petuchov, K.A. Pocheikin, P.G. Pochil, O.P. Pokalev, M.I. Rosanov, V.Yu. Rubzov, A.V. Rzhetshizki, S.I. Sinegovsky, I.A. Sokalsky, Ch. Spiering, O. Streicher, V.A. Tarashansky, T. Thon, I.I. Trofimenko, R. Wischnewski: Nucl. Phys., B (Proc. Suppl.), 35, p. 290 (1994).

Belolaptikov, I.A., L.B. Bezrukov, B.A. Borisovets, N.M. Budnev, A. G. Chensky, I.A. Danilchenko, Zh.A.M. Djilkibaev, V.I. Dobrynin, G.V. Domogatsky, L.A. Donskych, A.A. Doroshenko, S.V. Fialkovsky, A.A. Garus, O.A. Gress, T.A. Gress, H. Heukenkamp, A. Karle, A.M. Klabukov, A.I. Klimov, S.I. Klimushin, A.P. Koshechkin, J. Krabi, V.F. Kulepov, L.A. Kuzmichov, B.K. Lubsandorzhiev, M.B. Milenin, T. Mikolajski, R.R. Mirgazov, N.I. Moseiko, S.A. Nikiforov, E.A. Osipova, A.I. Panfilov, Yu.V. Parfenov, A.A. Pavlov, D.P. Petuchov, K.A. Pocheikin, P.G. Pochil, P.A. Pokolev, M.I. Rosanov, V.Yu. Rubzov, S.I. Sinegovsky, I.A. Sokalsky, Ch. Spiering, O. Streicher, V.A. Tarashansky, T. Thon, I.I. Trofimenko, Ch. Wiebusch, R. Wischnewski: PICRC 1, p. 536 (1995a).

Belolaptikov, I.A., L.B. Bezrukov, B.A. Borisovets, N.M. Budnev, A. G. Chensky, I.A. Danilchenko, Zh.A.M. Djilkibaev, V.I. Dobrynin, G.V. Domogatsky, L.A. Donskych, A.A. Doroshenko, S.V. Fialkovsky, O.N. Gaponenko, A.A. Garus, O.A. Gress, T.A. Gress, H. Heukenkamp, A.M. Klabukov, A.I. Klimov, S.I. Klimushin, A.P. Koshechkin, J. Krabi, V.F. Kulepov, L.A. Kuzmichov, B.K. Lubsandorzhiev, N.I. Maseiko, M.B. Milenin, T. Mikolajski, R.R. Mirgazov, N.I. Moseiko, S.A. Nikiforov, P. Mohrmann, E.A.

Osipova, A.I. Panfilov, Yu.V. Parfenov, A.A. Pavlov, D.P. Petuchov, K.A. Pocheikin, P.G. Pochil, P.A. Pokolev, M.I. Rosanov, V.Yu. Rubzov, S.I. Sinegovsky, I.A. Sokalsky, Ch. Spiering, O. Streicher, V.A. Tarashansky, T. Thon, I.I. Trofimenko, R. Wischnewski: Nucl. Phys., B (Proc. Suppl.) 43, p. 241 (1995b).

Belolaptikov, I.A., L.B. Bezrukov, B.A. Borisovets, N.M. Budnev, E.V. Bugaev, A.G. Chensk, I.A. Danilchenko, J.-A.M. Djilkibaev, V.I. Dobrynin, G.V. Domogatsky, L.A. Donskych, A.A. Doroshenko , G.N. Dudkin, V.Yu. Egorov, S.V. Fialkovsky, A.A. Garus, A. Gaponenko, A.V. Golikov, 0.A. Gress, T.A. Gress, M.N. Gushtan, R. Heller, V.B. Kabikov, H. Heukenkamp, A. Karle, A.M. Klabukov, A.I. Klimov, S.I. Klimushin, A.P. Koshechkin, J. Krabi, V.F. Kulepov, L.A. Kuzmichov, 0.Yu. Lanin, A.L. Lopin, B.K. Lubsandorzhiev, M.B. Milenin, T. Mikolajski, R.R. Mirgazov, A.V. Moroz, N.I. Moseiko, M.N. Nemchenko, S.A. Nikiforov, N.V. Ogievetsky, E.A. Osipova, A.N. Padusenko, A.I. Panfilov, Yu.V. Parfenov, A.A. Pavlov, D.P. Petukhov, K.A. Pocheikin, P.G. Pokhil, P.A. Pokolev, M.I. Rosanov, V.Yu. Rubzov, A.V. Rzhestshitski, S.I. Sinegovsk, I.A. Sokalski, Ch. Spiering, 0. Streicher, A.A. Sumanov, L. Tanko, T. Thon, B.A. Tarashanski, I.I. Trofimenko, Ch. Wiebusch, R. Wischnewski, and V.L. Zurbanov: Astropart. Phys., 7, p. 263 (1997).

Bugaev, Edgar V., Vadim A. Naumov, Sergey I. Sinegovsky, Akeo Misaki, Nobusuke Takahashi, and Elena S. Zaslavskaya: Proceedings of Nestor Workshop, p. 268 (1993).

Bugaev, Edgar V., Vadim A. Naumov, Sergey I. Sinegovsky, Akeo Misaki, Nobusuke Takahashi, and Elena S. Zaslavskaya: Università degli Studi di Firenze, Dipartimento di Fisica and Instituto Nationale di Fisica Nucleare Sezione di Firenza, Preprint DFF 204/4/1994 (1994).

Davitaev, L.N., V.M. Fyodorov, Yu.A. Trubkin, Yu.N. Vavilov: Acta Phys. Acad. Sci. Hung., 29, Suppl. 4, p. 53 (1970).

Fyodorov, V.M., V.P. Pustovetov, Yu.A. Trubkin, and A.V. Kirilenkov: PICRC, 8, p. 39 (1985).

Fyodorov, V.M.: Nucl. Instr. Methods,A 248, p. 221 (1986).

Halzen, Francis, and John G. Learned: Proc. International Symposium on Very High Energy Cosmic Ray Interactions, Lodz, Poland (M. Giler, ed.), Vol. 1 (contributed papers), p. 371 (1988).

Higashi, S., T. Kitamura, S. Miyamoto, Y. Mishima, T. Takahashi, and Y. Watase: Nuovo Cimento, 43A, p. 334 (1966).

Learned, J.G.L., ed.: DUMAND 1979 Summer Workshops at Khabarovsk

and Lake Baikal, published by the University of Hawaii, Honolulu (1980).

Lowder, D.M., T. Miller, P.B. Price, A. Westphal, S.W. Barwick, F. Halzen, and R. Morse: Nature, 353, p. 331 (1991).

Markov, M.A.: in Proceedings of the 1960 Annual International Conference on High Energy Physics , Rochester, ed. E.C.G. Sudarshan, J.H. Tinlot, and A. Melissinos (Uni. of Rochester/Interscience, Rochester, N.Y.), p. 578 (1960).

Markov, M.A., and I.M. Zheleznykh: Nucl. Phys., 27, p. 385 (1961).

Miyake, S.: J. Phys. Soc. Japan, 18, p. 1093 (1963).

Percy, J.C., and I.W. Rogers: PICRC 6, p. 99 (1977).

Resvanis, L.K., ed.: Proc. 2nd NESTOR Workshop, Pylos, Greece, published by the University of Athens (1992a).

Resvanis, L.K.: Proc. 2nd NESTOR Workshop, Pylos, Greece, (L.K. Resvanis, ed.), University of Athens, p. 1 (1992b).

Resvanis, L.K., ed.: Proc. 3rd NESTOR Workshop, Pylos, Greece, published by the University of Athens, (1993).

Resvanis, L.K.: Nucl. Phys., B (Proc. Suppl.) 48, p. 425 (1996).

Roberts, A., ed.: Proc. 1978 DUMAND Summer Workshop, Volume 1, Array Studies (1979a) published by Scripps Institution of Oceanography, Code A-010, La Jolla, CA 92093 (1979a).

Roberts, A., ed.: Proc. 1978 DUMAND Summer Workshop, Volume 2, UHE Interactions, Neutrino Astronomy (1979b), published by Scripps Institution of Oceanography, Code A-010, La Jolla, CA 92093 (1979b).

Roberts, A.: Rev. Mod. Phys., 64, p. 259 (1992).

Rogers, I.W., M. Tristam, and G. Le Dallic: PICRC 10, p. 313 (1981).

Rogers, I.W., and M. Tristam: PICRC, 7, p. 32 (1983).

Rogers, I.W., and M. Tristam: J. Phys. G., 10, p. 983 (1984).

Stenger, V.J., ed.: DUMAND 80, Proc. 1980 International DUMAND Symposium, Volumes 1 and 2 (1981), published by the University of Hawaii, Honolulu (1981).

Thron, J.L., W.W.M. Allison, G.J. Alner, I. Ambats, D.S. Ayres, L.J. Balka, G.D. Barr, W.L. Barrett, D. Benjamin, P.M. Border, C.B. Brooks, J.H. Cobb, D.J.A. Cockerill, H. Courant, J.W. Dawson, D.M. Demuth, V.W. Edwards, B. Ewen, T.H. Fields, C. Garcia-Garcia, R.H. Giles, G.L. Giller, M.C. Goodman, R.N. Gray, S.J. Heilig, N. Hill, J.H. Hoftiezer, D.J. Jankowski, K.

Johns, T. Kafka, S.M.S. Kasahara, J. Kochocki, W. Leeson, P.J. Litchfield, N.P. Longley, F.V. Lopez, M.J. Lowe, W.A. Mann, M.L. Marshak, E.N. May, D. Maxam, L. McMaster, R.H. Milburn, W.H. Miller, C.P. Minor, A. Napier, W.P. Oliver, G.F. Pearce, D.H. Perkins, E.A. Peterson, L.E. Price, D.M. Roback, D.B. Rosen, K. Ruddick, B. Saitta, D.J. Schmid, J. Schlereth, J. Schneps, P.D. Shield, M.A. Shupe, N. Sundaralingam, M.A. Thomson, L.M. Tupper, G. Villaume, S.J. Werkema, N. West, and C.A. Woods, Soudan 2 Collaboration: Phys. Rev., D 46, p. 4846 (1992).

Vavilov, Yu.N., L.N. Davitaev, Yu.A. Trubkin, and V.M. Fyodorov: Izv. Akad. Nauk. SSSR, Ser. Fiz., 2, p. 1977 (1970); Bull. Acad. Sci. USSR, Phys. Ser. 34, p. 1759 (1970).

Vavilov, Yu.N., Yu.A. Trubkin, and V.M. Fyodorov: Sov. J. Nucl. Phys., 18, p. 434 (1974).

Wilkins, G., ed.: Proc. 1978 DUMAND Summer Workshop, Volumes 3, Oceanographic and Ocean Engineering Studies, published by Scripps Institution of Oceanography, Code A-010, La Jolla, CA 92093 (1979).

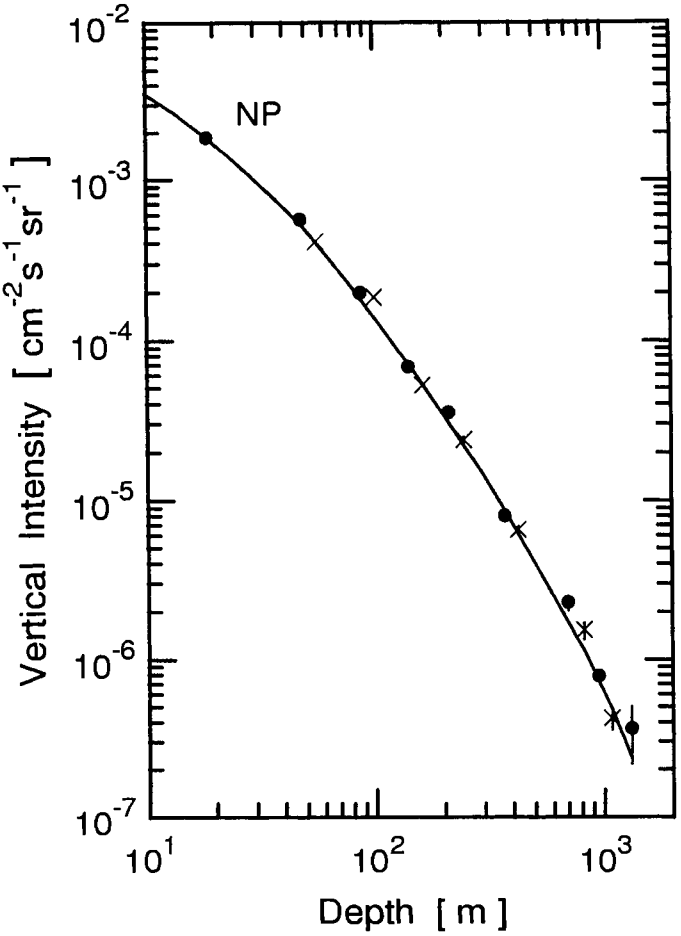

Figure 4.70: Observed muon intensities as a function of depth in sea water. Shown are data from vertical and inclined measurements. In the latter case depth corresponds to the slant depth. The solid line represents the Durham sea level muon spectrum converted to the underwater conditions (Higashi et al., 1966). NP is the normalizing point.

• vertical measurements | × oblique measurements

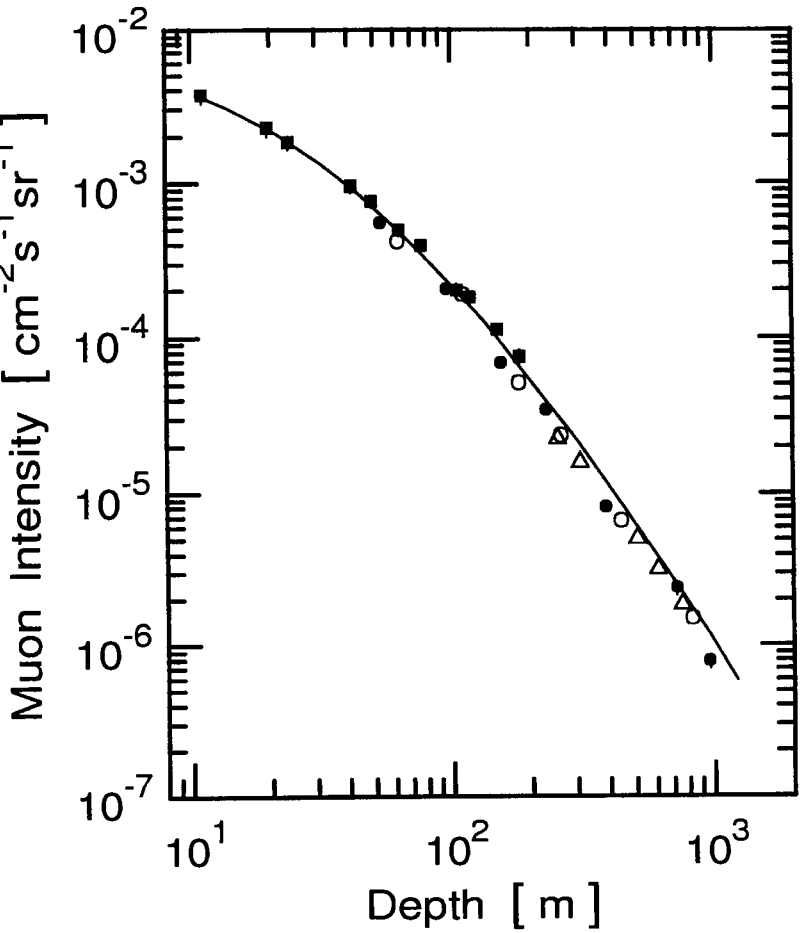

Figure 4.71: Compilation of early vertical and oblique muon intensities versus depth in fresh and sea water from different experiments. For the oblique data depth refers to the slant depth. The solid curve is from a calculation by Bugaev et al. (1993, 1994).

■ Rogers and Tristam (1984) | △ Davitaev et al. (1970)
• Higashi et al. (1966), vertical | ○ Higashi et al. (1966), oblique

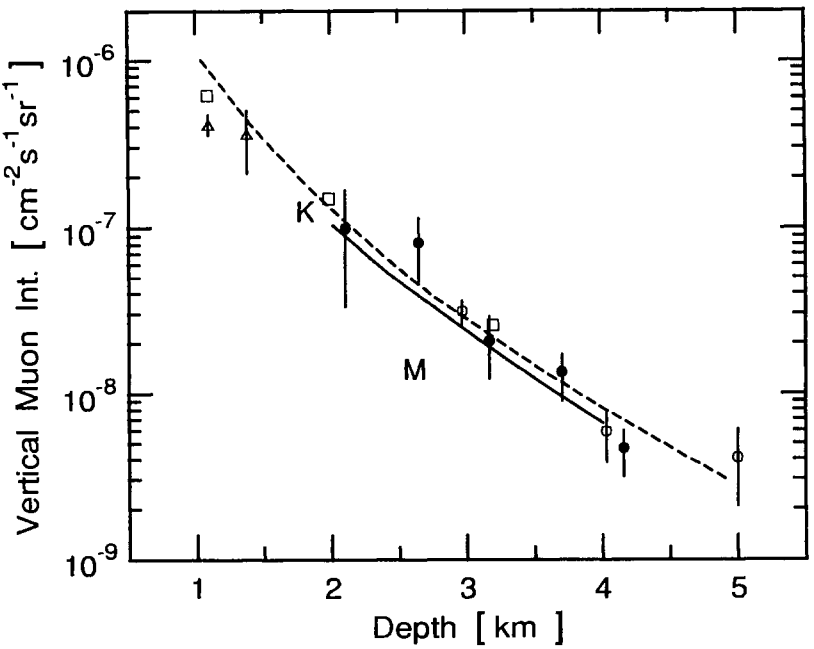

Figure 4.72: Comparison of different experimental vertical underwater muon intensities versus depth below 1000 m. The errors indicated are both systematic and statistical. The solid curve (M) is the distribution predicted by the Miyake formula (Miyake, 1963), the dashed curve (K) shows result of inclined data from other experiments converted to vertical intensity using a correction of Kobayakawa (after Babson et al., 1990).

• Babson et al. (1990)	△ Higashi et al. (1966)
□ Vavilov et al. (1970)	o Fyodorov et al. (1985)

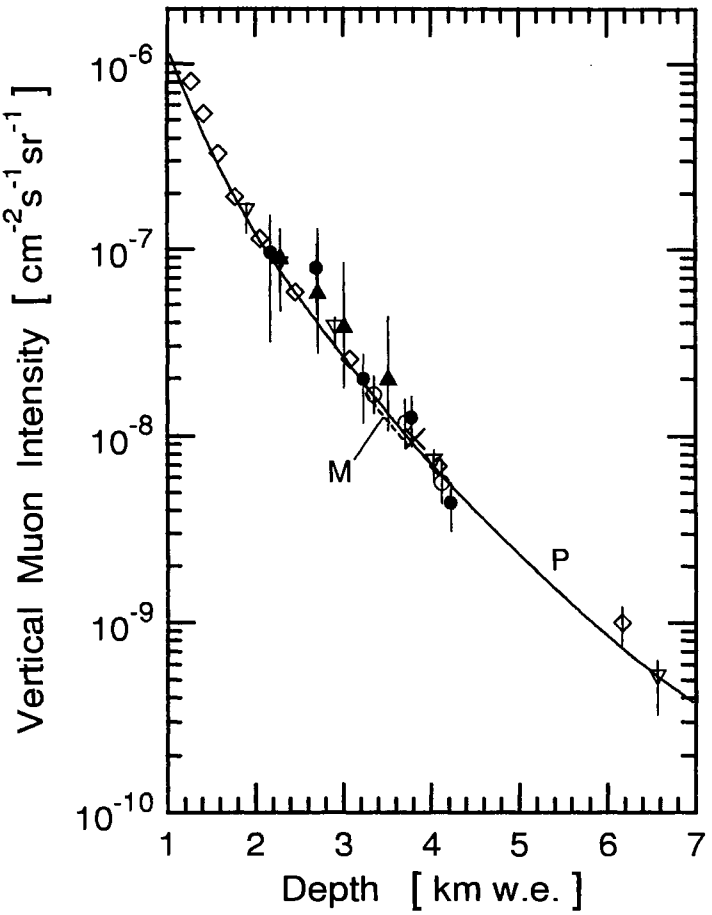

Figure 4.73: Summary of vertical muon intensity measurements versus depth obtained with different installations. The three sets of NESTOR data apply to slightly different locations at the Pylos, Greece, site in the Mediterranean (Anassontzis et al., 1993) and were recorded at different dates (▲ Oct. 1989, o July 1991, × Nov. 1992). The solid curve labeled P is from the parametrization of Thron et al. (1992), the short dashed curve represents a section obtained with the Miyake formula, adapted to sea water (Miyake, 1963). The remaining data are as listed below.

◇ Belolaptikov et al. (1997) | • Babson et al. (1990)
▽ Andres et al. (2000)

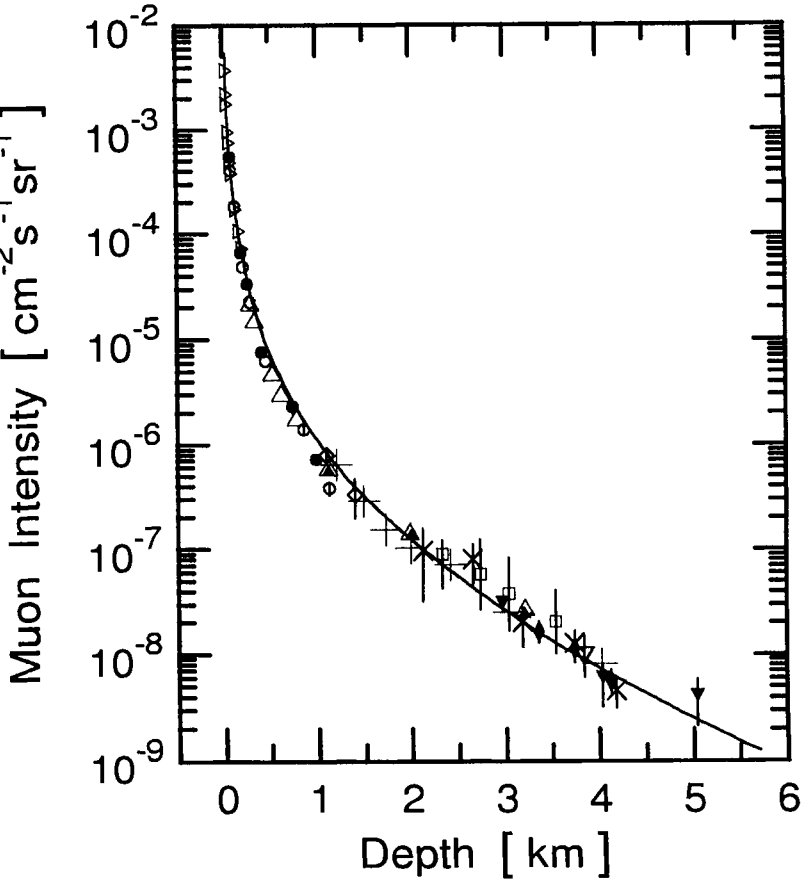

Figure 4.74: Compilation of vertical muon intensities versus depth in water from different experiments. Note that the data by Belolaptikov et al. (1995a and 1995b) were obtained from inclined measurements that were converted to vertical intensities. The solid curve is from a calculation by Bugaev et al. (1993, 1994).

▷ Rogers and Tristam (1984)	△ Davitaev et al. (1970)
• Higashi et al. (1966) vertical	○ Higashi et al. (1966) oblique
▲ Vavilov et al. (1974)	▼ Fyodorov et al. (1985, 1986)
× Babson et al. (1990)	▽ Resvanis (1992b)
□ Anassontzis et al. (1993)	◆ Anassontzis et al. (1993)
◇ Belolaptikov et al. (1993b)	+ Belolaptikov et al. (1995a, b)

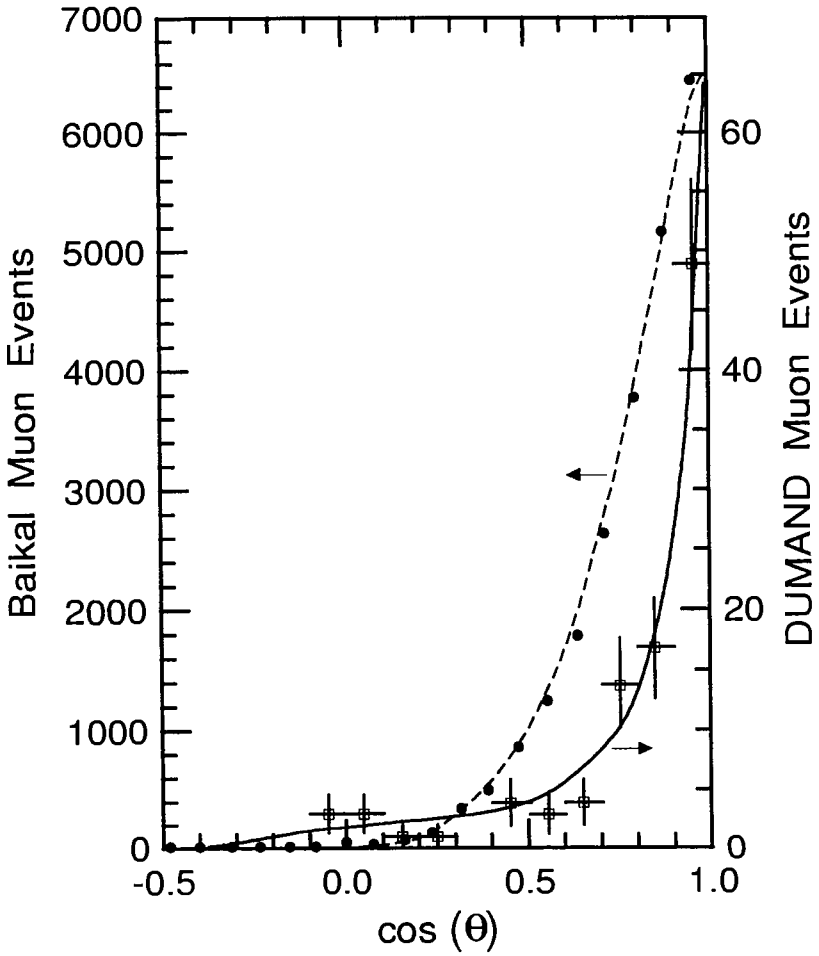

Figure 4.75: Zenith angle distributions of reconstructed muon tracks at great depth in water. Shown are the results from measurements made with the Lake Baikal array NT-36 (•, dashed curve), located at a nominal depth of 1170 m (Belolaptikov et al.,1993a), and the DUMAND Short Prototype String in the Pacific at a nominal depth of 4000 m (□, solid curve) (Babson et al., 1990). The vertical error bars of the DUMAND data are statistical. The dashed (Baikal) and solid (DUMAND) curves are from Monte Carlo simulations.

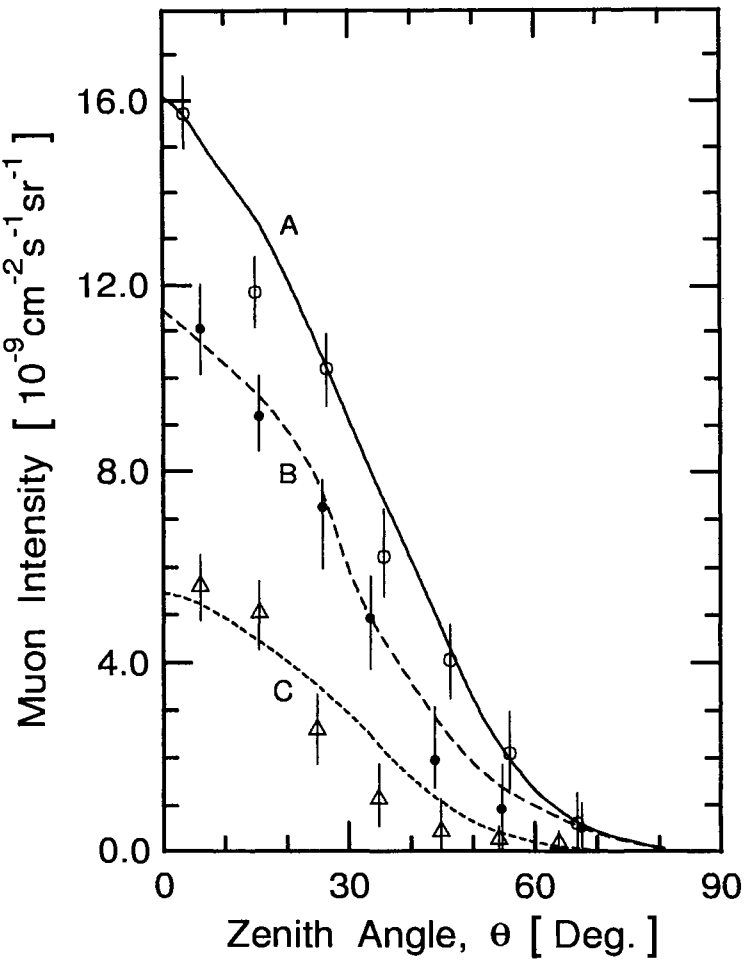

Figure 4.76: Zenith angle, θ, distribution of muons in the Mediterranean measured by the NESTOR Collaboration with six prototype optical detector modules at the NESTOR site, off the coast of Pylos, Greece (Anassontzis et al., 1995). Shown are the actually measured intensities at depths as indicate below and fits to the data of the form $I(\theta) = I_0 \cdot cos^m(\theta)$.

Symbol	Depth [m]	m	Curve
○	3338	4.0 ± 0.8	A
●	3697	4.5 ± 0.8	B
△	4108	4.8 ± 0.8	C

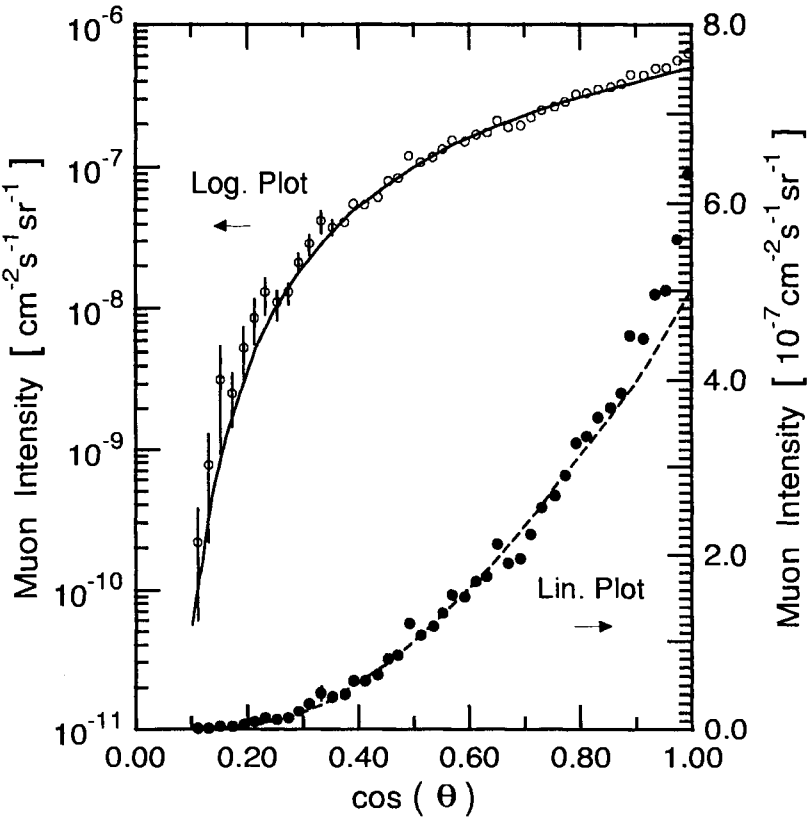

Figure 4.77: Zenith angle distribution of muons in Lake Baikal. Shown is the logarithmic (left) and linear (right) representation of the absolute intensity versus $\cos(\theta)$ measured at a depth of 1170 m. The solid line is a calculated distribution for stochastic energy losses (Belolaptikov et al., 1995a and 1995b).

4.5 Neutrinos, General and Atmospheric

4.5.1 Introduction

The presently accepted view is that there exist three flavors of neutrinos, namely the electron neutrino, ν_e, the muon neutrino, ν_μ, and the tau neutrino, ν_τ, and the corresponding antineutrinos, $\overline{\nu}_e$, $\overline{\nu}_\mu$ and $\overline{\nu}_\tau$, respectively.

Besides the particle physics aspects we can also classify neutrinos according to their origin as *terrestrial* or *extraterrestrial* neutrinos. The former can be the result of cosmic ray interactions in the atmosphere producing so-called *atmospheric neutrinos*, or they can be of *radioactive* origin from β-decay of unstable isotopes. When discussing extraterrestrial neutrinos we usually distinguish between neutrinos of *solar* and those of *astrophysical* origin.

Terrestrial Neutrinos of Radioactive Origin

Terrestrial neutrinos from β-decay originate from radioactive isotopes in the Earth, mostly from the Thorium-, Neptunium-, Uranium- and Actinium series of naturally radioactive heavy elements and their daughter products, and are electron antineutrinos. It is estimated that this flux amounts to about $7 \cdot 10^6$ cm^{-2}s^{-1}, assuming an effective thickness of the Earth's crust of 15 km (Young, 1973). Of this flux only about 10^5 cm^{-2}s^{-1} have energies above the threshold for detection by the reaction

$$\overline{\nu}_e(> 1.8\text{MeV}) + p \rightarrow n + e^+ \tag{4.59}$$

In addition cosmic ray induced radioactivity in the atmosphere and the top layer of the Earth's crust contribute through beta decay to the terrestrial neutrino and antineutrino flux.

But also the fission processes that take place in *nuclear reactors* and their by-products make locally significant contributions to the antineutrino flux. Neutrinos from β-decay are electron neutrinos and antineutrinos and are of comparatively low energy, mostly in the keV to MeV range.

Cosmic Ray Induced Atmospheric Neutrinos

Neutrinos from interactions of primary and secondary cosmic rays in the atmosphere can be of any kind. It is the specific interaction process that determines the flavor. Atmospheric neutrinos cover a wide range of energies similar to that of the cosmic radiation.

Secondary cosmic ray hadrons that enter the Earth's crust are predominantly of low energy. They dissipate most of their remaining energy in hadronic collisions and, if they carry electric charged, through ionization losses over relatively short path lengths because of the high density of the medium in which they propagate. The latter applies to muons as well. Therefore unstable particles such as pions, kaons and muons decay nearly at rest, producing only low energy muon and electron neutrinos and antineutrinos.

Solar Neutrinos

Solar neutrinos are the product of the nuclear fusion processes that take place in the Sun and are electron neutrinos of low energy (< 20MeV). Various processes contribute to the flux of solar neutrinos, some contribute line spectra, others continuum spectra. Because of the significance of the Sun and the mechanisms that take place within it, we have devoted a special section in Chapter 6 (Section 6.6) to the topic of solar neutrinos.

Astrophysical Neutrinos

Neutrinos of astrophysical origin span the full range of the spectrum, from the lowest energy relic big bang neutrinos to the highest energy cosmic ray induced neutrinos resulting from interactions of the cosmic radiation with the interstellar and intergalactic medium, and the photon field. All flavors of neutrinos and their antiparticles can occur in this category, depending on the source process from which they emerge.

Theoretical considerations have been extended to include even higher energy neutrinos that could be produced in the decay of supermassive GUT-(Grand Unified Theory) scale particles resulting from the decay of cosmic strings and topological defects. A separate section is devoted to astrophysical neutrinos, including the recorded neutrino data from the supernova SN-1987A in Chapter 5, Section 5.5.

4.5.2 Experimental Aspects and Detection Methods

General Comments

Because of the small cross sections of neutrinos ($\sim 10^{-38}$ cm^2 at 1 GeV, see below for details) very large detectors (or high accelerator beam intensities) are needed to obtain a reasonable rate of neutrino reactions, and background is a major issue. Different experimental methods and techniques are employed for the detection of neutrinos, depending on the flavor and the energy

regime under investigation.

For the detection of the very low energy solar neutrinos (ν_e) radiochemical methods as well as large-scale liquid scintillation detectors are being used; for the more energetic solar neutrinos the water Cherenkov technique is employed. The advantage of the two latter methods over the radiochemical method is that the data are accessible in real time and supply also directional information, which is not available from the radiochemical method.

For the detection of atmospheric neutrinos large water Cherenkov as well as scintillation detectors, a variety of purely electronic tracking calorimeters and hybrid detectors have been used successfully. The different experimental techniques are briefly discussed in the appropriate sections mentioned above.

Until very recently all solar and cosmic ray neutrino experiments have been carried out deep underground, in order to achieve adequate shielding of the detectors from the unwanted components of the cosmic radiation, to reduce background. However, the extremely low intensity predicted for ultrahigh energy astrophysical neutrinos require much larger detectors than those used for low energy solar and even moderately energetic atmospheric neutrino studies to achieve a reasonable event rate.

Moreover, large detectors permit a much better reconstruction of very energetic events that have long trajectories and background rejection is greatly improved. Detector volumes on the order of 1 km^3 are needed for this task, to pursue neutrino astronomy successfully. At the same time the relatively high counting rate of a huge detector would enable us to carry out neutrino tomography of the Earth and thus open up entirely new possibilities for geology and planetology (Bosetti et al., 1989; Crawford et al., 1995; Jain et al., 1999).

The construction of suitable cavities deep underground can no longer be considered for practical as well as economic reasons. The ideal solution to this problem is to use giant optical Cherenkov detector matrices at great depth (several kilometers) in the ocean or the polar ice caps, to detect and analyze the neutrino induced reactions.

These media (water and ice) serve at the same time as targets for the neutrino reactions that take place within the detector volume or its surroundings and as Cherenkov radiators to observe and reconstruct the charged particle trajectories of the events, to identify the neutrino signatures (see Section 4.4). In addition, the overburden acts as shield.

Up to date no energy spectra of astrophysical (cosmic) neutrinos have been measured. The only non-solar extraterrestrial neutrino signature so far

identified was the neutrino burst from the supernova SN-1987A (see Chapter 5, Section 5.5 for details and references). However, the flux of the low energy solar and atmospheric components have been well explored, the ratio R of the two common neutrino flavors $(\nu_\mu+\overline{\nu}_\mu)/(\nu_e+\overline{\nu}_e)$ of the atmospheric component has been measured, and very rudimentary data of the solar and the low energy portion of the atmospheric neutrino spectra have been determined.

Remaining Problems and Puzzles

Several puzzles such as the discrepancies between the predicted and measured neutrino flux from the Sun, known as the *solar neutrino problem* (SNP) (Bahcall, 1999; Smirnov, 1999) and the disparity between the predicted and measured ratio of electron to muon neutrinos of the atmospheric neutrino flux, commonly known as the *atmospheric neutrino anomaly* or the *ratio-of-ratio problem*, suggest that neutrinos may in fact be subject to oscillations (Beier et al., 1992; Perkins, 1993). It is beyond the scope of this book to elaborate on these problems. However, we will briefly summarize the results from atmospheric neutrino measurements that are indicative for the existence of neutrino oscillations and the difficulties that are involved in the interpretation of the data, including the problem of the up/down flux symmetry, in this section.

4.5.3 Atmospheric Neutrino Production, Properties

Production Channels

So-called atmospheric neutrinos are the decay products of unstable particles, such as pions, kaons, muons and charmed particles that are produced in collisions of primary and secondary cosmic rays with atmospheric target nuclei such as N, O, Ar, etc.. In these collisions neutrinos of all flavors and their antiparticles are produced. However, tau neutrino (antineutrino) production via the decays of heavy charmed mesons such as the charmed D- and F-mesons must be considered only at laboratory energies on the order of $\sim$1 TeV/nucleon and more. The dominating production process of atmospheric neutrinos and antineutrinos in the sub-GeV to multi-GeV energy range is the $\pi \rightarrow \mu \rightarrow e$ decay chain, i.e.,

$$\pi^+ \rightarrow \mu^+ + \nu_\mu \tag{4.60}$$

$$\mu^+ \rightarrow e^+ + \nu_e + \overline{\nu}_\mu \tag{4.61}$$

and

Table 4.28: Neutrino Reactions in Heavy and Common Water (Bemporad, 1996)

Reaction			Q-Value MeV
a)	CC	$\nu_e + d \rightarrow p + p + e^-$	-1.44
b)	CC	$\overline{\nu}_e + d \rightarrow n + n + e^+$	-4.03
c)	NC	$\nu_x + d \rightarrow p + n + \nu_x$	-2.2
d)	CC	$\overline{\nu}_e + p \rightarrow n + e^+$	-1.8
e)	ES	$\nu_x + e \rightarrow \nu_x + e$	0

ν_x stands for $\nu_e, \overline{\nu}_e, \nu_\mu, \overline{\nu}_\mu, \nu_\tau$, and $\overline{\nu}_\tau$.

$$\pi^- \rightarrow \mu^- + \overline{\nu}_\mu \tag{4.62}$$

$$\mu^- \rightarrow e^- + \overline{\nu}_e + \nu_\mu \tag{4.63}$$

Charged kaons ($K^\pm$) contribution to the same decay channel but are much less abundant at low energies. At much higher energies the decay of

$$K_L^0 \rightarrow \pi^\pm + e^\pm + \overset{(-)}{\nu}_e \tag{4.64}$$

with a branching fraction of 38.7% is the chief contributor to the atmospheric ν_e and $\overline{\nu}_e$ flux.

Neutrino Cross Sections

Neutrinos can undergo charged current (CC), neutral current (NC) or elastic scattering (ES) reactions. The different reaction types that can occur in water and heavy water are summarized in Table 4.28, where ν_x stands for any kind of neutrino or antineutrino. Disregarding the large Cherenkov detector matrices in water or ice, water and heavy water are the combined target and detector materials of Super-Kamiokande (Koshiba, 1992), the largest underground neutrino experiment in operation today, and of the Sudbury Neutrino Observatory, SNO, now beginning operation (McDonald, 1996 and 1999), respectively.

Table 4.29: Cross Sections for Neutrino Elastic Scattering.
(Bemporad, 1996)

Reaction	Cross Section
$\nu_e + e^-$	$\sigma = 0.92 \cdot 10^{-43} \left[\frac{E_\nu}{10MeV}\right] \ cm^2$
$\overline{\nu}_e + e^-$	$\sigma = 0.39 \cdot 10^{-43} \left[\frac{E_{\overline{\nu}}}{10MeV}\right] \ cm^2$
$\nu_\mu + e^-$	$\sigma = 0.16 \cdot 10^{-43} \left[\frac{E_\nu}{10MeV}\right] \ cm^2$
$\overline{\nu}_\mu + e^-$	$\sigma = 0.13 \cdot 10^{-43} \left[\frac{E_{\overline{\nu}}}{10MeV}\right] \ cm^2$

At very low energies the neutrino cross section, σ_ν, rises logarithmically. In the MeV region it is on the order of 10^{-44} cm^2 and rises linearly with energy. The cross sections for elastic scattering of neutrinos of the two common flavors and their antiparticles are given in Table 4.29.

For inelastic processes above about 1 GeV where the cross section is on the order of 10^{-38} cm^2 it rises linearly. In this energy range we can write

$$\sigma_\nu \simeq 10^{-38} \cdot E_\nu \ \ [\mathrm{cm}^2\,\mathrm{GeV}^{-1}\,\mathrm{nucleon}^{-1}] \ , \tag{4.65}$$

with E in GeV. Above the W and Z intermediate boson thresholds the cross section saturates. For antineutrinos the cross section is approximately $\frac{1}{3}$ of that of the neutrinos. Theoretical and experimental cross sections for charged current reactions of muon neutrinos and antineutrinos are illustrated in Figs. 4.78 and 4.79 (Hikasa et al., 1992; Frati et al., 1993).

Neutrino Flavor Ratio

For neutrino energies $\leq$1 GeV a *naive* calculation of the relative number of each neutrino type based on the decay channels listed above and in the absence of neutrino oscillations leads to the predictions that the ratio

$$\frac{N_{\nu_\mu} + N_{\overline{\nu}_\mu}}{N_{\nu_e} + N_{\overline{\nu}_e}} \approx 2 \tag{4.66}$$

and

$$\frac{N_{\nu_\mu}}{N_{\overline{\nu}_\mu}} \approx 1 \ , \tag{4.67}$$

where N_{ν_μ} ($N_{(\overline{\nu}_\mu)}$) and N_{ν_e} ($N_{\overline{\nu}_e}$) are the number of ν_μ ($\overline{\nu}_\mu$) and ν_e ($\overline{\nu}_e$), respectively. Because of the excess of protons over neutrons in the primary cosmic radiation there is an excess of ν_e over $\overline{\nu}_e$ in the atmospheric neutrino flux (Gaisser et al., 1987). Thus,

$$\frac{N_{\nu_e}}{N_{\overline{\nu_e}}} \approx \frac{\mu^+}{\mu^-} < 1 \tag{4.68}$$

The lepton-antilepton asymmetries increase with increasing energy and are non-trivial functions of the energy and the zenith angle. They also depend weakly on the atmospheric depth of observation (Lipari, 1993).

At higher energies muon neutrinos are expected to be the dominating kind because muons are less likely to decay and thus contribute less and less to the neutrino flux in the atmosphere with increasing energy, causing the ν_e ($\overline{\nu}_e$) fraction to diminish (see Chapter 1, Subsections 1.3.3) and 1.3.4.

Consequently, the ratio of eq. 4.66 decreases with increasing energy because muons are more and more likely to reach the ground before decaying. Comparison of the decay length to the energy-loss length of muons in the Earth leads to the conclusion that virtually all muons that reach the ground stop before decay (or capture) occurs. Therefore muons that reach the ground do not contribute to neutrinos with energy > 100 MeV, which makes their detection even for electron neutrinos via electron scattering difficult.

Up/Down Symmetry of Neutrino Flux and Geomagnetic Effects

Because of the very small but energy dependent cross sections of neutrino reactions given in eq. 4.65 and illustrated in Figs. 4.78 and 4.79 it is evident that neutrinos of energy <100 TeV remain essentially unaffected when traversing the Earth. Thus, the upward and downward fluxes should be symmetrical in the absence of neutrino oscillations, provided that the cosmic ray beam is fully isotropic.

Unfortunately the *east-west effect*, asymmetries and anomalies of the geomagnetic and magnetospheric fields and the highly complex and time dependent geomagnetic cutoff conditions disturb the isotropy of the cosmic radiation and therefore the up-down symmetry of the cosmic ray induced atmospheric neutrino flux (for details see Chapter 1, Section 1.8 and Chapter

6, Section 6.2). Careful consideration must therefore be given to these effects when carrying out neutrino flux calculations (Agrawal et al., 1996; Barr et al., 1989; Battistoni et al., 2000; Bugaev and Naumov, 1989; Cheung and Young, 1990; Gaisser and Stanev, 1995; Gaisser, 1999; Honda et al., 1990, 1995 and 1999; Lipari et al., 1998).

Muon Polarization and Neutrino Spectra

Muons produced in the cosmic radiation are polarized, μ^+ have on average negative helicity and μ^- positive helicity. For accurate calculations the *muon polarization* must be taken into account because the neutrino spectra produced in muon decay depend on the polarization (Dermer, 1986; Barr et al., 1988; Barr et al., 1989; Volkova, 1989; Lee and Koh, 1990; Lipari, 1993; Gaisser et al., 1995).

Neutrino Oscillations

If neutrinos have mass, it is possible that the weak interaction eigenstates $(\nu_e, \nu_\mu, \nu_\tau)$ are distinct from their mass eigenstates (m_1, m_2, m_3), and there could be vacuum oscillations of the type $\nu_\mu \leftrightarrow \nu_e$ in analogy to the $K^0, \overline{K^0}$ system (Pontecorvo, 1946 and 1967; Maki et al., 1962; Bilenky and Pontecorvo, 1978). Thus, if neutrino oscillations exist then the ratio $(\nu_e + \overline{\nu}_e)/(\nu_\mu + \overline{\nu}_\mu)$ of eq. 4.66 could be affected.

For a two-neutrino oscillation hypothesis, i.e., $\nu_\mu \leftrightarrow \nu_e$ or $\nu_\mu \leftrightarrow \nu_\tau$, the probability for a neutrino produced in a flavor state a to be observed in a flavor state b after traveling a distance L in vacuum is given by

$$P_{a\to b} \;=\; \sin^2(2\theta)\,\sin^2\left(\frac{1.27\Delta m^2[\mathrm{eV}^2]\cdot L[\mathrm{km}]}{E_\nu[\mathrm{GeV}]}\right) \quad , \tag{4.69}$$

where E_ν is the neutrino energy, θ is the mixing angle between the flavor eigenstates and the mass eigenstates, and $\Delta m^2 = |m_1^2 - m_2^2|$ is the mass squared difference. (In the recent experiment of Apollonio et al. (1998) no evidence was found for neutrino oscillations in the disappearance mode $\overline{\nu}_e \leftrightarrow \overline{\nu}_x$ for the parameter region given approximately by $\Delta m^2 > 0.9 \cdot 10^{-3}$ eV^2 for maximum mixing and $\sin^2(2\theta) > 0.18$.)

For detectors near the surface of the Earth, the neutrino flight distance, and therefore the oscillation probability, is a function of the zenith angle of the neutrino trajectory. Vertically downward-going neutrinos travel about 15 km while vertically upward-going neutrinos travel roughly 13,000 km before reaching the detector.

The bulk of the downward-going muons in an underground detector are originally high energy atmospheric muons resulting from cosmic ray interactions in the atmosphere that have survived and retained sufficient energy to enter or even penetrate the detector; they are not neutrino induced muons. Only a tiny fraction of the downward-going muons are the result of neutrino interactions. If the latter take place in the detector overburden they are undistinguishable from atmospheric muons. However, if the neutrino reaction occurs inside the detector the event can be recognized as being due to a neutrino reaction. On the other hand, upward going muons that are observed in underground detectors are due exclusively to neutrino reactions in the rock below the detector or within it.

Typical events have neutrino energies of about 10 GeV if they are fully contained in a large detector such as Superkamiokande (50.000 m^3 of water) and about 100 GeV for through-going muons (Kajita, 2000). The wide energy spectrum from a few hundred MeV to about 100 GeV that is available for such experiments and the range of flight distances just mentioned make measurements of atmospheric neutrinos sensitive to neutrino oscillations with a Δm^2 down to about 10^{-4} eV^2.

It was pointed out by Wolfenstein (1978 and 1979) that whereas muon neutrinos interact only via neutral currents with the electrons in a medium, electron neutrinos interact both by charged and neutral currents. This fact leads to incoherence over a characteristic distance L_0 (Wolfenstein length, $9.0 \cdot 10^6$ m in the Earth on average) between the two types of waves. Therefore oscillations are damped and destroyed and limit the sensitivity of underground experiments (Ramana Murthy, 1983; Mikheyev and Smirnov, 1986).

4.5.4 Theoretical Neutrino Spectra and Data

General Comments on Computational Methods

In principle the energy spectra of atmospheric neutrinos and their antiparticles can be calculated from the primary cosmic ray spectrum on top of the atmosphere with the help of a Monte Carlo simulation or analytically. Apart from uncertainties concerning the particle physics aspects the accuracy of this method hinges on our knowledge of the primary spectrum and the varying and complex heliospheric, magnetospheric and geomagnetic cutoff conditions. The latter affect the low energy region of the primary spectrum which consists predominantly of protons and alpha particles, and may cause significant spectral shape and intensity differences between different locations on Earth. This is illustrated in Fig. 5.23 of Chapter 5, Section 5.2.

Another approach to obtain the atmospheric neutrino spectra is to determine first the parent pion and kaon spectra from experimentally determined muon spectra at ground level (sea level and mountain altitudes) as well as from balloon measurements across the atmosphere. The procedure then is to compute the neutrino fluxes from the decays of these particles.

This method, too, harbors many uncertainties, also with respect to kaons, and the evolution of the muon spectrum as a function of atmospheric depth is not very well known, particularly at higher altitudes. Due to different production cross sections and threshold energies of the processes involved, the muons are most likely to come from pions, but muon neutrinos result from the decay of kaons and other particles as well, but with much smaller probabilities and at higher energies.

It is somewhat uncertain to predict the $\nu_\mu/\overline{\nu}_\mu$ ratio because of the uncertainty in the $K/\overline{K}$ ratio, particularly at higher energies. The ν_e flux from kaons is about a factor of 30 lower than the ν_μ flux because it results from a 3-body decay mode of the kaon. In addition energetic electron neutrinos are also produced in muon decays together with muon neutrinos. These problems had been discussed by several authors (Gaisser et al., 1987; Lipari, 1993; Perkins, 1993; Honda, 1999).

Neutrino Spectra from Early Calculations

The energy spectra of cosmic ray induced atmospheric neutrinos had been calculated by numerous authors through the years and likewise the detector responses. Many of the early calculations of neutrino intensities and spectra were based on a limited set of assumptions and are therefore inaccurate (Zatsepin and Kuzim, 1962; Osborne et al., 1965; Cowsik et al., 1966; Tam and Young, 1970; Volkova and Zatsepin, 1972; Choi and Young, 1975; Margolis et al., 1978; Allkofer et al., 1979a, 1979b; and Dedenko et al., 1979) . An early summary of muon neutrinos at ground level is given by Osborne (1973) and on electron neutrinos by Young (1973).

In Fig. 4.80 we show the theoretical low energy atmospheric electron neutrino and antineutrino spectra obtained by Young (1973) for two different geomagnetic latitudes at sea level. The latitude effect is evident. High energy vertical and horizontal differential electron and muon neutrino and antineutrino spectra at sea level had been calculated by Allkofer et al. (1979a and 1979b). These spectra, shown in Figs. 4.81 and 4.82, were derived from atmospheric muon spectra under the assumptions that the exponent, δ, of the differential muon spectrum is -2.8 and that the K/π-ratio is 0.15 and 0.3, respectively. High energy integral spectra for vertical and horizontal muon

neutrinos are shown in Fig. 4.83 together with a rather speculative spectrum of neutrinos from direct production processes (Allkofer et al., 1979a) (for details see caption).

Neutrino Spectra from Recent Calculations

Recent atmospheric neutrino flux calculations are mostly based on full Monte Carlo simulations. Some are taking into account solar modulation, geomagnetic and other effects mentioned above with great care, including improved interaction models. Few calculations are three-dimensional, many are still one-dimensional. Generally speaking, the accuracy of the calculations has been stepped up significantly. Calculations of more recent date are those of Agrawal et al., 1996; Barr et al., 1989; Battistoni et al., 2000; Bugaev and Naumov, 1989; Cheung and Young, 1990; Gaisser and Stanev, 1995; Honda et al., 1990 and 1995; Lipari, 1993; Lipari et al., 1998.

An analytical calculation of the atmospheric neutrino flux of more recent data was carried out by Bhattacharyya and Pal (1990), however, without including geomagnetic effects. Much of the more recent theoretical work on atmospheric neutrinos focuses on the question whether neutrino oscillations do exist or not. In the following we present a small selection of data from the numerous new and very detailed calculations that have become available during the last few years.

In Tables 4.30 and 4.31 we give the muon and electron neutrino and antineutrino differential intensities, respectively, for energies from 0.2 to 10^8 GeV and a range of zenith angles from 0° (vertical downward) to 90° (horizontal) for solar minimum from the work of Mitsui et al. (1986). Table 4.32 shows the downward differential and integral fluxes of electron and muon neutrinos and antineutrinos from the same work. We have plotted the integral flux spectra of $(\nu_\mu + \overline{\nu}_\mu)$ and $(\nu_e + \overline{\nu}_e)$ of Table 4.32 in Fig. 4.84. The differential and Integral fluxes of downward-going prompt muon neutrinos from the decay of charmed particles from the work of Mitsui et al. (1986) is listed in Table 4.33 and their differential intensity in vertical and horizontal directions in Table 4.34.

Similarly, Cheung and Young (1990) who's early work is summarized in Fig. 4.80 have extensively studied the upward/downward asymmetries of the low energy neutrino fluxes $(\nu_\mu, \overline{\nu}_\mu, \nu_e, \overline{\nu}_e)$ at different sites caused by the latitude dependence of the geomagnetic cutoff for primary protons in the energy range between 0.1 and 1 GeV, including the effects of solar activity.

Tables 4.35 and 4.36 show an analogous set of data from an analytic

calculation of Lipari (1993). From these tables we have plotted in Fig. 4.85 the spectra of the differential intensities of $(\nu_\mu + \overline{\nu}_\mu)$ and $(\nu_e + \overline{\nu}_e)$ in vertical and horizontal directions. In addition, Tables 4.37 and 4.38 list the $(\nu_\mu/\overline{\nu}_\mu)$ and $(\nu_e/\overline{\nu}_e)$ ratios which result from the work of Lipari (1993). A more recent set of data of the intensity of atmospheric muon and electron neutrinos and antineutrinos combined of energy $\geq$1 GeV from a calculation of Agrawal et al. (1996) is shown in Tables 4.39 to 4.42.

The atmospheric muon spectra, their zenith angle dependence and the muon charge ratio that result from the basic calculations of Lipari (1993) and Agrawal et al. (1996) from which the neutrino data discussed here were derived are presented in Chapter 3, Section 3.6 . Both of these calculations are based on a number of assumptions and approximations and disregard geomagnetic effects. However, Agrawal et al. include in their work a table of geomagnetic correction factors for the zenith angle dependence of upward going $(\nu_\mu + \overline{\nu}_\mu)$ for several experimental locations (Table 4.43).

A compilation of neutrino spectra of two flavors from different sources is shown in Fig. 4.86 (Koshiba, 1992).

Up/Down Asymmetry and Ratio-of-Ratios

More specific theoretical results that are related to neutrino oscillations, such as the zenith angle and azimuthal distributions and the ratio-of-ratio problem, are displayed jointly with the corresponding experimental data in the next subsection.

4.5.5 Experimental Results, Early Work

Historical Summary

The pioneering cosmic ray neutrino experiments that used electronic and not radiochemical techniques were the comparatively large installation set up by Reines and collaborators in the East Rand Proprietary Mine (ERPM) near Johannerburg, South Africa (Reines et al., 1965; Crouch et al., 1970), and the more modest experiment set up by Menon, Miyake, Wolfendale and collaborators in a deep mine in the Kolar Gold Fields (KGF), in Karnataka, Southern India (Achar et al., 1965; Krishnaswamy et al., 1970).

These experiments were followed by a new generation of more sophisticated installations, many of which were primarily designed to be used as proton decay detectors, but also to search for various forms of dark matter and for other tasks.

Table 4.30: Differential Atmospheric Muon Neutrino Intensities at Solar Minimum (Mitsui et al., 1986).

$\nu_\mu, \bar{\nu}_\mu$	$(\nu_\mu + \bar{\nu}_\mu)$ Intensity $[\mathrm{cm}^{-2}\,\mathrm{s}^{-1}\,\mathrm{sr}^{-1}\,\mathrm{GeV}^{-1}]$									
Energy	Zenith Angle θ									
[GeV]	0°	30°	45°	60°	75°	80°	84°	87°	90°
0.2	1.34	1.35	1.43	1.51	1.61	1.71	1.82	2.03	2.08
0.3	$6.86 \cdot 10^{-1}$	$7.06 \cdot 10^{-1}$	$7.34 \cdot 10^{-1}$	$7.68 \cdot 10^{-1}$	$8.32 \cdot 10^{-1}$	$8.94 \cdot 10^{-1}$	$9.61 \cdot 10^{-1}$	1.07	1.11
0.5	$2.06 \cdot 10^{-1}$	$2.16 \cdot 10^{-1}$	$2.25 \cdot 10^{-1}$	$2.45 \cdot 10^{-1}$	$2.58 \cdot 10^{-1}$	$2.78 \cdot 10^{-1}$	$3.01 \cdot 10^{-1}$	$3.37 \cdot 10^{-1}$	$3.46 \cdot 10^{-1}$
1	$3.62 \cdot 10^{-2}$	$3.87 \cdot 10^{-2}$	$4.15 \cdot 10^{-2}$	$4.51 \cdot 10^{-2}$	$4.79 \cdot 10^{-2}$	$5.14 \cdot 10^{-2}$	$5.51 \cdot 10^{-2}$	$6.27 \cdot 10^{-2}$	$6.47 \cdot 10^{-2}$
2	$5.39 \cdot 10^{-3}$	$5.76 \cdot 10^{-3}$	$6.30 \cdot 10^{-3}$	$6.98 \cdot 10^{-3}$	$7.80 \cdot 10^{-3}$	$8.30 \cdot 10^{-3}$	$9.00 \cdot 10^{-3}$	$1.03 \cdot 10^{-3}$	$1.07 \cdot 10^{-3}$
3	$1.70 \cdot 10^{-3}$	$1.84 \cdot 10^{-3}$	$2.04 \cdot 10^{-3}$	$2.26 \cdot 10^{-3}$	$2.60 \cdot 10^{-3}$	$2.87 \cdot 10^{-3}$	$3.03 \cdot 10^{-3}$	$3.64 \cdot 10^{-3}$	$3.80 \cdot 10^{-3}$
5	$3.69 \cdot 10^{-4}$	$3.88 \cdot 10^{-4}$	$4.26 \cdot 10^{-4}$	$4.93 \cdot 10^{-4}$	$6.03 \cdot 10^{-4}$	$6.69 \cdot 10^{-4}$	$7.45 \cdot 10^{-4}$	$8.55 \cdot 10^{-4}$	$8.80 \cdot 10^{-4}$
10	$4.29 \cdot 10^{-5}$	$4.74 \cdot 10^{-5}$	$5.28 \cdot 10^{-5}$	$6.08 \cdot 10^{-5}$	$7.89 \cdot 10^{-5}$	$9.15 \cdot 10^{-5}$	$1.08 \cdot 10^{-4}$	$1.21 \cdot 10^{-4}$	$1.25 \cdot 10^{-4}$
20	$5.09 \cdot 10^{-6}$	$5.57 \cdot 10^{-6}$	$6.28 \cdot 10^{-6}$	$7.35 \cdot 10^{-6}$	$9.62 \cdot 10^{-6}$	$1.18 \cdot 10^{-5}$	$1.41 \cdot 10^{-5}$	$1.65 \cdot 10^{-5}$	$1.74 \cdot 10^{-5}$
50	$3.06 \cdot 10^{-7}$	$3.36 \cdot 10^{-7}$	$4.01 \cdot 10^{-7}$	$4.56 \cdot 10^{-7}$	$6.01 \cdot 10^{-7}$	$7.23 \cdot 10^{-7}$	$8.80 \cdot 10^{-7}$	$1.05 \cdot 10^{-6}$	$1.15 \cdot 10^{-6}$
100	$3.61 \cdot 10^{-8}$	$3.96 \cdot 10^{-8}$	$4.58 \cdot 10^{-8}$	$4.94 \cdot 10^{-8}$	$7.14 \cdot 10^{-8}$	$8.42 \cdot 10^{-8}$	$1.01 \cdot 10^{-7}$	$1.19 \cdot 10^{-7}$	$1.31 \cdot 10^{-7}$
200	$4.22 \cdot 10^{-9}$	$4.61 \cdot 10^{-9}$	$5.34 \cdot 10^{-9}$	$5.99 \cdot 10^{-9}$	$8.51 \cdot 10^{-9}$	$9.90 \cdot 10^{-9}$	$1.17 \cdot 10^{-8}$	$1.35 \cdot 10^{-8}$	$1.48 \cdot 10^{-8}$
500	$2.30 \cdot 10^{-10}$	$2.52 \cdot 10^{-10}$	$2.87 \cdot 10^{-10}$	$3.33 \cdot 10^{-10}$	$4.68 \cdot 10^{-10}$	$5.35 \cdot 10^{-10}$	$6.23 \cdot 10^{-10}$	$7.02 \cdot 10^{-10}$	$7.53 \cdot 10^{-10}$
10^3	$2.29 \cdot 10^{-11}$	$2.54 \cdot 10^{-11}$	$2.91 \cdot 10^{-11}$	$3.49 \cdot 10^{-11}$	$4.96 \cdot 10^{-11}$	$5.62 \cdot 10^{-11}$	$6.49 \cdot 10^{-11}$	$7.19 \cdot 10^{-11}$	$7.71 \cdot 10^{-11}$
$2 \cdot 10^3$	$2.18 \cdot 10^{-12}$	$2.46 \cdot 10^{-12}$	$2.86 \cdot 10^{-12}$	$3.57 \cdot 10^{-12}$	$5.32 \cdot 10^{-12}$	$6.11 \cdot 10^{-12}$	$7.07 \cdot 10^{-12}$	$7.78 \cdot 10^{-12}$	$8.20 \cdot 10^{-12}$
$5 \cdot 10^3$	$8.68 \cdot 10^{-14}$	$9.91 \cdot 10^{-14}$	$1.18 \cdot 10^{-13}$	$1.55 \cdot 10^{-13}$	$2.51 \cdot 10^{-13}$	$3.01 \cdot 10^{-13}$	$3.61 \cdot 10^{-13}$	$4.03 \cdot 10^{-13}$	$4.24 \cdot 10^{-13}$
10^4	$7.19 \cdot 10^{-15}$	$8.25 \cdot 10^{-15}$	$9.93 \cdot 10^{-15}$	$1.33 \cdot 10^{-14}$	$2.28 \cdot 10^{-14}$	$2.82 \cdot 10^{-14}$	$3.49 \cdot 10^{-14}$	$4.00 \cdot 10^{-14}$	$4.24 \cdot 10^{-14}$
$2 \cdot 10^4$	$5.80 \cdot 10^{-16}$	$6.67 \cdot 10^{-16}$	$8.07 \cdot 10^{-16}$	$1.10 \cdot 10^{-15}$	$1.93 \cdot 10^{-15}$	$2.46 \cdot 10^{-15}$	$3.13 \cdot 10^{-15}$	$3.66 \cdot 10^{-15}$	$3.92 \cdot 10^{-15}$
$5 \cdot 10^4$	$2.04 \cdot 10^{-17}$	$2.54 \cdot 10^{-17}$	$2.85 \cdot 10^{-17}$	$3.90 \cdot 10^{-17}$	$7.04 \cdot 10^{-17}$	$9.87 \cdot 10^{-17}$	$1.18 \cdot 10^{-16}$	$1.41 \cdot 10^{-16}$	$1.52 \cdot 10^{-16}$
10^5	$1.60 \cdot 10^{-18}$	$1.85 \cdot 10^{-18}$	$2.24 \cdot 10^{-18}$	$3.09 \cdot 10^{-18}$	$5.60 \cdot 10^{-18}$	$7.29 \cdot 10^{-18}$	$9.53 \cdot 10^{-18}$	$1.14 \cdot 10^{-17}$	$1.24 \cdot 10^{-17}$
$2 \cdot 10^5$	$1.26 \cdot 10^{-19}$	$1.45 \cdot 10^{-19}$	$1.76 \cdot 10^{-19}$	$2.43 \cdot 10^{-19}$	$4.41 \cdot 10^{-19}$	$5.76 \cdot 10^{-19}$	$7.55 \cdot 10^{-19}$	$9.06 \cdot 10^{-19}$	$9.82 \cdot 10^{-19}$
$5 \cdot 10^5$	$3.97 \cdot 10^{-21}$	$4.58 \cdot 10^{-21}$	$5.58 \cdot 10^{-21}$	$7.59 \cdot 10^{-21}$	$1.35 \cdot 10^{-20}$	$1.81 \cdot 10^{-20}$	$2.39 \cdot 10^{-20}$	$2.90 \cdot 10^{-20}$	$3.16 \cdot 10^{-20}$
10^6	$2.52 \cdot 10^{-22}$	$2.90 \cdot 10^{-22}$	$3.54 \cdot 10^{-22}$	$4.81 \cdot 10^{-22}$	$8.57 \cdot 10^{-22}$	$1.15 \cdot 10^{-21}$	$1.15 \cdot 10^{-21}$	$1.84 \cdot 10^{-21}$	$2.00 \cdot 10^{-21}$
$2 \cdot 10^6$	$1.60 \cdot 10^{-23}$	$1.84 \cdot 10^{-23}$	$2.24 \cdot 10^{-23}$	$3.05 \cdot 10^{-23}$	$5.42 \cdot 10^{-23}$	$7.26 \cdot 10^{-23}$	$9.56 \cdot 10^{-23}$	$1.16 \cdot 10^{-22}$	$1.26 \cdot 10^{-22}$
$5 \cdot 10^6$	$4.17 \cdot 10^{-25}$	$4.80 \cdot 10^{-25}$	$5.84 \cdot 10^{-25}$	$7.94 \cdot 10^{-25}$	$1.41 \cdot 10^{-24}$	$1.89 \cdot 10^{-24}$	$2.48 \cdot 10^{-24}$	$3.00 \cdot 10^{-24}$	$3.27 \cdot 10^{-24}$
10^7	$2.64 \cdot 10^{-26}$	$3.04 \cdot 10^{-26}$	$3.70 \cdot 10^{-26}$	$5.02 \cdot 10^{-26}$	$8.91 \cdot 10^{-26}$	$1.19 \cdot 10^{-25}$	$1.56 \cdot 10^{-25}$	$1.89 \cdot 10^{-25}$	$2.06 \cdot 10^{-25}$
$2 \cdot 10^7$	$1.68 \cdot 10^{-27}$	$1.93 \cdot 10^{-27}$	$2.34 \cdot 10^{-27}$	$3.18 \cdot 10^{-27}$	$5.63 \cdot 10^{-27}$	$7.51 \cdot 10^{-27}$	$9.83 \cdot 10^{-27}$	$1.19 \cdot 10^{-26}$	$1.29 \cdot 10^{-26}$
$5 \cdot 10^7$	$4.36 \cdot 10^{-29}$	$5.01 \cdot 10^{-29}$	$6.09 \cdot 10^{-29}$	$8.26 \cdot 10^{-29}$	$1.46 \cdot 10^{-28}$	$1.95 \cdot 10^{-28}$	$2.54 \cdot 10^{-28}$	$3.06 \cdot 10^{-28}$	$3.33 \cdot 10^{-28}$
10^8	$2.76 \cdot 10^{-30}$	$3.17 \cdot 10^{-30}$	$3.85 \cdot 10^{-30}$	$5.22 \cdot 10^{-30}$	$9.21 \cdot 10^{-30}$	$1.23 \cdot 10^{-29}$	$1.60 \cdot 10^{-29}$	$1.93 \cdot 10^{-29}$	$2.09 \cdot 10^{-29}$

Table 4.31: Differential Atmospheric Electron Neutrino Intensities at Solar Minimum (Mitsui et al., 1986).

$\nu_e, \overline{\nu}_e$	$(\nu_e + \overline{\nu}_e)$ Intensity [$cm^{-2} s^{-1} sr^{-1} GeV^{-1}$]								
Energy	Zenith Angle θ								
[GeV]	0°	30°	45°	60°	75°	80°	84°	87°	90°
0.2	$6.53 \cdot 10^{-1}$	$6.60 \cdot 10^{-1}$	$6.67 \cdot 10^{-1}$	$6.74 \cdot 10^{-1}$	$6.80 \cdot 10^{-1}$	$6.87 \cdot 10^{-1}$	$6.94 \cdot 10^{-1}$	$7.01 \cdot 10^{-1}$	$7.13 \cdot 10^{-1}$
0.3	$3.24 \cdot 10^{-1}$	$3.36 \cdot 10^{-1}$	$3.47 \cdot 10^{-1}$	$3.59 \cdot 10^{-1}$	$3.70 \cdot 10^{-1}$	$3.82 \cdot 10^{-1}$	$3.94 \cdot 10^{-1}$	$4.05 \cdot 10^{-1}$	$4.27 \cdot 10^{-1}$
0.5	$8.65 \cdot 10^{-2}$	$9.22 \cdot 10^{-2}$	$9.80 \cdot 10^{-2}$	$1.04 \cdot 10^{-1}$	$1.10 \cdot 10^{-1}$	$1.15 \cdot 10^{-1}$	$1.21 \cdot 10^{-1}$	$1.27 \cdot 10^{-1}$	$1.39 \cdot 10^{-1}$
1	$1.27 \cdot 10^{-2}$	$1.41 \cdot 10^{-2}$	$1.58 \cdot 10^{-2}$	$1.81 \cdot 10^{-2}$	$2.15 \cdot 10^{-2}$	$2.26 \cdot 10^{-2}$	$2.34 \cdot 10^{-2}$	$2.39 \cdot 10^{-2}$	$2.44 \cdot 10^{-2}$
2	$1.56 \cdot 10^{-3}$	$1.80 \cdot 10^{-3}$	$2.18 \cdot 10^{-3}$	$2.75 \cdot 10^{-3}$	$3.30 \cdot 10^{-3}$	$3.48 \cdot 10^{-3}$	$3.60 \cdot 10^{-3}$	$3.70 \cdot 10^{-3}$	$3.77 \cdot 10^{-3}$
3	$4.14 \cdot 10^{-4}$	$4.89 \cdot 10^{-4}$	$5.88 \cdot 10^{-4}$	$7.66 \cdot 10^{-4}$	$1.05 \cdot 10^{-3}$	$1.12 \cdot 10^{-3}$	$1.19 \cdot 10^{-3}$	$1.23 \cdot 10^{-3}$	$1.25 \cdot 10^{-3}$
5	$7.07 \cdot 10^{-5}$	$8.58 \cdot 10^{-5}$	$1.05 \cdot 10^{-4}$	$1.42 \cdot 10^{-4}$	$2.09 \cdot 10^{-4}$	$2.37 \cdot 10^{-4}$	$2.68 \cdot 10^{-4}$	$2.95 \cdot 10^{-4}$	$3.03 \cdot 10^{-4}$
10	$6.26 \cdot 10^{-6}$	$7.94 \cdot 10^{-6}$	$9.63 \cdot 10^{-6}$	$1.35 \cdot 10^{-5}$	$2.38 \cdot 10^{-5}$	$2.94 \cdot 10^{-5}$	$3.57 \cdot 10^{-5}$	$4.27 \cdot 10^{-5}$	$4.58 \cdot 10^{-5}$
20	$5.18 \cdot 10^{-7}$	$6.58 \cdot 10^{-7}$	$8.07 \cdot 10^{-7}$	$1.15 \cdot 10^{-6}$	$2.23 \cdot 10^{-6}$	$3.08 \cdot 10^{-6}$	$4.18 \cdot 10^{-6}$	$5.42 \cdot 10^{-6}$	$6.37 \cdot 10^{-6}$
50	$2.07 \cdot 10^{-8}$	$2.46 \cdot 10^{-8}$	$3.10 \cdot 10^{-8}$	$4.61 \cdot 10^{-8}$	$9.20 \cdot 10^{-8}$	$1.35 \cdot 10^{-7}$	$2.02 \cdot 10^{-7}$	$2.84 \cdot 10^{-7}$	$3.83 \cdot 10^{-7}$
100	$2.07 \cdot 10^{-9}$	$2.43 \cdot 10^{-9}$	$3.21 \cdot 10^{-9}$	$4.34 \cdot 10^{-9}$	$8.03 \cdot 10^{-9}$	$1.17 \cdot 10^{-8}$	$1.78 \cdot 10^{-8}$	$2.62 \cdot 10^{-8}$	$3.70 \cdot 10^{-8}$
200	$2.04 \cdot 10^{-10}$	$2.40 \cdot 10^{-10}$	$3.23 \cdot 10^{-10}$	$4.16 \cdot 10^{-10}$	$6.92 \cdot 10^{-10}$	$9.65 \cdot 10^{-10}$	$1.43 \cdot 10^{-9}$	$2.11 \cdot 10^{-9}$	$3.01 \cdot 10^{-9}$
500	$9.43 \cdot 10^{-12}$	$1.11 \cdot 10^{-11}$	$1.38 \cdot 10^{-11}$	$1.83 \cdot 10^{-11}$	$3.03 \cdot 10^{-11}$	$3.91 \cdot 10^{-11}$	$5.36 \cdot 10^{-11}$	$7.40 \cdot 10^{-11}$	$1.03 \cdot 10^{-10}$
10^3	$8.69 \cdot 10^{-13}$	$1.04 \cdot 10^{-13}$	$1.30 \cdot 10^{-12}$	$1.76 \cdot 10^{-12}$	$2.91 \cdot 10^{-12}$	$3.69 \cdot 10^{-12}$	$4.75 \cdot 10^{-12}$	$6.16 \cdot 10^{-12}$	$8.18 \cdot 10^{-12}$
$2 \cdot 10^3$	$7.60 \cdot 10^{-14}$	$9.16 \cdot 10^{-14}$	$1.17 \cdot 10^{-13}$	$1.61 \cdot 10^{-13}$	$2.76 \cdot 10^{-13}$	$3.46 \cdot 10^{-13}$	$4.40 \cdot 10^{-13}$	$5.37 \cdot 10^{-13}$	$6.61 \cdot 10^{-13}$
$5 \cdot 10^3$	$2.85 \cdot 10^{-15}$	$3.46 \cdot 10^{-15}$	$4.47 \cdot 10^{-15}$	$6.33 \cdot 10^{-15}$	$1.12 \cdot 10^{-14}$	$1.46 \cdot 10^{-14}$	$1.84 \cdot 10^{-14}$	$2.23 \cdot 10^{-14}$	$2.52 \cdot 10^{-14}$
10^4	$2.31 \cdot 10^{-16}$	$2.82 \cdot 10^{-16}$	$3.65 \cdot 10^{-16}$	$5.23 \cdot 10^{-16}$	$9.51 \cdot 10^{-16}$	$1.23 \cdot 10^{-15}$	$1.61 \cdot 10^{-15}$	$1.95 \cdot 10^{-15}$	$2.16 \cdot 10^{-15}$
$2 \cdot 10^4$	$1.85 \cdot 10^{-17}$	$2.25 \cdot 10^{-17}$	$2.93 \cdot 10^{-17}$	$4.22 \cdot 10^{-17}$	$7.80 \cdot 10^{-17}$	$1.02 \cdot 10^{-16}$	$1.35 \cdot 10^{-16}$	$1.60 \cdot 10^{-16}$	$1.80 \cdot 10^{-16}$
$5 \cdot 10^4$	$6.49 \cdot 10^{-19}$	$7.91 \cdot 10^{-19}$	$1.03 \cdot 10^{-18}$	$1.48 \cdot 10^{-18}$	$2.70 \cdot 10^{-18}$	$3.54 \cdot 10^{-18}$	$4.74 \cdot 10^{-18}$	$5.83 \cdot 10^{-18}$	$6.24 \cdot 10^{-18}$
10^5	$5.12 \cdot 10^{-20}$	$6.24 \cdot 10^{-20}$	$8.11 \cdot 10^{-20}$	$1.15 \cdot 10^{-19}$	$2.00 \cdot 10^{-19}$	$2.65 \cdot 10^{-19}$	$3.60 \cdot 10^{-19}$	$4.27 \cdot 10^{-19}$	$4.70 \cdot 10^{-19}$
$2 \cdot 10^5$	$3.56 \cdot 10^{-21}$	$4.44 \cdot 10^{-21}$	$5.50 \cdot 10^{-21}$	$7.88 \cdot 10^{-21}$	$1.28 \cdot 10^{-20}$	$1.71 \cdot 10^{-20}$	$2.31 \cdot 10^{-20}$	$2.81 \cdot 10^{-20}$	$3.38 \cdot 10^{-20}$
$5 \cdot 10^5$	$9.94 \cdot 10^{-23}$	$1.15 \cdot 10^{-22}$	$1.44 \cdot 10^{-22}$	$2.08 \cdot 10^{-22}$	$3.36 \cdot 10^{-22}$	$4.50 \cdot 10^{-22}$	$6.13 \cdot 10^{-22}$	$7.40 \cdot 10^{-22}$	$8.46 \cdot 10^{-22}$
10^6	$6.42 \cdot 10^{-24}$	$7.28 \cdot 10^{-24}$	$9.03 \cdot 10^{-24}$	$1.33 \cdot 10^{-23}$	$2.12 \cdot 10^{-23}$	$2.87 \cdot 10^{-23}$	$3.89 \cdot 10^{-23}$	$4.71 \cdot 10^{-23}$	$5.28 \cdot 10^{-23}$
$2 \cdot 10^6$	$4.03 \cdot 10^{-25}$	$4.56 \cdot 10^{-25}$	$5.75 \cdot 10^{-25}$	$8.57 \cdot 10^{-25}$	$1.35 \cdot 10^{-24}$	$1.82 \cdot 10^{-24}$	$2.44 \cdot 10^{-24}$	$2.97 \cdot 10^{-24}$	$3.34 \cdot 10^{-24}$
$5 \cdot 10^6$	$1.06 \cdot 10^{-26}$	$1.21 \cdot 10^{-26}$	$1.48 \cdot 10^{-26}$	$2.28 \cdot 10^{-26}$	$3.44 \cdot 10^{-26}$	$4.73 \cdot 10^{-26}$	$6.41 \cdot 10^{-26}$	$7.73 \cdot 10^{-26}$	$8.66 \cdot 10^{-26}$
10^7	$6.71 \cdot 10^{-28}$	$7.40 \cdot 10^{-28}$	$9.39 \cdot 10^{-28}$	$1.46 \cdot 10^{-27}$	$2.20 \cdot 10^{-27}$	$2.99 \cdot 10^{-27}$	$4.04 \cdot 10^{-27}$	$4.86 \cdot 10^{-27}$	$5.47 \cdot 10^{-27}$
$2 \cdot 10^7$	$4.29 \cdot 10^{-29}$	$4.65 \cdot 10^{-29}$	$5.99 \cdot 10^{-29}$	$9.26 \cdot 10^{-29}$	$1.39 \cdot 10^{-28}$	$1.90 \cdot 10^{-28}$	$2.58 \cdot 10^{-28}$	$3.07 \cdot 10^{-28}$	$3.46 \cdot 10^{-28}$
$5 \cdot 10^7$	$1.12 \cdot 10^{-30}$	$1.20 \cdot 10^{-30}$	$1.57 \cdot 10^{-30}$	$2.48 \cdot 10^{-30}$	$3.65 \cdot 10^{-30}$	$4.92 \cdot 10^{-30}$	$6.63 \cdot 10^{-30}$	$7.98 \cdot 10^{-30}$	$8.93 \cdot 10^{-30}$
10^8	$7.14 \cdot 10^{-32}$	$7.64 \cdot 10^{-32}$	$9.96 \cdot 10^{-32}$	$1.57 \cdot 10^{-31}$	$2.31 \cdot 10^{-31}$	$3.11 \cdot 10^{-31}$	$4.19 \cdot 10^{-31}$	$5.03 \cdot 10^{-31}$	$5.63 \cdot 10^{-31}$

Table 4.32: Downward-going Atmospheric Neutrino Flux from Kaon, Pion and Muon Decays. (Mitsui et al., 1986)

Neutrino Energy [GeV]	Differential Flux $[\mathrm{cm}^{-2}\,\mathrm{s}^{-1}\,\mathrm{GeV}^{-1}]$		Integral Flux $[\mathrm{cm}^{-2}\,\mathrm{s}^{-1}]$	
	$\nu_\mu, \overline{\nu}_\mu$	$\nu_e, \overline{\nu}_e$	$\nu_\mu, \overline{\nu}_\mu$	$\nu_e, \overline{\nu}_e$
0.2	9.83	4.28	1.79	$7.68 \cdot 10^{-1}$
0.3	5.09	2.29	1.09	$4.56 \cdot 10^{-1}$
0.5	1.59	$6.66 \cdot 10^{-1}$	$5.17 \cdot 10^{-1}$	$2.07 \cdot 10^{-1}$
1	$2.91 \cdot 10^{-1}$	$1.17 \cdot 10^{-1}$	$1.69 \cdot 10^{-1}$	$6.34 \cdot 10^{-2}$
2	$4.57 \cdot 10^{-2}$	$1.72 \cdot 10^{-2}$	$4.99 \cdot 10^{-2}$	$1.67 \cdot 10^{-2}$
3	$1.51 \cdot 10^{-2}$	$5.13 \cdot 10^{-3}$	$2.33 \cdot 10^{-2}$	$7.10 \cdot 10^{-3}$
5	$3.38 \cdot 10^{-3}$	$1.02 \cdot 10^{-3}$	$8.61 \cdot 10^{-3}$	$2.34 \cdot 10^{-3}$
10	$4.39 \cdot 10^{-4}$	$1.15 \cdot 10^{-4}$	$2.18 \cdot 10^{-3}$	$4.98 \cdot 10^{-4}$
20	$5.45 \cdot 10^{-5}$	$1.17 \cdot 10^{-5}$	$5.34 \cdot 10^{-4}$	$9.84 \cdot 10^{-5}$
50	$3.40 \cdot 10^{-6}$	$5.33 \cdot 10^{-7}$	$8.02 \cdot 10^{-5}$	$1.09 \cdot 10^{-5}$
100	$3.90 \cdot 10^{-7}$	$4.91 \cdot 10^{-8}$	$1.85 \cdot 10^{-5}$	$1.94 \cdot 10^{-6}$
200	$4.58 \cdot 10^{-8}$	$4.24 \cdot 10^{-9}$	$4.18 \cdot 10^{-6}$	$3.39 \cdot 10^{-7}$
500	$2.48 \cdot 10^{-9}$	$1.70 \cdot 10^{-10}$	$5.47 \cdot 10^{-7}$	$3.46 \cdot 10^{-8}$
10^3	$2.58 \cdot 10^{-10}$	$1.55 \cdot 10^{-11}$	$1.13 \cdot 10^{-7}$	$6.25 \cdot 10^{-9}$
$2 \cdot 10^3$	$2.68 \cdot 10^{-11}$	$1.40 \cdot 10^{-12}$	$2.26 \cdot 10^{-8}$	$1.11 \cdot 10^{-9}$
$5 \cdot 10^3$	$1.24 \cdot 10^{-12}$	$5.60 \cdot 10^{-14}$	$2.50 \cdot 10^{-9}$	$1.09 \cdot 10^{-10}$
10^4	$1.12 \cdot 10^{-13}$	$4.75 \cdot 10^{-15}$	$4.40 \cdot 10^{-10}$	$1.81 \cdot 10^{-11}$
$2 \cdot 10^4$	$9.64 \cdot 10^{-15}$	$3.89 \cdot 10^{-16}$	$7.41 \cdot 10^{-11}$	$2.92 \cdot 10^{-12}$
$5 \cdot 10^4$	$3.57 \cdot 10^{-16}$	$1.37 \cdot 10^{-17}$	$6.71 \cdot 10^{-12}$	$2.48 \cdot 10^{-13}$
10^5	$2.83 \cdot 10^{-17}$	$1.03 \cdot 10^{-18}$	$1.06 \cdot 10^{-12}$	$3.55 \cdot 10^{-14}$
$2 \cdot 10^5$	$2.23 \cdot 10^{-18}$	$6.89 \cdot 10^{-20}$	$1.60 \cdot 10^{-13}$	$4.63 \cdot 10^{-15}$
$5 \cdot 10^5$	$7.01 \cdot 10^{-20}$	$1.81 \cdot 10^{-21}$	$1.18 \cdot 10^{-14}$	$3.03 \cdot 10^{-16}$
10^6	$4.44 \cdot 10^{-21}$	$1.14 \cdot 10^{-22}$	$1.49 \cdot 10^{-15}$	$3.84 \cdot 10^{-17}$
$2 \cdot 10^6$	$2.81 \cdot 10^{-22}$	$7.26 \cdot 10^{-24}$	$1.88 \cdot 10^{-16}$	$4.87 \cdot 10^{-18}$
$5 \cdot 10^6$	$7.30 \cdot 10^{-24}$	$1.89 \cdot 10^{-25}$	$1.22 \cdot 10^{-17}$	$3.17 \cdot 10^{-19}$
10^7	$4.61 \cdot 10^{-25}$	$1.20 \cdot 10^{-26}$	$1.54 \cdot 10^{-18}$	$4.02 \cdot 10^{-20}$
$2 \cdot 10^7$	$2.91 \cdot 10^{-26}$	$7.59 \cdot 10^{-28}$	$1.95 \cdot 10^{-19}$	$5.10 \cdot 10^{-21}$
$5 \cdot 10^7$	$7.54 \cdot 10^{-28}$	$1.98 \cdot 10^{-29}$	$1.26 \cdot 10^{-20}$	$3.33 \cdot 10^{-22}$
10^8	$4.75 \cdot 10^{-29}$	$1.26 \cdot 10^{-30}$	$1.59 \cdot 10^{-21}$	$4.21 \cdot 10^{-23}$

Table 4.33: Differential and Integral Flux of Downward-going Muon Neutrinos from the Decay of Charmed Particles (Mitsui et al., 1986).

Neutrino Energy [Gev]	Flux Differential $[cm^{-2} s^{-1} GeV^{-1}]$	Flux Integral $[cm^{-2} s^{-1}]$
10^4	$2.29 \cdot 10^{-15}$	$1.36 \cdot 10^{-11}$
10^5	$4.79 \cdot 10^{-18}$	$2.68 \cdot 10^{-13}$
10^6	$7.91 \cdot 10^{-21}$	$3.96 \cdot 10^{-15}$
10^7	$7.98 \cdot 10^{-24}$	$3.55 \cdot 10^{-17}$
$2 \cdot 10^7$	$8.60 \cdot 10^{-25}$	$7.23 \cdot 10^{-18}$
$5 \cdot 10^7$	$3.98 \cdot 10^{-26}$	$7.71 \cdot 10^{-19}$
10^8	$3.40 \cdot 10^{-26}$	$1.24 \cdot 10^{-19}$
$2 \cdot 10^8$	$2.61 \cdot 10^{-28}$	$1.70 \cdot 10^{-20}$
$5 \cdot 10^8$	$6.36 \cdot 10^{-30}$	$8.84 \cdot 10^{-22}$
10^9	$2.62 \cdot 10^{-31}$	$7.29 \cdot 10^{-23}$

Table 4.34: Differential Intensities of Prompt Muon Neutrinos for Vertical Downward-going ($\theta = 0°$) and Horizontal ($\theta = 90°$) Direction. (Mitsui et al., 1986)

Neutrino Energy [Gev]	Differential Intensity $[cm^{-2} s^{-1} sr^{-1} GeV^{-1}]$ $\theta = 0°$	$\theta = 90°$
10^4	$3.65 \cdot 10^{-16}$	$3.65 \cdot 10^{-16}$
10^5	$7.62 \cdot 10^{-19}$	$7.62 \cdot 10^{-19}$
10^6	$1.26 \cdot 10^{-21}$	$1.26 \cdot 10^{-21}$
10^7	$1.27 \cdot 10^{-24}$	$1.27 \cdot 10^{-24}$
$2 \cdot 10^7$	$1.36 \cdot 10^{-25}$	$1.38 \cdot 10^{-25}$
$5 \cdot 10^7$	$5.90 \cdot 10^{-27}$	$6.78 \cdot 10^{-27}$
10^8	$4.61 \cdot 10^{-28}$	$6.33 \cdot 10^{-28}$
$2 \cdot 10^8$	$2.83 \cdot 10^{-29}$	$5.38 \cdot 10^{-29}$
$5 \cdot 10^8$	$6.77 \cdot 10^{-31}$	$1.32 \cdot 10^{-30}$
10^9	$2.88 \cdot 10^{-32}$	$5.36 \cdot 10^{-32}$

Table 4.35: Muon Neutrino Intensities, $\nu_\mu + \overline{\nu}_\mu$, at Sea Level.
(Lipari, 1993)

Neutrino Energy GeV	$(\nu_\mu + \overline{\nu}_\mu)$ Intensity $[\mathrm{cm}^{-2}\mathrm{s}^{-1}\mathrm{sr}^{-1}\mathrm{GeV}^{-1}]$								
	$\cos(\theta)$								
	1	0.6	0.4	0.3	0.2	0.1	0.05	0.0
1.0	$3.64 \cdot 10^{-2}$	$4.11 \cdot 10^{-2}$	$4.43 \cdot 10^{-2}$	$4.63 \cdot 10^{-2}$	$4.85 \cdot 10^{-2}$	$5.12 \cdot 10^{-2}$	$5.26 \cdot 10^{-2}$	$5.30 \cdot 10^{-2}$
3.16	$1.31 \cdot 10^{-3}$	$1.52 \cdot 10^{-3}$	$1.70 \cdot 10^{-3}$	$1.82 \cdot 10^{-3}$	$1.96 \cdot 10^{-3}$	$2.11 \cdot 10^{-3}$	$2.17 \cdot 10^{-3}$	$2.19 \cdot 10^{-3}$
10.0	$4.46 \cdot 10^{-5}$	$5.20 \cdot 10^{-5}$	$5.90 \cdot 10^{-5}$	$6.43 \cdot 10^{-5}$	$7.18 \cdot 10^{-5}$	$8.22 \cdot 10^{-5}$	$8.73 \cdot 10^{-5}$	$8.98 \cdot 10^{-5}$
31.6	$1.42 \cdot 10^{-6}$	$1.69 \cdot 10^{-6}$	$1.92 \cdot 10^{-6}$	$2.10 \cdot 10^{-6}$	$2.37 \cdot 10^{-6}$	$2.81 \cdot 10^{-6}$	$3.10 \cdot 10^{-6}$	$3.30 \cdot 10^{-6}$
100	$4.08 \cdot 10^{-8}$	$5.00 \cdot 10^{-8}$	$5.84 \cdot 10^{-8}$	$6.47 \cdot 10^{-8}$	$7.38 \cdot 10^{-8}$	$8.79 \cdot 10^{-8}$	$9.77 \cdot 10^{-8}$	$1.07 \cdot 10^{-7}$
316	$1.09 \cdot 10^{-9}$	$1.37 \cdot 10^{-9}$	$1.63 \cdot 10^{-9}$	$1.83 \cdot 10^{-9}$	$2.12 \cdot 10^{-9}$	$2.56 \cdot 10^{-9}$	$2.84 \cdot 10^{-9}$	$3.07 \cdot 10^{-9}$
1000	$2.59 \cdot 10^{-11}$	$3.48 \cdot 10^{-11}$	$4.27 \cdot 10^{-11}$	$4.87 \cdot 10^{-11}$	$5.72 \cdot 10^{-11}$	$6.98 \cdot 10^{-11}$	$7.71 \cdot 10^{-11}$	$8.17 \cdot 10^{-11}$
3160	$4.93 \cdot 10^{-13}$	$7.28 \cdot 10^{-13}$	$9.63 \cdot 10^{-13}$	$1.15 \cdot 10^{-12}$	$1.42 \cdot 10^{-12}$	$1.81 \cdot 10^{-12}$	$2.01 \cdot 10^{-12}$	$2.12 \cdot 10^{-12}$
$1.00 \cdot 10^4$	$7.90 \cdot 10^{-15}$	$1.24 \cdot 10^{-14}$	$1.74 \cdot 10^{-14}$	$2.18 \cdot 10^{-14}$	$2.87 \cdot 10^{-14}$	$3.98 \cdot 10^{-14}$	$4.61 \cdot 10^{-14}$	$4.91 \cdot 10^{-14}$
$3.16 \cdot 10^4$	$1.17 \cdot 10^{-16}$	$1.88 \cdot 10^{-16}$	$2.72 \cdot 10^{-16}$	$3.49 \cdot 10^{-16}$	$4.79 \cdot 10^{-16}$	$7.07 \cdot 10^{-16}$	$8.48 \cdot 10^{-16}$	$9.18 \cdot 10^{-16}$
$1.00 \cdot 10^5$	$1.67 \cdot 10^{-18}$	$2.72 \cdot 10^{-18}$	$3.97 \cdot 10^{-18}$	$5.15 \cdot 10^{-18}$	$7.18 \cdot 10^{-18}$	$1.09 \cdot 10^{-17}$	$1.33 \cdot 10^{-17}$	$1.46 \cdot 10^{-17}$
$3.16 \cdot 10^5$	$2.37 \cdot 10^{-20}$	$3.87 \cdot 10^{-20}$	$5.67 \cdot 10^{-20}$	$7.38 \cdot 10^{-20}$	$1.03 \cdot 10^{-19}$	$1.59 \cdot 10^{-19}$	$1.96 \cdot 10^{-19}$	$2.14 \cdot 10^{-19}$

Table 4.36: Electron Neutrino Intensities, $\nu_e + \overline{\nu}_e$, at Sea Level. (Lipari, 1993)

Neutrino Energy GeV	$(\nu_e + \overline{\nu}_e)$ Intensity $[\mathrm{cm}^{-2}\mathrm{s}^{-1}\mathrm{sr}^{-1}\mathrm{GeV}^{-1}]$							
	$\cos(\theta)$							
	1	0.6	0.4	0.3	0.2	0.1	0.05	0.0
1.0	$1.46 \cdot 10^{-2}$	$1.90 \cdot 10^{-2}$	$2.22 \cdot 10^{-2}$	$2.41 \cdot 10^{-2}$	$2.63 \cdot 10^{-2}$	$2.89 \cdot 10^{-2}$	$3.02 \cdot 10^{-2}$	$3.05 \cdot 10^{-2}$
3.16	$3.76 \cdot 10^{-4}$	$5.64 \cdot 10^{-4}$	$7.28 \cdot 10^{-4}$	$8.41 \cdot 10^{-4}$	$9.77 \cdot 10^{-4}$	$1.13 \cdot 10^{-3}$	$1.18 \cdot 10^{-3}$	$1.20 \cdot 10^{-3}$
10.0	$7.42 \cdot 10^{-6}$	$1.24 \cdot 10^{-5}$	$1.78 \cdot 10^{-5}$	$2.23 \cdot 10^{-5}$	$2.91 \cdot 10^{-5}$	$3.87 \cdot 10^{-5}$	$4.37 \cdot 10^{-5}$	$4.62 \cdot 10^{-5}$
31.6	$1.34 \cdot 10^{-7}$	$2.21 \cdot 10^{-7}$	$3.32 \cdot 10^{-7}$	$4.39 \cdot 10^{-7}$	$6.25 \cdot 10^{-7}$	$9.80 \cdot 10^{-7}$	$1.24 \cdot 10^{-6}$	$1.43 \cdot 10^{-6}$
100	$2.71 \cdot 10^{-9}$	$4.00 \cdot 10^{-9}$	$5.69 \cdot 10^{-9}$	$7.40 \cdot 10^{-9}$	$1.07 \cdot 10^{-8}$	$1.81 \cdot 10^{-8}$	$2.50 \cdot 10^{-8}$	$3.26 \cdot 10^{-8}$
316	$5.77 \cdot 10^{-11}$	$8.16 \cdot 10^{-11}$	$1.08 \cdot 10^{-10}$	$1.33 \cdot 10^{-10}$	$1.80 \cdot 10^{-10}$	$2.89 \cdot 10^{-10}$	$3.99 \cdot 10^{-10}$	$5.49 \cdot 10^{-10}$
1000	$1.10 \cdot 10^{-12}$	$1.62 \cdot 10^{-12}$	$2.17 \cdot 10^{-12}$	$2.65 \cdot 10^{-12}$	$3.43 \cdot 10^{-12}$	$4.96 \cdot 10^{-12}$	$6.31 \cdot 10^{-12}$	$8.09 \cdot 10^{-12}$
3160	$1.80 \cdot 10^{-14}$	$2.81 \cdot 10^{-14}$	$3.93 \cdot 10^{-14}$	$4.91 \cdot 10^{-14}$	$6.50 \cdot 10^{-14}$	$9.26 \cdot 10^{-14}$	$1.12 \cdot 10^{-13}$	$1.30 \cdot 10^{-13}$
$1.00 \cdot 10^4$	$2.70 \cdot 10^{-16}$	$4.34 \cdot 10^{-16}$	$6.25 \cdot 10^{-16}$	$7.99 \cdot 10^{-16}$	$1.09 \cdot 10^{-15}$	$1.61 \cdot 10^{-15}$	$1.95 \cdot 10^{-15}$	$2.17 \cdot 10^{-15}$
$3.16 \cdot 10^4$	$3.90 \cdot 10^{-18}$	$6.32 \cdot 10^{-18}$	$9.23 \cdot 10^{-18}$	$1.19 \cdot 10^{-17}$	$1.66 \cdot 10^{-17}$	$2.52 \cdot 10^{-17}$	$3.08 \cdot 10^{-17}$	$3.39 \cdot 10^{-17}$
$1.00 \cdot 10^5$	$5.54 \cdot 10^{-20}$	$9.02 \cdot 10^{-20}$	$1.32 \cdot 10^{-19}$	$1.72 \cdot 10^{-19}$	$2.41 \cdot 10^{-19}$	$3.70 \cdot 10^{-19}$	$4.55 \cdot 10^{-19}$	$5.00 \cdot 10^{-19}$
$3.16 \cdot 10^5$	$7.85 \cdot 10^{-22}$	$1.28 \cdot 10^{-21}$	$1.88 \cdot 10^{-21}$	$2.45 \cdot 10^{-21}$	$3.44 \cdot 10^{-21}$	$5.30 \cdot 10^{-21}$	$6.53 \cdot 10^{-21}$	$7.17 \cdot 10^{-21}$

Table 4.37: Muon Neutrino/Antineutrino Ratio, (ν_μ / $\overline{\nu}_\mu$), at Sea Level. (Lipari, 1993)

Neutrino Energy GeV	Ratio ($\nu_\mu/\overline{\nu}_\mu$) cos($\theta$) 1	0.6	0.4	0.3	0.2	0.1	0.05	0.00
1.0	1.18	1.13	1.10	1.08	1.07	1.05	1.04	1.04
3.16	1.29	1.21	1.16	1.13	1.10	1.07	1.06	1.06
10.0	1.44	1.35	1.28	1.23	1.18	1.12	1.10	1.09
31.6	1.63	1.53	1.45	1.40	1.33	1.23	1.19	1.16
100	1.90	1.76	1.67	1.60	1.52	1.42	1.35	1.29
316	2.20	2.07	1.96	1.89	1.79	1.66	1.59	1.52
1000	2.38	2.32	2.26	2.20	2.11	1.98	1.91	1.85
3160	2.42	2.41	2.40	2.38	2.34	2.27	2.23	2.19
$1.00 \cdot 10^4$	2.43	2.43	2.42	2.42	2.42	2.40	2.39	2.38
$3.16 \cdot 10^4$	2.42	2.43	2.43	2.43	2.43	2.42	2.42	2.42
$1.00 \cdot 10^5$	2.42	2.42	2.42	2.42	2.43	2.43	2.43	2.43

Table 4.38: Electron Neutrino/Antineutrino Ratio, (ν_e / $\overline{\nu}_e$), at Sea Level. (Lipari, 1993)

Neutrino Energy GeV	Ratio ($\nu_e/\overline{\nu}_e$) cos(θ) 1	0.6	0.4	0.3	0.2	0.1	0.05	0.00
1.0	1.32	1.32	1.32	1.31	1.31	1.31	1.31	1.31
3.16	1.32	1.32	1.32	1.32	1.31	1.31	1.31	1.31
10.0	1.32	1.32	1.32	1.32	1.32	1.32	1.31	1.31
31.6	1.32	1.32	1.32	1.32	1.32	1.32	1.32	1.32
100	1.35	1.33	1.33	1.32	1.32	1.32	1.32	1.32
316	1.44	1.40	1.37	1.36	1.34	1.33	1.33	1.33
1000	1.54	1.51	1.47	1.45	1.42	1.38	1.37	1.37
3160	1.60	1.58	1.56	1.54	1.52	1.48	1.46	1.45
$1.00 \cdot 10^4$	1.62	1.61	1.61	1.60	1.59	1.57	1.55	1.55
$3.16 \cdot 10^4$	1.63	1.62	1.62	1.62	1.61	1.61	1.60	1.60
$1.00 \cdot 10^5$	1.63	1.63	1.63	1.63	1.62	1.62	1.62	1.62

Table 4.39: Atmospheric ν_μ and $\overline{\nu}_\mu$ Intensities as a Function of Zenith Angle. The values are $dN_\nu/d(\ln E_\nu)$, in units of $[\mathrm{cm}^{-2}\,\mathrm{s}^{-1}\,\mathrm{sr}^{-1}]$ and apply to solar minimum. Geomagnetic effects are disregarded (after Agrawal et al., 1996).

Neutrino Energy GeV]	Intensity $[\mathrm{cm}^{-2}\,\mathrm{s}^{-1}\,\mathrm{sr}^{-1}]$					
	$\cos(\theta) = 1.00$		$\cos(\theta) = 0.75$		$\cos(\theta) = 0.50$	
	ν_μ	$\overline{\nu}_\mu$	ν_μ	$\overline{\nu}_\mu$	ν_μ	$\overline{\nu}_\mu$
1	$1.88 \cdot 10^{-2}$	$1.74 \cdot 10^{-2}$	$1.99 \cdot 10^{-2}$	$1.90 \cdot 10^{-2}$	$2.09 \cdot 10^{-2}$	$2.08 \cdot 10^{-2}$
2	$5.38 \cdot 10^{-3}$	$4.97 \cdot 10^{-3}$	$5.79 \cdot 10^{-3}$	$5.53 \cdot 10^{-3}$	$6.31 \cdot 10^{-3}$	$6.16 \cdot 10^{-3}$
3	$2.47 \cdot 10^{-3}$	$2.23 \cdot 10^{-3}$	$2.74 \cdot 10^{-3}$	$2.55 \cdot 10^{-3}$	$3.03 \cdot 10^{-3}$	$2.89 \cdot 10^{-3}$
5	$9.63 \cdot 10^{-4}$	$8.36 \cdot 10^{-4}$	$1.07 \cdot 10^{-3}$	$9.51 \cdot 10^{-4}$	$1.20 \cdot 10^{-3}$	$1.07 \cdot 10^{-3}$
10	$2.77 \cdot 10^{-4}$	$2.21 \cdot 10^{-4}$	$2.89 \cdot 10^{-4}$	$2.46 \cdot 10^{-4}$	$3.31 \cdot 10^{-4}$	$2.78 \cdot 10^{-4}$
20	$7.19 \cdot 10^{-5}$	$5.46 \cdot 10^{-5}$	$7.65 \cdot 10^{-5}$	$6.16 \cdot 10^{-5}$	$8.72 \cdot 10^{-5}$	$7.18 \cdot 10^{-5}$
30	$3.23 \cdot 10^{-5}$	$2.34 \cdot 10^{-5}$	$3.58 \cdot 10^{-5}$	$2.59 \cdot 10^{-5}$	$4.01 \cdot 10^{-5}$	$3.07 \cdot 10^{-5}$
50	$1.16 \cdot 10^{-6}$	$7.99 \cdot 10^{-6}$	$1.28 \cdot 10^{-5}$	$9.07 \cdot 10^{-6}$	$1.45 \cdot 10^{-5}$	$1.08 \cdot 10^{-5}$
100	$2.80 \cdot 10^{-6}$	$1.73 \cdot 10^{-6}$	$3.11 \cdot 10^{-6}$	$1.99 \cdot 10^{-6}$	$3.59 \cdot 10^{-6}$	$2.39 \cdot 10^{-6}$
200	$6.71 \cdot 10^{-7}$	$3.67 \cdot 10^{-7}$	$7.37 \cdot 10^{-7}$	$4.26 \cdot 10^{-7}$	$8.62 \cdot 10^{-7}$	$5.28 \cdot 10^{-7}$
300	$2.69 \cdot 10^{-7}$	$1.43 \cdot 10^{-7}$	$3.21 \cdot 10^{-7}$	$1.75 \cdot 10^{-7}$	$3.71 \cdot 10^{-7}$	$2.14 \cdot 10^{-7}$
500	$8.95 \cdot 10^{-8}$	$4.40 \cdot 10^{-8}$	$1.02 \cdot 10^{-7}$	$5.23 \cdot 10^{-8}$	$1.25 \cdot 10^{-7}$	$6.64 \cdot 10^{-8}$
1000	$1.82 \cdot 10^{-8}$	$8.37 \cdot 10^{-9}$	$2.18 \cdot 10^{-8}$	$1.04 \cdot 10^{-8}$	$2.72 \cdot 10^{-8}$	$1.34 \cdot 10^{-8}$
2000	$3.33 \cdot 10^{-9}$	$1.50 \cdot 10^{-9}$	$4.10 \cdot 10^{-9}$	$1.87 \cdot 10^{-9}$	$5.53 \cdot 10^{-9}$	$2.58 \cdot 10^{-9}$
3000	$1.21 \cdot 10^{-9}$	$5.33 \cdot 10^{-10}$	$1.53 \cdot 10^{-9}$	$6.73 \cdot 10^{-10}$	$2.08 \cdot 10^{-9}$	$9.59 \cdot 10^{-10}$
5000	$3.33 \cdot 10^{-10}$	$1.41 \cdot 10^{-10}$	$4.28 \cdot 10^{-10}$	$1.80 \cdot 10^{-10}$	$5.98 \cdot 10^{-10}$	$2.60 \cdot 10^{-10}$
10000	$5.27 \cdot 10^{-11}$	$2.21 \cdot 10^{-11}$	$6.89 \cdot 10^{-11}$	$2.86 \cdot 10^{-11}$	$1.01 \cdot 10^{-10}$	$4.32 \cdot 10^{-11}$

Table 4.40: Atmospheric ν_μ and $\overline{\nu}_\mu$ Intensities as a Function of Zenith Angle. The values are $dN_\nu/d(\ln E_\nu)$, in units of $[\mathrm{cm}^{-2}\,\mathrm{s}^{-1}\,\mathrm{sr}^{-1}]$ and apply to solar minimum. Geomagnetic effects are disregarded (after Agrawal et al., 1996).

Neutrino Energy GeV]	Intensity $[\mathrm{cm}^{-2}\,\mathrm{s}^{-1}\,\mathrm{sr}^{-1}]$					
	$\cos(\theta) = 0.25$		$\cos(\theta) = 0.15$		$\cos(\theta) = 0.05$	
	ν_μ	$\overline{\nu}_\mu$	ν_μ	$\overline{\nu}_\mu$	ν_μ	$\overline{\nu}_\mu$
1	$2.24 \cdot 10^{-2}$	$2.29 \cdot 10^{-2}$	$2.35 \cdot 10^{-2}$	$2.40 \cdot 10^{-2}$	$2.40 \cdot 10^{-2}$	$2.38 \cdot 10^{-2}$
2	$7.01 \cdot 10^{-3}$	$7.08 \cdot 10^{-3}$	$7.45 \cdot 10^{-3}$	$7.61 \cdot 10^{-3}$	$7.78 \cdot 10^{-3}$	$7.77 \cdot 10^{-3}$
3	$3.47 \cdot 10^{-3}$	$3.38 \cdot 10^{-3}$	$3.65 \cdot 10^{-3}$	$3.68 \cdot 10^{-3}$	$3.83 \cdot 10^{-3}$	$3.89 \cdot 10^{-3}$
5	$1.41 \cdot 10^{-3}$	$1.34 \cdot 10^{-3}$	$1.50 \cdot 10^{-3}$	$1.47 \cdot 10^{-3}$	$1.61 \cdot 10^{-3}$	$1.63 \cdot 10^{-3}$
10	$3.89 \cdot 10^{-4}$	$3.55 \cdot 10^{-4}$	$4.22 \cdot 10^{-4}$	$3.94 \cdot 10^{-4}$	$4.74 \cdot 10^{-4}$	$4.59 \cdot 10^{-4}$
20	$1.06 \cdot 10^{-4}$	$9.03 \cdot 10^{-5}$	$1.15 \cdot 10^{-4}$	$1.01 \cdot 10^{-4}$	$1.33 \cdot 10^{-4}$	$1.23 \cdot 10^{-4}$
30	$4.74 \cdot 10^{-5}$	$3.95 \cdot 10^{-5}$	$5.34 \cdot 10^{-5}$	$4.53 \cdot 10^{-5}$	$6.10 \cdot 10^{-5}$	$5.58 \cdot 10^{-5}$
50	$1.77 \cdot 10^{-5}$	$1.38 \cdot 10^{-5}$	$1.98 \cdot 10^{-5}$	$1.60 \cdot 10^{-5}$	$2.34 \cdot 10^{-5}$	$1.98 \cdot 10^{-5}$
100	$4.51 \cdot 10^{-6}$	$3.20 \cdot 10^{-6}$	$5.00 \cdot 10^{-6}$	$3.74 \cdot 10^{-6}$	$6.00 \cdot 10^{-6}$	$4.80 \cdot 10^{-6}$
200	$1.10 \cdot 10^{-6}$	$7.04 \cdot 10^{-7}$	$1.23 \cdot 10^{-6}$	$8.29 \cdot 10^{-7}$	$1.49 \cdot 10^{-6}$	$1.09 \cdot 10^{-6}$
300	$4.82 \cdot 10^{-7}$	$3.02 \cdot 10^{-7}$	$5.34 \cdot 10^{-7}$	$3.40 \cdot 10^{-7}$	$6.49 \cdot 10^{-7}$	$4.45 \cdot 10^{-7}$
500	$1.67 \cdot 10^{-7}$	$9.93 \cdot 10^{-8}$	$1.82 \cdot 10^{-7}$	$1.09 \cdot 10^{-7}$	$2.18 \cdot 10^{-7}$	$1.43 \cdot 10^{-7}$
1000	$3.71 \cdot 10^{-8}$	$1.91 \cdot 10^{-8}$	$4.26 \cdot 10^{-8}$	$2.29 \cdot 10^{-8}$	$5.07 \cdot 10^{-8}$	$3.01 \cdot 10^{-8}$
2000	$7.93 \cdot 10^{-9}$	$3.88 \cdot 10^{-9}$	$9.39 \cdot 10^{-9}$	$4.72 \cdot 10^{-9}$	$1.14 \cdot 10^{-8}$	$6.01 \cdot 10^{-9}$
3000	$3.12 \cdot 10^{-9}$	$1.44 \cdot 10^{-9}$	$3.77 \cdot 10^{-9}$	$1.72 \cdot 10^{-9}$	$4.75 \cdot 10^{-9}$	$2.45 \cdot 10^{-9}$
5000	$9.37 \cdot 10^{-10}$	$4.20 \cdot 10^{-10}$	$1.14 \cdot 10^{-9}$	$5.03 \cdot 10^{-10}$	$1.50 \cdot 10^{-9}$	$6.91 \cdot 10^{-10}$
10000	$1.71 \cdot 10^{-10}$	$7.07 \cdot 10^{-11}$	$2.08 \cdot 10^{-10}$	$8.82 \cdot 10^{-11}$	$2.91 \cdot 10^{-10}$	$1.25 \cdot 10^{-10}$

Table 4.41: Atmospheric ν_e and $\overline{\nu}_e$ Intensities as a Function of Zenith Angle. The values are $dN_\nu/d(\ln E_\nu)$, in units of $[\mathrm{cm}^{-2}\,\mathrm{s}^{-1}\,\mathrm{sr}^{-1}]$ and apply to solar minimum. Geomagnetic effects are disregarded (after Agrawal et al., 1996).

Neutrino Energy GeV]	Intensity $[\mathrm{cm}^{-2}\,\mathrm{s}^{-1}\,\mathrm{sr}^{-1}]$					
	$\cos(\theta) = 1.00$		$\cos(\theta) = 0.75$		$\cos(\theta) = 0.50$	
	ν_e	$\overline{\nu}_e$	ν_e	$\overline{\nu}_e$	ν_e	$\overline{\nu}_e$
1	$8.23 \cdot 10^{-3}$	$6.51 \cdot 10^{-3}$	$9.75 \cdot 10^{-3}$	$7.24 \cdot 10^{-3}$	$1.15 \cdot 10^{-2}$	$8.85 \cdot 10^{-3}$
2	$2.03 \cdot 10^{-3}$	$1.56 \cdot 10^{-3}$	$2.54 \cdot 10^{-3}$	$2.00 \cdot 10^{-3}$	$3.16 \cdot 10^{-3}$	$2.46 \cdot 10^{-3}$
3	$7.87 \cdot 10^{-4}$	$6.66 \cdot 10^{-4}$	$1.04 \cdot 10^{-3}$	$8.17 \cdot 10^{-4}$	$1.36 \cdot 10^{-3}$	$1.11 \cdot 10^{-3}$
5	$2.50 \cdot 10^{-4}$	$2.02 \cdot 10^{-4}$	$3.09 \cdot 10^{-4}$	$2.58 \cdot 10^{-4}$	$4.35 \cdot 10^{-4}$	$3.52 \cdot 10^{-4}$
10	$4.15 \cdot 10^{-5}$	$3.68 \cdot 10^{-5}$	$5.99 \cdot 10^{-5}$	$4.83 \cdot 10^{-5}$	$8.60 \cdot 10^{-5}$	$7.18 \cdot 10^{-5}$
20	$7.77 \cdot 10^{-6}$	$6.47 \cdot 10^{-6}$	$1.01 \cdot 10^{-5}$	$8.39 \cdot 10^{-6}$	$1.57 \cdot 10^{-5}$	$1.30 \cdot 10^{-5}$
30	$2.82 \cdot 10^{-6}$	$2.35 \cdot 10^{-6}$	$3.66 \cdot 10^{-6}$	$3.03 \cdot 10^{-6}$	$5.76 \cdot 10^{-6}$	$4.61 \cdot 10^{-6}$
50	$7.44 \cdot 10^{-7}$	$6.25 \cdot 10^{-7}$	$1.05 \cdot 10^{-6}$	$7.80 \cdot 10^{-7}$	$1.51 \cdot 10^{-6}$	$1.22 \cdot 10^{-6}$
100	$1.48 \cdot 10^{-7}$	$1.16 \cdot 10^{-7}$	$1.77 \cdot 10^{-7}$	$1.52 \cdot 10^{-7}$	$2.67 \cdot 10^{-7}$	$1.96 \cdot 10^{-7}$
200	$2.46 \cdot 10^{-8}$	$2.37 \cdot 10^{-8}$	$3.59 \cdot 10^{-8}$	$2.55 \cdot 10^{-8}$	$5.01 \cdot 10^{-8}$	$3.87 \cdot 10^{-8}$
300	$1.14 \cdot 10^{-8}$	$7.41 \cdot 10^{-9}$	$1.25 \cdot 10^{-8}$	$1.03 \cdot 10^{-8}$	$2.01 \cdot 10^{-8}$	$1.22 \cdot 10^{-8}$
500	$3.29 \cdot 10^{-9}$	$2.15 \cdot 10^{-9}$	$3.83 \cdot 10^{-9}$	$2.63 \cdot 10^{-9}$	$5.26 \cdot 10^{-9}$	$3.90 \cdot 10^{-9}$
1000	$5.86 \cdot 10^{-10}$	$3.67 \cdot 10^{-10}$	$7.46 \cdot 10^{-10}$	$4.58 \cdot 10^{-10}$	$9.70 \cdot 10^{-10}$	$6.29 \cdot 10^{-10}$
2000	$1.00 \cdot 10^{-10}$	$6.23 \cdot 10^{-11}$	$1.26 \cdot 10^{-10}$	$7.80 \cdot 10^{-11}$	$1.75 \cdot 10^{-10}$	$1.14 \cdot 10^{-10}$
3000	$3.51 \cdot 10^{-11}$	$2.15 \cdot 10^{-11}$	$4.50 \cdot 10^{-11}$	$2.71 \cdot 10^{-11}$	$6.42 \cdot 10^{-11}$	$4.06 \cdot 10^{-11}$
5000	$9.24 \cdot 10^{-12}$	$5.45 \cdot 10^{-12}$	$1.18 \cdot 10^{-11}$	$7.01 \cdot 10^{-12}$	$1.73 \cdot 10^{-11}$	$1.07 \cdot 10^{-11}$
10000	$1.47 \cdot 10^{-12}$	$8.46 \cdot 10^{-13}$	$1.90 \cdot 10^{-12}$	$1.13 \cdot 10^{-12}$	$2.79 \cdot 10^{-12}$	$1.67 \cdot 10^{-12}$

Table 4.42: Atmospheric ν_e and $\overline{\nu}_e$ Intensities as a Function of Zenith Angle. The values are $dN_\nu/d(\ln E_\nu)$, in units of $[\mathrm{cm}^{-2}\,\mathrm{s}^{-1}\,\mathrm{sr}^{-1}]$ and apply to solar minimum. Geomagnetic effects are disregarded (after Agrawal et al., 1996).

Neutrino Energy GeV]	Intensity $[\mathrm{cm}^{-2}\,\mathrm{s}^{-1}\,\mathrm{sr}^{-1}]$					
	$\cos(\theta) = 0.25$		$\cos(\theta) = 0.15$		$\cos(\theta) = 0.05$	
	ν_e	$\overline{\nu}_e$	ν_e	$\overline{\nu}_e$	ν_e	$\overline{\nu}_e$
1	$1.36 \cdot 10^{-2}$	$1.02 \cdot 10^{-2}$	$1.40 \cdot 10^{-2}$	$1.15 \cdot 10^{-2}$	$1.48 \cdot 10^{-2}$	$1.17 \cdot 10^{-2}$
2	$4.09 \cdot 10^{-3}$	$3.26 \cdot 10^{-3}$	$4.58 \cdot 10^{-3}$	$3.55 \cdot 10^{-3}$	$4.89 \cdot 10^{-3}$	$3.83 \cdot 10^{-3}$
3	$1.90 \cdot 10^{-3}$	$1.48 \cdot 10^{-3}$	$2.16 \cdot 10^{-3}$	$1.68 \cdot 10^{-3}$	$2.38 \cdot 10^{-3}$	$1.90 \cdot 10^{-3}$
5	$6.72 \cdot 10^{-4}$	$5.42 \cdot 10^{-4}$	$7.93 \cdot 10^{-4}$	$6.50 \cdot 10^{-4}$	$9.47 \cdot 10^{-4}$	$7.54 \cdot 10^{-4}$
10	$1.46 \cdot 10^{-4}$	$1.21 \cdot 10^{-4}$	$1.88 \cdot 10^{-4}$	$1.56 \cdot 10^{-4}$	$2.47 \cdot 10^{-4}$	$2.02 \cdot 10^{-4}$
20	$2.89 \cdot 10^{-5}$	$2.35 \cdot 10^{-5}$	$3.98 \cdot 10^{-5}$	$3.22 \cdot 10^{-5}$	$5.84 \cdot 10^{-5}$	$4.70 \cdot 10^{-5}$
30	$1.10 \cdot 10^{-5}$	$9.05 \cdot 10^{-6}$	$1.52 \cdot 10^{-5}$	$1.27 \cdot 10^{-5}$	$2.53 \cdot 10^{-5}$	$1.99 \cdot 10^{-5}$
50	$2.97 \cdot 10^{-6}$	$2.43 \cdot 10^{-6}$	$4.26 \cdot 10^{-6}$	$3.65 \cdot 10^{-6}$	$7.28 \cdot 10^{-6}$	$6.25 \cdot 10^{-6}$
100	$4.89 \cdot 10^{-7}$	$4.18 \cdot 10^{-7}$	$7.43 \cdot 10^{-7}$	$6.30 \cdot 10^{-7}$	$1.40 \cdot 10^{-6}$	$1.12 \cdot 10^{-6}$
200	$8.48 \cdot 10^{-8}$	$6.79 \cdot 10^{-8}$	$1.16 \cdot 10^{-7}$	$9.16 \cdot 10^{-8}$	$2.43 \cdot 10^{-7}$	$1.87 \cdot 10^{-7}$
300	$3.05 \cdot 10^{-8}$	$2.49 \cdot 10^{-8}$	$4.19 \cdot 10^{-8}$	$3.34 \cdot 10^{-8}$	$7.62 \cdot 10^{-8}$	$6.28 \cdot 10^{-8}$
500	$8.42 \cdot 10^{-9}$	$6.94 \cdot 10^{-9}$	$1.11 \cdot 10^{-8}$	$8.57 \cdot 10^{-9}$	$2.00 \cdot 10^{-8}$	$1.62 \cdot 10^{-8}$
1000	$1.52 \cdot 10^{-9}$	$9.78 \cdot 10^{-10}$	$1.98 \cdot 10^{-9}$	$1.47 \cdot 10^{-9}$	$3.30 \cdot 10^{-9}$	$2.61 \cdot 10^{-9}$
2000	$2.68 \cdot 10^{-10}$	$1.78 \cdot 10^{-10}$	$3.86 \cdot 10^{-10}$	$2.42 \cdot 10^{-10}$	$5.20 \cdot 10^{-10}$	$4.02 \cdot 10^{-10}$
3000	$1.01 \cdot 10^{-10}$	$6.45 \cdot 10^{-11}$	$1.28 \cdot 10^{-10}$	$8.35 \cdot 10^{-11}$	$2.01 \cdot 10^{-10}$	$1.40 \cdot 10^{-10}$
5000	$2.86 \cdot 10^{-11}$	$1.79 \cdot 10^{-11}$	$3.55 \cdot 10^{-11}$	$2.25 \cdot 10^{-11}$	$5.41 \cdot 10^{-11}$	$3.40 \cdot 10^{-11}$
10000	$4.84 \cdot 10^{-12}$	$2.93 \cdot 10^{-12}$	$6.05 \cdot 10^{-12}$	$3.63 \cdot 10^{-12}$	$8.76 \cdot 10^{-12}$	$5.38 \cdot 10^{-12}$

Table 4.43: Geomagnetic Correction Coefficients for Zenith Angle Dependence of Upward-going ν_μ and $\overline{\nu}_\mu$ for Several Experimental Locations (Agrawal et al., 1996).

Location	Neutrino Energy [GeV]	Correction Coefficients												
		Solar Maximum						Solar Minimum						
		cos(θ)						cos(θ)						
		-1.00	-0.75	-0.50	-0.25	-0.15	-0.05	-1.00	-0.75	-0.50	-0.25	-0.15	-0.05
Kamio-kande	1.0	0.75	0.70	0.69	0.64	0.60	0.56	0.75	0.70	0.69	0.64	0.61	0.57
	2.0	0.92	0.88	0.87	0.83	0.78	0.75	0.92	0.88	0.88	0.84	0.79	0.75
	3.0	0.99	0.96	0.95	0.90	0.88	0.85	1.00	0.96	0.96	0.90	0.88	0.85
	5.0	1.00	0.98	1.00	0.94	0.94	0.93	1.00	0.98	1.00	0.94	0.94	0.93
IMB	1.0	0.89	0.90	0.91	0.91	0.87	0.78	0.98	0.99	1.00	1.00	0.94	0.84
	2.0	0.96	0.96	0.97	0.97	0.95	0.90	0.98	0.99	1.00	1.00	0.97	0.91
	3.0	1.00	0.98	1.00	0.98	0.99	0.96	1.00	0.99	1.00	1.00	0.99	0.96
	5.0	1.00	0.99	1.00	0.99	0.99	0.99	1.00	1.00	1.00	1.00	0.99	0.99
Fréjus	1.0	0.86	0.87	0.87	0.82	0.75	0.68	0.92	0.93	0.92	0.86	0.79	0.72
Gran Sasso	2.0	0.96	0.95	0.96	0.95	0.88	0.83	0.98	0.97	0.98	0.96	0.90	0.84
	3.0	1.00	0.98	1.00	0.97	0.95	0.@1	1.00	1.00	1.00	0.97	0.96	0.91
	5.0	1.00	0.99	1.00	0.98	0.97	0.96	1.00	1.00	1.00	0.99	0.98	0.97
Soudan SNO	1.0	0.89	0.90	0.90	0.92	0.89	0.83	0.98	0.99	1.00	1.00	0.97	0.89
	2.0	0.96	0.96	0.97	0.98	0.96	0.93	0.98	0.99	1.00	1.00	0.98	0.94
	3.0	1.00	0.99	1.00	0.99	0.99	0.98	1.00	1.00	1.00	1.00	1.00	0.98
	5.0	1.00	1.00	1.00	1.00	0.99	0.99	1.00	1.00	1.00	1.00	1.00	0.99

This newer generation of experiments, some of which are still in operation, includes the following installations: The detectors near Park City (Utah) (Bergeson et al., 1965; Hendricks et al., 1970), at Baksan in Southern Russia (Alexeyev et al., 1979), another one at the Kolar Gold Fields (Krishnaswami et al., 1983), the NUSEX and LSD experiments in the Mont Blanc tunnel (Battistoni et al., 1983; Aglietta et al., 1985), the IMB (LoSecco et al., 1985), Kamiokande I and II (Arisaka et al., 1985; Beier, 1986), Fréjus (Berger et al., 1987 and 1989), Soudan I and II (Ayres et al., 1985; Ambats et al., 1987), MACRO (Stone et al., 1985) and, most recently, the Superkamiokande (Suzuki, 1994) and SNO (McDonald, 1996) experiments, to mention only the large underground efforts.

Presently the new generation of very large three-dimensional Cherenkov detector matrices such as the Lake Baikal installation (Balkanov et al., 1999) or the deep ocean detector arrays such as the pioneering but discontinued DUMAND (Deep Underwater Muon And Neutrino Detector) experiment (Grieder, 1986 and 1993), the NESTOR muon and neutrino telescope now under construction (Resvanis, 1996), the ANTARES project (Hubbard, 1999; Moscoso et al., 1999) and the operational AMANDA array located deep in the polar ice cap at Antarctica (Andrés et al., 1999) are expected to detect and identify ultrahigh energy astrophysical neutrinos in the near future.

Neutrino Flux and Intensities

The pioneering experiments mentioned above and many of the early successors have measured the intensity of neutrino induced upward or horizontal muons but could not reconstruct or analyze the neutrino events in detail. We have summarized the results of these experiments together with the intensity measurements recorded by the large and sophisticated modern detectors in Table 4.44.

4.5.6 Experimental Results, Modern Work

Experimental Identification of Neutrino Flavor

Experiments cannot directly determine whether a particular event was initiated by a ν_μ ($\overline{\nu}_\mu$) or a ν_e ($\overline{\nu}_e$), but they can differentiate between muons and electrons resulting from a neutrino interaction. In the sub- to multi-GeV region muons resulting from a muon neutrino reaction make clean non-showering single tracks whereas electrons produce electron-photon showers. This implies that for example in a water tank muons produce fairly clean optical Cherenkov rings. On the other hand, electrons produce circular light

Table 4.44: Upward-going and Horizontal Muon Intensities Underground

Experiment	Intensity $[10^{-13}\,cm^{-2}\,s^{-1}\,sr^{-1}]$	Energy [GeV]	Reference
Baksan	1.92 ± 0.44	> 2	Boliev et al. (1981)
	2.36 ± 0.12	> 1	Boliev et al. (1990)
	2.77 ± 0.17	> 1	Boliev et al. (1991)
	2.08 ± 0.14	> 3	Frati et al. (1993)*
	2.72 ± 0.16	> 1	Boliev et al. (1995)
ERPM	4.10 ± 0.60	> 0.1	Reines (1969)
	3.70 ± 0.60	> 0.1	Crouch et al. (1970)
horizontal	4.59 ± 0.42	> 0.1	Crouch et al. (1978)
vertical	2.23 ± 0.20	> 0.1	Crouch et al. (1978)
Fréjus	3.67 ± 0.66	> 0.2	Rhode et al. (1996)
IMB	2.41 ± 0.21	> 2	Svoboda et al. (1987)
	2.26 ± 0.11	> 2	Becker-Szendy et al. (1990)
	1.92 ± 0.11	> 3	Frati et al. (1993)*
Kamiokande	2.05 ± 0.18	> 2	Oyama et al. (1987)
	2.04 ± 0.13	> 3	Mori et al. (1991)
	$1.94 \pm 0.0.10^{+0.07}_{-0.06}$	> 1.6	Kajita (1999)
KGF	3.4 ± 0.8		Krishnaswami et al. (1970)
LVD	8.3 ± 0.26	> 1	Sartorelli et al. (1995)
MACRO	1.2 ± 0.2	> 1	Ronga (2000)
$\cos(\theta) = -0.05$	7.0 ± 2.4	> 1	Ronga (2000)
Superkamiokande	$1.75 \pm 0.07 \pm 0.09$	> 1.6	Kajita (1999)

* Data rescaled by Frati et al. (1993) to E >3GeV for comparison with Kamiokande.

patches with fuzzy edges. At higher energies ν_μ ($\overline{\nu}_\mu$) initiated reactions, too, get more complex and are more difficult to interpret.

If in a detector an event resembles a muon (electron), it is assumed that a ν_μ (ν_e) or $\overline{\nu}_\mu$ ($\overline{\nu}_e$) initiated the interaction and the event is designated $\mu-like$ ($e-like$). The ratio of the quotient of eq. 4.66 obtained experimentally to the one determined theoretically is called the *ratio of ratios* and is defined as

$$R = \frac{(N_{\mu-like}/N_{e-like})_{measured}}{(N_{\mu-like}/N_{e-like})_{theoretical}} \simeq \frac{(N_{\nu_\mu}/N_{\nu_e})_{measured}}{(N_{\nu_\mu}/N_{\nu_e})_{theoretical}} \ , \qquad (4.70)$$

where $N_{\mu-like}$ stands for $(\nu_\mu+\overline{\nu}_\nu)$-like and N_{e-like} for $(\nu_e+\overline{\nu}_e)$-like initiated events. This ratio is one of the two relevant experimental quantities for studying neutrino oscillations.

Neutrino Intensity Measurements and Spectra

The atmospheric neutrino intensities measured by the large modern detectors are listed together with those from the early experiments in Table 4.44. In Fig. 4.87 we show the depth-intensity plot of the Fréjus experiment for through-going and stopping muons (Rhode, 1993). The asymptotic intensity is evidently due to neutrino induced muons. Only few spectral measurements were made. In Fig. 4.88 we show the energy spectra of electron $(\nu_e+\overline{\nu}_e)$ and muon neutrinos $(\nu_\mu+\overline{\nu}_\mu)$ that were measured with the fine-grained Fréjus detector (Rhode et al., 1995 and 1996).

For neutrino energies >1 GeV Rhode et al. (1995) have parameterized the differential atmospheric neutrino spectra using the expression

$$j_\nu(E) = j_0 E_\nu^{-\gamma} \left(\frac{1}{1+6E_\nu/E_\pi(\theta)} + \frac{0.213}{1+1.44E_\nu/E_{K^\pm}(\theta)} \right) \ , \qquad (4.71)$$

where $E_{\pi^\pm}(\theta)$ and $E_{K^\pm}(\theta)$ are the zenith angle dependent critical energies accounting for the $\pi^\pm$ and $K^\pm$ decay length, respectively. These authors find that a fit to their data for $E_\nu \geq 3$ GeV leads to a spectral index for the atmospheric muon neutrino intensity of

$$\gamma = 2.66 \pm 0.05(\text{stat.}) \pm 0.03(\text{syst.}) \qquad (4.72)$$

and

$$j_0 = (2.5 \pm 0.2(\text{stat.}) \pm 0.3(\text{syst.})) \cdot 10^{-2} \ [\text{cm}^2\,\text{s}^{-1}\,\text{sr}^{-1}\,\text{GeV}^{\gamma-1}] \ . \qquad (4.73)$$

Momentum distributions of e-like and μ-like events recorded with the Super-Kamiokande detector are illustrated in Figs. 4.89 and 4.90, respectively (Fukuda et al., 1998).

Zenith Angle Dependence and Neutrino Oscillations

Fig. 4.91 shows a plot of the ratio of stopping to through-going muons versus zenith angle, measured with the Super-Kamiokande detector and theoretical distributions with and without oscillations. The observed ratio of the (stopping/through-going) muon flux, R, obtained by Kajita (2000) is

$$R = 0.235 \pm 0.018(\text{stat.})^{+0.013}_{-0.011}\text{syst.}) \tag{4.74}$$

whereas the calculated value is

$$R = 0.37^{+0.049}_{-0.044} \tag{4.75}$$

Other sets of data to investigate neutrino oscillations based on zenith angle distributions are presented in Fig. 4.92 from measurements with the MACRO detector (Ronga, 1999 and 2000) and in Fig. 4.93 from Super-Kamiokande (Scholberg, 1999). Both sets use upward through-going muons. An additional set of data showing the full range of zenith angle measurements, from the downward to the upward direction, carried out on e-like and μ-like fully and partially contained events at Super-Kamiokande is illustrated in Fig. 4.94 together with predicted distributions (Scholberg, 1999).

Because of the many uncertainties involved in the determination of the absolute neutrino intensity and its zenith angle dependence as well as because of theoretical problems concerning the simulations, discussed before, it is impossible to get a clear-cut answer whether neutrino oscillations occur or not from these measurements.

Azimuthal Distribution and East-West Effect

The azimuthal distributions of e-like and μ-like events and the corresponding theoretical predictions reflect the various geomagnetic problems and question of local isotropy of the low energy primary cosmic radiation, discussed earlier. Fig. 4.95 which shows measured azimuthal distributions from Super-Kamiokande and predictions illuminates the problems (Scholberg, 1999; Futagami et al., 1999).

Measured Neutrino Flavor Ratios

Neutrino flavor ratio measurements yield information about neutrino oscillations that are independent of the knowledge of the absolute flux of atmospheric neutrinos. Measurements from different experiments can be compared with less inherent ambiguities. The flavor ratio is at present the most reliable experimental signature for neutrino oscillations.

The method to search for neutrino oscillations by this method is to compare the experimentally determined flavor ratio with Monte Carlo predictions (Hirata et al., 1992). The latter are made for a specific measurement and a given set of oscillation parameters Δm^2 and $\sin^2(2\theta)$, described before, and for the same calculation without oscillation. The measure that is used for comparison is the previously mentioned ratio of ratios, R, defined above. We have listed the results for R from different experiments and for different analyses carried out through the years by various authors in Table 4.45.

Table 4.45: Summary of Ratio-of-Ratios Results, R

Experiment	Ratio-of-Ratios R	Reference
Fréjus contained	$0.87 \pm 0.13 \pm 0.08$	a)
Fréjus uncontained	1.04 ± 0.13	a)
Fréjus all	$0.99 \pm 0.13 \pm 0.08$	b)
IMB-1	0.68 ± 0.08	c)
IMB-3 Ring Events	$0.54 \pm 0.05 \pm 0.11$	d)
IMB-3 μ-Decay Events	0.64 ± 0.07	d)
Kamiokande Sub-GeV	$0.60^{+0.06}_{-0.05} \pm 0.05$	e)
Kamiokande Multi-GeV	$0.57^{+0.08}_{-0.07} \pm 0.07$	e)
MACRO	$0.73 \pm 0.09 \pm 0.06 \pm 0.12$	f)
MACRO $< E_\mu > = 100$ GeV	$0.74 \pm 0.036 \pm 0.046 \pm 0.13$	g)
NUSEX	$0.99 \pm 0.40 \pm 0.00$	h)
Super-Kamiokande Sub-GeV	$0.63 \pm 0.03 \pm 0.05$	i)
Super-Kamiokande Sub-GeV	$0.63 \pm 0.03 \pm 0.05$	i)
Super-Kamiokande Multi-GeV	$0.65 \pm 0.05 \pm 0.08$	j)
Super-Kamiokande <1.3 GeV	$0.668^{0.024}_{0.023} \pm 0.052$	j)
Super-Kamiokande >1.3 GeV	$0.663^{0.044}_{0.041} \pm 0.079$	k)
Soudan-II	$0.64 \pm 0.11 \pm 0.06$	l)

a) Meyer (1993) (see also Berger et al., 1990), b) Rhode et al. (1995), c) Haines et al. (1986), d) Casper et al. (1991), Becker-Szendy et al. (1992), e) Fukuda et al. (1994), f) Ahlen et al. (1995), g) Ronga (1999), h) Aglietta et al. (1989), i) Fukuda et al., (1998), j) Kajita (1999), k) Kaneyuki et al. (1999), l) Allison et al. (1997 and 1999), Peterson (1999).

With the exception of the Fréjus and NUSEX experiments, the bulk of

the experimental results listed in Table 4.45 agree with each other and are consistently lower than expected, which leads to the conclusion that neutrino oscillations may be the cause for the discrepancy.

In Fig. 4.96 we show the resulting $\nu_\mu \rightarrow \nu_\tau$ oscillation confidence level contours of allowed regions deduced from the combined data of fully contained and partially contained upward going muons in Superkamiokande (Scholberg, 1999).

References

[h] Achar, C.V., M.G.K. Menon, V.S. Narasimham, P.V. Ramana-Murthy, B.V. Sreekantan, K. Hinotani, S. Miyake, D.R. Creed, J.L. Osborne, J.B.M. Pattison, and A.W. Wolfendale: PICRC, 2, p. 1012 (1965).

Aglietta, M., G. Badino, G.F. Bologna, C. Castagnoli, W. Fulgione, P. Galeotti, O. Saavedra, G.C. Trinchero, S. Vernetto, V.L. Dadykin, V.B. Korchagin, P.V. Korchagin, A.S. Malgin, F.G. Ryassny, O.G. Ryazhskaya, V.P. Talochkin, G.T. Zatsepin, V.F. Yakushev: PICRC, 8, p. 108 (1985).

Aglietta, M., G. Battistoni, E. Bellotti, C. Bloise, G. Bologna, C. Broggini, P. Campana, C. Castagnoli, A. Castellina, V. Chiarella, O. Cremonesi, D. Cundy, B. D'Ettore Piazzoli, E. Fiorini, W. Fulgione, P. Galeotti, E. Iarocci, C. Liguori, G. Mannocchi, G. Murtas, P. Negri, G. Nicoletti, P. Picchi, M. Price, A. Pullia, S. Ragazzi, O. Saavedra, L. Satta, S. Vernetto, and L. Zanotti: Europhys. Lett., 8, p. 611 (1989).

Agrawal, Vivek, T.K. Gaisser, P. Lipari, and T. Stanev: Phys. Rev., D 53, p. 1314 (1996).

Ahlen, S., M. Ambrosio, R. Antolini, G. Auriemma, R. Baker, A. Baldini, G.C. Barbarino, B.C. Barish, G. Battistoni, R. Bellotti, C. Bemporad, P. Bernardini, H. Bilokon, V. Bisi, C. Bloise, C. Bower, S. Bussino, F. Cafagna, M. Calicchio, D. Campana, M. Carboni, M. Castellano, S. Cecchini, F. Cei, P. Celio, V. Chiarella, R. Cormack, A. Corona, S. Coutu, G. De Cataldo, H. Dekhissi, C. De Marzo, E. Diehl, I. De Mitri, M. De Vincenzi, A. Di Credico, 0. Erriquez, C. Favuzzi, C. Forti, P. Fusco, G. Giacomelli, G. Giannini, N. Giglietto, M. Grassi, P. Green, A. Grillo, F. Guarino, P. Guarnaccia, C. Gustavino, A. Habig, K. Hanson, A. Hawthorne, R. Heinz, J.T. Hong, E. Iarocci, E. Katsavounidis, E. Kearns, S. Kyriazopoulou, E. Lamanna, C. Lane, D.S. Levin, P. Lipari, G. Liu, R. Liu, N.P. Longley, M.J. Longo, Y. Lu, G. Ludlam, G. Mancarella, G. Mandrioli, A. Margiotta-Neri, A. Marini, D. Martello, A. Marzari-Chiesa, M.N. Mazziotta, D.G. Michael, S. Mikheyev, L. Miller, M. Mittelbrunn, P. Monacelli, T. Montaruli, M. Monteno, S. Mufson,

J. Musser, D. Nicoló, R. Nolty, S. Nutter, C. Okada, C. Orth, G. Osteria, 0. Palamara, S. Parlati, V. Patera, L. Patrizii, R. Pazzi, C.W. Peck', J. Petrakis, S. Petrera, N.D. Pignatano, P. Pistilli, V. Popa, A. Rainó, J. Reynoldson, F. Ronga, A. Sanzgiri, F. Sartogo, C. Satriano, L. Satta, E. Scapparone, K. Scholberg, A. Sciubba, P. Serra-Lugaresi, M. Severi, M. Sitta, P. Spinelli, M. Spinetti, M. Spurio, R. Steinberg, J.L. Stone, L.R. Sulak, A. Surdo, G. Tarlé, V. Togo, V. Valente, C.W. Walter, R. Webb, and W. Worstell. MACRO Collaboration: Phys. Lett., B 357, p. 481 (1995).

Alexeyev, E.N., V.V. Alexeyenko, Yu.M. Andreyev, V.N. Bakatanov, A.N. Budkevich, A.E. Chudakov, M.D. Gal'perin, A.A. Gitelson, V.I. Gurentsov, A.E. Danshin, V.A. Dogujaev, V.L. Dadykin, Ya.S. Elensky, V.A. Kozyarivsky, I.M. Kogai, N.F. Klimenko, A.A. Kiryishin, Yu.N. Konovalov, B.A. Makoev, V.Ya. Markov, Yu.Ya. Markov, Yu.V. Malovichko, N.A. Metlinsky, A.R. Mikhelev, S.P. Mikheyev, Yu.S. Novosel'tsev, V.G. Sborshikov, V.V. Sklyarov, Yu.V. Sten'kin, V.I. Stepanov, Yu.R. Sula-Petrovsky, T.I. Tulupova, A.V. Voevodsky, V.I. Volchenko, and V.N. Zakidyshev: PICRC, 10, p. 276 (1979).

Allison, W.W.M., G.J. Alner, D.S. Ayres, W.L. Barrett, C. Bode, P.M. Border, C.B. Brooks, J.H. Cobb, D.J.A. Cockerill, R.J. Cotton, H. Courant, D.M. DeMuth, T.H. Fields, H.R. Gallagher, C. Garcia-Garcia, M.C. Goodman, R.N. Gray, K. Johns , T. Kafka, S.M.S. Kasahara, W. Leeson, P.J. Litchfield, N.P. Longley, M.J. Lowe, W.A. Mann, M.L. Marshak, E.N. May, R.H. Milburn, W.H. Miller, L. Mualem, A. Napier, W. Oliver, G.F. Pearce, D.H. Perkins, E.A. Peterson, D.A. Petyt, L.E. Price, D.M. Roback, K. Ruddick, D.J. Schmid, J. Schneps, M.H. Schub, R.V. Seidlein, M.A. Shupe, A. Stassinakis, N. Sundaralingam, J.Thomas, J.L. Thron, V. Vassiliev, G. Villaume, S.P. Wakely, D. Wall, S.J. Werkema, N. West, and U.M. Wielgosz: Phys. Lett., B 391, p. 491 (1997).

Allison, W.W.M., G.J. Alner, D.S. Ayres, G. Barr, W.L. Barrett, C. Bode, P.M. Border, C.B. Brooks, J.H. Cobb, R.J. Cotton, H. Courant, D.M. DeMuth, T.H. Fields, H.R. Gallagher, C. Garcia-Garcia, M.C. Goodman, R. Gran, T. Joffe-Minor, T. Kafka, S.M.S. Kasahara, W. Leeson, P.J. Litchfield, N.P. Longley, W.A. Mann, M.L. Marshak, R.H. Milburn, W.H. Miller, L. Mualem, A. Napier, W. Oliver, G.F. Pearce, E.A. Peterson, D.A. Petyt, L.E. Price, K. Ruddick, M. Sanchez, J. Schneps, M.H. Schub, R.V. Seidlein, A. Stassinakis, J.L. Thron, V. Vassiliev, G. Villaume, S. Wakely, D. Wall, N. West, and U.M. Wielgosz: Phys. Lett., B 449, p. 137 (1999).

Allkofer, O.C., T. Kitamura, A. Odada, and W. Vernon: PICRC, 10, p. 411 (1979a).

Allkofer, O.C., T. Kitamura, A. Okada, and W. Vernon: Proc. 1978 DUMAND Summer Workshop, A. Roberts (ed), 1, p. 37 (1979b).

Ambats, I., D. Ayres, W. Barrett, J. Dawson, T. Fields, M.C. Goodman, F. Lopez, E. May, L. Price, J. Schlereth, J. Thron, H. Courant, U. DasGupta, D. Feyma, K. Heller, S. Heppelman, K. Johns, T. Joyce, M. Marshak, E. Peterson, D. Rosen, K. Ruddick, M. Shupe, S. Werkema, W. Allison, G. Barr, C. Brooks, J. Cobb, R. Giles, A. Gilgrass, L. Kirby-Gallagher, D. Perkins, P. Shields, N. West, J. Alner, D. Cockerill, C. Garcia, P. Litchfield, G. Pearce, C. Roberts, E. Wallis, C. Woods, S. Yarker, D. Benjamin, T. Kafka, J. Kochocki, A. Mann, R. Milburn, A. Napier, W. Oliver, B. Saitta, J. Schneps, K. Shaw, and N. Sundarlingam, Soudan Collaboration: PICRC, 6, p. 246 (1987).

Andrés, E.C., P. Askebjer, S.W. Barwick, R.C. Bay, L. Bergström, A. Biron, J. Booth, 0. Botner, A. Bouchta, S. Carius, M. Carlson, W. Chinowsky, D. Chirkin, J. Conrad, C.G.S. Costa, D. Cowen, E. Dalberg, T. DeYoung, J. Edsjö, P. Ekström, A. Goobar, L. Gray, A. Hallgren, F. Halzen, R. Hardtke, S. Hart, Y. He, C.P. de los Heros, G. Hill, P.0. Hulth, S. Hundertmark, J. Jacobsen, A. Jones, V. Kandhadai, A. Karl, J. Kim, H. Leich, M. Leuthold, P. Lindahl, I. Liubarsky, P. Loaiza, D. Lowder, P. Marciniewski, T.C. Miller, P. Miocinovic, P.C. Mock, R. Morse, M. Newcomer, P. Niessen, D. Nygren, R. Porrata, D. Potter, P.B. Price, G. Przybylski, W. Rhode, S. Richter, J. Rodriguez, P. Romenesko, D. Ross, H. Rubinstein, T. Schmidt, E. Schneider, R. Schwarz, U. Schwendicke, G. Smoot, M. Solarz, V. Sorin, C. Spiering, P. Steffen, R. Stokstad, 0. Streicher, I. Taboada, T. Thon, S. Tilav, C. Walck, C.H. Wiebusch, R. Wischnewski, K. Woschnagg, W. Wu, G. Yodh, S. Young: Nucl. Phys., B (Proc. Suppl.) 77, p. 474 (1999).

Apollonio, M., A. Baldini, C. Bemporad, E. Caffau, F. Cei, Y. Déclais, H. de Kerret, B. Dieterle, A. Etenko, J. George, G. Giannini, M. Grassi, Y. Kozlov, W. Kropp, D. Kryn, M. Laiman, C.E. Lane, B. Lefièvre, I. Machulin, A. Martemyanov, V. Martemyanov, L. Mikaelyan, D. Nicolò, M. Obolensky, R. Pazzi, G. Pieri, L. Price, S. Riley, R. Reeder, A. Sabelnikov, G. Santin, M. Skorokhvatov, H. Sobel, J. Steele, R. Steinberg, S. Sukhotin, S. Tomshaw, D. Verson, and V. Vyrodov: Phys. Lett., B 420, p. 397 (1998).

Arisaka, Katsushi, Takaaki Kajita, Masatoshi Koshiba, Masayuki Nakahata, Yuichi Oyama, Atsuto Suzuki, Masato Takita, Yoji Totsuka, Tadashi Kifune, Teruhiro Suda, Kasuke Takahashi, and Kazumasa Miyano: J. Phys. Soc. Japan, 54, p. 3213 (1985).

Ayres, D.S., W.L. Barrett, J.W. Dawson, T.H. Fields, M.C. Goodman, J. Hoftiezer, E.N. May, N.K. Mondal, L.E. Price, J.L. Schlereth, J.L. Thron,

T. Kafka, W.A. Mann, R. Milburn, A. Napier, W. Oliver, J. Schneps, H. Courant, K. Heller, S. Heppelmann, T. Joyce, M. Marshak, E. Peterson, K. Ruddick, M. Shupe, W.W.M. Allison, G. Barr, C.B. Brooks, J.H. Cobb, D.H. Perkins, P. Shield, D. Cockerill, P.J. Lichtfield, G.F. Pearce, and E.W.G. Wallis: PICRC, 8, p. 267 (1985).

Bahcall, John, N.: Nucl. Phys., B (Proc. Suppl.), 77, p. 64 (1999).

Balkanov, V.A., I.A. Belolaptikov, L.B. Bezrukov, N.M. Budnev, A.G. Chensky, I.A. Danilchenko, Zh.-A.M. Djilkibaev, G.V. Domogatsky, A.A. Doroshenko, S.V. Fialkovsky, 0.N. Gaponenko, A.A. Garus, T.I. Gress, A.M. Klabulov, A.I. Klimov, S.I. Klimushin, A.P. Koshechkin, E.V. Kuznetzov, V.F. Kulepov, L.A. Kuzmichev, S.V. Lovtzov, B.K. Lubsandorzhiev, M.B. Milenin, R.R. Mirgazov, A.V. Moroz, N.I. Moseiko, V.A. Netikov, E.A. Osipova, A.I. Panfilov, Yu.V. Parfenov, A.A. Pavlov, E.N. Pliskovsky, P.G. Pohil, E.G. Popova, M.I. Rozanov, V.Yu. Rubzov, I.A. Sokalski, Ch. Spiering, 0. Streicher, B.A. Tarashansky, T. Thon, R.V. Vasiljev, R. Wischnewski, I.V. Yashin. Baikal Collaboration: Nucl. Phys., B (Proc. Suppl.) 77, p. 486 (1999).

Barr, Stephen, T.K. Gaisser, Paolo Lipari, and Serap Tilav: Phys. Lett., B 214, p. 3532 (1988).

Barr, Giles, T.K. Gaisser, and Todor Stanev: Phys. Rev., D 39, p. 3532 (1989).

Battistoni, G., E. Bellotti, G. Bologna, P. Campana, C. Castagnoli, A. Castellina, V. Chiarella, D.C. Cundy, B. D'Ettorre-Piazzoli, E. Fiorini, P. Galeotti, R. Iarocci, C. Liguori, G. Mannocchi, G.P. Murtas, P. Negri, G. Nicoletti, P. Picchi, A. Pullia, M. Price, S. Ragazzi, M. Rollier, O. Saavedra, L. Satta, L. Trasatti, S. Vernetto, and L. Zanotti: PICRC, 11, p. 466 (1983).

Battistoni, G., A. Ferrari, P. Lipari, T. Montaruli, P.R. Sala, and T. Rancati: Astropart. Phys., 12, p. 315 (2000).

Becker-Szendy, R., C.B. Bratton, D.R. Cady, D. Casper, R. Claus, M. Crouch, S.T. Dye, W. Gajewski, M. Goldhaber, T.J. Haines, P.G. Halverson, T.W. Jones, D. Kielczewska, W.R. Kropp, J.G. Learned, J.M. LoSecco, C. McGrew, S. Matsuno, J. Matthews, M.S. Mudan, L. Price, F. Reines, J. Schultz, D. Sinclair, H.W. Sobel, J.L. Stone, L.R. Sulak, R. Svoboda, G. Thornton, and J.C. van der Velde: Phys. Rev., D 42, p. 2974 (1990).

Becker-Szendy, R., C.B. Bratton, D. Casper, S.T. Dye, W. Gajewski, M. Goldhaber, T.J. Haines, P.G. Halverson, D. Kielczewska, W.R. Kropp, J.G. Learned, J.M. LoSecco, S. Matsuno, G. McGrath, C. McGrew, R. Miller, L.R. Price, F. Reines, J. Schultz, H.W. Sobel, J.L. Stone, L.R. Sulak, and R.

Svoboda: Phys. Rev., D 46, p. 3720 (1992).

Beier, E.W.: Proc. Seventh Workshop on Grand Unification / ICOBAN 86, ed. J. Arafune (Toyama, Japan), p. 79 (1986).

Beier, E.W., E.D. Frank, W. Frati, S.B. Kim, A.K. Mann, F.M. Newcomer, R. Van Berg, W. Zhang, K.S. Hirata, K. Inoue, T. Ishida, T. Kajita, K. Kihara, M. Nakahata, K. Nakamura, S. Ohara, A. Sakai, N. Sato, Y. Suzuki, Y. Totsuka, Y. Yaginuma, M. Mori, Y. Oyama, A. Suzuki, K. Takahashi, M. Yamada, M. Koshiba, K. Nishijima, T. Kajimura, T. Suda, T. Tajima, K. Miyano, H. Miyata, H. Takei, Y. Fukuda, E. Kodera, Y. Nagashima, M. Takita, H. Yokoyama, K. Kaneyuki, Y. Takeuchi, and T. Tanimori: Phys, Lett., B. 283, p. 446 (1992).

Bemporad, C.: Nucl. Phys., B (Proc. Suppl.) 48, p. 412 (1996).

Berger, Ch., A. Hofmann, H. Mönch, F. Raupach, P. Schleper, G. Schmitz, J. Tutas, B. Voigtländer, C. Arpesella, Y. Benadjal, Ph. Bernaudin, D. Blum, C. Bourdarious, J. Brugnon, M. Corazzi, G. Deuzet, B. Dudelzak, P. Eschstruth, S. Jullian, D. Lalanne, F. Laplanche, C. Longuemare, C. Paulot, A. Reboux, Ph. Roy, J.L. Saury, G. Szklarz, L. Behr, R.W. Bland, F. Bousser, A. Debraine, B. Degrange, R. Marbot, U. Nguyen-Khac, B. Pietrzyk, J. Raguet, P. Serri, S. Tisserant, M. Arignon, M. Arnaud, A. Baracat, P. Bareyre, R. Barloutaud, R. Benait, A. Borg, G. Chardin, E. Coulareau, L. Di Ciaccio, D. Edmunds, J. Ernwein, G. Gerbier, J.F. Glicenstein, J. Heitzmann, M.A. Jabiol, M. Jacquet, W. Kolton, Y. Laigneau, C. Mathis, L Mosca, L. Moscoso, P. Paillier, S. Palanque, J. Pelle, B. Tallini, K.H. Becker, H.J. Daum, S. Denski, R. Hinners, W. Kohrs, B. Kuznik, R. Mayer, H. Meyer, D. Ortmann, J. Peters, M. Schubnell, J. Thierjung, P. Wintgen, and Y. Wei: Fréjus Collaboration Nucl. Ins. and Methods, A 262 , p. 463 (1987).

Berger, Ch., M. Fröhlich, H. Mönch, R. Nisius, F. Raupach, P. Schleper, Y. Benadjal, D. Blum, C. Bourdarios, B. Dudelzak, P. Eschstruth, S. Jullian, D. Lalanne, F. Laplanche, C. Longuemare, C. Paulot, O. Perdereau, Ph. Roy, G. Szklarz, L. Behr, B. Degrange, U. Nguyen-Khac, S. Tisserant, C. Arpesella, P. Bareyre, R. Barloutaud, A. Borg, G. Chardin, J. Ernwein, J.F. Glicenstein, L. Mosca, L. Moscoso, J. Becker, K.H. Becker, H.J. Daum, S. Demski, B. Jacobi, B. Kuznik, R. Mayer, H. Meyer, R. Möller, M. Schubnell, B. Seyffert, Y. Wei, and P. Wintgen: Phys. Lett., B 227, p. 489 (1989).

Berger, Ch., M. Fröhlich, H. Mönch, R. Nisius, F. Raupach, P. D. Blum, C. Bourdarios, B. Dudelzak, P. Eschstruth, S. Jullian, D. Lalanne, F. Laplanche, C. Longuemare, C. Paulot, O. Perdereau, Ph. Roy, G. Szklarz, L. Behr, B. Degrange, U. Nguyen-Khac, S. Tisserant, C. Arpesella, P. Bareyre, R.

Barloutaud, A. Borg, G. Chardin, J. Ernwein, J.F. Glicenstein, L. Mosca, L. Moscoso, J. Becker, K.H. Becker, H.J. Daum, B. Jacobi, B. Kuznik, H. Meyer, R. Möller, M. Schubnell, and Y. Wei: Phys. Lett., B 245, p. 305 (1990).

Bergeson, H.E., L.K. Hilton, J.W. Keuffel, M. Morris, J.L. Parker, R.O. Stenerson, and C.J. Wolfson: PICRC, 2, p. 1048 (1965).

Bhattacharyya, D.P., and Pratibha Pal: PICRC, 10, p. 26 (1990).

Bilenky, S.M., and B.M. Pontecorvo: Phys. Rep., 41, p 225 (1978).

Boliev, M.M., A.V. Butkevich, A.E. Chudakov, B.A. Makoev, S.P. Mikheyev, and V.N. Zakidyshev: PICRC, 7, p. 106 (1981).

Boliev, M.M., A.V. Butkevich, A.E. Chudakov, S.P. Mikheyev, M.V. Skarzhinskaya, and V.N. Zakidyshev: PICRC, 10, p. 20 (1990).

Boliev, M.M., et al.: Proc. 3rd Internat. Workshop on Neutrino Telescopes, Venice, Italy, 1991, ed. M. Baldo-Ceolin (INFN, Padova), p. 235 (1991).

Boliev, M.M., A.V. Butkevich, A.E. Chudakov, S.P. Mikheyev, O.V. Suvorova, and V.N. Zakidyshev: PICRC, 1, p. 686, (1995).

Bosetti, P., P.K.F. Grieder, P. Minkowski, B. Barish, J. Elliott, W. Gajewski, W. Kropp, L. Price, F. Reines, H. Sobel, J. Babson, R. Becker-Szendy, R., J.G. Learned, S. Matsuno, D. O'Connor, A. Roberts, V.J. Stenger, V.Z. Peterson, G. Wilkins, O.C. Allkofer, P. Koske, M. Preischel, J. Rathlev, T. Kitamura, H. Bradner, K. Mitsui, Y. Ohashi, A. Okada, J. Clem, C.E. Roos, M. Webster, U. Camerini, M. Jaworski, R. March, R. Morse: DUMAND Proposal 1989, Dept. of Physics and Astronomy, University of Hawaii (1989).

Bugaev, E.V., and V.A. Naumov: Phys. Lett., B 232, p. 391 (1989).

Casper, D., R. Becker-Szendy, C.B. Bratton, D.R. Cady, R. Claus, S. T. Dye, W. Gajewski, M. Goldhaber, T.J. Haines, P.G. Halverson, T.W. Jones, D. Kielczewska, W.R. Kropp, J.G. Learned, J.M. LoSecco, C. McGrew, S. Matsuno, J. Matthews, M.S. Mudan, L. Price, F. Reines, J. Schultz, D. Sinclair, H.W. Sobel, J.L. Stone, L.R. Sulak, R. Svoboda, G. Thornton, and J.C. van der Velde: Phys. Rev. Lett., 66, p. 2561 (1991).

Chen, H.H., W.R. Kropp, H.W. Sobel, and F. Reines: Phys. Rev., D 4, p. 99 (1971).

Cheung, T., and E.C.M. Young: PICRC, 10, p. 16 (1990).

Choi, M.C. and E.C.M. Young: PICRC, 6, p. 2134 (1975).

Cowsik, R., Y. Pal, and S.N. Tandon: Proc. Indian Acad. Sci., 63A, p. 217 (1966).

Crawford, H.J., R. Jeanloz, B. Romanowicz and the DUMAND Collaboration: PICRC, 1, p. 804 (1995).

Crouch, M.F., H.S. Gurr, W.R. Kropp, J. Lathrop, B.S. Meyer, F. Reines, J.P.F. Sellschop, and H.W. Sobel: Acta Phys. Hung., 29, Suppl., 4, p. 327 (1970).

Crouch, M.F., P.B. Landecker, J.F. Lathrop, F. Reines, W.G. Sandie, H.W. Sobel, H. Coxell and J.P.F. Sellschop: Phys. Rev., D 18, p. 2239 (1978).

Dedenko, L.G., I.M. Zheleznykh, V.A. Kuzmin, and E.A. Tajnov: Sov. J. Nucl. Phys., 30, p. 554 (1979).

Dermer, C.D.: Astrophys. J., 307, p. 47 (1986).

Eichten, E., I. Hinchcliffe, K. Lane, and C. Quigg: Rev. Mod. Phys., 56, p. 579 (1984).

Eichten, E., I. Hinchcliffe, K. Lane, and C. Quigg: Rev. Mod. Phys., 58, p. 1065 (1986).

Frati, W., T.K. Gaisser, A.K. Mann, and Todor Stanev: Phys. Rev., D 48, p. 1140 (1993).

Fukuda, Y., T. Hayakawa, K. Inoue, T. Ishida, S. Joukou, T. Kajita, S. Kasuga, Y. Koshio, T. Kumita, K. Matsumoto, M. Nakahata, K. Nakamura, A. Sakai, M. Shiozawa, J. Suzuki, Y. Suzuki, Y. Totsuka, K.S. Hirata, K. Kihara, M. Mori, Y. Oyama, A. Suzuki, M. Yamada, M. Koshiba, K. Nishijima, T. Kajimura, T. Suda, A.T. Suzuki, T. Ishizuka, M. Koga, K. Miyano, H. Miyata, H. Okazawa, H. Takei, T. Hara, N. Kishi, Y. Nagashima, M. Takita, A. Yoshimoto, Y. Hayato, K. Kaneyuki, Y. Takeuchi, T. Tanimori, S. Tasaka, K. Nishikawa, E.W. Beier, E.D. Frank, W. Frati, S.B. Kim, A.K. Mann, F.M. Newcomer, R. Van Berg, and W. Zhang, (Kamiokande Collaboration): Phys. Lett., B 335, p. 237 (1994).

Fukuda, Y., T. Hayakawa, K. Inoue, K. Ishihara, H. Ishino, S. Joukou, T. Kajita, S. Kasuga, Y. Koshio, T. Kumita, K. Matsumoto, M. Nakahata, K. Nakamura, K. Okumura, A. Sakai, M. Shiozawa, J. Suzuki, Y. Suzuki, T. Tomoeda, Y. Totsuka, K.S. Hirata, K. Kihara, Y. Oyama, M. Koshiba, K. Nishijima, T. Horiuchi, K. Fujita, S. Hatakeyama, M. Koga, T. Maruyama, A. Suzuki, M. Mori, T. Kajimura, T. Suda, A.T. Suzuki, T. Ishizuka, K. Miyano, H. Okazawa, T. Hara, Y. Nagashima, M. Takita, T. Yamaguchi, Y. Hayato, K. Kaneyuki, T. Suzuki, Y. Takeuchi, T. Tanimori, S. Tasaka, E. Ichihara, S. Miyamoto, and K. Nishikawa. (Kamiokande Collaboration): Phys. Rev. Lett., 77, p. 1683 (1996).

Fukuda, Y., T. Hayakawa, E. Ichihara, K. Inoue, K. Ishihara, H. Ishino, Y. Itow, T. Kajita, J. Kameda, S. Kasuga, K. Kobayashi, Y. Kobayashi

Y. Koshio , K. Martens, M. Miura, M. Nakahata, S. Nakayama, A. Okada, M. Oketa , K. Okumura, M. Ota, N. Sakurai, M. Shiozawa, Y. Suzuki, Y. Takeuchi, Y. Totsuka, S. Yamada, M. Earl, A. Habig, J.T. Hong, E. Kearns, S.B. Kim, M. Masuzawa, M.D. Messier, K. Scholberg, J.L. Stone, L.R. Sulak, C.W. Walter, M. Goldhaber, T. Barszczak, W. Gajewski, P.G. Halverson, J. Hsu, W.R. Kropp, L.R. Price, F. Reine, H.W. Sobel, M.R. Vagins, K.S. Ganezer, W.E. Keig, R.W. Ellsworth, S. Tasaka, J.W. Flanagan, A. Kibayashi, J.G. Learned, S. Matsuno, V. Stenger, D. Takemori, T. Ishii, J. Kanzaki, T. Kobayashi, K. Nakamura, K. Nishikawa, Y. Oyama, A. Sakai, M. Sakuda, O. Sasaki, S. Echigo, M. Kohama, A.T. Suzuki, T.J. Haines, E. Blaufuss, R. Sanford, R. Svoboda, M.L. Chen, Z. Conner, J.A. Goodman, G.W. Sullivan, M. Mori, F. Goebel, J. Hill, C.K. Jung, C. Mauger, C. McGrew, E. Sharkey, B. Viren, C. Yanagisawa, W. Doki, T. Ishizuka, Y. Kitaguchi, H. Koga, K. Miyano, H. Okazawa, C. Saji, M. Takahata, A. Kusano, Y. Nagashima, M. Takita, T. Yamaguchi, M. Yoshida, M. Etoh , K. Fujita, A. Hasegawa, T. Hasegawa, S. Hatakeyama, T. Iwamoto, T. Kinebuchi, M. Koga, T. Maruyama, H. Ogawa, M. Saito, A. Suzuki, F. Tsushima, M. Koshiba, M. Nemoto, K. Nishijima, T. Futagami, Y. Hayato, Y. Kanaya, K. Kaneyuki, Y. Watanabe, D. Kielczewska, R. Doyle, J. George, A. Stachyra, L. Wai, J. Wilkes, K. Young, Super-Kamiokande Collaboration: Phys. Lett., B 433, p. 9 (1998).

Futagami, T., Y. Fukuda, T. Hayakawa, K. Inoue, K. Ishihara, H. Ishino, Y. Itov, T. Kajita, J. Kameda, S. Kasuga, K. Kobayashi, Y. Kobayashi, Y. Koshio, M. Miura, M. Nakahata, S. Nakayama, Y. Obayashi, A. Okada, K. Okumura, N. Sakurai, M. Shiozawa, Y. Suzuki, H. Takeuchi, Y. Takeuchi, Y. Totsuka, S. Yamada, M. Earl, A. Habig, E. Kearns, M.D. Messier, K. Scholberg, J.L. Stone, L.R. Sulak, C.W. Walter, M. Goldhaber, T. Barsczak, D. Casper, W. Gajewski, W.R. Kropp, S. Mine, L.R. Price, M. Smy, H.W. Sobel, M.R. Vagins, K.S. Ganezer, W.E. Keig, R.W. Ellsworth, S. Tasaka, A. Kibayashi, J.G. Learned, S. Matsuno, V. Stenger, D. Takemori, T. Ishii, J. Kanzaki, T. Kobayashi, K. Nakamura, K. Nishikawa, Y. Oyama, A. Sakai, M. Sakuda, O. Sasaki, S. Echigo, M. Kohama, A.T. Suzuki, T.J. Haines, E. Blaufuss, B.K. Kim, R. Sanford, R. Svoboda, M.L. Chen, J.A. Goodman, G.W. Sullivan, J. Hill, C.K. Jung, K. Martens, C. Mauger, C. McGrew, E. Sharkey, B. Viren, C. Yanagisawa, W. Doki, M. Kirisawa, S. Inaba, K. Miyano, H. Okazawa, C. Saji, M. Takahashi, M. Takahata, K. Higuchi, Y. Nagashima, M. Takita, T. Yamaguchi, M. Yoshida, S.B. Kim, M. Etoh, A. Hasegawa, T. Hasegawa, S. Hatakeyama, T. Iwamoto, M. Koga, T. Maruyama, H. Ogawa, J. Shirai, A. Suzuki, F. Tsushima, M. Koshiba, Y. Hatakeyama, M. Koike, M. Nemoto, K. Nishijima, H. Fyjiyasu, Y. Hayato, Y. Kanaya, K. Kaneyuki,

Y. Watanabe, D. Kielczewska, J.S. George, A.L. Stachyra, L.L. Wai, R.J. Wilkes, and K.K. Young, Super-Kamiokande Collaboration: Phys. Rev. Lett., 82, p. 5194 (1999).

Gaisser, T.K.: Nucl. Phys., B (Proc. Suppl.) 77, p. 133 (1999).

Gaisser, T.K., and Todor Stanev: PICRC, 1, p. 694 (1995).

Gaisser, Thomas K., Francis Halzen, and Todor Stanev: Physics Reports, 258, p. 173 (1995).

Gaisser, T.K., Todor Stanev, and Giles Barr: PICRC, 6, p. 169 (1987).

Grieder, P.K.F.: in "Neutrinos and the Present-day Universe", eds. Thierry Montmerle and Michel Spiro, ISBN 2-7272-0103-6 Edition Doc. CEN Saclay 86-45 (1986).

Grieder, P.K.F.: Proceedings of Nestor Workshop, Pylos, Greece, 1993, ed. L.K. Resvanis, University of Athems, Greece, p. 168 (1993).

Haines, T.J., R.M. Bionta, G. Blewitt, C.B. Bratton, D. Casper, R. Claus, B.G. Cortez, S. Errede, G.W. Foster, W. Gajewski, K.S. Ganezer, M. Goldhaber, T.W. Jones, D. Kielczewska, W.R Kropp, J.G. Learned, E. Lehmann, J.M. LoSecco, J. Matthews, H.S. Park, L.R. Price, F. Reinse, J. Schultz, S. Seidel, E. Shumard, D. Sinclair, H.W. Sobel, J.L. Stone, L. Sulak, R. Svoboda, J.C. Van der Velde, and C. Wuest: Phys. Rev. Lett., 57, p. 1986 (1986).

Hendricks, M.B., H.E. Bergeson, R.B. Coats, J.W. Keuffel, M.O. Larson, J.L. Osborne, S. Ozaki, and R.O. Stenerson: Acta Phys. Acad. Sci. Hung., 29, Suppl. 4, p. 313 (1970).

Hikasa, K., K. Hagiwara, and S. Kawabata, R.M. Barnett, D.E. Groom, T.G.Trippe, C.G. Wohl, and G.P. Yost, B. Armstrong, G.S. Wagman, J. Stone, F.C. Porter, R.J. Morrison, R.E. Cutkosky, L. Montanet, K. Gieselmann, M. Aguilar-Benitez, C. Caso, R.L. Crawford, M. Roos, N.A. Törnqvist, K.G. Hayes, G. Höhler, D.M. Manley, K.A. Olive, P.E. Shrock, S. Eidelman, R.H. Schindler, J.J. Hernandez, G. Conforto, and R.A. Eichler, Particle Data Group: Phys. Rev., D 45, S 1, p. III 82 (1992).

Hirata, K.S., K. Inoue, T. Ishida, T. Kajita, K. Kihara, M. Nakahata, K. Nakamura, S. Ohara, A. Sakai, N. Sato, Y. Suzuki, Y. Totsuka, Y. Yaginuma, M. Mori, Y. Oyama, A. Suzuki, K. Takahashi, M. Yamada, M. Koshiba, K. Nishijima, T. Kajimura, T. Suda, T. Tajima, K. Miyano, H. Miyata, H. Takei, Y. Fukuda, E. Kodera, Y. Nagashima, M. Takita, H. Yokoyama, K. Kaneyuki, Y. Takeuchi, T. Tanimori, E.W. Beier, E.D. Frank, W. Frati, S.B. Kim, A.K. Mann, F.M. Newcomer, R. Van Berg, and W. Zhang, (Kamiokande Collaboration): Phys. Lett., B 280, p. 146 (1992).

Honda, M.: Nucl. Phys., B (Proc. Suppl.) 77, p. 140 (1999).

Honda, M., K. Kasahara, K. Hidaka, and S. Midorikawa: Phys. Lett., B 248, p. 193 (1990).

Honda, M., T. Kajita, K. Kasahara, and S. Midorikawa: Phys. Rev., D 52, p. 4985 (1995).

Hubbard, Richard, J., ANTARES Collaboration: PICRC, 2, p. 436 (1999).

Jain, Pankaj, John P. Ralston, and George M. Fichter: Astropart. Phys., 12, p. 193 (1999).

Kajita, Takaaki: Nucl. Phys., B (Proc. Suppl.) 77, p. 123 (1999).

Kajita, Takaaki: Nucl. Phys. B (Proc. Suppl.) 85, p. 44 (2000).

Kaneyuki, K., Super-Kamiokande Collaboration: PICRC, 2, p. 184 (1999).

Koshiba, M.: Physics Reports, 220, Nr. 5 and 6, p. 229 - 381 (1992).

Krishnaswamy, M.R., M.G.K. Menon, V.S. Narasimham, H. Sesaki, S. Kino, S. Miyake, R. Craig, A.J. Parsons, and A.W. Wolfendale: Acta Phys. Acad. Sci. Hung., 29, Suppl. 4, p. 319 (1970).

Krishnaswami, M.R., M.G.K. Menon, N.K. Mondal, V.S. Narasimham, B.V. Sreekantan, Y. Hayashi, N. Ito, S. Kawakami, and S. Miyake: PICRC, 7, p. 95 (1983).

Lee, H., and Y.S. Koh: Nuovo Cimento, 105 B, p. 883 (1990).

Lipari, P.: Astropart. Phys., 1, p. 195 (1993).

Lipari, Paolo, Todor Stanev, and T.K. Gaisser: Phys. Rev., D 58 , p. 073003 (1998).

LoSecco, J.M., R.M. Bionta, G. Blewitt, C.B. Bratton, D. Casper, P. Chrysicopoulou, R. Claus, B.G. Cortez, S. Errede, G.W. Foster, W. Gajewski, K. S. Ganezer, M. Goldhaber, T.J. Haines, T.W. Jones, D. Kielczewska, W.R. Kropp, J.G. Learned, E. Lehmann, H.S. Park, F. Reines, J. Schultz, S. Seidel, E. Shumard, D. Sinclair, H.W. Sobel, J.L Stone, L. Sulak, R. Svoboda, J. van der Velde, and C. Wuest: PICRC, 8, p. 116 (1985).

Maki, Ziro, Masami Nakagawa, and Shoichi Sakata: Progr. Theor. Phys., 28, p. 870 (1962).

Margolis, S.H., D.N. Schramm, and R. Silberberg: Astrophys. J., 221, p. 990 (1978).

McDonald, A.B.: Nucl. Phys., B (Proc. Suppl.) 48, p. 357 (1996).

McDonald, A.B.: Nucl. Phys., B (Proc. Suppl.) 77, p. 43 (1999).

Meyer, H.: Proc. Baton Rouge Workshop on Atmospheric Neutrinos, R. Svoboda, ed. (1993).

Mikheyev, S.P. and A.Y. Smirnov: Nuov. Cim., 9, p. 17 (1986).

Mitsui, K., Y. Minorikawa, and H. Komori: Nuovo Cimento, 9 C, N. 5, p. 995 (1986).

Mori, M., M.M. Nojiri, Y. Oyama, A. Suzuki, K. Takahashi, M. Yamada, H. Takei, K. Miyano, H. Miyata, K.S. Hirata, K. Inoue, T. Ishida, T. Kajita, K. Kihara, M. Nakahata, K. Nakamura, N. Sato, Y. Suzuki, Y. Totsuka, Y. Yaginuma, M. Koshiba, K. Nishijima, T. Suda, T. Tajima, Y. Fukuda, E. Kodera, Y. Nagashima, M. Takita, K. Kaneyuki, T. Tanimori, E.W. Beier, E.D. Frank, W. Frati, S.B. Kim, A.K. Mann, F.M. Newcomer, R. van Bern, and W. Zhang: Phys. Lett., B 270, p. 89 (1991).

Moscoso, L.: PICRC, 2, p. 440 (1999).

Osborne, J.L., S.S. Said, and A.W. Wolfendale: Proc. Phys. Soc., 86, p. 93 (1965).

Osborne, J.L.: A.W. Wolfendale, (Ed.) Cosmic rays at ground level, The Institute of Physcis, London, Chapter 5, p. 85 (1973).

Owens, J.F.: Phys. Lett, B 266, p. 126 (1991).

Oyama, Y., K. Hirata, T. Kajita, M. Koshiba, N. Nakahata, N. Sato, A. Suzuki, M. Takita, Y. Totsuka, T. Kifune, T. Suda, K. Nakamura, K. Takahashi, T. Tanimori, K. Miyano, M. Yamada, E.W. Beier, L.R. Feldscher, S.B. Kim, A.K. Mann, F.M. Newcomer, R. van Berg, and W. Zhang:Phys. Rev. Lett., 59, p. 2604 (1987).

Perkins, D.H.: Nucl. Phys., B 399, p. 3 (1993).

Peterson, Earl (Soudan Collaboration): Nucl. Phys., B (Proc. Suppl.) 77, p. 111 (1999).

Pontecorvo, B.: Chalk River Report PD-205 (1946).

Pontecorvo, B.: Zh. Eksp. Theor. Fiz., 53, p. 1717 (1967).

Pontecorvo, B.: J.E.T.P., 26, (5), p. 984 (1968).

Ramana-Murthy, P.V.: PICRC, 7, p. 125 (1983).

Reines, F., M.F. Crouch, T.L. Jenkins, W.R. Kropp, H.S. Gurr, G.R. Smith, H.W. Sobel, J.P.F. Sellschop, and B. Meyer: PICRC, 2, p. 1051 (1965).

Reines, F.: Proc. Topical Conf. on Weak Interactions, CERN, p. 101 (1969).

Resvanis, L.K.: Nucl. Phys., B (Proc. Suppl.) 48, p. 425 (1996).

Rhode, Wolfgang: Ph. D. Thesis, Fachbereich Physik, Bergische Universität,

Gesamthochschule Wuppertal, Germany. WUB-DIS 93-11 (1993).

Rhode, W., et al. (Fréjus Collaboration): PICRC, 1, p. 726 (1995).

Rhode, W., K. Daum, P. Bareyre, R. Barloutaud, G. Chardin, B. Degrange, J. Ernwein, B. Kuznik, H. Meyer, L. Mosca, L. Moscoso, O. Perdereau, M. Schubnell, S. Tisserant, and Y. Wei: Astropart. Phys., 4, p. 217 (1996).

Ronga, F. (MACRO Collaboration): Nucl. Phys., B (Proc. Suppl.) 77, p. 117 (1999).

Ronga, F. (MACRO Collaboration): Nucl. Phys., B (Proc. Suppl.) 87, p. 135 (2000).

Sartorelli et al. LVD Collaboration: PICRC, 1, p. 734 (1995).

Scholberg, Kate (Superkamiokande Collaboration): arXiv:hep-ex/9905016, 11 May (1999).

Smirnov, A.Yu.: Nucl. Phys., B (Proc. Suppl.), 77, p. 98 (1999).

Stone, J., MACRO Collaboration: PICRC, 8, p. 226 (1985).

Svoboda, R., R.M. Bionta, G. Blewitt, C.B. Bratton, D. Casper, P. Chrysicopoulou, A. Ciocio, R. Claus, B. Cortez, S.T. Dye, S. Errede, G.W. Foster, W. Gajewski, K.S. Ganezer, M. Goldhaber, T.J. Haines, T.W. Jones, D. Kielczewska, W.R. Kropp, J.G. Learned, J.M. LoSecco, J. Matthews, H.S. Park, F. Reines, J. Schultz, S. Seidel, E. Shumard, D. Sinclair, H.W. Sobel, J.L. Stone, L.R. Sulak, G. Thornton, J.C. van der Velde, and C. Wuest: Astrophys. J., 315, p. 420 (1987).

Tam, A.C. and E.C.M. Young: Acta Phys. Acad. Sci. Hung., 29, Suppl. 4, p. 307 (1970).

Volkova, L.V.: Yad. Fiz., 31, p. 784 (1980); Sov. J. Nucl. Phys., 31, p. 1510 (1980).

Volkova, L.V.: in Cosmic Gamma Rays, Neutrinos and Related Astrophysics, Proc. of the NATO Advanced Study Intitute, ed. M.M. Shapiro and J.P. Wefel, NATO ASI Series B: Physics Vol. 270 (Plenum, New York), p. 139 (1989).

Volkova, L.V. and G.T. Zatsepin: Sov. J. Nucl. Phys., 14, p. 117 (1972).

Wolfenstein, L.: Phys. Rev., D 17, p. 2369 (1978).

Wolfenstein, L.: Phys. Rev., D 20, p. 2634 (1979).

Young, E.C.M.: A.W. Wolfendale, (Ed.) Cosmic rays at ground level, The Institute of Physcis, London, Chapter 6, p. 105 (1973).

Zatsepin, G.T. and V.A. Kuzim: Sov. Phys. JETP, 14, p. 1294 (1962).

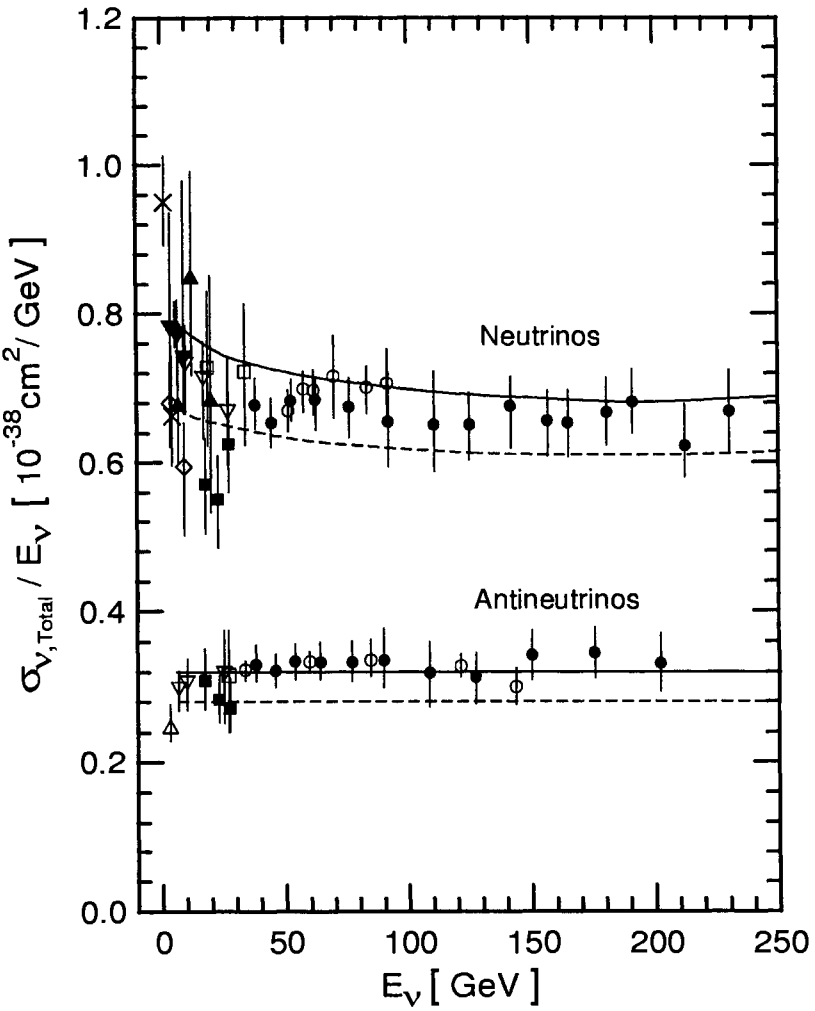

Figure 4.78: Compilation of charged current total cross section data, $\sigma_{\nu,Total}$, for muon neutrinos and antineutrinos divided by E_ν as a function of neutrino energy, E_ν. The curves are calculated cross sections from the work of Frati et al. (1993) using the structure functions of Eichten et al. (1984) (solid curves) and Owens (1991) (dashed curves). The experimental data compilation is after Hikasa et al., 1992).

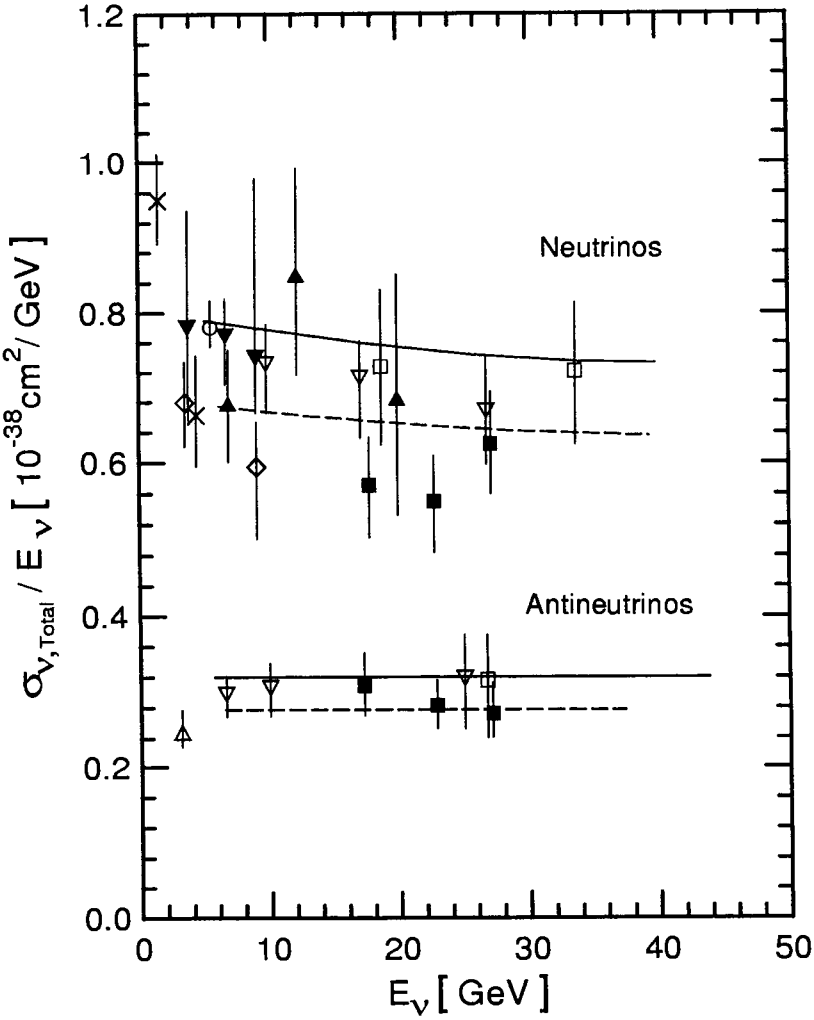

Figure 4.79: Enlargement of the low energy portion of Fig. 4.78, showing the charged current total cross section data, $\sigma_{\nu,Total}$, for muon neutrinos and antineutrinos divided by E_ν as a function of neutrino energy, E_ν. The curves are calculated cross sections from the work of Frati et al. (1993) using the structure functions of Eichten et al. (1984) (solid curves) and Owens (1991) (dashed curves). The experimental data compilation is after Hikasa et al., 1992).

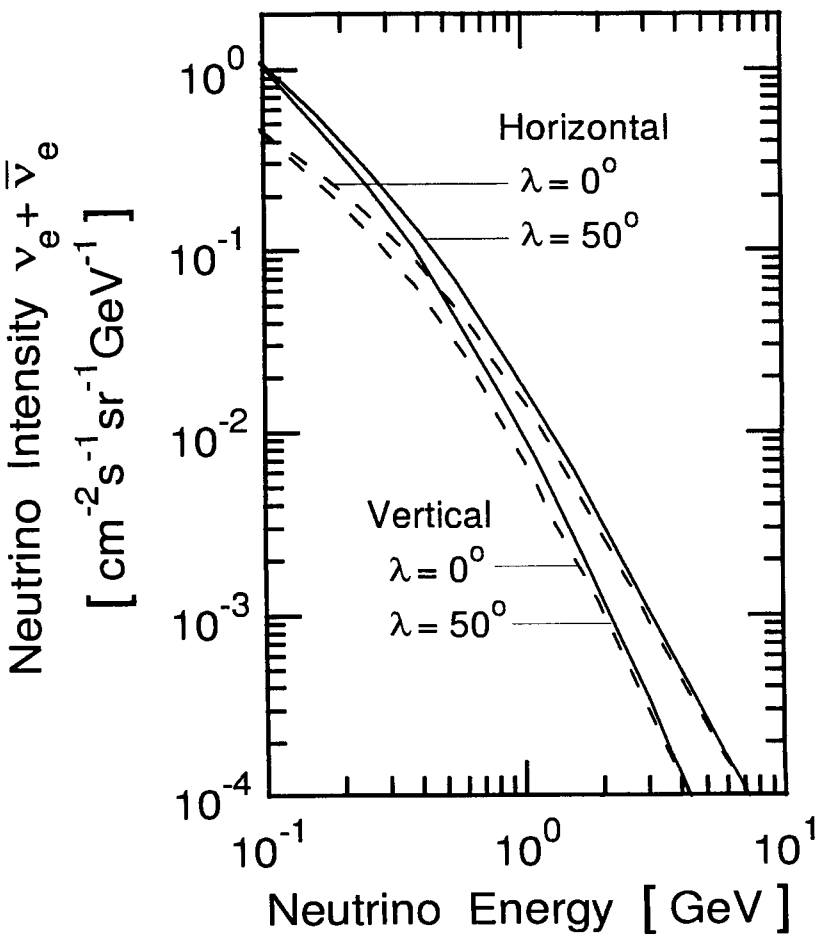

Figure 4.80: Theoretical differential energy spectra of atmospheric electron neutrinos and antineutrinos combined, in horizontal and vertical directions, respectively, at sea level and geomagnetic latitudes of 0° and 50° (Young, 1973).

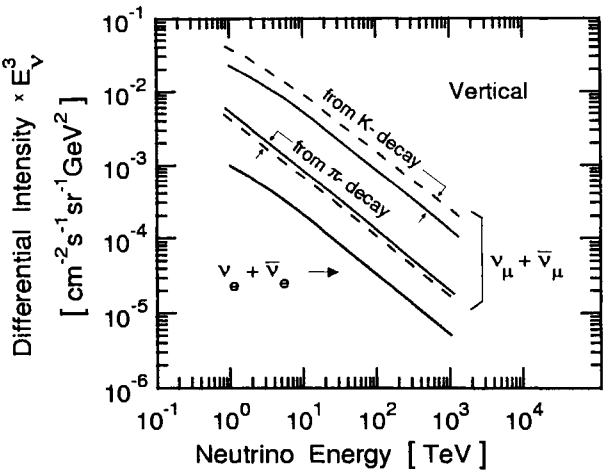

Figure 4.81: Theoretical vertical differential energy spectra of neutrinos of atmospheric origin at sea level for a differential muon spectrum of the form $j_\mu(E) \propto E^{-2.8}$. The solid curves are for the ratio $K/\pi = 0.15$, the dashed curves for $K/\pi = 0.3$. The electron neutrinos are shown for comparison (Allkofer et al., 1979a and 1979b).

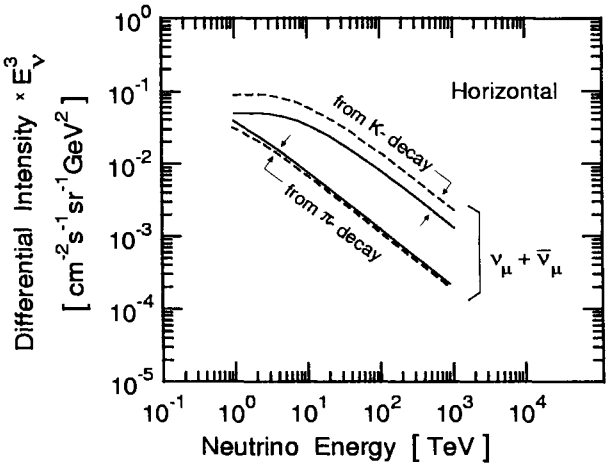

Figure 4.82: Theoretical horizontal differential energy spectra of neutrinos of atmospheric origin at sea level for a differential muon spectrum of the form $j_\mu(E) \propto E^{-2.8}$. The solid curves are for the ratio $K/\pi = 0.15$, the dashed curves for $K/\pi = 0.3$ (Allkofer et al., 1979a and 1979b).

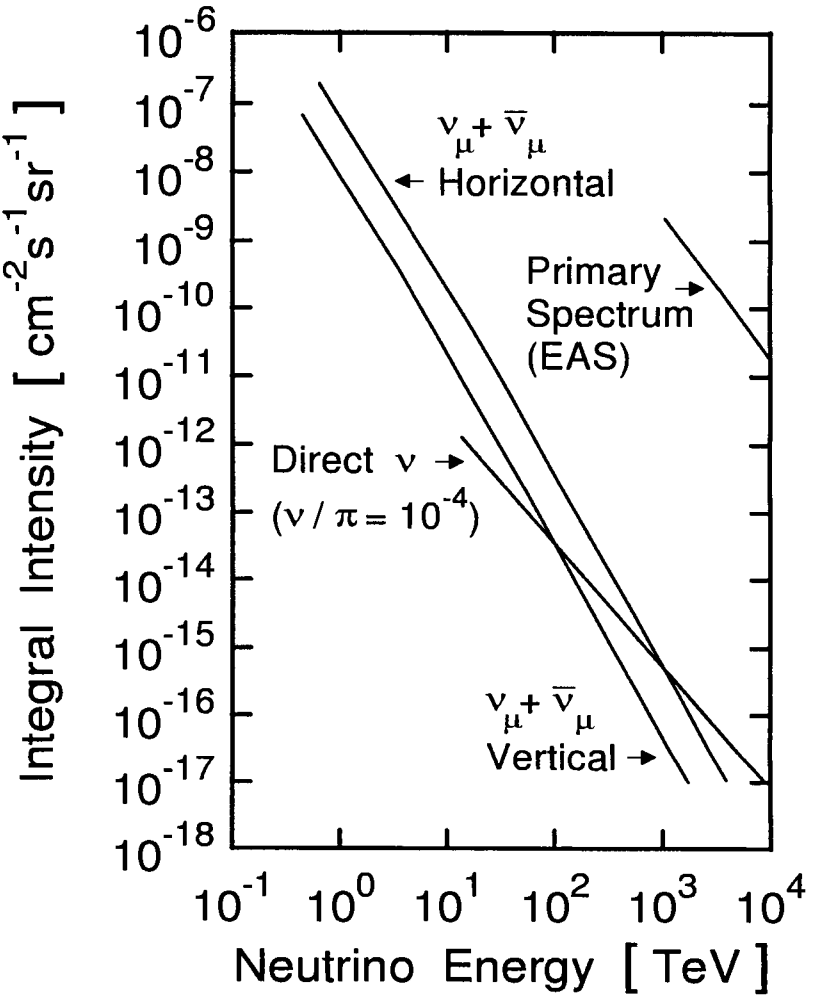

Figure 4.83: Theoretical horizontal and vertical integral energy spectra of atmospheric neutrinos. (Allkofer et al., 1979a, b).

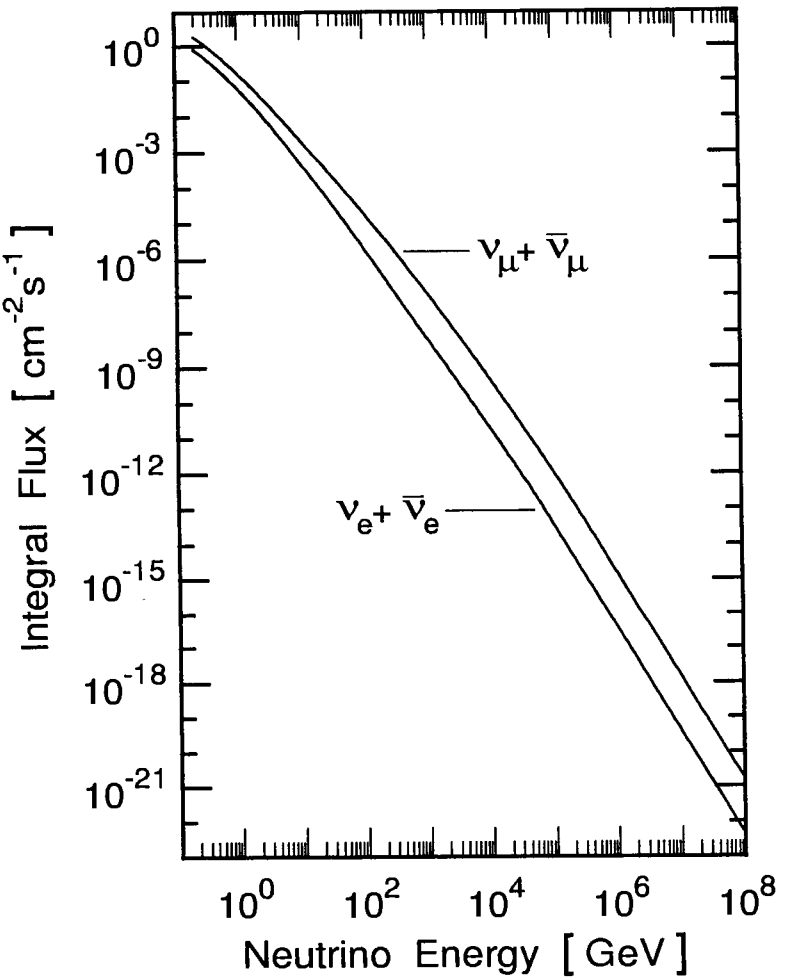

Figure 4.84: Integral energy spectra (flux) of atmospheric muon and electron neutrinos and antineutrinos from the calculations of Mitsui et al. (1986). The two curves are the plots of the data listed in columns 4 and 5 of Table 4.32.

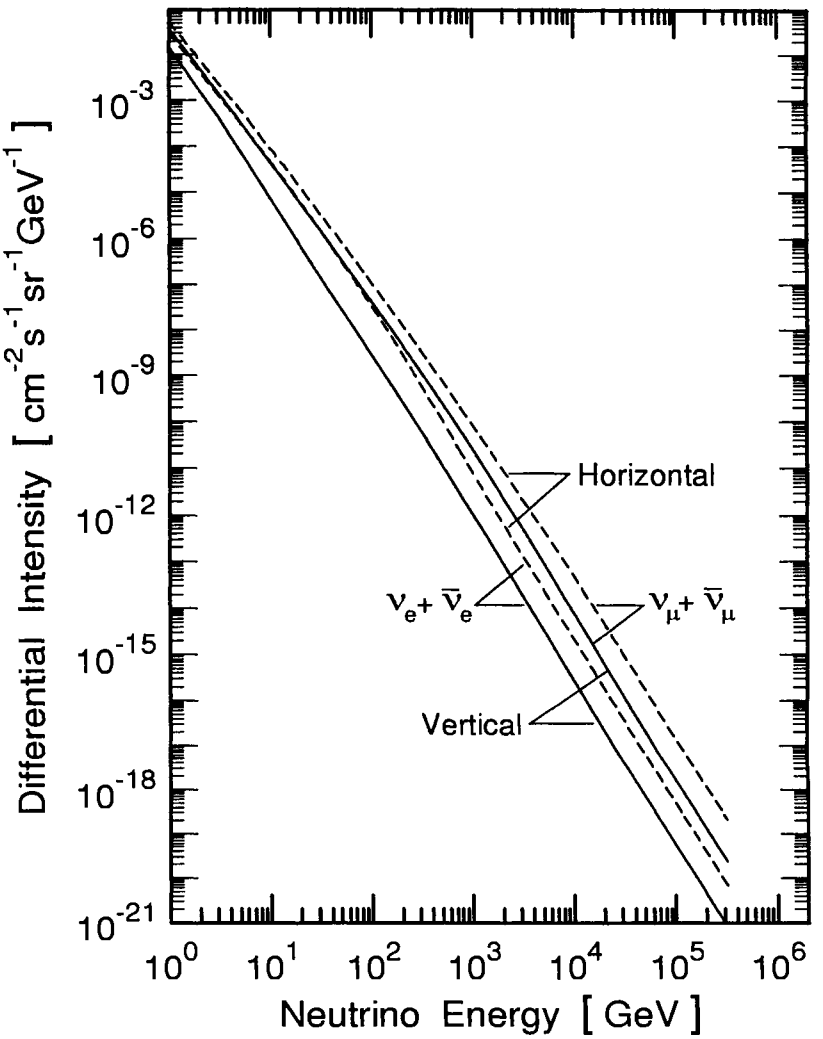

Figure 4.85: Differential energy spectra (intensity) of vertical and horizontal atmospheric muon and electron neutrinos and antineutrinos from the calculations of Lipari (1993). The four curves are the plots of the data listed in columns 2 and 9 of Tables 4.35 and 4.36, respectively.

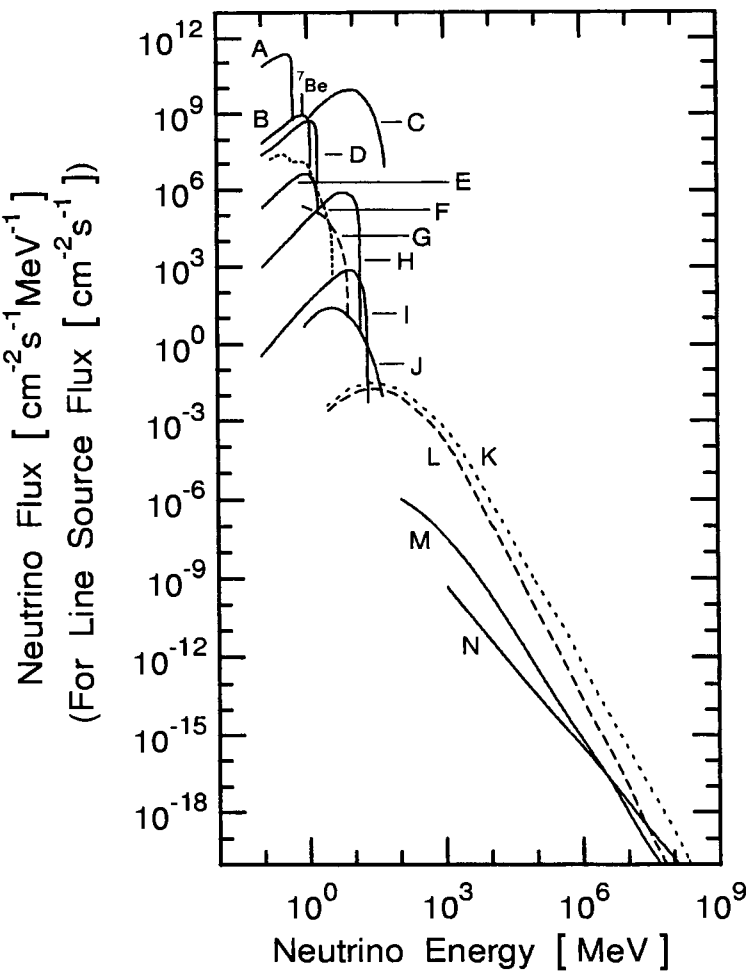

Figure 4.86: Compilation of theoretical differential energy spectra of neutrinos and antineutrinos of two flavors from terrestrial and extraterrestrial sources as listed below (Koshiba, 1992).

A	Solar pp	B	Solar ^{13}N	C	Type II SN
D	Solar ^{15}O	E	Solar ^{17}F	F	$\overline{\nu}_e$ Terrestrial
G	$\overline{\nu}_e$ Reactors	H	Solar ^{8}B	I	Solar hep
J	Relic SN	K	$\nu_\mu + \overline{\nu}_\mu$ Atmos.	L	$\nu_e + \overline{\nu}_e$ Atmos.
M	Galactic	N	Cygnus X-3		

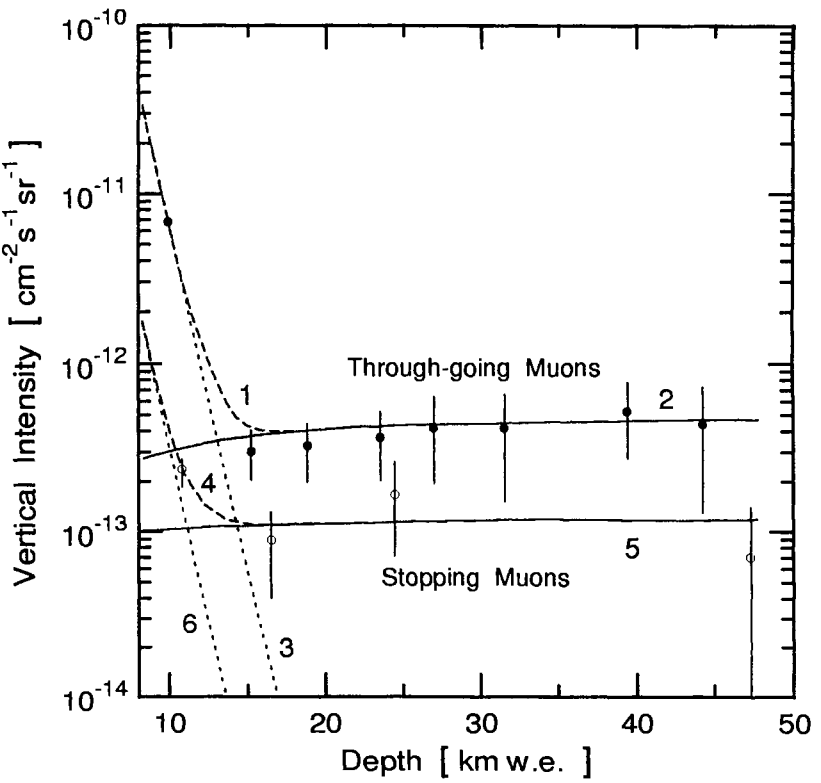

Figure 4.87: Vertical depth-intensity relation of through-going and stopping muons recorded with the Fréjus detector at very large depths (Rhode 1993). Curves 2 and 5 are theoretical distributions for through-going and stopping neutrino induced muons, respectively, curves 3 and 6 are analogous distributions for atmospheric muons. Curves 1 and 4 are the sums of curves 2 and 3, and 5 and 6, respectively. Intensities recorded at zenith angles $\theta > 0°$ as seen by the detector were multiplied by $\cos(\theta^*)$ for conversion to vertical intensity. θ^* is the local zenith angle measured at the point of creation of the particle in the atmosphere and not as seen at the detector).

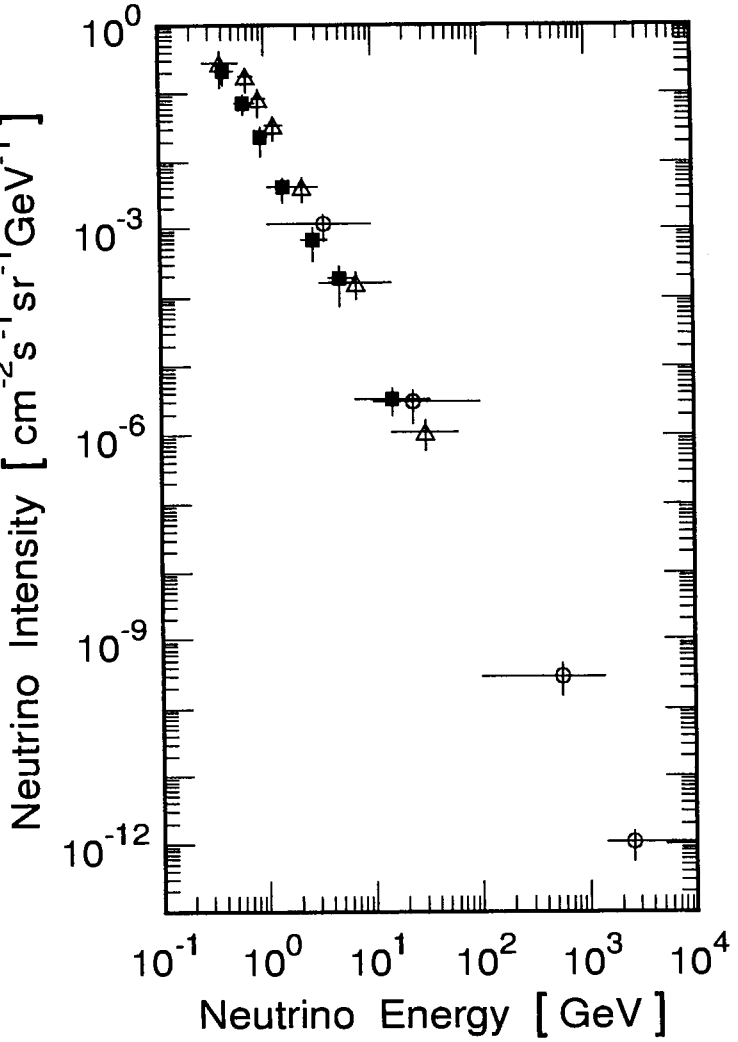

Figure 4.88: Absolute electron neutrino ($\nu_e + \overline{\nu}_e$) and muon neutrino ($\nu_\mu + \overline{\nu}_\mu$) spectra in the ranges 320 MeV $\leq E_{\nu_e,\overline{\nu}_e} \leq$ 30 GeV and 250 MeV $\leq E_{\nu_\mu,\overline{\nu}_\mu} \leq$ 10 TeV, respectively, averaged over the zenith angle as measured with the Fréjus detector (Rhode et al., 1995 and 1996).

- ■ $\nu_e, \overline{\nu}_e$
- △ $\nu_\mu, \overline{\nu}_\mu$ contained + semi-contained
- ○ $\nu_\mu, \overline{\nu}_\mu$ induced muons

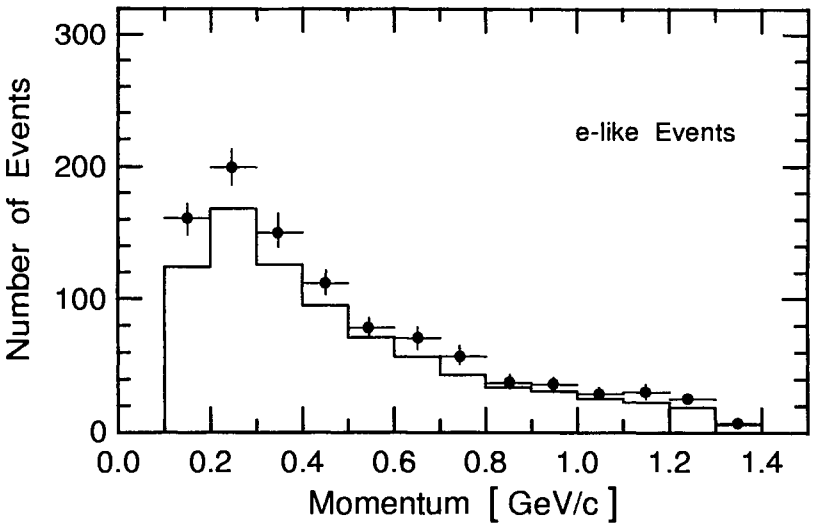

Figure 4.89: Momentum distribution of e-like events in the Superkamiokande detector. The histogram is the distribution obtained from the Monte Carlo simulation (Fukuda et al., 1998).

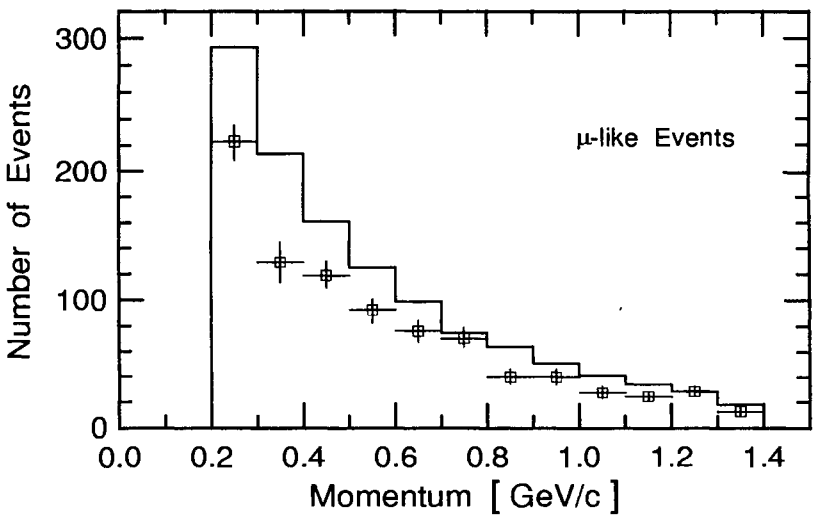

Figure 4.90: Momentum distribution of μ-like events in the Superkamiokande detector. The histogram is the distribution obtained from the Monte Carlo simulation (Fukuda et al., 1998).

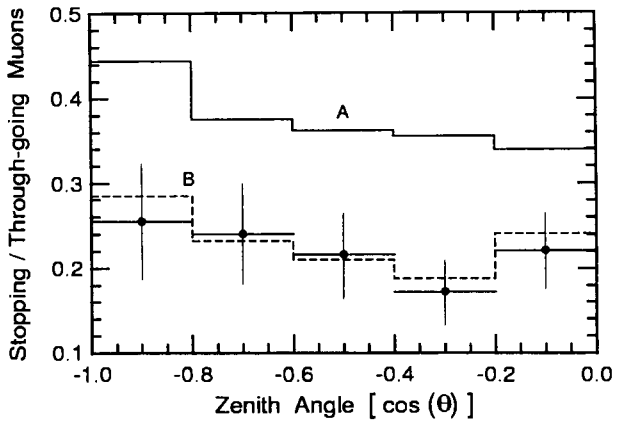

Figure 4.91: Ratio of stopping to through-going muons as a function of the cosine of the zenith angle, θ. The dots are the experimental data, the solid histogram (A) represents the normalized no-oscillation flux prediction, and the dashed histogram (B) is the best fit prediction for oscillations with $\sin^2(2\theta) = 1.0$ and $\Delta m^2 = 3.5 \cdot 10^{-3}$ eV^2 (after Scholberg, 1999).

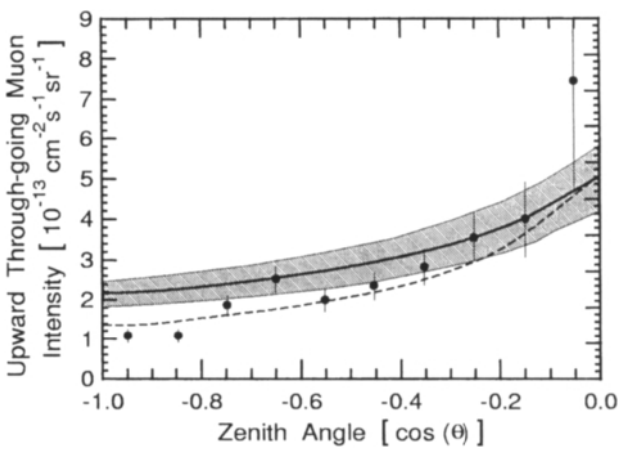

Figure 4.92: Zenith angle distribution in units of $\cos(\theta)$ of flux of upward through-going muons with energy >1 GeV for data and Monte Carlo events for the combined MACRO data. The solid curve shows the expectation for no oscillations and the shaded region represents the 17% uncertainty in the expectation. The dashed line is the result of the prediction for an oscillated flux with $\sin^2(2\theta) = 1$ and $\Delta m^2 = 0.0025$ eV^2 (after Ronga, 1999 and 2000).

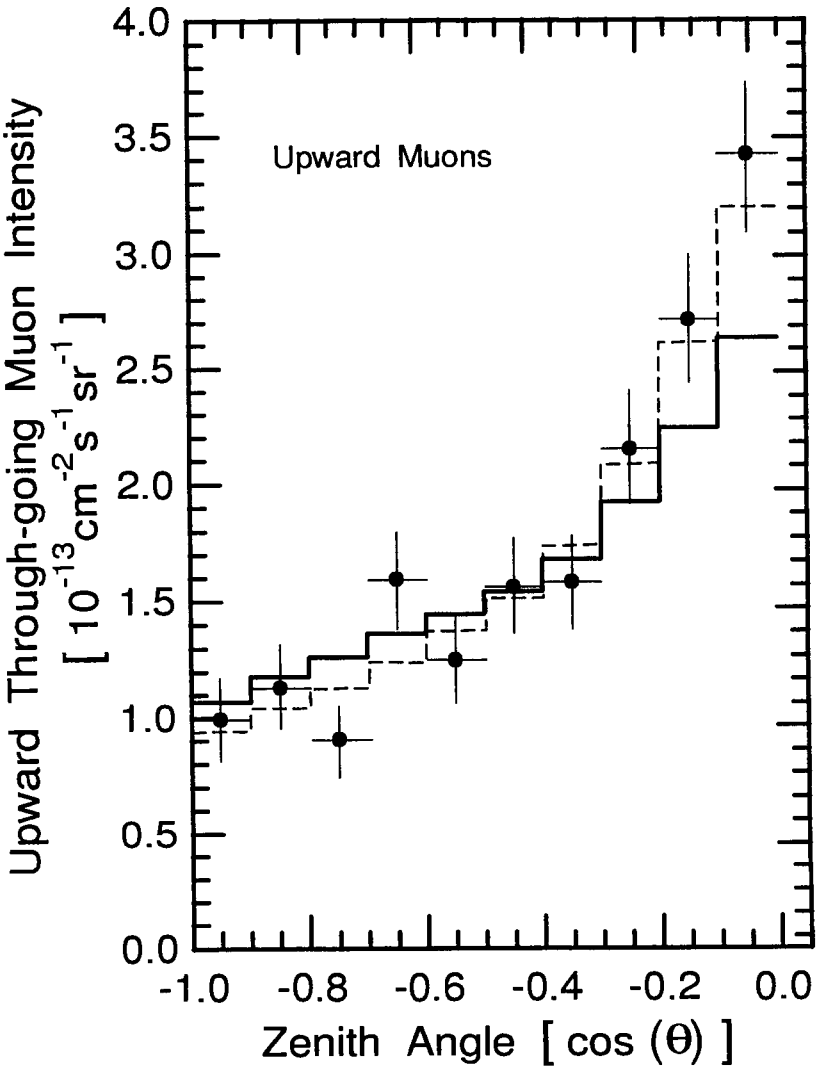

Figure 4.93: Zenith angle distribution in units of $\cos(\theta)$ of upward through-going muons. The dots are the experimental data, the solid line represents the normalized no-oscillation flux prediction, and the dashed line is the best fit prediction for oscillations, $\sin^2(2\theta) = 1.0$ and $\Delta m^2 = 3.5 \cdot 10^{-3}$ eV^2 (after Scholberg, 1999).

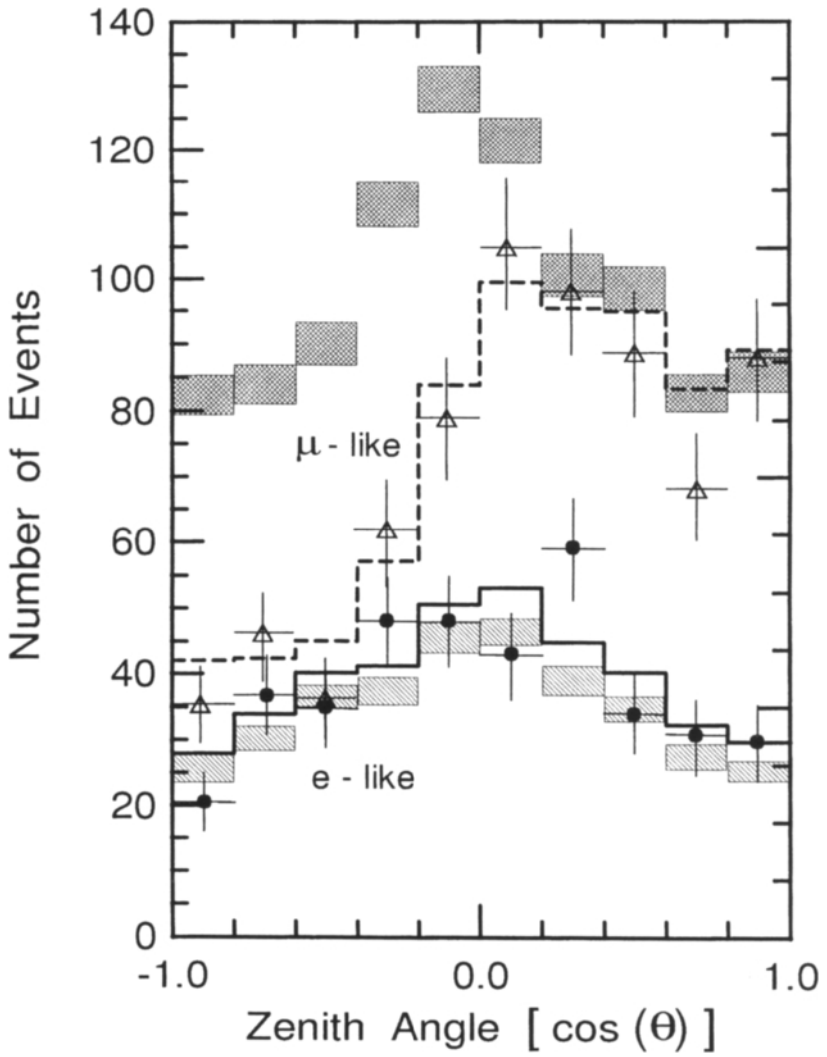

Figure 4.94: Zenith angle distribution in units of $\cos(\theta)$ for e-like ($\bullet$) and μ-like ($\triangle$) multi-GeV (fully and partially contained) events. The hatched and cross-hatched rectangles indicate the Monte Carlo no-oscillation predictions with statistical errors and the solid and dashed histograms the oscillation prediction for the best fit parameters, $\sin^2(2\theta) = 1.0$ and $\Delta m^2 = 3.5 \cdot 10^{-3}$ eV^2, for e-like and μ-like events, respectively (after Scholberg, 1999; see also Kajita, 2000).

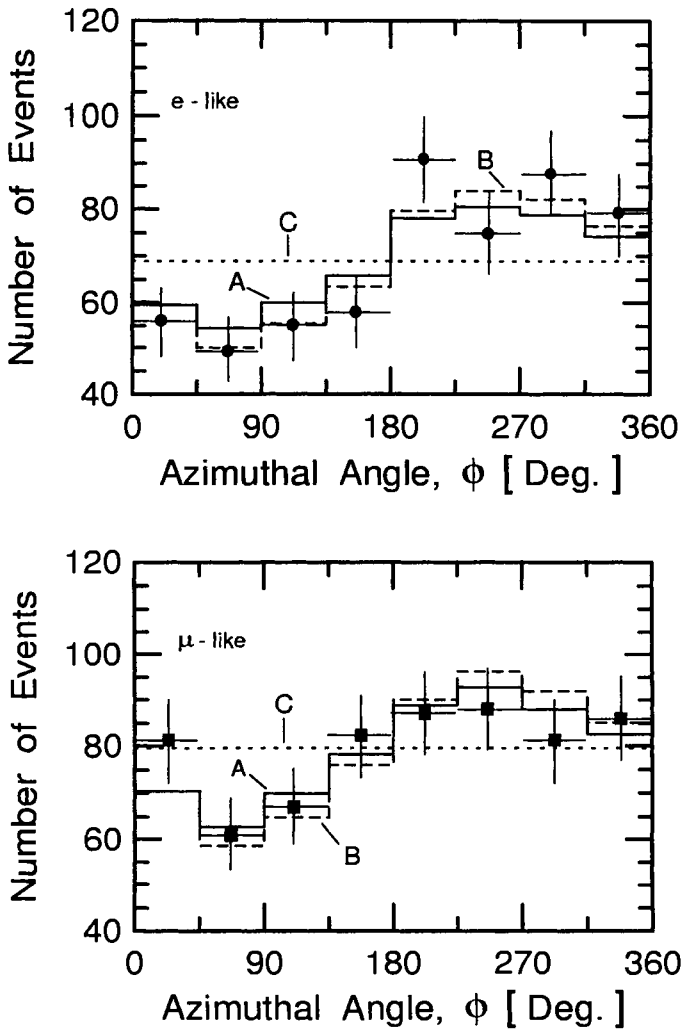

Figure 4.95: Illustration of the east-west effect. Shown is the azimuthal distribution of low energy near horizontal e-like (upper figure) and μ-like (lower figure) experimental data together with the Monte Carlo predictions of Honda et al. (1995 and 1996) (solid histogram, A) and Lipari et al. (1998) (dashed line, B) of the flux. The azimuthal angle $\phi = 0$ corresponds to particles going to the north and $\phi = 180°$ to particles going south. The expected deficit of neutrinos from the east due to the geomagnetic cutoff of the charged primaries is observed (after Scholberg, 1999).

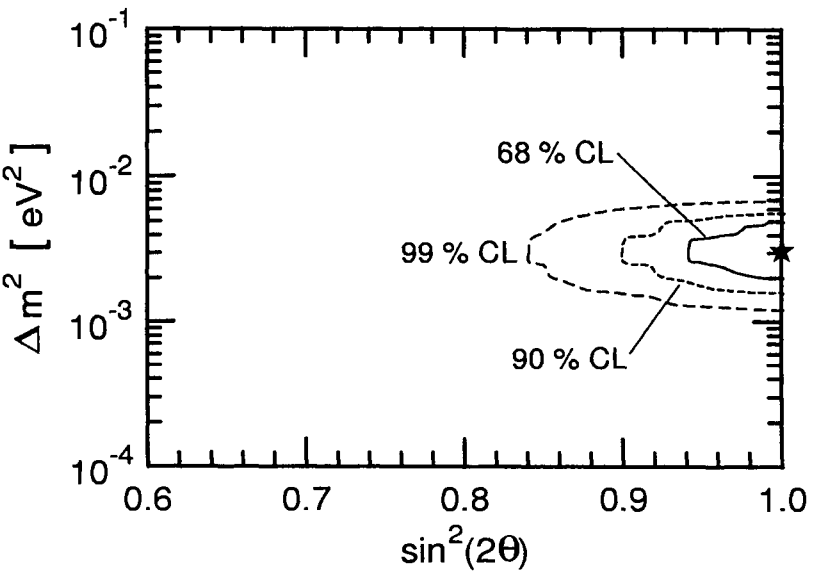

Figure 4.96: Resulting $\nu_\mu \rightarrow \nu_\tau$ oscillation confidence level contours of allowed regions deduced from the combined data of fully contained and partially contained upward going muons in Superkamiokande. The best fit value ($\star$) is at $\sin^2(2\theta) = 1.0$ and $\Delta m^2 = 3.2 \cdot 10^{-3}$ eV^2, corresponding to χ^2/d.o.f. of 70.2/82 (after Scholberg, 1999).

Chapter 5

Primary Cosmic Radiation

An excellent historic review of the discovery of the cosmic radiation by Victor Hess (Hess, 1912) and of the great efforts that followed in the years until the beginning of world war II, including the ionization measurements in the atmosphere to an altitude of 16 km by Piccard during his spectacular first manned stratospheric balloon flight in 1931 (Piccard and Cosyns, 1932) is given by Eugster and Hess (1940). It must be remembered that at that time essentially nothing was known of the world of particle physics. The significant progress that was made in cosmic ray research in the period that followed until the late fifties was summarized by Peters (1959).

It should also be mentioned that at a relatively early stage of cosmic ray research, since the early thirties, Eugster, himself a pathologist with a profound interests in cosmic ray physics, conducted pioneering studies over decades on the biological effects of the cosmic radiation. Some of this work he did in collaboration with Hess and is also summarized in the account mentioned above (see also Eugster and Hauptmann, 1934).

5.1 Introduction

Under the term *cosmic radiation* we usually mean the flux of energetic particles that enter the Earth's atmosphere from outer space. The bulk of this radiation is of hadronic nature and seems to be of galactic origin but the ultra energetic tail of the spectrum with energies in excess of about 10^9 GeV is probably of extragalactic origin.

The galactic component is believed to be essentially isotropic outside the heliosphere whereas propagation effects within it cause an anisotropy on the order of 1%. Recently some authors have suggested that there may be a

local source that could contribute to irregularities in the hadron spectrum, and that there may be a radial gradient of cosmic rays in our Galaxy (Erlykin and Wolfendale, 1997 and 1999; Erlykin et al., 1997a and 1997b), but the idea is not widely accepted.

The low energy portion of the cosmic ray spectrum is subject to strong variability due to solar modulation, following the 11 year solar cycle. The modulation effects decrease with increasing particle rigidity and become negligible for particles with rigidities in excess of a few GV (or approximately 5 GeV/nucleon). Cosmic ray modulation is highly complex and a vast field of its own. For this reason this subject is not treated in detail in this book, only some basic modulation phenomena in connection with spectral influences are described in this chapter and in Chapter 6, Section 6.3.

The isotropic flux at sunspot minimum is about 4 protons $cm^{-2}s^{-1}$, at sunspot maximum it is about 2 protons $cm^{-2}s^{-1}$ at 1 *astronomical unit* [AU]. A one year exposure to the galactic cosmic radiation at 1 AU yields a dose of $\sim$ 10 rads at sunspot minimum and $\sim$4 rads at maximum (West et al., 1977).

The origin of the cosmic radiation is still a matter of scientific debate. Various objects in our Galaxy had been proposed as likely particle injectors and different acceleration mechanisms are known to have the ability to accelerate or possibly reaccelerate cosmic rays to energies of about 10^6 to 10^7 GeV, some even to 10^9 GeV (Völk and Biermann, 1988; Biermann 1993 and 1997). However, it remains a mystery where and how the most energetic particles with energies of 10^{10} GeV and beyond acquire their energy (Nagano and Watson, 2000), though various more or less exotic models and processes have been proposed.

Since the arrival directions of these particles do not seem to show any significant anisotropy if we disregard three particular events with energies $\geq 4 \cdot 10^{10}$ GeV (Teshima, 2000), a possible enhancement from the directions of Cygnus and the Galactic Center (Hayashida et al., 1999; Clay et al., 2000), their sources must be very distant in order to allow for directional randomization by the magnetic fields in space. If so it is a puzzle how these particles can reach our part of the universe across large distances without being subject to the Greisen-Zatsepin-Kuzmin (GZK) cutoff, expected to occur around $(3-5) \cdot 10^{10}$ GeV for protons (Zatsepin, 1951; Greisen, 1966; Zatsepin and Kuzmin, 1966; Kuzmin and Zatsepin, 1968).

This cutoff is due to interactions of the cosmic rays with the cosmic microwave background radiation (CMBR), predicted by Alpher et al. (1948 and 1950), Gamow (1948) and Dicke et al. (1965), and discovered by Penzias and

Wilson (1965), that degrade the energy of the particles via photo-pion production and fragment nuclei. The mean free path for photo-pion production is $\sim$6 Mpc.

To our present and experimentally confirmed knowledge the primary cosmic radiation consists chiefly of hadrons, at lower energies mostly protons and alpha particles, but also heavier nuclei up to iron and beyond. With increasing energy the fraction of heavier nuclei increases and thus the average mass of the primaries (for a review see Wolfendale, 1973; Smart and Shea, 1985; Swordy, 1994; Watson, 1997) . This trend seems to reverse at ultrahigh energies where we have indications from air shower experiments that the composition seems to change in favor of lighter nuclei and protons, possibly for reasons mentioned above.

There is a small diffuse flux of gamma rays whose spectrum exhibits a general power law behavior with some structure and the spectra of a large number of X-ray and gamma ray point sources superimposed on it which had been discovered through the years (Giacconi et al., 1962). Today, the latter are part of the rapidly evolving field of gamma ray astronomy which spans over an energy range from less than 0.5 MeV into the multi-PeV and possibly EeV domain (for a review see Weekes, 1988; Ong, 1998; see also Section 5.4).

Some of the point sources emit extremely energetic photons, some continuously like the Crab nebula in our own Galaxy, others show remarkable flaring activity like the AGN object Markarian 501, or the distant blazars. Others seem to have disappeared completely from the high energy scenario like Cygnus X-3, located at the fringes of our Galaxy (Weekes, 1988).

In 1963 a small flux of energetic electrons (negatrons and positrons) at the level of about one percent of the hadronic flux has also been identified (De Shong et al., 1964) (see Section 5.3). Part of this flux is probably due to the pion - muon - electron (or positron) decay chain resulting from energetic collisions of the primary hadronic component with the interstellar medium and to interactions with the background radiation field.

A contribution is also expected from pair production of energetic photons of various origin in encounters with interstellar matter and very likely from objects such as the Crab which is well known for its highly polarized synchrotron radiation, revealing the presence of energetic electrons in magnetic fields. However, the electron component below $\simeq$20 MeV is dominated by Jovian electrons (Eraker and Simpson, 1981).

In 1979 experimental evidence of the detection of a very small flux of antiprotons in the cosmic radiation was claimed (see Section 5.6). The question

whether this flux is entirely of secondary nature, being the result of collisions of the primary radiation with interstellar matter only, or contains a primordial component, too, remained unanswered (Golden et al., 1978, 1979a and 1979b; Bogomolov et al., 1979). So far no antinuclei have been identified.

In addition there must be a very large flux of neutrinos and antineutrinos of all flavors of extraterrestrial origin (Learned and Mannheim, 2000) which so far has evaded identification except for the neutrino burst from the supernova SN-1987a (Aglietta et al., 1987; Alekseev et al., 1987; Bionta et al., 1987; Hirata et al., 1987 and 1988) (see Section 5.5) and the continuous flux of solar neutrinos, discussed in Chapter 6, Section 6.6 (for a comprehensive review see Koshiba, 1992).

It is expected that there must be numerous neutrino point sources of different energy regimes within our Galaxy and beyond. Their detection is only a matter of time. They are expected to play a key role for finding the sources of the cosmic radiation (Learned, 1993; Gaisser et al., 1995) (see also Sections 4.5 and 5.5).

The solar contribution to the local cosmic radiation, frequently referred to as *solar cosmic rays*, *energetic solar particles* (ESP) or *solar energetic particles* (SEP), concerns the very low energy portion of the spectrum only ($E < 50$ MeV) and is of sporadic nature (see Chapter 6, Section 6.4). The sources of energetic solar particles are usually *solar flare events*. It is mostly protons and electrons that are ejected but also small quantities of heavier elements may be involved. Rarely solar flare particles may attain energies of several GeV (Mandzhavidze, 1993; Ruffolo, 1997). In the region between about 100 MeV and 1 GeV there is a so-called *anomalous cosmic ray component* (Panasyuk, 1993; Jokipii and Kòta, 1997) (see Chapter 6, Section 6.5).

At very rare occasions solar neutrons can be observed at Earth. To arrive as such they must be sufficiently energetic to avoid decay during transit, i.e., $E_n > \approx 100$ MeV (Kocharov, 1993). To be detectable at ground level their energy must exceed 250 MeV. Topics concerning energetic solar particles, anomalous cosmic rays and solar neutrons are discussed briefly in Chapter 6, Section 6.4.

The differential energy spectra of all components of the cosmic radiation in space with kinetic energy larger than a few GeV can be described by a power law of the form

$$j(E) \propto E^{-\gamma} , \tag{5.1}$$

where j is the intensity, E the kinetic energy per nucleon and γ the spectral index.

At energies above a few GeV the value of γ is approximately 2.7 for the hadronic component and remains constant over many decades of energy, up to the so-called *knee* at $\simeq 3 \cdot 10^6$ GeV, originally discovered by Kulikov and Khristiansen (1958), where the spectrum steepens and γ reaches a value of $\simeq 3.0$ with slightly falling tendency to reach about 3.15 at 10^9 GeV. At ultra high energies, beyond the so-called *ankle* at $\simeq 10^{10}$ GeV, where the extragalactic component is probably dominating, the spectrum appears to flatten with $\gamma \sim 2.7$.

References

Aglietta, M., G. Badino, G. Bologna, C. Castagnoli, A. Castellina, V.L. Dadykin, W. Fulgione, P. Galeotti, F.F. Kalchukov, V.B. Kortchaguin, P.V. Kortchaguin, A.S. Malguin, V.G. Ryassny, O.G. Ryazhskaya, O. Saavedra, V.P. Talochkin, G. Trinchero, S. Vernetto, G.T. Zatsepin, and V.F. Yakushev: Europhys. Lett., 3 (12), p. 1315 (1987).

Alekseev, E.N., L.N. Alekseeva, V.I. Volchenko, and I.V. Krivosheina: Pis'ma Zh. Eksp. Teor. Fiz., 45, No. 10, p. 461 (1987) and JETP Lett., 45, No. 10, p. 589 (1987).

Alpher, R.A., H.A. Bethe, and G. Gamow: Phys. Rev., 73, p. 803 (1948).

Alpher, R.A., and R.C. Herman: Rev. Mod. Phys., 22, p. 153 (1950).

Biermann, P.L.: Astron. Astrophys., 271, p. 649 (1993).

Biermann, P.L.: in Cosmic Winds and the Heliosphere, ed. J.R. Jokipii et al., University of Arizona Press, Tucson, p. 887 (1997).

Bionta, R.M., G. Blewitt, C.B. Bratton, D. Casper, A. Ciocio, R. Claus, B. Cortez, M. Crouch, S.T. Dye, S. Errede, G.W. Foster, W. Gajewski, K.S. Ganezer, M. Goldhaber, T.J. Haines, T.W. Jones, D. Kielczewska, W.R. Kropp, J.G. Learned, J.M. LoSecco, J. Matthews, R. Miller, M.S. Mudan, H.S. Park, L.R. Price, F. Reines, J. Schultz, S. Seidel, E. Shumard, D. Sinclair, H.W. Sobel, J.L. Stone, L.R. Sulak, R. Svoboda, G. Thornton, J.C. van der Velde, and C. Wuest: Phys. Rev. Lett., 58, p. 1494 (1987).

Bogomolov, E.A., N.D. Lubyanaya, V.A. Romanov, S.V. Stepanov, and M.S. Shulakova: PICRC, 1, p. 330 (1979).

Clay, R.W., B.R. Dowson, J. Bowen, and M. Debes: Astropart. Phys., 12, p. 249 (2000).

De Shong, J.A., R.H. Hildebrand, and P. Meyer: Phys. Rev. Lett., 12, p. 3 (1964).

Dicke, R.H., P.J.E. Peebles, P.G. Roll, and D.T. Wilkinson: Astrophys. J., 142, p. 414 (1965).

Eraker, J.H., and J.A. Simpson: PICRC, 3, p. 279 (1981).

Erlykin, A.D., and A.W. Wolfendale: PICRC, 4, p. 85 (1997).

Erlykin, A.D., and A.W. Wolfendale: PICRC, 3, p. 140 (1999).

Erlykin, A.D., A. Smialkowski, and A.W. Wolfendale: PICRC, 3, p. 113 (1997a).

Erlykin, A.D., A. Smialkowski, and A.W. Wolfendale: Astropart. Phys., 8, p. 283 (1997b).

Eugster, J., und W. Hauptmann: Strahlentherapie, 49. Band (1934).

Eugster, J., und V.F. Hess: Die Weltraumstrahlung (Kosmische Strahlung) und ihre biologische Wirkung. Orell Füssli Verlag, Zürich (1940).

Gaisser, Thomas K., Francis Halzen, and Todor Stanev: Physics Reports, 258, p. 173 - 236 (1995).

Gamow, G.: Nature, 162, p. 680 (1948).

Giacconi, Riccardo, Herbert Gursky, Frank R. Paolini, and Bruno B. Rossi: Phys. Rev. Lett., 9, p. 439 (1962).

Golden, R.L., G.D. Badhwar, J.L. Lacy, and J.E. Zipse: Nucl. Instr. Meth., 148, p. 179 (1978).

Golden, R.L., S. Horan. B.G. Mauger, G.D. Badhwar, J.L. Lacy, S.A. Stephens, R.R. Daniel, and J.E. Zipse: PICRC, 12, p. 76 (1979a).

Golden, R.L., S. Horan. B.G. Mauger, G.D. Badhwar, J.L. Lacy, S.A. Stephens, R.R. Daniel, and J.E. Zipse: Phys. Rev. Lett., 43, p. 1196 (1979b).

Greisen, K.: Phys. Rev. Lett., 16, p. 748 (1966).

Hayashida, N., M. Nagano, D. Nishikawa, H. Ohoka, N. Sakaki, M. Sasaki, M. Takeda, M. Teshima, R. Torii, T. Yamamoto, S. Yoshida, K. Honda, N. Kawasumi, I. Tsushima, N. Inoue, E. Kusano, K. Shinozaki, N. Souma, K. Kadota, F. Kakimoto, K. Kamata, S. Kawaguchi, Y. Kawasaki, H. Kitamura, Y. Matsubara, K. Murakami, Y. Uchihori, and H. Yoshii: Astropart. Phys., 10, p. 303 (1999).

Hess, V.F.: Phys. ZS. 13, p. 1084 (1912).

Hirata, K., T. Kajita, M. Koshiba, M. Nakahata, Y. Oyama, N. Sato, A.

Suzuki, M. Takita, Y. Totsuka, T. Kifune, T, Suda, K. Takahashi, T. Tanimori, K. Miyano, M. Yamada, E.W. Beier, L.R. Feldscher, S,B. Kim, A.K. Mann, F.M. Newcomer, R. Van Berg, W. Zhang, and B.G. Cortez: Phys. Rev. Lett., 58, p. 1490 (1987).

Hirata, K., T. Kajita, M. Koshiba, M. Nakahata, Y. Oyama, N. Sato, A. Suzuki, M. Takita, Y. Totsuka, T. Kifune, T, Suda, K. Takahashi, T. Tanimori, K. Miyano, M. Yamada, E.W. Beier, L.R. Feldscher, W. Frati, S,B. Kim, A.K. Mann, F.M. Newcomer, R. Van Berg, W. Zhang, and B.G. Cortez: Phys. Rev., D 38, p. 448 (1988).

Jokipii, J.R., and J. Kòta: PICRC, 8, p. 151 (1997).

Kocharov, G.E.: PICRC, 5, p. 483, eds. Leahy, Hicks and Venkatesan, World Scientific, Singapore (1993).

Koshiba, M.: Physics Reports, 220, Nr. 5 & 6, p. 229 - 381 (1992).

Kulikov, G.V., and G.B. Khristiansen: JETP, 35, p. 635 (1958).

Kuzmin, V.A., and G.T. Zatsepin: Can. J. Phys., 46, p. S617 (1968).

Learned, J.G.: in "Cosmic Rays 92 - Astrophysical, High Energy and Heliospheric Processes", P.K.F. Grieder, ed., Nucl. Phys. B (Proc. Suppl.) 33A, B, p. 77 (1992).

Learned, J.G., and K. Mannheim: Ann. Rev. Nucl. and Part. Sci., 50, p. 679 (2000).

Mandzhavidze, Natalie: PICRC, 5, p. 157, eds. Leahy, Hicks and Venkatesan, World Scientific, Singapore (1993).

Nagano, M., and A.A. Watson: Rev. Mod. Phys., 72, p. 689 (2000).

Ong, René A.: Phys. Rep., 305, p. 93 (1998).

Panasyuk, M.I.: PICRC, 5, 455, eds. Leahy, Hicks and Venkatesan, World Scientific, Singapore (1993).

Penzias, A.A, and R.W. Wilson: Astrophys. J., 142, p. 419 (1965).

Peters, B.: J. Geophys. Res., 64, No. 2, p. 155 (1959).

Piccard, A., and M. Cosyns: Comptes rendus de l'academie de mathem., 195, No. 1, p. 604 (1932).

Ruffolo, D.: PICRC, 8, p. 109 (1997).

Smart, D.F., and M.A. Shea: in "Handbook of Geophysics and Space Environment", Adolph S. Jursa, ed., Air Force Geophysical Laboratory (1985).

Swordy, Simon: PICRC, 5, p. 243 (1994); eds. D.A. Leahy, R.B. Hicks, and D. Venkatesan. World Scientific Publishing Co., Singapore (1994).

Teshima, M.: PICRC, Invited and Rapporteur Papers, AIP Conf. Proc., 516, p. 365 (2000).

Völk, H.J., and P.L. Biermann: Astrophys. J. Lett., 333, p. L65 (1988).

Watson, A.A.: PICRC, 8, p. 257 (1997).

Weekes, Trevor, C.: Physics Reports, 160, Nr. 1 & 2 (1988).

West, G.S. Jr., S.J. Wright, and H.C. Euler, eds.: "Space and Planetary Environment Criteria Guidelines for use in Space Vehicle Developments". NASA-TM-78119 (1977).

Wolfendale, A.W.: in "Cosmic Rays at Ground Level". A.W. Wolfendale, ed., The Institute of Physics, London (1973).

Zatsepin, G.T.: Dokl. Akad. Nauk SSSR, 80, p. 577 (1951).

Zatsepin, G.T. and V.A. Kuzmin: Zh. Eksperim. Teor. Fiz. Letters, 4, p. 114 (1966).

5.2 Hadrons, Spectra and Composition

5.2.1 Introduction

The hadronic component covers an enormous energy range. At or near the Earth the low energy observational limit is given by the geomagnetic cutoff and, if detection takes place within the atmosphere, by an additional atmospheric cutoff. On the opposite side of the spectrum, where the most energetic particles so far detected exceed 10^{20} eV, detector size and statistics impose a limit to exploration.

The low energy component up to rigidities of a few GV is subject to solar modulation and exhibits a large variability that may be as much as a factor of two or more in intensity. The modulation effects are rigidity dependent and diminish with increasing particle rigidity. They become negligible at a rigidity of about 10 GV.

The chemical (or mass) composition of the hadronic component ranges from protons to the actinide elements, and seems to manifest a non-trivial energy dependence. This may be linked to source composition, mass dependent acceleration and propagation. Our knowledge concerning the details of the composition decreases rapidly with increasing energy because of the rapid fall of the spectrum, resulting in poor statistics. In addition, there are technical problems in connection with particle identification and energy or momentum measurements.

Presently direct measurements of the energy and composition of the cosmic radiation are limited to the region below $\sim 10^5$ GeV per particle. The low energy component was explored with instruments on board of satellites, space stations, and balloons using a wide variety of techniques and instruments. Much effort has recently been invested into the determination of isotope ratios at low energies.

Balloon-borne experiments flown near the fringes of the atmosphere using electronic detectors such as spectrometers, Cherenkov counters, calorimeters, transition radiation detectors, combinations of the latter and more advanced systems, or nuclear emulsion, recording and identifying individual particles have yielded excellent data in the region between the geomagnetic and/or atmospheric cutoff and about 10^5 GeV. In this energy range energy spectra of particles of distinct charge, mass or mass groups had been measured recently by the JACEE (Cherry, 1997a, 1997b and 1999) and RUNJOB experiments (Apanasenko et al., 1997a, 1997b, 1999a and 1999b). However, deviations in slope and intensity of some of the components observed by these two

experiments remain, as is evident from the data shown below.

At higher energies the composition is still very uncertain and partly subject to speculations. This is because the determination of both, the energy and the nature (mass and/or charge) of the primaries, are based on very indirect methods using large ground-based installations that detect air showers initiated by these particles.

Air showers are highly complex phenomena and represent another vast branch of cosmic ray and astroparticle physics research which is beyond the scope of this book (see Galbraith, 1958; Khristiansen, 1980; Sokolsky, 1989). Air showers are used to explore the primary spectrum to the highest energies, up to and beyond 10^{11} GeV.

5.2.2 All-Particle Spectrum

The all-particle energy spectrum is the spectrum of all primary cosmic ray hadrons combined, irrespective of charge or mass. Thus, it comprises all the species of the elements and isotopes of the entire chart of the nuclides. This spectrum spans over an enormous energy range of more than ten decades, from less than 1 GeV to over 10^{11} GeV. The intensity is usually expressed in GeV per nucleus [GeV/nucleus].

The all-particle spectrum is assembled from data of many different experiments. The low energy data are from satellite measurements made well outside the Earth's atmosphere as well as from balloon-borne measurements made at the fringes of the atmosphere. In either case we are dealing with direct detection of individual nuclear species. The low energy component is subject to strong variability because of solar modulation. At rigidities in excess of about 10 GV solar modulation becomes irrelevant.

Balloon-borne measurements require in addition corrections for energy losses and nuclear interactions of the primaries with constituents of the residual atmosphere that also lead to spallation and fragmentation of primary nuclei and thus to a change of composition before detection. Spallation and fragmentation cause losses as well as enhancement of specific nuclei.

For direct measurements on board of satellites a wide variety of electronic detection systems is being used whereas superconducting magnetic spectrometers and other electronic instruments as well as nuclear emulsion, mostly in the form of elaborate emulsion stacks or emulsion chambers, are employed in balloon experiments. Depending on the kind of instrument used charge and energy or even mass (isotope) and momentum can be determined. At present direct measurements can be made to energies as high as about 100

TeV/nucleus. This energy limit is imposed by the physical size of the detectors and the rapidly falling spectrum, i.e., the diminishing intensity with increasing energy and thus the lack of events.

At higher energies the data for the all-particle spectrum are obtained with ground based equipment. A limited data sample is from large emulsion chambers located at mountain altitudes between 3776 m to 5450 m a.s.l. (Mt. Fujii, Japan, 3776 m; Pamir Mountains, Tadjikistan 3860 m and 4380 m; Mt. Chacaltaya, Bolivia, 5260 m, and Mt. Kanbala, Tibet, 5450 m; see Table C.3 in the Appendix). However, the very high energy data are acquired with air shower arrays located anywhere from sea level to over 5000 m a.s.l..

These measurements cannot identify the mass of the particles that initiate the showers, only their energy. The latter can be determined to an accuracy of about 20 percent or worse. However, with the data of highly sophisticated arrays that record simultaneously observables of different kinds of particles in a shower and possess a large hadron calorimeter, or a fly's eye type installation that can get the longitudinal shower profile, or a well equipped air Cherenkov array, the mass group (protons, light or heavy nuclei) of the primaries initiating the showers can be estimated.

In the mid-range the primary energy spectrum can also be derived from the high energy muon spectrum, and an estimate of the mass groups involved can be obtained from multi muon measurements.

In Fig. 5.1 we show the all-particle energy spectrum over the energy range from 1 MeV to over 100 EeV (10^{20} eV) in normal double logarithmic representation. This spectrum was assembled from the results of a large number of experiments using very different techniques. The low energy portion with the saddle and hump is subject to strong variability because of solar modulation. This part of the spectrum below 10 GeV, as shown in Fig. 5.1, is valid for a particular date. Its shape is characteristic but the exact intensities change continuously. With increasing energy (rigidity) of the particles the modulation effects decrease and become negligible above about 10 GeV, where the primary beam is dominated by protons and alpha particles.

Above 10 GeV the primary spectrum seems to be almost featureless except for a slight change of slope around $3 \cdot 10^{15}$ eV. The two straight sections of the spectrum can be described with two power laws of the form

$$j(E) \propto E^{-\gamma_{1,2}} \tag{5.2}$$

with $\gamma_1 = 2.68$ and $\gamma_2 = 3.15$, as indicated in Fig. 5.1 by the solid and dashed lines. The region of the spectrum where the two lines intersect is

known as the *knee* (Kulikov and Khristiansen, 1958).

If the intensity $j(E)$ of the differential energy spectrum is multiplied with the corresponding energy E to some fixed power α, i.e., $j(E) \cdot E^{\alpha}$, where α is usually chosen to be equal to the average slope of the spectral region under investigation, and again plotted in double logarithmic representation, the spectrum lies along a horizontal line. Any change of slope of the spectrum will now be strongly emphasized, causing a rapid deviation from the horizontal.

This is illustrated in the all-particle differential spectra shown in Figs. 5.2 and 5.4. Here we have plotted the quantity $j(E) \cdot E^{\alpha}$ with α set to 2.5 and 2.75, respectively. References for the contributions to the data are listed in the figure captions. The features of the knee of the spectrum are now well emphasized. The two plots a) and b) of Fig. 5.3 are a magnification of the knee region of Fig. 5.2, showing only the data points between 10^5 and 10^8 GeV, one part of the data in a) the other in b), for better comparison.

There is a great wealth of information in the so-called knee region of the spectrum that is being studied with many medium size air shower experiments located at different altitudes, such as Akeno (Akeno, Japan) (Hayashida et al., 1997; Nagano et al., 1984 and 1992), BASJE (Yoshii et al., 1995) and Chacaltaya (Bradt et al., 1965; Inoue et al., 1997) (both at Mt. Chacaltaya, Bolivia), CASA-MIA (Glasmacher et al., 1999a and 1999b), CASA-BLANCA (Cassidy et al., 1997; Fortson et al., 1999), DICE (Boothby et al., 1997a and 1997b; Kieda and Swordy, 1999) (all Dugway, Utah, U.S.A.), EAS-TOP (Gran Sasso, Italy) (Aglietta et al., 1995; EAS-TOP Collaboration, 1997), HEGRA (Canary Islands) (Cortina et al., 1997; Wiebel-Sooth et al., 1997; Röhring et al., 1999), KASCADE (Karlsruhe, Germany) (Klages et al., 1997; Hörandel et al., 1999; Kampert et al., 1999), Kobe (Japan) (Asakimori, 1990), Moscow (Russia) (Fomin et al., 1991; Khristiansen et al., 1995), Mt. Norikura (Japan) (Ito et al., 1997), Ooty (India) (Acharya et al., 1981; Gupta et al., 1997), SPASE and VULCAN (South Pole) (Dickinson et al., 1999), Tien Shan (Kazakhstan) (Antonov et al., 1995; Nesterova et al., 1995; Danilova et al., 1995; Nikolsky, 1997), Tunka (Russia, Siberia) (Gress et al., 1997), Yangbajing (Tibet, China) (Amenomori et al., 1996a and 1999), and others. Some of these installations are of recent date. For details see Appendix, Table C.1).

In Fig. 5.5 we show a selection of mostly recent results of some of the arrays listed above together with the classical data from the Proton satellite (Akimov et al., 1970; Grigorov et al., 1970, 1971a, 1971b and 1971c) and recent JACEE data from balloon flights (Asakimori et al., 1993a and 1993b; Cherry et al., 1995, 1997a, 1997b and 1999).

Table 5.1: Primary Spectral Indices Below (γ_1) and Above (γ_2) the Knee. E_k is the energy at which the knee is seen (Castellina, 2000).

Experiment	γ_1	γ_2	E_k [PeV]	Ref.
EAS-TOP	2.76 ± 0.03	3.19 ± 0.06	$2.7 - 4.1$	a)
KASCADE	2.70 ± 0.05	3.10 ± 0.07	$4.0 - 5.0$	b)
KASCADE	2.66 ± 0.12	3.03 ± 0.16	5.0 ± 0.5	c)
CASA	2.66 ± 0.02	3.00 ± 0.05	smooth	d)
Akeno	2.62 ± 0.12	3.02 ± 0.05	$\simeq 4.7$	e)
Tibet	2.60 ± 0.04	3.00 ± 0.05	smooth	f)
Tunka	2.60 ± 0.02	3.00 ± 0.06	$\simeq 4.0$	g)
BLANCA	2.72 ± 0.02	2.95 ± 0.02	$2.0^{+0.4}_{-0.2}$	h)
DICE	$\simeq 2.7$	$\simeq 3.0$	$\simeq 3.0$	i)
HEGRA	2.67 ± 0.03	$3.33^{+0.33}_{-0.41}$	$3.4^{+1.3}_{-0.7}$	j)
HEGRA	$2.72^{+0.02}_{-0.03}$	$3.22^{+0.47}_{-0.59}$	$3.98^{+4.66}_{-0.83}$	k)

a) Aglietta M. et al. (1999); b) Kampert et al. (1999); c) Hörandel et al. (1999); d) Glasmacher et al. (1999a); e) Nagano et al. (1984); f) Amenomori et al. (1996b); g) Gress et al. (1997); h) Fowler et al. (2000); i) Kieda and S.P.Swordy (1999); j) Rohring et al. (1999); k) Arqueros et al. (1999).

There is still much debate where exactly the knee is located and whether the change of slope is continuous and extends over a wider energy range or is rather sudden. Different experiments give different answers. In Table 5.1 we present a list compiled by Castellina (2000) of the spectral indices below and above the knee from a number of experiments and the energy where the knee is seen.

What exactly causes the knee is still a puzzle. However, we know that different constituents of the radiation, such as H, He, the CNO and Fe groups manifest different spectra at high energies, as will be discussed in the next subsection. In particular, the spectra of the different elements or mass groups do not show all the same spectral slope, some spectra drop-off more rapidly at high energy. Consequently, the superposition of the different spectra to form the all-particle spectrum must lead inevitably to irregularities in the latter (see Schatz, 2001).

Other factors such as rigidity dependent confinement (or leakage) could cause the knee in the spectrum and because of the elemental mix in the composition, irregularities in the knee region. Source properties, too, could in principle cause similar effects. Without going into any details concerning

acceleration and propagation of the cosmic rays, we show as an example in Fig. 5.6 the results of a model calculation.

The latter is based on the assumption of particle injection into the Galaxy with a power law spectrum, $E^{-\gamma}$, with a constant spectral index of -2.3 for all components at the source, with a diffusion escape, τ_{esc}, that is proportional to $E^{-\delta}$ with $\delta = 0.4$, and a rigidity of 10^{15} V with appropriate source abundances (Webber, 1983) (see also Müller, 1989; Swordy et al., 1990 and Subsection 5.2.3 where the elemental composition of the cosmic radiation is discussed).

In Figs. 5.7 to 5.12 we show the upper end of the explored primary spectrum. These spectra were acquired by the five giant air shower arrays, Akeno-AGASA (Japan), Haverah Park (GB), Yakutsk (Russia), Volcano Ranch (U.S.A.) and SUGAR (Aus.), and the Fly's Eye (U.S.A.). All intensities in these figures are multiplied with $E^{3.0}$. Each of these installations has or had its particularity. We will only point out that the spectrum of the SUGAR array of the University of Sydney (Aus.) is based essentially on muon measurements at shallow depth underground (Brownlee et al., 1968), whereas the other spectra were derived using chiefly the photon-electron component with an admixture of muons. The Fly's Eye is basically an air fluorescence detector with an unavoidable and varying contribution of Cherenkov light being collected, and the Yakutsk array makes use of both, air Cherenkov and particle density distribution measurements on the ground.

Some of these arrays have been taken out of service quite some time ago and those remaining in operation are subject to modification or extension from time to time. Changes may, of course, affect calibration and can influence the resulting spectrum. Figure 5.13 shows a compilation of the six spectra in a single plot without modification or normalization of the data. Teshima (1993) in a similar summary has normalized the energies of the spectra from the more recent experiments (Fly's Eye, Yakutsk and Haverah Park) with respect to the Akeno spectrum and constructed a *Grand Unified* energy spectrum, shown in Fig. 5.14.

The results presented in Figs. 5.7 to 5.14 show clearly a further change of slope of the spectrum around 10^{19} eV where γ decreases from $\simeq$3.0 to reach again a value of $\gamma \simeq 2.7$. This change of slope is known as the *ankle* of the primary spectrum. From these spectra it is difficult to draw a clear-cut conclusion whether the Greisen-Zatsepin-Kuzmin (GZK) cutoff (Zatsepin, 1951; Greisen, 1966; Zatsepin and Kuzmin, 1966; Kuzmin and Zatsepin, 1968) becomes effective or not. This cutoff which is briefly discussed in Section 5.1 is expected to appear around $(3 - 5) \cdot 10^{19}$ eV. It is due to interactions of the ultrahigh energy primary cosmic radiation with the cosmic microwave

background radiation (CMBR) (Penzias and Wilson, 1965) that lead to significant energy losses of the particles which initially populate the high end of the spectrum (Hill and Schramm, 1985; Baltrusaitis et al., 1985; Berezinsky and Grigorieva, 1988; Stecker, 1989; Protheroe and Johnson, 1996; Hillas 1999). It is expected that the questions concerning the GZK cutoff will be answered by the huge Auger array, now under construction in Argentina (Cronin, 1992, 1999 and 2001; Guérard, 1999; Watson, 1992).

A consequence of the GZK cutoff implies that the sources of the most energetic cosmic ray particles would have to lie within 50 Mpc of the observer to avoid the cutoff. This, however, could lead to anisotropies which so far have escaped detection. For ultra energetic particles from larger distances a pileup in the spectral region just around or below the expected cutoff could occur (Hill and Schramm, 1985), and nuclei would not arrive as such because of dissociation. In Fig. 5.7 a theoretical primary spectrum is plotted together with experimental Akeno and AGASA data that would be expected for extragalactic sources, distributed uniformly in the Universe, including the effect of the GZK cutoff (Takeda et al., 1998; Yoshida and Teshima, 1993).

Several mechanisms have been proposed to circumnavigate the GZK cutoff problem; for distant sources by invoking rather exotic processes and particles (e.g. Protheroe and Stanev, 1996; see also Section 5.5), by introducing a Galactic wind (Biermann et al., 2000), or, assuming galactic sources, by invoking specific source objects that accelerate chiefly iron nuclei in rather conventional processes and subsequent propagation through the Galaxy that accounts for an approximately isotropic distribution (e.g. Olinto et al., 1999).

Up to date more than 10 events had been detected that are claimed to have energies $> 10^{20}$ eV (Yoshida and Dai, 1998). The most energetic event had an energy of $(3^{+0.36}_{-0.54}) \cdot 10^{20}$ eV (300 EeV) (Bird et al., 1993a and 1995). From these observations it appears that the GZK-cutoff is violated. Recent analyses of the ultrahigh energy portion of the cosmic ray spectrum in the light of the GZK-cutoff were carried out by Watson (1992 and 1995), Hayashida et al. (1994 and 1997), Yoshida et al. (1995), and Wiebel-Sooth and Biermann (1998).

In Table 5.2 we have summarized the value of the spectral index, γ, obtained by some of the large experiments over different regions of the primary all-particle spectrum and in Table 5.3 the intensities at 10^{19} eV. In Table 5.4 we have reproduced the data of Kieda and Swordy (1999) showing the absolute intensities over the knee region which they have obtained with the DICE installation.

Table 5.2: Spectral Indices γ of Differential Spectra Determined by Different Experiments Between $5 \cdot 10^{15}$ eV and 10^{20} eV.

Site	γ	Energy Range [eV]
Akeno[1)]	3.02 ± 0.03	$5 \cdot 10^{15} - 6.3 \cdot 10^{17}$
Akeno Array 1[1)]	3.24 ± 0.18	$6.3 \cdot 10^{17} - 6.3 \cdot 10^{18}$
Akeno Array 20[1)]	3.16 ± 0.08	$6.3 \cdot 10^{17} - 6.3 \cdot 10^{18}$
Akeno Array 20[1)]	3.04 ± 0.04	$5 \cdot 10^{15} - 6.3 \cdot 10^{19}$
AGASA Array [2)]	2.67	below knee
AGASA Array [2)]	3.07	above knee
Chacaltaya[1)]	3.0	$10^{16} - 2 \cdot 10^{18}$
Fly's Eye[2)]	3.01 ± 0.06	$2 \cdot 10^{17} - 4 \cdot 10^{17}$
Fly's Eye[3)]	3.27 ± 0.02	$4 \cdot 10^{17} - 3 \cdot 10^{18}$
Fly's Eye[3)]	2.71 ± 0.10	$3 \cdot 10^{18} - 4 \cdot 10^{19}$
Fly's Eye Mono[3)]	3.07 ± 0.01	$2 \cdot 10^{17} - 8 \cdot 10^{19}$
Fly's Eye Stereo[3)]	3.18 ± 0.02	$2 \cdot 10^{17} - 4 \cdot 10^{19}$
Haverah Park[4)]	3.01 ± 0.02	$3 \cdot 10^{17} - 4 \cdot 10^{17}$
Haverah Park[4)]	$3.14^{+0.05}_{-0.06}$	$4 \cdot 10^{17} - 4 \cdot 10^{18}$
Yakutsk[5)]	2.98 ± 0.06	$3 \cdot 10^{17} - 2 \cdot 10^{18}$
Yakutsk[5)]	3.23 ± 0.08	$2 \cdot 10^{18} - 10^{19}$
Grand	3.02 ± 0.03	$\leq 10^{17.8 \pm 0.2}$
Unified	3.20 ± 0.05	$10^{17.8 \pm 0.2} - 10^{18.9 \pm 0.2}$
Spectrum[6)]	2.6 ± 0.1	$\geq 10^{18.9 \pm 0.2}$
Akeno [1)]	2.8 ± 0.3	
Fly's Eye[1)]	2.90 ± 0.12	Above Ankle
Haverah Park[1)]	2.7 ± 0.2	($\geq 10^{19}$)
Yakutsk[1)]	2.65 ± 0.17	

[1)] Nagano et al. (1992); [2)] Stanev et al. (1993); [3)] Bird et al. (1994);
[4)] Watson, 1991; Lawrence et al. (1991); [5)] Efimov et al. (1991); [6)] Teshima (1993)

5.2.3 Charge Resolved Energy Spectra and Chemical Composition

General Comments and Overview

A large number of measurements have been carried out through the years to obtain charge resolved energy spectra, to determine the chemical or elemen-

Table 5.3: All-Particle Differential Intensities $j(E)$ at 10^{19} eV.
(Watson, 1992; Wiebel-Sooth and Biermann, 1998)

Array Name	Intensity $j(E)$ $[\mathrm{cm}^{-2}\,\mathrm{s}^{-1}\,\mathrm{sr}^{-1}\,\mathrm{eV}^{-1}]$
Akeno AGASA	$2.91 \cdot 10^{-37}$
Fly's Eye	$2.38 \cdot 10^{-37}$
Haverah Park	$2.22 \cdot 10^{-37}$
Yakutsk	$3.39 \cdot 10^{-37}$

Table 5.4: Absolute Intensities of Primaries versus Energy
DICE Experiment (Kieda and Swordy, 1999).

Energy [GeV]	Intensity $[\mathrm{m}^{-2}\mathrm{sr}^{-1}\mathrm{s}^{-1}\mathrm{GeV}^{-1}]$	Error $[\mathrm{m}^{-2}\mathrm{sr}^{-1}\mathrm{s}^{-1}\mathrm{GeV}^{-1}]$
$3.55 \cdot 10^{5}$	$3.61 \cdot 10^{-11}$	$5.0 \cdot 10^{-13}$
$4.47 \cdot 10^{5}$	$2.08 \cdot 10^{-11}$	$3.0 \cdot 10^{-13}$
$5.62 \cdot 10^{5}$	$1.15 \cdot 10^{-11}$	$1.8 \cdot 10^{-13}$
$7.08 \cdot 10^{5}$	$6.19 \cdot 10^{-12}$	$1.1 \cdot 10^{-13}$
$8.91 \cdot 10^{5}$	$3.22 \cdot 10^{-12}$	$6.5 \cdot 10^{-14}$
$1.12 \cdot 10^{6}$	$1.67 \cdot 10^{-12}$	$3.9 \cdot 10^{-14}$
$1.41 \cdot 10^{6}$	$9.06 \cdot 10^{-13}$	$2.4 \cdot 10^{-14}$
$1.78 \cdot 10^{6}$	$4.96 \cdot 10^{-13}$	$1.5 \cdot 10^{-14}$
$2.24 \cdot 10^{6}$	$2.63 \cdot 10^{-13}$	$9.6 \cdot 10^{-15}$
$2.82 \cdot 10^{6}$	$1.42 \cdot 10^{-13}$	$6.1 \cdot 10^{-15}$
$3.55 \cdot 10^{6}$	$7.34 \cdot 10^{-14}$	$3.8 \cdot 10^{-15}$
$4.47 \cdot 10^{6}$	$3.33 \cdot 10^{-14}$	$2.3 \cdot 10^{-15}$
$5.62 \cdot 10^{6}$	$1.63 \cdot 10^{-14}$	$1.4 \cdot 10^{-15}$
$7.08 \cdot 10^{6}$	$7.11 \cdot 10^{-15}$	$8.2 \cdot 10^{-16}$
$8.91 \cdot 10^{6}$	$5.57 \cdot 10^{-15}$	$6.4 \cdot 10^{-16}$
$1.12 \cdot 10^{7}$	$2.07 \cdot 10^{-15}$	$3.5 \cdot 10^{-16}$
$1.4l \cdot 10^{7}$	$9.99 \cdot 10^{-16}$	$2.1 \cdot 10^{-16}$
$1.78 \cdot 10^{7}$	$4.30 \cdot 10^{-16}$	$1.2 \cdot 10^{-16}$
$2.24 \cdot 10^{7}$	$1.13 \cdot 10^{-16}$	$5.7 \cdot 10^{-17}$
$2.82 \cdot 10^{7}$	$1.12 \cdot 10^{-16}$	$5.0 \cdot 10^{-17}$

tal and mass compositions, and even isotope ratios of the cosmic radiation in the vicinity of the Earth and their energy dependencies. At low energies the chemical composition is relatively well known and we also have a fair knowledge of the isotopic composition. However, our information fades rapidly with increasing energy because of the rapidly falling spectrum which yields low counting rates and large statistical errors. In addition there are significant technical problems at high energies.

The most exhaustive data exist on low energy protons and helium nuclei because these particles are the most abundant. Because of the rapid decrease of the data on individual nuclei with increasing energy many authors handle the heavier and less abundant nuclei in groups. Frequently 5, 6 or even 7 elemental groups are formed, depending on the wealth of data that is available. Hydrogen (or protons) and helium nuclei are usually handled separately because there are enough data that insure adequate statistics, but the elements C N O, Ne-Si, and Fe-Ni are often grouped together to form three representative sets of nuclides for the analysis. It is therefore customary to refer to these groups as the H or p, the He, C N O, Ne-Si, and Fe-groups. Other authors prefer to classify the nuclei beyond helium ($Z > 2$) into the *light* or L ($3 \leq Z \leq 5$), *medium* or M ($6 \leq Z \leq 9$), *heavy* or H ($10 \leq Z \leq 20$), *very heavy* or VH ($21 \leq Z \leq 30$), and *ultra heavy* or UH ($Z > 31$) group of elements.

Chemical Composition at Low and Medium Energies

Major efforts to explore the cosmic radiation began after world war II with balloon-borne emulsion stacks and cloud chambers located at high altitude. The discovery of heavy nuclei in the primary radiation with the help of nuclear emulsion by Freier et al. (1948a and 1948b) and Bradt and Peters (1948) was a significant landmark for the field. Numerous experiments with balloon-borne equipment and later on measurements made on board of satellites yielded a great wealth of data. At present satellite measurements are still quite limited in the energy range they can explore but they offer many other advantages such as no residual atmosphere above the instrument. On the other hand emulsion stacks and emulsion chambers lack accurate mass determination but can explore in principle the highest energies and are essentially only event rate limited.

In the following we present from the great wealth of data that are available a very limited selection of compilations, including also some results of older measurements for comparison. With the help of a list of additional references the interested reader should find access to further, more detailed data.

In Figs. 5.15 and 5.16 we present the differential and integral energy spectra, respectively, of hydrogen (protons), helium and of the sum of carbon and oxygen nuclei from old balloon experiments (Webber and Lezniak, 1974), covering an energy range from 10 MeV/nucleon to $\leq$1000 GeV/nucleon. In the low energy region of Fig. 5.15 three spectra are shown for each, hydrogen and helium nuclei. They manifest the effect of solar modulation, corresponding to different epochs of solar activity, ranging from solar minimum (low solar activity) for the top curves to solar maximum for the bottom curves (high solar activity). It is evident from this figure that solar modulation effects can be disregarded in most cases beyond about 5 GeV/nucleon.

A similar set of differential spectra assembled from several experiments of more recent date which also includes iron nuclei is shown in Fig. 5.17 (Cherry, 1997b). Figures 5.18 and 5.19 show high energy differential and integral energy spectra of protons and helium nuclei obtained with modern emulsion experiments (Apanasenko et al., 1997c, 1997d, 1997e, 1999a and 1999b; Cherry, 1997a; Parnell et al., 1989; Shibata, 1997).

Another set of data from particle-by-particle measurements carried out with satellite and mostly balloon-borne experiments is compiled in Figs. 5.20, 5.21 and 5.22. The data show differential spectra of protons and helium nuclei, and of the CNO, NeMgSi and Fe-group nuclei. The spectra of Figs. 5.20 and 5.21 are multiplied by the energy per nucleon to the power of 2.5 ($E^{2.5}$/nucleon) whereas in Fig. 5.22, which shows the all-particle spectrum to the highest energies observed for direct detection, the spectrum is multiplied by the energy per nucleus to the power of 2.5 ($E^{2.5}$/nucleus). This representation has the advantage that it emphasizes the differences between the data from different experiments and the changes in spectral slope.

The differential intensities of medium and heavy nuclei and of groups of nuclear species compiled by Swordy et al. (1993) and Ichimura et al. (1993b and 1993d) are listed in Tables 5.5, 5.6 and 5.7, respectively. Note that the intensities given by Ichimura et al. (1993b) are multiplied by $E^{2.5}$.

A new precision measurement of the primary proton energy spectrum at relatively low energies has recently been made with the BESS-98 instrument on a balloon flight from Lynn Lake, Manitoba (Canada) (360 m a.s.l.), in 1998 under a residual atmosphere of about 5 g/cm^2 by Sanuki et al. (1999) (see also Nozaki, 2000). The instrument covered an energy range from 1 to 120 GeV. The result is presented in Fig. 5.23 together with data from earlier experiments of other authors as listed in the caption.

Similar measurements were carried out by Bellotti et al. (1999) with

the MASS-91 instrument on September 23, 1991 from Fort Sumner, NM (U.S.A.) (1270 m a.s.l.) and by Boezio et al. (1999) August 8/9, 1994 from Lynn Lake with the CAPRICE-94 instrument. The former measured the proton and helium spectra from 2.5 - 100 GeV and from 0.8 - 50 GeV, respectively, while the latter investigated hydrogen (protons and deuterons) over an energy range from 0.15 - 200 GeV and helium nuclei from 0.2 - 100 GeV. The results are given in Tables 5.8 to 5.11.

Wiebel-Sooth and Biermann (1998) have assembled the most comprehensive recent compilation of charge resolved cosmic ray energy spectra of individual nuclei from Z = 1 to Z = 28 and of four groups of nuclei, including the Ne-S ($10 \leq Z \leq 16$), Cl-Ca ($17 \leq Z \leq 20$), Sc-Mn ($21 \leq Z \leq 25$), and Fe-Ni ($26 \leq Z \leq 28$). The authors have fitted essentially all relevant data that are available in the literature, using the CERN MINUIT fitting program (CERN, 1992), to determine the spectral index, γ, and the absolute intensity coefficient, j_0, normalized at 1 TeV for a simple power law representation of the form

$$j(E) = j_0 E^{-\gamma} \tag{5.3}$$

of the measured spectra above an energy of $Z \cdot 10$ GeV/nucleus, where solar modulation ceases to affect the spectra. The values of j_0 and γ for individual nuclei and elemental groups are given in Tables 5.12, 5.13 and 5.14, including the χ^2 values. Note that E, the energy per nucleus, must be inserted in TeV. In Figs. 5.24 to 5.32 we have reproduced the spectra of Wiebel-Sooth and Biermann (1998) for H, He, C, N, O, Si, Ne-S, Fe and Fe-Ni.

From the large number of data on individual species of nuclei, particularly at low energy where statistics are good, the relative abundance of the elements (and isotopes) in the cosmic radiation can be determined. In Table 5.15 the relative abundances of the chemical elements in the cosmic radiation at low energy ($E \geq 5$ GeV) are summarized (Hillier, 1984). Listed, too, for comparison are the abundances of the elements in the solar system, mostly from meteorite measurements.

A comparison between the so-called solar system abundance of the chemical elements (Cameron 1973, 1981 and 1982; Grevesse et al., 1996) and the abundance of the elements in the cosmic radiation at low energy ($\leq$1.5 GeV) is presented in Fig. 5.33 (Simpson, 1983, 1997; Wefel, 1991) and Fig. 5.34 (Wiebel-Sooth and Biermann, 1998).

Chemical Composition at High Energies

With increasing primary energy the intensity of the cosmic radiation drops very rapidly and direct detection of individual particles becomes essentially impossible because of lack of events. Beyond about 100 TeV per nucleus only indirect methods of primary mass determination are available, using air shower techniques, that harbor large inherent errors. There the nature of the primaries can only be inferred from air shower observables recorded at ground level in conjunction with simulation calculations.

Sophisticated air shower arrays that record simultaneously different observables and are coupled with air Cherenkov or air scintillation observations that reveal data on the longitudinal development of the showers as well yield the best data. However, the information is still inadequate to go beyond a coarse assignment of the likely mass group of the primary initiating the shower (Grieder, 1977; Khristiansen 1980; Gaisser, 1990). Frequently, one distinguishes only between primary protons and iron nuclei in order to get a better mass signature and stronger differentiation.

This situation is well illustrated in Figs. 5.35 to 5.39. Figure 5.35 is an older compilation (Webber, 1983) which covers an energy range that overlaps well with direct observations. It shows besides the well established all-particle spectrum summary spectra of helium, of carbon and oxygen combined (C+O), the LH-group (light-heavy) and of iron, with the regions of uncertainty indicated. Shown, too, is the all-particle spectrum derived from muon measurements at ground level (Klemke et al., 1981).

Furthermore, data points from direct measurements of protons are also given. Some of these overlap with the lower end of the air shower energy range and the modern collider energy region. Data from collider experiments are important to calibrate and adjust air shower simulation models and their parameters from which the primary mass and energy are computed. A rough indication of the average mass number, A, of the primaries as deduced from the data of this compilation is given at different energies between 10 and 10^5 GeV/nucleus on top in Fig. 5.35. According to this work the average mass of the primaries increases from 1.8 to 13.0 over the energy range considered. This trend is also evident when plotting the fraction of the major elemental components of the cosmic radiation relative to the total differential intensity, as is shown in Fig. 5.36 (Ichimura et al., 1993b).

Figure 5.37 (Swordy et al., 1993, extended by the author) illustrates the present situation concerning the composition of the primary cosmic radiation at high energies. Shown are again data from single particle measurements

and the familiar all-particle spectrum. Above about 10^4 GeV/nucleus the scatter of the data points from the individual particle experiments is very large and likewise the error bars. On the other hand, the air shower data points that make up the largest portion of the all-particle spectrum start at a few 10^4 GeV, with tiny error bars up to about 10^8 GeV. They overlap for about two decades at the low energy side with the satellite data of Grigorov et al. (1971a).

Because of the large uncertainties of the mass of the primaries initiating air showers, the authors frequently specify the average mass rather than specific percentages of mass groups (light, heavy, etc.) over particular energy intervals. In Fig. 5.38 we present a compilation of the energy dependence of the average primary mass derived from air shower experiments. It is customary to plot $< \ln(A) >$ as a function of primary energy rather than A to compress the scatter of the data. Included in the figure are also some data from direct measurements.

The disagreement between different experiments above 1 PeV (10^{15} eV) is very large. The major reason for the large scatter of the data is the indirect mass determination method that is based on multi-parameter air shower data in conjunction with simulation calculations. Uncertainties concerning the models, in particular the interaction processes, that get worse with increasing energy lead to the large spread in the average primary mass. This is well illustrated in the three analyses of the KASCADE data over the knee region of the spectrum shown in Fig. 5.39, using either hadrons, electrons or both combined (Engler et al., 1999; Kampert et al., 1999).

If one disregards older data the general agreement is somewhat better. When computing the average mass using data from many indirect experiments (Fig. 5.38) one gets a value of $< \ln(A) > \simeq 2$ ($< A > \simeq 7.4$) just before the knee of the spectrum at $\simeq 10^{15}$ eV. Above 10^{16} eV a relatively dramatic change seems to occur, reaching $< \ln(A) > \simeq 3.5$ ($< A > \simeq 33$). At even higher energies the composition appears to get lighter again. Proton dominance cannot be excluded at the highest energies, also on theoretical grounds, due to dissociation of nuclei at ultrahigh energies when interacting with the cosmic microwave background radiation.

5.2.4 Isotopic Composition

The isotopic composition of the cosmic radiation had been investigated with considerable efforts mostly during the last decade. Emphasis was given to isotope ratios that are relevant to link local observations to likely sources

and source spectra as well as to determine the so-called *escape length*, the *confinement time*, the density of the interstellar medium and the matter column through which the cosmic ray particles must penetrate to reach our region of space. The experimental work is restricted to low energies because of lack of intensity, but also for purely practical reasons which limit the size of spectrometers on board of satellites. On the other hand low energy measurements are strongly influenced by solar modulation and must cope with all sorts of background problems (see also Chapter 6).

In Table 5.16 we list the results of some recent isotope ratio measurements. For an extensive compilation of isotope ratios the reader is referred to the summary of Wiebel-Sooth and Biermann (1998).

5.2.5 Conclusions from Composition Observations

When comparing the measured cosmic ray composition around 1 GeV per nucleon with terrestrial and solar abundances (Fig. 5.33), one finds that the cosmic radiation is enhanced in the Li, Be, B and the sub-iron elements. This enhancement is due to spallation of the primary cosmic ray nuclei during their propagation through the interstellar space where the particles are subject to interactions with the interstellar medium and the photon field (Garcia-Munoz et al., 1987; Wefel, 1991; Simpson, 1983 and 1997).

The cosmic rays as they are observed near Earth consist therefore of a mixture of a truly *primary* and a *secondary* component. To the former group belong the elements ^{1}H, ^{4}He, C, O, Ne, Mg, Si, and Fe; to the latter ^{3}He, Li, Be, B, F, and Z = 21 - 25. The ratios of various elements and isotopes, e.g., the ratio B/C or (Z = 21-25)/Fe, and the energy dependence of these ratios play an important role in the determination of the amount of matter the cosmic rays have traversed on their way from the source to the observer and to estimate the confinement time.

In addition, *radioactive isotopes* like ^{10}Be* give valuable complementary timing information. From the abundance of ^{10}Be* and its half life ($\tau \simeq 2 \cdot 10^6$ y) one can compute the age of the cosmic radiation. In an early calculation Shapiro and Silberberg (1970) obtained a confinement time of only $3 \cdot 10^6$ y. Later work based on ^{10}Be* of a few 100 MeV/nucleon and average interstellar densities of ~ 0.25 atoms/cm^3 yielded values of $\sim 10^7$y (Wiedenbeck and Greiner, 1980; Garcia-Munoz et al., 1977 and 1987; Dwyer and Meyer, 1987). Most recently Yanasak et al. (2001) obtain for an interstellar hydrogen density of 0.34 ± 0.04 atoms/cm^3 a confinement time of $(1.5 \pm 0.16) \cdot 10^7$ y. Connell et al. (1997) have summarized the results of recent work, including

studies where other isotopes had been used, such as $^{26}Al^*$, $^{36}Cl^*$ and $^{54}Mn^*$.

From the above mentioned studies one obtains for the amount of matter traversed by the cosmic rays in the interstellar space, i.e., in our Galaxy, a value of 7 - 10 g/cm^2 at energies of about 1 GeV/nucleon. Above a few GeV/nucleon where solar modulation and magnetospheric effects become small, the ratio of secondary to primary cosmic rays is observed to decrease with increasing energy, suggesting that the cosmic ray mean path length, Λ_{esc}, in the interstellar medium decreases with increasing energy approximately as $E^{-0.6}$. At about 1 TeV/nucleon it is $\sim$1 g/cm^2 (Müller, 1989; Swordy, 1995; Cherry, 1997a; Davis et al., 2000).

Table 5.5: Differential Intensity per Total Particle Energy (Swordy et al., 1993)

Element	Energy [GeV/Nucleus]	Differential Intensity [cm^{-2} s^{-1} sr^{-1} GeV^{-1}]	Reference
C	127	$(2.71 \pm 0.052) \cdot 10^{-7}$	a
(Z = 6)	194	$(8.42 \pm 0.35) \cdot 10^{-8}$	a
	420	$(1.01 \pm 0.14) \cdot 10^{-8}$	a
	871	$(1.280 \pm 0.164) \cdot 10^{-9}$	b
	1230	$(5.22 \pm 0.86) \cdot 10^{-10}$	b
	2480	$(8.66 \pm 0.9) \cdot 10^{-11}$	b
	18000	$(3.63 \pm 0.85) \cdot 10^{-13}$	b
0	169	$(2.06 \pm 0.038) \cdot 10^{-7}$	a
(Z = 8)	259	$(6.60 \pm 0.27) \cdot 10^{-8}$	a
	560	$(7.91 \pm 1.1) \cdot 10^{-9}$	a
	1160	$(1.180 \pm 0.113) \cdot 10^{-9}$	b
	1640	$(4.61 \pm 0.63) \cdot 10^{-10}$	b
	3310	$(7.26 \pm 0.75) \cdot 10^{-11}$	b
	24000	$(3.68 \pm 0.76) \cdot 10^{-13}$	b
Ne	223	$(2.39 \pm 0.05) \cdot 10^{-8}$	a
(Z = 10)	340	$(7.740 \pm 0.326) \cdot 10^{-9}$	a
	735	$(8.69 \pm 1.19) \cdot 10^{-10}$	a
	1050	$(4.43 \pm 0.60) \cdot 10^{-10}$	b
	1290	$(2.06 \pm 0.33) \cdot 10^{-10}$	b
	1740	$(7.88 \pm 1.6) \cdot 10^{-11}$	b
	3260	$(1.75 \pm 0.18) \cdot 10^{-11}$	b
	21600	$(7.15^{+6.8}_{-3.9}) \cdot 10^{-14}$	b
Mg	254	$(2.71 \pm 0.055) \cdot 10^{-8}$	a
(Z = 12)	389	$(8.780 \pm 0.367) \cdot 10^{-9}$	a
	840	$(1.000 \pm 0.119) \cdot 10^{-9}$	a
	1200	$(4.47 \pm 0.57) \cdot 10^{-10}$	b
	1470	$(2.56 \pm 0.33) \cdot 10^{-10}$	b
	1990	$(1.09 \pm 0.15) \cdot 10^{-10}$	b
	3790	$(2.03 \pm 0.17) \cdot 10^{-11}$	b
	24700	$(1.75^{+0.84}_{-0.58}) \cdot 10^{-13}$	b
Si	296	$(1.92 \pm 0.04) \cdot 10^{-8}$	a
(Z = 14)	454	$(6.610 \pm 0.278) \cdot 10^{-9}$	a
	980	$(7.94 \pm 1.09) \cdot 10^{-10}$	a
	1400	$(3.38 \pm 0.55) \cdot 10^{-10}$	b
	1720	$(1.76 \pm 0.33) \cdot 10^{-10}$	b
	2320	$(7.6 \pm 1.4) \cdot 10^{-11}$	b
	4400	$(1.33 \pm 0.17) \cdot 10^{-11}$	b
	28800	$(1.99^{+4.8}_{-1.6}) \cdot 10^{-14}$	b
Fe	594	$(7.000 \pm 0.170) \cdot 10^{-9}$	a
(Z = 26)	907	$(2.540 \pm 0.109) \cdot 10^{-9}$	a
	1960	$(3.28 \pm 0.45) \cdot 10^{-10}$	a
	2950	$(1.11 \pm 0.20) \cdot 10^{-10}$	b
	3320	$(7.91 \pm 1.2) \cdot 10^{-11}$	b
	3840	$(5.87 \pm 1.0) \cdot 10^{-11}$	b
	4570	$(3.36 \pm 0.54) \cdot 10^{-11}$	b
	6460	$(1.34 \pm 0.19) \cdot 10^{-11}$	b
	12400	$(2.67 \pm 0.5) \cdot 10^{-12}$	b
	36300	$(1.65^{+0.7}_{-0.5}) \cdot 10^{-13}$	b
	87500	$(1.65^{+1.6}_{-0.9}) \cdot 10^{-14}$	b

References: a, HEAO 3 (Engelmann et al., 1990); b, CRN (Müller et al., 1991b).

Table 5.6: Absolute Intensities of Heavy Elements Multiplied by $E^{2.5}$. The numbers in parenthesis are the number of events per bin. The energy is given in GeV per nucleon [GeV/N]. (Ichimura et al., 1993b)

Energy Range	Differential Intensity × $E^{2.5}$ [m^{-2} s^{-1} sr^{-1} (GeV/Nucleon)$^{1.5}$]		
[GeV/N]	Silicon (Z = 14)	Sulfur (Z = 16)	Calcium (Z = 20)
3.98 - 5.01	0.90 ± 0.14 (40)	0.168 ± 0.400 (18)	0.155 ± 0.036 (18)
5.01 - 6.31	1.15 ± 0.16 (50)	0.175 ± 0.041 (18)	
6.31 - 7.94	1.24 ± 0.17 (50)	0.248 ± 0.051 (24)	0.110 ± 0.033 (11)
7.94 - 10.0	1.89 ± 0.22 (72)	0.234 ± 0.052 (20)	
10.0 - 12.6	1.80 ± 0.24 (58)	0.364 ± 0.070 (27)	0.208 ± 0.052 (16)
12.6 - 15.9	2.04 ± 0.27 (55)	0.304 ± 0.072 (18)	
15.9 - 20.0	2.12 ± 0.30 (49)	0.396 ± 0.091 (19)	0.212 ± 0.092 (6)
20.0 - 25.1	2.01 ± 0.33 (36)	0.428 ± 0.106 (16)	0.178 ± 0.040 (20)
25.1 - 31.6	2.14 ± 0.39 (30)	0.381 ± 0.076 (25)	0.140 ± 0.040 (12)
31.6 - 39.8	1.76 ± 0.22 (66)	0.386 ± 0.074 (27)	0.201 ± 0.056 (13)
39.8 - 50.1	1.42 ± 0.22 (41)	0.354 ± 0.084 (18)	0.187 ± 0.062 (9)
50.1 - 63.1	1.72 ± 0.27 (41)	0.437 ± 0.109 (16)	0.169 ± 0.069 (6)
63.1 - 79.4	1.66 ± 0.27 (39)	0.452 ± 0.130 (12)	0.271 ± 0.100 (7)
79.4 - 100	1.38 ± 0.28 (24)	0.423 ± 0.150 (8)	0.213 ± 0.106 (4)
100 - 126	1.20 ± 0.30 (15)	0.396 ± 0.132 (9)	0.129 ± 0.074 (3)
126 - 159	1.40 ± 0.39 (13)		
159 - 200	1.04 ± 0.39 (7)	0.296 ± 0.209 (2)	0.051 ± 0.051 (1)
200 - 251	0.59 ± 0.26 (5)	0.352 ± 0.203 (3)	
251 - 316			
316 - 398	0.70 ± 0.40 (3)	0.386 ± 0.273 (2)	
398 - 501			
501 - 631	0.36 ± 0.36 (1)		
631 - 794			
794 - 1000			

Table 5.7: Absolute Intensities of Heavy Elements Multiplied by $E^{2.5}$. The numbers in parenthesis are the number of events per bin. The energy is given in GeV per nucleon [GeV/N]. (Ichimura et al., 1993b)

Energy Range	Differential Intensity × $E^{2.5}$ [m^{-2} s^{-1} sr^{-1} (GeV/Nucleon)$^{1.5}$]		
[GeV/N]	Iron (Z = 26)	Z = 17 - 20	Z = 21 - 25
3.98 - 5.01	1.11 ± 0.15 (56)	0.375 ± 0.065 (33)	0.302 ± 0.050 (36)
5.01 - 6.31	1.20 ± 0.16 (58)	0.453 ± 0.072 (40)	0.308 ± 0.051 (37)
6.31 - 7.94	1.45 ± 0.18 (66)	0.407 ± 0.071 (33)	0.437 ± 0.063 (48)
7.94 - 10.0	1.42 ± 0.19 (57)	0.510 ± 0.083 (38)	0.525 ± 0.072 (53)
10.0 - 12.6	1.35 ± 0.20 (47)	0.381 ± 0.076 (25)	0.495 ± 0.075 (44)
12.6 - 15.9	1.37 ± 0.22 (38)	0.527 ± 0.098 (29)	0.488 ± 0.061 (64)
15.9 - 20.0	1.51 ± 0.26 (34)	0.542 ± 0.111 (24)	
20.0 - 25.1	1.54 ± 0.30 (27)	0.598 ± 0.130 (21)	0.299 ± 0.092 (19)
25.1 - 31.6	1.26 ± 0.32 (18)	0.745 ± 0.166 (20)	0.385 ± 0.103 (14)
31.6 - 39.8	1.62 ± 0.41 (16)	0.641 ± 0.178 (13)	0.414 ± 0.055 (57)
39.8 - 50.1	1.68 ± 0.48 (12)	0.425 ± 0.075 (32)	0.391 ± 0.062 (40)
50.1 - 63.1	1.36 ± 0.51 (7)	0.396 ± 0.084 (22)	0.2920.062 (22)
63.1 - 79.4	1.55 ± 0.29 (29)	0.420 ± 0.102 (17)	0.328 ± 0.077 (18)
79.4 - 100	1.65 ± 0.35 (22)	0.441 ± 0.122 (13)	0.291 ± 0.065 (20)
100 - 126	1.38 ± 0.38 (13)	0.357 ± 0.099 (13)	
126 - 159	1.34 ± 0.45 (9)		0.289 ± 0.118 (6)
159 - 200	1.05 ± 0.47 (5)	0.214 ± 0.107 (4)	0.202 ± 0.117 (3)
200 - 251	1.37 ± 0.48 (8)		0.222 ± 0.111 (4)
251 - 316		0.247 ± 0.143 (3)	
316 - 398	1.22 ± 0.61 (4)		0.218 ± 0.154 (2)
398 - 501			
501 - 631	1.39 ± 0.98 (2)	0.221 ± 0.221 (1)	0.163 ± 0.163 (1)
631 - 794			
794 - 1000			
1000 - 1260	1.09 ± 1.09 (1)		0.191 ± 0.191 (1)
1260 - 1590			

Table 5.8: Differential Proton Intensities at the Top of the Atmosphere. (Bellotti et al., 1999) (MASS-91)

Energy Range [GeV]	Mean Energy [GeV]	Intensity $[cm^{-2}s^{-1}sr^{-1}GeV^{-1}]$
2.55 - 2.95	2.77	$(2.310 \pm 0.048) \cdot 10^{-3}$
2.95 - 3.41	3.21	$(5.184 \pm 0.071) \cdot 10^{-3}$
3.41 - 3.93	3.68	$(8.690 \pm 0.092) \cdot 10^{-3}$
3.93 - 4.52	4.22	$(8.346 \pm 0.085) \cdot 10^{-3}$
4.52 - 5.19	4.85	$(6.766 \pm 0.072) \cdot 10^{-3}$
5.19 - 5.95	5.56	$(5.480 \pm 0.060) \cdot 10^{-3}$
5.95 - 6.81	6.36	$(4.204 \pm 0.048) \cdot 10^{-3}$
6.81 - 7.78	7.28	$(3.283 \pm 0.040) \cdot 10^{-3}$
7.78 - 8.89	8.31	$(2.490 \pm 0.032) \cdot 10^{-3}$
8.89 - 10.1	9.49	$(1.918 \pm 0.026) \cdot 10^{-3}$
10.1 - 11.6	10.8	$(1.390 \pm 0.021) \cdot 10^{-3}$
11.6 - 13.2	12.3	$(1.066 \pm 0.017) \cdot 10^{-3}$
13.2 - 15.1	14.1	$(7.63 \pm 0.13) \cdot 10^{-4}$
15.1 - 17.2	16.1	$(5.52 \pm 0.10) \cdot 10^{-4}$
17.2 - 19.7	18.3	$(3.89 \pm 0.08) \cdot 10^{-4}$
19.7 - 22.5	21.0	$(2.79 \pm 0.06) \cdot 10^{-4}$
22.5 - 25.7	24.0	$(1.95 \pm 0.05) \cdot 10^{-4}$
25.7 - 29.5	27.5	$(1.40 \pm 0.04) \cdot 10^{-4}$
29.5 - 33.9	31.6	$(9.61 \pm 0.29) \cdot 10^{-5}$
33.9 - 39.0	36.3	$(6.52 \pm 0.22) \cdot 10^{-5}$
39.0 - 52.2	44.8	$(3.60 \pm 0.10) \cdot 10^{-5}$
52.2 - 71.0	60.3	$(1.67 \pm 0.06) \cdot 10^{-5}$
71.0 - 99.1	83.0	$(7.2 \pm 0.3) \cdot 10^{-6}$

Table 5.9: Differential Helium Intensities at the Top of the Atmosphere. (Bellotti et al., 1999) (MASS-91)

Energy Range [GeV]	Mean Energy [GeV]	Intensity $[cm^{-2}s^{-1}sr^{-1}GeV^{-1}]$
0.841 - 1.00	0.927	$(3.30 \pm 0.34) \cdot 10^{-4}$
1.00 - 1.19	1.11	$(6.53 \pm 0.49) \cdot 10^{-4}$
1.19 - 1.40	1.30	$(1.77 \pm 0.1) \cdot 10^{-3}$
1.40 - 1.64	1.52	$(2.72 \pm 0.14) \cdot 10^{-3}$
1.64 - 1.92	1.78	$(2.70 \pm 0.13) \cdot 10^{-3}$
1.92 - 2.24	2.08	$(2.19 \pm 0.11) \cdot 10^{-3}$
2.24 - 2.62	2.42	$(1.69 \pm 0.09) \cdot 10^{-3}$
2.62 - 3.03	2.82	$(1.35 \pm 0.07) \cdot 10^{-3}$
3.03 - 3.51	3.26	$(1.01 \pm 0.05) \cdot 10^{-3}$
3.51 - 4.06	3.77	$(7.48 \pm 0.41) \cdot 10^{-4}$
4.06 - 4.68	4.36	$(5.78 \pm 0.32) \cdot 10^{-4}$
4.68 - 5.39	5.02	$(4.58 \pm 0.26) \cdot 10^{-4}$
5.39 - 6.20	5.77	$(3.17 \pm 0.19) \cdot 10^{-4}$
6.20 - 7.13	6.64	$(2.38 \pm 0.15) \cdot 10^{-4}$
7.13 - 8.20	7.63	$(1.62 \pm 0.11) \cdot 10^{-4}$
8.20 - 9.42	8.77	$(1.19 \pm 0.08) \cdot 10^{-4}$
9.42 - 10.8	10.1	$(8.75 \pm 0.65) \cdot 10^{-5}$
10.8 - 12.4	11.6	$(5.36 \pm 0.45) \cdot 10^{-5}$
12.4 - 14.3	13.3	$(4.44 \pm 0.38) \cdot 10^{-5}$
14.3 - 16.5	15.3	$(2.86 \pm 0.27) \cdot 10^{-5}$
16.5 - 19.1	17.7	$(1.86 \pm 0.20) \cdot 10^{-5}$
19.1 - 22.1	20.5	$(1.42 \pm 0.16) \cdot 10^{-5}$
22.1 - 25.7	23.7	$(9.8 \pm 1.1) \cdot 10^{-6}$
25.7 - 35.0	29.7	$(4.8 \pm 0.5) \cdot 10^{-6}$
35.0 - 49.1	41.0	$(2.0 \pm 0.27) \cdot 10^{-6}$

Table 5.10: Measured Intensity of Protons and Hydrogen (p + ^{2}D) at Top of Atmosphere (CAPRICE-94) (Boezio et al., 1999).

Kinetic Energy Range [GeV]	Mean Kinetic Energy [GeV]	Intensity*) $[cm^{-2}s^{-1}sr^{-1}(GeV/Nucleon)^{-1}]$ Protons	Hydrogen
0.15 - 0.23	0.21	$(1.24 \pm 0.02) \cdot 10^{-1}$	$(1.25 \pm 0.02) \cdot 10^{-1}$
0.23 - 0.33	0.30	$(1.39 \pm 0.02) \cdot 10^{-1}$	$(1.42 \pm 0.02) \cdot 10^{-1}$
0.33 - 0.47	0.42	$(1.41 \pm 0.01) \cdot 10^{-1}$	$(1.44 \pm 0.01) \cdot 10^{-1}$
0.47 - 0.62	0.55	$(1.32 \pm 0.01) \cdot 10^{-1}$	$(1.35 \pm 0.01) \cdot 10^{-1}$
0.62 - 0.78	0.70	$(1.20 \pm 0.02) \cdot 10^{-1}$	$(1.22 \pm 0.01) \cdot 10^{-1}$
0.78 - 1.12	0.95	$(9.87 \pm 0.10) \cdot 10^{-2}$	$(1.01 \pm 0.01) \cdot 10^{-1}$
1.12 - 1.48	1.29	$(7.39 \pm 0.06) \cdot 10^{-2}$	$(7.56 \pm 0.05) \cdot 10^{-2}$
1.48 - 1.85	1.66	$(5.45 \pm 0.04) \cdot 10^{-2}$	$(5.61 \pm 0.04) \cdot 10^{-2}$
1.85 - 2.23	2.03	$(4.18 \pm 0.04) \cdot 10^{-2}$	$(4.28 \pm 0.03) \cdot 10^{-2}$
2.23 - 2.61	2.41	$(3.17 \pm 0.09) \cdot 10^{-2}$	$(3.27 \pm 0.03) \cdot 10^{-2}$
2.61 - 3.00	2.80	$(2.50 \pm 0.07) \cdot 10^{-2}$	$(2.58 \pm 0.02) \cdot 10^{-2}$
3.00 - 3.39	3.19	$(2.01 \pm 0.06) \cdot 10^{-2}$	$(2.09 \pm 0.02) \cdot 10^{-2}$
3.39 - 3.84	3.60	$(1.61 \pm 0.05) \cdot 10^{-2}$	$(1.64 \pm 0.02) \cdot 10^{-2}$
3.84 - 4.40	4.11	$(1.26 \pm 0.03) \cdot 10^{-2}$	$(1.28 \pm 0.01) \cdot 10^{-2}$
4.40 - 5.13	4.75	$(9.66 \pm 0.10) \cdot 10^{-3}$	$(9.66 \pm 0.10) \cdot 10^{-3}$
5.13 - 6.10	5.59	$(6.86 \pm 0.07) \cdot 10^{-3}$	$(6.86 \pm 0.07) \cdot 10^{-3}$
6.10 - 7.46	6.73	$(4.64 \pm 0.05) \cdot 10^{-3}$	$(4.64 \pm 0.05) \cdot 10^{-3}$
7.46 - 9.49	8.38	$(2.78 \pm 0.03) \cdot 10^{-3}$	$(2.78 \pm 0.03) \cdot 10^{-3}$
9.5 - 12.8	11.0	-	$(1.45 \pm 0.02) \cdot 10^{-3}$
12.8 - 19.4	15.6	-	$(5.82 \pm 0.08) \cdot 10^{-4}$
19.4 - 22.2	20.7	-	$(2.82 \pm 0.08) \cdot 10^{-4}$
22.2 - 25.8	23.9	-	$(1.88 \pm 0.06) \cdot 10^{-4}$
25.8 - 30.8	28.1	-	$(1.13 \pm 0.04) \cdot 10^{-4}$
30.8 - 38.1	34.1	-	$(7.60 \pm 0.25) \cdot 10^{-5}$
38.1 - 49.7	43.2	-	$(4.06 \pm 0.15) \cdot 10^{-5}$
49.7 - 71.3	58.8	-	$(1.57 \pm 0.07) \cdot 10^{-5}$
71.3 - 90.8	80.0	-	$(7.21 \pm 0.49) \cdot 10^{-6}$
90.8 - 124.8	105.4	-	$(2.80 \pm 0.23) \cdot 10^{-6}$
124.8 - 199.1	154.3	-	$(1.15 \pm 0.11) \cdot 10^{-6}$

*) The quoted errors are a combination of statistical and systematic errors.

Table 5.11: Measured Intensity of Helium Nuclei at Top of Atmosphere. (CAPRICE-94) (Boezio et al., 1999)

Kinetic Energy Range [GeV/Nucleon]	Mean Kinetic Energy [GeV/nucleon]	Helium Intensity*) $[cm^{-2}s^{-1}sr^{-1}(GeV/Nucleon)^{-1}]$
0.20 - 0.26	0.23	$(1.94 \pm 0.08) \cdot 10^{-2}$
0.26 - 0.38	0.32	$(2.10 \pm 0.04) \cdot 10^{-2}$
0.38 - 0.53	0.46	$(1.84 \pm 0.03) \cdot 10^{-2}$
0.53 - 0.69	0.61	$(1.54 \pm 0.03) \cdot 10^{-2}$
0.69 - 0.85	0.77	$(1.22 \pm 0.02) \cdot 10^{-2}$
0.85 - 1.03	0.94	$(9.49 \pm 0.20) \cdot 10^{-3}$
1.03 - 1.21	1.12	$(7.86 \pm 0.18) \cdot 10^{-3}$
1.21 - 1.39	1.30	$(6.48 \pm 0.16) \cdot 10^{-3}$
1.39 - 1.60	1.49	$(5.23 \pm 0.13) \cdot 10^{-3}$
1.60 - 1.87	1.73	$(3.90 \pm 0.10) \cdot 10^{-3}$
1.87 - 2.22	2.04	$(3.20 \pm 0.08) \cdot 10^{-3}$
2.2 - 2.7	2.4	$(2.25 \pm 0.06) \cdot 10^{-3}$
2.7 - 3.4	3.0	$(1.51 \pm 0.04) \cdot 10^{-3}$
3.4 - 4.4	3.8	$(9.24 \pm 0.26) \cdot 10^{-4}$
4.4 - 6.0	5.1	$(4.90 \pm 0.15) \cdot 10^{-4}$
6.0 - 9.3	7.4	$(2.04 \pm 0.07) \cdot 10^{-4}$
9.3 - 10.7	9.9	$(9.80 \pm 0.74) \cdot 10^{-5}$
10.7 - 12.5	11.5	$(6.97 \pm 0.54) \cdot 10^{-5}$
12.5 - 15.0	13.6	$(4.33 \pm 0.36) \cdot 10^{-5}$
15.0 - 18.6	16.6	$(2.47 \pm 0.23) \cdot 10^{-5}$
18.6 - 24.4	21.2	$(1.26 \pm 0.13) \cdot 10^{-5}$
24.4 - 35.2	28.9	$(5.33 \pm 0.62) \cdot 10^{-6}$
35.2 - 45.0	39.5	$(2.67 \pm 0.46) \cdot 10^{-6}$
45.0 - 62.0	52.2	$(1.04 \pm 0.22) \cdot 10^{-6}$
62.0 - 99.1	76.7	$(6.20 \pm 1.20) \cdot 10^{-7}$

*) The quoted errors are a combination of statistical and systematic errors.

Table 5.12: Intensity and Spectral Index of the Elements from ^{1}H to ^{28}Ni in the Cosmic Radiation.
(for details see text)
(Wiebel-Sooth and Biermann, 1998)

Element	Z	Intensity j_0 $[(\mathrm{cm}^2 \mathrm{s\,sr\,TeV/Nucleus})^{-1}]$	γ	χ^2/df
H	1	$(11.51 \pm 0.41) \cdot 10^{-6}$	2.77 ± 0.02	0.70
He	2	$(7.19 \pm 0.20) \cdot 10^{-6}$	2.64 ± 0.02	2.63
Li	3	$(2.08 \pm 0.51) \cdot 10^{-7}$	2.54 ± 0.09	0.90
Be	4	$(4.74 \pm 0.48) \cdot 10^{-8}$	2.75 ± 0.04	0.37
B	5	$(8.95 \pm 0.79) \cdot 10^{-8}$	2.95 ± 0.05	0.45
C	6	$(1.06 \pm 0.01) \cdot 10^{-6}$	2.66 ± 0.02	1.42
N	7	$(2.35 \pm 0.08) \cdot 10^{-7}$	2.72 ± 0.05	1.91
0	8	$(1.57 \pm 0.04) \cdot 10^{-6}$	2.68 ± 0.03	1.70
F	9	$(3.28 \pm 0.48) \cdot 10^{-8}$	2.69 ± 0.08	0.47
Ne	10	$(4.60 \pm 0.10) \cdot 10^{-7}$	2.64 ± 0.03	3.14
Na	11	$(7.54 \pm 0.33) \cdot 10^{-8}$	2.66 ± 0.04	0.36
Mg	12	$(8.01 \pm 0.26) \cdot 10^{-7}$	2.64 ± 0.04	0.10
Al	13	$(1.15 \pm 0.15) \cdot 10^{-7}$	2.66 ± 0.04	1.24
Si	14	$(7.96 \pm 0.15) \cdot 10^{-7}$	2.75 ± 0.04	0.10
P	15	$(2.70 \pm 0.20) \cdot 10^{-8}$	2.69 ± 0.06	0.68
S	16	$(2.29 \pm 0.24) \cdot 10^{-7}$	2.55 ± 0.09	0.44
Cl	17	$(2.94 \pm 0.19) \cdot 10^{-8}$	2.68 ± 0.05	2.36
Ar	18	$(8.36 \pm 0.38) \cdot 10^{-8}$	2.64 ± 0.06	0.45
K	19	$(5.36 \pm 0.15) \cdot 10^{-8}$	2.65 ± 0.04	4.58
Ca	20	$(1.47 \pm 0.12) \cdot 10^{-7}$	2.70 ± 0.06	0.60
Sc	21	$(3.04 \pm 0.19) \cdot 10^{-8}$	2.64 ± 0.06	0.81
Ti	22	$(1.13 \pm 0.14) \cdot 10^{-7}$	2.61 ± 0.06	5.67
V	23	$(6.31 \pm 0.28) \cdot 10^{-8}$	2.63 ± 0.05	6.83
Cr	24	$(1.36 \pm 0.12) \cdot 10^{-7}$	2.67 ± 0.06	3.41
Mn	25	$(1.35 \pm 0.14) \cdot 10^{-7}$	2.46 ± 0.22	5.38
Fe	26	$(1.78 \pm 0.18) \cdot 10^{-6}$	2.60 ± 0.09	1.81
Co	27	$(7.51 \pm 0.37) \cdot 10^{-9}$	2.72 ± 0.09	1.13
Ni	28	$(9.96 \pm 0.43) \cdot 10^{-8}$	2.51 ± 0.18	5.47

Table 5.13: Intensity and Spectral Index of Elemental Groups from ^{10}Ne to ^{28}Ni in the Cosmic Radiation.
(for details see text)
(Wiebel-Sooth and Biermann, 1998)

Element	Z	Intensity j_0 $[(\mathrm{cm}^2\mathrm{s\,sr\,TeV/Nucleus})^{-1}]$	γ	χ^2/df
Ne - S	10 - 16	$(3.34 \pm 0.18) \cdot 10^{-6}$	2.69 ± 0.03	4.02
Cl - Ca	17 - 20	$(3.35 \pm 0.15) \cdot 10^{-7}$	2.74 ± 0.03	0.35
Sc - Mn	21 - 25	$(4.23 \pm 0.10) \cdot 10^{-7}$	2.77 ± 0.04	2.04
Fe - Ni	26 - 28	$(1.97 \pm 0.10) \cdot 10^{-6}$	2.62 ± 0.03	0.12

Table 5.14: Intensity and Spectral Index of Elemental Groups from ^{1}H to ^{28}Ni in the Cosmic Radiation.
(for details see text)
(Wiebel-Sooth and Biermann, 1998)

Element	Z	Intensity j_0 $[(\mathrm{cm}^2\mathrm{s\,sr\,TeV/Nucleus})^{-1}]$	γ
low	1 - 2	$(18.81 \pm 0.76) \cdot 10^{-6}$	2.71 ± 0.02
Li - B	3 - 5	$(3.49 \pm 0.40) \cdot 10^{-7}$	2.72 ± 0.06
Be + B	4 - 5	$(1.36 \pm 0.11) \cdot 10^{-7}$	2.90 ± 0.04
medium	6 - 8	$(2.86 \pm 0.06) \cdot 10^{-6}$	2.67 ± 0.02
high	10 - 16	$(2.84 \pm 0.19) \cdot 10^{-6}$	2.66 ± 0.03
very high	17 - 26	$(1.34 \pm 0.09) \cdot 10^{-6}$	2.63 ± 0.03
Sc - Mn	21 - 25	$(4.74 \pm 0.20) \cdot 10^{-7}$	2.63 ± 0.03
Fe - Ni	26 - 28	$(1.89 \pm 0.10) \cdot 10^{-6}$	2.60 ± 0.04
He - Ni	2 - 28	$(15.80 \pm 1.35) \cdot 10^{-6}$	2.64 ± 0.04
all particles	1 - 28	$(27.47 \pm 2.43) \cdot 10^{-6}$	2.68 ± 0.02

Table 5.15: Relative Abundances of Low Energy Cosmic Rays ($E \geq 5$ GeV). The data are normalized to 100 at carbon (Hillier, 1984).

Element	Group	Z	Cosmic Rays	Solar System
H		1	26000	270000
He		2	3600	18728
Li		3	18 ± 2	$4.2 \cdot 10^{-4}$
Be	L	4	10.5 ± 1	$6.9 \cdot 10^{-6}$
B		5	28 ± 1	$3.0 \cdot 10^{-3}$
C		6	100	100
N	M	7	25 ± 2	31.7
0		8	91 ± 4	182
F		9	1.7 ± 0.4	$2.1 \cdot 10^{-2}$
Ne		10	16 ± 2	29.2
Na		11	2.7 ± 0.4	0.51
Mg		12	19 ± 1	8.99
Al		13	2.8 ± 1	0.72
Si		14	14 ± 2	8.47
P	H	15	0.6 ± 0.2	$8.1 \cdot 10^{-2}$
S		16	3 ± 0.4	4.24
Cl		17	0.5 ± 0.2	$4.83 \cdot 10^{-2}$
A		18	1.5 ± 0.3	0.99
K		19	0.8 ± 0.2	$3.6 \cdot 10^{-2}$
Ca		20	2.2 ± 0.5	0.611
Sc		21	0.4 ± 0.2	$3.0 \cdot 10^{-4}$
Ti		22	1.7 ± 0.3	$2.35 \cdot 10^{-2}$
V		23	0.7 ± 0.3	$2.22 \cdot 10^{-3}$
Cr		24	1.5 ± 0.4	0.108
Mn	VH	25	0.9 ± 0.2	$7.88 \cdot 10^{-2}$
Fe		26	10.8 ± 1.4	7.03
Co		27	< 0.2	$1.87 \cdot 10^{-2}$
Ni		28	0.4 ± 0.1	0.407
Cu		29	-	$4.58 \cdot 10^{-3}$
Zn		30	-	$1.05 \cdot 10^{-2}$
		31-35	$\sim 5 \cdot 10^{-3}$	$2.1 \cdot 10^{-3}$
		36-40	$\sim 5 \cdot 10^{-4}$	$9.4 \cdot 10^{-4}$
	UH	41-60	$\sim 5 \cdot 10^{-4}$	$3.0 \cdot 10^{-4}$
		61-80	$\sim 2 \cdot 10^{-4}$	$4.7 \cdot 10^{-5}$
		> 80	$\sim 10^{-4}$	$4.0 \cdot 10^{-5}$

Table 5.16: The Isotopic Composition of the Cosmic Radiation. (Wiebel-Sooth and Biermann, 1998)

Isotopes	Measured Ratio [%]	Energy [MeV/nucleon]	References
^{7}Be/Be	56.3 ± 1.3	68 - 135	Connell (1997)
	52.4 ± 2.9	43 - 113	Lukasiak et al. (1994a)
	57.2 ± 4.9	43 - 113	Lukasiak et al. (1997a)
	54.6 ± 2.9	60 - 185	Wiedembeck and Greiner (1980)
^{9}Be/Be	39.1 ± 1.3	68 - 135	Connell (1997)
	43.3 ± 3.7	37 - 98	Lukasiak et al. (1994a)
	38.1 ± 4.1	37 - 98	Lukasiak et al. (1997a)
	39.0 ± 2.9	60 - 185	Wiedembeck and Greiner (1980)
^{10}Be/Be	4.6 ± 0.6	68 - 135	Connell (1997)
	4.3 ± 1.5	35 - 92	Lukasiak et al. (1994a)
	4.7 ± 1.3	35 - 92	Lukasiak et al. (1997a)
	6.4 ± 1.5	60 - 185	Wiedembeck and Greiner (1980)
^{10}B/B	$23.8^{+1.1}_{-0.8}$	85 - 205	Krombel and Wiedenbeck (1988)
	30.2 ± 1.5	45 - 119	Lukasiak et al. (1997a)
^{13}C/^{12}C	6.3 ± 0.2	129	Connell and Simpson (1997a)
	5.97 ± 0.46	48 - 126	Lukasiak et al. (1994b)
	6.29 ± 0.33	48 - 126	Webber et al. (1996)
	7.0 ± 0.6	130 - 300	Wiedembeck and Greiner (1981)
^{17}O/^{16}O	1.21 ± 0.06	152	Connell and Simpson (1997a)
	1.35 ± 0.24	57 - 150	Lukasiak et al. (1994b)
	1.57 ± 0.16	57 - 150	Webber et al. (1996)
^{18}O/^{16}O	1.47 ± 0.07	152	Connell and Simpson (1997a)
	1.62 ± 0.23	55 - 145	Lukasiak et al. (1994b)
	1.54 ± 0.14	55 - 145	Webber et al. (1996)
^{21}Ne/^{20}Ne	23.0 ± 0.9	168	Connell and Simpson (1997a)
	19.7 ± 3.7	65 - 172	Lukasiak et al. (1994b)
	22.2 ± 1.8	65 - 150	Webber et al. (1997)
^{22}Ne/^{20}Ne	59.0 ± 1.7	168	Connell and Simpson (1997a)
	60.7 ± 6.0	63 - 167	Lukasiak et al. (1994b)
	53.3 ± 2.9	65 - 150	Webber et al. (1997)

Table 5.16: The Isotopic Composition of the Cosmic Radiation (continued). (Wiebel-Sooth and Biermann, 1998)

Isotopes	Measured Ratio [%]	Energy [MeV/nucleon]	References
$^{25}Mg/^{24}Mg$	20.5 ± 0.6	190	Connell and Simpson (1997a)
	16.9 ± 2.6	72 - 192	Lukasiak et al. (1994b)
	22.3 ± 1.3	73 - 169	Webber et al. (1997)
$^{26}Mg/^{24}Mg$	23.1 ± 0.7	190	Connell and Simpson (1997a)
	22.6 ± 2.4	70 - 187	Lukasiak et al. (1994b)
	25.7 ± 1.3	73 - 169	Webber et al. (1997)
$^{26}Al/^{27}Al$	6.1 ± 0.7	370	Simpson and Connell (1998)
	6.4 ± 0.8	370	Connell and Simpson (1997b)
	8.3 ± 2.4	77 - 206	Lukasiak et al. (1994c)
$^{29}Si/^{28}Si$	8.2 ± 0.4	210	Connell and Simpson (1997a)
	7.8 ± 0.9	80 - 187	Webber et al. (1997)
	$10.9^{+2.4}_{-1.4}$	100 - 300	Wiedembeck and Greiner (1981)
$^{30}Si/^{28}Si$	6.3 ± 0.3	210	Connell and Simpson (1997a)
	8.6 ± 1.5	77 - 206	Lukasiak et al. (1994b)
	6.9 ± 0.6	80 - 187	Webber et al. (1997)
	$8.4^{+2.0}_{-1.4}$	100 - 300	Wiedembeck and Greiner (1981)
$^{33}S/^{32}S$	18.6 ± 3.8	86 - 230	Webber et al. (1997)
$^{34}S/^{32}S$	26.2 ± 3.1	86 - 230	Webber et al. (1997)
$^{36}Cl/Cl$	6.4 ± 2.0	240	Connell et al. (1997)
$^{54}Fe/^{56}Fe$	11.4 ± 0.6	200 - 420	Connell and Simpson (1997c)
	9.04 ± 0.86	100 - 300	Lukasiak et al. (1997b)
$^{55}Fe/^{56}Fe$	5.4 ± 0.4	200 - 420	Connell and Simpson (1997c)
	< 6.0	100 - 300	Lukasiak et al. (1994b)
$^{57}Fe/^{56}Fe$	$3.9^{+0.35}_{-0.38}$	200 - 420	Connell et al. (1997)
	< 6.3	100 - 300	Lukasiak et al. (1997b)
$^{58}Fe/^{56}Fe$	$0.34^{+0.10}_{-0.14}$	200 - 420	Connell and Simpson (1997c)
	0.83 ± 0.48	100 - 300	Lukasiak et al. (1997b)

References

Abu-Zayyad, T., G. Archbold, K. Belov, J. Belz, J. Boyer, Z. Cao, G. Chen, R.W. Clay, B.R. Dawson, B.D. Dieterle, R. Gray, B. Jones, C.C.H. Jui, D. Kieda, K. Kim, B. Knapp, W. Lee, E.C. Loh, E.J. Mannel, G. Martin, J.N. Matthews, J.A.J. Matthews, J. Meyer, R. Mumford, K. Reil, M. Seman, M. Shaevitz, K.M. Simpson, J. Smith, P. Sokolsky, C. Song, S.F. Taylor, S.B. Thomas, L. Wiencke, T. Vanderveen, and X. Zhang: PICRC, 3, p. 264 (1999).

Acharya, B.S., S. Naranan, M.V.S. Rao, K. Srivaprasad, B.V. Sreekantan, and Srikantha Rao: PICRC, 9, p. 162 (1981).

Acharya, B.S., M.V.S. Rao, K. Srivaprasad, and B.V. Sreekantan: PICRC, 9, p. 191 (1983).

Adelaide Group: after Shirasaki et al., (1997).

Afanasiev, B.N., M.N. Dyakonov, T.A. Egorov, V.P. Egorova, N.N. Efremov, V.M. Grigoryev, A.V. Glushkov, A.A. Ivanov, S.P. Knurenkov, V.A. Kolosov, A.D. Krasilnikov, G.B. Khristiansen, I.T. Makarov, A.A. Mikhailov, E.S. Nikiforova, S.I. Nikolsky, V.A. Orlov, M.I. Pravdin, I.Ye. Sleptsov, N.I. Sleptsov, V.R. Sleptsova, and G.G. Struchkov: PICRC, 2, p. 756 (1995).

AGASA Collaboration: PICRC, 3, p. 252 (1999).

Aguirre, C., H. Aoki, K. Hashimoto, K. Honda, N. Inoue, N. Kawasumi, Y. Maeda, N. Martinic, T. Matano, N. Ohmori, A. Ohsawa, K. Shinozaki, M. Tamada, R. Ticona, and I. Tsushima: Phys. Rev., D 62, p. 0120XX (2000). (in print)

Aglietta, M., B. Alessandro, P. Antonioli, F. Arneodo, L. Bergamasco, M. Bertaina, A. Bosio, A. Castellina, C. Castagnoli, A. Chiavassa, G. Cini, B. D'Ettore Piazzoli, G. Di Sciascio, W. Fulgione, P. Galeotti, P.L. Ghia, M. Iacovacci, G. Mannocchi, C. Melagrana, N. Mengotti Silva, C. Morello, G. Navarra, H. Nogima, L. Riccati, O. Saavedra, G.C. Trinchero, P. Vallania, and S. Vernetto, EAS-TOP Collaboration: PICRC, 2, p. 732 (1995).

Aglietta, M., B. Alessandro, P. Antonioli, F. Arneodo, L. Bergamasco, M. Bertaina, C. Castagnoli, A. Castellina, A. Chiavassa, G. Cini-Castagnoli, B. D'Ettore Piazzoli, G. Di Sciascio, W. Fulgione, P. Galeotti, P.L. Ghia, M. Iacovacci, G. Mannocchi, C. Morello, G. Navarra, O. Saavedra, G.C. Trinchero, P. Vallania, S. Vernetto, and C. Vigorito: Astropart. Phys., 10, p. 1 (1999).

Akimov, V.V., N.L. Grigorov, V.E. Nesterov, I.D. Rapoport, I.A. Savenko, G.A. Skuridin, and A.F. Titenkox: Acta Phys. Acad. Sci. Hung., 29, Suppl.

1, p. 517 (1970).

Amenomori. M., E. Konishi, H. Nanjo, K. Kasahara, S. Torii, Y. Yuda, T. Shorai, N. Tateyama, T. Taira, I. Mito, M. Shibata, H. Sugimoto, K. Taira, and N. Hotta. Phys. Rev., D 25, p. 2807 (1982).

Amenomori, M., Z. Cao, B.Z. Dai, L.K. Ding, Y.X. Feng, Z.Y. Feng, K. Hibino, N. Hotta, Q. Huang, A.X. Huo, H.G. Jia, G.Z. Jiang, S.Q. Jiao, F. Kajino, K. Kasahara, Labaciren, S.M. Liu, D.M. Mei, L. Meng, X.R. Meng, Mimaciren, K. Mizutani, J. Mu, H. Nanjo, M. Nishizawa, A. Oguro, M. Ohnishi, I. Ohta, T. Ouchi, J.R. Ren, To. Saito, M. Sakata, Z.Z. Shi, M. Shibata, T. Shirai, H. Sugimoto, X.X. Sun, K. Taira, Y.H. Tan, N. Tateyama, S. Torii, H. Wang, C.Z. Wen, Y. Yamamoto, G.C. Yu, P. Yuan, T. Yuda, C.S. Zhang, H.M. Zhang L. Zhang, Zhasang, Zhaxiciren, and W.D. Zhou: PICRC, 2, p. 736 (1995).

Amenomori, M., B.Z. Dai, L.K. Ding, Z.Y. Feng, K. Hibino, N. Hotta, Q. Huang, A.X. Huo, A.Y. Jia, F. Kajino, K. Kasahara, Labaciren , S.M. Liu, D.M. Mei, L. Meng, X.R. Meng, K. Mizutani, J. Mu, H. Nanjo, M. Nishizawa, M. Ohnishi, I. Ohta, T. Ouchi, J.R. Ren, To. Saito, M. Sakata, Z.Z. Shi, M. Shibata, A. Shiomi, T. Shirai, H. Sugimoto, K. Taira, Y.H. Tan, N. Tateyama, S. Torii, H. Wang, Y. Yamamoto, G.C. Yu, P. Yuan, T. Yuda, C.S. Zhang, H.M. Zhang, Zhasang, Zhaxiciren, and W.D. Zhasang: Astrophys. J., 464, p. 954 (1996a).

Amenomori, M., Z. Cao, B.Z. Dai, L.K. Ding, Z.Y. Feng, K. Hibino, N. Hotta, Q. Huang, A.X. Huo, H.Y. Jia, G.Z. Jiang, F. Kajino, K. Kasahara, Labaciren , S.M. Liu, D.M. Mei, L. Meng, X.R. Meng, Mimaciren, K. Mizutani, J. Mu, H. Nanjo, M. Nishizawa, M. Ohnishi, I. Ohta, T. Ouchi, J.R. Ren, To. Saito, M. Sakata, Z.Z. Shi, M. Shibata, A. Shiomi, T. Shirai, H. Sugimoto, X.X. Sun, K. Taira, Y.H. Tan, N. Tateyama, S. Torii, H. Wang, C.Z. Wen, Y. Yamamoto, G.C. Yu, P. Yuan, T. Yuda, C.S. Zhang, H.M. Zhang, L. Zhang, Zhasang, Zhaxiciren, and W.D. Zhou: Astrophys. J., 461, p. 408 (1996b).

Amenomori, M., S. Ayabe, P.Y. Cao, Danzengloubu, L.K. Ding, Z.Y. Feng, Y. Fu, H.W. Guo, M. He, K. Hibino, N. Hotta, J. Huan, Q. Huang, A.X. Huo, S. Inazumi, M. Inoue,K. Iwasaki, K. Izu, A.Y. Jia, F. Kajino, K. Kasahara, Y. Katayose, T. Kobayashi, Labaciren , J.Y. Li, H. Lu, S.L. Lu, G.X. Luo, X.R. Meng, K. Mizutani, J. Mu, H. Nanjo, M. Nishizawa, M. Ohnishi, I. Ohta, T. Ouchi, J.R. Ren, To. Saito, M. Sakata, Z.Z. Shi, M. Shibata, A. Shiomi, T. Shirai, H. Sugimoto, K. Taira, Y.H. Tan, N. Tateyama, T. Tateyama, S. Torii, T. Utsugi, C.R. Wang, H. Wang, P.X. Wang, X.W. Xu, Y. Yamamoto, G.C. Yu, A.F. Yuan, T. Yuda, C.S. Zhang, H.M. Zhang, J.L. Zhang, N.J.

Zhang, X.Y. Zhang, Zhaxisangzhu, Zhaxiciren, and W.D. Zhou: PICRC, 3, p. 211 (1999).

Anand, K.C., R.R. Daniel, and S.A. Stephens: Can. J. Phys., 46, p. S-652 (1968a).

Anand, K.C., R.R. Daniel, and S.A. Stephens, B. Bhowmilk, C.S. Kirshina, P.P. Aditya, and R.K. Puri: Proc. Ind. Acad. Sci., 67, p. 138 (1968b).

Anders, E., and N. Grevesse: Geochin. Cosmochim. Acta, 53, p. 197 (1989).

Antonov, R.A., A.M. Anokhina, V.I. Galkin, E.E. Korosteleva, L.A. Kuzmichev, K.V. Mandritskaya, E.A. Petrova, T.M. Roganova, G.A. Samsonov, and W. Tkaczyk: PICRC, 2, p. 776 (1995).

Apanasenko, A.V., M. Fujii, M. Hareyama, G. Hashimoto, M. Ichimura, E. Kamioka, T. Kobayashi, N.M. Kotunova, S. Kuramata, V.I. Lapshin, A.K. Managadze, H. Matsutani, T. Misu, H. Nanjo, S.I. Nikolsky, K. Ogura, D.S. Oshuev, I.V. Rakobolskay, T.M. Roganova, G.P. Sazhina, H. Semba, T. Shibata, T. Shiota, H. Sugimoto, L.G. Sveshnikova, Z. Watanabe, I.V. Yashin, E.A. Zamchalova, G.T. Zatsepin, and I.S. Zayarnaya: PICRC, 4, p. 137 (1997a).

Apanasenko, A.V., et al.: PICRC, 4, p. 141 (1997b).

Apanasenko, A.V., et al.: PICRC, 4, p. 133 (1997c).

Apanasenko, A.V., et al.: PICRC, 5, p. 9 (1997d).

Apanasenko, A.V., et al.: PICRC, 5, p. 13 (1997e).

Apanasenko, A.V., V.A. Beresovskaya, M. Fujii, V.I. Galkin, M. Hareyama, M. Ichimura, S. Ito, E. Kamioka, T. Kitami, T. Kobayashi, V. Kopenkin, S. Kuramata, Y. Kuriyama, V.I. Lapshin, A.K. Managadze, H. Matsutani, H. Mikami, N.P. Misnikova, R.A. Mukhamedshin, M. Namiki, H. Nanjo, S.N. Nazarov, S.I. Nikolsky, T. Oe, S. Ohta, V.I. Osedlo, D.S. Oshuev, P.A. Publichenko, I.V. Rakobolskaya, T.M. Roganova, M. Saito, G.P. Sazhina, Yu.N. Shabanova, T. Shibata, H. Sugimoto, L.G. Sveshnikova, K. Takahashi, T. Tsutiya, V.M. Taran, H. Semba, N. Yajima, T. Yamagami, K. Yamamoto, I.V. Yashin, E.A. Zamchalova, G.T Zatsepin, and I.S. Zayarnaya: PICRC, 3, p. 163 (1999a).

Apanasenko, A.V., et al.: PICRC, 3, p. 167 (1999b).

Arqueros, F., et al.: ASTRO-PH/9908202.

Asakimori, K.: PICRC, 3, p. 129 (1990).

Asakimori, K., T.H. Burnett, M.L. Cherry, M.J. Christl, S. Dake, J.H. Derrickson, W.F. Fountain, M. Fuki, J.C. Gregory, T. Hayashi, R. Holynski,

J. Iwai, A. Iyono, W.V. Jones, A. Jurak, J.J. Lord, O. Miyamura, H. Oda, T. Ogata, T.A. Parnell, F.E. Roberts, S. Strausz, Y. Takahashi, T. Tominaga, J.W. Watts, J.P. Wefel, B. Wilczynska, H. Wilczynski, R.J. Wilkes, W. Wolter, and B. Wosiek: PICRC, 2, p. 57 (1991a).

Asakimori, K., et al.: PICRC, 2, p. 97 (1991b).

Asakimori, K., et al.: PICRC, 2, p. 21 (1993a).

Asakimori, K., et al.: PICRC, 2, p. 25 (1993b).

Asakimori, K., T.H. Burnett, M.L. Cherry, K. Chevli, M.J. Christl, S. Dake, J.H. Derrickson, W.F. Fountain, M. Fuki, J.C. Gregory, T. Hayashi, R. Holynski, J. Iwai, A. Iyono, J. Johnson, W.V. Jones, M. Kobayashi, J. Lord, O. Miyamura, K.H. Moon, H. Oda, T. Ogata, E.D. Olson, T.A. Parnell, F.E. Roberts, K. Sengupta,T. Shiina, S.C. Strausz, T. Sugitate, Y. Takahashi, T. Tominaga, J.W. Watts, J.P. Wefel, B. Wilczynska, H. Wilczynski, R.J. Wilkes, W. Wolter, H. Yokomi, and E. Zager: PICRC, 2, p. 707 (1995).

Asakimori, K., et al.: LSU Space Science/Particle Astrophysics Preprint 7/28/97 (1997).

Asakimori, K., T.H. Burnett, M.L. Cherry, K. Chevli, M.J. Christl, S. Dake, J.H. Derrickson, W.F. Fountain, M. Fuki, J.C. Gregory, T. Hayashi, R. Holynski, J. Iwai, A. Iyono, J. Johnson, M. Kobayashi, J. Lord, O. Miyamura, K.H. Moon, B.S. Nilsen, H. Oda, T. Ogata, E.D. Olson, T.A. Parnell, F.E. Roberts, K. Sengupta,T. Shiina, S.C. Strausz, T. Sugitate, Y. Takahashi, T. Tominaga, J.W. Watts, J.P. Wefel, B. Wilczynska, H. Wilczynski, R.J. Wilkes, W. Wolter, H. Yokomi, and E. Zager: Astrophys. J., 502, p. 278 (1998).

Badhwar, G.D., R.R. Daniel, T. Cleghorn, R.L. Golden, J.L. Lacy, S.A. Stephens, and J.E. Zipse: PICRC, 11, p. 155 (1977).

Balasubrahmanyan, V.K., and J.F. Ormes: Astrophys. J., 186, p. 109 (1973).

Baltrusaitis, R.M., R. Cady, G.L. Cassiday, R. Cooper, J.W. Elbert, P.R. Gerhardy, S. Ko, E.C. Loh, Y. Mizumoto, M. Salamon, P. Sokolsky, and D. Steck: Phys. Rev. Lett., 54, p. 1875 (1985).

Barbiellini, G. G. Basini, R. Bellotti, M. Bocciolini, M. Boezio, U. Bravar, F. Cafagna, P. Carlson, M. Casolini, M. Castellano, M. Circella, A. Codino, G. De Cataldo, C. De Marzo, M. De Pascale, N. Finetti, T. Francke, N. Giglietto, R.L. Golden, C. Grimani, M. Hof, W. Menn, J.W. Mitchell, A. Morselli, J.F. Ormes, P. Papini, A. Perego, S. Piccardi, P. Picozza, M. Ricci, P. Schiavon, M. Simon, R. Sparvoli, P. Spillantini, P. Spinelli, S.A. Stephens, S.J. Stochaj, R.E. Streitmatter, M. Suffert, A. Vacchi, N. Weber, and N.

Zampa: PICRC, 3, p. 369 (1997).

Bellotti, R., F. Cafagna, M. Circella, C.N. De Marzo, R.L. Golden, S.J. Stochaj, M.P. De Pascale, A. Morselli, P. Picozza, S.A. Stephens, M. Hof, W. Menn, M. Simon, J.W. Mitchell, J.F. Ormes, R.E. Streitmatter, N. Finetti, C. Grimani, P. Papini, S. Piccardi, P. Spillantini, G. Basini, and M. Ricci: Phys. Rev., D 60, p. 052002-1 (1999).

Berezinsky, V.S., and S.I. Grigorieva: Astron. Astrophys., 199, p. 1 (1988).

Bernlöhr, K., W. Hofmann, G. Leffers, V. Matheis, M. Panter, and R. Zink: Astropart. Phys., 8, p. 253 (1998).

Biermann, Peter L., Eun-Joo Ahn, Gustavo Medina - Tanco, and Todor Stanev: Nucl. Phys., B (Proc. Suppl.) 87, p. 417 (2000).

Binns, W.R., N.R. Brewster, D.J. Fixsen, T.L. Garrard, M.H. Israel, J. Klarmann, B.J. Newport, E.C. Stone, and C.J. Waddington: Astrophys. J., 297, p. 111 (1985).

Binns, W.R., T.L. Garrard, P.S. Gibner, M.H. Israel, M.P. Kertzman, J. Klarmann, B.J. Newport, E.C. Stone, and C.J. Waddington: Astrophys. J., 346, p. 997 (1989).

Bird, D.J., S.C. Corbató, H.Y. Dai, B.R. Dawson, J.W. Elbert, B.L. Emerson, M.A. Huang, D.B. Kieda, M. Lou, S. Ko, C.G. Larsen, E.C. Loh, M.H. Salamon, J.D. Smith, P. Sokolsky, P. Sommers, J.K.K. Tang, and S.B. Thomas: PICRC, 2, p 34 (1993a).

Bird, D.J., S.C. Corbató, H.Y. Dai, B.R. Dawson, J.W. Elbert, T.K. Gaisser, M.H.A. Huang, D.B. Kieda, S. Ko, C.G. Larsen, E.C. Loh, M.H. Salamon, J.D. Smith, P. Sokolsky, P. Sommers, T. Stanev, S. Tilav, J.K.K. Tang, and S.B. Thomas: PICRC, 2, p 38 (1993b).

Bird, D.J., S.C. Corbató, H.Y. Dai, B.R. Dawson, J.W. Elbert, B.L. Emerson, K.D. Green, M.A. Huang, D.B. Kieda, M. Lou, S. Ko, C.G. Larsen, E.C. Loh, M.H. Salamon, J.D. Smith, P. Sokolsky, P. Sommers, J.K.K. Tang, and S.B. Thomas: Astrophys, J., 424, p. 491 (1994).

Bird, D.J., S.C. Corbató, H.Y. Dai, J.W. Elbert, K.D. Green, M.A. Huang, D.B. Kieda, S. Ko, C.G. Larsen, E.C. Loh, M.Z. Luo, M.H. Salamon, J.D. Smith, P. Sokolsky, P. Sommers, J.K.K. Tang, and S.B. Thomas: Astrophys, J., 441, p. 144 (1995).

Boezio, M., P. Carlson, T. Francke, N. Weber, M. Suffert, M. Hof, W. Menn, M. Simon, S.A. Stephens, R. Bellotti, F. Cafagna, M. Castellano, M. Circella, C. De Marzo, N. Finetti, P. Papini, S. Piccardi, P. Spillantini, M. Ricci, M. Casolino, M.P. De Pascale, A. Morselli, P. Picozza, R. Sparvoli, G. Bar-

biellini, U. Bravar, P. Schiavon, A. Vacchi, N. Zampa, J.W. Mitchell, J.F. Ormes, R.E. Streitmatter, R.L. Golden, and S.J. Stochaj: Astrophys. J., 518, p. 457 (1999).

Boothby, K., M. Chantell, K.D. Green, D.B. Kieda, J. Knapp, C.G. Larsen, and S.P. Swordy: Astrophys. J., 491, p. L-35 (1997a).

Boothby, K., K.D. Green, D.B. Kieda, J. Knapp, C.G. Larsen, and S.P. Swordy : PICRC, 5, p. 193 (1997b).

Bower, A.J., G. Cunningham, C.D. England, J. Lloyd-Evans, R.J.O. Reid, R. Walker, and A.A. Watson: PICRC, 9, p. 166 (1981).

Bradt, H.L., and B. Peters: Phys. Rev., 74, p. 1828 (1948).

Bradt, H.L., G. Clark, M. La Pointe, V. Domingo, I. Escobar, K. Kamata, K. Murakami, K. Suga, and Y. Toyoda. PICRC, 2, p. 715 (1965).

Brownlee, R.G., A.J. Fisher, L. Goorevich, P.C. Kohn, C.B.A. McCusker, H.B. Ogelman, A.F. Parkinson, L.S. Peak, M.H. Rathgeber, M.J. Ryan, and M.M. Winn: Can. J. Phys., 46, p. 259 (1968).

Bryanski, S.V., Y.V. Vasilchenko, O.A. Gress, T.I. Gress, G.N. Dudkin, A.I. Klimov, V.S. Khlytchieva, L.A. Kuzmichev, B.K. Lubsandorziev, E.A. Osipova, V.N. Padalko, L.V. Pan'kov, Y.V. Parfenov, P.G. Pochil, V.V. Prosin, and Y.A. Semeney: PICRC, 2, p. 725 (1995).

Buckley, J., J. Dwyer, D. Müller, S. Swordy, and K.K. Tang: PICRC, 1, p. 599 (1993).

Buckley, J., J. Dwyer, D. Müller, S. Swordy, and K.K. Tang: Astrophys. J., 429, p. 736 (1994).

Bugaev, Edgar V., Vadim A. Naumov, Sergey I. Sinegovsky, Akeo Misaki, Nobusuke Takahashi, and Elena S. Zaslavskaya: Proceedings of Nestor Workshop, p. 268 (1993).

Burnett, T.H., S. Dake, J.H. Derrickson, W.F. Fountain, M. Fuki, J.C. Gregory, T. Hayashi, R. Holynski, J. Iwai, W.V. Jones, A. Jurak, J.J. Lord, O. Miyamura, H. Oda, T. Ogata, T.A. Parnell, E. Roberts, T. Shibata, S. Strausz, T. Tabuki, Y. Takahashi, T. Tominaga, J.W. Watts, J.P. Wefel, B. Wilczynska, H. Wilczynski, R.J. Wilkes, W. Wolter, and B. Wosiek: PICRC, 3, p. 97 (1990a).

Burnett, T.H., et al.: PICRC, 3, p. 101 (1990b).

Burnett, T.H., et al.: Astrophys. J., 349, L25 (1990c).

Byrnak, B., N. Lund, I.L. Rasmussen, M. Rotenberg, J. Engelmann, P. Goret, and E. Juliusson: PICRC, 2, p. 29 (1983).

Caldwell, J.H.: Astrophys. J., 218, p. 269 (1977).

Cameron, A.G.W.: Space Sci. Rev., 15, p 121 (1973).

Cameron, A.G.W.: Elementary and Nuclide Abundances in the Solar System, in Essays in Nuclear Astrophysics, eds. C.A. Barnes, D.D. Clayton and D.N. Schramm, Cambridge Univ. Press, Cambridge, p. 23 (1981).

Cameron, A.G.W.: Astrophys. Space Sci., 82, p. 123 (1982).

Cassidy, M., L.F. Fortson, J.W. Fowler, C.H. Jui, D.B. Kieda, E.C. Loh, R.A. Ong, P. Sommers: PICRC, 5, p. 189 (1997).

Castellina, A.: Paper presented at the XI. Internat Symposium on Very High Energy Cosmic Ray Interactions, Campinas, Brazil, 2000. To appear in Nucl. Phys., B (Proc. Suppl.) (2001).

CERN Program Library Long Writeup D-506: MINUIT Function Minimizing and Error Analysis Program Package (1992).

Cherry, M.L., Asakimori, K., T.H. Burnett, K. Chevli, M.J. Christl, S. Dake, J.H. Derrickson, W.F. Fountain, M. Fuki, J.C. Gregory, T. Hayashi, R. Holynski, J. Iwai, A. Iyono, J. Johnson, W.V. Jones, M. Kobayashi, J. Lord, O. Miyamura, K.H. Moon, H. Oda, T. Ogata, E.D. Olson, T.A. Parnell, F.E. Roberts, K. Sengupta,T. Shiina, S.C. Strausz, T. Sugitate, Y. Takahashi, T. Tominaga, J.W. Watts, J.P. Wefel, B. Wilczynska, H. Wilczynski, R.J. Wilkes, W. Wolter, H. Yokomi, and E. Zager: PICRC, 2, p. 728 (1995).

Cherry, Michael, L. (for the JACEE Collaboration): PICRC, 4, p. 1 (1997a).

Cherry, Michael, L.: Proc. Sixth Conference on Interactions of Particle and Nuclear Physics, Big Sky, Montana, May (1997b).

Cherry, Michael, L. (for the JACEE Collaboration): PICRC, 3, p. 187 (1999).

Chiba, N., N. Hayashida, K. Honda, M. Honda, S. Imaizumi, N. Inoue, K. Kadota, F. Kakimoto, K. Kamata, S. Kawaguchi, N. Kawasumi, Y. Matsubara, K. Murakami, M. Nagano, H. Ohoka, Y. Suzuki, M. Teshima, I. Tsushima, S. Yoshida, and H. Yoshii: PICRC, 2, p. 42 (abstract) (1993).

Connell, J.J.: PICRC, 3, p. 385 (1997).

Connell, J.J., and J.A. Simpson: PICRC, 3, p. 381 (1997a).

Connell, J.J., and J.A. Simpson: PICRC, 3, p. 393 (1997b).

Connell, J.J., and J.A. Simpson: Astrophys. J., 475, p. L-61 (1997c).

Connell, J.J., M.A. DuVernois, and J.A. Simpson: PICRC, 3, p. 397 (1997).

Cortina, J., D. Horns, H. Kornmayer, A. Lindner, A. Moralejo, R. Plaga, A.

Röhring, and the HEGRA Collaboration: PICRC, 4, p. 69 (1997).

Cronin, J.W.: Nucl. Phys., B (Proc. Suppl.) 28B, p. 213 (1992).

Cronin, James, W.: Rev. Mod. Phys., 71, p. S-165 (1999).

Cronin, J.W.: Paper presented at the XI. Internat Symposium on Very High Energy Cosmic Ray Interactions, Campinas, Brazil, 2000. To appear in Nucl. Phys., B (Proc. Suppl.) (2001).

Cunningham, G., A.M.T. Pollock, R.J.O. Reid, and A.A. Watson: PICRC, 2, p. 303 (1977).

Cunningham, G., A.M.T. Pollock, R.J.O. Reid, and A.A. Watson: Astrophys. J., 236, p. L71 (1980).

Danilova, E.V., N.V. Kabanova, S.I. Nikolsky, V.A. Romakhin: PICRC, 1, p. 285 (1995).

Davis, A.J., R.A. Mewaldt, W.R. Binns, E.R. Christian, A.C. Cummings, J.S. George, P.L. Hink, R.A. Leske, T.T. von Rosenvinge, M.E. Wiedenbeck, and N.E. Yanasak: Proc. ACE 2000 Symposium, ed., Richard A. Mewaldt et al., CP528, AIP, p. 421 (2000).

Dickinson, J.E., J.R. Gill, S.P. Hart, J.A. Hinton, J. Lloyd-Evans, K. Rochester, A.A. Watson, T.K. Gaisser, T.C. Miller, G.M. Spiczak, and T. Stanev: PICRC, 3, p. 136 (1999).

Diminstein, O.S., Efimov, N.N., and M.I. Pravdin: Bull. Naushno-Tech. Inf. Yakutsk, 9., p 537 (1982).

Doronina,I.V., M.N. Dyakonov, S.P. Knurenko, V.A. Kolosov, A.D. Krasilnikov, V.N. Pavlov, and I.Ye. Sleptsov: PICRC, 3, p. 150 (1990).

Dwyer, R., and P. Meyer: PICRC, 1, p. 321 (1987).

Dwyer, J., J. Buckley, D. Müller, S. Swordy, and K.K. Tang: PICRC, 1, p. 587 (1993).

Dyakonov, M.N., N.N. Efimov, T.A. Egorov, A.V. Glushkov, S.P. Knurenko, V.A. Kolosov, I.T. Markov, V.N. Pavlov, P.D. Petrov, M.I. Pravdin, I.Ye. Sleptsov, and G.G. Strucjkov: PICRC, 2, p. 93 (1991).

EAS-TOP Collaboration: PICRC, 4, p. 125 (1997).

Efimov, N.N., T.A. Egorov, A.V. Glushkov, M.I. Pravdin, and I. Ye. Sleptsov: Proc. ICRR Internat. Symp. on "Astrophys. Aspects of Most Energetic Cosmic Rays, Kofu, Japan, 1990, eds M. Nagano and F. Takahara (World Scientific, Singapore), p. 20 (1991).

Engelmann, J.J., P. Goret, E. Juliusson, L. Koch-Miramond, N. Lund, P. Masse, I.L. Rasmussen, and A. Souloul: Astron. and Astrophys., 148, p. 12

(1985).

Engelmann, J.J., P. Ferrando, A. Soutoul, P. Goret, E. Juliusson, L. Koch-Miramond, N. Lund, P. Masse, B. Peters, N. Petrou, and I.L. Rasmussen: Astron. and Astrophys., 233, p. 96 (1990).

Engler, J., T. Antoni, W.D. Apel, F. Badea, K. Bekk, K. Bernlöhr, E. Bollmann, H. Bozdog, I.M. Brancus, A. Chilingarian, K. Daumiller, P. Doll, F. Fessler, H.J. Gils, R. Glasstetter, R. Haeusler, W. Hafemann, A. Haungs, D. Heck, J.R. Hörandel, T. Holst, K.-H. Kampert, H. Keim, J. Kempa, H.O. Klages, J. Knapp, H.J. Mathes, H.J. Mayer, J. Milke, D. Mühlenberg, J. Oehlschläger, M. Petcu, H. Rebel, M. Risse, M. Roth, G. Schatz, F.K. Schmidt, T. Thouw, H. Ulrich, A. Vardanyan, B. Vulpescu, J.H. Weber, J. Wentz, T. Wibig, T. Wiegert, D. Wochele, J. Wochele, and J. Zabierowski: PICRC, 1, p. 349 (1999).

Fan, C.Y., G. Gloeckler, and J.A. Simpson: Phys. Rev. Lett., 17, p. 329 (1966).

Fichtel, Carl E, and John Linsley: PICRC, 2, p. 288 (1985).

Fomin, Yu.A., G.B. Khristiansen, G.B. Kulikov, V.G. Pogorely, V.I. Solovjeva, V.P. Sulakov, and A.V. Trubitsyn: PICRC, 2, p. 85 (1991).

Fomin, Yu.A., N.N. Kalmykov, G.B. Khristiansen, G.V. Kulikov, A.I. Pavlov, V.I. Solovjeva, V.P. Sulakov, E.A. Vishnevskaya, and M.Yu. Zotov: Proc. 16th European Cosmic Ray Symposium, Alcalá, Spain, ed. José Medina, Departamento de Fisica, Universidad de Alcalá, Spain, p. 261 (1998).

Fortson, L.F., J.W. Fowler, C.H. Jui, D. Kieda, R.A. Ong, C.L. Pryke, and P. Sommers: PICRC, 3, p. 125 (1999).

Fowler, J.W., et al.: ASTRO-PH/0003190.

Fowler, P.H., R.N.F. Walker, M.R.W. Masheder, R.T. Moses, A. Worley, and A.M. Gry: Astrophys. J., 314, p. 739 (1987).

Freier, Phyllis, E.J. Lofgren, E.P. Ney, F. Oppenheimer, H.L. Bradt, and B. Peters: Phys. Rev., 74, p. 213 (1948a).

Freier, Phyllis, E.J. Lofgren, E.P. Ney, and F. Oppenheimer: Phys. Rev., 74, p. 1818 (1948b).

Freier, P.S., and C.J. Waddington: J. Geophys. Res., 73, p. 4261 (1968).

Gaisser, Thomas K.: Cosmic Ray and Particle Physics. Cambridge University Press (1990).

Galbraith, W.: Extensive Air Showers, Butterworths Scientific Publications, London (1958).

Garcia-Munoz, M., G.M. Mason, and J.A. Simpson: Astrophys. J., 217, p. 859 (1977).

Garcia-Munoz, M., J.A. Simpson, T.G. Guzik, J.P. Wefel, and S.H. Margolis: Astrophys. J., Suppl., 217, p. 859 (1987).

Glasmacher, M.A.K., M.A. Catanese, M.C. Chantell, C.E. Covault, J.W. Cronin, B.E. Fick, L.F. Fortson, J.W. Fowler, K.D. Green, D.B. Kieda, J. Matthews, B.J. Newport, D.F. Nitz, R.A. Ong, S. Oser, D. Sinclair, and J.C. van der Velde: Astropart. Phys., 10, p. 291 (1999a).

Glasmacher, M.A.K., M.A. Catanese, M.C. Chantell, C.E. Covault, J.W. Cronin, B.E. Fick, L.F. Fortson, J.W. Fowler, K.D. Green, D.B. Kieda, J. Matthews, B.J. Newport, D.F. Nitz, R.A. Ong, S. Oser, D. Sinclair, and J.C. van der Velde: Astropart. Phys., 12, p. 1 (1999b).

Gregory, J.C., T. Ogata, T. Saito, R. Holynski, A. Jurak, W. Wolter, B. Wosiek, S. Dake, M. Fukui, T. Tominaga, E.M. Friedlander, H.H. Heckmann, R.W. Huggett, S. Hunter, W.V. Jones, Y. Takahashi, T.A. Parnell, J. Watts, O. Miyamura, T.H. Burnett, J.J. Lord, R.J. Wilkes, T. Hayashida, J. Iwai, and T. Tabuki: PICRC, 9, p. 154 (1981).

Greisen, K.: Phys. Rev. Lett., 16, p. 748 (1966).

Gress, O.A., T.I. Gress, G.B. Khristiansen, E.E. Korosteleva, L.A. Kuzmichev, B.K. Lubsandorzhiev, L.V. Pan'kov, Yu.V. Parfenov, P.G. Pohil, P.A. Pokolev, V.V. Prosin, and Yu.A. Semeney: PICRC, 4, p. 129 (1997).

Grevesse, N., A. Noels, and A.J. Sauvel: in "Standard Abundances" in Cosmic Abundances, eds. S.S. Holt and G. Sonneborn, ASP Conference Series, 99, p. 117 (1996).

Grieder, P.K.F.: Rivista del Nuovo Cimento, 7, p. 1 (1977).

Grigorov, N.L., Y.V. Gubin, I.D. Rapoport, I.A. Savenko, B.M. Yakovlev, V.V. Akimov, and V.E. Nesterov: Sov. J. Nucl. Phys., 11, p. 588 (1970).

Grigorov, N.L., Y.V. Gubin, I.D. Rapoport, I.A. Savenko, B.M. Yakovlev, V.V. Akimov, and V.E. Nesterov: PICRC, 5, p. 1746 (1971a).

Grigorov, N.L., N.A. Mamontova, I.D. Rapoport, I.A. Savenko, V.V. Akimov, and V.E. Nesterov: PICRC, 5, p. 1752 (1971b).

Grigorov, N.L., I.D. Rapoport, I.A. Savenko, V.E. Nesterov, V.L. Prokhin: PICRC, 5, p. 1760 (1971c).

Grunsfeld, J.M., J. L'Heureux, P. Meyer, D. Müller, and S.P. Swordy: Astrophys. J. Lett., 327, p. L31 (1988).

Guérard, C.K.: Nucl. Phys. B (Proc. Suppl.) 75A, p. 380 (1999).

Gupta, S.K., Y. Aikawa, Y. Hayashi, N. Ikeda, N. Ito, S. Kawakami, S. Miyake, D.K. Mohanty, M. Sasano, K. Sivaprasad, B.V. Sreekantan, and S.C. Tonwar: PICRC, 4, p. 153 (1997).

Hara, T., N. Hayashida, M. Honda, F. Ishikawa, K. Kamata, T. Kifune, Y. Mizumoto, M. Nagano, G. Tanahashi, and M. Teshima: PICRC, 9, p. 198 (1983).

Hayashida, N., K. Honda, M. Honda, S. Imaizumi, N. Inoue, K. Kadota, F. Kakimoto, K. Kamata, S. Kawaguchi, Y. Kawasaki, N. Kawasumi, Y. Matsubara, K. Murakami, M. Nagano, H. Ohoka, M. Takeda, M. Teshima, I. Tsushima, S. Yoshida, and H. Yoshii: Phys. Rev. Lett., 73, p. 391 (1994).

Hayashida, N., K. Honda, M. Honda, N. Inoue, K. Kadota, F. Kakimoto, K. Kamata, S. Kawaguchi, Y. Kawasaki, N. Kawasumi, H. Kitamura, H. Lafoux, Y. Matsubara, K. Murakami, M. Nagano, D. Nishikawa, H. Ohoka, N. Sakaki, M. Sasaki, N. Souma, M. Takeda, M. Teshima, I. Tsushima, Y. Uchihori, S. Yoshida, and H. Yoshii: PICRC, 4, p. 145 (1997).

Hill, C.T., and D.N. Schramm: Phys. Rev, D 31, p. 564 (1985).

Hillas, A.M.: Nucl. Phys., B (Proc. Suppl. 75A, p. 109 (1999).

Hillier, R.: Gamma-Ray Astronomy, Clarendon Press, Oxford (1984).

Honda, M., T. Kajita, K. Kasahara, and S. Midorikawa: Phys. Rev., D 52, p. 4985 (1995).

Hörandel, J.R., T. Antoni, W.D. Apel, F. Badea, K. Bekk, K. Bernlöhr, E. Bollmann, H. Bozdog, I.M. Brancus, A. Chilingarian, K. Daumiller, P. Doll, J. Engler, F. Fessler, H.J. Gils, R. Glasstetter, R. Haeusler, W. Hafemann, A. Haungs, D. Heck, T. Holst, K.H. Kampert, H. Keim, J. Kempa, H.O. Klages, J. Knapp, H.J. Mathes, H.J. Mayer, J. Milke, D. Mühlenberg, J. Oehlschläger, M. Petcu, H. Rebel, M. Risse, M. Roth, G. Schatz, F.K. Schmidt, T. Thouw, H. Ulrich, A. Vardanyan, B. Vulpescu, J.H. Weber, J. Wentz, T. Wibig, T. Wiegert , D. Wochele, J. Wochele, and J. Zabierowski: PICRC, 1, p. 337 (1999).

Hörandel, J.R., for the KASCADE Collaboration: Proc. 16th European Cosmic Ray Symposium, Alcalá, Spain, ed. José Medina, Departamento de Fisica, Universidad de Alcalá, Spain, p. 579 (1998).

Ichimura, M., E. Kamioka, K. Kirii, M. Kitazawa, T. Kobayashi, M. Kogawa, S. Kuramata, K. Maruguchi, H. Matsutani, A. Mihashi, H. Mito, T. Murabayashi, T. Nakamura, K. Nakazawa, H. Nanjo, K. Ohba, T. Ohuchi, T. Ozawa, T. Shibata, K. Shibuta, H. Sugimoto, Z. Watanabe, and Y. Yamada: PICRC, 2, p. 5 (1993a).

Ichimura, Masakatsu, Masataka Kogawa, Shuichi Kuramata, Hiroyuki Mito, Takayuki Murabayashi, Hirotada Nanjo, Takahiro Nakamura, Katsuyuki Ohba, Tatsumi Ohuchi, Tomohiko Ozawa, Yoshoyuki Yamada, Hideya Matsutani, Zenjiro Watanabe, Kazuo Shibuta, Hisahiko Sugimoto, and Kazuma Nakazawa: Phys. Rev. D 48, p. 1949 (1993b).

Ichimura, M., E. Kamioka, K. Kirii, M. Kitazawa, T. Kobayashi, M. Kogawa, S. Kuramata, K. Maruguchi, H. Matsutani, A. Mihashi, H. Mito, T. Murabayashi, T. Nakamura, K. Nakazawa, H. Nanjo, K. Ohba, T. Ohuchi, T. Ozawa, T. Shibata, K. Shibuta, H. Sugimoto, Z. Watanabe, and Y. Yamada: PICRC, 2, p. 9 (1993c).

Ichimura, Masakatsu, Masataka Kogawa, Shuichi Kuramata, Hiroyuki Mito, Hirotada Nanjo, Takahiro Nakamura, Katsuyuki Ohba, Tomohiko Ozawa, Yoshoyuki Yamada, Hideya Matsutani, Zenjiro Watanabe, Eiji Kamioka, Motoyasu Kitazawa, Tadashi Kobayashi, Atsusi Mihashi, Toru Shibata, Katsuyuki Maryguchi, Tatsumi Ohuchi, and Hisahiko Sugimoto: PICRC, 1, p. 591 (1993d).

Inoue, N., K. Honda, K. Hashimoto, N. Kawasumi, I. Tsushima, T. Matano, A. Ohsawa, N. Ohmori, R. Ticona, and N. Martinic: PICRC, 4, p. 113 (1997).

Ito, N., S. Kawakami, Y. Hayashi, T. Matsuyama, M. Sasano, N. Ikeda, and Y. Aikawa: PICRC, 4, p. 117 (1997).

Ivanenko, I.P., N.L. Grigorov, V.Ya. Shestoperov, Yu.V. Basina, P.V. Vakulov, Yu.Ya. Vasil'ev, R.M. Golynskaya,L.B. Grigor'eva, D.A. Zhuravlev, V.I. Zatsepin, A.E. Kazakova, V.D. Kozlov, I.P. Kumpan, Yu.A. Laputin, L.G. Mishchenko, V.M. Nikanorov, L.P. Papina, V.V. Platonov, D.M. Podorozhnyi, I.D. Rapoport, G.A. Samsonov, L.G. Smolenskii, V.A. Sobinyakov, V.K. Sokolov, G.E. Tambovtsev, Ch.A. Tret'yakova, Yu.V. Trigubov, I.M. Fateeva, L.A. Khein, L.O. Chikova, V.Ya. Shiryaeva, B.M. Yakovlev, and I.V. Yashin: Sov. J. Nucl. Phys., 45, p. 664 (1987).

Ivanenko, I.P., I.D. Rapoport, V.Ya. Shestoperov, Yu.V. Basina, P.V. Vakulov, Yu.Ya. Vasiliev, R.M. Golinskaya, L.B. Grigorieva, A.E. Kazakova, I.P. Kumpan, L.G. Mischenko, V.M. Nikanorov, L.P. Papina, V.V. Platonov, G.A. Samsonov, L.G. Smolensky, V.A. Sobinyakov, A.N. Turundaevskyi, Yu.V. Trigubov, I.M. Fateeva, A.N. Fedorov, L.A. Hein, L.O. Chikova, V.Ya. Shiryaeva, B.M. Yakovlev, and I.V. Yashin: PICRC, 3, p. 77 (1990).

Ivanenko, I.P., V.Ya. Shestoperov, L.O. Chikova, I.M. Fateeva, L.A. Hein, D.M. Podoroznyi, I.D. Rapoport, G.A. Samsonov, V.A. Sobinyakov, A.N. Turundaevskyi, I.V. Yashin: PICRC, 2, p. 17 (1993).

Iwai, J., T. Ogata, I. Ohta, Y. Takahashi, and T. Yanagita: PICRC, 8, p. 1 (1979).

Juliusson, E.: PICRC, 1, p. 178 (1973).

Juliusson, E.: Astrophys. J., 191, p. 331 (1974).

Kamioka, E., M. Hareyama, M. Ichimura, T. Kobayashi, H. Komatsu, S. Kuramata, K. Maruguchi, H. Matsutani, A. Mihashi, H. Mito, T. Nakamura, H. Nanjo, T. Ouchi, T. Ozawa, T. Shibata, H. Sugimoto, and Z. Watanabe: Astropart. Phys., 6, p. 155 (1997).

Kampert, K.-H., T. Antoni, W.D. Apel, F. Badea, K. Bekk, K. Bernlöhr, E. Bollmann, H. Bozdog, I.M. Brancus, A. Chilingarian, K. Daumiller, P. Doll, J. Engler, F. Fessler, H.J. Gils, R. Glasstetter, R. Haeusler, W. Hafemann, A. Haungs, D. Heck, J.R. Hörandel, T. Holst, J. Kempa, H.O. Klages, J. Knapp, H.J. Mathes, H.J. Mayer, J. Milke, D. Mühlenberg, J. Oehlschläger, M. Petcu, H. Rebel, M. Risse, M. Roth, G. Schatz, F.K. Schmidt, T. Thouw, H. Ulrich, A. Vardanyan, B. Vulpescu, J.H. Weber, J. Wentz, T. Wibig, T. Wiegert, D. Wochele, J. Wochele, and J. Zabierowski: PICRC, 3, p. 159 (1999).

Kawamura, Yasuhiro, Hideya Matsutani, Hirotada Nanjyo, Katsuya Teraoka, Kimio Toda, Masakatsu Ichimura, Keisuke Kirii, Tadashi Kobayashi, Yasuo Niihori, Toru Shibata, Kazuo Shibuta, and Yasuko Yoshizumi: Phys. Rev., D 40, p. 729 (1989).

Kawamura, Y., H. Matsutani, H. Nanjyo, M. Saito, K. Toda, Z. Watanabe, M. Ichimura, E. Kamioka, M. Kitazawa, K. Kirii, T. Kobayashi, T. Shibata, K. Shibuta, H. Sugimoto, and K. Nakazawa: PICRC, 3, p. 85 (1990a).

Kawamura, Y., H. Matsutani, H. Nanjyo, M. Saito, K. Teraoka, K. Toda, Z. Watanabe, M. Ichimura, E. Kamioka, K. Kirii, T. Kobayashi, T. Shibata, K. Shibuta, Y. Yoshizumi, H. Sugimoto, and K. Nakazawa: PICRC, 3, p. 89 (1990b).

Khristiansen, G.B.: Cosmic Rays of Superhigh Energies. Karl Thiemig Verlag, München (1980).

Khristiansen, G.B., Yu.A. Fomin, N.N. Kalmykov, G.V. Kulikov, S.S. Ostapchenko, V.I. Solovjeva, V.P. Sulakov, and A.V. Trubitsyn: PICRC, 2, p. 772 (1995).

Kieda, D.B, and S.P. Swordy: PICRC, 3, p. 191 (1999).

Klages, H.O., W.D. Apel, K. Bekk, E. Bollmann, H. Bozdog, I.M. Brancus, M. Brendle, A. Chilingarian, K. Daumiller, P. Doll, J. Engler, M. Föller, P. Gabriel, H.J. Gils, R. Glasstetter, A. Haungs, D. Heck, J. Hörandel, K.-H.

Kampert, H. Keim, J. Kempa, J. Knapp, H.J. Mathes, H.J. Mayer, H.H. Milke, D. Mühlenberg, J. Oehlschläger, M. Petcu, U. Raidt, H. Rebel, M. Roth, G. Schatz, H. Schieler, G. Schmalz, H.J. Simonis, T. Thouw, J. Unger, G. Völker, B. Vulpescu, G.J. Wagner, J. Wdowczyk, J. Weber, J. Wentz, Y. Wetzel, T. Wibig, T. Wiegert , D. Wochele, J. Wochele, J. Zabierowski, S. Zagromski , B. Zeitnitz: Proc. 9th Internat. Symposium on Very High Energy Cosmic Ray Interactions, Karlsruhe (1996). Nucl. Phys., 52B, p. 92 (1997).

Klemke, G., G. Bella, W.D. Dau, H. Jokisch, Y. Oren, A. Liland, K. Carstensen, and O.C. Allkofer: PICRC, 9, p. 150 (1981).

Krombel, K.E., and M.E. Wiedenbeck: Astrophys. J., 328, p. 940 (1988).

Kulikov, G.V., and G.B. Khristiansen: Sov. Phys. JETP, 35, p. 635 (1958).

Kuzmin, V.A., and G.T. Zatsepin: Can. J. Phys., 46, p. S617 (1968).

Labrador, A.W., R.A. Mewaldt: PICRC, 3, p. 68 (1995).

Lawrence, M.A., R.J.O. Reid, and A.A. Watson: J. Phys., G, 17, p. 733 (1991).

Lezniak, J.A., and W.R. Webber: Astrophys. J., 223, p. 676 (1978).

Linsley, John: PICRC, 12, p. 135 (1983).

Linsley, John, and Carl E. Fichtel: PICRC, 2, p. 284 (1985).

Linsley, John, and Alan Watson: Phys. Rev. Lett., 46, p. 459 (1981).

Lukasiak, A., P. Ferrando, F.B. McDonald, and W.R. Webber: Astrophys. J., 423, p. 426 (1994a).

Lukasiak, A., P. Ferrando, F.B. McDonald, and W.R. Webber: Astrophys. J., 426, p. 366 (1994b).

Lukasiak, A., F.B. McDonald, and W.R. Webber: Astrophys. J., 430, p. L-69 (1994c).

Lukasiak, A., F.B. McDonald, and W.R. Webber: PICRC, 3, p. 389 (1997a).

Lukasiak, A., F.B. McDonald, and W.R. Webber: PICRC, 3, p. 357 (1997b).

Menn, W., L.M. Barbier, E.R. Christian, A.J. Davis, R.L. Golden, M. Hof, K.E. Krombel, F. Krizmanic, A.W. Labrador, R.A. Mewaldt, J.W. Mitchell, J.F. Ormes, I.L. Rasmussen, O. Reimer, S.M. Schindler, M. Simon, S.J. Stochaj, R.E. Streitmatter, W.R. Webber: PICRC, 3, p. 409 (1997).

Minagawa, G.: Astrophys. J., 248, p. 847 (1981).

Müller, Dietrich: Adv. Space Res., 9, No. 12, p. (12)31 (1989).

Müller, Dietrich, John M. Grunsfeld, Jacques L'Heureux, Peter Meyer, and Simon P. Swordy: PICRC, 2, p. 25 (1991a).

Müller, Dietrich, Simon P. Swordy, Peter Meyer, Jacques L'Heureux, and John M. Grunsfeld: Astrophys. J., 374, p. 356 (1991b).

Nagano, M., T. Hara, Y. Hatano, N. Hayashida, S. Kawaguchi, K. Kamata, T. Kifune, and Y. Mizumoto: J. Phys., G, 10, p. 1295 (1984).

Nagano, M., M. Teshima, Y. Matsubara, H.Y. Dai, T. Hara, N. Hayashida, M. Honda, H. Ohoka, and S. Yoshida: J. Phys., G, 18, p. 423 (1992).

Nesterova, N.M., A.P. Chubenko, P.A. Djatlov, and L.I. Vildanova: PICRC, 2, p. 748 (1995).

Nikolsky, S.I., N.V. Kabanova, J.N. Stamenov, and V.D. Janminchev: PICRC, 8, p. 335 (1979).

Nikolsky, S.I., I.I. Stamenov, and S.Z. Ushev: Zh. Eksp. Teor. Fiz., 87, p. 18 (1984a).

Nikolsky, S.I., I.I. Stamenov, and S.Z. Ushev: Sov. Phys. JETP, 60, p. 10 (1984b).

Nikolsky, S.I.: PICRC, 6, p. 105 (1997).

Nozaki, M., BESS Collaboration: PICRC, Invited and Rapporteur Papers, AIP Conf. Proc., 516, p. 330 (2000).

Olinto, A.V., R.I. Epstein, and P. Blasi: PICRC, 4, p. 361 (1999).

Ormes, J.F., and W.R. Webber: PICRC, 1, p. 349 (1965).

Orth, C.D., A. Buffington, G.F. Smoot, and T.S. Mast: Astrophys. J., 226, p. 1147 (1978).

Palamara, O. MACRO Collaboration: PICRC, 2, p. 689 (1995).

Papini, P., C. Grimani, G. Basini, F. Bongiorno, M.T. Brunetti, A. Codino, R.L. Golden, B.L. Kimbell, F. Massimo Brancaccio, M. Menichelli, M. Miozza, A. Morselli, J.F. Ormes, M.P. de Pascale, P. Picozza, M. Ricci, I. Salvatori, S. Spillantini, S.A. Stephens, S.J. Stochaj, R.E. Streitmatter, and W.R. Webber: PICRC, 1, p. 579 (1993).

Parnell, T.A., T.H. Burnett, S. Dake, J.H. Derrickson, W.F. Fountain, M. Fuki, J.C. Gregory, T. Hayashi, R. Holynski, J. Iwai, W.V. Jones, A. Jurak, J.J. Lord, O. Miyamura, H. Oda, T. Ogata, F.E. Roberts, S. Strausz, T. Tabuki, Y. Takahashi, T. Tominaga, J.W. Watts, J.P. Wefel, B. Wilczynska, H. Wilczynski, R.J. Wilkes, W. Wolter, and B. Wosiek: Adv. Space Res., 9, No. 12, p. (12)45 (1989).

Penzias, A.A, and R.W. Wilson: Astrophys. J., 142, p. 419 (1965).

Petrera, S.: Nuovo Cimento, 19C, p. 737 (1996).

Pravdin, M.I., M.N. Dyakonov, A.V. Glushkov, T.A. Egorov, V.P. Egorova, A.A. Ivanov, G.B. Khristiansen, S.P. Knurenko, V.A. Kolosov, A.D. Krasilnikov, I.T. Makarov, S.I. Nikolsky, V.A. Orlov, I.Ye. Sleptsov, V.R. Sleptsova, and G.G. Struchkov: PICRC, 3, p. 292 (1999).

Protheroe, R.J., and P.A. Johnson: Astropart. Phys., 4, p. 253 (1996).

Protheroe, R.J., and Todor Stanev: Phys. Rev. Lett., 77, p. 3708 (1996).

Ramaty, R., and V.K. Balasubrahmanyan: Science, 180, p. 731 (1973).

Röhring, A., J. Cortina, S. Denninghoff, D. Horns, H. Kronmayer, A. Lindner, A. Moralejo, R. Plaga, W. Wittek, and the HEGRA Collaboration: PICRC, 1, p. 214 (1999).

Ryan, M.J., J.F. Ormes, and V.K. Balasubrahmanyan: Phys. Rev. Lett., 28, p. 985 (1972), and erratum, Phys. Rev. Lett., 28, p. 1497 (1972).

Sanuki, T., M. Motoki, H. Matsumoto, E.S. Seo, J.Z. Wang, K. Abe, K. Anraku, Y. Asaokal, M. Fujikawa, M. Imori, M. Ishino, T. Maeno, Y. Makida, N. Matsui, H. Matsunaga, J. Mitchell, T. Mitsui, A. Moiseev, J. Nishimura, M. Nozaki, S. Orito, J. Ormes, T. Saeki, M. Sasaki, Y. Shikaze, T. Sonoda, R. Streitmatter, J. Suzuki, K. Tanaka, I. Ueda, N. Yajima, T. Yamagami, A. Yamamoto, T. Yoshida, and K. Yoshimura: PICRC, 3, p. 93 (1999).

Schatz, G.: Submitted to Elsevier Preprint (2001).

Seo, E.S., J.F. Ormes, R.E. Streitmatter, S.J. Stochaj, W.V. Jones, S.A. Stephens, and T. Bowen: Astrophys. J., 378, p. 763 (1991).

Shapiro, M.M., R. Silberberg, and C.H. Tsao: Acta Phys. Acad. Sci. Hung., 29, Suppl. 1, p. 471 (1970).

Shibata, T.: Nuovo Cimento, 19 C, p, 713 (1996).

Shibata, T.: after Watson (1997).

Shibata, T.: Nucl. Phys., B (Proc. Suppl.) 75A, p. 22 (1999).

Shirasaki, Y.: Master Thesis, Tokyo Inst. of Technology, Meguro, Tokyo (1994).

Shirasaki, Y., F. Kakimoto, S. Ogio, N. Tajima, K, Nishi, N. Gironda, T. Kaneko, N. Takeda, H. Yoshii, T. Baba, S. Sano, K. Murakami, Y. Toyoda, Y. Matsubara, Y. Yamada, S. Shimoda, H. Nakatani, E. Gotoh, Y. Mizumoto, W. Velasquez, A. Velarde, and P. Miranda: PICRC, 4, p. 53 (1997).

Simon, M., H. Spiegelhauer,, W.K.H. Schmidt, F. Siohan, J. Ormes, V.K. Balasubrahmanyan, and J.F. Arens: Astrophys. J., 239, p. 712 (1980).

Simpson, J.A.: Elemental and Isotopic Composition of the Galactic Cosmic Rays, in Ann. Rev. of Nucl. and Particle Phys. (Ann/ Reviews, Inc., Palo Alto, Calif.), 33 (1983).

Simpson, J.A.: PICRC, 8, p. 4 (1997).

Simpson, J.A., and J.J. Connell: Astrophys. J., 497, p. L-85 (1998).

Smith, L.H., A. Buffington, G.F. Smoot, L.W. Alvarez, and M.A. Wahlig: Astrophys. J., 180, p. 978 (1973).

Sokolsky, Pierre: Introduction to Ultrahigh Energy Cosmic Ray Physics, Frontiers in Physics, Vol. 76, Addison-Weskey Publishing Co., New York (1989).

Stanev, Todor, Peter L. Biermann, and Thomas K. Gaisser: Astron. Astrophys., 274, p. 902 (1993).

Stecker, F.W.: Nature, 342, p. 401 (1989).

Swordy, Simon P.: PICRC, 2, p. 697 (1995).

Swordy, Simon P.: Proc. 16th European Cosmic Ray Symposium, Alcalá, Spain, ed. José Medina, Departamento de Fisica, Universidad de Alcalá, Spain, p. 265 (1998).

Swordy, Simon P., Dietrich Müller, Peter Meyer, Jaques L'Heureux, and John M. Grunsfeld: Astrophys. J., 349, p. 625 (1990).

Swordy, Simon P., Jacques L'Heureux, Peter Meyer, and Dietrich Müller: Astrophys. J., 403, p. 658 (1993).

Swordy, S.P., Barwick, S.W., J.J. Beatty, C.R. Bower, C. Chaput, S. Coutu, G. de Nolfo, D. Ficenec, J. Knapp, D.M. Lowder, S. McKee, D. Müller, J.A. Musser, S.L. Nutter, E. Schneider, K.K. Tang, G. Tarlé, A.D. Tomasch, and E. Torbet: PICRC, 2, p. 652 (1995).

Takeda, M., N. Hayashida, K. Honda, N. Inoue, K. Kadota, F. Kakimoto, K. Kamata, S. Kawaguchi, Y. Kawasaki, N. Kawasumi, H. Kitamura, E. Kusano, Y. Matsubara, K. Murakami, M. Nagano, D. Nishikawa, H. Ohoka, N. Sakaki, K. Shinozaki, N. Souma, M. Teshima, R. Torii, I. Tsushima, Y. Uchihori, T. Yamamoto, S. Yoshida, and H. Yoshii: Phys. Rev. Lett., 81, p. 1163 (1998).

M. Tamada: J. Phys., G 20, p. 487 (1994).

Teshima, M.: PICRC, 5, p. 257 (1993).

Verma, R.P., T.N. Rengarajan, S.N. Tandon, S.V. Damle, and Yash Pal: Nature, 240, p. 135 (1972).

Von Rosenvinge, T.T., W.R. Webber, and J.F. Ormes: Astrophys. Space

Sci., 5, p. 342 (1969).

Watson, A.A.: Proc. 12th European Cosmic Ray Symp. (Nottingham), Nucl. Phys., B, p. 16 (1991).

Watson, A.A.: Nucl. Phys., B (Proc. Suppl.) 28B, p. 3 (1992).

Watson, A.A.: Proc. 1994 Snowmass Summer Study. Eds. E.W. Kolb and R.D. Pecci, p. 126 (1995).

Watson, A.A.: PICRC, 8, p. 257 (1997).

Webber, W.R.: in Composition and Origin of Cosmic Rays, M.M. Shapiro ed., D. Reidel Publishing Co., Dordrecht, p. 25 (1983).

Webber, W.R., and J.A. Lezniak: Astrophys. Space Sci., 30, p. 361 (1974).

Webber, W.R., J.A. Lezniak, J.C. Kish, and S.V. Damle: Nature Phys. Sci., 241, p. 96 (1973).

Webber, W.R., R.L. Golden, and S.A. Stephens: PICRC, 1, p. 325 (1987).

Webber, W.R., A. Lukasiak, F.B. McDonald, and P. Ferrando: Astrophys. J., 457, p. 435 (1996).

Webber, W.R., A. Lukasiak, and F.B. McDonald: Astrophys. J., 476, p. 766 (1997).

Wefel, J.P.: in "Cosmic Rays, Supernovae, and the Interstellar Medium", eds. M.M. Shapiro, R. Silbergerg, and J.P. Wefel, Kluwer, Dordrecht, p. 29 (1991).

Wiebel-Sooth, Barbara: Thesis Univ. of Wuppertal, WUB-Dis 98-9 (1998).

Wiebel-Sooth, Barbara, and Peter L. Biermann: Cosmic Rays, Landolt - Börnstein, Springer Verlag (1998).

Wiebel-Sooth, Barbara, Peter L. Biermann, and Hinrich Meyer:: PICRC, 2, p. 656 (1995).

Wiebel-Sooth, B., W. Rhode, and the HEGRA Collaboration: PICRC, 4, p. 121 (1997).

Wiedenbeck, M.E., and D.E. Greiner: Astrophys. J., 239, p. L-139 (1980).

Wiedenbeck, M.E., and D.E. Greiner: Astrophys. J., 247, p. L-119 (1981).

Winn, M.M., J. Ulrichs, L. Horton, C.B.A. McCusker, and L.S. Peak: PICRC, 9, p. 499 (1985).

Winn, M.M., J. Ulrichs, L.S. Peak, C.B.A. McCusker, and L. Horton,: J. Phys., G, 12, p. 653 (1986).

Yanasak, N.E., M.E. Wiedenbeck, W.R. Binns, E.R. Christian, A.C. Cummings, A.J. Davis, J.S. George, P.L. Hink, M.H. Israel, R.A. Leske, M. Li-

jowski, R.A. Mewaldt, E.C. Stone, T.T. von Rosenvinge: Adv. Space Res., Report of 33rd COSPAR Meeting, Warsaw (2000) (in press).

Yoshida, Shigeru: Rapporteur Paper XXVI Internat. Cosmic Ray Conf. (1999), AIP Conf. Proc., 516, p. 180, Brenda L. Dingus, David B. Kieda and Michael H. Salamon eds., American Institute of Physics (2000).

Yoshida, Shigeru, and Hongyue Dai: J. Phys. G., 24, p. 905 (1998).

Yoshida, Shigeru, and Masahiro Teshima: Progr. Theor. Phys., 89, p. 833 (1993).

Yoshida, S., Nagano, M., N. Hayashida, K. Honda, M. Honda, S. Imaizumi, N. Inoue, K. Kadota, F. Kakimoto, K. Kamata, S. Kawaguchi, N. Kawasumi, Y. Matsubara, K. Murakami, M. Nagano, H. Ohoka, M. Teshima, I. Tsushima, and H. Yoshii: Astropart. Phys., 3, p. 105 (1995).

Yoshii, H., T. Baba, T. Kaneko, F. Kakimoto, S. Ogio, Y. Shirasaki, N. Gironda, Y. Toyoda, K. Murakami, Y. Matsubara, Y. Mizumoto, K. Nishi, N. Tajima, S. Shimoda, H. Nakatani, Y. Yamada, E. Gotoh, W. Velasquez, and A. Velarde: PICRC, 2, p. 703 (1995).

Zatsepin, G.T.: Dokl. Akad. Nauk SSSR, 80, p. 577 (1951).

Zatsepin, G.T. and V.A. Kuzmin: Zh. Eksp. Teor. Fiz. Letters, 4, p. 114 (1966).

Zatsepin, V.I., E.A. Zamchalova, A.Ya. Varkovitskaya, N.V. Sokolskaya, G.P. Sazhina, N.G. Ryabova, and K.V. Mandritskaya: PICRC, 3, p. 81 (1990).

Zatsepin, V.I., E.A. Zamchalova, A.Ya. Varkovitskaya, N.V. Sokolskaya, G.P. Sazhina, and T.V. Lazareva: PICRC, 2, p. 13 (1993).

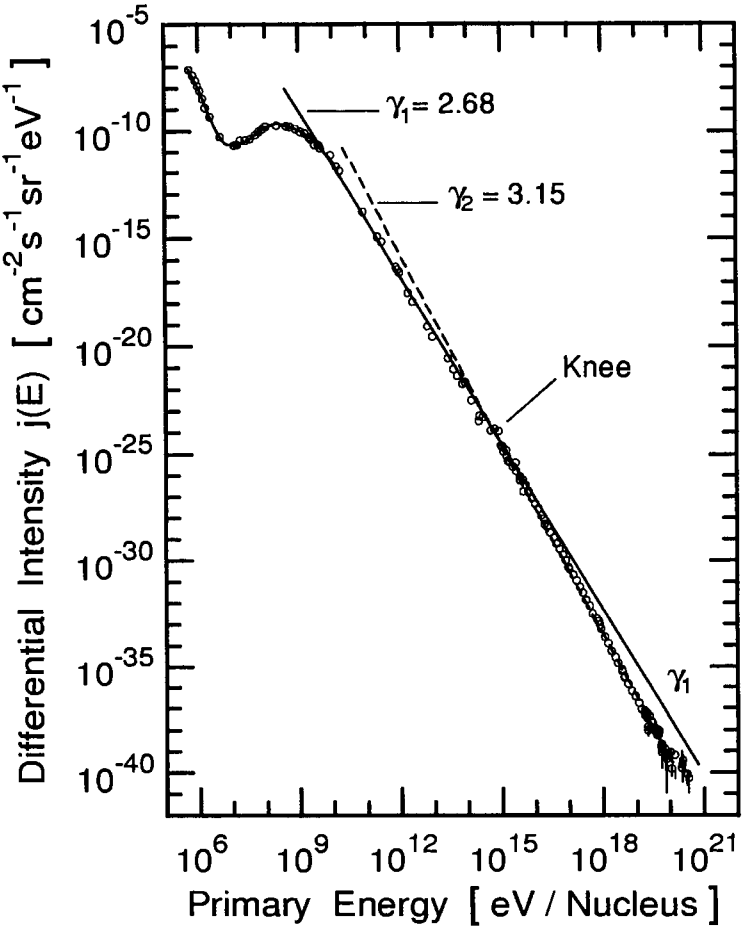

Figure 5.1: Differential energy spectrum of the all-particle hadronic cosmic radiation. The dip around 10 MeV is the result of the superposition of the rapidly falling solar and anomalous components with increasing energy and the slower falling intensity of the galactic cosmic radiation with decreasing energy. Above about 10 GeV where the solar modulation has a negligible effect the spectrum appears to be almost featureless in this representation, except for a slight change of slope, as indicated by the two power law fits of the form $j(E) \propto E^{-\gamma}$ with spectral indices γ_1 and γ_2 as indicated.

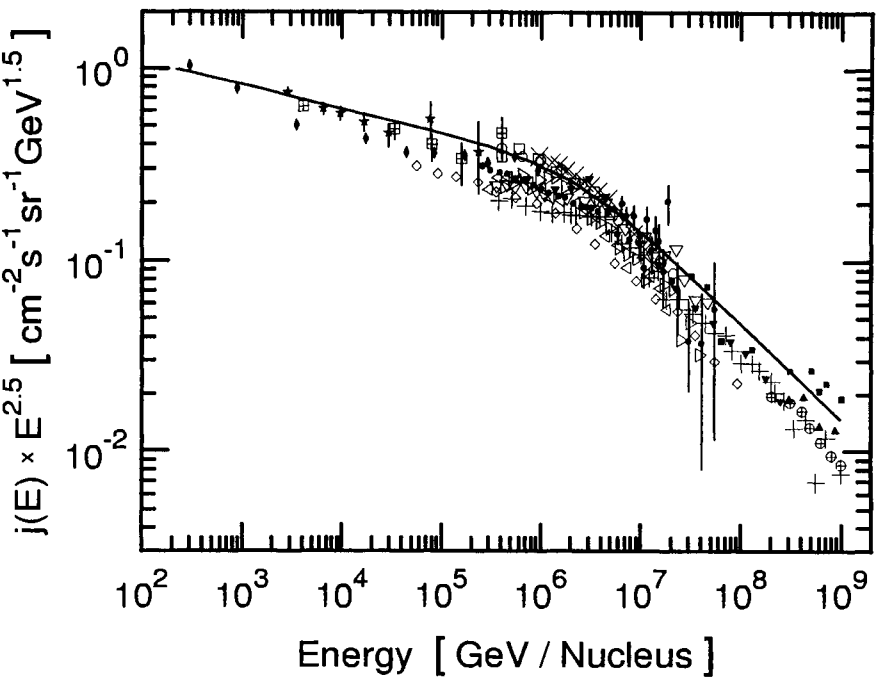

Figure 5.2: All-particle differential energy spectrum of primary cosmic rays. The intensity, $j(E)$, is multiplied with $E^{2.5}$, E being the primary energy in GeV, to compress the spectrum and to emphasize spectral features and differences between the results of different experiments. The solid line is the spectrum according to the NSU model (Bugaev et al., 1993). The knee in the spectrum is evident.

- ♦ PROTON 4 (Grigorov et al., 1971a)
- ⊞ JACEE (Asakimori et al., 1991a, b)
- • Kascade (Hörandel et al., 1999)
- × EAS-TOP (Aglietta et al., 1999)
- ○ Tibet (Amenomori et al., 1995, 1996a)
- ▷ Kobe (Asakimori, 1990)
- ▽ Tunka (Gress et al., 1997)
- ▲ Haverah Park (Lawrence et al., 1991)
- ■ Yakutsk (Dyakonov et al., 1991)
- ★ Sokol (Ivanenko et al., 1993)
- ◇ Norikura (Ito et al., 1997)
- □ HEGRA (Cortina et al., 1997; Röhring et al., 1999)
- ◁ DICE (Boothby et al., 1997a, b; Kieda and Swordy, 1999)
- ▼ MSU (Fomin et al., 1991)
- ⊕ Fly's Eye (Bird et al., 1994)
- \+ Akeno (Nagano et al., 1984)

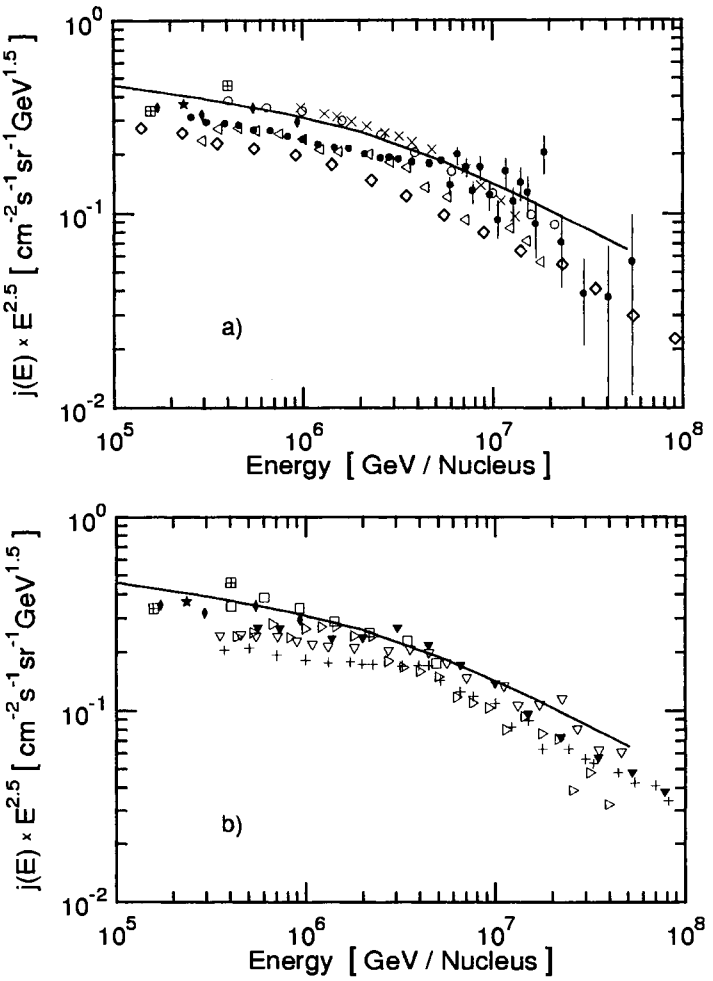

Figure 5.3: Knee region only of Fig. 5.2 with the full data set split between plots a) and b) for better comparison.

- ♦ PROTON 4 (Grigorov et al., 1971a)
- ⊞ JACEE (Asakimori et al., 1991a, b)
- • Kascade (Hörandel et al., 1999)
- × EAS-TOP (Aglietta et al., 1999)
- ○ Tibet (Amenomori et al., 1995, 1996a)
- ▷ Kobe (Asakimori, 1990)
- ▽ Tunka (Gress et al., 1997)
- \+ Akeno (Nagano et al., 1984)
- ★ Sokol (Ivanenko et al., 1993)
- ◇ Norikura (Ito et al., 1997)
- □ HEGRA (Cortina et al., 1997) Röhring et al., 1999)
- ◁ DICE (Boothby et al., 1997a, b) Kieda and Swordy, 1999)
- ▼ MSU (Fomin et al., 1991)

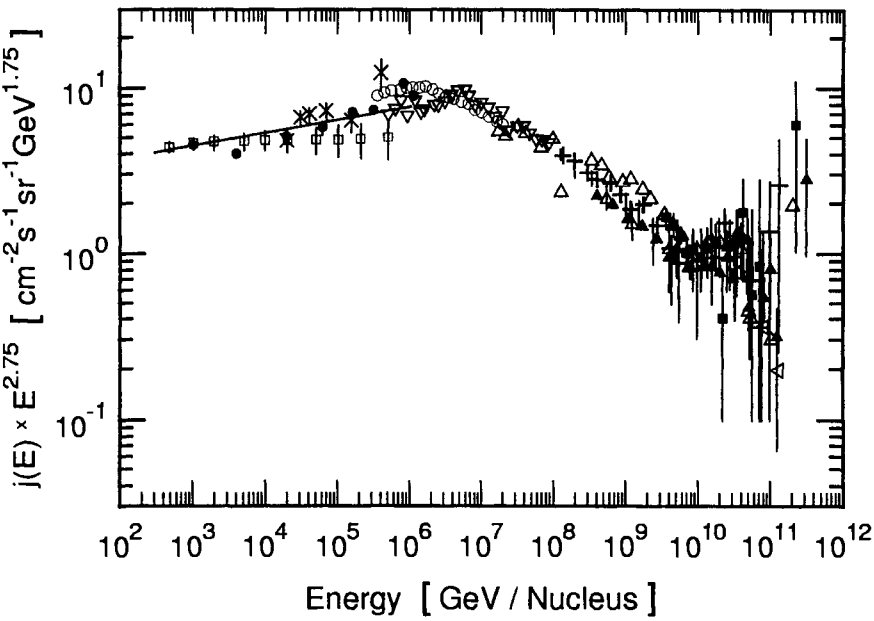

Figure 5.4: All-particle cosmic ray differential energy spectrum constructed with data from many experiments. The differential intensity, $j(E)$, is multiplied with $E^{2.75}$, E being the primary energy in GeV, to compress the spectrum and to emphasize spectral features and differences between the results from different experiments. The bend in the spectral slope represents the knee in the spectrum. The lower energy data up to about 10^6 GeV are from direct measurements on top of the atmosphere and on board of satellites, the higher energy data are from air shower measurements, as listed below. The solid line indicates the averaged low energy portion of the spectrum.

- □ Ichimura et al., (1993a)
- ▲ Fly's Eye (Bird et al., 1994)
- ▽ Akeno (Nagano et al., 1984)
- ■ AGASA (Yoshida et al. (1995)
- △ Yakutsk (Dyakonov et al., 1991)
- • PROTON 4 (Grigorov et al., 1971a)
- × JACEE (Asakimori et al., 1993a, 1993b)
- ○ Tien Shan (Nesterova et al., 1995)
- ◁ Yakutsk (Afanasiev et al. (1995)
- \+ Haverah Park (Lawrence et al., 1991)

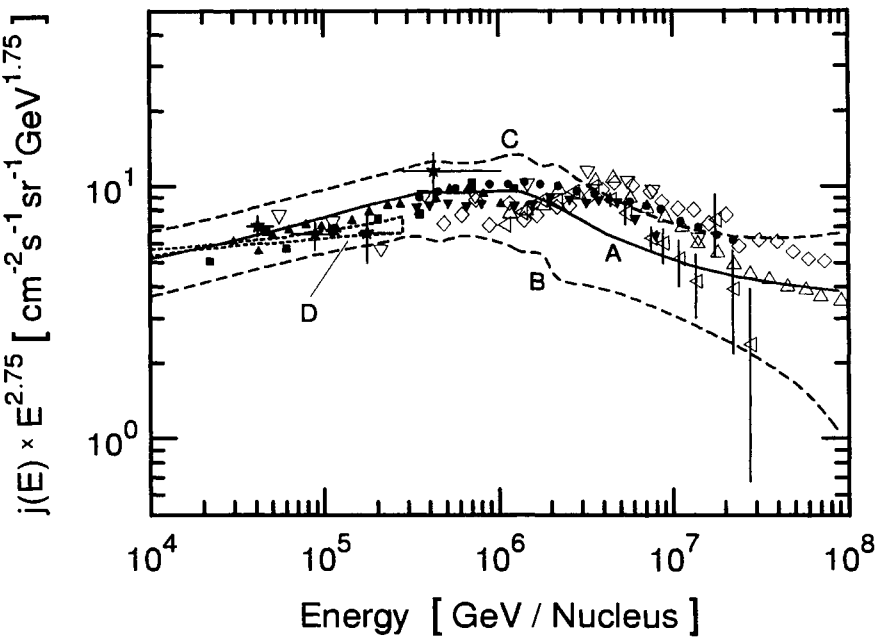

Figure 5.5: Compilation of all-particle differential spectra. The solid symbols are high altitude air shower and direct balloon and satellite measurements, the open symbols are sea level or near sea level air shower measurements ($\geq$950 g/cm^2), as listed below. The solid and dashed lines represent the spectrum with upper and lower limits derived from muons detected with MACRO (Palamara et al., 1995), and the dotted region shows the result of a summary of direct measurements after Wiebel-Sooth et al., (1995). Note that the intensity, $j(E)$, is multiplied by $E^{2.75}$. For details see text (for recent summaries see Petrera, 1996; Wiebel-Sooth and Biermann, 1998).

▲	BASJE, 520 g/cm^2 (Yoshii et al., 1995)
▼	BASJE, 520 g/cm^2 (Shirasaki, 1994)
★	JACEE Balloon ~4 g/cm^2 (Asakimori et al., 1993a, b and Ichimura et al., 1993a)
■	Proton Satellite (Grigorov et al., 1971a)
•	Yangbajing, 606 g/cm^2 (Amenomori et al., 1995)
◇	Akeno, 970 g/cm^2 (Nagano et al., 1984)
◁	Tunka, 950 g/cm^2 (Bryanski et al., 1995)
△	Moscow, 1000 g/cm^2 (Fomin et al., 1991)
▽	Yakutsk, 1020 g/cm^2 (Efimov et al., 1991)

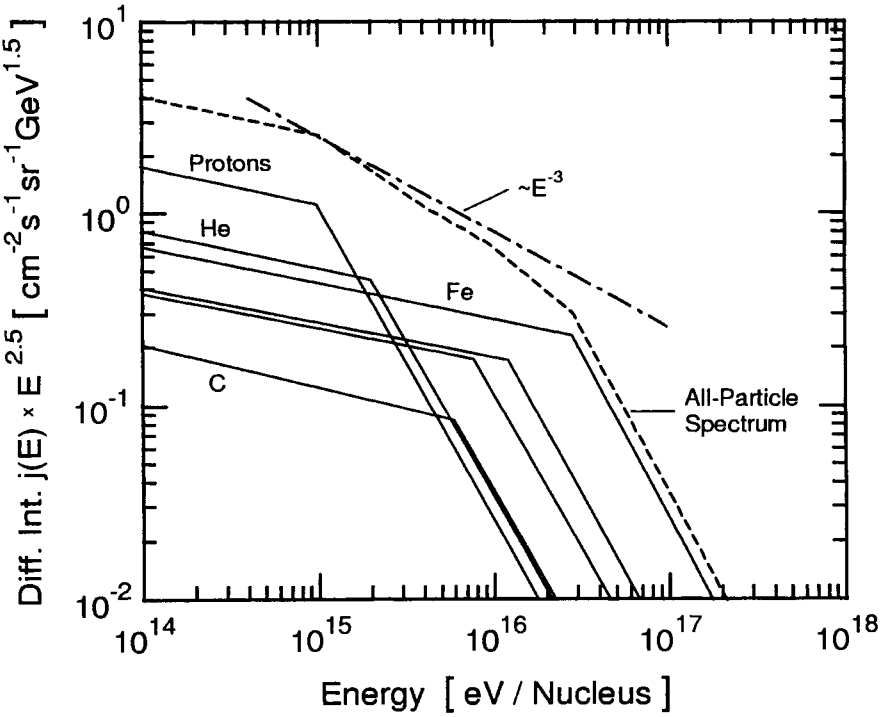

Figure 5.6: All-particle spectrum constructed by summing the spectra of the individual constituents. These spectra are based on the assumption of a constant injection spectrum of the form $E^{-\gamma}$ with $\gamma = 2.3$ for all charge components and a propagation with an energy dependent diffusion escape $\propto E^{-0.4}$ up to $\sim 10^{15}$ eV, E being the energy of the particle, with appropriate source abundances. For an upper limit of these spectra imposed by a particle rigidity of 10^{15} V, as assumed in this example, the all-particle spectrum shown here results. For comparison a spectral slope of -3.0 is also indicated (after Webber, 1983). Such a model can produce a smooth extended knee region in the spectrum. Another component with a flatter spectrum extending to ultrahigh energies would then be responsible for the observed spectral region above 10^{18} eV. Note that the intensity is multiplied by $E^{2.5}$, E being in GeV.

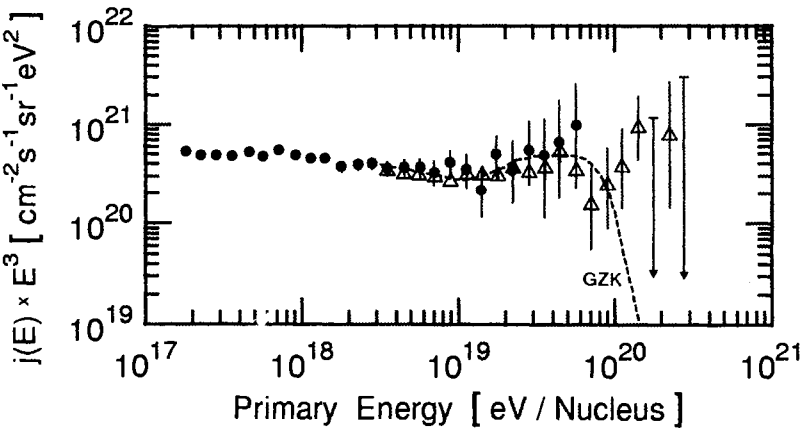

Figure 5.7: All-particle primary differential energy spectrum obtained with the Akeno (•) (Nagano et al., 1992; Chiba et al., 1993) and AGASA (△) (Takeda et al., 1998; AGASA, 1999) installations. The dashed curve labeled GZK represents the spectrum expected for extragalactic sources including the GZK cutoff effect (Yoshida and Teshima, 1993; see also Yoshida et al., 1995; Yoshida, 2000). Note that the differential intensity, $j(E)$, is multiplied by E^3.

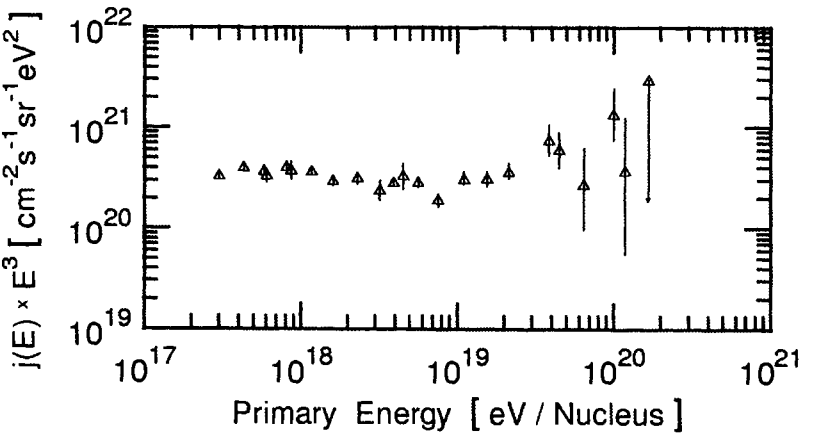

Figure 5.8: All-particle primary differential energy spectrum obtained with the Haverah Park installation (Lawrence et al., 1991). Note that the differential intensity, $j(E)$, is multiplied by E^3.

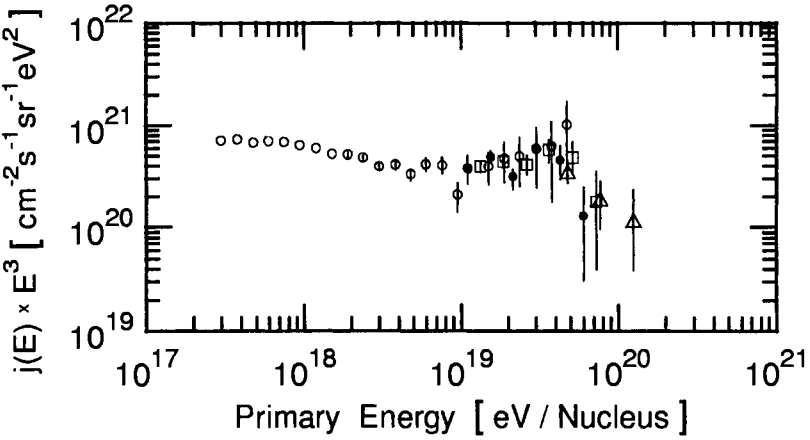

Figure 5.9: All-particle primary differential energy spectrum obtained with the Yakutsk installation (Efimov et al., 1991; Afanasiev et al., 1995; Pravdin et al. 1999) for different trigger conditions (○ 500 m, • 1000 m) and zenith angles (○, □, •, $\theta < 50°$; △, $\theta < 60°$). Note that the differential intensity, $j(E)$, is multiplied by E^3.

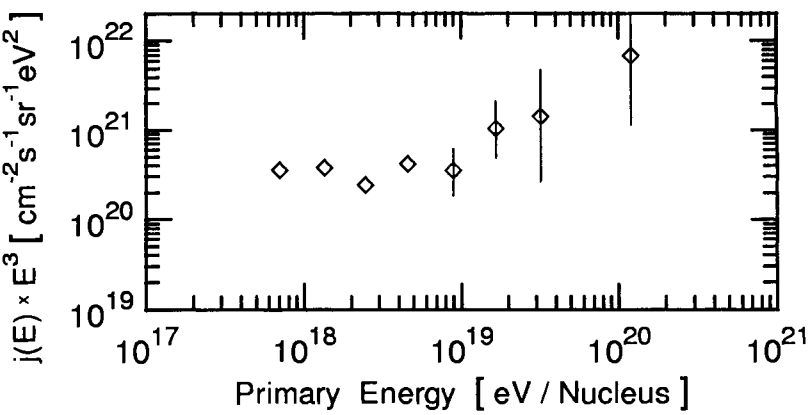

Figure 5.10: All-particle primary differential energy spectrum obtained with the Volcano Ranch installation (Cunningham et al., 1977 and 1980). Note that the differential intensity, $j(E)$, is multiplied by E^3.

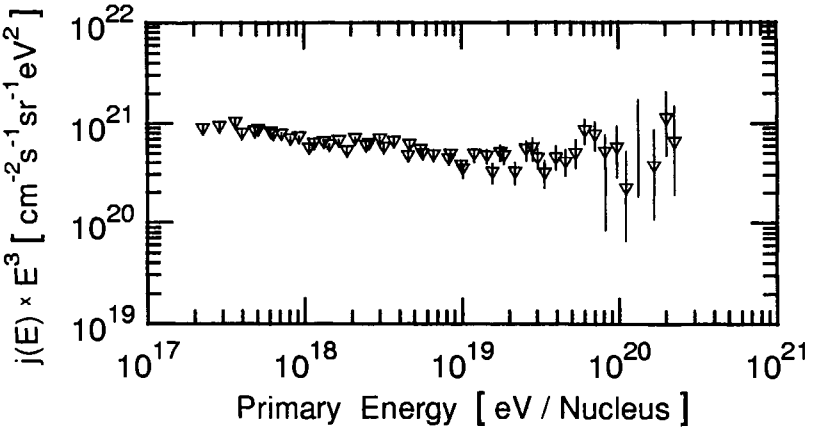

Figure 5.11: All-particle primary differential energy spectrum obtained with the SUGAR installation (Winn et al., 1985 and 1986). Note that the differential intensity, $j(E)$, is multiplied by E^3.

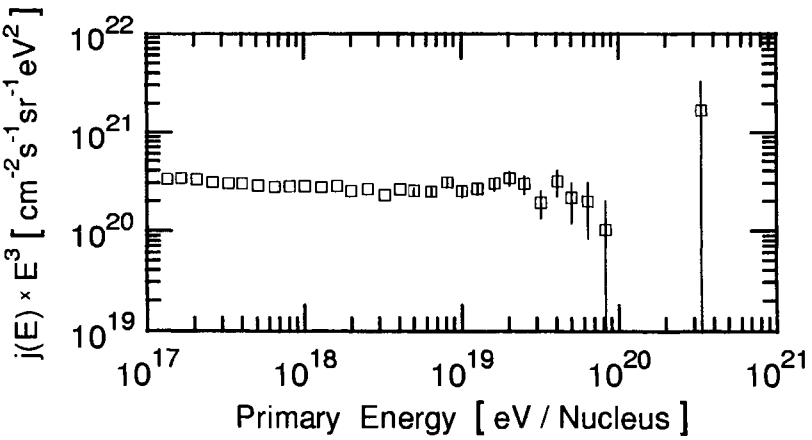

Figure 5.12: All-particle primary differential energy spectrum obtained with the Fly's Eye installation (Bird et al., 1994; see also Abu-Zayyad, 1999). Note that the differential intensity, $j(E)$, is multiplied by E^3.

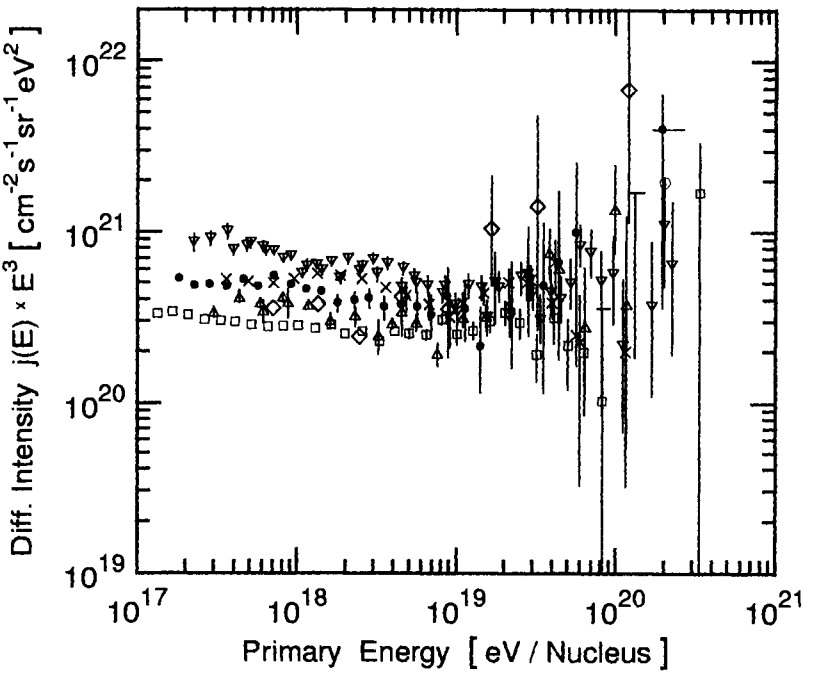

Figure 5.13: All-particle primary differential energy spectra derived from the results of the giant air shower arrays, operated during different epochs. Shown are the results from Akeno (Japan), the Fly's Eye (U.S.A.), Haverah Park (GB), SUGAR (Aus.), Volcano Ranch (US), and Yakutsk (Russia). Note that the differential intensity, $j(E)$, is multiplied by E^3. (Compilation by the author.)

- • Akeno (Nagano et al., 1992)
- ○ Akeno, re-analyzed (Chiba et al., 1993)
- △ Haverah Park (Lawrence et al., 1991)
- × Yakutsk (Efimov et al., 1991)
- □ Fly's Eye (Bird et al., 1994)
- ◇ Volcano Ranch (Fichtel & Linsley, 1985)
- ▽ SUGAR (Winn et al., 1985)

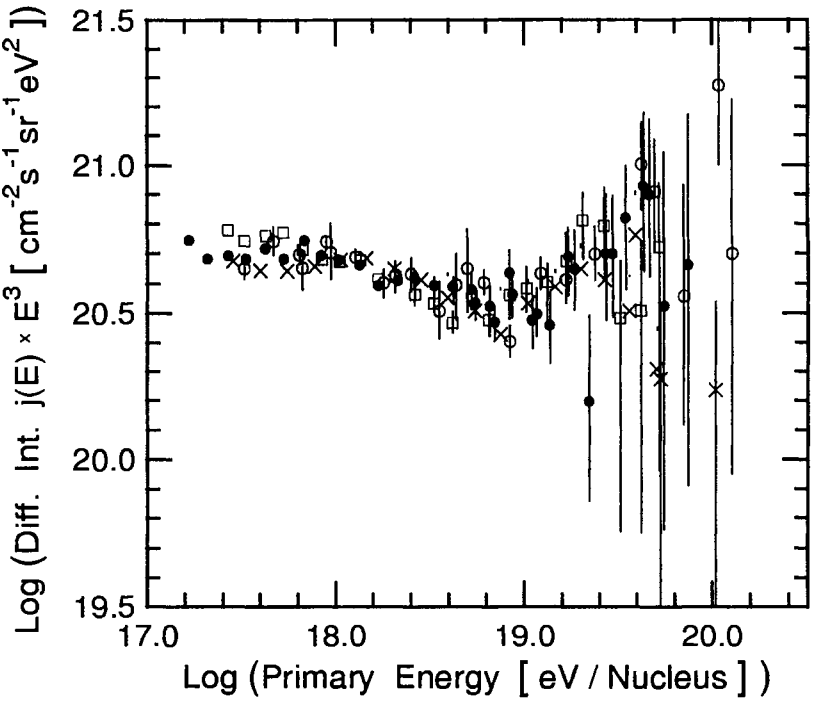

Figure 5.14: *Grand-Unified* all-particle cosmic ray differential energy spectrum. The experimental data are a selection of the data in the previous figure (Fig. 5.13) but normalized with respect to Akeno according to the method outlined by Teshima (1993), i.e., the energy scales are shifted to follow the AGASA (Akeno Giant Air Shower Array) results (Yoshida et al., 1995). All intensities are multiplied with E^3, as before. Note that with respect to the previous figures the normalization moves the data points along the abscissa and the ordinate because of the multiplication with E^3.

- • Akeno (Nagano et al., 1992; Chiba et al., 1993)
- o Haverah Park (Lawrence et al., 1991)
- × Yakutsk (Efimov et al., 1991)
- □ Fly's Eye (Bird et al., 1993a)

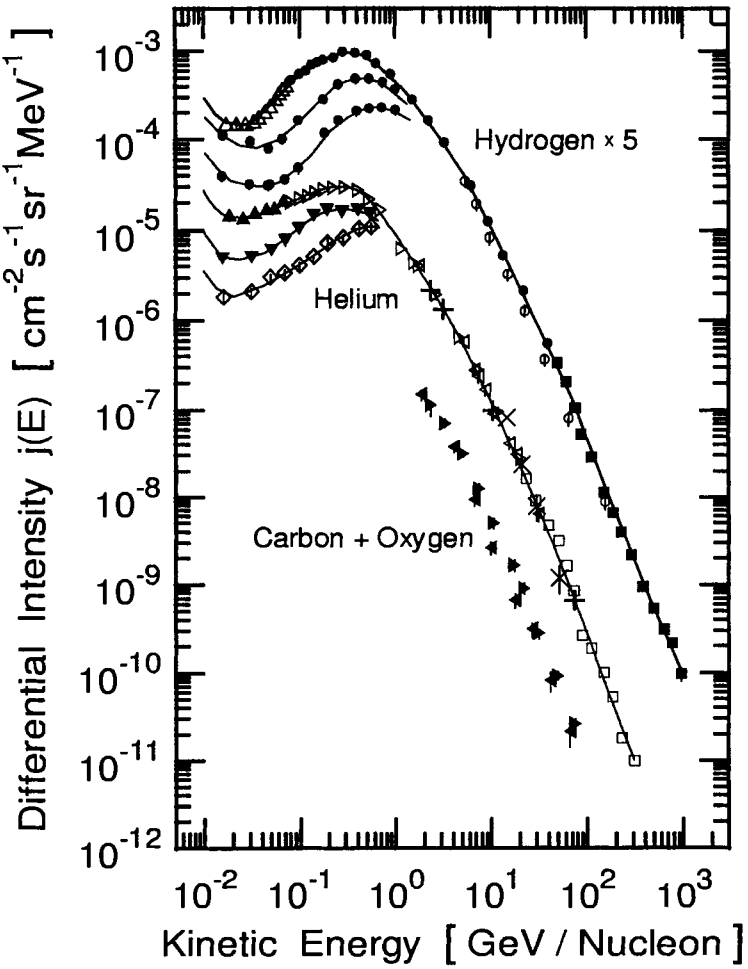

Figure 5.15: Differential energy spectra of cosmic ray hydrogen (protons) and helium nuclei recorded at different times. The solar modulation effect is evident. The data points are from several older experiments as listed below. Also shown are two data sets for carbon and oxygen nuclei combined. The curves are smoothed best fits to the data (after Webber and Lezniak, 1974).

•, ▷, ▼, ◇	Ormes and Webber (1965), von Rosenvinge et al. (1969), Webber et al. (1973)	○	Smith et al. (1973)
		+	Anand et al. (1968b)
		×	Verma et al. (1972)
□, ■	Ryan et al. (1972)	▶	Smith et al. (1973)
△, ▲	Fan et al. (1966)	◀	Balasubrahmanyan and Ormes (1973)

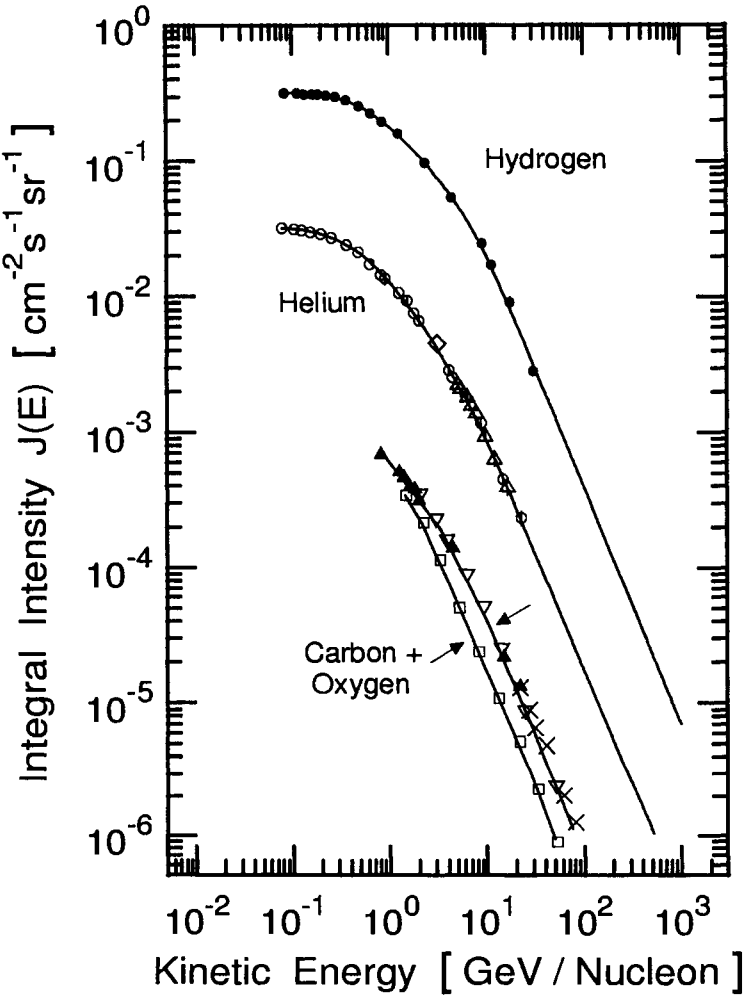

Figure 5.16: Integral energy spectra of cosmic ray hydrogen (protons) and helium nuclei. The data points are from several older experiments as listed below. Also shown are two data sets for carbon and oxygen nuclei combined. The curves are smoothed best fits to the data (after Webber and Lezniak, 1974).

•, ○	Ormes and Webber (1965), von Rosenvinge et al. (1969),	◇	Smith et al. (1973)
		△	Anand et al. (1968b)
▲	Webber et al. (1973)	×	Juliusson (1973)
□	Balasubrahmanyan and Ormes (1973)		

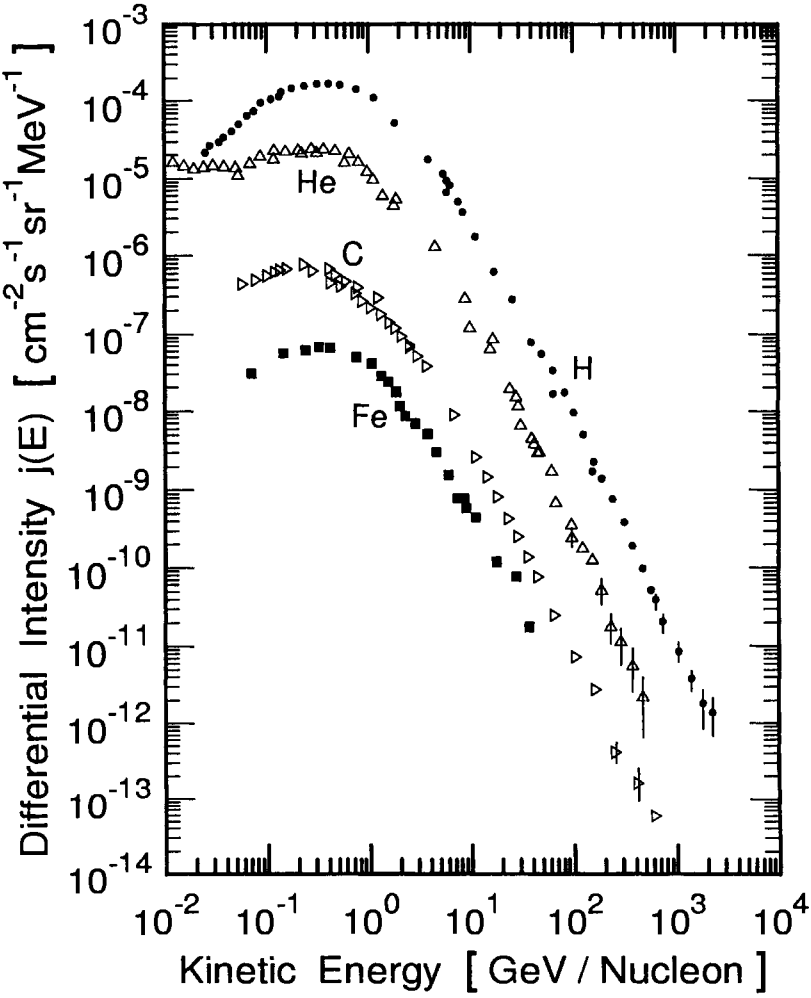

Figure 5.17: Examples of differential energy spectra of protons, helium, carbon and iron nuclei as measured by different experiments on a direct particle-by-particle basis. The spectra of the individual elements follow the expected power law. However, it can be noticed that the spectral slope of iron is somewhat flatter than the slopes of the other elements shown (Cherry, 1997b).

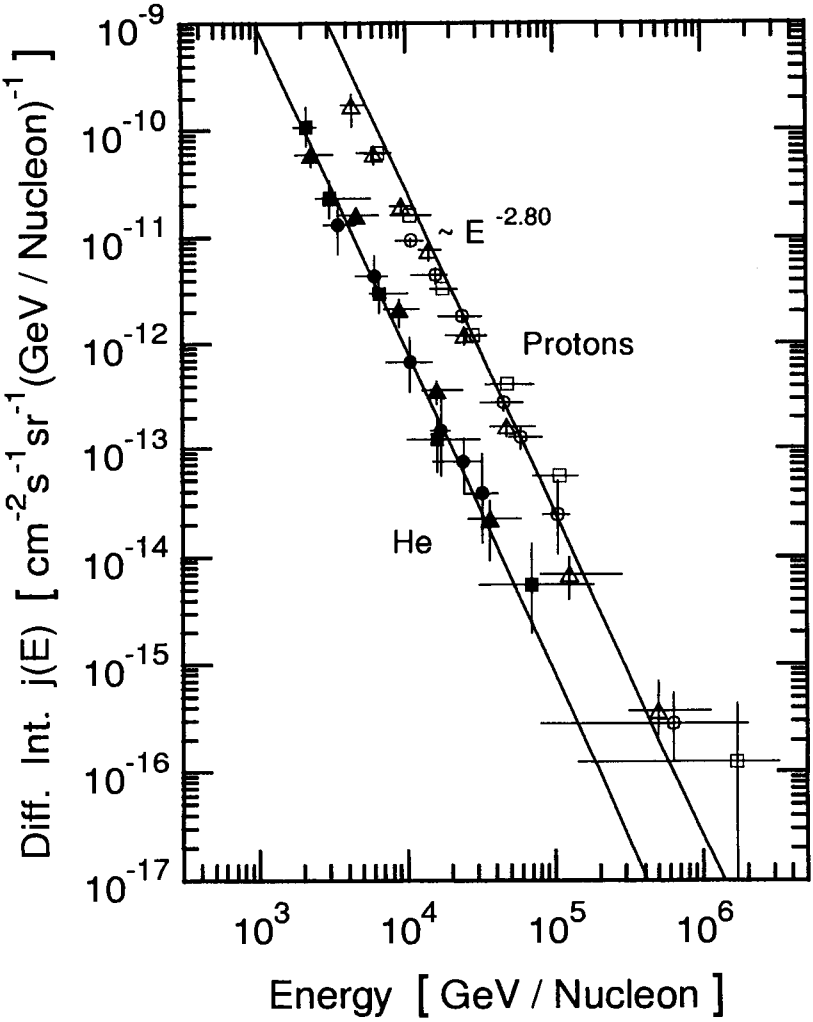

Figure 5.18: Differential energy spectra of protons and helium as measured by the balloon-borne emulsion experiments JACEE and RUNJOB. The two lines represent power law spectra with a spectral index of -2.80. Recent JACEE data show for He a slope of -2.68 (see Shibata, 1997, Watson, 1997).

△	protons	▲	He	JACEE (Parnell et al., 1989)
○	protons	●	He	RUNJOB (Apanasenko et al., 1997d, e)
□	protons	■	He	RUNJOB (Apanasenko et al., 1999a, b)

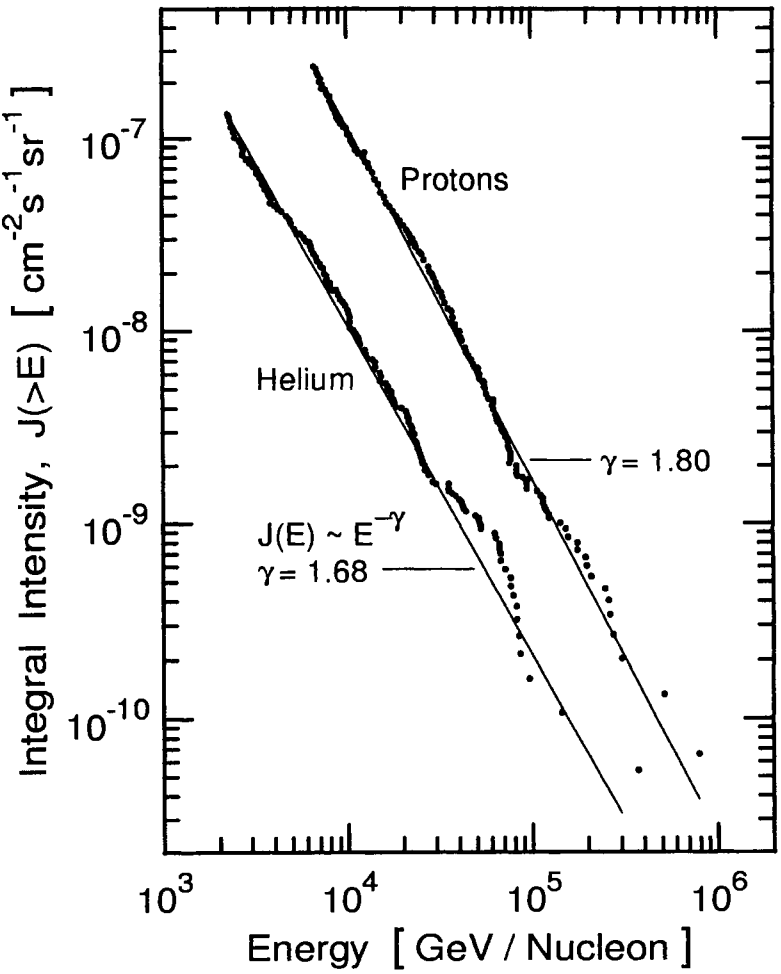

Figure 5.19: Integral energy spectra of protons and helium as measured by the balloon-borne emulsion experiments JACEE-1 to JACEE-12. The data are the result of a cumulative exposure of 644 m^2 hr. The dip in the proton spectrum between 60 TeV and 100 TeV and in the He spectrum between 20 TeV and 30 TeV is characteristic of the point-to-point correlation in an integral plot. The straight lines are maximum likelihood fits with power law indices $\gamma_p = 1.80 \pm 0.04$ and $\gamma_{He} = 1.68 \pm 0,06$ for the proton and helium spectra, respectively (Cherry, 1997a and 1999).

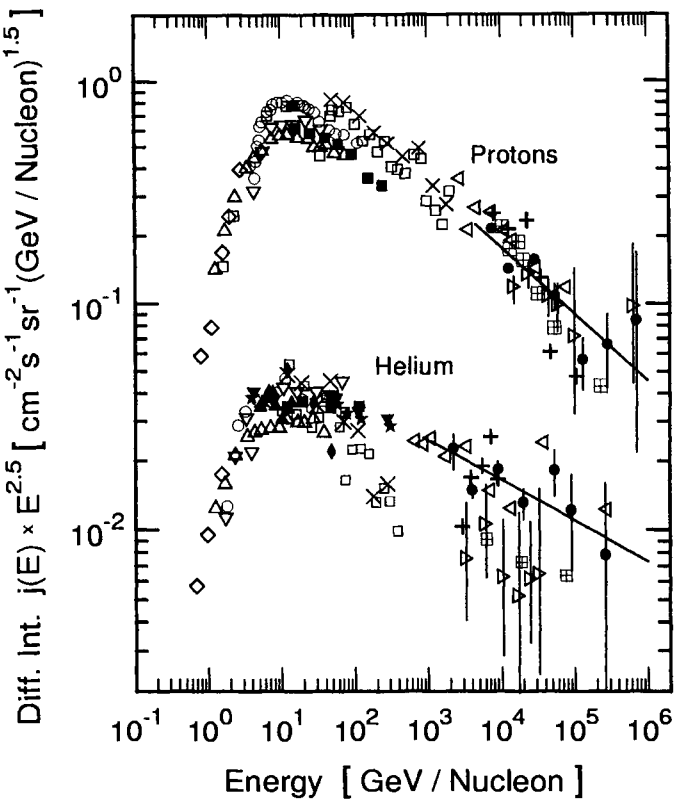

Figure 5.20: Differential energy spectra of protons and helium as measured by the balloon-borne emulsion experiments JACEE 1 to JACEE 12 (Asakimori et al., 1997; also Cherry et al., 1997a), RUNJOB 95 (Apanasenko et al., 1999a and 1999b; Shibata, 1999), and a number of other experiments, as listed below. Note that the differential intensity, $j(E)$, is multiplied by $E^{2.5}$.

×	Ryan et al. (1972)	◇	Freier and Waddington (1968)
▲	Anand et al. (1968a)	•	Asakimori et al. (1997, 1998)
♦	Verma et al. (1972)	□	Ramaty et al. (1973)
▽	Smith et al. (1973)	○	Badhwar et al. (1977)
△	Seo et al. (1991)	▼	Dwyer et al. (1993)
◁	Ivanenko et al. (1993)	+	Ichimura et al. (1993a, b)
⊞	Zatsepin et al. (1993)	■	Swordy et al. (1995)
★	Swordy et al. (1993)	▷	Shibata (1999)

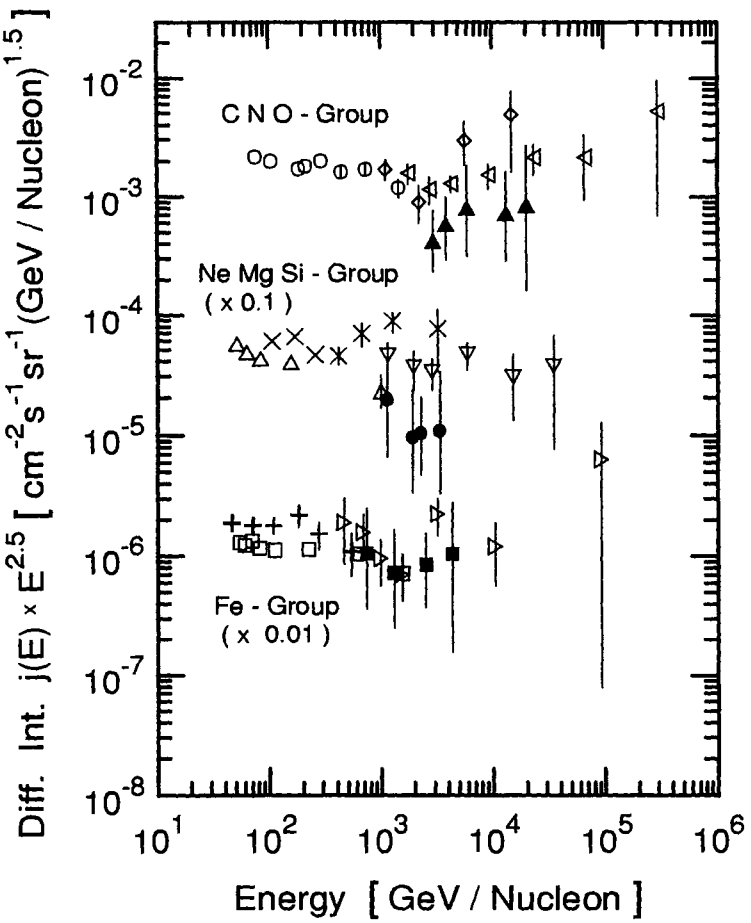

Figure 5.21: Differential energy spectra of the C-N-O, Ne-Mg-Si and Fe groups measured by different experiments, as indicated below. The intensities are multiplied by $E^{2.5}$. In addition the intensities of the Ne-Mg-Si and Fe groups are plotted a factor of 10 and 100 lower, respectively, as indicated, for better distinction (Shibata, 1997, after Watson, 1997; Shibata, 1999).

- o, △, □ CRN (Müller et al., 1991b)
- ◁, ▽, ▷ JACEE (Cherry et al., 1997a and Asakimori et al., 1991a)
- ▲, ●, ■ RUNJOB-95 (Apanasenko et al., 1997a, b; 1999b)
- ◇, ×, + SOKOL (Ivanenko et al., 1993)

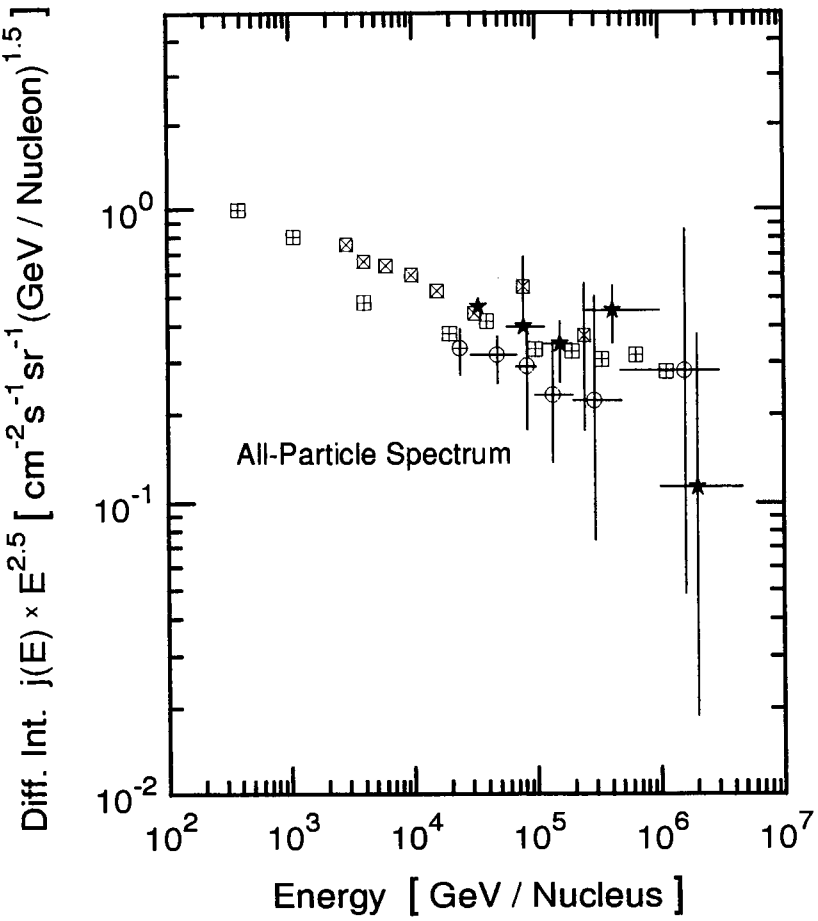

Figure 5.22: Differential all-particle spectrum assembled from data obtained by different direct measurements as listed below. Note that the intensities are multiplied by $E^{2.5}$ and the energy is given per incident nucleus (Shibata, 1997, after Watson, 1997; Shibata, 1999).

- ⊞ Proton (Satellite), Grigorov et al. (1971a)
- ⊠ SOKOL (Satellite), Ivanenko et al. (1993)
- ★ JACEE (Emulsion), Asakimori et al. (1993b)
- ⊕ RUNJOB-95 (Emulsion) Apanasenko et al. (1997a, b, c; 1999b)

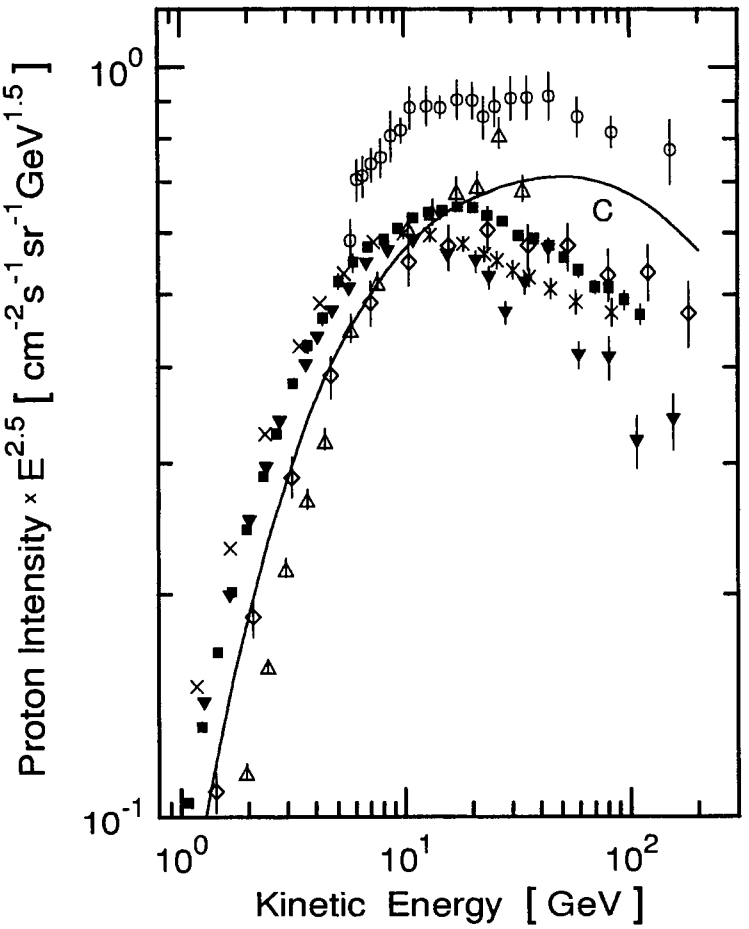

Figure 5.23: Absolute differential proton spectrum determined with the BESS-98 instrument (Sanuki et al., 1999; Nozaki, 2000) and earlier spectra obtained by other authors as specified below. The solid curve, C, is the assumed primary proton spectrum used by Honda et al. (1995) to compute the neutrino flux, discussed in Chapter 4, Section 4.5

- ■ Sanuki et al. (1999), BESS-98
- ▼ Barbiellini et al. (1997), CAPRICE-94
- △ Papini et al. (1993) MASS-89
- ○ Webber et al. (1987)
- × Seo et al. (1991) LEAP
- ◇ Menn et al. (1997) IMAX-92

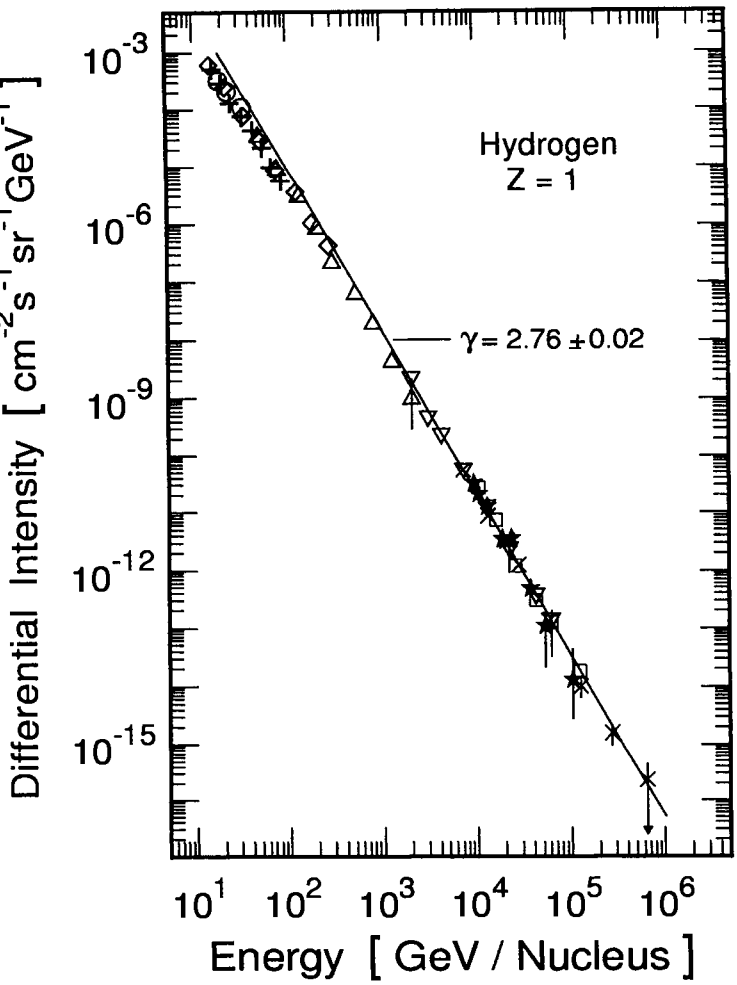

Figure 5.24: Differential energy spectrum of primary hydrogen nuclei (protons) compiled from the data of several experiments as listed below (after Wiebel-Sooth and Biermann, 1998).

- o Ivanenko et al. (1987, 1990, 1993)
- □ Zatsepin et al. (1990, 1993)
- × Asakimori et al. (1991a, b; 1993a, b; 1997a, b), Burnett et al. (1990a, b), Parnell et al. (1989)
- \+ Barbiellini et al. (1997)
- △ Ryan et al. (1972)
- ▽ Papini et al. (1993)
- ◇ Menn et al. (1997)
- ★ Ichimura et al. (1993a, b, c), Kawamura et al. (1989, 1990a, b)

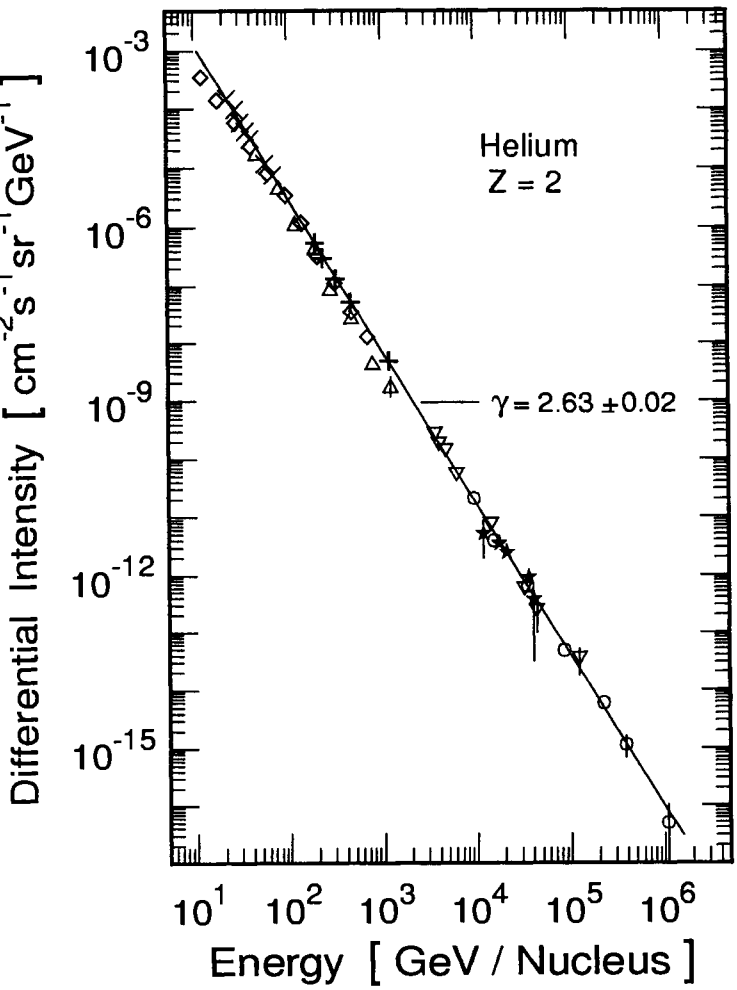

Figure 5.25: Differential energy spectrum of primary helium nuclei compiled from the data of several experiments as listed below (after Wiebel-Sooth and Biermann, 1998).

- ◇ Menn et al. (1997)
- ▽ Ivanenko et al. (1987, 1990, 1993)
- ○ Asakimori et al. (1991a, b; 1993a, b; 1997a, b), Burnett et al. (1990a, b), Parnell et al. (1989)
- × Papini et al. (1993)
- \+ Buckley et al. (1993, 1994)
- △ Ryan et al. (1972)
- ★ Ichimura et al. (1993a, b, c), Kawamura et al. (1989), Kawamura et al. (1990a, b)

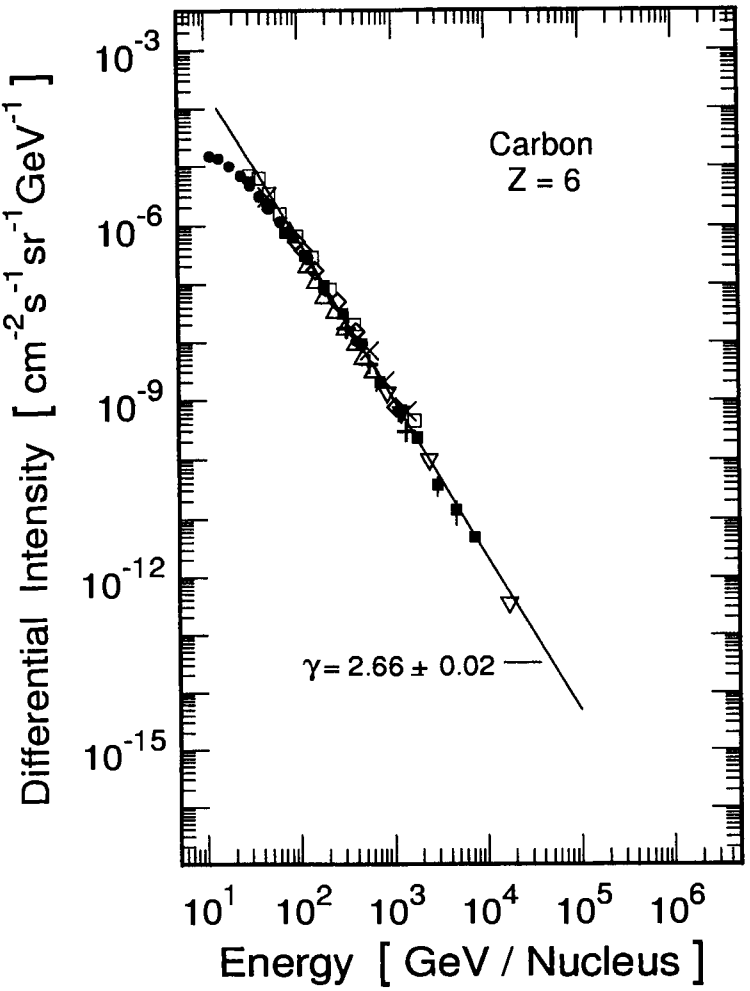

Figure 5.26: Differential energy spectrum of primary carbon nuclei compiled from the data of several experiments as listed below (after Wiebel-Sooth and Biermann, 1998).

•	Engelmann et al. (1985, 1990)	□	Simon et al. (1980)
△	Lezniak & Webber (1978)	×	Buckley et al. (1993, 1994)
▽	Swordy et al. (1990, 1993), Müller et al. (1989, 1991a, b), Grunsfeld et al. (1988)	□	Orth et al. (1978)
		+	Juliusson (1974)
		◇	Caldwell (1977)

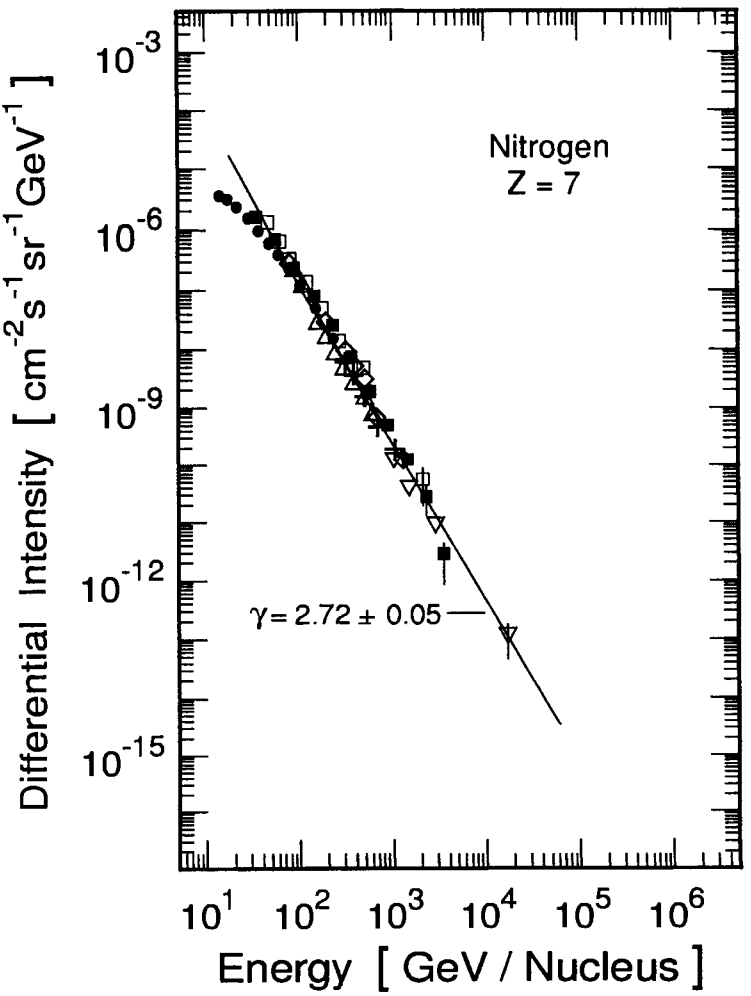

Figure 5.27: Differential energy spectrum of primary nitrogen nuclei compiled from the data of several experiments as listed below (after Wiebel-Sooth and Biermann, 1998).

- • Engelmann et al. (1985, 1990)
- ▽ Swordy et al. (1990, 1993), Müller et al. (1989, 1991a, b), Grunsfeld et al. (1988)
- △ Lezniak & Webber (1978)
- □ Simon et al. (1980)
- □ Orth et al. (1978)
- \+ Juliusson (1974)
- ◇ Caldwell (1977)

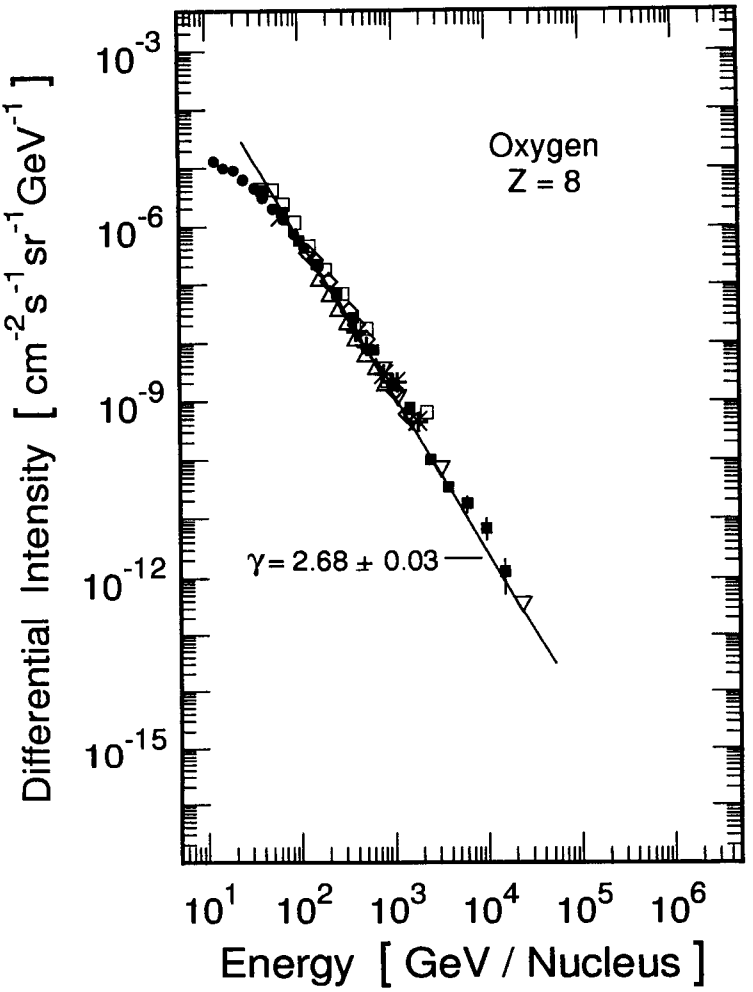

Figure 5.28: Differential energy spectrum of primary oxygen nuclei compiled from the data of several experiments as listed below (after Wiebel-Sooth and Biermann, 1998).

•	Engelmann et al. (1985, 1990)	□	Simon et al. (1980)
△	Lezniak & Webber (1978)	×	Buckley et al. (1993, 1994)
▽	Swordy et al. (1990, 1993), Müller et al. (1989, 1991a, b), Grunsfeld et al. (1988)	□	Orth et al. (1978)
		+	Juliusson (1974)
		◇	Caldwell (1977)

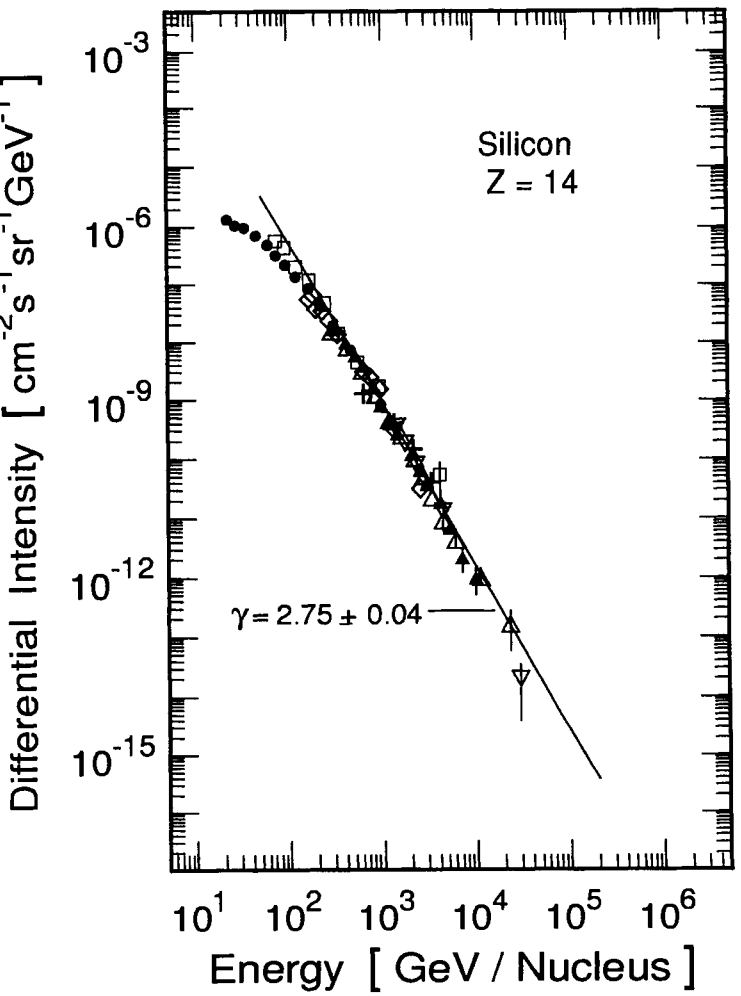

Figure 5.29: Differential energy spectrum of primary silicone nuclei compiled from the data of several experiments as listed below (after Wiebel-Sooth and Biermann, 1998).

- • Engelmann et al. (1985, 1990)
- ▽ Swordy et al. (1990, 1993), Müller et al. (1989, 1991a, b), Grunsfeld et al. (1988)
- △ Kamioka et al. (1997)
- ◇ Caldwell (1977)
- □ Orth et al. (1978)
- \+ Juliusson (1974)
- ★ Ichimura et al. (1993a, b, c) Kawamura et al. (1990a, b)

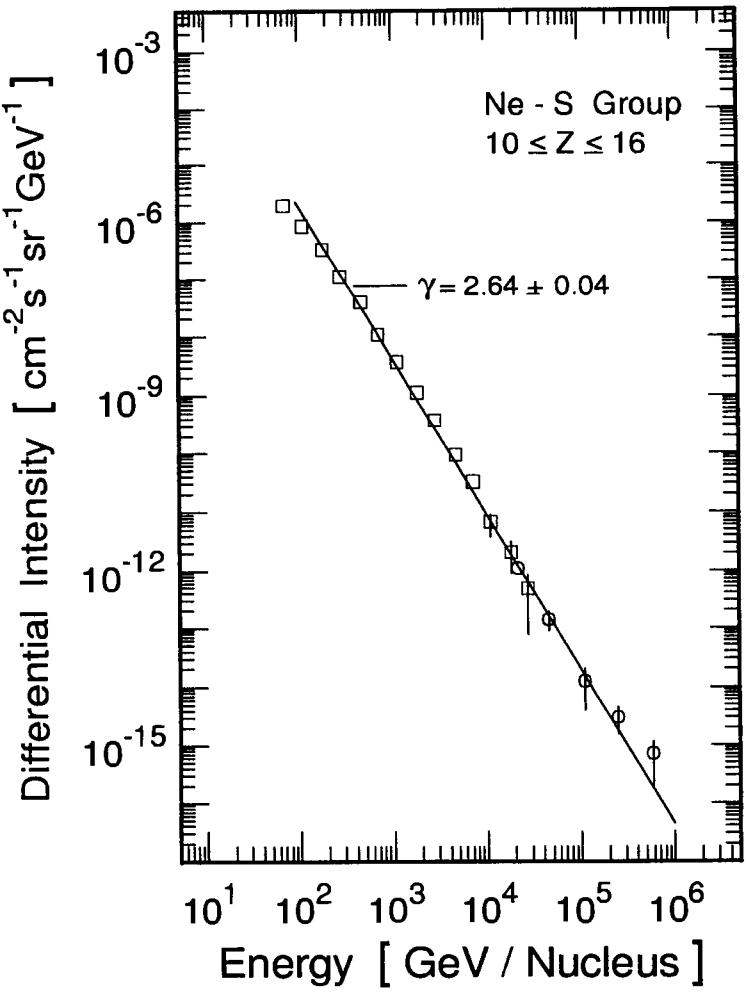

Figure 5.30: Differential energy spectrum of the primary group neon to sulfur compiled from the data of several experiments as listed below (after Wiebel-Sooth and Biermann, 1998).

- o Asakimori et al. (1991a, b; 1993a, b; 1997), Burnett et al. (1990a, b), Parnell et al. (1989)
- □ Simon et al. (1980)

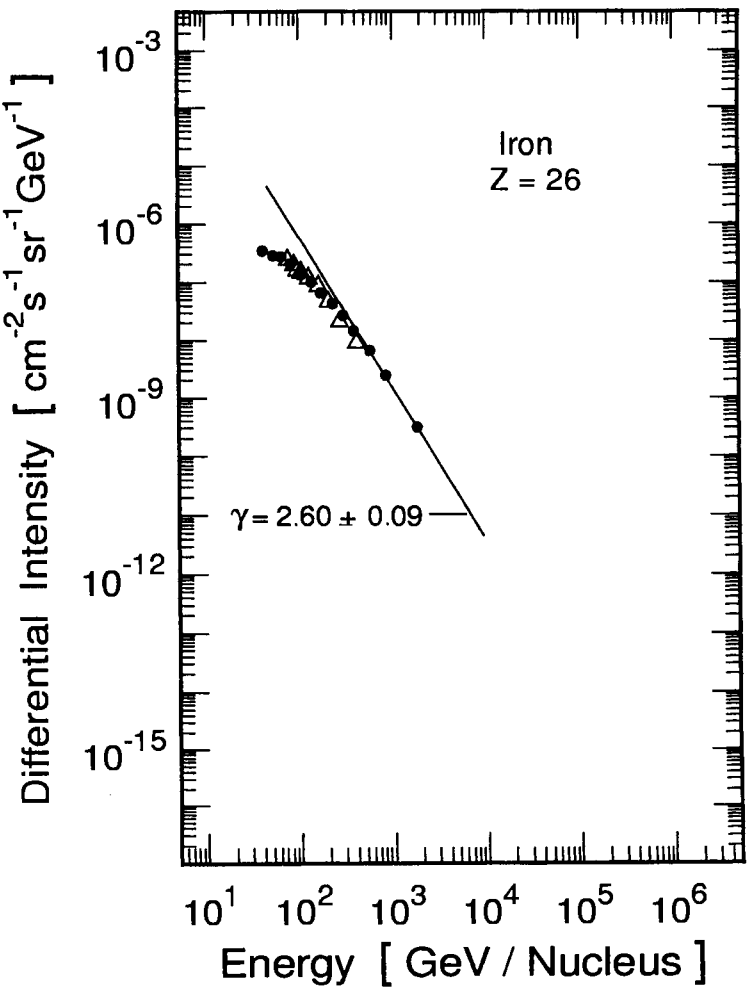

Figure 5.31: Differential energy spectrum of primary iron nuclei compiled from the data of several experiments as listed below (after Wiebel-Sooth and Biermann, 1998).

• Engelmann et al. (1985, 1990) | △ Minagawa (1981)

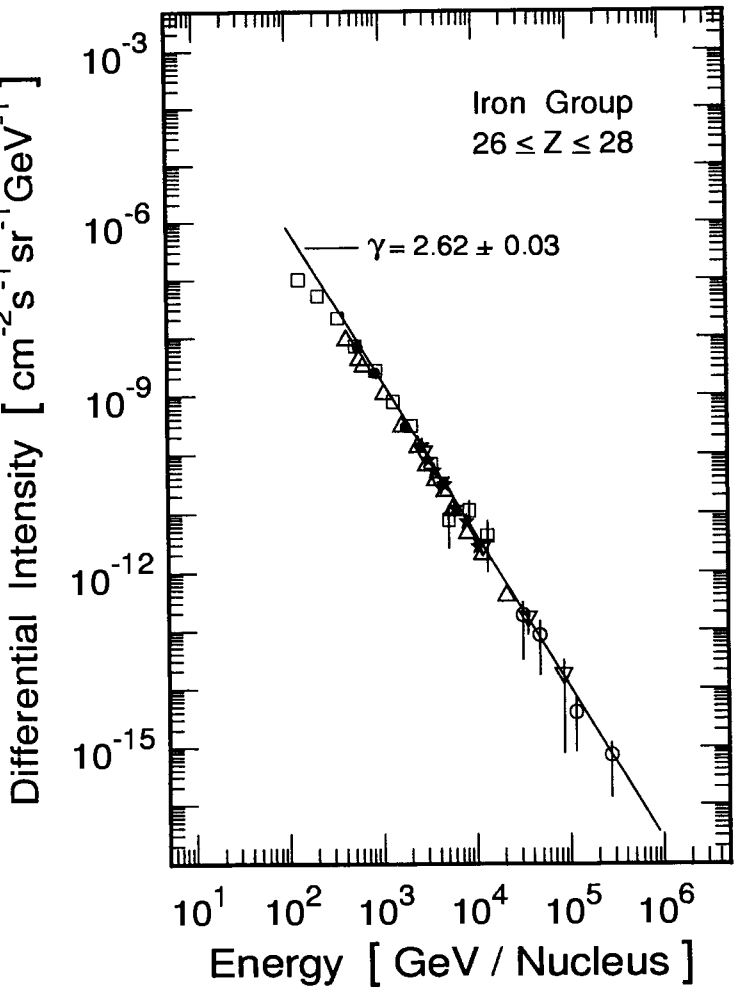

Figure 5.32: Differential energy spectrum of the primary iron group compiled from the data of several experiments as listed below (after Wiebel-Sooth and Biermann, 1998).

- • Engelmann et al. (1985, 1990)
- □ Simon et al. (1980)
- △ Kamioka et al. (1997)
- ○ Asakimori et al. (1991a, b; 1993a, b; 1997a, b), Burnett et al. (1990a, b), Parnell et al. (1989)
- ★ Ichimura et al. (1993a, b, c), Kawamura et al. (1990a, b)
- \+ Buckley et al. (1993, 1994)
- ▽ Swordy et al. (1990, 1993), Müller et al. (1989, 1991a, b), Grunsfeld et al. (1988)

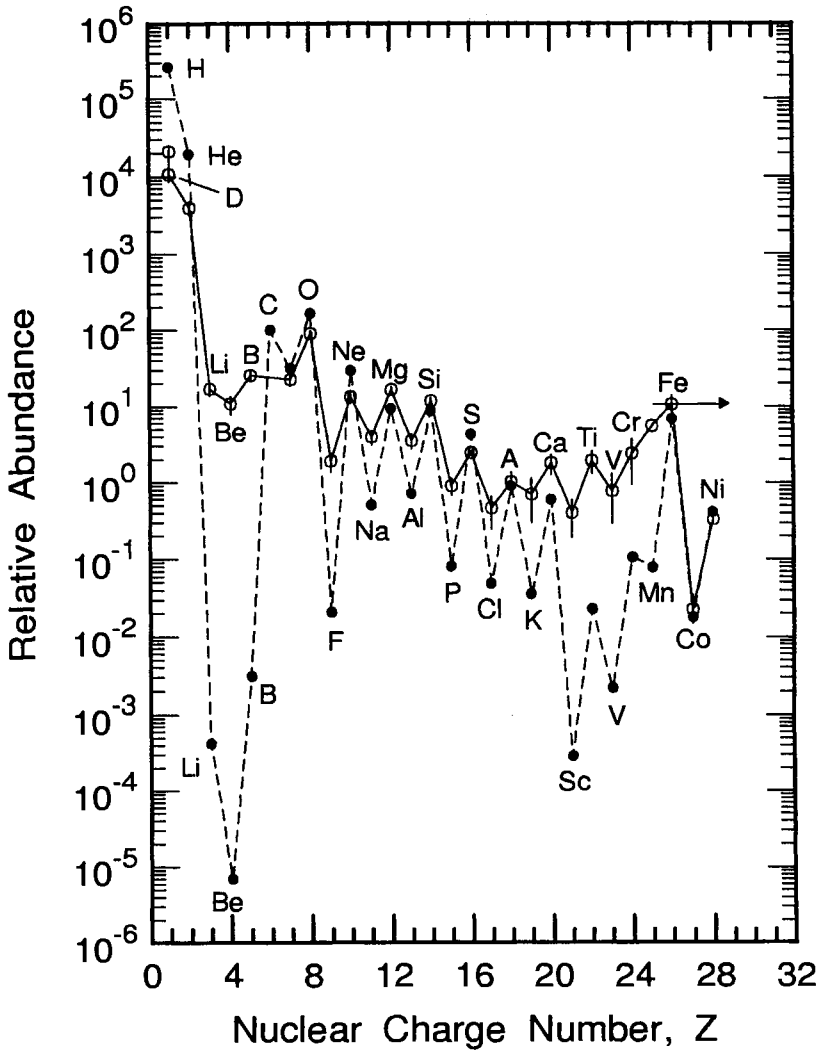

Figure 5.33: Relative elemental composition from hydrogen to nickel in the galactic cosmic radiation at ≥ 1 GeV/nucleon kinetic energy arriving near the top of the Earth's atmosphere (o) compared to the solar system or "universal" abundances according to Cameron (1973, 1981 and 1982) (•) (see also Anders and Grevesse, 1989). The data are normalized to the cosmic ray carbon abundance, set to 100 %, obtained with the satellite IMP-8 (Wefel, 1991; Simpson, 1983 and 1997).

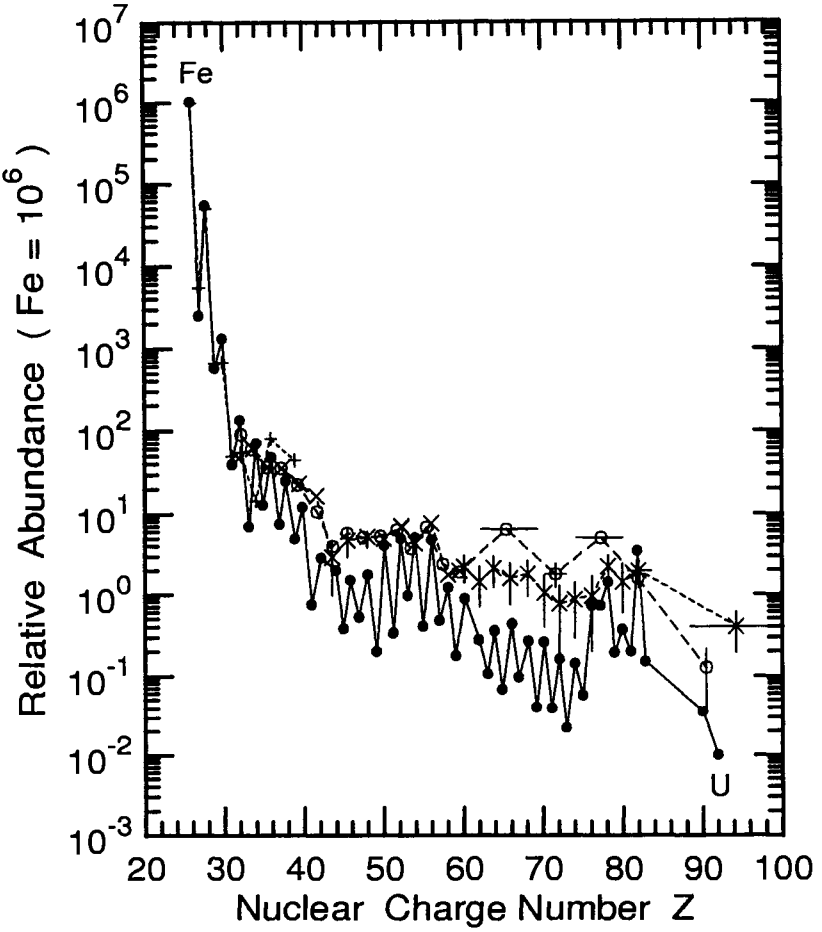

Figure 5.34: Relative elemental composition from iron to fermium in the galactic cosmic radiation at kinetic energies $\geq$1.5 GeV/nucleon arriving near the top of the Earth's atmosphere compared to the solar system or "universal" abundances according to Cameron (1973, 1981 and 1982) (•) (see also Anders and Grevesse, 1989). The data include the following experiments: o, Binns et al. (1985 and 1989); ×, Fowler et al. (1987); +, Byrnak et al. (1983). They are normalized to iron at 10^6 (after Wiebel-Sooth and Biermann, 1998).

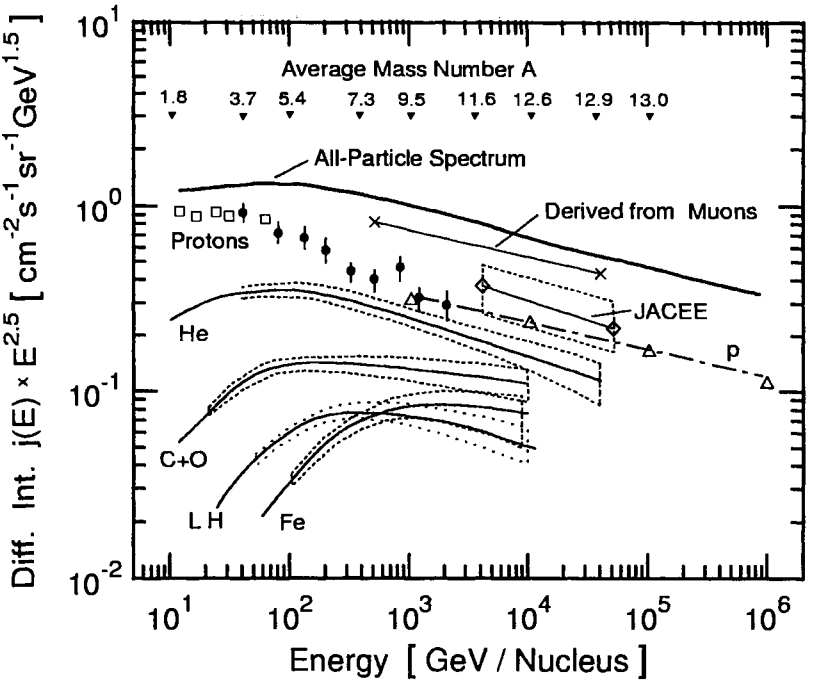

Figure 5.35: Summary spectra of the major components of the primary cosmic radiation (p, He, C+O, LH-group (light-heavy), Fe) resulting from older direct measurements, including emulsion chambers, and the all-particle spectrum made up of the sum of all the constituents. Contributions to the proton-only spectrum from individual experiments are listed below. Also shown is part of the all-particle spectrum obtained from muon measurements (×) at sea level (Klemke et al., 1981). Dotted curves above and below solid spectra indicate error bands. The chain line is the proton spectrum obtained from a summary of Iwai et al. (1979). The numbers across the figure above the spectra indicate the average mass number of the incident nuclei at the particular energy (Webber, 1983). Note that the results of old experiments may deviate significantly from each other in intensity (up to factor of 2 or more) and/or spectral shape for specific elements or elemental groups because of poor statistics.

□ Grigorov et al. (1971a)	• Ryan et al., (1972)
△ Iwai et al., (1979)	◇ Gregory et al. (1981)

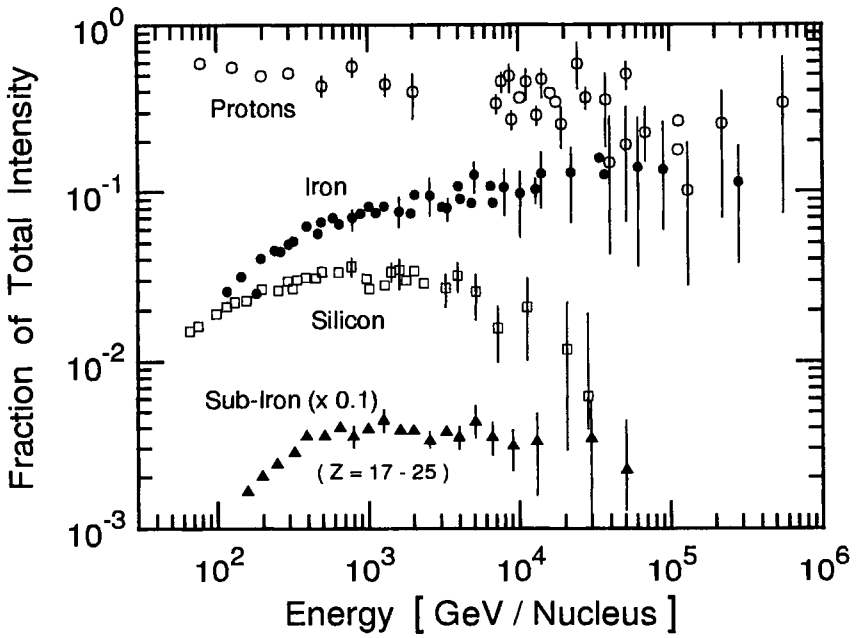

Figure 5.36: Energy dependence of the fraction of typical cosmic ray elemental representatives, p, Fe, Si and the sub-iron group ($17 \leq Z \leq 25$), relative to the total differential intensity. Included are date from different experiments (Ichimura et al., 1993b). The trend towards an increasing presence of the heavier masses in the primary radiation at least up to about 10^5 GeV, where the knee region of the all-particle spectrum is approached is evident, particularly the steady increase of the fraction of iron nuclei. (See also the rapporteur paper of Shibata, 1996.)

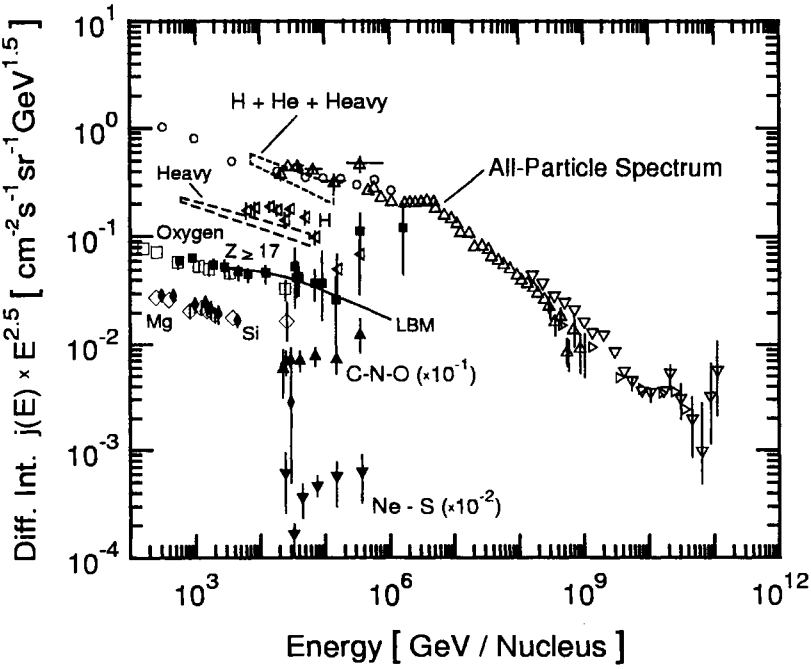

Figure 5.37: All-particle spectrum assembled from data of different experiments, including direct measurements as well as air shower experiments, as indicated below. The region of the all-particle spectrum surrounded by short dashes and labeled *H+He+Heavy* is a compilation from different direct measurements and includes all particles (JACEE, Asakimori et al., 1991a). The lower region that is surrounded by longer dashes and labeled *Heavy* shows the spectrum of heavy particles ($Z \geq 6$), excluding hydrogen and helium. These data are the sum of all the measurements of Swordy et al. (1993) listed in Table 5.5. The curve labeled LBM is the iron spectrum from a calculation using the leaky box model (Swordy et al., 1993). The spectra of individual elements and elemental groups include data from different experiments (CNR: Müller et al., 1991b; HEAO-3: Engelmann et al., 1990; JACEE 1-8: Asakimori et al., 1993a,b; see also Burnett et al., 1990c).

- ○ Proton Satellite (Grigorov et al., 1971a)
- △ Akeno Array (Nagano et al., 1984)
- ▷ Yakutsk Array (Diminstein et al., 1982)
- ▽ Haverah Park Array (Bower et al., 1981)

◁ Hydrogen	▲ C-N-O	□ Oxygen	▼ Ne-S
◇ Magnesium	◆ Silicone	■ Iron Group ($Z \geq 17$)	

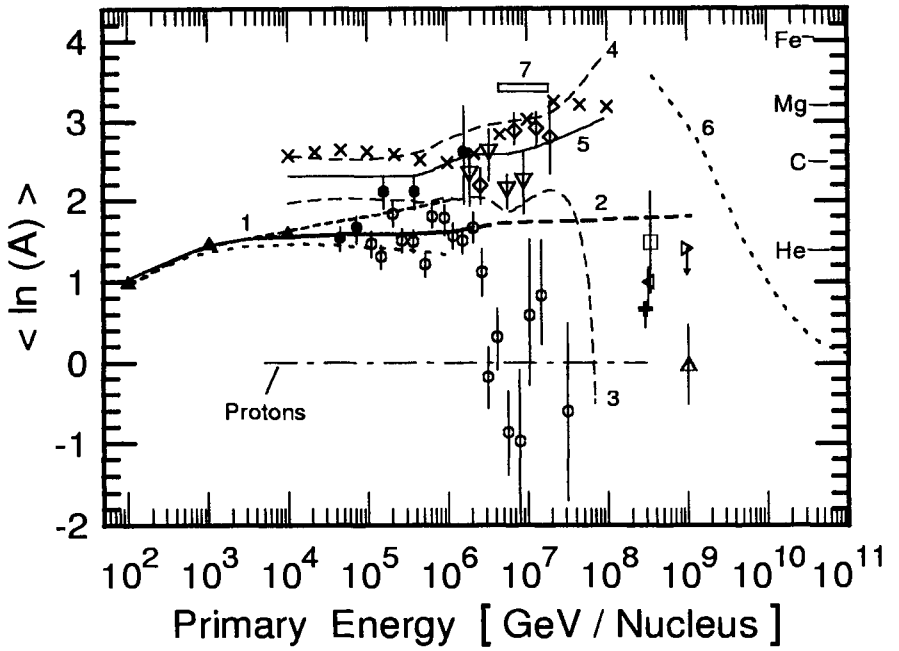

Figure 5.38: Compilation of data on the energy dependence of the average primary mass at very high energies. Shown is the value of ln(A) as a function of particle energy, A being the particle mass number. The solid curve 1 and short-dashed curves above and below it represent direct measurements and upper and lower boundaries, respectively (Ichimura et al., 1993a). Curve 2 is the prediction of the NSU-model (Nikolsky et al., 1984a and 1984b; see also Bugaev et al., 1993). Curves 3, 4 and 5 are results from MACRO using muons, representing upper and lower boundaries and the center value (Palamara, 1995). Curve 6 is the interpretation of Fly's Eye data (Bird et al., 1993b) and region 7 is the result from Adelaide (1989).

- ▲ Linsley (1983) direct measurements
- o Acharya et al. (1983)
- ◇ Shirasaki et al. (1997) BASJE
- □ Doronina et al. (1990)
- \+ Linsley & Fichtel (1985) Volcano Ranch
- △ Linsley and Watson (1981)
- • Asakimori et al. (1995) JACEE
- ▽ Nikolsky et al. (1979)
- × Swordy (1995)
- ◁ Hara (1983)
- ▷ Linsley & Fichtel (1985) various EAS data

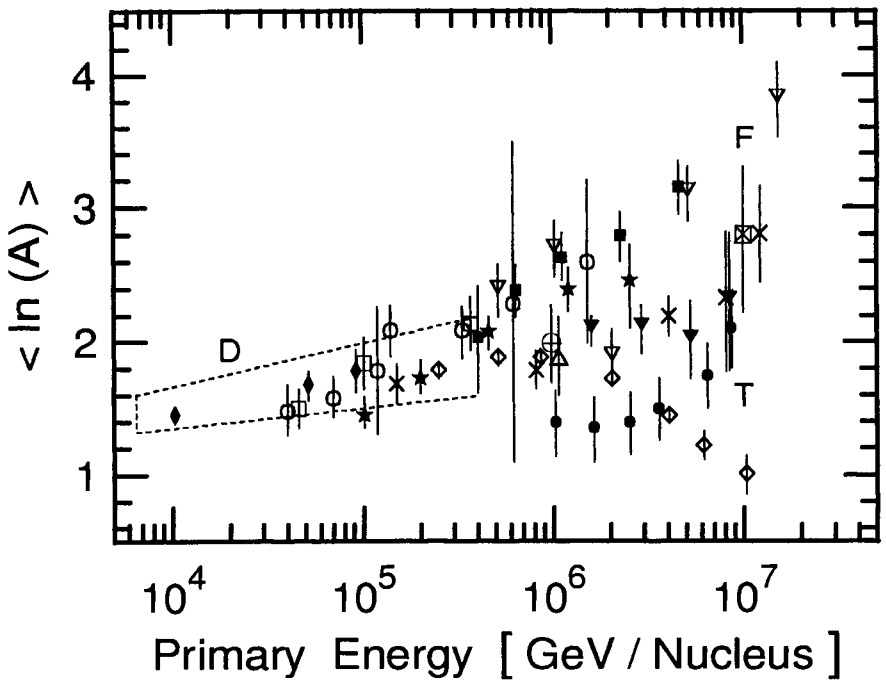

Figure 5.39: Very recent compilation of data on the energy dependence of the average primary mass in the knee region. Shown is the mean logarithmic mass, <ln(A)>, as a function of particle energy, A being the particle mass number. The short-dashed lines identify the region within which the mean masses resulting from direct measurements of individual particles fall (D). Data points □, ○, ⊕ represent results from direct measurements and ♦ is from the compilation of Wiebel-Sooth (1998). The data point ⊠ is the result of a combined air shower, hadron calorimeter and emulsion chamber experiment at Mt. Chacaltaya (Aguirre et al., 2000). Regions F and T identify the results of simulation calculations based on models of heavy and proton dominance (Amenomori et al., 1982 and Tamada, 1994), respectively (after Aguirre et al. 2000). The remaining data points are from air shower experiments (see also the compilation of Hörandel, 1998).

- ■ Engler et al. (1999) KASCADE, Hadrons
- ▼ Engler et al. (1999) KASCADE, Electrons
- • Engler et al. (1999) KASCADE, combined
- ★ Bernlöhr et al. (1998) HEGRA
- ▽ Shirasaki et al. (1997) BASJE
- □ Asakimori et al. (1995) JACEE
- ○ Apanasenko et al. (1999b) RUNJOB
- ♦ Wiebel-Sooth (1998)
- ⊕ Shibata (1999)
- △ Watson (1997)
- ◇ Swordy (1998) DICE
- × Fomin et al. (1998) MSU
- ⊠ Aguirre et at. (2000) BASJE

5.3 Electrons (Positrons and Negatrons)

5.3.1 Introduction

Contrary to common usage where negatively charged electrons, i.e., negatrons, are commonly referred to as electrons and positively charged electrons as positrons, we will strictly distinguish in this section between the two kinds of particles to avoid confusion. We shall use the term electrons only for both kinds of particles, negatrons and positrons, combined.

The importance of measuring the charge ratio of the electron component of the cosmic radiation to determine their source was first pointed out by Ginzburg (1958) and Hayakawa et al. (1958). In addition, cosmic ray electrons are also a unique probe to study conditions existing in different regions of space.

Until 1960 all attempts to find electrons in the primary cosmic radiation had failed (Critchfield et al., 1952). The first evidence for their existence was delivered by Earl (1961) and Meyer and Vogt (1961) in two separate balloon-borne experiments during 1960. The former used a cloud chamber launched from Minneapolis, Minnesota (USA), that was flown at 4.5 g/cm^2 of residual atmosphere whereas the latter have used a scintillation counter telescope launched from Fort Churchill, Manitoba (CND), flying at comparable altitudes (3 to 5 g/cm^2 of overburden).

Pioneering experimental work with a magnetic spectrometer that permitted charge separation was carried out by the Chicago group. The first experimental determination of the ratio of positrons to electrons was made by De Shong et al. (1964). Subsequently major efforts ware made by other researchers to extend the measurements to determine the spectra of positrons and negatrons and their ratio over a wider energy range using basically the same technique (Hartman et al., 1965; L'Heureux and Meyer, 1965 and 1968; Bland et al., 1966; Daniel and Stephens, 1966; Hartman, 1967; L'Heureux et al., 1968; Beuermann et al., 1969 and 1970; Fanselow et al., 1969; Kniffen et al., 1970; L'Heureux et al., 1972).

Parallel to this work measurements to study the flux of electrons in the cosmic radiation without charge sign resolution were carried out with nuclear emulsion (emulsion chambers, EC) (Freier and Waddington, 1965; Waddington and Freier, 1965; Daniel and Stephens, 1965a and 1965b; Anand et al, 1968, 1970a and 1973; Matsuo et al., 1975; Aizu et al., 1977; Taira et al., 1979; Nishimura et al., 1970, 1980 and 1981), with spark chamber and scintillator combinations (Agrinier et al., 1964 and 1965), and with more sophisticated

electronic detector systems such as total absorption spectrometers, calorimeters and transition radiation detectors (L'Heureux, 1967; Scheepmaker and Tanaka, 1971; Zatsepin, 1971; Ishii et al., 1973; Müller and Meyer, 1973; Meegan and Earl, 1975; Hartmann et al., 1977; Prince, 1979; Tang, 1984), and with hybrid detector systems using a combination of emulsion and electronic detection (Freier et al., 1977). For reviewing the early work the reader is referred to Daniel and Stephens (1970 and 1975).

Müller and Tang (1985 and 1987) have used their combination transition radiation and shower detector telescope in conjunction with the east-west asymmetry at a specific geomagnetic cutoff rigidity (Hawaii) to achieve charge separation in order to determine the ratio of positrons to electrons, $(e^+/(e^+ + e^-))$. Earlier attempts using this technique were made by Daniel and Stephens (1965a, 1965b, 1967 and 1970) who pioneered this method of separating electrons and positrons, and by Bland et al. (1966) and Agrinier et al. (1969), however, without much success due to poor statistics and systematic uncertainties.

More recent experiments using spectrometers with superconducting magnets were carried out by Buffington et al. (1975), Barbiellini et al. (1996) (CAPRICE-94), Barwick et al. (1995 and 1997) (HEAT-94 and HEAT-95), Basini et al. (1995) (MASS2/MASS-91), Golden et al. (1987, 1994) (MASS/MASS-89) and Golden et al. (1996) (MASS/TS93). Lately a new calorimetric device using scintillating fibers had been developed and used by Torii et al. (1995 and 1997) (BETS). The names in parenthesis are acronyms of some of these experiments (see Appendix D.1). But also work with emulsion stacks is being continued (Nishimura et al., 1997). In the following we summarize some of the data acquired by these and earlier experiments.

5.3.2 Energy Spectra

An early compilation of the results of measurements of the spectrum of the electron component in the cosmic radiation on top of the atmosphere using different experimental techniques and covering a wide range of energies is shown in Fig. 5.40 (Fanselow et al., 1969). Included are the data from the balloon-borne experiments of Anand et al. (1968 and 1970a), Beuermann et al. (1969 and 1970), Bleeker et al. (1968 and 1970), Fanselow et al. (1969), L'Heureux and Meyer (1968), and Webber (1968). Also shown are two sets of low energy data from measurements carried out in 1967 and 1968 on board the satellites IMP-IV (McDonald and Simnett 1968) and OGO-5 (Fan et al., 1969), respectively. The straight portion of curve C drawn in Fig. 5.40 can be well represented by a single power law of the form

$$\frac{dJ(E)}{dE} = 1.26 \cdot 10^{-2} E^{-(2.62 \pm 0.05}\ [\mathrm{cm^{-2}\,s^{-1}\,sr^{-1}\,GeV^{-1}}]\ . \qquad (5.4)$$

However, at higher energies the spectrum begins to drop more rapidly and exhibits a spectral index of approximately -3.6 (see also Fig. 5.43). The curved portion of C (Fig. 5.40) which covers the energy range below 5 GeV was derived from the observed non-thermal galactic radio emission of interstellar electrons between 10 MHz and 400 MHz (Anand et al., 1970a; see also Cummings et al., 1973).

The extensive measurements of Fanselow et al. (1969) were made with a magnetic spectrometer in combination with a counter telescope and spark chambers (Hartman, 1967). The balloon carrying the instrument was flown in 1965 and for longer periods (45 hours) in June 1966 from Fort Churchill, Manitoba (CND) during a period of minimum solar activity. The data were acquired at an altitude equivalent to 3.2 g/cm^2 of residual atmosphere. The measurements covered the energy range from 170 MeV to 14.3 GeV. A finite flux of positrons was observed up to 4 GeV.

The results of the work of Fanselow et al. are summarized in Table 5.17 where the intensities measured in 1965 and 1966 are listed separately as well as the weighted average of both years. They are also illustrated in Fig. 5.41, showing the positron and electron spectra separately (Fanselow et al., 1969). Both spectra can be represented by single power laws for energies $\geq$860 MeV over the explored energy range.

In a subsequent experiment Buffington et al. (1975) have measured the differential and integral intensities of cosmic ray positrons and negatrons separately. The results are listed in Tables 5.18 and 5.19. The combined all-electron differential intensities of this work are included in the compilation shown in Fig. 5.42 which summarizes the data from fourteen other experiments, as listed in the caption of this figure.

Another early compilation of electron spectra is shown in Fig. 5.43. Included are data from the work of Anand et al. (1973), Ishii et al. (1973), Müller and Meyer (1973), Meegan and Earl (1975), Silverberg (1976), Freier et al. (1977), Hartmann et al. (1977) and Nishimura et al. (1980). Some of these experiments employed nuclear emulsion as detectors, others counters. Also indicated is the spectrum of background atmospheric secondary electrons at a residual atmosphere of 4 g/cm^2 and a single power law fit to the emulsion data of Freier et al. (1977). The differential spectrum of Anand et al. (1973) that was obtained with hypersensitized nuclear emulsion is given in Table 5.20.

Table 5.17: Positron and Electron Intensities on Top of Atmosphere (ToA). (Fanselow et al., 1969)

Energy Interval at ToA [GeV]	0.053 - 0.088 [1]	0.088 - 0.173 [1]	0.173 - 0.44	0.44 - 0.86	0.86 - 1.70	1.70 - 4.2	4.2 - 8.4	8.4 - 14.3
Energy Interval at Magnet [GeV]	0.042 - 0.076	0.076 - 0.161	0.161 - 0.43	0.43 - 0.84	0.84 - 1.69	1.69 - 4.2	4.2 - 8.4	8.4 - 14.3
Energy for diff. Intensity Pt. [GeV]	0.069	0.125	0.28	0.63	1.23	2.7	6.0	11.0
1965								
Total No. of $(e^+ + e^-)$	26	130	131	98	100	71	2.1	7
Positron Intensity $[(m^2\ s\ sr\ GeV)^{-1}]$	150± 121%	143± 40%	33± 45%	2.6± 215%	1.4± 96%	0.27± 122%	0.0± 0.23 [2]	0.10± 190%
Electron Intensity $[(m^2\ s\ sr\ GeV)^{-1}]$	416± 59%	367± 22%	71± 28%	44± 23%	31± 15%	7.9± 17%	1.6± 37%	0.36± 101%
Positive Fraction	0.36± 0.31	0.39± 0.11	0.45± 0.14	0.06± 0.12	0.047± 0.043	0.035± 0.041	0.00± 0.13	0.26± 0.43
1966								
Total No. of $(e^+ + e^-)$	82	354	454	343	325	256	64	34
Positron Intensity $[(m^2\ s\ sr\ GeV)^{-1}]$	118± 109%	107± 37%	12± 80%	5.5± 75%	2.6± 32%	0.40± 44%	0.016± 339%	0.077± 171%
Electron Intensity $[(m^2\ s\ sr\ GeV)^{-1}]$	410± 41%	212± 24%	67± 22%	44± 16%	26.4± 11%	8.2± 10%	1.0± 27%	0.61± 46%
Positive Fraction	0.29± 0.24	0.51± 0.11	0.18± 0.12	0.12± 0.08	0.098± 0.028	0.049± 0.020	0.015± 0.050	0.12± 0.19
Weighted Average for 1965 and 1966								
Positron Intensity $[(m^2\ s\ sr\ GeV)^{-1}]$	128± 82%	119± 28%	18.5± 44%	4.5± 74%	2.3± 31%	0.37± 42%	0.015± 349%	0.084± 128%
Electron Intensity $[(m^2\ s\ sr\ GeV)^{-1}]$	412± 34%	255± 17%	68± 17%	44± 13%	27.5± 9%	8.1± 9%	1.1± 22%	0.51± 43%
Positive Fraction	0.31± 0.19	0.45± 0.08	0.29± 0.09	0.10± 0.07	0.083± 0.024	0.046± 0.018	0.013± 0.05	0.15± 0.18

1) Likely to include reentrant albedo electrons (positrons and negatrons).
2) Actual error.

Table 5.18: Differential Intensities of Negatrons, Positrons and Electrons Outside Atmosphere (Buffington et al., 1975).

E_{min} [GeV]	E_{max} [GeV]	$\overline{E}$ [GeV]	Diff. Intensity $[cm^{-2}\,s^{-1}\,sr^{-1}\,GeV^{-1}]$
		e^-	
4	7	5.1	$(1.02\pm0.07\cdot10^{-4}$
7	9.4	8.0	$(2.5$ - $3.0)\cdot10^{-5}$
9.4	14	11.2	$(8.5\pm1.1)\cdot10^{-6}$
14	28	18.8	$(1.7\pm0.3)\cdot10^{-6}$
28	inf	63	$(1.1\pm0.2)\cdot10^{-7}$
		e^+	
4	7	5.1	$(7\pm2)\cdot10^{-6}$
7	9.4	8.0	$(2\pm1)\cdot10^{-6}$
9.4	14	11.2	$(4\pm4)\cdot10^{-7}$
14	28	18.8	$(5\pm3)\cdot10^{-7}$
28	00	63	$(2\pm2)\cdot10^{-8}$
		$(e^+ + e^-)$	
4	7	5.1	$(1.09\pm0.08\cdot10^{-4}$
7	9.4	8.0	$(2.7\pm0.3)\cdot10^{-5}$
9.4	14	11.2	$(8.6\pm1.3)\cdot10^{-6}$
14	18	18.8	$(2.2\pm0.6)\cdot10^{-6}$
28	inf	63	$(1.3\pm0.4)\cdot10^{-7}$

Figure 5.44 shows theoretical positron spectra that are based on different cosmic ray propagation models as listed in the caption (Stephens, 1981; Stephens, 1985; Stephens and Golden, 1987). Some data points from early measurements (Fanselow et al., 1969; Buffington et al., 1975; Hartman and Pellerin, 1976), and the more recent data of Golden et al. (1987) have been added to the figure for comparison.

Absolute differential and integral intensities of negatrons at the top of the atmosphere were measured by Golden et al. (1984) and are listed in Table 5.21. Results of positron measurements of Golden et al., (1987) are given in Table 5.22. These data together with data of Tang (1984), Garcia-Munoz et al., (1986), and the recent measurements of Evenson et al. (1991), Golden et al. (1994) and Barbiellini et al. (1997) which all have charge separation

Table 5.19: Integral Intensity of e^+ and $(e^+ + e^-)$ Above Atmosphere. (Buffington et al., 1975)

Energy[1] [GeV]	Number[2] e^+	Intensity $[cm^{-2}s^{-1}sr^{-1}GeV^{-1}]$	
		e^+	$(e^+ + e^-)$
4[3]	28± 7	$(3.7\pm0.9)\cdot10^{-5}$	$(4.82\pm0.35)\cdot10^{-4}$
7.0	9.5± 3.5	$(1.6\pm0.6)\cdot10^{-5}$	$(1.55\pm0.15)\cdot10^{-4}$
9.4	6.3± 2.5	$(1.1\pm0.5)\cdot10^{-5}$	$(9.0\pm0.9)\cdot10^{-5}$
14.0	5± 2.2	$(1.0\pm0.5)\cdot10^{-5}$	$(5.0\pm0.09)\cdot10^{-5}$
28.0	1± 1	$(2.5\pm0.25)\cdot10^{-6}$	$(1.9\pm0.05)\cdot10^{-5}$

[1] Equivalent energy above atmosphere. [2] Net incident number of positrons after deduction of atmospheric secondaries. [3] Geomagnetic cutoff.

capability are presented in Fig. 5.45. The results of the measurements of Barbiellini et al. (1997) using the instrument CAPRICE-94 are also given numerically in Table 5.23 (see also Barbiellini et al., 1996).

In addition we give in Table 5.24 the intensities at the top of the atmosphere from a later analysis of the CAPRICE-94 experiment (Boezio et al., 2000), those of HEAT-94 in Table 5.25 (Barwick et al., 1998) and the data of Kobayashi et al. (1999) from the emulsion chamber experiment in Table 5.26. In the first two tables negatron and positron intensities are given separately and in Table 5.25 also the sum of both. Barwick et al. (1998) specify a power law fit to their spectra, given in eq. 5.5.

$$j(E) = j_0 E^{-\alpha} \quad [m^{-2}s^{-1}sr^{-1}GeV^{-1}] \tag{5.5}$$

The following values apply for α and j_0 for negatrons and positrons separately and for E in GeV.

Particles	α	j_0
Negatrons	3.086 ± 0.081	227 ± 45
Positrons	3.31 ± 0.23	24 ± 12

To conclude the spectral aspects of cosmic ray electrons we present in Figs. 5.46 and 5.47 a compilation of a large number of experimental spectra in another representation, frequently used, that emphasizes the differences

Table 5.20: Differential Intensity of Primary Electrons $(e^+ + e^-)$. (Anand et al., 1973)

Energy [GeV]	Number of $(e^+ + e^-)$	Differential Intensity $[\mathrm{cm}^{-2}\,\mathrm{s}^{-1}\,\mathrm{sr}^{-1}\mathrm{GeV}^{-1}]$
12 - 15.5	10	$(1.48 \pm 0.5) \cdot 10^{-5}$
15.5 - 21	12	$(4.45 \pm 1.5) \cdot 10^{-6}$
21 - 30	7	$(7.87 \pm 3.1) \cdot 10^{-7}$
30 - 40	7	$(4.10 \pm 1.9) \cdot 10^{-7}$
40 - 50	19	$(4.24 \pm 1.13) \cdot 10^{-7}$
50 - 70	23	$(2.08 \pm 0.48) \cdot 10^{-7}$
70 - 90	17	$(1.15 \pm 0.32) \cdot 10^{-7}$
90 - 110	17	$(6.30 \pm 2.1) \cdot 10^{-8}$
110 - 130	15	$(3.65 \pm 1.12) \cdot 10^{-8}$
130 - 150	10	$(1.61 \pm 0.7) \cdot 10^{-8}$
150 - 175	8	$(9.14 \pm 4.4) \cdot 10^{-9}$
175 - 210	9	$(8.03 \pm 3.2) \cdot 10^{-9}$
210 - 240	7	$(6.38 \pm 2.75) \cdot 10^{-9}$
240 - 290	6	$(2.88 \pm 1.1) \cdot 10^{-9}$
290 - 350	5	$(2.01 \pm 0.97) \cdot 10^{-9}$
350 - 500	3	$(4.25 \pm 3.7) \cdot 10^{-10}$
500 - 750	2	$(1.645 \pm 1.62) \cdot 10^{-10}$

between the various experimental results. There we have multiplied the electron intensity of each data point by the energy to the third power (E^3) and plotted as a function of energy. Fig. 5.46 is a compilation of data covering a period of almost 30 years and Fig. 5.47 shows the results of the most recent experiments. Also included are the results of the new BETS instrument mentioned before (Torii et al., 1997), the emulsion chamber data of Kobayashi et al. (1999) and the spectral distribution of interstellar electrons derived from non-thermal galactic radio emission by Webber (1980).

5.3.3 Positron Fraction

The energy dependence of the positron fraction, $e^+/(e^+ + e^-)$, resulting from the work of Fanselow et al. (1969 and 1971) also listed in Table 5.17 is plotted in Fig. 5.48 together with the results of Agrinier et al. (1970), Buffington et al. (1975), Beuermann et al. (1969), Daugherty et al. (1975) and Müller

Table 5.21: Absolute Negatron Intensities (Golden et al., 1984).

Rigidity[1] [GV/c]	Number e^-	$\overline{E}_p$ [2] [GeV]	ΔE_p [3] [GeV]	Intensity j_P [1] $[(cm^2\,s\,sr\,GeV)^{-1}]$	$\overline{E}_G$ [4] [GeV]	Intensity j_G [5] $[(cm^2\,s\,sr\,GeV)^{-1}]$
3.33 - 3.57	65±9	3.45	0.24	$(4.2\pm0.6)\cdot10^{-5}$	4.68	$(3.50\pm1.56)\cdot10^{-4}$
3.57 - 3.85	61±8	3.70	0.27	$(3.7\pm0.5)\cdot10^{-5}$	5.01	$(2.17\pm0.58)\cdot10^{-4}$
3.85 - 4.17	93±10	4.00	0.32	$(4.7\pm0.5)\cdot10^{-5}$	5.39	$(1.77\pm0.28)\cdot10^{-4}$
4.17 - 4.56	128±12	4.35	0.38	$(5.4\pm0.5)\cdot10^{-5}$	5.83	$(1.33\pm0.16)\cdot10^{-4}$
4.56 - 5.00	183±14	4.76	0.45	$(6.6\pm0.5)\cdot10^{-5}$	6.35	$(1.00\pm0.10)\cdot10^{-4}$
5.00 - 5.56	235±16	5.26	0.55	$(6.9\pm0.5)\cdot10^{-5}$	6.99	$(7.6\pm0.7)\cdot10^{-5}$
5.56 - 6.25	284±17	5.88	0.69	$(6.7\pm0.4)\cdot10^{-5}$	7.78	$(6.2\pm0.5)\cdot10^{-5}$
6.25 - 7.14	254±16	6.66	0.89	$(4.6\pm0.3)\cdot10^{-5}$	8.77	$(3.6\pm0.3)\cdot10^{-5}$
7.14 - 8.33	234±16	7.69	1.18	$(3.3\pm0.2)\cdot10^{-5}$	10.08	$(2.5\pm0.2)\cdot10^{-5}$
8.33 - 10.00	227±15	9.09	1.65	$(2.3\pm0.2)\cdot10^{-5}$	11.85	$(1.7\pm0.1)\cdot10^{-5}$
10.00 - 12.50	168±14	11.10	2.46	$(1.1\pm0.1)\cdot10^{-5}$	14.42	$(8.2\pm0.8)\cdot10^{-6}$
12.50 - 16.67	120±13	14.27	4.07	$(5.1\pm0.6)\cdot10^{-6}$	18.45	$(3.5\pm0.4)\cdot10^{-6}$
16.67 - 25.00	74±10	19.95	7.94	$(1.6\pm0.2)\cdot10^{-6}$	25.69	$(0.11\pm0.2)\cdot10^{-6}$
25.00 - 50.00	49±10	33.08	21.79	$(4.1\pm0.8)\cdot10^{-5}$	42.47	$(2.6\pm0.5)\cdot10^{-5}$
50.00 - ∞	41±24	91.67	159.10	$(4.9\pm2.9)\cdot10^{-5}$	119.40	$(1.4\pm0.8)\cdot10^{-5}$

[1] At payload. [2] Effective mean energy at payload. [3] Effective energy interval at payload. [4] Effective mean energy in galaxy. [5] In galaxy.

Table 5.22: Positron Intensities on Top of the Atmosphere (Golden et al., 1987)

Rigidity [GV/ c]	Number e^+	$\overline{E}$ [GeV]	ΔE [GeV]	Intensity $[(cm^2\,s\,sr\,GeV)^{-1}]$
3.57 - 4.17	25.8±5.3	4.90	0.76	$(1.2\pm0.6)\cdot10^{-5}$
4.17 - 5.00	47.5±7.4	5.79	1.06	$(1.0\pm0.3)\cdot10^{-5}$
5.00 - 6.25	39.4±7.7	7.09	1.59	$(4.1\pm1.1)\cdot10^{-6}$
6.26 - 8.33	39.9±7.7	9.14	2.65	$(2.3\pm0.6)\cdot10^{-6}$
8.33 - 12.5	14.3±8.1	12.9	5.30	$(3.3\pm2.9)\cdot10^{-7}$
12.5 - 25.0	28.7±9.6	22.0	15.9	$(3.0\pm1.1)\cdot10^{-7}$
25.0 - 50.0	0.5±11.5	44.1	31.8	$(0.0\pm1.4)\cdot10^{-7}$

and Tang (1985). Shown, too, in this figure are predictions from calculations of Protheroe (1982) using different models, and of Cummings et al. (1973) based on work of Ramaty and Lingenfelter (1968). In Fig. 5.49 we have plotted another set of curves showing the energy dependence of the positron to electron ratio resulting from a variety of different cosmic ray propagation models and some experimental points for comparison.

A compilation of a large number of measured positron to electron ratios resulting from many different experiments, including recent work, is pre-

Table 5.23: Negatron and Positron Data Summary of CAPRICE-94. (Barbiellini et al., 1997)

Energy Bin at Spectrometer	Observed Number of Particles		Median Energy at ToA[1]	Intensity at ToA[1] $[(\mathrm{cm}^2\,\mathrm{s\,sr\,GeV})^{-1}]$		Positron Ratio at ToA[1]
	e^-	e^+		e^-	e^+	$e^+/(e^+ + e^-)$
[GeV]			[GeV]			
0.25 - 0.4	199	148	0.485	$(1.01\pm0.16)\cdot10^{-3}$	$(1.7\pm1.3)\cdot10^{-4}$	0.143±0.099
0.4 - 0.6	419	164	0.73	$(1.37\pm0.11)\cdot10^{-3}$	$(2.2\pm0.6)\cdot10^{-4}$	0.138±0.036
0.6 - 0.8	413	128	1.01	$(1.33\pm0.085)\cdot10^{-3}$	$(2.4\pm0.4)\cdot10^{-4}$	0.152±0.023
0.8 - 1.05	388	101	1.33	$(9.72\pm0.57)\cdot10^{-4}$	$(1.7\pm0.26)\cdot10^{-4}$	0.151±0.021
1.05 - 1.5	539	99	1.82	$(7.33\pm0.36)\cdot10^{-4}$	$(9.7\pm1.3)\cdot10^{-5}$	0.117±0.015
1.5 - 2.0	427	60	2.475	$(5.06\pm0.28)\cdot10^{-4}$	$(5.6\pm0.9)\cdot10^{-5}$	0.099±0.015
2.0 - 3.0	420	44	3.49	$(2.21\pm0.12)\cdot10^{-4}$	$(1.8\pm0.3)\cdot10^{-5}$	0.076±0.013
3.0 - 5.0	279	31(5.6)[2]	5.33	$(7.9\pm0.5)\cdot10^{-5}$	$(6.0\pm2.0)\cdot10^{-6}$	0.071±0.018
5.0 - 10.0	159	28(10.4)[2]	9.43	$(1.14\pm0.09)\cdot10^{-5}$	$(9.0\pm4.0)\cdot10^{-7}$	0.074±0.028

[1] Top of Atmosphere.
[2] The numbers in parentheses are the estimated proton background

sented in Fig. 5.50. Indicated, too, are expected ratios of a leaky box model calculation of Protheroe (1982) and the result of a calculation by Clem et al. (1996) showing upper and lower limits. To resolve the cluster of data around

Table 5.24: Negatron and Positron Intensities as a Function of Energy at Top of Atmosphere (CAPRICE-94) (Boezio et al., 2000).

Energy Range [GeV]	Mean Energy [GeV]	Intensity*) $[m^{-2}s^{-1}sr^{-1}GeV^{-1}]$ e^-	e^+
0.46 - 0.61	0.54	$(1.3 \pm 0.2) \cdot 10^1$	3.9 ± 1.7
0.61 - 0.75	0.68	$(1.6 \pm 0.2) \cdot 10^1$	3.2 ± 1.1
0.75 - 0.90	0.83	$(1.5 \pm 0.1) \cdot 10^1$	2.7 ± 0.8
0.90 - 1.05	0.97	$(1.4 \pm 0.1) \cdot 10^1$	3.4 ± 0.7
1.05 - 1.19	1.12	$(1.3 \pm 0.1) \cdot 10^1$	2.5 ± 0.5
1.19 - 1.34	1.26	9.3 ± 0.9	2.1 ± 0.5
1.34 - 1.48	1.41	10.0 ± 0.9	1.1 ± 0.3
1.48 - 1.84	1.66	8.4 ± 0.6	1.4 ± 0.2
1.84 - 2.21	2.02	7.4 ± 0.5	$(6.8 \pm 1.5) \cdot 10^{-1}$
2.21 - 2.57	2.39	6.3 ± 0.5	$(7.6 \pm 1.5) \cdot 10^{-1}$
2.57 - 2.93	2.75	4.9 ± 0.4	$(3.9^{+1.3}_{-1.0} \cdot 10^{-1}$
2.93 - 3.30	3.11	3.3 ± 0.3	$(2.1^{+1.0}_{-0.7} \cdot 10^{-1}$
3.30 - 3.66	3.48	2.1 ± 0.2	$(2,0^{+0.9}_{-0.7} \cdot 10^{-1}$
3.66 - 4.39	4.01	2.0 ± 0.2	$(2.1^{+0.6}_{-0.5} \cdot 10^{-1}$
4.39 - 5.11	4.74	1.2 ± 0.1	$(1.2^{+0.5}_{-0.4} \cdot 10^{-1}$
5.11 - 5.84	5.47	$(8.4 \pm 1.0) \cdot 10^{-1}$	$(4.6^{+3.7}_{-2.5} \cdot 10^{-2}$
5.84 - 7.29	6.51	$(4.5 \pm 0.5) \cdot 10^{-1}$	$(25^{+2.1}_{-1.5} \cdot 10^{-2}$
7.29 - 10.20	8.58	$(1.8 \pm 0.2) \cdot 10^{-1}$	$(2.7^{+1.1}_{-0.9} \cdot 10^{-2}$
10.20 - 14.56	12.11	$(6.3 \pm 1.0) \cdot 10^{-2}$	$(3.7^{+5.1}_{-3.5} \cdot 10^{-3}$
14.6 - 20.4	17.1	$(1.9^{+0.5}_{-0.4} \cdot 10^{-2}$	-
20.4 - 27.6	23.6	$(9.1^{+3.5}_{-2.6} \cdot 10^{-3}$	-
27.6 - 43.6	34.3	$(1.7^{+1.2}_{-0.8} \cdot 10^{-3}$	-

*) The quoted errors are a combination of statistical and systematic errors.

8 GeV we have somewhat expanded the plot and redrew it in Fig. 5.51. In addition we have added the most recent data obtained by CAPRICE-94 (Boezio et al., 2000) and CAPRICE-98 (Boezio et al., 1999). The results obtained by CAPRICE-94 and CAPRICE-98 are given in numeric form in Tables 5.27 and 5.28, respectively.

Table 5.25: Differential Electron Intensities at Top of Atmosphere. (Barwick et al., 1998) (HEAT-94)

Mean Energy	Intensity $[m^{-2}s^{-1}sr^{-1}GeV^{-1}]$		
GeV]	e^-	e^+	$e^+ + e^-$
5.45	1.13 ± 0.12	0.076 ± 0.016	1.20 ± 0.13
7.16	0.548 ± 0.057	0.0405 ± 0.0070	0.589 ± 0.062
11.1	0.141 ± 0.016	$(9.2^{+2.1}_{-2.0}) \cdot 10^{-3}$	0.151 ± 0.017
18.9	0.0278 ± 0.0033	$(1.00^{+0.52}_{-0.38}) \cdot 10^{-3}$	0.0288 ± 0.0035
34.5	$(3.64^{+0.62}_{-0.58}) \cdot 10^{-3}$	$(2.1^{+1.9}_{-1.1}) \cdot 10^{-4}$	$(3.84^{+0.64}_{-0.83}) \cdot 10^{-3}$
66.4	-	-	$(3.30^{+1.11}_{-0.83}) \cdot 10^{-4}$

Table 5.26: Electron Spectrum Observed from Sanriku, Japan The measurement was made at an altitude of 36 km. (Kobayashi et al., 1999).

Energy Range [GeV]	$< E >$ [GeV]	N^*_{Obs}	N^{**}_{prim}	Intensity, j $[m^{-2}s^{-1}sr^{-1}GeV^{-1}$	$E^3 \cdot j$ $[m^{-2}s^{-1}sr^{-1}GeV^2$
30 - 50	37.9	6	6.0	$(4.30 \pm 1.76) \cdot 10^{-3}$	234 ± 96
60 - 100	75.8	9	9.0	$(3.30 \pm 1.10) \cdot 10^{-4}$	144 ± 48
100 - 150	121	8	7.2	$(8.55 \pm 3.38) \cdot 10^{-5}$	152 ± 60
150 - 200	172	4	3.6	$(2.70 \pm 1.52) \cdot 10^{-5}$	138 ± 77
200 - 300	243	7	5.4	$(5.55 \pm 2.78) \cdot 10^{-6}$	80 ± 40
300 - 400	345	9	6.4	$(2.71 \pm 1.31) \cdot 10^{-6}$	111 ± 54
400 - 600	486	24	19.6	$(9.94 \pm 2.53) \cdot 10^{-6}$	114 ± 29
600 - 800	690	13	10.4	$(3.33 \pm 1.18) \cdot 10^{-7}$	109 ± 39
800 - 1000	892	20	14.2	$(1.30 \pm 0.42) \cdot 10^{-7}$	92 ± 30
1000 - 1500	1214	17	10.1	$(3.04 \pm 1.29) \cdot 10^{-8}$	54 ± 23
1500 - 3000	2068	10	5.2	$(5.21 \pm 3.32) \cdot 10^{-9}$	46 ± 29

* N_{obs} Observed number of electrons.

** N_{prim} Number of electrons after correcting for energy losses and atmospheric secondary electrons.

5.3.4 Atmospheric Secondary Electron Contamination

When carrying out balloon experiments the detectors are always in a residual atmosphere of a few grams. This thin overburden acts as target for the

Table 5.27: Positron Fraction v/s Energy at Top of Atmosphere (ToA). The measurement was made from Lynn Lake (Canada) August 8/9, 1994 with the CAPRICE-94 (Boezio et al., 2000).

Energy Range at Instrument [GeV]	Mean Energy at ToA [GeV]	Positron Fraction*) $e^+/(e^+ + e^-)$
0.3 - 0.4	0.54	0.223 ± 0.081
0.4 - 0.6	0.75	0.160 ± 0.034
0.6 - 0.8	1.04	0.177 ± 0.025
0.8 - 1.1	1.40	0.144 ± 0.019
1.1 - 1.5	1.90	0.106 ± 0.015
1.5 - 2.0	2.55	0.092 ± 0.014
2.0 - 3.0	3.56	0.082 ± 0.015
3.0 - 5.0	5.61	$0.070^{+0.019}_{-0017}$
5.0 - 7.0	8.58	$0.129^{+0.049}_{-0.039}$
7.0 - 10.0	12.11	$0.056^{+0.073}_{-0.049}$

*) The quoted errors are a combination of statistical and systematic errors.

Table 5.28: Positron Fraction v/s Energy at Top of Atmosphere (ToA). The measurement was made from Ft. Sumner, NM (USA) May 28-29, 1998 with the CAPRICE-98 (Boezio et al., 1999).

Energy Range at Instrument [GeV]	Observed Number		Median Energy at ToA [GeV]	Positron Fraction $e^+/(e^+ + e^-)$
	e^+	e^-		
2.5 - 3.0	14	67	4.09	$0.072^{+0.058}_{-0.045}$
3.0 - 4.0	16	169	5.19	$0.033^{+0.023}_{-0.018}$
4.0 - 5.5	12	223	6.96	$0.029^{+0.019}_{-0.014}$
5.5 - 8.0	12	155	9.77	$0.051^{+0.026}_{-0.020}$
8.0 - 12.0	5	70	14.43	$0.041^{+0.041}_{-0.026}$
12.0 - 25.0	3	52	25.04	$0.034^{+0.048}_{-0.027}$

primary electron flux which is subject to interactions, producing atmospheric secondaries in electromagnetic cascading processes that contaminate the primary beam. The secondary contribution must be properly accounted for and

Table 5.29: Intensities of Atmospheric Secondary Negatrons and Positrons at 5.7 $g\,cm^{-2}$ (HEAT-94) (Barwick et al., 1998).

Energy [GeV]	Intensity $[m^{-2}s^{-1}sr^{-1}GeV^{-1}]$	
	e^-	e^+
5.0 - 6.0	$(1.8 \pm 0.6) \cdot 10^{-2}$	$(2.4 \pm 0.6) \cdot 10^{-2}$
6.0 - 8.9	$(7.6 \pm 2.3) \cdot 10^{-3}$	$(9.7 \pm 2.2) \cdot 10^{-3}$
8.9 - 14.8	$(2.1 \pm 0.6) \cdot 10^{-3}$	$(2.5 \pm 0.7) \cdot 10^{-3}$
14.8 - 26.5	$(4 \pm 1) \cdot 10^{-4}$	$(5.3 \pm 1.1) \cdot 10^{-4}$
26.5 - 50.0	$(7 \pm 2) \cdot 10^{-5}$	$(9 \pm 2) \cdot 10^{-5}$
50.0 - 100.0	$(1.1 \pm 0.7) \cdot 10^{-5}$	$(1.2 \pm 0.7) \cdot 10^{-5}$

Table 5.30: Secondary to Primary Electron Ratio at 6 $g\,cm^{-2}$ (HEAT-94) (Barwick et al., 1998).

Energy [GeV]	Ratio (Secondary / Primary)	
	Monte Carlo	Measured
4.5 - 6.0	0.04 ± 0.01	0.04 ± 0.03
6.0 - 8.9	0.04 ± 0.01	0.04 ± 0.03
8.9 - 14.8	0.04 ± 0.01	0.01 ± 0.03
14.8 - 26.5	0.05 ± 0.01	0.01 ± 0.03
26.5 - 50.0	0.06 ± 0.02	-

subtracted from the total flux to obtain the primary intensity.

Barwick et al. (1998) have determined the contribution of secondary negatrons and positrons under an overburden of 5.7 $g\,cm^{-2}$ in the energy range between 5 and 100 GeV. The results are given in Table 5.29. The same authors give also the measured and theoretically expected ratios of secondary to primary electrons $(e^+ + e^-)$ at an atmospheric depth of 6 $g\,cm^{-2}$ for different energy bins (Table 5.30).

5.3.5 Theoretical Contributions

Various astrophysical objects and processes have been proposed by numerous authors as sources of cosmic ray electrons. However, it is generally believed

and very likely that apart form discrete sources that inject electrons into the interstellar space the bulk of the cosmic ray positrons presumably arise from collisions of primary protons and nuclei with interstellar matter. Their intensity and energy spectrum can therefore be calculated on the basis of cosmic ray propagation models. In order to compare predicted spectra in the Galaxy with observations made in the vicinity of the Earth one has to account properly for solar modulation effects.

In addition energy losses due to synchrotron radiation and Compton collisions lead to an equilibrium spectrum which is steeper than the source spectrum above some critical energy which depends on the average diffusion time from the Galaxy, the average strength of the galactic magnetic fields and the energy density of the electromagnetic radiation (Ramaty and Lingenfelter, 1966; Shen 1967; Jokipii and Meyer, 1968; Simnett and McDonald, 1969).

Many authors have carried out calculations to estimate flux and spectral features of the electron component in the Galaxy as well as in the vicinity of the Earth, taking into account the effects of solar modulation, and calculated the positron to negatron ratio, using quite different cosmic ray propagation and modulation models (Perola and Scarsi, 1966; Perola et al., 1967; Webber, 1967; Ramaty et al., 1970; Cowsik and Wilson, 1973; Bulanov and Dogiel, 1974; Badhwar and Stephens, 1976; Ginzburg and Ptuskin, 1976; Owens, 1976; Ramaty and Westergaard, 1976; French and Osborne, 1976; Giler et al., 1977; Owens and Jokipii, 1977; Peters and Westergaard, 1977; Stecker and Jones, 1977; Lezniak and Webber, 1979; Tan and Ng, 1981a and 1981b; Protheroe, 1981; Webber, 1987; Chi et al., 1995; Atoyan et al., 1995).

The results of some predictions have been included in a number of figures presented in this section, showing measured spectra and charge ratios (Anand et al., 1968 and 1970b; Cummings et al., 1973; Buffington et al., 1975; Nishimura et al., 1980; Stephens, 1981; Protheroe, 1982; Stephens, 1985; Dogiel et al., 1986; Stephens and Golden, 1987; Clem et al., 1996).

References

Agrinier, B., Y. Koechlin, B. Parlier, G. Boella, G. Degli Antoni, C. Dilworth, L. Scarsi, and G. Sironi: Phys. Rev. Lett., 13, p. 377 (1964).

Agrinier, B., Y. Koechlin, B. Parlier, J. Vasseur, C.J. Bland, G. Boella, Antonio Degli, C. Dilworth, L. Scarsi, and G. Sironi: PICRC, 2, p. 331, (1965).

Agrinier, B., Y. Koechlin,B. Parlier, J. Paul, J. Vasseur, G. Boella, G. Sironi,

A. Russo, and L. Scarsi: Lett. Nuovo Cimento, 1, p. 53 (1969).

Agrinier, B., Y. Koechlin,B. Parlier, J. Paul, J. Vasseur, G. Boella, G. Sironi, A. Russo, and L. Scarsi: Acta Phys. Hung., 29, Suppl., 1, p. 203 (1970).

Aizu, E., H. Hiraiwa, M. Fujii, J. Nishimura, T. Taira, T. Kobayashi, K. Niu, J.J. Lord, R.J. Wilkes, and R. Golden: PICRC, 1, p. 372 (abstract) (1977).

Anand, K.C., R.R. Daniel, and S.A. Stephens: Phys. Rev. Lett., 20, p. 764 (1968).

Anand, K.C., R.R. Daniel, and S.A. Stephens: Acta Phys. Hung., 29, Suppl., 1, p. 229 (1970a).

Anand, K.C., R.R. Daniel, and S.A. Stephens: Acta Phys. Hung., 29, Suppl., 1, p. 235 (1970b).

Anand, K.C., R.R. Daniel, and S.A. Stephens: PICRC, 1, p. 235 (1973).

Atoyan, A.M., F.A. Aharonian, and H.J. Völk: PICRC, 3, p. 21 (1995).

Badhwar, G.D., and S.A. Stephens: Phys. Rev., D, 14, p. 356 (1976).

Barbiellini, G., G. Basini, R. Bellotti, M. Bocciolini, M. Boezio, F. Massimo Brancaccio, U. Bravar, F. Cafagna, M. Candusso, P. Carlson, M. Casolino, M. Castellano, M. Circella, A. Codino, G. De Cataldo, C. De Marzo, M.P. De Pascale, N. Finetti, T. Francke, N. Giglietto, R.L. Golden, C. Grimani, M. Hof, B. Marangelli, W. Menn, J.W. Mitchell, A. Morselli, J.F. Ormes, P. Papini, A. Perego, S. Piccardi, P. Picozza, M. Ricci, P. Schiavon, M. Simon, R. Sparvoli, P. Spillantini, P. Spinelli, S.A. Stephens, S.J. Stochaj, R.E. Streitmatter, M. Suffert, A. Vacchi, N. Weber, and N. Zampa: Astron. Astrophys., 309, L15 (1996).

Barbiellini, G., G. Basini, R. Bellotti, M. Bocciolini, M. Boezio, U. Bravar, F. Cafagna, P. Carlson, M. Casolino, M. Castellano, M. Circella, A. Codino, G. De Cataldo, C. De Marzo, M.P. De Pascale, N. Finetti, T. Francke, N. Giglietto, R.L. Golden, C. Grimani, M. Hof, W. Menn, J.W. Mitchell, A. Morselli, J.F. Ormes, P. Papini, A. Perego, S. Piccardi, P. Picozza, M. Ricci, P. Schiavon, M. Simon, R. Sparvoli, P. Spillantini, P. Spinelli, S.A. Stephens, S.J. Stochaj, R.E. Streitmatter, M. Suffert, A. Vacchi, N. Weber, and N. Zampa: PICRC, 4, p. 221 (1997).

Barwick, S.W., J.J. Beatty, C.R. Bower, C. Chaput, S. Coutu, G. de Nolfo, D. Ficenec, J. Knapp, D.M. Lowder, S. McKee, D. Müller, J.A. Musser, S.L. Nutter, E. Schneider, S.P. Swordy, K.K. Tang, G. Tarlé, A.D. Tomasch, and E. Torbet: Phys. Rev. Lett., 75, p. 390 (1995).

Barwick, S.W., J.J. Beatty, A. Bhattacharyya, C.R. Bower, C.J. Chaput, S. Coutu, G.A. de Nolfo, J. Knapp, D.M. Lowder, S. McKee, D. Müller, J.A.

Musser, S.L. Nutter, E. Schneider, S.P. Swordy, G. Tarlé, A.D. Tomasch, and E. Torbet: Astrophys.J., 482, p. L191 (1997).

Barwick, S.W., J.J. Beatty, C.R. Bower, C.J. Chaput, S. Coutu, G. de Nolfo, M.A. DuVernois, D. Ellithorpe, D. Ficenec, J. Knapp, D.M. Lowder, S. McKee, D. Müller, J.A. Musser, S.L. Nutter, E. Schneider, S.P. Swordy, G. Tarlé, A.D. Tomasch, and E. Torbet: Astrophys.J., 498, p. 779 (1998).

Basini, G., R. Bellotti, F. Bongiorno, M.T. Brunetti, F. Cafagna, M. Circella, A. Codino, G. De Cataldo, C.N. De Marzo, M.P. De Pascale, N. Finetti, N. Giglietto, R.L. Golden, C. Grimani, M. Hof, F. Massimo Brancaccio, M. Menichelli, J.W. Mitchell, A. Morselli, J.F. Ormes, P. Papini, S. Piccardi, P. Picozza, M. Ricci, I. Salvatori, M. Simon, P. Spillantini, P. Spinelli, S.A. Stephens, S.J. Stochaj, and R.E. Streitmatter: PICRC, 3, p. 1 (1995).

Beuermann, K.P., C.J. Rice, E.C. Stone, and R.E. Vogt: Phys. Rev. Lett., 22, p. 412 (1969).

Beuermann, K.P., C.J. Rice, E.C. Stone, and R.E. Vogt: Acta Phys. Acad. Sci. Hung., 29, Suppl. 1, p. 173 (1970).

Bland, C.J., G. Boella, Antoni Degli, C. Dilworth, L. Scarsi, G. Sirono, B. Agrinier, Y. Koechlin, B. Parlier, and J. Vasseur: Phys. Rev. Lett., 17, p. 813 (1966).

Bleeker, J.A.M., J.J. Burger, A.J.M. Deerenberg, A. Scheepmaker, B.N. Swanenburg, and Y. Tanaka: Can. J. Phys., 46, p. S522 (1968).

Bleeker, J.A.M., J.J. Burger, A.J.M. Deerenberg, H.C. van de Hulst, A. Scheepmaker, B.N. Swanenburg, and Y. Tanaka: Acta Phys. Acad. Sci. Hung., 29, Suppl. 1, p. 217 (1970).

Boezio, M., M.L. Ambriola, G. Barbiellini, S. Bartalucci, R. Bellotti, D. Bergström, V. Bidoli, U. Bravar, F. Cafagna, P. Carlson, M. Casolino, M. Castellano, F. Ciacio, M. Circella, C. De Marzo, M.P. De Pascale, T. Francke, N. Finetti, S. Grinstein, M. Hof, F. Khalchukov, J. Kremer, W. Menn, J.W. Mitchell, A. Morselli, J.F. Ormes, P. Papini, S. Piccardi, P. Picozza, M. Ricci, P. Schiavon, M. Simon, R. Sparvoli, P. Spillantini, S.A. Stephens, S.J. Stochaj, R.E. Streitmatter, M. Suffert, A. Vacchi, and N. Zampa: PICRC, 3, p. 57 (1999).

Boezio, M., P. Carlson, T. Francke, N. Weber, M. Suffert, M. Hof, W. Menn, M. Simon, S.A. Stephens, R. Bellotti, F. Cafagna, M. Castellano, M. Circella, C. De Marzo, N. Finetti, P. Papini, S. Piccardi, P. Spillantini, M. Ricci, M. Casolino, M.P. De Pascale, A. Morselli, P. Picozza, R. Sparvoli, G. Barbiellini, U. Bravar, P. Schiavon, A. Vacchi, N. Zampa, C. Grimani, J.W. Mitchell, J.F. Ormes, R.E. Streitmatter, R.L. Golden, and S.J. Stochaj: As-

trophys. J., 532, p. 653 (2000).

Buffington, A., Orth, C.D., and G.F. Smoot: Astrophys. J., 199, p. 669 (1975).

Bulanov, S.V., and V.A. Dogiel: Astrophys. Space Sci., 29, p. 305 (1974).

Burger, J.J., B.N. Swanenburg: PICRC, 5, p. 3061 (1973).

Chi, X., K.S. Cheng, and E.C.M. Young, PICRC, 3, p. 25, (1995).

Clem, John M., David P. Clements, Joseph Espositi, Paul Evenson, David Huber, Jaques L'Heureux, Peter Meyer, and Christian Constantin: Astrophys. J., 464, p. 507 (1996).

Cowsik, R, and L.W. Wilson: PICRC, 1, p. 500 (1973).

Critchfield, C.L., E.P. Ney, and Sophie Oleksa: Phys. Rev., 85, p. 461 (1952).

Cummings, A.C., E.C. Stone, and R.E. Vogt: PICRC, 1, p. 335 (1973).

Daniel, R.R., and S.A. Stephens: PICRC, 1, p. 335 (1965a).

Daniel, R.R., and S.A. Stephens: Phys. Rev. Lett., 15, p. 769 (1965b).

Daniel, R.R., and S.A. Stephens: Phys. Rev. Lett., 17, p. 935 (1966).

Daniel, R.R., and S.A. Stephens: Proc. Indian Acad. Sci., 65a, p. 319 (1967).

Daniel, R.R., and S.A. Stephens: Space Sci. Rev., 10, p. 599 (1970).

Daniel, R.R., and S.A. Stephens: Space Sci. Rev., 17, p. 45 (1975).

Daugherty, J.K., R.C. Hartman, and P.J. Schmidt: Astrophys. J., 198, p. 493 (1975).

De Shong, J.A., R.H. Hildebrand, and P. Meyer: Phys. Rev. Lett., 12, p. 3 (1964).

Dogiel, V.A., A.V. Gurevich, Ya.N. Istomin, G.S. Sharov, and K.P. Zybin: Plasma Astrophys., ESA, SP-251, p. 287 (1986).

Du Vernois, M.A., S.W. Barwick, J.J. Beatty, A. Bhattacharyya, C.R. Bower, S. Coutu, S. McKee, D. Müller, J.A. Musser, S.L. Nutter, S.P. Swordy, G. Tarlé, and A.D. Tomasch: PICRC, 3, p. 49 (1999).

Earl, James, A.: Phys. Rev. Lett., 6, p. 125 (1961).

Evenson, P., Evelyn Tuska, Joseph Esposito, and Peter Meyer: PICRC, 3, p. 505 (1991).

Fan, C.Y., J. L'Heureux, and Peter Meyer: Phys. Rev. Lett., 23, p. 877 (1969).

Fanselow, J.L., R.C. Hartman, R.H. Hildebrand, and Peter Meyer: Astrophys. J., 158, p. 771 (1969).

Fanselow, J.L., R.C. Hartman, Peter Meyer, and P.J. Schmidt: Astrophys. Space Sci., 14, p. 301 (1971).

Freier, P.S., and C.J. Waddington: J. Geophys. Res., 70, p. 5753 (1965).

Freier, Phyllis, Charles Gilman, and C.J. Waddington: Astrophys. J., 213, p. 588 (1977).

French, D.K., and J.L. Osborne: Nature, 260, p. 372 (1976).

Garcia-Munoz, M., P. Meyer, K.R. Pyle, and J.A. Simpson: J. Geophys. Res., 91, No. A3, p. 2858 (1986).

Giler, M., J. Wdowczyk, and A.W. Wolfendale: J. Phys. A, 10, p. 843 (1977).

Ginzburg, V.L.: Progress in Elementary and Cosmic Ray Physics, Vol. 4, Amsterdam: North Holland Publishing Co. (1958).

Ginzburg, V.L., and V.S. Ptuskin: Rev. Mode. Phys., 48, p. 161 (1976).

Golden, R.L., B.G. Mauger, G.D. Badhwar, R.R. Daniel, J.L. Lacy, S.A. Stephens, and J.E. Zipse: Astrophys. J., 287, p. 622 (1984).

Golden, R.L., S.A. Stephens, B.G. Mauger, G.D. Badhwar, R.R. Daniel, S. Horan, J.L. Lacy, and J.E. Zipse: Astron. Astrophys., 188, p. 145 (1987).

Golden, R.L., C. Grimani, B.L. Kimbell, S.A. Stephens, S.J. Stochaj, W.R. Webber, G. Basini, F. Bongiorno, F. Massimo Brancaccio, M. Ricci, J.F. Ormes, R.E. Streitmatter, P. Papini, P. Spillantini, M.T. Brunetti, A. Codino, M. Menichelli, I. Salvatori, M.P. De Pascale, A. Morselli, and P. Picozza: Astrophys. J., 436, p. 769 (1994).

Golden, R.L., S.J. Stochaj, S.A. Stephens, F. Aversa, G. Barbiellini, M. Boezio, U. Bravar, A. Colavita, F. Fratnik,P. Schiavon, A. Vacchi, N. Zampa, J.W. Mitchell, J.F. Ormes, R.E. Streitmatter, R. Bellotti, F. Cafagna, M. Castellano, M. Circella, G. De Cataldo, C. De Marzo, N. Giglietto, B. Marangelli, A. Rainò, P. Spinelli, M. Bocciolini, N. Finetti, P. Papini, A. Perego, S. Piccardi, P. Spillantini, G. Basini, F. Massimo Brancaccio, M. Ricci, M.T. Brunetti, A. Codino, C. Grimani, M. Menichelli, V. Bidoli, M. Candusso, M. Casolino, M.P. De Pascale, A. Morselli, P. Picozza, R. Sparvoli, M. Hof, W.Menn, and M. Simon: Astrophys. J., 457, p. L103 (1996).

Hartman, R.C., Peter Meyer, and R.H. Hildebrand: J. Geophys. Res., 70, p. 2713 (1965).

Hartman, R.C.: Astrophys. J., 150, p. 371 (1967).

Hartman, R.C. and C.J. Pellerin: Astrophys. J., 204, p. 927 (1976).

Hartmann, Gernot, Dietrich Müller, and Thomas Prince: Phys. Rev. Lett., 38, p. 1368 (1977).

Hayakawa, S., K. Ito, and Y. Terashima: Progr. Theoret. Phys. Suppl., 6, p. 1 (1958).

Ishii, C., T. Kobayashi, N. Shigibara, K. Yokoi, M. Matsuo, J. Nishimura, T. Taira, and K. Niu: PICRC, 5, p. 3073 (1973).

Jokipii, J.R., and P. Meyer: Phys. Rev. Lett., 20, p. 752 (1968).

Kniffen, D.A., T.L. Cline, and C.E. Fichtel: Acta Phys. Acad. Sci. Hung., 29, Suppl. 1, p. 187 (1970).

Kobayashi, T., J. Nishimura, Y. Komori, T. Shirai, N. Tateyama, T. Taira, K. Yoshida, and T. Yuda: PICRC, 3, p. 61 (1999).

Lezniak, J.A., and W.R. Webber: Astrophys. Space. Sci., 63, p. 35 (1979).

L'Heureux, J., and P. Meyer: Phys. Rev. Lett., 15, p.93 (1965).

L'Heureux, Jaques: Astrophys. J., 148, p. 399 (1967).

L'Heureux, J., and P. Meyer: Can. J. Phys., 46, p. S892 (1968).

L'Heureux, J., P. Meyer, S.D. Verma, and R.E. Vogt: Can. J. Phys., 46, p. S896 (1968).

L'Heureux, Jaques, C.Y. Fan, and Peter Meyer: Astrophys. J., 171, p. 363 (1972).

Marar, T.M.K., P.S. Freier, and C.J. Waddington: J. Geophys. Res., 76, p. 1625 (1971).

Marsden, P.L., R. Jakeways, and I.R. Calder: PICRC, 1, p. 110 (1971).

Matsuo, M., E. Mikumo, J. Nishimura, K. Niu, and T. Taira: PICRC, 7, p. 2550 (1971).

Matsuo, M., J. Nishimura, T. Kobayashi, K. Niu, E. Aizu, H. Hiraiwa, and T. Taira: PICRC, 12, p. 4132 (1975).

McDonald, F.B., and G.M. Simnett: NASA preprint X-611-68-450 (1968).

Meegan, C.A.: Ph.D. Thesis University of Maryland (1973), available as Technical Report No. 74-055

Meegan, Charles A., and James A. Earl: Astrophys. J., 197, p. 219 (1975).

Meyer, Peter, and Rochus Vogt: Phys. Rev. Lett., 6, p. 193 (1961).

Müller, D., and P. Meyer: Astrophys. J., 186 (1973).

Müller, Dietrich, and Jonathan Tang: PICRC, 2, p. 378 (1985).

Müller, Dietrich, and Kwok-Kwong Tang: Astrophys. J., 312, p. 183 (1987).

Müller, D., S.W. Barwick, J.J. Beatty, A. Bhattacharyya, C.R. Bower, C.J. Chaput, S. Coutu, G.A. de Nolfo, M.A. Du Vernois, J. Knapp, D.M. Lowder, S. McKee, J.A. Musser, S.L. Nutter, E. Schneider, S.P. Swordy, G. Tarlé, A.D. Tomasch, and E. Torbet: PICRC, 4, p. 237 (1997).

Nishimura, J., E. Mikumo, I. Mito, K. Niu, I. Ohta, and T. Taira: Acta Phys. Hung., 29, Suppl., 1, 239 (1970).

Nishimura, J., M. Fujii, T. Taira, E. Aizu, H. Hiraiwa, T. Kobayashi, K. Niu, I. Ohta, R.L. Golden, T.A. Koss, J.J. Lord, and R.J. Wilkes: Astrophys. J., 238, p. 394 (1980).

Nishimura, J.: Japan-U.S. Primary Electron Collaboration. PICRC, 2, p. 94 (1981).

Nishimura, Jun, T. Kobayashi, Y. Komori, and N. Tateyama: PICRC, 3, p. 29 (1995).

Nishimura, J., T. Kobayashi, Y. Komori, T. Shirai, N. Tateyama, and K. Yoshida: PICRC, 4, p. 233 (1997).

Ormes, J., and P.S. Freier: Astrophys. J., 222, p. 471 (1978).

Oran, W.A., G.M. Frey, Jr., and C.P. Wang: J. Geophys. Res., 74, p. 53 (1969).

Owens, A.J.: Astrophys. Space Sci., 40, p. 357 (1976).

Owens, A.J., and J.R. Jokipii: Astrophys. J., 227, p. 676 (1977).

Perola, G.L, and L. Scarsi: Nuovo Cimento, 46, p. 718 (1966).

Perola, G.C., L. Scarsi, and G. Sironi: Nuovo Cimento, 53 B, p. 459 (1967).

Peters, B., and N.J. Westergaard: Astrophys. Space. Sci., 48, p. 21 (1977).

Prince, Thomas A.: Astrophys. J., 227, p. 676 (1979).

Protheroe, R.J.: Astrophys. J., 251, p. 387 (1981).

Protheroe, R.J.: Astrophys. J., 254, p. 391 (1982).

Ramaty, R. and R.E. Lingenfelter: Phys. Rev. Lett., 17, p. 1230 (1966).

Ramaty, R. and R.E. Lingenfelter: Phys. Rev. Lett., 20, p. 120 (1968).

Ramaty, R., D.V. Reames, and R.E. Lingenfelter: Phys. Rev. Lett, 24, p. 913 (1970).

Ramaty, R., and N.J. Westergaard: Astrophys. Space Sci., 45, p. 143 (1976).

Scheepmaker, A., and Y. Tanaka: Astron. Astrophys., 11, p. 53 (1971).

Schmidt, P.J.: J. Geophys. Res., 77, p. 3295 (1972).

Shen, C.S.: Phys. Rev. Lett.: 19, p. 399 (1967).

Silverberg, R.F., J.F. Ormes, and V.K. Balasubrahmanyan: PICRC, 1, p. 347 (1973).

Silverberg, Robert, F.: J. Geophys. Res., 81, p. 3944 (1976).

Simnett, G.M., and F.B. McDonald: Astrophys. J., 157, p. 1435 (1969).

Stecker, F.W., and F.C. Jones: Astrophys. J., 217, p. 843 (1977).

Stephens, S.A.: PICRC, 2, p. 214 (1981).

Stephens, S.A.: PICRC, 2, p. 390 (1985).

Stephens, S.A., and R.L. Golden: Space Sci. Rev., 46, p. 31 (1987).

Taira, T., M. Fujii, J. Nishimura, E. Aizu, H. Hiraiwa, T. Kobayashi, I. Ohta, K. Niu, J.J. Lord, R.J. Wilkes, T. Koss, and R.L. Golden: PICRC, 1, p. 478 (1979).

Tan, L.C., and L.K. Ng: J. Phys. G 7, p. 1123 (1981a).

Tan, L.C., and L.K. Ng: J. Phys., G 7, p. 1135 (1981b).

Tan, L.C., and L.K. Ng: Astrophys. J., 269, p. 751 (1983).

Tang, K.-K.: Astrophys. J., 278, p. 881 (1984).

Tang, Kwok-Kwong, and Dietrich Müller: PICRC, 2, p. 88 (1987).

Torii, S., J. Nishimura, K. Kasahara, T. Tamura, N. Tateyama, K. Yoshida, T. Yamagami, T. Kobayashi, H. Murakami, and T. Yuda: PICRC, 3, p. 575 (1995).

Torii, S., J. Nishimura, N. Tateyama, T. Tamura, K. Yoshida, T. Yamagami, S. Ohta, M. Namiki, H. Murakami, T. Kobayashi, Y. Komori, K. Kasahara, and T. Yuda: PICRC, 4, p. 241 (1997).

Torii, S., K. Kasahara, T. Kobayashi, Y. Komori, H. Murakami, J. Nishimura, T. Ouchi, Y. Saito, T. Tamura, N. Tateyama, T. Yamagami, K. Yoshida, and T. Yuda: PICRC, 3, p. 53 (1999).

Waddington, C.J., and P.S. Freier: PICRC, 1, p. 339 (1965).

Webber, W.R.: J. Geophys. Res., 72, p. 5949 (1967).

Webber, W.R.: J. Geophys. Res., 73, p. 4905 (1968).

Webber, W.R., and J.M. Rockstroh: J. Geophys. Res., 78 (1973).

Webber, W.R., G.A. Simpson, and H.V. Cane: Astrophys. J., 236, p. 448 (1980).

Webber, W.R.: PICRC, 2, p. 80 (1987).

Zatsepin, V.I.: PICRC, 5, p. 1720 (1971).

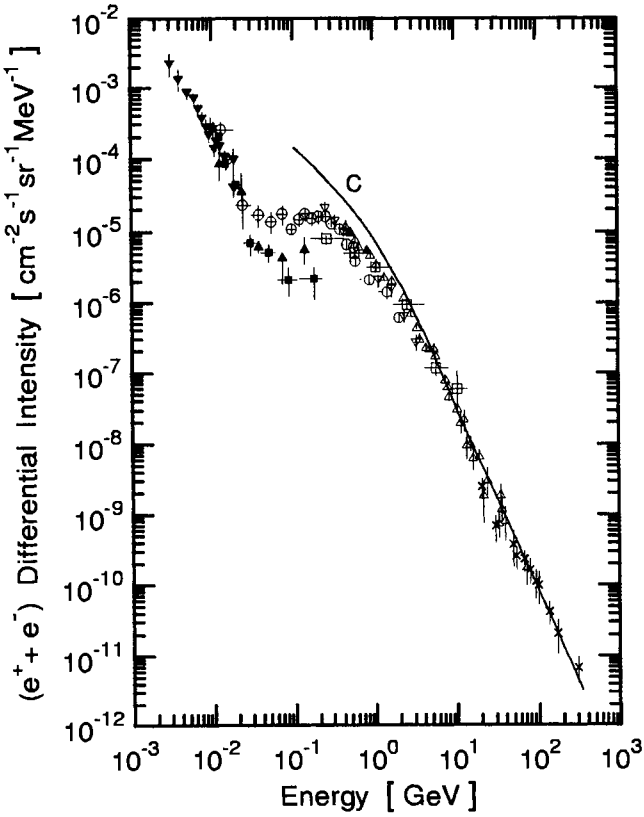

Figure 5.40: Energy spectrum of primary cosmic ray electrons, $(e^+ + e^-)$, on top of the atmosphere. Shown is a compilation of data from different experiments as listed below (Fanselow et al., 1969 and 1971). Curve C is a combination of a theoretical spectrum derived from non-thermal radio emission of electrons (below 5 GeV) and a power law fit to the data above 5 GeV (Anand et al., 1968; see text).

×	Anand et al. (1968)	△	Bleeker et al. (1968, 1970)
o	Webber (1968)	▲	Beuermann et al. (1969, 1970)
□	Fanselow et al. (1969)	▽	L'Heureux and Meyer (1968)
■	Fan et al. (1969)	▼	McDonald and Simnett (1968) and Simnett & McDonald (1969)

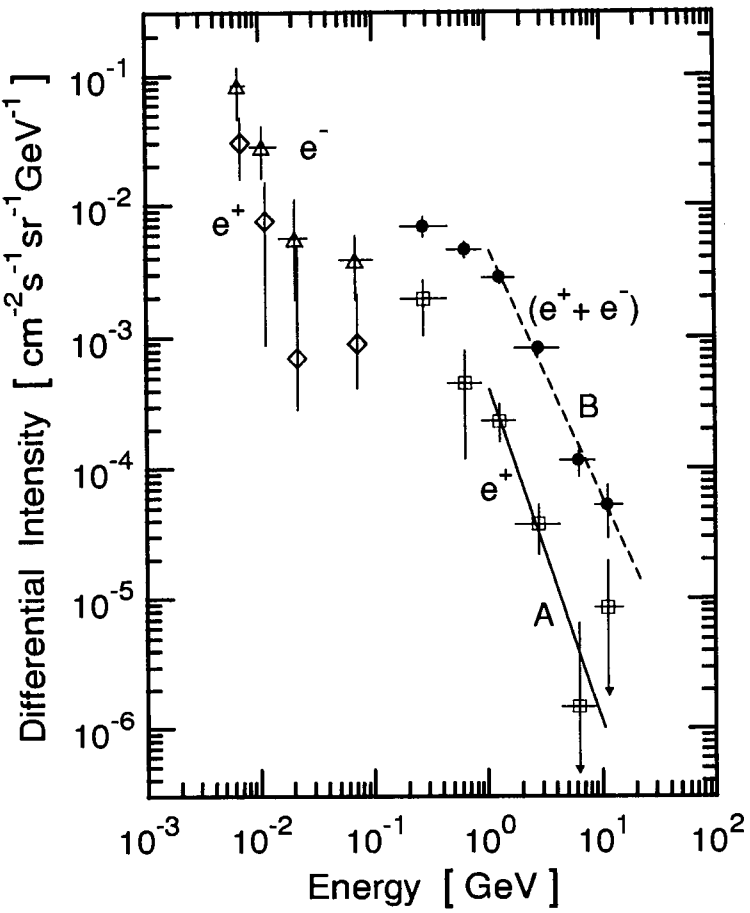

Figure 5.41: Energy spectra of positrons, negatrons and all electrons ($e^+ + e^-$) from two experiments, as indicated below. The lines A and B are least square fits of power laws to the data of Fanselow et al. (1969) for energies $\geq$860 MeV .

◇ e^+	△ e^-	Beuermann et al. (1970)
□ e^+	• $e^+ + e^-$	Fanselow et al. (1969)

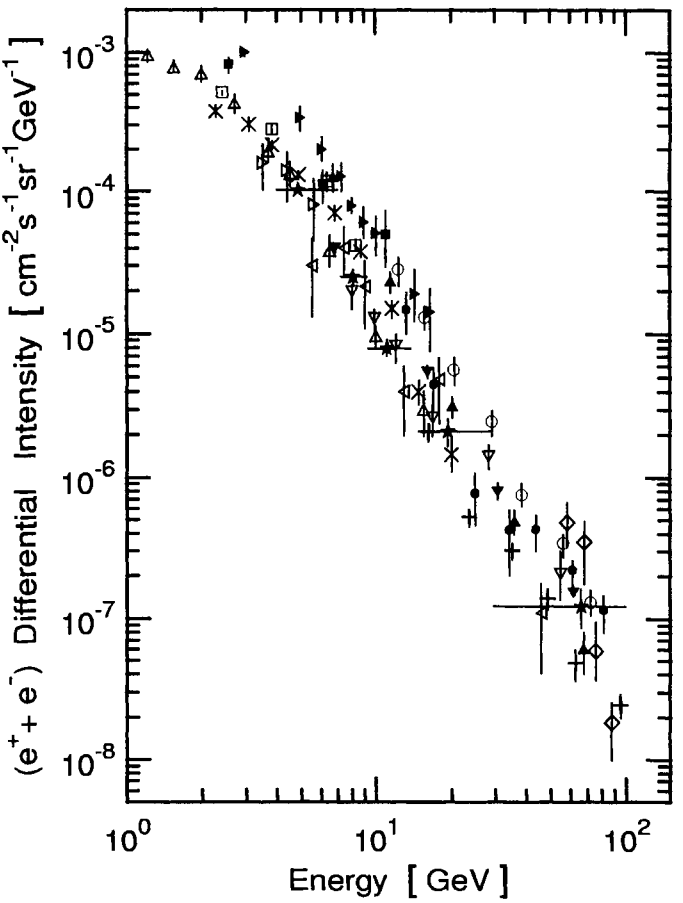

Figure 5.42: Compilation of differential energy spectra of electrons in the primary cosmic radiation measured by different experiments as listed below.

- ⋆ Buffington et al. (1975)
- • Anand et al. (1973)
- ■ Fanselow et al. (1969)
- ▶ Marsden et al. (1971)
- ▲ Meegan (1973)
- ▷ Oran et al. (1969)
- o Silverberg et al. (1973)
- ▼ Zatsepin (1971)
- ▽ Agrinier et al. (1969, 1970)
- □ Burger & Swanenburg (1973)
- ◁ Marar et al. (1971)
- ◇ Matsuo et al. (1971)
- \+ Müller & Meyer (1973)
- × Schmidt (1972)
- △ Webber & Rockstroh (1973)

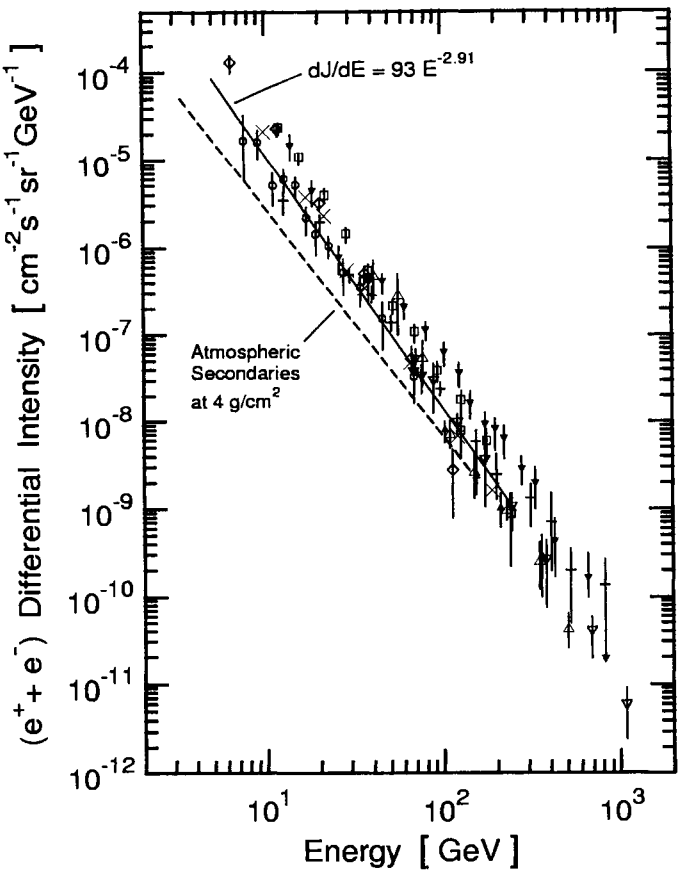

Figure 5.43: Compilation of measured differential intensities of primary cosmic ray electrons ($e^+ + e^-$) outside the atmosphere as a function of energy. Included are data from counter as well as emulsion experiments. The dashed line indicates the intensity of secondaries at a residual atmosphere of 4 g/cm^2 and the solid line is a single power law fit to the data of Freier et al. (1977).

o Freier et al. (1977)	◇ Meegan & Earl (1975)
× Hartmann et al. (1977)	▼ Anand et al. (1973)
▲ Ishii et al. (1973)	□ Silverberg (1976)
– Müller & Meyer (1973)	△ Ishii et al. (1973)
▽ Nishimura et al. (1980)	

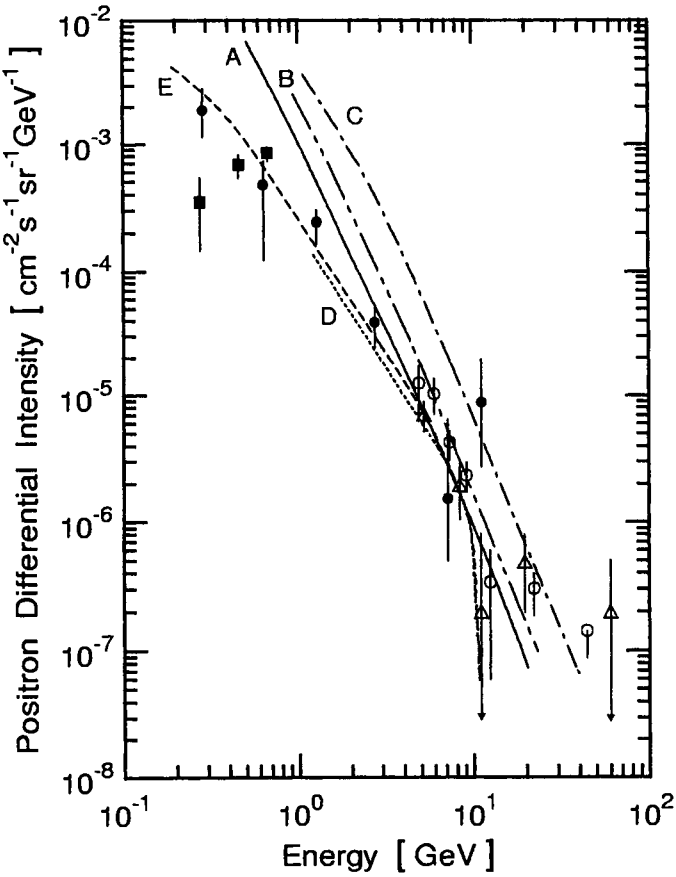

Figure 5.44: Measured differential energy spectrum of positrons in the primary cosmic radiation compared with predictions from different models. Curve A is the result of the modified closed galaxy model (MCGM) with a mean density of 0.1 atom/cm^3 (Stephens, 1981), curves B and C are for supernovæexploding in dense clouds using the nested and modified leaky box models (NLBM and MLBM), respectively (Stephens, 1985). Curves D and E are for dark matter annihilation, curve D for higgsino and curve E for photino annihilation (Stephens and Golden, 1987).

• Fanselow et al. (1969) | ■ Hartman and Pellerin (1976)
△ Buffington et al. (1975) | o Golden et al. (1987)

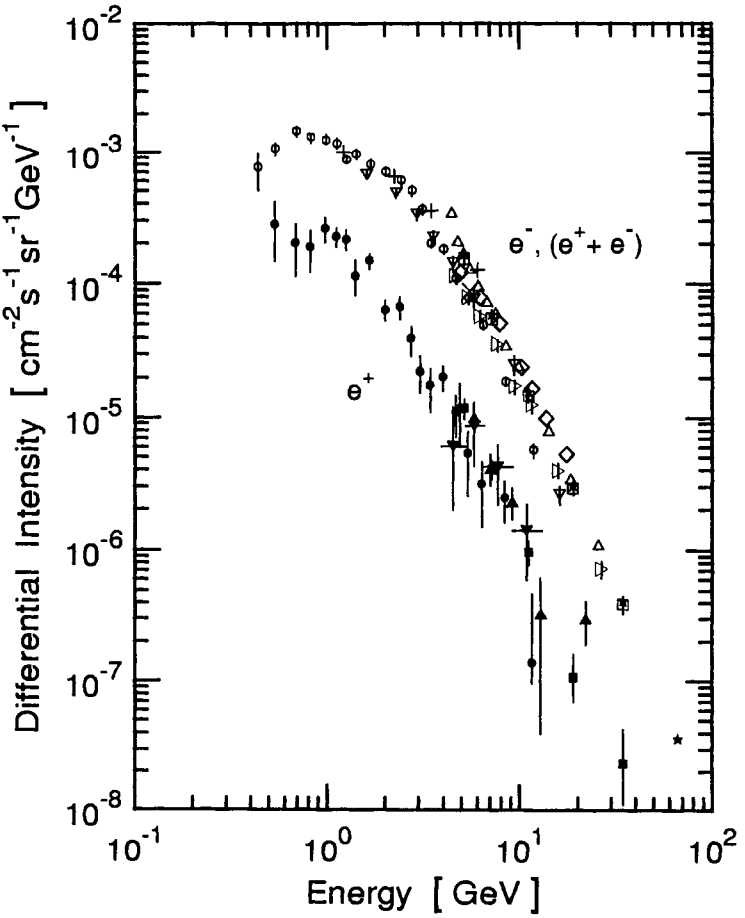

Figure 5.45: Positron, negatron and all-electron spectra obtained from several experiments, as listed below. The date apply to the top of the atmosphere.

▲	e^+	Golden et al. (1987)	•	e^+	Barbiellini et al. (1997)
△	e^-	Golden et al. (1984)*	○	e^-	Barbiellini et al. (1997)
▼	e^+	Golden et al. (1994)*	×	$e^+ + e^-$	Evenson et al. (1991)
		* measured at payload	+	$e^+ + e^-$	Garcia-Munoz et al. (1986)
▽	e^-	Golden et al. (1994)	◇	$e^+ + e^-$	Tang (1984)
■	e^+	Müller et al. (1997)	⋆	$e^+ + e^-$	Müller et al. (1997)
□	e^-	Müller et al. (1997)	▷	e^-	Basini et al. (1995)

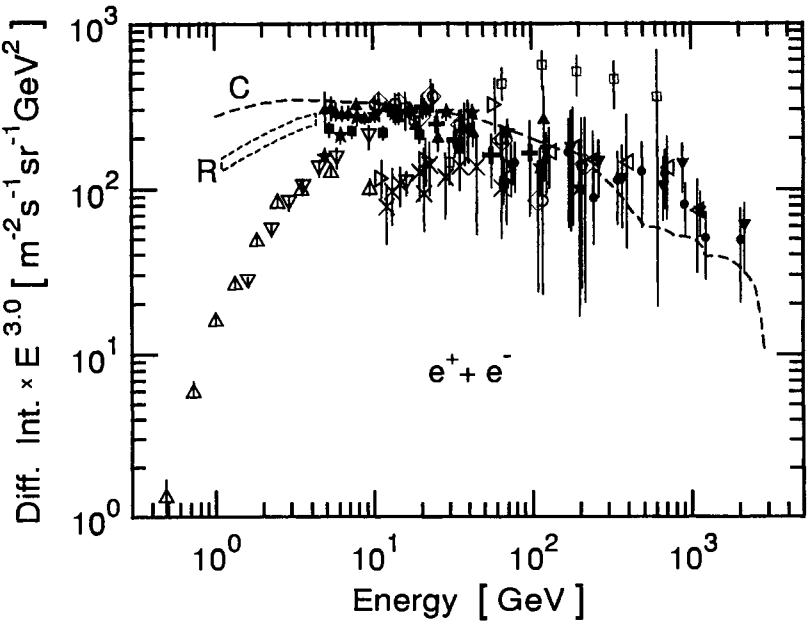

Figure 5.46: Compilation of experimentally determined primary electron intensities on top of the atmosphere multiplied by the energy to the third power and plotted as a function of energy. This representation spreads the differences between the various experiments. Curve C shows the electron spectrum resulting from the contributions of all nearby supernovae according to a model calculation of Nishimura et al. (1997) (see also Ormes and Freier, 1978; Nishimura et al., 1995). The enclosed region R marks the electron spectrum calculated by Webber et al. (1980) from intensity measurements of the diffuse galactic radio continuum.

□ Anand et al. (1968, 1970a)	△ Barbiellini et al. (1997)
▷ Buffington et al. (1975)	× Freier et al. (1977)
▲ Golden et al. (1984)	▽ Golden et al. (1994)
◇ Hartmann et al. (1977)	■ Müller et al. (1997)
◁ Nishimura et al. (1980)	▼ Nishimura et al. (1981)
• Nishimura et al. (1997)	o Prince (1979)
★ Tang (1984)	+ Torii et al. (1997)

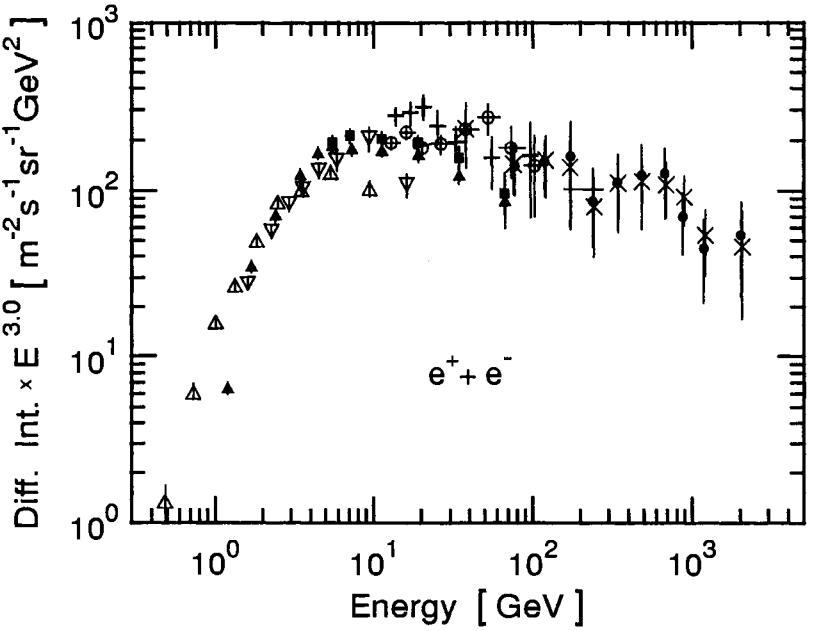

Figure 5.47: Compilation of mostly recent electron energy spectra (positrons and negatrons combined) at the top of the atmosphere. Note that the intensities are multiplied by the energy to the third power. The plot includes data from the following experiments.

- ▽ Golden et al. (1994)
- • Nishimura et al. (1995), EC
- △ Barbiellini et al. (1997), CAPRICE-94
- \+ Torii et al. (1997), BETS-95
- ○ Torii et al. (1999), BETS-97/98
- ■ Barwick et al. (1998), HEAT-94
- × Kobayashi et al. (1999), EC
- ▲ DuVernois et al. (1999), HEAT-94+95

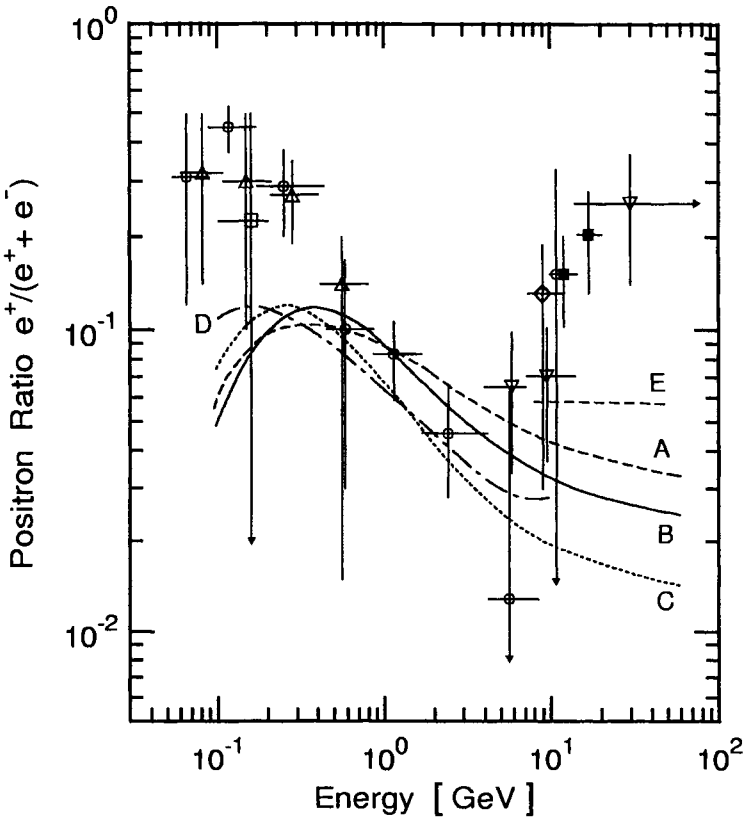

Figure 5.48: Positron fraction of cosmic ray electrons on top of the atmosphere as a function of energy. The experimental points are as listed below. The curves represent predictions from different model calculations: A is for the leaky box model, B for the halo and C for the dynamical halo model (Protheroe 1982, after Müller and Tang 1985); D is the ratio obtained by Cummings et al. (1973) using the non-thermal radio background and the positron calculation of Ramaty and Lingenfelter (1968), and E is the result expected from all interactions of cosmic ray protons and nuclei with the interstellar gas (Buffington et al., 1975).

o Fanselow et al. (1969, 1971)	◇ Agrinier et al. (1970)
△ Daughtery et al. (1975)	▽ Buffington et al. (1975
■ Müller and Tang (1985)	□ Beuermann et at. (1969)

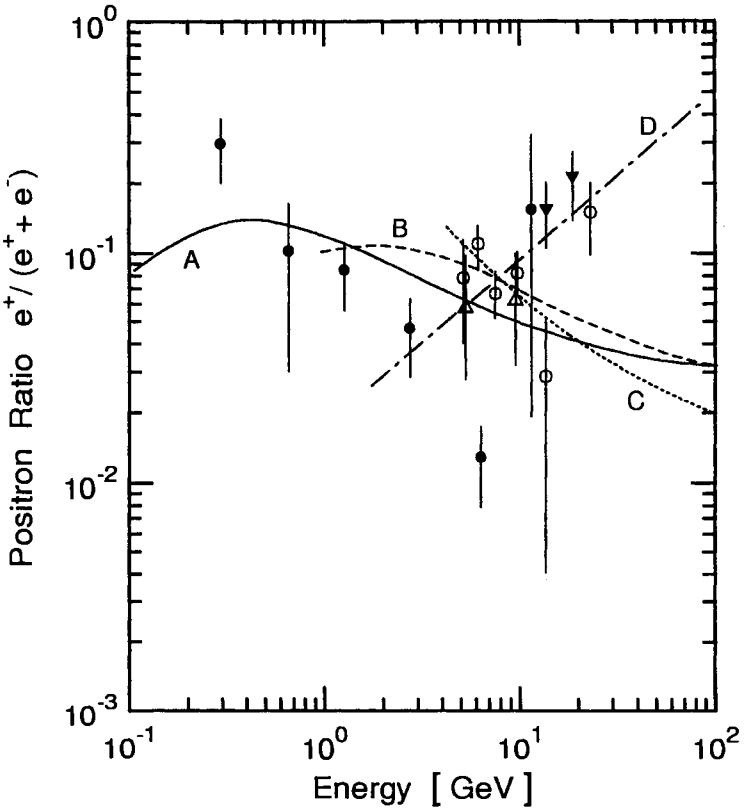

Figure 5.49: Comparison of experimental and theoretical positron fractions in the primary cosmic radiation as a function of energy. The curves represent predictions from different models. Curve A is based on the modified closed galaxy model and curve B is for supernovae exploding in dense clouds (Stephens and Golden, 1987). Curve C is the result of the non-uniform model (Tan and Ng, 1983), and line D is for acceleration in dense clouds (Dogiel et al., 1986) (after Stephens and Golden, 1987).

• Fanselow et al. (1969)	o Golden et al. (1987)
△ Buffington et al. (1975)	▼ Müller and Tang (1987)

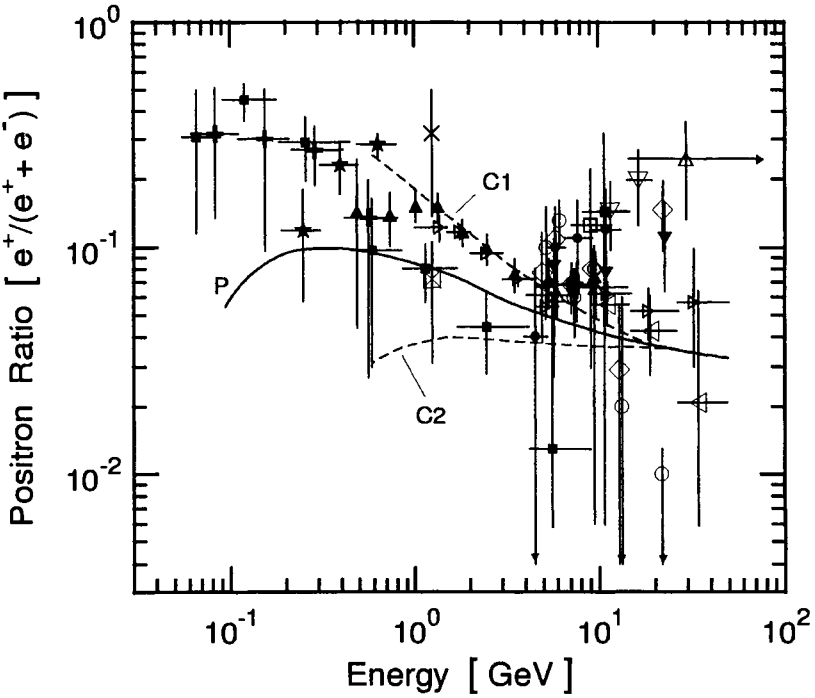

Figure 5.50: Compilation of the results of positron fraction measurements as listed below. Included are most of the available data from balloon-borne magnetic spectrometer measurements and from measurements of Agrinier et al. (1969) and Müller and Tang (1985 and 1987) using the geomagnetic east-west asymmetry. The solid curve P is the prediction of the leaky box model of Protheroe (1982) and the two dashed curves C1 and C2 show the boundaries of the effect of solar modulation from the work of Clem et al. (1996). The date apply to the top of the atmosphere.

□ Agrinier et al. (1970)	▲ Barbiellini et al. (1997)
◁ Barwick et al. (1995)	▷ Barwick et al. (1997)
△ Buffington et al. (1975)	× Clem et al. (1996)
+ Daugherty et al. (1975)	■ Fanselow et al. (1969, 1971)
o Golden et al. (1984)	◇ Golden et al. (1987)
• Golden et al. (1994)	▼ Golden et al. (1996)
⋆ Hartmann et al. (1977)	▽ Müller & Tang (1985, 1987)

⊠ Clem et al. (1996) adjusted to solar polarity state 1960

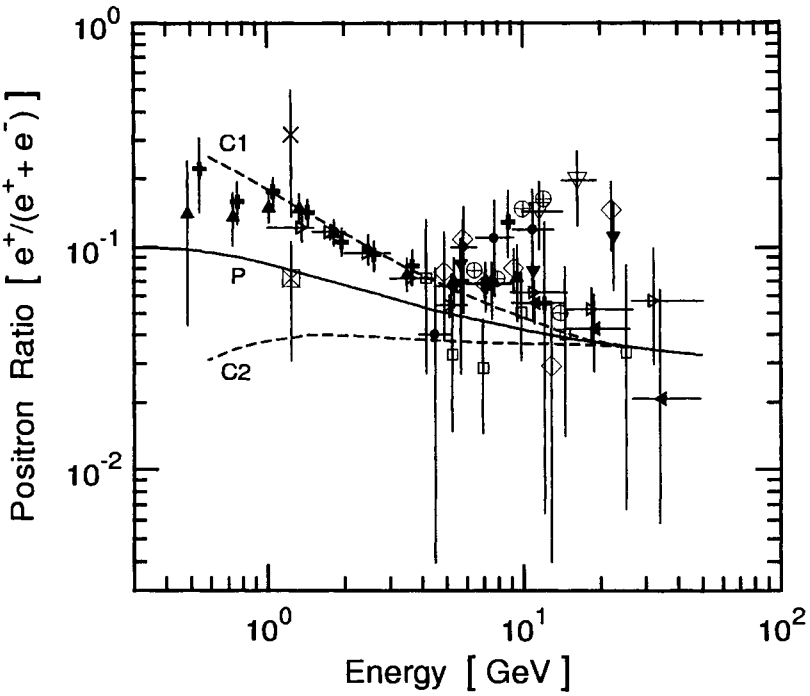

Figure 5.51: This figure is an expanded plot of Fig. 5.50, showing only the results of the most recent measurements of the positron fraction. Note that the symbol of the data of Barwick et al. (1995) was changed for better legibility. In addition we have added the date of Basini et al. (1995). The central cluster of data points at 7 GeV and ratio 0.067 includes 4 data points; one data point each of the work of Golden et al. (1987), Barwick et al. (1995), Golden et al. (1996), and Barwick et al. (1997). The curves P, C1 and C2 are the same as those in Fig. 5.50. The date apply to the top of the atmosphere.

▲ Barbiellini et al. (1997)	◀ Barwick et al. (1995)
▷ Barwick et al. (1997)	⊕ Basini et al. (1995)
◇ Golden et al. (1987)	• Golden et al. (1994)
▼ Golden et al. (1996)	▽ Müller & Tang (1987)
□ Boezio et al. (1999)	+ Boezio et al. (2000)
× Clem et al. (1996)	

⊠ Clem et al. (1996) adjusted to solar polarity state 1960

5.4 X- and Gamma Rays

5.4.1 Introduction

It was the discovery of radio emission from the Milky Way by Jansky in 1932 (Jansky, 1932, 1933a and 1933b) that marks the beginning of the systematic search for electromagnetic radiation from space other than optical. Eventually, these efforts led to the discoveries of galactic and extragalactic radio sources, the 21 cm hydrogen line, radio galaxies and finally to the discovery of X- and gamma radiation (Giacconi et al., 1962; Kraushaar et al., 1972) and the cosmic microwave background radiation (CMBR) (Penzias and Wilson, 1965). The term *gamma ray* is a generic one that includes photons of energy >0.511 MeV.

The spectrum of electromagnetic radiation from space covers an enormous range, over more than 30 orders of magnitude, from radio waves to ultrahigh energy gamma rays. This is illustrated in Fig. 5.52 which shows the so-called *grand unified photon spectrum* (GUPS) of the *diffuse extragalactic background radiation* (DEBRA) (Ressell and Turner, 1990). This spectrum was assembled from data obtained by many separate experiments through the years.

Modern astronomy employs the entire range of the electromagnetic spectrum from radio waves to gamma rays. Each spectral range provides information, which is unique and cannot be obtained by other means. Gamma radiation represents the most energetic part of the electromagnetic spectrum and yields direct information about high energy processes in the Universe.

X- and gamma ray astronomy are complementary to cosmic ray particle physics and open completely new perspectives that can help to reveal locations of potential sources of cosmic rays. During the past two decades these disciplines have evolved rapidly into vast and highly specialized fields of science.

Since charged particles are subject to deflection when propagating in magnetic fields, the arrival direction of charged cosmic rays cannot reveal the direction of location of their source because of the presence of randomly oriented magnetic fields in space. On the other hand, gamma rays are not deflected by magnetic fields and are therefore pointing toward their source.

Nevertheless, like charged particles, gamma rays, too, are subject to interactions with the photon fields in space and interstellar matter (cf Chapter 5, Section 5.2). As a result they cannot propagate indefinitely without being scattered and loosing a large fraction of their energy.

The cross section for a photon - photon head on collision between a photon of energy E_γ and a background photon of energy E_b, for the production of pairs of particles with mass m is given by (Wdowczyk et al., 1972; see also Jauch and Röhrlich, 1955)

$$\sigma_1 = \pi r_0^2 \left(\frac{m}{\omega}\right)^2 \left\{2 \ln\left(\frac{2\omega}{m}\right) - 1\right\} \tag{5.6}$$

for $\omega >> m$, i.e., in the extreme relativistic region, and

$$\sigma_2 = \pi r_0^2 \left(1 - \frac{m^2}{\omega^2}\right)^{1/2} \tag{5.7}$$

for ω close to m, i.e., in the classical region. In either case

$$\omega = \sqrt{E_\gamma E_b} \tag{5.8}$$ and $$r_0 = \frac{e^2}{mc^2} \tag{5.9}$$

For the interaction length we can write

$$\lambda_{int} = \frac{1}{n\sigma} \tag{5.10}$$

where n is the number of target photons per unit volume.

Figure 5.53 shows the energy dependence of the interaction length, λ_{int}, of photons with the various electromagnetic radiation fields in space. The most important process is electron pair production but at a sufficiently high value of E_γ muon pair production sets in, too.

Gamma ray experiments are carried out in space on board of satellites, at the fringes of the atmosphere with balloon-borne instruments and at ground level. Space and balloon-borne gamma ray astronomy extends over more than five orders of magnitude in energy and aims at the low energy radiation that cannot be detected at ground level because of atmospheric absorption. It is based on direct detection of the photons with spectrometers whereas ground-based measurements employ indirect methods, such as air shower techniques, mostly air Cherenkov methods for the energy range from $\sim$100 GeV to $\sim$100 TeV, and common air shower arrays or hybrid systems at higher energies.

At present the energy range between about 10 GeV and a few 100 GeV is difficult to explore. The rapidly decreasing event rate with increasing energy and the size and weight limits of conventional satellite detectors sets an upper energy limit to space-bound spectral gamma ray investigations. On the other hand the low energy cutoff for ground-based measurements using the air Cherenkov technique is given by the column density of the atmosphere, its

absorption properties, and the detector sensitivity. Presently the installation with the lowest threshold for ground based observations is the Cangaroo narrow-beam imaging Cherenkov telescope at Woomera (Australia) (160 m a.s.l.) (Bhat, 1997; Matsubara, 1997), and for conventional arrays it is the air shower array at Yangbajing in Tibet (Amenomori et al., 1999a; Yuda, 1996).

In the following, after a brief general survey, we present a summary of recent data on the diffuse galactic and cosmic gamma ray background. This is followed by a few comments on point sources, including a limited set of tabulated data of low and high energy gamma ray sources. As examples we present some spectral data of the Crab Nebula and pulsar, and of Markarian 501. Finally, we outline the relevance of gamma ray line spectra.

We do not elaborate on the vast and rapidly evolving subjects of X- and gamma ray astronomy, nor do we discuss the many discrete sources and their individual properties. We only give a general overview, focusing mostly on gamma radiation. The interested reader is referred to the detailed literature for these and related topics, such as the books by P.V. Ramana Murthy and A.W. Wolfendale (1993), Hillier (1984), Chupp (1976), and Stecker (1971), as well as conference proceedings and reviews (e.g., Weekes, 1988; Trümper, 1993; Ong, 1998; Buckley, 2000). A short but interesting account of the early history of gamma ray astronomy is given by Pinkau (1996).

5.4.2 General Survey of Gamma Radiation

When discussing cosmic gamma ray sources we distinguish between point sources, extended sources, and the diffuse galactic and diffuse cosmic radiation. Superimposed on a continuum are γ-ray emission lines that signal the presence of distinct radioactive isotopes which reveal locations where nucleosynthesis or nuclear reactions are taking place, and positron-electron annihilation lines.

Since the discovery of the first X-ray source by Giacconi et al. (1962) and the discovery of Kraushaar et al. (1972) who showed that the Milky Way could be seen in the light of gamma rays, a large number of experiments had been carried out, covering the spectral range from some 10 keV to PeV, using all available techniques, to search for gamma ray sources. Balloon and space-borne measurements explore the energy region up to $\sim$30 GeV whereas ground-based measurements cover the range above a $\sim$100 GeV, as explained earlier. Besides carrying out general searches for distinct X- and gamma ray sources in space, the galactic center but also particular objects in our own

Galaxy as well as extragalactic objects and the diffuse background were the targets of intense scientific investigations during the past two decades.

The COS-B detector made the first complete gamma ray map of the Milky Way and the Compton Observatory carried out the first all-sky survey. The latter, which has a sensitivity that is about ten times higher than that of COS-B, produced the first all-sky gamma ray map in the energy window from about 1 MeV to more than 1 GeV and acquired a great wealth of new data (cf Schönfelder, 1993a, 1993b, 1996 and references listed therein). The systematic analysis of the data from this experiment revealed that *spin-down pulsars* and *X-ray binaries* are the most intense permanent sources in our Galaxy and that the interstellar medium itself is a strong, though extended source of radiation.

In addition, supernova remnants and interstellar clouds had been identified as gamma ray contributors superimposed on the large-scale emission, and a large number of *gamma ray lines* from nucleosynthesis and nuclear reactions have been observed, mostly in the direction of the galactic center. In extragalactic space *gamma ray blazars*, i.e., certain types of active galactic nuclei (AGN) emitting high energy gamma rays, had been discovered (Hartman et al., 1999), and measurements of the diffuse cosmic gamma ray background have been significantly improved in recent years. On the other hand, the origin of cosmic *gamma ray bursts*, i.e., short astrophysical bursts of MeV gamma radiation, remains uncertain. They seem to be of cosmological origin and it appears that at least some are correlated with high-z (redshift) extragalactic objects (Piran, 1999).

The galactic plane stands out clearly against the rest of the sky. Part of its emission is due to discrete sources, the brightest are Crab, Geminga, Vela and the Cygnus region. The dominant galactic emission, however, is attributed to the diffuse galactic component that comes from interstellar space. Superimposed on this radiation is the diffuse cosmic gamma ray background. There are many discrete sources at medium and high galactic latitudes. Most of them are gamma ray blazars.

It is worth noting that there are sources which are visible only at low energies and not at high energies, and vice versa; in addition, there seems to be much more structure and scattering at low energies. At higher energies the emission shows a stronger concentration towards the galactic plane. Most of the sources along the galactic plane remain unidentified.

The ground-level work focuses mostly on the search for ultra high energy sources that could be potential sources of energetic cosmic rays. The first upper limits of the diffuse ultra high energy gamma ray background were

determined by Toyoda et al. (1965) with the air shower installation at Mt. Chacaltaya (5200 m a.s.l.) in Bolivia and by Firkowski et al. (1965) with the installation at Lodz (s.l.) in Poland, using so-called muon-poor air showers.

Subsequently high energy point sources such as the Crab Nebula and Pulsar , and others were discovered (Weekes et al., 1989). Some of the sources appear to have ceased their one-time high activity, such as Cygnus X-3 (Vladimirsky et al., 1973; Neshpor et al., 1979; Samorski and Stamm, 1983, and Protheroe, 1987). For reviews of ground-based high energy gamma ray astronomy the reader is referred to the articles by Weekes (1988), Dogiel (1996), Bhat (1997) and Ong (1998), and proceedings of workshops (see Kifune, 1995 and 1996; Völk and Aharonian, 1996; de Jager, 1997; Buckley, 2000; Dorman, 2000).

5.4.3 Diffuse Galactic Gamma Radiation

The diffuse galactic continuum emission is believed to be primarily due to interactions of cosmic ray nuclei with interstellar matter. The galactic plane stands out clearly with respect to the rest of the Galaxy at all energies. Superimposed on the diffuse galactic radiation is the contribution from the extragalactic diffuse radiation which is usually taken as being isotropic. The two are difficult to separate, as will be discussed later. In addition there are low energy photons.

The three major components of the diffuse galactic gamma ray emission are a) from the decay of neutral pions (π^0) that result chiefly from nuclear interactions of cosmic rays with the interstellar medium, b) from bremsstrahlung of cosmic ray electrons, and c) from inverse Compton scattering of cosmic ray electrons with photons of the galactic radiation fields. Measurements of the intensity of the diffuse gamma radiation yield information on the cosmic ray and matter (hydrogen) densities and on the density gradient of the cosmic radiation.

An early compilation of data on the differential energy spectrum of the diffuse gamma radiation for high galactic latitudes and the energy range from 100 keV to 1 GeV was made by Fichtel et al. (1978) and is illustrated in Fig. 5.54. In this work an attempt was made to estimate the fractions of the contributions from the isotropic and galactic components.

More recently, the gamma ray spectrum of the inner part of the Galaxy ($|l| \leq 60°$) has been measured over the entire space-borne gamma ray astronomy range from about 100 keV to over 10 GeV and is shown in Fig. 5.55. The data include results from SIGMA at low energies, from COMP-

TEL at medium energies, and from COS-B at high energies (Strong et al., 1994; Schönfelder, 1996).

In the analysis of the COMPTEL data the authors have assumed that the gamma ray intensity from the direction of the galactic plane contains five different components: the neutral hydrogen component, the molecular hydrogen component, the inverse Compton component, a contribution from gamma ray sources and a contribution from the cosmic diffuse background. The resulting intensity spectrum from the inner Galaxy ($-60° < l < +60°$, $-20° < b < +20°$) connects well to the SIGMA spectrum at lower energies and to the COS-B spectrum at higher energies.

Also indicated in Fig. 5.55 are theoretical predictions for the contributions of electron bremsstrahlung, inverse Compton scattering, and π^0-decay to the X- and gamma ray flux. The two electron induced components were calculated from the equilibrium cosmic ray electron spectrum derived from a three-dimensional diffusion model (Strong et al., 1996). The sum of the three theoretical components gives a reasonable fit to the overall spectrum. It appears that below 1 MeV and above 100 GeV the inverse Compton component dominates even within the galactic plane.

A similar but still more recent analysis of data from the COMPTEL and EGRET instruments of measurements of the inner Galaxy, taken over a somewhat smaller longitudinal region and lower galactic latitude range, is presented in Fig. 5.56 (Strong et al., 1999a; see also Strong et al., 1996 and Paul, 1997). Note that the ordinates of Figs. 5.55 and 5.56 are multiplied with E^2 to emphasize the slope variations of the spectrum.

A summary of spectral measurements at high galactic latitudes towards the galactic poles ($|b| \geq 70°$) for $z_h = 4$ kpc is shown in Fig. 5.57 together with predicted spectra from the main contributing processes, from a calculation of Strong et al. (1999a).

Figures 5.58 and 5.59 are two additional plots showing compilations of diffuse galactic gamma ray spectral measurements. In the first (Fig. 5.58) the data are shown in the usual double logarithmic representation whereas in the second (Fig. 5.59) the flux is multiplied by the energy squared (Purcell et al., 1995 and 1996). The galactic region from where the data were collected are indicated. In either figure the 511 keV positron-electron annihilation line, discussed later, is evident.

In Fig. 5.60 we show an evaluation of data from the EGRET instrument of measurements of the diffuse emission of the inner Galaxy ($300° \leq l \leq 60°$, $|b| \leq 10°$) (~ 0.73 sr) which covers the energy range from about 30 MeV

Table 5.31: Diffuse Cosmic Gamma Ray Intensities.
(Schönfelder et al., 1980)

Energy [MeV]	Intensity $[cm^{-2}s^{-1}sr^{-1}MeV^{-1}]$
1.1 - 2.0	$(1.2 \pm 0.7) \cdot 10^{-2}$
2 - 3	$(4.8 \pm 2.0) \cdot 10^{-3}$
3 - 5	$(1.75 \pm 0.6) \cdot 10^{-3}$
5 - 10	$(6.75 \pm 2.5) \cdot 10^{-4}$
10 - 20	$(5.4 \pm 5.0) \cdot 10^{-5}$

to 50 GeV. Shown, too, are the contributions from the different processes according to a model calculation (Hunter et al., 1997).

5.4.4 Diffuse Cosmic Gamma Radiation

The determination of the cosmic background radiation is a very difficult task. The reason is that an absolute measurement is required and that the background problem is extremely serious. Measurements must be made with the instrument pointing away from the galactic center and disk, at high galactic latitude, and preferentially in the direction of the *galactic anti-center* ($90° \leq l \leq 270°$).

In Table 5.31 we give the results of a measurement of the diffuse cosmic gamma ray component with the balloon-borne large-area Compton telescope of Schönfelder et al. (1980).

From these and earlier measurements it is known that the diffuse cosmic gamma ray background spectrum exhibits the so-called *MeV-bump*. Several processes were suggested to explain the feature. However, according to Kappadath et al. (1995) the analysis of the COMPTEL data does not support the existence of the bump above 2 MeV.

The data are consistent with extrapolations from higher and lower energies. Between 0.75 and 1.8 MeV only upper limits exist. These limits still allow for a small bump, but only in this small energy interval, as is shown in Fig. 5.61 (Kappadath et al., 1995). Figure 5.62 shows the spectrum of the diffuse cosmic X- and gamma ray background radiation assembled from measurements of several experiments (Schönfelder, 1996).

Kappadath et al. (1995) show that adding the 5 GV rigidity dependent

background measured with COMPTEL to the diffuse cosmic gamma ray component yields flux levels that agree well with the earlier balloon measurements of White et al. (1977) and Schönfelder et al. (1980), carried out from Palestine, Texas (rigidity 5 GV) (Fig. 5.61). It is therefore concluded that the balloon data contained an unidentified instrumental background component. A similar effect could explain the MeV bump that was observed in the Apollo XV data, since the measurement was performed at a cutoff rigidity that was essentially zero (Trombka et al., 1977).

The origin of the diffuse cosmic gamma ray background remains an open question. The gamma ray measurements of AGNs raise the question whether a real diffuse component is still needed to understand the cosmic background spectrum. Unresolved blazars and AGNs may explain at least part of the high energy gamma ray background, as Quasars and Seyfert galaxies have explained most of the X-ray background.

An estimate of the contribution of galaxy clusters to the diffuse cosmic gamma ray background has been made some time ago by Houston et al. (1984). These authors obtain for the contribution of clusters out to a Hubble radius of 6000 Mpc to the universal gamma ray flux, $J_{\gamma,EG}$, assuming no evolutionary effects, values of

$$J_{\gamma,EG}(35 - 100\,\mathrm{MeV}) \simeq 6.3 \cdot 10^{-4}\ \mathrm{photons\ cm^{-2}\,s^{-1}} \qquad (5.11)$$

and

$$J_{\gamma,EG}(> 100\,\mathrm{MeV}) \simeq 1.1 \cdot 10^{-4}\ \mathrm{photons\ cm^{-2}\,s^{-1}}\ . \qquad (5.12)$$

Thus, they conclude that the cluster contribution can amount to a significant fraction.

5.4.5 Point Sources

In Table 5.32 we show an older list of very high energy gamma ray sources which have been observed with ground based installations (Weekes, 1988). Some relevant parameters, including the nature of the sources and the gamma ray flux at a particular energy are given. A more recent list, shown in Table 5.33, produced by the HEGRA group has also been included (Karle et al., 1995).

Unfortunately many of the high energy point sources have not been seen at comparable levels since their discovery and seem to have faded away. The most prominent example is Cygnus X-3, illustrated in Fig. 5.63 (Borione et al., 1995; see also Hillas, 1996). Shown are the initially estimated integral

Table 5.32: List of Very High Energy Gamma Ray Point Sources (Weekes, 1988)

Source	Periodicity	Hemi-sphere	Energy	Flux $[cm^{-2}s^{-1}]$	Distance [kpc]
Pulsars					
Crab	33 ms	N	1 TeV	$4 \cdot 10^{-12}$	2.0
Vela	89.2 ms	S	1 Tev	$3 \cdot 10^{-12}$	0.5
PSR 1937+21	1.56 ms	N	1 Tev	$2 \cdot 10^{-11}$	5
PSR 1953+29	6.13 ms	N	1 TeV	$1.2 \cdot 10^{-12}$	3.5
PSR 1802-23	112 ms	S	1 TeV	$2.3 \cdot 10^{-10}$	2.7
Binary X-Ray Sources					
Cygnus X-3	4.8 h	N	1 TeV	$5 \cdot 10^{-11}$	> 11.4
			100 TeV	10^{-13}	
			1 PeV	$2 \cdot 10^{-14}$	
Hercules X-1	1.24 s	N	1 Tev	$3 \cdot 10^{-11}$	5
			0.5 PeV	$3 \cdot 10^{-12}$	
4U0115+63	3.61 s	N	1 TeV	$7 \cdot 10^{-11}$	5
Vela X-1	8.96 d	S	1 TeV	$2 \cdot 10^{-11}$	1.4
		S	3 PeV	$9 \cdot 10^{-15}$	
Cen X-3	2.09 d	S	? PeV	?	10
LMC X-4	1.41 d	S	10 Pev	$5 \cdot 10^{-15}$	50
Supernova Remnants					
Crab Nebula	steady	N	1 TeV	$1 \cdot 10^{-11}$	2
	variable		1 PeV	$1 \cdot 10^{-13}$	
Radio Galaxies					
Cen A	steady	S	1 TeV	$4 \cdot 10^{-12}$	4400

flux levels derived from measurements made with the Kiel and subsequently the Haverah Park array and an anticipated spectrum (curve C) (Samorski and Stamm, 1983; Lloyd-Evans et al., 1983). Also plotted are upper limits determined with other installation during later epochs.

Significant galactic point sources are the Crab Nebula and pulsar, the Vela pulsar, Cyg X-1, the Gregory-Taylor radio source GT 0236+610 (COS-B source 2CG135+01), and a strong unidentified source at 1-18°. Extragalactic sources include 3C273 and Cen-A. In addition the region around the Large

Table 5.33: Flux Limits of some Gamma Ray Point Source Candidates (Karle et al., 1995)

Object	$E_{th}^{*)}$ [TeV]	$\sigma^{**)}$	Flux $[\cdot 10^{-13}\ \mathrm{cm}^{-2}\,\mathrm{s}^{-1}]$
Cygnus X-3	25.1	1.16	4.09
Cygnus X-1	24.1	-0.79	1.97
Hercules X-1	23.3	-0.54	2.24
Crab-Nebula	24.2	-0.78	1.78
Geminga	24.3	-0.03	2.38
AM Her	27.8	1.79	4.59
AE Aqr	33.5	0.77	3.44
V404 Cyg	24.3	0.44	3.20
SS Cyg	25.9	-0.14	2.46
SS 433	28.1	-0.09	2.64
4U 0115+63	52.2	-0.88	1.09
1E 2259+586	40.6	-1.15	1.14
PSR 1855+09	26.2	-1.10	1.77
PSR 1937+21	24.2	-0.91	1.92
PSR 1953+29	23.9	0.42	3.27
PSR 1957+20	24.1	-1.06	1.84
2CG 028+15	31.2	1.70	4.92
2CG 034+00	33.3	-2.16	1.02
2CG 054+03	23.8	-0.48	2.32
2CG 070+06	24.1	-1.51	1.51
2CG 076+00	24.6	1.46	4.67
2CG 078+02	24.8	-0.03	2.62
2CG 082+03	26.2	1.22	4.05
2CG 135+01	41.5	0.73	2.65
2CG 139+00	39.6	-0.73	1.25
NGC 4151	25.2	1.39	4.27
3C 273	33.2	-0.17	2.29
3C 279	29.7	0.59	3.23
Mrk 421	25.3	-1.71	1.24
Mrk 501	24.0	0.79	3.72
Mrk 1505	25.7	-1.50	1.34
Mrk 1506	30.0	-1.15	1.46
QSO 2200+420	25.8	-0.64	2.01
PKS 0528+134	25.4	1.07	3.70
PKS 2251+158	25.0	1.24	4.71

*) E_{th} Energy threshold for 50% detection efficiency. **) σ Statistical significance.

Magellanic Cloud (LMC) shows enhanced emission of an unknown nature. Of the firmly established point sources the Crab has become a sort of reference

source or "standard candle".

In Fig. 5.64 we show the differential energy spectrum of the Crab Nebula over the energy range from 100 keV to 100 TeV. It is the most significant galactic gamma ray source. The continuous curves indicate the contributions from different processes according to model calculations of de Jager et al. (1995). A compilation of new differential flux data of the Crab Nebula is presented in Fig. 5.65 and the flux detected with the HEGRA detector is given in Table 5.34 (Aharonian et al., 2000). According to these authors the Crab spectrum can be fitted in the energy range between 1 and 20 TeV by a simple power law as given below with energy E in units of TeV.

$$\frac{dJ_\gamma}{dE} = (2.79 \pm 0.02 \pm 0.5) \cdot 10^{-11} E^{(-2.59 \pm 0.03 \pm 0.05)} \quad [\text{ph cm}^{-2}\ \text{s}^{-1}\ \text{TeV}^{-1}] \tag{5.13}$$

A fit with a logarithmic steepening of the power law spectrum yields

$$\frac{dJ_\gamma}{dE} = (2.67 \pm 0.01 \pm 0.5) \cdot 10^{-11} E^{(-2.47 \pm 0.1 \pm 0.05 - (0.11 \pm 0.10)\log(E))} \quad [\text{ph cm}^{-2}\ \text{s}^{-1}\ \text{TeV}^{-1}] \tag{5.14}$$

The integral spectrum of the Crab Nebula is given in Fig. 5.66, and a compilation of data points from ground-based measurements, covering the high energy range from 0.3 TeV to almost 100 TeV, and upper limits to 1 PeV, in Fig. 5.67. Finally the spectrum of the Crab pulsar is shown in Fig. 5.68.

Spin-down pulsars are known to be isolated rotating neutron stars and gamma ray emitters. It is interesting to note that the peaks of the light curves in the different wavelength regions of the spectrum, i.e., optical, radio, X- and gamma ray, of many objects are not in phase. An exception is the Crab pulsar where the different wavelength regimes are in phase.

Active galactic nuclei (ANG) are the most powerful compact objects in the Universe. A supermassive object, probably a black hole, is presumably located at the center of each, and the accretion of matter is most likely the power source. The EGRET instrument detected about 50 AGNs with blazar properties (Fichtel, 1996). A list of strong AGN sources is given by Hunter (1995) and is reproduced in Table 5.35.

Powerful high energy extragalactic gamma ray sources are Markarian 421 (Punch et al., 1992) and Markarian 501 (Quinn et al., 1996). Of these two

Table 5.34: Crab Nebula Differential Gamma Ray Spectrum.
(Aharonian et al., 2000)

Energy [TeV]	dJ_γ/dE [ph cm^{-2} s^{-1} TeV^{-1}]	σ_{stat} [ph cm^{-2} s^{-1} TeV^{-1}]	σ_{syst} [ph cm^{-2} s^{-1} TeV^{-1}]
0.65	$7.44 \cdot 10^{-11}$	$5.25 \cdot 10^{-12}$	$(+2.31 - 1.79) \cdot 10^{-11}$
0.87	$3.74 \cdot 10^{-11}$	$2.50 \cdot 10^{-12}$	$(+5.98 - 5.61) \cdot 10^{-12}$
1.16	$1.95 \cdot 10^{-11}$	$1.39 \cdot 10^{-12}$	$(+1.94 - 1.94) \cdot 10^{-12}$
1.54	$9.25 \cdot 10^{-12}$	$1.58 \cdot 10^{-13}$	$(+8.32 - 7.40) \cdot 10^{-13}$
2.05	$4.25 \cdot 10^{-12}$	$1.03 \cdot 10^{-13}$	$(+3.42 - 2.97) \cdot 10^{-13}$
2.74	$2.20 \cdot 10^{-12}$	$7.72 \cdot 10^{-14}$	$(\pm 1.54) \cdot 10^{-13}$
3.65	$9.78 \cdot 10^{-13}$	$5.17 \cdot 10^{-14}$	$(\pm 5.87) \cdot 10^{-14}$
4.87	$4.43 \cdot 10^{-13}$	$3.25 \cdot 10^{-14}$	$(\pm 2.66) \cdot 10^{-14}$
6.49	$2.32 \cdot 10^{-13}$	$3.40 \cdot 10^{-14}$	$(\pm 1.39) \cdot 10^{-14}$
8.66	$1.20 \cdot 10^{-13}$	$2.45 \cdot 10^{-14}$	$(\pm 7.19) \cdot 10^{-15}$
11.55	$5.64 \cdot 10^{-14}$	$1.68 \cdot 10^{-14}$	$(\pm 3.38) \cdot 10^{-15}$
15.40	$2.28 \cdot 10^{-14}$	$1.07 \cdot 10^{-14}$	$(\pm 1.36) \cdot 10^{-15}$
20.54	$1.14 \cdot 10^{-14}$	$7.55 \cdot 10^{-15}$	$(\pm 6.85) \cdot 10^{-16}$

relatively nearby sources (both have similar redshifts of $z \approx 0.03$), Mrk 501 entered in March 1997 a state of remarkably flaring activity that lasted for almost half a year exhibiting highly variable and strong gamma ray emission. In spite of the fact that Mrk 501 is approximately 100,000 times further away than Crab its TeV gamma ray flux frequently exceeded that of Crab by a factor of 2 to 10 (Amenomori et al., 1999b). Fig. 5.69 shows spectral measurements of this object made with several installations.

5.4.6 Gamma Ray Line Spectra

Gamma Ray Lines from Nucleosynthesis and Nuclear Reactions

Gamma ray line spectroscopy is a powerful tool, for studying chemical element production and nuclear reactions in the Universe. A lists of the most important radioactive isotopes that are produced in nucleosynthesis processes is shown in Table 5.36. The decay times range from a few months to more than one million years.

Of particular interest is the radio isotope ^{26}Al with its 1.809 MeV gamma line. Due to its long decay time of $1.04 \cdot 10^6$ years ^{26}Al traces galactic nucleosynthesis processes over the past million years. The COMPTEL telescope

Table 5.35: Strong AGN Gamma Sources Detected by EGRET (Fichtel et al., 1994; Hunter, 1995)

Source ID	Flux E>100 MeV [$\cdot 10^{-6}$ cm^{-2} s^{-1}]	Photon Spectral Index	z	Other Names
0202+149	0.26 ± 0.06	2.5 ± 0.1		4C+15.05,PKS
0208−512	1.1 ± 0.07	1.7 ± 0.1	1.003	PKS
0234+285	0.16 ± 0.04		1.213	4C+28.0,PKS
0235+164	0.82 ± 0.09	2.0 ± 0.2	0.94	OD+160,PKS
0420−014	0.45 ± 0.10	1.9 ± 0.3	0.92	OA 129,PKS
0446+112	1.04 ± 0.19	1.8 ± 0.3		PKS
0454−463	0.13 ± 0.03		0.858	PKS
0528+134	1.13 ± 0.08	2.6 ± 0.1	2.06	OG+147,PKS
0537−441	0.32 ± 0.08	2.0 ± 0.2	0.894	PKS
0716+714	0.50 ± 0.12	2.4 ± 0.3		
0804+499	2.9		1.43	
0827+243	0.18 ± 0.04		2.046	
0836+710	0.34 ± 0.10	1.9 ± 0.4	2.17	4C+71.07
0954+658	0.20	1.7 ± 0.2	0.368	
1101+384	0.15 ± 0.03	1.9 ± 0.1	0.031	Mrk 421
1156+295	0.63 ± 0.15		0.729	4C+29.45
1219+285	0.17 ± 0.04		0.102	ON 231
1222+216	0.17 ± 0.03		0.435	4C21.35
1226+023	0.14 ± 0.03	2.4 ± 0.1	0.158	3C273
1253−055	2.7 ± 0.1	1.9 ± 0.1	0.538	3C 279
1313−333	1.3		1.21	
1406−076	0.97 ± 0.09		1.494	OQ−010,PKS
1510−089	0.21 ± 0.05		0.361	OR−17,PKS
1606+106	0.33 ± 0.05	2.2 ± 0.3	1.23	4C+10.45
1611+343	0.33 ± 0.06		1.40	
1622−253	0.42 ± 0.05			PKS
1633+382	1.00 ± 0.08	1.9 ± 0.1	1.81	4C+38.4
1739+522	0.36 ± 0.05		1.38	4C+51.37
1741−038	0.23 ± 0.05		1.054	OT−68,PKS
2022−077	0.63 ± 0.11	1.5 ± 0.2		NRAO 629
2052−474	0.25 ± 0.05		1.489	PKS
2230+114	0.27 ± 0.04	2.6 ± 0.2	1.037	CTA 102
2251+158	0.81 ± 0.06	2.2 ± 0.1	0.859	3C 454.3

produced an all-sky map in 1.809 MeV ^{26}Al emission lines. On this map the galactic plane stands out clearly. There is only weak emission of the 1.809 MeV line from medium latitudes and no measurable signal from high latitudes (Schönfelder, 1996).

Table 5.36: Gamma Lines from Nucleosynthesis Processes (Schönfelder, 1996)

Decay Chain	Mean Life [y]	Emission, γ [MeV]
$^{56}Ni \rightarrow ^{56}Co \rightarrow ^{56}Fe$	0.31	e^+, 0.847, 1.238
$^{57}Ni \rightarrow ^{57}Co \rightarrow ^{57}Fe$	1.1	0.014, 0.122
$^{22}Na \rightarrow ^{22}Ne$	3.8	e^+, 1.275
$^{44}Ti \rightarrow ^{44}Sc \rightarrow ^{44}Ca$	78	e^+, 0.068, 0.078, 1.156
$^{60}Fe \rightarrow ^{60}Co \rightarrow ^{60}Ni$	$2.2 \cdot 10^6$	0.059, 1.173, 1.332
$^{26}Al \rightarrow ^{26}Mg$	$1.1 \cdot 10^6$	e^+, 1.809

511 keV Positron-Electron Annihilation Line

The 511 keV positron-electron annihilation line is another important observable (Kinzer, 1996). Strong annihilation radiation signals the presence of high positron density and implies the presence of matter in interaction with the cosmic radiation. Observations from different positions along the galactic plane are consistent with the existence of a bulge component of about 10 degrees radius around the Galactic center, and of a much thinner disk component along the plane.

5.4.7 Gamma Ray Fraction of Cosmic Radiation

Several experiments have been carried out to determined the fraction of the *isotropic* gamma ray content in the total cosmic ray flux. The selection criterion in the search for gamma ray initiated showers when using air shower arrays is to look for muon-poor showers, i.e., showers that have a muon content which is typically $\leq 5\%$ of that of normal showers. In Fig. 5.70 we show a compilation of Sasano et al. (1999) of the isotropic gamma ray to cosmic ray ratio covering the primary energy range from about 30 TeV to 10^4 TeV that includes the results of five different investigations.

References

Aglietta, M., B. Alessandro, P. Antonioli, F. Arneodo, L. Bergamasco, A. Campos Fauth, C. Castagnoli, A. Castellina, C. Cattadori, A. Chiavassa, G. Cini, B. D'Ettore Piazzoli, G. Di Sciascio, W. Fulgione, P. Galeotti, P.L. Ghia, M. Iacovacci, G. Mannocchi, C. Morello, G. Navarra, L. Riccati, O.

Saavedra, G.C. Trinchero, P. Vallania, and S. Vernetto: PICRC, 1, p. 216 (1993).

Aglietta, M., B. Alessandro, P. Antonioli, F. Arneodo, L. Bergamasco, A. Campos Fauth, C. Castagnoli, A. Castellina, C. Cattadori, A. Chiavassa, G. Cini, B. D'Ettore Piazzoli, G. Di Sciascio, W. Fulgione, P. Galeotti, P.L. Ghia, R. Granella, M. Iacovacci, A. Lima de Godoi, G. Mannocchi, C. Melagrana, N. Mengotti, C. Morello, G. Navarra, H. Nogima, L. Riccati, O. Saavedra, G.C. Trinchero, P. Vallania, and S. Vernetto, and C. Vigorito: Astropart. Phys., 6, p. 71 (1996).

Aharonian, F.A., A.G. Akhperjanian, J.A. Barrio, K. Bernlöhr, H. Bojahr, I. Calle, J.L. Contreras, J. Cortina. S. Denninghoff, V. Fonsexa, J.C. Gonzales, N. Götting, G. Heinzelmann, M. Hemberger, G. Hermann, A. Heusler, W. Hofmann, D. Horns, A. Ibarra, R. Kankanyan, M. Kestel, J. Kettler, C. Köhler, A. Kohnle, A. Konopelko, H. Kornmeyer, D. Kranich, H. Krawczynski, H. Lampeitl, A. Lindner, E. Lorenz, F. Lucarelli, N. Magnussesn, O. Mang, H. Meyer, R. Mirzoyan, A. Moralejo, L. Padilla, M. Panter, R. Plaga, A. Plyasheshnikov, J. Prahl, G. Pühlhofer, G. Rauterberg, A. Röhring. V. Sahakian, M. Samorski, M. Schilling, D. Schmele, F. Schröder, W. Stamm, M. Tluczykont, H.J. Völk, B. Wiebel-Sooth, C. Wiedner, M. Willmer, and W. Wittek: Astrophys. J., 539, p. 317 (2000).

Akerlof, C.W., J. DiMarco, H. Levy, D. Meyer, P. Radusewicz, R. Tschirhart, and Z. Yama: Proc. Gamma Ray Observatory Science Workshop (NASA / GSFC), ed. W.N. Johnson (Washington: Naval Research Laboratory) 4 (1989).

Alexandreas, D.E., G. Allen, D. Berley, S. Biller, R.L. Burman, D.R. Cady, M. Cavalli-Sforza, C.Y. Chang, D. Coyne, C. Dion, G.M. Dion, D. Dorfan, R.W. Ellsworth, S.J. Freedman, B.K. Fujikawa, J.A. Goodman, T.J. Haines, C.M. Hoffman, L. Kelley, S. Klein, D.A. Krakauer, P.W. Kwok, X,-Q. Lu, D.E. Nagle, M. Potter, V.D. Sandburg, C. Sinnis, A. Shoup, M.J. Stark, P.R. Vishwanath, D.D. Weeks, D.A. Williams, J.-P. Wu, G.B. Yodh, and W.P. Zhang (CYGNUS Collaboration): Astrophys. J., 405, p. 353 (1993a).

Alexandreas, D.E., G.E. Allen, D. Berley, S. Biller, R.L. Burman, M. Cavalli-Sforza, C.Y. Chang, M.L. Chen, P. Chumney, D. Coyne, C.L. Dion, G.M. Dion, D. Dorfan, R.W. Ellsworth, J.A. Goodman, T.J. Haines, M. Harmon, C.M. Hoffman, L. Kelley, S. Klein, D.E. Nagle, D.M. Schmidt, R. Schnee, C. Sinnis, A. Shoup, M.J. Stark, D.D. Weeks, D.A. Williams, J.-P. Wu, T. Yang, G.B. Yodh, and W.P. Zhang: PICRC, 1, p. 373 (1993b).

Alexandreas, D.E., et al.: PICRC, 1, p. 353 (1993c).

Amenomori, M., Z. Cao, L.K. Ding, Z.Y. Feng, K. Hibino, N. Hotta, Q. Huang, A.X. Huo, H.Y. Jia, G.Z. Jiang, S.Q. Jiao, F. Kajino, K. Kasahara, Labaciren, D.M. Mei, L. Meng, X.R. Meng, Mimaciren, K. Mizutani, J. Mu, H. Nanjo, M. Nishizawa, Nusang, A. Oguro, M. Ohnishi, I. Ohta, J.R. Ren, To. Saito, M. Sakata, Z.Z. Shi, M. Shibata, T. Shirai, H. Sugimoto, X.X. Sun, K. Taira, Y.H. Tan, N. Tateyama, S. Torii, M. Tsukamoto, H. Wang, C.Z. Wen, Y. Yamamoto, X.Y. Yao, G.C. Yu, P. Yuan,T. Yuda, J.G. Zeng, C.S. Zhang, H.M. Zhang, L. Zhang, Zhasang, Zhaxiciren, and W.D. Zhou: PICRC, 1, p. 342 (1993).

Amenomori, M., Z. Cao, L.K. Ding, Z.Y. Feng, K. Hibino, N. Hotta, Q. Huang, A.X. Huo, H.Y. Jia, G.Z. Jiang, S.Q. Jiao, F. Kajino, K. Kasahara, Labaciren, D.M. Mei, L. Meng, X.R. Meng, Mimaciren, K. Mizutani, J. Mu, H. Nanjo, M. Nishizawa, Nusang, A. Oguro, M. Ohnishi, I. Ohta, J.R. Ren, To. Saito, M. Sakata, Z.Z. Shi, M. Shibata, T. Shirai, H. Sugimoto, X.X. Sun, A. Tai, K. Taira, Y.H. Tan, N. Tateyama, S. Torii, H. Wang, C.Z. Wen, Y. Yamamoto, X.Y. Yao, G.C. Yu, P. Yuan,T. Yuda, J.G. Zeng, C.S. Zhang, H.M. Zhang, L. Zhang, Zhasang, Zhaxiciren, and W.D. Zhou: PICRC, 3, p. 181 (1997).

Amenomori, M., S. Ayabe, P.Y. Cao, Danzengluobu, L.K. Ding, Z.Y. Feng, Y. Fu, W.W. Guo, M. He, K. Hibino, N. Hotta, Q. Huang, A.X. Huo, K. Izu, H.Y. Jia, F. Kajino, K. Kasahara, Y. Katayose, Labaciren, J.Y. Li, H. Lu, S.L. Lu, G.X. Luo, X.R. Meng, K. Mizutani, J. Mu, H. Nanjo, M. Nishizawa, M. Ohnishi, I. Ohta, T. Ouchi, J.R. Ren, To. Saito, M. Sakata, T. Sasaki, Z.Z. Shi, M. Shibata, A. Shiomi, T. Shirai, H. Sugimoto, K. Taira, Y.H. Tan, N. Tateyama, S. Torii, T. Utsugi, C.R. Wang, H. Wang, H.Y. Wang, P.X. Wang, X.M. Xu, Y. Yamamoto, G.C. Yu, A.F. Yuan, T. Yuda, C.S. Zhang, H.M. Zhang, J.L. Zhang, N.J. Zhang, X.Y. Zhang, Zhaxisangzhu, Zhaxiciren, and W.D. Zhou: PICRC, 3, p. 456 (1999a).

Amenomori, M., S. Ayabe, P.Y. Cao, Danzengluobu, L.K. Ding, Z.Y. Feng, Y. Fu, W.W. Guo, M. He, K. Hibino, N. Hotta, Q. Huang, A.X. Huo, K. Izu, H.Y. Jia, F. Kajino, K. Kasahara, Y. Katayose, Labaciren, J.Y. Li, H. Lu, S.L. Lu, G.X. Luo, X.R. Meng, K. Mizutani, J. Mu, H. Nanjo, M. Nishizawa, M. Ohnishi, I. Ohta, T. Ouchi, J.R. Ren, To. Saito, M. Sakata, T. Sasaki, Z.Z. Shi, M. Shibata, A. Shiomi, T. Shirai, H. Sugimoto, K. Taira, Y.H. Tan, N. Tateyama, S. Torii, T. Utsugi, C.R. Wang, H. Wang, X.W. Xu, Y. Yamamoto, G.C. Yu, A.F. Yuan, T. Yuda, C.S. Zhang, H.M. Zhang, J.L. Zhang, N.J. Zhang, X.Y. Zhang, Zhaxisangzhu, Zhaxiciren, and W.D. Zhou: Astrophys. J., 525, p. L93 (1999b).

Barrau, A.: PhD Thesis, Université Joseph Fourier, Grenoble, France (1998).

Bartlett, L.M.: Ph.D. Thesis, University of Maryland (1994).

Bertsch, D.L., and D.A. Kniffen: Astrophys. J., 270, p. 305 (1983).

Bhat, Chaman, L.: PICRC, 8, p. 211 (1997).

Bloemen, H., W. Hermsen, B.N. Swanenburg, C.P. de Vries, R. Diehl, V. Schönfelder, H. Steinle, A.W. Strong, A. Connors, M. McConnell, D. Morris, G. Stacy, K. Bennett, and C. Winkler: Astrophys. J., Suppl. Ser. 92, p. 419 (1994).

Bloemen, H., et al.: Astroph. Lett. Comm. (3rd INTEGRAL Workshop) (1999) in press (after Strong et al., 1999a).

Borione, A., M.A. Catanese, C.E. Covault, J.W. Cronin, B.E. Fick, K.G. Gibbs, K.D. Green, D.B. Kieda, T.A. McKay, J. Matthews, B.J. Newport, D.F. Nitz, R.A. Ong, L.J. Rosenberg, D. Sinclair, and J.C. van der Velde: PICRC, 1, p. 286 (1993).

Borione, A., M. Catanese, C.E. Covault, J.W. Cronin, B.E. Fick, L.F. Fortson, K.G. Gibbs, M.A.K. Glasmacher, K.D. Green, D.B. Kieda, J. Matthews, B.J. Newport, D. Nitz, R.A. Ong, D. Sinclair, and J.C. van der Velde: PICRC, 2, p. 430 (1995).

Borione, A., M.A. Catanese, M.C. Chantell, C.E. Covault, J.W. Cronin, B.E. Fick, L.F. Fortson, J.F. Fowler, K.G. Gibbs, M.A.K. Glasmacher, K.D. Green, D.B. Kieda, J. Matthews, B.J. Newport, D.F. Nitz, R.A. Ong, L.J. Rosenberg, D. Sinclair, and J.C. van der Velde: Astrophys. J., 481, p. 313 (1997).

Bratolyubova-Tsulukidze, L.I., N.L. Grigorov, L.F. Kalinkin, A.S. Melioransky, Ye.A. Pryakhin, I.A. Savenho, and V.Ya. Yufarkin: Geomagnetism and Aeronomy (Soviet), 11, p. 585 (1971).

Buckley, J.H.: Rapporteur Paper XXVI Internat. Cosmic Ray Conf. (1999), AIP Conf. Proc., 516, p. 195 (2000)..

Carter-Lewis, D.A., S. Biller, P.J. Boyle, J.H. Buckley, A. Burdett, J. Bussons Gordo, M.A. Cantanese, M.F. Cawley, D.J. Fegan, J.P. Finley, J.A. Gaidos, A.M. Hillas, F. Krennrich, R.C. Lamb, R.W. Lessard, C. Masterson, J.E. McEnery, G. Mohanty, J. Quinn, A.J. Rodgers, H.J. Rose, F.W. Samuelson,G.H. Sembroski, R. Srinivasan, T.C. Weekes, M. West, J.A. Zweerink: PICRC, 3, p. 161 (1997).

Chantell, M.C., C.E. Covault, J.W. Cronin, B.E. Fick, L.F. Fortson, J.W. Fowler, K.D. Green, B.J. Newport, R.A. Ong, S. Oser, M.A. Catanese, M.A.K. Glasmacher, J. Matthews, D.F. Nitz, D. Sinclair, J.C. Van der Velde, and D.B. Kieda: Phys. Rev., 79, p. 1805 (1997).

Chupp, E.L.: Gamma Ray Astronomy, Reidel, Dordrecht (1976).

Claret, A., F. Lebrun, J. Paul, A.W. Strong, J.P. Roques, L. Bouchet, I. Malet, P. Mandrou, N. Khavenson, A. Dyachkov, V. Kovtunenko, R. Kremnev, N. Kuleshova, A. Sheikhet, K. Sukhanov, and I. Tserenin: Adv. Space Res., 15, No 5, p. 57 (1995).

Clear, J., K. Bennett, R. Buccheri, I.A. Grenier, W. Hermsen, H.A. Mayer-Hasselwander, and B. Sacco: Astron. Astrophys., 174, p. 85 (1987).

Daniel, R.R., G. Joseph, and P.J. Lavakare: Astrophys. and Space Sci., 18, p. 462 (1972).

De Jager, O.C., A.K. Harding, P. Sreekumar, and M.S. Strickmann: PICRC, 2, p. 174 (1995).

De Jager,O.C., A.K. Harding, P.F. Michelson, H.I. Nel, P.L. Nolan, P. Sreekumar, and D.J. Thompson: Astrophys. J., 457, p. 253 (1996).

De Jager, O.C.: Towards a Major Atmospheric Cherenkov Detector - V. Kruger National Park Workshop on TeV Gamma Ray Astrophysics. O.C. de Jager, ed., Space Research Unit, Potchefstroom University for CHE, Potchefstroom, South Africa (1997).

Djannati-Atai, A.: Ph.D. Thesis, Univ. of P. et M. Curie (Paris) (1994) (unpublished).

Djannati-Atai, THEMISTOCLE Collaboration: PICRC, 2, p. 315 (1995).

Dogiel, V.A.: Nuovo Cimento, 19 C, p. 671 (1996).

Dorman, L.I.: Rapporteur Paper XXVI Internat. Cosmic Ray Conf. (1999), AIP Conf. Proc., 516, p. 283 (2000)..

Fichtel, C.: Astron. Astrophys., Suppl. Ser., 120, p. 23 (1996).

Fichtel, C.E., R.C. Hartman, D.A. Kniffen, D.J. Thompson, G.F. Bignami, H. Ögelman, M.E. Özel, and T. Tümer: Astrophys. J., 198, p. 163 (1975).

Fichtel, C.E., G.A. Simpson, and D.J. Thompson: Astrophys. J., 222, p. 833 (1978).

Fichtel, C.E., D.L. Bertsch, R.C. Hartmann, S.D. Hunter, G. Kanbach, D.A. Kniffen, P.W. Kwok, Y.C. Lin, J.R. Mattox, H.A. Mayer-Hasselwander, P.F. Michelson, C. von Montigny, P.L. Nolan, K. Pinkau, H. Rothermel, E.J. Schneid, M. Sommer, P. Sreekumar, and D.J. Thompson: Astron. Astrophys., Suppl. Ser., 97, p. 13 (1993).

Fichtel, C.E., D.L. Bertsch, J. Chiang, B.L. Dingus, J.A. Esposito, J.M. Fierro, R.C. Hartmann, S.D. Hunter, G. Kanbach, D.A. Kniffen, P.W. Kwok, Y.C. Lin, J.R. Mattox, H.A. Mayer-Hasselwander, L. McDonald, P.F. Michel-

son, C. von Montigny, P.L. Nolan, K. Pinkau, H.-D. Radecke, H. Rothermel, P. Sreekumar, M. Sommer, E.J. Schneid, D.J. Thompson, and T. Willis: Astrophys. J., Suool. Ser., 94, p. 511 (1994).

Firkowski, R., J. Gawin, J. Hibner, J. Wdowczyk, A. Zawadski, and R. Maze: PICRC, 2, p. 696 (1965).

Fukada, Y., S. Hayakawa, I. Kashara, F. Makino, and Y. Tanaka: Nature, 254, p. 398 (1975).

Gehrels, N., and J. Tueller: Astrophys. J., 407, p. 597 (1993).

Gendron, K., et al.: preprint (1995), after Schönfelder (1996).

Ghia, P.L., EAS-TOP Collaboration: PICRC, 2, p. 421 (1995).

Giacconi, Riccardo, Herbert Gursky, Frank R. Paolini, and Bruno Rossi: Phys. Rev. Lett., 9, p. 439 (1962).

Goret, Ph., T. Palfrey, A. Tabary, G. Vacanti, and R. Bazer-Bachi: Astron Astrophys., 270, p. 401 (1993).

Gruber, D.E.: in "The X-Ray Background", eds. X. Barcons and A.C. Fabian, Cambridge University Press, p. 45 (1992).

Harris, M.J., G.H. Share, M.D. Leising, R.L. Kinzer, and D.C. Messina: Astrophys. J., 362, p. 135 (1990).

Hartman, R.C., D.L. Bertsch, S.D. Bloom, A.W. Chen, P. Deines-Jones, J.A. Esposito, C.E. Fichtel, D.P. Friedlander, S.D. Hunter, L.M. McDonald, P. Sreekumar, D.J. Thompson, B.B. Jones, Y.C. Lin, P.F. Michelson, P.L. Nolan, W.F. Tompkins, G. Kanbach, H.A. Mayer-Hasselwander, A. Mücke, M. Pohl, O. Reimer, D.A. Kniffen, E.J. Schneid, C. von Montigny, R. Mukherjee, and B.L. Dingus: Astrophys. J. Suppl., 123, p. 79 (1999).

Hasinger, G.: in "The X-Ray Background", eds. X. Barcons and A.C. Fabian, Cambridge University Press, p. 229 (1992).

Hasinger, G.: Astron. Astrophys., Suppl. Ser., 120, p. 607 (1996).

Hayashida, N., H. Hirasawa, F. Ishikawa, H. Lafoux, M. Nagano, D. Nishikawa, T. Ouchi, H. Ohoka, M. Ohnishi, N. Sakaki, M. Sasaki, H. Shimodaira, M. Teshima, R. Torii, T. Yamamoto, S. Yoshida, T. Yuda, Y. Hayashi, N. Ito, S. Kawakami, Y. Kawasaki, T. Matsuyama, M. Sasano, and T. Takahashi, N. Chamoto, F. Kajino, M. Sakata, T. Sugiyama, M. Tsukiji, Y. Yamamoto, N. Inoue, E. Kusano, K. Mizutani, A. Shiomi, K. Hibino, T. Kashiwagi, J. Nishimura, E.C. Loh, P. Sokolsky, S.F. Taylor, K. Honda, N. Kawasumi, I. Tsushima, Y. Uchihori, H. Kitamura, M. Chikawa, S. Kabe, Y. Mizumoto, H. Yoshii, N. Hotta, To. Saito, M. Nishizawa, H. Kuramochi, and K.Sakumoto: Astrophys. J., 504, p. L71 (1998).

Herterich, W., K. Pinkau, H. Rothermel, and M. Sommer: PICRC, 1, p. 21 (1973).

Hillas, A.M.: Nature, 312, p. 50 (1992).

Hillas, A.M.: Rapporteur Paper 24th Internat. Cosmic Ray Conf., Rome, Italy (1995), Nuovo Cimento, 19C, p. 701 (1996).

Hillas, A.M., C.W. Akerlof, S.D. Biller, J.H. Buckley, D.A. Carter-Lewis, M. Catanese, M.F. Cawley, D.J. Fegan, J.P. Finley, J.A. Gaidos, F. Krennrich, R.C. Lamb, M.J. Lang, G. Mohanty, M. Punch, P.T. Reynolds, A.J. Rodgers, H.J. Rose, A.C. Rovero, M.S. Schubnell, G.H. Sembroski, G. Vacanti, T.C. Weekes, M. West, and J. Zweerink: Astrophys. J., 503, p. 744 (1998).

Hillier, R.: Gamma Ray Astronomy, Clarendon Press, Oxford (1984).

Hopper, V.D., O.B. Mace, J.A. Thomas, P. Albats, G.M. Frye, Jr., G.B. Thomson, and J.A. Staib: Astrophys. J. Lett., 186, p. L-55 (1973).

Houston, B.P., A.W. Wolfendale, and E.C.M. Young: J. Phys., G, 10, p. L-147 (1984).

Hunter, S.D.: Nucl. Phys., B (Proc. Suppl.) 38, p. 447 (1995).

Hunter, S.D., D.L. Bertsch, J.R. Catelli, T.M. Dame, S.W. Digel, B.L. Dingus, J.A. Esposito, C.E. Fichtel, R.C. Hartman, G. Kanbach, D.A. Kniffen, Y.C. Lin, H.A. Mayer-Hasselwander, P.F. Michelson, C. von Montigny, R. Mukherjee, P.L. Nolan, E. Schneid, P. Sreekumar, P. Thaddeus, and D.J. Thompson: Astrophys. J., 481, p. 205 (1997).

Jansky, Karl, G.: Proc. I.R.E., 20, 1920 (Dec. 1932).

Jansky, Karl, G.: Nature, 132, p. 66 (1933a).

Jansky, Karl, G.: Popular Astronomy, 41, p. 548 (1933b).

Jauch, J.M., and F. Röhrlich: "The Theory of Photons and Electrons", Addison Wesley, Cambridge, Mass (1955).

Kappadath, Ch., J. Ryan, K. Bennett, H. Bloemann, D. Forrest, W. Hermsen, R.M. Kippen, M. McConnell, V. Schönfeldet, R. vam Dijk, M. Varendorff, G. Weidenspointner, and C. Winkler: PICRC, 2, p. 230 (1995).

Kappadath, S.C.: PhD Thesis, University of New Hampshire, USA (1998).

Karle, A., F. Arqueros, K.H. Becker, E. Faleiro, J. Fernandez, P. Fernandez, V. Fonseca, V. Haustein, G. Heinzelmann, V. Henke, I. Holl, F. Just, H. Krawczynski, F. Krennrich, M. Kühn, A. Lindner, E. Lorenz, S. Martinez, V. Matheis, M. Merck, H. Meyer, R. Mirzoyan, N. Müller, R. Plaga, J. Prahl, D. Renker, M. Rozanska, M. Samorski, H. Sander, K. Sauerland, D. Schmele, R. Sooth, W. Stamm, and B. Wiebel: Astropart. Phys., 4, p. 1 (1995).

Karle, A., S. Martinez, R. Plaga, F. Arqueros, K.H. Becker, S.M. Bradbury, J. Fernandez, P. Fernandez, V. Fonseca, B. Funk, V. Haustein, G. Heinzelmann, V. Henke, H. Krawczynski, F. Krennrich, M. Kühn, A. Lindner, E. Lorenz, N. Magnussen, V. Matheis, M. Merck, H. Meyer, R. Mirzoyan, N. Müller, D. Petry, J. Prahl, C. Prosch, D. Renker, W. Rhode, M. Rozanska, M. Samorski, H. Sander, D. Schmele, R.N. Sooth, W. Stamm, S. Westerhoff, and B. Wiebel-Sooth, and M. Willmer: Phys. Lett., B 347, p. 161 (1995).

Kifune, T.: Proceedings of Tokyo Workshop "Towards a Major Atmospheric Cherenkov Telescope III, ed. T. Kifune (Universal Academy Press, Tokyo (1995).

Kifune, T.: Nuovo Cimento, 19 C, p. 953 (1996).

Kinzer, R.L., W.R. Purcell, W.N. Johnson, J.D. Kurfess, G. Jung, and J. Skibo: Astron. Astrophys., Suppl. Ser., 120, p. 317 (1996).

Kinzer, R.L., W.R. Purcell, and J.D. Kurfess: Astrophys. J., 515, p. 215 (1999).

Kniffen, D.A., D.L. Bertsch, B.L. Dingus, J.A. Esposito, C.E. Fichtel, R.C. Hartman, S.D. Hunter, G. Kanbach, Y.C. Lin, H.A. Mayer-Hasselwander, M. Merck, P.F. Michelson, C. von Montigny, A. Mücke, R. Mukherjee, P.L. Nolan, M. Pohl, E. Schneid, P. Sreekumar, D.J. Thompson, and T.D. Willis: Proc. 3rd Compton Symp. , Astron. Astrophys., Suppl. Ser. 120, p. 615 (1996).

Konopelko, A., F. Aharonian, A. Akhperjanian, F. Arqueros, G. Aslanian, A. Beglarian, S. Bradbury, J. Cortina, A. Daum, T. Deckers, J. Fernandez, V. Fonseca, B. Funk, J.C. Gonzalez, W. Greve, G. Heinzelmann, M. Hemberger, G. Hermann, M. Hess, A. Heusler, I. Holl, W. Hofmann, R. Kankanian, A. Karle, O. Kirstein, C. Köhler, A. Kohnle, H. Krawczynski, F. Krennrich, A. Lindner, E. Lorenz, N. Magnussen, S. Martinez, M. Merck, H. Meyer, R. Mirzoyan, H. Möller, A. Moralejo, N. Müller, L. Padilla, M. Panter, D. Petry, R. Plaga, A. Plyasheshnikov, J. Prahl, C. Prosch, G. Rauterberg, W. Rhode, D. Renker, V. Sahakian, M. Samorski, J.A. Sanchez, K. Sauerland, D. Schmele, E. Smarsch, R.N. Sooth, W. Stamm, M. Ulrich, H.J. Völk, S. Westerhoff, B. Wiebel-Sooth, C.A. Wiedner, M. Willmer, and H. Wirth: Astropart. Phys., 4, p. 199 (1996).

Konopelko, A.K., et al.: preprint (astro-ph/9901093) (1999).

Kraushaar, W.L., and G.W. Clark, G.P. Garmire, R. Broken, P. Higbie, V. Leong, and T. Thorsos: Astrophys. J., 177, p. 341 (1972).

Krennrich, F., R. Mirzoyan, N. Müller, H. Sander, F. Aharonian, A.G. Akhperjanian, F. Arqueros, K.H. Becker, A.S. Beglarian, R. Eckmann, E. Faleiro,

J. Fernandez, P. Fernandez, V. Fonseca, P. Friedrich, W. Greve, V. Haustein, G. Heinzelmann, A. Heusler, I. Holl, F. Just, R.S. Kankanian, A. Karle, M. Kühn, E. Lorenz, S. Martinez, M. Merck, H. Meyer, R. Plaga, A.V. Plyasheshnikov, J. Prahl, D. Renker, W. Rhode, M. Rozanska, V. Sahakian, M. Samorski, K. Sauerland, R.N. Sooth, W. Stamm, B. Wiebel, C. Wiedner, and H. Wirth: PICRC, 1, p. 251 (1993).

Kuo, Fu-Shong, G.M. Frye, Jr., and A.D. Zych: Astrophys. J. Lett., 186, p. L-51 (1973).

Lewis, D.A., C.W. Akerlof, D.J. Fegan, A.M. Hillas, R.C. Lamb, D.I. Meyer, G. Mohanty, and T.C. Weekes: PICRC, 1, p. 279 (1993).

Lockwood, J.A., W.R. Webber, L.A. Friling, J. Macri, and L. Hsieh: Astrophys. J., 248, p. 1194 (1981).

Lloyd-Evans, J., R.N. Coy, A. Lambert, J. Lapikens, M. Patel, R.J.O. Reid, and A.A. Watson: Nature, 305, p. 784 (1983).

Mandrou, P., A. Bui-Van, G. Vedrenne, and M. Niel: Astrophys. J., 237, p. 424 (1980).

Matsubara, Y., CANGAROO Collaboration: Towards a Major Atmospheric Cherenkov Detector - V. Kruger National Park Workshop on TeV Gamma Ray Astrophysics. O.C. de Jager, ed., Space Research Unit, Potchefstroom University for CHE, Potchefstroom, South Africa, P. 447 (1997).

Matthews, J., D. Ciampa, K.D. Green, J. Kolodziejczak, D. Nitz, D. Sinclair, G. Thornton, J.C. Van der Velde, G.L. Cassiday, R. Cooper, S.C. Corbado, B.R. Dawson, J.W. Elbert, B.E. Fick, D.B. Kieda, S. Ko, D.F. Liebing, E.C. Loh, M.H. Salamon, J.D. Smith, P. Sokolsky, S.B. Thomas, and B. Wheeler: Astrophys. J., 375, p. 202 (1991).

Mattox, J.R., O.C. de Jager, and A.K. Harding: in Isolated Pulsars, ed. K.A. van Riper, R. Epstein, and C. Ho. Cambridge University Press, p. 298 (1992).

Mazets, E.P., S.V. Golenetskii, V.N. Il'inskii, Yu.A. Gur'yan, and T.V. Kharitonova: Astrophys. and Space Sci., 33, p. 347 (1975).

McCammon, D., and W.T. Sanders: Annu. Rev. Astron. Astrophys., 28, p. 657 (1990).

Merck, M., A. Karle, M. Kühn, F. Aharonian, F. Arqueros, K.H. Becker, R. Eckmann, E. Faleiro, J. Fernandez, P. Fernandez, V. Fonseca, P. Friedrich, W. Greve, V. Haustein, G. Heinzelmann, I. Holl, F. Just, F. Krennrich, E. Lorenz, S. Martinez, H. Meyer, A. Heusler, R. Mirzoyan, N. Müller, R. Plaga, J. Prahl, D. Renker, W. Rhode, M. Rozanska, M. Samorski, H. Sander, K.

Sauerland, R.N. Sooth, W. Stamm, B. Wiebel, C. Wiedner, and H. Wirth: PICRC, 1, p. 361 (1993).

Much, R., K. Bennett, R. Buccheri, M. Busetta, R. Diehl, D. Forrest, W. Hermsen, L. Kuiper, G.G. Lichti, M. McConnell, J. Ryan, V. Schönfelder, H. Steinle, A. Strong, and M. Varendorff: Astron. Astrophys., 299, p. 435 (1995).

Neshpor, Y.I., A.A. Stepanian, V.P. Fomin, S.A. Gerasimov, B.M. Vladimirsky, and Y.L. Ziskin: Astrophys. Space Sci., 61, p. 349 (1979).

Neshpor, Yu.I., O.R. Kalekin, A.A. Stepanian, V.P. Fomin, A.P. Kornienko, V.G. Shitov, and Yu.L. Zyskin: PICRC, 2, p. 385 (1995).

Ong, René A.: Phys. Rep., 305, p. 93 (1998).

Osborne, J.L., A.W. Wolfendale, and L. Zhang: J. Phys. G, 20, p. 1089 (1994).

Parlier, B., M. Forichon, T. Montmerle, B. Agrinier, G. Boella, L. Scarsi, M. Niel, and R. Palmeira: PICRC, 4, p. 1393 (1975).

Paul, J.A., K. Bennett, G.F. Bignami, R. Buccheri, P. Caraveo, W. Hermsen, G. Kanbach, H.A. Mayer-Hasselwander, L. Scarsi, B.N. Schwanenburg, and R.D. Wills: Astron. Astrophys., 63, p. L-31 (1978).

Paul, Jacques: PICRC, 8, p. 193 (1997).

Penzias, A.A., and R.W. Wilson: Astrophys. J., 142, p. 419 (1965).

Pinkau, K.: Astron. Astrophys., Suppl. Ser., 120, p. 43 (1996).

Piran, Tsvi: Phys. Rep., 314, p. 575 (1999).

Prahl, J. (HEGRA Collaboration): PICRC, 2, p. 354 (1995a).

Prahl, J., et al.: (1995b), after Borione et al., (1997).

Protheroe, R.J.: PICRC, 8, p. 21 (1987).

Punch, M., C.W. Ackerlof, M.F. Cawley, M. Chantell, D.J. Fegan, S. Fennell, J.A. Gaidos, J. Hagan, A.M. Hillas, Y. Jiang, A.D. Kerrick, R.C. Lamb, M.A. Lawrence, D.A. Lewis, D.I. Meyer, G. Mohanty, K.S. O'Flaherty, P.T. Reynolds, A.C. Rovero, M.S. Schubnell, G. Sembroski, T.C. Weekes, T. Whitaker, and C. Wilson: Nature, 358, p. 477 (1992).

Purcell, W.R., D.A. Grabelsky, M.P. Ulmer, W.N. Johnson, R.L. Kinzer, J.D. Kurfess, M.S. Strickman, G. Jung, J.G. Skibo, M.D. Leising, L. Bouchet, P. Mandrou, J.P. Roques, and G. Vedrenne: PICRC, 2, p. 211 (1995).

Purcell, W.R., D.A. Grabelsky, M.P. Ulmer, W.N. Johnson, R.L. Kinzer, J.D. Kurfess, M.S. Strickman, G. Jung, J.G. Skibo, M.D. Leising, L. Bouchet, P.

Mandrou, J.P. Roques, and G. Vedrenne: Astron. Astrophys., Suppl. Ser., 120, p. 389 (1996).

Quinn, J., C.W. Akerlof, S. Biller, J. Buckley, D.A. Carter-Lewis, M.F. Cawley, M. Catanese, V. Connaughton, D.J. Fegan, J.P. Finley, J. Gaidos, A.M. Hillas, R.C. Lamb, F. Krennrich, R. Lessard, J.E. McEnery, D.I. Meyer, G. Mohanty, A.J. Rodgers, H.J. Rose, M.S. Schubnell, G.H. Sembroski, T.C. Weekes, C. Wilson, and J. Zweerink: Astrophys. J., 456, p. L86 (1996).

Ramana-Murthy, Poolla, V., and Arnold W. Wolfendale: Gamma Ray Astronomy, 2nd edition, Cambridge University Press (1993).

Ressell, M. Ted, and Michael S. Turner: Comments Astrophys., 14, No. 6, p. 323 (1990).

Sakurazawa, K., T. Tanimori, S.A. Dazeley, P.G. Edwards, S. Hara, T. Hara, Y. Hayami, S. Kamei, T. Kifune, R. Kita, T. Konishi, A. Masaike, Y. Matsubara, Y. Matsuoka, Y. Mizumoto, M. Mori, H. Muraishi, Y. Muraki, T. Naito, K. Nishijima, S. Ogio, J.R. Patterson, M.D. Roberts, G.P. Rowell, T. Sako, R. Susukita, A. Suzuki, R. Suzuki, T. Tamura, G.J. Thornton, S. Yanagita, T. Yoshida, and T. Yoshikoshi: PICRC, 3, p. 165 (1997).

Samorski, M., and W. Stamm: Astrophys. J., 268, p. L-17 (1983).

Samuelson, F.W., S.D. Biller, I.H. Bond, P.J. Boyle, S.M. Bradbury, A. Breslin, J.H. Buckley, A.M. Burdett, J. Bussóns Gordo, D.A. Carter-Lewis, M. Catanese, M.F. Cawley, D.J. Fegan, J.P. Finley, J.A. Gaidos, T. Hall, A.M. Hillas, F. Krennrich, R.C. Lamb, R.W. Lessard, J.E. McEnery, C. Masterson, J. Quinn, A.J. Rodgers, H.J. Rose, G.H. Sembroski, R. Srinivasan, V.V. Vassiliev, T.C. Weekes, and J. Zweerink: Astrophys. J., 501, p. L17 (1998).

Sasano, M., Y. Aikawa, N.V. Gopalakrishnan, S.K. Gupta, Y. Hayashi, N. Ito, S. Kawakami, D.K. Mohanti, K.C. Ravindran, K. Sasaki, K. Sivaprasad, B.V. Sreekantan, H. Tanaka, S.C. Tonwar, and K. Viswanathan: PICRC, 4, p. 85 (1999).

Schönfelder, V.: Cosmic Rays 92 - Astrophysical, High Energy and Heliospheric Processes. Proc. 13th Europ. Cosmic Ray Symp., Geneva, 1992, ed. P.K.F. Grieder. Nucl. Phys., B (Proc. Suppl.) 33A/B, p. 113 (1993b).

Schönfelder, V.: Nuovo Cimento, 19 C, p. 805 (1996).

Schönfelder, V., G. Lichti, J. Daugherty, and C. Moyano: PICRC, 1, p. 8 (1975).

Schönfelder, V., F. Graml, and F.P. Penningsfeld: Astrophys. J., 240, p. 350 (1980).

Schönfelder, V., H. Aarts, K. Bennett, H. de Boer, J. Clear, W. Collmar,

A. Connors, A. Deerenberg, R. Diehl, A. von Dordrecht, J.W. den Herder, W. Hermsen, M. Kippen, L. Kuiper, G. Lichti, J. Lockwood, J. Macri, M. McConnell, D. Morris, R. Much, J. Ryan, G. Simpson, M. Snelling, G. Stacy, H. Steinle, A. Strong, B.N. Swanenburg, B. Taylor, C. de Vries, and C. Winkler: Astrophys. J., Suppl. Ser., 86, p. 657 (1993a).

Share, G.H., R.L. Kinzer, and N. Seeman: Astrophys. J., 187, p. 511 (1974).

Sinitsyna, V.G., S.I. Nikolsky, A.Y. Alaverdian, S.P. Vorobiov, Sh.B. Matiazov, G.F. Platonov, V.B. Strigin, and I.M. Usmanov: PICRC, 2, p. 334 (1995).

Skibo, J.G., R. Ramaty, and W.R. Purcell: Astron. Astrophys., Suppl. Ser., 120, p. 403 (1996).

Stecker, F.W.: Cosmic Gamma Rays, NASA SP-249 National Aeronautics and Space Administration, Washington, D.C. (1971).

Strong, A.W., and J.R. Mattox: Astron. and Astrophys., 308, p. L 21 (1996).

Strong, A.W., J.B.G.M. Bloemen, T.M. Dame, I.A. Grenier, W. Hermsen, F. Lebrun, L.-A. Nyman, A.M.T. Pollock, and P. Thaddeus: Astron. Astrophys., 207, p. 1 (1988).

Strong, A.W., K. Bennett, H. Bloemen, R. Diehl, W. Hermsen, D. Morris, V. Schönfelder, J.G. Stacy, C. de Vries, M. Varendorff, C. Winkler, and G. Youssefi: Astron. Astrophys., 292, p. 82 (1994).

Strong, A.W., K. Bennett, H. Bloemen, R. Diehl, W. Hermsen, W. Purcell, V. Schönfelder, J.G. Stacy, C. Winkler, and G. Youssefi: Proc. 3rd Compton Symposium, Astron. Astrophys., Suppl. Ser., 120, p. 381 (1996).

Strong, Andrew W., Igor V. Moskalenko, and Olaf Reimer: PICRC, 4, p. 52 (1999a).

Strong, A.W., I.V. Moskalenko, and O. Reimer: (1999b) (astro-ph/9811284).

Tanimori, T., T. Tsukagoshi, T. Kifune, P.G. Edwards, M. Fujimoto, T. Hara, N. Hayashida, Y. Matsubara, Y. Mizumoto, Y. Muraki, S. Ogio, J.R. Patterson, M.D. Roberts, G. Rowell, T. Suda, T. Tamura, M. Teshima, G.J. Thornton, Y. Watase, and T. Yoshikoshi: Astrophys. J., 429, L-61 (1994).

Tanimori, T., K. Sakurazawa, S.A. Dazeley, P.G. Edwards, T. Hara, Y. Hayami, S. Kamei, T. Kifune, T. Konishi, Y. Matsubara, T. Matsuoka, Y. Mizumoto, A. Masaike, M. Moei, H. Muraishi, Y. Muraki, T. Naito, S. Oda, S. Ogio, T. Osaki, J.R. Patterson, M.D. Roberts, G.P. Rowell, A. Suzuki, R. Suzuki, T. Sako, T. Tamura, G.J. Thornton, R. Susukita, S. Yanagita, T. Yoshida, and T. Yoshikoshi: Astrophys. J., L33 (1998).

Toyoda, Y., K. Suga, K. Murakami, H. Hasegawa, S. Shibata, V. Domingo, I. Escobar, K. Kamata, H. Bradt, G. Clark, and M. LaPoint: PICRC, 2, p. 708 (1965).

Trombka, J.I., C.S. Dyer, L.G. Evans, M.J. Bielefeld, M. Seltzer, and A.E. Metzger: Astrophys. J., 212, p. 925 (1977).

Trümper, J.: Cosmic Rays 92 - Astrophysical, High Energy and Heliospheric Processes. Proc. 13th Europ. Cosmic Ray Symp., Geneva, 1992, ed. P.K.F. Grieder. Nucl. Phys., B (Proc. Suppl.) 33A/B, p. 126 (1993).

Vacanti, G., M.F. Cawley, E. Colombo, D.J. Fegan, A.M. Hillas, P.W. Kwok, M.J. Lang, R.C. Lamb, D.A. Lewis, D.J. Macomb, K.S. O'Flaherty, P.T. Reynolds, and T.C. Weekes: Astrophys. J., 377, p. 467 (1991).

Vedrenne, G., F. Albernhe, I. Martin, and R. Talon: Astron. Astrophys., 15, p. 50 (1971).

Vladimirsky, B.M., A.A. Stepanian, and V.P. Fomin: PICRC, 1, p. 456 (1973).

Völk, H.J., and F.A. Aharonian: Proceedings of Heidelberg Workshop, 1994; eds. H.J. Völk and F.A. Aharonoan, Space Sci. Rev., 75, Nos. 1-2 (1996).

Wdowczyk, J., W. Tkaczyk, and A.W. Wolfendale: J. Phys. A, 5, p. 1419 (1972).

Weekes, T.C.: Phys. Rep., 160, Nos. 1 & 2, p. 1 (1988).

Weekes, T.C., M.F. Cawley, D.J. Fegan, K.G. Gibbs, A.H. Hillas, P.W. Kwok, R.C. Lamb, D.A. Lewis, D. Macomb, N.A. Porter, P.T. Reynolds, and G. Vacanti: Astrophys. J., 342, p. 379 (1989).

Weekes, T.C., et al.: AIP Conf. Proc., 304, p. 270. Proc. 2nd Compton Symp., eds. C.E. Fichtel, N. Gehrels, and J.P. Norris (New York, AIP) (1994).

Weidenspointer, G., et al.: Astroph. Lett. Comm. (3rd INTEGRAL Workshop) (1999) in press (after Strong et al., 1999a).

White, R. Stephen, Bruce Dayton, Shin H. Moon, James M. Ryan, Robert B. Wilson, and Allen D. Zych: Astrophys. J., 218, p. 920 (1977).

Yamasaki, N.Y., T. Ohashi, F. Takahara, S. Yamauchi, T. Kamae, K. Makishima, and K. Koyama: Astron. Astrophys., Suppl. Ser., 120, p. 393 (1996).

Yuda, Y.: Proc. Internat. Symp. on Extremely High Energy Cosmic Rays: Astrophysics and Future Observations, ed. M. Nagano, University of Tokyo, Institute for Cosmic Ray Research, 175 (1996).

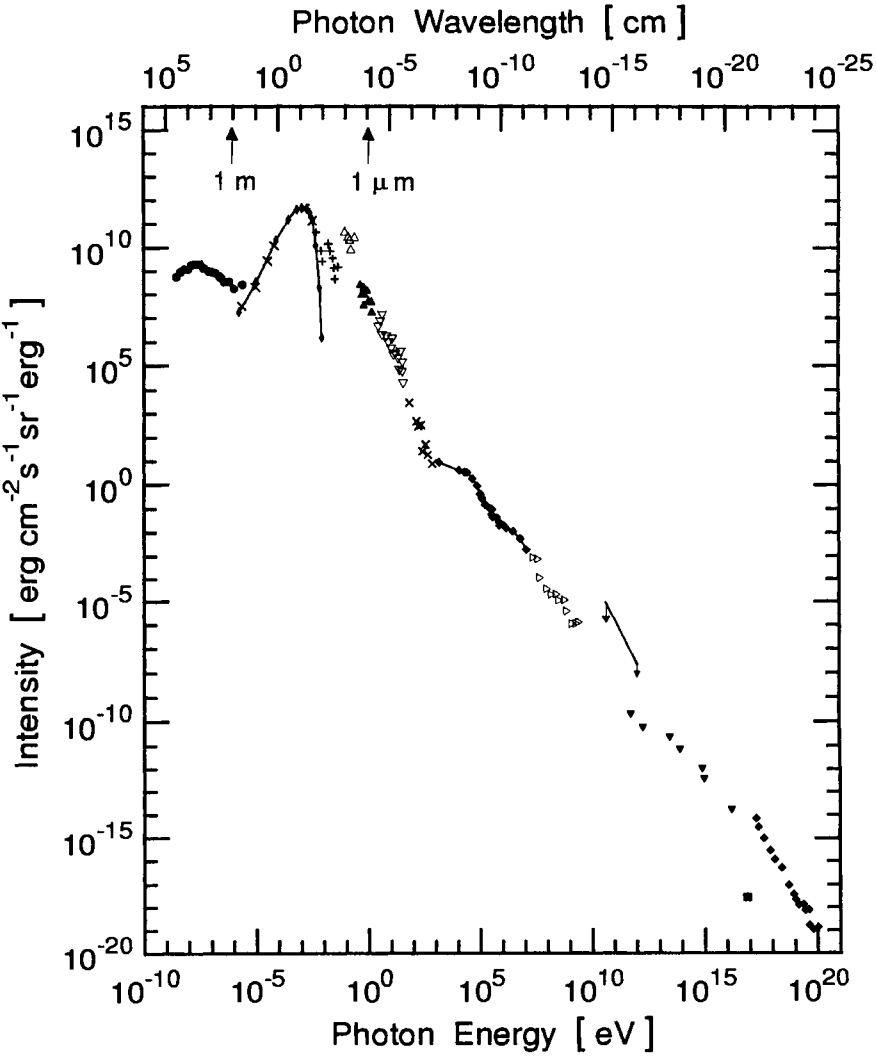

Figure 5.52: The grand unified photon spectrum (GUPS) of the diffuse extragalactic background radiation (after Ressell and Turner, 1990). The figure is a compilation of a large number of experimental data. For details see Ressel and Turner (1990) and references listed therein.

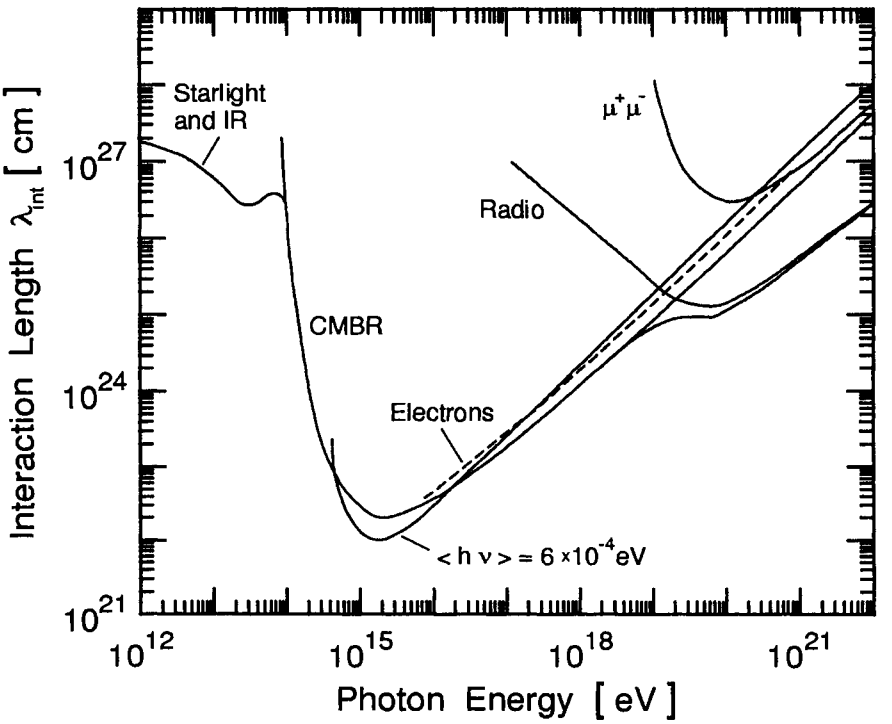

Figure 5.53: Interaction length, λ_{int}, against photon energy for collisions of energetic photons with photons of the various radiation fields in space. Unless stated otherwise the process concerned is electron pair production (e^+e^-). Also shown is the interaction length for electrons by way of inverse Compton effect with black body photons (after Wdowczyk et al., 1972).

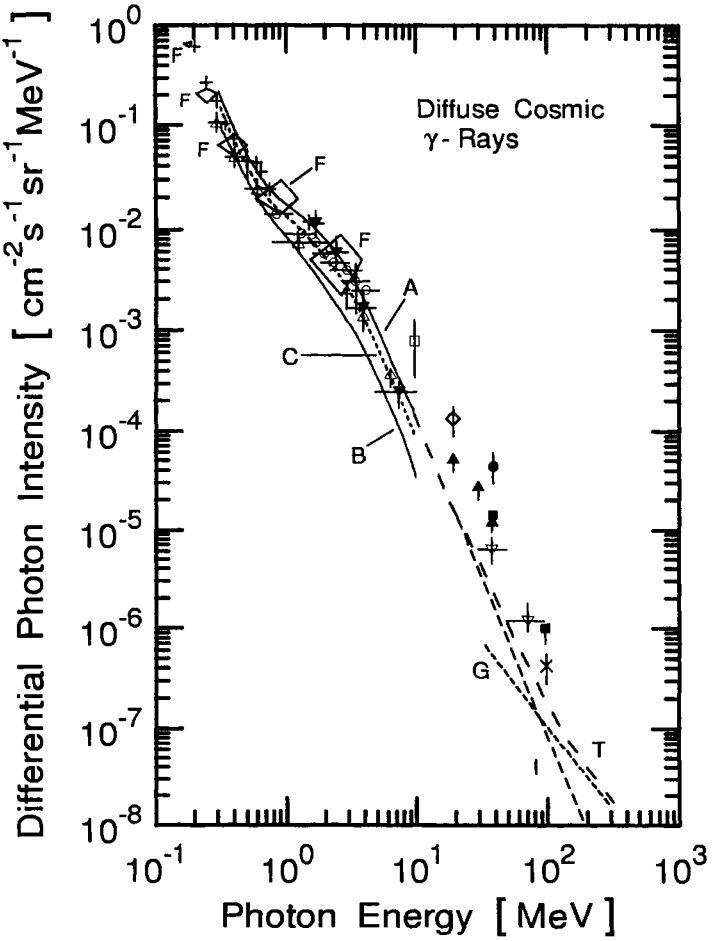

Figure 5.54: Compilation of early balloon and satellite data from measurements of the diffuse gamma ray spectrum (after Fichtel et al., 1978). The curves A, B and C are from the summary of Trombka et al. (1977), I and G are the isotropic and high latitude galactic components, respectively, and T is the sum. The trapezoidal fields, F, are the data of Fukada et al. (1975) (after Fichtel et al., 1978) .

+	Mazets et al. (1975)	△	Daniel et al. (1972)
o	Vedrenne et al. (1971)	▲	Share et al. (1974)
▼	Schönfelder et al. (1975)	□	Kuo et al. (1973)
■	Hopper et al. (1973)	◇	Parlier et al. (1975)
×	Kraushaar et al. (1972)	•	Herterich et al. (1973)
▽	Bratolyubova et al. (1971)	F	Fukada et al. (1975)

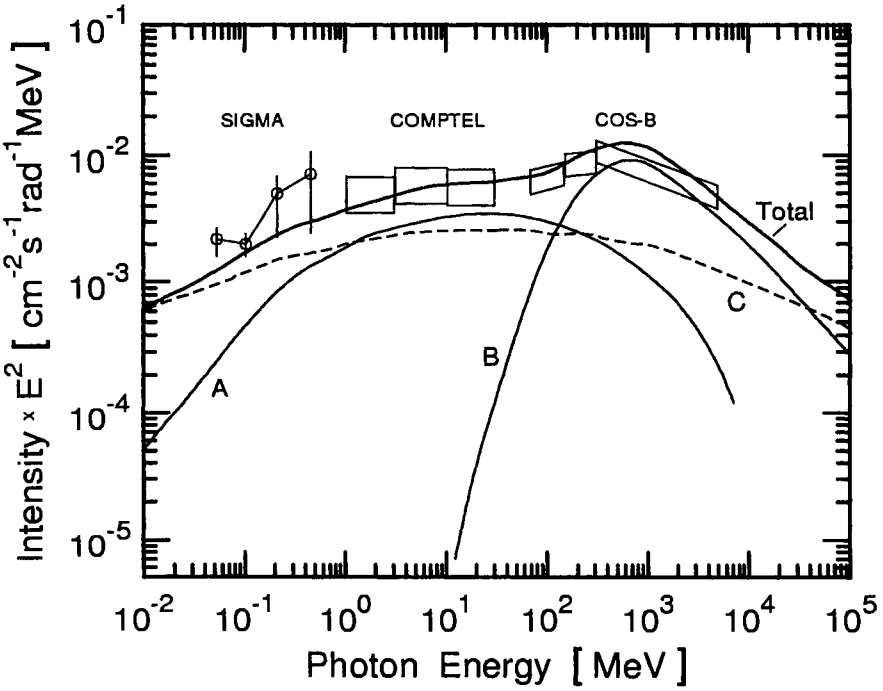

Figure 5.55: The diffuse gamma ray spectrum of the inner Galaxy ($300° < l < 60°$), integrated over $|b| < 20°$, derived from COMPTEL data (Strong et al., 1994) together with values from COS-B (Strong et al., 1988). Also included are results from SIGMA around $l = 315°$ (Claret et al., 1995). The curves A, B, and C are theoretical spectra representing the contribution from bremsstrahlung, π^0-decay and inverse Compton effect, respectively (after Schönfelder, 1996).

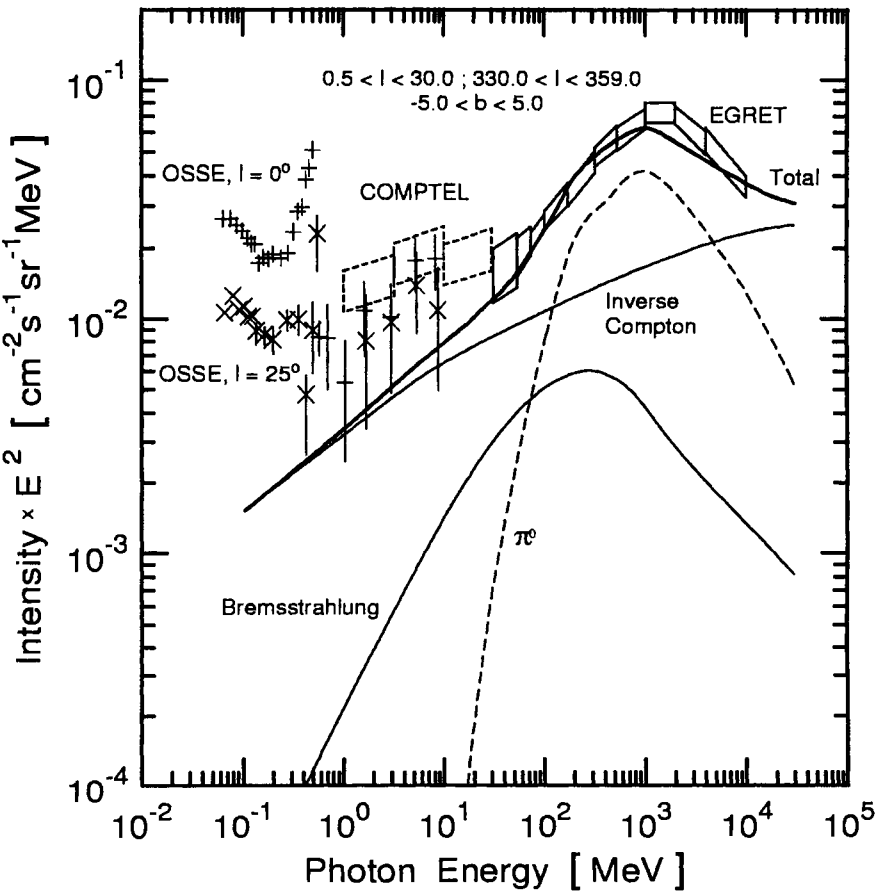

Figure 5.56: Gamma ray energy spectrum of the inner Galaxy ($300° \leq l \leq 30°$, $|b| \leq 5°$) compared with model calculations of Strong et al. (1999a) using an electron injection index of -1.8 and a modified nucleon spectrum. The curves show the contributions from the different processes considered, as indicated in the figure. The experimental data are from EGRET (Strong and Mattox, 1996), COMPTEL (Strong et al, 1999b) and OSSEE for $l = 0°$ and 25° (Kinzer et al., 1999) (after Strong et al., 1999a).

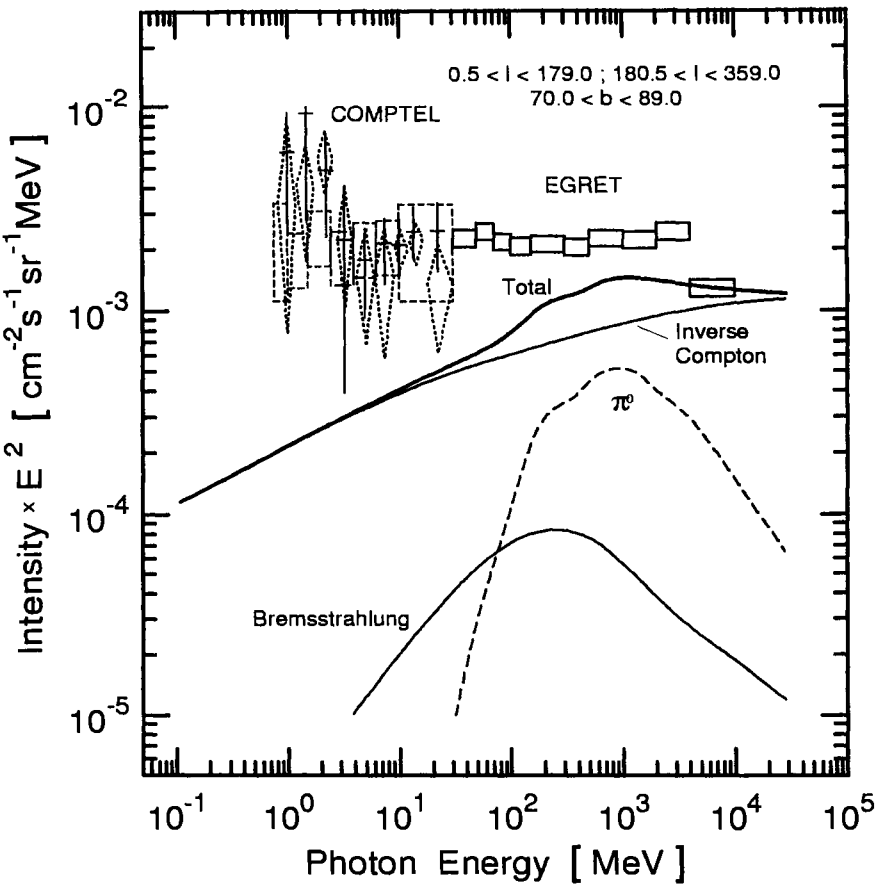

Figure 5.57: Energy spectrum of gamma rays from high galactic latitudes ($|b| \geq 70°$, all longitudes) for $z_h = 4$ kpc. The solid boxes apply to EGRET, total intensity from cycle 1-4 data. The COMPTEL high-latitude total intensity data are from Bloemen et al. (1999) (dashed boxes), Kappadath (1998) (dotted diamond shaped boxes) and Weidenspointner et al. (1999) (+). The curves represent the result of model calculations of Strong et al. (1999a) of the galactic gamma ray components due to bremsstrahlung, inverse Compton scattering and neutral pion decay (after Strong et al., 1999a).

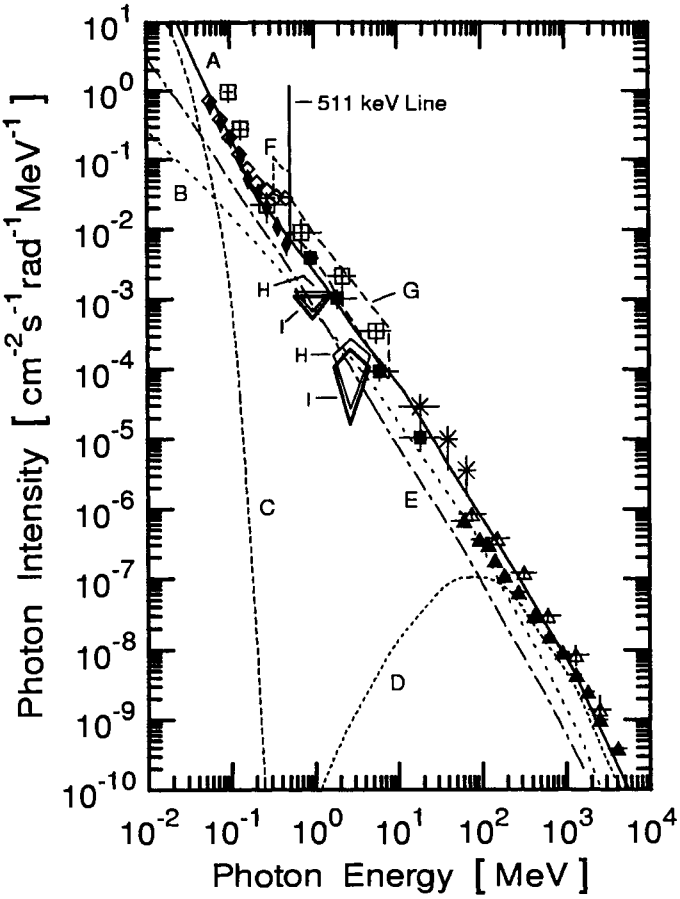

Figure 5.58: Compilation of more recent satellite data on the *diffuse galactic* gamma ray emission. The solid curve, A, indicates the best-guess spectrum of Gehrels and Tueller (1993). Curves B, C, D and E represent the contributions from inverse Compton, 10 keV thermal bremsstrahlung, π^0-decay, and non-thermal bremsstrahlung. The distribution is relatively flat in longitude within $\sim 25°$ of the galactic center. The 511 keV annihilation line and the positron continuum also shown are observed primarily within 10° of the galactic center (after Purcell et al., 1995 and 1996).

◇, H	Purcell et al. (1995, 1996) $l = 0°$	■	Bloemen et al. (1994) and Strong et al. (1994) COMPTEL
◆, I	Purcell et al. (1995, 1996) OSSE $l = 25°$ & 339°	▲	Fichtel et al. (1993) EGRET
×	Bertsch & Kniffen (1983) balloon	□	Mandrou et al. (1980) balloon
F, G	Harris et al. (1990) SMM	△	Paul et al. (1978) COS-B

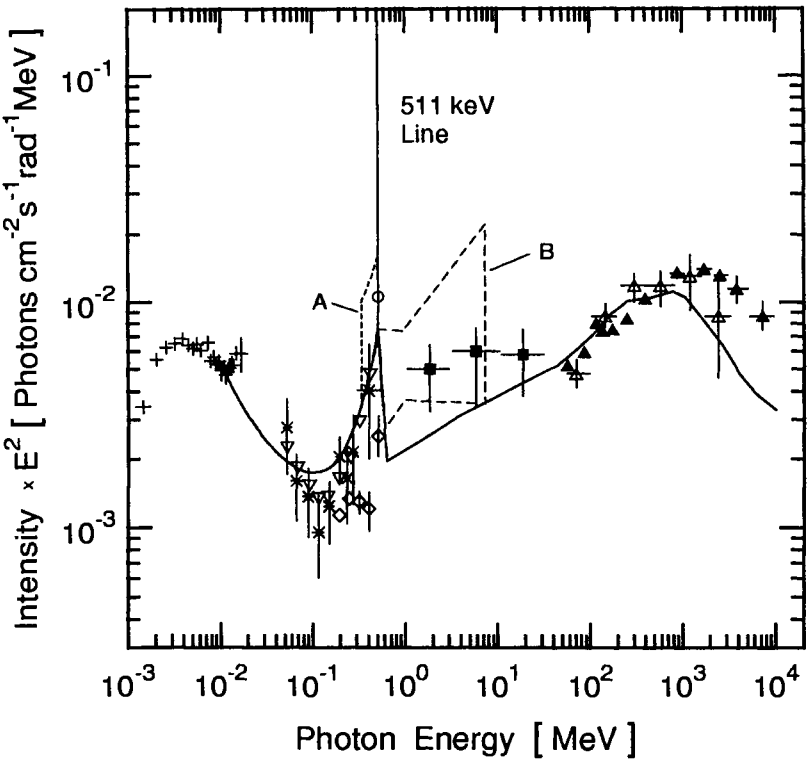

Figure 5.59: Diffuse Gamma ray intensity spectrum of the inner Galaxy observed with satellite-based instruments. The data are the same as those in Fig. 5.58 except for the missing balloon and Ginga data (after Purcell et al., 1996). The curve represents the data of the model of Skibo et al. (1996).

▽	OSSEE ($-5° < l < 5°$; $-2° < b < 2°$); Purcell et al. (1996)
◇, ○	OSSEE ($20° < l < 30°$; $334° < l < 344°$; $-2° < b < 2°$); Purcell et al. (1996)
■	COMPTEL ($-60° < l < 60°$; $-20° < b < 20°$); Bloemen et al. (1994) and Strong et al. (1994)
▲	EGRET ($-10° < l < 10°$; $-5° < b < 5°$); Fichtel et al. (1993)
△	COS-B ($-5° < l < 15°$; $-10° < b < 10°$); Paul et al. (1978)
A, B	SMM ($-65° < l < 65°$); Harris et al. (1990)
+	Ginga; × Welcome-1; Yamasaki et al. (1996)

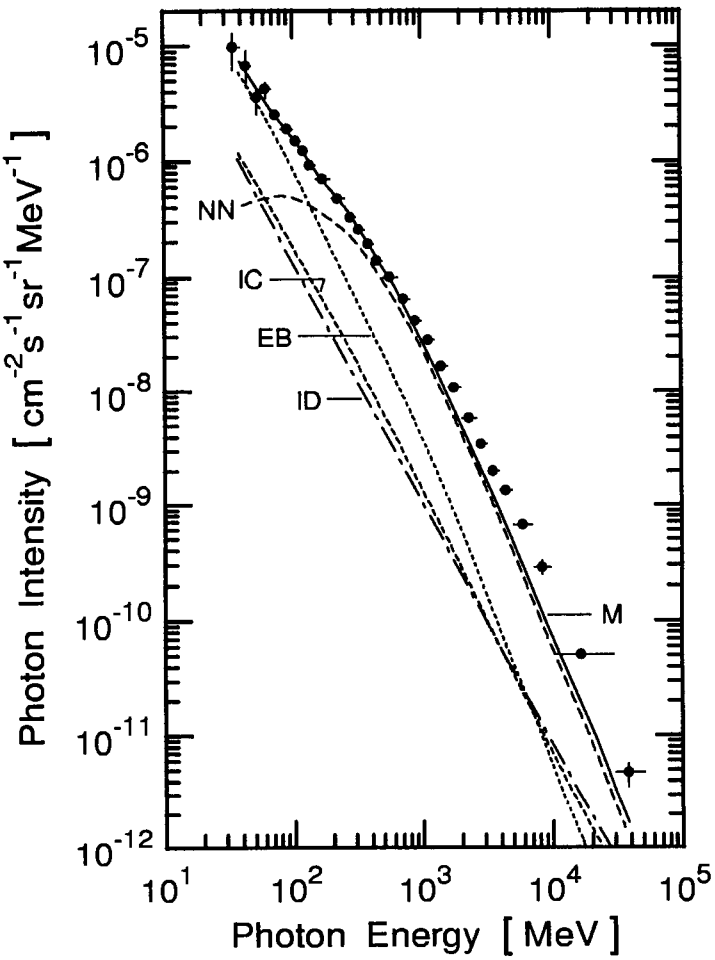

Figure 5.60: Average diffuse gamma ray spectrum of the inner Galaxy region, $300° \leq l \leq 60°$; $|b| \leq 10°$ (0.73 sr). Shown are the data of EGRET and results of model calculations. Curves NN, IC, EB and ID represent the π^0 contribution from nucleon-nucleon interactions, inverse Compton scattering, electron bremsstrahlung, and the isotropic diffuse emission, respectively. Curve M is the best-fit model calculation plus the isotropic diffuse emission (after Hunter et al., 1997).

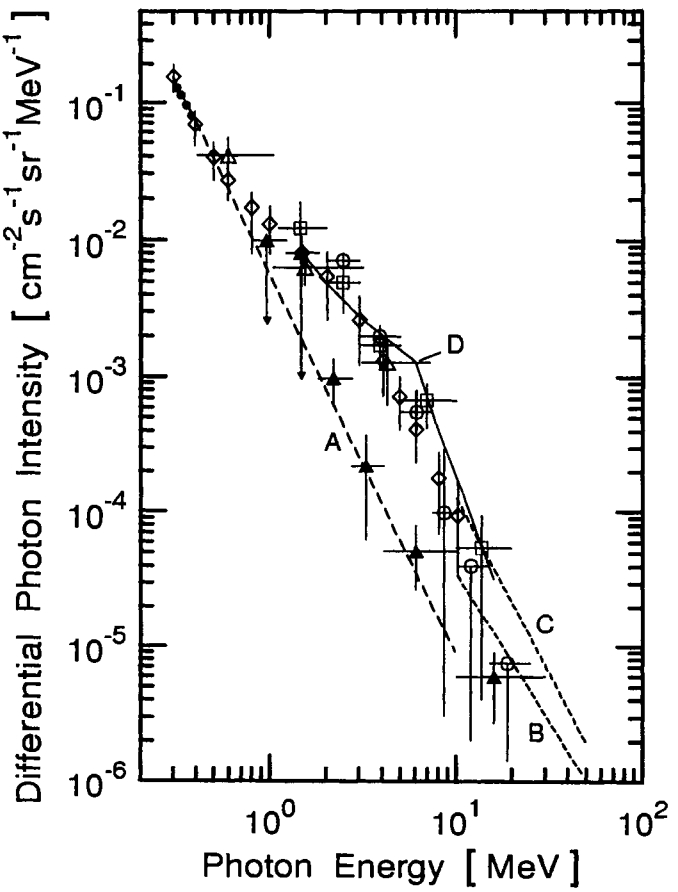

Figure 5.61: The *diffuse cosmic* (extragalactic) gamma ray background between 0.8 MeV and 30 MeV. Shown are the COMPTEL data in the direction of Virgo ($l \sim 270°, b \sim 65°$) together with results from earlier work, as indicated below. The dashed curve A is the extrapolation from the low energy measurements of Mazets et al. (1975), curves B and C are extrapolations from measurements at higher energies of Fichtel et al. (1975). Curve D is the sum of the COMPTEL diffuse cosmic and the 5 GV *rigidity dependent* background fluxes. The data of Trombka et al. (1977), White et al. (1977), and Schönfelder et al. (1980) lie close to curve D (*MeV-bump*), implying that they contain unidentified background (after Kappadath et al., 1995).

▲ Kappadath et al. (1995), COMPTEL
□ Schönfelder et al. (1980), balloon
△ Lockwood et al. (1981), balloon
○ White et al. (1977), balloon
● Mazets et al. (1975), satellite
◇ Trombka et al. (1977), satellite

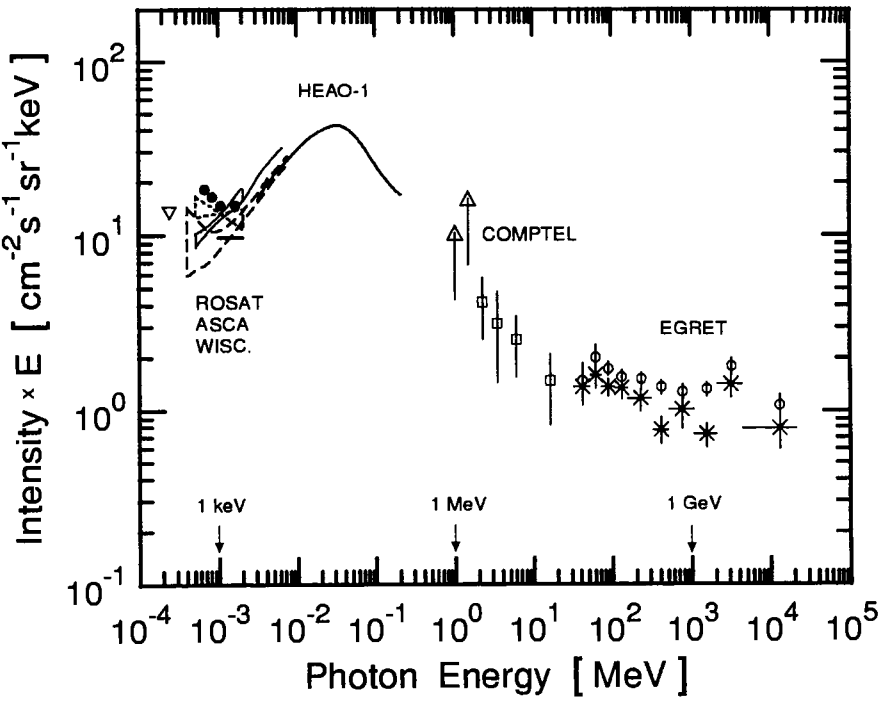

Figure 5.62: The *diffuse cosmic* (extragalactic) X- and γ-ray background. The plot is the $\nu \cdot f(\nu)$ representation, showing the emitted power per decade of energy. The data are from ROSAT, ASCA, the Wisconsin group, HEAO-1, COMPTEL, and EGRET (after Schönfelder, 1996).

△	Kappadath et al. (1995) (upper limits only)
□	Kappadath et al. (1995)
o	Kniffen et al. (1996)
×	Osborne et al. (1994)
HEAO-1	Gruber (1992)
ROSAT	Hasinger (1992, 1996)
ASCA	Gendron et al. (1995)
WISC.	McCammon and Sanders (1990)

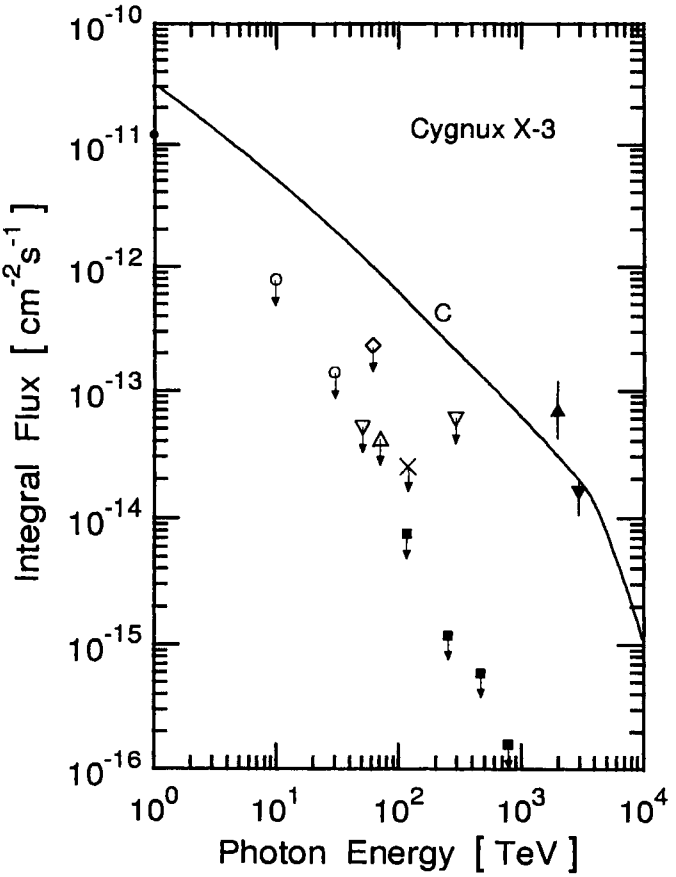

Figure 5.63: The fading high energy gamma ray flux from Cygnus X-3. Shown are the initial integral flux level estimates derived from the measurements made with the Kiel (Samorski and Stamm, 1983) and Haverah Park (Lloyd-Evans et al., 1983) arrays and the anticipated spectrum (curve C) (Hillas, 1984). Also plotted are the results of measurements made during later epochs with different installations that yielded only upper limits (Borione et al., 1995; Hillas, 1996).

▲ Samorski & Stamm (1983) Kiel
o Amenomori et al. (1993) Tibet
▽ Aglietta et al. (1993) EAS-TOP
△ Merck et al. (HEGRA)
× Borione et al. (1995) CASA-MIA neutral particles
▼ Lloyd-Evans et al. (1983) Haverah Park
• Neshpor et al. (1995) Crimean Obs.
◇ Alexandreas et al. (1993a, b) CYGNUS
■ Borione et al. (1995) CASA-MIA

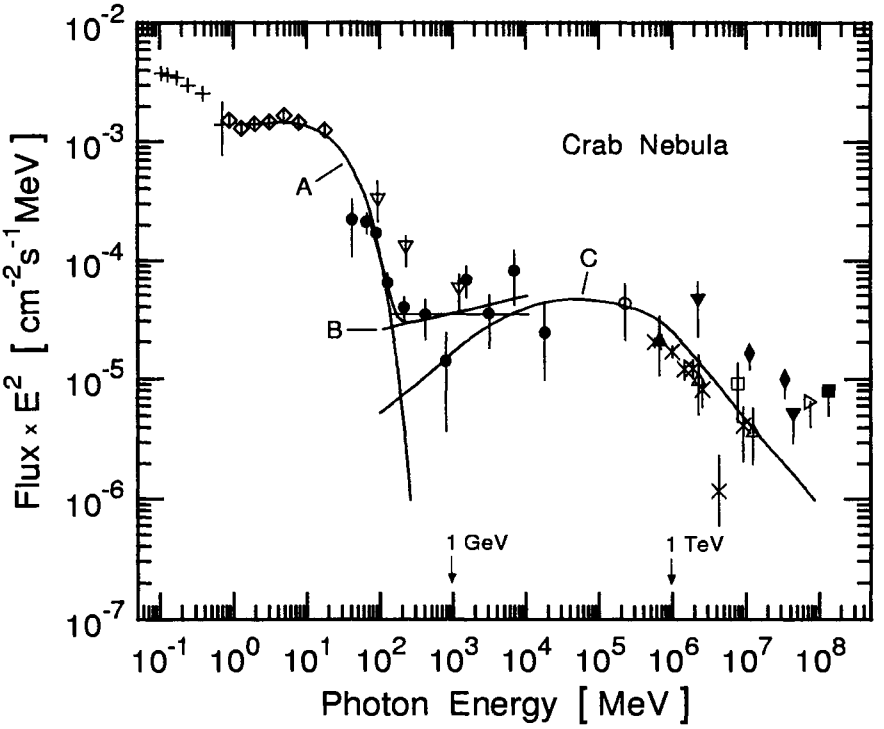

Figure 5.64: The unpulsed Crab Nebula differential photon spectrum, multiplied by E^2. The experiments are listed in the table below. The best fit synchrotron cutoff plus hard power law components are indicated by curves A and B, respectively, and the inverse Compton power law by curve C (after De Jager et al., 1995).

+	Bartlett et al. (1994) GRIS	◇	Much et al. (1995) COMPTEL
▽	Clear et al. (1987), and Mattox et al. (1992) COS-B	■	Borione et al. (1993) CASA-MIA
▲	Goret et al. (1993) ASCAT	○	Akerlof et al. (1989) Gamma Star
♦	Amenomori et al. (1993) Tibet	▼	Krennrich et al. (1993) HEGRA
•	De Jager et al. (1996) EGRET	□	Tanimori et al. (1994) Cangaroo
×	Weekes et al. (1994) Whipple	▷	Alexandreas et al. (1993a) Cygnus
		△	Djannati-Atai et al. (1994) Thémistocle

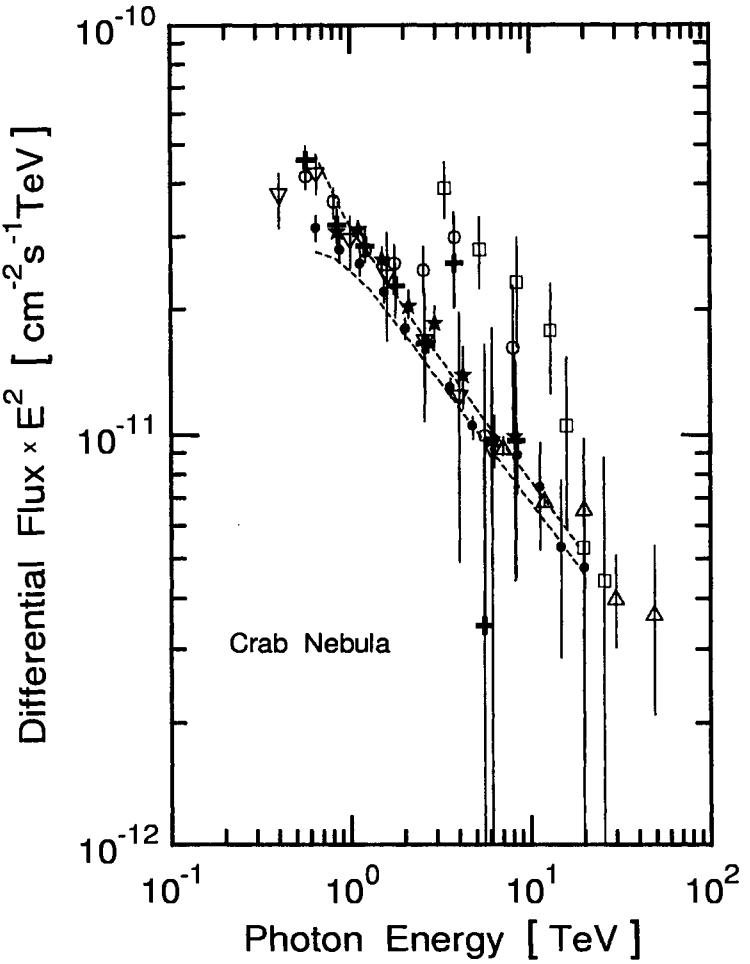

Figure 5.65: Differential energy spectra of the Crab Nebula determined by different groups (Aharonian et al., 2000). The HEGRA data (•) were obtained with the imaging air Cherenkov telescope. The dashed lines indicate the HEGRA error band.

+ ○ ⋆	Hillas et al. (1998) Whipple
△	Tanimori et al. (1998) Cangaroo
▽	Barrau (1998) CAT
□	Amenomori et al. (1999a) Tibet
•	Aharonian et al. (2000) HEGRA

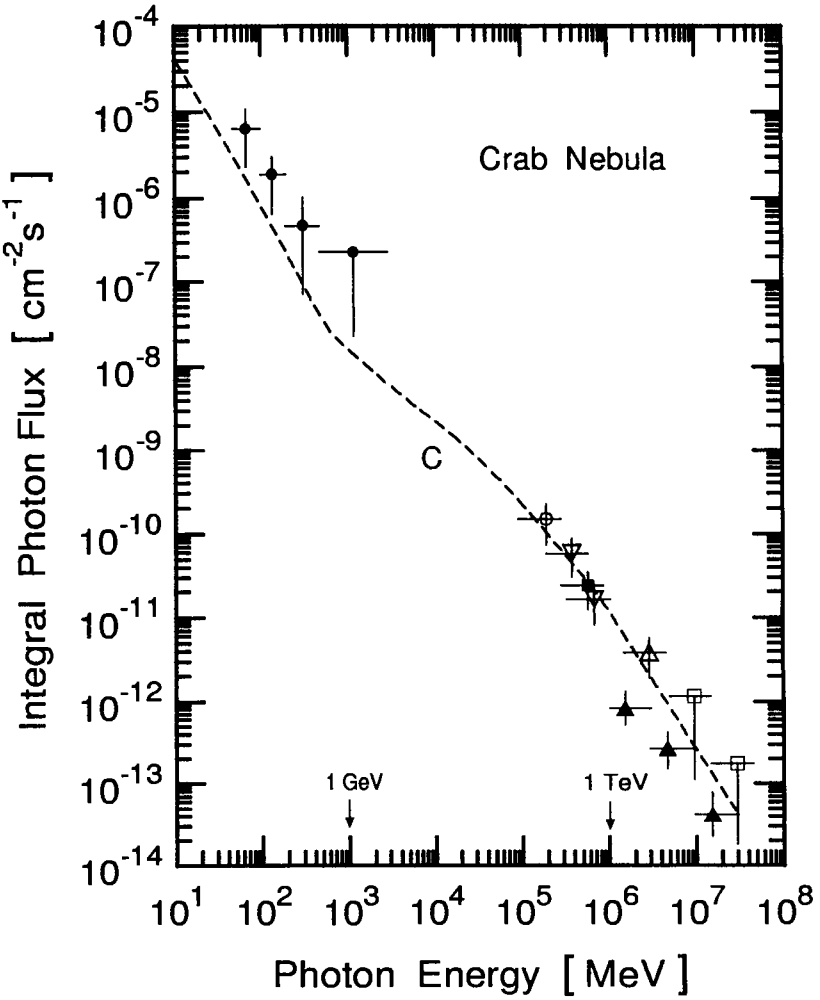

Figure 5.66: Wide-range gamma ray integral energy spectrum of the Crab Nebula (after Sinitsyna et al., 1995). Included are data of the satellite COS-B and results from ground based measurements, as given in the table.

• Paul et al. (1978) COS-B	o Akerlof et al. (1989) Sandia
▽ Vacanti et al. (1991) Whipple	■ Goret et al. (1993) ASGAT
△ Djannati-Atai et al. (1995) Thémistocle	□ Amenomori et al. (1997) Tibet
▲ Sinitsyna et al. (1995) SHALON	C Sinitsyna et al. (1995)

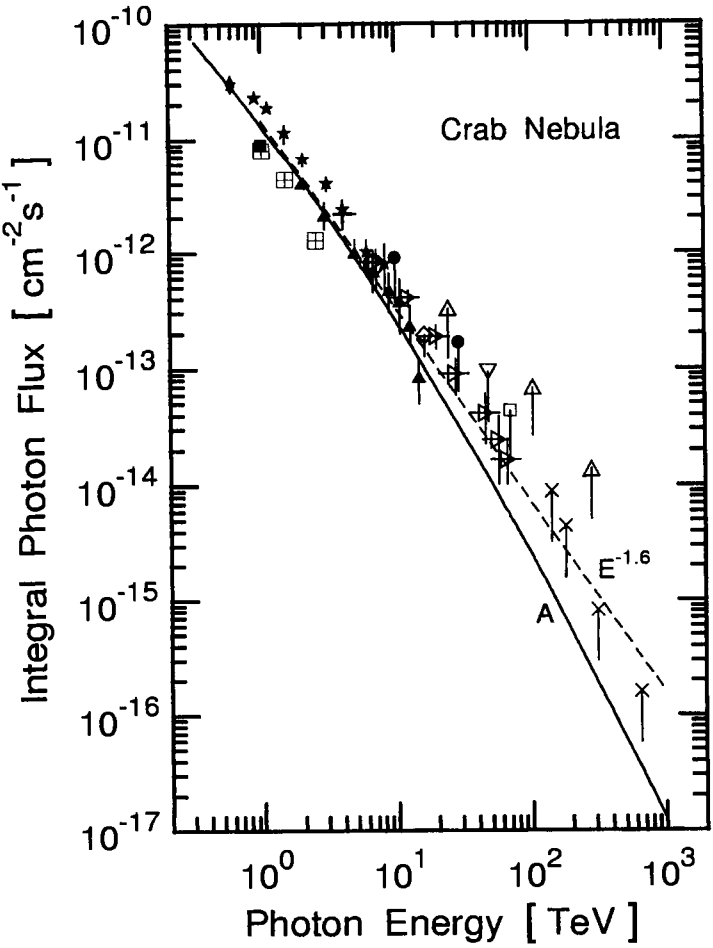

Figure 5.67: Gamma ray flux and flux limits from the Crab measured by many experiments, as listed below.

- ▲ Djannati-Atai et al. (1995) (Thémis)
- □ Alexandreas et al. (1993a, b) (Cygnus)
- × Borione et al. (1997) (CASA-MIA)
- ★ Carter-Lewis et al. (1997) (Whipple)
- \+ Sakurazawa et al. (1997) (Cangaroo)
- ▷ Sakurazawa et al. (1997) (Cangaroo)
- ○ Tanimori et al. (1994) (Cangaroo)
- A De Jager et al. (1996) (Model)
- ■ Lewis et al. (1993) (Whipple)
- ◇ Prahl et al. (1995a) (AIROBICC)
- ▽ Prahl et al. (1995b) (HEGRA)
- ⊞ Konopelko et al. (1996) HEGRA
- △ Ghia et al. (1995) (EAS-Top)
- • Amenomori et al. (1993) (Tibet)
- ♦ Goret et al. (1993) (ASGAT)

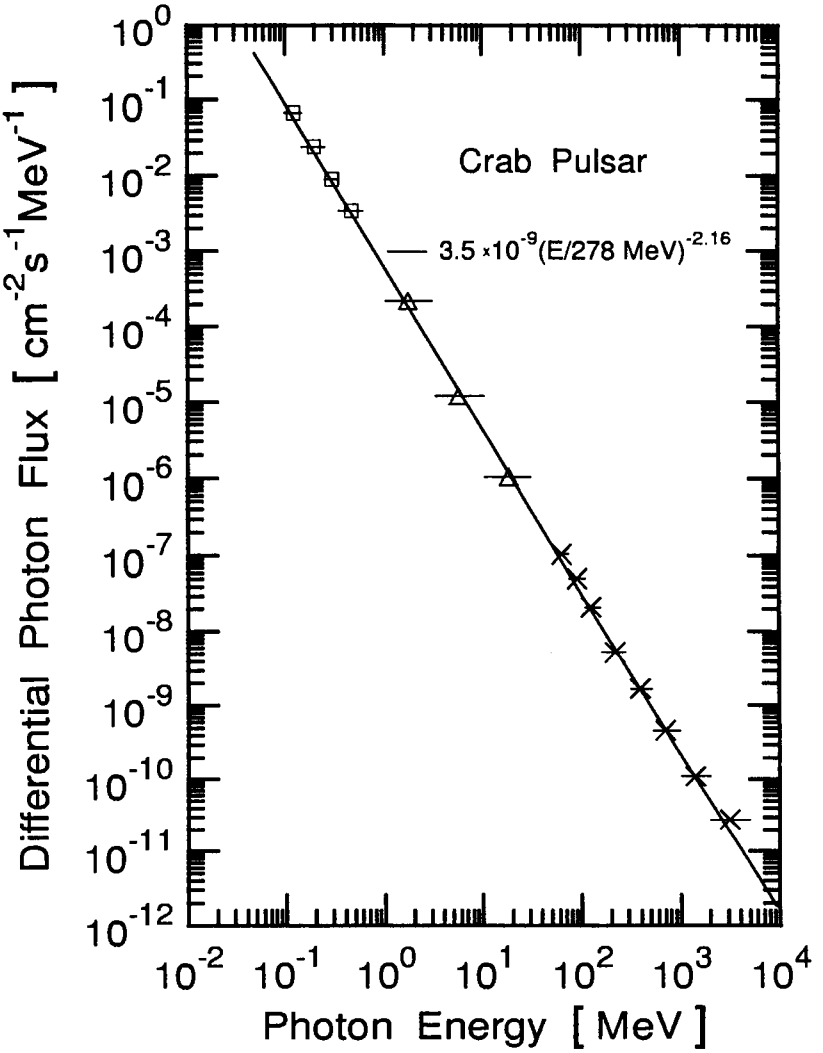

Figure 5.68: Differential energy spectrum of the pulsed photon emission from the Crab Pulsar measured by the OSSE, COMPTEL, and EGRET instruments on the Gamma Ray Observatory, GRO (Schönfelder, 1993a).

□ OSSE
△ COMPTEL
× EGRET

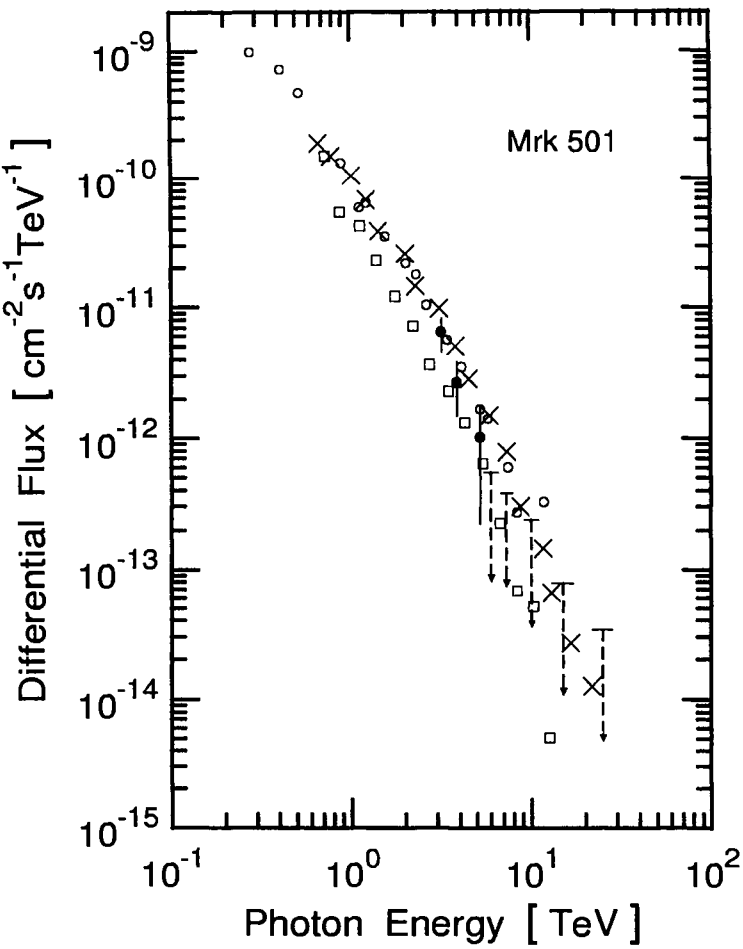

Figure 5.69: Differential gamma ray energy spectra of Markarian 501 observed with different installations. The data from the Tibet array are averaged over the period from 1997 February 27 to 1997 August 25 and the upper limit data (dashed lines) are the 2 σ confidence levels (Amenomori et al., 1999b).

- o Samuelson et al. (1998) Whipple
- × Konopelko et al. (1999) HEGRA
- □ Hayashida et al. (1998) Tibet
- • Amenomori et al. (1999b) Tibet

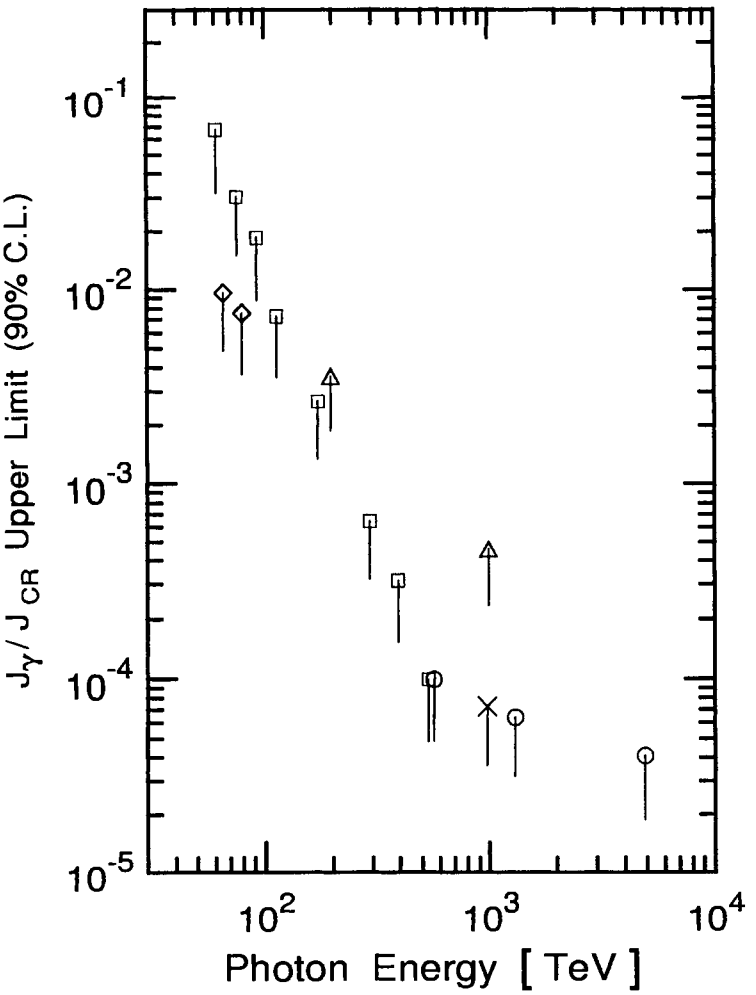

Figure 5.70: Upper limits of the flux ratio of isotropic gamma rays to cosmic rays determined by five different experiments as listed below (Sasano et al., 1999).

- □ Sasano et al. (1999) Ooty
- × Aglietta et al. (1996) EAS-TOP
- ◇ Karle et al. (1995) HEGRA
- △ Matthews et al. (1991) Utah
- o Chantell et al. (1997) CASA-MIA

5.5 Neutrinos and Antineutrinos

5.5.1 General Comments

Disregarding the continuous flux of neutrinos from the Sun, the only extraterrestrial (astrophysical) neutrinos (antineutrinos) that have so far been identified are those from the neutrino burst of the type II supernova of February 23, 1987, called SN-1987A.

It was the collapse of the blue supergiant star Sanduleak (-69°, 202) in the Large Magellanic Cloud (LMC) which is at a distance of about 55 kpc from our location. The first confirmed observation of optical brightening was by Garradd, February 23.44 and Shelton, February 24.23 at the Las Campanas Observatory in Chile (Garradd, 1987; Shelton, 1987).

Supernovae of type II are believed to involve stars of masses greater than about 8 solar masses wherein the central core of about 1.5 solar masses can no longer withstand the pressure of its internal gravitational force and collapses to a *neutron star* (Zwicky, 1965; for a review see Burrows, 1988 and 1990; Bethe, 1990). The latter has an enormous nuclear density of approximately 10^{14} g/cm^2 and a radius of only about 10 km. The highly excited outer shell of the star radiates energy over much of the electromagnetic spectrum.

The release of the binding energy of the neutron star which amounts to about 0.1 to 0.2 solar masses (approximately 10^{53} erg) occurs through the emission of neutrinos (Chiu, 1964; Colgate and White, 1966; Woosley et al., 1986). The process responsible for neutrino emission is primarily the formation of the neutron star through the reaction

$$e^- + p \rightarrow \nu_e + n \tag{5.15}$$

and in the rapid cooling of the neutron star. The average neutrino energy expected from model calculations is in the vicinity of 15 MeV. Considering an estimated total energy emitted by SN-1987A of about $3 \cdot 10^{53}$ erg yields a neutrino burst of $10^{57} - 10^{58}$ neutrinos in a time interval of just a few seconds.

5.5.2 Neutrinos from the Supernova SN-1987A

Four installations claimed observation of the neutrino burst from SN-1987A. They comprise the installations LSD in the Mont Blanc tunnel (Italy-France) (Castagnoli, 1987a and 1987b; Aglietta et al., 1987a and 1987b), Kamiokande II (Japan) (Hirata et al., 1987), IMB-3 (Irvine-Michigan-Brookhaven) near Cleveland, Ohio, (U.S.A.) (Bionta et al., 1987), and Baksan in southern Rus-

Table 5.37: Event Sequence and Energy of SN-1987A Neutrino (Antineutrino) Events in the LSD Detector (Aglietta et al., 1987a).

Event No.	Event Time [UT]	Electron Energy [MeV]
1	2h52m36s.79	7
2	2h52m40s.65	8
3	2h52m41s.01	11
4	2h52m42s.70	7
5	2h52m43s.80	9

sia (Alekseev et al., 1987). The LSD and Baksan detectors are liquid scintillation detectors whereas Kamiokande II and IMB-3 are water Cherenkov detectors. The depths of these detectors are specified by the respective groups as 5200 hg/cm^2 standard rock (SR) (LSD), 850 m water equivalent (w.e.) (Baksan), 2400 m w.e. (Kamiokande II) and 1570 m w.e. (IMB-3).

The detectors Kamiokande II, IMB-3 and Baksan recorded the first neutrino event of the burst on February 23, 1987, at 7:35:35 UT, 7:35:41 UT and 7:36:11 UT, respectively. The Torino group operating the LSD detector reported registration of a neutrino burst on February 23, 1987 at 02:52:36 UT, thus, 4.72 hours prior to the previously mentioned three quasi-coincident observations (Castagnoli, 1987a and 1987b; Aglietta et al., 1987a). For a detailed review see for example Koshiba (1992).

The time sequence of arrival and the energy of the neutrinos (antineutrinos) recorded in the LSD and Baksan detectors are listed in Tables 5.37 and 5.38 (Aglietta et al., 1987a; Alexeyev et al., 1987 and 1988), those recorded with Kamiokande II and IMB-3 in Tables 5.39 and 5.40 (Hirata et al., 1988; Bratton et al., 1988), respectively. In addition Kamiokande II and IMB-3 have also determined the angle of emission of the electrons identifying the neutrino (antineutrino) events in the detectors with respect to the supernova. These data are also given in Tables 5.39 and 5.40.

In Fig. 5.71 we show the time sequences of arrival of the neutrino (antineutrino) events recorded in the Kamiokande II, IMB-3 and Baksan detectors along the abscissa and the energy of the detected electrons along the ordinate (Hirata et al., 1988; Bratton et al., 1988; Alexeyev et al., 1988). The sequences are plotted with a common origin for the first event registered

Table 5.38: Event Sequence and Energy of SN-1987A Neutrino (Antineutrino) Events in the Baksan Detector (Alexeyev et al., 1988).

Event No.	Event Time [UT]	Electron Energy [MeV]
1	7h36m11s.82	12±2.4
2	7h36m12s.25	18±3.6
3	7h36m13s.53	23.3±4.7
4	7h36m19s.51	17±3.4
5	7h36m20s.92	20.1±4.0

Table 5.39: Characteristics of Contained SN-1987A Neutrino (Antineutrino) Events in the Kamiokande II Detector (Hirata et al., 1988).

Event No.	Event Time [UT]	Electron Energy [MeV]	Track Angle [deg]
1	7h35m35s.00	20.0± 2.9	18± 18
2	7h35m35s.11	13.5± 3.2	40± 27[a)]
3	7h35m35s.30	7.5± 2.0	108± 32
4	7h35m35s.32	9.2± 2.7	70± 30
5	7h35m35s.51	12.8± 2.9	135± 23
6[b)]	7h35m35s.69	6.3± 1.7	68± 77
7	7h35m36s.54	35.4± 8.0	32± 16
8	7h35m36s.73	21.0± 4.2	30± 18
9	7h35m36s.92	19.8± 3.2	38± 22
10	7h35m44s.22	8.6± 2.7	122± 30
11	7h35m45s.43	13.0± 2.6	49± 26
12	7h35m47s.44	8.9± 1.9	91± 39

[a)] New value, old value was $(15 \pm 27)°$ (Hirata et al., 1987).

[b)] Later discarded as background.

in each detector. Note that the re-analyzed data of Bratton et al. (1988) and not the original data of Bionta et al. (1987) are shown for the IMB-3 experiment.

Table 5.40: Characteristics of Contained SN-1987A Antineutrino[a] Events in the IMB-3 Detector (Bratton et al., 1988).

Event No.	Event Time [UT]	Electron Energy [MeV]	Track Angle[b] [deg]
1	7h35m41s.37	38±7	80±10
2	7h35m41s.79	37±7	44±15
3	7h35m42s.02	28±6	56±20
4	7h35m42s.52	39±7	65±20
5	7h35m42s.94	36±9	33±15
6	7h35m44s.06	36±6	52±10
7	7h35m46s.38	19±5	42±20
8	7h35m46s.96	22±5	104±20

[a] The data are interpreted as being all due to $\overline{\nu}_e(p,n)e^+$ reactions.

[b] With respect to direction away from SN-1987A. Note that because of inoperative photomultipliers the detector had a bias against triggering on tracks moving toward LMC.

The angular distributions of the electron tracks of the neutrino (antineutrino) reactions in the Kamiokande II and IMB-3 detectors with respect to the direction of SN-1987A are shown in Figure 5.72. This figure is in the form of a scatter plot with $\cos(\theta_{e,LMC})$ along the abscissa, $\theta_{e,LMC}$ being the polar angle between the electron track and the direction pointing away from the Large Magellanic Cloud, and the electron energy along the ordinate. Two sets of IMB-3 data are shown. The second set with error bars is the result of a re-analysis with improved energy measurements, reduced energy uncertainties, re-assessed trigger efficiency and timing (Bratton et al., 1988).

Of the different neutrino (antineutrino) reactions that can take place in the water target of a detector and lead to electrons or positrons that produce the Cherenkov signal, the two most likely to occur are the absorption of an electron antineutrino by a free proton,

$$\overline{\nu}_e + p_{free} \rightarrow n + e^+ \ , \tag{5.16}$$

and, with a roughly 100 times smaller probability at 10 MeV, neutrino - electron scattering,

$$\nu_e + e^- \rightarrow \nu_e' + e^{-\prime} \ . \tag{5.17}$$

In the absorption reaction ($\overline{\nu}_e + p_{free} \rightarrow n + e^+$) the e^+ is emitted essentially isotropically, whereas in the scattering reaction ($\nu_e + e^- \rightarrow \nu_e' + e^{-\prime}$) the $e^{-\prime}$ preserves the initial neutrino direction within an r.m.s. angle of 28° at about 10 MeV.

For neutrinos and antineutrinos of energy ≥ 30 MeV the reactions

$$\nu_e + {}^{16}O \rightarrow {}^{16}F + e^- \tag{5.18}$$

and

$$\overline{\nu}_e + {}^{16}O \rightarrow {}^{16}N + e^+ \tag{5.19}$$

contribute comparable numbers of electrons and positrons, respectively, in a water Cherenkov detector but the cross section of either reaction is about 10 times smaller than for the absorption of $\overline{\nu}_e$ on free protons (see Chapter 4, Section 4.5 for details).

Scintillation detectors such as Baksan or LSD are most sensitive to the absorption process $\overline{\nu}_e + p_{free} \rightarrow n + e^+$. For neutrinos of energy >30 MeV they are also sensitive to the reaction

$$\nu_e + {}^{12}C \rightarrow {}^{12}N + e^- \ . \tag{5.20}$$

Due to the large cross section of the neutral current reaction

$$\nu_x + {}^{12}C \rightarrow {}^{12}C^* + \nu_x' \tag{5.21}$$

and the subsequent γ emission of ^{12}C*

$${}^{12}C^* \rightarrow {}^{12}C + \gamma \ \ (15.1 \text{ MeV}) \ \ 96\% \tag{5.22}$$

scintillation detectors based on C_nH_{2n} compounds are also able to detect neutrinos of any flavor (ν_x) with a threshold energy of ~16 MeV (Ryazhskaya et al., 1993).

After a careful analysis, considering the different reaction processes and the energy dependent detector efficiency the Kamiokande team came to the conclusion that probably all but one of the events are due to $\overline{\nu}_e + p_{free} \rightarrow n + e^+$ reactions and that the resulting *integrated $\overline{\nu}_e$ flux of the burst* in the detector was approximately

$$J_{\overline{\nu}_e}(\geq 8.8\,\text{MeV}) \simeq 1.1 \cdot 10^{10} \ \ \text{cm}^{-2} \tag{5.23}$$

for neutrinos of energy $\geq$8.8 MeV. This leads to a $\overline{\nu}_e$ luminosity of the supernova SN-1987A of about $9 \cdot 10^{52}$ erg for an observed average energy of 15

MeV and amounts to a total energy emitted by neutrino - antineutrino pairs of all flavors of $\sim 3 \cdot 10^{53}$ erg. The corresponding neutron star temperature is $kT \approx 4$ MeV. An upper limit for the masses of ν_e and $\overline{\nu}_e$ ranging from a few eV to 24 eV was obtained on the grounds of a variety of assumptions (Hirata et al., 1988).

The IMB-3 data were interpreted as being all due to $\overline{\nu}_e(p,n)e^+$ reactions. After accounting for all corrections and assuming for simplicity a 32 MeV monochromatic $\overline{\nu}_e$ beam, the $\overline{\nu}_e$ flux at the detector thus obtained for the burst was $8 \cdot 10^8$ cm^{-2}. The total $\overline{\nu}_e$ luminosity of SN-1987A is given as $1.3 \cdot 10^{52}$ erg above the detector threshold of 20 MeV (Bionta et al., 1987, Bratton et al., 1988).

For the Baksan detector the integrated $\overline{\nu}_e$ luminosity was estimated to be $(18.6 \pm 8.5) \cdot 10^{52}$ erg, disregarding absorption in the outer layers of the supernova (Alexeyev et al., 1988).

5.5.3 Energetic Neutrinos from Astrophysical Sources

General Comments

High energy neutrino astronomy is a rapidly evolving young field of science. Great efforts were made during the last decade to estimate the intensities of high energy neutrinos from astrophysical sources. We will only very briefly touch this complex theoretical subject and call attention to the fact that the anticipated discovery of high and ultrahigh energy neutrinos, mostly the easier detectable ν_μ and $\overline{\nu}_\mu$ from point sources, with the various huge underwater or under ice detector matrices now under construction or in the planning phase may well be the key to locate at least some of the sources of ultrahigh energy cosmic rays (Markov, 1960; Markov and Zheleznykh, 1961; Grieder, 1986; Barwick et al., 1992; Roberts, 1992; Learned, 1993; Gaisser et al., 1995).

There are basically two kinds of sources to consider. One category includes the previously mentioned point sources such as pulsars, binary systems, active galactic nuclei (AGN), blazars, gamma ray bursters (GRB), supernovae, and possibly other compact objects (Stecker et al., 1991 and 1992a; Szabo and Protheroe, 1992 and 1994; Protheroe, 1999). The other are diffuse sources that could generate a rather significant more or less isotropic background.

Neutrino Point Sources and Spectra

In Fig. 5.73 we show as examples the predicted neutrino fluxes from model calculations for the two active galactic nuclei, NGC4151 and 3C273 from the work of Stecker et al. (1991, 1992a and 1992b) and another spectrum for 3C273 from a calculation of Szabo and Protheroe (1994), using different assumptions. Also shown is the spectrum of supernova remnants (Volkova, 1980), the atmospheric ν_μ and $\overline{\nu}_\mu$ background spectrum from a calculation of Stecker (1979) and the spectra of solar and SN-1987A neutrinos.

The theoretical results presented here are just a small sample of the numerous contributions made to the field up to date by many authors, using different models and assumptions (for further details see Berezinsky et al., 1991; for comprehensive reviews see Koshiba, 1992; Learned, 1993; Gaisser et al., 1995). Further details concerning atmospheric neutrinos are given in Chapter 4, Section 4.5.

Diffuse Neutrino Sources and Spectra

Interactions of cosmic rays with the background radiation or with interstellar matter in our own and other galaxies but also in intergalactic space could produce a diffuse background with a spectrum that extends to the highest energies (Stecker, 1979; Volkova, 1980; Berezinsky and Learned, 1992; Yoshida and Teshima, 1993).

In addition the large number of unresolved AGNs, GRBs and blazars are likely to produce a relatively strong diffuse flux of high energy neutrinos of all flavors (Stecker et al., 1992b). Finally, topological defects could be another, though highly speculative, source of very energetic neutrinos (Protheroe and Stanev, 1996; Sigl et al., 1997; Birkel and Sarkar, 1998; Yoshida et al., 1997; Protheroe, 1999).

Neutrino spectra of various diffuse sources from older calculations are illustrated in Fig. 5.74 together with the atmospheric background (Stecker, 1979 and 1992b; Berezinsky and Learned 1992; Szabo and Protheroe, 1992 and 1994; Yoshida and Teshima, 1993). When comparing the neutrino intensity from unresolved AGNs shown in this figure with the flux of discrete sources shown in Fig. 5.73 it is readily recognized that the former could easily mask distant point sources.

The results of another set of calculations of the diffuse high energy neutrino flux from a variety of sources are summarized in Figs. 5.75 to 5.78. In Fig. 5.75 we show the muon neutrino $(\nu_\mu + \overline{\nu}_\mu)$ spectra from interactions of the cosmic radiation with the interstellar medium arriving from the direction

of the galactic center ($l = 0°$, $b = 0°$) and perpendicular to it ($b = 0°$) from calculations of Ingelman and Thunman (1996), Domokos et al. (1993) and Berezinsky et al. (1993).

Also shown in the same figure are the spectra resulting from interactions of the cosmic radiation with the cosmic microwave background radiation (CMBR) for different cosmic ray spectral and source assumptions, as outlined in the captions (Protheroe and Johnson, 1995 and 1996; Lee 1996; Hill and Schramm, 1985). The recent atmospheric neutrino spectrum of Lipari (1993) which represents the background for any extraterrestrial neutrino flux measurements is also shown.

Another set of neutrino spectra due to proton blazars and $p\gamma$ and $pp + p\gamma$ processes (Mannheim, 1995; Protheroe, 1997; Halzen and Zas, 1997), and from gamma ray bursters (Waxman and Bahcall, 1997) are shown in Fig. 5.76.

Topological defects could be another yet highly speculative source of very high energy neutrinos. The results of four calculations using different sets of topological model parameters and assumptions, such as different X-particle masses and magnetic field strengths, specified in the caption, are presented in Fig. 5.77 (Protheroe and Stanev, 1996; Sigl et al., 1997; Birkel and Sarkar, 1998; Yoshida et al., 1997).

Spectra of so-called "visible particles" (p, n, γ, e) that are associated with the decay of massive X-particles from topological defects resulting from the calculation of Protheroe and Stanev (1996) that produced the neutrino spectrum shown in Fig. 5.77 (curve A), are displayed in Fig. 5.78 together with the neutrino spectrum. Also indicated are gamma ray data in the GeV energy range from SAS-II and EGRET satellite measurements (Thompson and Fichtel, 1982; Fichtel, 1996), and from the HEGRA experiment at 1 TeV (Karle, 1995). These spectra set stringent limits on topological models and their many parameters.

5.5.4 Experimental Upper Limits of Neutrino Fluxes from Astrophysical Point Sources

Upper limits for the flux of extraterrestrial neutrinos from established high energy gamma ray sources were obtained by some experiments (Svoboda et al., 1987; Koshiba, 1992; Miller et al., 1994; Barish, 1995; Ambrosio et al., 2001). In Table 5.41 we give the upper limits for the muon neutrino flux ($\nu_\mu + \overline{\nu}_\mu$) from several likely sources as determined by the IMB experiment (Becker-Szendy et al., 1995).

Table 5.41: IMB Flux Limits on Prospective Astrophysical Neutrino Point Sources.
(Becker-Szendy et al., 1995)

Source	Events within 1σ	Expected Background Events	90% CL μ-Flux $[\cdot 10^{-14}\text{cm}^{-2}\text{s}^{-1}]$	90% CL ν-Flux $[\cdot 10^{-6}\text{cm}^{-2}\text{s}^{-1}]$
Crab PSR	2	0.56	4.3	4.8
Vela PSR	0	0.72	0.78	0.85
Cyg X−3	0	0.50	4.1	4.5
Geminga	1	0.43	3.1	3.5
Her X−1	1	0.38	4.3	4.8
LMC X−4	0	1.0	0.66	0.75
Sco X−1	3	0.54	3.4	3.8
Vela X−1	0	1.1	0.84	0.95
3C273	0	0.79	1.5	3.3
3C279	1	0.60	2.0	2.4
Cen A	0	0.76	0.80	0.9
Mrk421	0	0.40	3.3	3.6
NGC1068	0	0.70	1.4	1.6
NGC4151	2	0.43	7.7	8.5
SN1987a	0	0.59	1.2	1.3

The analysis is based on simulated events from point sources with a power law spectrum, $E^{-\gamma}$, with spectral index $\gamma = 2$ which yields a Gaussian point spread of $\sigma = 3.4°$. Listed in the table is the number of upward going muons detected by IMB within 1σ of the sources along with a background estimated from randomizing the event arrival times, and the 90% confidence limits (CL) on the muon and neutrino fluxes. No significant neutrino excesses were found with this experiment.

A more recent and very extensive analysis had been carried out by the MACRO Collaboration (Ambrosio et al., 2001). Their results are presented in Table 5.42.

From the data presented here it is evident that the search for extraterrestrial neutrino sources must be carried out at energies well beyond the point where the atmospheric neutrino spectrum is being overtaken by the flatter spectra of astrophysical sources, where the latter make the dominating con-

Table 5.42: MACRO Flux Limits on Prospective Astrophysical Neutrino Point Sources. (Ambrosio et al., 2001)

90% CL of neutrino induced muon flux limits for the MACRO detector list of 42 sources. Corresponding limits on the neutrino flux are given in the last column for $E_{\nu\ min} = 1$ GeV. These limits are calculated for a spectral index $\gamma = 2.1$ and for $E_\mu > 1$ GeV, including the decrease in efficiency at very high energies. The reduction factors for a 3° half width cone are included. These limits include the effect of absorption of neutrinos in the Earth. The flux upper limits are calculated with the unified approach of Feldman and Cousins (1998).

Source	Decl. δ (degrees)	Events in 3°	Backgr. in 3°	ν-induced μ-Flux Limits [10^{-14} cm^{-2} s^{-1}]	ν-Flux Limits [10^{-6} cm^{-2} s^{-1}]
SMC X-1	-73.5	3	2.1	0.62	1.18
LMCX-2	-72.0	0	2.0	0.15	0.33
LMCX-4	-69.5	0	2.0	0.15	0.29
SN1987A	-69.3	0	2.0	0.15	0.31
GX301-2	-62.7	2	1.8	0.53	1.10
Cen X-5	-62.2	2	1.7	0.55	1.04
GX304-1	-61.6	2	1.7	0.54	1.05
CENXR-3	-60.6	1	1.7	0.36	0.68
CirXR-1	-57.1	5	1.7	1.18	2.21
2U1637-53	-53.4	0	1.7	0.19	0.36
MX1608-53	-52.4	0	1.7	0.20	0.38
GX339-4	-48.8	6	1.7	1.62	3.00
ARA XR1	-45.6	3	1.6	1.00	1.87
VelaP	-45.2	1	1.5	0.51	0.94
GX346-7	-44.5	0	1.5	0.23	0.43
SN1006	-41.7	1	1.3	0.56	1.04
VelaXR-1	-40.5	0	1.3	0.26	0.55
2U1700-37	-37.8	1	1.3	0.58	1.08
L10	-37.0	2	1.1	0.91	1.72
SGR XR-4	-30.4	0	0.9	0.34	0.63
Gal Cen	-28.9	0	0.9	0.34	0.65
GX1+4	-24.7	0	0.9	0.36	0.67
Kep1604	-21.5	2	0.9	1.12	2.12
GX9+9	-17.0	0	0.9	0.40	0.75
Sco XR-1	-15.6	1	0.9	0.85	1.59
Aquarius	-1.0	3	0.8	2.09	3.95
4U0336+01	0.6	1	0.8	1.17	2.19

Table 5.42: MACRO Flux Limits on Prospective Astrophysical Neutrino Point Sources. (Ambrosio et al., 2001)
(continued)

Source	Decl. δ (degrees)	Events in 3°	Backgr. in 3°	ν-induced μ-Flux Limits [10^{-14} cm^{-2} s^{-1}]	ν-Flux Limits [10^{-6} cm^{-2} s^{-1}]
AQL XR-1	0.6	0	0.8	0.57	1.18
2U1907+2	1.3	0	0.8	0.58	1.27
SER XR-1	5.0	0	0.7	0.67	1.41
SS433	5.7	0	0.7	0.67	1.27
2U0613+09	9.1	1	0.6	1.52	3.02
Geminga	18.3	0	0.5	1.12	2.10
Crab	22.0	1	0.4	2.52	4.70
2U0352+30	31.0	2	0.3	5.98	11.43
Cyg XR-1	35.2	0	0.2	3.24	6.24
Her X-1	35.4	0	0.2	3.30	6.96
Cyg XR-2	38.3	0	0.1	4.99	10.61
Mkn 421	38.4	0	0.1	5.00	9.56
Mkn 501	40.3	0	0.1	5.73	10.69
Cyg X-3	40.9	0	0.1	6.59	12.49
Per XR-1	41.5	0	0.1	7.51	13.99

tribution to the total flux of neutrinos and antineutrinos. This, however, will only be possible with a giant detector matrix with an effective volume on the order of 1 km^3, as mentioned earlier. High angular resolution of such a detector is of paramount importance because it reduces the background rate per pixel, improves the signal to noise ratio and sensitivity, and lowers the minimum detectable flux (Bosetti et al., 1982 and 1989; Roberts, 1992; Anassontzis et al., 1995; see also Chapter 4, Section 4.5).

References

Aglietta, M., G. Badino, G. Bologna, C. Castagnoli, A. Castellina, V.L. Dadykin, W. Fulgione, P. Galeotti, F.F. Kalchukov, V.B. Kortchaguin, P.V. Kortchaguin, A.S. Malguin, V.G. Ryassny, O.G. Ryazhskaya, O. Saavedra, V.P. Talochkin, G. Trinchero, S. Vernetto, G.T. Zatsepin, and V.F. Yakushev: Europhys. Lett., 3 (12), p. 1315 (1987a).

Aglietta, M., G. Badino, G. Bologna, C. Castagnoli, A. Castellina, V.L. Dadykin, W. Fulgione, P. Galeotti, F.F. Kalchukov, V.B. Kortchaguin, P.V.

Kortchaguin, A.S. Malguin, V.G. Ryassny, O.G. Ryazhskaya, O. Saavedra, V.P. Talochkin, G. Trinchero, S. Vernetto, G.T. Zatsepin, and V.F. Yakushev: Europhys. Lett., 3 (12), p. 1321 (1987b).

Alekseev, E.N., L.N. Alekseeva, V.I. Volchenko, and I.V. Krivosheina: Pis'ma Zh. Eksp. Teor. Fiz., 45, No. 10, p. 461 (1987) and JETP Lett., 45, No. 10, p. 589 (1987).

Alexeyev, E.N., L.N. Alexeyeva, A.E. Chudakov, and I.V. Krivosheina: PICRC, 6, p. 277 (1987).

Alexeyev, E.N., L.N. Alexeyeva, I.V. Krivosheina, and V.I. Volchenko: Physics Lett., B 205, p. 209 (1988).

Ambrosio, M., R. Antolini, G. Auriemma, D. Bakari, A. Baldini, G.C. Barbarino, B.C. Barish, G. Battistoni, R. Bellotti, C. Bemporad, P. Bernardini, H. Bilokon, V. Bisi, C. Bloise, C. Bower, M. Brigida, S. Bussino, F. Cafagna, M. Calicchio, D. Campana, M. Carboni, S. Cecchini, F. Cei, V. Chiarella, B.C. Choudhary, S. Coutu, G. De Cataldo, H. Dekhissi, C. De Marzo, I. De Mitri, J. Derkaoui, M. De Vincenzi, A. Di Credico, 0. Erriquez, C. Favuzzi, C. Forti, P. Fusco, G. Giacomelli, G. Giannini, N. Giglietto, M. Giorgini, M. Grassi, L. Gray, A. Grill, F. Guarino, C. Gustavino, A. Habig, K. Hanson, R. Heinz, E. Iarocci, E. Katsavounidis, I. Katsavounidis, E. Kearns, H. Kim, S. Kyriazopoulou, E. Lamanna, C. Lane, D. S. Levin, P. Lipari, N.P. Longley, M.J. Longo, F. Loparco, F. Maaroufi, G. Mancarella, G. Mandrioli, S. Manzoor, A. Margiotta, A. Marini, D. Martello, A. Marzari-Chiesa, M.N. Mazziotta, D.G. Michael, S. Mikheyev, L. Miller, P. Monacelli, T. Montaruli, M. Monteno, S. Mufson, J. Musser, D. Nicolò, R. Nolty, C. Okada, C. Orth, G. Osteria, M. Ouchrif, 0. Palamara, V. Patera, L. Patrizii, R. Pazzi, C.W. Peck, L. Perrone, S. Petrera, P. Pistilli, V. Popa, A. Rainò, J. Reynoldson, F. Ronga, C. Satriano, L. Satta, E. Scapparone, K. Scholberg, A. Sciubba, P. Serra, M. Sioli, M. Sitta, P. Spinelli, M. Spinetti, M. Spurio, R. Steinberg, J.L. Stone, L.R. Sulak, A. Surdo, G. Tarlè, V. Togo, M. Vakili, E. Vilela, C.W. Walter, and R. Webb, MACRO Collaboration: Astrophys. J., January (2001).

Anassontzis, E., P. Assimakopoulus, M. Barone, G. Fanourakis, C. Goudis, G. Grammatikakis, P. Hantzion, P. Ioannou, S. Katsanevas, C. Markou, J. McNutt, L. Moraitis, A. Nicolaidis, P. Pramantiotis, L.K. Resvanis, I. Siotis, S.A. Sotiriou, G. Voulgaris, P.K.F. Grieder, P. Minkowski, E. Torrente, L. Sulak, A.E. Ball, B. Langeset, H. Bradner, S. Bottai, A. Cartacci, L. Dell'Angelo, M.P. DePascale, F. Grianti, B. Monteleoni, V.A. Naumov, V. Valente, J.G. Learned, V.J. Stenger, U. Keusen, P. Koske, J. Rathlev, G. Voigt, G. DeMarchis, L. Piccari, M. Bonori, A. Capone, F. Massa, E.

Valente, I.F. Barinov, A.V. Butkevich, L.G. Dedenko, A.O. Deineko, V.A. Gaidash, S.K. Karaevsky, A.A. Mironovich, A.A. Permyakov, N.M. Surin, A.V. Trenikhin, L.A. Zakharov, I.M. Zheleznykh, V.A. Zhukov, T.A. Demidova, A.P. Eremeev, M.N. Platonov, V.K. Rucol, N.A. Sheremet, V.I. Albul, V.V. Ledenev, A.A. Paramonov, N. de Botton, P.H. Carton, M. Cribier, F. Feinstein, Ph. Gorest, J.-C. Languillat, S. Loucatos, L. Moscoso, J.-P. Passérieux, Ph. Rebourgeard, F. Rondeaux, J. Poinsignon, Y. Sacquin, J.-P. Schuller, A. Tabary, D. Vignaud, D. Vilanova, U. Camerini, R. March: NESTOR Proposal 1995, Dept. of Physics, University of Athens (1995).

Barish, Barry, C.: Nucl. Phys., B (Proc. Suppl.) p. 469 (1995).

Barwick, S., F. Halzen, D. Lowder, T. Miller, R. Morse, P.B. Price, and A. Westphal: J. Phys., G 18, p. 225 (1992).

Becker-Szendy, R., C.B. Bratton, D. Casper, S.T. Dye, W. Gajewski, K. Ganezer, M. Goldhaber, T.J. Haines, P.G. Halverson, D. Kielczewska, W.R. Kropp, J.G. Learned, J. LoSecco, G. McGrath, C. McGrew, M. Masuzawa, S. Matsuno, R.S. Miller, L. Price, F. Reines, J. Schultz, H.W. Sobel, J. Stone, L.R. Sulak, R. Svoboda, and M. Vagins: Nucl. Phys., B (Proc. Suppl.) 38, p. 331 (1995).

Berezinsky, V.S., and L.M. Ozernoy: Astron. Astrophys., 98, p. 50 (1981).

Berezinsky, V.S., S.V. Bulanov, V.A. Dogiel, V.L. Ginzberg, and V.S. Ptuskin: Astrophysics of Cosmic Rays (Amsterdam), Elsevier (1991).

Berezinsky, V.S., and John G. Learned: in Proc. of the Workshop on "High Energy Neutrino Astrophysics"; eds. V.J. Stenger, J.G. Learned, S. Pakvasa, and X. Tata, World Scientific, Singapore, p. 43 (1992).

Berezinsky, V.S., T.K. Gaisser, F. Halzen, and T. Stanev: Astropart. Phys. 1, p. 281 (1993).

Berezinsky, V.: Nucl. Phys., B (Proc. Suppl.) 38, p. 363 (1995).

Bethe, H.A.: Rev. Mod. Phys., 62, p. 801 (1990).

Bionta, R.M., G. Blewitt, C.B. Bratton, D. Casper, A. Ciocio, R. Claus, B. Cortez, M. Crouch, S.T. Dye, S. Errede, G.W. Foster, W. Gajewski, K.S. Ganezer, M. Goldhaber, T.J. Haines, T.W. Jones, D. Kielczewska, W.R. Kropp, J.G. Learned, J.M. LoSecco, J. Matthews, R. Miller, M.S. Mudan, H.S. Park, L.R. Price, F. Reines, J. Schultz, S. Seidel, E. Shumard, D. Sinclair, H.W. Sobel, J.L. Stone, L.R. Sulak, R. Svoboda, G. Thornton, J.C. van der Velde, and C. Wuest: Phys. Rev. Lett., 58, p. 1494 (1987).

Bird, D.J., S.C. Corbato, H.Y. Dai, J.W. Elbert, K.D. Green, M.A. Huang, D.B. Kieda, S. Ko, C.G. Larsen, E.C. Loh, M.Z. Luo, M.H. Salamon, J.D.

Smith, P. Sokolsky, P. Sommers, J.K.K. Tang, and S.B. Thomas: Astrophys. J., 441, p. 144 (1995).

Birkel, M., and S. Sarkar: Preprint hep-ph/9804285 (1998).

Bosetti, P., P.K.F. Grieder, P. Minkowski, B. Barish, J. Elliott, W. Gajewski, W. Kropp, L. Price, F. Reines, H. Sobel, J. Babson, R. Becker-Szendy, J.G. Learned, S. Matsuno, D. O'Connor, A. Roberts, V.J. Stenger, V.Z. Peterson, G. Wilkins, O.C. Allkofer, P. Koske, M. Preischel, J. Rathlev, T. Kitamura, H. Bradner, K. Mitsui, Y. Ohashi, A. Okada, J. Clem, C.E. Roos, M. Webster, U. Camerini, M. Jaworski, R. March, R. Morse: DUMAND Proposal 1982, Dept. of Physics and Astronomy, University of Hawaii (1982).

Bosetti, P., P.K.F. Grieder, P. Minkowski, B. Barish, J. Elliott, W. Gajewski, W. Kropp, L. Price, F. Reines, H. Sobel, J. Babson, R. Becker-Szendy, J.G. Learned, S. Matsuno, D. O'Connor, A. Roberts, V.J. Stenger, V.Z. Peterson, G. Wilkins, O.C. Allkofer, P. Koske, M. Preischel, J. Rathlev, T. Kitamura, H. Bradner, K. Mitsui, Y. Ohashi, A. Okada, J. Clem, C.E. Roos, M. Webster, U. Camerini, M. Jaworski, R. March, R. Morse: DUMAND Proposal 1989, Dept. of Physics and Astronomy, University of Hawaii (1989).

Bratton, C.B., D. Casper, A. Ciocio, R. Claus, M. Crouch, S.T. Dye, S. Errede, W. Gajewski, M. Goldhaber, T.J. Haines, T.W. Jones, D. Kielczewska, W.R. Kropp, J.G. Learned, J.M. LoSecco, J. Matthews, R. Miller, M.S. Mudan, L.R. Price, F. Reines, J. Schultz, S. Seidel, D. Sinclair, H.W. Sobel, J.L. Stone, L.R. Sulak, R. Svoboda, G. Thornton, J.C. van der Velde: Phys. Rev., D, 37, p. 3361 (1988).

Burrows, A.: in Supernova, ed. A.G. Petschek, Springer, Berlin (1988).

Burrows, A.: Ann. Rev. Nucl. Part. Sci., 40, p. 181 (1990).

Castagnoli, C: Internat. Astronomical Union Circular (IAUC) No. 4323 (1987a).

Castagnoli, C: ibid No. 4332 (1987b).

Chiu, H.Y.: Ann. Phys. (N.Y.), 26, p. 364 (1964).

Colgate, S.A., and R.H. White: Astrophys. J., 143, p. 626 (1966).

Crouch, M.F., P.B. Landecker, J.F. Lathrop, F. Reines, W.G. Sandie, H.W. Sabel, H. Coxell and J.P.F. Sellschop: Phys. Rev., D 18, p. 2239 (1978).

Domokos, G., B. Elliott, ans S. Kovesi-Domokos: J. Phys. G, 19, p. 899 (1993).

Fichtel, C.: Proc. of the 3rd. Compton Observatory Symposium (Astronomy and Astron. Astrophys., Suppl. Ser., 120, p. 23 (1996).

Gaisser, Thomas K., Francis Halzen, and Todor Stanev: Physics Reports, 258, p. 173 - 236 (1995).

Garradd, G.: Internat. Astronomical Union Circular (IAUC) No. 4316 (1987).

Grieder, P.K.F.: in "Neutrinos and the Present-day Universe", eds. Thierry Montmerle and Michel Spiro, ISBN 2-7272-0103-6 Edition Doc. CEN Saclay 86-45 (1986).

Halzen, F., and E. Zas: Astrophys. J., 488, p.669 (1997).

Hill, C.T., and D.N. Schramm: Phys. Rev., D 31, p. 564 (1985).

Hirata, K.S., T. Kajita, M. Koshiba, M. Nakahata, Y. Oyama, N. Sato, A. Suzuki, M. Takita, Y. Totsuka, T. Kifune, T. Suda, K. Takahashi, T. Tanimori, K. Miyano, M. Yamada, E.W. Beier, L.R. Feldscher, S.B. Kim, A.K. Mann, F.M. Newcomer, R. Van Berg, W. Zhang, and B.G. Cortez: Phys. Rev. Lett., 58, p. 1490 (1987).

Hirata, K.S., T. Kajita, M. Koshiba, M. Nakahata, Y. Oyama, N. Sato, A. Suzuki, M. Takita, Y. Totsuka, T. Kifune, T. Suda, K. Takahashi, T. Tanimori, K. Miyano, M. Yamada, E.W. Beier, L.R. Feldscher, W. Frati, S.B. Kim, A.K. Mann, F.M. Newcomer, R. Van Berg, W. Zhang, and B.G. Cortez: Phys. Rev., D, 38, p. 448 (1988).

Ingelman, G., and M. Thunman: Preprint, hep-ph/9604286 (1996).

Karle, A.: Phys. Lett., B 347, p. 161 (1995).

Koshiba, M.: Physics Reports, 220, Nr. 5 & 6, p. 229 - 381 (1992).

Learned, John G.: in "Cosmic Rays 92 - Astrophysical, High Energy and Heliospheric Processes", ed., P.K.F. Grieder, Nucl. Phys., B, (Proc. Suppl.) 33A, B, p. 77 (1993).

Lee, S.: Preprint astro-ph/9604098 (1996).

Lipari, P.: Astropart. Phys., 1, p. 195 (1993).

Mannheim, K.: Astropart. Phys., 3, p. 295 (1995).

Markov, M.A.: in "Proceedings of the 1960 Annual International Conference on High Energy Physics" , Rochester, ed. E.C.G. Sudarshan, J.H. Tinlot, and A. Melissinos (Uni. of Rochester/Interscience, Rochester, N.Y.), p. 578 (1960).

Markov, M.A., and I.M. Zheleznykh: Nucl. Phys., 27, p. 385 (1961).

Miller, R.S., R. Becker-Szendy, C.B. Bratton, J. Breault, D. Casper, S.T. Dye, W. Gajewski, M. Goldhaber, T.J. Haines, P.G. Halverson, D. Kielczewska, W.R. Kropp, J.G. Learned, J.M. LoSecco, S. Matsuno, J. Matthews,

G. McGrath, C. McGrew, L. Price, F. Reines, J. Schultz, D. Sinclair, H.W. Sobel, J.L. Stone, L.R. Sulak, R. Svoboda, and J.C. van der Velde: Astrophys. J., 428, p. 629 (1994).

Protheroe, R.J.: in Proc. IAU Colloq. 163, Accretion Phenomena and Related Outflows, ed. D. Wickramasinghe et al., ASP Conf. series, Vol 121, p. 585, astro-ph/9607165 (1997).

Protheroe, R.J.: Nucl. Phys. (Proc. Suppl.), B 77, p. 465 (1999).

Protheroe, R.J., and P.A. Johnson: Astropart. Phys., 4, p. 253 (1995), and erratum, Astropart. Phys., 5, p. 215 (1996).

Protheroe, R.J., and Todor Stanev: Phys. Rev. Lett., 77, p. 3708 (1996).

Ryazhskaya, O.G., V.G. Ryasny, and O. Saavedra: Nuovo Cimento, 106 A, p. 257 (1993).

Roberts, A.: Rev. Mod. Phys., 64, p. 259 (1992).

Shelton, I.: Internat. Astronomical Union Circular (IAUC) No. 4316 (1987).

Sigl. Günter, Sangjin Lee, David Schramm, and Paolo Coppi: Phys. Lett., B 392, p. 129 (1997).

Stecker, F.W.: Astrophys. J., 228, p. 919 (1979).

Stecker, F.W., C. Done. M.H. Salamon, and P. Sommers: Phys. Rev. Lett., 66, p. 2697 (1991).

Stecker, F.W., C. Done. M.H. Salamon, and P. Sommers: Phys. Rev. Lett., 69, p. 2738 (1992a) Errata.

Stecker, F.W., C. Done. M.H. Salamon, and P. Sommers: in Proc. of the Workshop on "High Energy Neutrino Astrophysics"; eds. V.J. Stenger, J.G. Learned, S. Pakvasa, and X. Tata, World Scientific, Singapore, p. 1 (1992b).

Svoboda, R., R.M. Bionta, G. Blewitt, C.B. Bratton, D. Casper, P. Chrysicopoulou, A. Ciocio, R. Claus, B. Cortez, S.T. Dye, S. Errede, G.W. Foster, W. Gajewski, K.S. Ganezer, M. Goldhaber, T.J. Haines, T.W. Jones, D. Kielczewska, W.R. Kropp, J.G. Learned, J.M. LoSecco, J. Matthews, H.S. Park, F. Reines, J. Schultz, S. Seidel, E. Shumard, D. Sinclair, H.W. Sobel, J.L. Stone, L.R. Sulak, G. Thornton, J.C. van der Velde, and C. Wuest: Astrophys. J., 315, p. 420 (1987).

Szabo, A.P., and R.J. Protheroe: in Proc. of the Workshop on "High Energy Neutrino Astrophysics"; eds. V.J. Stenger, J.G. Learned, S. Pakvasa, and X. Tata, World Scientific, Singapore, p. 24 (1992).

Szabo, A.P., and R.J. Protheroe: Astropart. Phys., 2, p. 375 (1994).

Thompson, D.J., and C.E. Fichtel: Astron. Astrophys., 109, p. 352 (1982).

Volkova, L.V.: Yad. Fiz., 31, p. 1510 (1980); Sov. J. Nucl. Phys., 31, p. 784 (1980).

Waxman, Eli, and John Bahcall: Phys. Rev. Lett.,78, p. 2292 (1997).

Woosley, S.E., J. Wilson, and R. Mayle: Astrophys. J., 302, p. 19 (1986).

Yoshida, Shigeru, and Masahiro Teshima: Progr. Theor. Phys., 89, p. 833 (1993).

Yoshida, S., H. Dai, C.C.H. Jui, and P. Sommers: Astropart. Phys., 479, p 547 (1997).

Zwicky, F.: in Stellar Structure, eds. G.P. Kuiper and B.M. Middlehurst, University of Chicago Press, Chicago (1965).

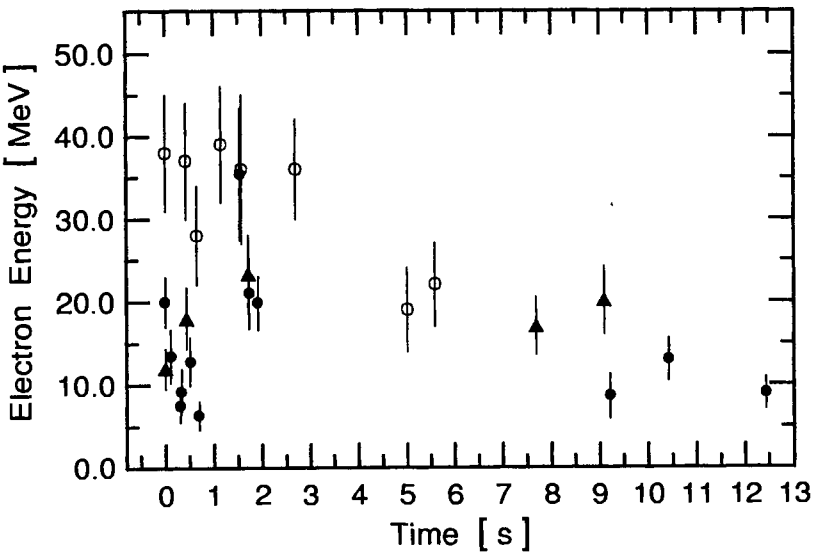

Figure 5.71: Compilation of the time - energy distribution of the 5, 8 and 12 neutrino events from the neutrino burst of the supernova SN-1987A recorded with the Baksan (▲) (Alexeyev et al., 1987 and 1988), IMB-3 (o) (Bratton et al., 1988), and Kamiokande II (•) (Hirate et al., 1987 and 1988) detectors, respectively, on February 23, 1987. IMB-3 and Kamiokande II are water Cherenkov detectors, Baksan is a liquid scintillation detector. The exact time of occurrence of the first event of the neutrino burst recorded is slightly different for each experiment but was set to zero in the plot to have a common origin for better comparison. The exact universal time (UT) of occurrence of each event including those of the LSD detector (Aglietta et al., 1987a), not shown here, are listed in Tables 5.37 to 5.40.

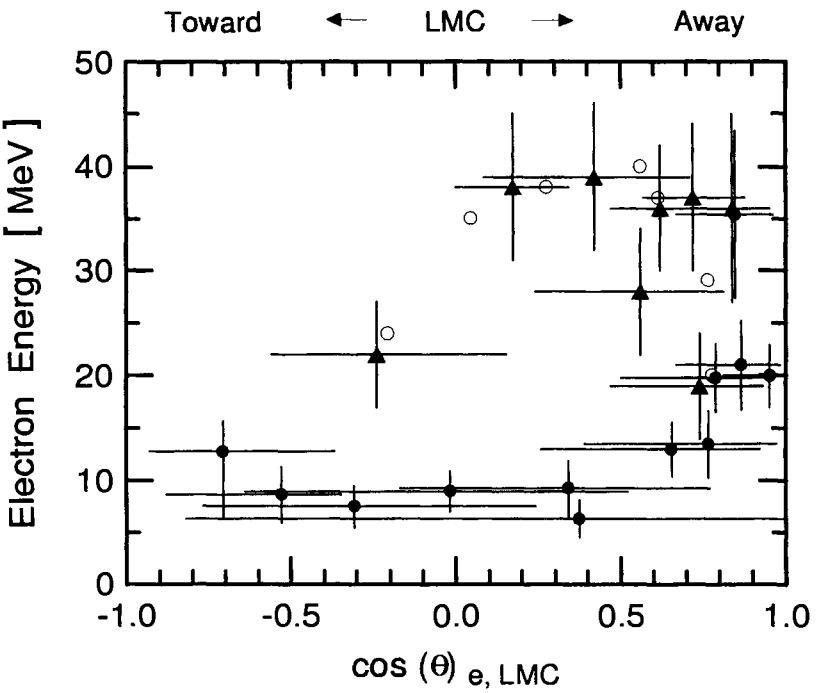

Figure 5.72: Energy - direction plot of the electrons resulting from the neutrino reactions in the Kamiokande II (•) (Hirata et al., 1988) and IMB-3 (○, ▲) detectors (Bionta et al, 1987; Bratton et al., 1988). The data points of Bratton et al. (1988) (▲) are the result of a re-analysis of the measurements of Bionta et al. (1987), shown without error bars. $\theta_{e,LMC}$ is the angle of the electron track in the detector with respect to the direction away from the supernova SN-1987A in the Large Magellanic Cloud (LMC). Note that at the time of the neutrino burst the IMB-3 detector had a directional trigger bias against events oriented toward SN-1987A because of inoperative photomultipliers in the detector (Bionta et al., 1987).

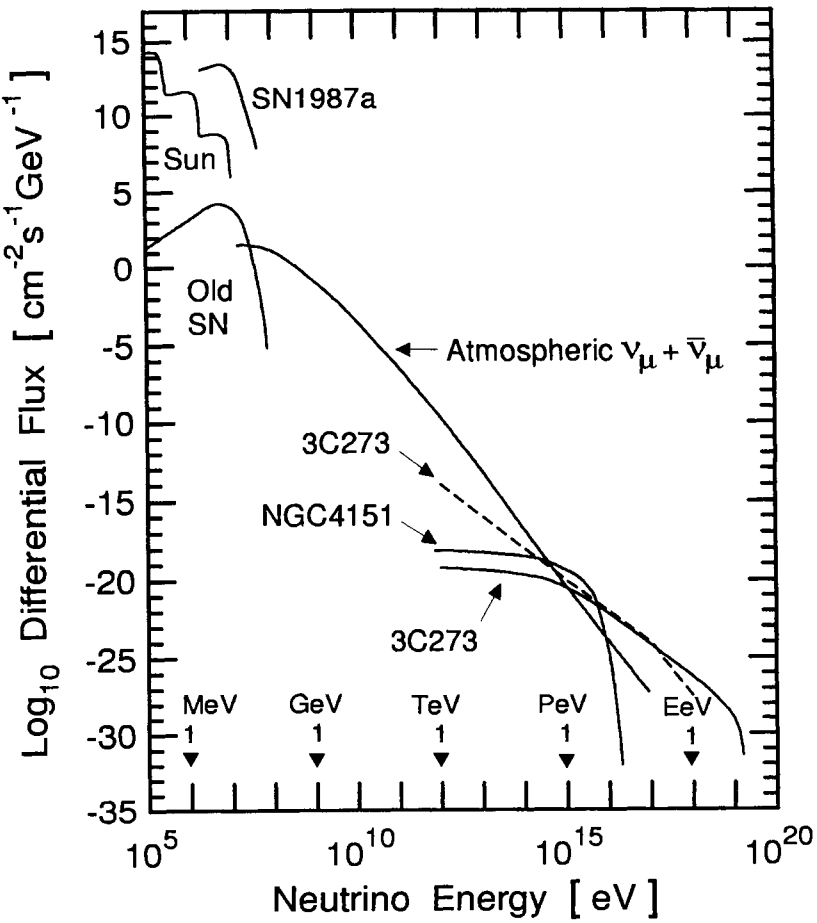

Figure 5.73: Differential energy spectra of neutrinos of some point sources. The atmospheric flux applies to 2π steradian (Volkova, 1980; Koshiba, 1992). The ν_μ ($\overline{\nu}_\mu$) spectra of the two point sources, NGC4151, the brightest radio-quiet AGN, and 3C273, the brightest radio-loud AGN, (solid curves) are from a calculation of Stecker et al. (1991, 1992a and 1992b). The dashed line labeled 3C273 is a neutrino spectrum of this object from the work of Szabo and Protheroe (1994) using different assumptions. The calculation is based on assumed X-ray luminosities of $L_X = 3 \cdot 10^{43}$ erg s^{-1} and $L_X = 10^{47}$ erg s^{-1}, and distances of $4.5 \cdot 10^{25}$ cm and $3 \cdot 10^{27}$ cm for NGC4151 and 3C273, respectively. The ν_e, $\overline{\nu}_e$ intensity is half of that of the ν_μ, $\overline{\nu}_\mu$ intensity. The solar and supernova fluxes are taken from Koshiba (1992).

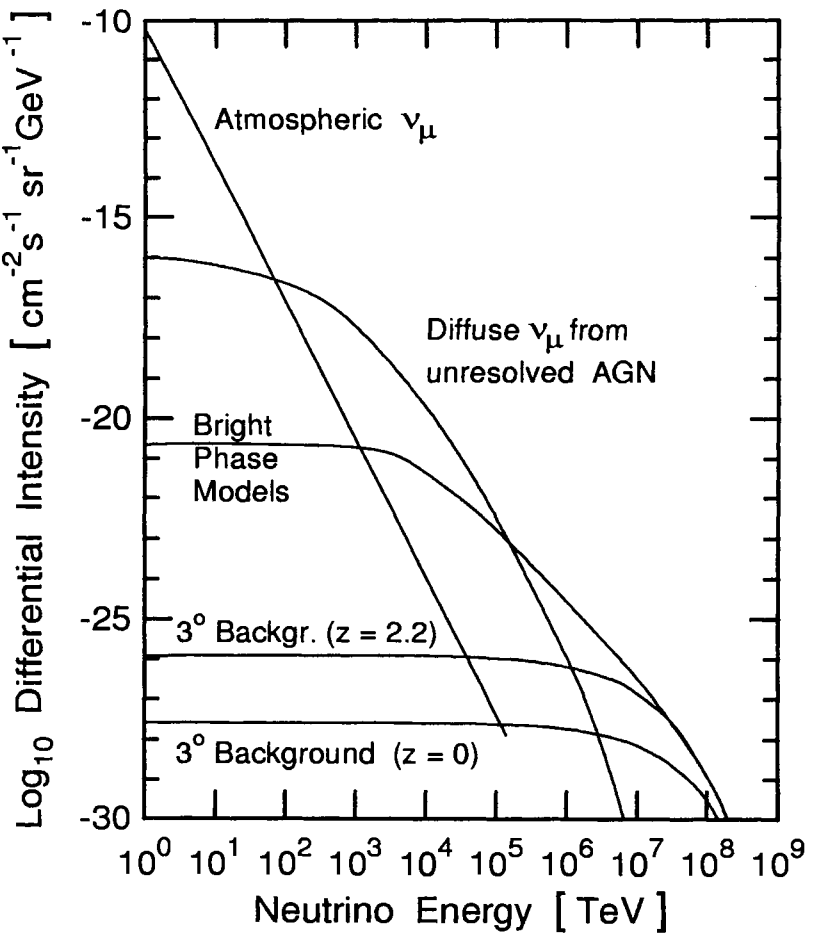

Figure 5.74: Predicted spectra of some diffuse astrophysical high energy neutrino sources ($\nu_\mu + \overline{\nu}_\mu$). The spectrum of the diffuse neutrinos from unresolved AGNs is the integrated $\nu_\mu + \overline{\nu}_\mu$ intensity and is from a calculation of Stecker et al. (1991 and 1992a). Also shown is the background expected from photo-meson production of the extragalactic high energy cosmic rays with the cosmic background radiation for z = 0 and integrated over cosmic time to red a shift of z = 2.2 (Stecker et al., 1992b), and to galaxy formation according to Berezinsky et al. (1991), labeled "bright phase models" (see also Berezinsky, 1995). The horizontal atmospheric neutrino spectrum from high energy cosmic rays interacting in the Earth's atmosphere is also indicated (Stecker, 1979; Crouch et al., 1978; Volkova, 1980) (see also Berezinsky and Ozernoy, 1981).

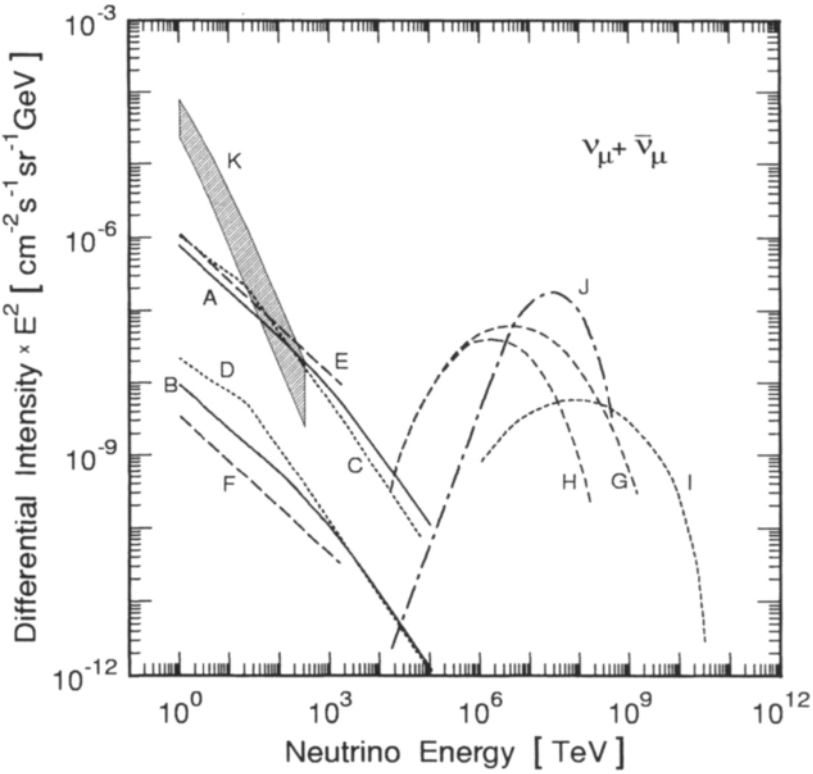

Figure 5.75: Predicted diffuse muon neutrino and antineutrino intensities from cosmic ray interactions with the interstellar medium. Curves A and B are from the work of Ingelman and Thunman (1996), C and D from Domokos et al. (1993), and E and F from Berezinsky et al. (1993). Curves A, C and E are for the galactic coordinates $l = 0°$, $b = 0°$, curves B, D and F for $b = 90°$. The hatched area, K, represents the atmospheric neutrino background for the zenith angle range from $\theta = 0°$ (vertical, lower boundary of hatched area K) to $\theta = 90°$ (horizontal, upper boundary of K), after Lipari (1993). Curves G to J are neutrino intensities from cosmic ray interactions with the microwave background: G is for a maximum cosmic ray energy of $3 \cdot 10^{21}$ eV, H for $E_{max} = 3 \cdot 10^{20}$ eV (Protheroe and Johnson, 1995 and 1996); I is from the work of Lee (1996) assuming that the highest energy cosmic rays are due to gamma ray bursters (GRB); and J is from the work of Hill and Schramm (1985) (after Protheroe, 1999).

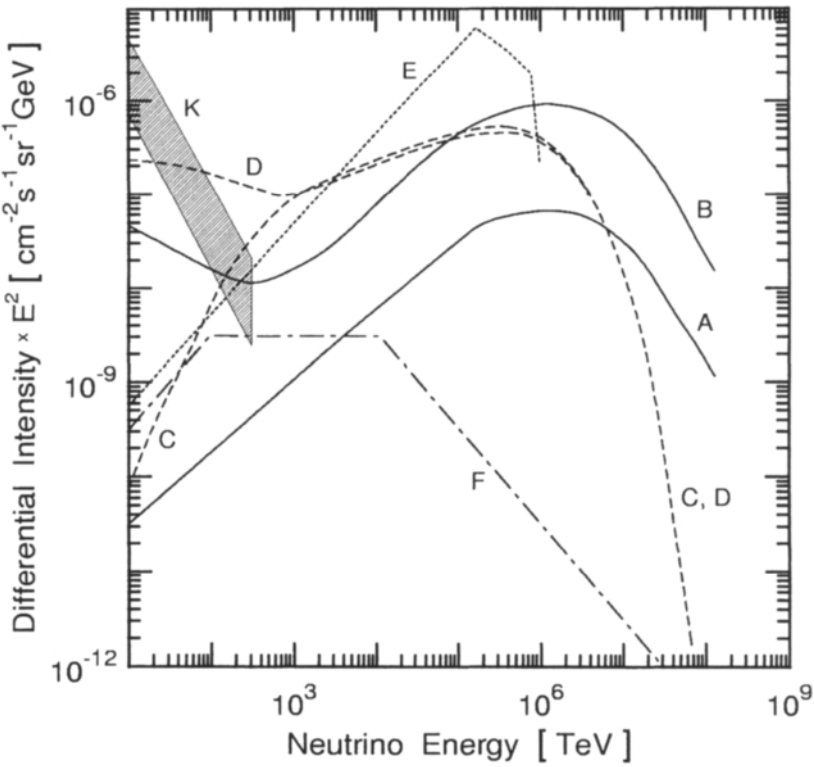

Figure 5.76: Prediction of the diffuse muon neutrino and antineutrino intensities from blazars according to calculations of Mannheim (1995) for $p\gamma$ (model A), curve A, and $pp + p\gamma$ (model B) processes, curve B, and likewise Protheroe (1997) curves C and D, respectively. Curve E is from the work of Halzen and Zas (1997) for $p\gamma$ only. Curve F shows the contribution from gamma ray bursters (GRB) according to Waxman and Bahcall (1997) (after Protheroe, 1999). The hatched area, K, shows the atmospheric neutrino background after Lipari (1993) over the entire zenith angle range from 0° (vertical, lower boundary of K) to 90° (horizontal, upper boundary of K).

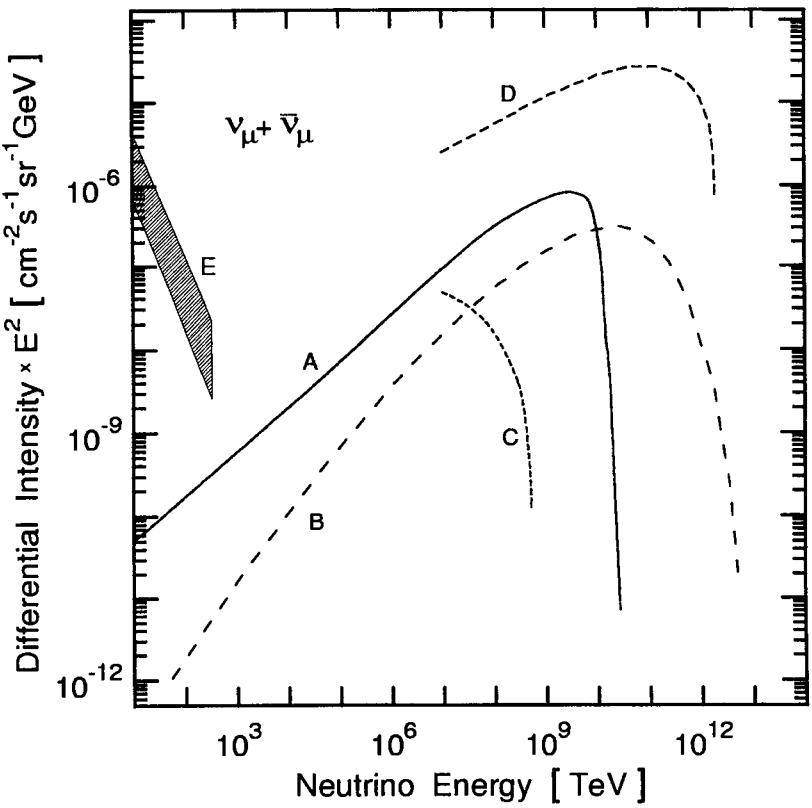

Figure 5.77: Highly speculative muon neutrino and antineutrino intensities from model calculations of topological defects (for details see Protheroe, 1999 and references therein). Curve A which is based on $M_X c^2 = 10^{14.1}$ GeV and a magnetic field of $B = 10^{-9}$ G is just ruled out according to Protheroe and Stanev (1996), and curve B for $M_X c^2 = 2 \cdot 10^{16}$ GeV and $B = 10^{-12}$ G is classified as just allowed according to Sigl et al. (1997). Curve C is from the work of Birkel and Sarkar (1998) for $M_X c^2 = 10^{12}$ GeV, $B = 0$ G; and D is from Yoshida et al. (1997) for $M_X c^2 = 10^{16}$ GeV and $B = 0$ G. The hatched area, E, indicates the atmospheric neutrino background from the calculation of Lipari (1993) for the full zenith angle range from 0° (vertical, lower limit of E) to 90° (horizontal, upper limit of E).

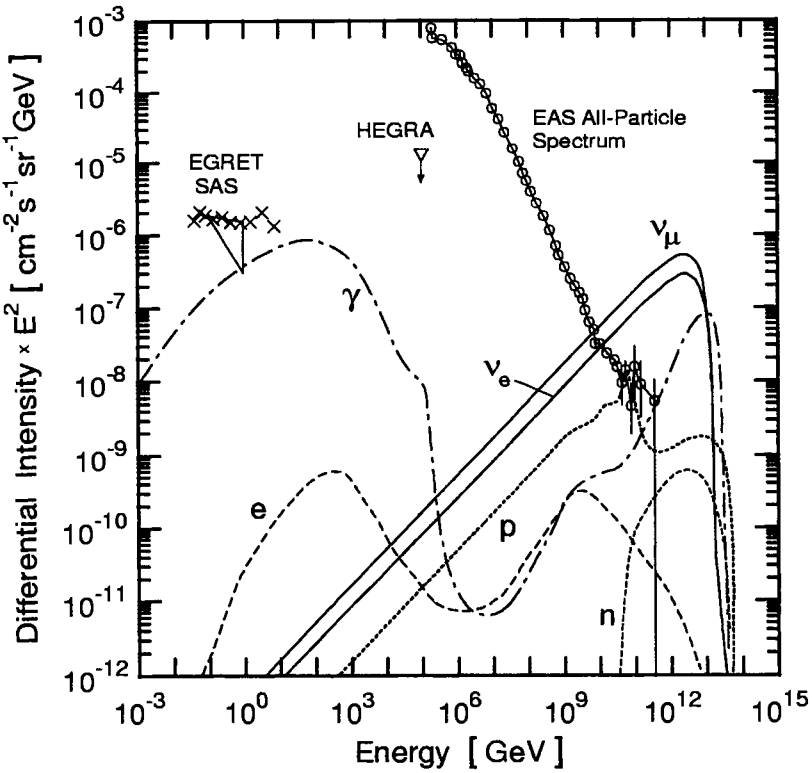

Figure 5.78: Muon neutrino ($\nu_\mu + \overline{\nu}_\mu$) and electron neutrino ($\nu_e + \overline{\nu}_e$) intensities from topological defects according to model calculations of Protheroe and Stanev (1996) using an injection spectrum that follows approximately an $E^{-1.5}$ dependence and extends up to $\sim M_X c^2/2$, containing ~3% nucleons and 97% pions. The curves labeled p, n, γ and e are product spectra of M_X-decays and set bounds for the models and parameters (see text). The curves apply for $M_X c^2 = 10^{14.1}$ GeV, a magnetic field of $B = 10^{-9}$ G and a model parameter of $p = 2$ (constant injection), where $Q(t) = Q_0(t/t_0)^{-2+p}$ is the injection rate per evolving volume. The spectra of observable particles are normalized to the $3 \cdot 10^{11}$ GeV point of the cosmic ray spectrum, outlined by circles, as determined from air shower measurements (Bird et al., 1995). Indicated, too, are gamma ray intensities measured with the SAS-II (Thompson and Fichtel, 1982) and EGRET (Fichtel, 1996) satellite instruments and a HEGRA point at 100 TeV (Karle, 1995).

5.6 Antiprotons and Antimatter

5.6.1 Discovery of Cosmic Ray Antiprotons

The question whether antimatter such as antiprotons, antideuterons, antihelium, etc., exist in the primary cosmic radiation is of great relevance from the astrophysical and cosmological point of view (Steigman, 1976). It is also linked to the fundamental question of charge symmetry in the Universe. Speculations that antiprotons may be present in the cosmic radiation appeared in the literature (Fradkin, 1955 and 1956) soon after their discovery at the Bevatron accelerator at Berkeley by Chamberlain et al. (1955). It should be mentioned in this context that prior to the official discovery of the antiproton, Amaldi et al. (1955) observed a cosmic ray induced event in stripped nuclear emulsion after an exposure at high altitude in Sardinia, Italy, in 1953 which they have interpreted as being most likely an antiproton, a particle which had never been observed before.

Antiprotons are produced in energetic collisions of the primary radiation with the constituents of the interstellar medium, i.e., gas and dust particles. These antiprotons are therefore not true primaries but must be referred to as secondary antiprotons (for a review see Stephens and Golden, 1987; Basini et al., 1989). Speculations that primordial antimatter, i.e., $\overline{p}$, $\overline{He}$, etc., if present in the cosmic radiation, originates from antimatter galaxies or even distant antimatter portions of the universe are extremely unlikely on the grounds of the well known intensity and homogeneity of the diffuse gamma ray background. Likewise, theories that suggest a cosmological origin of antimatter through the decay of a variety of hypothetical particles are highly speculative.

The flux of cosmic ray antiprotons is also regarded as a test to investigate the amount of matter traversed by the cosmic radiation in the Galaxy and to test the validity of models of cosmic ray propagation (Shen et al., 1968; Suh, 1971; Gaisser and Maurer, 1973; Gaisser and Levy, 1974; Badhwar et al., 1975; Steigman, 1977; Bhattacharyya et al., 1978).

Evidence for the discovery of antiprotons in the cosmic radiation was first claimed by Golden et al. (1978, 1979a and 1979b) and Bogomolov et al. (1979) in balloon-borne experiments, after previous attempts by different groups have failed except for setting upper bounds to the flux of antiprotons (Haskin et al., 1959; Aizu et al., 1961; Grigorov et al., 1961; Apparao et al., 1967 and 1968, Bogomolov et al., 1971).

The instrument of Golden et al. (1979a and 1979b) was launched in

1979, from Palestine, Texas. The measurements were made under an average residual atmosphere of 5.4 g/cm^2. The geomagnetic cutoff during the flight varied from 4.55 GV/c to 5.55 GV/c and the data acquisition period lasted $2.84 \cdot 10^4$ s ($\simeq$ 7.89 hrs). A total of 28.4 events was attributed to galactic antiprotons, yielding a $\overline{p}/p$-ratio of $(5.2 \pm 1.5) \cdot 10^{-4}$ in the rigidity interval between 5.6 GV/c and 12.5 GV/c.

Some details of this experiment in which a superconducting magnet spectrometers had been used in conjunction with other devices are given in Chapter 2, Section 2.8. Problems that are faced by the experimenters in connection with the severe background, including deduction of the locally (atmospherically, etc.,) produced antiprotons from the total sample to isolate the small fraction of cosmic ray antiprotons, are also outlined in that section.

5.6.2 Detection Methods

In early attempts to search for antimatter in the cosmic radiation several authors have used nuclear emulsion in balloon experiments to identify low energy antiprotons or antimatter through their annihilation signatures, but without success (Haskin et al., 1959; Aizu et al., 1961; Grigorov et al., 1961; Apparao et al., 1968). In a later experiment Bogomolov et al. (1971 and 1979) used a small permanent magnet spectrometer for charge identification and a combination of scintillation and Cherenkov detectors, and spark chambers. A modified version of this instrument was used in subsequent flights (Bogomolov et al., 1987). Another technique was employed by Buffington et al. (1972, 1979 and 1981) who flew a spark chamber calorimeter with photographic recording of the annihilation events and a combination of scintillation counters for trigger selection.

Today most of the modern antimatter search experiments use highly sophisticated detector systems and many use a superconducting magnetic spectrometer as charge sign indicator. These instruments (BESS, CAPRICE, HEAT, IMAX, LEAP, MASS, PBAR, etc.) are state of the art and flown with balloons at the fringes of the atmosphere (3 - 5 g/cm^2), like their predecessors.

Measurements made on board of satellites or space stations have the great advantage that they do not have to cope with the strong background caused by the residual atmosphere, a problem common to balloon experiments, and that they offer long exposure times . Several projects are presently under way to explore the cosmic ray antiproton flux with instruments orbiting in space and to search for antinuclei such as $\overline{He}$ and $\overline{C}$. The most sophisticated

and promising new project is at present the PAMELA telescope (Adriani et al., 1997). Another much publicized project called AMS may not yield the anticipated results because it lacks a sufficient number of tracking planes for reconstructing the particle trajectories. Small-angle scattering of energetic particles could therefore easily lead to wrong charge assignment and consequently to matter/antimatter misinterpretation.

An interesting indirect method to estimate an upper limit of the flux of cosmic ray antiprotons, originally based on ideas of Peters (1963), was used during the early stages of the cosmic antiproton hunt by Brooke and Wolfendale (1964). These authors used the ratio of pions to protons measured at an atmospheric depth of 800 g/cm^2 (Lal et al., 1963) and the observed ratio of negative to positive particles that interact and produce neutrons at sea level (Brooke et al., 1964). The data were first evaluated under the assumption that no antiprotons are present and from the difference of particle ratios the fraction of antiprotons can then be inferred. The method is not applicable at low energies where the interaction cross sections of protons and antiprotons are different.

This approach was repeated later in a more refined form by Stephens and Golden (1987). Stephens did also estimate the fraction of antiprotons in the cosmic radiation from the charge ratio of muons, μ^+/μ^-, in the atmosphere (Stephens, 1983 and 1985), and Durgaprasad and Kunte (1971) derived an estimate from the flux values of singly-charged particles in conjunction with the east-west asymmetry of the cosmic radiation.

5.6.3 Measured Antiproton Intensities and $\overline{p}/p$ Ratios

The determination of the intensity of the antiproton flux and of the energy spectrum of antiprotons in the vicinity of the Earth is a difficult task. For instrumental reasons (annihilation of low energy $\overline{p}$ in the detector modules, limitation of the maximum detectable momentum and background problems) present measurements of antiprotons with balloon-borne detectors are limited to the energy range from about 0.1 GeV to less than 30 GeV. One of the foremost problems is the rejection of the π^--background.

Like all low energy particles, antiprotons, too, are subject to solar modulation. Their intensity varies with time which makes even comparisons with other not time-like experiments problematic. To reveal the interstellar antiproton spectrum the locally observed spectrum must be demodulated.

Many experimenters specify only the ratio of antiprotons to protons, $\overline{p}/p$, which they observe after having isolated the antiprotons from the high back-

ground of negatively charged particles and proton spill-over (see Section 2.8 Fig. 2.173), and after having subtracted the local contribution of antiprotons produced in interactions in the atmosphere and the instrument. The accuracy of the determination of the locally produced number of antiprotons and of the $\overline{p}/p$ ratio depends crucially on the flux of the primary cosmic radiation which itself is subject to variability and inaccuracy. Frequently the reason for not specifying the antiproton intensity are calibration and detector efficiency uncertainties.

The essential results of the great efforts which had been made over several decades in the search of antiprotons are presented here in compact form without discussing experimental aspects unless a particular feature warrants it. In Table 5.43 we summarize the available data of measured and estimated $\overline{p}/p$-ratios, and in Table 5.44 the measured differential intensities of antiprotons in the cosmic radiation on top of the atmosphere resulting from the pioneering work.

The data of the experiment of Golden et al. (1979a and 1979b) had been re-analyzed over a somewhat wider range of rigidity, resulting in a total of 41.5 galactic antiproton events as compared to the first analysis mentioned above that isolated 28.4 events only. The 41.5 events were divided into several energy intervals to get an indication of the shape of the antiproton spectrum, however, only over a very limited energy range (Golden et al., 1984).

In their early series of $\overline{p}/p$ measurements, not listed in the Table 5.43, Bogomolov et al. (1971) obtained an upper limit for the antiproton to proton flux ratio of $\overline{p}/p = 3 \pm 3 \cdot 10^{-3}$ at 2.3 - 5.3 GeV and cutoff rigidity $P_c \sim 3.2$ GV. In later measurements made at different geomagnetic cutoff rigidities these authors specified values of $\overline{p}/p = 6 \pm 4 \cdot 10^{-4}$ for the energy range 2 - 5 GeV and $P_c \sim 3.5$ GV, (Bogomolov et al., 1979). The three sets of data of the same authors listed in Table 5.43 were obtained at cutoff rigidities of 0.6 GV, 2.9 GV and 3.0 - 3.5 GV, respectively. The measurements were made with a permanent magnet spectrometer at residual atmospheres between 7 and 12 g/cm^2.

Subsequent to the pioneering work many more experiments were carried out employing mostly superconducting magnets and a variety of sophisticated detectors to confirm the results of the teams of Golden and Bogomolov, to improve the statistics and, above all, to determine the shape of the spectrum of cosmic ray antiprotons. Particular efforts were made to explore the sub-GeV region where Buffington et al. (1981) obtained a high $\overline{p}/p$-ratio in a measurement which, if confirmed, would have astrophysical implications, perhaps indicating the presence of primordial antimatter. But all of the later

Table 5.43: Measured and Estimated Fraction of Antiprotons in the Cosmic Radiation. (Early Work)

Energy GeV	Ratio $(\overline{p}/p) \cdot 10^4$	Reference
0.1-0.15	<3	Apparao et al. (1967, 1968)
0.05 - 0.15	<4.3	Apparao et al. (1985)
0.12 - 0.22	<30	Rao and Yock (1987)
0.13 - 0.32	2.2±0.6	Buffington et al. (1981)
0.2 - 0.8	≤ 9	Aizu et al. (1961)
0.2 - 2.0	$0.6^{+1.4}_{-0.5}$	Bogomolov et al. (1987)
2.0 - 5.0	3^{+4}_{-2}	Bogomolov et al. (1987)
2.0 - 2.5	$2.4^{+2.4}_{-1.3}$	Bogomolov et al. (1990)
4.7 - 11.3	6.8±1.7	Golden et al. (1984)
4.4	2.73±5.46	Golden et al. (1984)
5.0	<0.82	Golden et al. (1984)
5.8	5.61±2.99	Golden et al. (1984)
6.8	6.10±2.72	Golden et al. (1984)
8.2	9.50±3.17	Golden et al. (1984)
10.2	12.23±3.80	Golden et al. (1984)
13.4	3.36±2.87	Golden et al. (1984)
≥16	170 ± 650	Durgaprasad and Kunte (1971)
100-200	<700	Stephens (1985)
$> 10^3$	<500	Brooke and Wolfendale (1964)
$10^3 - 1.5 \cdot 10^3$	<1700	Stephens (1985)
$10^4 - 1.5 \cdot 10^4$	<1000	Stephens (1985)
$> 3 \cdot 10^4$	<1400	Stephens (1985)

generation experiments found much lower ratios.

It is worth mentioning that the evaluation of a new generation low energy (≤170 MeV) antiproton search experiments with emulsion is currently under way (Taira et al., 1990) but no data are yet available. Major progress can be expected from the previously mentioned new or improved generation of instruments. For instance, the PAMELA instrument that will be launched into a polar orbit with an altitude of 700 km will have the capability to detect antiprotons in the energy range between ≃70 MeV and 100 GeV (Adriani et al., 1997).

Table 5.44: Differential Intensity of Antiprotons in the Cosmic Radiation. (Early Work)

Energy GeV	$\bar{p}$ Intensity $[cm^{-2}s^{-1}sr^{-1}GeV^{-1}]$	Reference
0.06-0.15	$< 4.0 \cdot 10^{-5}$	Apparao et al. (1985)
0.12-0.22	$< 3.0 \cdot 10^{-4}$	Rao and Yock (1987)
0.13-0.32	$(1.7 \pm 0.5) \cdot 10^{-5}$	Buffington et al. (1981)
0.2-2.0	$(5.0^{+10.0}_{-4.0}) \cdot 10^{-6}$	Bogomolov et al. (1987)
2.0-5.0 *	$(5.8^{+7.7}_{-3.9}) \cdot 10^{-6}$	Bogomolov et al. (1987)
4.7-11.3 *	$(3.8 \pm 0.95) \cdot 10^{-6}$	Golden et al. (1984)
4.4 *	$(3.22 \pm 6.44) \cdot 10^{-6}$	Golden et al. (1984)
5.5 *	$< 7.8 \cdot 10^{-7}$	Golden et al. (1984)
5.8 *	$(4.1 \pm 2.2) \cdot 10^{-6}$	Golden et al. (1984)
6.8 *	$(3.2 \pm 1.4) \cdot 10^{-6}$	Golden et al. (1984)
8.2 *	$(3.4 \pm 1.1) \cdot 10^{-6}$	Golden et al. (1984)
10.2 *	$(2.8 \pm 0.9) \cdot 10^{-6}$	Golden et al. (1984)
13.4 *	$(4.2 \pm 3.6) \cdot 10^{-7}$	Golden et al. (1984)

* These intensity values are estimated using the $\bar{p}/p$ ratios given in Table 1 and the observed proton spectrum (see Stephens and Golden, 1987, and the original references).

The results of the more recent experiments to determine the $\bar{p}/p$-ratio and the intensity of antiprotons in the cosmic radiation are summarized in Tables 5.45 and 5.46, respectively. The flights of Bogomolov et al. (1990) apply to a geomagnetic cutoff rigidity of 3 - 3.5 GV and residual atmospheres between 7 and 10 g/cm^2. The instruments PBAR and LEAP were flown from Prince Albert, Canada, at slightly less than 5 g/cm^2 and cutoff rigidities around 0.65 GV; CAPRICE-94, IMAX-92, BESS-93 and BESS-95 were flown from Lynn Lake, Canada, at 4 to 5 g/cm^2 and cutoffs between 0.3 and 0.5 GV, and MASS-91 (MASS-2) from Fort Sumner, New Mexico, at 5.8 g/cm^2 and a cutoff of about 4.5 GV.

Compilations of the data of the experiments listed in Tables 5.43 to 5.46 together with theoretical predictions that are based on different cosmic ray propagation models, summarized below, are presented in Figs. 5.79 to 5.85.

An attempt to estimate the antiproton fraction in the high energy cosmic radiation was made by Amenomori et al., (1995), using the Tibet air shower array at Yangbajing (606 g/cm^2, 4300 m a.s.l.). These authors used

Table 5.45: Measured and Estimated Fraction of Antiprotons in the Cosmic Radiation. (Recent Experiments)

Energy GeV	Ratio $(\bar{p}/p)$	Reference NAME of Experiment
2.0 - 5.0	$2.4^{+2.4}_{-1.3}$	Bogomolov et al. (1990)
0.205 - 0.64	$4.6 \cdot 10^{-5}$	Ahlen et al. (1988), PBAR
0.1 - 0.6	$2.8 \cdot 10^{-5}$	Salamon et al. (1990), PBAR
0.64 - 1.58	$6.1 \cdot 10^{-5}$	Barwick et al. (1990),
0.1 - 1.58	$2.0 \cdot 10^{-5}$	PBAR
0.6 - 2.0	$2.5^{+3.2}_{-1.9} \cdot 10^{-5}$	Barbiellini et al. (1997) and
2.0 - 3.2	$1.9^{+1.6}_{-1.0} \cdot 10^{-4}$	Boezio et al. (1997), CAPRICE-94
3.7 - 19	$1.24^{+0.68}_{-0.51} \cdot 10^{-4}$	Hof et al. (1996), MASS-91
0.2 - 1.0	$4.0^{+4.2}_{-2.4} \cdot 10^{-5}$	
1.0 - 2.6	$6.4^{+3.8}_{-2.7} \cdot 10^{-5}$	Labrador et al. (1995), IMAX-92
2.6 - 3.2	$1.9^{+1.8}_{-1.2} \cdot 10^{-4}$	
0.25 - 1.0	$3.14^{+3.4}_{-1.9} \cdot 10^{-5}$	
1.0 - 2.6	$5.36^{+3.5}_{-2.4} \cdot 10^{-5}$	Mitchell et al. (1996), IMAX-92
2.6 - 3.2	$1.94^{+1.8}_{-1.1} \cdot 10^{-5}$	
0.12 - 0.36	$3.5 \cdot 10^{-5}$	Streitmatter et al. (1989), LEAP
0.12 - 0.86	$1.8 \cdot 10^{-5}$	Streitmatter et al. (1990), LEAP
0.6 - 1.2	$2.3 \cdot 10^{-4}$	Moats et al. (1990), LEAP
0.2 - 0.6	$5.2^{+4.4}_{-2.8} \cdot 10^{-6}$	Moiseev et al. (1997), BESS-93
0.175 - 0.3	$0.78^{+0.81+0.18}_{-0.45-0.18} \cdot 10^{-5}$	
0.3 - 0.5	$0.74^{+0.45+0.12}_{-0.31-0.12} \cdot 10^{-5}$	
0.5 - 0.7	$0.77^{+0.52+0.12}_{-0.35-0.12} \cdot 10^{-5}$	Matsunaga et al. (1997, 1998),
0.7 - 1.0	$1.01^{+0.54+0.17}_{-0.40-0.17} \cdot 10^{-5}$	BESS-95
1.0 - 1.4	$1.99^{+0.85+0.32}_{-0.66-0.32} \cdot 10^{-5}$	
10^4	0.22	Amenomori et al. (1995) *

* Using air showers and shadow of sun.

Table 5.46: Differential Intensity of Antiprotons in the Cosmic Radiation. (Recent Experiments)

Energy GeV	$\overline{p}$ Intensity $[cm^{-2}s^{-1}sr^{-1}GeV^{-1}]$	Reference Name of Experiment
0.6 - 2.0	$1.9^{+2.4}_{-1.4} \cdot 10^{-6}$	Barbiellini et al. (1997) and
2.0 - 3.2	$5.3^{+4.5}_{-2.9} \cdot 10^{-6}$	Boezio et al. (1997), CAPRICE-94
0.25 - 1.0	$2.31^{+2.5}_{-1.4} \cdot 10^{-6}$	
1.0 - 2.6	$2.11^{+1.4}_{-1.0} \cdot 10^{-6}$	Mitchell et al. (1996), IMAX-92
2.6 - 3.2	$3.46^{+3.1}_{-2.0} \cdot 10^{-6}$	
0.2 - 0.6	$6.4^{+5.5}_{-3.5} \cdot 10^{-7}$	Moiseev et al. (1997), BESS-93
0.175 - 0.3	$1.36^{+1.41+0.30}_{-0.79-0.30} \cdot 10^{-6}$	
0.3 - 0.5	$1.36^{+0.83+0.23}_{-0.57-0.23} \cdot 10^{-6}$	
0.5 - 0.7	$1.22^{+0.81+0.20}_{-0.55-0.22} \cdot 10^{-6}$	Matsunaga et al. (1998), BESS-95
0.7 - 1.0	$1.25^{+0.67+0.22}_{-0.50-0.22} \cdot 10^{-6}$	
1.0 - 1.4	$1.85^{+0.79+0.31}_{-0.61-0.31} \cdot 10^{-6}$	
3.7 - 6.3	$8.2^{+10.3}_{-6.6} \cdot 10^{-7}$	
6.3 - 11.6	$4.2^{+4.2}_{-2.7} \cdot 10^{-7}$	Basini et al. (1999), MASS-91
11.6 - 24.1	$2.1^{+1.7}_{-1.1} \cdot 10^{-7}$	

the shadowing effect of the sun and the moon in conjunction with the geomagnetic and heliospheric magnetic fields. The upper limit of the antiproton to proton ratio resulting from this work was found to be <0.22 at energies around 10 TeV.

5.6.4 Antinuclei

So far the only claim for the detection of antimatter beyond antiprotons was made by Apparao et al. (1983) who observed an event in an emulsion stack that can be interpreted as being an *antitriton*, $\overline{T}$. The stack was flown in 1972 above Fort Churchill, Canada, for over 13 hours at an atmospheric depth of only 1.7 g/cm^2. The kinetic energy of the particle was approximately 150 MeV and it traversed 2.3 cm of emulsion before interacting. Unless produced in the residual atmosphere the $\overline{T}$ must be of relatively local origin because

of its expected short half life (12.323 years for T). Considering the smallness of the residual atmosphere and the amount of interstellar and interplanetary matter the antitriton passed through in a few half-lives, the authors estimated the probability of its formation in a primary proton initiated interaction to be $\leq 10^{-9}$.

All other efforts to search for antideuteron, $\overline{D}$, antihelium, $\overline{He}$, and heavier antinuclei did not yield positive results, only upper limits could be established. The results of the different experiments are summarized in Table 5.47. The data of Smoot et al. (1975), Badhwar et al. (1978) and Ormes et al. (1995 and 1997) have a confidence level of 95% or better. The recent data of Ormes et al. (1995 and 1997) and Nozaki et al. (1999) were obtained with the BESS instrument and give the lowest upper limit. The next generation instruments such as PAMELA can search for antinuclei up to 30 GeV/antinucleon with a sensitivity of better than 10^{-7} for the $\overline{He}/He$ ratio (Adriani et al., 1997).

5.6.5 Theoretical Studies

Antiproton to Proton Ratio and Antiproton Intensities

Numerous authors have studied the question of the origin of antiprotons in the cosmic radiation and the implications of their existence. Many have made attempts to estimate their intensity, the $\overline{p}/p$-ratio and the energy spectrum theoretically, using a variety of models of cosmic ray propagation in the Galaxy (Shen et al., 1968; Suh, 1971; Gaisser and Maurer, 1973; Gaisser and Levy, 1974; Badhwar et al., 1975; Steigman, 1977; Peters and Westergaard, 1977; Bhattacharyya et al., 1978; Stephens, 1981b; Webber and Potgieter, 1989; Stephens, 1989; Gaisser and Schaeffer, 1992; Heinbach and Simon, 1995; Simon et al., 1998). Some of the results of these calculations are included in the data summaries shown in Figs. 5.79 to 5.85.

Most of these calculations are based on some form of Leaky Box Model for the propagation of cosmic rays in the Galaxy and on the assumption that antiprotons found in the cosmic radiation are the result of interactions of the primary cosmic radiation with the interstellar medium and are therefore secondary particles. More recently the concept of distributed and diffuse re-acceleration had been introduced (Heinbach and Simon, 1995; Simon and Heinbach, 1996) that yield different spectral features and $\overline{p}/p$ energy dependencies. Mitsui et al. (1996) have also investigated the contribution from evaporating primordial black holes and neutralino annihilations (Fig. 5.84).

One of the first calculations to estimate the $\overline{p}/p$-ratio was carried out by

Table 5.47: Measured and Estimated Fraction of Antinuclei in the Cosmic Radiation.

Nuclear Charge $\lvert\overline{Z}\rvert$	Rigidity GV/c	Ratio $(\overline{Z}/Z)$	Reference
	0.25 - 0.5	$2.2 \cdot 10^{-5}$	Buffington et al. (1981)
	1.0 - 16	$0.85 \cdot 10^{-6}$	Nozaki et al. (1999, 2000)
	1.6 - 16	$8.1 \cdot 10^{-6}$	Ormes et al. (1997)
	1.2 - 10.4	$1.4 \cdot 10^{-3}$	Evenson (1972)
	10 - 25	$8 \cdot 10^{-2}$	Evenson (1972)
	< 2.7	$7 \cdot 10^{-3}$	Aizu et al. (1961)
	4 - 33	$5 \cdot 10^{-4}$	Smoot et al. (1975)
	33 - 100	$2 \cdot 10^{-2}$	Smoot et al. (1975)
≥ 2	2.5 - 5	$1.7 \cdot 10^{-4}$	Badhwar et al. (1978)*
	2.5 - 5	$8.8 \cdot 10^{-5}$	Badhwar et al. (1978)
	2.5 - 5	$5.8 \cdot 10^{-5}$	Badhwar et al. (1978)**
	2 - 17.2	$1.0 \cdot 10^{-4}$	Badhwar et al. (1978)
	5 - 17.2	$1.6 \cdot 10^{-4}$	Badhwar et al. (1978)
	17.2 - 50	$< 1 \cdot 10^{-2}$	Badhwar et al. (1978)
	14 - 100	$1 \cdot 10^{-2}$	Verma et al. (1972)
	14 - 30	$< 2 \cdot 10^{-2}$	Verma et al. (1972)
	30 - 50	$< 2 \cdot 10^{-2}$	Verma et al. (1972)
	50 - 100	$< 1 \cdot 10^{-1}$	Verma et al. (1972)
	< 100	$7 \cdot 10^{-3}$	Damle et al. (1973)
	< 3	$2 \cdot 10^{-2}$	Grigorov et al. (1963, 1964)
	< 4	$2 \cdot 10^{-2}$	Ivanova et al. (1968a, 1968b)
≥ 3	4 - 33	$8 \cdot 10^{-5}$	Smoot al. (1975)
	33 - 100	$6 \cdot 10^{-3}$	Smoot al. (1975)
	4 - 125	$5 \cdot 10^{-3}$	Golden et al (1974)
	4 - 10	$8 \cdot 10^{-3}$	Golden et al (1974)
	10 - 50	$1.3 \cdot 10^{-2}$	Golden et al (1974)
	60 - 125	$1.5 \cdot 10^{-1}$	Golden et al (1974)
≥ 6	<2.7	$1 \cdot 10^{-2}$	Aizu et al. (1961)
	10 - 18	$8 \cdot 10^{-2}$	Greenhill et al. (1971)

* data from 1975 flight; ** combined data

Gaisser and Maurer (1973), using the basic ideas outlined above. Employing parameterized expressions for the production cross section of antiprotons from accelerator data (see also Stephens, 1981a; Tan and Ng, 1982 and 1983c), these authors predict that the ratio $\bar{p}/p \simeq 10^{-5}$ around 2 GeV, increasing rapidly to 10^{-4} around 6 GeV and reaching an asymptotic value of $4.6 \cdot 10^{-4}$ beyond 10^5 GeV. An interstellar column of matter of 5 g/cm^2 was assumed to have been traversed by the primary radiation. The energy dependence of the antiproton production rate in interstellar space is shown in Fig. 5.86. The curve is based on a calculation using the demodulated primary proton spectrum after Stephens and Golden (1987).

An early attempt to calculate the absolute antiproton spectrum in the Galaxy was carried out by Gaisser and Levy (1974). They did also calculate the spectrum in the vicinity of the Earth, accounting for solar modulation effects. This work was followed by calculations of Szabelski et al. (1980), Stephens (1981a and 1981b), Protheroe (1981) and Tan and Ng (1981, 1983a and 1983b) and others. In general the different predictions of the antiproton spectrum and $\bar{p}/p$-ratio agree within a factor of two.

From the calculations mentioned above one can infer that the antiproton lifetime is at least comparable to the cosmic ray storage time which is believed to be on the order of 10^7 years and that most of the matter traversed by high energy cosmic rays is encountered after their acceleration.

Solar Modulation Effects

The low energy cosmic ray antiproton flux arriving at Earth is subject to solar modulation (Perko, 1987 and 1992; Boella et al., 1998). Antiprotons with energies $\leq$1 GeV observed at 1 AU appear to be primarily the result of *adiabatic deceleration* of higher energy antiprotons. Their intensity varies therefore much less over the solar cycle than does that of low energy protons because most of the antiprotons are produced with energies of several GeV (Fig. 5.86), where the effects of solar modulation are much less. Perko (1987) has calculated the average energy loss for antiprotons due to adiabatic deceleration against the outflow of solar wind for the periods when low energy measurements were made.

In their investigation of solar modulation effects on the flux of cosmic ray antiprotons, Labrador and Mewaldt (1995 and 1997) note that the shape of the antiproton spectrum is not affected significantly over a solar cycle but that the $\bar{p}/p$-ratio at several hundred MeV varies approximately one order of magnitude. They point out that the latter is chiefly due to the variation of the proton flux rather than to variations of the antiproton flux, as pointed

out before (for details see Chapter 6, Section 6.3). In Fig. 5.87 we show the interstellar proton spectrum after Webber and Potgieter (1989) used by Labrador and Mewaldt (1995 and 1997) together with modulated proton spectra as well as the corresponding spectra of antiprotons. The $\overline{p}/p$-ratio obtained by the same authors using interstellar proton and antiproton fluxes according to Webber and Potgieter (1989) and Gaisser and Schaeffer (1992) are shown in Fig. 5.88.

Another recent study of the expected enhancement of the cosmic ray antiproton flux at solar minimum was carried out by Mitsui et al. (1996), using different models of antiproton sources.

Flux of Antinuclei

On theoretical grounds, partly based on the calculations mentioned above, the flux of antinuclei from cosmic ray interactions with the interstellar medium is estimated to be approximately a factor of 10^{-8} lower than the flux of antiprotons. The best present result in the search for antimatter yields an upper limit for the $\overline{He}/He$ ratio of $8 \cdot 10^{-6}$ (Ormes et al., 1997, see Subsection 5.6.4).

References

O. Adriani, M. Ambriola, G. Barbiellini, L.M. Barbier, S. Bartalucci, G. Basini, R. Bellotti, D. Bergstrom, M. Boezio, V. Bonvicini, F.M. Brancaccio, U. Bravar, F. Cafagna, R. Cardarelli, P. Carlson, M. Casolino, M. Castellano, G. Castellini, E.R. Christian, F. Ciacio, M. Circella, R. D'Alessandro, A.J. Davis, G. De Cataldo, C.N. De Marzo, M.P. De Pasca]e, T. Francke, C. Fuglesang, A.M. Galper, F. Giannini, N. Giglietto, M. Hof, S.V. Koldashov, M.G. Korotkov, J.F. Krizmanic, B. Marangelli, W. Menn, R.A. Mewaldt, V.V. Mikhailov, N. Mirizzi, J.W. Mitchell, A.A. Moiseev, A. Morselli, J.F. Ormes, J.V. Ozerov, P. Papini, A. Perego, S. Piccardi, P. Picozza, M. Ricci, P. Schiavon, S.M. Schindler, M. Simon, R. Sparvoli, P. Spillantini, P. Spinelli, S.A. Stephens, D.E. Stilwell, S.J. Stochaj, R.E. Streitmatter, F. Taccetti, A. Vacchi, V. Vignoli, S.A. Voronov, N. Weber, N. Zampa: PICRC, 5, p. 49 (1997).

Ahlen, S.P., S. Barwick, J.J. Beatty, C.R. Bower, G. Gerbier, R.M. Heinz, D. Lowder, S. McKee, S. Mufson, J.A. Musser, P.B. Price, M.H. Salamon, G. Tarlé, A. Tomasch, and B. Zhou: Phys. Rev. Lett., 61, p. 145 (1988).

Aizu, H., Y. Fujimoto, S. Hasegawa, M. Koshiba, I. Mito, J. Nishimura, K. Yokoi, and M. Schein: Phys. Rev., 121, p. 1206 (1961).

Amaldi, E., C. Castagnoli, G. Cortini, C. Franzinetti, and A. Manfredini: Nuovo Cimento, 1, p. 492 (1955).

Amenomori, M., Z. Cao, B.Z. Dai, L.K. Ding, Y.X. Feng, Z.Y. Feng, K. Hibino, N. Hotta, Q. Huang, A.X. Huo, H.G. Jia, G.Z. Jiang, S.Q. Jiao, F. Kajino, K. Kasahara, Labaciren, S.M. Liu, D.M. Mei, L. Meng, X.R. Meng, Mimaciren, K. Mizutani, J. Mu, H. Nanjo, M. Nishizawa, A. Oguro, M. Ohnishi, I. Ohta, T. Ouchi, J.R. Ren, To. Saito, M. Sakata, T. Sasaki, Z.Z. Shi, M. Shibata, T. Shirai, H. Sugimoto, X.X. Sun, K. Taira, Y.H. Tan, N. Tateyama, S. Torii, H. Wang, C.Z. Wen, Y. Yamamoto, G.C. Yu, P. Yuan, T. Yuda, C.S. Zhang, H.M. Zhang L. Zhang, Zhasang, Zhaxiciren, and W.D. Zhou: PICRC, 3, p. 84 (1995).

Apparao, K.M.V.: Nature, 215, p. 727 (1967).

Apparao, K.M.V.: Can. J. Phys., 46, p. S654 (1968).

Apparao, K.M.V., N. Durgaprasad, S.A. Stephens, and S. Biswas: PICRC, 2, p. 75 (1983).

Apparao, K.M.V., S. Biswas, N. Durgaprasad, and S.A. Stephens: PICRC, 2, p. 326 (1985).

Badhwar, G.D., R.L. Golden, and J.L. Lacy: Astrophys. Space Sci., 37, p. 283 (1975).

Badhwar, G.D., R.L. Golden, J.L. Lacy, J.E. Zipse, and R.R. Daniel: Nature, 274, p. 137 (1978).

Barbiellini, G. G. Basini, R. Bellotti, M. Bocciolini, M. Boezio, U. Bravar, F. Cafagna, P. Carlson, M. Casolini, M. Castellano, M. Circella, A. Codino, G. De Cataldo, C. De Marzo, M. De Pascale, N. Finetti, T. Francke, N. Giglietto, R.L. Golden, C. Grimani, M. Hof, W. Menn, J.W. Mitchell, A. Morselli, J.F. Ormes, P. Papini, A. Perego, S. Piccardi, P. Picozza, M. Ricci, P. Schiavon, M. Simon, R. Sparvoli, P. Spillantini, P. Spinelli, S.A. Stephens, S.J. Stochaj, R.E. Streitmatter, M. Suffert, A. Vacchi, N. Weber, and N. Zampa: PICRC, 4, p. 217 (1997).

Barwick, S.W., S.P. Ahlen, J.J. Beatty, C.R. Bower, R.M. Heinz, D.M. Lowder, S. McKee, J.L. Miller, S.L. Mufson, J.A. Musser, P.B. Price, M.H. Salamon, G. Tarle, A. Tomasch, and B. Zhou: PICRC, 3, p. 273 (1990).

Basini, G., A. Morselli, and M. Ricci: Rivista del Nuovo Cimento, 12, p. 1 (1989).

Basini, G., R. Bellotti, M.T. Brunetti, F. Cafagna, M. Circella, A. Codino, C. De Marzo, M.P. De Pascale. R.L. Golden, C. Grimani, M. Hoi, M. Menichelli, W. Menn, J.W. Nutchen, A. Morsein, J.F. Ormes, P. Papini, C. Pfeifer, S.

Piccardi, P. Picozza, M. Ricci, M. Simon, P. Spillantini, S.A. Stephens, S.J. Stochaj, and R.E. Streitmatter: PICRC, 3, p. 77 (1999).

Bhattacharyya, D.P., K. Sarkar, and D. Basu: Annalen der Physik, 35, p. 371 (1978).

Boella, G., M. Gervasi, M.A.C. Potenza, P.G. Rancoita, and I. Usoskin: Astropart. Phys., 9, p. 261 (1998).

Boezio, M., P. Carlson, T. Francke, N. Weber, M. Suffert, M. Hof, W. Menn, M. Simon, S.A. Stephens, R. Bellotti, F. Cafagna, M. Circella, G. De Cataldo, C. De Marzo, N. Giglietto, P. Spinelli, M. Bocciolini, P. Papini, A. Perego, S. Piccardi, P. Spillantini, G. Basini, M. Ricci,A. Codino, N. Finetti, C. Grimani, M. Candusso, M. Casolino, M.P. De Pascale, A. Morselli, P. Picozza, R. Sparvoli, G. Barbiellini, U. Bravar, P. Schiavon, A. Vacchi, N. Zampa, J.W. Mitchell, J.F. Ormes, R.E. Streitmatter, R.L. Golden, and S.J. Stochaj: Astrophys. J., 487, p. 415 (1997).

Bogomolov, E.A., N.D. Lubyanaya, and V.A. Romanov: PICRC, 5, p. 1730 (1971).

Bogomolov, E.A., N.D. Lubyanaya, V.A. Romanov, S.V. Stepanov, and M.S. Shulakova: PICRC, 1, p. 330 (1979).

Bogomolov, E.A., G.I. Vasilyev, S.Yu. Kurt'kov, N.D. Lubyanaya, V.A. Romanov, S.V. Stepanov, and M.S. Shulakova: PICRC, 2, p. 72 (1987).

Bogomolov, E.A., G.I. Vasilyev, S.Yu. Kurt'kov, N.D. Lubyanaya, V.A. Romanov, S.V. Stepanov, and M.S. Shulakova: PICRC, 3, p. 288 (1990).

Brooke, G., and A.W. Wolfendale: Nature, 202, p. 480 (1964).

Brooke, G., M.A. Meyer, and A.W. Wolfendale: Proc. Phys. Soc., 83, p. 871 (1964).

Buffington, A., L.H. Smith, G.F. Smoor, L.W. Alvarez, and M.A. Wahlig: Nature (London), 236, p. 335 (1972).

Buffington, A., C.R. Pennypacker, P.M. Lubin, and C.F. Smoot: PICRC, 1, p. 337 (1979).

Buffington, Andrew, Stephen M. Schindler, and Carlton R. Pennypacker: Astrophys. J., 248, p. 1179 (1981).

Chamberlain, Owen, Emilio Segrè, Clyde Wiegand, and Thomas Ypsilantis: Phys. Rev., 100, p. 947 (1955).

Damle, V., Y. Pal, T.N. Rengarajan, S.N. Tandon, and R.P. Verma: PICRC, 1, p. 231 (1973).

Durgaprasad, N., and P.K. Kunte: Nature, 234, p. 74 (1971).

Evenson, P.: Astrophys. J., 176, p. 797 (1972).

Fradkin, M.I.: J. Eksper. Theor. Phys. USSR, 29, p. 147 (1955).

Fradkin, M.I.: Soviet Phys., JETP, 2, p. 87 (1956).

Gaisser, T.K., and E.H. Levy: Phys. Rev., D 10, p. 1731 (1974).

Gaisser, T.K., and R. Maurer: Phys. Rev. Lett., 30, p. 1264 (1973).

Gaisser, Thomas K., and Robert T.Schaeffer: Astrophys. J., 394, p. 174 (1992).

Golden, R.L., J.H. Adams, Jr., G.D. Badhwar, C.L. Deney, H.H. Heckman, and P.L. Lindstrom: Astrophys. J., 192, p. 747 (1974).

Golden, R.L., G.D. Badhwar, J.L. Lacy, and J.E. Zipse: Nucl. Instr. Meth., 148, p. 179 (1978).

Golden, R.L., S. Horan, B.G. Mauger, G.D. Badhwar, J.L. Lacy, S.A. Stephens, R.R. Daniel, and J.E. Zipse: PICRC, 12, p. 76 (1979a).

Golden, R.L., S. Horan, B.G. Mauger, G.D. Badhwar, J.L. Lacy, S.A. Stephens, R.R. Daniel, and J.E. Zipse: Phys. Rev. Lett., 43, p. 1196 (1979b).

Golden, R.L., B.G. Mauger, S. Nunn, and S. Horan: Astrophys. Letters, 24, p. 75 (1984).

Greenhill, J.G., A.R. Clarke, and H. Elliot: Nature (London), 230, p. 170 (1971).

Grigorov, N.L., D.A. Zhuraulev, M.A. Kondrateva, I.D. Rapaport, and I.A. Savenkov: Artificial Earth Satellites, 10, p. 96 (1961).

Grigorov, N.L., D.A. Zhuraulev, M.A. Kondrateva, I.D. Rapaport, and I.A. Savenkov: Zh. Eksp. Teor. Fiz., 45, p. 394 (1963).

Grigorov, N.L., D.A. Zhuraulev, M.A. Kondrateva, I.D. Rapaport, and I.A. Savenkov: Sov. Phys., JETP, 18, p.272 (1964).

Haskin, D.M., P.L. Jain, E. Lohrmann, M. Schein, and M. Teucher: PICRC, 3, p. 123 (1959).

Heinbach, U., and M. Simon: Astrophys. J., 441, p. 209 (1995).

Hof, M., R.L. Golden, S.J. Stochaj, G. Basini, F. Bongiorno, F. Massimo Brancaccio, M.T. Brunetti, A. Codino, C. Grimani, M. Menichelli, J.W. Mitchell, A. Morselli, J.F. Ormes, P. Papini, M.P. de Oascale, C. Pfeifer, S. Piccardi, P. Picozza, M. Ricci, I. Salvatori, M. Simon, S. Spillantini, S.A. Stephens, R.E. Streitmatter, and W.R. Webber: PICRC, 3, p. 60 (1995).

Hof, M., W. Menn, C.Pfeifer, M. Simon, R.L. Golden, S.J. Stochaj, S.A. Stephens, G. Basini, M. Ricci, F. Massimo Brancaccio, P. Papini, P. Spillan-

tini,M.P. De Pascale, A. Morselli, P. Picozza, M.T. Brunetti, A. Codino. C. Grimani, M. Menichelli, J.W. Mitchell, J.F. Ormes, and R.E. Streitmatter: Astrophys. J., 467, p. L33, (1996).

Ivanova, N.S., Yu.F. Gagarin, and V.N. Kulikov: Kosm. Issled., 6, 83 (1968a).

Ivanova, N.S., Yu.F. Gagarin, and V.N. Kulikov: Cosmic Res., U.S.S.R., 6, p. 69 (1968b).

Labrador, A.W., R.A. Mewaldt: PICRC, 3, p. 68 (1995).

Labrador, A.W., R.A. Mewaldt: Astrophys. J., 480, p. 371 (1997).

Labrador, A.W., W. Menn, L.M. Barbier, E.R. Christian, A.J. Davis, R.L. Golden, M. Hof, K.E. Krombel, R.A. Mewaldt, J.W. Mitchell, J.F. Ormes, O. Reimer, S.M. Schindler, M. Simon, S.J. Stochaj, R.E. Streitmatter, I.L. Rasmussen, and W.R. Webber: PICRC, 3, p. 64 (1995).

Lal, S., R. Raghavan, T.N. Rangaswamy, B.V. Sreekantan, and A. Subrahmanian: PICRC, 5, 260 (1963).

Maki, K., Mitsui, T., and S. Orito: Phys. Rev. Lett., 76, p. 3474 (1996).

Matsunaga, H., H. Matsumoto, S. Orito, K. Yoshimura, A. Mosiev, K. Anraku, R. Golden, M. Imori, S. Inaba, B. Kimbell, N. Kimura, Y. Makida, J. Mitchell, M. Motoki, J. Nishimura, M. Nozaki, J. Ormes, T. Saeki, T. Sanuki, R. Streitmatter, J. Suzuki, K. Tanaka, I. Ueda, N. Yajima, T. Yamagami, A. Yamamoto, and T. Yoshida: PICRC, 4, p. 225 (1997).

Matsunaga, H., S. Orito, H. Matsumoto, K. Yoshimura, A. Mosiev, K. Anraku, R. Golden, M. Imori, Y. Makida, J. Mitchell, M. Motoki, J. Nishimura, M. Nozaki, J. Ormes, T. Saeki, T. Sanuki, R. Streitmatter, J. Suzuki, K. Tanaka, I. Ueda, N. Yajima, T. Yamagami, A. Yamamoto, and T. Yoshida: Phys. Rev. Lett., 81, p. 4052 (1998).

Mitchell, J.W., L.M. Barbier, E.R. Christian, J.F. Krizmanic, K. Krombel, J.F. Ormes, R.E. Streitmatter, A.W. Labrador, A.J. Davis, R.A. Mewaldt, S.M. Schindler, R.L. Golden, S.J. Stochaj, W.R. Webber, W. Menn, M. Hof, O. Reimer, M. Simon, and I.L. Rasmussen: Phys. Rev. Lett., 76, p. 3057 (1996).

Mitsui, T.: Ph.D. Thesis, University of Tokyo (1996).

Mitsui, T., K. Maki, and S. Orito: Phys. Lett., B 389, p. 169 (1996).

Moats, A., T. Bowen, R.E. Streitmatter, S.J. Stochaj, J.F. Ormes, L. Barbier, R.L. Golden, S.A. Stephens, and J.L. Evans: PICRC, 3, p. 284 (1990).

Moiseev, A., K. Yoshimura, I. Ueda, K. Anraku, R. Golden, M. Imori, S.

Inaba, B. Kimbell, N. Kimura, Y. Makida, H. Matsumoto, H. Matsunaga, J. Mitchell, M. Motoki, J. Nishimura, M. Nozaki, S. Orito, J. Ormes, T. Saeki, E.S. Seo, S. Stochaj, R. Streitmatter, J. Suzuki, K. Tanaka, N. Yajima, T. Yamagami, A. Yamamoto, and T. Yoshida: Astrophys. J., 474, p. 479 (1997).

Nozaki, M., M. Sasaki, T. Saeki, K. Abe, K. Anraku, Y. Asaoka, M. Fujikawa, M. Imori, M. Ishino, T. Maeno, Y. Makida, N. Matsui, H. Matsumoto, H. Matsunaga, J. Mitchell, T. Mitsui, A. Moiseev, M. Motoki, J. Nishimura, S. Orito, J. Ormes, T. Sanuki, E.S. Seo, Y. Shikaze, T. Sonoda, R. Streitmatter, J. Suzuki, K. Tanaka, I. Ueda, J.Z. Wang, N. Yajima, T. Yamagami, A. Yamamoto, T. Yoshida, and K. Yoshimura: PICRC, 3, p. 85 (1999).

Nozaki, M., et al.: PICRC, Invited and Rapporteur Papers, AIP Conf. Proc., 516, p. 330 (2000).

Orito, S., K. Yoshimura, I. Ueda, K. Anraku, R. Golden, M. Imori, S. Inaba, B. Kimbell, N. Kimura, Y. Makida, H. Matsumoto, H. Matsunaga, J. Mitchell, M. Motoki, J. Nishimura, M. Nozaki, J. Ormes, T. Saeki, R. Streitmatter, J. Suzuki, K. Tanaka, N. Yajima, T. Yamagami, A. Yamamoto, and Y. Yoshida: PICRC, 3, p. 76 (1995).

Ormes, J.F., K. Anraku, R. Golden, M. Imori, S. Inaba, B. Kimbell, N. Kimura, Y. Makida, H. Matsumoto, H. Matsunaga, J. Mitchell, M. Motoki, J. Nishimura, M. Nozaki, S. Orito, T. Saeki, R.E. Streitmatter, J. Suzuki, K. Tanaka, I. Ueda, N. Yajima, T. Yamagami, A. Yamamoto, T. Yoshida, and K. Yoshimura: PICRC, 3. p. 92 (1995).

Ormes, J.F., A.A. Moiseev, T. Saeki, K. Anraku, S. Orito, R.L. Golden, M. Imori, S. Inaba, B. Kimbell, N. Kimura, Y. Makida, H. Matsumoto, H. Matsunaga, J. Mitchell, M. Motoki, J. Nishimura, M. Nozaki, R.E. Streitmatter, J. Suzuki, K. Tanaka, I. Ueda, N. Yajima, T. Yamagami, A. Yamamoto, T. Yoshida, and K. Yoshimura: Astrophys. J., 482, p. L187 (1997).

Perko, J.S.: Astron. Astrophys., 184, p. 119 (1987).

Perko, J.S.: Astrophys. J., 397, p. 153 (1992).

Peters, B.: PICRC, 5, p. 423 (1963).

Peters, B., and N.J. Westergaard: Astrophys. Space Sci., 48, p. 21 (1977).

Pfeifer, Ch., S. Roesler, and M. Simon: Phys. Rev., C, 54, p. 882 (1996).

Protheroe, R.J.: Astrophys. J., 251, p. 387 (1981).

Rao, A.C.R., and P.C.M. Yock: Europhys. Letters, 3, p. 1049 (1987).

Salamon, M.H., S. McKee, J.A. Musser, G. Tarle, A. Tomasch, C.R. Bower, R.M. Heinz, J.L. Miller, S.L. Mufson, S.W. Barwick, G. Gerbier, D.M. Low-

der, P.B. Price,B. Zhou, J.J. Beatty, and S.P. Ahlen: Astrophys. J., 349, p. 78 (1990).

Shen, C.S., G.B. Berkey: Phys. Rev., 171, p. 1344 (1968).

Suh, P.K.: Astron. Astrophys., 15, p. 206 (1971).

Simon, Manfred, U. Heinbach, and Ch. Koch: Astrophys. J., 320, p. 699 (1987).

Simon, M., A. Molnar, and S. Roesler: Astrophys. J., 499, p. 250 (1998).

Smoot, G.F., A. Buffington, and C.D. Orth: Phys. Rev. Lett., 35, p. 258 (1975).

Stecker, F.W., and A.W. Wolfendale: Nature, 309, p. p.37 (1984).

Stecker, F., and A.W. Wolfendale: PICRC, 2, p. 354 (1985).

Steigman, G.: Ann. Rev. Astron. Astrophys, 14, p. 399 (1976).

Steigman, G.: Astrophys. J., 217, p. L131 (1977).

Stephens, S.A.: PICRC, 2, p. 214 (1981a).

Stephens, S.A.: Astrophys. Space Sci., 76, p. 87 (1981b).

Stephens, S.A.: PICRC, 9, p. 167 (1983).

Stephens, S.A.: Astron. and Astrophys., 149, p. 1 (1985).

Stephens, S.A., and R.L. Golden: Space Sci. Rev., 46, p. 31 (1987).

Stephens, S.A.: Adv. Space Res., 9, No 12, p. (12)55 (1989).

Streitmatter, R.E., S.J. Stochaj, J.F. Ormes, R.L. Golden, S.A. Stephens, T. Bowen, A. Moats, J. Lloyd-Evans: Adv. Space Res., 9, (12) p 65 (1989).

Streitmatter, R.E., S.J. Stochaj, J.F. Ormes, R.L. Golden, S.A. Stephens, T. Bowen, A. Moats, J. Lloyd-Evans, L. Barbier, and E.S. Seo: PICRC, 3, p. 277 (1990).

Szabelski, J., J. Wdowczyk, and A.W. Wolfendale: Nature, 285, p. 386 (1980).

Taira, T., T. Shirai, N. Tateyama, S. Torii, J. Nishimura, M. Fujii, T. Kobayashi, H. Aizu, Y. Yoshimori, S. Tanaka, and A. Nishio: PICRC, 3, p. 281 (1990).

Tan, L.C., and L.K. Ng: J. Phys., G 7, p. 123 (1981).

Tan, L.C., and L.K. Ng: Phys. Rev., D 26, p. 1179 (1982).

Tan, L.C., and L.K. Ng: J. Phys. G 9, p. 227 (1983a).

Tan, L.C., and L.K. Ng: Astrophys. J., 269, p. 751 (1983b).

Tan, L.C., and L.K. Ng: J. Phys. G 9, p. 1289 (1983c).

Verma, R.P., T.N. Rengarajan, S.N. Tandon, S.V. Damle, and Y. Pal: Nature (London), 240, p. 135 (1972).

Webber, W.R., and M.S. Potgieter: Astrophys. J., 344, p. 779 (1989).

Weber, N.: Ph.D. Thesis, University of Stockholm, Sweden (1997).

Yoshimura, K., S. Orito, I. Ueda, K. Anraku, R. Golden, M. Imori, S. Inaba, B. Kimbell, N. Kimura, Y. Makida, H. Matsumoto, H. Matsunaga, J. Mitchell, M. Motoki, J. Nishimura, M. Nozaki, J. Ormes, T. Saeki, R. Streitmatter, J. Suzuki, K. Tanaka, N. Yajima, T. Yamagami, A. Yamamoto, and Y. Yoshida: Phys. Rev. Lett., 75, p. 3792 (1995).

Yoshimura, K., T. Maeno, S. Orito, H. Matsunaga, K. Abe, K. Anraku, Y. Asaoka, M. Fujikawa, M. Imori, M. Ishino, Y. Makida, N. Matsui, H. Matsumoto, J. Michell, T. Mitsuil, A. Moiseev, M. Motoki, J. Nishimura, M. Nozaki, J. Ormes, T. Saeki, T. Sanuki, M. Sasaki, E.S. Seo, Y. Shikaze, T. Sonoda, R. Streitmatter, J. Suzuki, K. Tanaka, I. Ueda, J.Z. Wang, Y. Yajima, T. Yamagami, A. Yamamoto, and T. Yoshida: PICRC, 3, p. 81 (1999).

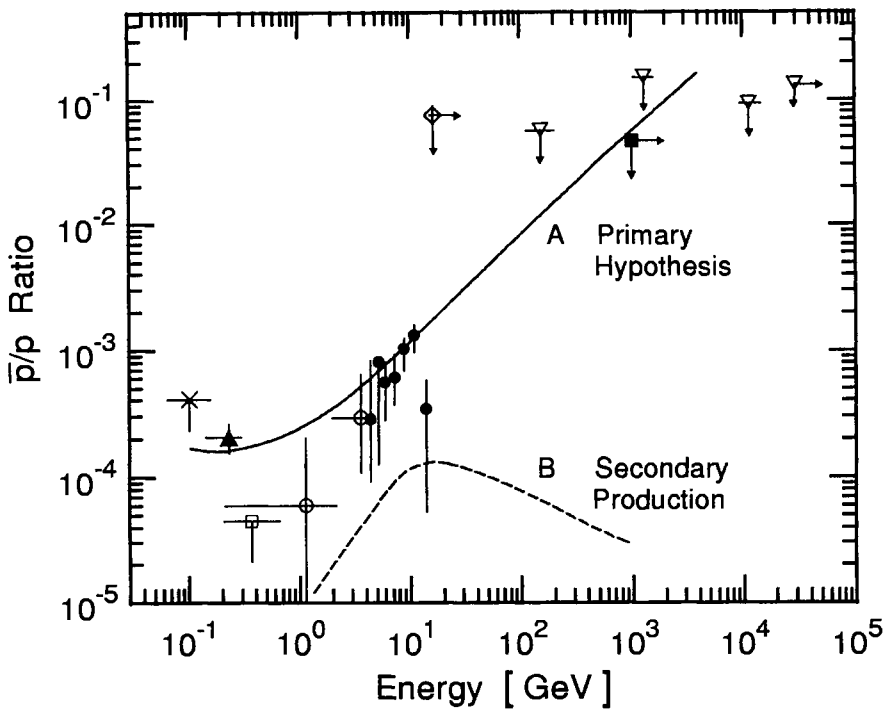

Figure 5.79: Ratio of cosmic ray antiprotons to protons, $\bar{p}/p$, as a function of kinetic energy at the top of the atmosphere. Shown are early data obtained with different experiments in direct measurements and by indirect methods. The solid curve, A, is the primary antiproton hypothesis of Stecker and Wolfendale (1985), the dashed curve, B, shows the ratio due to secondary production (Stephens and Golden, 1987).

× Apparao et al. (1985)	▲ Buffington et al. (1981)
• Golden et al. (1984)	○ Bogomolov et al. (1987)
□ Ahlen et al. (1988)	■ Brooke and Wolfendale (1964)
▽ Stephens (1985)	◇ Durgaprasad and Kunte (1971)

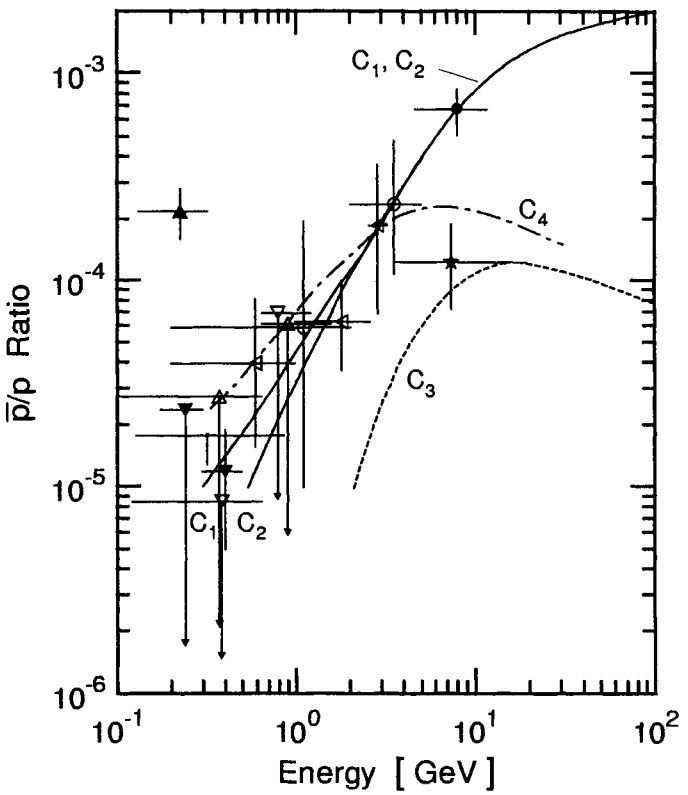

Figure 5.80: Low energy cosmic ray antiproton to proton ratios obtained with different experiments and theoretical expectations based on various models. Curves C_1 and C_2 show the range for the closed galaxy model (Peters and Westergaard, 1977) as calculated by Protheroe (1981), C_3 is the result of the leaky box model as calculated by Protheroe (1981), and C_4 is the prediction of Webber and Potgieter (1989).

★	Hof et al. (1996) MASS-91	▲	Buffington et al. (1981)
•	Golden et al. (1984)	◁	Labrador et al. (1995, 1997) IMAX-92
▼	Orito et al. (1995) BESS-93	△	Salamon et al. (1990) PBAR
▽	Stochaj et al. (1985) LEAP	○	Bogomolov et al. (1987, 1990)

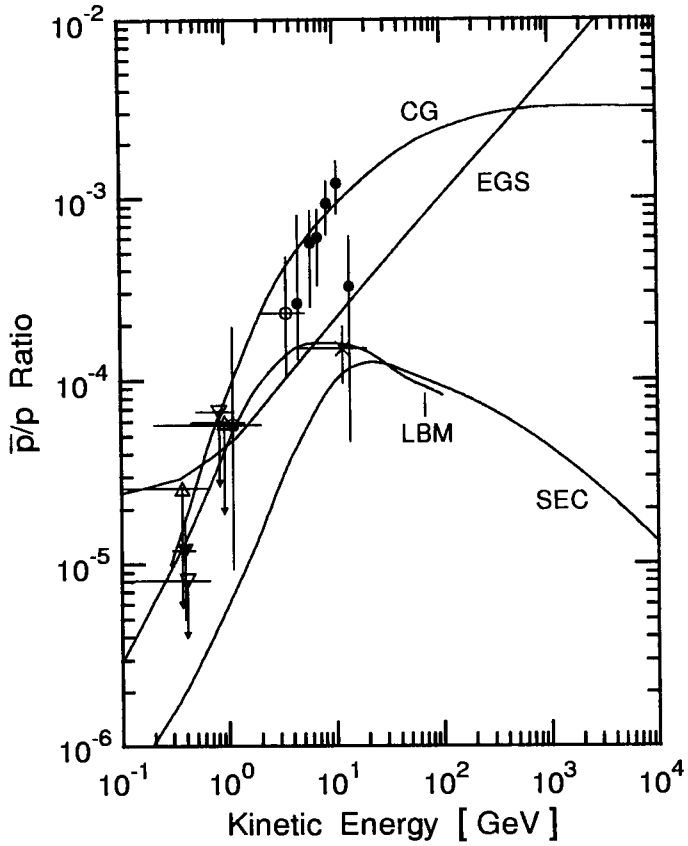

Figure 5.81: Compilation of cosmic ray antiproton to proton ratios from different experiments as listed below, compared with different theoretical predictions: CG, closed galaxy model; SEC, secondary production (Protheroe, 1981); EGS, extragalactic sources model (Stecker and Wolfendale, 1984); LBM, leaky box model (Gaisser and Schaefer, 1992), modulated to the 1 AU value applicable for the epoch of 1976.

•	Golden et al. (1984)	○	Bogomolov et al. (1979)
▽	Moats et al. (1990) LEAP	△	Salamon et al. (1990) PBAR
×	Hof et al. (1995) MASS-91	▼	Yoshimura et al. (1995) BESS-93

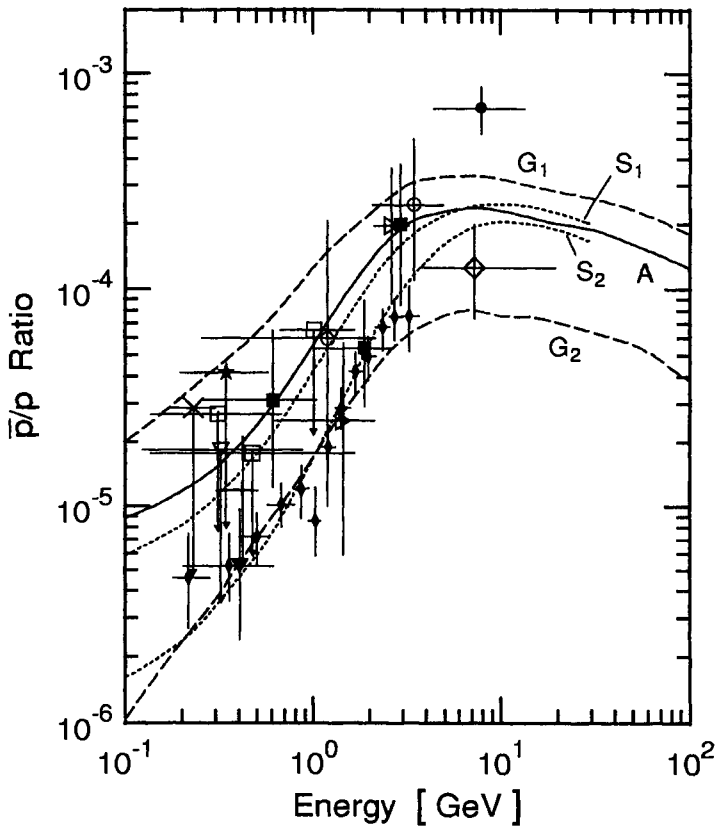

Figure 5.82: Compilation of antiproton to proton ratios on top of the atmosphere from different experiments, as listed below. The solid curve, A, is the calculated ratio obtained by modulating the Webber and Potgieter (1989) interstellar spectra to the 1992 levels, the dashed curves, G_1 and G_2, are extrema calculated by Gaisser and Schaeffer (1992), and curves S_1 and S_2 are from a recent calculation of Simon et al. (1998) based on the standard leaky box model.

- o Bogomolov et al. (1987, 1990)
- ▷ Barbiellini et al. (1997) and Boezio et al. (1997), CAPRICE-94
- ▼ Moiseev et al. (1997), BESS-93
- ▽ Streitmatter et al. (1990), LEAP
- × Yoshimura et al. (1995), BESS-93 175 - 300 MeV
- ♦ Yoshimura et al. (1999), BESS-95+97
- • Golden et al. (1984)
- ★ Ahlen et al. (1988), PBAR
- ■ Mitchell et al. (1996), IMAX-92
- ◇ Hof et al (1996), MASS-91
- □ Salamon et al. (1990), PBAR
- \+ Yoshimura et al. (1995), BESS-93 300 - 500 MeV

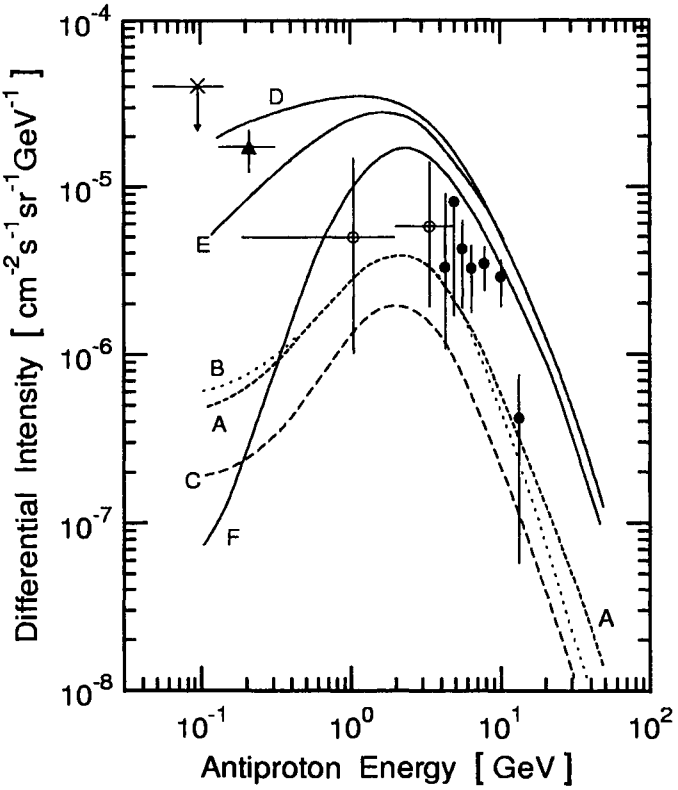

Figure 5.83: Differential cosmic ray antiproton intensities on top of the atmosphere as a function of kinetic energy obtained with different experiments, as listed below. The dashed curves A and C and the dotted curve B show the expected antiproton intensities based on the standard leaky box model, the nested leaky box model and the modified leaky box model, respectively (Stephens and Golden, 1987). The solid curves D (Stephens and Golden, 1987), E (Tan and Ng, 1983a), and F (Stephens, 1981a) are predictions of different models of cosmic ray propagation based on closed galaxy models.

× Apparao et al. (1985) | ▲ Buffington et al. (1981)
o Bogomolov et al. (1987) | • Golden et al. (1984)

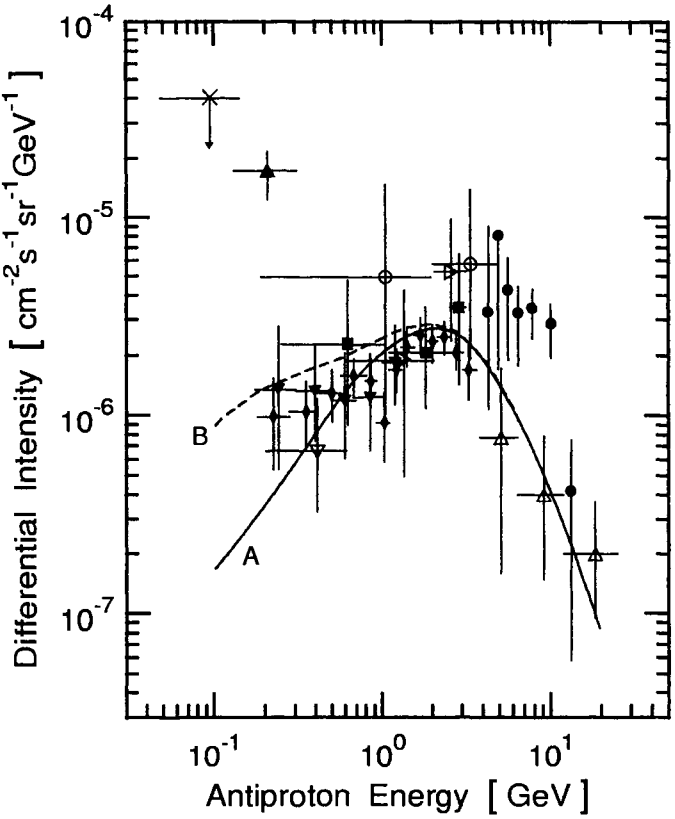

Figure 5.84: Compilation of cosmic ray antiproton intensities measured on top of the atmosphere by different balloon experiments. The theoretical spectra A and B are from the work of Maki et al. (1996), Mitsui (1996) and Mitsui et al. (1996). Curve A is for the standard leaky box model (SLBM), curve B for primordial black holes plus SLBM contributions.

- × Apparao et al. (1985)
- ▲ Buffington et al. (1981)
- • Golden et al. (1984)
- o Bogomolov et al. (1987)
- △ Basini et al. (1999), MASS-91
- ■ Mitchell et al. (1996), IMAX-92
- ▷ Barbiellini et al. (1997) and Boezio et al. (1997), CAPRICE-94
- ▽ Moiseev et al. (1997), BESS-93
- ▼ Matsunaga et al. (1997, 1998), BESS-95
- ♦ Yoshimura et al. (1999), BESS-95+97

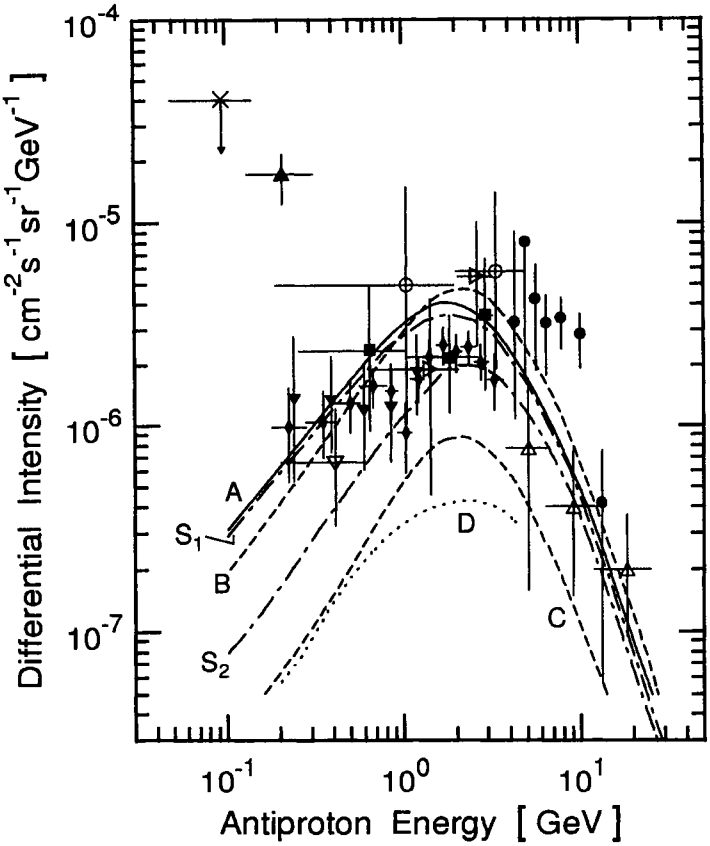

Figure 5.85: Same experimental data as in Fig. 5.84 but different model predictions. The solid curve A is the Webber and Potgieter (1989) antiproton spectrum with the modulation parameter adjusted to fit the data of the IMAX experiment. Curves B and C are the upper and lower limits obtained by Gaisser and Schaeffer (1992), modulated to the 1992 levels (Mitchell et al., 1996), and curve D is the theoretical spectrum of atmospheric antiprotons at 5 g/cm^2 according to Pfeifer et al. (1996). Curves S_1 and S_2 are from a recent calculation of Simon et al. (1998).

- × Apparao et al. (1985)
- ▲ Buffington et al. (1981)
- • Golden et al. (1984)
- ○ Bogomolov et al. (1987)
- △ Basini et al. (1999), MASS-91
- ■ Mitchell et al. (1996), IMAX-92
- ▷ Barbiellini et al. (1997) and Boezio et al. (1997), CAPRICE-94
- ▽ Moiseev et al. (1997), BESS-93
- ▼ Matsunaga et al. (1997, 1998), BESS-95
- ♦ Yoshimura et al. (1999), BESS-95+97

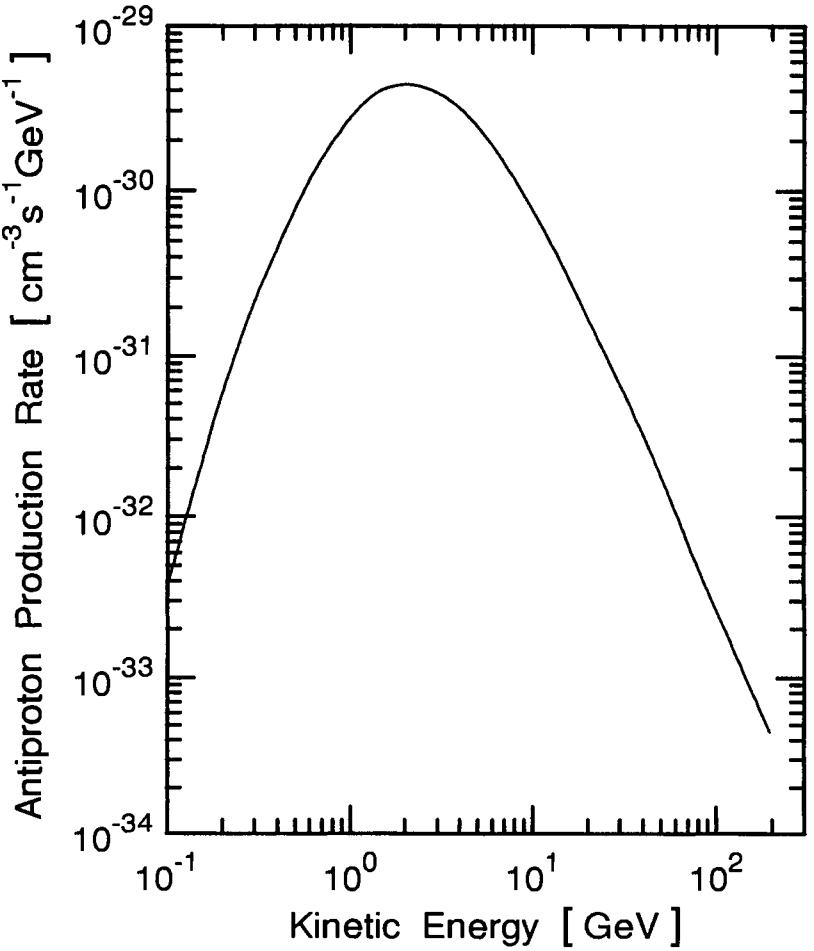

Figure 5.86: Production spectrum of antiprotons in interstellar space based on the demodulated proton spectrum of Stephens and Golden (1987). The curve was obtained for a matter density in interstellar space of 1 H-atom/cm^3. A very similar spectrum is obtained with a simple power law spectrum in rigidity for the protons of the form $j_p(R) \propto R^{-2.75}$, where R is the proton rigidity.

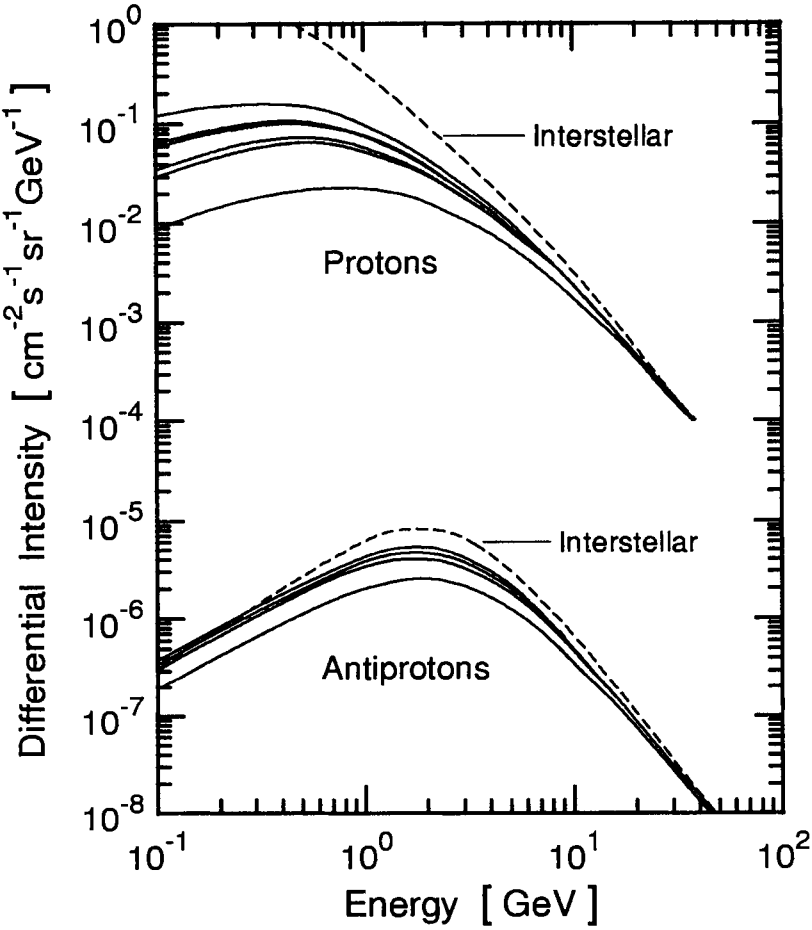

Figure 5.87: Interstellar proton spectrum (top portion of figure) calculated by Webber and Potgieter (1989) (dashed line) and proton spectra modulated to the 1987 (solar minimum), 1993, 1979, 1992, 1980, and 1990 (solar maximum) levels (solid lines, from top to bottom). Likewise (bottom portion of figure), in the same sequence the corresponding antiproton spectra (Labrador and Mewaldt, 1995 and 1997).

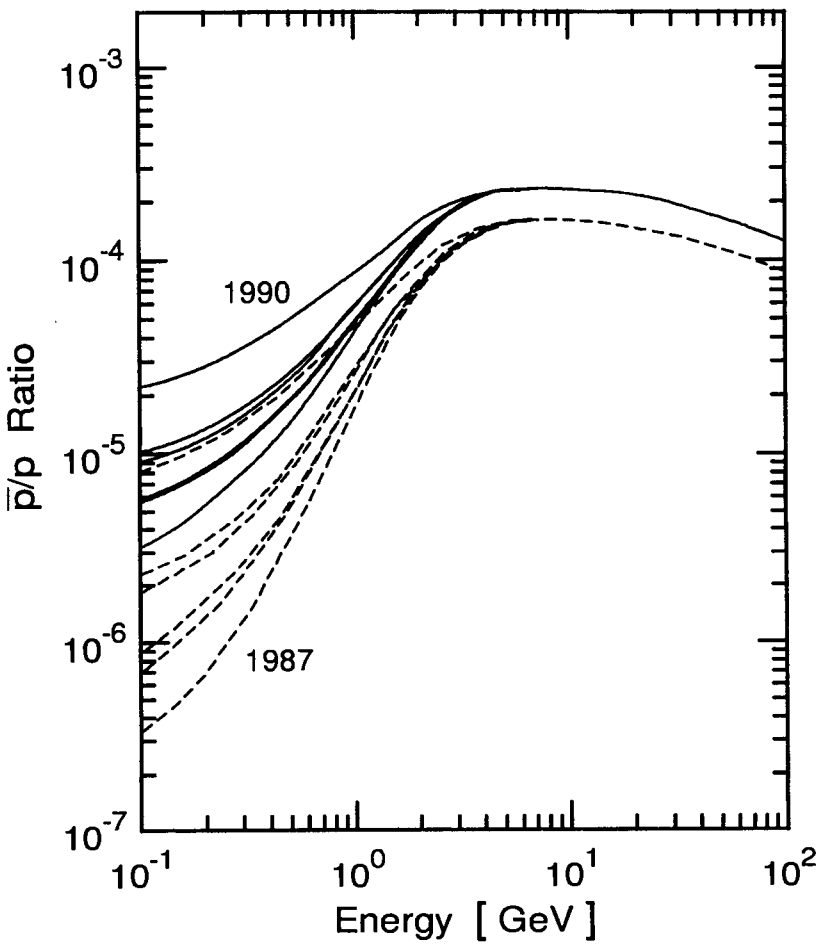

Figure 5.88: Antiproton to proton ratios calculated from interstellar proton and antiproton fluxes of Webber and Potgieter (1989) (solid curves), and the median Gaisser and Schaeffer (1992) fluxes (dashed curves), for epochs of different solar activity. The curves are (from top to bottom) for 1990 (solar maximum), 1980, 1992, 1979, 1993, and 1987 (solar minimum). (Labrador and Mewaldt, 1995 and 1997).

This Page Intentionally Left Blank

Chapter 6

Heliospheric Phenomena

The *heliosphere* is that region of space where solar influences manifest themselves and dominate. It extends for about 120 AU from the Sun. Its boundary, called *heliopause*, lies beyond the *termination shock*, there where the heliospheric magnetic field carried by the *solar wind* interacts with the interstellar medium. The magnetic field configuration of the heliosphere and that of the enclosed *magnetosphere* are outlined in the next section.

Many of the heliospheric cosmic ray phenomena involve very complex processes and represent highly specialized fields of research of their own that are far beyond the scope of this book. We only outline some of the more basic heliospheric topics for reasons of completeness and definition, and present a very limited set of data in the appropriate sections. For further details the reader is referred to the specialized literature (see e.g. Parker 1963 and 1965; Schopper et al., 1967; Dorman 1974; Allkofer 1975; Kunow 1992; Longair 1992; Moraal 1993; Fisk et al., 1998).

6.1 Introduction

The *solar activity* affects the shape of the cosmic ray energy spectrum up to about 10 GeV/nucleon, i.e., a rigidity of ~10 GV for protons (~20 GV for He) because of the magnetic disturbances it causes. The amplitude of this activity is time dependent and manifests periodic as well as aperiodic features. Periodic occurrences such as the *11-year sunspot cycle* as well as the *27-day rotation* of the Sun play an important role. Apart from *solar flares* (SF) and *coronal mass ejections* (CME) that occur at random but with a frequency that appears to have some correlation with the *sunspot number*, there are indications that other periodicities may exist. In addition, the solar magnetic field *reverses polarity* every 22 years, superimposing accompanying

effects. The time variation of the cosmic radiation due to solar activity is called *solar modulation* (Quenby, 1967; Moraal, 1993).

On Earth the fluxes and spectra from the eastern and western directions are different up to rigidities of about 60 GV, because of the geomagnetic field and the positive charge dominance of the primary radiation. This is called the *east - west effect* or *east - west asymmetry.* Due to the *geomagnetic cutoff* imposed by the geomagnetic field, the energy spectra manifest a *latitude dependence* for rigidities up to about 15 GV at vertical incidence, called the *latitude effect.*

There exists also a *longitude effect* which is due to the fact that the geomagnetic dipole axis is inclined with respect to the Earth's axis of rotation and laterally displaced. In addition there are *magnetic anomalies.* The most significant one is the *South Atlantic anomaly,* off the coast of Brazil. All these effects are altitude and time dependent.

References

Allkofer, O.C.: Introduction to Cosmic Radiation, Thiemig Verlag, München (1975).

Dorman, L.I.: Cosmic Rays: Variation and Space Exploration, Amsterdam, North-Holland Publishing Company (1974).

Fisk, L.A., J.R. Jokipii, G.M. Simnett, R. von Steiger, and K.-P. Wenzel (eds.): Cosmic Rays in the Heliosphere. Space Science Series of ISSI. Kluwer Academic Publishers, Dordrecht. Space Sci. Rev., 83 (1998).

Kunow, H.: Proc. of the First Soltip Symposium, Liblice, Czechoslovakia 1991, p. 165. Fischer, S., and M. Vandas editors. Published by the Astronomical Institute of Czechoslovak Academy of Sciences, Prague, Czechoslovakia (1992).

Longair, Malcolm, S.: High Energy Astrophysics. Cambridge University Press, Cambridge, 2nd. ed. (1992).

Moraal, H.: in Cosmic Rays 92 - Astrophysical, High Energy and Heliospheric Processes. Proc. 13th European Cosmic Ray Symposium, Geneva, Switzerland, 1992. Ed. P.K.F. Grieder. Nucl. Phys. B (Proc. Suppl.) 33A,B, p. 161 (1993).

Parker, E.N.: Interplanetary Dynamical Processes. Interscience Monographs and Texts in Physics and Astronomy. J. Wiley and Sons N.Y. and London (1963).

Parker, E.N.: PICRC, 1, p. 26 (1965).

Quenby, J.J.: The Time Variations of the Cosmic Ray Intensity. Handbuch der Physik, Kosmische Strahlung XLVI/2, p. 310, Berlin, Springer Verlag (1967).

Schopper, E., E. Lohrmann, and G. Mauck: Nukleonen in der Atmosphäre. Handbuch der Physik, Kosmische Strahlung XLVI/2, p. 372, Berlin, Springer Verlag (1967).

6.2 Heliospheric, Magnetospheric and Terrestrial Magnetic Fields

6.2.1 Introduction

The combined effects of the magnetic fields of the Sun and the Earth, and the *solar wind* form a highly complex electromagnetic configuration that influences the propagation of the cosmic radiation as it enters the heliosphere and magnetosphere, and approaches the Earth. We have excellent knowledge of the geomagnetic field and detailed data of large portions of the magnetic field in the magnetosphere. However, both field components are superimposed and time dependent, and both can be subject to sudden and significant changes.

The interplanetary and heliospheric magnetic fields have been explored for a long time with many space probes and we have a fair understanding of the magnitude and orientation of the fields, at least in the explored regions, but the situation is complex and also time dependent. In the following we discuss very briefly the basic features of the *heliospheric* and the Earth's *magnetospheric magnetic fields* and the principal consequences that result for the cosmic radiation, including geomagnetic effects.

6.2.2 Heliospheric Magnetic Field and Solar Wind

The *heliosphere* is that region of space surrounding the Sun that is dominated by the *solar wind* (Parker, 1957, 1958a, 1958b and 1963). The solar wind flows continuously away from the Sun into space with a velocity of about 300 km/s to 800 km/s. It manifests latitude, longitude and time dependence, and consists mainly of hydrogen, some helium and other nuclei, all highly ionized, and an approximately equal number of electrons. It is therefore electrically neutral and a *plasma*. The solar wind is subject to variations that are coupled with solar activity.

Table 6.1: Solar Wind Composition

(von Steiger et al., 2000)

Abundance ratios obtained with SWICS/Ulysses during four ~300-day periods. The numbers denote averages of daily values with their 1σ variability. Photospheric values are from Grevesse and Sauval (1998).

Element	FIP	Maximum	South	North	Minimum	Photosphere
He	24.59	95.9 ± 35.1	72.7 ± 7.9	73.6 ± 8.2	84.0 ± 33.0	126
C	11.26	0.670 ± 0.071	0.683 ± 0.040	0.703 ± 0.037	0.670 ± 0.086	0.489
N	14.53	0.069 ± 0.038	0.111 ± 0.022	0.116 ± 0.021	0.088 ± 0.035	0.123
O	13.62	1 ± 0	1 ± 0	1 ± 0	1 ± 0	1
Ne	21.56	0.091 ± 0.025	0.082 ± 0.013	0.084 ± 0.013	0.104 ± 0.027	0.178
Mg	7.65	0.147 ± 0.045	0.105 ± 0.025	0.108 ± 0.022	0.143 ± 0.055	0.0560
Si	8.15	0.167 ± 0.047	0.115 ± 0.023	0.102 ± 0.023	0.132 ± 0.042	0.0525
S	10.36	0.049 ± 0.016	0.056 ± 0.013	0.051 ± 0.014	0.051 ± 0.021	0.0316
Fe	7.87	0.120 ± 0.039	0.092 ± 0.017	0.081 ± 0.014	0.106 ± 0.044	0.0468

In Table 6.1 we list long-term average values of the elemental composition of the solar wind according to von Steiger et al. (2000) for different epochs and spatial locations. The data cover the time span from 1991 to 1998 and include the following measurements:

a) low latitude, relatively quiet, *slow solar wind* at post-maximum solar activity period (September 1991 to June 1992) (column 3, Table 6.1);

b) high latitude, *fast stream* from south polar coronal hole (January to October 1994) (column 4);

c) high latitude, *fast stream* from north polar coronal hole (July 1995 to April 1996) (column 5);

d) low latitude, *slow solar wind* at post-minimum solar activity (July 1997 to April 1998) (column 6).

Also given in Table 6.1 are the first ionization potentials of the elements (FIP) and the photospheric abundances after Grevesse and Sauval (1998).

The isotopic composition of the solar wind is given in Table 6.2 and was taken from the summary of Wimmer et al. (1999a).

Because of the high conductivity of the interplanetary plasma the solar wind transports the *frozen-in magnetic field* from the Sun into space. Due to the rotation of the Sun the field lines are not radial but describe approx-

Table 6.2: Summary of the Isotopic Composition of the Solar Wind

(Wimmer et al., 1999a, corrected)

Isotopes	Source[1)]	Ratio	Ref.[2)]	Solar[3)]
$^4He/^3He$	ASW	2450 ± 500	(1)	2050 ± 20
$^4He/^3He$	SSW	2450 ± 150	(2)	2050 ± 20
$^4He/^3He$	FSW	3030 ± 250	(2)	2050 ± 20
$^{14}N/^{15}N$	ASW	200 ± 60	(3)	272
$^{16}O/^{18}O$	SSW	450 ± 130	(4)	498
$^{20}Ne/^{21}Ne$	SSW	440 ± 110	(5)	420 ± 50
$^{20}Ne/^{22}Ne$	SSW	13.8 ± 0.7	(5)	13.7 ± 0.3
$^{20}Ne/^{22}Ne$	SSW	13.64 ± 0.7	(6)	13.7 ± 0.3
$^{25}Mg/^{24}Mg$	SSW	0.128 ± 0.011	(7)	0.1266
$^{25}Mg/^{24}Mg$	FSW	0.132 ± 0.013	(7)	0.1266
$^{25}Mg/^{24}Mg$	SSW	0.130 ± 0.007	(8)	0.1266
$^{25}Mg/^{24}Mg$	CME	0.117 ± 0.021	(9)	0.1266
$^{26}Mg/^{24}Mg$	SSW	0.138 ± 0.012	(7)	0.1394
$^{26}Mg/^{24}Mg$	FSW	0.153 ± 0.013	(7)	0.1394
$^{26}Mg/^{24}Mg$	SSW	0.137 ± 0.010	(8)	0.1394
$^{26}Mg/^{24}Mg$	CME	0.146 ± 0.024	(9)	0.1394
$^{29}Si/Si$	SSW	0.0454 ± 0.002	(6)	0.0463
$^{29}Si/^{28}Si$	CME	0.056 ± 0.016	(9)	0.0506
$^{30}Si/Si$	SSW	0.0326 ± 0.002	(6)	0.0310
$^{30}Si/^{28}Si$	CME	0.036 ± 0.015	(9)	0.0336
$^{40}Ca/^{44}Ca$	ASW	50 ± 8	(10)	47.153
$^{40}Ca/^{42}Ca$	ASW	128 ± 47	(10)	151.04
$^{54}Fe/^{56}Fe$	SSW	$0.085^{+0.005}_{-0.022}$	(11)	0.063
$^{54}Fe/^{56}Fe$	SSW	0.065 ± 0.003	(12)	0.063
$^{57}Fe/^{56}Fe$	SSW	< 0.05	(11)	0.023

1) SSW slow solar wind; FSW fast solar wind; CME coronal mass ejection; ASW average solar wind

2) (1) Bodmer and Bochsler (1998); (2) Gloeckler and Geiss (1998); (3) Kallenbach et al. (1998a); (4) Collier et al. (1998); (5) Kallenbach et al. (1997); (6) Wimmer et al. (1998); (7) Bochsler et al. (1997); (8) Kucharek et al. (1998); (9) Wimmer et al. (1999b); (10) Kallenbach et al. (1998b); (11) Oetliker et al. (1997); (12) Wurz (1999)

3) Solar system values are those of Anders and Grevesse (1989).
For noble gases the solar wind values for He are those of Coplan et al. (1984) and Geiss et al. (1972), for Ne those of Geiss et al. (1972).

imately *Archimedean spirals* centered at the Sun (Parker, 1963). Particles which flow outwards with constant velocity move in radial direction, following the revolving spirals. The orientation of the heliospheric magnetic field in the ecliptic along the spirals has a *sector structure*. It reverses direction in successive sectors, pointing predominantly towards the Sun and then again away from it. The Earth sweeps across a sector in about 6 to 7 days for a typical 4-sector structure. A more realistic model has recently been proposed by Fisk (1996).

At the outer fringes of the heliosphere, at an estimated distance of about 100±20 AU, the solar wind meets the interstellar medium (Axford, 1996). There it interacts with the interstellar wind and a termination shock occurs. The interstellar wind is believed to act in the Galaxy in an analogous way as the solar wind in the heliosphere.

A *bow shock* occurs where the onflowing interstellar wind first encounters the presence of the heliospheric field (Parker, 1961). The region between the bow shock and the *heliopause* which separates the *heliospheric cavity* from interstellar space is called the *heliosheath*. Variation of the solar activity affects the magnetic field in the heliosphere and the spectrum of the cosmic radiation within it. Figure 6.1 shows an approximate outline of the magnetic field and plasma flow configurations in the heliosphere.

Disturbances due to local solar activity, such as *solar flares* (SF) or *coronal mass ejections* (CME), cause irregularities in the flow of the solar wind and the associated magnetic field. So-called magnetic bottles are formed that act as scattering regions for the incident low energy cosmic radiation and can influence its intensity and energy spectrum near the Earth. If the Earth is engulfed in such a disturbance the event causes geomagnetic disturbances , called *magnetic storms* . At distances >10 AU there may be *global merged interaction regions* (GMIR) that may affect the cosmic ray intensity at Earth.

6.2.3 Geomagnetic and Magnetospheric Fields

At the surface of the Earth the magnetic field varies between 30 μT (0.3 G) and 60 μT (0.6 G), depending on the geographic location (or geomagnetic latitude). Some details concerning the properties of the *geomagnetic field*, such as the *geomagnetic cutoff*, are discussed in Chapter 1 and references to specific literature are listed there.

The magnetic field measured on Earth or in the atmosphere is the result of the superposition of the purely geomagnetic field, which itself is not homogeneous and changes slowly with time, and the field components caused by

external currents and other internal and external influences that may cause additional slow or sudden variations.

The resulting field interacts with the onstreaming solar wind and forms a magnetic field configuration, called the *magnetosphere*, that resembles a picture as described above for the heliosphere, but on a smaller scale. Figure 6.2 shows a cross-sectional view of the magnetic field in and around the magnetosphere, embedded in the solar wind, in a plane perpendicular to the ecliptic that passes through the centers of the Earth and the Sun.

The much weaker fields of the heliosphere affect the cosmic radiation essentially over the entire heliospheric volume, whereas geomagnetic effects that are of much larger magnitude mark their influence on a much more local level, over a comparatively small volume. The latter is confined to the magnetosphere which is bound by the *magnetopause.*

The relatively strong geomagnetic field in the vicinity of the Earth imposes a cutoff for low energy particles that varies as a function of geomagnetic latitude, which is different from the geographic latitude because the Earth's magnetic dipole axis does not coincide with its axis of rotation. At the magnetic poles the geomagnetic cutoff is zero whereas at the geomagnetic equator it is $\simeq$15 GV for vertical incidence. In addition to the geomagnetic cutoff there is an altitude dependent atmospheric cutoff which is present everywhere, preventing low energy particles from reaching ground level because of interactions with the atmospheric constituents.

Solar activity disturbs the magnetospheric magnetic field configuration and can change the cutoff conditions for cosmic rays and solar particles significantly. It may also lead to partial discharges of the *radiation belts* in the Earth's polar regions, causing *aurora* effects.

Depending on the rigidity and direction of propagation of the cosmic radiation the particles are more or less deflected from their original trajectories by the magnetic fields encountered while approaching the Earth. Some of the particles may never reach the Earth's surface because they may be deflected back into space, others may dissipate their energy in the atmosphere before reaching ground.

To illustrate the radial dependence of the gyroradius of a particle moving in the inner magnetosphere, we show in Fig. 6.3 the relation between the gyroradius and the rigidity of a particle at four radial distances from the center of the Earth, and for two geomagnetic latitudes.

6.2.4 Interplanetary Magnetic Fields

The interplanetary magnetic field has been explored by numerous satellites. In the inner heliosphere the radial field as measured by Ulysses is about 3.5 nT (35 μG) at 1 AU and shows significant variations in amplitude and direction with time and position of the space probe (Smith et al., 1995; Balogh, 1996; Fisk, 1997). It was also found that the relation

$$B_r \cdot r^2 \simeq 3.5 \quad [\mathrm{nT(AU)^2}] \,, \tag{6.1}$$

where B_r is the radial component of the magnetic field in units of [nT] and r the distance from the Sun in units of [AU], holds for the region explored by Ulysses (Smith and Balogh, 1995). In the outer heliosphere the magnetic field is estimated to be probably $\leq$1 nT (Axford, 1990).

Galactic and Intergalactic Magnetic Fields are discussed in Chapter 7, Section 7.2.

References

Axford, W.I.: in S. Grzedzielski and D.E. Page, eds., Physics of the Outer Heliosphere, Pergamon Press, Oxford, 7-15 (1990).

Axford, W.I.: Space Sci. Rev., 78, p. 9 (1996).

Balogh, André: Space Sci. Rev., 78, p. 15 (1996).

Bochsler, P., H. Balsiger, R. Bodmer, Th. Zurbuchen, G. Gloeckler, D.C. Hamilton, M. Collier, and D. Hovestadt: Phys. Chem Earth, 22, p. 401 (1997).

Bodmer, R., and P. Bochsler: Astron. Astrophys., 337, p. 921 (1998).

Collier, Michael R., D.C. Hamilton, G. Gloeckler, G. Ho, P. Bochsler, R. Bodmer, and R. Sheldon: J. Geophys. Res., 103, p. 7 (1998).

Coplan, M.A., K.W. Ogilvie, P. Bochsler, and J. Geiss: Sol. Phys., 93, p. 415 (1984).

Fisk, L.A.: J. Geophys. Res., 101, p. 15547 (1996).

Fisk, L.A.: PICRC, 8, p. 27 (1997).

Geiss, J., F. Buehler, H. Cerutti, P. Eberhardt, and Ch. Filleux: in Apollo 16 Prelim. Sci. Rep., 14.1 - 14.10, NASA SP-315 (1972).

Gloeckler, G., and J. Geiss: Space Sci. Rev., 84, p. 275 (1998).

Grevesse, N., and A.J. Sauval: Space Sci. Rev., 5, p. 161 (1998).

Kallenbach, R., F.M. Ipavich, P. Bochsler, S. Hefti, D. Hovestadt, H. Grünwaldt, M. Hilchenbach, W.I. Axford, H. Balsiger, A. Bürgi, M.A. Coplan, A.B. Galvin, J. Geiss, F. Gliem, G. Gloeckler, K.C. Hsieh, B. Klecker, M.A. Lee, S. Livi, G.G. Managadze, E. Marsch, E. Möbius, M. Neugebauer, K.-U. Reiche, M. Scholer, M.I. Verigin, B. Wilken, and P. Wurz: J. Geophys. Res., 102, p. 26895 (1997).

Kallenbach, R., J. Geiss, F.M. Ipavich, G. Gloeckler, P. Bochsler, F. Gliem, M. Hilchenbach, and D. Hovestadt. Astrophys. J., 507, L-185 (1998a).

Kallenbach, R., F.M. Ipavich, P. Bochsler, S. Hefti, P. Wurz, M.R. Aellig, A.B. Galvin, J. Geiss, F. Gliem, G. Gloeckler, H. Grünwaldt, M. Hilchenbach, D. Hovestadt, and B. Klecker: Astrophys. J., 498, p. L-75 (1998b).

Kucharek, H., F.M. Ipavich, R. Kallenbach, P. Bochsler, D. Hovestadt, H. Grünwaldt, M. Hilchenbach, W.I. Axford, H. Balsiger, A. Bürgi, M.A. Coplan, A.B. Galvin, J. Geiss, F. Gliem, G. Gloeckler, K.C. Hsieh, D.J. Judge, B. Klecker, M.A. Lee, S. Livi, G.G. Managadze, E. Marsch, E. Möbius, M. Neugebauer, H.S. Ogawa, K.-U. Reiche, M. Scholer, M.I. Verigin, B. Wilken, and P. Wurz: J. Geophys. Res., 103, p. 26805 (1998).

Oetliker, M., D. Hovestadt, B. Klecker, M.R. Collier, G. Gloeckler, D.C. Hamilton, F.M. Ipavich, P. Bochsler, and G.G. Managadze: Astrophys. J., 474, p. L-69 (1997).

Parker, E.N.: Phys. Rev., 107, p. 924 (1957).

Parker, E.N.: Astrophys. J., 128, p. 664 (1958a).

Parker, E.N.: Phys. Rev., 109, p. 1874 (1958b).

Parker, E.N.: Astrophys. J., 134, p. 20 (1961).

Parker, E.N.: Interplanetary Dynamical Processes. Interscience Monographs and Texts in Physics and Astronomy. J. Wiley and Sons N.Y. and London (1963).

Smith, Edward, J., and A. Balogh: Geophys. Res. Lett, 22, p. 3317 (1995).

Smith, E.J., M. Neugebauer, A. Balogh, S.J. Bame, R.P. Lepping, and B.T. Tsurutani: Space Sci. Rev., 72, p. 165 (1995).

Von Steiger, R., N.A. Schwadron, L.A. Fisk, J. Geiss, G. Gloeckler, S. Hefti, B. Wilken, R.F. Wimmer-Schweingruber, and T.H. Zurbuchen: J. Geophys. Res., 105, p. 27217 (2000).

Wimmer-Schweingruber, R.F., Peter Bochsler, and Olivier Kern: J. Geophys. Res., 103, p. 20621 (1998).

Wimmer-Schweingruber, R.F., P. Bochsler, and P. Wurz: Isotopes in the

Solar Wind: New Results from ACE, SOHO, and WIND, in Solar Wind Nine. (S.R. Habbal, R. Esser, J.V. Hollweg, P. Isenberg eds.) p. 147 (1999a).

Wimmer-Schweingruber, Robert F., Peter Bochsler, George Gloeckler, Fred M. Ipavich, Johannes Geiss, Reinald Kallenbach, Len A. Fisk, Simon Hefti, and Thomas H. Zurbuchen: Geophys. Res. Lett., 26, p. 165 (1999b).

Wurz, P.: "Heavy Ions in the Solar Wind: Results from SOHO / CELIAS / MTOF", Habilitation Thesis, University of Bern, Switzerland (1999).

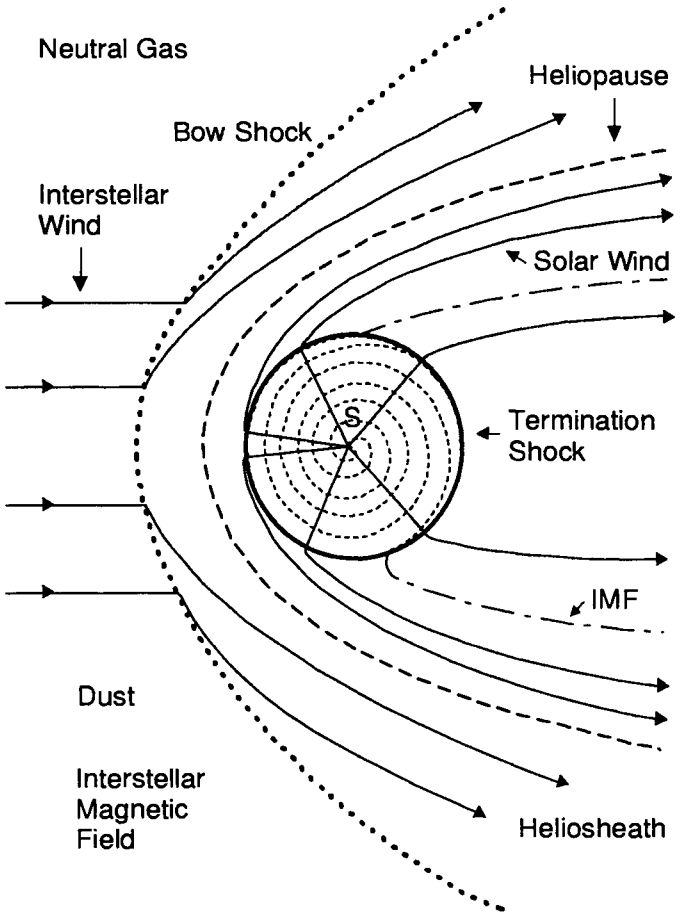

Figure 6.1: Approximate configuration of the heliospheric magnetic field and plasma flows derived and constructed from measurements made by Voyager 1 and 2 in the plane of the ecliptic and from out of ecliptic measurements made by Ulysses on its voyage over the solar polar regions in conjunction with the modified Parker model (Parker, 1958a and 1963; Fisk, 1996 and 1997). The termination shock is also indicated.

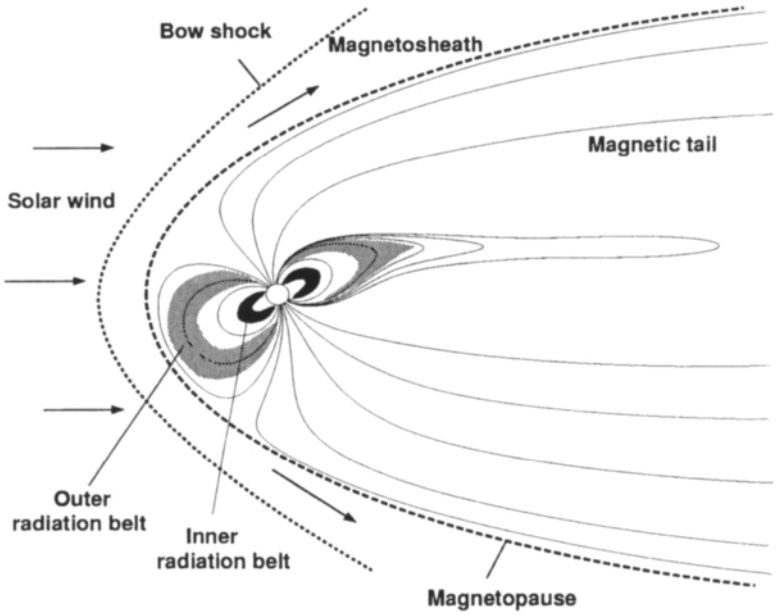

Figure 6.2: The Earth's magnetosphere embedded in the solar wind. Because of the inclination of the Earth's axis of rotation of 23° with respect to a line perpendicular to the ecliptic, and because of the deviation of the Earth's magnetic dipole axis from its axis of rotation of about 11°, the magnetosphere is not symmetric (the figure shows the extreme position). Interaction between the solar wind and the geomagnetic field leads to the bow shock, the magnetosheath and the magnetopause. The geomagnetic field is confined to the space within the magnetopause. Also shown are the Earth's radiation belts (courtesy of L. Desorgher).

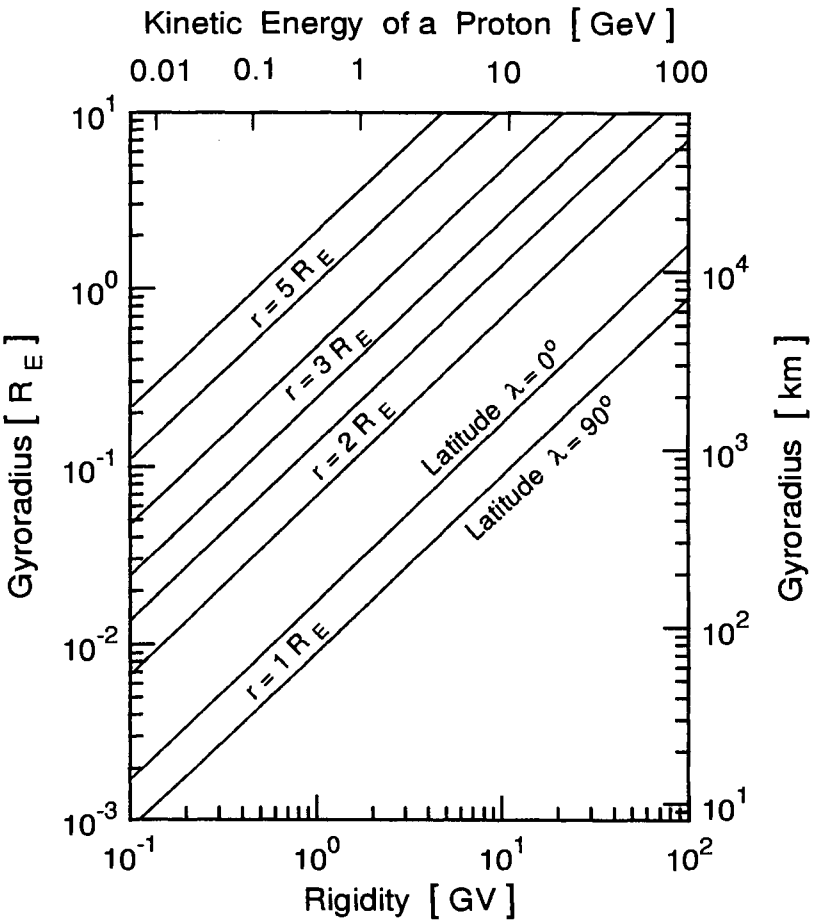

Figure 6.3: Radius of gyration of charged particles in the Magnetosphere, in units of Earth radii [R_E] and kilometers [km], as a function of rigidity at different distances, r, from the Earth's center, and geomagnetic latitudes between $\lambda = 0°$ (equator) and $\lambda = 90°$ (poles) (courtesy E. Flückiger, University of Bern). On top of the graph we have marked the kinetic energy of a proton corresponding to the rigidity marked on the abscissa.

6.3 Time Variation and Modulation Effects

6.3.1 Introduction

To a first approximation, the intensity of the cosmic radiation at sea level can be considered as constant. However, careful measurements over many years have revealed that there exist periodic as well as aperiodic intensity variations. Both kinds of variations are caused by solar activity and are referred to as *solar modulation effects* (Parker, 1965; Sandström, 1965; Quenby, 1967; Moraal, 1993; Kudela, 1997 and references listed therein).

Likewise, geomagnetic activity causes long-term latitude dependent variations . In addition, changing meteorological and seasonal conditions, such as barometric pressure and temperature, affect the effective thickness and scale height of the atmosphere, causing secondary intensity variations of the cosmic ray flux on Earth.

Solar Time and Diurnal Variations

Solar time is our daily time, from noon to noon. It is the time required for one complete revolution of the Earth about its axis with respect to the Sun. Many directional variations that we observe in heliospheric coordinates are recurrent in solar time and are called *solar diurnal variations.* Astronomical features, however, are recurrent in *sidereal time.*

Sidereal Time and Sidereal Variations

One *sidereal day* is the time required for the Earth to make one complete 360° revolution about its axis with respect to a fixed star, or a distant galaxy. Therefore *directional features* of cosmic ray intensity that are of interstellar, galactic or even extragalactic origin, such as radiation from a distant point source, will appear periodically in *sidereal time* or manifest *sidereal variations.*

Solar time and sidereal time differ by one part in 365, the sidereal day being shorter. A difference of one day arises in a cycle of one year because of the orbital motion of the Earth around the Sun. To distinguish sidereal from solar variations, or from other effects, measurements must be made for extended periods, say one year, or even several years to improve the statistics.

6.3.2 Atmospherically Induced Variations

Atmospherically induced intensity variations are investigated by measurements of the flux of muons and nucleons in the lower parts of the atmosphere, from sea level to mountain altitudes. In some cases muons are also monitored at shallow depth underground to reduce background effects. The nucleonic component is studied with the help of so-called *neutron monitors* (NM) (Simpson and Uretz, 1953; Hatton, 1971). It is mostly the abundant low energy neutrons, that are produced in the atmosphere by relatively low energy cosmic ray hadrons in interactions with nuclei of air constituents, to which the neutron monitor responds.

Muons which are the decay products of charged pions resulting from similar nuclear interactions have different propagation characteristics in the atmosphere than the nucleonic component, and the two components do not respond alike to changes of the atmosphere (see Chapter 1) (for details see Allkofer, 1975; Gaisser, 1990; Kudela, 1997; Bazilevskaya and Svirzhevskaya, 1998).

Nucleonic Component

For precise interpretation of the measurements the entire atmospheric column must be taken into account. The fractional change of intensity, $\Delta j_n/j_n$, recorded by a neutron monitor, e.g., at sea level, due to a pressure change, Δp, at the location of the neutron monitor can be approximated by the expression

$$\Delta j_n/j_n \;=\; -\alpha_N \, \Delta p \;\;, \tag{6.2}$$

where α_N is the *pressure coefficient* of the nucleonic component. $\alpha_N \simeq 9.6 \cdot 10^{-3}$ [mm^{-1} Hg] for atmospheric pressure changes measured in [mm Hg]. Thus, if the pressure is higher than the reference pressure, i.e., if $\Delta p > 0$, the neutron flux is reduced because a larger column of atmosphere must be traversed to reach sea level.

Muonic Component

As mentioned before, muon production and propagation in the atmosphere are determined by a different mix of processes than the nucleonic component and the muon flux responds in a different way to changes of atmospheric parameters. The general trend with respect to pressure changes in the atmosphere described by eq. 6.2 remains, but it is less pronounced because muon propagation is mainly subject to ionization losses only. The previous relation

can therefore be rewritten for the fractional change of the muon intensity, $\Delta j_\mu / j_\mu$, due to a pressure change, Δp, as

$$\Delta j_\mu / j_\mu = -\alpha_\mu \Delta p \ , \tag{6.3}$$

where α_μ is the *pressure coefficient* of the muonic component. $\alpha_\mu \simeq 2.15 \cdot 10^{-3}$ [mm^{-1} Hg] for atmospheric pressure changes measured in [mm Hg].

Because of muon decay an additional variation of the intensity of muons arises when the altitude of the main production layer changes. If the altitude increases, the path lengths of the muons to sea level gets larger and the probability for decay increases. We can therefore write an analogous equation for the fractional intensity change of muons, $\Delta j_\mu / j_\mu$, recorded by a muon detector at sea level due to a change of production height, Δh, in the atmosphere as we did previously for changes in pressure. Thus,

$$\Delta j_\mu / j_\mu = -\alpha_{\mu h} \Delta h \ , \tag{6.4}$$

where $\alpha_{\mu h}$ is the *decay* or *altitude coefficient* of the muonic component. $\alpha_{\mu h} = 5 \cdot 10^{-5}$ [m^{-1}] for changes of the height of the production layer in the atmosphere, measured in [m].

Finally, a third atmospheric effect which is due to the competition between interaction and decay of charged pions must be considered. The probabilities for both processes depend on the density of the atmosphere at the location of propagation of the pion. When the temperature in the main production layer for pions in the atmosphere increases, which is between about 100 mb and 200 mb, the density decreases and the competition between decay and interaction changes slightly in favor of decay, yielding more muons (cf Chapter 1). This temperature change, ΔT, causes the muon intensity to increase with increasing temperature and can be described by the relation

$$\Delta j_\mu / j_\mu = \alpha_{\mu T} \Delta T \ , \tag{6.5}$$

where $\alpha_{\mu T}$ is the *temperature coefficient* for muons. $\alpha_{\mu T} \simeq 10^{-3}$ [$^\circ C^{-1}$] per degree of temperature change in the region between 100 mb and 200 mb. Note that this effect is positive in contrast to the others.

It must be emphasized that for accurate measurements, the altitude dependence of all the coefficients mentioned in this subsection must be properly included as well as the energy dependence of the coefficients that are relevant for correcting the muon intensity.

Both the nucleonic and muonic components show large *seasonal effects* because of seasonal variations of the production layer. For muons this corresponds to a combination of barometric and temperature effects. In Fig. 6.4 we show the relative seasonal variation of the cosmic ray muon intensity during 1969 (after Allkofer and Jokisch, 1973).

6.3.3 Solar Diurnal Variations

For many years the cosmic ray intensity measured on Earth has been observed to undergo a periodic variation with a periodicity of one *solar day*. This solar diurnal variation is approximately sinusoidal and has a maximum soon after noon, local time, as shown in Fig. 6.5. It reflects the interaction of the solar wind and interplanetary magnetic field with the cosmic radiation. The typical amplitude of the variation is about 0.3% with respect to the mean for the nucleonic and 0.1% for the muonic intensities. Fourier analysis of the diurnal variation shows that it is not quite sinusoidal and contains a second harmonic, called the *semi-diurnal variation*. Its amplitude is $< 0.02\%$ for the nucleonic component (Fig. 6.5).

An important characteristic of any modulation process is its variation with rigidity. Since the origin of the modulation is always the interaction of charged cosmic ray particles with the changing magnetic fields in interplanetary and magnetospheric space, solar modulation is rigidity dependent. The fractional change in intensity can therefore be written as

$$\Delta j(P)/j(P) = \kappa P^{-\delta} \quad , \tag{6.6}$$

For the diurnal variation $\delta \approx 0$ up to a limiting rigidity, P_L, above which the diurnal anisotropy disappears. Thus

$$\Delta j(P)/j(P) = \kappa \quad \text{for } P < P_L \tag{6.7}$$

$$\Delta j(P)/j(P) = 0 \quad \text{for } P > P_L \tag{6.8}$$

P_L changes during the solar cycle and has a value of about 55 GV at solar minimum and approaches 100 GV at solar maximum.

The origin of the solar diurnal modulation is believed to be linked with the solar wind and its frozen-in magnetic field that interacts with the cosmic radiation. Since the magnetic field co-rotates with the Sun and likewise the low energy cosmic ray particles that are spiraling around the magnetic field

lines, particles moving in the same direction as the Earth along its orbit have a flux excess of about 0.4% compared to those moving in opposite direction.

6.3.4 Sidereal Variations and Anisotropies

If the galactic cosmic radiation is not isotropic a periodic variation of the intensity should be observable in sidereal time because of the rotation of the Earth. The period would have to be one sidereal day. Thus by searching for sidereal variations, anisotropies could be discovered that could reveal sources of cosmic radiation.

However, excluding gamma ray point sources, in all the years of cosmic ray research only very minor indications of anisotropies could be found, that have proven to be difficult to confirm. For energies less than 10^{14} eV a sidereal variation with an amplitude of 0.1% and a possible increase of amplitude with energy proportional to $E^{0.5}$ had been found (Sakakibara, 1965), and around 10^{17} eV an amplitude of $(1.7 \pm 0.4)\%$ (Lloyd-Evans et al., 1983; Kifune et al., 1986).

Recently the existence of a definite asymmetry in the latitude distribution of the amplitude of the first harmonic of the sidereal diurnal variation above 500 GV has been confirmed by Munakata et al. (1995) and Mori et al. (1995) (see also Kudela, 1997). Likewise, very recently the Akeno group in Japan has reported a $\sim$4% anisotropy around 10^{18} eV from an analysis of 216.000 extensive air showers recorded over the past 15 years (Hayashida et al., 1999a). In addition, the AGASA group observed a remarkable clustering of events on the celestial sphere. They registered one triplet and two doublets with energies above $4 \cdot 10^{19}$ eV whose arrival directions are within 2.5° (Hayashida et al., 1999b; see also Chapter 5, Section 5.2).

6.3.5 Compton-Getting Effect

If the cosmic radiation is truly isotropic it is certainly not with respect to the Earth as a frame of reference. This fact was realized by Compton (1933) and Compton and Getting (1935). Under the assumptions made at that time (rectilinear motion of the particles and empty space between planets, stars and galaxies) the authors came to the conclusion that the frame of reference in which cosmic rays are isotropic cannot be in significant rotation relative to distant galaxies, provided that nothing entrains the particles locally.

Considering the rotation of our Galaxy, the motion of the Sun within it and of the Earth along its orbit, Compton and Getting further concluded that if the cosmic radiation is isotropic, our speed with respect to their source

must be about the speed of the galactic rotation. It then follows that a *sidereal diurnal effect* with an amplitude of ~1% would have to result, with a maximum when an observer on Earth is looking forward. If modified for geomagnetic effects in mid latitudes and propagation through the atmosphere, the effect is reduced by about a factor of ten to ~0.1%. Modern estimates yield an even lower amplitude (Gleeson and Axford, 1968; Forman, 1970). However, no such effect could yet be found experimentally.

6.3.6 Forbush Decreases

Continuous monitoring of the cosmic ray intensity has revealed that on many occasions, on a world-wide scale, the cosmic ray intensity decreased between a few percent and about 20%. The decrease occurs rather suddenly, within a few hours or less, but the subsequent recovery to the previous level takes days or even weeks. Such events are usually associated with so-called *geomagnetic storms* and are called *Forbush decreases* (Forbush, 1957, 1958a and 1958b). Typical events are illustrated in Fig. 6.6 which shows the response of a neutron monitor.

Although details are not yet well known, the general mechanism responsible for Forbush decreases is generally believed to be a solar wind effect. At the time of occurrence of a *solar flare* (SF) or a *coronal mass ejection* (CME) from an active region of the Sun, the ejected plasma cloud with associated magnetic fields may have a higher velocity than the normal plasma stream and may produce a shock wave. A *magnetic bottle* may be formed with relatively high field strength and, if the Earth is within it, the low energy galactic cosmic radiation is prevented from reaching it.

6.3.7 27-Day Variations

Sometimes similar cosmic ray flux anomalies may be observed at mean intervals of 27-days. This quasi-periodic recurrence of certain effects is a well known phenomenon and linked to the 27-day rotational period of the Sun which identifies the events as being of solar origin. Frequently, they are related to sunspot activity and *corotating interaction regions* (CIR). Forbush decreases, too, may have a similar recurrence.

6.3.8 11-Year and 22-Year Variations

By monitoring the cosmic ray flux over many years, it has been found that the average flux varies with a period of about 11 years. This period is equivalent

to the 11-year solar cycle (Schwabe cycle, Schwabe, 1843) and is anticorrelated with the solar activity, i.e., during high solar activity which means many sunspots, the cosmic ray intensity is lower, and vice versa, during the quiet Sun when there are fewer sunspots the cosmic ray intensity is higher. At high latitude the peak-to-peak variation over a solar cycle is usually $\simeq$15% for the neutron intensity and $\simeq$4.5% for the muon intensity, measured at ground level. This behavior is illustrated in Fig. 6.7 for the neutron rate, for the epoch 1954 to 1965, i.e., for solar cycle number 19 (Webber, 1967a). Solar cycles are numbered, beginning with 1750. Previous solar cycles, prior to 1750, have negative numbers. Solar cycle 23 began with the solar minimum in 1996. The maximum of solar cycle 23 is expected to occur in the fall of the year 2000.

The 11-year variations are due to changing magnetic conditions in the heliosphere that influence the penetration of low energy galactic cosmic rays into the heliosphere. Stronger magnetic fields and an enhanced degree of turbulence reduce their intensity in the heliosphere or prevent them from entering the inner heliosphere because of deflection. This reduces the local intensity of the cosmic radiation and, hence, the flux of particles responsible for producing the flux of atmospheric secondaries that are detected by the monitoring instruments on Earth. The 11-year cosmic ray intensity variation is anticorrelated with the solar activity.

More subtle additional variations are observed that are probably linked to the *polarity reversal* of the heliospheric magnetic field which occurs at successive sunspot maxima ($\sim$11 years apart) and has a periodicity of approximately 22 years, called the Hale cycle. The alternation of the shape of the cosmic ray maxima between more sharply and more rounded peaks every 11 years seems to be one of these variations.

In Fig. 6.8 we show how the 11-year modulation affects the primary proton and helium spectra. Indicated are the average spectra as well as the minimum and maximum levels that occur during solar maxima and minima, respectively. From this figure it is seen that modulation effects cease to influence particles having energies larger than a few GeV/nucleon.

A compilation of proton spectra obtained from different experiments during different levels of solar activity is illustrated in Fig. 6.9. The intensity variation of low energy protons (130 MeV $< E <$ 225 MeV) in interplanetary space observed on board of the satellites IMP-8 and Pioneer 10 at $\sim$1 AU and at larger distances, respectively, during the last 15 years is presented in Fig. 6.10.

6.3.9 Long-Term Variations

Cosmic ray particles produce both, *stable* and *unstable isotopes* in nuclear reactions in meteorites, in the atmosphere, on Earth and in the Earth's crust, such as ^{3}He, ^{10}Be, ^{32}Si, ^{36}Cl, ^{39}Ar, ^{53}Mn, ^{59}Ni, ^{81}Kr and others, depending on the target material. The production rate of these so-called *cosmogenic nuclides* (see Section 7.2) depends primarily on the intensity and the spectrum of the cosmic radiation, on the location of the specific sample and on the production cross sections (Lal and Peters, 1967; Reedy et al., 1983).

Under the assumption that the intensity of the cosmic radiation and its composition did not change with time, the reaction products can be used for *nuclear chronology*, to determine the so-called *radiation* or *exposure age* of meteorites (Honda, 1967; Caffee et al., 1988), to date trees, the deep ice in the polar regions and other terrestrial objects (Beer, 1997). They are also an important key for deducing past climatic conditions on Earth.

On the other hand, from the fraction of radioactive isotopes such as ^{10}Be and from stable elemental abundances in the cosmic radiation, the average age of cosmic ray particles, τ_{CR}, can be determined. It was found to be about 10^7 years. There seems to be a slight energy dependence which goes approximately as $\tau_{CR} \propto E^{-0.6}$ (more recent work suggests that the energy dependence may be $\propto E^{-0.3}$). From these studies it appears that the more energetic particles are younger (Müller, 1989; see also Section 5.2).

Cosmic Ray History Archived in Meteorites

From the known production cross sections of stable and radioactive nuclides produced by cosmic rays in nuclear reactions in meteorites and in conjunction with the mean decay time of unstable nuclides, information on the variation of the flux of the cosmic radiation over long time spans can be obtained.

Generally speaking we can say that from this work it had been deduced that the average flux of the cosmic radiation has been more or less constant over the past 500 years, that the variation over the past $5 \cdot 10^5$ years remained on average within fluctuations of about 10%, and that over time scales of millions of years its variation did not exceed a factor of two (Vogt et al., 1990).

Iron meteorites appear to be those small bodies that had been exposed longest to the cosmic radiation in space, some as long as 10^9 y and more. They retain a record of any changes in the cosmic ray intensity that may have occurred over the last few hundred million years. Detection of changes can be achieved by comparing ages based on various pairs of cosmogenic

isotopes, one radioactive and one stable (Anders, 1962). Meteorites that show simple exposure histories, i.e., agreement of the ages determined with different isotope pairs, e.g., $^{26}Al/^{21}Ne$ and $^{40}K/^{41}K$, imply a constant average intensity of the cosmic radiation for the last 10^9 years (1 Gy) (Lipschutz et al., 1965).

Other authors found in some cases in meteorites that had a complex exposure history disparities that could imply a 50% increase in the cosmic ray flux within the last few million years (Voshage, 1962 and 1967; Hampel and Schaeffer, 1979). On the other hand Marti et al. (1984) rule out such a change in the flux variability on a million year time scale based on ^{10}Be data but find evidence for a change of about 50% on a time scale of $10^8 - 10^9$ years in iron meteorites (see also Aylmer et al., 1988; Lavielle et al., 1999).

However, there may have been short periods of significantly higher cosmic ray intensities than at present which may have been caused by nearby supernova explosions that require more subtle techniques to be discovered. Furthermore, the solar activity manifests additional cycles and irregularities that are not so well established as those mentioned above, such as the 207 year De Vries cycle (De Vries, 1958), the 70 year Maunder minimum (1645 - 1715 AD) (Maunder, 1894 and 1902; Eddy 1976 and 1983) and possibly a 2100 to 2400 year cycle (Houtermans, 1971; Dergachev and Chistyakov, 1995) that affect the heliospheric magnetic field and consequently the intensity and spectrum of the low energy (<10 GeV) cosmic radiation arriving at Earth.

Supernova Explosions Revealed in Thermoluminescence Records of Sediments

Cini et al. (1982 and 1983) and Attolini et al. (1983) detected evidence for periods of sharply elevated radiation levels in sediments of the Tyrrhenian Sea, off the coast of Livorno, Italy, using thermoluminescence, that coincide with the dates of historical supernovae explosions. This is illustrated in Fig. 6.11. A relatively high rate of sedimentation takes place in that region (up to 20 cm/1000 y), partly from wind-carried dust from the Sahara and of other origin.

More recent work by Cini et al. (1997) using thermoluminescence on shallow cores from the Ionian Sea spans the epoch of the last 3000 years. From the known sedimentation rate any section of a drill core can be dated very accurately (Cini et al., 1990; Bonino et al., 1993). The authors suggest that the dust was probably exposed in the stratosphere to an elevated flux of gamma rays from the supernovae. The first attempt to detect supernovae

explosions in terrestrial material was made by Rood et al. (1979).

Cosmic Ray Intensity Variations Deduced from Radioactive Isotopes in Tree Rings and Polar Ice

Extensive studies of the ^{14}C contents in tree trunks, of ^{36}Cl and ^{10}Be in polar ice cores and of other cosmogenic nuclides in terrestrial samples have revealed that the intensity of the cosmic radiation at Earth that is responsible for the production of these nuclides, i.e., the relatively intense but low energy component that is influenced by solar modulation, must have been subject to variations in the past.

The variations appear to be correlated with solar activity and changes of the heliospheric and geomagnetic fields that affect the intensity and spectral shape of the cosmic radiation up to a few GeV/nucleon. It is not trivial to separate effects due to changes of the geomagnetic field from those of the heliospheric magnetic field. The latter are inferred from past sunspot records whereas the former hinge on very delicate measurements of the magnetic remanence and other properties of sea floor sediments (Meynadier et al., 1992; Tric et al., 1992).

Todays ^{14}C record extends back to about 12,000 y (12 ky) BP (before present, i.e., 10,000 y BC) and were obtained in conjunction with *dendrochronological* research (e.g. Stuiver and Reimer, 1993; Dergachev and Chistyakov, 1995). This is illustrated in Fig. 6.12 which shows the per mil deviation of the atmospheric $^{14}C/^{12}C$ ratio, $\Delta^{14}C$, in tree rings as a function of age with respect to the official 1950 reference value (Stuiver et al., 1998).

For a constant irradiation of the atmosphere by the cosmic radiation and therefore a constant production rate of cosmogenic nuclides within it, the $\Delta^{14}C$ plot would show a straight horizontal line provided that no changes occurred within the terrestrial carbon system. (See Section 7.2 for cosmogenic nuclide production.) Therefore the concentration of ^{14}C in the samples today would have to follow a smooth exponentially falling curve, characterized by the half-life of ^{14}C of 5730 y when plotted as a function of time. However, it is evident from Fig. 6.12 that in the past the atmospheric $^{14}C/^{12}C$ ratio was most of the time higher than today due to a higher production rate, which indicates a higher level of cosmic ray intensity.

The records that are based on ^{10}Be and ^{36}Cl measured in polar ice cores reach back to more than 100,000 years. This is illustrated in Fig. 6.13. There curve A shows the atmospheric ^{36}Cl flux determined from the measured ^{36}Cl concentration in the GRIP (Greenland Ice Project) ice core from

Summit, Greenland, as a function of age (Baumgartner et al., 1998; Beer, 1997 and 2000). Curve D of this figure shows the corresponding geomagnetic field intensity as reconstructed from sediment cores from the Somali Basin (Meynadier et al., 1992).

From these *paleomagnetic* data the geomagnetically controlled ^{36}Cl production rate was calculated (curve C). Because of uncertainties in the time scales of the two data sets (the measured ^{36}Cl concentrations and the magnetic field strengths) Baumgartner et al. (1998) shifted the time scale of the magnetic records slightly to match the wiggles of the re-calculated ^{36}Cl flux, curve B, to the major wiggles of the measured ^{36}Cl flux of the GRIP time scale, curve A, as good as possible. This work confirms that the cosmic ray intensity on Earth was subject to significant variations in the past.

References

Allkofer, O.C., H. Jokisch: Nuovo Cimento, 15A, p. 371 (1973).

Allkofer, O.C.: Introduction to Cosmic Radiation, Thiemig Verlag, München (1975).

Anders, E.: Rev. Mod. Phys., 2, p. 287 (1962).

Apparao, Krishna, M.V.: Composition of Cosmic Radiation. Topics in Astrophysics, Gordon and Breach Science Publishers, London (1975).

Attolini, M.R., G. Bonino, G. Cini-Castagnoli, and M. Galli: PICRC, 9, p. 321 (1983).

Aylmer, D., V. Bonanno, G.F. Herzog, H. Weber, J. Klein, and R. Middleton: Earth Planet. Sci. Lett., 88, p. 107 (1988).

Baumgartner, S., J. Beer, J. Masarik, G. Wagner, L. Meynadier, and H.-A. Synal: Science, 279, p. 1330 (1998).

Bazilevskaya, G.A., and A.K. Svirzhevskaya: Space Sci. Rev., 85, No. 3, p. 431 (1998).

Beer, J.: Proc. Internat. School of Physics, Enrico Fermi, Course CXXXIII, G. Cini Castagnoli and A. Provenzale, eds. IOS Press, Amsterdam (1997).

Beer, J.: Space Sci. Rev., in print (2000).

Bonino, G., G. Cini-Castagnoli, E. Callegari, and G.M Zhu: Nuovo Cimento, C 16, p. 155 (1993).

Caffee, M.W., J.N. Goswami, C.M. Hohenberg, K. Marti, and R.C. Reedy: in "Meteorites and the Early Solar System", John F. Kerridge and Mildred Shapley Matthews, eds.. The University of Arizona Press (1988).

Cini-Castagnoli, G., G. Bonino, and S. Miono: Nuovo Cimento, 5C, N. 4, p. 488 (1982).

Cini-Castagnoli, G., G. Bonino, and S. Miono: PICRC, 2, p. 389 (1983).

Cini-Castagnoli, G., G. Bonino, F. Caprioglio, A. Provenzale, M. Serio, anf G.M. Zhu: Geophys. Res. Lett., 17, p. 1937 (1990).

Cini-Castagnoli, G., G. Bonino, P. Della Monica, and C. Taricco: in "Past and Present Variability of the Solar-Terrestrial System: Measurements, Data Analysis and Theoretical Models". Proc. Internat. School of Physics E. Fermi, Varenna, 1996, ed. C. Cini-Castagnoli, IOS Press, Amsterdam (1997).

Compton, A.H.: Phys. Rev., 43, p. 387 (1933).

Compton, A.H., and I.A. Getting: Phys. Rev., 47, p. 817 (1935).

De Vries, H.: Proc. K. Ned. Akad. Wet., B 61, No. 2, p. 94 (1958).

Dergachev, Valentin, and Vladimir Chistyakov: Proc. 15th Internat. ^{14}C Conf., G.T. Cook, D.D. Harkness, B.F. Miller, and E.M. Scott: Radiocarbon, 37, No. 2, p. 417 (1995).

Eddy, John, A.: Science, 192, No. 4245, p. 1189 (1976).

Eddy, John, A.: Solar Physics, 89, p. 195 (1983).

Forbush, S.E.: Proc. Nat. Acad. Sci., 43, p. 28 (1957).

Forbush, S.E.: Trans. Am. Geophys. Union, 39, p. 100 (1958a).

Forbush, S.E.: J. Geophys. Res., 63, p. 651 (1958b).

Forman, Miriam, A.: Planet Scpace Sci., 18, p. 25 (1970).

Gaisser, Thomas K.: Cosmic Ray and Particle Physics. Cambridge University Press (1990).

Gleeson, L.J., and W.I. Axford: Astrophys. Space Sci., 2, p. 431 (1968).

Hampel, W. and O.A. Schaeffer: Earth Plant. Sci. Lett., 42, p. 348 (1979).

Hatton, C.J.: Progr. Elementary Particle and Cosmic Ray Phys., 10, p. 1 (1971).

Hayashida, N., K. Honda, N. Inoue, K. Kadota, F. Kakimoto, F. Kakizawa, K. Kamata, S. Kawaguchi, Y. Kawasaki, N. Kawasumi, E. Kusano, Y. Matsubara, K. Mase, T. Minagawa, K. Murakami, M. Nagano, D. Nishikawa, H. Ohoka, S. Osone, N. Sakaki, M. Sasaki, K. Shinozaki, M. Takeda, M. Teshima, R. Torii, I. Tsushima, Y. Uchihori, T. Yamamoto, S. Yoshida, and H. Yoshii: PICRC, 3, p. 256 (1999a).

Hayashida, N., K. Honda, N. Inoue, K. Kadota, F. Kakimoto, F. Kakizawa, K. Kamata, S. Kawaguchi, Y. Kawasaki, N. Kawasumi, E. Kusano, Y. Mat-

subara, K. Mase, T. Minagawa, K. Murakami, M. Nagano, D. Nishikawa, H. Ohoka, S. Osone, N. Sakaki, M. Sasaki, K. Shinozaki, M. Takeda, M. Teshima, R. Torii, I. Tsushima, Y. Uchihori, T. Yamamoto, S. Yoshida, and H. Yoshii: PICRC, 3, p. 276 (1999b).

Honda, M.: Effects of Cosmic Rays on Meteorites. Handbuch der Physik, Kosmische Strahlung XLVI/2, p. 613, Berlin, Springer Verlag (1967).

Houtermans, J. C.: Ph.D. Dissertation, University of Bern, Switzerland (1971).

Kifune, T., T. Hara, Y. Hatano, N. Hayashida, M. Honda, K. Kamata, M. Nagano, K. Nishijima, G. Tanahashi, and M. Teshima: J. Phys., G 12, p. 129 (1986).

Kudela, K.: PICRC, 8, p. 175 (1997).

Lal, D., and B. Peters: in Handbuch der Physik (Springer-Verlag, Heidelberg, Germany), 46, p. 551 (1967).

Lavielle, B., K. Marti, J.-P. Jeannot, K. Nishiizumi, and M. Caffee: Earth Planet. Sci. Lett., 170, p. 93 (1999).

Lipschutz, M.E., P. Singer, and E. Anders: J. Geophys. Res., 70, p. 1473 (1965).

Lloyd-Evans, J., and A.A. Watson: Invited Talks 8th European Cosmic Ray Symposium, Rome, 1982, eds. N. Iucci, M. Storini, S. Cecchini, F. Massaro, Technoprint, Bologna, Italy (1983).

Marti, K., B. Lavielle, and S. Regnier: Lunar Planet. Sci., XV, p. 511 (1984).

Masarik, J., and J. Beer: J. Geophys. Res., 104, No. D10, p. 12099 (1999).

Maunder, E.W.: Knowledge, 17, p. 173 (1894).

Maunder, E.W.: Knowledge, 25, p. 129 (1902).

Meynadier, L., J.P. Valet, R. Weeks, N.J. Shackleton, and V.L. Hagee: Earth Planet. Sci. Lett., 114, p. 39 (1992).

Moraal, H., and M.S. Mulder: PICRC, 5, p. 222 (1985).

Moraal, H.: Nucl. Phys. B (Proc. Suppl.) 33A,B, p. 161 (1993).

Mori, S., S. Yasue, K. Munakata, et al.: J. Geomagn Geoelectr., 47, p. 1097 (1995).

Müller, Dietrich: Adv. Space Res., 9, No. 12, p. (12)31 (1989).

Munakata, K., S. Yasue, S. Mori, et al.: J. Geomagn Geoelectr., 47, p. 1103 (1995).

Ormes, J.F., and W.R. Webber: Can. J. Phys., 46, p. S883 (1968).

Parker, E.N.: PICRC, 1, p. 26 (1965).

Potgieter, Marius, S.: PICRC, 5, p. 213, eds. Leahy, Hicks and Venkatesan, World Scientific, Singapore (1993).

Quenby, J.J.: The time Variations of the Cosmic Ray Intensity. Handbuch der Physik, Kosmische Strahlung XLVI/2, p. 310, Berlin, Springer Verlag (1967).

Reedy, R.C., J.R. Arnold, and D. Lal: Ann. Rev. Nucl. Part. Sci., 33, p. 505 (1983).

Rood, R.T., C.L. Sarazin, E.J. Zeller, and B.C. Parker: Nature, 282, p. 701 (1979).

Sakakibara, S.: J. Geomag. Geoelectr. Japan, 17, p. 99 (1965).

Sandström, A. E.: Cosmic-ray physics. Amsterdam: North-Holland Publishing Company 1965

Schwabe, H.: Astron. Nachr., 20, No. 495 (1843).

Simpson, J.A., and R.B. Uretz: Phys. Rev., 90, p. 44 (1953).

Smart, D.F., and M.A. Shea: p 6-14 in "Handbook of Geophysics and Space Environment", Adolph S. Jursa, ed., Air Force Geophysical Laboratory (1985).

Stuiver, Minze, and Paul J. Reimer: Radiocarbon, 35, p. 215 (1993).

Stuiver, M., P.J. Reimer, E. Bard, J.W. Beck, G.S. Burr, K.A. Hughen, B. Kromer, G. McCormac, J. Van der Plicht, and M. Spurk: INTCAL98 Radiocarbon age calibration, 24,000-0 cal BP. Radiocarbon, 40, p. 1041 (1998).

Tric, Emmanuel, Jean-Pierre Valet, Piotr Tucholka, Martine Paterne, Laurent Labeyrie, Francois Guichard, Lisa Tauxe, and Michel Fontugne: J. Geophys. Res., 97, p. 9337 (1992).

Vogt, F., G.F. Herzog, and R.C. Reedy: Rev. Geophys., 28, p. 253 (1990).

Voshage, H.: Zeitschr. Naturf., 17a, p. 422 (1962).

Voshage, H.: Zeitschr. Naturf., 22, p. 477 (1967).

Webber, W.R.: (1967a), after Apparao (1975).

Webber, William, R.: J. Geophys. Res., 72, p. 5949 (1967b).

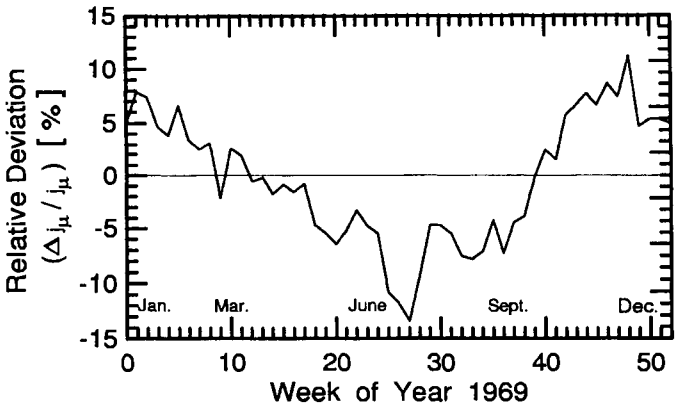

Figure 6.4: Seasonal variation of the cosmic ray muon intensity at sea level. Shown are the relative deviations of the average weekly counting rates from January to December, 1969 (after Allkofer and Jokisch, 1973).

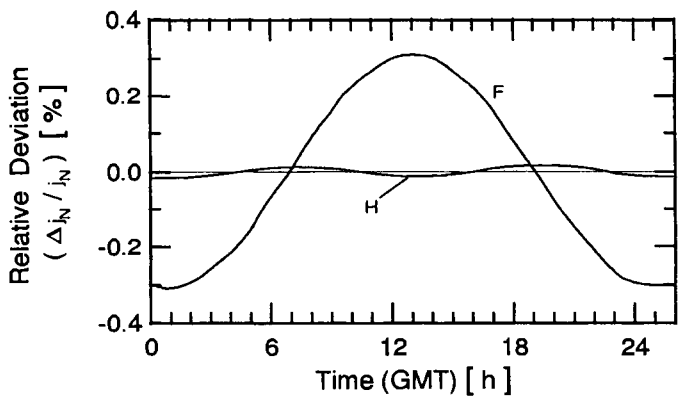

Figure 6.5: Diurnal variation of the nucleonic component (curve F) recorded at sea level with a neutron monitor. The maximum is about 1 hour past noon local time. The time dependence is almost sinusoidal except for a weak semi-diurnal component (curve H). The amplitude of this second harmonic is $< 0.02\%$ (after Sandström, 1965).

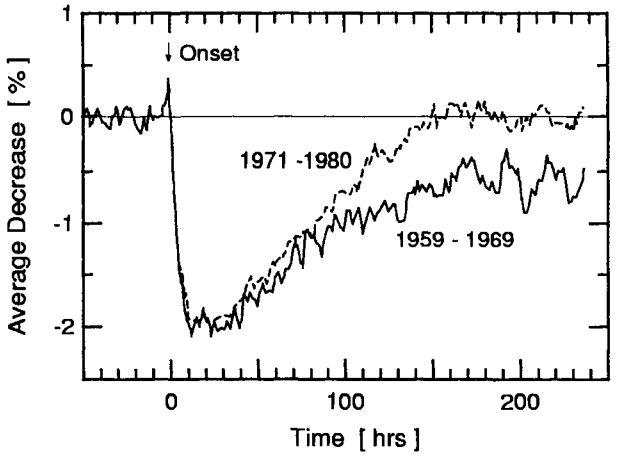

Figure 6.6: Plot of "averaged" Forbush decreases as observed with the neutron monitor at Hermanus (South Africa) during the epochs 1959 - 1969 (solid curve) and 1971 - 1980 (dashed curve), respectively. The difference in the recoveries and asymptotic levels between the two epochs is evident and, according to Moraal and Mulder (1985), may be due to drift effects.

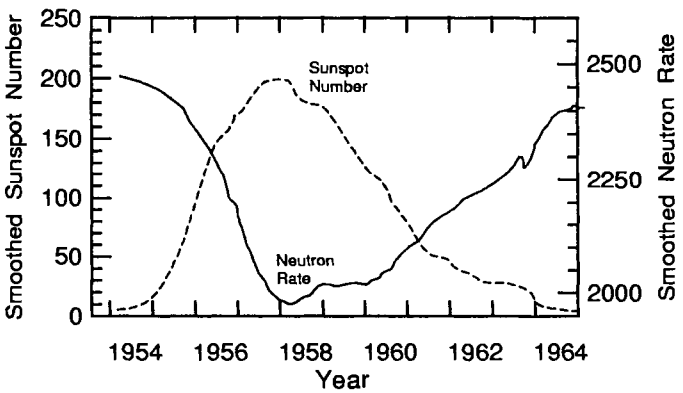

Figure 6.7: Variation of the neutron monitor counting rate at Mt. Washington (NH) and the sunspot number recorded over a period of eleven years, from one sunspot minimum to the other. The anticorrelation of the two observables is evident, however, the sunspot maximum occurs about one year earlier than the neutron monitor minimum. The latter is being referred to as the modulation maximum (Webber, 1967a, after Apparao, 1975).

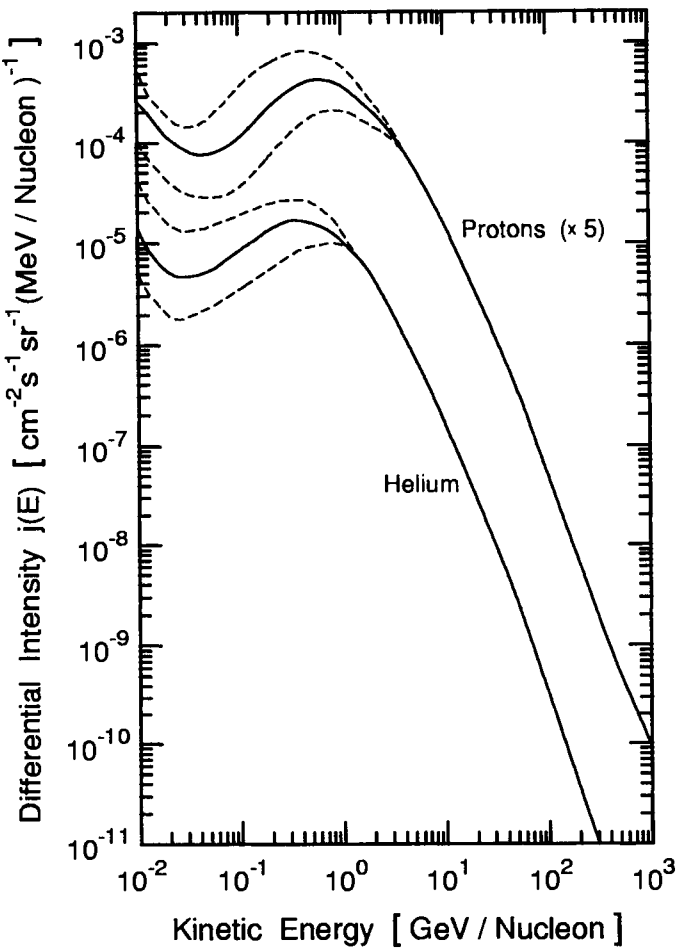

Figure 6.8: Typical differential energy spectra of primary cosmic ray protons and helium nuclei. The solid lines show the average spectra. The modulation effects are illustrated by the dashed lines; the upper lines indicate the intensity during solar minimum and the lower during solar maximum. Note that the proton intensities are multiplied by a factor of 5 to avoid overlapping with the helium spectra. The modulation effects cease at higher energies (after Smart and Shea, 1985).

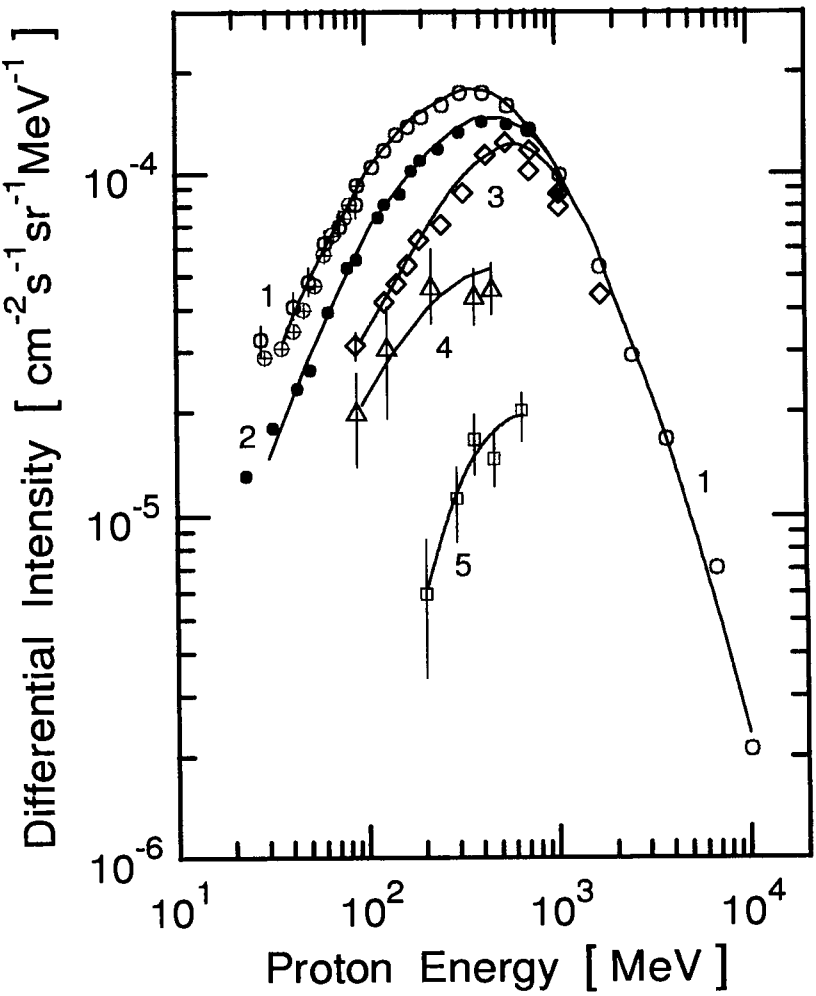

Figure 6.9: Time variation of the proton spectrum with solar activity measured at five different epochs. Curves 1 to 5 correspond to successively increasing solar activity (Ormes and Webber, 1968; Webber, 1967b; Apparao, 1975).

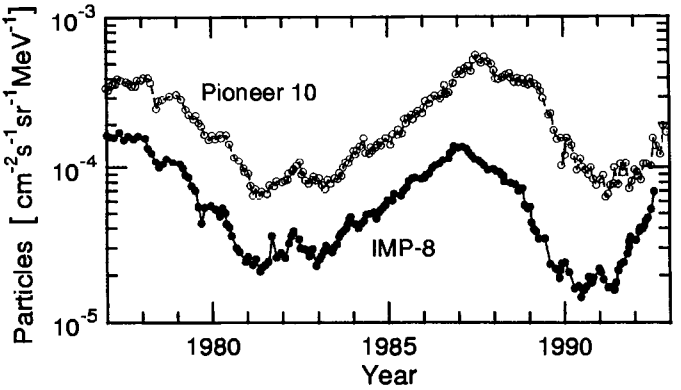

Figure 6.10: Intensity variations of cosmic ray protons having energies between 130 MeV and 225 MeV, measured with instruments on board of the satellites Pioneer 10 and IMP-8 over a period of over 15 years during their journey through space (after Potgieter, 1993).

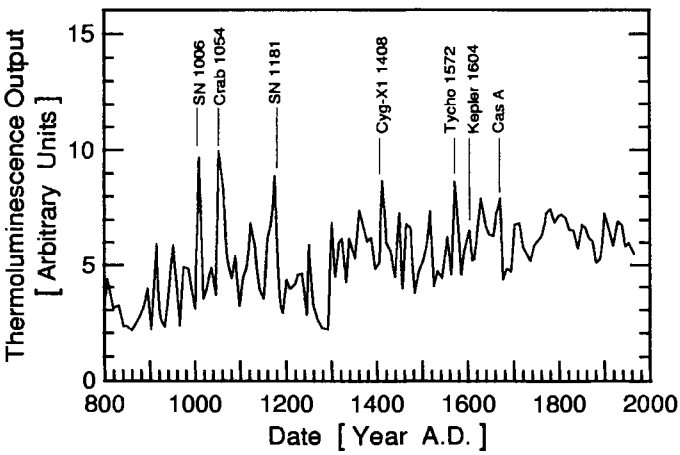

Figure 6.11: Thermoluminescence output from a sea floor core from the Tyrrhenian Sea as a function of time. The pronounced peaks indicate epochs of elevated radiation exposures of the dust in the stratosphere prior to sedimentation that correspond with dates of historical supernovae explosions, as indicated. The core dating is based on the known sedimentation rate (Cini et al., 1983).

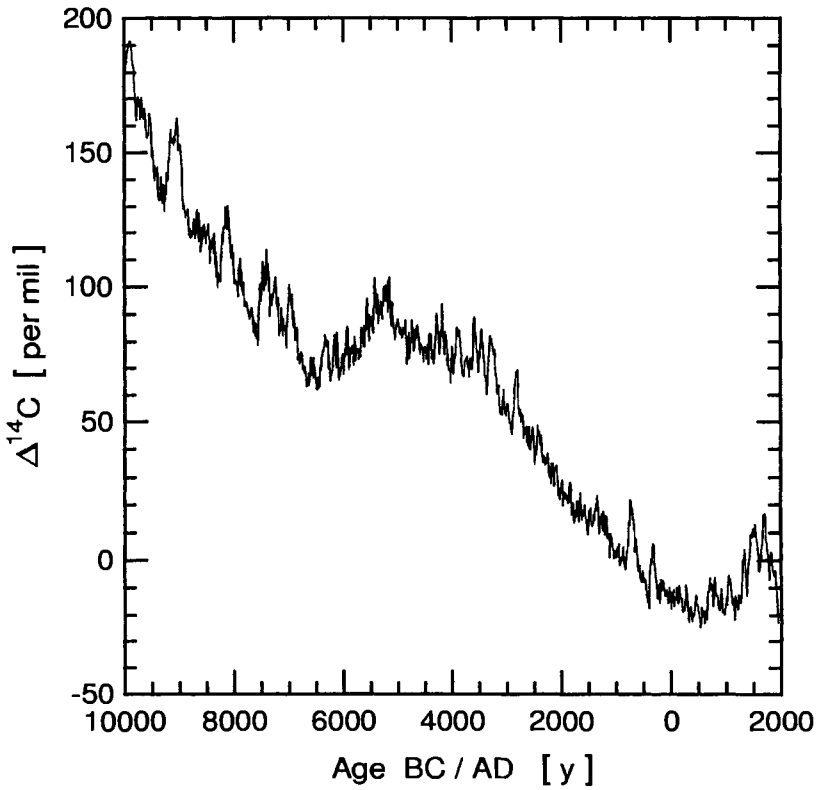

Figure 6.12: The per mil deviation of the atmospheric $^{14}C/^{12}C$ ratio, $\Delta^{14}C$, from today's standard value, as deduced from measurements in tree rings for the last 12,000 years. Note that the most recent point of the curve (on the right hand side) begins with the year 1950. This is defined as year *zero* (0) BP (before present). More recent samples show contributions from nuclear bombs and falsify the interpretation. The curve shows that in the past the $^{14}C/^{12}C$ ratio in the atmosphere was most of the time higher than today due to a higher production rate, which implies a higher cosmic ray intensity (Stuiver et al., 1998).

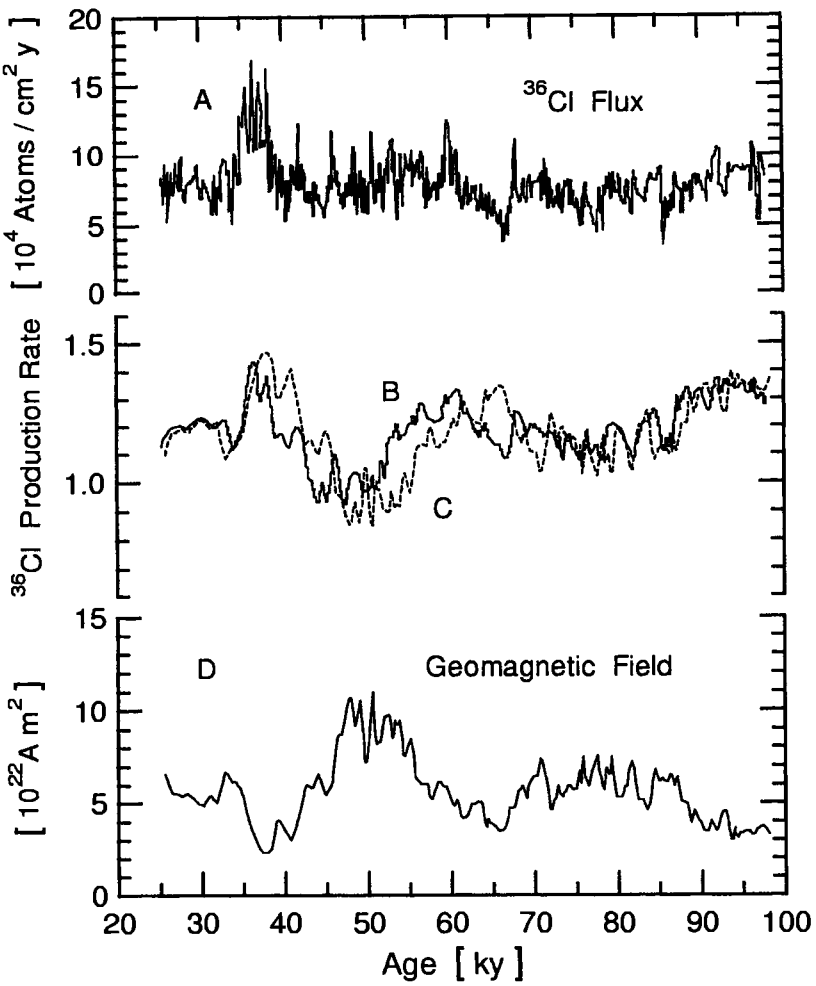

Figure 6.13: Curve A shows the ^{36}Cl flux in the atmosphere derived from the measured ^{36}Cl concentrations in the GRIP (Greenland Ice Project) ice core from Summit, Greenland. Curve D is the geomagnetic field intensity (virtual axial dipole moment) as reconstructed from paleomagnetic measurements on three sediment cores from the Somali Basin (Meynadier et al., 1992). The geomagnetically controlled ^{36}Cl production rate calculated on its own time scale from the data of curve D is represented by the dashed curve C. Curve B shows the geomagnetically controlled ^{36}Cl production rate shifted in time to match the major wiggles of curve A (after Baumgartner et al., 1998).

6.4 Energetic Solar Particles and Photons

6.4.1 Introduction

In comparison to the universal cosmic ray spectrum that extends to energies well over 10^{10} GeV, particles emitted by the Sun, even in the most violent solar processes, are of very low energy. Their spectrum extends at most up to about 10 GeV, in some cases particles having energies as high as 50 GeV were reported (e.g. Karpov et al., 1997). However, with respect to the bulk of the radiation from the Sun, corpuscular or other, particles that are associated with energetic solar events, such as *solar flares* (SF) or *coronal mass ejections* (CME), that may reach energies as high as 10 GeV and more, are of comparatively high energy for the solar regime. Thus, the term *energetic solar particles* (ESP) or *solar energetic particles* (SEP), i.e., energetic with respect to solar wind particles. In the following we will use the first term.

Not all solar flare events produce particle fluxes that are observable on Earth. Whether or not a solar flare causes an observable flux of particles on Earth depends on its strength and on its location at the Sun with respect to the position of the Earth. The accepted view that energetic solar particles are accelerated in association with solar flares or coronal mass ejections is based on the fact that they are time correlated with these phenomena. However, the recently observed association of particle fluxes in the MeV range with interplanetary shocks suggests that fast coronal mass ejections could be another significant contributor of MeV particles in space (Smart, 1996). The mechanisms by which particles are accelerated to the energies observed in a solar flare are not yet fully understood although various models have been proposed.

6.4.2 Solar Flares

Solar flares are sporadic local eruptions of the chromosphere. They develop suddenly and rapidly, in minutes, and cover a relatively small region of the solar surface. Initially they manifest themselves by a localized sudden brightening. The duration of a solar flare ranges from about 20 minutes to as much as 3 hours.

Flares are accompanied with the emission of a broad spectrum of electromagnetic radiation, including X- and gamma ray emission, and relatively energetic particles, predominantly protons but also electrons, helium and small quantities of heavier nuclei. Sometimes the flux levels of particles and radiation are very high, several orders of magnitude higher than the galactic

cosmic ray flux. Simultaneously shock waves and magnetic disturbances are generated which may affect the magnetosphere if the Earth lies within the zone of influence of a flare.

The increase of the electromagnetic radiation is particularly strong in the short wavelength region, around <2000 Å. Solar flares are classified according to size. Lately solar flare particle observations are classified according to the type of associated solar flare soft-X-ray emission into *impulsive* and *gradual* events. Impulsive soft X-ray events are usually of short duration ($\leq$1h), whereas gradual soft-X-ray events last many hours and are called *long duration events* (LDE).

It has been observed that flares originating in the western hemisphere of the Sun are more likely to produce solar particles capable of reaching the Earth than flares in the eastern hemisphere. This is a consequence of the interplanetary magnetic field configuration. The number of flares is inversely proportional to their size. At times of high solar activity, up to 10 events per day can occur. There are only few events per year with very large fluxes. Correlations of the number and intensity of flares with the number and size of sunspots have been observed.

6.4.3 Photons and Particles from Solar Flares

Photon Emission

Solar flares emit a wide spectrum of electromagnetic radiation which can extend over a wavelength range from less than 10^{-11} cm ($\sim$ 2 MeV) (X- and gamma radiation) to more than 10^{6} cm ($\sim$ 10^{-10} eV or 30 kHz radio waves). The associated emission of gamma rays in solar flares was discovered by Chupp et al. (1973). The sources of optical flare emissions are the chromosphere and the corona. In general, the maximum brightness only lasts a few minutes.

Of particular interest are the soft and hard X-rays, and the gamma rays. Most of the observations today are made with satellite based instruments in space. Measurements made over the energy range from 30 keV to 2 MeV of the X-ray emission from powerful flares indicate that the spectrum cannot be described by a single power law. A break exists around 170 keV as shown in Fig. 6.14. The spectrum consists of a bremsstrahlung continuum from accelerated electrons with an admixture of γ-rays from π°-decay and a superposition of γ-ray emission lines (Rank et al., 1997).

The gamma ray emission lines that are observed are believed to be due to accelerated ions that travel down magnetic loops and impact on denser

material in the chromosphere or photosphere, causing nuclear reactions. Individual flare spectra may vary greatly in slope and shape. In some spectra the emission lines are clearly visible above the bremsstrahlung continuum, in others it is difficult to identify them (Yoshimori et al., 1995).

Charged Particle Emission

Protons and Nuclei: Solar flares and/or coronal mass ejections are also sources of energetic particles. In most cases the energy spectrum of solar particles terminates at energies $\leq$10 GeV, however, in some cases observation of particles with energies as high as 50 GeV and more had been reported. In many cases the energy determination is very indirect via secondary observations and in conjunction with simulation calculations. The particles are believed to originate in the chromosphere of the Sun. Only a small fraction of the flares observed produce particles that can be detected on Earth, either directly at the fringes of the atmosphere, or indirectly through their interactions in the atmosphere at ground level with neutron monitors. The latter are then referred to as *ground level enhancements* or *ground level events* (GLE). Frequently only one ground level enhancement is observed per year, preferentially at high latitude.

Besides protons and helium nuclei the heavier elements up to iron are also present in energetic solar events. The particle composition is related to the first ionization potential of the individual elements and the charge state of individual ions is linked to the temperature of the source plasma (Oetliker et al., 1995; Leske et al., 1995). Charge state measurements have been carried out over an energy range from about 1 MeV into the region of 10 - 100 MeV, depending on the element. The question whether the composition of energetic solar particles is related to either the coronal or the solar wind composition has not yet been answered.

Electrons: The presence of X-rays and gamma rays in solar flares indicates that electrons must be present that are accelerated into the MeV energy range. Satellite measurements show that electron events associated with impulsive X-ray events have a characteristic double power law spectrum, suggesting a two-stage acceleration mechanism. On the other hand, electron events associated with long-duration X-ray events had a characteristic single power law spectrum (Dröge, 1995a and 1995b).

Charged Particle Energy Spectra

The slope and shape of the energy spectrum of solar particles changes with time during a flare. The most energetic particles ($\geq$1 GeV) are the first to arrive with a delay of only a few minutes after visual recognition of the flare. Lower energy particles then appear in increasing numbers while the high energy particles fade away (Allkofer and Simon, 1970). The rigidity spectrum, $j(P,t)$, can be approximated by the expression

$$j(P,t) = I_0(t)e^{-P/G(t)} \quad , \tag{6.9}$$

where P is the rigidity in [MV] ($P = pc/ze$, see Chapter 1), I_0 the flare parameter characterizing the intensity expressed in [$\mathrm{cm^{-2}\,s^{-1}\,sr^{-1}}$], and $G(t)$ is the slope of the spectrum in [MV].

The slope of the spectrum is steeper for flares with small values of G, and vice versa. The values of G range from 40 MV to 400 MV and those of I_0 from 2 to 1000 protons $\mathrm{cm^{-2}\,s^{-1}\,sr^{-1}}$. The spectra steepen with time. Frequently the fluxes of energetic solar particles are orders of magnitude (up to $\sim$1000 times) higher than the galactic cosmic ray flux and flare spectra are steeper. These properties are illustrated in Fig. 6.15 which shows the evolution of the energy spectrum of solar flare particles in the flare of May 7, 1978 and the galactic cosmic ray spectrum for comparison (Debrunner et al., 1983a).

Neutron Emission

The possibility that neutrons might be present in solar flare events and detectable at Earth was first suggested by Biermann, Haxel and Schluter (1951). However, it was not until 1980 that the existence of $\sim$400 MeV neutrons was detected in space near Earth with detectors on board the SMM (Solar Maximum Mission) satellite, following an impulsive solar flare (Chupp et al., 1982).

Simultaneous observation of solar flare neutrons in space and at ground level with neutron monitors took place in 1982 (Chupp et al., 1987). The ground based observations were made with the neutron monitors at Jungfraujoch (Switzerland) (46.5° N, 8.0° E, 3554 m a.s.l.) (Debrunner et al., 1983b), at Lomnicky Stit (Czechoslovakia) (49.2° N, 20.2° E, 2632 m) (Efimov et al., 1983), and a faint signal could be recognized in the data of the neutron monitor at Rome (Italy) (41.9° N, 12.5° E, 60 m) (Iucci et al., 1985).

In Fig. 6.16 we show the data recorded with the neutron monitor at Jungfraujoch, the corresponding evidence from the satellite based measure-

ment and the associated gamma ray signature of the flare, also from the satellite measurement (Chupp et al., 1987). From these data and the detector responses the time dependence of the production spectra of neutrons in solar flares was attempted to be disentangled. To produce the recorded ground level event at Jungfraujoch neutrons must have an energy in excess of 300 MeV. The energy spectrum of solar flare neutrons seems to extend to about 2 - 4 GeV, with an almost cutoff-like sharp drop around 4 GeV.

With the help of satellite based measurements Evenson et al. (1983 and 1985) could observe in some events solar neutron decay protons near the Earth. Furthermore, the detection of the 2.223 MeV gamma line from the n-p-capture delivers additional proof of the existence of neutrons at the Sun (Chupp, 1982; Share et al., 1982; Prince et al., 1982). Based on X- and gamma ray measurements and various assumptions, Dunphy and Chupp (1991) estimated the time integrated energy spectrum of the solar neutrons of the solar flare of March 6, 1989. It is reproduced in Fig. 6.17 (see also Takahashi et al., 1991).

6.4.4 Ionospheric Effects

The interaction between the solar wind and the geomagnetic field determine shape and properties of the magnetosphere. Disturbances and irregularities in the steady flow of the solar wind due to solar activity affect the shape of the magnetosphere and influence the cutoff conditions. As a consequence energetic solar particles, mostly protons but also heavier nuclei and electrons, may have easier access at times to the inner magnetosphere and can reach the Earth.

The arrival of radiation increases the electron density in the upper atmosphere by photoionization and other processes, causing *sudden ionospheric disturbances* (SID). The ionization is particularly strong in the polar regions, where low energy protons of 5 to 20 MeV, the most abundant in flare processes, can enter easily along the field lines. This process is called *Polar Cap Absorption* (PCA) and may cause *aurora* effects that can impair temporarily local or world-wide radio communication.

References

Allkofer, O.C., and M. Simon: Atompraxis, 16, Heft 3, p. 1 (1970).

Biermann, L., O. Haxel, and A. Schluter: Zeitschr. f. Naturforschung, 6a, p. 47 (1951).

Chupp, E.L., D.J. Forrest, P.R. Higbie, A.N. Suri, C. Tsai, and P.P Dunphy: Nature, 241, p. 333 (1973).

Chupp, E.L., D.J. Forrest, J.M. Ryan, J. Heslin, C. Rippin, K. Pinkau. G. Kanbach, E. Rieger, and G.H. Share: Astrophys. J., Lett., 263, p. L-95 (1982).

Chupp, E.L., H. Debrunner, E. Flückiger, D.J. Forrest, F. Golliez, G. Kanbach, W.T. Vestrand, J. Cooper, and G. Share: Astrophys. J., 318, p. 913 (1987).

Debrunner, H., E. Flückiger, H. Neuenschwander, M. Schubnell, and J.A. Lockwood: PICRC, 4, p. 144 (1983a).

Debrunner, H., E. Flückiger, E.L. Chupp, and D.J. Forrest: PICRC, 4, p. 75 (1983b).

Dröge, W.: PICRC, 4, p. 187 (1995a).

Dröge, W.: PICRC, 4, p. 191 (1995b).

Dunphy, P.P, and E.L. Chupp: PICRC, 3, p. 65 (1991).

Efimov, Yu., E. G.E. Kocharov, and K. Kudela: PICRC, 10, p. 276 (1983).

Evenson, P., P. Meyer, and K.R. Pyle: Astrophys. J., 274, p. 875 (1983).

Evenson, P., R. Kroeger, and P. Meyer: PICRC, 4, p. 130 (1985).

Iucci, N., M. Parisi, C. Signorini, M. Storini, and G. Villoresi: PICRC, 4, p. 134 (1985).

Karpov, S.N., L.I. Miroshnichenko, and E.V. Vashenyuk: PICRC, 1, p. 205 (1997).

Leske, R.A., J.R. Cummings, R.A. Mewaldt, E.C. Stone, and T.T. von Rosenvinge: PICRC, 4, p. 461 (1995).

Oetliker, M., B. Klecker, D. Hovestadt, M. Scholer, J.B. Blake, M. Looper, and R.A. Mewaldt: PICRC, 4, p. 470 (1995).

Prince, T.A., D.J. Forrest, E.L. Chupp, G. Kanbach, and G.H. Share: PICRC, 4, p. 79 (1983).

Rank, G., H. Debrunner, L. Kocharov, G. Kovaltsov, J. Lockwood, M. McConnell, P. Nieminen, J. Ryan, and V. Schönfelder: PICRC, 1, p. 1 (1997).

Share, G.H., D.J. Forrest, E.L. Chupp, and E. Rieger: Bull. Am. Astron. Soc., 14, p. 875 (1982).

Smart, D.F.: Rapporteur Talk, XXIV. ICRC, Rome (1995). Nuovo Cimento, 19C, N.5, p. 765 (1996).

Takahashi, K., E. Sakamoto, M. Matsuoka, K. Nishi, Y. Yamada, S. Shimoda, T. Shikata, M. Wada: PICRC, 3, p. 37 (1991).

Yoshimori, M., K. Morimoto, K. Suga, T. Matsuda, and K. Kawabata: PICRC, 4, p. 102 (1995).

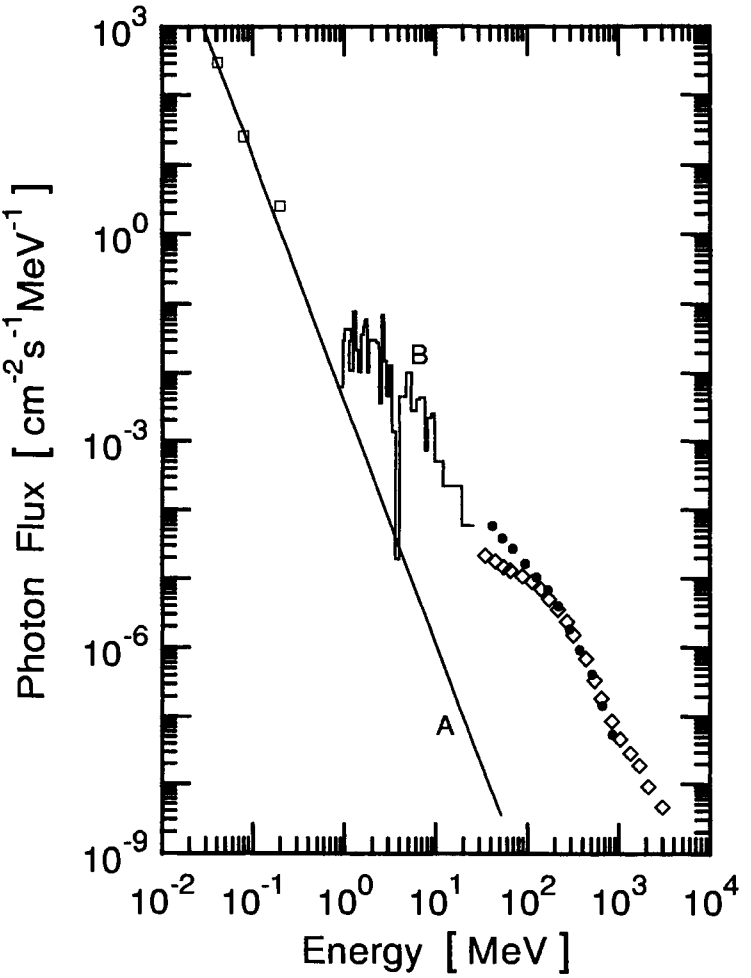

Figure 6.14: Composite X- and γ-ray spectrum of the extended phase of the June 15, 1991 solar flare using data from several experiments. The data from the CGRO instrument have been scaled up by a factor of about 4 to compensate for the different observation times (after Rank et al., 1997). The spectrum which extends beyond 3 GeV shows a break around 170 keV.

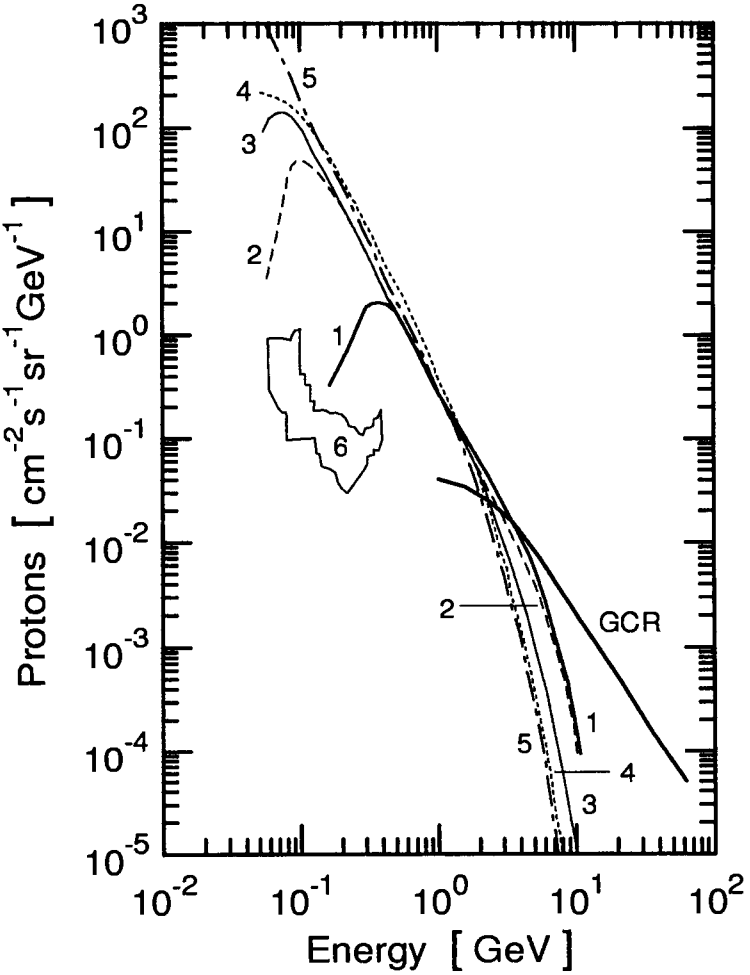

Figure 6.15: Energy spectra of solar protons observed during the solar flare event of May 7, 1978. Curves 1 to 5 show the evolution of the particle spectrum for the time intervals listed below. Shown, too, for comparison are the galactic cosmic ray spectrum (curve GCR) and the range of the cosmic ray background level at low energies (region 6) (after Debrunner et al., 1983a).

1 0335 - 0345 UT	2 0345 - 0400 UT	3 0400 - 0415 UT
4 0415 - 0430 UT	5 0430 - 0450 UT	

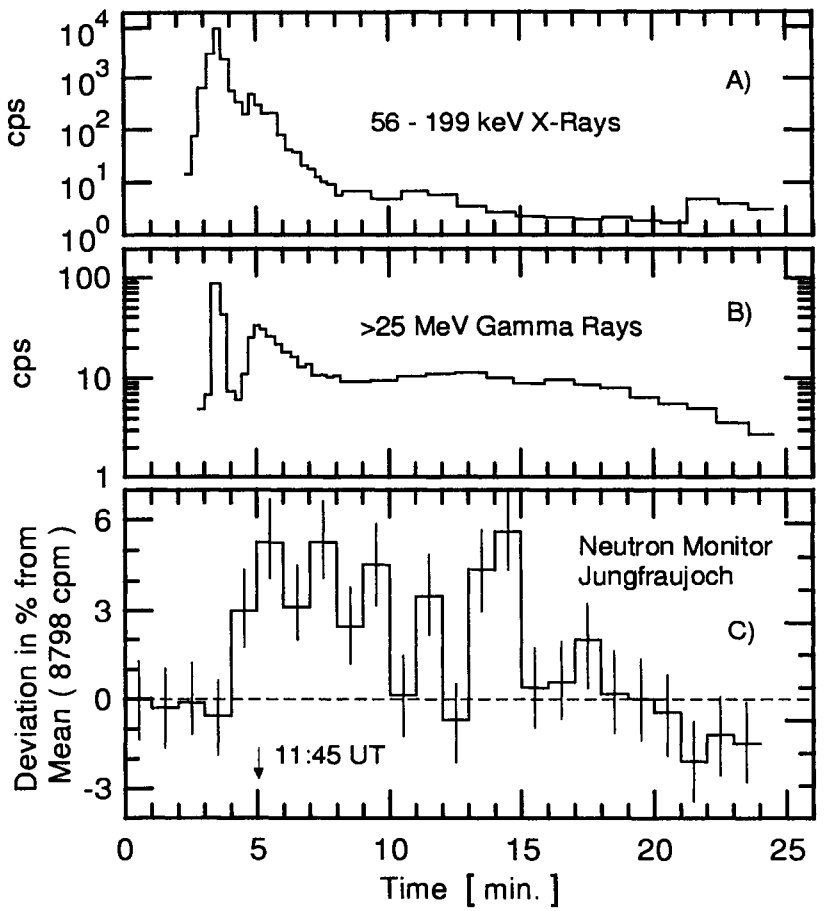

Figure 6.16: Time profile of the responses of two of the tree detectors on board of the SMM satellite (histograms A and B) and of the Jungfraujoch neutron monitor (histogram C) to the June 3, 1982 solar flare event (after Chupp et al., 1987). The peak X-ray counting rate is uncertain because of technical limitations.

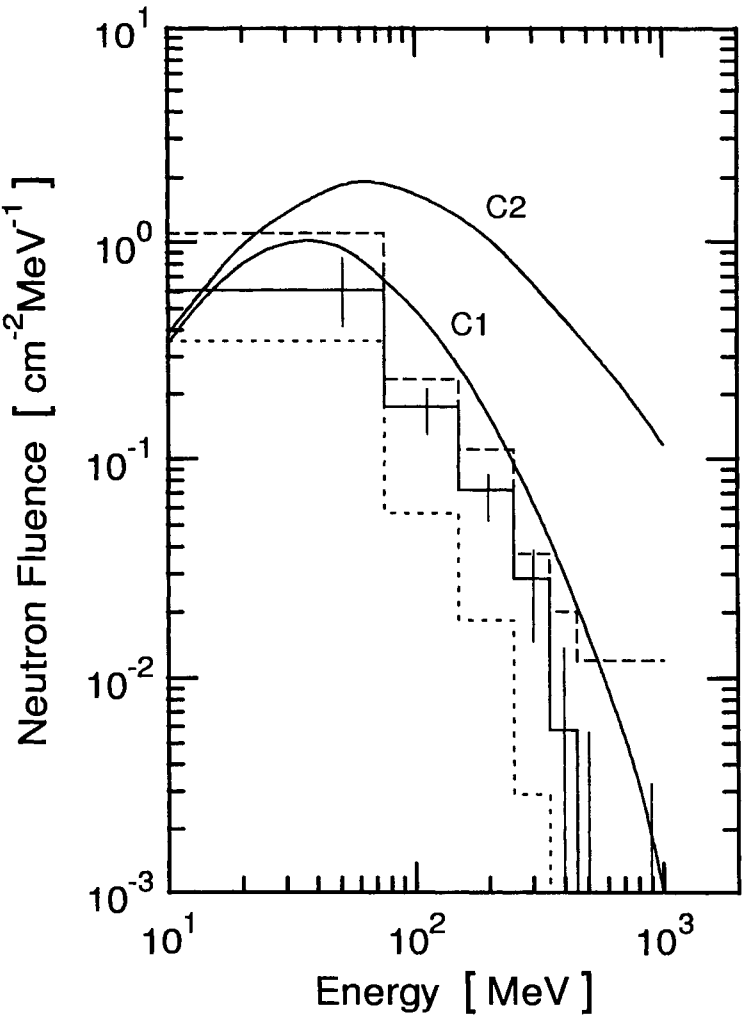

Figure 6.17: Time integrated solar neutron spectrum at the Earth from the flare of March 6, 1989 (histograms). Spectrum and envelope (dotted and dashed histograms) depend on the production time. The solid line with error bars represents the most likely spectrum. Curves C1 and C2 refer to neutron spectra obtained using Bessel function and power law proton spectra, respectively, that were obtained from gamma ray data in an isotropic, thick-target model (after Dunphy and Chupp, 1991).

6.5 Anomalous Cosmic Rays

6.5.1 Introduction

In 1972 as the solar cycle approached minimum modulation, Garcia-Munoz et al. (1973a, 1973b, 1973c and 1973d) discovered that the abundance ratio $^4He/^1H$ became ≥ 1 at low energy (<30 MeV) and that the low energy helium and proton spectra evolved into an anomalous combination of spectral forms that could not be fitted with previously successful models and methods. In particular, the observed combination of a flat helium spectrum and a steep proton spectrum that persisted for about two years was interpreted as being *anomalous* in that the spectra could not be fitted by a simple extension of the previously successful solar modulation calculations of Garcia-Munoz et al. (1973c). This is illustrated in Figs. 6.18, 6.19 and 6.20. In an overview of the complete cosmic ray energy spectrum we show in Fig. 6.21 where exactly the anomalous cosmic rays fit into the picture.

These authors concluded therefore that the explanation for this observation was beyond the then current framework of solar modulation theory. Further investigations revealed that the Sun appeared to be an unlikely source of these anomalies, since the low-energy radial gradients of hydrogen and helium, measured by Pioneer 10 outward to ~4 AU (astronomical units), were small but not negative (McKibben et al., 1973; Simpson et al., 1974). From their analysis Garcia-Munoz et al. (1973c and 1975) concluded that in the case of helium, the ^4He isotope component in excess of the calculated flux level must be an *anomalous component.*

At about the same time Hovestadt et al. (1973) and McDonald et al. (1974) discovered from their measurements made in 1972 that low energy nitrogen and oxygen spectra exhibited an anomalous composition. This result was confirmed by Garcia-Munoz et al. (1975) who did also find anomalous nitrogen and oxygen components at energies $\leq$20 MeV/Nucleon. Later on other elements were found to have anomalous components, such as argon (von Rosenvinge and McDonald, 1975; Klecker et al., 1977), carbon (Cummings and Stone, 1987), and hydrogen (Christian et al., 1988). Subsequently, *anomalous cosmic rays* (ACR) became a subject of intense study (for reviews see Jokipii, 1998; Klecker et al., 1998; Klecker, 1999).

6.5.2 Theoretical Aspects

A qualitative explanation concerning the origin and formation of the anomalous cosmic ray component was offered by Fisk et al. (1974) who suggested

that anomalous cosmic rays were the result of heliospheric acceleration (by some unspecified mechanism) of freshly-ionized, initially neutral interstellar particles. Interstellar neutral atoms which stream into the inner heliosphere have a probability of being ionized by solar ultraviolet radiation or by charge exchange with solar wind ions. They are subsequently swept outward and then accelerated. This explains very nicely the composition and spectrum of the anomalous component, since only initially neutral particles can participate in the process.

Specific acceleration mechanisms were then proposed by several authors that are based on the general diffusion theory for the transport of energetic charged particles, developed by Parker (1965), Axford (1965), Gleeson and Axford (1967), Jokipii and Parker (1970), and others (for reviews see Jokipii, 1971; Völk, 1975).

Pesses et al. (1981) pointed out that many features of the anomalous component could be explained if the acceleration of ACR occurs at the termination shock of the solar wind by the mechanism of diffusive shock acceleration. This, however, requires that the initially neutral interstellar gas, after getting ionized in the inner heliosphere, be convected into the outer heliosphere for acceleration at the termination shock.

Jokipii (1986) presented results from a quantitative two-dimensional numerical simulation of this model, in which the full transport equation was solved. Many authors have since contributed to the theory and added refinements to the simulations such as the considerable deviation of the magnetic field from the classical Parker Archimedean spiral, which had been discovered by Ulysses (Jokipii and Kòta, 1989; Jokipii et al., 1995; Jokipii, 1996).

Lately the theory has further evolved and anomalous cosmic rays seem to be the consequence of acceleration of interstellar pick-up ions, from their original energy of a few keV to more than 1 GeV, at the termination shock of the solar wind, at a heliocentric distance of about 90 AU to 120 AU. According to Jokipii and Kòta (1997) models which incorporate such acceleration in a global transport model can account naturally for the observed energy spectrum, charge states, composition and spatial distribution. However, the direct acceleration of pick-up ions at the termination shock seems to be more difficult.

Acceleration of these low energy particles at propagating shocks in the inner heliosphere is found to be much easier. A new scenario of initial acceleration or pre-acceleration at propagating or co-rotating shocks in the inner solar system is consistent with observations of both low energy particles and approximately 100 MeV anomalous cosmic rays in the inner heliosphere. The

theory as it stands now can fairly well explain the experimental observations.

6.5.3 Current Status of Anomalous Cosmic Rays

It is now established that anomalous cosmic rays are composed of fluxes of helium, nitrogen, oxygen, neon, argon, protons and low levels of carbon (Klecker, 1995; Oetliker et al., 1997), which are observed in the inner heliosphere to be enhanced at energies ranging from 20 MeV to about 300 MeV. Recently some authors have claimed to have discovered additional anomalous components such as silicone, sulfur and even iron (Takashima et al., 1997; Stone and Cummings, 1997).

There have been numerous measurements of the radial and latitudinal gradients of the anomalous component (McKibben et al., 1979; McDonald and Lal, 1986; Cummings et al., 1987; Simpson, 1995; Stone and Cummings, 1997). In particular it was found that in the inner solar system the radial gradient of the anomalous oxygen is as high as 16% per AU, whereas in the outer solar system it is 3% per AU. The increase of the intensities of six anomalous species (O, N, Ne, C, Ar, S) with increasing heliocentric distance is shown in Fig. 6.22 and the energy spectra of the same species at 1 AU in Fig. 6.23 (Stone and Cummings, 1997). The magnitude of the radial gradient computed with modern models is quite consistent with that observed, both in absolute magnitude and in radial variation.

Mewaldt et al. (1996) have reported that at energies above some 16 MeV/Nucleon, multiply charged ACR Oxygen atoms are observed and they become dominant at higher energies. For a recent review the reader is referred to the rapporteur paper on ACR presented at the 26th International Cosmic Ray Conference 1999 by Klecker (2000).

References

Anand, K.C., R.R. Daniel, and S.A. Stephens, R. Bhowmik, C.S. Krishna, P.K. Aditya, and R.K. Puri: Proc. Ind. Acad. Sci., 67, p. 138 (1968).

Axford, W.I.: Planetary Space Sci., 13, p. 115 (1965).

Christian, E.R., A.C. Cummings, and E.C. Stone: Astrophys. J., 334, p. L-77 (1988).

Cummings, A.C., and E.C. Stone: PICRC, 3, p. 413 (1987).

Cummings, A.C., E.C. Stone, and W.R. Webber: Geophys. Res. Letters, 14, p. 174 (1987).

Fisk, L.A., B. Kozlovsky, and R. Ramaty: Astrophys. J., 190, p. L-35 (1974).

Garcia-Munoz, M., G.M. Mason, and J.A. Simpson: Proc. of the Fall Annual Meeting of the AGU, San Francisco, 1972 December, reported in Trans. Am. Geophys. Union, 54, No. 3, p. 130 (1973a).

Garcia-Munoz, M., G.M. Mason, and J.A. Simpson: Bull. Am. Phys. Soc., 18, p. 567 (1973b).

Garcia-Munoz, M., G.M. Mason, and J.A. Simpson: Astrophys. J. Lett., 182, p. L-81 (1973c).

Garcia-Munoz, M., G.M. Mason, and J.A. Simpson: PICRC, 2, p. 1304 (1973d).

Garcia-Munoz, M., G.M. Mason, and J.A. Simpson: Astrophys. J., 202, p. 265 (1975).

Gleeson, L., and W.I. Axford: Astrophys. J., 149, p. L-115 (1967).

Hovestadt, D., O. Vollmer, G. Gloeckler, and C.Y. Fan: Phys. Rev. Lett., 31, p. 650 (1973).

Jokipii, J.R., and E.N. Parker: Astrophys. J., 160, p. 735 (1970).

Jokipii, J.R.: Rev. Geophys. Space Phys., 9, p. 27 (1971).

Jokipii, J.R.: J. Geophys. Res., 91, p. 2929 (1986).

Jokipii, J.R., and J. Kòta: Geophys. Res. Letters, 16, p. 1 (1989).

Jokipii, J.R., J. Kòta, J. Giacalone, T.S. Horbury, and E.J. Smith: Geophys. Res. Letters, 22, p. 3385 (1995).

Jokipii, J.R., and J. Kòta: PICRC, 8, p. 151 (1997).

Jokipii, J.R.: Space Sci. Rev. 86, p. 161 (1998).

Juliusson, E: Astrophys. J., 191, p. 331 (1974).

Klecker, B.: Space Sci. Rev., 72, p. 419 (1995).

Klecker, B., R.A. Mewaldt, J.W. Bieber, A.C. Cummings, L. Drury, J. Giacalone, J.R. Jokipii, F.C. Jones, M.B. Krainev, M.A. Lee, J.A. LeRoux, R.G. Marsden, F.B. McDonald, R.B. McKibben, C.D. Steenberg,M.G. Baring, D.C. Ellison, L.J. Lanzerotti, R.A. Leske, J.E. Mazur, H. Moraal, M. Oetliker, V.S. Ptuskin, R.S. Selesnick, and K.J. Trattner: Space Sci. Rev., 83, p. 259 (1998).

Klecker, B.: Adv. Space Res., 23, p. 521 (1999).

Klecker, Berndt: Rapporteur Paper XXVI Internat. Cosmic Ray Conf. (1999), AIP Conf. Proc., 516, p. 140, Brenda L. Dingus, David B. Kieda and Michael H. Salamon eds., American Institute of Physics (2000).

McDonald, F.B., B.J. Teegarden, J.H. Trainor, and W.R. Webber: Astrophys. J., 187, p. L-105 (1974).

McDonald, F.B. and N. Lal: Geophys. Res. Letters, 13, p. 781 (1986).

McKibben, R.B., J.J. O'Gallagher, J.A. Simpson, and A.J. Tuzzolino: Astrophys. J. Lett., 181, L-9 (1973).

McKibben, R.B., K.R. Pyle, and J.A. Simpson: Astrophys. J., 227, L-147 (1979).

Mewaldt, R.A., R.S. Selesnick, J.R. Cummings, E.C. Stone, and T.T. von Rosenvinge: Astrophys. J., 466, p. L-43 (1996).

Parker, E.N.: Planetary Space Sci., 13, p. 9 (1965).

Pesses, M.E., J.R. Jokipii, and D. Eichler: Astrophys. J., 246, p. L-85 (1981).

Rygg, T.A., and J.A. Earl: J. Geophys. Res., 76, p. 7445 (1971).

Rygg, T.A., J.J. O'Gallagher, and J.A. Earl: J. Geophys. Res., 79, p. 4127 (1974).

Simpson, J.A., T.F. Conlon, J.J. O'Gallagher, R.B. McKibben, and A.J. Tuzzolino: Solar Wind Three, 1974 July, Conference Proceedings (University of California, Los Angeles), p. 214 (1974).

Simpson, J.A.: Adv. Space Res., 16, p. 135 (1995).

Smith, L.H., A. Buffington, G.F. Smoot, L.W. Alvarez, and M.A. Wahlig: Astrophys. J., 180, p. 978 (1973).

Stone, E.C., and A.C. Cummings: PICRC, 2, p. 289 (1997).

Takashima, T., T. Doke, T. Hayashi, J. Kikuchi, K. Itsumi, M. Kobayashi, H. Shirai, N. Takehana, N. Hasebe, K. Kondoh, T. Kohno, K. Munakata, C. Kato, S. Yanagita, Y. Yamada, D.V. Reames, and T.T. von Rosenvinge: PICRC, 2, p. 285 (1997).

Von Rosenvinge, T.T., J.F. Ormes, and W.R. Webber: Astrophys. Space Sci., 3, p. 80 (1969).

Von Rosenvinge, T.T., and F.B. McDonald: PICRC, 2, p. 792 (1975).

Völk, Heinrich, J.: Rev. Geophys. Space Phys., 13, p. 547 (1975).

Webber, W.R.: PICRC, 5, p. 3568 (1973).

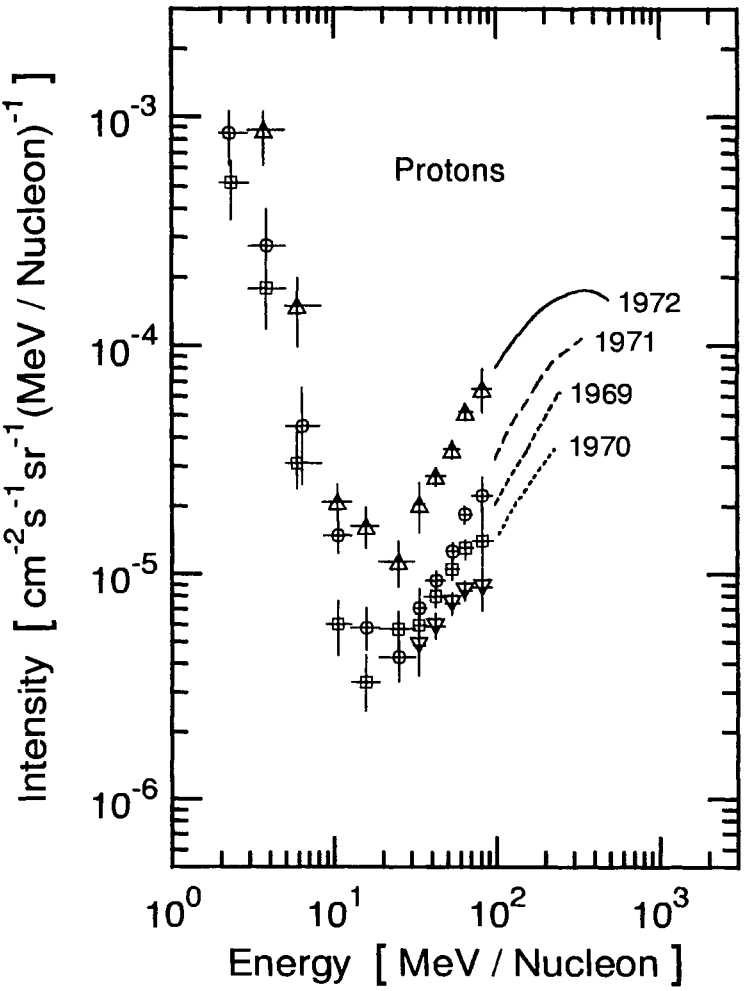

Figure 6.18: Quiet-time proton spectra for 1969, 1970,1971, and 1972 measured on different IMP satellites by different authors (for details see Garcia-Munoz et al., 1975). The curves are from balloon measurements (Rygg and Earl, 1971; Rygg et al., 1974, after Garcia-Munoz et al., 1975).

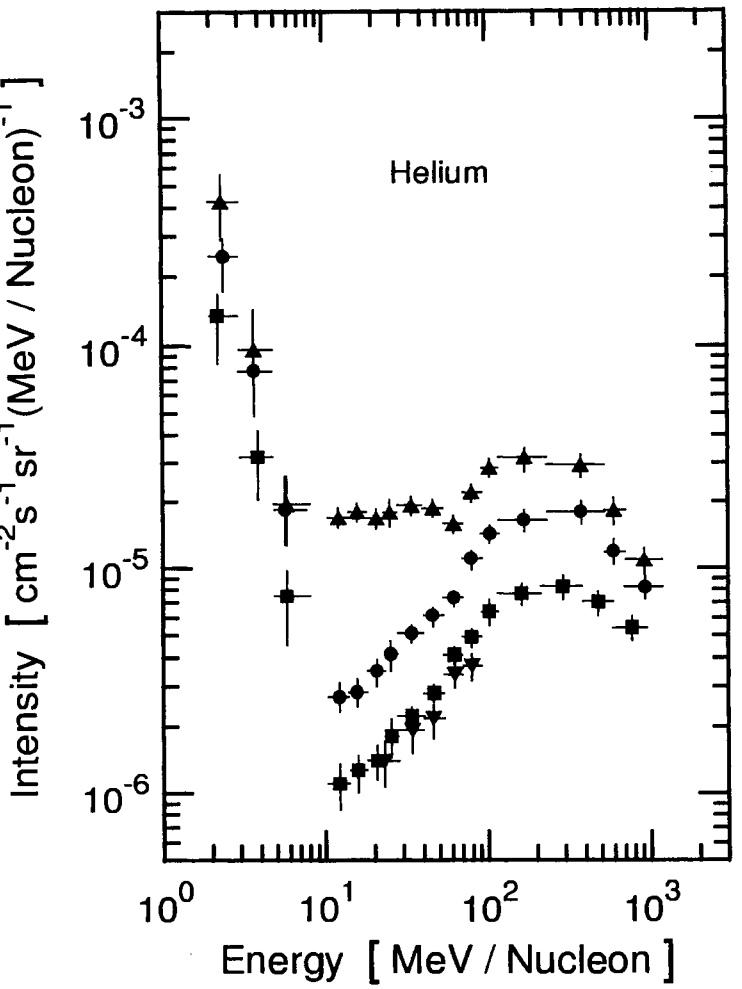

Figure 6.19: Quiet-time helium spectra for 1969 (■), 1970 (▼), 1971 (●), and 1972 (▲) measured on different IMP satellites by different authors (for details see Garcia-Munoz et al., 1975). At energies <95 MeV the helium spectra are ^{4}He, above the data are ^{3}He+^{4}He (after Garcia-Munoz et al., 1975). The anomalous behavior of He around 20 MeV in 1972 is evident.

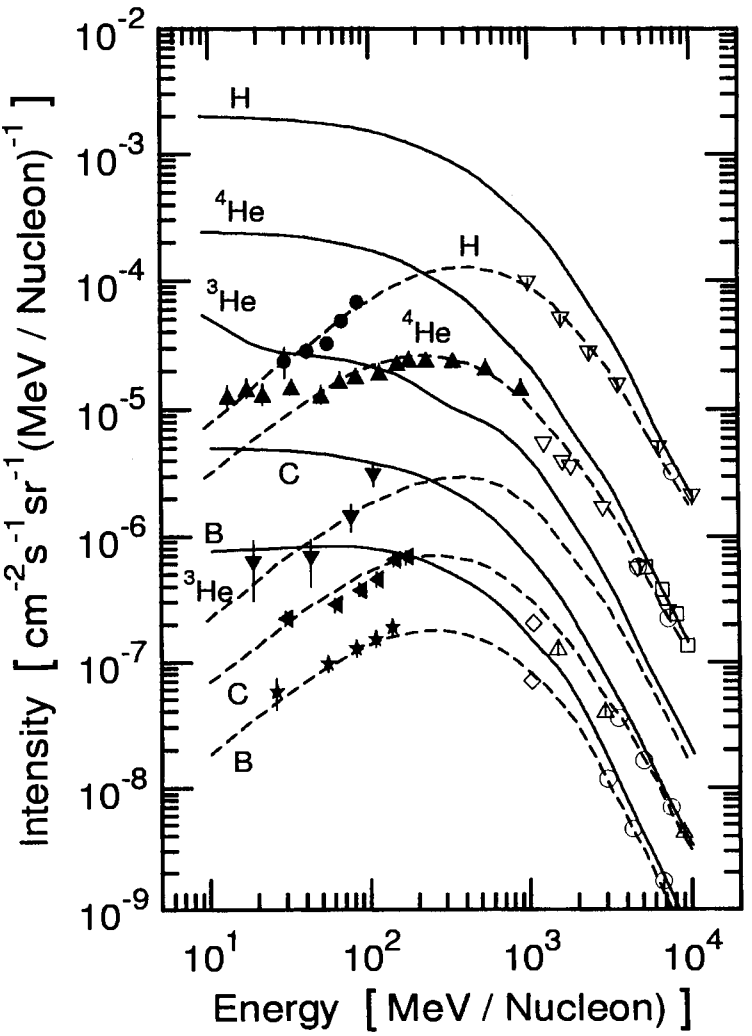

Figure 6.20: Quiet-time low-energy measurements from IMP-7 (solid symbols). At energies <95 MeV the helium spectrum is ^{4}He, above it is ^{3}He+^{4}He. The higher energy data (open symbols) are from balloon measurements (∇ Webber, 1973; $\square$ Anand et al., 1968; $\circ$ Smith et al., 1973; $\triangle$ von Rosenvinge, et al., 1969; $\diamond$ Juliusson, 1974). The solid lines are local interstellar spectra and the dashed lines are calculated spectra accounting for solar modulation (Garcia-Munoz et al., 1975).

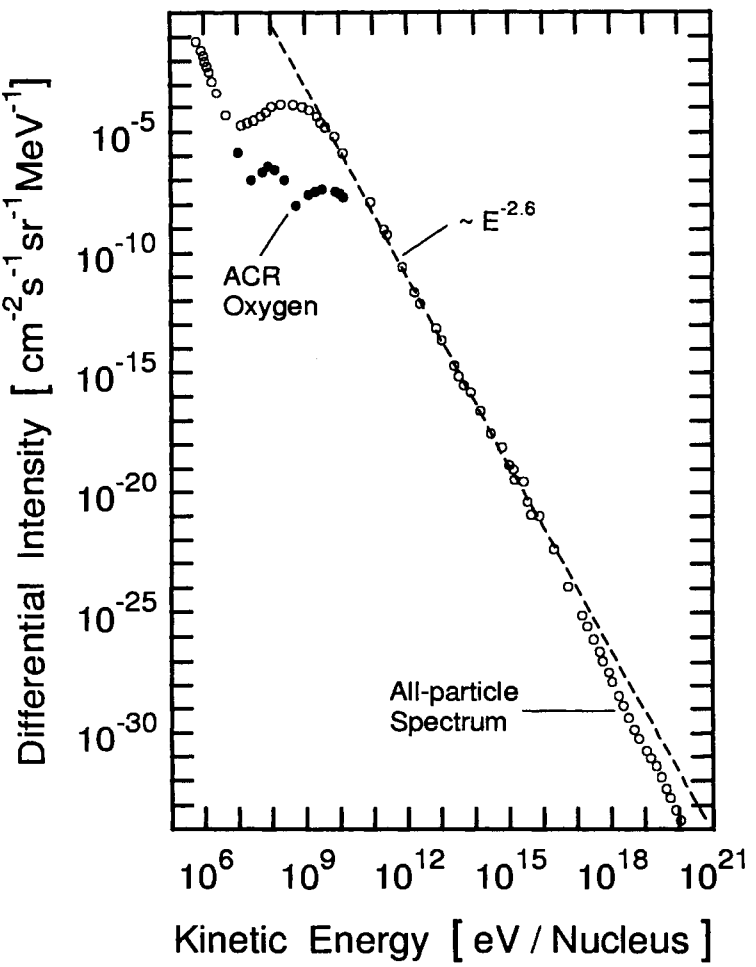

Figure 6.21: The observed spectrum of cosmic rays (o), ranging from the lowest energies, dominated by heliospheric particles, to the very highest energies which are probably of extragalactic origin. Anomalous oxygen (•) produces the peak at some 10^8 eV (after Jokipii and Kòta, 1997). The dashed line which represents a power law with spectral index of -2.6 fits the experimental data between 10^{10} eV and 10^{16} eV very well.

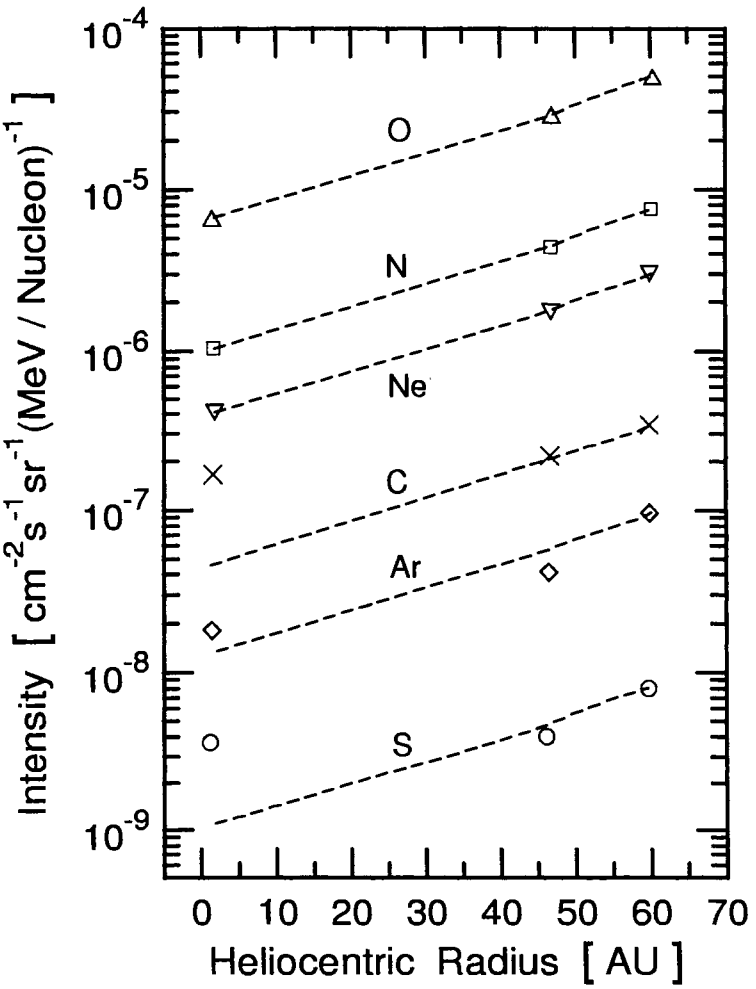

Figure 6.22: Increase of six anomalous cosmic ray species (O, N, Ne, C, Ar, S) with increasing heliospheric radius. The measurements were made on board of the spacecrafts WIND, Voyager 2 and Voyager 1 at heliocentric distances of 1 AU, 45.3 AU, and 58.6 AU, respectively (Stone and Cummings, 1997).

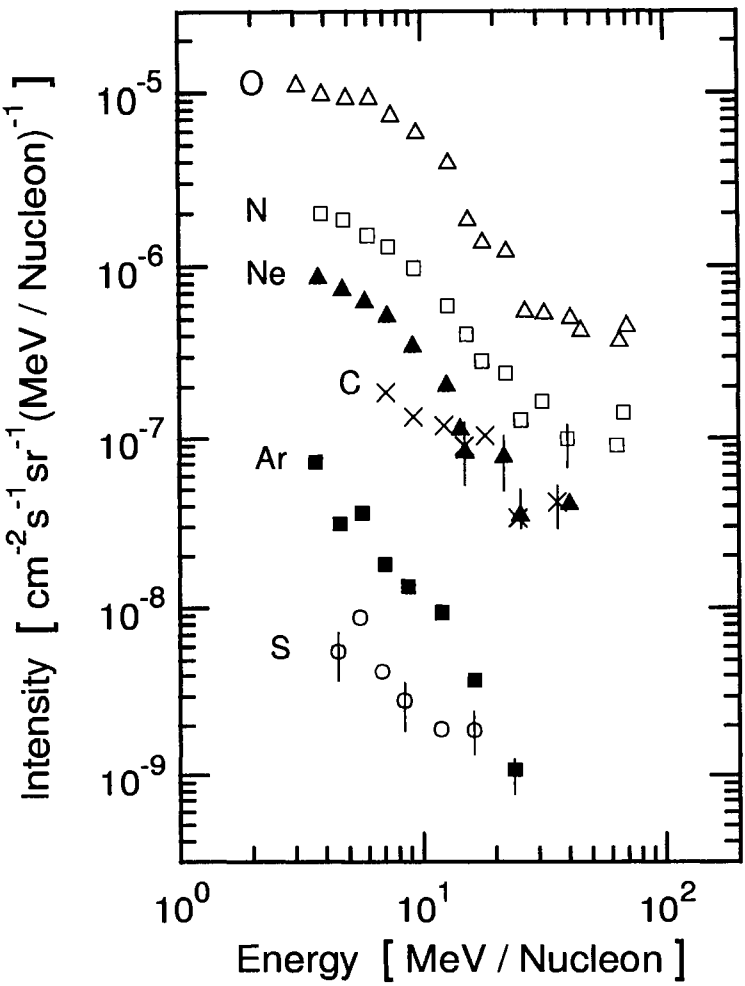

Figure 6.23: Energy spectra of the same six anomalous cosmic ray species (O, N, Ne, C, Ar, S) as shown in Fig. 6.22 observed during the period 1993/307 to 1996/100 at a heliocentric distance of 1 AU. The spectra have similar shapes at large distances (Stone and Cummings, 1997).

6.6 Solar Neutrinos

6.6.1 Introduction

Each solar model predicts different contributions to the overall solar neutrino spectrum and to the steady outward flux of neutrinos from the Sun from the various thermonuclear processes that are involved. The simplest model which can be developed with minimum special assumptions, called the *Standard Solar Model* (SSM), was developed by several authors, in particular by J. Bahcall (Bahcall et al., 1968; Bahcall and Ulrich, 1988; Bahcall, 1989 and references listed therein, Bahcall and Pinsonneault, 1992) and Turck-Chièze et al. (1988). More recently, model refinements, extensions and related topics were discussed by Turck-Chièze (1993), Turck-Chièze and Lopes (1993), Bahcall and Pinsonneault (1995), Bahcall et al. (1998) and Brun et al. (1998).

According to the SSM eight principal nuclear reactions and decays produce solar neutrinos. Six produce continuous energy spectra and two produce neutrino lines. The processes and the resulting neutrino energies are listed in Table 6.3 together with the neutrino fluxes predicted by Bahcall and Ulrich (1971 and 1988).

Table 6.3: Neutrino Generating Fusion Processes in the Sun.

Reaction	Neutrino Energy MeV	Calculated* Flux at 1 AU $[10^{10}$ cm^{-2} s$^{-1}]$
$p + p \rightarrow {}^2\mathrm{H} + e^+ + \nu_e$ (pp)	≤ 0.420	$6.0 \cdot (1 \pm 0.02)$
$p + e^- + p \rightarrow {}^2\mathrm{H} + \nu_e$ (pep)	1.442	$0.014 \cdot (1 \pm 0.05)$
${}^3\mathrm{He} + p \rightarrow {}^4\mathrm{He} + e^+ + \nu_e$ (hep)	≤ 18.77	$8 \cdot 10^{-7}$
${}^7\mathrm{Be} + e^- \rightarrow {}^7\mathrm{Li} + \nu_e$	0.862 (89,7%)	$0.47 \cdot (1 \pm 0.15)$
	0.384 (10.3%)	included above
${}^8\mathrm{B} \rightarrow {}^8\mathrm{Be}^* + e^+ + \nu_e$	≤ 15	$5.8 \cdot 10^{-4} \cdot (1 \pm 0.37)$
${}^{13}\mathrm{N} \rightarrow {}^{13}\mathrm{C} + e^+ + \nu_e$	≤ 1.199	$0.06 \cdot (1 \pm 0.50)$
${}^{15}\mathrm{O} \rightarrow {}^{15}\mathrm{N} + e^+ + \nu_e$	≤ 1.732	$0.05 \cdot (1 \pm 0.58)$
${}^{17}\mathrm{F} \rightarrow {}^{17}\mathrm{O} + e^+ + \nu_e$	≤ 1.740	$5.2 \cdot 10^{-4} \cdot (1 \pm 0.46)$

* Bahcall and Ulrich (1971 and 1988)

More recent flux predictions and neutrino capture rates for ^{37}Cl and ^{71}Ga targets used in the two classical radiochemical experiments, Homestake and GALLEX, discussed below, are listed in Table 6.4.

Table 6.4: Standard Solar Model Predictions.
Solar neutrino fluxes and capture rates in chlorine and gallium: Columns 3 and 4 have 1σ uncertainties for all sources (combined quadratically) (Bahcall et al., 1998); columns 5 and 6 are from earlier calculations (Bahcall and Pinsonneault, 1992; see also Bahcall and Ulrich, 1971 and 1988).

Source	Calculated Flux at 1 AU $[10^{10}$ cm^{-2} s$^{-1}]$	Capture Rates ^{37}Cl SNU	Capture Rates ^{71}Ga SNU	Capture Rates ^{37}Cl SNU	Capture Rates ^{71}Ga SNU
(*pp*)	$5.94(1.00^{+0.01}_{-0.01})$	0.0	69.6	0.0	70.8
(*pep*)	$1.39 \cdot 10^{-2}(1.00^{+0.01}_{-0.01})$	0.2	2.8	0.2	3.0
(*hep*)	$2.10 \cdot 10^{-7}$	0.0	0.0	0.03	0.06
^{7}Be	$4.80 \cdot 10^{-1}(1.00^{+0.09}_{-0.09})$	1.15	34.4	1.1	34.3
	included above				
^{8}B	$5.15 \cdot 10^{-4}(1.00^{+0.19}_{-0.14})$	5.9	12.4	6.1	14.0
^{13}N	$6.05 \cdot 10^{-2}(1.00^{+0.19}_{-0.13})$	0.1	3.7	0.1	3.8
^{15}O	$5.32 \cdot 10^{-2}(1.00^{+0.22}_{-0.15})$	0.4	6.0	0.3	6.1
^{17}F	$6.33 \cdot 10^{-4}(1.00^{+0.12}_{-0.11})$	0.0	0.1	0.003	0.06
Total		$7.7^{+1.2}_{-1.0}$	129^{+8}_{-6}	7.9 ± 2.6	132^{+20}_{-17}

The theoretical solar neutrino spectra resulting from the above listed processes are shown in Fig. 6.24. The thresholds of the dedicated solar neutrino experiments are indicated. In order to test the model the solar neutrino flux must be verified experimentally. However, because of the very small neutrino cross section which is of the order of 10^{-44} cm^2 in the MeV range (for details see Chapter 4, Section 4.5), very large volume detectors are required. In order to reduce background caused by cosmic rays the detectors must be placed deep underground and well shielded from the natural radioactivity of the surrounding rock. Several large detectors are currently in operation. They are briefly described below and the results are summarized.

Two different kinds of principles are currently used for the detection of solar neutrinos. One employs the *radiochemical* method, initially proposed by Pontecorvo (1946), that requires special processing and off-line electronic

counting. The other is based on neutrino electron scattering and some specific neutrino reactions (see Subsection 6.6.9), and use direct on-line *opto-electronic* recording of the events.

A third method, the so called *geochemical* method, is presently in an exploratory phase. It uses the process ($\nu_e + {}^{98}\mathrm{Mo} \rightarrow {}^{98}\mathrm{Tc}^* + e^-$) on natural ${}^{98}\mathrm{Mo}$ in rock deep underground. Since ${}^{98}\mathrm{Tc}$ has a mean life of 4.2 million years its decay time is too long such that special mass spectrometric methods must be used on a typical sample of about 10^7 atoms. The same technique is also explored on ${}^{205}\mathrm{Tl}$, i.e., ($\nu_e + {}^{205}\mathrm{Tl} \rightarrow e^- + {}^{205}\mathrm{Pb}$). This process has the lowest threshold, 0.054 MeV.

Finally, new radiochemical processes are being explored, using ${}^{7}\mathrm{Li}$ ($\nu_e + {}^{7}\mathrm{Li} \rightarrow e^- + {}^{7}\mathrm{Be}$), ${}^{127}\mathrm{I}$ ($\nu_e + {}^{127}\mathrm{I} \rightarrow e^- + {}^{127}\mathrm{Xe}$), and ${}^{82}\mathrm{Br}$ ($\nu_e + {}^{81}\mathrm{Br} \rightarrow e^- + {}^{81}\mathrm{Kr}$) (Bahcall, 1989).

6.6.2 The Solar Neutrino Unit (SNU)

Because of the rare occurrence of neutrino induced reactions, it is convenient to use as unit for the neutrino capture or reaction rate the SNU (*Solar Neutrino Unit*): The SNU is defined as the product of a characteristic calculated solar neutrino flux, in units of [$\mathrm{cm}^{-2}\ \mathrm{s}^{-1}$], multiplied by a theoretical cross section for neutrino absorption or scattering, in units of [cm^2]. The unit of SNU is therefore events per target atom per second. Its numeric value is $10^{-36}\ \mathrm{s}^{-1}$ (Davis, 1973). Thus,

$$1\ \mathrm{SNU} = 10^{-36}\ [\mathrm{s}^{-1}]\,. \tag{6.10}$$

6.6.3 The Solar Neutrino Problem and Recent Results

For about thirty years, the first and for a long time only operating solar neutrino experiment (Homestake) measured a solar neutrino flux that was consistently about a factor of two lower than theoretical predictions based on the standard solar model (Davis, 1969, 1970, Cleveland et al., 1995). This fact is known as the *solar neutrino problem.*

The predicted rate, R_{pred}, for capturing solar neutrinos in the Homestake chlorine experiment described below is (Bahcall et al., 1998)

$$R_{pred} = 7.7^{+1.2}_{-1.0}\ \mathrm{SNU}\,, \tag{6.11}$$

whereas the observed rate, R_{obs}, is (Lande et al., 1999)

$$R_{obs} = 2.56 \pm 0.16 \text{ SNU} . \quad (6.12)$$

More recently, other experiments confirmed the flux deficiency of solar neutrinos (Hirata et al., 1990a; Anselmann et al., 1993; Abdurashitov et al., 1994; Davis, 1994). An interesting comparison of the results of the different experiments is presented by Anselmann et al. (1995a) together with a discussion of the theoretical implications (see also Langacker, 1999).

The present data show that there is a lack of ^{8}B and ^{7}Be neutrinos while they are consistent with the full flux of *pp* neutrinos. The latest data from the two gallium experiments, GALLEX and SAGE, discussed below, also tend to indicate a deficiency of ^{7}Be neutrinos, if it is assumed that these experiments detect the full flux of *pp* neutrinos.

The current models of the solar interior and of neutrino propagation are not strongly constrained by experimental data. Model modification is not a trivial matter. Nonstandard models are all in conflict with at least one apparently established fact.

One possible way out of the dilemma would be *neutrino oscillations*, in particular the Mikheyev-Smirnov-Wolfenstein (MSW) neutrino matter oscillation effect (Wolfenstein, 1978, 1979, 1986; Mikheyev and Smirnov, 1986a, 1986b, 1986c, 1986d), or vacuum oscillations (Maki et al., 1962; Pontecorvo, 1967, 1968) (see also Smirnov, 1999). That, however, would have far reaching consequences for particle physics and astrophysics (see Chapter 4, Section 4.5 and Chapter 5, Section 5.5).

Evidence in support of another type of neutrino oscillations comes from the study of atmospheric neutrinos, specifically from the so-called ratio of ratios analysis of predicted and measured $(\nu_e + \overline{\nu}_e)$ and $(\nu_\mu + \overline{\nu}_\mu)$ fluxes (see Chapter 4, Section 4.5), but no definite proof has yet been delivered, confirming the existence of neutrino oscillations. A review of the early history of the solar neutrino problem is found in Bahcall (1989) and a more recent summary reviewing the different models in Bahcall (1999).

In connection with the solar neutrino problem, two important questions need to be answered: Are there ^{7}Be neutrinos emitted by the Sun, and, can the neutrino oscillation hypothesis be tested in a model independent way (see also Chapter 4, Section 4.5).

6.6.4 Homestake Chlorine Detector and Data

The Homestake chlorine based detector is the first and oldest major solar neutrino experiment. It is located in the Homestake Gold Mine, Lead, South Dakota (USA), at a depth of 1480 m (4400 hg/cm^2 or 4100 m w.e.) and consists of $3.8{\cdot}10^5$ liters or 615 tons of perchloroethylene (C_2Cl_4) (Davis et al., 1968). Detection of neutrinos is based on the neutrino capture reaction,

$$^{37}\mathrm{Cl}\,(\nu_e,\, e^-)\,^{37}\mathrm{Ar}\;;\; E_{th} = 814\;\;\mathrm{keV}\;. \tag{6.13}$$

The number of ^{37}Cl target atoms in the tank is $2.18{\cdot}10^{30}$. The threshold for the reaction is 814 KeV. The argon is extracted from the liquid by purging with helium gas, and the decay of the recovered argon gas ($^{37}\mathrm{Ar} \rightarrow\; ^{37}\mathrm{Cl}$, 90% by 2.82 keV K-orbital electron capture with a half life of 35.0 days, resulting in the release of Auger electrons, and the remaining 10% via the emission of soft X-rays) is counted in tiny proportional counters.

The detector is sensitive to all neutrino generating reactions in the Sun except for $p-p$ fusion, namely to ^{7}Be electron capture, decay of ^{13}C, ^{15}N and ^{8}B, and to the process $(p+e^-+p)$. ^{8}B is the main contributor. The neutrino capture rates on ^{37}Cl as predicted by the SSM are given in Table 6.4.

Early measurements yielded a neutrino capture rate per ^{37}Cl atom in the detector of $(2.5{\pm}1.4)\cdot 10^{-36}$ s^{-1}, or 2.5 ± 1.4 SNU (Davis, 1969, 1970). Background handling is discussed elsewhere (Wolfendale et al., 1972; Cassiday, 1973; Zatsepin et al., 1981; Bahcall and Holstein, 1986; Bahcall and Ulrich, 1988). Operational details can be found in Cleveland (1983) and Cleveland et al. (1995).

The number of ^{37}Ar atoms in the detector at any given time is

$$\Sigma(\Phi_i\sigma_i + Background)\cdot N_oT_o(1-e^{-t/T_o}) \tag{6.14}$$

where Φ_i is the electron neutrino flux from the $i-th$ neutrino generating reaction in the Sun, σ_i is the average cross section for these neutrinos, $N_o = 2.18\cdot 10^{30}$ the number of target atoms in the detector tank, $T_o = 50.5$ days the mean lifetime of ^{37}Ar, and t is the time since the last argon extraction.

Figure 6.25 shows the observed rates from 1970 to 1991 (Davis, 1993). Large fluctuations occur and the data suggest a periodic variation. However there seems to be no clear correlation with the Sun spot number. In a recent paper the results from the different periods of operation are summarized and the errors of the measurements are discussed (Cleveland et al., 1995). The data are presented in Table 6.5 together with a more recent overall flux (Lande et al., 1999) added by the author and illustrated in Fig. 6.26.

Table 6.5: Homestake Observed ^{37}Cl Capture Rates.

Period	Average Neutrino Flux
1970 - 1977	2.52 ± 0.41 SNU
1977 - 1985	2.27 ± 0.30 SNU
1986 - 1993	2.78 ± 0.35 SNU
overall - 1995	2.55 ± 0.25 SNU
overall - 1999	2.56 ± 0.16 SNU

6.6.5 GALLEX Detector and Data

The GALLEX detector, now shut-down, was located at the Gran Sasso National Laboratory (LNGS), Italy, at a depth of 3300 m water equivalent of standard rock. It is now replaced by a new experiment called Gallium Neutrino Observatory (GNO) (Kirsten, 1999). Gallex consisted of a tank of 101 metric tons of concentrated aqueous gallium chloride solution, containing 30.3 tons of Gallium, i.e., 76.3 tons of $GaCl_3$, 21 tons H_2O, and 3.7 tons HCl. The density was 1.9 g/cm^3 (Anselmann et al., 1992, 1994; Henrich, 1996). Detection of the neutrinos was based on the neutrino capture reaction,

$$^{71}\mathrm{Ga}\,(\nu_e,\, e^-)\,^{71}\mathrm{Ge}\ ;\ E_{th} = 233.2\ \mathrm{keV}\ . \tag{6.15}$$

The threshold energy for this process is 233.2 keV and the half-life of ^{71}Ge is 11.4 days. The neutrino capture rates for a ^{71}Ga detector predicted by the SSM are given in Table 6.4.

GALLEX was the first experiment that was sensitive to the *pp* process and the first to record neutrinos from this process. The total predicted SSM neutrino capture rate was 128±8 SNU (1σ) (Bahcall and Pinsonneault, 1992; Turck-Chièze and Lopes, 1993). Of this flux 58% (74 SNU) were expected from *pp* (and *pep*) neutrinos, 26% from ^{7}Be neutrinos, 10% from ^{8}B, and 6% from ^{13}N and ^{15}O.

On average 0.7 ^{71}Ge atoms were produced per day by this reaction in the tank. The parasitic reaction, $^{71}\mathrm{Ga}(p,n)^{71}\mathrm{Ge}$, resulting from protons produced in photo-nuclear processes by energetic penetrating muons deep underground produced about 0.04 ^{71}Ga atoms per day.

The ^{71}Ge atoms were extracted as volatile germanium tetrachloride by nitrogen purging together with approximately 1 mg of a stable germanium

isotope that was added for process monitoring. After further processing the Auger electrons and X-rays from the electron capture decay of ^{71}Ge to ^{71}Ga of 10.4 keV (K-shell) and 1.2 keV (L-shell) were recorded (Henrich and Ebert, 1992).

The results from a total of 65 runs (GALLEX I - IV) are shown in Fig. 6.27 (Kirsten, 1999). Summaries of different groups of runs are found in Anselmann et al. (1992, 1993, 1994, 1995b, 1995c), Kirsten (1993) and Henrich (1996). The combined result for the capture rate of solar neutrinos from this experiment is (Kirsten, 1999)

$$R_{obs} = (78 \pm 8) \text{ SNU} . \tag{6.16}$$

This corresponds to (60±6)% of the SSM expectation or, what is noteworthy, to 107% of what is expected for the combined *pp* and *pep* neutrino flux alone. As mentioned before, the most recent data from GALLEX and those from SAGE, presented below, tend to indicate a deficit of ^{7}Be neutrinos, if it is assumed that the full flux of *pp* neutrinos is detected.

Background, processing and other problems are discussed in Kirsten et al. (1994), and Anselmann and Hartmann (1994). Uncertainties in the solar neutrino flux are discussed by Haxton (1999). The implications of these results are discussed by Anselmann et al. (1995a) and Kirsten (1999).

6.6.6 SAGE Detector and Data

The SAGE (Soviet-American-Gallium-Experiment) detector is located at the Baksan Laboratory in the Northern Caucasus Mountains (Mt. Andyrchi), in southern Russia, at a depth of 4700 m w.e. underground (Pomansky, 1986, 1988). It uses 60 tons of metallic liquid gallium (T $\geq$ 30° C, ρ_{Ga} = 6 g/cm^3). Apart from the extraction the procedures are similar to the GALLEX experiment.

First results were reported by Abazov et al. (1991a, 1991b). After a detector upgrade the data were in better agreement with other experiments (Gavrin et al., 1993, 1994; Zatsepin, 1993; Abdurashitov et al., 1994). The overall results for the best fit value of the ^{71}Ga capture rate at SAGE for the full operating period from January 1990 to December 1997, totaling 57 runs after excluding the problem period from November 1993 through June 1994, is (Abdurashitov et al., 1999)

$$R_{obs} = 66.9^{+7.1}_{-6.8}\,(\text{stat.})\,^{+5.4}_{-5.7}\,(\text{syst.}) \text{ SNU} . \tag{6.17}$$

Figure 6.28 shows the full data set and the lumped data of the different operating periods since the beginning of the experiment (Abdurashitov et al., 1995 and 1999). The problems during the initial phase are evident. The overall GALLEX data are also shown for comparison.

6.6.7 Kamiokande Detector and Data

The Kamiokande neutrino detector, now out of service, was a 3000 ton water Cherenkov detector located at a depth of 1000 m underground (~2700 m w.e.) at 36.4° N, 137.3° E, and 25.8° N geomagnetic latitude (Hirata et al., 1989, 1990a). A detector of this kind is a real time detector responding to all three kinds of neutrino flavors and their antiparticles via neutrino scattering processes and reactions of the neutrinos in the water, provided that the process and/or detector thresholds are exceeded.

The process that is relevant for the detection of solar neutrinos with such a detector is elastic scattering of electron neutrinos on electrons,

$$\nu_e + e^- \rightarrow \nu_e' + e^{-\prime} \ , \tag{6.18}$$

though the process $\overline{\nu}_e + p \rightarrow e^+ + n$ is detectable, too. Detection was based on the Cherenkov signature of the electrons with a design threshold of $\geq$6 MeV. Only the most inner 680 tons were used for solar neutrino studies. Because of the relatively high threshold Kamiokande could only observe part of the ^{8}B and *hep* neutrino spectra (cf. Fig. 6.24) (Suzuki, 1993). Under actual operating conditions the threshold level for event selection was initially set to an energy of 9.3 MeV for the electrons (Hirata et al., 1989). In the course of time and with improving background handling capability the threshold had been lowered to 7.5 MeV and later to 7.0 MeV (Hirata et al., 1990a, 1991b; Fukuda et al., 1996).

Solar neutrino recording with the Kamiokande detector began in January 1987. The results of the three different series of measurements called Kamiokande I, II and III, corresponding to different detector operating conditions, were reported by Hirata et al. (1990b, 1991a, 1991b), Suzuki (1993) and Fukuda et al. (1996). More recently, for an assumed shape of the ^{8}B neutrino spectrum a time averaged flux of

$$\Phi_\nu \ = \ (2.89^{+0.22}_{-0.21} \pm 0.35) \cdot 10^6 \ \ \mathrm{cm^{-2}\,s^{-1}} \tag{6.19}$$

was specified by Suzuki (1995). For the ratio, r, of the measured to the SSM predicted flux the same author gives the value of

$$r = 0.54 \pm 0.06\,(\text{stat.}) \pm 0.06\,(\text{syst.}) \tag{6.20}$$

for the selected data sample pointing toward the Sun, and

$$r = 0.51 \pm 0.04\,(\text{stat.}) \pm 0.06\,(\text{syst.}) \tag{6.21}$$

for all the data. Figure 6.29 illustrates the time variation of the data over a period of nearly 7 years, expressed as the ratio between measured and predicted fluxes (Suzuki, 1995).

Since the direction of the elastically scattered electrons is correlated with that of the incident neutrinos within an angle θ_e such that $E_e\theta_e^2 \leq 2m_e$, where $0 \leq E_e \leq E_\nu$, E_e being the electron energy, θ_e the scattering angle, m_e the electron mass and E_ν the neutrino energy, the approximate arrival direction of the neutrino could be identified. Directionality is useful for extracting solar neutrinos (see Figure 6.30). The angular resolution of the Kamiokande detector was $\Delta\theta_e \simeq 26°$ at 10 MeV (28° for Kamiokande II) and dominated by the Coulomb scattering of the recoil electrons in the water.

Directionality in the antineutrino scattering process of atmospheric neutrinos is lost but the antineutrino energy is directly measurable through the recoil electron energy with the help of the relation $E_{\overline{\nu}} = E_{e^+} + 1.8$ MeV. The cross section for this process is about 20 times larger than for neutrino scattering.

6.6.8 Super-Kamiokande (SK) Detector and Data

This new 50 kt water Cherenkov detector, also located at Kamiokande, is the first second generation neutrino detector of its kind. It has a fiducial mass of 22.5 kt for the detection of solar neutrinos (Suzuki, 1994) and began operating May 31, 1996. Its principle of operation is the same as that of the Kamiokande detector. It was designed for a threshold energy of 5 MeV. The same basic observables are being measured with the SK detector as before with Kamiokande, but the data are acquired at a much faster rate, with better statistics and better resolution.

The angular distribution of the events with respect to the direction toward the Sun are shown in Fig. 6.30 for the first 300 days of operation (Fukuda et al., 1998) and for the 504 day period (Suzuki, 1999). A similar set of data, not shown here, was obtained with the previously discussed Kamiokande detector (Suzuki, 1995), showing the same peaking toward the Sun but with poorer statistics and larger fluctuations.

The daytime/nighttime fluxes were also investigated with the SK detector to search for neutrino matter oscillations. The fluxes were corrected for seasonal intensity variations due to the eccentricity of the Earth's orbit to a distance of 1 AU. The following values were obtained (Suzuki, 1999; Kajita, 2000): For daytime

$$\Phi_\nu = (2.37 \pm 0.07\,(\text{stat.})\,^{+0.08}_{-0.07}\,(\text{syst.})) \cdot 10^6 \ \text{cm}^{-2}\,\text{s}^{-1} \tag{6.22}$$

and for nighttime

$$\Phi_\nu = (2.48^{+0.07}_{0.06}\,(\text{stat.})\,^{+0.08}_{-0.07}\,(\text{syst.})) \cdot 10^6 \ \text{cm}^{-2}\,\text{s}^{-1}\,. \tag{6.23}$$

The nighttime/daytime ratio resulting from this work is

$$\frac{N}{D} - 1 = 0.047 \pm 0.042\,(\text{stat.}) \pm 0.008\,(\text{syst.})\,. \tag{6.24}$$

A search for seasonal effects due to the eccentricity of the Earth's orbit that could reveal neutrino vacuum oscillations was also carried out. The result is illustrated in Fig. 6.31 together with the expected variations for no oscillations. No significant deviation is observed.

The recoil energy spectrum of the electrons is illustrated in Fig. 6.32 together with the theoretical spectrum predicted by the SSM of Bahcall et al. (1998) (Fukuda et al., 1999).

The flux of ^{8}B solar neutrinos determined with the 22.5 kt fiducial volume of the Super-Kamiokande detector over the period from May 31, 1996 to March 25, 1998 is

$$\Phi_\nu = (2.44 \pm 0.05\,(\text{stat.})\,^{+0.09}_{-0.07}\,(\text{syst.})) \cdot 10^6 \ \text{cm}^{-2}\,\text{s}^{-1}\,. \tag{6.25}$$

The ratio, r, of the measured to the predicted SSM flux is

$$r = 0.473^{+0.010}_{-0.009}\,(\text{stat.})\,^{+0.017}_{-0.014}\,(\text{syst.}) \tag{6.26}$$

using the prediction of Bahcall et al. (1998). It is

$$r = 0.368^{+0.008}_{-0.007}\,(\text{stat.})\,^{+0.013}_{-0.011}\,(\text{syst.}) \tag{6.27}$$

for the prediction of Bahcall and Pinsonneault (1995), and

$$r = 0.506^{+0.011}_{-0.010}\,(\text{stat.})\,^{+0.018}_{-0.015}\,(\text{syst.}) \tag{6.28}$$

when compared with the work of Brun et al. (1998) (Suzuki, 1999).

6.6.9 New and Future Detectors

Many new solar neutrino detector project studies evolved in recent years that are reviewed by Bellotti (1995), Cremonesi (1999), Kirsten (1999) and Lanou (1999). In the following we give a very brief account of some new detectors that have just come into service or will soon be commissioned.

BOREXINO

This detector, of which a prototype is in operation at the Gran Sasso Laboratory, consists of an extremely pure scintillator target that is heavily shielded by 1 kt of de-ionized water against environmental radioactivity. It is a real time solar neutrino detector and aimed at the detection of the 862 keV ^{7}Be neutrino line via electron scattering (eq. 6.18) with a threshold of about 250 keV (Bonetti, 1992; Oberauer, 1999).

SNO

The SNO (Sudbury Neutrino Observatory), located at the INCO Creighton Mine near Sudbury, Ontario (Canada), at a depth of about 2000 m (~5900 m w.e.), uses 1 kt of heavy water (D_2O), surrounded by 7 kt of light water (Chen, 1985; Ewan, 1992a and 1992b; Bemporad, 1996; McDonald, 1999). The detector can measure the electron neutrino flux via the charged current reaction

$$\nu_e + d \rightarrow p + p + e^- \tag{6.29}$$

and the flux of neutrinos (and antineutrinos) of any flavor, ν_x ($\overline{\nu}_x$), via the neutral current reaction

$$\nu_x + d \rightarrow p + n + \nu_x \, . \tag{6.30}$$

In addition it responds to the elastic neutrino scattering reaction

$$\nu_x + e^- \rightarrow e^{-\prime} + \nu_x' \, . \tag{6.31}$$

The threshold for the charged current reaction ($\nu_e + e^- \rightarrow e^{-\prime} + \nu_e'$) is about 5 MeV in electron energy, corresponding to a neutrino energy of ~6.4 MeV. The threshold for the neutral current reaction is 2.2 MeV. Therefore both reactions will be sensitive only to neutrinos from the ^{8}B decay in the Sun. Additional details concerning this detector and the neutrino reactions that are accessible with it are discussed in Chapter 4, Section 4.5.

Contrary to the Kamiokande detector directional correlation is inadequate to be employed for selecting solar neutrinos (McDonald, 1999).

ICARUS

The proposed ICARUS detector is a 5 kt liquid argon imaging chamber (Time Projection Chamber, TPC) with a high spatial resolution (2 mm), planned to be operated in the Gran Sasso underground laboratory. It was initially intended to be used as a proton decay detector, but also to study atmospheric neutrinos and, in conjunction with a neutrino beam from CERN, neutrino oscillations (ICARUS Collab., 1994). The detector is planned in modular units. The first step is the construction of a 600 t module, now underway (Vignoli et al., 2000). Detection is based on the elastic scattering reaction and it will also observe the reaction

$$^{40}\mathrm{Ar} + \nu_e, \rightarrow {}^{40}\mathrm{K} + e^- + \gamma \tag{6.32}$$

which has a Q-value of -5.85 MeV.

References

Abazov, A.I., D.N. Abdurashitov, O.L. Anosov, L.A. Eroshkina, E.L. Faizov, V.N. Gavrin, A.V. Kalikhov, T.V. Knodel, I.I. Knyshenko, V.N. Kornoukhov, S.A. Mezentseva, I.N. Mirmov, A.I. Ostrinsky, V.V. Petukhov, A.M. Pshukov, N.Ye. Revzin, A.A. Shikhin, P.V. Timofeyev, E.P. Veretenkin, V.M. Vermul, Yu. Zakharov, G.T. Zatsepin, and V.I. Zhandarov, T.J. Bowles, B.T. Cleveland, S.R. Elliott, H.A. O'Brian, D.L. Wark, J.F. Wilkerson, R. Davis, Jr., K. Lande, M.L. Cherry, R.T. Kouzes, SAGE Collaboration: Nucl. Phys. B (Proc. Suppl), 19, p. 84 (1991a).

Abazov, A.I., O.L. Anosov, E.L. Faizov, V.N. Gavrin, A.V. Kalikhov, T.V. Knodel, I.I. Knyshenko, V.N. Kornoukhov, S.A. Mezentseva, I.N. Mirmov, A.I. Ostrinsky, A.M. Pshukov, N.Ye. Revzin, A.A. Shikhin, P.V. Timofeyev, E.P. Veretenkin, V.M. Vermul, and G.T. Zatsepin, T.J. Bowles, B.T. Cleveland, S.R. Elliott, H.A. O'Brian, D.L. Wark, J.F. Wilkerson, R. Davis, Jr., K. Lande, M.L. Cherry, R.T. Kouzes, SAGE Collaboration: Phys. Rev. Lett., 67, p. 3332 (1991b).

Abdurashitov, J.N., E.L. Faizov, V.N. Gavrin, A.O. Gusev, A.V. Kalikhov, T.V. Knodel, I.I. Knyshenko, V.N. Kornoukhov, I.N. Mirmov, A.M. Pshukov, A.M. Shalagin, A.A. Shikhin, P.V. Timofeyev, E.P. Veretenkin, V.M. Vermul, G.T. Zatsepin, T.J. Bowles, J.S. Nico, W.A. Teasdale, D.L. Wark, J.F. Wilkerson, B.T. Cleveland, T. Daily, R. Davis Jr., K. Lande, C.K. Lee, P.W. Wildenhain, S.R. Elliott, M.L. Cherry, and R.T. Kouzes (SAGE Collaboration): Phys. Lett., B 328, p. 234 (1994).

Abdurashitov, J.N., E.L. Faizov, V.N. Gavrin, A.O. Gusev, A.V. Kalikhov, T.V. Knodel, I.I. Knyshenko, V.N. Kornoukhov, I.N. Mirmov, A.M. Pshukov, A.M. Shalagin, A.A. Shikhin, P.V. Timofeyev, E.P. Veretenkin, V.M. Vermul, G.T. Zatsepin, T.J. Bowles, J.S. Nico, W.A. Teasdale, D.L. Wark, J.F. Wilkerson, B.T. Cleveland, R. Davis, Jr., T. Daily, K. Lande, C.K. Lee, P.W. Wildenhain, S.R. Elliott, and M.R. Cherry: SAGE Collaboration: Nucl. Phys. B (Proc. Suppl), 38, p. 60 (1995).

Abdurashitov, T.J. Bowles, M.L. Cherry, B.T. Cleveland, T. Daily, R. Davis, Jr., S.R. Elliott, J.N., V.N. Gavrin, S.V. Girin, V.V. Gorbachev, T.V. Ibragimova, A.V. Kalikhov, N.G. Khairnasov, T.V. Knodel, K. Lande, C.K. Lee, I.N. Mirmov, S.N. Nico, A.A. Shikhin, W.A. Teasdale, E.P. Veretenkin, V.M. Vermul, D.L. Wark, P.V. Wildenhain, J.F. Wilkerson, V.E. Yants, and G.T. Zatsepin, SAGE Collaboration: Nucl. Phys. B (Proc. Suppl), 77, p. 20 (1999).

Anselmann, P., W. Hampel, G. Heusser, J. Kiko, T. Kirsten, E. Pernicka, R. Plaga, U. Rönn, M. Sann, C. Schlosser, R. Wink, M. Wójcik, R. von Ammon, K.H. Ebert, T. Fritsch, K. Hellriegel, E. Henrich, L. Stieglitz, F. Weirich, M. Balata, E. Bellotti, N. Ferrari, H. Lalla, T. Stolarczyk, C. Cattadori, O. Cremonesi, E. Fiorini, S. Pezzoni, L. Zanotti, F. von Feilitzsch, R. Mössbauer, U. Schanda, G. Berthomieu, E. Schatzmann, I. Carmi, I. Dostrovsky, C. Bacci, P. Belli, R. Bernabei, S. d'Angelo, L. Paoluzi, S. Charbit, M. Cribier, G. Dupont, L. Gosset, J. Rich, M. Spiro, C. Tao, D. Vignaud, R.L. Hahn, F.X. Hartmann, J.K. Rowley, R.W. Stoenner, and J. Weneser, GALLEX Collaboration: Phys. Lett. B, 285, p. 376 (1992).

Anselmann, P., W. Hampel, G. Heusser, J. Kiko, T. Kirsten, M. Laubenstein, E. Pernicka, S. Pezzoni, R. Plaga, U. Rönn, M. Sann, C. Schlosser, R. Wink, M. Wójcik, R. von Ammon, K.H. Ebert, T. Fritsch, K. Hellriegel, E. Henrich, L. Stieglitz, F. Weirich, M. Balata, N. Ferrari, H. Lalla, E. Bellotti, C. Cattadori, O. Cremonesi, E. Fiorini, L. Zanotti, M. Altmann, F. von Feilitzsch, R. Mössbauer, U. Schanda, G. Berthomieu, E. Schatzmann, I. Carmi, I. Dostrovsky, C. Bacci, P. Belli, R. Bernabei, S. d'Angelo, L. Paoluzi, S. Charbit, M. Cribier, J. Rich, M. Spiro, T. Stolarczyk, C. Tao, D. Vignaud, R.L. Hahn, F.X. Hartmann, J.K. Rowley, R.W. Stoenner, and J. Weneser, GALLEX Collaboration: Phys. Lett. B, 314, p. 445 (1993).

Anselmann, P., and F.X. Hartmann: Progr. Part. Nucl. Phys. 32, p. 35 (1994).

Anselmann, P., W. Hampel, G. Heusser, J. Kiko, T. Kirsten, M. Laubenstein, E. Pernicka, S. Pezzoni, U. Rönn, M. Sann, C. Schlosser, R. Wink, M. Wójcik, R. von Ammon, K.H. Ebert, T. Fritsch, K. Hellriegel, E. Henrich, L.

Stieglitz, F. Weirich, M. Balata, N. Ferrari, H. Lalla, E. Bellotti, C. Cattadori, O. Cremonesi, E. Fiorini, L. Zanotti, M. Altmann, F. von Feilitzsch, R. Mössbauer, U. Schanda, G. Berthomieu, E. Schatzmann, I. Carmi, I. Dostrovsky, C. Bacci, P. Belli, R. Bernabei, S. d'Angelo, L. Paoluzi, A. Bevilacqua, S. Charbit, M. Cribier, L. Gosset, J. Rich, M. Spiro, T. Stolarczyk, C. Tao, D. Vignaud, R.L. Hahn, F.X. Hartmann, J.K. Rowley, R.W. Stoenner, and J. Weneser, GALLEX Collaboration: Phys. Lett., B, 327, p. 377 (1994).

Anselmann, P., W. Hampel, G. Heusser, J. Kiko, T. Kirsten, M. Laubenstein, E. Pernicka, S. Pezzoni, U. Rönn, M. Sann, C. Schlosser, R. Wink, M. Wójcik, R. von Ammon, K.H. Ebert, T. Fritsch, K. Hellriegel, E. Henrich, L. Stieglitz, F. Weirich, M. Balata, N. Ferrari, H. Lalla, E. Bellotti, C. Cattadori, O. Cremonesi, E. Fiorini, L. Zanotti, M. Altmann, F. von Feilitzsch, R. Mössbauer, U. Schanda, G. Berthomieu, E. Schatzmann, I. Carmi, I. Dostrovsky, C. Bacci, P. Belli, R. Bernabei, S. d'Angelo, L. Paoluzi, A. Bevilacqua, S. Charbit, M. Cribier, L. Gosset, J. Rich, M. Spiro, T. Stolarczyk, C. Tao, D. Vignaud, R.L. Hahn, F.X. Hartmann, J.K. Rowley, R.W. Stoenner, and J. Weneser, GALLEX Collaboration: Nucl. Phys. B (Proc. Suppl.), 38, p. 68 (1995a).

Anselmann, P., R. Fockenbrock, W. Hampel, G. Heusser, J. Kiko, T. Kirsten, M. Laubenstein, E. Pernicka, S. Pezzoni, U. Rönn, M. Sann, F. Spielker, R. Wink, M. Wójcik, R. von Ammon, K.H. Ebert, T. Fritsch, D. Heidt, E. Henrich, C. Schlosser, L. Stieglitz, F. Weirich, M. Balata, H. Lalla, E. Bellotti, C. Cattadori, O. Cremonesi, N. Ferrari, E. Fiorini, L. Zanotti, M. Altmann, F. von Feilitzsch, R. Mössbauer, U. Schanda, G. Berthomieu, E. Schatzmann, I. Carmi, I. Dostrovsky, C. Bacci, P. Belli, R. Bernabei, S. d'Angelo, L. Paoluzi, A. Bevilacqua, S. Charbit, M. Cribier, G. Dupont, L. Gosset, J. Rich, M. Spiro, T. Stolarczyk, C. Tao, D. Vignaud, J. Boger, R.L. Hahn, F.X. Hartmann, J.K. Rowley, R.W. Stoenner, and J. Weneser, GALLEX Collaboration: Phys. Lett. B, 342, p. 440 (1995b).

Anselmann, P., W. Hampel, G. Heusser, J. Kiko, T. Kirsten, M. Laubenstein, E. Pernicka, S. Pezzoni, U. Rönn, M. Sann, C. Schlosser, R. Wink, M. Wójcik, R. v. Ammon, K.H. Ebert, T. Fritsch, D. Heidt, E. Henrich, L. Stieglitz, F. Weirich, M. Balata, H. Lalla, E. Bellotti, C. Cattadori, O. Cremonesi, N. Ferrari, E. Fiorini, L. Zanotti, M. Altmann, F. v. Feilitzsch, R. Mössbauer, U. Schanda, G. Berthomieu, E. Schatzmann, I. Carmi, I. Dostrovsky, C. Bacci, P. Belli, R. Bernabei, S. d'Angelo, L. Paoluzi, A. Bevilacqua, S. Charbit, M. Cribier, L. Gosset, J. Rich, M. Spiro, T. Stolarczyk, C. Tao, D. Vignaud, J. Boger, R.L. Hahn, F.X. Hartmann, J.K. Rowley, R.W. Stoenner, and J. Weneser, GALLEX Collaboration: Phys. Lett. B, 357, p. 237 (1995c).

Bahcall, J.N.: Neutrino Astrophysics, Cambridge University Press (1989).

Bahcall, John N.: Phys. Lett., 338 B, p. 276 (1994).

Bahcall, John N.: Phys. Rev., C 56, p. 3391 (1997).

Bahcall, John N.: Nucl. Phys. B (Proc. Suppl.) 77, p. 64 (1999).

Bahcall, J.N., and B.R. Holstein: Phys. Rev. C, 33, p. 2121 (1986).

Bahcall, J.N., and M.H. Pinsonneault: Rev. Mod. Phys., 64, p. 885 (1992).

Bahcall, J.N., and M. Pinsonneault: Rev. Mod. Phys., 67, p. 781 (1995).

Bahcall, J.N., and K. Ulrich: Astrophys. J., 170, p. 593 (1971).

Bahcall, J.N., and R.K. Ulrich: Rev. Mod. Phys., 60, p. 297 (1988).

Bahcall, J.N., N.A. Bahcall, and G. Shaviv: Phys. Rev. Lett., 20, p. 1209 (1968).

Bahcall, John N., Sarbani Basu, and M.H. Pinsonneault: Phys. Lett., B 433, p. 1 (1998).

Bellotti, E.: Nucl. Phys. B (Proc. Suppl.) 38, p. 90 (1995).

Bemporad, C.: Nucl. Phys. B (Proc. Suppl.) 48, p. 412 (1996).

Bonetti, S.: Nucl. Phys. B (Proc. Suppl.) 28 A, p. 486 (1992).

Brun, A.S., S. Turck-Chièze, and P. Morel: Astrophys. J., 506, p. 913 (1998).

Cassiday, G.L.: PICRC, 3, p.1958 (1973).

Chen, H.H.: Phys. Rev. Lett., 55, p. 1534 (1985).

Cleveland, B.T.: Nucl. Instr. Methods, 214 p. 451 (1983).

Cleveland, B.T., T. Daily, R. Davis, Jr., J. Distel, K. Lande, C.K. Lee, P. Wildenhain, and J. Ullman: Nucl. Phys. B (Proc. Suppl.), 38, p. 47 (1995).

Cremonesi, O.: Nucl. Phys., B (Proc. Suppl.) 77, p. 369 (1999).

Davis, Jr., Raymond, Don S. Harmer, and Kenneth C. Hoffman: Phys. Rev. Lett., 20, p. 1205 (1968).

Davis, R.: Proc. Moscow Conf. on Neutrino Physics and Neutrino Astrophysics, 2, p. 99 (1969).

Davis, Jr., R.: Acta Acad. Scient. Hung. Suppl., 4, p. 371 (1970).

Davis, Jr., Raymond, and John C. Evans: PICRC, 3, p. 2001 (1973).

Davis, Jr., Raymond: Proc. Internat. Symp. on Neutrino Astrophysics, Takayama, Japan. Frontiers of Neutrino Astrophysics, p. 47, Universal Academy Press, Inc., Tokyo, Japan. Y. Suzuki, and K. Nakamura, ed. (1993).

Davis, R.: Prog. in Part. and Nucl. Phys., 32, p 13 (1994).

Ewan, G.T.: Nucl. Instr. Methods, A 314, p. 373 (1992a).

Ewan, G.T.: Physics in Canada, 48, p. 112 March (1992b).

Fukuda, Y., T. Hayakawa, K. Inoue, K. Ishihara, H. Ishino, S. Joukou, T. Kajita, S. Kasuga, Y. Koshio, T. Kumita, K. Matsumoto, M. Nakahata, K. Nakamura, K. Okumura, A. Sakai, M. Shiozawa, J. Suzuki, Y. Suzuki, T. Tomoeda, Y. Totsuka, K.S. Hirata, K. Kihara, Y. Oyama, M. Koshiba, K. Nishijima, T. Horiuchi, K. Fujita, S. Hatakeyama, M. Koga, T. Maruyama, A. Suzuki, M. Mori, T. Kajimura, T. Suda, A.T. Suzuki, T. Ishizuka, K. Miyano, H. Okazawa, T. Hara, Y. Nagashima, M. Takita, T. Yamaguchi, Y. Hayato, K. Kaneyuki, T. Suzuki, Y. Takeuchi, T. Tanimori, S. Tasaka, E. Ichihara, S. Miyamoto, and K. Nishikawa: Phys. Rev. Lett., 77, p. 1683 (1996).

Fukuda, Y., T. Hayakawa, E. Ichihara, K. Inoue, K. Ishihara, H. Ishino, Y. Itov, T. Kajita, J. Kameda, S. Kasuga, K. Kobayashi, Y. Kobayashi, Y. Koshio, K. Martens, M. Miura, M. Nakahata, S. Nakayama, A. Okada, M. Oketa, K. Okumura, M. Ota, N. Sakurai, M. Shiozawa, Y. Suzuki, Y. Takeuchi, Y. Totsuka, S. Yamada, M. Earl, A. Habig, J.T. Hong, E. Kearns, S.B. Kim, M. Masuzawa, D.D. Messier, K. Scholberg, J.L. Stone, L.R. Sulak, C.W. Walter, M. Goldhaber, T. Barsczak, W. Gajewski, P.G. Halverson, J. Hsu, W.R. Kropp, L.R. Price, F. Reines, H.W. Sobel, M.R. Vagins, K.S. Ganezer, W.E. Keig, R.W. Ellsworth, S. Tasaka, J.W. Flanagan, A. Kibayashi, J.G. Learned, S. Matsuno, V. Stenger, D. Takemori, T. Ishii, J. Kanzaki, T. Kobayashi, K. Nakamura, K. Nishikawa, Y. Oyama, A. Sakai, M. Sakuda, O. Sasaki, S. Echigo, M. Kohama, A.T. Suzuki, T.J. Haines, E. Blaufuss, R. Sanford, R. Svoboda, M.L. Chen, Z. Conner, J.A. Goodman, G.W. Sullivan, M. Mori, J. Hill, C.K. Jung, C. Mauger, C. McGrew, E. Sharkey, B. Viren, C. Yanagisawa, W. Doki, T. Ishizuka, Y. Kitaguchi, H. Koga, K. Miyano, H. Okazawa, C. Saji, M. Takahata, A. Kusano, Y. Nagashima, M. Takita, T. Yamaguchi, M. Yoshida, M. Etoh, K. Fujita, A. Hasegawa, T. Hasegawa, S. Hatakeyama, T. Iwamoto, T. Kinebuchi, M. Koga, T. Maruyama, H. Ogawa, A. Suzuki, F. Tsushima, M. Koshiba, M. Nemoto, K. Nishijima, T. Futagami, Y. Hayato, Y. Kanaya, K. Kaneyuki, Y. Watanabe, D. Kielczewska, R. Doyle, J. George, A. Stachyra, L. Wai, J. Wilkes, and K. Young. Phys. Rev. Lett., 81, p. 1158 (1998).

Fukuda, Y., T. Hayakawa, E. Ichihara, K. Inoue, K. Ishihara, H. Ishino, Y. Itov, T. Kajita, J. Kameda, S. Kasuga, K. Kobayashi, Y. Kobayashi, Y. Koshio, M. Miura, M. Nakahata, S. Nakayama, A. Okada, K. Okumura, N. Sakurai, M. Shiozawa, Y. Suzuki, Y. Takeuchi, Y. Totsuka, S. Yamada, M.

Earl, A. Habig, E. Kearns, D.D. Messier, K. Scholberg, J.L. Stone, L.R. Sulak, C.W. Walter, M. Goldhaber, T. Barsczak, D. Casper, W. Gajewski, P.G. Halverson, J. Hsu, W.R. Kropp, L.R. Price, F. Reines, M. Smy, H.W. Sobel, M.R. Vagins, K.S. Ganezer, W.E. Keig, R.W. Ellsworth, S. Tasaka, J.W. Flanagan, A. Kibayashi, J.G. Learned, S. Matsuno, V.J. Stenger, D. Takemori, T. Ishii, J. Kanzaki, T. Kobayashi, S. Mine, K. Nakamura, K. Nishikawa, Y. Oyama, A. Sakai, M. Sakuda, O. Sasaki, S. Echigo, M. Kohama, A.T. Suzuki, T.J. Haines, E. Blaufuss, B.K. Kim, R. Sanford, R. Svoboda, M.L. Chen, Z. Conner, J.A. Goodman, G.W. Sullivan, J. Hill, C.K. Jung, K. Martens, C. Mauger, C. McGrew, E. Sharkey, B. Viren, C. Yanagisawa, W. Doki, K. Miyano, H. Okazawa, C. Saji, M. Takahata, Y. Nagashima, M. Takita, T. Yamaguchi, M. Yoshida, S.B. Kim, M. Etoh, K. Fujita, A. Hasegawa, T. Hasegawa, S. Hatakeyama, T. Iwamoto, H. Koga, T. Maruyama, H. Ogawa, J. Shirai, A. Suzuki, F. Tsushima, M. Koshiba, M. Nemoto, K. Nishijima, T. Futagami, Y. Hayato, Y. Kanaya, K. Kaneyuki, Y. Watanabe, D. Kielczewska, R. Doyle, J. George, A. Stachyra, L. Wai, J. Wilkes, and K. Young: Phys. Rev. Lett., 82, p. 2430 (1999).

Gavrin, V., et al., SAGE Collaboration: XXVI Int. Conf. on High Energy Physics, Dallas , 1992, J. Stanford, (ed.), p. 1101 (1993).

Gavrin, V., E.L. Faizov, A.V. Kalikhov, T.V. Knodel, I.I. Knyshenko, V.N. Kornoukhov, I.N. Mirmov, A.I. Ostrinsky, A.M. Pshukov, A.A. Shikhin, P.V. Timofeyev, E.P. Veretenkin, V.M. Vermul, G.T. Zatsepin, T.J. Bowles, S.R. Elliott, J.S. Nico, W.A. Teasdale, D.L. Wark, J.F. Wilkerson, B.T. Cleveland, T. Daily, R. Davis, Jr., K. Lande, C.K. Lee, P. Wildenhain, M.L. Cherry, and R.T. Kouzes, SAGE Collaboration: Nucl. Phys. B (Proc. Suppl), 35, p. 412 (1994).

Haxton, W.C.: Nucl. Phys. B (Proc. Suppl), 77, p. 73 (1999).

Henrich, E.: Forschungszentrum Karlsruhe, Technik und Umwelt, Nachrichten, 28, p. 29 (1996).

Henrich, E., and K.H. Ebert: Angew. Chem., Int. Ed. (Engl.) 31, p. 1283 (1992).

Hirata, K.S., T. Kajita, K. Kifune, K. Kihara, M. Nakahata, K. Nakamura, S. Ohara, Y. Oyama, N. Sato, M. Takita, Y. Totsuka, and Y. Yaginuma, M. Mori, A. Suzuki, K. Takahashi, T. Tanimori, and M. Yamada, M. Koshiba, T. Suda, K. Miyano, H. Miyata, H. Takei, K. Kaneyuki, Y. Nagashima, and Y. Suzuki, E.W. Beier, L.R. Feldscher, E.D. Frank, W. Frati, S.B. Kim, A.K. Mann, F.M. Newcomer, R. Van Berg, and W. Zhang: Phys. Rev. Lett., 63, p. 16 (1989).

Hirata, K.S., K. Inoue, T. Kajita, T. Kifune, K. Kihara, M. Nakahata, K. Nakamura, S. Ohara, N. Sato, Y. Suzuki, Y. Totsuka, Y. Yaginuma, M. Mori, Y. Oyama, A. Suzuki, K. Takahashi, M. Yamada, M. Koshiba, T. Suda, T. Tajima, K. Miyano, H. Miyata, H. Takei, Y. Fukuda, E. Kodera, Y. Nagashima, M. Takita, K. Kaneyuki, T. Tanimori, E.W. Beier, L.R. Feldscher, E.D. Frank, W. Frati, S.B. Kim, A.K. Mann, F.M. Newcomer, R. Van Berg, and W. Zhang: Phys. Rev. Lett., 65, p. 1297 (1990a).

Hirata, K.S., K. Inoue, T. Kajita, T. Kifune, K. Kihara, M. Nakahata, K. Nakamura, S. Ohara, N. Sato, Y. Suzuki, Y. Totsuka, Y. Yaginuma, M. Mori, Y. Oyama, A. Suzuki, K. Takahashi, M. Yamada, M. Koshiba, T. Suda, T. Tajima, K. Miyano, H. Miyata, H. Takei, Y. Fukuda, E. Kodera, Y. Nagashima, M. Takita, K. Kaneyuki, T. Tanimori, E.W. Beier, L.R. Feldscher, E.D. Frank, W. Frati, S.B. Kim, A.K. Mann, F.M. Newcomer, R. Van Berg, and W. Zhang: Phys. Rev. Lett., 65, p. 1301 (1990b).

Hirata, K.S., K. Inoue, T. Kajita, K. Kihara, M. Nakahata, K. Nakamura, S. Ohara, N. Sato, Y. Suzuki, Y. Totsuka, Y. Yaginuma, M. Mori, Y. Oyama, A. Suzuki, K. Takahashi, M. Yamada, M. Koshiba, K. Nishijima, T, Suda, T. Tajima, K. Miyano, H. Miyata, H. Takei, Y. Fukuda, E. Kodera, Y. Nagashima, M. Takita, K. Kaneyuki, T. Tanimori, E.W. Beier, L.R. Feldscher, E.D. Frank, W. Frati, S,B. Kim, A.K. Mann, F.M. Newcomer, R. Van Berg, and W. Zhang: Phys. Rev. Lett, 66, p. 9 (1991a).

Hirata, K.S., K. Inoue, T. Ishida, T. Kajita, K. Kihara, M. Nakahata, K. Nakamura, S. Ohara, N. Sato, Y. Suzuki, Y. Totsuka, Y. Yaginuma, M. Mori, Y. Oyama, A. Suzuki, K. Takahashi, M. Yamada, M. Koshiba, K. Nishijima, T. Suda, T. Tajima, K. Miyano, H. Miyata, H. Takei, Y. Fukuda, E. Kodera, Y. Nagashima, M. Takita, K. Kaneyuki, T. Tanimori, E.W. Beier, L.R. Feldscher, E.D. Frank, W. Frati, S.B. Kim, A.K. Mann, F.M. Newcomer, R. Van Berg, and W. Zhang: Phys. Rev., D 44, p. 2241 (1991b).

ICARUS Collaboration: ICARUS II - A second generation proton decay experiment and neutrino observatory at Gran Sasso Laboratory. LNGS report - 94/99, vol. 1 (1994).

Kajita, Takaaki: Nucl. Phys. B (Proc. Suppl.) 85, p. 44 (2000).

Kirsten, T.: Proc. Internat. Symp. on Neutrino Astrophysics, Takayama, Japan. Frontiers of Neutrino Astrophysics, p. 83, Universal Academy Press, Inc., Tokyo, Japan. Y. Suzuki and K. Nakamura, ed. (1993).

Kirsten, T., F.X. Hartmann, R. Wink, and P. Anselmann: Nucl. Phys. B (Proc. Suppl.) 35, p. 418 (1994).

Kirsten, T.A.: Nucl. Phys. B (Proc. Suppl.) 77, p. 26 (1999).

Koshiba, M.: Physics Reports, 220, Nr. 5 & 6, p. 229 - 381 (1992).

Lande, K., B.T. Cleveland, R. Davis, Jr., J. Distel, P. Wildenhain, J. Abdurashitov, V.N. Gavrin, I. Mirmov, E. Veretenkin, V.E. Yants, and Yu.S. Khomyakov: Nucl. Phys. B (Proc. Suppl.) 77, p. 13 (1999).

Langacker, P.: Nucl. Phys. B (Proc. Suppl.) 77, p. 241 (1999).

Lanou, Robert E., Jr.: Nucl. Phys. B (Proc. Suppl.) 77, p. 241 (1999).

Maki, Ziro, Masami Nakagawa, and Shoichi Sakata: Progr. Theor. Phys., 28, p. 870 (1962).

McDonald, A.B.: Nucl. Phys. B (Proc. Suppl.) 77, p. 43 (1999).

Mikheyev, S.P., and A.Yu. Smirnov: Sov. J. Nucl. Phys., 42, p. 913 (1986a).

Mikheyev, S.P., and A.Yu. Smirnov: Sov. Phys. JETP, 64, p. 4 (1986b).

Mikheyev, S.P., and A.Yu. Smirnov: Nuovo Cimento, 9 C, p. 17 (1986c).

Mikheyev, S.P., and A.Yu. Smirnov: Proc. 12th Internat Conf. on Neutrino Physics and Astrophysics, Sendai, Japan, T. Kitagaki and H. Yuta ed. (Singapore: World Scientific), p. 1 (1986d).

Oberauer, L.: Nucl. Phys. B (Proc. Suppl.) 77, p. 48 (1999).

Pomansky,A.A: Nucl. Instr. Meth., B 17, p. 406 (1986).

Pomansky,A.A: Nucl. Instr. Meth., A 271, p. 254 (1988).

Pontecorvo, B.: Chalk River Report PD-205 (1946).

Pontecorvo, B.: Zh. Eksp. Theor. Fiz., 53, p. 1717 (1967).

Pontecorvo, B.: J.E.T.P., 26, (5), p. 984 (1968).

Smirnov, A.Yu.: Nucl. Phys. B (Proc. Suppl.) 77, p. 98 (1999).

Suzuki, Y.: Proc. Internat. Symp. on Neutrino Astrophysics, Takayama, Japan, 1992. Frontiers of Neutrino Astrophysics, p. 61, Universal Academy Press, Inc., Tokyo, Japan. Y. Suzuki, and K. Nakamura, ed. (1993).

Suzuki, Y.: Nucl. Phys. B (Proc. Suppl.) 35, p. 273 (1994).

Suzuki, Yoichiro: Nucl. Phys. B (Proc. Suppl.) 38, p. 54 (1995).

Suzuki, Y., Super-Kamiokande Collaboration: Nucl. Phys. B (Proc. Suppl.) 77, p. 35 (1999).

Turck-Chièze, S., S. Cahen, M. Cassé, and C. Doom: Astrophys. J., 335, p. 415 (1988).

Turck-Chièze, S.: Nucl. Phys. B 31, p. 129 (1993).

Turck-Chièze, S., and I. Lopes: Astrophys. J., 408, p. 347 (1993).

Vignoli, C., F. Arneodo, A. Badertscher, E. Barbieri, P Benetti, A. Bario di Tigliole, R. Brunetti, A. Bueno, E. Calligarich, M. Campanelli, F. Carli, C. Carpanese, D. Cavalli, F. Cavanna, P. Cennini, S. Centro, A. Cesana, C. Chen, Y. Chen, C. Cinquini, D. Cline, I. De Mitri, R. Dolfini, D. Favaretto, A. Ferrari, A. Gigli Berzolari, P. Goudsmit, K. He, X. Huang, Z. Li, F. Lu, J. Ma, G. Mannocchi, F. Mauri, D. Mazza, L. Mazzone, C. Montanari, G.P. Nurzia, S. Otwinowski, 0. Palamara, D. Pascoli, A. Pepato, L. Periale, S. Petrera, G. Piano-Mortari, A. Piazzoli, P. Picchi, F Pietropaolo, T. Rancati, A. Rappoldi, G.L. Raselli, D. Rebuzzi, J.P. Revol, J. Rico, M. Rossella, C. Rossi, A. Rubbia, C. Rubbia, P. Sala, D. Scannicchio, F. Sergiampietri, S. Suzuki, M. Terrani, S. Ventura, M. Verdecchia, H. Wang, J. Woo, G. Xu, Z. Xu, C. Zhang, Q. Zhang and S. Zheng, ICARUS Collaboration: Nucl. Phys. B (Proc. Suppl.) 85, p. 119 (2000).

Wolfendale, A.W., E.C.M. Young, and R. Davis, Jr.: Nature, Phys. Sci., 238, p. 130 (1972).

Wolfenstein, L.: Phys. Rev. D, 17, p. 2369 (1978).

Wolfenstein, L.: Phys. Rev. D, 20, p. 2634 (1979).

Wolfenstein, L.: Proc. 12th Internat Conf. on Neutrino Physics and Astrophysics, Sendai, Japan, T. Kitagaki and H. Yuta ed. (Singapore: World Scientific), p. 1 (1986).

Zatsepin, G.T, A.V. Koplylov, and E.K. Shirokova: Yad. Fiz., 33, p. 378 (1981).

Zatsepin, George: Proc. Internat. Symp. on Neutrino Astrophysics, Takayama, Japan. Frontiers of Neutrino Astrophysics, p. 71, Universal Academy Press, Inc., Tokyo, Japan. Y. Suzuki and K. Nakamura, ed. (1993).

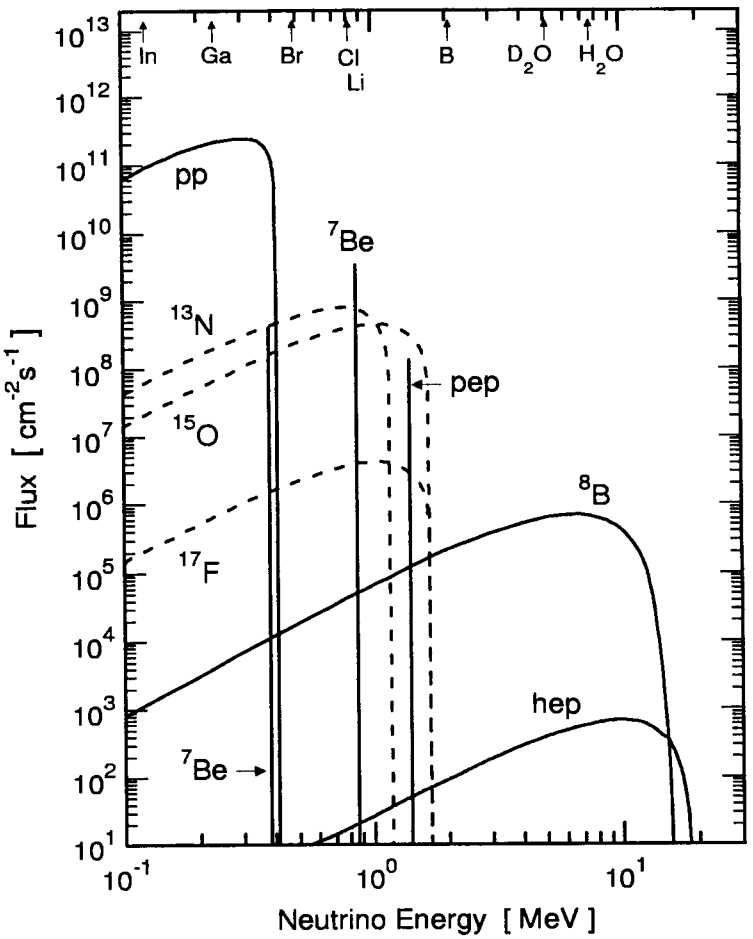

Figure 6.24: Solar neutrino energy spectra as predicted by the Standard Solar Model. Neutrino fluxes apply to a distance of 1 AU from the Sun. Line fluxes are given in number per cm^2 per s. Spectra from *pp* chain processes are drawn with solid lines, those from the CNO cycle in dotted lines (after Bahcall, 1989). The threshold energies for neutrino induced reactions with the elements listed at the top of the figure are indicated by arrows (Ga 0.233 MeV, Cl 0.814 MeV). The Cherenkov threshold in water for electrons ($\theta_{Ch} = 0°$) is 0.26 MeV. However, to reject detector noise and background Kamiokande used threshold levels of 7.0 MeV and higher and Super-Kamiokande of 6.5 MeV and higher.

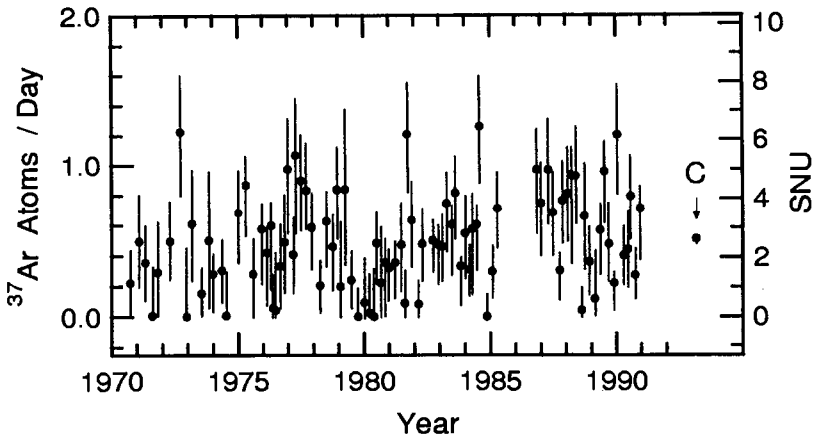

Figure 6.25: Summary of the Homestake results from 1970 to 1991. The combined ^{37}Ar production rate of all runs from 1970 to 1991 (small dots) is 0.509±0.031 atoms per day in 615 t of C_2Cl_4, corresponding to 2.28±0.23 SNU, (C), identified by arrow (Davis, 1993).

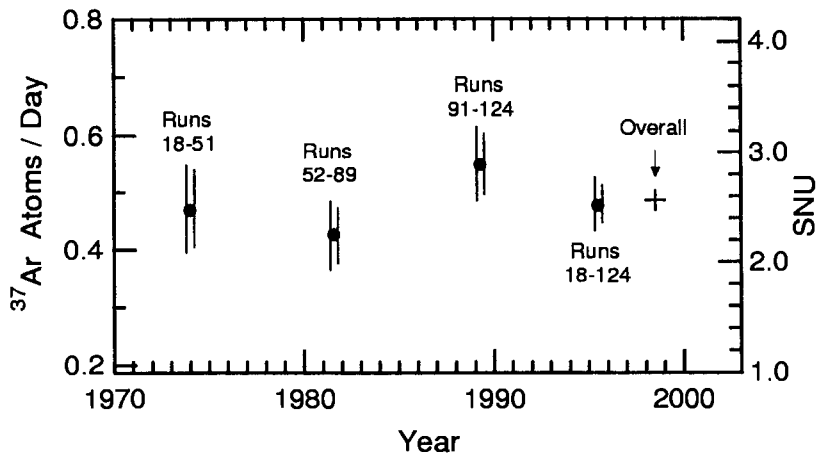

Figure 6.26: Time averaged ^{37}Ar production rate at Homestake as given in Table 6.5 covering the period from 1970 to 1993 (Cleveland et al., 1995), and on to 1998 (Lande (1999). The separate total of runs 18 to 124 is also indicated and the overall result (+). The two sets of error bars apply to two different energy windows for the 2.82 keV peak of the ^{37}Ar K-orbital capture; the larger errors are for FWHM, the smaller for 2 FWHM. In the latter case the overall rate up to 1993 is 2.52±0.23 SNU (Cleveland et al., 1995) and to 1998 it is 2.56±0.16 (Lande et al., 1999).

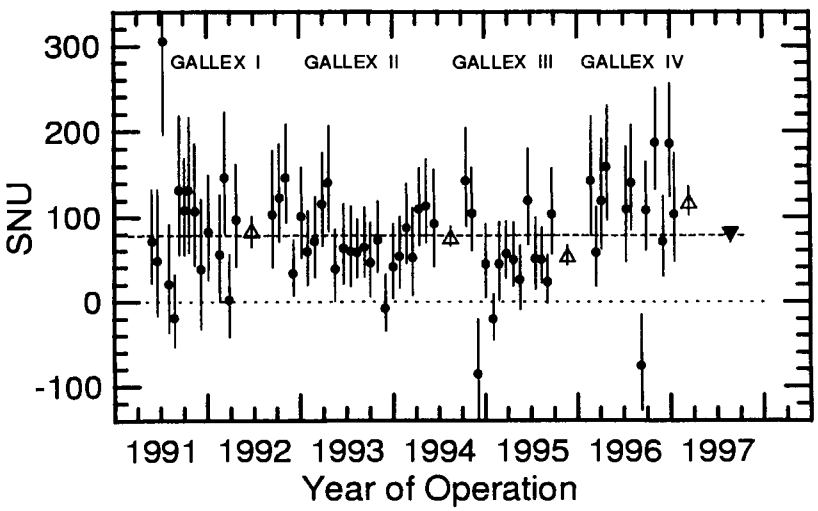

Figure 6.27: Overview of the ^{71}Ge production rate in the GALLEX detector, showing the net SNU production after subtraction of side reaction contributions. Error bars are $\pm 1\sigma$, statistical only. The symbols $\triangle$ indicate the average values for the four series of runs and $\blacktriangledown$ represents the mean global value for the total of all 65 runs. (Kirsten, 1999).

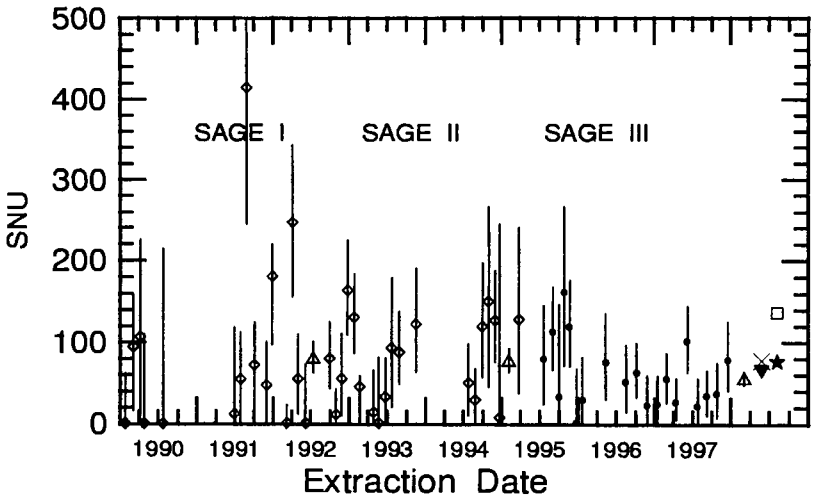

Figure 6.28: Best fit values and 1σ uncertainties for each SAGE run in the period from January 1990 to December 1997. Ten runs made between November 1993 and June 1994 are not included. The symbols $\triangle$ represent the combined results of the three experiments SAGE I, II and III, respectively, $\blacktriangledown$ is the result of the total exposure period, $\square$ indicates the SSM prediction of Bahcall (1994), and $\bigstar$ the theoretically possible minimum (Bahcall, 1997), after Abdurashitov et al. (1999). $\times$ shows the overall result of GALLEX (Kirsten, 1999).

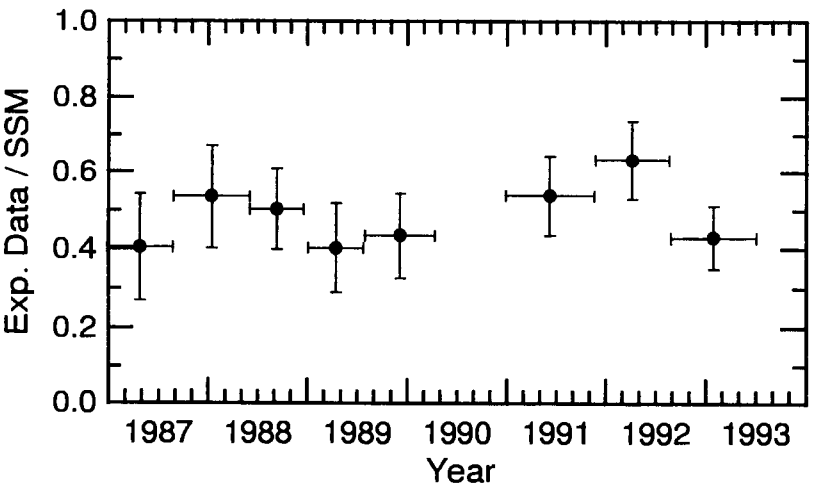

Figure 6.29: The 200-day plot of the ratio of experimental Kamiokande data to standard solar model predictions (Suzuki, 1995).

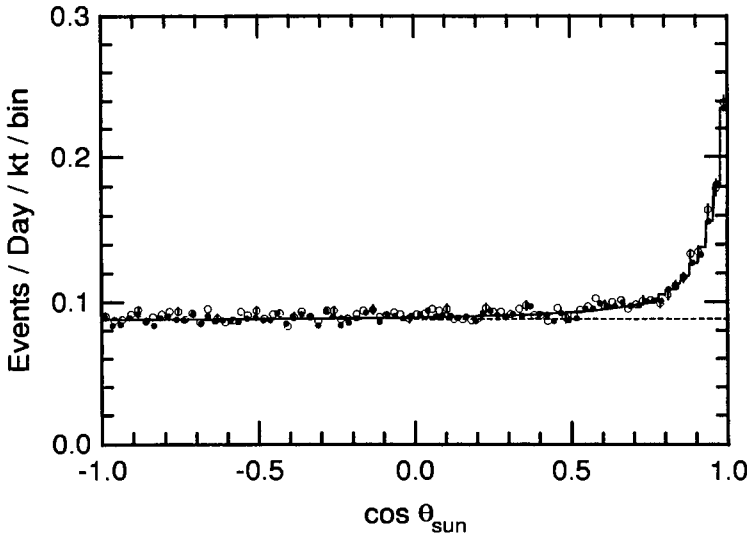

Figure 6.30: Angular distribution of the neutrino events in Super-Kamiokande. The strong peaking toward the Sun at $\cos(\theta_{Sun}) = 1.0$ is evident. θ_{Sun} is the event arrival angle with respect to the direction of the Sun. The two sets of data apply to the first 300 days (o) (Fukuda et al., 1998) and to the first 504 days of operation (•) (Suzuki, 1999).

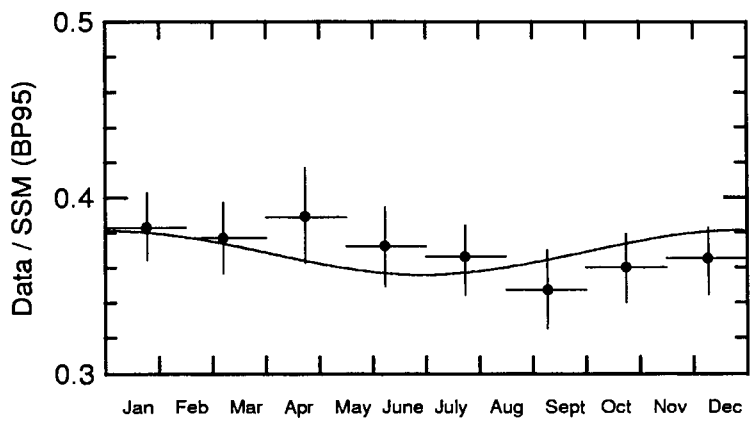

Figure 6.31: Solar neutrino flux presented in 1.5 months time intervals, recorded with the 22.5 kt Super-Kamiokande detector during 504 days, covering an energy window from 6.5 MeV to 20 MeV to investigate neutrino vacuum oscillations. The continuous curve shows the variation expected because of the eccentricity of the Earth's orbit (Suzuki, 1999).

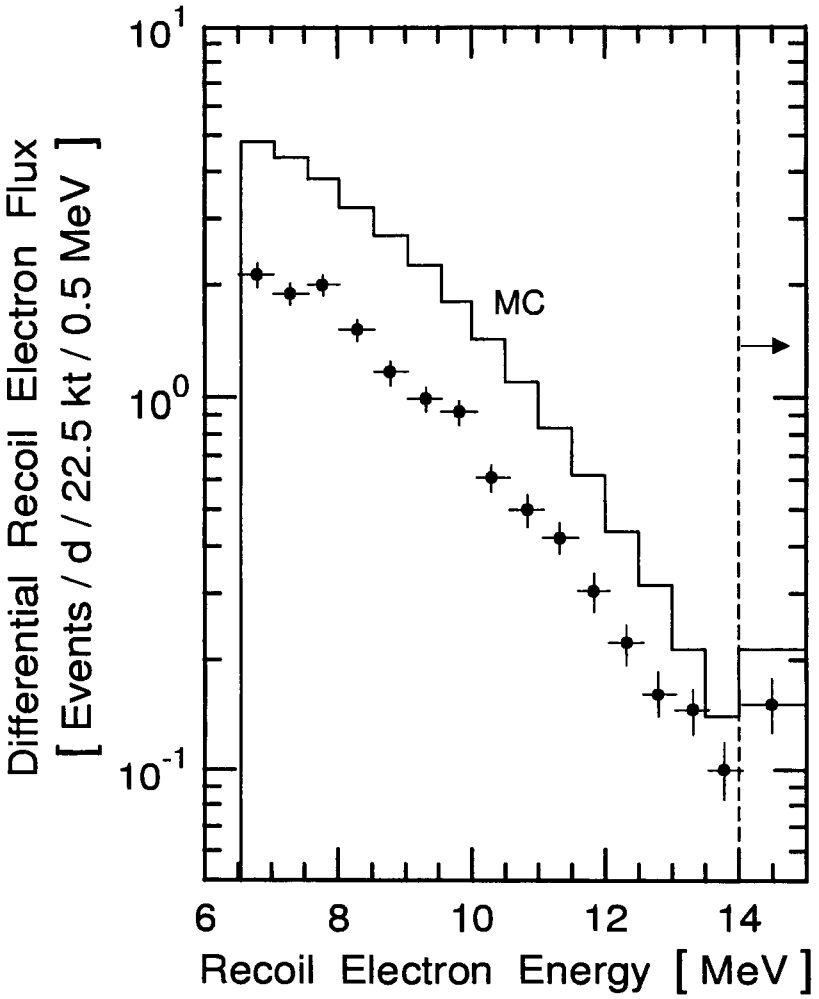

Figure 6.32: Measured recoil electron energy spectrum of solar neutrinos (•). The histogram (MC) shows the expectation from the SSM (Bahcall and Pinsonneault, 1998). The vertical error bars represent the total error (statistical and systematic) (Fukuda et al., 1999)

Chapter 7

Miscellaneous Topics

7.1 General Comments

In this chapter we present a variety of more or less stand-alone topics which, however, are closely linked to some specific aspects of cosmic ray physics. Some of the topics cannot be found easily in readily available cosmic ray literature because they may belong primarily to other disciplines of science. Additional and/or complementary data in tabulated or graphic form concerning specific topics not included here may be found in the Appendix.

7.2 Cosmogenic Nuclides

7.2.1 Introductory Comments

As a by-product of the interactions of the cosmic radiation in meteorites, in the Earth's atmosphere, the soil and in objects on the ground a wide variety of isotopes, both stable and radioactive, are produced in the respective bodies. These isotopes or nuclides are referred to as *cosmogenic nuclides.* Some of them are spallation or fragmentation products, others are the results of decay processes of nuclear reactions, or even neutron capture.

After production these isotopes may remain embedded in the host body as is the case for meteorites or they may be subject to transport if produced in the atmosphere and subsequently deposited in some archive, e.g., in tree rings, sediments, etc.. In Table 7.1 we present a list of cosmogenic nuclides, stable and radioactive, that are frequently found in meteorites together with their half-lives and the main parent targets. Likewise, in the first three columns of Table 7.2 we list the relevant isotopes that are produced in the

Table 7.1: Cosmogenic Nuclides Frequently Found in Meteorites (Caffee et al., 1988)

Nuclide	Half-life(*) [y]	Main Targets
^{3}H	12.3	O, Mg, Si, Fe
^{3}He, ^{4}He	S	O, Mg, Si, Fe
^{10}Be	$1.6 \cdot 10^{6}$	O, Mg, Si, Fe
^{14}C	5730	O, Mg, Si, Fe
^{20}Ne, ^{21}Ne, ^{12}Ne	S	Mg, Al, Si, Fe
^{22}Na	2.6	Mg, Al, Si, Fe
^{26}Al	$7.1 \cdot 10^{5}$	Si, Al, Fe
^{36}Cl	$3.0 \cdot 10^{5}$	Fe, Ca, K, Cl
^{36}Ar, ^{38}Ar	S	Fe, Ca, K
^{37}Ar	35 days	Fe, Ca, K
^{39}Ar	269	Fe. Ca, K
^{40}K	$1.3 \cdot 10^{9}$	Fe
^{39}K, ^{41}K	S	Fe
^{41}Ca	$1.0 \cdot 10^{5}$	Ca, Fe
^{46}Sc	84 days	Fe
^{48}V	16 days	Fe
^{53}Mn	$3.7 \cdot 10^{6}$	Fe
^{54}Mn	312 days	Fe
^{55}Fe	2.7	Fe
^{59}Ni	$7.6 \cdot 10^{4}$	Ni
^{60}Co	5.27	Co, Ni
^{81}Kr	$2.1 \cdot 10^{5}$	Rb, Sr, Zr
^{78}Kr, ^{80}Kr, ^{82}Kr, ^{83}Kr	S	Rb, Sr, Zr
^{129}I	$1.6 \cdot 10^{7}$	Te, Ba, La, Ce
$^{124-132}Xe$	S	Te, Ba, La, Ce, (I)

(*) S denotes that the nuclide is stable.

terrestrial atmosphere, including their half-lives and corresponding parent targets.

As mentioned in Section 6.3 many of these isotopes can be used either to determine the so-called exposure or radiation age of meteorites or the cosmic ray exposure age of terrestrial samples. In more sophisticated analyses one can gather information on the time variation of the cosmic ray intensity in the past. In the following we will very briefly consider the production of

Table 7.2: Cosmogenic Isotopes Produced in the Atmosphere. (Beer, 1997 and 2000b)

Cosmogenic Isotope	Half-life	Target Element	Production Rate(**) [Atoms $cm^{-2} s^{-1}$]	Global Inventory (estimated)
^{3}H(*)	12.3 y	N, O	0.2	3 kg
^{7}Be	53.4 d	N, O	0.06	20 g
^{10}Be	$1.5 \cdot 10^{6}$ y	N, O	0.03	200 tons
^{14}C(*)	5730 y	N	2	70 tons
^{26}Al	$7.3 \cdot 10^{5}$ y	Ar	0.000092	700 kg
^{32}Si	140 y	Ar	0.00025	0.5 kg
^{36}Cl(*)	$3 \cdot 10^{5}$ y	Ar	0.005	20 tons
^{129}I(*)	$1.6 \cdot 10^{7}$ y	Xe	0.000021	17 tons

(*) Isotopes that are also produced artificially. In addition, ^{129}I is a natural product of spontaneous fission of ^{238}U.

(**) Estimated mean global values in full atmospheric column.

cosmogenic nuclides in the atmosphere and in rock.

7.2.2 Cosmogenic Nuclides in the Atmosphere

Many authors have studied production, transport and natural archiving of cosmogenic nuclides. Pioneering work in this field initially based predominantly on experimental efforts was carried out by Lal and Peters (1967). Subsequently, with the availability of more accurate interaction and production cross sections mathematical models were constructed to compute more and more reliable production rates of cosmogenic nuclides in the atmosphere (Hess et al., 1961; Newkirk, 1963; Lingenfelter, 1963, Oeschger et al., 1969; Light et al., 1973; O'Brian, 1979; Blinov, 1988; Masarik and Reedy, 1995).

The production rate of cosmogenic nuclides of type i, P_i, at depth z can be expressed analytically as

$$P_i(z) = \sum_j N_j \sum_k \int_0^\infty \sigma_{ijk}(E_k J_k(E_k, z) dE_k \quad , \tag{7.1}$$

where N_j is the number of atoms of target element j per kilogram of sample material, e.g., the atmosphere, $\sigma_{ijk}(E_k)$ is the cross section for the production

of nuclei of type i from the target element j by particles of type k with energy E_k, and $J_k(E_k, z)$ is the total flux of particles of type k with energy E_k at location z inside the sample. The particle flux $J_k(E_k, z)$ is usually calculated with the help of a Monte Carlo simulation. In Table 7.2, columns 4 and 5, the estimated mean global production rates and the global inventory are listed (Beer, 1997).

The bulk of the galactic cosmic radiation that is responsible for the production of cosmogenic nuclides, i.e., the relatively intense but low energy component with energies <10 GeV/nucleon, is subject to solar modulation effects. Those are accounted for with the so-called *solar modulation parameter*, Φ, expressed in units of [MeV]. Castagnoli and Lal (1980) have derived an expression given below, that describes the flux of the dominating proton component of the galactic cosmic radiation, taking into account solar modulation.

$$J(E_p, \Phi) = C_p \left(\frac{E_p(E_p + 2m_pc^2)(E_p + x + \Phi)^{-2.5}}{(E_p + \Phi)(E_p + 2m_pc^2 + \Phi)} \right) \qquad (7.2)$$

Here $x = 780 \exp(-2.5 \cdot 10^{-4} E_p)$, E_p [MeV] is the kinetic energy of the protons, Φ [MeV] is the solar modulation parameter, m_pc^2 [MeV] is the rest mass energy of the proton (938 MeV), and $C_p = 1.244 \cdot 10^6$ cm^{-2}s^{-1}MeV^{-1} is the normalizing factor. Analogous formulas had been developed for primaries other than protons (Lal, 1988).

Very recently Masarik and Beer (1999) have introduced a new theoretical model for simulating the processes that are relevant for the production of cosmogenic nuclides in the atmosphere and carried out extensive Monte Carlo calculations. The latter are based on the CERN GEANT and the MCNP program packages to compute in a first step the nucleon flux in the atmosphere (protons and neutrons), from which they calculated the production rates of the various cosmogenic nuclides in the atmosphere. The atmospheric composition which the authors have used for their calculations (and for the soil in other calculations) are given in Table 7.3.

The calculations include solar modulation as well as geomagnetic latitude effects and data are available for all atmospheric depths. Some of the results of this work are given in Table 7.4 where the global average production rates of five isotopes in nine latitude intervals and the global averages are listed.

Additional data are presented in Figs. 7.1 to 7.6 where we show a selection of spectra and distributions from their vast work. Figures 7.1 and 7.2 show differential energy spectra of protons and neutrons at four different atmospheric depths ranging from 30 g/cm^2 to 990 g/cm^2 and geomagnetic

Table 7.3: Elemental Compositions Adopted for Calculations (Masarik and Beer, 1999)

Element	Weight Fraction	
	Soil	Atmosphere
H	0.002	-
N	-	0.755
0	0.473	0.232
Na	0.025	-
Mg	0.040	-
Al	0.060	-
Si	0.290	-
Ar	-	0.013
Ca	0.050	-
Fe	0.060	-

latitude ranges of $\lambda = 0° - 10°$ (equatorial region) and $\lambda = 80° - 90°$ (polar region), respectively. Comparison of the two figures reveals the influence of the geomagnetic effect. The integral proton and neutron fluxes as a function of atmospheric depth for the same two latitude ranges are plotted in Fig. 7.3. The spectra and distributions of these figures were obtained with a solar modulation parameter of 550 MeV.

For the production rates of cosmogenic nuclides we present two examples, ^{10}Be (Fig. 7.4) and ^{14}C (Fig. 7.5). These figures show the production rates per square centimeter and second in the full atmospheric column as a function of the solar modulation parameter, Φ, for nine geomagnetic latitude intervals from the equator to the poles of width 10°, and the global averages. The curves for ^{36}Cl, not shown, are very similar in shape to those of ^{10}Be, but the production rate is about a factor of ten lower. The dependence of the production rate per gram of air and second of ^{10}Be and ^{36}Cl as a function of depth in the atmosphere, for a solar modulation parameter of 550 MeV and nine intervals of latitude from the equator to the poles are illustrated in Fig. 7.6.

Table 7.4: Latitudinal and Global Average Production Rates of Cosmogenic Nuclides in the Earth's Atmosphere for Long-Term Mean Solar Activity and Modulation Factor $\Phi = 550$ MeV, for Present Geomagnetic Field Intensity (Masarik and Beer, 1999).

Nuclide	Production Rates [atoms $cm^{-2} s^{-1}$] in Atmospheric Column							
	Latitude [deg.]							Global
	0 - 10	10 - 20	20 - 30	30 - 40	40 - 50	50 - 60	60 - 90	Average
^{3}H	0.118	0.129	0.159	0.224	0.380	0.565	0.602	0.281
^{7}Be	0.0148	0.0161	0.0197	0.0285	0.0478	0.071	0.0740	0.0354
^{10}Be	0.00775	0.00841	0.0104	0.0147	0.0248	0.0368	0.0386	0.0184
^{14}C	0.83	0.90	1.10	1.56	2.63	3.92	4.55	2.02
^{36}Cl	0.000791	0.000860	0.00105	0.00151	0.00252	0.00375	0.00396	0.00188

7.2.3 Cosmogenic Nuclides in Rock

Similar work as discussed above for the atmosphere was also carried out for solids such as rock (e.g., Beer, 2000a). However, in comparison to cosmogenic nuclides produced in the atmosphere that are naturally stored as *differential records* in tree rings or sediments, cosmogenic nuclides produced in rocks are accumulated. Thus, such samples contain *integral records.* For rock and similar archives erosion and diffusion may play an important role and must be considered.

We can write for the concentration C of a radionuclide as a function of depth z and time t in rock (Beer, 2000a)

$$\frac{\partial C(z,t)}{\partial t} = P(z) + \epsilon \frac{\partial C(z,t)}{\partial z} - \lambda C(z,t) \tag{7.3}$$

with

$$P(z) = P_0 \cdot e^{-\frac{\rho z}{\Lambda}} \tag{7.4}$$

where $C(z,t)$ [atoms g^{-1}] is the isotope concentration, z [cm] the depth, t [s] the time, ϵ [cm My^{-1}] the erosion rate, λ [y^{-1}] the decay constant, $P(z)$ [atoms $g^{-1}y^{-1}$] the production rate at depth z, P_0 the production rate at the surface, ρ [$g\,cm^{-3}$] the rock density, and Λ [$g\,cm^{-2}$] the production attenuation length. Note that the production rate depends on altitude and geomagnetic latitude.

If the following conditions are fulfilled, the differential equation 7.3 can be solved analytically:

- The rock in which the isotope production takes place has to be a closed system, i.e., there should be no leakage in either direction, from the inside out, and vice versa.
- The production rate at the surface of the rock should be constant or have a known time dependence.
- The erosion rate should be constant or must follow a known time dependence.
- The production attenuation length should be constant and must be known.

The solution of eq. 7.3 has the form

$$C(t,z) = \frac{P_0}{(\rho\epsilon/\Lambda)+\lambda)} \cdot \left(e^{-\frac{\rho z}{\Lambda}}\right) \cdot \left(1 - e^{-(\frac{\rho\epsilon}{\Lambda}+\lambda)t}\right) + C_0 \cdot e^{-\lambda t} + \Sigma P_{other} \quad (7.5)$$

The first term describes the dependence of the concentration C as a function of depth z and time t, the second, C_0, represents the concentration which is initially present at the time the exposure starts, and P_{other} includes all contributions other than those due to cosmic rays.

Figure 7.7 illustrates two examples, one for ^{10}Be, the other for ^{26}Al production in quartz as a function of exposure time for assumed production rates of 1 and 6 atoms $g^{-1}\,y^{-1}$, respectively, and erosion rates of 0, 5 and 10 cm My^{-1} for either case. A useful graph for quick reference when carrying out practical measurements is presented in Fig. 7.8. There we have plotted the percentage of decayed atoms of radioactive substances as a function of the half-life for measuring periods of 1 day, 1 week, 1 month and 1 year, respectively.

References

Beer, J.: Proc. Internat. School of Physics, Enrico Fermi, Course CXXXIII, G. Cini Castagnoli and A. Provenzale, eds. IOS Press, Amsterdam (1997).

Beer, J.: Space Sci. Rev., in print (2000a).

Beer, J.: private communication (2000b).

Blinov, A.: in Secular Solar and Geomagnetic Variations in the last 10,000 Years, eds., F.R. Stephenson and A.W. Wolfendale, p. 329, Kluwer Acad., Norwell, Mass. (1988).

Caffee, M.W., J.N. Goswami, C.M. Hohenberg, K. Marti, and R.C. Reedy: in "Meteorites and the Early Solar System", John F. Kerridge and Mildred Shapley Matthews, eds.. The University of Arizona Press (1988).

Castagnoli, G.C., and D. Lal: Radiocarbon, 22, p. 133 (1980).

Hess, W.N., E.H. Canfield, and R.E. Lingenfelter: J. Geophys. Res., 66, p. 665 (1961).

Lal, D.: in Solar Terrestrial Relationships, eds., G.C. Castagnoli and D. Lal, Soc. Italiana di Fisica, Bologna, Italy, p. 216 (1988).

Lal, D., and B. Peters: in Handbuch der Physik (Springer-Verlag, Heidelberg, Germany), 46, p. 551 (1967).

Light, E.S., M. Merker, H.J. Vershell, R.B. Mendel, and S.A. Korff: J. Geophys. Res., 78, p. 2741 (1973).

Lingenfelter, R.E.: Rev. Geophys., L-35 (1963).

Masarik, J., and J. Beer: J. Geophys.Res., 104, No. D10, p. 12099 (1999).

Masarik, J., and R.C. Reedy: Geochim. Cosmochim. Acta, 58, p. 5307 (1995).

Newkirk, L.L.: J. Geophys. Res., 68, p. 1825 (1963).

O'Brian, K.: J. Geophys. Res., 84, p. 423 (1979).

Oeschger, H., J. Houtermans, H. Loosli, and M. Wahlen: in Radiocarbon Variations and Absolute Chronology, ed. I.U. Olsen. John Wiley, New York (1969).

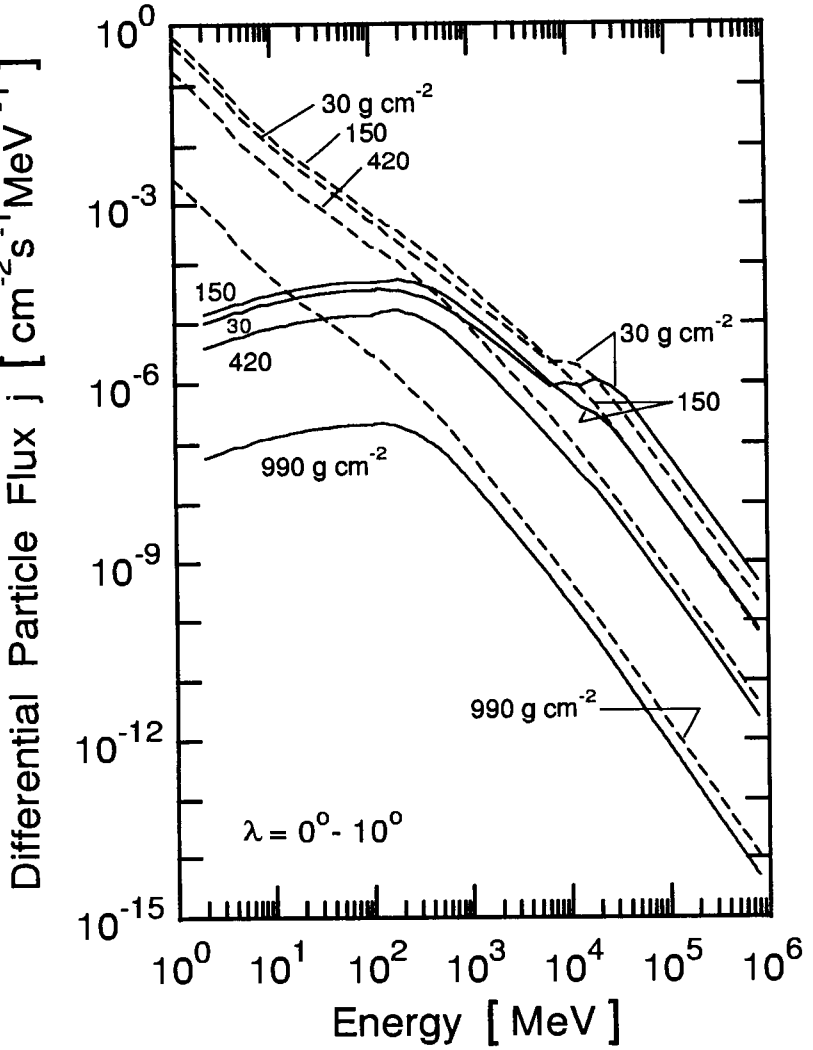

Figure 7.1: Differential proton (solid curves) and neutron (dashed curves) fluxes in the Earth's atmosphere at four depths (30, 150, 420 and 990 g/cm^2), for a solar modulation parameter of $\Phi = 550$ MeV and the geomagnetic latitude range $0° \leq \lambda \leq 10°$ (after Masarik and Beer, 1999).

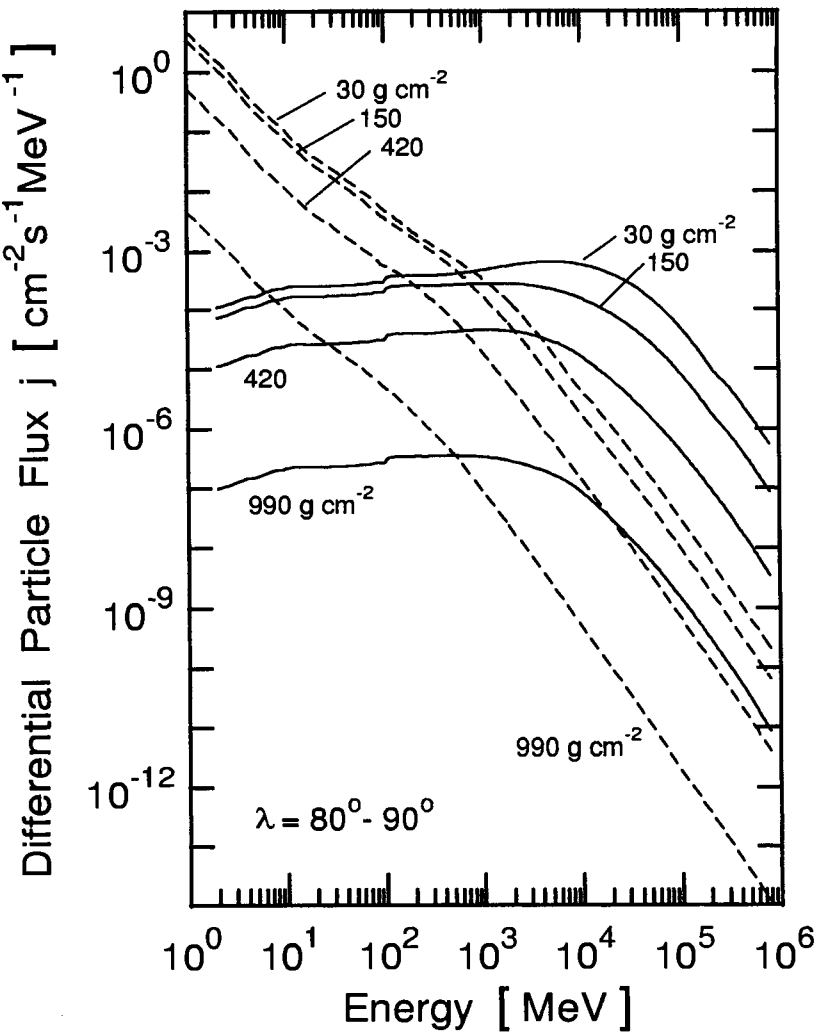

Figure 7.2: Differential proton (solid curves) and neutron (dashed curves) fluxes in the Earth's atmosphere at four depths (30, 150, 420 and 990 g/cm^2), for a solar modulation parameter of $\Phi = 550$ MeV and the geomagnetic latitude range $80° \leq \lambda \leq 90°$ (after Masarik and Beer, 1999).

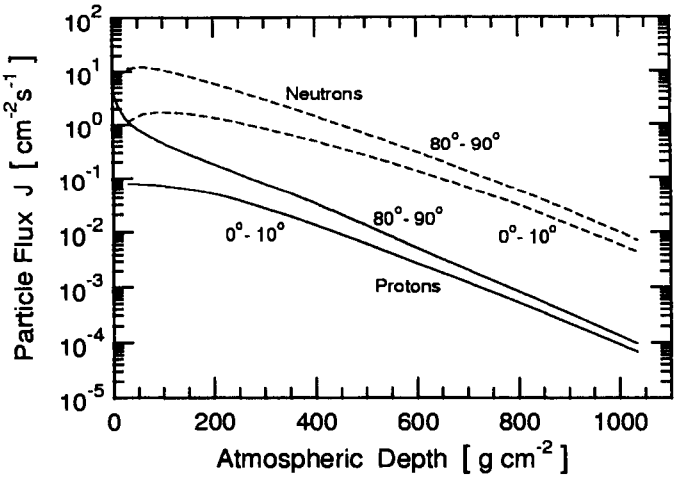

Figure 7.3: Integral proton (solid lines) and neutron (dashed lines) fluxes for energies > 1 MeV in the Earth's atmosphere, a solar modulation parameter of $\Phi = 550$ MeV and two latitude ranges, $0° \leq \lambda \leq 10°$ and $80° \leq \lambda \leq 90°$ (after Masarik and Beer, 1999).

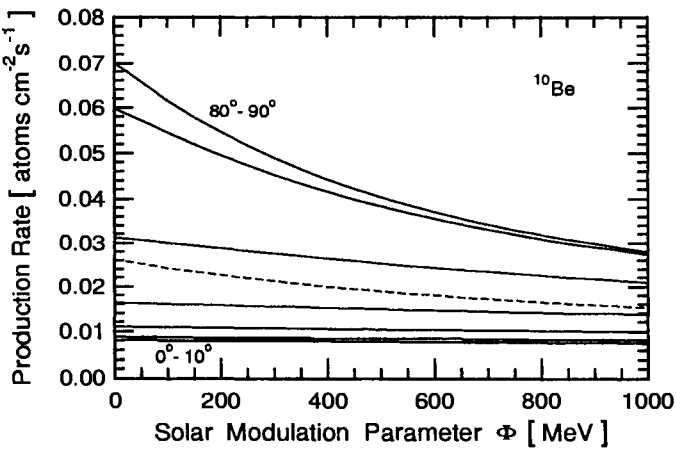

Figure 7.4: Dependence of the ^{10}Be production rate in the Earth's atmosphere on the solar modulation parameter, Φ. Each line represents a latitude interval of width 10°. Shown are the nine intervals that cover the full range, from the equator (0° to 10°) to the poles (80° to 90°) (after Masarik and Beer, 1999).

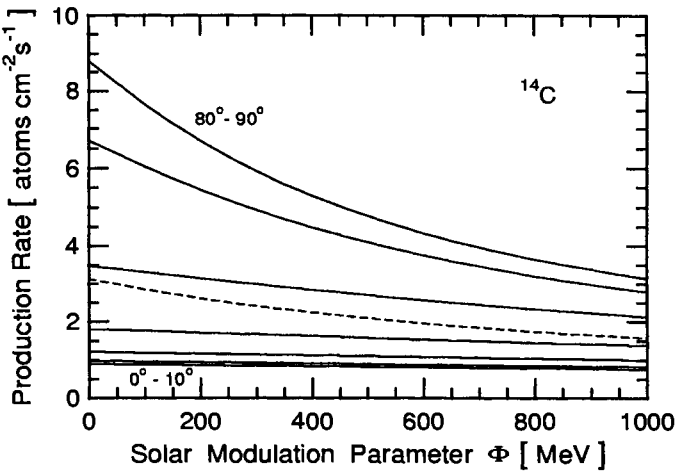

Figure 7.5: Dependence of the ^{14}C production rate in the Earth's atmosphere on the solar modulation parameter, Φ. Each line represents a latitude interval of width 10°. Shown are the nine intervals that cover the full range, from the equator (0° to 10°) to the poles (80° to 90°) (after Masarik and Beer, 1999).

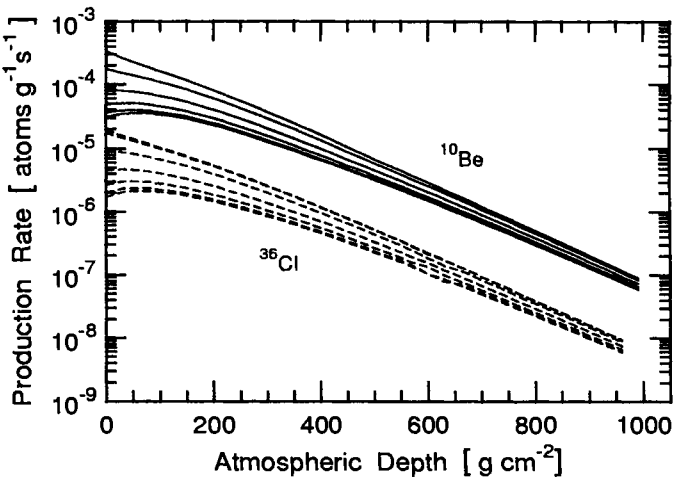

Figure 7.6: Depth dependent production rates of ^{10}Be (solid curves) and ^{36}Cl (dashed curves) in the Earth's atmosphere for a solar modulation parameter of $\Phi = 550$ MeV and nine geomagnetic latitude intervals of width 10°, from the equator to the pole (after Masarik and Beer, 1999).

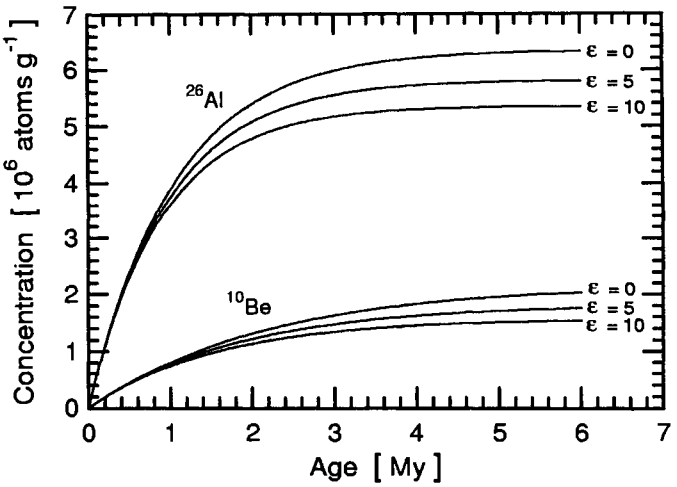

Figure 7.7: Concentration of the cosmogenic nuclides ^{10}Be and ^{26}Al in rock (quartz, SiO_2) at depth zero as a function of exposure time, assuming production rates of 1 atom $g^{-1}y^{-1}$ (^{10}Be) and 6 atoms $g^{-1}y^{-1}$ (^{26}Al), respectively, for three different erosion rates, ϵ [cm/My] (Beer, 2000).

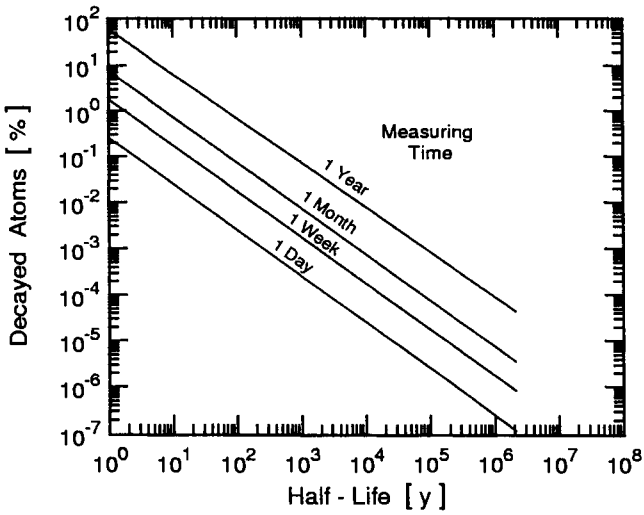

Figure 7.8: Percentage of decayed atoms as a function of half-life for four different measuring times (1 day, 1 week, 1 month and 1 year) (Beer, 1997).

7.3 Galactic and Intergalactic Magnetic Fields

7.3.1 Introduction

The magnetic fields that are present more or less everywhere in space affect the propagation of the cosmic radiation. Charged particles are deflected and follow curved trajectories. Consequently their arrival direction at detection cannot reveal the direction of the location of their source. In addition, apart from interactions of the cosmic radiation with the interstellar medium and the photons of the radiation field in space that degrade the energy of the primary hadronic component, cosmic ray electrons may lose energy via various electromagnetic processes, in particular via synchrotron radiation when propagating in magnetic fields.

The effects of the geomagnetic, the magnetospheric and the heliospheric magnetic fields are discussed in Chapter 6, Section 6.2 and will not be considered here. Some details concerning the geomagnetic cutoff and references related to this subject are presented in Chapter 1, Section 1.8.

7.3.2 Galactic Magnetic Fields

Our knowledge of the galactic magnetic field is very limited. Today we know that there exist two field components, a large-scale so-called regular field and many so-called small-scale irregular field regions with dimensions between about 10 pc and 100 pc. The latter have larger field strength than the regular field and are associated with galactic clouds.

The existence of the galactic magnetic field was deduced from the discovery of the linear polarization of starlight which is due to the alignment of dust grains in the magnetic field (Hall, 1949; Hiltner, 1949). Polarization alone permits to determine the direction of the field, but not the magnitude. An early attempt to estimate the magnetic field strength using gamma and X-ray intensities is discussed by Clark (1963).

More recently, on the basis of the theory of magnetic alignment proposed by Jones and Spitzer (1967), a field strength of 0.3 nT (3μG) is needed to explain the observed polarization. In a review Ellis and Axon (1978) estimated the direction of the regular field to point towards $l \simeq 45°$ within 500 pc, and beyond but within distances $\leq$2kpc towards $l \simeq 60°$ in our location. Other authors using the polarization method found for the direction of the regular field $l \simeq 70°$ (Mathewson and Milne, 1965), $l \simeq 60°$ (Berkhuijsen,

1971), and $l \simeq 45°$ (Spoelstra, 1984).

There are several indirect methods to determine the magnetic field strength in the Galaxy. Some are suitable for the large-scale regular field, others apply to the small irregular field regions. The well known Zeeman splitting method is a widely used technique, but it is applicable only to cloud regions of sufficiently high densities, emitting narrow lines.

The emissivity of the diffuse galactic synchrotron radiation produced by relativistic electrons gyrating in the galactic magnetic field together with the experimentally determined electron spectrum can be used to determine the large-scale magnetic field strength. Using this method Phillipps et al. (1981) obtained a total field strength of 0.4 nT (4μG), whereas Beuermann et al. (1985) deduced for different assumptions a field strength of 0.9 nT ($\simeq 9\mu$G).

The Faraday rotation method is considered by several authors to be one of the best to measure the galactic magnetic field and many have used pulsar rotation methods (Rand and Lyne, 1994). We briefly summarize the results of some authors that have used this method.

Manchester (1974) used pulsars that are located within <2 kpc from the Sun and obtained a field strength of $B_{reg} = 0.22 \pm 0.04$ nT ($2.2 \pm 0.4\,\mu$G) and direction of $l = 94 \pm 11°$ for the regular field. Thomson and Nelson (1980) found $B_{reg} = 0.35 \pm 0.03$ nT ($3.5 \pm 0.3\,\mu$G) and $l_0 = 74 \pm 10°$. In addition these authors found a field reversal toward the inner Galaxy at a distance of $D_{rev} \simeq 170 \pm 90$ pc. They also specify a range of values for the irregular field from $B_{irr} = 0.4$ nT to 1.4 nT ($4\,\mu$G to 14μG) for scale lengths of 10 pc to 100 pc.

Rand and Kulkarni (1989) derived a field strength of $B_{reg} = 0.16 \pm 0.02$ nT ($1.6 \pm 0.2\,\mu$G) and $l = 96 \pm 4°$ for a distance $D < 3$ kpc and a field reversal at $D_{rev} = 600 \pm 80$ pc toward the inner Galaxy, and for the irregular field $B_{irr} = 0.5$ nT ($5\,\mu$G). In their work, Chi and Wolfendale (1990) have restricted the analysis to distances $D < 1.4$ kpc to avoid the problem of the curvature of the spiral arms and likely large-scale irregularities. They obtained the following results: $B_{reg} = 0.10 \pm 0.04$ nT ($1.0 \pm 0.4\,\mu$G), $l = 80 \pm 19°$ in the outer Galaxy, and $B_{reg} = 0.32 \pm 0.1$ nT ($3.2 \pm 1.0\,\mu$G), $l = 57 \pm 14°$ and a field reversal at $D_{rev} = 190 \pm 90$ pc in the inner Galaxy.

Chi and Wolfendale (1990) conclude that the regular component of the local galactic field appears to be aligned along the local spiral arms with a reversal of the field direction in the interarm region, and that the regular field strength is stronger in the interarm region than in the arm region. Thus the large-scale structure of the galactic magnetic field can be represented by

a bisymmetric spiral. For the irregular field they specify a value of $B_{irr} = 0.6$ nT (6 μG).

In many studies a *typical average* value of 0.3 nT (3μG) is taken for the interstellar magnetic field strength in the *galactic disk* (thickness $\sim \pm 300$ to ± 500 pc from the galactic plane). Other authors consider 0.6 nT (6 μG) a more appropriate typical value near the Sun which decreases slowly with increasing radial distance from the galactic center (Beck et al., 1996). For the random fields in the Milky Way Ohno and Shibata (1993) specify 0.4 - 0.6 nT (4 - 6 μG). The field strength is generally assumed to decreases with increasing perpendicular distance from the galactic plane and is expected to have a value of 0.02 - 0.1 nT (0.2 - 1 μG) in the *halo* (Han and Qiao, 1994). These values must be considered with the necessary caution (For a review see Beck et al., 1996).

7.3.3 Intergalactic Magnetic Fields

The estimates of the magnetic field strength in intergalactic space are highly speculative and vary widely. Some authors use for trajectory estimates in their calculations of the Greisen - Zatsepin - Kuzmin (GZK) cosmic ray cutoff (Zatsepin, 1951; Greisen, 1966; Zatsepin and Kuzmin, 1966; Kuzmin and Zatsepin, 1968) values around 10^{-4} nT (1 nG) (Teshima, 1993). In their early work Ginzburg and Syrovatskii (1964) and Ginzburg (1969) estimated the field strength in intergalactic space to be approximately one to two orders of magnitude lower than the galactic field, i.e., <0.01 nT (< 0.1 μG), a value which in today's view appears to be rather high.

For their studies of topological defect models as a source of ultrahigh energy cosmic rays, intergalactic field strengths ranging from 10^{-7} nT (1 pG) to 10^{-4} nT (1 nG) are being considered (Sigl et al, 1997; Protheroe and Johnson, 1996; Protheroe and Stanev, 1996). There is evidence from indirect measurements that the magnetic field in the Virgo cluster is about 0.15 nT (1.5 μG) (Vallée 1990, 1991 and 1993). Across cosmological distances recent field strength estimates range from values as low as $\sim 2 \cdot 10^{-6}$ nT ($\sim$20 pG) to $\leq 10^{-4}$ nT ($\leq$1 nG) (Kronberg, 1994; Biermann, 1995; see also Biermann, 1997 for a brief summary).

7.3.4 Magnetic Fields of Astrophysical Objects

Magnetic fields in astrophysical objects and in different regions of the Universe vary widely. The respective field strengths are of great importance when discussing acceleration mechanisms of cosmic rays and aspects of mag-

netic confinement. In Fig. 7.9 we have reproduced an instructive plot from a summary of Hillas (1984) that we have slightly modified. Plotted is the magnetic field strength versus size (linear dimension) of a variety of astrophysical objects and regions of the Universe that are likely cosmic ray accelerators.

Shown, too, are two lines that represent the loci of twice the gyroradii, $2r_L$, (diameter of circle of gyration) of a proton and an iron nucleus, respectively, of energy 10^{20} eV over the range of magnetic field strength considered. The gyroradius, r_L, in units of [pc] of a relativistic particle of electric charge Z and energy E in units of [PeV] (10^{15} eV) in a magnetic field with a component normal to the velocity vector of strength B [μG] is given by the expression

$$r_L \;=\; 1.08\frac{E}{Z\cdot B} \quad [\mathrm{pc}]\,. \tag{7.6}$$

Objects plotted below the proton or iron lines would be unable to accelerate the respective particle to 10^{20} eV because of lack of sufficient confinement. Thus, only some neutron stars, AGNs, radio galaxies, galactic clusters and the intergalactic medium (IGM) enter into consideration for the acceleration of the most energetic cosmic rays.

References

Berkhuijsen, E.M.: Astron. Astrophys., 14, p. 359 (1971).

Beck, Rainer, Axel Brandenburg, David Moss, Anvar Shukurov, and Dmitry Sokoloff: Ann. Rev. Astron. Astrophys., 34, p. 155 (1996).

Beuermann, K., G. Kanbach, and E.M. Berkhuijsen: Astron. Astrophys., 153, p. 17 (1985).

Biermann, P.L.: Trends in Astroparticle Physics, ed. L. Bergström, P. Carlson, P.O. Hult, and H. Dnellman: Nucl. Phys., B (Proc. Suppl.) 43, p, 221 (1995).

Biermann, Peter, L.: J. Phys., G 23, p. 1 (1997).

Chi, X., and A.W. Wolfendale: J. Phys., G, 16, p. 1409 (1990).

Clark, G.W.: Nuovo Cimento, XXX, N. 3, p. 727 (1963).

Ellis, R.S., and D.J. Axon: Astrophys. Space Sci., 54, p. 425 (1978).

Ginzburg, V.L., and S.I. Syrovatskii: The Origin of Cosmic Rays. Oxford, Pergamon Press (1964).

Ginzburg, V.L.: The Astrophysics of Cosmic Rays, 2nd. ed., Jerusalem, Israel, Program for Scientific Transactions (1969).

Greisen, K.: Phys. Rev. Lett., 16, p. 748 (1966).

Hall, J.S.: Science, 109, p. 166 (1949).

Han, J.L., and G.J. Qiao: Astron. Astrophys., 288, p. 759 (1994).

Hillas, A.M.: Ann. Rev. Astron. Astrophys., 22, p. 425 (1984).

Hiltner, W.A.: Astrophys. J., 109, p. 471 (1949).

Jones, R.V., and L. Spitzer: Astrophys. J., 147, p. 943 (1967).

Kronberg, P.P.: Rep. Progr. Phys., 57, p. 325 (1994).

Kuzmin, V.A., and G.T. Zatsepin: Can. J. Phys., 46, p. S617 (1968).

Manchester, R.N.: Astrophys. J., 188, p. 637 (1974).

Mathewson, D.S., and D.K. Milne: Austr. J. Phys., 18, p. 635 (1965).

Ohno, H., and S. Shibata: MNRAS, 260, p. 953 (1993).

Phillipps, S., S. Kearsey, J.L. Osborne, C.G.T. Haslam, and H. Stoffel: Astron. Astrophys., 103, p. 405 (1981).

Rand, R.J., and S.R. Kulkarni: Astrophys. J., 343, p. 760 (1989).

Rand, R.J., and A.G. Lyne: MNRAS, 268, p. 497 (1994).

Spoelstra, T.A.T.: Astron. Astrophys., 135, p. 238 (1984).

Teshima, M.: PICRC, 5, p. 257 (1993).

Thomson, C.R., and A.H. Nelson: Mon. Not. R. Astr. Soc., 191, p. 863 (1980).

Vallée, J.P.: Astron. J., 99, p. 459 (1990).

Vallée, J.P.: Astron. Astrophys., 251, p. 411 (1991).

Vallée, J.P.: Mon. Not. R. Astron. Soc., 264, p. 665 (1993).

Zatsepin, G.T.: Dokl. Akad. Nauk SSSR, 80, p. 577 (1951).

Zatsepin, G.T. and V.A. Kuzmin: JETP Lett., 4, p. 78 (1966).

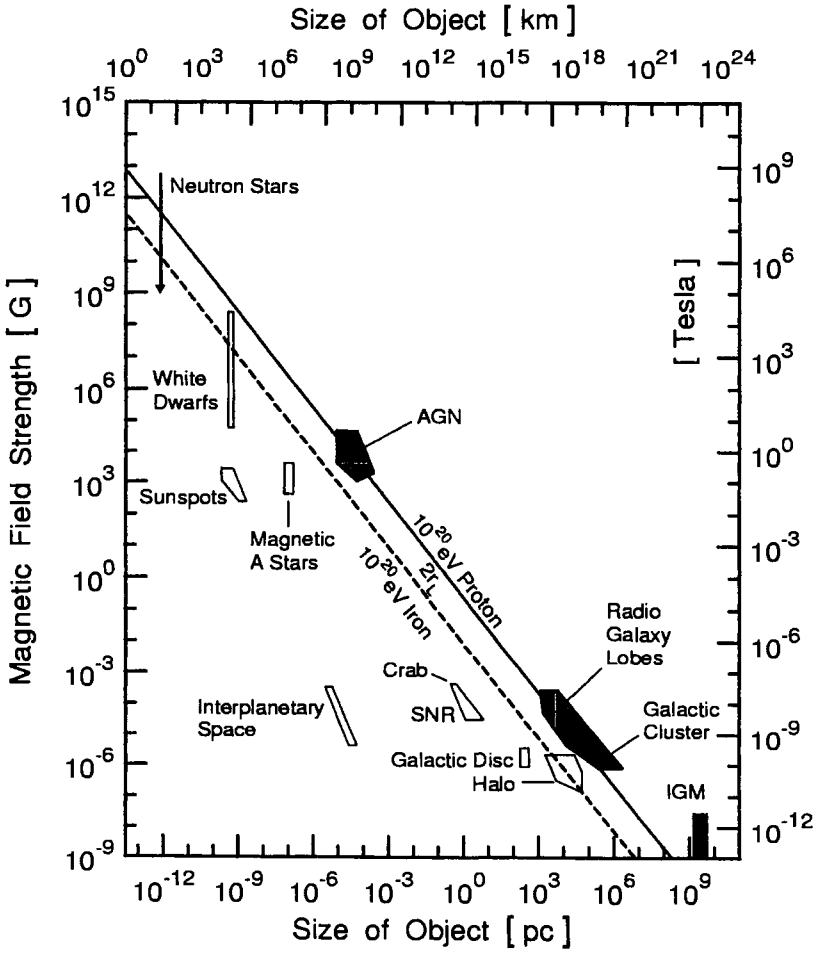

Figure 7.9: Size and magnetic field strength of likely objects and sites of ultrahigh energy cosmic ray acceleration (Hillas, 1984, modified). The solid and dashed lines represent the loci of twice the gyroradii, $2r_L$, of 10^{20} eV protons and iron nuclei, respectively, in the magnetic fields considered here. Only some neutron stars, active galactic nuclei (AGN), radio galaxies, galactic clusters and the intergalactic medium (IGM) are likely scenarios to accelerate cosmic rays to the highest energies observed.

7.4 Antarctic Atmosphere

7.4.1 General Comments

The antarctic atmosphere is significantly different from the standard atmosphere because of the extremely low temperature. It is therefore necessary to use a special parametrization of the barometer formula to determine the atmospheric overburden in order to calculate cosmic ray intensities or the development of extensive air showers. For very accurate work one must also distinguish between the four yearly seasons that cause marked differences in atmospheric properties.

7.4.2 Determination of Atmospheric Profile and Data

The Bartol and Leeds groups that operate SPASE, the South Pole Air Shower Experiment, located at the Pole at an altitude of 2834 m a.s.l. and having an overburden of 688 $\mathrm{g\,cm^{-2}}$ (mean value between days 168 and 220 of 1997), have carried out several sets of balloon flights during the mid Antarctic winter of 1997 to get atmospheric profiles (Hinton, 1999). They calculate the atmospheric overburden, $X(h,i)$, using five altitude zones, i, each with a different atmospheric scale height, $h_s(i)$, with the expression

$$X(h,i) = a(i) + b(i) \cdot \exp - \left(\frac{h}{h_s(i)}\right) \quad [\mathrm{g\,cm^{-2}}] \,, \tag{7.7}$$

where $a(i)$ and $b(i)$ are zone dependent parameters. The five zones and the parameters are defined in Table 7.5 below.

Table 7.5: Antarctic Atmosphere Data (J.A. Hinton).

Zone i	Altitude h [km]	Overburden X [$\mathrm{g\,cm^{-2}}$]	a(i) [$\mathrm{g\,cm^{-2}}$]	b(i) [$\mathrm{g\,cm^{-2}}$]	c(i) [m]
1	0.0 - 3.96	1079.5 - 582.6	146.66	932.8	5208
2	3.96 - 8.53	582.6 - 287.9	-110.33	1119.8	8255
3	8.53 - 17.68	287.9 - 59.73	-6.80	1182.0	6145
4	17.68 - 100.0	59.73 - 0.000017	0.00	1511.7	5472
5	100.0 - 10^{27}	Column Density (1.28 $\mathrm{mg\,cm^{-2}}$)			

With respect to zone 5, i.e. the top layer of the atmosphere, the author of Table 7.5 considers for his calculations the overburden to increase linearly from 0 $g\,cm^{-2}$ at 10^{27} km to a column density of 0.00128 $g\,cm^{-2}$ at altitude 100 km.

References

Hinton, Jim: Dept. of Physics, University of Leeds, GB, private communication (1999).

7.5 Optical and Related Properties of Water and Ice

7.5.1 General Comments

Water and ice are most transparent in the blue-green wavelength region. The transmissivities of these media are usually measured in the laboratory using samples from well defined locations in the water or ice body under investigation (geographic coordinates and depth). Such measurements are made with a so-called *monochromator*. This instrument consists of a light source of given wavelength, producing a highly collimated well defined beam of light that is aimed at a column of given length (usually 1 meter) containing the medium under test, and a photometric detector that measures the light intensity at the column exit. Measurements made with such an instrument are referred to as *good geometry* measurements. They are important for establishing the fundamental optical properties of the media and for characterizing their image forming characteristics.

Both scattering and absorption reduce the light flux that reaches the detector. In ocean water scattering of blue-green light is sharply peaked in the forward direction. Generally speaking, in clean water 97% of all photons are propagated within a half-cone of 5° (Jerlov, 1968). Under such conditions good geometry measurements show that the scattering coefficient amounts to only about 10% of the attenuation coefficient.

With an instrument that has a small acceptance geometry and a base length of about one meter, most of the scattered light is lost (Khanaev and Kuleshov, 1992). Because of the long attenuation length of clear water a much longer base line is desirable to obtain accurate results, such that in-situ measurements become necessary. Another option to improve short base

line measurements would be to use light of longer wavelength, where the attenuation is stronger, and then convert the result to the shorter wavelength.

In-situ measurements are usually more difficult and require more elaborate instruments. This is particularly so for measurements made in the open ocean. There special support equipment is required on board the ships and, for accurate measurements, ships need *dynamical positioning* and possibly *wave motion compensation systems*, as had been used for the DUMAND prototype system tests (Babson et al., 1990). Both are extremely costly. Frequently large acceptance *poor geometry* instruments are used for this task in clear water that determine the transmission length (or transmission distance) rather than the attenuation length (Bradner and Blackington 1984; Anassontzis et al. 1992). The former is a more realistic parameter than the attenuation length when dealing with large surface poor geometry detectors, as discussed below, because the measurement accepts photons, originally lost by scattering, that are back scattered into the beam and recorded by the detector, a situation that applies to the large underwater and under ice Cherenkov detector matrices.

7.5.2 Definitions

In the following we will briefly define frequently used terms.

Attenuation is the sum of two processes, *absorption* and *scattering* . Both are wavelength dependent. Attenuation can be expressed by the *attenuation coefficient*, $\epsilon(\lambda)$ [m^{-1}], or the *attenuation length* , $L_{att}(\lambda)$ [m]. Since the scattering coefficient in clean ocean water is much smaller than the absorption coefficient, attenuation of light from a monochromatic point source in such a medium can be considered to be exponential.

The attenuation coefficient, ϵ, is defined as

$$\epsilon = \left(\frac{1}{L_L - L_S}\right) \cdot \ln\left(\frac{I_S - I_0}{I_L - I_0}\right) \quad [m^{-1}] \,. \tag{7.8}$$

L_S and L_L are the distances of the near and far positions, respectively, of the detector from the light source, or the lengths of the two measuring cells or columns containing the water sample. I_S and I_L are the light intensities at the near and far detector positions, measured from the source, and I_0 is the background or noise intensity. The concept of attenuation is used in good geometry measurements where a well collimated narrow beam of light is used and scattered light is lost, i.e., does not enter the detector.

The attenuation length is the reciprocal of the attenuation coefficient and is expressed in meters. It is used in measurements with well collimated light beams.

Absorption is due to interaction of the photons with the atomic electrons of the molecules of the medium, whereby the photons are removed from the total flux of light. Suspended particles cause chiefly scattering but may also contribute to absorption. It can be expressed by the *absorption coefficient* , $\kappa(\lambda)$ [m^{-1}], or the *absorption length* , $L_{abs}(\lambda)$ [m] . Absorption is defined analogous to attenuation.

Scattering of light is the redistribution of light without loss of intensity. It is due to small particles. In water the wavelength dependence of scattering is proportional to λ^{ν} where λ is the wavelength and ν depends on the particle size. For large particles (> 1 μm) ν is of the order of 0.3, whereas for smaller particles (< 1 μm) ν is about 1.7 to 2.0. Scattering can be expressed by the *scattering coefficient*, $\sigma(\lambda)$ [m^{-1}], or the *scattering length*, $L_{scat}(\lambda)$ [m]. The standard procedure to determine scattering is done with the *nephelometer.* This instrument measures the amount of light that is scattered out of a test beam at an angle of 90° by particles suspended in the medium under investigation.

The scattering coefficient can be represented by the following expression.

$$\sigma = 2\pi \int_0^{\pi} \beta(\theta)\, sin(\theta)\, d\theta \tag{7.9}$$

where

$$\beta = dI(\theta)/E\, dV \tag{7.10}$$

and dI is the intensity emanating from a volume element dV when illuminated by *irradiance* E.

Transmission length, $L_{trans}(\lambda)$ [m], is defined as the distance in a medium after which the light intensity I falls to the (1/e)-th value. Some authors use the term *transmission distance* in place of transmission length to avoid confusion with the attenuation length.

The light intensity recorded by a detector in a transmission measurement includes photons that are backscattered into the test beam after having been scattered out of it before. Transmission length or distance is commonly used for poor geometry (wide beam) measurements where the attenuation of light can be assumed to decrease exponentially (Jerlov, 1968). Frequently isotropically emitting light sources are used for transmission measurements.

The calculation of the transmission length in a medium is based on the comparison of the light intensities, I_S and I_L, at two different distances from the light source, L_S and L_L, respectively. Neglecting background, the following relation is valid for the transmission length.

$$L_{trans} = \frac{L_L - L_S}{\ln\left(\frac{L_S^2 \cdot I_S}{L_L^2 \cdot I_L}\right)} \quad [\mathrm{m}] \,. \tag{7.11}$$

The symbols have the same meaning as defined before for attenuation.

Transmittance, T [%], is the percentage of light that reaches a detector after having traversed a column of water of length 1 m.

Detailed studies on the generation and propagation of Cherenkov light in water resulting from the relativistic motion of charged particles had been carried out by many authors (Roberts 1979a and 1979b; Bugaev et al., 1986). A *standard ocean* mostly tailored for the DUMAND site (Hawaii) was defined by Bradner (1979). Details concerning the propagation of Cherenkov light in ice, including bubbly ice, had been investigated by Askebjer et al. (1995) and Tilav et al. (1995). In the following we summarize the essential data and relations that are relevant for optical Cherenkov detectors in water and ice.

7.5.3 Depth Profiles of Ocean Parameters

Apart from ocean currents that are of interest at all depths for the deployment, installation and successful operation of a detector array on the ocean floor, the water transparency (or optical attenuation) is of primary concern when operating a Cherenkov detector matrix in this medium. Additional parameters may be essential, particularly when working in the ocean, to operate sonar systems that are needed to determine the exact location of modules of non-rigid arrays. Consequently, extensive environmental investigations have to be carried out and had been carried out at prospective sites of giant future arrays prior to installation. We give here only a very brief summary of the results obtained from this work that is relevant in the context of this volume.

Figures 7.10 and 7.11 are summary plots showing the depth profiles of some of the most relevant data of two ocean sites. Figure 7.10 shows the depth profiles of the temperature, density, salinity and optical transmission at the most favorable wavelength (approx. 480 nm) in the Pacific ocean, at the DUMAND Keahole Point site, about 30 km off-shore west of Kailua Kona, Hawaii (Harvey et al., 1978 and 1979; Zaneveld, 1981). A similar set

of measurements made at the NESTOR site in the Mediterranean near Pylos, Greece, is illustrated in Fig. 7.11, showing also the depth dependence of the velocity of sound (Anassontzis et al., 1993b). Additional depth profiles of the optical attenuation are given below.

7.5.4 Optical Attenuation in Water and Ice

In order to assess the relative clarity of a given water sample, one needs a reference point. Pure water would be the ideal reference. Unfortunately, attenuation values for pure water are not very well known. For reasons of comparison , however, we list in Table 7.6 the transmittance, T, the attenuation coefficient, ϵ, and the scattering coefficient, σ, obtained by Clarke and James (1939), Sullivan (1963), and Morel (1973) over a broad wavelength window.

Exploratory measurements at various sites around the world had been carried out by several groups that are interested in the construction of large deep ocean Cherenkov detector matrices for cosmic ray, astrophysics and particle physics research, and neutrino astronomy. A great wealth of additional information is also available form oceanographic research projects that are, however, not specifically related to one of the prospective detector sites mentioned earlier. In the following we present exclusively data from locations where Cherenkov arrays are planned and measurements with prototypes had been performed. The data are ordered according to the medium in which the measurements were made, i.e., fresh water, sea water and ice.

It is important to note that for poor geometry detector arrays, i.e., arrays that use typically large surface detector modules, such as the Baikal, DUMAND, NESTOR and all the newer similar array projects that are embedded in an environment of clean water, the main process that is responsible for the attenuation of light is absorption. Scattering in such a medium is strongly peaked in the forward direction such that most of the scattered photons of a well collimated test beam of light, directed at one of the modules, are collected. For situations as encountered under these conditions it is therefore often more practical to use transmission length rather than attenuation length as common optical key parameter (c.f. Fig. 7.10).

In ice the situation is different because of the possibility of the presence of small air bubbles, layers of dust particles, particular molecules such as hydrates of H_2, O_2 or air, or of crystalline and other structures that may have special optical properties that may provoke heavy scattering. At shallower depth in ice ($\leq$500 m) it is known that the density of air bubbles can be very large and their size may be such that scattering is totally dominating.

Table 7.6: Measured Optical Parameters of Pure Water

Wavelength [nm]	T [% /m]		ϵ [m^{-1}]		σ [m^{-1}]
	1)	2)	1)	2)	3)
375	95.6		0.045		0.00768
400	95.8		0.043		0.00581
425	96.8		0.033		0.00447
450	98.1		0.019		0.00349
475	98.2		0.018		0.00276
500	96.5		0.036		0.00222
525	96.0		0.041		0.00179
550	93.3		0.069		0.00149
575	91.3	89.7*	0.091	0.109*	0.00125
600	83.3	75.2	0.186	0.272	0.00109
625	79.6	73.7	0.228	0.305	
650	75.0	70.4	0.288	0.351	
675	69.3	64.5	0.367	0.438	
700	60.7	52.3	0.500	0.648	
725	29.	17.	1.24	1.75	
750	9.	7.	2.40	2.68	
775	9.	7.	2.40	2.63	
800	18.		2.05		

* Measurement at 580 nm. 1) Clarke and James (1939); 2) Sullivan (1963); 3) Morel (1973).

Under such conditions track reconstruction of charged particles based on the emission of Cherenkov light becomes impossible.

Optical Attenuation in Fresh Water

Detailed measurements of the absorption coefficient κ and the scattering coefficient σ over the wavelength window from 350 nm to 600 nm in fresh

water were made by the Lake Baikal collaboration at a depth of 1000 m at the detector site, located about 4.5 km from shore, where the maximum depth of the lake is 1370 m (Belolaptikov et al., 1991). The results are shown in Fig. 7.12.

More recent data of the attenuation length from the same site taken at different times of the year are illustrated in Fig. 7.13 (Belolaptikov et al., 1993a). The surveys were made over several years and illustrate significant variations, resulting from the major seasonal variations to which the lake and its environment are subjected (see also Sherstyankin, 1980).

Optical Attenuation in Sea Water

The ocean at the DUMAND site in the Pacific is up to date the most extensively studied environment of a prospective detector site. The ocean parameters had been monitored sporadically over a period of many years (Harvey et al., 1979; Zaneveld, 1981; Smith and Baker, 1981; Bradner and Blackington, 1981 and 1984; Aoki et al., 1985 and 1986; Babson et al., 1990). They cover the wavelength window from 350 nm to 550 nm. No seasonal changes were observed. The results of this work are shown in Fig. 7.14. In addition the depth profiles of the attenuation length at four different wavelengths, namely 400 nm, 450 nm, 500 nm and 550 nm, were also determined at this site (Fig. 7.15).

Likewise, several in-situ measurements of the water transparency were made at the NESTOR site near Pylos, Greece, in the Mediterranean down to depths of almost 4000 m, employing a large acceptance instrument (Karabashev and Kuleshov, 1988; Anassontzis et al., 1992; Khanaev and Kuleshov, 1992). This work yields a mean transmission length at depths between 1000 m and 3650 m of $L_{trans} = 55 \pm 10$ m at 480 nm, as shown in Fig. 7.16. Detailed values for different depths in the wavelength window from 310 nm to 610 nm are illustrated in Fig. 7.17, and tabulated in Table 7.7.

In addition numerous water samples were collected at different depths and attenuation measurements were made in the laboratory, using a tight acceptance instrument (Anassontzis et al., 1993b). From this work attenuation coefficients of $0.025 \leq \epsilon \leq 0.04$ m^{-1} were obtained. Based on the assumption that the ratio $\Lambda = \sigma/\epsilon \simeq 0.5$, where σ and ϵ are the scattering and attenuation coefficients as defined above, an absorption length of $L_{abs} = 67 \pm 8$ m was obtained. These data are in agreement with earlier measurements by Shifrin (1983). Anassontzis et al. (1992) also note that the transparency below 1500 m seems to be uniform at all locations in the area.

Table 7.7: Transmission Length, L_{trans}, at Different Depths in the Mediterranean (Anassontzis et al., 1992).

Site	Sea Floor [m]	Depth [m]	L_{trans} [m]
a	3727	200	40 ± 8
		1000	52 ± 11
		2000	52 ± 11
		3000	52 ± 11
		3500	52 ± 10
		3650	54 ± 10
b	4160	1000	52 ± 10
		3500	55 ± 17
		3900	62 ± 21
c	3600	100	36 ± 6
		1000	58 ± 13
		2000	45 ± 8
		3000	46 ± 7
		3500	52 ± 5

Optical Attenuation in Ice

The optical attenuation of light in bubble-free laboratory ice was studied by Warren (1984). He found for the attenuation length a value of ~25 m at 470 nm. In-situ measurements in Greenland ice at a depth of 217 m made by the AMANDA (Antarctic Muon And Neutrino Detector Array) collaboration yielded an attenuation length of ~18 m (Lowder et al., 1991a and 1991b; Barwick et al., 1992). This work was continued at different depths in the Antarctic ice cap at the South Pole by the same collaboration (Askebjer et al., 1995). Early measurements at this site indicated that at shallower depth, around 800 m ($\simeq$ 700 m w.e.) from the surface, the attenuation length was unexpected long. However, the fast rising leading edge of the laser light pulse at the source had a poor rise time, an excessive delay and a long exponentially decaying tail at the detector after traversing many meters of ice, making it impossible to reconstruct muon trajectories. At greater depth the situation is better.

It was then recognized that this was due to unexpected frequent scattering of the photons from the light source on numerous tiny air bubbles enclosed

in the ice (Askebjer et al., 1995). This came as a surprise since core samples from other sites at the Antarctic indicated that the existence of bubbles in ice should cease to exist at depths greater than ~500 m. The mean size of the bubbles was on the order of 100 μm and their separation millimeters. It was found that with increasing depth the bubble density was decreasing and improved temporal properties were obtained.

The scattering length depends on bubble density, bubble size and shape. For spherical bubbles the scattering length can be expressed as

$$L_{scat} = \frac{1}{n_{bub} \cdot < \pi r^2 >_{bub}} \tag{7.12}$$

where n_{bub} is the number density of bubbles and $< \pi r^2 >_{bub}$ is their average geometrical cross section. Dust particles typically have radii that are 1/10 to 1/100 that of air bubbles.

Askebjer et al. (1995) show that the propagation of Cherenkov photons in bubbly ice is well described by random walk with absorption and can be expressed by

$$u(d,t) = \left(\frac{1}{(4\pi Dt)^{3/2}} e^{-\frac{d^2}{4Dt}} \right) e^{-\frac{c_i t}{L_{abs}}} . \tag{7.13}$$

$D \simeq 4L_{scat}c_i/3$, $c_i = c/n_{ice}$, c being the velocity of light, n_{ice} the index of refraction of ice, L_{scat} the scattering length, and L_{abs} the absorption length.

These authors conclude that there is a direct relation between the fall time of the pulse of late photons at the detector and the absorption length (see also Tilav et al., 1995). The results of this work and of the studies by Price et al. (1995) are given in Figs. 7.18 and 7.19 which show the inverse scattering length, $1/L_{scat}$, and the absorption length, L_{abs}, respectively, as a function of depth in ice at the South Pole.

Subsequent measurements made at depths between 810 m and 1000 m in the ice at the same site at wavelengths of 410 nm, 415 nm, 420 nm, 435 nm, 450 nm, 475 nm, 500 nm, 550 nm, 590 nm, and 610 nm confirmed the long absorption length of $\sim$ 215 m at 400 nm, a value of 59$\pm$3 m at 515 nm and the rapid fall with increasing wavelength, reaching ~10 m at 610 nm. Likewise, the relatively short scattering length of ~0.1 m at 800 m with increasing tendency toward greater depth was also confirmed (Erlandsson et al., 1995). The results of this work are presented in Figs. 7.20 and 7.21, respectively. In another study Tilav et al. (1995) obtain for the maximum

absorption length in the depth range 800 m $\leq z \leq$ 1000 m about 300 m at wavelength 400 nm.

Additional studies of chemical and optical properties of polar ice , with the aim to identify the different causes for scattering were made by Price (1995) and Price et al. (1995). These authors come to the conclusion that at depths between 1500 m and 2000 m the scattering length, L_{scat} is controlled by dust, ice bifringence, and air hydrate crystals. Moreover, scattering by insoluble dust is forward-peaked ($< \cos(\theta) > \simeq 0.9$), and L_{scat}(dust) is shortest ($\sim$15 m) at a depth of approximately 1700$\pm$50 m, and 40 m to 60 m at other depths. Small angle scattering at air hydrate crystals may be of some concern but Rayleigh scattering seems to be negligible. In an earlier analysis Miller (1969) determined the relation between temperature, pressure, depth and the dissociation pressure of N_2, O_2 and air hydrated in ice (Fig. 7.22).

7.5.5 Optical Background in Water and Ice

The level of optical background in a medium intended to be used as Cherenkov radiator for the reconstruction of charged particle trajectories is together with the optical attenuation or transmission length of prime importance. Comprehensive investigation were carried out by the Baikal, DUMAND and AMANDA collaborations. Other teams have also made valuable contributions to this field. In the following we present a summary of this work.

Optical Background in Fresh Water

Data on the optical background in Lake Baikal were obtained by Belolaptikov et al. (1991). Since no ^{40}K is present in the lake the background is probably due mostly to a mixture of *bioluminescence* and chemoluminescence, and is subject to significant seasonal and yearly variations. The background intensity as a function of depth is shown in Fig. 7.23 and the seasonal changes are indicated in Fig. 7.24.

Optical Background in Sea Water

Several authors have studied the optical background in the sea at prospective array sites. Under quiet conditions Cherenkov light from the decay products of ^{40}K, chiefly beta decay (89.3%), is the dominating source of optical background. The consequences of ^{40}K for deep ocean Cherenkov detectors are discussed by Roberts (1979c). A very detailed analysis of the role of ^{40}K in the ocean was made by Geelhood (1982). ^{40}K produces about 43 Cherenkov quanta between 300 nm and 650 nm per disintegration. Approximately 13

^{40}K disintegrations occur per second per liter. Assuming an optical attenuation length of 20 m to 25 m in the ocean the ambient isotropic flux anywhere is about 120 to 150 photons $\mathrm{cm}^{-2}\,\mathrm{sec}^{-1}$.

Bioluminescence is another source of optical background in the deep sea, emitting predominantly green light. Apart from fluorescent fish and other creatures it is mostly micro-organisms and bacteria that can produce a significant level of luminescence. Turbulence above a certain level can cause high levels of *stimulated bioluminescence* at all depths in the sea. It can be caused by objects, including the measuring equipment itself, that are dragged or moving in the water with a velocity greater than a critical value with respect to the surrounding water masses. The critical velocity may be different for different sites. Ship tethered equipment usually follows the up and down movements of ships caused by wave motion. This is frequently adequate to generate a high level of stimulated bioluminescence, even at great depth. *Wave motion compensating tethering systems* help to reduce stimulated bioluminescence and are recommended for accurate measurements.

A typical bioluminescence light bursts from observations of Abin et al. (1987) is shown in Fig. 7.25. The onset is relatively fast and the decay time on the order of one second. Occasionally spontaneous bioluminescence storms are observed that may last for minutes. They are relatively local, covering volumes of meters to several tens of meters across.

Exhaustive studies of the optical background including bioluminescence both in the quiescent and stimulated state were made at the DUMAND Keahole Point site by Bradner et al. (1987), Aoki et al. (1985 and 1986) and Babson et al. (1990). Aoki et al. (1985 and 1986) studied also the short-time behavior of the optical background at different depths. The results are illustrated in Fig. 7.26. These authors have also determined the pulse height spectrum and the depth profile of the background level at the previously mentioned site.

Both, ship and bottom tethered measurements were made. The latter were made 100 m above the ocean floor and are free of stimulated bioluminescence. The background was due essentially to ^{40}K. The results of this work are shown in Fig. 7.27. Referring to this figure, the intensities described by the curves representing the fits to the ship tethered data by Aoki et al. (1986) (curve A) and Bradner et al. (1987) (curve B) can be expressed by eqs 7.14 and 7.15, respectively.

$$I(z) \;=\; 3.72 \cdot 10^5 \exp -(z/877) \quad [\mathrm{quanta\,cm^{-2}s^{-1}}] \qquad (7.14)$$

and

$$I(z) \;=\; 2.008 \cdot 10^5 \exp\, -(z/960) \quad [\text{quanta}\,\text{cm}^{-2}\text{s}^{-1}]\,, \tag{7.15}$$

where z [m] is the depth in meters.

Abin et al. (1987) carried out investigations in the Pacific and the Sea of Japan, and Bannykh et al. (1985 and 1987) in the Black Sea and the Atlantic. The data are also shown in Fig. 7.27. These authors found that the light intensity in the Atlantic could be described by the expression

$$I(z, 2\pi) \;=\; 400\,\epsilon^{-1} \exp\, -(0.5\,z) \quad [\text{quanta}/2\pi\,\text{sr}\,\text{cm}^2\,\text{s}]\,, \tag{7.16}$$

where $I(z, 2\pi)$ is the number of photons having wavelengths between 300 nm and 600 nm, incident on a hemisphere of area 1 cm^2 per second, ϵ is the attenuation coefficient for the same spectral band, and z is the depth in km.

Numerous measurements were made by other authors at other locations that are of no particular interest in regard to prospective Cherenkov detector sites. However, comparison of the results obtained by Losee (1982) who studied bioluminescence in the Gulf Stream down to 3650 m off the coast of North Carolina with the data found at the sites mentioned above shows that the general features of bioluminescence are the same. The time profiles obtained in the Gulf Stream show minimum rise times of approximately 50 μs. Sunlight could be detected to depths as low as 350 m.

Optical Background in Ice

There is essentially no relevant optical background in polar ice. The mechanisms that may contribute to optical background in polar ice are natural radioactivity producing Cherenkov light, scintillation or fluorescence, and thermoluminescence. According to Price et al. (1995) background Cherenkov radiation due to ^{40}K decay stored in dust and salt in South Pole ice is only $2 \cdot 10^{-6}$ times as intense as that due to ^{40}K in the ocean. Pure ice has an extremely low efficiency for fluorescence, on the order of $\sim 10^{-6}$ per eV absorbed, and for thermoluminescence approximately 10^{-11} to 10^{-10} per eV absorbed (Ghormley, 1956; Grossweiner and Matheson, 1954). The fluorescence emission peaks at $\sim$ 390 nm. Thermoluminescence is the emission at $\sim -190°$ C and $\sim -140°$ C of energy stored in ice that has been heavily irradiated at a lower temperature and then warmed. It is therefore of no concern to natural ice.

7.5.6 Sedimentation in the Ocean

The only studies concerning sedimentation in connection with water Cherenkov array sites and detector systems in the ocean were made by the DUMAND Collaboration at the Maui and Keahole Point sites in the Pacific near Hawaii. They were of exploratory nature (Zaneveld, 1981). According to Zaneveld, the rate at which a flat area is covered by settling particles is given by

$$A_t = \int_{D_l}^{D_\mu} \frac{\pi D^2}{4} w_s(D) f(D) dD \tag{7.17}$$

where A_t is the fractional surface covered, D_l and D_μ are the upper and lower limits of the diameter of the settling particles, $w_s(D)$ is the settling velocity of a particle of diameter D, and $F(D)dD$ is the number of particles per unit volume with sizes between D and $D + dD$.

If we assumes Stoke's settling law for particles we may set $w_s(D) = K_s D^2$ where $K_s = 3.403 \cdot 10^{-1}\ \mu\text{m}^{-1}\text{s}^{-1}$ at 5°C and 3.5% salinity, for a density of particle matter of 2. The cumulative size distribution $g(D) = \int_0^D f(D)dD$ is commonly measured in the ocean and has been found to be well represented by the hyperbolic distribution $g(D) = ND^{-C}$. Typically in the deep ocean, $C = 3$, and D is expressed in μm. Combining the above leads to

$$A_t = \int_{D_l}^{D_\mu} \frac{\pi D^2}{4} (K_s D^2)(DND^{-C-1}) dD \ . \tag{7.18}$$

It is known that $N = 10^4$ corresponds to a total particle volume of about 10^{-7} m^3/m^3 for $C = 3$. At the DUMAND site there are about 20 μg/l or about 10^{-6} m^3/m^3 if the matter density of particles is twice that of water. Substituting for $N = 10^3$, $D_l = 0.04$ μm and $D_\mu = 40$ μm in the above equation yields

$$A_t \simeq 2.8 \cdot 10^{-3} \quad \text{day}^{-1}$$

Thus, in 60 days about 15% of a given area would be covered. However, these are very rough estimates and experimental studies show that the coverage is only about 3% at the Maui site and slightly more at the Keahole Point site after 60 days. Curved surfaces would also show lower coverage than suggested by the above calculation (Zaneveld, 1981).

References

Abin, A.V., V.M. Aunutdiniv, V.G. Alalichin, V.V. Borog, S.B. Gavshin, I.A. Danilchenko, I.V. Penin, A.A. Petrukhin, G.A. Potapov, I.I. Yashin, V.H. Gorchakov, V.I. Ilichov, V.V. Kobiliansky, A.I. Miagky, Yu.M. Charlamov: PICRC, 6, p. 273 (1987).

Anassontzis, E.G, P. Ioannou, Chr. Kourkoumelis, L.K. Resvanis, and H. Bradner: Proc. 2nd. NESTOR Workshop, October 19 - 21, 1992, Pylos, Greece, (L.K. Resvanis, ed.), University of Athens, Greece, p. 270 (1992).

Anassontzis, E.G, P. Asproloupos, I. Chatzantonakis, P. Ioannou, G. Kalkanis, S. Katsanevas, C. Kourkoumelis, L. Moraitis, P. Pramantiotis, L.K. Resvanis, S. Sotiriou, N. Vassilopoulos, G. Voulgaris, M. Barone, I. Siotis, G. Contopoulos, P. Hatzios, H. Bradner, G. Fanourakis, G. Gramatikakis, S. Bottai, L. Dell'Angelo, B. Monteleoni, V. Naumov, J.G. Learned, V.J. Stenger, U. Keusen, P. Koske, J. Rathlev, G. Voigt, I.F. Barinov, A.O. Deineko, V.A. Gaidash, M.A. Markov, A.A. Permyakov, N.N. Surin, L.M. Zakarov, I.M. Zheleznykh, V.A. Zhukov, A.P. Eremeev, V.V. Ledenev, M.N. Platonov, V.K. Rucol, N.A. Sherement, U. Camerini, and R. March: Proc. 3rd NESTOR Workshop, October 19 - 21, 1993, Pylos, Greece, (L.K. Resvanis, ed.), University of Athens, Greece, p. 614 (1993b).

Aoki, T., T. Kitamura, S. Matsuno, K. Mitsui, Y. Ohashi, A. Okada, D.R. Cady, J.G. Learned, D. O'Connor, S. Dye, P.W. Gorham, M. Webster, C. Wilson, and P. Grieder: PICRC, 8, p. 53 (1985).

Aoki, T., T. Kitamura, S. Matsuno, K. Mitsui, Y. Ohashi, A. Okada, D.R. Cady, J.G. Learned, D. O'Connor, S. Dye, P.W. Gorham, M. Webster, C. Wilson, and P. Grieder: Nuovo Cimento, 9C, p. 642 (1986).

Askebjer, P., S.W. Barwick, L. Bergström, A. Bouchat, S. Carius, A. Coulthard, K. Engel, B. Erlandsson, A. Goobar, L. Gray, A. Hallgren, F. Halzen, P.O. Hulth, J. Jacobson, S. Johansson, V. Kandhadai, I. Liubarsky, D. Lowder, T. Miller, P.C. Mock, R. Morse, R. Porrata, P.B. Price, A. Richards, H. Rubinstein, E. Schneider, Q. Sun, S. Tilav, C. Walck, and G. Yodh: Science, 267, p. 1147 (1995).

Babson, J., B. Barish, R. Becker-Szendy, H. Bradner, R. Cady, J. Clem, S.T. Dye, J. Gaidos, P. Gorham, P.K.F. Grieder, M. Jaworski, T. Kitamura, W. Kropp, J.G. Learned, S. Matsuno, R. March, K. Mitsui, D. O'Connor, Y. Ohashi, A. Okada, V. Peterson, L. Price, F. Reines, A. Roberts, C. Roos, H. Sobel, V.J. Stenger, M. Webster, and C. Wilson: Phys. Rev., D 42, p. 3613 (1990).

Bannykh, A.E., V.I. Beresnev, V.A. Gaidash, O.M. Gulkhandanyan, V.I.

Ivanov, M.A. Markov, V.T. Paka, I.V. Shtranikh, N.M. Surin, A.N. Volkov, and I.M. Zheleznykh: PICRC, 8, p. 57 (1985).

Bannykh, A.E., V.I. Beresnev, V.A. Gaidash, O.M. Gulkhandanyan, V.I. Ivanov, P.I. Krastev, M.A. Markov, A.A. Permyakov, V.O. Pozovnoi, I.V. Shtranikh, N.M. Surin, A.N. Volkov, and I.M. Zheleznykh, A.P. Eremeev, V.Yu. Maslov, and V.T. Paka: PICRC, 6, p. 269 (1987).

Barwick, S.W., F. Halzen, D.M. Lowder, T. Miller, R. Morse, P.B. Price, and A. Westphal: J. Phys. G, 18, p. 225 (1992).

Belolaptikov, I.A., L.B. Bezrukov, B.A. Borisovets, E.V. Bugaev, G.V. Domogatsky, L.A. Donskich, A.A. Doroshenko, M.D. Galperin, Zh.A.M. Djilkibaev, A.M. Klabukov, S.I. Klimushin, O.J. Lanin, B.K. Lubsandorzhiev, A.I. Panfilov, I.A. Sokalsky, I.I. Trofimenko, N.M. Budnev, A. G. Chensky, V.I. Dobrynin, O.A. Gress, A.P. Koshechkin, J.B. Lanin, G.A. Litunenko, A.V. Lopin, V.A. Naumov, M.I. Nemchenko, Yu.V. Parfenov, A.A. Pavlov, O.P. Pokalev, V.A. Primin, A.A. Shestakov, A.A. Sumanov, V.A. Tarashansky, V.L. Zurbanov, A.V. Golikov, E.S. Zaslavskaya, V.B. Kabikov, L.A. Kuzmichov, E.A. Osipova, G.N. Dudkin, V.Yu. Egorov, M.N. Gushtan, A.A. Lukanin, A.M. Ovcharov,V.M. Padalko, A.H. Padusenko, J. Krabi, T. Mikolajski, Ch. Spiering, R. Wischnewski, L. Jenek, D. Kiss, L. Tanko, Yu.S. Kusner, V.A. Poleschuk, and P.P. Sherstyankin: Nucl. Phys., B (Proc. Suppl.) 19, p. 388 (1991).

Belolaptikov, I.A., L.B. Bezrukov, B.A. Borisovets, N.M. Budnev, A. G. Chensky, Zh.A.M. Djilkibaev, V.I. Dobrynin, G.V. Domogatsky, L.A. Donskych, A.A. Doroshenko, S.V. Fialkovsky, O.A. Gress, A.V. Golikov, R. Heller, H. Heukenkamp, V.B. Kabikov, A.M. Klabukov, A.I. Klimov, S.I. Klimushin, T.A. Konopleva, A.P. Koshechkin, J. Krabi, V.F. Kulepov, L.A. Kuzmichov, O.J. Lanin, B.K. Lubsandorzhiev, M.B. Milenin, T. Mikolajski, R.R. Mirgazov, S.A. Nikiforov, N.V. Ogievietzky, E.A. Osipova, A.H. Padusenko, A.I. Panfilov, Yu.V. Parfenov, A.A. Pavlov, D.P. Petuchov, K.A. Pocheikin, P.G. Pochil, O.P. Pokalev, M.I. Rosanov, A¿V. Rzhetshizki, V.Yu. Rubzov, S.I. Sinegovsky, I.A. Sokalsky, Ch. Spiering, O. Streicher, V.A. Tarashansky, T. Thon, I.I. Trofimenko, R. Wischnewski, and V.L. Zurbanov: Proc. 3rd NESTOR Workshop, October 19 - 21, 1993, Pylos, Greece, (L.K. Resvanis, ed.), University of Athens, Greece, p. 213 (1993a).

Bradner, Hugh: Proc. 1978 DUMAND Summer Workshop, 1, p. 259 (1979). (A. Roberts, ed.) published by Scripps Institution of Oceanography, Code A-010, La Jolla, CA 92093 (1979).

Bradner, H., and G. Blackington: DUMAND 80, Proc. 1980 International DUMAND Symposium, 1, p. 9 (1981). (V.J. Stenger, ed.) Published by the

University of Hawaii, Honolulu (1981).

Bradner, H., and G. Blackington: Applied Optics, 23, p. 1009 (1984).

Bradner, H., M. Bartlett, G. Blackinton, J. Cleam, D. Karl, J.G. Learned, A. Lewis, S. Matsuno, D. O'Connor, W. Peatmen, M. Reichle, C. Roose, J. Waters, M. Webster, and M. Yarbrough: Deap-Sea Research, 34, p. 1831 (1987).

Bugaev, E.V., J.A.M. Djilkibaev, and M.D. Galpern: Nucl. Instr. Methods, A248, p. 219 (1986).

Clarke, G.L., and H.R. James: J. Opt. Soc. Amer., 29, p. 43 (1939).

Erlandsson, B., P. Askebjer, S.W. Barwick, L. Bergström, A. Bouchat, S. Carius, A. Goobar, L. Gray, A. Hallgren, F. Halzen, H. Heukenkamp, P.O. Hulth, J. Jacobson, S. Johansson, V. Kandhadai, A. Karle, I. Liubarsky, D. Lowder, T.C. Miller, P.C. Mock, R. Morse, R. Porrata, P.B. Price, A. Richards, H. Rubinstein, C. Spiering, Q. Sun, T. Thon, S. Tilav, C. Walck, R. Wischnewski, and G. Yodh: PICRC, 1, p. 1039 (1995).

Geelhood, B.D.: Proc. DUMAND 1982 Signal Processing Workshop, p. 30 (1982). (V.J. Stenger, ed.), University of Hawaii (1982).

Ghormley, J.A.: J. Chem. Phys., 24, p. 1111 (1956).

Grossweiner, L.I., and M.S. Matheson: J. Chem. Phys., 22, p. 1514 (1954).

Harvey, Robert, James E. Andrews, and J. Ronald Zaneveld: Preliminary DUMAND Site Evaluations: Maui Basin and Keahole Point Basin. Hawaii Institute of Geophysics Report, University of Hawaii, UNIHI-SEAGRANT-CR-78-02, HIG-78-2 (1978).

Harvey, Robert, James Andrews, and J. Ronald Zaneveld: Proc. 1978 DUMAND Summer Workshop, Vol. 3, p. 23 (1979). (G. Wilkins, ed.), published by Scripps Institution of Oceanography, Code A-010, La Jolla, CA 92093 (1979).

Jerlov, N.G.: Optical Oceanography, Elsevier Publ. Co. Amsterdam (1968).

Karabashev, G.S., and A.F. Kuleshov: Doc. Akad. Nauk, USSR, 298, No 2, p. 467 (1988).

Khanaev, S.A., and A.F. Kuleshov: Proc. 3rd NESTOR Workshop, October 19 - 21, 1992, Pylos, Greece, (L.K. Resvanis, ed.), University of Athens, Greece, p. 253 (1992).

Losee, Jon, R.,: Proc. DUMAND 1982 Signal Processing Workshop, p. 19 (1982) (V.J. Stenger, ed.), published by the University of Hawaii (1982).

Lowder, D.M., T. Miller, P.B. Price, A. Westphal, S.W. Barwick, F. Halzen,

and R. Morse: PICRC, 4, p. 654 (1991a).

Lowder, D.M., T. Miller, P.B. Price, A. Westphal, S.W. Barwick, F. Halzen, and R. Morse: Nature, 353, p. 331 (1991b).

Miller, Stanley, L.: Science, 165, p. 489 (1969).

Morel, A.: Optics of the Sea, AGARD Lecture Series, No 61 (1973).

Price, P.B.: Science, 267, p. 1802 (1995).

Price, P.B., P. Askebjer, S.W. Barwick, L. Bergström, A. Bouchat, S. Carius, B. Erlandsson, A. Goobar, L. Gray, A. Hallgren, F. Halzen, H. Heukenkamp, P.O. Hulth, J. Jacobson, S. Johansson, V. Kandhadai, A. Karle, I. Liubarsky, D.M. Lowder, T.C. Miller, P.C. Mock, R. Morse, R. Porrata, A. Richards, H. Rubinstein, C. Spiering, Q. Sun, S. Tilav, C. Walck, A.J. Westphal, R. Wischnewski, and G. Yodh: PICRC, 1, p. 777 (1995).

Roberts, A., ed.: Proc. 1978 DUMAND Summer Workshop, Volume 1, Array Studies (1979a). Published by Scripps Institution of Oceanography, Code A-010, La Jolla, CA 92093 (1979a).

Roberts, A., ed.: Proc. 1978 DUMAND Summer Workshop, Volume 2, UHE Interactions, Neutrino Astronomy (1979b). Published by Scripps Institution of Oceanography, Code A-010, La Jolla, CA 92093 (1979b).

Roberts, A.: Proc. 1978 DUMAND Summer Workshop, 1, p. 139 (1979c). (A. Roberts, ed.) published by Scripps Institution of Oceanography, Code A-010, La Jolla, CA 92093 (1979c).

Sherstyankin, P.P.: DUMAND 1979 Summer Workshops at Khabarovsk and Lake Baikal, p. 308 (1980). (J.G. Learned, ed.), published by the University of Hawaii, Honolulu (1980).

Shifrin, K.S.: Introduction in Ocean Optic, Leningrad, Gidrometeoizdat, p. 277 (1983).

Smith, R.S., and K.S. Baker: Appl. Opt., 20, p. 177 (1981).

Sullivan, S.A.: J. Opt. Soc. Amer., 53, p. 962 (1963).

Tilav, S., P. Askebjer, S.W. Barwick, L. Bergström, A. Bouchat, S. Carius, B. Erlandsson, A. Goobar, L. Gray, A. Hallgren, F. Halzen, H. Heukenkamp, P.O. Hulth, J. Jacobson, S. Johansson, V. Kandhadai, A. Karle, I. Liubarsky, D.M. Lowder, T.C. Miller, P.C. Mock, R. Morse, R. Porrata, P.B. Price, A. Richards, H. Rubinstein, C. Spiering, Q. Sun, T. Thon, C. Walck, R. Wischnewski, and G. Yodh: PICRC, 1, p. 1011 (1995).

Warren, S.G.: Appl. Optics., 23, p. 1225 (1984).

Zaneveld, J. Ronald V.: Proc. of the 1980 International DUMAND Sympo-

sium, July 24 - August 2, 1980, (V.J. Stenger, ed.), University of Hawaii, 1, p. 7 (1981).

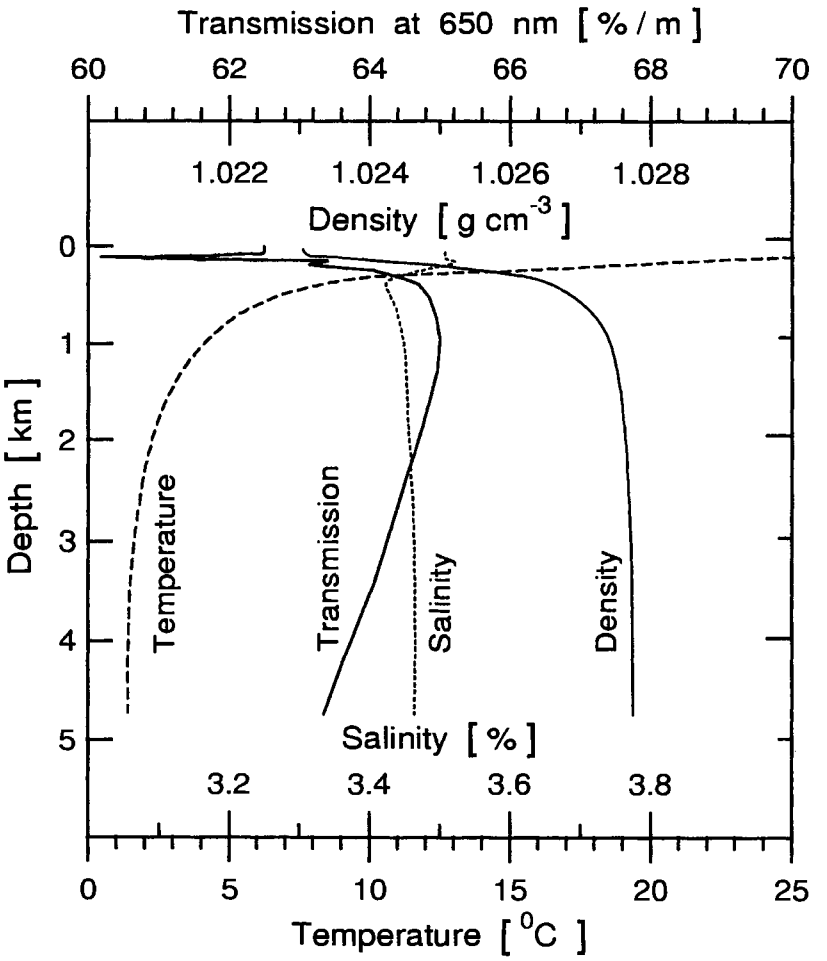

Figure 7.10: Depth profiles of optical transmission at 650 nm, salinity, density and temperature at the Keahole Point site, Hawaii, measured October 24, 1977 (Harvey et al., 1979). Note that the optical transmission in water increases rapidly with decreasing wavelength and reaches its maximum between 450 nm and 500 nm in sea water (c.f. Figs. 7.12, 7.13, 7.14 and 7.17).

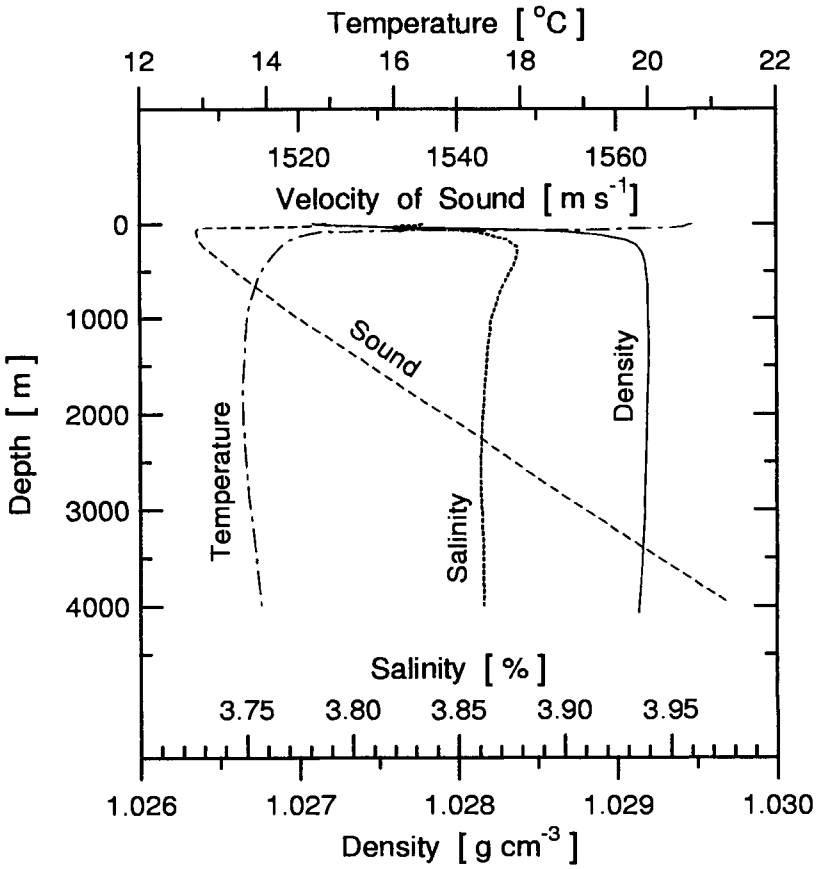

Figure 7.11: Environmental parameter profiles of the NESTOR detector site near Pylos, Greece, in the Mediterranean as a function of depth (Anassontzis et al., 1993b)

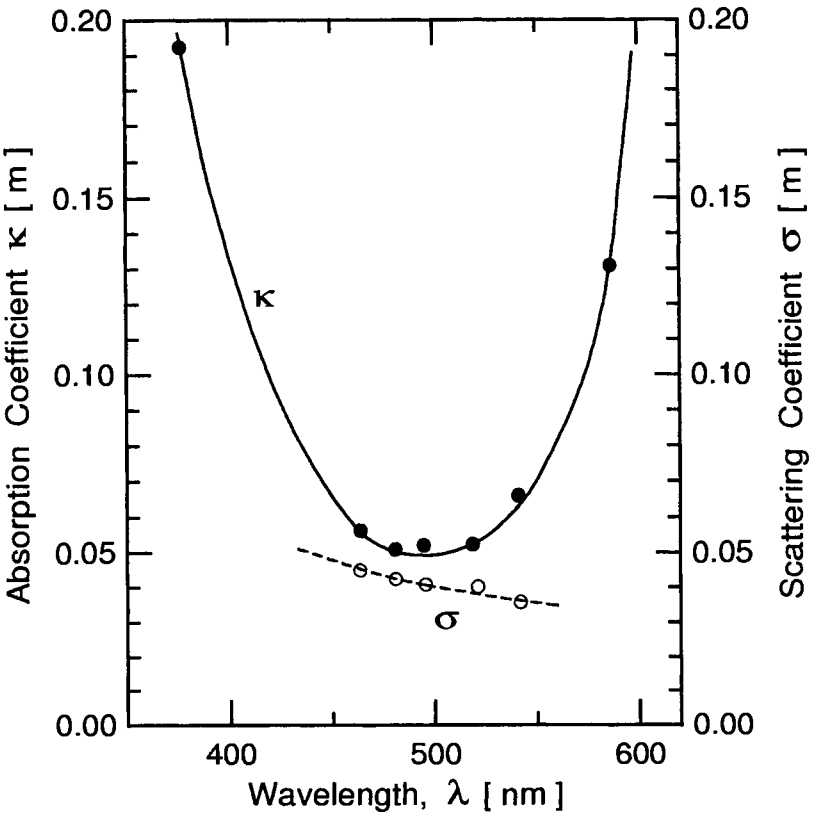

Figure 7.12: Optical absorption coefficient κ (solid line and full circles), and scattering coefficient σ (dashed line and open circles) measured in Lake Baikal at a depth of 1000 m as a function of wavelength λ (Belolaptikov et al., 1991).

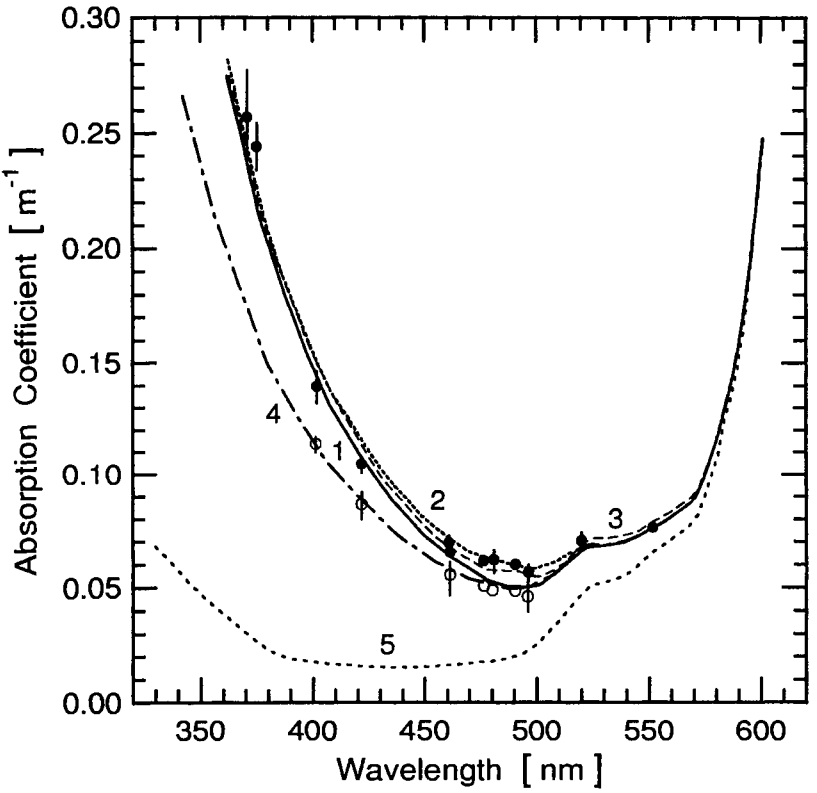

Figure 7.13: Optical absorption coefficient, $\kappa(\lambda)$, as a function of wavelength, λ, in Lake Baikal, and its seasonal variation (Belolaptikov et al., 1993a).

Curve	Date	Curve	Date	Curve	Date
• , 1	April 1993	2	June 1993	3	September 1993
○ , 4	November 1993	5	pure water		

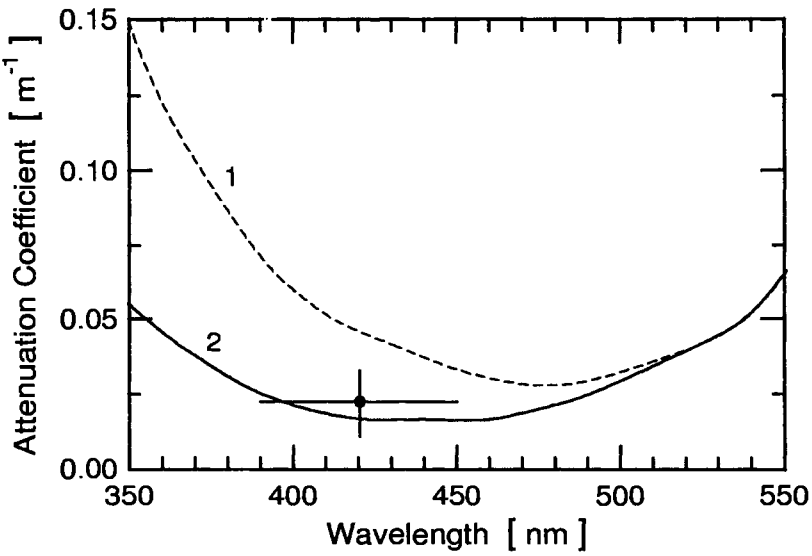

Figure 7.14: Optical attenuation coefficient as a function of wavelength of ocean water in the Pacific, 30 km west of Keahole Point, Hawaii, measured with the DUMAND short prototype string calibration system (•) (Babson et al., 1990). Also shown are earlier measurements of Zaneveld et al. (1981), curve 1, and Smith and Baker (1981), curve 2.

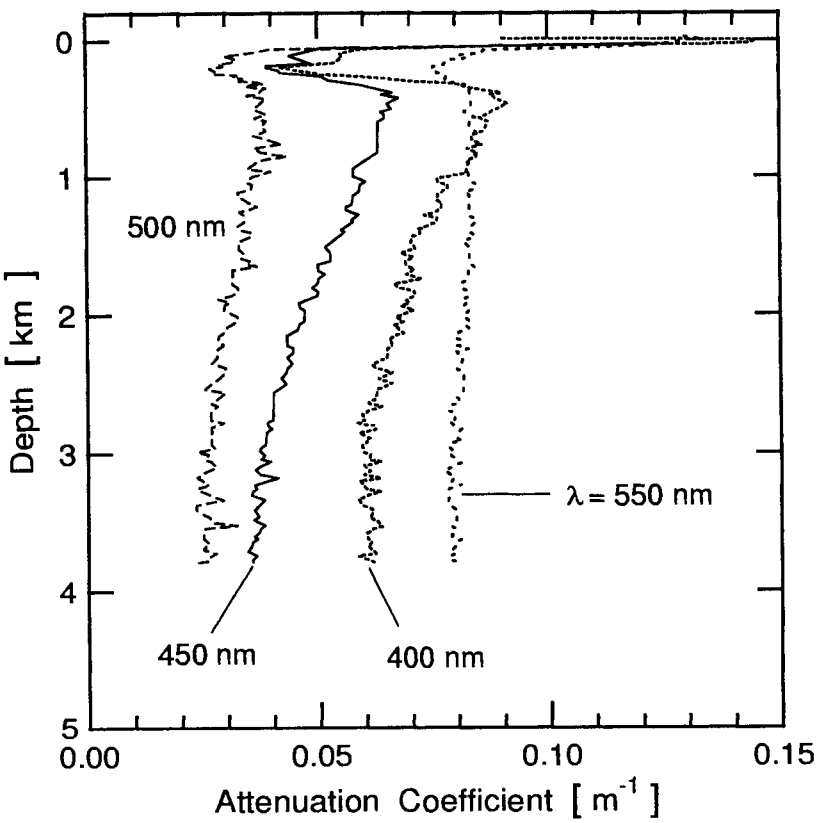

Figure 7.15: Optical attenuation coefficients for different wavelengths as a function of depth measured on April 1, 1980 in the Pacific, 30 km west of Keahole Point, Hawaii, at the DUMAND site. The rapid decrease of the attenuation in the first 500 m from the surface shows a spectral dependence proportional to λ^{-4}, which suggests a decrease in the concentration of submicrometer-sized particles with depth (Zaneveld, 1981).

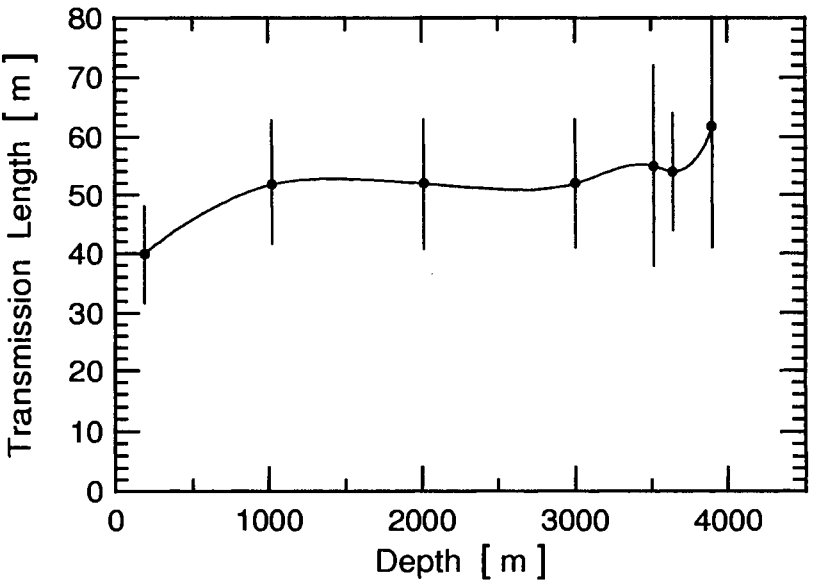

Figure 7.16: Optical transmission length at a wavelength of $\lambda = 480$ nm as a function of depth in the Mediterranean at the NESTOR site near Pylos, Greece. The data were obtained from in-situ measurements with a large acceptance instrument (Anassontzis et al., 1992 and 1993b). For definitions of terms see text.

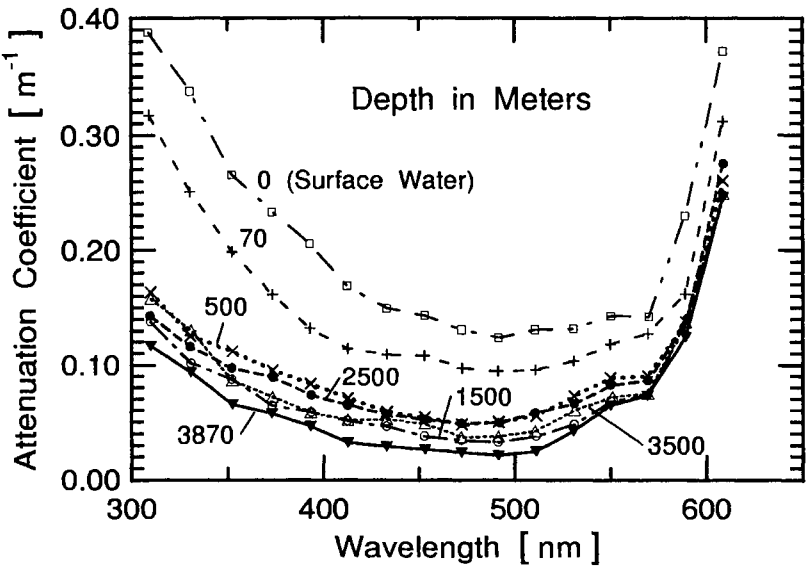

Figure 7.17: Typical optical attenuation coefficients versus wavelength of water samples taken at different depths in the Mediterranean at the NESTOR site near Pylos, Greece, determined in the laboratory with a narrow beam 1.1 m base line monochromator (Khanaev and Kuleshov, 1992). For definitions of terms see text.

□	0 m	+	70 m	×	500 m	○	1500 m
•	2500 m	△	3500 m	▼	3870 m		

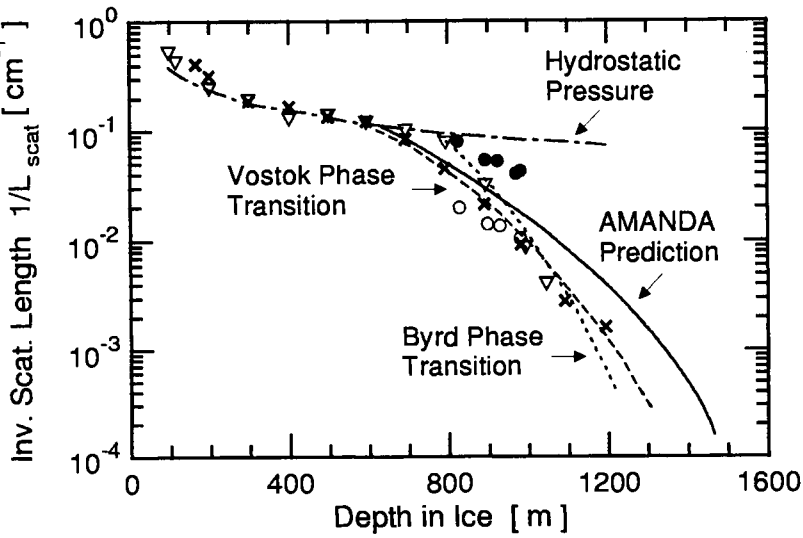

Figure 7.18: Inverse (reciprocal) of bubble to bubble scattering length, $1/L_{scat} = n\pi r^2$, in Antarctic ice as a function of depth. The data from the Vostok ($\times$) and Byrd (∇) sites are from microscopic examinations, those from AMANDA ($\bullet, \circ$) are from in-situ measurements. The full circles assume forward scattering from smooth-walled bubbles, the open circles isotropic scattering from rough-walled bubbles. The hydrostatic pressure curve shows the effect of bubble shrinkage at constant concentration. The other curves are the results of calculations and show the effect caused by a decreasing bubble concentration as a function depth (and time) due to H_2O molecule diffusion through air hydrate crystal walls (after Price, 1995).

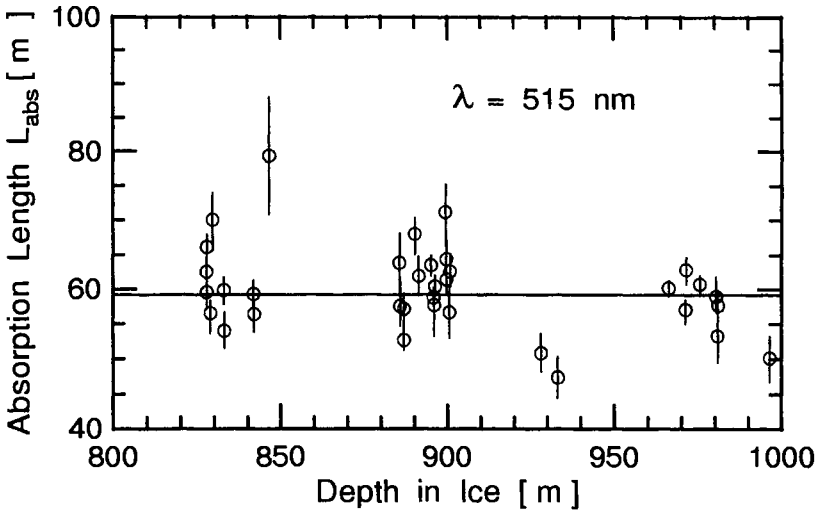

Figure 7.19: Measured optical absorption length, L_{abs}, at 515 nm in ice at the South Pole at depths between 800 m and 1000 m. The solid line shows the best fit which is at 59 m (Askebjer et al., 1995).

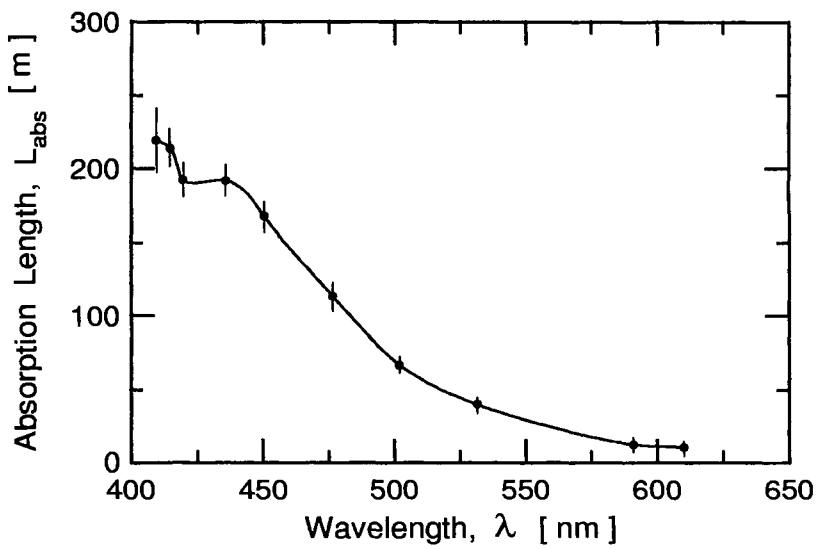

Figure 7.20: Optical absorption length as a function of wavelength in Antarctic ice at the AMANDA site. Each point represents an average of all arrival time distributions for that wavelength (Erlandsson et al., 1995).

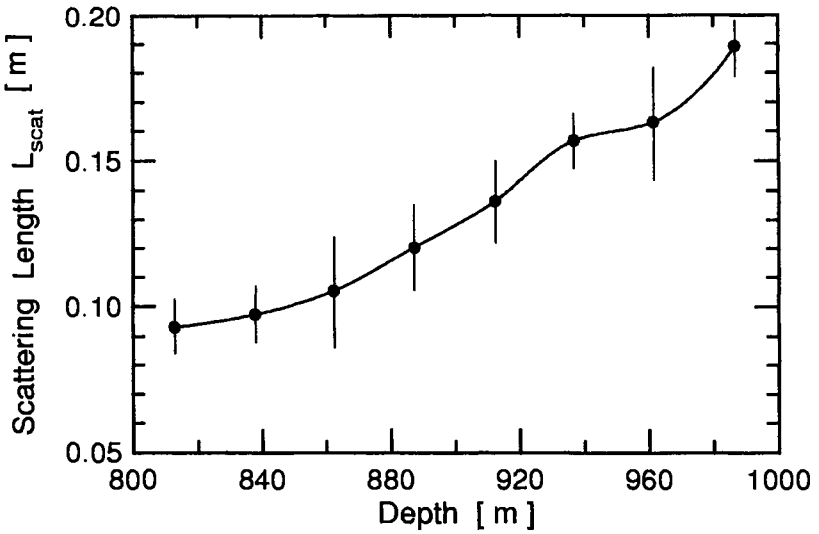

Figure 7.21: Optical scattering length as a function of depth in Antarctic ice. Each point is an average of all arrival time distributions for depths in an interval ± 12.5 m around that depth (Erlandsson et al., 1995).

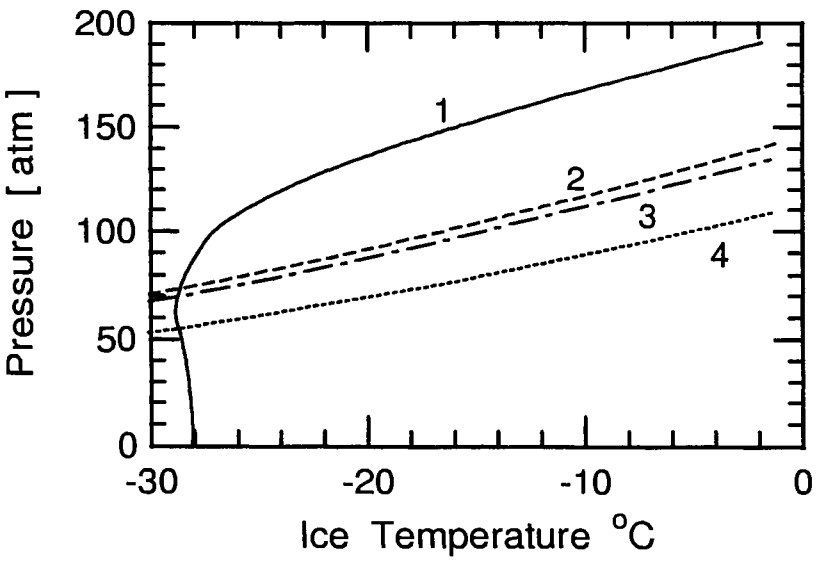

Figure 7.22: Relation between temperature and pressure depth of ice core (curve 1), and temperature and dissociation pressures of N_2 (curve 2), air hydrates (curve 3) and O_2 (curve 4) (Miller, 1969).

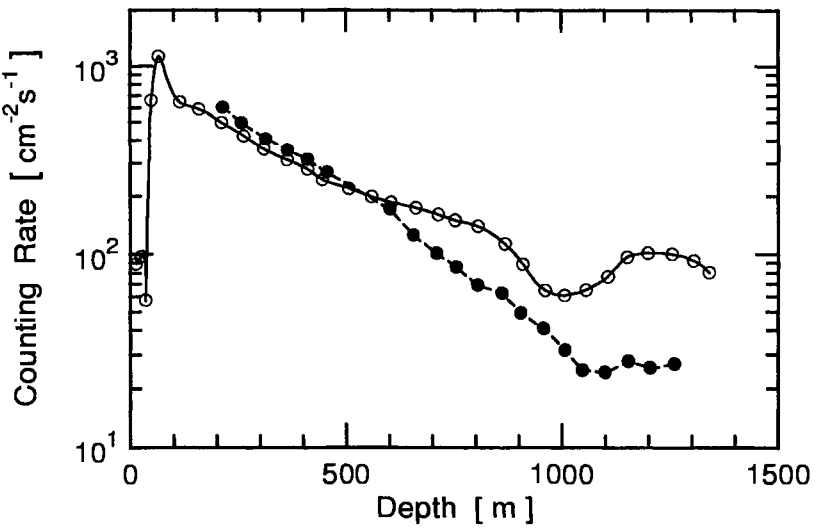

Figure 7.23: Intensity of single photoelectron pulses due to background luminescence in Lake Baikal as a function of depth. The open circles are the result of measurements made in March 1986, the closed circles are from March 1988 (Belolaptikov et al., 1991).

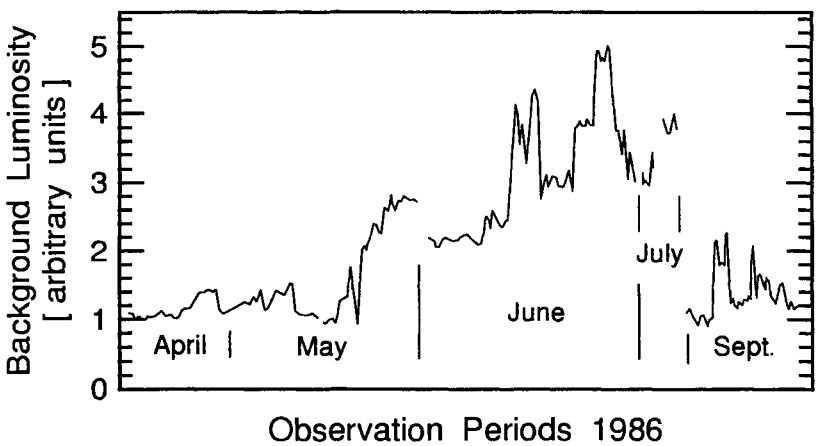

Figure 7.24: Long-term variation of the counting rate of single photoelectron pulses due to background luminescence in Lake Baikal at a depth of 1180 m. The detector was attached to a stationary string (Belolaptikov et al., 1991).

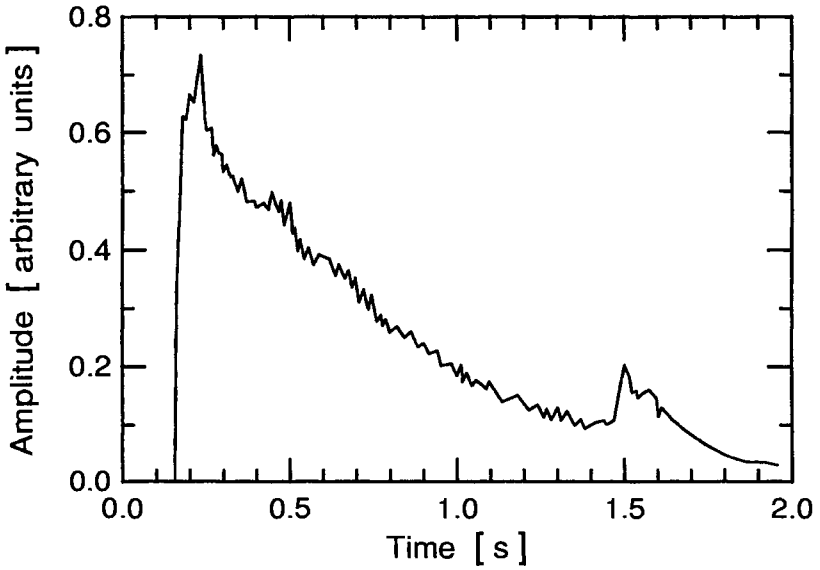

Figure 7.25: Typical time structure of the intensity variation of a sporadic bioluminescence light flash in the Pacific ocean, off the coast of Kona, near Keahole Point (Hawaii). The rise time is approximately 1 ms and the time constant of the exponential decay is 1 to 2 seconds (Abin et al., 1987).

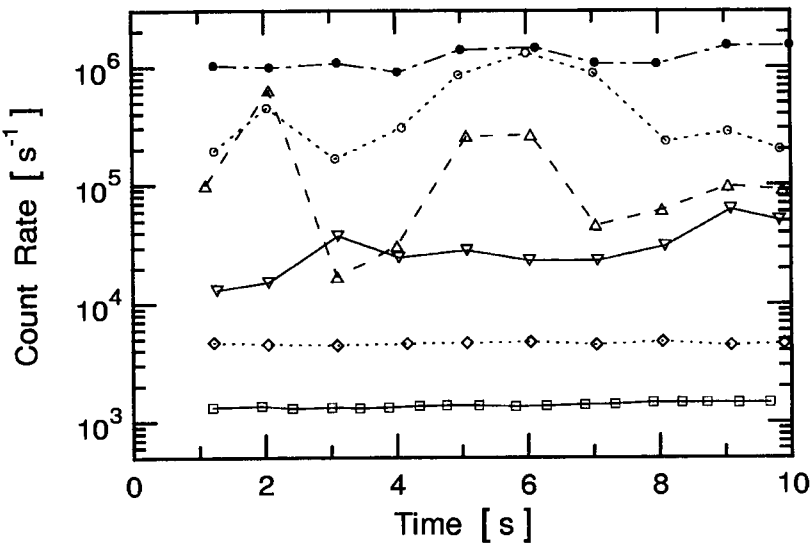

Figure 7.26: Short-time variation of the optical background counting rate in the Pacific ocean 30 km west of Keahole Point, Hawaii, and photomultiplier (PMT) dark current measurements at low temperature in the laboratory (Aoki et al., 1985 and 1986). Shown are ship tethered measurements made at depths of 1500 m, 2500 m, 3500 m and 4500 m, bottom tethered measurements 100 m above the sea floor located at a depth of 4700 m, and PMT dark current counting rates at 3°C.

- 1500 m | ○ 2500 m | △ 3500 m | ▽ 4500 m
  - ◇ bottom tethered 100 m above sea floor
  - □ photomultiplier dark noise at 3°C

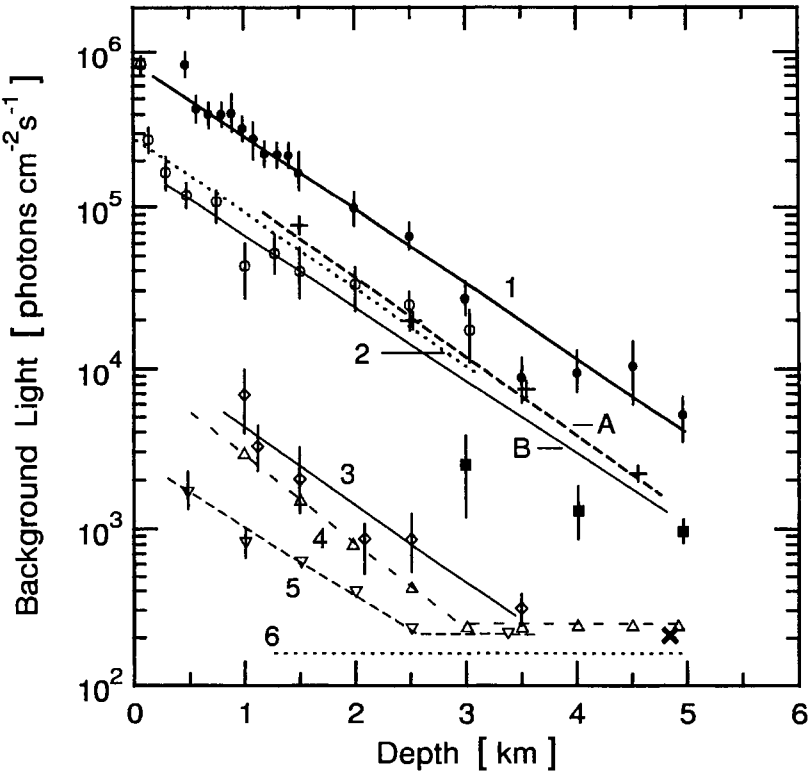

Figure 7.27: Compilation of data on the optical background underwater versus depth at widely different locations. The lines are fits to the measured data points. Line 3 and the associated data points are an extrapolation to zero velocity ($v = 0$ m/s) of the detector with respect to the bulk velocity of the surrounding water masses. For details see text.

•	1	Pacific Ocean, mean rate (Abin et al., 1987)
△	4	Pacific Ocean, minimum (Abin et al., 1987)
◇	3	Pacific, extrapolated to $v = 0$ (Abin et al., 1987)
○	2	Sea of Japan, mean rate (Abin et al., 1987)
▽	5	Sea of Japan, minimum (Abin et al., 1987)
■		South Atlantic (Bannykh et al., 1985)
+	A	Pacific Ocean (Aoki et al., 1985 and 1986)
×		Pacific Ocean, bottom tethered (Aoki et al., 1986)
	B	Pacific Ocean (Bradner et al., 1987)
	6	^{40}K level only

Appendix A

Miscellaneous Data: Tables

A.1 Comments to Tables

A.1.1 COSPAR Reference Atmosphere

In Table A.1 of this Appendix data of the International Standard COSPAR Atmosphere are listed. A graphic representation of the date is given in Chapter 1, Section 1.7.

A.1.2 Solar System Elemental Abundances

For the abundances of the elements in the solar system the compilation of Cameron (1973) is so frequently referred to that we have reproduced it in (Table A.2). More recent compilations of solar system elemental abundances based on meteorite measurements were made by Anders and Grevesse (1989). The same authors did also make a compilation of the abundances of the nuclides (see Grevesse et al., 1996).

A.1.3 Radiation Lengths and Critical Energies of Materials

In Table A.3 we present a collection of radiation lengths and critical energies of various elements and compounds, that are useful for common calculations of electromagnetic interaction processes.

A.1.4 Elements and their Material Parameters

Table A.4 lists the density, the atomic number and weight, and the mean ionization potential of various elements. Also given are the *density correction*

constants of Sternheimer (1984) to account for the density effect of ionization, δ, in the Bethe-Bloch equation, given here in the form derived by Petrukhin and Shestakov (1968).

$$-\left(\frac{dE}{dx}\right) = 2\pi N\alpha^2\lambda_e^2\frac{Zm_e}{A\beta^2}\left[\ln\left(\frac{2m_e\gamma^2\beta^2E'_m}{I^2(Z)}\right) - 2\beta^2 + \frac{E'^2_m}{4E^2} - \delta\right] . \quad \text{(A.1)}$$

The symbols stand for the following quantities:

$\alpha = 1/137.036$	fine structure constant
$N = 6.023 \cdot 10^{23}$	Avogadro's number
Z	atomic number of absorber
A	atomic weight of absorber
m_e	rest masses of electron
m_μ	rest masses of muon
$\beta = p/E$	
p	p muon momentum
E	E muon energy
$\gamma = E/m_\mu$	Lorentz factor of muon
$\lambda_e = 3.8616 \cdot 10^{-11}$ cm	Compton wavelength of electron
$I(Z)$	mean ionization potential of absorber and
E'_m	maximum energy transferable to electron

For E'_m we write

$$E'_m = \frac{2m_ep^2}{m_e^2 + m_\mu^2 + 2m_e\sqrt{p^2 + m_\mu^2}} , \quad \text{(A.2)}$$

and δ is the density correction constant,

$$\delta(X) = 4.6052\,X + a(X_1 - X)^m + C , \quad \text{for} X_0 < X < X_1 \quad \text{(A.3)}$$

and

$$\delta(X) = 4.6052\,X + C , \quad \text{for} X > X_1 . \quad \text{(A.4)}$$

A.1.5 Muon Energy Losses in Elements and Compounds

Using eq. A.1 and the constants given in Table A.4 Lohmann et al. (1985) have computed the energy loss of muons in the energy range from 1 to 10^4 GeV in various elements and compounds, as listed in Tables A.5 and A.6.

A.1.6 Units, Conversion Factors, Constants and Parameters

Some units and conversion factors frequently used in astrophysics and radiation dosimetry are listed in Tables A.7, A.8 and A.9, and some common constants are given in Table A.10.

A.2 COSPAR Reference Atmosphere

Table A.1: COSPAR International Reference Atmosphere:
30° N Annual Mean
(after Barnett and Chandra, 1990)

Pressure Scale Height[1]	Pressure [mb]	Geometric Height[2] [m]	Geopotential Height[3] [m]	Temperature [K]
17.50	2.544E-05	119656	117361	370.1
17.25	3.266E-05	116732	114545	324.8
17.00	4.194E-05	114192	112096	287.2
16.75	5.385E-05	111965	109948	256.9
16.50	6.914E-05	109982	108034	233.7
16.25	8.878E-05	108161	106275	218.1
16.00	1.140E-04	106471	104642	207.5
15.75	1.464E-04	104861	103085	199.6
15.50	1.880E-04	103319	101594	194.1
15.25	2.413E-04	101823	100146	189.9
15.00	3.099E-04	100364	98734	187.0
14.75	3.979E-04	98931	97345	185.0
14.50	5.109E-04	97518	95976	183.7
14.25	6.560E-04	96118	94619	182.8
14.00	8.423E-04	94727	93269	182.5
13.75	1.082E-03	93340	91924	182.5
13.50	1.389E-03	91953	90577	183.3
13.25	1.783E-03	90562	89226	185.2
13.00	2.290E-03	89158	87862	187.9
12.75	2.940E-03	87733	86477	191.2
12.50	3.775E-03	86284	85068	194.8
12.25	4.847E-03	84804	83628	198.6
12.00	6.224E-03	83298	82163	201.9

[1] The pressure scale height is minus the natural logarithm of pressure relative to the surface pressure; it is dimensionless (continued next page).

Table A.1: COSPAR International Reference Atmosphere (continued).

Pressure Scale Height[1]	Pressure [mb]	Geometric Height[2] [m]	Geopotential Height[3] [m]	Temperature [K]
11.75	7.992E-03	81766	80670	204.4
11.50	1.026E-02	80217	79161	206.3
11.25	1.318E-02	78662	77646	207.8
11.00	1.692E-02	77097	76120	209.2
10.75	2.172E-02	75521	74581	210.8
10.50	2.789E-02	73932	73031	212.5
10.25	3.582E-02	72333	71469	214.3
10.00	4.599E-02	70720	69893	216.4
9.75	5.905E-02	69087	68296	219.2
9.50	7.582E-02	67433	66678	222.6
9.25	9.736E-02	65754	65035	226.4
9.00	0.1250	64048	63364	230.4
8.75	0.1605	62308	61660	234.5
8.50	0.2061	60539	59926	238.9
8.25	0.2647	58739	58160	243.6
8.00	0.3398	56905	56361	248.5
7.75	0.4363	55029	54519	253.9
7.50	0.5603	53116	52639	259.1
7.25	0.7194	51170	50726	263.5
7.00	0.9237	49198	48786	266.5
6.75	1.1861	47213	46832	267.1
6.50	1.5230	45231	44880	266.0
6.25	1.9556	43265	42942	263.0
6.00	2.5110	41325	41030	258.8

[1] see previous page. [2] The geometric height or altitude of an element is its distance above the reference sea level terrestrial ellipsoid, given in meters (continued next page).

Table A.1: COSPAR International Reference Atmosphere (continued).

Pressure Scale Height[1]	Pressure [mb]	Geometric Height[2] [m]	Geopotential Height[3] [m]	Temperature [K]
5.75	3.2242	39425	39155	253.8
5.50	4.1399	37563	37316	248.7
5.25	5.3157	35737	35513	243.7
5.00	6.8255	33948	33744	238.9
4.75	8.7642	32198	32013	234.4
4.50	11.25	30479	30313	230.3
4.25	14.45	28788	28638	226.9
4.00	18.55	27120	26986	223.9
3.75	23.82	25478	25359	221.0
3.50	30.59	23860	23754	218.3
3.25	39.28	22267	22174	215.6
3.00	50.43	20697	20616	212.8
2.75	64.76	19151	19080	210.0
2.50	83.15	17625	17564	207.1
2.25	106.77	16116	16065	205.8
2.00	137.09	14604	14561	208.5
1.75	176.03	13055	13019	214.8
1.50	226.03	11450	11421	223.6
1.25	290.23	9771	9750	234.6
1.00	372.66	8011	7995	247.0
0.75	478.51	6148	6138	259.9
0.50	614.42	4197	4192	272.1
0.25	788.93	2166	2164	283.1
0.00	1013.00	57	57	295.1

[1,2] see previous pages. [3] The geopotential height above the reference sea level ellipsoid is given in meters. It can be considered to be its geometric height plus (or minus) a correction which depends upon latitude and height. The difference between geometric and geopotential height is zero at the surface at 30° N and increases with height; the difference varies with latitude.

A.3 Solar System Elemental Abundances

Table A.2: Abundances of the Elements in the Solar System
Normalized to Si = 10^6. (Cameron, 1973)
Notes refer to sources used for the compilation.
(see also Cameron, 1981 and 1982; Grevesse et al., 1996)

Element	Suess & Urey	Cameron (1968)	Cameron (1973)	Notes
1 H	$4.00 \cdot 10^{10}$	$2.6 \cdot 10^{10}$	$3.18 \cdot 10^{10}$	1
2 He	$3.08 \cdot 10^{9}$	$2.1 \cdot 10^{9}$	$2.21 \cdot 10^{9}$	2
3 Li	100	45	49.5	3
4 Be	20	0.69	0.81	25
5 B	24	6.2	350	25
6 C	$3.5 \cdot 10^{6}$	$1.35 \cdot 10^{7}$	$1.18 \cdot 10^{7}$	1, 4
7 N	$6.6 \cdot 10^{6}$	$2.44 \cdot 10^{6}$	$3.74 \cdot 10^{6}$	1, 4
8 0	$2.15 \cdot 10^{7}$	$2.36 \cdot 10^{7}$	$2.15 \cdot 10^{7}$	1, 4
9 F	1600	3630	2450	3
10 Ne	$8.6 \cdot 10^{6}$	$2.36 \cdot 10^{6}$	$3.44 \cdot 10^{6}$	2
11 Na	$4.38 \cdot 10^{4}$	$6.32 \cdot 10^{4}$	$6.0 \cdot 10^{4}$	3
12 Mg	$9.12 \cdot 10^{5}$	$1.050 \cdot 10^{6}$	$1.061 \cdot 10^{11}$	3
13 Al	$9.48 \cdot 10^{4}$	$8.51 \cdot 10^{4}$	$8.5 \cdot 10^{4}$	3
14 Si	$1.00 \cdot 10^{6}$	$1.00 \cdot 10^{6}$	$1.00 \cdot 10^{6}$	3
15 P	$1.00 \cdot 10^{4}$	$1.27 \cdot 10^{4}$	9600	3
16 S	$3.75 \cdot 10^{5}$	$5.06 \cdot 10^{5}$	$5.0 \cdot 10^{5}$	3, 5
17 Cl	8850	1970	5700	3, 5
18 Ar	$1.4 \cdot 10^{5}$	$2.28 \cdot 10^{5}$	$1.172 \cdot 10^{5}$	5
19 K	3160	3240	4200	3, 5
20 Ca	$4.90 \cdot 10^{4}$	$7.36 \cdot 10^{4}$	$7.21 \cdot 10^{4}$	3
21 Sc	28	33	35	6
22 Ti	2240	2300	2775	7
23 V	220	900	262	7
24 Cr	7800	$1.24 \cdot 10^{4}$	$1.27 \cdot 10^{4}$	3
25 Mn	6850	8800	9300	23
26 Fe	$6.00 \cdot 10^{5}$	$8.90 \cdot 10^{5}$	$8.3 \cdot 10^{5}$	23
27 Co	1800	2300	2210	23
28 Ni	$2.74 \cdot 10^{4}$	$4.57 \cdot 10^{4}$	$4.80 \cdot 10^{4}$	3
29 Cu	212	919	540	3

Table A.2: Abundances of the Elements in the Solar System Normalized to Si = 10^6. (Cameron, 1973) (continued)

Element	Suess & Urey	Cameron (1968)	Cameron (1973)	Notes
30 Zn	486	1500	1244	18
31 Ga	11.4	45.5	48	3
32 Ge	50.4	126	115	18
33 As	4.0	7.2	6.6	3
34 Se	67.6	70.1	67.2	18, 24
35 Br	13.4	20.6	13.5	24
36 Kr	51.3	64.4	46.8	8
37 Rb	6.5	5.95	5.88	9, 18
38 Sr	18.9	58.4	26.9	3, 10
39 Y	8.9	4.6	4.8	3
40 Zr	54.5	30	28	3
41 Nb	1.00	1.15	1.4	11
42 Mo	2.42	2.52	4.0	3
44 Ru	1.49	1.6	1.9	3
45 Rh	0.214	0.33	0.4	12
46 Pd	0.675	1.5	1.3	3
47 Ag	0.26	0.5	0.45	18
48 Cd	0.89	2.12	1.48	18
49 In	0.11	0.217	0.189	18
50 Sn	1.33	4.22	3.6	3
51 Sb	0.246	0.381	0.316	18
52 Te	4.67	6.76	6.42	18
53 I	0.80	1.41	1.09	3
54 Xe	4.0	7.10	5.38	13
55 Cs	0.456	0.367	0.387	18
56 Ba	3.66	4.7	4.8	3
57 La	2.00	0.36	0.445	14
58 Ce	2.26	1.17	1.18	14
59 Pr	0.40	0.17	0.149	14
60 Nd	1.44	0.77	0.78	14
62 Sm	0.664	0.23	0.226	14
63 Eu	0.187	0.091	0.085	14

Table A.2: Abundances of the Elements in the Solar System Normalized to Si = 10^6. (Cameron, 1973) (continued)

Element	Suess & Urey	Cameron (1968)	Cameron (1973)	Notes
64 Gd	0.684	0.34	0.297	14
65 Tb	0.0956	0.052	0.055	14
66 Dy	0.556	0.36	0.36	14
67 Ho	0.118	0.090	0.079	14
68 Er	0.316	0.22	0.225	14
69 Tm	0.0318	0.035	0.034	14
70 Yb	0.220	0.21	0.216	14
71 Lu	0.050	0.035	0.036	14
72 Hf	0.438	0.16	0.21	22
73 Ta	0.065	0.022	0.021	15
74 W	0.49	0.16	0.16	16
75 Re	0.135	0.055	0.053	17, 18
76 Os	1.00	0.71	0.75	6
77 Ir	0.821	0.43	0.717	18
78 Pt	1.625	1.13	1.4	6
79 Au	0.145	0.20	0.202	18
80 Hg	0.284	0.75	0.4	19
81 Tl	0.108	0.182	0.192	18
82 Pb	0.47	2.90	4	3
83 Bi	0.144	0.164	0.143	18
90 Th	-	0.034	0.058	6, 20
92 U	-	0.0234	0.0262	18, 21

Notes to Table A.2

1. Normalized to abundances in type-I carbonaceous chondrites by multiplying the solar abundance scale, H = 10^{12}, by 0.03175, which is an average of the ratios of the solar scale and meteoritic scale (Si = 10^6) for the elements Mg, Al, Si, P, S, Ca, Fe, and Ni.
2. Based upon solar flare cosmic rays (Bertsch et al., 1972), for which He/O = 103 ± 10 and Ne/O = 0.16 ± 0.03.
3. Type-I carbonaceous chondrites (Mason, 1971).
4. Solar photospheric composition adopted by Withbroe (1971).
5. Choice of abundance influenced by semi-equilibrium interpolation between ^{28}Si and ^{40}Ca.
6. Weighted mean of carbonaceous chondrites (Mason, 1971).
7. Weighted mean of type-I and -II carbonaceous chondrites (Mason, 1971).

8. Average of the geometric interpolations of ^{84}Kr between ^{80}Se and ^{88}Sr and of ^{83}Kr between ^{81}Br and ^{85}Rb.

9. Present abundance 5.77. Adopted value includes correction for ^{87}Rb decay since solar system formation.

10. Present abundance 27. Adopted value allows for growth of ^{87}Sr since solar system formation.

11. Very little meteorite data: 0.3 in L6, 1.6 in LL6 chondrites (Mason, 1971). Value is an interpolation between ^{91}Zr and ^{95}Mo.

12. Very little meteorite data: 0.4 in H5, 0.31 in L6, 0.70 in LL6, and 0.36 in E4 chondrites (Mason, 1971).

13. Fitted to Te and I to form a continuous abundance peak with the same odd-even abundance ratios centered at mass numbers 127 and 129. Carbonaceous chondrite isotope ratios used.

14. There is little variation in rare Earth abundances among meteorite classes, but type-I carbonaceous chondrite measurements are not as good as those in ordinary chondrites. Hence the latter values were chosen (Mason, 1971) but multiplied by 1.20 to normalize to Orgeuil and Ivuna type-I carbonaceous chondrites (Urey, 1964).

15. No data on C1 meteorites. Value chosen is average of H-group meteorites (Mason, 1971) and is possibly low.

16. Average of C2 and C3 meteorites (Mason, 1971) omitting higher values of Rieder and Wanke (1968).

17. Present value 0.050 has been corrected for decay of ^{187}Re since formation of solar system.

18. Measurements in C1 chondrites (Krähenbühl et al., 1973).

19. Mercury has enormous variations in meteorites, and the carbonaceous chondrite values are one to two orders of magnitude too high for nuclear systematics. The value chosen is a representative value for enstatite chondrites (Mason, 1971).

20. Present value 0.046, corrected for decay since formation of solar system.

21. Present value 0.0098, corrected for decay since formation of solar system.

22. The C1 values of Ehmann and Rebagay (1970) are surprisingly high, since there is no indication that there should be fractionation of Zr or Hf among carbonaceous chondrites. The adopted value was obtained by dividing the C1 Zr abundance of Ehmann and Rebagay by the average chondritic Zr/Hf ratio.

23. Average C1 values of Schmitt et al. (1972).

24. Average C1 value of Goles et al. (1967).

25. See Cameron et al. (1973a).

A.4 Radiation Lengths and Critical Energies

Table A.3: Radiation Length and Critical Energy of Materials.
(after Nishimura 1967; Barnett et al., 1996; extended by author)

Material	Z	A	Radiation Length χ_0		Critical Energy*
			g/cm^2	cm	Mev
H	1	1.008	63.05	752300	350
He	2	4.003	94.32	560000	250
Li	3	6.940	82.76	155	138
Be	4	9.000	65.19	35.3	-
C	6	12.010	42.70	18.8	-
C**	6	12.010	43.3	16.9	79
N	7	14.008	38.6	33100	85
O	8	16.000	34.6	25800	75
Ne	10	20.600	28.94	24.0	-
Al	13	26.980	24.01	8.9	40
Si	14	28.090	21.82	9.36	37.5
Ar	18	39.948	19.55	14.0	35.2
Fe	26	55.85	13.84	1.76	20.7
Cu	29	63.54	12.86	1.43	18.8
Br	35	79.916	11.5	3.71	15.7
Ag	47	10.988	9.0	0.86	11.9
I	53	126.910	8.5	1.74	10.7
W	74	183.85	6.76	0.35	8.08
Pb	82	207.19	6.37	0.56	7.40
Compound Materials					
Air: (Z = 7.4) N 75.52%, O 23.14%, Ar 1.3%			36.66	30420	81.0
Borosilicate Glass (Pyrex)			28.3	12.7	-
CO_2			36.2	18310	-
Fused Quartz SiO_2			27.05	10.3	47.3
LiH			80.0	113	157
Lucite, Plexiglas			40.55	$\simeq$34.4	-
Nuclear Emulsion, G5			11.4	2.98	16.4
Polyethylene CH_2=CH_2			44.8	$\simeq$47.9	-
Polystyrene C_6H_5CH=CH_2			43.8	42.4	-
Water H_2O (Z = 6.6)			36.08	36.1	73.0

* Density effect for solids included. For gaseous media at 20° C and atmospheric pressure. The critical energy is approximately given by 500 MeV/Z. ** For graphite.

A.5 Elements and their Material Parameters

Table A.4: Elements and their Material Parameters.
(after Sternheimer, 1984)

Material	Density	Z	A	I	Density correction constants				
	[g/cm^3]			[eV]	$-C$	X_0	X_1	a	m
Hydrogen	0.063	1	1.008	21.8	3.263	.476	1.922	.135	5.625
Deuterium	0.140	1	2.014	21.8	2.942	.200	2.000	.347	3.000
Helium	0.125	2	4.003	41.8	4.517	.473	2.000	.657	3.000
Lithium	0.534	3	6.940	40.0	3.122	.130	1.640	.951	2.499
Beryllium	1.848	4	9.012	63.7	2.785	.059	1.692	.804	2.434
Boron	2.370	5	10.810	76.0	2.848	.031	1.969	.562	2.451
Carbon	2.265	6	12.011	78.0	2.868	-.018	2.342	.261	2.870
Nitrogen	0.808	7	14.007	82.0	3.998	.304	2.000	.533	3.000
Oxygen	1.140	8	15.999	95.0	3.948	-.287	2.000	.523	3.000
Fluorine	1.108	9	18.998	115.0	4.413	-.200	3.000	.159	3.000
Neon	1.207	10	20.170	137.0	4.632	.200	3.000	.169	3.000
Sodium	0.971	11	22.990	149.0	5.053	.288	3.196	.078	3.645
Magnesium	1.740	12	24.305	156.0	4.530	.150	3.067	.082	3.617
Aluminum	2.699	13	26.982	166.0	4.240	.171	3.013	.080	3.635
Silicon	2.330	14	28.086	173.0	4.435	.201	2.872	.149	3.255
Sulfur	2.000	16	32.060	180.0	4.666	.158	2.716	.340	2.646
Chlorine	1.560	17	35.453	174.0	4.887	.200	3.000	.181	3.000
Argon	1.393	18	39.948	188.0	5.217	.201	3.000	.196	3.000
Potassium	0.862	19	39.098	190.0	5.642	.385	3.172	.198	2.923
Calcium	1.550	20	40.080	191.0	5.040	.323	3.119	.156	3.075
Chromium	7.180	24	51.996	257.0	4.178	.034	3.045	.154	2.990
Manganese	7.440	25	54.938	272.0	4.270	.045	3.107	.150	2.980
Iron	7.874	26	55.847	286.0	4.291	-.001	3.153	.147	2.963
Nickel	8.902	28	58.710	311.0	4.312	-.057	3.185	.165	2.843
Copper	8.960	29	63.546	322.0	4.419	-.025	3.279	.143	2.904
Zinc	7.133	30	65.380	330.0	4.691	.005	3.367	.147	2.865
Germanium	5.323	32	72.590	350.0	5.141	.338	3.610	.072	3.331
Bromine	3.120	35	79.904	343.0	5.641	.339	3.000	.217	3.000
Tin	7.310	50	118.690	488.0	5.534	.288	3.296	.187	2.858
Iodine	4.930	53	126.905	491.0	5.949	.055	3.260	.238	2.728
Barium	3.500	56	137.330	491.0	6.315	.419	3.455	.183	2.891
Tungsten	19.300	74	183.850	727.0	5.406	.217	3.496	.155	2.845
Lead	11.350	82	207.200	823.0	6.202	.378	3.807	.094	3.161
Bismuth	9.747	83	208.980	823.0	6.351	.415	3.825	.094	3.167
Uranium	18.950	92	238.029	890.0	5.869	.226	3.372	.197	2.817

A.6 Muon Energy Loss in Various Elements

Table A.5: Energy Loss of Muons in Various Elements.
(after Lohmann et al., 1985)
Included are energy losses due to ionization, bremsstrahlung, pair production and nuclear interactions.

Energy	Energy Loss, dE/dX [GeV g^{-1} cm^2]			
[GeV]	Carbon	Aluminum	Iron	Lead
1	$1.830 \cdot 10^{-3}$	$1.723 \cdot 10^{-3}$	$1.561 \cdot 10^{-3}$	$1.251 \cdot 10^{-3}$
2	$1.943 \cdot 10^{-3}$	$1.843 \cdot 10^{-3}$	$1.682 \cdot 10^{-3}$	$1.372 \cdot 10^{-3}$
4	$2.053 \cdot 10^{-3}$	$1.958 \cdot 10^{-3}$	$1.802 \cdot 10^{-3}$	$1.494 \cdot 10^{-3}$
6	$2.113 \cdot 10^{-3}$	$2.022 \cdot 10^{-3}$	$1.870 \cdot 10^{-3}$	$1.569 \cdot 10^{-3}$
8	$2.155 \cdot 10^{-3}$	$2.066 \cdot 10^{-3}$	$1.919 \cdot 10^{-3}$	$1.626 \cdot 10^{-3}$
10	$2.187 \cdot 10^{-3}$	$2.100 \cdot 10^{-3}$	$1.958 \cdot 10^{-3}$	$1.674 \cdot 10^{-3}$
15	$2.245 \cdot 10^{-3}$	$2.163 \cdot 10^{-3}$	$2.032 \cdot 10^{-3}$	$1.777 \cdot 10^{-3}$
20	$2.287 \cdot 10^{-3}$	$2.211 \cdot 10^{-3}$	$2.091 \cdot 10^{-3}$	$1.868 \cdot 10^{-3}$
30	$2.350 \cdot 10^{-3}$	$2.285 \cdot 10^{-3}$	$2.189 \cdot 10^{-3}$	$2.037 \cdot 10^{-3}$
40	$2.400 \cdot 10^{-3}$	$2.348 \cdot 10^{-3}$	$2.275 \cdot 10^{-3}$	$2.201 \cdot 10^{-3}$
50	$2.444 \cdot 10^{-3}$	$2.404 \cdot 10^{-3}$	$2.357 \cdot 10^{-3}$	$2.364 \cdot 10^{-3}$
60	$2.484 \cdot 10^{-3}$	$2.457 \cdot 10^{-3}$	$2.436 \cdot 10^{-3}$	$2.527 \cdot 10^{-3}$
70	$2.521 \cdot 10^{-3}$	$2.508 \cdot 10^{-3}$	$2.513 \cdot 10^{-3}$	$2.690 \cdot 10^{-3}$
80	$2.557 \cdot 10^{-3}$	$2.558 \cdot 10^{-3}$	$2.590 \cdot 10^{-3}$	$2.855 \cdot 10^{-3}$
90	$2.591 \cdot 10^{-3}$	$2.606 \cdot 10^{-3}$	$2.666 \cdot 10^{-3}$	$3.020 \cdot 10^{-3}$
100	$2.624 \cdot 10^{-3}$	$2.655 \cdot 10^{-3}$	$2.741 \cdot 10^{-3}$	$3.186 \cdot 10^{-3}$
120	$2.689 \cdot 10^{-3}$	$2.749 \cdot 10^{-3}$	$2.893 \cdot 10^{-3}$	$3.521 \cdot 10^{-3}$
140	$2.752 \cdot 10^{-3}$	$2.843 \cdot 10^{-3}$	$3.044 \cdot 10^{-3}$	$3.860 \cdot 10^{-3}$
160	$2.814 \cdot 10^{-3}$	$2.936 \cdot 10^{-3}$	$3.195 \cdot 10^{-3}$	$4.201 \cdot 10^{-3}$
180	$2.875 \cdot 10^{-3}$	$3.029 \cdot 10^{-3}$	$3.347 \cdot 10^{-3}$	$4.545 \cdot 10^{-3}$
200	$2.935 \cdot 10^{-3}$	$3.121 \cdot 10^{-3}$	$3.499 \cdot 10^{-3}$	$4.890 \cdot 10^{-3}$
220	$2.995 \cdot 10^{-3}$	$3.214 \cdot 10^{-3}$	$3.652 \cdot 10^{-3}$	$5.238 \cdot 10^{-3}$
240	$3.055 \cdot 10^{-3}$	$3.306 \cdot 10^{-3}$	$3.805 \cdot 10^{-3}$	$5.586 \cdot 10^{-3}$
260	$3.114 \cdot 10^{-3}$	$3.398 \cdot 10^{-3}$	$3.958 \cdot 10^{-3}$	$5.937 \cdot 10^{-3}$
280	$3.173 \cdot 10^{-3}$	$3.490 \cdot 10^{-3}$	$4.112 \cdot 10^{-3}$	$6.290 \cdot 10^{-3}$
300	$3.232 \cdot 10^{-3}$	$3.583 \cdot 10^{-3}$	$4.265 \cdot 10^{-3}$	$6.643 \cdot 10^{-3}$
350	$3.379 \cdot 10^{-3}$	$3.814 \cdot 10^{-3}$	$4.652 \cdot 10^{-3}$	$7.531 \cdot 10^{-3}$
400	$3.525 \cdot 10^{-3}$	$4.045 \cdot 10^{-3}$	$5.040 \cdot 10^{-3}$	$8.425 \cdot 10^{-3}$

Table A.5: Energy Loss of Muons in Various Elements (continued). Included are energy losses due to ionization, bremsstrahlung, pair production and nuclear interactions.

Energy	Energy Loss, dE/dX [GeV g^{-1} cm^2]			
[GeV]	Carbon	Aluminum	Iron	Lead
450	$3.671 \cdot 10^{-3}$	$4.277 \cdot 10^{-3}$	$5.429 \cdot 10^{-3}$	$9.323 \cdot 10^{-3}$
500	$3.816 \cdot 10^{-3}$	$4.509 \cdot 10^{-3}$	$5.821 \cdot 10^{-3}$	$1.023 \cdot 10^{-2}$
600	$4.108 \cdot 10^{-3}$	$4.974 \cdot 10^{-3}$	$6.607 \cdot 10^{-3}$	$1.204 \cdot 10^{-2}$
700	$4.399 \cdot 10^{-3}$	$5.442 \cdot 10^{-3}$	$7.395 \cdot 10^{-3}$	$1.387 \cdot 10^{-2}$
800	$4.691 \cdot 10^{-3}$	$5.911 \cdot 10^{-3}$	$8.189 \cdot 10^{-3}$	$1.570 \cdot 10^{-2}$
900	$4.983 \cdot 10^{-3}$	$6.380 \cdot 10^{-3}$	$8.985 \cdot 10^{-3}$	$1.754 \cdot 10^{-2}$
1000	$5.276 \cdot 10^{-3}$	$6.852 \cdot 10^{-3}$	$9.782 \cdot 10^{-3}$	$1.939 \cdot 10^{-2}$
1500	$6.744 \cdot 10^{-3}$	$9.222 \cdot 10^{-3}$	$1.380 \cdot 10^{-2}$	$2.869 \cdot 10^{-2}$
2000	$8.220 \cdot 10^{-3}$	$1.161 \cdot 10^{-2}$	$1.785 \cdot 10^{-2}$	$3.806 \cdot 10^{-2}$
3000	$1.119 \cdot 10^{-2}$	$1.642 \cdot 10^{-2}$	$2.600 \cdot 10^{-2}$	$5.691 \cdot 10^{-2}$
4000	$1.418 \cdot 10^{-2}$	$2.125 \cdot 10^{-2}$	$3.419 \cdot 10^{-2}$	$7.584 \cdot 10^{-2}$
5000	$1.719 \cdot 10^{-2}$	$2.611 \cdot 10^{-2}$	$4.241 \cdot 10^{-2}$	$9.484 \cdot 10^{-2}$
6000	$2.020 \cdot 10^{-2}$	$3.098 \cdot 10^{-2}$	$5.065 \cdot 10^{-2}$	$1.139 \cdot 10^{-1}$
7000	$2.323 \cdot 10^{-2}$	$3.587 \cdot 10^{-2}$	$5.892 \cdot 10^{-2}$	$1.329 \cdot 10^{-1}$
8000	$2.626 \cdot 10^{-2}$	$4.076 \cdot 10^{-2}$	$6.719 \cdot 10^{-2}$	$1.520 \cdot 10^{-1}$
9000	$2.930 \cdot 10^{-2}$	$4.566 \cdot 10^{-2}$	$7.548 \cdot 10^{-2}$	$1.711 \cdot 10^{-1}$
10000	$3.235 \cdot 10^{-2}$	$5.057 \cdot 10^{-2}$	$8.377 \cdot 10^{-2}$	$1.902 \cdot 10^{-1}$

A.7 Muon Energy Loss in Compounds

Table A.6: Energy Loss of Muons in Various Compounds.
(after Lohmann et al., 1985)
Included are energy losses due to ionization, bremsstrahlung, pair production and nuclear interactions.

Energy	Energy Loss, dE/dX [GeV g^{-1} cm^2]		
[GeV]	Std. Rock	Water	Concrete
1	$1.787 \cdot 10^{-3}$	$2.087 \cdot 10^{-3}$	$1.813 \cdot 10^{-3}$
2	$1.907 \cdot 10^{-3}$	$2.213 \cdot 10^{-3}$	$1.934 \cdot 10^{-3}$
4	$2.024 \cdot 10^{-3}$	$2.336 \cdot 10^{-3}$	$2.052 \cdot 10^{-3}$
6	$2.090 \cdot 10^{-3}$	$2.405 \cdot 10^{-3}$	$2.118 \cdot 10^{-3}$
8	$2.135 \cdot 10^{-3}$	$2.452 \cdot 10^{-3}$	$2.163 \cdot 10^{-3}$
10	$2.170 \cdot 10^{-3}$	$2.488 \cdot 10^{-3}$	$2.198 \cdot 10^{-3}$
15	$2.234 \cdot 10^{-3}$	$2.554 \cdot 10^{-3}$	$2.263 \cdot 10^{-3}$
20	$2.282 \cdot 10^{-3}$	$2.602 \cdot 10^{-3}$	$2.311 \cdot 10^{-3}$
30	$2.355 \cdot 10^{-3}$	$2.674 \cdot 10^{-3}$	$2.385 \cdot 10^{-3}$
40	$2.416 \cdot 10^{-3}$	$2.731 \cdot 10^{-3}$	$2.447 \cdot 10^{-3}$
50	$2.470 \cdot 10^{-3}$	$2.781 \cdot 10^{-3}$	$2.502 \cdot 10^{-3}$
60	$2.520 \cdot 10^{-3}$	$2.826 \cdot 10^{-3}$	$2.553 \cdot 10^{-3}$
70	$2.569 \cdot 10^{-3}$	$2.869 \cdot 10^{-3}$	$2.602 \cdot 10^{-3}$
80	$2.615 \cdot 10^{-3}$	$2.910 \cdot 10^{-3}$	$2.649 \cdot 10^{-3}$
90	$2.661 \cdot 10^{-3}$	$2.949 \cdot 10^{-3}$	$2.696 \cdot 10^{-3}$
100	$2.706 \cdot 10^{-3}$	$2.988 \cdot 10^{-3}$	$2.741 \cdot 10^{-3}$
120	$2.794 \cdot 10^{-3}$	$3.063 \cdot 10^{-3}$	$2.831 \cdot 10^{-3}$
140	$2.881 \cdot 10^{-3}$	$3.135 \cdot 10^{-3}$	$2.920 \cdot 10^{-3}$
160	$2.966 \cdot 10^{-3}$	$3.207 \cdot 10^{-3}$	$3.007 \cdot 10^{-3}$
180	$3.052 \cdot 10^{-3}$	$3.278 \cdot 10^{-3}$	$3.094 \cdot 10^{-3}$
200	$3.137 \cdot 10^{-3}$	$3.347 \cdot 10^{-3}$	$3.181 \cdot 10^{-3}$
220	$3.222 \cdot 10^{-3}$	$3.417 \cdot 10^{-3}$	$3.267 \cdot 10^{-3}$
240	$3.306 \cdot 10^{-3}$	$3.486 \cdot 10^{-3}$	$3.353 \cdot 10^{-3}$
260	$3.391 \cdot 10^{-3}$	$3.555 \cdot 10^{-3}$	$3.440 \cdot 10^{-3}$
280	$3.475 \cdot 10^{-3}$	$3.623 \cdot 10^{-3}$	$3.526 \cdot 10^{-3}$
300	$3.560 \cdot 10^{-3}$	$3.692 \cdot 10^{-3}$	$3.612 \cdot 10^{-3}$
350	$3.771 \cdot 10^{-3}$	$3.862 \cdot 10^{-3}$	$3.827 \cdot 10^{-3}$
400	$3.983 \cdot 10^{-3}$	$4.032 \cdot 10^{-3}$	$4.042 \cdot 10^{-3}$

Table A.6: Energy Loss of Muons in Various Compounds (continued). Included are energy losses due to ionization, bremsstrahlung, pair production and nuclear interactions.

Energy	Energy Loss, dE/dX [GeV g^{-1} cm^2]		
[GeV]	Std. Rock	Water	Concrete
450	$4.194 \cdot 10^{-3}$	$4.202 \cdot 10^{-3}$	$4.258 \cdot 10^{-3}$
500	$4.406 \cdot 10^{-3}$	$4.372 \cdot 10^{-3}$	$4.473 \cdot 10^{-3}$
600	$4.831 \cdot 10^{-3}$	$4.711 \cdot 10^{-3}$	$4.906 \cdot 10^{-3}$
700	$5.258 \cdot 10^{-3}$	$5.050 \cdot 10^{-3}$	$5.340 \cdot 10^{-3}$
800	$5.685 \cdot 10^{-3}$	$3.390 \cdot 10^{-3}$	$5.775 \cdot 10^{-3}$
900	$6.113 \cdot 10^{-3}$	$5.731 \cdot 10^{-3}$	$6.211 \cdot 10^{-3}$
1000	$6.543 \cdot 10^{-3}$	$6.071 \cdot 10^{-3}$	$6.648 \cdot 10^{-3}$
1500	$8.702 \cdot 10^{-3}$	$7.782 \cdot 10^{-3}$	$8.845 \cdot 10^{-3}$
2000	$1.088 \cdot 10^{-2}$	$9.502 \cdot 10^{-3}$	$1.106 \cdot 10^{-2}$
3000	$1.525 \cdot 10^{-2}$	$1.296 \cdot 10^{-2}$	$1.551 \cdot 10^{-2}$
4000	$1.966 \cdot 10^{-2}$	$1.644 \cdot 10^{-2}$	$1.999 \cdot 10^{-2}$
5000	$2.408 \cdot 10^{-2}$	$1.994 \cdot 10^{-2}$	$2.448 \cdot 10^{-2}$
6000	$2.852 \cdot 10^{-2}$	$2.345 \cdot 10^{-2}$	$2.899 \cdot 10^{-2}$
7000	$3.297 \cdot 10^{-2}$	$2.697 \cdot 10^{-2}$	$3.352 \cdot 10^{-2}$
8000	$3.743 \cdot 10^{-2}$	$3.049 \cdot 10^{-2}$	$3.805 \cdot 10^{-2}$
9000	$4.190 \cdot 10^{-2}$	$3.403 \cdot 10^{-2}$	$4.259 \cdot 10^{-2}$
10000	$4.637 \cdot 10^{-2}$	$3.758 \cdot 10^{-2}$	$4.714 \cdot 10^{-2}$

A.8 Units and Conversion Factors

Table A.7: Astrophysical Units and Conversion Factors.

Unit	Name	Corresponds to
1 [y]	Year	$3.156 \cdot 10^7$ s 10^{-9} Æon
1 [AU]	Astronomical Unit	$1.4960 \cdot 10^{13}$ cm $4.848 \cdot 10^{-3}$ pc $1.581 \cdot 10^{-5}$ ly
1 [pc]	Parsec	$3.0857 \cdot 10^{18}$ cm $2.06265 \cdot 10^5$ AU 3.262 ly
1 [ly]	Light Year	$9.4605 \cdot 10^{17}$ cm 0.3066 pc $6.324 \cdot 10^4$ AU
1 [eV]	Electronvolt	$1.6021892 \cdot 10^{-19}$ J or Ws
1 [J]	Joule	$6.241 \cdot 10^{18}$ eV 10^7 erg
1 [Jy]	Jansky	10^{-30} W cm^{-2} Hz^{-1}
1 [R]	Rayleigh	10^6 ph cm^{-2} s^{-1} per column
1 [T]	Tesla	10^4 G or 1 V s m^{-2}
1 [G]	Gauss	10^{-4} T
1 [γ]	Gamma	10^{-5} G 1 nT

Table A.8: Pressure Units and Conversion Factors.

Unit	Name	Corresponds to
1 [Pa]	Pascal	1 N m^{-2} $7.5 \cdot 10^{-3}$ Torr $9.87 \cdot 10^{-6}$ atm. 0.01 mbar

Table A.9: Radiation Dosimetry, Units and Conversion Factors.

Unit	Name	Corresponds to
1 [Bq]	Becquerel	1 disintegration s^{-1}
1 [Ci]	Curie	$3.7 \cdot 10^{10}$ Bq
1 [Gy]	Gray	1 J kg^{-1} $6.24 \cdot 10^{12}$ MeV kg^{-1} 100 rad
1 [R]	Röntgen	$2.58 \cdot 10^{-4}$ coul kg^{-1} air
1 [Sv]	Sievert	100 rem (roentgen equivalent man) 1 Gy$\cdot \omega_R$ (ω_R, radiation weight factor)

A.9 Constants and Parameters

Table A.10: Constants and Parameters.

Depth of atmosphere	1033 g cm^{-2}
Gas constant	8.314 J K^{-1} g^{-1} mol^{-1}
Effective temperature of atmosphere	219 K
Effective molecular weight of air	28.966
Density of air at s.l., 10°C, 76 cm Hg	0.00124 g cm^{-3}
Energy loss of relativistic muons in air	2.225 MeV g^{-1} cm^{-2}
Velocity of light	$2.9978 \cdot 10^{10}$ cm s^{-1}
Electron rest mass	0.511 MeV
Muon rest mass	105.659 MeV
Charged pion rest mass	139.570 MeV
Neutral pion rest mass	134.976 MeV
Charged kaon rest mass	493.677 MeV
Proton rest mass	938.272 MeV
Neutron rest mass	939.566 MeV
Mean life of muon at rest	$2.20 \cdot 10^{-6}$ s
Mean life of pion at rest	$2.616 \cdot 10^{-8}$ s
Mean life of kaon at rest	$1.240 \cdot 10^{-8}$ s
Mean life of neutron at rest	887.0 s

References

Anders, E., and N. Grevesse: Geochin. Cosmochim. Acta, 53, p. 197 (1989).

Barnett, J.J., and S. Chandra: Adv. Space Res., 10, No. 12, p. (12)7 (1990).

Barnett, R.M., C.D. Carone, D.E. Groom, T.G. Trippe, C.G. Wohl, B. Armstrong, P.S. Gee, G.S. Wagman, F. James, M. Mangano, K. Mönig, L. Montanet, J.L. Feng, H. Murayama, J.J. Hernàndez, A. Manohar, M. Aguilar-Benitez, C. Caso, M. Roos, N.A. Törnqvist, K.G. Hayes, K. Hagiwara, S. Kawabata, K. Nakamura, M. Tanabashi, K. Olive, K. Honscheid, P.R. Burchat, R.E. Shrock, S. Eidelman, R.H. Schindler, A. Gurtu, K. Hikasa, G. Conforto, R.L. Workman, C. Grab, and C. Amsler: Phys. Rev., D 54, 1 (1996).

Bertsch, D.L., C.E. Fichtel, and D.V. Reames: Astrophys. J., 171, p. 169 (1972).

Cameron, A.G.W.: in "Origin and Distribution of the Elements", L.H. Ahrens (ed.), Pergamon Press, Oxford (1968).

Cameron, A.G.W.: Space Sci. Rev., 15, p 121 (1973).

Cameron, A.G.W., S.A. Colgate, and L. Grossman: Nature, 243, p. 204 (1973).

Cameron, A.G.W.: Essays in Nuclear Astrophysics, eds. Barnes, Clayton and Schramm, Cambridge Univ. Press, Cambridge, p. 23 (1981).

Cameron, A.G.W.: Astrophys. Space Sci., 82, p. 123 (1982).

Ehmann, W.D., and T.V. Rebagay: Geochim. Cosmochim. Acta, 34, p. 649 (1970).

Goles, G.G., L.P. Greenland, and D.Y. Jerome: Geochim. Cosmochim. Acta, 31, p. 1771 (1967).

J.A. Hinton: Dept. of Physics, University of Leeds, GB, private communication (1999).

Krähenbühl, U., J.W. Morgan, R. Ganapathy, and E. Anders: Geochim. Cosmochim. Acta, 37, p. 1353 (1973).

Lohmann, W., R. Kopp, and R. Voss: CERN Yellow Report 85-03 (1985).

Mason, B., ed.: Handbook of Elemental Abundances in Meteorites, Gordon and Breach Science Publishers, New York (1971).

Nishimura, J.: Handbuch der Physik, 46/2, p. 1, Springer Verlag, Berlin (1967).

Petrukhin, A.A., and V.V. Shestakov: Can. J. Phys., 46, p. S377 (1968).

Rieder, R., and H. Wanke: in "Meteorite Research", P.M. Millman, ed., P. Reidel Publishing Co., Dordrecht (1969).

Schmitt, R.A., G.G. Goles, R.A. Smith, and T.W. Osborn: Meteoritics, 7, p. 131 (1972).

Urey, H.: Rev. Geophys, 2, p. 1 (1964).

Withbroe, G.L.: "The Chemical Composition of the Photosphere and Corona", in Menzel Symposium on Solar Physics, Atomic Spectra, and Gaseous Nebulae, National Bureau of Standards Special Pub. No. 353, p. 127 (1971).

Appendix B

Miscellaneous Data: Figures

B.1 Comments to Figures

Some of the data presented in the following figures are complementary to topics discussed in the previous chapters, others are not directly related but may be useful for quick reference. Background material, where relevant, can be found in the references given below.

References

Becker-Szendy, R., C.B. Bratton, D.R. Cady, D. Casper, R. Claus, M. Crouch, S.T. Dye, W. Gajewski, M. Goldhaber, T.J. Haines, P.G. Halverson, T.W. Jones, D. Kielczewska, W.R. Kropp, J.G. Learned, J.M. LoSecco, C. McGrew, S. Matsuno, J. Matthews, M.S. Mudan, L. Price, F. Reines, J. Schultz, D. Sinclair, H.W. Sobel, J.L. Stone, L.R. Sulak, R. Svoboda, G. Thornton, and J.C. van der Velde: Phys. Rev., D 42, p. 2974 (1990).

Ganezer, Kenneth S., Super-Kamiokande Collaboration: PICRC, 2, p. 328 (1999).

Hirata, K.S., T. Kajita, K. Kifune, K. Kihara, M. Nakahata, K. Nakamura, S. Ohara, Y. Oyama, N. Sato, M. Takita, Y. Totsuka, Y. Yaginuma, M. Mori, A. Suzuki, K. Takahashi, T. Tanimori, M. Yamada, M. Koshiba, T. Suda, K. Miyano, H. Miyata, H. Takei, K. Kaneyuki, Y. Nagashima, Y. Suzuki, E.W. Beier, L.R. Feldscher, E.D. Frank, W. Frati, S.B. Kim, A.K. Mann, F.M. Newcomer, R. Van Berg, and W. Zhang: Phys. Lett., B, 220, p. 308 (1989).

Kielczewska, Danuta: Rapporteur Paper XXVI Internat. Cosmic Ray Conf. (1999), AIP Conf. Proc., 516, p. 225 (2000).

Kyker, Granvil, C., Jr., and Abraham R. Liboff: J. Geophys. Res., 83, p. 5539 (1978).

Shiozawa, M.: Proc. Internat. Conf. on High Energy Physics, Osaka, Japan, July 2000, World Scientific (in press).

Smart, D.F., and M.A. Shea: p 6-14 in "Handbook of Geophysics and Space Environment", Adolph S. Jursa, ed., Air Force Geophysical Laboratory (1985).

B.2 Kinetic Energy - Rigidity Conversion

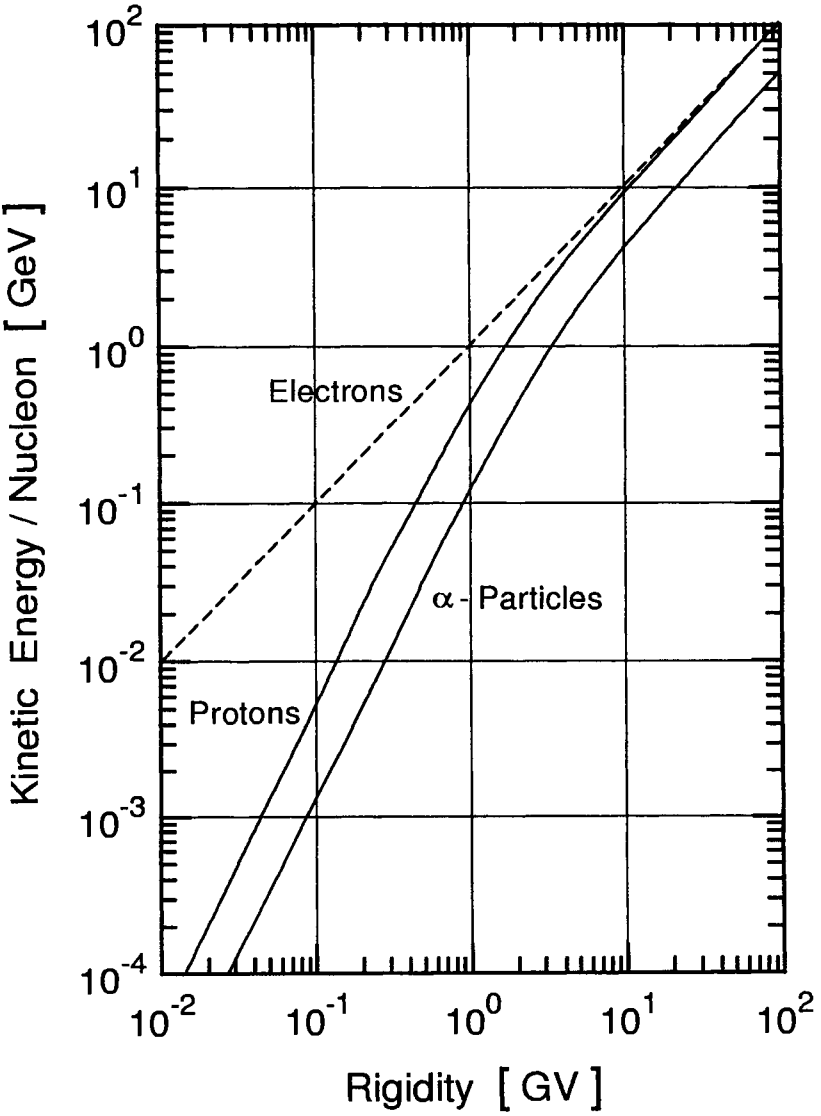

Figure B.1: Kinetic energy as a function of rigidity for electrons, protons and alpha particles.

B.3 Gyroradius versus Proton Energy

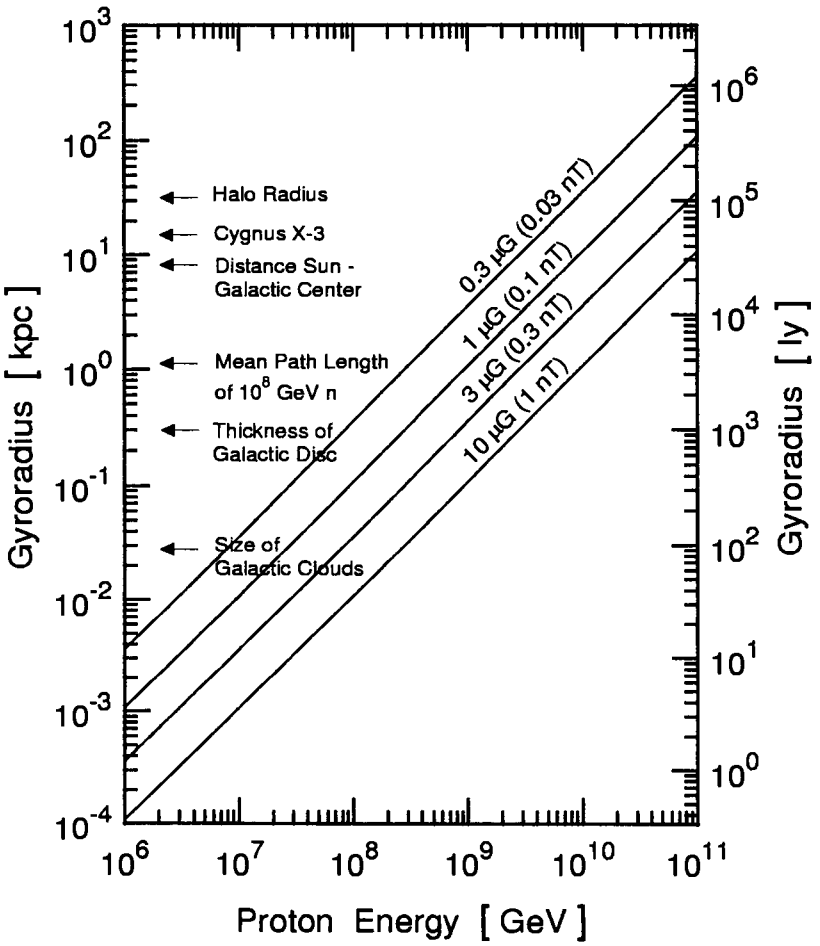

Figure B.2: Gyroradius in kiloparsec [kpc] and light years [ly] of a proton versus proton energy in magnetic fields of 0.3 μG (0.03 nT), 1 μG (0.1 nT), 3 μG (0.3 nT), and 10 μG (1 nT). Indicated, too, are the sizes of some astrophysical objects and regions, the distance to Cygnus X-3, and the mean path length traveled by a 10^8 GeV neutron before decay.

B.4 Ionization versus Depth in Atmosphere

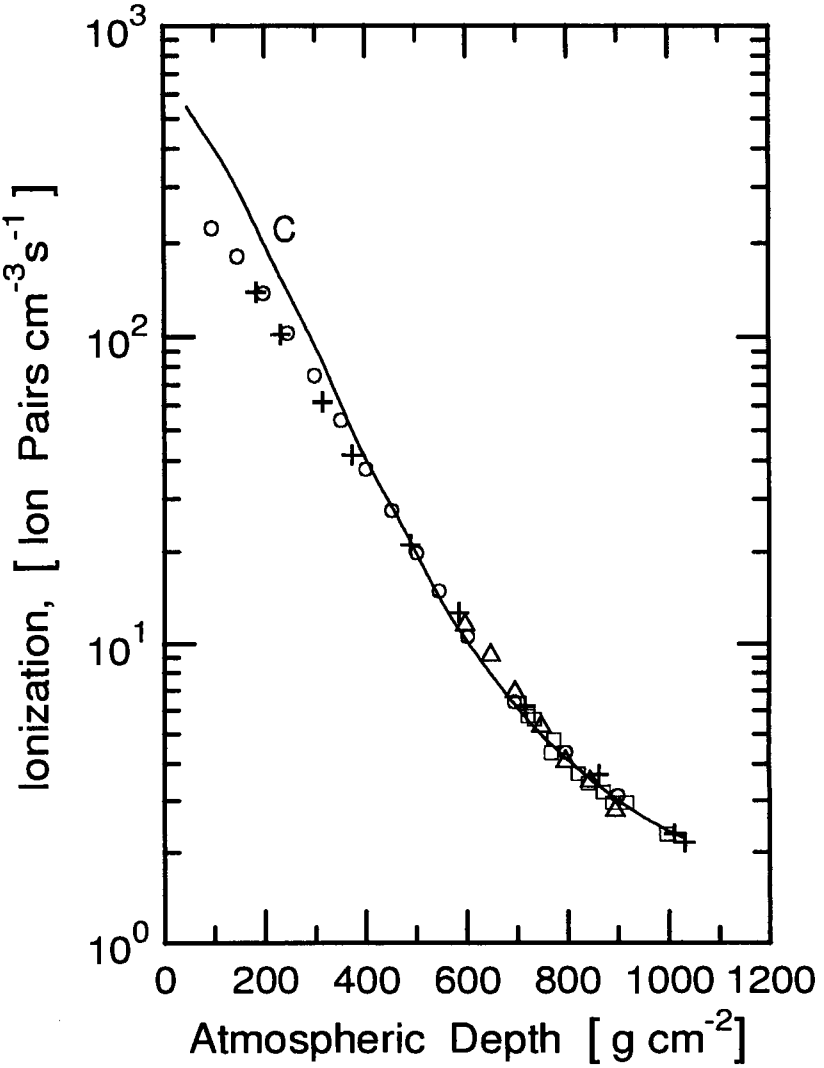

Figure B.3: Measured (symbols) and calculated (curve C) variation of the cosmic ray induced ionization as a function of depth in the atmosphere. The data are normalized to a sea level value of 2.15 ion pairs per cubic centimeter and second at sea level (Kykler and Liboff, 1978; Smart and Shea, 1985).

B.5 Nucleon Lifetime Limits

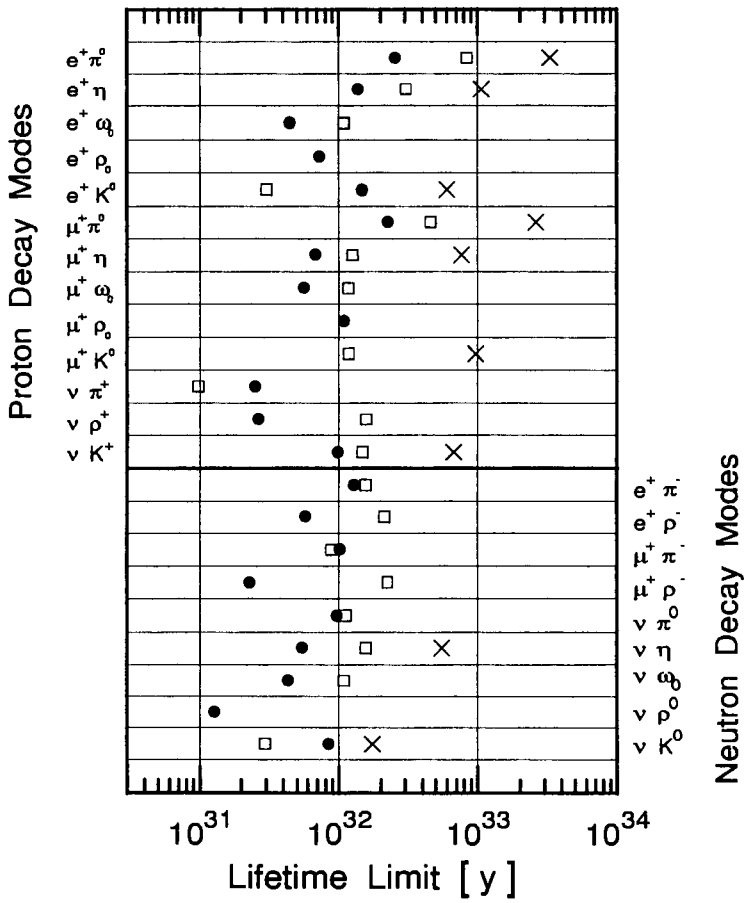

Figure B.4: Preliminary nucleon lifetime limits at 90% c.l. obtained by Super-Kamiokande and the previous best limits from the IMB and Kamiokande detectors (Shiozawa, 2000; see also Kielczewska, 2000).

× Super-Kamiokande (Ganezer et al., 1999)
• Kamiokande (Hirate et al., 1989)
□ IMB (Becker-Szendy et al., 1992; McGrew et al., 1999)

Appendix C

Cosmic Ray Experiments of Past and Present

C.1 Cosmic Ray Ground Level Facilities

C.1.1 Comments to Tables

In the following we present some lists of different types of ground based cosmic ray experiments of the past and present.

In Table C.1 we present an extensive list of air shower arrays. The altitudes of the arrays are listed together with the corresponding atmospheric depths. The latter are in most cases the vertical atmospheric depths, however, sometimes authors may specify a different value in different publications for the same array. The reason for these discrepancies is that in some cases authors consider the slant depth for the average near vertical shower, e.g., $\sim 15°$, as compared to the depth for perfectly vertical showers that are the exception.

In Tables C.2 we list major gamma ray air Cherenkov detectors. Many are narrow-beam detectors, some are stereo type installations, some telescope arrays, and some are hybrid type detectors. A recent list and detailed description of narrow-beam Cherenkov experiments is given by Bhat (1997).

In Table C.3 we list emulsion chamber experiments and their locations.

In Table C.4 we list some balloon spectrometer experiments, the years of the flights, the locations and altitudes from where the launches took place, the range of altitudes where the data were taken and the particles that were under investigation (the list is incomplete).

C.1.2 EAS Array Sites of Past and Present

Table C.1: List of EAS Array Sites of Past and Present.

Name, Place, Country (nearest major city)	Altitude a.s.l. m	Atmospheric Depth g/cm^2
AGASA, see Akeno	-	-
Agassiz, (Boston) USA[1]	183	1020
Akeno, (Kofu), Japan	900	930
ANI/Aragatz, (Erevan), Armenia [2]	3250	695
Auger, (Malargue), Argentina[2]	1469	800
Bagnères de Bigorre, France	456	965
Baksan, Kabardian-Balkarian Rep., Russia	1700	820
Buckland Park, (Adelide), SA, Australia	s.l.	1033
CASA-BLANCA, (Dugway), Utah, USA	1435	870
CASA-MIA, (Dugway), Utah, USA	1435	870
Chacaltaya, (La Paz), Bolivia	5230	530
Cornell, (Ithaca), NY, USA[1]	260	998
Cygnus, (Los Alamos), NM, USA	2220	800
Dugway, UT, USA	1450	865
Durham, England[1]	60	1025
EAS-TOP, Gran Sasso, Italy	2005	820
EAS-1000, (Alma Ata), Kazakhstan[2]	500	970
Echo Lake, Colorado, USA[1]	3260	715
El Alto, (La Paz), Bolivia[1]	4200	630
Evans, Mt., Colorado, USA[1]	4300	615
Fly's Eye 1, (Dugway), Utah, USA	1585	860
Fly's Eye 2, (Dugway), Utah, USA	1435	870
GASP, (Cherenkov) South Pole[3]	2834	688
GRAND, (South Bend), Indiana, USA	200	1018
GREX, Haverah Park, (Leeds), England	212	1018
Gulmarg, (Srinagar), Kashmir, India[1]	2743	740
Haverah Park, (Leeds), England[1]	212	1018
HEGRA, La Palma, Canary Islands	2200	800
Homestake, South Dakota, USA (surface)	488	978
Issik-Kul Lake, (Alma Ata), Kazakhstan[2]	1600	845
JANZOS, New Zealand	1640	840
KASCADE, Karlsruhe, Germany	110	1022
Kiel, Germany[1]	s.l.	1033

Table C.1: List of EAS Array Sites of Past and Present (continued).

Name, Place, Country (nearest major city)	Altitude m	Atmospheric Depth g/cm^2
Kobe, Japan	s.l.	1033
KGF, Kolar Gold Fields, (Karnataka), India	920	920
Liang Wang, Mt., Yun-Nan, China[2]	2700	745
Lodz, Poland	230	1000
MILARGO, (Los Alamos), N.M., U.S.A.	2630	747
Moscow, Russia	192	1020
Musala Mountain, Bulgaria[1]	2925	713
NASCA, see Akeno	-	-
Norikura, Mt., (Matsumoto), Japan	2770	750
Ohya, (Nikko), Japan	149	1020
Ootacamund, (Mysor), India	2200	800
Pamir, Tadzhikistan (new Station)	4380	596
Pic du Midi, Pyrenees, France[1]	2855	729
Plateau Rosa, Italy	3500	675
Samarkand, Uzbekistan	750	958
SPASE, South Pole (Antarctica)	2834	688[3]
SPICA, see Akeno	-	-
SUGAR, (Narrabri), Australia[1]	260	998
Sulphur Mountain, Alberta, Canada[1]	2285	800
Sydney, Australia	30	1016
Tibet, Yangbajing, (Lhasa), China	4370	606
Tien Shan, (Alma Ata), Kazakhstan	3340	690
Tokyo, INS, Japan[1]	59	1020
Tunka Valley, near Baikal Lake, Russia	680	948
UMC array, see CASA/MIA/Fly's Eye	-	-
Verrières (Paris), France[1]	100	1020
Volcano Ranch, (Albuquerque), N.M., USA[1]	1768	834
Yakutsk, Siberia, Russia	105	1020

[1] Shut-down. [2] Under construction or partial operation. [3] Non-standard altitude - pressure relation applies (see Chapter 7, Section 7.4).

Note: Some of the atmospheric depths listed above do not correspond exactly to the vertical air column at the specified altitude, but to the effective air column of an incident trajectory subtending a mean zenith angle of about 10° to 15°. This zenith angular cut is frequently used to select a reasonable number of quasi vertical events for analysis.

C.1.3 Air Cherenkov Array/Telescope Sites

Table C.2: List of TeV Gamma Ray Air Cherenkov Array / Telescope Sites[1].

Name, Place, Country (nearest major city)	Altitude m	Atmospheric Depth g/cm^2
Akeno, Kofu, Japan	900	930
ASGAT, Targasonne, France	1650	840
BIGRAT, Woomera, South Australia	160	1000
Cangaroo, Woomera, South Australia	160	1000
CAT, Thémis, France	1650	842
Crimean AP Obs., Nauchny, Ukraina	2100	800
DICE, Dugway, UT, USA	1435	870
GASP 1, South Pole	3300	695
GRAPES, Ootacamund, India	2200	800
Haleakala, Maui, Hawaii, USA[2]	3297	695
HEGRA, La Palma, Canary Islands	2200	800
Mark-6, near Narrabri, Australia	250	998
Mount Cedar, Utah, USA	1600	847
PACT, Pachmarhi, India	1075	920
Nooigedacht, Potchefstrom, S. A.	1429	880
Shalon Alatoo, near Tien Shan, Kazakhstan	3338	671
TACTIC 1, 2, Mt Abu, India	1300/1700	875/833
Thémistocle, Targasonne, France	1650	840
Whipple Obs., Mt. Hopkins, Arizona, USA	2380	730

[1] Some systems have thresholds as low as 0.1 TeV. [2] Shut-down.

References

Bhat, Chaman, L.: PICRC, 8, p. 211 (1997)..

C.1.4 Emulsion Chamber Sites

Table C.3: List of Major Emulsion Chamber Sites.

Name, Place, Country (nearest major city)	Altitude m	Atmospheric Depth g/cm^2
Chacaltaya, BASJE, (La Paz), Bolivia(1)	5230	540
Fuji, Mt., Japan	3776	650
Kanbala, Mt., Tibet, China	5450	520
Pamir Mountains, Tadzhikistan (Old Station)(2)	3860	625
Pamir Mountains, Tadzhikistan (New Station)	4380	596

(1) coupled with dedicated counter array. (2) shut-down.

C.2 Balloon Experiments

Table C.4: List of Some Balloon Experiments

Experiment	Flight Year	Launch Location Name	m a.s.l.	Altitude [g/cm^2]	Particles Investigated
BESS[1]	1993-95	Lynn Lake	360	4 - 5	$p, \bar{p}$, He , $\overline{He}$
BESS[1]	1995	Tsukuba	s.l.	1020	$\mu^{\pm}$
BESS[1]	1997-99	Lynn Lake	360	4 - 5	$\mu^{\pm}, p, \bar{p}, He, \overline{He}$
BESS[1]	1998	Tsukuba	s.l.	1020	$\mu^{\pm}$
MASS[1]	1989	Prince Albert	600	910 - 5	$\mu^{\pm}, \bar{p}, e^{\pm}$
MASS[1]	1991	Ft. Sumner	1270	886 - 5.8	$\mu^{\pm}, p, \bar{p}, e^{\pm}$, He
IMAX[1]	1992	Lynn Lake	360	960 - 5	$\mu^{\pm}, \bar{p}$
CAPRICE[1]	1994	Lynn Lake	360	1000 - 3.9	$\mu^{\pm}, p, \bar{p}, e$
CAPRICE[1]	1997	Ft. Sumner	1270	886 - 3.9	$\mu^{\pm}, \bar{p}$
CAPRICE[1]	1998	Ft. Sumner	1270	886 - 5	$\mu^{\pm}, e^{\pm}$
HEAT[1]	1994	Ft. Sumner	1270	850 - 5.7	$e^{\pm}$
HEAT[1]	1995	Lynn Lake	360	960 - 4.8	$\mu^{\pm}, e^{\pm}$
LEAP[1]	1987	Prince Albert	600	4.7	$\bar{p}$
PBAR[1]	1987	Prince Albert	600	(36 km)	$p, \bar{p}$
BETS	1995	Sanriku	s.l.	(38 km)	e
BETS	1997	Sanriku	s.l.	(35 - 36 km)	e
BETS	1998	Sanriku	s.l.	(34 - 35 km)	e

[1] spectrometer experiments.

C.3 Underground, Underwater, Under Ice Experiments

Table C.5: Underground, Underwater and Under Ice Muon and Neutrino Detectors of Past and Present.

Detector	Location	Technique	Depth [hg/cm^2]
AMANDA	South Pole	Cherenkov in ice	1800[1]
Artyomowsk	Ukraina	Liquid scintillator	600
Antares[2,3]	Mediterranean	Water Cherenkov	2350[1]
Baikal	Lake Baikal	Water Cherenkov	1300[1]
Baksan	Caucasus (Rus)	Liquid scintillator	850
BOREXINO[2]	Gran Sasso (I)	Boron reaction	3100
CWI[4]	South Africa	Liquid scintillator	8890
DUMAND[4]	Hawaii	Water Cherenkov	4500[1]
Fréjus[4]	France	Geiger & flash tubes	4000 m.w.e.
GALLEX	Gran Sasso	Gallium solution	3100
Holborn[4]	England	Plastic scintillators	71.6 ± 1.2
Homestake	S.D. (USA)	Scintillators	4200 m.w.e.
HPW[4]	Utah (USA)	Water Cherenkov	1700 m.w.e.
Ikarus[2]	Gran Sasso (I)	Liquid Argon	3100
IMB[4]	Cleveland (US)	Water Cherenkov	1570
Kamiokande	Japan	Water Cherenkov	2700 m.w.e.
KGF[4]	Karnataka (Ind)	Scintillators	730
KGF[4]	Karnataka (Ind)	Water Cherenkov	1590
KGF[4]	Karnataka (Ind)	Scint. + flash tubes	~7400 m.w.e.
LSD	Mont Blanc (I)	Liquid scintillator	5200
LVD	Gran Sasso (I)	Liq. scint., str. tubes	3100
MACRO	Gran Sasso (I)	Liq. scint., str. tubes	3100
NESTOR[2,3]	Pylos (GR)	Water Cherenkov	3800[1]
NUSEX	Mont Blanc (I)	Streamer tubes/Fe	5000
SAGE	Baksan, Russia	Liquid Gallium	4715 m.w.e.
SNO	Sudbury(Canada)	D_20	~6300 m.w.e.
SOUDAN II	S.D. (USA)	Drift tubes/concrete	2100
Super-Kamiokande	Japan	Water Cherenkov	
RAMAND	Antarctica	Radio detection	

[1] bottom module; [2] under construction; [3] prototype; [4] shut-down.

Appendix D

Miscellany

D.1 Acronyms of some Experiments

AGASA: Akeno Giant Air Shower Array, Akeno (Japan).

AIROBICC: AIR shower OBservation with Cherenkov Counters, La Palma (Canary Islands).

ANI: (translated from Russian) Hadron surface investigations, Mount Aragats (Armenia).

ASGAT: Air Shower and Gamma Array Telescope, Targasonne (France).

AMANDA: Antarctic Muon And Neutrino Detector Array (South Pole).

BASJE: Brazilian Air Shower Joint Experiment, Mt. Chacaltaya (Bolivia).

BESS: Balloon Experiment with Superconducting Solenoid (Japanese - American).

BETS: Balloon-borne Electron Telescope with Scintillating fibers.

BOREXINO: BORon solar neutrino EXperiment, Gran Sasso (Italy).

CAPRICE: Cosmic Anti-Particle Ring-Imaging Cherenkov Experiment (on satellite).

CASA-MIA: Chicago Air Shower Array - MIchigan muon Array, Dugway, UT (USA).

CAT: Cherenkov Array at Thémis (1650 m a.s.l.) (France).

CELESTE: ChErenkov Low Energy Sampling and Timing Experiment (heliostat) at Thémis (France).

COMPTEL: COMPton TELescope on GRO (on satellite).

CRN: Cosmic Ray Nuclei experiment (on Spacelab).

CWI: Case - Witwatersrand - Irvine, Witwatersrand (S.A.).

Acronyms of some Experiments (continued).

DICE: Dugway Imaging Cherenkov Experiment, Dugway, UT (USA).

DUMAND: Deep Underwater Muon And Neutrino Detector (Hawaii, closed).

EAS-TOP: Extensive Air Shower array on TOP of Gran Sasso (Italy).

EGRET: Energetic Gamma Ray Experiment Telescope (on satellite).

GALLEX: GALLium solar neutrino EXperiment, Gran Sasso (Italy).

GASP: Gamma Array at South Pole (Cherenkov within SPASE).

GLAST: Gamma ray Line ASTronomy (on satellite).

GRAND: Gamma Ray Astrophysics at Notre Dame, IN, (USA).

GRAPES: Gamma Ray Astronomy at Pe(V) EnergieS, Ootacamund (2200 m a.s.l.) (India).

GREX: Gamma Ray EXperiment, Haverah Park (GB).

GRO: Gamma Ray Observatory (on satellite).

HEAO-x: High Energy Astronomical Observatory, satellite carrying different experiments.

HEAT: High Energy Antimatter Telescope (balloon-borne)

HEGRA: High Energy Gamma Ray Array, La Palma (Canary Islands).

IMAX: International Matter/Antimatter eXperiment (balloon-borne).

IMB: Irvine Michigan Brookhaven, Cleveland, Ohio (USA).

JACEE: Japanese-American Cooperative Emulsion Experiment (balloon-borne).

JANZOS: Japan - Australia - New Zealand Observation of Supernova, (NZ).

KASCADE: Karlsruhe Air Shower and Central Array DEtector (Germany).

KGF: Kolar Gold Fields, Karnataka (India).

LEAP: Low Energy AntiProton experiment.

LSD: Large Scintillation Detector, Mont Blanc (Italy).

LVD: Large Volume Detector, Gran Sasso (Italy).

MACRO: Monopole And Cosmic Ray Observatory, Gran Sasso (Italy).

MAGICT: Major Atmospheric Gamma Ray Imaging Telescope, at HEGRA, (Canary Islands).

MASS: Matter Antimatter Space Spectrometer.

Acronyms of some Experiments (continued).

MILAGRO: Multi - Institutional Los Alamos Gamma-Ray Observatory, Los Alamos, NM (2630 m a.s.l.) (USA).

NESTOR: NEutrinos from Supernovae and TeV sources Ocean Range, Pylos (Greece).

NUSEX: NUcleon Stability EXperiment, Mont Blanc (Italy).

PBAR: Antiproton experiment.

RAMAND: RAdio Muon And Neutrino Detector (Antarctica).

RICE: Radio Ice Cherenkov Experiment (Antarctica).

RICH: Ring-Imaging CHerenkov detector (balloon-borne).

RUNJOB: RUssian Nippon JOint Balloon experiment (balloon-borne).

SAGE: Soviet American (liquid) Gallium Experiment, Artyomovsk (Russia).

SAS: Small Astronomical Satellite

SNO: Solar Neutrino Observatory, Sudburry (Canada).

SPASE: South Pol Air Shower Experiment (3350 m a.s.l.) (Antarctica).

STACEE: Solar Tower Air ChErenkov Experiment (heliostat) at Sandia, NM (USA).

SUGAR: Sydney University Giant Airshower Recorder, Narrabri (Aus.) (closed).

TACT: Time sampling Air Cherenkov gamma Telescope, Tien Shan (Kazakhstan, 3300 m).

TACTIC: Te(V) Air Cherenkov Telescope Imaging Camera, Mount Abu (India).

7TA: 7-Telescope Array, Dugway, UT (USA).

D.2 List of Symbols

	Latin Letters
a	constant
A	mass number, atomic weight, area
A_T	target mass number
A_x	normalization constant for particle type x
b	constant, galactic latitude
B	constant, magnetic field strength
c	velocity of light, constant
C	constant
E	energy
E_c	critical energy
g	terrestrial gravitational constant
h	altitude, height above sea level
h_c	critical height for decay or interaction
h_s	scale height of atmosphere
I	ionization constant
$I(\theta, \phi)$	directional intensity
I_v	vertical intensity
j(E)	differential energy spectrum
J_1	particle flux
J_2	omnidirectional intensity
$J(\geq E)$	integral energy spectrum
k	inelasticity
K, K_x	charge ratio, of particle type x
l	geometric path length, galactic longitude
L_X	decay length
m_e	rest mass of electron
$m_{0,X}$	rest mass of particle X
$m_{\pi,K}$	rest mass of pion, kaon
$< M >$	mean molecular mass
M_p	proton rest mass
M	magnetic dipole momentum
n	index of refraction, exponent of distribution, constant secondary particle multiplicity
n_{ch}	charged particle multiplicity
n_i	number of molecules of type i per cm^3

List of Symbols (continued).

Latin Letters

N_A	Avogadro's number
N_c	number of charged hadrons
N_n	number of neutral hadrons
$N(x)$	number of particles of type x
p	momentum
P	rigidity, pressure
P_c	effective cutoff rigidity, usually vertical
P_{est}	estimated cutoff rigidity
P_h	horizon-limited rigidity
P_l	lower cutoff rigidity
P_L	limiting cutoff rigidity
P_m	main cutoff rigidity
P_s	Störmer cutoff rigidity
P_{sh}	shadow cutoff rigidity
P_u	upper cutoff rigidity
P_1	first discontinuity rigidity
r	radial distance, radius
	ratio of stopping to penetrating muons
r_e	classical radius of the electron
R	universal gas constant
R_E	Earth's radius
R_μ	range of muons in matter
s	center of mass energy squared
	charge excess
S_x	survival probability of particle type x
t	time
T	absolute temperature
v	velocity
x	coordinate, linear distance
X	atmospheric depth, column density, overburden (vertical)
	depth in matter
X_s	slant depth in matter, atmosphere
y	coordinate
z	coordinate, depth in water
	projectile charge

List of Symbols (continued).

Latin Letters

Z atomic number (electr. charge of nucleus)
target charge,

Greek Letters

α fine structure constant
asymmetry coeff. of neutron flux
exponent, ratio

β v/c

γ Lorentz factor,
exponent of power law spectrum

γ_x spectral exponent of particle type x

δ density effect parameter,
exponent of differential spectrum

ϵ small quantity, constant

ζ angle of local magnetic zenith

η elasticity

θ zenith angle

κ ratio of twin to single muon events

λ geomagnetic latitude

λ_d mean free path for decay

λ_i interaction mean free path

Λ attenuation length

ρ density of matter

σ cross section

σ_{el} elastic cross section

σ_i interaction cross section

σ_{ij} cross section for process ij

σ_T total cross section

τ mean life of particle

τ_0 mean life of particle at rest

ϕ azimuthal angle

Φ flux, magnetic
solar modulation parameter

χ radiation length

ω $d\omega$ annular element of solid angle

Ω $d\Omega$, element of solid angle

D.3 List of Abbreviations

ACR	anomalous cosmic rays
AU	astronomical unit
a.s.l.	above sea level
BP	before present
CIR	corotating interaction region
CKP	Cocconi-Koester-Perkins model
CLP	cutoff latitude positive
CME	coronal mass ejection
CR	cosmic rays
CRS	cosmic ray storm
DEBRA	diffuse extragalactic background radiation
Diff.	differential
EAS	extensive air shower
EMF	extra-galactic magnetic field
ESP	energetic solar particles
FIP	first ionization potential
GCR	galactic cosmic rays
GLE	ground level event, enhancement
GM	Geiger-Müller counter
GMF	galactic magnetic field
GMIR	global merged interaction regions
GZK	Greisen-Zatsepin-Kuzmin cutoff
HCS	heliospheric current sheet
hg	hectograms
HMF	heliospheric magnetic field
IMF	interstellar magnetic field, interplanetary magnetic field
Int.	integral
ISM	interstellar medium
ISMF	interstellar magnetic field
LDE	long duration events
LISM	local interstellar medium
MIR	merged interaction regions
m.w.e.	meters water equivalent
NCS	neutral current sheet
NM	neutron monitor
PCA	polar cap absorption

List of Abbreviations (continued)

PM	photomultiplier
PMT	photomultiplier tube
SAC	solar active cycle
SC	sudden commencement
SCR	solar cosmic rays
SEP	solar energetic particles
SF	solar flare
SID	sudden ionospheric disturbance
SN	supernova
SR	standard rock
STP	standard temperature and pressure
UT	universal time

D.4 List of Cosmic Ray Conferences

1.	Cracow, Poland	(1947)
2.	Como, Italy	(1949)
3.	Bagneres de Bigorre, France	(1953)
4.	Guanjuato, Mexico	(1955)
5.	Varenna, Italy	(1957)
6.	Moscow, U.S.S.R.	(1959)
7.	Kyoto, Japan	(1961)
8.	Jaipur, India	(1963)
9.	London, England	(1965)
10.	Calgary, Canada	(1967)
11.	Budapest, Hungary	(1969)
12.	Hobart, Tasmania, Aus.	(1971)
13.	Denver, CO, U.S.A.	(1973)
14.	Munich, Germany	(1975)
15.	Plovdiv, Bulgaria	(1977)
16.	Kyoto, Japan	(1979)
17.	Paris, France	(1981)
18.	Bangalore, India	(1983)
19.	La Jolla, CA, U.S.A.	(1985)
20.	Moscow, U.S.S.R.	(1987)
21.	Adelaide, Aus.	(1990)
22.	Dublin, Irland	(1991)
23.	Calgary, Canada	(1993)
24.	Rome, Italy	(1995)
25.	Durban, South Africa	(1997)
26.	Salt Lake City, UT, U.S.A.	(1999)
27.	Hamburg, Germany	(2001)

Index

N